VOLUME 32
SEPTEMBER 1971

THE
JOURNAL OF
PHYSICS
AND
CHEMISTRY
OF SOLIDS

AN
INTERNATIONAL
JOURNAL

Editor-in-Chief
HARVEY BROOKS
Cambridge, Mass.

Associate Editors

H. B. G. CASIMIR
Eindhoven

B. CHALMERS FRAZER
and
DAVID E. COX
Brookhaven

JACQUES FRIEDEL
Paris

I. M. LIFSHITZ
Khar'kov

PERGAMON PRESS NEW YORK · OXFORD · LONDON · PARIS

THE JOURNAL OF PHYSICS AND CHEMISTRY OF SOLIDS

Editors

Prof. Harvey Brooks (*Editor-in-Chief*), *217 Pierce Hall, Harvard University, Cambridge 38, Mass., U.S.A.*
Prof. Dr. H. B. G. Casimir, *N.V. Philips' Gloeilampenfabrieken, Eindhoven, The Netherlands*
Dr. B. Chalmers Frazer and **Dr. David E. Cox** (*Assistant Editor*), *Brookhaven National Laboratory, Upton, Long Island, New York, U.S.A.*
Prof. Jacques Friedel, *Laboratoire de Physique des Solides, Bâtiment 210, Faculté des Sciences, 91-Orsay, France*
Prof. I. M. Lifshitz, *Chief, Theoretical Department, Institute of Physical Problems, Moscow V-334, Vorobevskoe Shosse 2, U.S.S.R.*

Editorial Advisory Board

U.S.A.
E. N. Adams, White Plains, N.Y.
D. Alpert, Urbana, Ill.
L. Apker, Schenectady, N.Y.
J. Bardeen, Urbana, Ill.
D. S. Billington, Oak Ridge, Tenn.
R. G. Breckenridge, Canoga Pk., Calif.
Leo Brewer, Berkeley, Calif.
E. Burstein, Philadelphia, Penn.
J. A. Burton, Murray Hill, N.J.
N. Cabrera, Charlottesville, Va.
G. C. Danielson, Ames, Iowa
G. J. Dienes, Long Island, N.Y.
J. C. Fischer, Schenectady, N.Y.
H. K. Henisch, University Park, Penn.
F. Herman, San Jose, Calif.
C. Herring, Murray Hill, N.J.
A. R. von Hippel, Cambridge, Mass.
J. H. Hollomon, Norman, Okla.
W. V. Houston, Houston, Texas
H. B. Huntington, Troy, N.Y.
H. M. James, Lafayette, Ind.
C. Kittel, Berkeley, Calif.
W. Kohn, La Jolla, Calif.
J. A. Krumhansl, Ithaca, N.Y.
A. W. Lawson, Riverside, Calif.
H. W. Leverenz, Princeton, N.J.
O. T. Marzke, Pittsburgh, Penn.
B. T. Matthias, La Jolla, Calif.
L. R. Maxwell, Silver Spring, Md.
J. E. Mayer, La Jolla, Calif.
J. W. Mitchell, Charlottesville, Va.
E. W. Montroll, Rochester, N.Y.
D. Pines, Urbana, Ill.
M. H. L. Pryce, Los Angeles, Calif.
G. T. Rado, Washington, D.C.
H. Reiss, Thousand Oaks, Calif.
J. R. Reitz, Dearborn, Mich.
A. Rose, Princeton, N.J.
R. A. Smith, Cambridge, Mass.
R. Smoluchowski, Princeton, N.J.
F. H. Spedding, Ames, Iowa
J. Tauc, Providence, R.I.
D. Turnbull, Cambridge, Mass.
J. H. Van Vleck, Cambridge, Mass.
B. E. Warren, Cambridge, Mass.
E. P. Wigner, Princeton, N.J.
B. H. Zimm, La Jolla, Calif.

Canada
R. E. Burgess, Vancouver
W. B. Pearson, Ottawa

United Kingdom
A. Charlesby, Shrivenham, Berks.
W. J. Dunning, Bristol
F. C. Frank, Bristol
H. Jones, London
A. B. Pippard, Cambridge
O. C. Simpson, Baldock, Herts.
K. W. H. Stevens, Nottingham
F. C. Tompkins, London

Czechoslovakia
B. Velicky, Prague

France
E. F. Bertaut, Grenoble
J. Bok, Paris
B. Dreyfus, Grenoble
A. Guinier, Orsay
A. Herpin, Gif-sur-Yvette
B. Jacrot, Grenoble
Louis Néel, Grenoble

Germany
Ulrich Dehlinger, Stuttgart
R. Hilsch, Gottingen
G. Leibfried, Aachen
E. Mollwo, Erlangen
H. Pick, Stuttgart
W. Welker, Erlangen

Israel
I. Estermann, Haifa

Italy
F. G. Fumi, Genova

Japan
Toshinosuke Muto, Tokyo

The Netherlands
G. W. Rathenau, Eindhoven

Sweden
J. O. Linde, Stockholm
Per-Olov Lowdin, Uppsala

Switzerland
G. Busch, Zurich

U.S.S.R.
G. S. Zhdanov, Moscow

Publishing and Advertising Offices

American Continent: Pergamon Press Inc., Maxwell House, Fairview Park, Elmsford, N.Y. 10523.
Rest of the World: Pergamon Press Ltd., Headington Hill Hall, Oxford OX3 0BW, England.

Published monthly. Annual subscription for libraries, research establishments and all other multiple-reader institutions, £60 ($150.00); private individuals, whose departmental libraries subscribe, may obtain this Journal for their personal use at a reduced price of £10 ($25.00) per annum, including postage. All subscription enquiries are to be addressed to The Manager, Subscriptions Department, Pergamon Press, Headington Hill Hall, Oxford OX3 0BW, England. Back issues are available, write for Back Issues Price Lists.

Copyright © 1971 Pergamon Press Ltd.

PERGAMON PRESS
MAXWELL HOUSE, FAIRVIEW PARK, ELMSFORD, N.Y. 10523
HEADINGTON HILL HALL, OXFORD OX3 0BW

J. Phys. Chem. Solids, 1971, Vol. 32, pp. i–xvi. Pergamon Press. Printed in Great Britain

Author and Title Index to Volume 32

References with (T) are to Technical Notes; (E) to [illegible]

Agarwal, S. K. (see **Jain, S. C.**). **32**, 897

Agulló-López, F. and F. Jaque. Role of interstitial aggregation of the *F*-coloring cu[illegible] halides. **32**, 2009 (T)

Aizu, K. Phenomenological lattice-dynamical theory of ferroelasticity. **32**, 1959

Akimoto, S. I. (see **Syono, Y.**). **32**, 243

Alder, B. J. (see **Gass, D. M.**). **32**, 1797

Alder, B. J. (see **Bennett, C. H.**). **32**, 2111

Alderson, J. E. A. and C. M. Hurd. Spin component of the Hall effect and transve[illegible] resistance in dilute alloys containing magnetic solutes. **32**, 2075

Alderson, J. E. A. (see **Hurd, C. M.**). **32**, 175

Alex, K. and R. B. McLellan. A quasi-chemical approach to the thermodynamics of ternary solid solutions containing both substitutional and interstitial solute atoms. **32**, 449

Allan, G. (see **Lannoo, M.**). **32**, 637

Allred, W. P. (see **Skolnik, L. H.**). **32**, 1

Almassy, M. Y. (see **Holt, J. B.**). **32**, 2129

Amrhein, E. M. and H. Heil. Dielectric absorption of polymers from the millimeter to the infrared region. **32**, 1925

Anastassakis, E. and E. Burstein. Morphic effects—I. Effects of external forces on photon-optical phonon interactions. **32**, 313

Anastassakis, E. and E. Burstein. Morphic effects—II. Effects of external forces on the frequencies of the $q \sim 0$ optical phonons. **32**, 563

Anderson, J. S. and R. Burch. Lattice energies and heats of formation of the Ti_nO_{2n-1} shear phases. **32**, 923

Ancker-Johnson, B. (see **Dick, C. L., Jr.**). **32**, 2151

Atkinson, C. On the numerical solution of the one-dimensional diffusion equation in a semi-infinite sample. **32**, 749 (T)

Averbach, B. L. (see **Tobin, P. J.**). **32**, 1721

Avinor, M. and M. Pasternak. Hyperfine interaction on ^{57}Fe impurity in ferromagnetic MnSb. **32**, 1395 (T)

AuCoin, T. R. (see **Streever, R. L.**). **32**, 519

Bahl, M. K. (see **Bhide, V. G.**). **32**, 1001

Baratoff, A. (see **Benedek, R.**). **32**, 1015

Barrer, R. M. and D. E. W. Vaughan. Trapping of inert gases in sodalite and cancrinite crystals. **32**, 731

Barruel, F. (see **Chamberod, A.**). **32**, 881

Barsch, G. R. (see **Chang, Z. P.**). **32**, 27

Barsch, G. R. (see **Fancher, D. L.**). **32**, 1303

Bartels, R. A. (see **Potter, W. N.**). **32**, 2363

Bastin, A., C. Lewiner, O. Betbeder-Matibet et P. Nozieres. Quantum oscillations of the Hall effect of a fermion gas with random impurity scattering. **32**, 1811

Basu, C. and U. S. Ghosh. Estimation of bonding parameters and overlap integrals in octahedral iron group complexes from magnetic susceptibility and anisotropy data. **32**, 2259 (T)

Bates, J. B. and M. H. Brooker. Determination of longitudinal optical mode frequencies by polarized specular reflectance infrared spectroscopy. **32**, 2403

Batra, I. P. and B. H. Schechtman. Pulse induced photocurrents and field distributions in photoconductor-dielectric structures. **32**, 769

Baughman, R. H. and D. Turnbull. Vacancy formation parameters in organic crystals. **32**, 1375

Bean, A. R. and R. C. Newman. The solubility of carbon in pulled silicon crystals **32**, 1211

Beck, P. A. (see **Mishra, S.**). **32**, 1979

Benedek, R. and A. Baratoff. The influence of lattice strain on the electrical resistivity of vacancies in simple metals. **32**, 1015

Bennet, A. J. and L. M. Roth. Electronic structure of defect centers in SiO_2. **32**, 1251

Bennett, C. H. and B. J. Alder. Persistence of vacancy motion in hard sphere crystals. **32**, 2111

Bhattacharyya, B. D. Lattice-ion interactions of Fe^{2+} ion in a tetrahedral environment. **32**, 2357

Bhide, V. G. and M. K. Bahl. X-ray K-absorption studies of niobium selenides and tellurides. **32**, 1001

Biran, A., P. A. Montano and U. Shimony. Mössbauer measurements of $BiFeO_3$ and $BiFeO_3$–$PbZrO_3$ systems. **32**, 327

Björck, G. (see **Hörnfeldt, S.**). **32**, 753

Bloom, S. Band structures of GaN and AlN. **32**, 2027

Boer, K. W. (see **Schubert, R.**). **32**, 77

Boucher, B., R. Buhl and M. Perrin. Propriètes et structure magnétique de Mn_3O_4. **32**, 2429

Bowler, B. (see **Searle, T. M.**). **32**, 591

Brabers, V. A. M. Cation migration, cation valencies and the cubic-tetragonal transition in $Mn_xFe_{3-x}O_4$. **32**, 2181

Bradbury, M. I. and D. J. Newman. New superexchange model applied to Gd^{3+} pairs in $LaCl_3$ and $EuCl_3$. **32**, 627

Bray, P. J. (see **Kriz, H. M.**). **32**, 303 (T)

Brebrick, R. F. Composition stability limits for the rocksalt-structure phase $(Pb_{1-y}Sn_y)_{1-x}Te_x$ from lattice parameter measurements. **32**, 551

Brews, J. R. (see **Hwang, C. J.**). **32**, 837

Broerman, J. G. A. A conjecture on the anomalous mobility of α-Sn. **32**, 1283

Brooker, M. H. (see **Bates, J. B.**). **32**, 2403

Brooks, W. P. (see **Graham, R. A.**). **32**, 2311

Brüesch, P. and C. Schüler. Raman and infrared spectra of crystals with α-$NeFeO_2$ structure. **32**, 1025

Buchanan, D. N. E. (see **Robbins, M.**). **32**, 717

Buck, O., D. O. Thompson and C. A. Wert. The effect of hydrogen on the low temperature internal friction of a niobium single crystal. **32**, 2331

Buhl, R. (see **Boucher, B.**). **32**, 2429

Buisson, G. (see **Ollivier, G.**). **32**, 1189

Burch, R. (see **Anderson, J. S.**). **32**, 923

Burstein, E. (see **Anastassakis, E.**). **32**, 313

Burstein, E. (see **Anastassakis, E.**). **32**, 563

Burstein, E. (see **Portigal, D. L.**). **32**, 603

Burstein, E. (see **Salaneck, W.**). **32**, 2285

Busch, G., M. Campagna, F. Hulliger and H. C. Siegmann. Electronic energy levels in ferromagnetic Eu_3P_2 and Eu_3As_2. **32**, 2173

Calecki, D. Phénomènes galvanomagnétiques non lineaires B-Théorie quantique. 32, 1835
Campagna, M. (see **Busch, G.**). 32, 2173
Canali, C., G. Ottaviani and A. A. Quaranta. Drift velocity of electrons and holes and associated anisotropic effects in silicon. 32, 1707
Capellmann, H. Superconductors with magnetic impurities in a singlet ground state. 32, 2439
Caplan, P. J. (see **Streever, R. L.**). 32, 519
Carter, G. C. and J. C. Swartz. Nuclear magnetic resonance Knight shifts and quadrupole effects in transition metal diborides. 32, 2415
Carrander, K. (see **Hörnfeldt, S.**). 32, 753
Casalot, A., P. Dougier and P. Hagenmüller. Sur l'évolution des propriétés physiques de la perovskite $GdCoO_3$ entre 77–1200 K. 32, 407 (E)
Casamayou, L. (see **Saravia, L. R.**). 32, 1075
Casey, H. C. Jr., M. B. Panish and K. B. Wolfstirm. Influence of surface band bending on the incorporation of impurities in semiconductors: Te in GaAs. 32, 571
Catalano, E. and H. R. Leider. Calorimetric evidence of molecular hydrogen in irradiated lithium hydride. 32, 1297
Cate, R. C. and J. C. Thompson. Low-temperature electronic properties of $LI(NH_3)_4$. 32, 443
Chakravarti, A. K. and P. K. Dubey. Hot-electron Faraday effect in nonparabolic semiconductors. 32, 905 (T)
Chakravorty, D. Energy of migration of anion vacancy and interstitial in calcium fluoride. 32, 1091 (T)
Chamberod, A., F. Barruel and J. Paulevé. Étude par anisotropie magnétique du début de la mise en order d'un alliage Fe–Ni 50–50 irradié aux neutrons. 32, 881
Chan Sai-Kit. *F*-electrons in a strong crystal field. The relationship between paramagnetic and saturation moments. 32, 1111
Chang, R. and L. M. Falicov. Pseudopotential calculations of relaxation and formation energy of a vacancy in aluminum. 32, 465
Chang, Z. P. and G. R. Barsch. Pressure dependence of the elastic constants of RbCl, RbBr and RbI. 32, 27
Chattopadhyay, D. and B. R. Nag. Effect of the non-equivalent intervalley scattering on the high-field conductivity characteristics of *n*-Ge. 32, 2749
Chester, M. and C. C. Coleman. Electroabsorption in HgI_2. 32, 223
Chowdari, B. V. R. Electron paramagnetic resonance study of Mn^{2+} in $(NH_4)_2$ $Mg_2(SO_4)_3$ and $(NH_4)_2Zn_2(SO_4)_3$ crystals. 31, 1408 (E)
Chung, M. F. The effects of bulk doping on the ESR signal of clean Si surfaces. 32, 475
Cohen, E. (see **Finkman, E.**). 32, 2423
Coleman, C. C. (see **Chester, M.**). 32, 223
Conti, L. G. and R. D'Alessandro. ^{81}Br magnetic resonance in fresh silver bromide. 32, 1092 (T)

Cook, B. E. and P. G. LeComber. The optical properties of anthracene crystals in the vacuum ultraviolet. 32, 1321
Coulson, C. A. and F. P. Larkins. Isolated single vacancy in diamond–I. Electronic structure. 32, 2245
Craig, R. S. (see **Deenadas, C.**). 32, 1853
Craig, R. S. (see **Van Diepen, A. M.**). 32, 1867
Craig, R. S. (see **Nasu, S.**). 32, 2773
Craig, R. S. (see **Nasu, S.**). 32, 2779

Craig, R. S. (see **Neumann, H. H.**). **32**, 2788 (T)
Craig, R. S. (see **Wallace, W. E.**). **32**, 805
Crawford, R. W. (see **Holt, J. B.**). **32**, 2129
Cucureancu, E. (see **Rezlescu, N.**). **32**, 1096 (T)
Cuddy, L. J. (see **Swartz, J. C.**). **32**, 685
Cutler, P. H. (see **King, W. F. III**). **32**, 761
Cyrot-Lackmann, F. (see **Ducastelle, F.**). **32**, 285

D'Alessandro, R. (see **Conti, L. G.**). **32**, 1092 (T)
Dansas, P. Étude de la réorientation des complexes lacune-impureté divalente dans NaCl dopé. **32**, 2699
Davison, S. G. (see **Stéslicka, M.**). **32**, 1917
Deenadas, C., A. W. Thompson, R. S. Craig and W. E. Wallace. Low temperature heat capacities of laves phase lanthanide-aluminum compounds. **32**, 1853
Deenadas, C. (see **Wallace, W. E.**). **32**, 805
De Gonzalez, C. O. and N. E. W. de Reca. Isotope effect in orin diffusion in Fe/3% Si alloy. **32**, 1067
De Reca, N. E. W. (see **de Gonzalez, C. O.**). **32**, 1067
Dianoux, A. J. (see **Rigny, P.**). **32**, 1175
Dianoux, A. J. (see **Rigny, P.**). **32**, 1901
Dick, C. L., Jr. and B. Ancker-Johnson. Impact ionization in *P*-type InSb. **32**, 2151
Dismukes, J. P., R. T. Smith and J. G. White. Physical properties and crystal structure of a new semiconducting I–III–VI$_2$ compound, CuScS$_2$. **32**, 913
Doremus, R. H. Delayed elasticity resulting from periodic stress-induced atomic diffusion. **32**, 2211
Dougier, P. (see **Casalot, A.**). **32**, 407
Dougier, P. (see **Casalot, A.**). **32**, 407 (*E*)
Drickamer, H. G. (see **Moller, H. S.**). **32**, 745 (T)
Dubey, P. K. (see **Chakravarti, A. K.**). **32**, 905 (T)
Ducastelle, F. and F. Cyrot-Lackmann. Moments developments – II. Application to the crystalline structures and the stacking fault energies of transition metals. **32**, 285
Dujarin, Marie-Martine and Marie-Luce Theye. Investigation of the optical properties of Ag by means of thin semi-transparent films. **32**, 2033
Duwez, P. (see **Sinha, A. K.**). **32**, 267

Edwards, D. F. (see **She, C. Y.**). **32**, 1887
Edwards, J. and R. F. Frindt. Anisotropy in the resistivity of NbSe$_2$. **32**, 2217
Ekstig, B. (see **Ramqvist, L.**). **32**, 149
Emmenegger, F. P. and H. Roetschi. Dielectric properties of some niobates and tungstates. **32**, 787
Endoh, Y. (see **Syono, Y.**). **32**, 243
Evans, H. (see **Taylor, M. J.**). **32**, 2021
Ewald, A. W. (see **Wagern, R. J.**). **32**, 697
Ewald, A. W. (see **Lavine, C. F.**). **32**, 1121

Falicov, L. M. (see **Chang, R.**). **32**, 465

Fancher, D. L. and G. R. Barsch. Lattice theory of alkali halide solid solutions – III. Pressure dependence of solid solubility and spinodal decomposition. 32, 1303
Fano, V. and I. Ortalli. A study on some Co–Te compositions by Mössbauer spectroscopy. 32, 2305
Feigelson, R. (see **Ikushima, A.**). 32, 417
Filinski, I. and B. Wojtowicz-Natanson. Low temperature 'edge emission' of CdSe. 32, 2409
Filinski, I., B. Wojtowicz-Natanson and J. M. Hvam. Spontaneous and stimulated emission from CdSe at high excitation levels. 32, 2193
Finkman, E., Z. Kam, E. Cohen and G. Gilat. Accurate numerical method for calculating spectra in solids – IV. Extension to trigonal crystals. 32, 2423
Fischer, E. S. and M. H. Manghnani. Effects of change in volume and c/a ratio on the pressure derivatives of the elastic moduli of G.C.P. Ti and Zr. 32, 657
Fischer, P., D. Schwarzenbach and H. M. Rietveld. Crystal and magnetic structure of silver diflouride – I. Determination of the AgF$_2$ structure. 32, 543
Flotow, H. E. (see **Rowe, J. M.**). 32, 41
Flükiger, R., F. Heiniger, A. Junod, J. Muller, P. Spitzli et J. L. Staudenmann. Chaleur spécifique et supraconductivité dans des alliages de structure A 15 à base de chrome. 32, 459
Foiles, C. L. Transport anomalies in dilute silver-rare earth alloys. 32, 1205
Foner, S. (see **Mishra, S.**). 32, 1979
Fredericks, W. J. (see **Krause, J. L.**). 32, 2673
Frindt, R. F. (see **Edwards, J.**). 32, 2217

Gabay, A. (see **Maniv, S.**). 32, 815
Gallagher, P. T. and W. A. Oates. Vibrational entropies of hydrogen in palladium-silver-hydrogen alloys by the isotopic solubility ratio method. 32, 2105
Galtier, M. (see **Montaner, MM. A.**). 32, 55
Gass, D. M., B. J. Alder and T. E. Wainwright. The thermal conductivity of a hard sphere solid. 32, 1797
Gaur, S. P., J. F. Vetelino and S. S. Mitra. Localized mode frequency for substitutional impurities in zinc blende type crystals. 32, 2737
Gautier, F. (see **Loegel, B.**). 32, 2723
Gerard, A., P. Imbert, H. Prange, F. Varret and M. Winterberger. Fe^{2+} impurities, isolated and in pairs, in ZnS and CdS studied by the Mössbauer effect. 32, 2091
Gerson, R. (see **Moreau, J. M.**). 32, 1315
Ghosh, B. (see **Roy, S. K. Dutta**). 32, 857
Ghosh, U. S. (see **Basu, C.**). 32, 2259 (T)
Gilat, G. (see **Finkman, E.**). 32, 2423
Gilchrist, J. and P. Monceau. Resistivity of superconducting alloys in the mixed state in a weak field. 32, 2101
Gomez, M. P., D. A. Stevenson and R. A. Huggins. Self-diffusion of Pb and Te in lead telluride. 32, 335
Gora, Thaddeus. Madelung energy and electronic structure of BaN$_6$ and α-PbN. 32, 529
Goto, Y. and S. Kachi. Studies on the mechanism of electric conduction in Fe-doped BaTiO$_3$ single crystals by applying Kerr effect. 32, 889
Gragg, J. E., Jr. The determination of atomic force constants in cubic solid solutions – I. Theory. 32, 1195
Graham, G. M. (see **Schlosser, W. F.**). 32, 927

Graham, R. A. and W. P. Brooks. Shock-wave compression of sapphire from 15 to 420 KBR. The effects of large anisotropic compressions. 32, 2311
Greedan, J. E. (see **Rao, V. U. S.**). 32, 2755
Greedan, J. E. The magnetic properties of EuliH$_3$. 32, 819
Greedan, J. E. Electrical resistivity and optical absorption in EuLiH$_3$ and SrLiH$_3$. 32, 1039
Gregers-Hansen, P. E. Measurements at 4·2 K of galvanomagnetic effects in bismuth in weak magnetic fields. 32, 1881
Gromb, S. (see **Lichanot, A.**). 32, 1947
Guggenheim, H. J. (see **Henderson, A. J., Jr.**). 32, 1047
Gulick, Joan M. (see **Hubble, F. F.**). 32, 2345
Gupta, S. K. and M. L. Narchal. Dynamic orientation by saturation of forbidden transitions. 32, 993

Haas, C. (see **Popma, T. J. A.**). 32, 581
Hagenmüller, P. (see **Casalot, A.**). 32, 407
Hagenmüller, P. (see **Casalot, A.**). 32, 407 (E)
Hamaguchi, Y. (see **Ishii, T.**). 32, 235
Hammarström, Å. (see **Hörnfeldt, S.**). 32, 753
Harris, L. B. Initial and discharge time-dependent conductivity in alkali halide single crystals. 32, 59
Haynes, W. M. Shear strengths of solid methane and argon to 8 Kbar at 77 K. 32, 791
Heaton, L. (see **Lander, G. H.**). 32, 427
Hedman, L. E. Magnetic properties of Au–Mn alloys with 10–20 at. % Mn. 32, 825
Heil, H. (see **Amrhein, E. M.**). 32, 1925
Heiniger, F. (see **Flükiger, R.**). 32, 459
Helbig, R. (see **Müller, G.**). 32, 1971
Helman, J. S. Exchange splitting of the degenerate levels of a magnetic impurity in an antiferromagnetic insulator. 32, 251
Henderson, A., J. Jr., H. Meyer and H. J. Guggenheim. The specific heat of RbMnF$_3$ and MnF$_2$ between 0·5 and 4·2° K. 32, 1047
Hess, K. and H. Kahlert. Harmonic mixing and energy relaxation of warm electrons in *n*-GaAs at low temperatures. 32, 2262 (T)
Hoch, M. J. R. (see **Webster, D. S.**). 32, 2663
Höchli, U. T. Theory of local oscillation of substitutional defects near a free surface. 32, 2231
Hodges, L. (see **Watson, R. E.**). 32, 709
Holliday, J. E. The electronic properties of titanium interstitial and intermetallic compounds from soft X-ray spectroscopy. 32, 1825
Holt, J. B., M. Y. Almassy and R. W. Crawford. Helium diffusion in LiH. 32, 2129
Hörnfeldt, S., Å. Hammarström, K. Carrander and G. Björck. The de Haas–van Alphen effect and the Fermi surface in Iridium. 32, 753
Hoshino, H. and M. Shimoji. Ionic conductivity of potassium bromide and sodium bromide crystal coloured with bromine. 32, 385
Huang, C. -Y. (see **Mostrom, M. A.**). 32, 799
Hubble, F. F., Joan M. Gulick and W. G. Moulton. Superconductivity in the K, Rb, and Cs tungsten fluoroxide bronzes. 32, 2345
Huber, D. L. Spin-spin relaxation near the Curie point. 32, 2145
Huggins, R. A. (see **Gomez, M. P.**). 32, 335

Hulliger, F. (see **Busch, G.**). **32**, 2173
Hurd, C. M. (see **Alderson, J. E. A.**). **32**, 2075
Hurd, C. M. and J. E. A. Alderson. Anisotropic temperature dependence of the Hall effect in Cu and some Cu–Zn crystals. **32**, 175
Hurle, D. T. J. (see **Logan, R. M.**). **32**, 1739
Hutchens, R. D. (see **Rao, V. U. S.**). **32**, 2755
Hvam, J. M. (see **Filinski, I.**). **32**, 2193
Hwang, C. J. and J. R. Brews. Electron activity coefficients in heavily doped semiconductors with small effective mass. **32**, 837

Ikushima, A. and R. Feigelson. Acoustic study of the critical phenomena in FeF_2 near the Néel temperature. **32**, 417
Imbert, P. (see **Gerard, A.**). **32**, 2091
Inoue, E. (see **Kokado, H.**). **32**, 2785 (T)
Isaacs, L. L. and D. J. Lam. The magnetic susceptibilities of hexagonal Tc–Ru, Tc–Rh, Ru–Rh alloys. **31**, 2581 (E)
Isaacs, L. L. (see **Ross, J. W.**). **32**, 747 (T)
Ishii, T. K. Naito, K. Oshima and Y. Hamaguchi. An X-ray and neutron diffraction study on a phase transition in the U_4O_9 phase. **32**, 235
Itoga, R. S. and C. R. Kannewurf. Electrical resistivity, Hall effect and optical absorption in TlS, $TlS_{0.5}Se_{0.5}$ and TlSe. **32**, 1099
Ivanov, E. K. (see **Zlatkin, L. B.**). **32**, 1733

Jain, S. C., S. K. Agarwal and G. D. Sootha. Optical and electron spin resonance absorption spectra of manganate ions in alkali halides. **32**, 897
James, W. J. (see **Moreau, J. M.**). **32**, 1315
Janot, C. et H. Scherrer. Etude par effet Mössbauer des propriétés dynamiques d'une impureté de fer dans le nickel. **32**, 191
Jaque, F. (see **Agulló-López, F.**). **32**, 2009 (T)
Jerome, D. (see **Jullien, R.**). **32**, 257
Joyes, P. Alternations in the secondary emission of molecular ions from noble metals. **32**, 1269
Jullien, R. et D. Jerome. Etude de l'ytterbium et des alliages ytterbium-baryum sous haute pression à basse température. **32**, 257
Junod, A. (see **Flükiger, R.**). **32**, 459

Kachi, S. (see **Goto, Y.**). **32**, 889
Kahlert, H. (see **Hess, K.**). **32**, 2262 (T)
Kaldis, E. P. Streit and P. Wachter. Luminescence properties of the monoclinic phase of ferromagnetic $Eu_2(II)\,SiO_4$. **32**, 159
Källne, E. (see **Ramqvist, L.**). **32**, 149
Kam, Z. (see **Finkman, E.**). **32**, 2423
Kannewurf, C. R. (see **Itoga, R. S.**). **32**, 1099
Kar, S. (see **Roy, S. K. Dutta**). **32**, 857
Karayianis, N. Theoretical energy levels and g values for the ^4I terms of Nd^{3+} and Er^{3+} in $LiYF_4$. **32**, 2385
Katzman, H., J. Moss and W. F. Libby. The heat capacity of indium antimonide – II. **32**, 2786 (T)
Kawamori, A. (see **Kuroda, N.**). **32**, 1233

Keating, D. T. On the scattering of X-rays by structures containing a random distribution of defects. 32, 2693

Kennedy, D. E. and M. J. Russ. The effect of annealing procedures on photoluminescence and electroluminescence in ZnTe. 32, 847

Kennedy, G. C. (see **Vaidya, S. N.**). 32, 2301

Kennedy, G. C. (see **Vaidya, S. N.**). 32, 951

Kerr, R. K. and C. F. Schwerdtfeger. Temperature dependence of the EPR spectrum of $CdIn_2S_4$: Mn^{2+}. 32, 2007 (T)

King, W. F. III and P. H. Cutler. A first principle pseudopotential calculation of the elastic shear constants of magnesium. 32, 761

Kogachi, M. and Y. Matsuo. Phase changes of the disordered In–Ng and Al–Mg alloys. 32, 2393

Kokado, H., T. Nakayama and E. Inoue. Enhanced conduction in ZnO crystals by excited oxygen molecules. 32, 2785 (T)

Koster, A. S. Influence of the chemical bond on the *K* emission spectrum of oxygen and fluorine. 32, 2685

Krause, J. L. and W. J. Fredericks. The simultaneous diffusion of Pb^{2+} and Cd^{2+} in purified *NaCl single crystals.* 32, 2673

Kriz, H. M. and P. J. Bray. Doubts concerning the structure of boracites. 32, 303 (T)

Kunz, A. B. and N. O. Lipari. Hartree–Fock determination of the energy bands and the optical properties of lithium bromide. 32, 1141

Kuroda, N. and A. Kawamori. Effects of phase transition on ESR and optical spectra in NH_4Cl: Cu^{2+}. 32, 1233

Lam, D. J. (see **Isaacs, L. L.**). 31, 2581 (E)

Lambert, M. (see **Taupin, C.**). 32, 2045

Lander, G. H. and L. Heaton. Magnetic moment distribution in $Fe_{0\cdot8}Cr_{0\cdot2}$. 32, 427

Langbein, D. Microscopic calculation of macroscopic dispersion energy. 32, 133

Lannoo, M. and G. Allan. Formation energy of vacancies in transition metals. 32, 637

Larkins, F. P. (see **Coulson, C. A.**). 32, 2245

Larkins, F. P. Electronic structure of the isolated vacancy in silicon. 32, 965

Larkins, F. P. Isolated single vacancy in diamond – II. Jahn–Teller effect. 32, 2123

Läuger, K. Über den einfluß der bindungsart und der kristallstruktur auf das $K\alpha_{1,2}$-röntgenspektrum von aluminum. 32, 609

Lavine, C. F. and A. W. Ewald. Two-band galvanomagnetic effects in gray tin. 32, 1121

Lax, B. (see **Rabitz, R.**). 32, 359

LeComber, P. G. (see **Cook, B. E.**). 32, 1321

Le Craw, R. C. (see **Sinha, K. P.**). 32, 373

Leider, H. R. (see **Catalano, E.**). 32, 1297

Levinson, L. M. and S. Shtrikman. Theory of elastic stiffness C_{33} of gadolinium in the spin rotation region. 32, 981

Lewiner, C. (see **Bastin, A.**). 32, 1811

Libby, W. F. (see **Katzman, H.**). 32, 2786 (T)

Lichanot, A. and S. Gromb. Domaine d'existence du sulfure d'étain et phénomène d'associations des lacunes d'étain. 32, 1947

Lipari, N. O. (see **Kunz, A. B.**). 32, 1141

Lodato, V. A. Line broadening of uranyl salts at low temperature. 32, 1087

Loegel, B. and F. Gautier. Origine de la résistivité dans le cobalt et ses alliages dilués. 32, 2723

Loehman, R. E. (see **Rao, C. N. R.**). **32**, 1147

Logan, R. M. and D. T. J. Hurle. Calculations of point defect concentrations and nonstoichiometry in GaAs. **32**, 1739

Logan, R. M. Analysis of heat treatment and formation of gallium-vacancy-tellurium complexes in GaAs. **32**, 1755

Loughlin, K. F. and D. M. Ruthven. The sorption of light paraffins in linde 5A zeolite. **32**, 2451 (T)

Low, W. (see **Maniv, S.**). **32**, 815

Macko, P. Thermoelectrical parameters of fast-neutron-irradiated Te–Se–Bi, Te–Sb–Bi and GeSi. **32**, 1181

Manne, R. (see **Ramqvist, L.**). **32**, 149

Manghani, M. H. (see **Rischer, E. S.**). **32**, 657

Maniv, S., W. Low and A. Gabay. EPR spectrum of Ws^{5+} in single crystals of Cs_2 $ZrCl_6$ and Cs_2 $HfCl_6$. **32**, 815

Marshall, D. J. (see **Taylor, M. J.**). **32**, 2021

Martin, J. J. (see **Whiteman, A. E.**). **32**, 2223

Marzouk, N. (see **Neumann, H. H.**). **32**, 2788 (T)

Marzouk, N. *(see* ***Nasu, S.****).* ***32****, 2779*

Masso, Jon D. (see **She, C. Y.**). **32**, 1887

Matsuo, Y. (see **Kogachi, M.**). **32**, 2393

Matzke, Hj. Fluorine self diffusion in LiF and NaF. **32**, 437

Mazieres, Ch. (see **Taupin, C.**). **32**, 2045

McCarthy, K. A. (see **Pappu, S. V.**). **32**, 1287

McLellan, R. B. (see **Alex, K.**). **32**, 449

Meijer, Paul H. E. A study of the crystal field parameters in thulium garnets. **32**, 2163

Meinke, P. P. M. (see **Schlosser, W. F.**). **32**, 927

Melz, P. J. Energy band structure of strained crystals: pseudopotential calculations for Ge and Si with trial calculations for GaAs and CdTe. **32**, 209

Meyer, H. (see **Myers, S. M.**). **32**, 867

Meyer, H. (see **Henderson, A. J., Jr.**). **32**, 1047

Meyer, O. and W. Scherber. Analysis of silicon nitride layers deposited from SiH_4 and N_2 on silicon. **32**, 1909

Michel, C. (see **Moreau, J. M.**). **32**, 1315

Millar, J. E. (see **Weber, M. J.**). **32**, 2275

Minematsu, K. (see **Takahashi, T.**). **32**, 1007

Misetich, A. A. (see **Watson, R. E.**). **32**, 709

Mishra, S., P. A. Beck and S. Foner. Paramagnetism in dilute alloys of Fe in $Cu_{0.8}Ni_{0.2}$. **32**, 1979

Misra, P. K. The magnetic pseudopotential of metals and alloys. **32**, 511

Mitra, S. S. (see **Gaur, S. P.**). **32**, 2737

Miyatani, K. (see **Takahashi, T.**). **32**, 1007

Moller, H. S. and H. G. Drickamer. Pressure dependence of the Curie temperature and magnetization in ferromagnetic PdFe alloys. **32**, 745 (T)

Monceau, P. (see **Gilchrist, J.**). **32**, 2101

Montaner, MM. A. et M. Galtier. Spectroscopie moleculaire–determination des constantes *optiques du chlorate de sodium entre 20 et 400* cm^{-1} *à partir du spectre de reflexion infra-*rouge. **32**, 55

Montano, P. A. (see **Biran, A.**). **32**, 327

Moore, W. J. Magnetic field effects on the excitation spectra of neutral group II double acceptors in germanium. **32**, 93

Moreau, J. M., C. Michel, R. Gerson and W. J. James. Ferroelectric $BiFeO_3$ X-ray and neutron diffraction study. **32**, 1315

Moss, J. (see **Katzman, H.**). **32**, 2786 (T)

Mostrum, M. A. and C. -Y. Huang. Collective coordinates of vibration for the trigonal XY Z molecular cluster. **32**, 799

Moulton, W. G. (see **Hubble, F. F.**). **32**, 2345

Mostoller, M. Phonon density of states for MgF^2. **32**, 2451 (T)

Mukerjee, S. N. (see **Sharma, B. L.**). **32**, 1397 (T)

Müller, G. and R. Helbig. Über ein Einbau von Kupfer in ZnO-einkristallen. **32**, 1971

Muller, J. (see **Flükiger, R.**). **32**, 459

Murarka, S. P. and R. A. Swalin. Cation self-diffusion in strontium oxide (SrO). **32**, 1277

Murarka, S. P. and R. A. Swalin. Cation self-diffusion in barium oxide (BaO). **32**, 2015

Musser, S. W. A new method for calculating the influence of force constant changes on the mean square displacements of surface atoms. **32**, 115

Myers, S. M., H. Meyer and J. P. Remeika. Longitudinal relaxation of ^{57}Fe nuclei in Yb-doped YIG. **32**, 867

Nag, B. R. (see **Chattopadhyay, D.**). **32**, 2749

Naito, K. (see **Ishii, T.**). **32**, 235

Nakayama, T. (see **Kokado, H.**). **32**, 2785 (T)

Narchal, M. L. (see **Gupta, S. K.**). **32**, 993

Natarajan, M. (see **Rao, C. N. R.**). **32**, 1147

Nasu, S., A. M. Van Diepen, H. H. Neumann and R. S. Craig. Specific heats of $LaIn_3$, $CeIn_3$ and $PrIn_3$ at temperatures between 1·5 and 4·2°K. **32**, 2773

Nasu, S., H. H. Neumann, N. Marzouk, R. S. Craig and W. E. Wallace. Specific heats of $LaNi_5$, $CeNi_5$, $PrNi_5$, $NdNi_5$ and $GdNi_5$ between 1·6 and 4°K. **32**, 2779

Nasu, S. (see **Neumann, H. H.**). **32**, 2788 (T)

Neckel, A. (see **Weinberger, P.**). **32**, 2063

Newman, D. J. (see **Stedman, G. E.**). **32**, 109

Newman, D. J. and G. E. Stedman. Analysis of the crystal field in rare-earth and substituted oxysulphide and vanadate systems. **32**, 535

Newman, D. J. (see **Bradbury, M. I.**). **32**, 627

Newman, D. J. (see **Stedman, G. E.**). **32**, 2001

Neumann, H. H. (see **Nasu, S.**). **32**, 2773

Neumann, H. H. (see **Nasu, S.**). **32**, 2779

Neumann, H. H., S. Nasu, R. S. Craig, N. Marzouk and W. E. Wallace. Specific heats of $LaNi_2$ and $NdNi_2$ between 1·6 and 4°K. **32**, 2788 (T)

Newman, R. C. (see **Bean, A. R.**). **32**, 1211

Nozieres, P. (see **Bastin, A.**). **32**, 1811

Noreland, E. (see **Ramqvist, L.**). **32**, 149

Novakovic, L., S. Stamenkovic and L. Vlahov. Quantum theory of ferroelectricity – II. Thermodynamic behaviour of the ferroelectric spins. **32**, 487

Oates, W. A. (see **Gallagher, P. T.**). **32**, 2105

Ollivier, G. and G. Buisson. Influence de la préparation chimique sur les structures magnétiques de Ca_2MnO_4. **32**, 1189

Onodera, Y. (see **Sakoda, S.**). **32**, 1365
Ortalli, I. (see **Fano, V.**). **32**, 2305
Osburn, C. M. and R. W. Vest. Electrical properties of NiO grain boundaries. **32**, 1355
Osburn, C. M. and R. W. Vest. Defect structure and electrical properties of NiO – II. Temperatures below equilibrium. **32**, 1343
Osburn, C. M. and R. W. Vest. Defect structure and electrical properties of NiO – I. High temperature. **32**, 1331
Oshima, K. (see **Ishii, T.**). **32**, 235
Ottaviani, G. (see **Canali, C.**). **32**, 1707

Panish, M. B. (see **Casey, H. C., Jr.**). **32**, 571
Pappu, S. V. and K. A. McCarthy. On the colloidal centers in irradiated sodium chloride crystals. **32**, 1287
Parke, S. Effect of temperature on the fluorescence of divalent manganese in glasses. **32**, 699
Parker, S. G., J. E. Pinnell and L. N. Swink. Epitaxial ZnSe on GaAs and Ge by HBr transport. **32**, 139
Parravicini, G. P. (see **Tosatti, E.**). **32**, 623
Pasternak, M. (see **Avinor, M.**). **32**, 1395 (T)
Paulevé, J. (see **Chamberod, A.**). **32**, 881
Perkowitz, S. Far infrared free-carrier absorption in N-type gallium arsenide. **32**, 2267
Perrin, M. (see **Boucher, B.**). **32**, 2429
Petrescu-Prahova, I. and N. N. Winogradoff. Photoluminescence in compensated *n*-type, Si-doped gallium arsenide. **32**, 1873
Philipp, H. R. Optical properties of non-crystalline Si, SiO, SiO_x and SiO_2. **32**, 1935
Pierce, R. D. (see **Robbins, M.**). **32**, 1789
Pinnell, J. E. (see **Parker, S. G.**). **32**, 139
Pistorius, C. W. F. T. Crystal structure of KCN IV at 50 kbar. **32**, 2761
Plurien, P. (see **Rigny, P.**). **32**, 1175
Plurien, P. (see **Rigny, P.**). **32**, 1901
Popma, T. J. A., C. Haas and B. Van Laar. Spin structure and magnetic anisotropy of Cr_5S_6 and rhombohedral Cr_2S_3. **32**, 581
Portigal, D. L. and E. Burstein. Magneto-spatial dispersion effects on the propagation of electromagnetic radiation in crystals. **32**, 603
Potter, W. N., R. A. Bartels and R. W. Watson. The pressure dependence of the elastic constants of the alkali chlorides. **32**, 2363
Prange, H. (see **Gerard, A.**). **32**, 2091
Purohit, R. K. (see **Sharma, B. L.**). **32**, 1397 (T)

Quaranta, A. A. (see **Canali, C.**). **32**, 1707

Rabitz, R. and B. Lax. Coupled magnetoplasma and phonon systems. **32**, 359
Ramqvist, L., B. Ekstig, E. Källne, E. Noreland and R. Manne. X-ray emission spectra of VC_x, NbC_x, TaC_x and ZrC. **32**, 149
Rao, C. N. R., M. Natarajan, G. V. Subba Rao and R. E. Loehman. Phase transitions and conductivity anomalies in solid solutions of VO_2 with TiO_2, NbO_2 and MoO_2. **32**, 1147
Rao, C. N. R. (see **Rao, G. V. Subba**). **32**, 345
Rao, G. V. Subba, B. M. Wanklyn and C. N. R. Rao. Electrical transport in rare earth orthochromites, -manganites and -ferrites. **32**, 345

Rao, R. Ramji (see **Srinivasan, R.**). 32, 1769
Rao, V. U. S., R. D. Hutchens and J. E. Greedan. Influence of the crystalline electric field on the Kondo resistivity of $Ce_xLa_{1-x}Pd_3$ ternaries. 32, 2755
Reid, J. S. and T. Smith. Improved Debye-Waller factors for some alkali halides. 31, 2689 (E)
Remeika, J. P. (see **Myers, S. M.**). 32, 867
Rezlescu, N. and E. Cuciureanu. Cation distribution and Curie temperature in the copper-manganese-zinc ferrites. 32, 1096 (T)
Rietveld, H. M. (see **Fischer, P.**). 32, 543
Rigny, P., A. J. Dianoux et P. Plurien. Résonance paramagnétique et déformation locale dans les complexes de type UF_6M. 32, 1175
Rigny, P., A. J. Dianoux et P. Plurien. Susceptibilité magnétique d'un electron $5f$ en coordination de huit. 32, 1901
Ritter, J. R., Jr. (see **Yean, D. H.**). 32, 653
Robbins, M., G. K. Wertheim, R. C. Sherwood and D. N. E. Buchanan. Magnetic properties and site distributions in the system $FeCr_2O_4$–$Fe_3O_4(Fe^{2+}Cr_{2-x}Fe_x{}^{3+}O_4)$. 32, 717
Robbins, M., R. D. Pierce and R. Wolfe. Magnetic properties of fluoride substituted orthoferrites. 32, 1789
Roetschi, H. (see **Emmenegger, F. P.**). 32, 787
Rosen, M. Elastic moduli or thulium and ytterbium from 4·2 to 300°K. 32, 2351
Ross, J. W. and L. L. Isaacs. Electrical transport properties of scandium and a scandium-0·5% gadolinium alloy. 32, 747 (T)
Roth, L. M. (see **Bennett, A. J.**). 32, 1251
Rowe, J. M., K. Skold, H. E. Flotow and J. J. Rush. Quasielastic neutron scattering by hydrogen in the α and β phases of vanadium hydride. 32, 41
Roy, S. K. Dutta, B. Ghosh and S. Kar. Magnetic study of a reversible phase transition in $CoZrF_6$, $6H_2O$, $Co_{1-x}Zn_xSiF_6$, $6H_2O$ and $Co_{1-x}Zn_xF_25Hf$, $6H_2O$. 32, 857
Rush, J. J. (see **Rowe, J. M.**). 32, 41
Russ, M. J. (see **Kennedy, D. E.**). 32, 847
Ruthven, D. M. (see **Loughlin, K. F.**). 32, 2451 (T)

Sadoc, J. F. Étude expérimentale de la susceptibilité magnétique des solutions de métaux de première série de transition dans l'aluminium. 32, 2765
Sakoda, S. and Y. Onodera. Theory of the effects of uniaxial stress on the exciton states in CuCl. 32, 1365
Salaneck, W., Y. Sawada and E. Burstein. The magneto-quantum-electric effect. 32, 2285
Saravia, L. R. and L. Casamayou. Calculation of the photoelectric effect in silicon. 32, 1075
Sawada, Y. (see **Salaneck, W.**). 32, 2285
Schechtman, B. H. (see **Batra, I. P.**). 32, 769
Scherber, W. (see **Meyer, O.**). 32, 1909
Scherrer, H. (see **Janot, C.**). 32, 191
Schirmer, O. F. Trapped-hole centers containing lithium in MgO, CaO and SrO. 32, 499
Schlosser, W. F., G. M. Graham and P. P. M. Meincke. The temperature and magnetic field dependence of the forced magnetostriction and thermal expansion of Invar. 32, 927
Schlosser, W. F. A model for the Invar alloys and the Fe–Ni system. 32, 939
Schmidbauer, E. Magnetization and lattice parameters of Ti substituted Fe–Cr spinels. 32, 71
Schubert, R. and K. W. Boer. Desorption of oxygen and its influence on the electrical properties of CdS single crystal platelets. 32, 77

Schüler, C. (see **Brüesch, P.**). **32,** 1025
Schwarzenbach, D. (see **Fischer, P.**). **32,** 543
Schwarz, K. (see **Weinberger, P.**). **32,** 2063
Schwerdtefeger, C. F. (see **Kerr, R. K.**). **32,** 2007 (T)
Schwerer, F. C. and J. Silcox. Low field magnetoresistance of nickel polycrystals. **32,** 199
Searle, T. M. and B. Bowler. Optical study of the excited state of the V′ centre in MgO. **32,** 591
Sellmyer, D. J. (see **Tobin, P. J.**). **32,** 1721
Shanks, H. R. (see **Whiteman, A. E.**). **32,** 2223
Sharma, B. L., R. K. Purohit and S. N. Mukerjee. Diffusion of mercury in indium arsenide. **32,** 1397 (T)
Sharp, E. J. (see **Weber, M. H.**). **32,** 2275
She, C. Y., Jon D. Masso and D. F. Edwards. Raman scattering by polarization wave uniaxial crystals. **32,** 1887
Sherwood, R. C. (see **Voorhoeve-Van Den Berg, J. M.**). **32,** 167
Sherwood, R. C. (see **Robbins, M.**). **32,** 717
Shimoji, M. (see **Hoshino, H.**). **32,** 385
Shimony, U. (see **Biran, A.**). **32,** 327
Shtrikman, S. (see **Levinson, L. M.**). **32,** 981
Siegmann, H. C. (see **Busch, G.**). **32,** 2173
Sigel, G. H., Jr. Vacuum ultraviolet absorption in alkali doped fused silica and silicate glasses. **32,** 2373
Silcox, J. (see **Schwerer, F. C.**). **32,** 199
Simmons, J. G. Theory of metallic contacts on high resistivity solids—I. Shallow traps. **32,** 1987
Sinha, A. K. and P. Duwez. Radial distribution function of amorphous Ni–Pt–P alloys. **32,** 267
Sinha, K. P. and R. C. Le Craw. Phonon-magnon relaxation effects in ferrimagnetic resonance (Europium Iron Garnet). **32,** 373
Skold, K. (see **Rowe, J. M.**). **32,** 41
Skolnik, L. H., W. P. Allred and W. G. Spitzer. An infrared localized vibrational mode technique for measuring segregation coefficients. **32,** 1
Smith, F. T. J. A high temperature study of native defects in ZnTe. **32,** 2201
Smith, G. C. (see **Wayman, M. L.**). **32,** 103
Smith, R. T. (see **Dismukes, J. P.**). **32,** 913
Smith, T. (see **Reid, J. S.**). **31,** 2689 (E)
Solbrig, A. W., Jr. Valence force potentials for calculating crystal vibrations in silicon. **32,** 1761
Sootha, G. D. (see **Jain, S. C.**). **32,** 897
Spitzer, W. G. (see **Skolnik, L. H.**). **32,** 1
Spitzli, P. (see **Flükiger, R.**). **32,** 459
Srinivasan, U. (see **Stéslicka, M.**). **32,** 1917
Srinivasan, R. and R. Ramji Rao. Anharmonic properties of the hexagonal metals, magnesium, zinc and beryllium—I. Lattice dynamics and third order elastic constants. **32,** 1769
Srivastava, J. P. Absorption spectrum of cobalt fluosilicate hexahydrate. **32,** 279
Stamenkovic, S. (see **Novakovic, L.**). **32,** 487
Staudenmann, J. L. (see **Flükiger, R.**). **32,** 459
Stedman, G. E. and D. J. Newman. Crystal field in rare-earth fluorides, II parameters for Er^{3+} and Nd^{3+} in LaF_3. **32,** 109
Stedman, G. E. (see **Newman, D. J.**). **32,** 535

Stedman, G. E. and D. J. Newman. Crystals field in rare-earth fluorides – III. Analysis of experimental data for the alkaline earth fluorides. 32, 2001

Stéslicka, M. S. G. Davison and U. Srinivasan. Electronic states of heavy diatomic crystals. 32, 1917

Stevenson, D. A. (see **Gomez, M. P.**). 32, 335

Stewart, A. T. (see **Trifthaüser, W.**). 32, 2711

Stewart, A. T. (see **Trifthaüser, W.**). 32, 2717

Streever, R. L., T. R. AuCoin and P. J. Caplan. Nuclear Magnetic resonance studies of Mn^{55} in the Mn substituted hexagonal ferrite $Ba_2Zn_{2-x}Fe_{12-y}Mn_{x+y}O_{22}$. 32, 519

Streit, P. (see **Kaldis, E.**). 32, 159

Stubican, V. S. (see **Whitney, W. P., II**). 32, 305

Suzuki, K. and O. Uemura. Knight shift, magnetic susceptibility and electrical resistivity of pure gallium and gallium-indium eutectic alloy in the normal and the supercooled liquid state. 32, 1801

Swalin, R. A. (see **Murarka, S. P.**). 32, 1277

Swalin, R. A. (see **Murarka, S. P.**). 32, 2015

Swartz, J. C. and L. J. Cuddy. Electrical resistivities of Fe(C) and Fe(N) solutions between 4 and 1300°K. 32, 685

Swartz, J. C. (see **Carter, G. C.**). 32, 2415

Swink, L. N. (see **Parker, S. G.**). 32, 139

Syono, Y. S., I. Akimoto and Y. Endox. High pressure synthesis of ilmenite and perovskite type $MnVO_3$ and their magnetic properties. 32, 243

Szymanska, W. (see **Zawadzki, W.**). 32, 1151

Takahashi, T., K. Minematsu and K. Miyatani. Single crystal growth and some properties of $HgCr_{2-x}In_xSe_4$ solid solutions. 32, 1007

Taupin, C., M. Lambert and Ch. Mazieres. Résonance électronique dans le lithium liquide. 32, 2045

Taylor, M. J., D. J. Marshall and H. Evans. Infra-red spectra of photochromic sodalites. 32, 2021

Taylor, R. (see **Trifthaüser, W.**). 32, 2711

Thompson, J. C. (see **Cate, R. C.**). 32, 443

Thompson, A. W. (see **Deenadas, C.**). 32, 1853

Thompson, A. W. (see **Wallace, W. E.**). 32, 805

Ting, C. S. Theory of magnetic susceptibility of dilute magnetic alloys. 32, 395

Tobin, P. J., D. J. Sellmyer and B. L. Averbach. Effect of indium impurities on the De Haas-Van Alphen effect in lead. 32, 1721

Tosatti, E. and G. P. Parravicini. Model semiconductor dielectric function. 32, 623

Trifthaüser, W. and A. T. Stewart. Positron annihilation angular correlation measurements in disordered systems: α brass. 32, 2717

Trifthaüser, W., A. T. Stewart and R. Taylor. Angular correlation measurements of annihilation radiation in ordered β brass. 32, 2711

Turnbull, D. (see **Baughman, R. H.**). 32, 1375

Uemura, O. (see **Suzuki, K.**). 32, 1801

Vaidya, S. N. and G. C. Kennedy. Effect of pressure on the melting of cesium chloride. 32, 2301

Vaidya, S. N. and G. C. Kennedy. Compressibility of 27 halides to 45 kbar. 32, 951

Van Diepen, A. M. (see **Nasu, S.**). **32**, 2773

Van Diepen, A. M., R. S. Craig and W. E. Wallace. Crystal field and magnetic heat capacity in PrIn$_3$ and CeIn$_3$. **32**, 1867

Van Doan, Nguyen. Vacancy flow effect on electromigration in silver. **32**, 2135

Van Laar, B. (see **Popma, T. J. A.**). **32**, 581

Varret, F. (see **Gerard, A.**). **32**, 2091

Vaughan, D. E. W. (see **Barrer, R. M.**). **32**, 731

Vest, R. W. (see **Osburn, C. M.**). **32**, 1331

Vest, R. W. (see **Osburn, C. M.**). **32**, 1343

Vest, R. W. (see **Osburn, C. M.**). **32**, 1355

Vetelino, J. F. (see **Gaur, S. P.**). **32**, 2737

Vlahov, A. (see **Novakovic, L.**). **32**, 487

Voorhoeve-Van Den Berg, J. M. and R. C. Sherwood. Low-temperature magnetic susceptibilities of NbSe$_2$ containing the first-row transition metals. **32**, 167

Wachter, P. (see **Kaldis, E.**). **32**, 159

Wagner, R. J. and A. W. Ewald. Free carrier reflectivity of gray tin single crystals. **32**, 697

Wainwright, T. E. (see **Gass, D. M.**). **32**, 1797

Wallace, W. E. (see **Deenadas, C.**). **32**, 1853

Wallace, W. E. (see **Van Diepen, A. M.**). **32**, 1867

Wallace, W. E. (see **Nasu, S.**). **32**, 2779

Wallace, W. E. (see **Neumann, H. H.**). **32**, 2788 (T)

Wallace, W. E., C. Deenadas, A. W. Thompson and R. S. Craig. Low temperature heat capacities of PrBi, PrSb, LaBi and LaSb. Crystal field effects in PrBi and PrSb. **32**, 805

Wanklyn, B. M. (see **Rao, G. V. Subba**). **32**, 345

Watson, R. E., A. A. Misetich and L. Hodges. The effect of S–D hybridization on charge and spin contact densities in noble and transition metals. **32**, 709

Watson, R. W. (see **Potter, W. N.**). **32**, 2363

Wayman, M. L. and G. C. Smith. Hydride formation in nickel–iron alloys. **32**, 103

Weber, M. J., E. J. Sharp and J. E. Miller. Optical spectra, relaxation, and energy transfer of Eu^{3+} and Cr^{3+} in a europium phosphate glass. **32**, 2275

Webster, D. S. and M. J. R. Hoch. Rotational phase transitions in molecular solids. **32**, 2663

Webster, P. J. Magnetic and chemical order in Heusler alloys containing cobalt and manganese. **32**, 1221

Weinberger, P. K. Schwarz and A. Neckel. Electronic band structure of ScN. **32**, 2063

Wertheim, G. K. (see **Robbins, M.**). **32**, 717

White, J. G. (see **Dismukes, J. P.**). **32**, 913

Whitehouse, J. E. Defect production in n-type germanium by electron irradiation at low temperatures. **32**, 677

Whiteman, A. E., J. J. Martin and H. R. Shanks. Thermal conductivity of cubic sodium tungsten bronzes. **32**, 2223

Whitney, W. O., II and V. S. Stubican. Interdiffusion studies in the system MgO–Al$_2$O$_3$. **32**, 305

Wiley, J. D. Donor-acceptor pairing in the system GaP (Zn. O). **32**, 2053

Window, B. Electric field gradients at ^{57}Fe nuclei in gold alloys. **32**, 1059

Winogradoff, N. N. (see **Petrescu-Prahova, I.**). **32**, 1873

Winterberger, M. (see **Gerard, A.**). **32**, 2091

Wojtowicz-Natanson, B. (see **Filinski, I.**). **32**, 2409

Wojtowicz-Natanson, B. (see **Filinski, I.**). 32, 2193
Wolfe, R. (see **Robbins, M.**). 32, 1789
Wolfstirn, K. B. (see **Casey, H. C., Jr.**). 32, 571
Wynblatt, P. On the contribution of divacancies to self diffusion in copper. **32,** 15

Yean, D. H. and J. R. Ritter, Jr. Estimates of isothermal bulk moduli for group IVA crystals with the zincblende structure. **32,** 653

Zawadzki, W. and W. Szymanski. Electron scattering and transport phenomena in *n*–InSb. **32,** 1151
Zlatkin, L. B. and E. K. Ivanov. Character disorder at transition from crystal to vitreous phase in semiconductors. **32,** 1733

PROGRESS IN SOLID STATE CHEMISTRY

Volume 5

Edited by H. Reiss

This volume is devoted primarily to the structural chemistry of solids and to the influence of such structure on chemical and physical properties.
Contents: Crystal Chemistry and Magnetic Structures of Substituted $Ca_2[Fe](fe)O_5$ by *S. Geller, R. W. Grant and U. Gonser*; Strukturchemie einiger Verbindungen der Übergangsmetalle mit den Elementen C, Si, Ge, Sn by *H. Nowotny*; Les Bronzes Oxygenes by *P. Hagenmuller*; Metallic Oxides by *J. B. Goodenough*; Electronic Structure, Coloration and Photodecomposition of the Alkali–Metal Azides by *D. A. Young*; Dipolar Impurities in Alkali Halides: Zeeman and Stark Effects of Sm^{2+} : K^+ Vacancy Pair Fluorescence, and Paralectric Resonance and Relaxation of CH- and KCl by *C. R. Chilver, F. K. Fong and L. A. Vredovoe.*
506 pages £12.00 hard cover

ADVANCES IN SOLID LIQUID FLOW IN PIPES AND ITS APPLICATION

Edited by Iraj Zandi

A collection of papers bringing together works of many individuals from various disciplines and concerning itself primarily with the transport of solid materials in pipelines. Presents not only a unified and exhaustive treatment of the area of solid–liquid flow, but also brings to the reader the highlights of research carried out in this field.
308 pages £8.00 hard cover

PROCEEDINGS OF THE THIRD PHOTOCONDUCTIVITY CONFERENCE

Edited by E. M. Pell

Contents: *SESSION A*: Photoconductivity General Semiconductors, *SESSION B*: Photoconductivity General, High Resistivity Materials; *SESSION C*: Photoconductivity General, Ionic Crystals; *SESSION D*. Mostly Ternary Compounds; *SESSION E* Impurities and Defects; *SESSION F*: Organic Materials Phonon Effects; *SESSION G*: Structures, Junctions, Barriers
424 pages £12.50 hard cover

ELECTROMAGNETIC WAVES IN STRATIFIED MEDIA

Second Revised Edition

J. R. Wait

The second edition of this book, which has been brought up to date in view of recent investigations, contains information on recent work on electromagnetic waves in stratified media, including several recent papers by the author. Additional references to the new sections have also been included.
640 pages £8.00 hard cover
International Series of Monographs in Electromagnetic Waves, Volume 3.

Pergamon

Microelectronics and Reliability

Editor in Chief
G W A Dummer

Published Bi-monthly

Founded in 1962

The increasing complexity of electronics and the widening field of application has raised problems of reliability; the importance of reliability measured against cost for different applications is now realised, devices need accurate control in manufacture and considerable testing for very low failure rates. This bi-monthly journal (published in English, French and German) combines the practical, theoretical and statistical aspects of reliability with the design, construction, engineering and testing of microelectronic systems, bringing an up-to-date continuity never previously achieved. Introduced in 1962, it is the only regular international journal in the world covering reliability in all its aspects.

A recent breakdown of the subscribers to the journal shows that it is read by university, government and industrial personnel from such diverse departments as: telecommunications technology, semiconductors, guided weapons, research and development, dynamics, computers, radar, electronics, aeronautics, engineering research, naval, electrical engineering, atomic, railway research, aviation, space research, underwater weapons, physics labs, engineering, mathematics, oceanic research, systems engineering, electronic engineering, missiles, standards, army.
Some recent papers are detailed below. The editor-in-chief, G W A Dummer, is particularly well qualified in both microelectronics and reliability, having initiated most of the early British Government work on microelectronics, and authored several books on reliability. He holds the MBE, the American Medal of Freedom, and is a Fellow of the IEEE, the IEE and the IERE. He was awarded the Wakefield Gold Medal by the Royal Aeronautical Society for his pioneering work on microelectronics.

Some recent papers

G H SCHWUTTKE: Silicon material problems in semiconductor device technology
S PRAKASH: Stochastic behaviour of a redundant electronic equipment with imperfect switching and opportunistic repairs
C M HART AND C MULDER: An all silicon timing circuit for automatic cameras
R W NEWCOMBE and B D O ANDERSON: Transfer function sensitivity for discrete and integrated circuits
A B BHATTACHARYYA, M L GUPTA and V K GARG: *Temperature coefficient calculations for* monolithic resistors.
Y CHAIGNEAU: La fiabilité en France
HIROYUKI AOE, YASUO YATSUI and TOSHIAKI HAYASHIDA: Dielectric properties of silicone thin films cross linked by an electron beam.
M J DOWNEY: Satellite reliability
J HARRIS: *Equipment reliability and the environment.*

Subscription: £20.00/$50.00 per annum

PERGAMON PRESS LTD
OXFORD NEW YORK SYDNEY TORONTO

6/71

metron

measurement • control • automation

The aim of METRON is to assist scientists, technologists and industrial managers searching for new techniques and developments in fields which go beyond measurement to application in control and automation.

A high-level, internationally recognized journal, METRON is published by Pergamon Press for the British Scientific Instrument Research Association (Sira) and presents information aimed at evaluating those publications outlining recent developments whilst providing a cumulative source of reference material. The reader is able to examine narrow subject areas and, at the same time, gain a picture of development along a broad front. The service rendered to technology is invaluable.

METRON's contents may be summarised under five separate headings:

Short critical reviews on selected topics. developments in technology, or fields of application with special problems.

Information reviews, which collate, organize, abstract and compare recent literature Subject divisions for review are those used previously for the abstracts section, and each subject will be reviewed at regular intervals

Current titles, to provide immediate information on newly published literature, bridging the gap before inclusion in the appropriate information review. Keywords allocated to entries are intended to assist rapid scanning.

Reviews of books of particular relevance to the subject of measurement and control, with listings of others

Subject and author indexes to permit location of single articles, either for narrow current awareness, or for problem solving.

Published monthly.

Annual subscription :	£20.00	\$50.00	A\$43.00
Two Years - saving 10% :	£36.00	\$90.00	A\$77.50
Single copies :	£ 4.00	\$10.00	A\$ 9.00

A special supplement to Volume 1, 1969 has been published on **PHOTON DETECTORS** - a survey of literature on phototubes and photocells by P J Geary and R G Burrows.

Contents include: Photoemissive Detectors, Photoconductive and Photovoltaic Detectors, Infrared Photon Detectors, Photon Coupling, Positon-Sensitive Photon Detectors.

Available at :	£4.00	\$10.00	A\$8.50
METRON subscribers :	£3.00	\$ 7.50	A\$6.50

Please write to dept. ED(t), for an inspection copy of METRON plus 1969 index, (supplement on approval), and information on related journals.

Pergamon Press

Headington Hill Hall Oxford OX3 0BW England

are these important journals in your library?

Acta Metallurgica and Scripta Metallurgica

Editor:
PROFESSOR BRUCE CHALMERS
Harvard University
Cambridge Massachusetts 02138
USA

Sponsored by: The American Society for Metals
The American Institute of Mining, Metallurgical and Petroleum Engineers
The American Society for Testing and Materials

ACTA METALLURGICA is an international journal for the science of metallic and non-metallic solids
It provides a medium for the publication of papers describing theoretical and experimental investigations that contribute to the understanding of the properties and behaviour of metals in terms of fundamental particles, forces and energies. Emphasis is placed on those aspects of the science of materials that are concerned with the relationship between the structure of solids and their properties

SCRIPTA METALLURGICA, the companion volume, is concerned with the same subject matter but provides a medium for shorter papers and letters which demand a more rapid publication process. Abstracts of both journals are in the original language of publication as well as English, French and German.
Both published monthly

Journal of Physics and Chemistry of Solids

Editor-in-Chief.
PROFESSOR HARVEY BROOKS
Harvard University
Cambridge Massachusetts 02138
USA

The purpose of this journal is to provide an international medium of publication in the field of solid state: the fields of interest are the statistical mechanics of condensed systems. As an international medium, the journal accepts manuscripts in French and German, as well as English. Short communications may be published as Technical Notes.
While the Journal publishes both experimental and theoretical papers it is generally interested in experimental papers only to the extent that they can throw light on fundamental processes and theories. Preference is given in publication to work on well-characterised materials, such as single crystals.
Published monthly

Solid State Communications

Editor-in-Chief:
PROFESSOR ELIAS BURSTEIN
University of Pennsylvania
Philadelphia Pennsylvania USA

A Supplement to the Journal of Physics and Chemistry of Solids
SOLID STATE COMMUNICATIONS is the international medium for the rapid publication of short communications on important developments in the solid sciences. The primary aim of the Journal is to give scientists working in this field immediate access to important work just completed. In keeping with this aim the Journal also publishes short versions of important papers being submitted to national journals.

Inspection Copies
Inspection copies of all Pergamon Learned Journals are available on request from Dept. ED (t), Pergamon Press, Oxford.

Pergamon Press
Headington Hill Hall Oxford OX3 0BW
Maxwell House Fairview Park Elmsford New York 10523 USA
Pergamon House 19a Boundary Street Rushcutters Bay NSW 2011 Australia

J. Phys. Chem. Solids **Pergamon Press 1971. Vol. 32, pp. 2015–2020. Printed in Great Britain.**

CATION SELF-DIFFUSION IN BARIUM OXIDE (BaO)*

S. P. MURARKA and R. A. SWALIN
Department of Chemical Engineering and Materials Science, University of Minnesota,
Minneapolis, Minn. 55455, U.S.A.

(*Received* 26 *January* 1971)

Abstract – Cation self-diffusion studies were carried out in BaO crystals in the temperature range $900°\text{C} \leqslant T \leqslant 1400°\text{C}$ and at oxygen partial pressures of one atm and 2×10^{-5}atm. ^{133}Ba isotope was used as tracer and Gruzin's residual activity method was employed. The bulk diffusion coefficient could be represented by the following equations:

$$D(1200\text{–}1400°\text{C}) = \left(1{\cdot}35\,{}^{+4{\cdot}97}_{-1{\cdot}06}\right) \times 10^4 \exp\left[-(4{\cdot}00 \pm 0{\cdot}067)\text{eV}/kT\right] \text{cm}^2/\text{sec}.$$

$$D(950\text{–}1100°\text{C}) = \left(1{\cdot}20\,{}^{+6{\cdot}52}_{-1{\cdot}01}\right) \exp\left[-(2{\cdot}81 \pm 0{\cdot}21)\text{eV}/kT\right] \text{cm}^2/\text{sec}.$$

The diffusion coefficients were found to be independent of changes in the oxygen partial pressure of the annealing atmosphere.

The data are interpreted in terms of various possible defect models.

1. INTRODUCTION

THE USE of BaO–SrO coated vacuum tube cathodes has stimulated efforts directed toward understanding their defect structures and semiconducting behavior. In BaO, Sproull and co-workers[1–6] investigated the properties of barium rich crystals. One important observation that emerges out of these studies is the existence of a 2·0 eV peak in the optical absorption spectra of BaO crystals which contained excess Ba, Ca, Mg or Al. This peak was associated with oxygen ion vacancies.

Carson *et al.*[7] made ESR measurements on BaO which contained excess Ba and observed the ESR spectrum from singly ionized oxygen vacancies (F^+ center), but could not correlate this with the 2·0 eV optical absorption. Recently Bessent *et al.*[8] by use of the Faraday rotation technique have demonstrated that in crystals irradiated with 2·5 MeV protons, the 2·0 eV band is due to singly ionized oxygen vacancies.

Reddington[9] has studied the cation self-diffusion in BaO and reported two diffusion processes: one resulted in the transportation of electrical charge (of about 2 electron units) and the other was non-charge transporting. The activation energies of diffusion were 12 ± 2·3 eV and 11 ± 2·2 eV respectively. Such large activation energies for barium mass transport are highly unlikely in view of the fact that energy of formation of BaO from constituent elements is only about 10 eV.

An investigation of the BaO–O_2 systems was made bt Kozlenko *et al.*[10], who suggested that oxygen enters the crystal lattice in two forms: as BaO_2 clusters and as a solid solution. At very low pressures of oxygen or at temperatures higher than 800°C it was determined that oxygen is mainly dissolved in neutral atomic form.

All these studies have attempted to yield an understanding of the defect structure of BaO. Further detailed work, however, is clearly needed especially at higher temperatures. In

---

*This research was supported by the National Science Foundation.

view of these, the cation self-diffusion studies in BaO were undertaken as part of a general study.

2. EXPERIMENTAL PROCEDURE AND RESULTS

Single crystals of BaO were grown in our laboratory by use of an induction coupled plasma torch device[11] as the heat source. BaO in powder form was obtained from F.M.C. Corporation and the typical analysis of this powder as quoted by suppliers is given in Table 1 together with the semi-quantitative spectrographic analysis of the single crystal grown from this powder. Single crystals as large as 8 mm × 3 mm × 2 mm were obtained.

Table 1. Analysis of the powder and crystals of BaO

BaO powder*		BaO crystal†	
BaO	99·5%	BaO	principal
BaS	0·1–0·6%	SrO	0·15%
$BaCO_3$	2·0%	MgO	0·004%
Fe_2O_3	0·012%	CaO	0·08%
Al_2O_3	0·020%	Fe_2O_3	0·003%
$BaSO_4$	0·07%	Al_2O_3	0·002%
		Cr_2O_3	0·002%

*Analysis furnished by the powder suppliers.

†Semi-quantitative spectrographic analysis.

These crystals were annealed in magnesia crucibles under pure dry argon along with an excess of BaO powder at 1250–1300°C for 48 hr. Most of the crystals thus obtained were clear and transparent and no residual thermal stresses could be detected in the X-ray back reflection Laue pattern of the transparent crystals. Such crystals were used in diffusion studies.

Details of the experimental procedure were described in an earlier paper on SrO[12] which will be hereafter referred to as Paper I. Only the essential differences will be described here. Radioactive ^{133}Ba was used as the tracer. This isotope has a half-life of 7·2 yr and emits gamma radiation of energies 0·057, 0·082, 0·3 and 0·36 MeV. The 0·36 MeV radiation was used in the present studies for monitoring this isotope. Labeled Ba-oxalate was precipitated from the chloride solution and the oxalate was ignited, after drying, at 1000°C to form the oxide. This radioactive oxide was used for evaporation as a thin film on the prepared crystal surfaces.

All the diffusion anneals were performed in single crystal magnesium oxide crucibles. Each crucible was partially filled with dry inactive BaO powder and some crystal chips of BaO. The diffusion specimen was sandwiched between two cleaved surfaces of MgO crystals and placed on top of the powder and chips in the crucible. This assembly was then placed in the isothermal zone of the furnaces.

Anneals were carried out in the temperature range of 900–1400°C. The temperature was controlled to within ± 1°C and measured to within ± 4°C. Anneals were carried out at several temperatures both in pure dry argon ($p_{O_2} = 2 \times 10^{-5}$ atm) and in pure dry oxygen (p_{O_2} = one atm).

Analysis of the diffusion profiles was carried out as described in Paper I

Figure 1 shows typical plots of the surface activity I vs. diffusion penetration distance X into the BaO crystals. Figure 2 shows typical $\log I^*$ vs. X^2 plots. As in case of SrO, the experimental data presented in Fig. 2 did not fit a single straight line and two intersecting lines were drawn. The one near the surface has considerably larger slope than the line at larger penetrations. In BaO while the first region was restricted to a maximum of about 30 μm, the second segment extended up to 350 μm.

Diffusion coefficients were calculated from both these segments. Figure 3 shows a plot of $\log D$ vs. $1/T$, where D represents the diffusion coefficient in the bulk. It is observed that there is no effect on the values of diffusion coefficient when the oxygen partial pressure is changed from 2×10^{-5} atm to one atm. The temperature dependence of D could be best

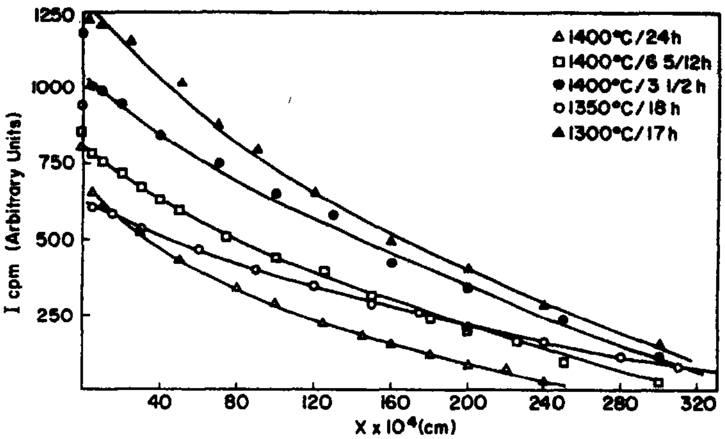

Fig. 1. Penetration profiles for cation self-diffusion in BaO ($p_{O_2} = 2\times 10^{-5}$ atm).

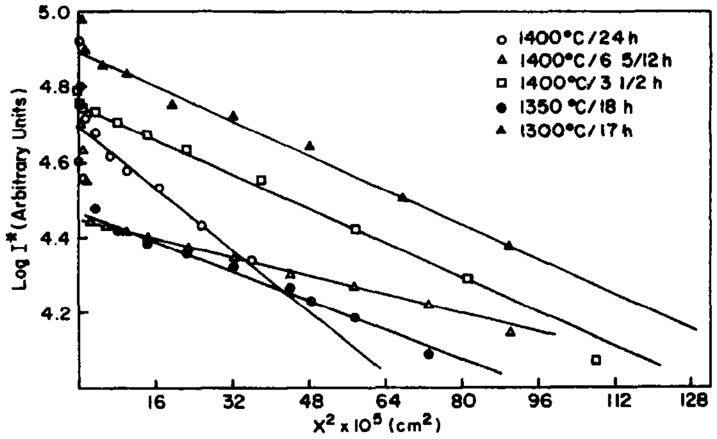

Fig. 2. Log I^* vs. X^2 plots for cation self-diffusion in BaO ($p_{O_2} = 2\times 10^{-5}$ atm).

described by the following (obtained from least square fit of the straight lines):

$$D(1200\text{–}1400^\circ\mathrm{C}) = \left(1{\cdot}35\,^{+4{\cdot}97}_{-1{\cdot}06}\right)\times 10^4 \exp\left[-\left(\frac{4{\cdot}00\pm 0{\cdot}067\ \mathrm{eV}}{kT}\right)\right]\mathrm{cm}^2/\mathrm{sec}$$

$$D(950\text{–}1100^\circ\mathrm{C}) = \left(1{\cdot}20\,^{+6{\cdot}52}_{-1{\cdot}01}\right)\exp\left[-\left(\frac{2{\cdot}81\pm 0{\cdot}21\ \mathrm{eV}}{kT}\right)\right]\mathrm{cm}^2/\mathrm{sec}$$

and

$$D(900\text{–}950^\circ\mathrm{C}) = 7{\cdot}52\times 10^{-8}\exp(-1{\cdot}05\ \mathrm{eV}/kT)\mathrm{cm}^2/\mathrm{sec}.$$

The limiting errors were calculated by a method described by Guest[14].

The last equation was based on only two data points at 900 and 950°C. The diffusion coefficient is much higher (beyond experimental error) than one would expect from extrapolation from results in the 950–1100°C

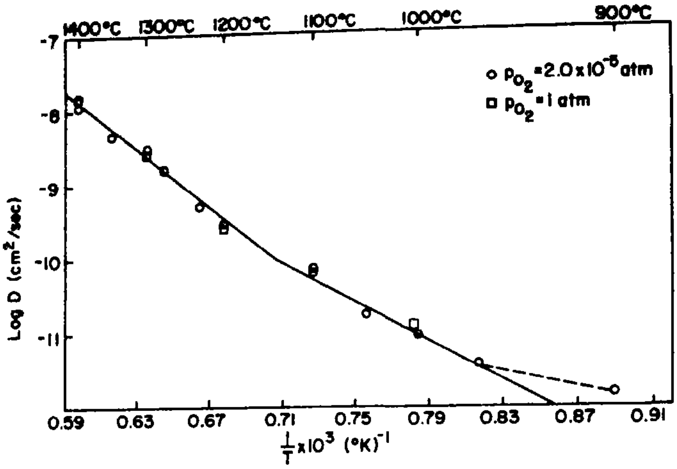

Fig. 3 Temperature dependence of cation self-diffusion coefficient D in BaO.

range. Reddington[9] also found that at lower temperatures the diffusivity was enhanced compared to extrapolation from high temperature values. He reported an activation energy of 0·3 to 0·44 eV at temperatures below 1075°C, which would seem to be supported by the present findings.

3. DISCUSSION

A detailed discussion of the diffusion coefficients obtained from the near surface region appears in Ref.[13]. It appears that the near surface region resulted from hydroxide layer formation. Thus the diffusion coefficient D from the second segment of the log I^* vs. X^2 curves will be considered to represent true volume diffusion[12].

The results of the present investigations do not agree with the studies of cation self-diffusion in BaO made by Reddington[9]. Reddington studied cation diffusion in BaO *in vacuo* by use of ^{140}Ba as the radioactive tracer. His results can be summarized as:

(i) Diffusion near the surface
$D(1077\text{–}1277^\circ\mathrm{C}) = 10^{31\pm 8} \exp [(-12 \pm 2{\cdot}3\ \mathrm{eV})/kT]\ \mathrm{cm^2/sec}$
$D(327\text{–}1077^\circ\mathrm{C}) = 3\times 10^{-10\pm 1} \exp [(-0{\cdot}3 \pm 0{\cdot}05\ \mathrm{eV})/kT]\ \mathrm{cm^2/sec}$.

(ii) Diffusion deep inside the crystal
$D(1077\text{–}1277^\circ\mathrm{C}) = 10^{29\pm 7} \exp [-(11 \pm 2{\cdot}2)\ \mathrm{eV}/kT]\ \mathrm{cm^2/sec}$
$D(327\text{–}1077^\circ\mathrm{C}) = 10^{-9\pm 1} \exp [(-0{\cdot}44 \pm 0{\cdot}03)\ \mathrm{eV}/kT]\ \mathrm{cm^2/sec}$.

Although it is difficult to determine the exact cause of the difference between his data and ours, some of the above numbers appear to be erroneous. For example, an activation energy of 11–12 eV yeilds a defect formation energy of 23 eV (for a combination of barium interstitial and a barium vacancy) and seems highly unlikely inasmuch as the dissociation energy of BaO is only about 10 eV. There is, however, a similarity observed in the two experimental investigations. In both, a near surface effect is observed where the diffusion coefficient in the near surface region is seemingly smaller by a factor of about 10 when compared with behavior in the bulk. The discontinuity in the slope of log D vs. $1/T$ curve occurred in both the cases at about 1100°C. Anomalously high diffusion coeffiients were obtained at lower temperatures leading to very small activation energies of diffusion.

Cation diffusion in bulk BaO could occur by either an interstitial or a vacancy mechanism.

In Paper I[12] equations were developed which relate the diffusion coefficient to the concentration of the migrating defect, which in turn, is dependent on the oxygen partial pressure in the diffusion annealing atmosphere. It can be shown that irrespective of the specific mechanism of incorporation of oxygen in the lattice, the diffusion coefficient should be dependent on P_{O_2} for a crystal in the intrinsic range.

In the present investigation (see Fig. 3) no significant change in the value of D was observed as a result of changes in P_{O_2} from 2×10^{-5} atm. to one atm. Three alternative mechanisms could explain this result.

(i) In view of the fact that cation self-diffusion in BaO was not influenced by changes in P_{O_2}, one is tempted to suggest that the whole temperature range of investigation is extrinsic. It is possible that there are impurities present which have different ionization levels lying in the band gap such that different impurities control the extrinsic defect levels in different temperature ranges, thus causing several discontinuities in the slope of the log D vs. $1/T$ plot. If this were so, it is very difficult to explain the relatively high activation energy of diffusion that was obtained for diffusion above 1150°C. The only heterovalent impurities present within spectrographic detection limits were Fe, Cr and Al (see Table 1). To what extent they could control the defect concentration is not actually known.

(ii) Barium self-diffusion could occur by a coupled mechanism in which both barium interstitials and cation vacancies take part in mass transfer (such a mechanism was suggested by Reddington[9] to explain his diffusion results). The total diffusion coefficient D is, then, a function of concentrations of both barium interstitial and cation vacancy. Since changes in the oxygen partial pressure has an opposite effect on the respective concentrations of these defects, a condition could be obtained for which D will be virtually independent of p_{O_2}.

(iii) Oxygen may be incorporated in the lattice in a form other than as interstitials or at anion sites (leading to concurrent formation of cation vacancies). There is some indirect evidence for example that oxygen forms oxygen molecule ions. ESR studies[15] of paramagnetic species adsorbed on the surface of MgO have identified the oxygen molecule ion as one of the defects on the surface. In BaO, the lattice dimensions are more accommodating for the existence of such a defect in the interior of the crystal. The formation of such a defect in BaO is also supported by the fact that the stability of peroxides increases as one moves through the series Mg, Ca, Sr and Ba. Recently Elo and Swalin[16] have studied the defect structure of BaO in the oxygen excess region of the nonstoichiometry by use of X-ray lattice parameter measurements, thermogravimetric measurements and absolute oxygen concentration analysis measurements in the temperature range 830–1400°C. Oxygen was seemingly incorporated in BaO lattice as a neutral defect with a small negative enthalpy of reaction.

$$\frac{1}{2}O_2\ (g) = \text{O(in crystal)} + \text{defect.}$$

The results can be explained semiquantitatively if it is assumed that oxygen goes to form oxygen molecule ions.

The principal conclusion of this work is that reasonable activation energies for the cation diffusion process are obtained which for our samples were independent of oxygen partial pressure. The results may be quantitatively interpreted in terms of impurity controlled diffusion, formation of equal numbers of oxygen interstitials and oxygen vacancies or as some form of oxygen complex such as O–O pairs. The last possibility is somewhat attractive since BaO_2 is a stable compound and crystallographically is a distorted NaCl structure in which O–O pairs exist.

REFERENCES

1. TYLER W. W. and SPROULL R. L., *Phys. Rev.* **83**, 548 (1951).
2. DASH W. C., *Phys. Rev.* **92**, 68 (1953).
3. SPROULL R. L., DASH W. C., TYLER W. W. and

MOORE A. R., *Rev. Scient. Instrum.* **22**, 410 (1951).
4. SPROULL R. L., BEVER R. S. and LIBOWITZ G., *Phys. Rev.* **92**, 77 (1953).
5. ZOLLWEG R. J., *Phys. Rev.* **100**, 671 (1955).
6. DOLOFF, R. T., *J. appl. Phys.* **27**. 1418 (1956).
7. CARSON J. W., HOLCOMB D. F. and RUCHARDT H., *J. Phys. Chem. Solids* **12**, 66 (1959).
8. BESSENT R. G., CAVENETT B. C. and HUNTER I. C., *J. Phys. Chem. Solids* **29**, 1523 (1968)
9. REDDINGTON R. W., *Phys. Rev.* **87**, 1066 (1952)
10. KOZLENKO T. A., KOVTUNENKO P. V., KISELEVA E. V. and BUNDEL A. A., *Russ. J. Phys. Chem.* **41**, 726 (1967).
11. GAMBINO R. J., *J. appl. Phys.* **36**, 656 (1965).
12. MURARKA S. P. and SWALIN R. A., *J. Phys. Chem. Solids* to be published.
13. MURARKA, S. P., Ph. D. Thesis *Cation Diffusion in Barium and Strontium Oxide Crystals*. University of Minnesota, June (1970).
14. GUEST P. G., in *Numerical Methods of Curve Fittings*. Cambridge University Press, London (1961).
15. HENDERSON B. and WERTZ J. E., *Adv. Phys.* **17**, 749 (1968).
16. ELO R. B. and SWALIN R. A., to be published.

J. Phys. Chem. Solids Pergamon Press 1971. Vol. 32, pp. 2021–2026. Printed in Great Britain.

INFRA-RED SPECTRA OF PHOTOCHROMIC SODALITES

M. J. TAYLOR, D. J. MARSHALL and H. EVANS
Royal Radar Establishment, Malvern, Worcestershire, England

(*Received* 24 *September* 1970; *in revised form* 31 *December* 1970)

Abstract—The i.r. spectra of synthetic sodalites from 10,000 cm^{-1} to 400 cm^{-1} are presented and discussed, and particular note is made of features which bear on the photochromic properties of these materials. There is evidence that the high temperature firing process, which develops the photochromic response of as-grown material, is necessary in order to remove OH$^-$ radicals from the sodalite cages.

INTRODUCTION

MEMBERS of the sodalite group of minerals are well known for their photochromic properties, which have been the subject of several recent studies[1–3]. Sodalites have an aluminosilicate framework structure and the photochromic effect has been most widely studied in members of the group which have the ideal composition $3(Na_2O \cdot Al_2O_3 \cdot 2SiO_2) \cdot 2NaCl$. However it is also possible to make various substitutions, such as Ge for Si, Ga for Al and other halides for Cl, and still obtain a photochromic material, although the induced colour may be different. The halide is located at the centre of the sodalite cage, surrounded by four sodium ions in tetrahedral coordination, and it has been established that the photochromic colouration is due to F-centres situated at halide vacancy sites. Optimum photochromism occurs in materials doped with about 0·5% w/w of sulphur, which appears to form a radical which acts as an electron donor. Sodalites containing high concentrations of sulphur are well known as the highly coloured ultramarines.

There is little published data on the infra-red spectra of sodalites. Milkey[4] has recorded the spectrum down to 660 cm^{-1} of Canadian natural sodalite as well as other minerals which have the sodalite structure, while Vierne and Brunel[5] give the reflection spectra of natural crystals down to about 400 cm^{-1}. Reflection spectra of synthetic sodalites powders have been reported by Avdeeva and Vorsina[6].

The spectra we present and discuss in this paper were obtained as part of a study of the photochromic effect in synthetic sodalites, and, while there is an obvious overall similarity between some of our spectra and these given by Avdeeva and Vorsina, detailed comparison is hampered by nonlinearities in their wavelength and frequency scales. Moreover their method of synthesis and the degree of crystallinity obtained are not made entirely clear.

SAMPLE PREPARATION

The sodalites used in our experiment were grown by the hydrothermal method. Samples of up to 0·5 gms of crystalline powder were produced in platinum capsules of 1·5 ml internal capacity heated under pressure in Tuttle-type autoclaves using a commerical apparatus made by Tem-Press Inc. The starting materials, which were fine powders of Analar quality or better, were weighed into the capsule, the appropriate alkaline solution was added from a hypodermic syringe and the capsule was sealed with a small arc-welder. The run lasted from 3 to 5 days at around 420°C and 550 bars. The autoclaves were then allowed to cool, the capsules opened and the product thoroughly washed and dried. The sodalites were produced as crystalline white powders consisting of euhedral rhombic dodecahedra usually about 25 μm across. Crystals up to about 0·5 mm in size could be produced if desired. To produce larger crystals, or to synthesize larger qualities of sodalite powder, platinum lined Morey-type autoclaves[7] with an internal capacity of 65 mls were used. According to the temperature gradient and concentrations employed these could be used to grow larger crystals or to produce about 15 gms at a time of uniform crystalline powder.

The products were identified by X-ray powder diffraction using Debye–Scherrer cameras; all the lines observed were indexed to a body centred cubic cell and there was usually no trace of any second phase. Analysis for halide and sulphur content was carried out by X-ray fluorescence or mass spectroscopy, and, as a check, a number of samples were fully analysed by classical wet chemical methods.

Absorption spectra were usually recorded on either of two i.r. instruments, a Perkin–Elmer model 21 and a Unicam model SP1200; occasional measurements were made on more powerful instruments. Powder spectra were obtained by conventional methods, the mull technique with a hexachlorobuta-1,3-diene mulling agent for spectra in the region 10,000 to 1700 cm^{-1}, and the KBr disc technique for spectra down to 400 cm^{-1}. The KBr was of Analar quality and typical discs contained 19·0 gms/cm^2, including 0·38 gm/cm^2 of the material under investigation; 13 mm dia. discs were compressed under 10 tons.

Evolution of water under heat treatment was studied by the technique of thermohygrometric analysis (THA)*, in which the sample is heated in a stream of argon under temperature programmed conditions (temperature rise 20°C per min.), the water evolved into the argon stream being continuously monitored with an electrolytic hygrometer.

RESULTS

1. *Hydroxyl bands in the region of* 3600 cm^{-1}

Spectra in this region are of particular interest since the concentration of OH or molecular water is believed to strongly affect the efficiency with which colour centres can be produced; to sensitize as-grown materials it is necessary to fire them in an atmosphere of hydrogen or inert gas for, typically, one hour at 800°C, and during this period there is a weight loss of the order of 1 per cent which is largely due to loss of hydroxyl groups. Hydroxyl enters the lattice from the alkaline solution during the growth process and OH groups partly substitute for the halide.

The spectra of single crystals and powders show a strong, narrow peak at $3635 \pm 0{\cdot}5$ cm^{-1} (Fig. 1) but in powders this line is partly obscured by a much broader peak centred at about 3400 cm^{-1}. Both bands can be attributed to the deformation oscillations of hydroxyl groups, as we shall discuss below. They are removed by the firing process, during which the rate of loss of hydroxyl is sufficiently great to shatter crystals of mm. dimensions, or at least to craze them to the extent that they become opaque, even when the rate of temperature rise is as little as two or three degrees per hour. With very thin slices, such as the one from which the spectra of Figs. 1(a) and (b) were obtained, the degree of crazing was sufficiently reduced that appreciable scatter occured only at the high frequency end of the spectrum.

Comparison of the powder and single crystal spectra, and the fact that the amplitude of the narrow 3635 cm^{-1} line in single crystal spectra is proportional to the sample thickness, suggests that surface effects are responsible for the broad band at 3400 cm^{-1}, whereas the 3635 cm^{-1} line comes from entities incorporated into the sodalite lattice. The sharpness of the 3635 cm^{-1} line and the fact that it lies close to the wavelength of the main stretching

---

*These measurements were undertaken by the Chemistry and Technical Services division of the General Electric Co. Ltd., Wembley, England.

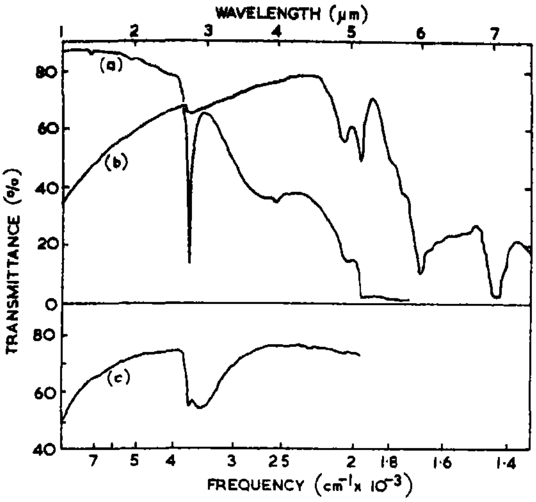

Fig. 1. (a) Absorption spectrum of a 173 μm thick slice of sodalite crystal. (b) Absorption spectrum of the same sample as for (a) but after being raised to 750°C at the rate of 12°C/hr. (c) Mull spectrum of a typical sodalite.

vibrational line of free, neutral OH (3569 cm^{-1} [8]), leave little doubt that it is due to the main stretching vibration of unassociated OH$^-$ groups. With the aid of deuterium exchange similar lines have been identified in other materials, including zeolites which contain the sodalite structural unit. In sodium chloride the main OH$^-$ absorption line occurs at 3654 cm^{-1}[9]. The first overtone in sodalite is also visible in Fig. 1, at 7060 cm^{-1}.

It is well known that the association of hydroxyl groups through hydrogen bonding tends to broaden the contour of the absorption, enhance its intensity and cause a shift to longer wavelengths. Thus the broader band at 3400 cm^{-1} is most probably due to adsorbed water molecules. However although most of this band is removed by drying at ~150°C an appreciable fraction remains, and baking at 400 to 500°C for an hour is necessary to completely remove it. A similar phenomenon has been observed with zeolites, and Angell and Schaffer[10] have suggested that this is because some of the water molecules are attached not only through the oxygen atom to a cation but also through both hydrogens to surface oxygens. Additional evidence of the importance of surface bonds in our sodalites is that this broad band at 3400 cm^{-1} can be generated by grinding the sodalite powder, which presumably exposes broken bonds. Powder which has been fired can be exposed to the atmosphere for many hours and still show no absorption in this region, whereas the broad band appears immediately after only light grinding with an agate pestle and mortar.

The difference between the hydroxyl groups responsible for the 3635 cm^{-1} and 3400 cm^{-1} bands is also apparent in their response to the firing process. Whereas the broad 3400 cm^{-1} band is progressively removed as the temperature is raised up to about 500°C, the sharp 3635 cm^{-1} line remains until much higher temperatures are reached, the actual temperature depending somewhat on the particle size but lying, typically, between 600 and 650°C. THA plots of the rate at which water is evolved as a function of temperature do in fact show two distinct peaks for a typical microcrystalline sodalite (Fig. 2(a)). The high temperature peak correlates with the disappearance of the 3635 cm^{-1} line and the low temperature peak with the disappearance of

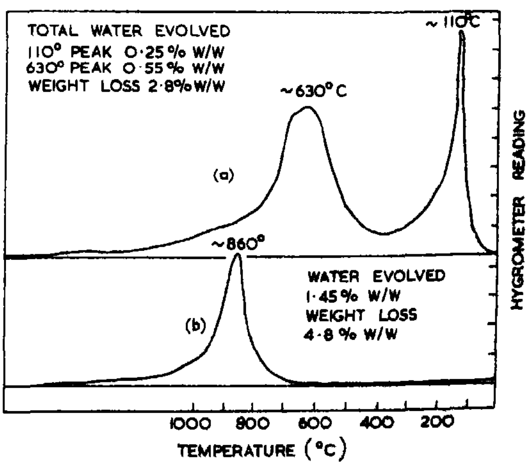

Fig. 2. THA curve of (a) a typical chlorosodalite powder, and (b) the chlorosodalite single crystal from which the slice for Figs. 1(a) and (b) was cut.

the broad 3400 cm^{-1} band. The low temperature peak has a 'tail' extending up to about 500°C, which is consistent with the behaviour of the broad band mentioned above. The precise location of the high temperature peak is presumably governed by the rate at which OH groups diffuse through the lattice and it is therefore not surprising that in the THA plot for single crystals of ~3 mm dimension (Fig. 2(b)) the peak occurs at a much higher temperature than for powders. As expected, no significant evolution of water occurs at low temperature for such single crystals.

The total weight loss after a THA run was always greater than the weight of water evolved, as calculated from the area under the THA curve. This is not entirely understood at present; the discrepancy was thought to be too large in most cases to be due to loss of fragments of material but might partly be due to evolution of sulphur and halide. The expected weight loss due to evolution of hydroxyl can be calculated from the measured halide and sulphur content of the material, assuming that those sodalite cages not occupied by halide or sulphur originally contain an OH^- radical. From the particular sample from which Figs. 1(a), 1(b) and 2(b) were obtained the expected loss calculated this way is 1·10 per cent w/w, corresponding to 32 per cent of the cages containing OH^- radicals at an equivalent concentration of $1{\cdot}1 \times 10^{23}$/cc. This agrees reasonably well with the THA result (Fig. 2(b)) if the detection of one water molecule corresponds to the loss of one hydroxyl. The width of the 3635 cm^{-1} line recorded in Fig. 1(b) was limited by the spectrometer resolution. Subsequent measurements under a resolution of 1·2 cm^{-1} gave the true linewidth as 9·7 cm^{-1} and a peak absorption constant of 230 cm^{-1} (the accuracy of these figures may be as low as ±20 per cent due to various interpretational difficulties). From these measurements one can calculate an oscillator strength of $f \sim 5{\cdot}10^{-5}$, assuming that the total concentration of OH^- radicals contributes to this line, an assumption which may not be justified, as we shall discuss in the final paragraph of this section.

Since the photochromic response of sulphur-doped sodalite powders develops progressively as the firing temperature is raised from about 500 to 800°C, coinciding with the disappearance of the 3635 cm^{-1} hydroxyl peak, it seems likely that the sites at which the *F*-centres are formed are some of those originally occupied by OH^- radicals. This will be discussed further in a future publication.

As we have previously remarked, there is considerable similarity between the spectra of sodalites and of some zeolites, and a sharp line at ~3640 cm^{-1} is shown by Linde Molecular sieves *X* and *Y*. There are various opinions concerning the location of the hydroxyl groups responsible for this line; Angell and Schaffer[10] suggest the hydroxyl groups are formed from proton attack on surface oxygens, while Ward[11] considers that they are probably located in the zeolite supercages, close to the faces of six membered oxygen rings. It is generally agreed, however, that the OH groups are attached to silicon atoms. As with the 3635 cm^{-1} line in sodalites, this line is only removed by heat treatment above about 600°C. Such similarities suggest that the hydroxyl groups in these zeolites may also be located within the sodalite cages.

The sodalite single crystal spectra show a general increase in transmission over the range 3000 cm^{-1} to about 1400 cm^{-1} on firing, and this may also be due to loss of hydroxyl; the most noticeable difference is the loss of the broad band at 2650 cm^{-1}, which is in the known water-band region. The weak line at 2550 cm^{-1} is probably due to sulphur, since it does not occur in the spectra of undoped material. This line also disappears on firing. S–H vibrational lines are known to occur in this region, so there is possibly some substitution of SH^- for OH^- in sulphur-doped material. The several strong lines around 2000, 1700 and 1430 cm^{-1}, which are unaffected by firing, are due to vibrations of the aluminosilicate lattice, which will be discussed in the next section.

THE SPECTRA AT LONGER WAVELENGTHS, DOWN TO 400 cm^{-1}

Well defined and reproducible peaks occur in this region which are due to distortion vibrations of the aluminosilicate framework. The spectrum of a typical chlorosodalite is shown in Fig. 3(a); variation of the halide does not significantly effect this spectrum, but differences occur on substitution of other cations for Al and Si (Figs. 3(b), 3(c)).

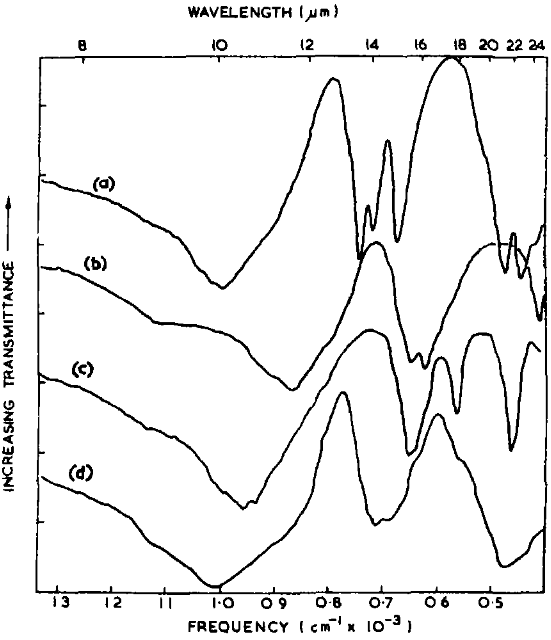

Fig. 3. KBr disc absorption spectra of (a) a typical chlorosodalite. (b) A chlorosodalite with Ge substituted for Si. (c) A chlorosodalite with Ga substituted for Al. (d) A hydroxysodalite fired at 800°C for 1 hr.

The standard firing procedure produces little observable change in these spectra, indicating that none of the bands are significantly perturbed by the presence of hydroxyl groups. However when a hydroxysodalite (containing no chlorine or sulphur) is fired there are marked changes in the spectrum (Fig. 3(d)), which is initially identical to that of a halide-containing sodalite. These differences result from collapse of the sodalite framework structure, and our X-ray diffraction analyses confirm that the product is a form of carnegieite. Thus it seems that the presence of an appreciable halide concentration in normal photochromic sodalite is essential to stabilize the lattice when the hydroxyl is removed. We have found that, in the absence of halide, similar concentrations of sulphur also prevent collapse.

As a consequence of the structural failure no *F*-centres can be generated in fired hydroxysodalites. However we find that an appreciable concentration of *F*-centres can be produced in such materials by firing them in such a way that only part of the OH content is removed, and the framework structure thus maintained.

The number of possible vibrations of this complex structure, in which the tetrahedrally co-ordinated SiO_4 and AlO_4 groups are linked by shared oxygens, is undoubtedly large, and detailed analysis is impossible at this stage. The band in the region of 1000 cm^{-1} is well-known in aluminosilicates[4, 12, 13] and thought to be due to stretching modes of the SiO_4 and AlO_4 groups; movement to lower frequencies on substitution of Ge for Si is consistent with this idea (Fig. 3(b)). The other bands in the spectrum down to 400 cm^{-1} may be more characteristic of the sodalite structure [4, 5] and it is thus reasonable that structural collapse affects these bands more, as has been noted above. However the striking similarity between the bands in the region of 700 cm^{-1} and bands in the spectra of various natural feldspars[14, 15, 16] suggests that the significant structural groups may not be those which uniquely characterize the sodalite structure.

Acknowledgements—The authors benefitted from the experimental assistance of C. R. Johnson and J. Lea, and are grateful to Dr. M. J. Payne for the high resolution measurements on the 3635 cm^{-1} line. This paper is published with the permission of the Controller, H. M. Stationery Office.

REFERENCES

1. HODGSON W. G., BRINEN J. S. and WILLIAMS E. F., *J. chem. Phys.* **47**, 3719 (1967).
2. WILLIAMS E. F., HODGSON W. G. and BRINEN J. S., *J. Am. ceram. Soc.* **52**, 139 (1969).
3. TAYLOR M. J., MARSHALL D. J., FORRESTER P. A. and McLAUGHLAN S. D. *Radio Electron. Eng.* **40**, July (1970).
4. MILKEY R. G., *Am. Mineral.* **45**, 990 (1960).
5. VIERNE R. and BRUNEL R., *Bull. Soc. Miner. Cristall.* **92**, 409 (1969).
6. AVDEEVA T. I. and VORSINA I. A., *Izv. Akad. Nauk SSSR Ser. Khim.* **10**, 2197 (1969).
7. BALLMAN A. A. and LAUDISE R. A., *Art and Science of Growing Crystals* (Edited by J. J. Gilman) p. 232. Wiley, New York (1965).
8. HERZBERG G., *Spectra of Diatomic Molecules* 2nd Ed., p. 506, D. Van Nostrand, Princeton, N.J. (1950).
9. WEDDING B. and KLEIN M. V., *Phys. Rev.* **177**, 1274 (1969).
10. ANGELL C. L. and SCHAFFER P. C., *J. Phys. Chem.* **69**, 3463 (1965).
11. WARD J. W., *J. Catal.* **9**, 396 (1967).
12. For example STUBICAN V. and ROY R., *Am. Mineral.* **46**, 32 (1961).
13. BELL R. J., BIRD N. F. and DEAN P., *Proc. Phys. Soc. (C), J. Phys.* **1**, 299 (1968).
14. EITEL W., *Silicate Science*, Vol. 1, p. 26, Academic Press, New York (1964).
15. LAVES F. and HAFNER ST., *Z. Kristallogr.* **108**, *52 (1956);* **109**, *204 (1957).*
16. THOMPSON C. S. and WADSWORTH M. E., *Am. Mineral.* **42**, 334 (1957).

J. Phys. Chem. Solids **Pergamon Press 1971. Vol. 32, pp. 2027–2032. Printed in Great Britain.**

BAND STRUCTURES OF GaN AND AlN

S. BLOOM
RCA Laboratories, Princeton, N. J. 08540, U.S.A.

(*Received* 28 *December* 1970)

Abstract – Pseudopotential band structures for GaN and AlN are calculated non-empirically by means of form factors synthesized from those of C, Ge and Ga in the case of GaN and from SiC and Al in the case of AlN. Good agreement with recent optical experiments is obtained for various gap energies.

1. INTRODUCTION

RECENT success[1] in the deposition of large, single-crystal films of GaN has spurred renewed experimental interest in this semiconductor. In particular, optical reflectivity measurements have been made up to 11 eV on both polycrystalline[2] and single-crystal [3] films, and the absorption edge has been studied[4]. This interest arises from the fact that this III–V compound has the large direct bandgap more commonly found in II–VI compounds but with, it is hoped, the easier dopability of the III–V systems. Thus GaN has potential usefulness for u.v. luminescent[5] devices and lasers. Similar considerations hold for the companion nitride, AlN, which has an even wider direct bandgap and, like GaN, has the hexagonal crystal structure. Room temperature optical absorption data [6, 7], have been taken on AlN single crystals and an OPW band structure has been estimated[8].

With new spectral data becoming available there is both the need and the opportunity for further band structure studies. In the present paper full-zone band structures for GaN and AlN are calculated by the pseudopotential method. However the commonly used empiricism, in which the form factors (Fourier transforms of the pseudopotential) are adjusted to force agreement with experimental bandgaps, is here avoided. Instead, the transferability property of the pseudopotentials of monatomic crystals is used; the form factors of GaN are synthesized from those of Ga and of the hypothetical IV–IV compound GeC, and the form factors of AlN are synthesized from those of Al and of SiC. Spin-orbit corrections[9] are neglected because of the lightness of the constituent elements.

2. METHOD AND CALCULATIONS

The pseudopotential method used here starts with that used by Bergstresser and Cohen in their well-known treatments of hexagonal[10] and cubic[11] binary compounds. The pseudopotential Hamiltonian

$$H = -(\hbar^2/2m)\nabla^2 + V(r) \qquad (1)$$

contains an effective potential which is expanded as a Fourier series in reciprocal lattice space. For binary compounds the expansion is written in two parts which are symmetric and antisymmetric with respect to interchange of the two atoms about their midpoint:

$$V(\mathbf{r}) = \sum_{G \leqslant G_0} [S^S(\mathbf{G})V_G{}^S + iS^A(\mathbf{G})V_G{}^A]e^{i\mathbf{G}\cdot\mathbf{r}}. \qquad (2)$$

The limited summation reflects the fact that the effective pseudopotential is sufficiently weak, because of cancellation between the kinetic and potential energies in the vicinity of atomic cores, that only a few Fourier terms suffice. The structure and form factors are given by[10]

$$S^S(\mathbf{G}) = \frac{1}{n}\sum_j e^{-i\mathbf{G}\cdot\boldsymbol{\delta}_j} \qquad (3)$$

$$S^A(\mathbf{G}) = -\frac{i}{n}\sum_j P_j e^{-i\mathbf{G}.\mathbf{a}_j} \tag{4}$$

$$V_G^{S,A}(12) = \frac{1}{\Omega_{12}}\int \frac{1}{2}[v_1(\mathbf{r}) \pm v_2(\mathbf{r})]_{12} e^{-i\mathbf{G}.\mathbf{r}} d^3\mathbf{r}. \tag{5}$$

This can be simplified through use of the transferability approximation for atomic pseudopotentials, as discussed by Phillips [12]. By writing

$$V_G(i) = \frac{1}{\Omega_i}\int v_i(\mathbf{r}) e^{-G.\mathbf{r}} d^3\mathbf{r}, \tag{6}$$

where Ω_i is the volume-per-atom of the monatomic solid consisting of atoms of type i, and by assuming that the atomic pseudopotential $v_i(\mathbf{r})$ is essentially independent of the particular crystalline environment of the atoms, (i.e., neglecting the dielectric screening at small G-values), we replace equation (5) by

$$V_G^{S,A}(12) = [\Omega_1 V_G(1) \pm \Omega_2 V_G(2)]/2\Omega_{12}. \tag{7}$$

The form factors for GaN are synthesized from the published form factors of C, Ge and Ga as follows. The symmetric form factors, V_G^S(GaN), are taken equal to those of the most closely corresponding IV–IV compound, GeC. This hypothetical cubic system would have essentially the same nearest-neighbor distance ($d = \bar{a}_{\text{cub}}\sqrt{\frac{3}{16}} = 2{\cdot}00$ Å, for a mean lattice constant $\bar{a}_{\text{cub}} = 4{\cdot}61$ Å) as has wurtzite GaN ($d = a_{\text{hex}}\sqrt{\frac{3}{8}} = 1{\cdot}95$ Å, for $a_{\text{hex}} = 3{\cdot}19$ Å). Silicon is not the appropriate choice since its nearest-neighbor separation is $d = 2{\cdot}36$ Å. The form factors for GeC are compounded graphically from a volume-weighted average of those of diamond [13] ($a_{\text{cub}} = 3{\cdot}57$ Å) and of germanium [11] ($a_{\text{cub}} = 5{\cdot}66$ Å):

$$V(\text{GeC}) = [(3{\cdot}57/4{\cdot}61)^3 V(C) + (5{\cdot}66/4{\cdot}61)^3 V(\text{Ge})]/2.$$

This is shown in Fig. 1 as V^S(GaN). The antisymmetric form factors of GaN are then obtained from equation (7); thus

$$V^A(\text{GaN}) = (\Omega_{\text{Ga}}/\Omega_{\text{GaN}})V(\text{Ga}) - V^S(\text{GaN}), \tag{8}$$

where the volumes-per-atom are $\Omega_{\text{Ga}} = 131{\cdot}4$ and $\Omega_{\text{GaN}} = 77{\cdot}3$ a.u. The gallium form factors shown in Fig. 1 are the '$V6$' values of Inglesfield [14].

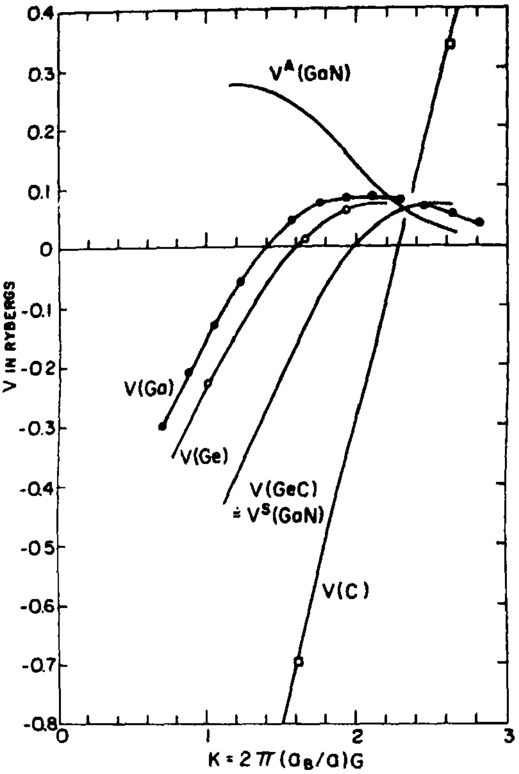

Fig. 1. Form factors for GaN, as calculated from published values for Ga, Ge and C, vs. the reciprocal lattice vector normalized with the appropriate cubic lattice constant.

The values of $V_G^{S,A}$ for 'cubic' GaN, as determined above and plotted in Fig. 1, are replotted vs. G^2 in Fig. 3. This latter figure is then used at those values of G^2 appropriate to the actual wurtzite structure, as discussed in Ref. [10].

A similar procedure is used for AlN. However now the corresponding IV–IV system is the real compound, SiC. This has a nearest neighbor distance of d = 1·88 Å, based on $a_{\text{cub}} = 4{\cdot}35$ Å, while wurtzite AlN, with $a_{\text{hex}} = 3{\cdot}10$ Å has d = 1·89 Å. The volumes-per-atom being essentially equal, the symmetric form factors V^S(AlN) can be taken equal to the published values[13] for V(SiC); these are shown in Fig. 2. Then equation (7) gives the antisymmetric values

$$V^A(\text{AlN}) = (\Omega_{\text{Al}}/\Omega_{\text{AlN}})\,V(\text{Al}) - V^S(\text{AlN}),$$

where the volumes-per-atom are $\Omega_{\text{Al}} = 111{\cdot}3$ a.u. and $\Omega_{\text{AlN}} = 69{\cdot}7$ a.u., and the aluminum form factors are from Animalu and Heine[15]. The $V^{S,A}$(AlN) values are replotted vs. G^2 in Fig. 3, for use at the wurtzite values of G^2.

The computer calculation follows that of Ref. [10]. The ratio of the wurtzite lattice constants is given its ideal value $c/a = \sqrt{8/3} = 1{\cdot}633$, which is an approximation since the actual values are $c/a = 5{\cdot}185/3{\cdot}189 = 1{\cdot}625$ for GaN[1], and $c/a = 4{\cdot}96/3{\cdot}10 = 1{\cdot}60$ for AlN[16]. The structure factors of equations (3) and (4) for wurtzite are $S^S(\mathbf{G}) = \cos[2\pi(l/6 + m/6 + n/4)]\cos(\tau n u)$ and $S^A(\mathbf{G}) = \cos[2\pi(l/6 + m/6 + n/4)]\sin(\pi n u)$, where the reciprocal lattice vectors are $\mathbf{G} = 2\pi(l\mathbf{a}^* + m\mathbf{b}^* + n\mathbf{c}^*)$, in terms of the primitive translation vectors. Again, the ideal value of the wurtzite parameter, $u = \frac{3}{8}$, is used. The form and structure factors are given in Table 1, at the ideal wurtzite values of G. As in Ref. [10], all plane waves having energies $|\mathbf{G} + \mathbf{k}|^2 \leq 10$ eV form the basis set of the Hamiltonian matrix, and waves of energy $10 < |\mathbf{G} + \mathbf{k}|^2 \leq 27$ eV form the perturbation set.

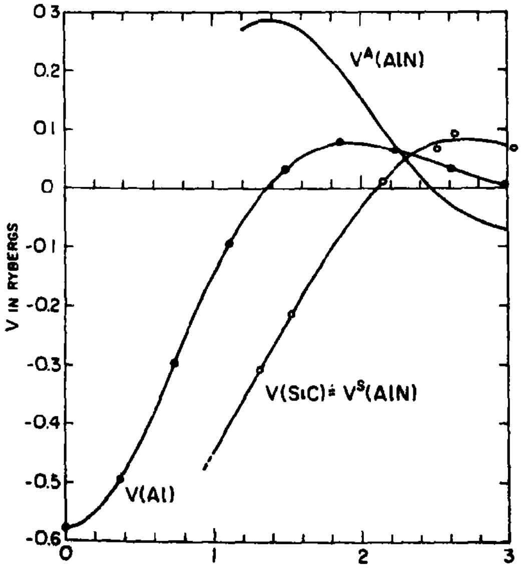

Fig. 2. Form factors for AlN, as calculated from published values for Al and cubic SiC.

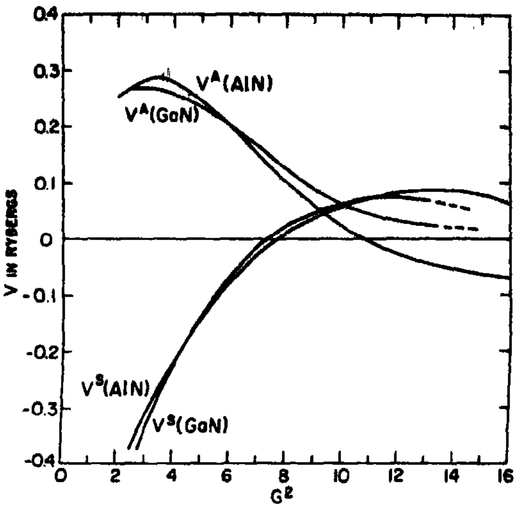

Fig. 3. Form factors for GaN and AlN vs. Square of reciprocal lattice vector.

3. RESULTS

The calculated band structures are shown in Figs. 4 and 5. In both compounds we find the Γ_1 to be higher than the Γ_6 valence band edge. For GaN, the fundamental, direct bandgaps are calculated to be 3·5 eV (∥) and 3·7 eV (⊥). The average agrees well with the various room-temperature experimental bandgaps of 3·4 eV[1], 3·5 eV[4], 3·6 eV[3] and 3·8 eV[2]. The bandgap calculated in the dielectric two-band model[17] is 4·8 eV. We calculate the $E_1 = \Gamma_{5v} \rightarrow \Gamma_{3c}$

Table 1. Wurtzite reciprocal lattice vectors, structure factors and form factors (in Ry*) for* GaN *and* AlN

G	G^2	$\|S^S(G)\|$	$\|S^A(G)\|$	GaN V^S	GaN V^A	AlN V^S	AlN V^A
000	0	1	0				
001	¾	0	0				
100	2−⅔	½	0	−0·38		−0·34	
002	3	0·71	0·71	−0·34	0·27	−0·31	0·28
101	3−5/12	0·33	0·80	−0·29	0·26	−0·27	0·28
102	5−⅔	0·35	0·35	−0·09	0·21	−0·09	0·22
003	6−¾	0	0				
210	8	1	0	0·02		0·01	
211	8−¾	0	0				
103	9−5/12	0·80	0·33	0·05	0·07	0·04	0·05
200	10−⅔	½	0	0·07		0·07	
212	11	0·71	0·71	0·07	0·04	0·07	−0·01
201	11−5/12	0·33	0·80	0·07	0·03	0·08	−0·02
004	12	0·00	1·00		0·03		−0·03
202	13−⅔	0·35	0·35	0·06	0·02	0·09	−0·05
104	14−⅔	0·00	0·50		0·01		−0·06
213	14−¾	0	0				

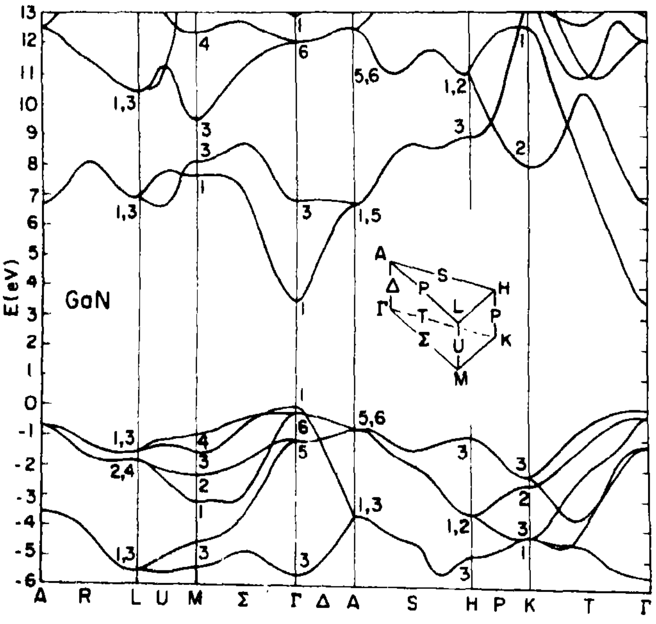

Fig. 4. Band structure of GaN. The numbers along the bands at the various symmetry points denote the irreducible representations of the particular point groups.

gap to be 7·9 eV, compared to 7·0 eV by Van Vechten; experimentally, Kosicki[2] sees a reflectivity peak near 6·8 eV whereas Harbeke[3] sees one at 7·2 at room temperature.

Reflectivity peaks are also measured at 9·5 and 10·7 eV. This calculation would assign the 9·5 eV peak to transitions near symmetry points *M* and/or *H*, rather than near Γ for

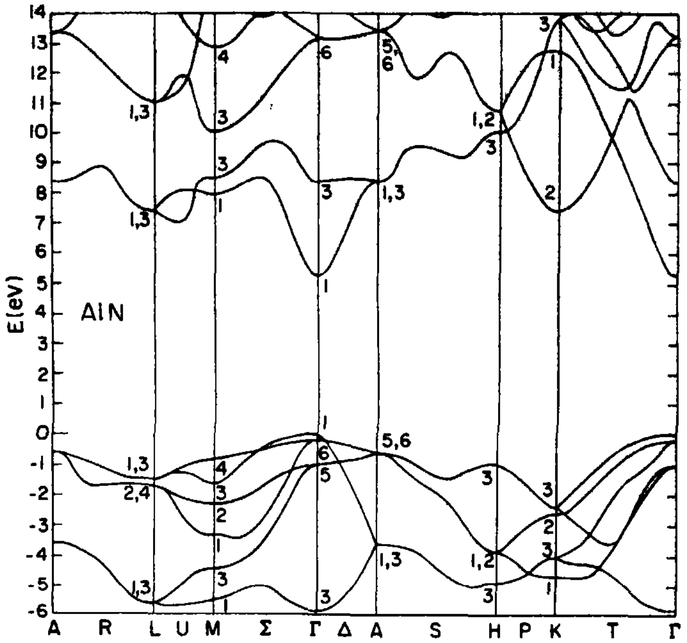

Fig. 5. Band structure of AlN.

which $E_0' = \Gamma_{1,6v} \rightarrow \Gamma_{1,6c}$ is over 12 eV here, although it is only 9·08 eV in the dielectric model[17]. The 10·7 eV peak corresponds to a calculated value at point K of $E_{2B} = K_{2v} \rightarrow K_{2c} = 10{\cdot}5$ eV, in agreement also with Van Vechten's[17] value of 10·96 eV. Other values calculated here are $E_{2A} = K_{3v} \rightarrow K_{2c} = 10{\cdot}2$, $E_1' = \Gamma_{5v} \rightarrow \Gamma_{6c} = 13{\cdot}3$, $E_{\mathrm{Ind}X} = \Gamma_{1v} \rightarrow H_{3c} =$ 8·9 eV; the dielectric model[17] values are 9·9, 12·2 and 6·4 eV, respectively. The calculated valence band is 23·2 eV wide, (the lowest band is not shown in Figs. 4 and 5).

For AlN the top of the valence band again has Γ_1 above Γ_6, the calculated bandgaps being 5·25 eV (‖) and 5·4 eV (⊥), in essential agreement with room temperature absorption data[6] of 5·74 eV (‖) and 5·88 eV (⊥). Thus both the ordering and the crystal-field splitting of 0·15 eV agree with experiment. The dielectric model[17] yields a value for this gap as high as 10·4 eV and Hejda's OPW calculation[8] gives a gap of only 2·4 eV, although Hejda, too, finds Γ_{1v} to be 0·15 eV above Γ_{6v}. Although the ordering and splitting of the $\Gamma_{1v,6v}$ bands agree with experiment for AlN, this is evidentally not so for GaN [3, 18]. However, not too much importance should be attached to this calculated ordering in either case; a slight empirical adjustment in one, or at most two, critical form factor is enough to re-order these two valence bands without affecting the other bands significantly. In fact Γ_{1v} is the most sensitive of all bands to form factor changes. With Γ_{6v} above Γ_{1v}, the band structure of GaN would have the connectivity of that of ZnS [10]. Other values calculated here for AlN are $E_1 = 9{\cdot}3$, $E_{2A} = 9{\cdot}8$, $E_{2B} = 10{\cdot}0$, $E_1' = 14{\cdot}2$ and $E_{\mathrm{Ind}X} = 10{\cdot}0$ eV; the dielectric model[17] gives 9·3, 10·0, 11·0, 12·2 and 8·4 eV, respectively. The valence band is calculated to be 22·1 eV wide, in essential agreement with Hejda's value of 20 eV.

It is of interest to note that form factors for nitrogen can be estimated through the use of the present results in the equation $\Omega_N V(N) = \Omega_{\mathrm{GaN}}[V^S(\mathrm{GaN}) - V^A(\mathrm{GaN})]$, or in the similar AlN equation. We find $\Omega_N V(N) = -36{\cdot}0, 0{\cdot}0,$

3·0 Ry via GaN, and $\Omega_N V(N) = -35{\cdot}5, 0{\cdot}0, 5{\cdot}2$ Ry via AlN, at points $K = 1{\cdot}5, 2{\cdot}3$ and $2{\cdot}5$ respectively, which is the important range for K. The agreement is a measure of the internal consistency.

Acknowledgements–The author is grateful to T. K. Bergstresser, J. Pankove and G. Harbeke for helpful discussions.

REFERENCES

1. MARUSKA H. P. and TIETJEN J. J., *Appl. Phys. Lett.* **15**, 327 (1969).
2. KOSICKI B. B., POWELL R J. and BURGIEL J. C., *Phys. Rev. Lett.* **24**, 1421 (1970).
3. HARBEKE G. and MEIER E. (unpublished).
4. PANKOVE J. I., MARUSKA H. P. and BERKEYHEISER J. E., *Appl. Phys. Lett.* **17**, 197 (1970).
5. PANKOVE J. I., BERKEYHEISER J. E., MARUSKA H P. and WITTKE J. P., *Solid State Commun.* **8**, 1051 (1970).
6. PASTERNAK J. and ROSKOVCOVA L., *Phys. Status Solidi* **26**, 591 (1968).
7. COX G. A., CUMMINS D. O., KAWABE K. and TREDGOLD R. H., *J. Phys. Chem. Solids* **28**, 543 (1967). Also, YIM W. M., STOFKO E. J., ETTENBERG M. and GILBERT S. L. (to be published).
8. HEJDA B., *Phys. Status Solidi* **32**, 407 (1969).
9. BLOOM S. and BERGSTRESSER T. K., *Phys. Status Solidi* **41**, 1 (1970).
10. BERGSTRESSER T. K. and COHEN M. L., *Phys. Rev.* **164**, 1069 (1967).
11. COHEN M. L. and BERGSTRESSER T. K., *Phys. Rev.* **141**, 789 (1966).
12. PHILLIPS J. C., *J. phys. Soc. Japan* **21** (supp.), 3 (1966).
13. JUNGINGER H. -G., van HAERINGEN W., *Phys. Status Solidi* **37**, 709 (1970).
14. INGLESFIELD J. E., *J. Phys. C. (Proc. Phys. Soc.)* **1**, 1337 (1968).
15. ANIMALU A. O. E. and HEINE V., *Phil. Mag.* **12**, 1249 (1965). Also, HARRISON W. A., *Pseudopotentials in the Theory of Metals*, Table 8–4, W. A. Benjamin, New York (1966).
16. JEFFREY G. A. and PARRY G. S., *J. chem. Phys.* **23**, 406 (1955).
17. VAN VECHTEN J. A., *Phys. Rev.* **187**, 1007 (1969).
18. DINGLE R., SELL D. D., STOKOWSKI S. E., DEAN P. J. and ZETERSTROM R. B., *Phys. Rev.* (to be published). *Note added in proof*: A small adjustment of a single GaN form factor, $V^s(103)$, from the value of 0·05–0·06 Ry has subsequently been made, as suggested in Section 3. This was found sufficient to put Γ_{6v} *above* Γ_{1v} (by 0·11 eV), in agreement with experiments. The bandgap values that result are now 3·7 eV (⊥) and 3·8 eV (∥R); the other energy differences throughout the zone are unchanged to within 0·1eV, and the K_{3v}, K_{2v} bands reverse positions.

J. Phys. Chem. Solids Pergamon Press 1971. Vol. 32, pp. 2033–2044. Printed in Great Britain.

INVESTIGATION OF THE OPTICAL PROPERTIES OF Ag BY MEANS OF THIN SEMI-TRANSPARENT FILMS

MARIE-MARTINE DUJARDIN and MARIE-LUCE THEYE
Institut d'Optique et Laboratoire d'Optique, Faculté des Sciences, Paris, France

(*Received* 22 *September* 1970; *in revised form* 22 *December* 1970)

Abstract—The optical constants of thin Ag films are determined from measurements of both their transmittance and reflectance. The complex dielectric constant is discussed in terms of intra and inter-band transitions, in relation with the film crystallographic structure. The optical mass of the conduction electrons is found to be very low, 0·87; their optical relaxation time to depend strongly on the film structure and to be smaller than their electrical relaxation time. The absorption due to interband transitions is considered. A supplementary absorption band related to film imperfections is observed in some cases. Plasma oscillations are also studied in relation with the film quality.

1. INTRODUCTION

AN INVESTIGATION of the influence of structural defects on the optical and electrical properties of thin metallic films presents a great interest from both fundamental and practical points of view. This is particularly true for Ag films, the properties of which often proved to be somewhat different from the bulk properties[1]. The interest in Ag films recently increased through studies of radiative and non-radiative surface plasmons and their excitation by light [2], the interpretation of the experimental results requiring an accurate knowledge of the optical constants of the films under investigation. On the other hand, detailed energy band computations were recently carried out for Ag[3–10] and allow a better identification of interband transitions which participate in optical absorption.

This paper presents an attempt at studying the optical properties of thin semi-transparent Ag films in a wide spectral range, in relation with the conditions of preparation and the crystallographic structure of these films. Section 2 describes the experimental procedures and Section 3 briefly comments on the results of structural studies by electron microscopy essentially. In Section 4, the optical data are discussed in terms of intra- and interband transitions. Plasma oscillations are also examined through the optical dielectric constant.

Further experimental results on d.c. electrical measurements and more thorough structural studies performed on Ag films deposited in ultra-high vacuum will be presented elsewhere[11].

2. EXPERIMENT

The Ag films under investigation were thin semi-transparent films with thicknesses ranging from 150 to 650 Å. They were deposited by evaporation of bulk (99·9% purity) Ag from tungsten boats in an improved oil diffusion pumped system (ultimate pressure: $2\cdot10^{-8}$ torr; pressure during evaporation: $5\cdot10^{-7}$ to 10^{-6} torr). The amorphous substrates (fused silica) were optically polished up to a supersmooth finish, then carefully chemically cleaned; some of them were submitted to a slight ionic cleaning, all were outgased by heating under vacuum. All the films investigated here were deposited on substrates at room temperature, as the vacuum system did not allow to solve the contamination problems arising during deposition at low temperature. Different deposition rates, from 10 to 200 Å/s, were tested. After their deposition, the films were annealed in the same vacuum (a few

10^{-7} torr), the annealing process being controlled by simultaneous measurements of the d.c. electrical resistance by a four point method[11].

The optical measurements were performed in air, as rapidly as possible, on a Cary 14 spectrophotometer fitted with a *V-W* absolute reflectance attachment. Both the transmittance T and reflectance R of the films at normal incidence were measured from 0·2 to 2·5 μ (6·2 to 0·5 eV). The real (n) and imaginary (k) parts of the complex index could thus be computed at each wavelength, provided that the film thickness d was known independently. This was achieved by using a method based on interference between X-rays reflected at grazing incidence on the two film surfaces [12, 13]. As this method is insensitive to the film structure and requires only flat and smooth parallel surfaces, its accuracy was very good, better than 1 per cent, in all cases.

This method of determining n and k from R and T is direct and accurate in general[14]; the results are exactly corrected for multiple reflections inside the transparent substrate, by successive approximations. However, it has been shown[15–18] that, for some combinations of n, k and d/λ, experimental errors on R and T have a very critical influence on the determination of n and k (especially of n). For this reason, for most of the Ag films, it was impossible to find any solution (n, k) corresponding to the experimental data (R, T) between 4 and 4·5 eV. As this spectral region precisely corresponds to the onset of interband transitions, any interpolation was difficult. Therefore, another method of computing n and k was tried in this critical region. It consists in determining n, k and d from R, T and δ_R (or R, T and δ_T) at three consecutive wavelengths, the phase changes δ_R and δ_T being related to the experimental R and T respectively by the Kramers-Kronig dispersion relations[19]. This method gives results in close agreement with those of the usual (R, T) method outside the critical region.

3. FILM STRUCTURE

The crystallographic structure of the Ag films was thoroughly investigated by means of X-ray and electron diffraction, and electron microscopy. These films are polycrystalline but continuous (for thicknesses as low as 150 Å); they are monocrystalline in thickness.* The grains are approximately oriented with their (111) compact planes parallel to the substrate surface, but there is no preferred orientation in the plane of the film. The best films had large (0·2 to 2μ) crystallites almost free of defects but still containing dislocations, separated by small areas of small (500 to 2000 Å) crystallites presenting a large amount of twin crystals and stacking faults. (Fig. 1).

The size and orientation of the crystallites strongly depend on the conditions of the film preparation, as well as the nature and amount of defects. It has been shown[11] that the recrystallization of the films is very sensitive to the surface state of the substrates (temperature, defects...) and to the presence of impurities, and that its mechanism is rather complex. In the present experiments, regularly recrystallized films free from structural defects (especially twin crystals) could not be obtained; it was noticed that holes appeared in the films during annealing before the recrystallization was achieved.

However, these films proved to be suitable samples for optical studies, mainly because of the quality of their surfaces. Investigation of the X-ray interference fringes [20] showed that the two surfaces limiting the films were parallel, and as flat and smooth as the substrate surface. Replicas of free surfaces showed the additional presence of steps (only a few Å high) along grain boundaries and twin crystals. Optical measurements confirmed the great smoothness of the film surfaces. (see Section 4).

Superficial contamination is of some importance in Ag[21]. It was shown that the contamination, which appears as isolated round

---

*i.e. the grains have the same thickness as the film.

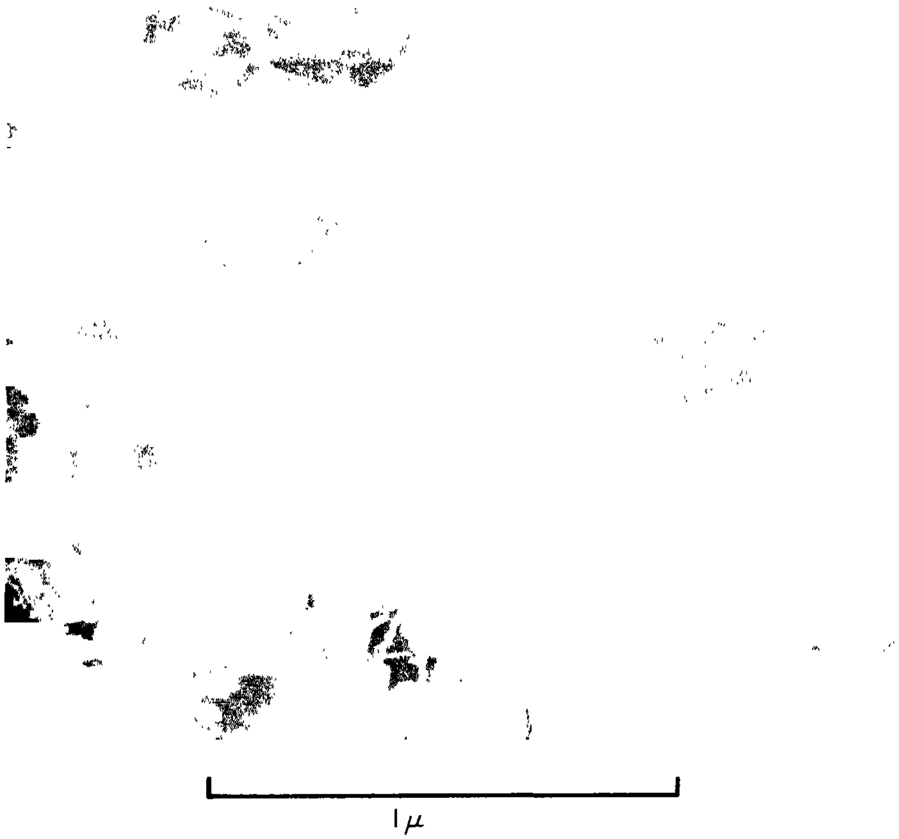

Fig. 1. Electron transmission micrograph of a 645 Å Ag film.

[*Facing page* 2034]

black spots on transmission micrographs, starts very slowly; it was practically nonexistent throughout the optical measurements. It was identified as cubic (α) Ag_2S, and shown to occur first along grain boundaries and twin crystals. After a few weeks, the contamination layer became continuous and the monoclinic phase of Ag_2S could be observed.

As mentioned above, the d.c. electrical resistivity ρ_e of the films was recorded during annealing in order to control the recrystallization process. The value at room temperature was used to give additional information on the conduction electrons. The best films in the present series of experiments had a resistivity close to 2 $\mu\Omega$cm when their thickness was larger than 300 Å; the resistivity increased when the thickness decreased (3 $\mu\Omega$cm for $d =$ 200 Å). The resistivity is of course very sensitive to the film structure. An interpretation of electrical data on Ag films in the framework of Fuchs' theory will be given elsewhere[11].

4. OPTICAL PROPERTIES

The mean values of n and k for well-crystallized Ag films from 0·2 to 0·6 μ are shown on Fig. 2, together with the data of Huebner *et al.*[1]. The uncertainty is a few per cent on n, 1 per cent on k. The present values are in qualitative agreement with those of Huebner *et al.*, but n is systematically larger. At higher wavelengths, where the optical properties are dominated by the conduction electrons, n and k vary with the film structure.

The discussion of the optical results will be conducted on the complex dielectric constant $\epsilon = \epsilon_1 + i\epsilon_2 = (n + ik)^2$. Different processes will be considered:

—at energies smaller than the onset of interband transitions $h\nu_t$, the absorption must be due to intraband transitions of the conduction electrons only. The results between 0·5 and 3·5 eV will be tentatively analysed along the lines of the Drude theory, possibly corrected for anomalous skin effect.

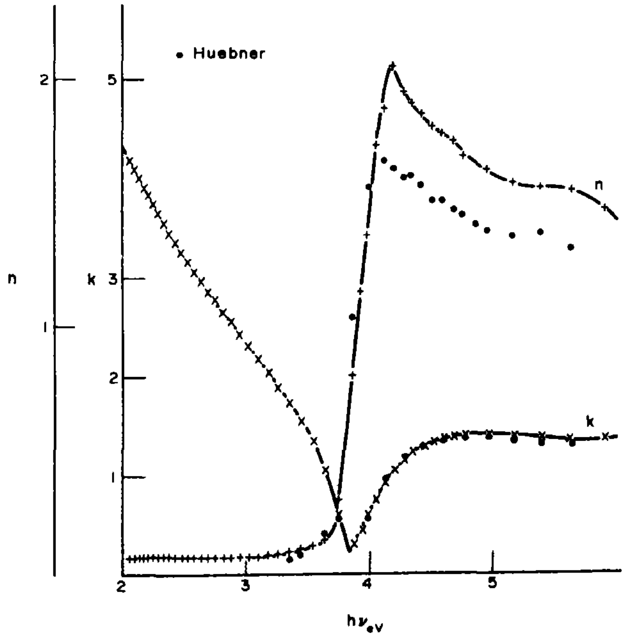

Fig. 2. Plot of n and k vs. energy for Ag films: (+) present work; (·) Huebner *et al.* (1964).

– at energies higher than $h\nu_i$, the absorption is also due to interband transitions. Their contribution to ϵ_2 is obtained by subtracting from the experimental value of ϵ_2 the contribution of intraband transitions computed through the Drude formula according to the analysis of the i.r. data.

– in some cases, an unexpected additional absorption is observed, which will be related to the presence of defects.

Although in the present experiments, plasma oscillations cannot be excited directly, information can be deduced from ϵ and from the energy loss function Im$(1/\epsilon)$.

It must be emphasized that the measured optical properties of the Ag films are not altered by any surface effect, like light scattering or surface excitations. In particular, except in the case of a few poorly crystallized films, direct excitation of surface plasmons with the help of surface roughness was never observed. Figure 3 shows $R(\lambda)$ for films of various thicknesses, and a curve $R_M(\lambda)$ which represents the reflectance of the corresponding bulk material, computed from the values of n and k for each film by:

$$R_M = \frac{(n-1)^2+k^2}{(n+1)^2+k^2}.$$

A reflectance curve obtained by Stanford *et al.*[22] on a rough opaque Ag film is also shown. No depression around 3500 Å can be seen on the present curves. Our very thin films are claimed to present the smoothest available Ag surfaces, even better than the surfaces of thick opaque films [23], in which the steps along grain boundaries grow higher.

4.1 *Intraband transitions*

The optical behaviour of the conduction electrons is characterized by two microscopic parameters: their optical effective mass m_0 and their optical relaxation time τ_0, or the corresponding wavelengths $\lambda_0 = (\pi m_0 c^2/Ne^2)^{1/2}$ (N is the number of conduction elec-

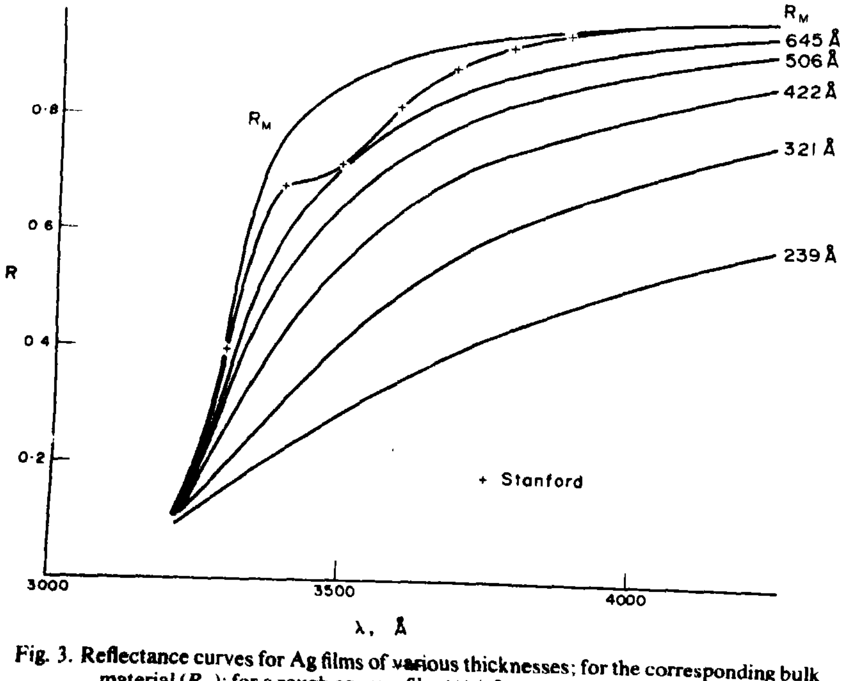

Fig. 3. Reflectance curves for Ag films of various thicknesses; for the corresponding bulk material (R_M); for a rough opaque film (+) (after Stanford *et al.* (1968)).

trons per unit volume, taken to be equal to the number of atoms per unit volume) and $\lambda_\tau = 2\pi c\tau_0$. As in the conditions of the experiments, $\omega\tau \gg 1$, the Drude relation can be written in the simple form:

$$\epsilon = P - \left(\frac{\lambda}{\lambda_0}\right)^2 + i\frac{\lambda^3}{\lambda_0^2\lambda_\tau} = \epsilon_1 + i\epsilon_2$$

(P being a constant polarization term). Such a behaviour of ϵ_1 and ϵ_2 in the i.r. was generally observed indeed; therefore, the ϵ_1 vs. λ^2 variation was used in order to determine m_0, then τ_0 was deduced from the variation of ϵ_2/λ vs. λ^2.

However, the experiments are performed in the conditions of anomalous skin effect: the penetration depth of the light δ and the film thickness d are of the same order of magnitude as the mean free path l. The interaction of light and electrons must then be reevaluated. It has been shown[24] that the value of m_0 deduced from the Drude analysis is still valid, but that the value of τ_0 must be corrected by a term which involves the scattering parameter p of the conduction electrons on the surfaces, and depends on the ratio d/δ. This corrective term vanishes when $p = 1$ (perfectly smooth surface); when $p \neq 1$ (partially scattering surface), the true relaxation time τ_0' (accounting for bulk scattering by phonons and defects only) is larger than the apparent Drude relaxation time, since part of the scattering is due to surfaces. Unfortunately, p is not known *a priori*. Therefore the analysis of the optical data in the i.r. cannot yield more than a relation between τ_0' and p.

For comparison with these optical results, a value of the electrical relaxation time τ_e was deduced for each film from the measured d.c. electrical resistivity at room temperature ρ_e, by means of the free-electron relation:

$$\tau_e = \frac{1}{\rho_e}\frac{m}{Ne^2}.$$

In this determination, m was taken to be equal to the bare electronic mass. As the film thickness d is of the same order of magnitude as the electron mean free path, this value of τ_e has to be corrected for size effects, by using the Fuchs' theory[11]. Here again, only a relation between the true electrical relaxation time τ_e' accounting for bulk scattering only and the scattering parameter p can be established by means of this theory.

We have however some idea of the value of p for our Ag films. Measurements of the film resistivity as a function of temperature were shown[11] to allow a determination of both p and the residual resistivity due to bulk defects only. p was found to be close to 0·5 for Ag films prepared in the same conditions (the only difference consisted in using an ion pumped ultra-high vacuum system) and having the same crystallographic structure as the films of the present work. The film surfaces are thus partially specular for the conduction electrons.

4.1.1 *Optical mass*. For most of the Ag films under investigation, it was found: $m_0 = 0{\cdot}87 \pm 0{\cdot}01$. This value was not very sensitive to the crystallographic structure of the films. No systematic variation with the film quality was observed, but the lowest values of m_0 were obtained for the best films.

The quoted value of m_0 is surprisingly low compared to either previous experimental values: 0·97[25], 1·03[26], or values computed from energy band calculations: 1·01[10], 0·95[7]. It is in closer agreement with the values recently determined for thick films by Hodgson[27]: $m_0 = 0{\cdot}89$ from internal reflection measurements, $m_0 = 0{\cdot}935$ from external reflection measurements. The same author found a similar discrepancy between internal and external reflection results for Au films[28], the lowest (internal) value of m_0 being also in close agreement with the value (0·94) obtained for thin semi-transparent Au films in experiments similar to those performed in the present work[29].

One may argue that the discrepancies between various experimental results come from differences in the sample structures, mainly in the sample surfaces, the quality of which is very important in experiments using reflection measurements only. The present value of m_0 is claimed to be valid since the film surfaces are very smooth indeed, and moreover since m_0 is mainly determined by the transmittance measurements. The presence of numerous structural defects in the films (grain boundaries, twin crystals...) does not seem to affect the value of m_0; according to the results obtained for Au, the defects would rather give rise to an enhancement of the optical mass[29].

The optical effective mass m_0 is related to an average of the electron velocity over the Fermi surface:

$$m_0^{-1} = \frac{1}{12\pi^3 N\hbar} \int v_F \, dS_F.$$

The Fermi surface of Ag departs markedly from a sphere in the (111) directions where it contacts the Brillouin zone boundaries[30–32]. The electron velocity, which is related to the gradient of energy in k space, varies on the Fermi surface. It is considerably lower on the 'necks' in the (111) directions than on the nearly spherical 'belly'; for example, from energy band calculations[10], the average Fermi velocities on the necks and on the belly are found to be $0{\cdot}8 \times 10^6$ and $1{\cdot}38 \times 10^6$ m/s respectively. A theoretical calculation of the optical mass ought therefore to take exactly into account both the shape of the Fermi surface and the distribution of electron velocity over the Fermi surface. The values of m_0 determined so far from energy band calculations are equal to or smaller than 1: $m_0 = 1{\cdot}01 \pm 0{\cdot}03$ (10); $m_0 = 0{\cdot}95 \pm 0{\cdot}05$ [7]. It is not unlikely that a more accurate knowledge of the Fermi surface properties in all directions of k space might lead to values of m_0 closer to our experimental value of 0·87. (A many-body enhancement of the optical mass, due to electron–electron and electron–phonon interaction, would not have to be considered, as it seems to be very small for Ag, of a few per cent only[10, 33]). It must also be reminded that our experimental value corresponds to films presenting a strong preferred orientation, the (111) planes being parallel to the film surfaces. This may affect the measured value of m_0, by making only limited areas of the Fermi surface 'effective' for the interaction of the electromagnetic field and the conduction electrons.

It seemed interesting to compare the optical effective mass m_0 to the thermal effective mass m_t, which is also related to an average of the electron velocity over the Fermi surface. One finds $m_t = 1{\cdot}01$ for Ag[34]. Therefore the thermal mass is greater than the optical mass, their ratio being equal to 1·16. According to simple arguments which do not take into account many-body effects (these effects, mainly the phonon-dressing, may modify appreciably m_t), one can write[35]:

$$\frac{m_t}{m_0} \propto \left(\frac{S_F}{S_F^0}\right)^2 \langle v_F \rangle_F \left\langle \frac{1}{v_F} \right\rangle_F$$

S_F^0 being the area of the sphere having the same volume as the actual Fermi surface of area S_F, and $\langle\,\rangle_F$ meaning the integral over the Fermi surface. The ratio m_t/m_0 thus depends on one hand on the distortion of the Fermi surface and its areas of contact with the Brillouin zone boundaries, on the other hand on the anisotropy of the Fermi velocity distribution. As S_F/S_F^0 is slightly smaller than 1[10], our result would confirm the strong anisotropy of the velocity distribution. It must be noticed that the value of the ratio m_t/m_0 determined for Au in similar experiments is of the same order as for Ag (1·16). This emphasizes the similarity between the properties of noble metals.

4.1.2 *Relaxation time.* The optical relaxation time τ_0 as deduced by means of the Drude formula was found to be extremely sensitive to the crystallographic structure of the film. It decreased drastically for poorly crystallized films with small grains and a large amount of defects, twin crystals and dislocations (especially for films deposited at low deposition rate or not annealed). A similar behaviour was observed for the electrical relaxation time τ_e; the variation of τ_e with film quality was however less important than the variation of τ_0.

As emphasized earlier, both true relaxation times, accounting for bulk scattering only, depend on the assumed value of the scattering parameter on the surfaces p, accounting for surface effects. From the analysis of the variation of the film resistivity with temperature[11], it seemed that the value of p was about the same (close to 0·5) independently of the film structure, which means that the reflection of the conduction electrons by the surfaces would remain partially specular even when the amount of defects inside the films increases. Therefore, grain boundaries and defects inside the grains, like twin crystals and dislocations, would play the major role in the decrease of τ_0 and τ_e when the film quality deteriorates.

For each film, the values of the optical and electrical relaxation times were compared. It was found that τ'_e was systematically larger than τ'_0, whatever the assumed value of p (between 0 and 1) might be; the ratio τ'_e/τ'_0 increased when the assumed value of p was increased. For example, for a 279 Å film:

$$(\lambda_\tau)_{\text{Drude}} = 33{\cdot}0\,\mu;\ \rho_e = 2{\cdot}34\,\mu\Omega\text{cm}$$

if $p = 1$, $\tau'_0 = 1{\cdot}75\times10^{-14}$ sec; $\tau'_e = 2{\cdot}47\times10^{-14}$ sec; $\tau'_e/\tau'_0 = 1{\cdot}41$

if $p = 0{\cdot}5$, $\tau'_0 = 2{\cdot}29\times10^{-14}$ sec; $\tau'_e = 3{\cdot}38\times10^{-14}$ sec; $\tau'_e/\tau'_0 = 1{\cdot}47$

if $p = 0$, $\tau'_0 = 3{\cdot}33\times10^{-14}$ sec; $\tau'_e = 5{\cdot}80\times10^{-14}$ sec; $\tau'_e/\tau'_0 = 1{\cdot}74$.

(It must be emphasized again that, in the analysis of the optical data, an effective electronic mass, equal to the optical mass deduced as explained in 4.1.1., was assumed, while in the analysis of the electrical data, the bare electronic mass was used).

For most films, assuming $p = 0{\cdot}5$, τ'_e/τ'_0 was comprised between 1·4 and 2. It was not possible to find a clear relation between these values and the film quality. A similar result was already obtained on bulk electropolished Ag samples [26] (surface effects were not taken into account): $\tau_0 = 1{\cdot}6\times10^{-14}$ sec; $\tau_e = 3{\cdot}7\times10^{-14}$ sec; $\tau_e/\tau_0 = 2{\cdot}3$. If the optical data are claimed not be modified by light scattering (either bulk – through inhomogeneities – or surface scattering), it must be deduced that the conduction electrons have different relaxation times when submitted to a static electric field and to a high frequency electromagnetic field.

It must however be noticed that the optical and electrical data give a direct measurement of the optical and electrical conductivities, and not of the corresponding relaxation times. These two conductivities involve different average values of the relaxation time over the Fermi surface. The discrepancy between the measured optical and electrical conductivities might thus simply be due to the anisotropy of the relaxation time over the Fermi surface [36], which would depend on the nature and amount of scattering defects in the films [29].

For some films, ϵ_2 did not exactly behave according to the Drude theory, but rather as:

$$\epsilon_2/\lambda = A\lambda^2 + B$$

B being a constant, the value of which was comprised between 0 and 1 μ^{-1}. The unexpected B term was also observed in thin Au films and was interpreted as showing a frequency dependence of the relaxation time, probably due to electron–electron interaction [29]. As in the case of Au films, the ratio of τ_e/τ_0 was found to be smaller (~ 1·2) for these films. But the presence of non-zero B term could not be definitely related to the poor structure of these films.

It was hoped that the study of Ag films, for which the onset of interband transitions occurs at high energy (~ 4 eV), (the optical properties being thus due to conduction electrons only up to high energies) could give more information about the optical behaviour of the conduction electrons, especially with respect to a possible variation of their relaxation time with frequency. Unfortunately, no definite interpretation can be deduced in this respect from the present work.

4.2 *Interband transitions*

Figure 4 shows the variation with energy of the total optical absorption ϵ_2/λ (1) in the interband transition range; the Drude contribution of intraband transitions (2) and the contribution of interband transitions only $\epsilon_2^{(i)}/\lambda$ (3) are also indicated (notice the constant term B). In general $\epsilon_2^{(i)}/\lambda$ does not depend on the film structure for $h\nu > 4$ eV, it is only slightly decreasing for films with very small grains (~ 500 Å).

4.2.1

The absorption edge is very steep and approximately linear with energy near the onset of interband transitions. The energy onset could thus be accurately determined:

$$h\nu_i = 3{\cdot}86 \pm 0{\cdot}01 \text{ eV}.$$

It does not depend on the film structure.

The difference in shape of the absorption edge of Au and Ag is very striking; it is more easily seen by comparing the quantities: $J(h\nu) = (h\nu)^2\epsilon_2^{(i)}$, which are proportional to the joint densities of states of Au and Ag (Fig. 5). In both cases, according to energy band calculations, the interband transitions of lowest energy are expected to occur from the top of the filled *d*-bands to the conduction band at the Fermi level in the vicinity of *L*. However, piezo-optical measurements on Ag single crystal[37] seem to show that transitions between conduction bands at L ($L_2 \rightarrow L_1$) also contribute at nearly the same energies in Ag, in agreement with the results of energy band calculations. Recent optical measure-

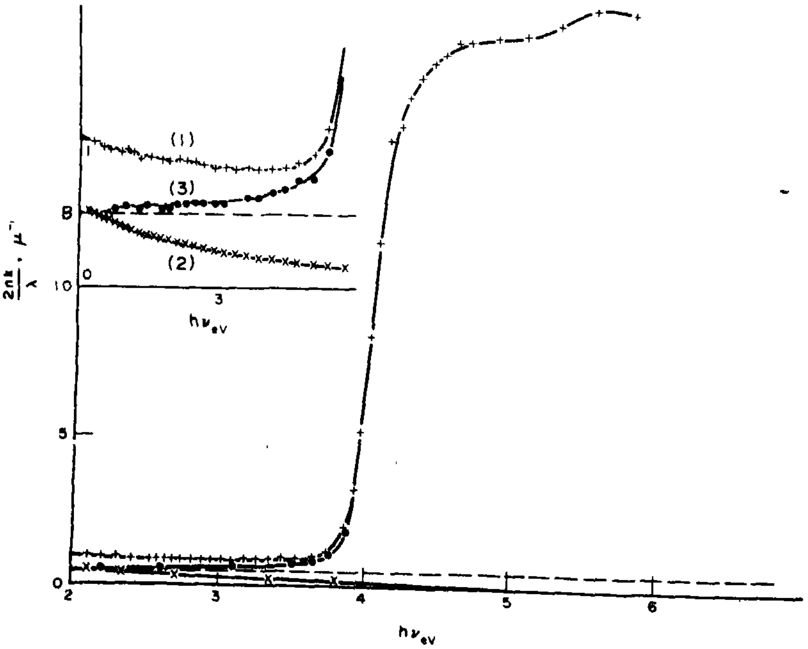

Fig. 4. Optical absorption for Ag film: (1) total; (2) due to intraband transitions (extrapolation); (3) due to interband transitions only.

ments as a function of temperature definitely prove the composite nature of the absorption edge in Ag; an absorption band probably due to $L_2 \rightarrow L_1$ transitions, which cannot be detected at room temperature, clearly separates and moves to lower energy on increasing temperature[38].

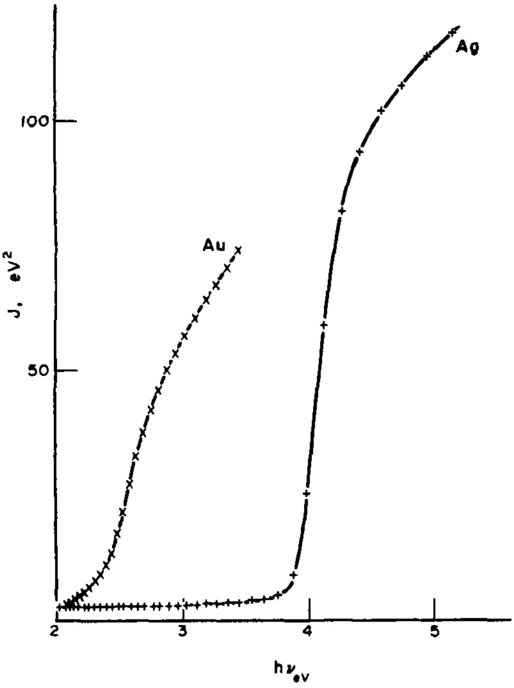

Fig. 5. $J(h\nu) = (h\nu)^2\epsilon_2^{(i)}$ for Au and Ag.

The present results are difficult to interpret in terms of precisely located interband transitions. The steepness of the edge could be related to some exciton-like effect between the excited electron and hole[37], or simply to the flatness of the *d*-band[40]. The bump observed in $\epsilon_2^{(i)}(\lambda)$ at about 5·6 eV cannot be due, as sometimes suggested, to transitions from the bottom of the *d*-band to the Fermi level, since the width of the *d*-band is approximately 3·5 eV[41]. According to energy band calculations, it would rather correspond to $X_5 \rightarrow X_4'$ transitions, which however are expected to be faint.

4.2.2

Below the onset of interband transitions, an absorption tail is observed, as shown in Fig. 4. This tail is approximately exponential, its intensity is smaller and it extends over a larger energy interval than in the case of Au[29]. It could be attributed to an Auger broadening of the absorption edge, due to the finite lifetime of the hole created at the top of the flat narrow *d*-band.

4.2.3

It must be emphasized again that, due to the smoothness of the film surfaces, for most films there is no excitation of surface plasmons: the ϵ_2 curves do not show the small bump at about 3·6 eV characteristic of this excitation [42].

4.3 *Supplementary absorption band*

For some poorly crystallized films, the optical absorption curves ϵ_2/λ display an anomalous bump at about 1·5 eV, as shown on Fig. 6. This supplementary absorption band, which is located well below the absorption edge, is always centered at approximately the same energy (1·5 eV) and its intensity increases with the amount of defects in the films. It must be related to the presence of some point defects or impurities, introducing localized energy levels. But an identification of these centers was not possible.

4.4 *Plasma oscillations*

Information on plasma oscillations can be gained from the optical dielectric constant. The plasmon frequency ω_p is such that:

$$\epsilon_1(\omega_p) = 0 \text{ with } \epsilon_2(\omega_p) \ll 1.$$

On the other hand, the energy loss function $\text{Im}(1/\epsilon) = \epsilon_2/\epsilon_1^2 + \epsilon_2^2$ must have a resonance peak at ω_p.

These conditions were simultaneously verified for all films at $\hbar\omega_p = 3{\cdot}77 \pm 0{\cdot}01$ eV, as shown on Fig. 7 for a 431 Å film ($\epsilon_2 \sim 0{\cdot}35$). This ω_p value is much smaller than the value

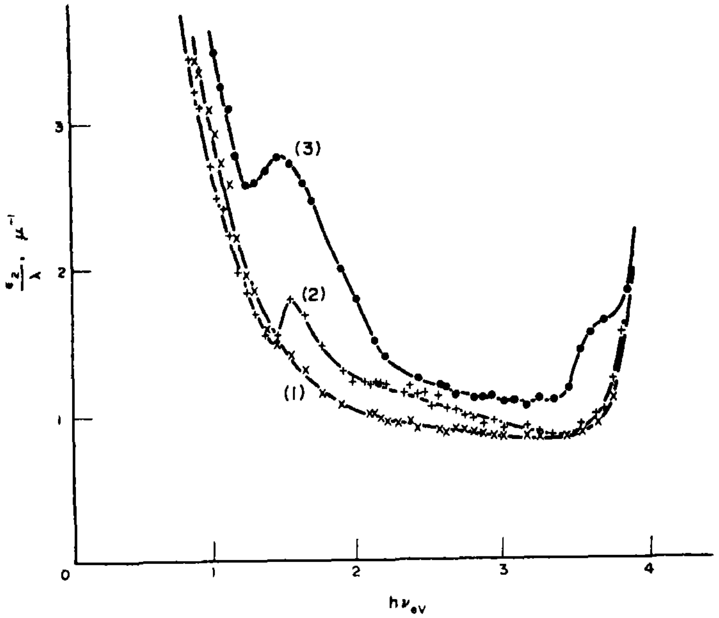

Fig. 6. ϵ_2/λ between 1 and 4 eV: (1) for a well crystallized film; (2) and (3) for poorly crystallized films, showing supplementary absorption bands.

which would correspond to a free electron gas of the same density as the conduction electron gas in Ag, $\omega_0(\hbar\omega_0 = 9{\cdot}2\text{ eV})$. This is due to the existence of interband transitions; these collective oscillations are rather due to a hybrid resonance of both *d* and *s–p* conduction electrons[36].

The width of the peak in $\text{Im}(1/\epsilon)$ is related to the damping of the conduction electrons, i.e. to $\epsilon_2(\omega_p)$. It was indeed observed that the width of the peak increased, while its intensity decreased drastically, for poorly crystallized films; at the same time, the value of ϵ_2 at ω_p (just below the absorption edge) increased. However, in contradistinction to the results of Schroeder[43], no variation of ω_p with the film structure was detected. Such a variation in Schroeder' *s* experiments could be due to a decrease of $\epsilon_2^{(i)}$ in the case of films with very small crystallites. Indeed, ϵ_1 can be written as follows:

$$\epsilon_1(\omega) = 1 + (\epsilon_a - 1) + \epsilon_1^{(i)} - \frac{\omega_0^2}{\omega^2}$$

where $(\epsilon_a - 1)$ accounts for the core polarization and $\epsilon_1^{(i)}$, the polarization term due to interband transitions, is related to $\epsilon_2^{(i)}$ by a Kramers–Kronig relation:

$$\epsilon_1^{(i)}(\omega) = \frac{2}{\pi}\int_0^\infty \frac{\omega'\epsilon_2^{(i)}(\omega')}{\omega'^2 - \omega^2}\,\mathrm{d}\omega'$$

ω_p satisfies $\epsilon_1^{(i)} = 0$ so that:

$$\omega_p = \frac{\omega_0}{(1 + (\epsilon_a - 1) + \epsilon_1^{(i)}(\omega_p))^{1/2}}.$$

If $\epsilon_2^{(i)}$ decreases, $\epsilon_1^{(i)}(\omega_p)$ decreases too, and ω_p increases.

5. CONCLUSION

The purpose of the present work was to determine the optical properties of thin Ag films and to investigate the influence of their crystallographic structure on these properties.

Obtaining well crystallized Ag films with large enough grains and a small amount of

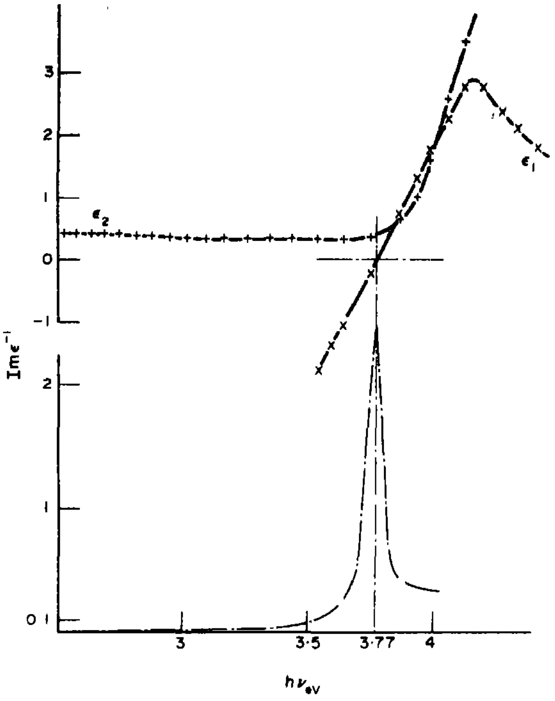

Fig. 7. ϵ_1, ϵ_2 and Im $(1/\epsilon)$ in the vicinity of the plasma frequency ω_p for a Ag film.

defects proved to be rather difficult. Improvements are expected from depositing the films in ultra-high vacuum at low temperature[11]. However, the film surfaces were certainly flatter and smoother than the surface of usual optical samples, which is important in order to prevent surface effects.

The optical results can be summarized as follows:

—a low value of the optical mass, independent of the film structure, was found: $m_0 = 0{\cdot}87$.

—the optical relaxation time strongly depends on the film structure, and is always smaller than the electrical relaxation time: $\tau_e/\tau_0 \sim 2$.

—the onset of interband transitions was accurately determined: $h\nu_i = 3{\cdot}86$ eV.

—in some cases a supplementary absorption band was observed, peaking at 1·5 eV, certainly related to the presence of impurity or defect centers.

—no displacement of the plasmon frequency ($\hbar\omega_p = 3{\cdot}77$ eV) with film structure was observed, only a damping of the resonance peak in Im$(1/\epsilon)$ for poor films.

Acknowledgements—The authors would like to thank Professor F. Abeles for his constant guidance and advices. They are indebted to Dr. M. Gandais who performed the electron microscopy studies and to V. Nguyen Van for his help in film preparation. Their thanks are also due to Dr. J. N. Hodgson for communicating his results on Ag films prior to publication. The research reported herein has been sponsored in part by the U.S. Department of the Army, through its European Research Office.

REFERENCES

1. HUEBNER R. H., ARAKAWA E. T., HAMM R. N. and MAC REA R. A. *J.O.S.A.* **54**, 1434 (1964).
2. RAETHER H., *J. Phys.* **31**, C1. 59 (1970).
3. SEGALL B., *G.E. Res. Lab. Report* 61 R.L. 2785 G (1961).
4. CHATTERJEE S. and SEN S. K., *Proc. Phys. Soc.* **91**, 749 (1967).
5. JACOBS R. L., *J. Phys. C.* (*Proc. Phys. Soc*) Ser. 2, **1**, 1296 (1968).
6. SNOW E. C., *Phys. Rev.* **172**, 708 (1968).
7. LEWIS P. E. and LEE P. M., *Phys. Rev.* **175**, 795. (1968).
8. BHATNAGAR S., *Phys. Rev.* **183**, 657 (1969).
9. BALLINGER R. A. and MARSHALL C. A. W., *J. Phys. C.* (*Solid State Phys.*) Ser. 2, **2**, 1822 (1969).
10. CHRISTENSEN N. E., *Phys. Status Solidi* **31**, 635 (1969).
11. NGUYEN VAN V., GANDAIS M. and DUJARDIN-COUZINEAU M. M., to be published.
12. KIESSIG H., *Ann. Phys.* **10**, 769 (1931).
13. UMRATH W., *Z. angew. Phys.* **22**, 406 (1967).
14. ABELES F. and THEYE M. L., *Surface Sci.* **5**, 325 (1966).
15. BAZIN C., *C.R.A.S.* **260**, 83 (1965).
16. GRANT P. M., *Technical Report N° HP 14*, Harvard University (1965).
17. NILSSON P. O., *Appl. Opt.* **7**, 435 (1968).
18. THEYE M. L., Thèse-Paris (1968).
19. FROISSART C., *Rev. Phys. Appl.* **4**, 397 (1969).
20. CROCE P., DEVANT G., SERE M. G. and VERHAEGHE M. F., *Surface. Sci.* **22**, 173 (1970).
21. BENNETT H. E., PECK R. L., BURGE D. K. and BENNETT J. M. *Phys. Rev.* **40**, 3351 (1969).
22. STANFORD J. L., BENNETT H. E., BENNETT J. M., ASHLEY E. J. and ARAKAWA E. T., *Bull. Am. Phys. Soc; Ser. 2.* **13**, 989 (1968).
23. BENNETT H. E., BENNETT J. M., ASHLEY E. J. and MOTYKA R. J., *Phys. Rev.* **165**, 755 (1968).
24. THEYE M. L., *Phys. Lett.* **25A**, 764 (1967).
25. SCHULZ L. G., *J.O.S.A.* **44**, 540 (1954).
26. ENRENREICH H. and PHILIPP H. R. *Phys. Rev.* **128**, 1622 (1962).
27. HODGSON J. N., Private communication (1970).
28. HODGSON J. N., *J. Phys. Chem. Solids* **29**, 2175 (1968).

29. THEYE M. L., *Phys. Rev.* **B2**, 3060 (1970).
30. SHOENBERG D., *Phil. Mag.* **5**, 105 (1960).
31. ROAF D. J., *Phil. Trans. Roy. Soc. (London)* **255**, 135 (1962).
32. BOHM H. V. and EASTERLING V. J., *Phys. Rev.* **128**, 1026 (1962).
33. O'SULLIVAN W. J., SWITENDICK A. C. and SCHIRBER J. E. to be published.
34. MARTIN D. L., *Phys. Rev.* **170**, 650 (1968).
35. COHEN M. H., *Phil. Mag.* **3**, 762 (1958).
36. RAYNE J. A., *Phys. Rev. Lett.* **3**, 512 (1959).
37. NILSSON P. O. and SANDELL B., *Solid State Commun.* **8**, 721 (1970).
38. LILJENVALL H. G. and MATHEWSON A. G., Chalmers University Report GIPR-031, Gothenburg (1970).
39. MAHAN G. D., *Phys. Rev. Lett.* **18**, 448 (1967).
40. EHRENREICH H., In *Optical properties and electronic structure of metals and alloys* p. 109 (Edited by F. Abeles), North Holland publishing Co, Amsterdam (1966).
41. EASTMAN D. E. and CASHION J. K., *Phys. Rev. Lett.* **24**, 310 (1970).
42. JASPERSON S. N. and SCHNATTERLY S. E., *Phys. Rev.* **188**, 759 (1969).
43. SCHRÖDER E., *Z. Phys.* **222**, 33 (1969).

J. Phys. Chem. Solids Pergamon Press 1971. Vol. 32, pp. 2045–2052. Printed in Great Britain.

RESONANCE ELECTRONIQUE DANS LE LITHIUM LIQUIDE

C. TAUPIN, M. LAMBERT et Ch. MAZIERES*
Laboratoire de Physique des Solides, Associé au C.N.R.S., Faculté des Sciences, 91, Orsay, France

(*Received* 22 *September* 1970; *in revised form* 21 *December* 1970)

Résumé – Les cristallites de lithium formés par irradiation aux neutrons thermiques dans le fluorure de lithium sont utilisés comme échantillons très purs de lithium. La variation thermique du spectre R.P.E., étudiée de l'ambiante à 300°C, montre que la fusion s'accompagne d'un élargissement des raies de 0,2 G. D'autre part, la largeur de raie augmente très rapidement avec la température dans la phase liquide. On discute des divers mécanismes de relaxation possibles expliquant les élargissements observés.

Abstract – Relaxation time measurements have been made on samples of *n*-irradiated lithium fluoride, which contain very pure particles of lithium metal. Thermal variation of C.E.S.R. line-width exhibits a broadening of 0·2 G at the melting point. In liquid state line-width increases very rapidly with temperature. These results are different from the results obtained by others on sodium. Several relaxation process are discussed.

INTRODUCTION

Ce sont les alcalins légers (Li, Na, K) qui, historiquement, ont permis la mise en évidence de la R.P.E. des électrons de conduction. Dans le cas de ces métaux simples, pour lesquels les temps de relaxation longitudinal et transverse sont égaux ($T_1 = T_2$), deux grandeurs physiques sont intéressantes: le temps de relaxation spin-réseau T_1 et le 'g-shift'. Dans le cas du lithium, la détermination du g-shift pose de nombreux problèmes, tant au point de vue théorique[2, 24], qu'expérimental[1, 23]. Ce travail se propose d'étudier le T_1, c'est à dire les mécanismes qui établissent le contact thermique entre le système de spins électroniques et le réseau.

Plusieurs études théoriques, antérieures aux expériences, ont traité ce problème[3, 4]. La plupart des mécanismes envisagés pour la relaxation de spin conduisent à des temps T_1 relativement longs pour le lithium ($T_1 > 10^{-6}\,s$).

L'étude expérimentale s'est faite en plusieurs étapes directement reliées aux progres réalisés dans la préparation du métal; alors que les premières études[5] ont montré que les impuretés déterminaient la relaxation, un travail plus récent[6] a prouvé l'existence d'une relaxation par la surface dans le cas de particules de lithium très pures et très fines (quelques centaines d'Å).

Or il existe des échantillons de lithium particulièrement purs: les amas métalliques qui précipitent au sein de cristaux de LiF fortement irradiés aux neutrons thermiques[7]. La résonance électronique de ces amas est connue depuis longtemps[8] et a déjà permis d'obtenir diverses informations:

– valeur de la probablité de présence de l'électron sur le noyau Li^7 par des expériences d'effet Overhauser[8]: le rapport de cette probablité sur un noyau métallique à la probablité sur un atome neutre est de 0,44.

– mise en évidence par Watts et Cousins de plusieurs mécanismes de relaxation dans la phase solide par l'étude de la variation thermique de T_1[9]. Ces auteurs distinguent trois termes: ΔH_{int} intrinsèque du lithium et linéaire en fonction de la température, ΔH_s lié à la relaxation superficielle, indépendant de la température à haute température et qui augmente à basse température lorsque le libre parcours moyen devient de l'ordre de grandeur des dimensions de la particule, ΔH_c lié aux défauts et impuretés fixes et indépendant de la température. Alors que ΔH_{int} est identique pour tous les cristallites, ΔH_s et ΔH_c sont très variables suivant l'échantillon.

---

*Laboratoire de Physico-Chimie Minérale, Faculté des Sciences, 91, Orsay, France.

La variation thermique de ces divers termes est rappelée sur la Fig. 1, reproduite de l'article de Watts et Cousins.

Toutefois, pour ces échantillons, se pose un problème d'identification des spectres car plusieurs types de défauts agglomérés coexistent après l'irradiation. Ces défauts sont essentiellement de deux sortes:

(1°) les plaquettes à deux dimensions formées de un ou deux plans atomiques de Li, parallèles aux plans {100} et dont les dimensions latérales varient autour de quelques dizaines d'Å.

(2°) les cristallites de lithium, de plusieurs centaines d'Å de côté et de structure définie c.f.c. (structure anormale) soit c.c. (structure normale). Par contre, leurs dimensions varient au sein d'un même échantillon.

Ces problèmes liés à l'inhomogénéité des échantillons, tant au point de vue de la nature des défauts que de leurs dimensions, peuvent néamoins être résolus grâce à des traitements thermiques appropriés des cristaux irradiés.

En effet ces divers amas évoluent par recuit. Une étude simultanée par plusieurs techniques[10, 13], en particulier diffusion des rayons X, μA.T.D. (microanalyse thermique différentielle) et R.P.E., a montré qu'après une phase de recristallisation (150°C à 200°C) la taille des cristallites croit progressivement entre 450 et 750°C, température à laquelle ils disparaissent. Par contre, après une phase de croissance dans toutes leurs dimensions, les plaquettes disparaissent complètement à 500°C.

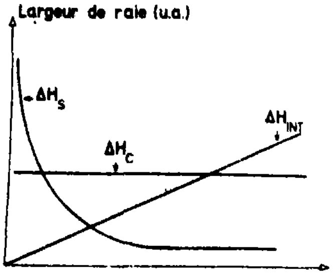

Fig. 1. Variation thermique des divers termes de l'analyse de Watts et Cousins (figure reproduite de leur article).

Nous rapportons ici les résultats d'une étude de la variation thermique du temps de relaxation T_1 dans la zone de température ambiante – 300°C qui permet donc d'observer pur le lithium:

- la phase solide jusqu'à 180°C,
- la fusion,
- la phase liquide de 180°C à 300°C.

En ce qui concerne la phase solide nos résultats sont en excellent accord avec ceux de Watts et Cousins[9]. De plus, nous avons observé, d'une part un élargissement de la raie de 0,2 G caractéristique de la fusion du lithium et d'autre part, un élargissement progressif, très important et réversible de la largeur de raie au cours du chauffage dans la phase liquide.

PARTIE EXPERIMENTALE

Les échantillons que nous avons utilisés étaient des lamelles de LiF fournies par Harshaw, de quelqules dixièmes de mm d'épaisseur, irradiées très fortement aux neutrons thermiques (dose voisine de $10^{19}\, n_{\text{th}}/\text{cm}^2$) au Centre d'Etudes Nucléaires de Grenoble*. Le flux était de l'ordre de $10^{13} n_{\text{th}}/\text{cm}^2 s$ et la température variait suivant les séries d'irradiation entre –100°C (lorsque les échantillons étaient refroidis extérieurement par de l'azote liquide) et +100°C (sans précautions particulières). De toute façon, l'état des cristallites après recuit des échantillons à 600°C est assez indépendant de leur température de formation.

---

*Nous tenons à exprimer nos vifs remerciements à Monsieur Doulat (C.E.N.G.) qui nous a donné toutes facilités pour effectuer plusieurs séries d'irradiation.

Nous avons utilisé un spectromètre Varian type 4502. Les expériences ont consisté à porter l'échantillon à des températures croissantes à l'intérieur de la cavité résonante, à l'aide de l'accessoire à température variable Varian (qui permet d'atteindre la température de 300°C, et possède une résolution en température de 1°C), et à observer le spectre R.P.E. à ces diverses températures.

Il faut rappeler que les raies de résonance de ces particules métalliques ont des formes anormales et sont en réalité la superposition de diverses raies de largeurs différentes[11]. Néanmoins, il est facile (cf. Appendice) d'analyser ces raies et de suivre leur évolution en étudiant par exemple les nombres sans dimensions N_6 et N_3 définis sur la Fig. 6. Les valeurs de ces nombres pour une raie lorentzienne ont été appelés N_{6L} et N_{3L}.

Les résultats de nos mesures sont rassemblés sur les Figs. 2 et 3. La Fig. 2 représente la variation de la largeur pic à pic et des nombres N_6 et N_3 caractéristiques de la forme de raie (cf. Appendice) en fonction de la température (de l'ambiante à 300°C) et pour en échantillon recuit à 612°C. La Fig. 3 représente avec une dilatation d'échelle la zone 160-200°C, la fusion du lithium étant située à 180°C. L'examen de ces deux figures montre que l'élévation de la température de l'échantillon, qui ne modifie pas la largeur de raie dans la phase solide jusque vers 120°C, produit par contre:

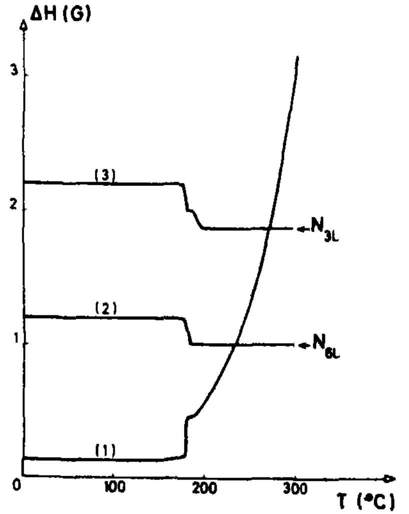

Fig. 2. Variation thermique de la largeur de raie (1) et des nombres N_6 (2) et N_3 (3). Les valeurs de ces nombres pour une lorentzienne sont indiquées par N_{6L} et N_{3L}.

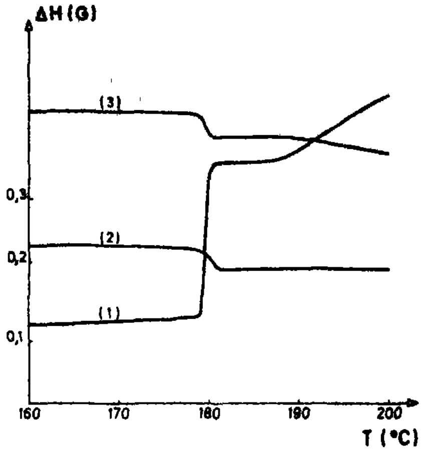

Fig. 3. Variation de la largeur de raie (1) et des nombres N_6 (2) N_3 (3) dans la zone de fusion.

– à la fusion un élargissement brutal de la raie qui passe de 0,13 G à 179°C à 0,41 G à 181°C. Cet élargissement brutal est précédé d'un élargissement plus faible et étalé sur quelques degrés.

– un élargissement progressif et très important de 200°C à 300°C.

A ces élargissements sont associés des changements de forme de la raie (courbes 2 et 3 des Figs. 2 et 3).

Nous décrirons tout d'abord les phénomènes observés, puis nous discuterons de leur interprétation en tenant compte à la fois des résultats obtenus sur les métaux liquides par d'autres mesures et des mécansimes de relaxation habituellement retenus pour le lithium.

1. *Zone de la fusion*

Les premières études expérimentales de la fusion du Li ont été faites par Enderby *et al.* [12] sur du lithium préparé par voie chimique. Rappelons les résultats de leurs expériences:

– la largeur de raie subit une discontinuité assez faible à la fusion; elle passe de 1,6 G dans l'état solide à 1,8 G dans l'état liquide,

– la susceptibilité paramagnétique électronique varie également très peu: elle augmente de 4 pour cent environ.

Nos expériences montrent donc un élargissement relatif de la raie beaucoup plus important (300%). Rappelons que la finesse de la raie est liée à la pureté exceptionnelle de ces échantillons[11]. Par contre, dans les deux cas, la valeur absolue de l'élargissement de la raie est sensiblement la même: alors que Enderby *et al.* mesurent 0,2 G, nos résultats varient suivant l'échantillon entre 0,1 et 0,3 G. Ce fait prouve que l'élargissement de 0,2 G est bien caractéristique de la fusion du lithium. En effet, la largeur de raie est proportionnelle à la probabilité de retournement du spin, et, lorsque plusieurs mécanismes de relaxation indépendants sont en compétition, les probabilités correspondantes s'ajoutent donc aussi les largeurs de raie. Aux termes de relaxation de l'état solide et responsables de la variété des largeurs de raies mesurées,[5, 6, 9, 11, 12] s'ajoute donc un terme supplémentaire qui correspond à un accroissement de la probabilité de retournement du spin de $3\,10^6 s^{-1}$. Ce terme est dû au changement d'état et est caractéristique du métal.

Deux remarques realtives à ces expériences de fusion des cristallites de Li observée par R.P.E. permettent de montrer que l'on peut, malgré l'inhomogénéité des échantillons de LiF irradié, séparer les effets spécifiques du Li de ceux dûs à la fois aux effets de taille et à la dispersion en taille.

(a) Rappelons que la fusion des cristallites a déjà été étudiée par l'un d'entre nous (Ch. Mazières) à l'aide de la microanalyse thermique différentielle (μA.T.D.)[13]. On observe pour un recuit de l'échantillon à 630°C deux pics de fusion (Fig. 4.a); l'un d'eux est situé à la température de fusion du Li et l'autre à une température inférieure de quelques degrés. Ce dernier pic a été attribué à la fusion de grains de Li plus petits et mal cristallisés[13]. Ces grains disparaissent après un recuit à 700°C comme le montre le pic unique de μA.T.D. que l'on observe alors (Fig. 4b).* Les courbes d'évolution de la lar-

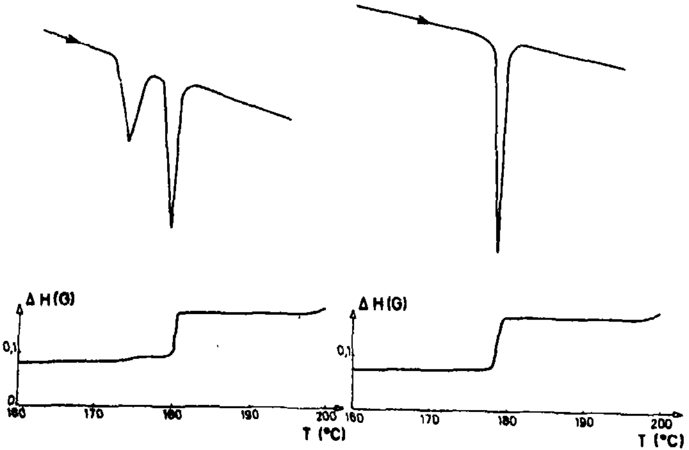

Fig. 4. Comparaison des profils de fusion (obtenus par μA.T.D.) et de la variation de la largeur de raie R.P.E. aprés (a) un recuit de l'échantillon à 630°C, (b) in recuit de l'échantillonà 710°C.

---

*Ce résultat tendrait à utiliser des échantillons recuits à haute température (700°C). En réalité le diamètre des cristallites est alors de l'ordre de grandeur de l'épaisseur de peau[11] et la forme des raies de Dyson[25] difficile à exploiter. Nous avons préféré recuire à une température intermédiaire (612°C) et analyser les raies observées par les méthodes indiquées dans l'appendice.

geur de raie R.P.E. montrent en effet deux élargissements isothermes des pics de fusion pour le premier recuit (Fig. 4(a)) et un seul élargissement pour le second (Fig. 4(b)). De plus la comparaison des courbes 2 et 3 de la Fig. 3 montre que le nombre N_3 (qui caractérise la forme de la raie loin du centre) évolue avant le nombre N_6. Ceci prouve que les cristallites responsables des composantes larges de la raie fondent les premiers; or il est légitime d'attribuer les raies les plus larges aux cristallites imparfaits[10, 11].

(b) La complexité des signaux R.P.E.[11] qui sont la superposition de plusieurs raies de largeurs et de facteurs g différents se retrouve dans l'état liquide tout au moins près du point de fusion. Ceci se traduit par la persistance après la fusion de nombres N_6 et N_3 différents de N_{6L} et N_{3L}. Toutefois ces nombres se rapprochent des valeurs caractéristiques des raies lorentziennes, ce qui montre une uniformisation des temps T_1.

2. *Phase liquide*

Un fait spectaculaire et, à notre connaissance, non encore signalé, est l'accroissement thermique très rapide de la relaxation dans l'état liquide. Cet effet est réversible. Entre 180 et 300°C, la largeur de raie est multipliée par un facteur qui, selon l'échantillon, varie de 2 à 7. De façon générale, après un palier de 180 à 190°C, la largeur de raie varie en T^{α} avec $\alpha > 1$.

La Fig. 2 correspond à l'un des échantillons pour lesquels l'effet est le plus important. Dans ce cas particulier la largeur de raie varie linéairement avec la température de 190 à 220°C ensuite s'ajoute à ce terme d'ordre 1 en T un terme d'ordre 2 au moins. Si l'on mesure simultanément les nombres caractéristiques de la forme de raie (courbes 2 et 3 de la Fig. 2) on constate qu'à partir de 200°C la raie (de 0,7 G à 200°C) est de forme lorentzienne, c'est à dire que l'on observe alors une raie pure. Pour d'autres échantillons la largeur de raie à 300°C varie de 0,4 à 0,6 G. Dans ces cas, la raie R.P.E. n'est pas une lorentzienne. Ceci signifie que pour l'échantillon ci-dessus un processus de relaxation très efficace (responsable d'une largeur de raie supérieure à 1 G) masque les effets de taille des cristallites.

DISCUSSION

Nos résultats relatifs à la phase solide sont en excellent accord avec ceux de Watts et Cousins[9]. Nous utiliserons donc leur analyse du processus de relaxation. Notons que les largeurs de raies importantes observées par ces auteurs sur des échantillons non recuits peuvent être interprétées par une diffusion des électrons sur les défauts d'empilement des plans {111} du lithium précipité[7]. C'est après un recuit à 150°C que disparaissent ces défauts et que s'affinent les raies R.P.E.[10].

Les processus de relaxation actuellement retenus pour la relaxation des spins électroniques dans la phase solide du Li sont le couplage spin-orbite et l'interaction entre spins électroniques au niveau de Fermi (mécanisme spin-courant de Overhauser). Pour ces deux processus, la largeur de raie varie linéairement avec la température. Rappelons que, d'après Watts et Cousins, le processus de relaxation intrinsèque responsable d'une largeur de raie de 45 mG à l'ambiante, contribue donc à une largeur de 75 mG à 180°C dans la phase solide. Alors que les informations expérimentales relatives à la fusion de Li sont compatibles avec un processus de relaxation par couplage spin-orbite, les résultats obtenus dans la phase liquide montreraient l'intervention d'autres mécanismes.

1. *Variation de T_1 associée à la fusion*

Les diverses mesures sur des échantillons très variés[11, 12], montrent donc que la fusion élargit la raie de 0,2 G. A la fusion plusieurs effets peuvent se produire:

— la fréquence des collisions orbitales double á peu près puisque la résistivité électrique passe de 15 à 25 $\mu\Omega$ cm (Fig. 5). Si le couplage spin-orbite varie peu, ce qui serait en accord avec la non variation du

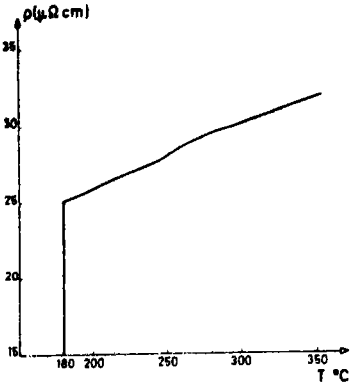

Fig. 5. Variation thermique de la résistivité électrique du lithium liquide (Clayton et Enderly 1961).

Knight-shift[14], la largeur de raie doit suivre les variations de la résistivité électrique, donc augmenter de 75 mG environ. L'accroissement observé, qui est de 200 mG est plus grand mais néanmoins du même ordre de grandeur.

— la fonction d'onde électronique peut être modifiée en raison de la disparition de la structure périodique; ce qui influerait à la fois sur le couplage spin-orbite et sur les interactions entre spins électroniques. Il est difficile d'évaluer alors l'effet produit; mais les variations nulles de Knight-shift, celles très faibles de la susceptibilité paramagnétique électronique semblent écarter cette hypothèse.

Il serait utile afin de suivre les modifications de la fonction d'onde de mesurer les variations du g-shift au cours de la fusion. Dans l'état solide, celui-ci est très faible: $g = g_0 - 2\ 10^{-6}$[1, 2]. Une variation même relativement importante est difficilement mesurable; toutefois l'examen des spectres semble montrer que g augmente de $3\ 10^{-6}$ (ce qui correspond à un déplacement de la raie de 10 mG) au cours de la fusion. ceci indiquerait que le comportement de l'électron dans le métal liquide est plus proche de celui de l'électron libre. D'autres résultats, en particulier de mesures optiques[14] ont déjà conduit à une telle conclusion.

En conclusion, l'effet observé s'explique bien en ne tenant compte que du seul couplage spin-orbite.

2. *Etude de la phase liquide de* 180 *à* 300°C

L'accroissement du processus de relaxation est ici très supérieur à l'accroissement correspondant de la résistivité électrique, qui n'est que de 20 pour cent[14] (Fig. 5). De plus, contrairement à la résistivité, la largeur de raie de varie pas linéairement avec la température. Ces deux résultats, obtenus sur les cristallites de lithium, sont très différents de ceux obtenus dans le cas du sodium pour lequel la largeur de raie ΔH augmente linéairement avec la température dans la phase liquide[15, 16]; de plus la pente de la droite obtenue pour ΔH dans le cas de Na est, bien que légèrement différente, du même ordre de grandeur que celle[17] de la résistivité électrique (mesurée, soit à volume, soit à pression constants).

Deux cas sont alors possibles:

(a) les conditions expérimentales de nos mesures sont en réalité très différentes de celles dans lesquelles ont été faites les mesures de résistivité,

(b) la largeur de raie est, pour Li, indépendante de la résistivité et due à un processus de relaxation autre que le couplage spin-orbite.

(a) Les conditions expérimentales de nos expériences sont en effet mal connues, en particulier celles relatives à la pression.

Les coefficients de dilatation volumique du solide LiF et du liquide Li étant notablement différents, on peut prévoir une augmentation de pression au cours du chauffage; cet effet dépend du contact entre les cristallites et la matrice. Connaissant la compressibilité du LiF ($4\ 10^{-5}\ \mathrm{at}^{-1}$) et supposant celle du lithium égale, les coefficients de dilatation du LiF ($3\ 10^{-5}\ {}^{\circ}\mathrm{C}^{-1}$), du Li supposé égal à celui du mercure ($2\ 10^{-4}\ {}^{\circ}\mathrm{C}^{-1}$) et en supposant qu'il y a contact entre le LiF et le Li à 180°C on peut évaluer la pression théorique à 300°C à 400 at. Or il existe des conditions pour lesquelles la résistivité électrique varie extrêmement vite avec la température: le voisinage d'une transition métal-non métal et en particulier la zone voisine du point critique. Les études les plus détaillées de cette zone ont été faites sur le mercure[18-20]: la résistivité y varie d'un facteur 10^5. La zone dans laquelle la résistivité varie rapidement avec la température et avec la pression, s'étend sur plusieurs centaines de degrés et plusieurs centaines de bars autour du point critique. Or les pressions critiques des alcalins sont faibles[21] (quelques centaines de bars). Pour le lithium elle se situe aux environs de 600 bars. Mais par contre les températures critiques des alcalins sont très élevées: pour le Li, celle-ci est évaluée à 3.200°C[21]. Un effet des fluctuations critiques sur la résistivité semble donc peu probable dans ces expériences à 600°K.

(b) Il semble que des expériences récentes [22] aient prouvé que la relaxation de spin dans le lithium soit produite par le mécanisme 'spin-courant' de Overhauser. Rappelons que parmi les interactions entre spins électroniques capables de relaxer le système de spin, Overhauser distingue:

- celles dont l'effet serait un double 'spin-flip' qui conduisent à l'ambiante à un temps de relaxation trop long mais variant linéairement avec le carré de la température.
- celles dont l'effet serait un simple 'spin-flip' conduisant à un temps de relaxation raisonnable et variant linéairement avec T.

Il serait intéressant de connaitre dans la phase liquide l'effet d'une élévation de température ou de pression sur ce mécanisme. En particulier, il serait séduisant d'expliquer la dispersion de nos résultats dans la phase liquide par des différences de pression à l'intérieur des cristallites, celles-ci étant dues à des contacts différents entre le LiF et le Li en raison des diverses températures d'irradiation. Au point de vue expérimental, la pression interne du Li peut être évaluée soit par des mesures précises de paramètre dans la phase solide, soit par la détermination de la température de fusion par μA.T.D.

CONCLUSION

Cette étude de la variation thermique du temps de relaxation a donc mis en évidence deux faits: élargissement défini des raies à la fusion et augmentation rapide de la relaxation dans la phase liquide. Le premier effet, déja signalé[16] caractéristique de la fusion s'explique bien à l'aide d'une relaxation par couplage spin-orbite. Par contre, le second effet nouveau bien qu'indépendant des effets de taille des cristallites pourrait être fonction de la pression interne. Il semble plus favorable au mécanisme 'spin-courant'. Pour interpréter cet effet, il faudrait à la fois contrôler la pression, et posséder de plus nombreuses informations quant à la phase liquide loin du point de fusion; en particulier toutes les techniques d'étude de la fonction d'onde (g-shiftpar R.P.E., Knight-shift en R.M.N., effet Overhauser, mesures optiques...) dont certaines sont aisément applicables à ce type d'échantillons améliorerait le connaissance de la phase du lithium liquide.

Remerciements—Les auteurs expriment leurs remerciements à Monsieur le Professeur J. Friedel pour de fructueuses discussions.

L'un d'entre eux (C.T.) remercie le referee delui avoir signalé des articles récents sur le g-shift dans le lithium.

APPENDICE—ANALYSE DES RAIES COMPLEXES

Plusieurs types d'expériences permettent de mettre en évidence la complexité d'une raie et de l'analyser.

(1°) *Etude de la forme de la raie*

On peut étudier cette forme grâce à quelques nombres définis sur la Fig. 6; ces nombres sont caractéristiques de la forme de raie. Sur cette figure sont indiquées les valeurs de ces nombres pour une gaussienne et une lorentzienne. Il est aisé de montrer[10], par exemple en effecuant des synthèses de raies, que ces nombres sont très sensibles à la composition d'une raie; ils peuvent en effet varier d'un facteur 2 sans que la raie composite manifeste de structure.

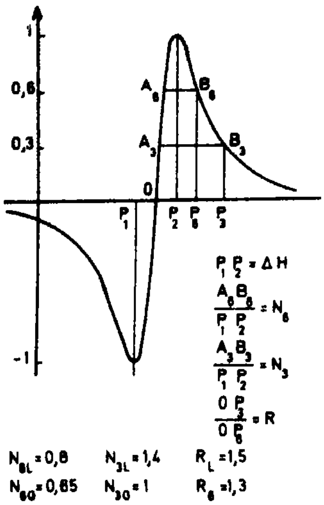

Fig. 6. Définition des nombres N_6 et N_3 utilisés pour l'étude de la forme de raie. On a indiqué les valeurs de ces nombres pour une gaussienne et une Lorentzienne.

L'étude de la déformation du signal en fonction du réglage de phase de la détection synchrone de la modulation B.F. du champ (100 khz dans notre cas) permet à la fois d'apprécier l'inhomogénétié des temps de relaxation et celles des facteurs *g* [10].

(3°) Saturation

On peut ainsi éliminer les raies fines et faire apparaitre les raies larges.

REFERENCES

1. PRESSLEY R. J. et BERK H. L., *Phys. Rev.* **140**, A 1207 (1965).
2. BIENENSTOCK A. et BROOKS H., *Phys. Rev.* **136**, A 784 (1964).
3. OVERHAUSER A. W., *Phys. Rev.* **89**, 689 (1953).
4. ELLIOTT R. J., *Phys. Rev.* **96**, 266 (1954).
5. FEHER G. et KIP A. F., *Phys. Rev.* **98**, 337 (1955).
6. GEN M. Y. et PETINOV V. I., *Soviet Phys. J.E.T.P.* **21**, 19 (1965).
7. LAMBERT M., *Thèse*, Paris (1958), LAMBERT M. et GUINIER A., *C.R. Acad. Sci.* **246**, 1678 (1958).
8. RYTER Ch., *Phys. Rev. Lett.* **5**, n°1, 10 (1960).
9. WATTS A. J. et COUSINS J. E., *Phys. Status Solidi* **30**, 105 (1968).
10. TAUPIN C., *Thèse*, Orsay (1968).
11. TAUPIN C., *J. Phys. Chem. Solids* **28**, 41 (1967).
12. ENDERBY J. E., TITMAN J. M. et WIGNALL G. D., *Phil. Mag.* **10**, 633 (1964).
13. LAMBERT M., MAZIÈRES Ch. et GUINIER A., *J. Phys. Chem. Solids* **18**, 129 (1961).
14. CUSACK N. E., *Rep. Prog. Phys.* **XXVI**, 361 (1963).
15. DEVINE R. A. B. et DUPREE R., *Phys. Lett. (Netherlands)* **30A**, n°3, 211 (1969).
16. DEVINE R. A. B. et DUPREE R., *Phil. Mag.* **21**, n° 172, 787 (1970).
17. LIEN S. Y. et SIVERTSEN J. M., *Phil. Mag.* **20**, n°166, 759 (1969).
18. FRANCK E. U. et HENSEL F., *Phys. Rev.* **147**, n°1, 147 (1966).
19. KIKOIN T. K. et SENCHENKOV A. P., *Fiz. Metal. Metalloved.* **24**, n°5, 843 (1967).
20. FRANCK E. U. et HENSEL F., *Rev. mod. Phys.* **40**, n°4, 697 (1968).
21. DILLON I. G., NELSON D. A. et SWANSON B. S., *J. chem. Phys.* **44**, n°11, 4229 (1966).
22. SMITHARD M. A. et COUSINS J. E., *Communication au XVIème Colloque Ampère*, Bucarest (1970).
23. VANDER V., *Phys. Rev.* **168**, 787 (1968).
24. OVERHAUSER de GRAAF, *Phys. Rev. Lett.* **22**, 127 (1969).
25. DYSON F. J., *Phys. Rev.* **98**, 349 (1955).

J. Phys. Chem. Solids Pergamon Press 1971. Vol. 32, pp. 2053–2062. Printed in Great Britain.

DONOR-ACCEPTOR PAIRING IN THE SYSTEM GaP(Zn, O)

J. D. WILEY
Bell Telephone Laboratories, Inc., Murray Hill, N.J. 07971, U.S.A.

(*Received* 14 *December* 1970)

Abstract—Equilibrium concentrations of Zn–O nearest-neighbor pairs in GaP have been calculated for Zn and O concentrations between 10^{16} and 10^{19} cm^{-3} at temperatures between 400 and 1200°K. The discrete nature of the host lattice is taken into account and the effects of strain-fields, bond mismatch, and electrostatic interactions on the Zn–O binding energy are discussed. The discrete and fluid models of ion pairing are compared and it is shown that, for the case of substitutional pairing in compound semiconductors, the fluid model can underestimate the pairing by as much as a factor of 3 depending on the temperature and ion concentrations.

1. INTRODUCTION

It is well known that interactions among point defects in solids can have a profound effect on the spatial distribution and electronic activity of these defects[1–4]. Uncharged defects (such as isoelectronic dopants) can interact through lattice distortion, bond mismatch, van der Waals forces, or other mechanisms which, in general, can be either attractive or repulsive. Perhaps the most important type of defect interaction, however, is the Coulomb attraction between ionized donors and acceptors which leads to the formation of donor-acceptor (DA) pairs in semiconductors [1, 2, 5]. The importance of DA pairs as centers for efficient radiative recombination has been emphasized in several recent reviews[5–7] and need not be discussed here. In the present paper, attention will be focused on the system GaP(Zn, O) and an attempt will be made to calculate the equilibrium concentration of nearest-neighbor Zn–O pairs as a function of temperature and doping levels.

In the past, most calculations of DA pairing in semiconductors have utilized the fluid model of Reiss, Fuller, and Morin[1] in which the host lattice is considered to be a dielectric continuum and the ions interact solely through a hard-sphere Coulomb interaction. At first sight, this method would seem to be the simplest since it avoids the complexities of a discrete lattice and is able to draw upon the large body of literature concerning the interaction of ions in electrolyte solutions[8–10]. Despite first appearances, however, the fluid model is not at all simple Among the difficulties encountered in the fluid model are the following: (1) The model leads to an integral equation for the *ionic distribution function* $g(r)$ which is difficult to solve satisfactorily. (2) The usual method of solving for $g(r)$ involves several approximations, the validity and consequences of which are difficult to assess[11]. (3) The model provides no simple route by which one could incorporate such refinements as non-Coulombic interactions or screening effects. (4) Finally, the fact that the discrete nature of the host has been ignored means that one cannot calculate the very quantity which is most useful: the concentration of substitutional *nearest neighbor* pairs. We will return to these points in Section 4.

Prener[12] has shown that, by converting certain integrals of the fluid model into sums, one can obtain an expression for the pair distribution function which reflects some features of the discrete lattice. This is an interesting approach but it leads to a temperature-dependent normalization parameter which is cumbersome to evaluate.

In view of the serious difficulties inherent in adapting a fluid model to the description of interactions among substitutional donors and acceptors, it seems preferable to introduce the discrete nature of the host at an early stage of the calculation. To this end, use will be made in the present calculation of a method first introduced by Lidiard[13] for the calculation of ion-vacancy complexes in NaCl.

Lidiard's approach is to recognize that the interacting ions will arrange themselves in such a way as to minimize the free energy of the system

$$F = E - TS = E - kT \ln W, \qquad (1)$$

where E is the internal energy, T is the temperature, S is the configurational entropy, and W is the number of distinguishable ways of constructing the system. The discrete nature of the host is introduced through W. In the simplest case, for example, one can consider only the formation of Coulomb bonded nearest-neighbor pairs and ignore interactions among unpaired ions. The internal energy is then taken to be

$$E = -\frac{P_1 e^2}{\epsilon a_1}, \qquad (2)$$

where P_1 is the number of nearest-neighbor pairs, ϵ is the dielectric constant of the host, and a_1 is the nearest-neighbor separation. The entropy term in this case is given by

$$W = \left[\frac{Z_1^{P_1} \prod_{S=0}^{P_1-1} (N-S)}{P_1!}\right]\left[\frac{(N-P_1)!}{(N-N_A)!(N_A-P_1)!}\right] \times \left[\frac{(N-P_1)!}{(N-N_D)!(N_D-P_1)!}\right] \qquad (3)$$

where Z_1 is the number of nearest-neighbor sites, N is the number of host atoms of either species and N_A and N_D are the numbers of acceptors and donors. For dimensional reasons N, N_A, N_D and P_1 must be pure numbers in equation (3) but they are easily converted to concentrations in the final expressions. Where no confusion can result, these quantities will be referred to interchangeably as numbers or concentrations.

The first bracketed term in equation (3) is the number of distinct ways of arranging P_1 pairs in the lattice by putting one member of the pair on one of the N sites of one sublattice and the other member of the pair on one of the Z_1 nearest-neighbor sites of the opposite sublattice. Having placed the P_1 pairs, there are now $N - N_A$ Ga atoms and $N_A - P_1$ acceptors to be placed on the $N - P_1$ vacant Ga sites. The number of distinct ways of filling these Ga sites is given in the second bracketed term. The third term applies to the $N - P_1$ remaining P sites in analogy to the Ga sites. In order to find the equilibrium concentration of pairs, P_1, we now substitute equations (2) and (3) into equation (1) and minimize F by setting $\mathrm{d}F/\mathrm{d}P_1 = 0$. This results in

$$\ln \frac{Z_1(N_A-P_1)(N_D-P_1)}{P_1(N-P_1)^2} + \frac{\mathrm{d}}{\mathrm{d}P_1} \sum_{S=0}^{P_1-1} \ln (N-S) + \frac{e^2}{\epsilon a_1 kT} = 0. \qquad (4)$$

In obtaining equation (4), use has been made of Stirling's approximation

$$\ln N! \approx N \ln N - N. \qquad (5)$$

If we now make use of the approximation $P_1 \ll N$ (an excellent approximation since $N \approx 2{\cdot}47 \times 10^{22}$ sites/cm^3 and P_1 is of the order of the doping level which is typically $\lesssim 10^{18}$ atoms/cm^3) we can write

$$\sum_{S=0}^{P_1-1} \ln (N-S) \approx P_1 \ln N. \qquad (6)$$

Thus

$$\ln \frac{Z_1(N_A-P_1)(N_D-P_1)N}{P_1(N-P_1)^2} + \frac{e^2}{\epsilon a_1 kT} = 0, \qquad (7)$$

or

$$\frac{P_1}{(N_A - P_1)(N_D - P_1)} \approx \frac{Z_1}{N} e^{e^2/\epsilon a_1 kT} \quad (8)$$

where use has been made of $P_1 \ll N$ again. Equation (8) is easily solved for the equilibrium pair concentration P_1.

If we make the identification

$$\Omega_1 = \frac{Z_1}{N} e^{e^2/\epsilon a_1 kT} = \frac{Z_1}{N} e^{\alpha_1}, \quad (9)$$

then equation (8) is the same as that derived by Reiss, Fuller, and Morin (equation (9·4) of Ref.[1]). The only difference is that we are now dealing strictly with nearest-neighbor pairs on discrete lattice sites and we have a simple expression for the equilibrium constant Ω.

In Section 2 the interaction energy will be considered more carefully and the above method will be generalized to include explicitly the formation of 1st, 2nd, ... Nth-neighbor pairs. Section 3 contains the results of the pairing calculations for GaP(Zn, O). In Section 4 a comparison will be made between the discrete and fluid models for ion pairing in semiconductors.

2. THEORY

(a) *Interaction among* Zn^- *and* O^+ *ions*

In what follows it will be assumed that we are dealing with a system of N_A ionized Zn acceptors and N_D ionized O donors which have entered the GaP lattice substitutionally on Ga and P sites respectively. The assumption of complete ionization is well satisfied at typical annealing temperatures provided $N_A > N_D$. The principal long-range interaction, then, is likely to be electrostatic. In general, the charge distributions around the Zn^- and O^+ will be distorted by bonding and the interaction energy will include all multipole terms consistent with the zincblende symmetry[14, 15]. For ion separations greater than 4th or 5th neighbors, however, the higher-order multipole terms amount to only a few milli-electron volts ($\leq$ 10 per cent of the monopole Coulomb term) and are negligible for present purposes. The multipole expansion breaks down for small Zn–O separations and it is difficult to estimate the deviation from Coulomb behavior. For simplicity, we will assume a Coulomb interaction $-e^2/\epsilon r$ at all separations. Srinivasan[16] has shown that $\epsilon(r)$ reaches its full value within one nearest-neighbor distance so that it is appropriate to use a constant ϵ ($\epsilon = 11 \cdot 1$ for GaP) even for nearest-neighbor separations between the ions.

In addition to the Coulomb interaction, it is possible for the ions to interact via their strain fields. If, for example, one impurity species were much smaller and the other much larger than the host atoms for which they substitute, then the lattice strain would be minimized if these ions were to occupy adjacent lattice sites. In the case of GaP (Zn, O) strain probably plays a negligible role in DA pair formation since the covalent radius of Zn is nearly identical to that of Ga[17]. Thus, despite the fact that O is much smaller than P and probably strains the lattice considerably, there is no way (on the basis of strain alone) for the O to distinguish between Zn and Ga.

Finally, the formation of covalent bonds may tend to enhance or inhibit pair formation. If Zn^- and O^+ are placed in a GaP lattice at *isolated* sites, 8 Ga–P bonds are broken and replaced by 4 Zn^-–P and 4 Ga–O^+ bonds. If the Zn^- and O^+ are placed on *adjacent* lattice sites, 7 Ga–P bonds are broken and replaced by 1 Zn^-–O^+, 3 Zn^-–P, and 3 Ga–O^+ bonds. The difference in energy between these two configurations is

$$\Delta E = E_{Zn-P} + E_{GaO^+} - E_{GaP} - E_{Zn^- O^+}, \quad (10)$$

where E_{XY} is the energy required to break one X–Y bond. As far as the formation of tetrahedral covalent bonds is concerned, Zn^- and Ga should be quite similar since Zn and Ga have identical electronegativities[18]. Thus, aside from Coulomb energies which are treated separately, one expects $E_{Zn-P} \approx E_{GaP}$, $E_{GaO^+} \approx E_{Zn-O^+}$, and $\Delta E \approx 0$. Here again, the remarkable similarity of Zn and Ga tends to eliminate any pairing energy. It is possible to use heats of formation or cohesive energies to construct other heuristic arguments[19, 20] all of which lead to the conclusion that the effects of bond energies in the GaP(Zn, O) system are probably small compared to the Coulomb energy. Note that the bond energy, to the extent that it is important at all, affects only the binding energy of nearest-neighbor pairs. Note also that bond energy mismatch could provide a very effective mechanism for forming *DA* pairs between isoelectronic substituents where there is no Coulomb interaction. It has been estimated that bond energies provide an attractive binding of $\Delta E \approx 0{\cdot}6$ eV for *B–N* pairs in the system GaP(*B*, *N*)[21].

In Section 1 the total interaction energy was taken to be solely the Coulomb energy of ions paired as nearest-neighbors. Clearly this overestimates the pairing by ignoring interactions among 'unpaired' ions. The easiest way to correct this is to calculate *explicitly* the number of ions paired as first, second . . .*N*th neighbors, and then allow the remaining ions to interact with each other in a collective or Debye–Hückel atmosphere[10, 13]. By *N*th-neighbor pairs we mean the following. A Zn^- ion at the origin will be said to be paired with an O^+ ion at a_n as an *N*th-neighbor pair provided there are *no other unpaired* O^+ *ions* within a distance a_n from the Zn^-. We will ignore the possibilities of multiple pairs (A Zn^- with two O^+ neighbors at the same distance, for example) and pairs involving ions of like sign. Using arguments based on the fluid model[1, 8, 9, 11] it is possible to show that ions separated by more than $b \approx e^2/2\epsilon kT$ can reasonably be considered to be 'unpaired' (their binding energy is small compared to kT) while those with separations smaller than b are paired. For the temperatures of interest here[22] (500°C $< T <$ 1000°C) b corresponds to 6–10 Å and includes the first 3–6 shells of neighbors on the opposite sublattice[23]. We will therefore write the total interaction energy as

$$E = -\sum_{j=1}^{m} \frac{P_j e}{\epsilon a_j} + E_{DH}(N_A, \beta, T), \tag{11}$$

where

$$\beta = \sum_{j=1}^{m} P_j. \tag{12}$$

In equation (11) P_j is the number of *j*th-neighbor pairs, a_j is their separation, and m will be chosen to be between 3 and 6. The Debye–Hückel term has the following meaning. If the total number of paired ions is β [equation (12)], then there are $N_A - \beta$ unpaired Zn^- ions, $N_A - N_D$ free holes, and $N_D - \beta$ unpaired O^+ ions. These charges are unpaired or unbound but they interact in such a way as to screen each other and thereby lower the total energy. This effect was first calculated by Debye and Hückel[24] who showed that each ion develops a time-averaged atmosphere of average thickness K^{-1} (also known as the Debye–Hückel screening length) where

$$K^2 = \frac{8\pi(N_A - \beta)e^2}{V\epsilon kT}. \tag{13}$$

In equation (13) the volume of the crystal, V, has been inserted explicitly and N_A and β are pure numbers. The total interaction energy of the unpaired ions is[10, 13]

$$E_{DH} = -\frac{(N_A - \beta)e^2}{\epsilon} \frac{K}{1 + Ka_{m+1}}, \tag{14}$$

where a_{m+1} is the distance of closest approach for the unpaired ions. As an illustration of the magnitudes of these quantities, if $N_A - \beta = 10^{18}$ and $V = 1\ \mathrm{cm}^3$ then $K^{-1} \approx 50$ Å at $T =$ 1000°K, and the interaction energy per ion $[E_{DH}/(N_A - \beta)]$ is $\approx$ 22 meV.

(b) *Calculation of the equilibrium pair concentrations*

Using the same reasoning as was given in Section 1, it is straightforward to show that equation (3) can be generalized for the explicit calculation of pairs out to *m*th-neighbors as follows:

$$W=\left[\prod_{j=1}^{m}\frac{Z_j^{P_j}\prod\limits_{S=0}^{P_j-1}\left(N-S-\sum\limits_{i<j}Z_iP_i\right)}{P_j!}\right]$$

$$\left[\frac{[(N-\beta)!]^2}{(N_A-\beta)!(N_D-\beta)!(N-N_A)!(N-N_D)!}\right]. \tag{15}$$

The sum over $i<j$ of Z_iP_i is an approximate term reflecting the fact that pairs of order i carry with them an 'excluded volume' in which no member of a higher-order pair can be placed. This is a consequence of the definition of 'pair'. Proceeding as before, equations (15) and (11) are substituted in equation (1) and the equilibrium condition $dF/dP_i=0$ is imposed[25]. This results in m simultaneous coupled equations to be solved for the P_j's. Upon making use of the approximation

$$S+\sum_{i<j}Z_iP_i\ll N.$$

(satisfied to better than 1 part in 1000) together with Stirling's approximation it can be shown that

$$\frac{P_j}{(N_A-\beta)(N_D-\beta)}=\Omega_j, \tag{16}$$

where

$$\Omega_j=\frac{Z_j}{N}e^{\alpha_j}, \tag{17}$$

and

$$\alpha_j=\frac{e^2}{\epsilon kT}\left[\frac{1}{a_j}-\frac{K}{1+Ka_{m+1}}\right]. \tag{18}$$

From equations (16) and (17) it is seen that the ratio of *j*th-neighbor pairs to 1st-neighbor pairs is simply

$$\frac{P_j}{P_1}=\frac{\Omega_j}{\Omega_1}=\frac{Z_j}{Z_1}e^{(\alpha_j-\alpha_1)}. \tag{19}$$

Since we are primarily interested in P_1, it is convenient to rewrite equation (16) for $j=1$ as follows:

$$\frac{P_1}{(N_A-\gamma P_1)(N_D-\gamma P_1)}=\Omega_1. \tag{20}$$

From the definition of β [equation (12) β is the sum of all pairs.] and equation (19) it is seen that

$$\gamma=\sum_{j=1}^{m}\frac{\Omega_j}{\Omega_1}. \tag{21}$$

Physically, γ is the ratio of all pairs to first-neighbor pairs. Once γ and Ω_1 are known, equation (20) is a simple quadratic in P_1. Higher order pairs can then be calculated from equation (19). If it were not for the concentration-dependence of the Debye-Hückel term, Ω_1 and γ would be immediately calculable [26]. As it is, K depends on β [equation (13)] and the calculation must be performed by setting $K=0$ the first time through and then repeating the calculation with the K term included. The convergence is quite rapid so that two iterations are usually sufficient.

3. RESULTS FOR GaP(Zn, O)

In Table 1 the radii a_j and occupation numbers Z_j are listed for the first 6 shells of neighbors[23] on the opposite sublattice in GaP. The nearest-neighbor distance in pure GaP is 2·36 Å and corresponds to the sum of the tetrahedral covalent radii for Ga and P. When Zn^- and O^+ occupy nearest-neighbor sites the separation will probably be somewhat less owing to the smaller covalent radius of oxygen[17, 18]. Since the sum of the covalent radii for Zn and O is 1·97 Å, a compromise value of 2·16 Å seems reasonable for the

Table 1. *The radii and occupation numbers for the first* 6 *shells of neighbors on the opposite sublattice in* GaP. *The radii are based on a lattice constant (unit cube edge) of* 5·45 Å

Shell number j	a_j (Å)	Z_j
1	2·36*	4
2	4·51	12
3	5·93	12
4	7·08	16
5	8·06	24
6	8·94	12

*This is the nearest-neighbor distance for pure GaP. See text for a discussion of the Zn–O separation.

Zn^-–O^+ nearest-neighbor separation when these ions are substituted in GaP[27]. Using $a_1 = 2·16$ Å, $\epsilon = 11·1$, and $m = 5$ (i.e., pairing ions separated by $a_j \leq a_5 = 8·06$ Å and including all other ions in the Debye–Hückel atmosphere) equilibrium pair concentrations have been calculated for various temperatures and doping levels. The results are shown in Figs. 1–3 where the quantity plotted along the ordinate is the fraction f of all donors (written as N_D or [O]) which are paired as nearest-neighbors with acceptors (the total acceptor concentration is denoted N_A or [Zn]), i.e.,

$$f \equiv P_1/[O]. \qquad (22)$$

For oxygen concentrations $[O] < 10^{17}$ cm^{-3}, f is essentially independent of [O] and Fig. 1 can be used even though it was calculated specifically for $[O] = 10^{17}$ cm^{-3}.

Figure 4 shows the temperature dependence of f for $[O] = 10^{17}$ cm^{-3} and 4 values of [Zn] (i.e., 4 vertical slices through Fig. 1). Knowing the general shapes of these curves, it is easy to estimate f for values of the parameters other than those specifically plotted in Figs. 1–4 by simply plotting a few points and interpolating.

In Fig. 5, f is plotted vs. T for $[O] = 10^{17}$, $[Zn] = 10^{18}$ cm^{-3} and $a_1 = 1·97$, 2·16, and 2·36 Å. These three radii correspond to Coulomb binding energies of 660, 600, and 550 meV, respectively [For GaP the Coulomb potential is $E_c(\text{eV}) = -1·3/r(\text{Å})$]. If it is desired to calculate f for other binding energies, the curves of Fig. 5 shift more-or-less rigidly at a rate of 3·9°K/0·01 Å.

It was mentioned earlier[25] that, as a matter of practical consequence, it is un-

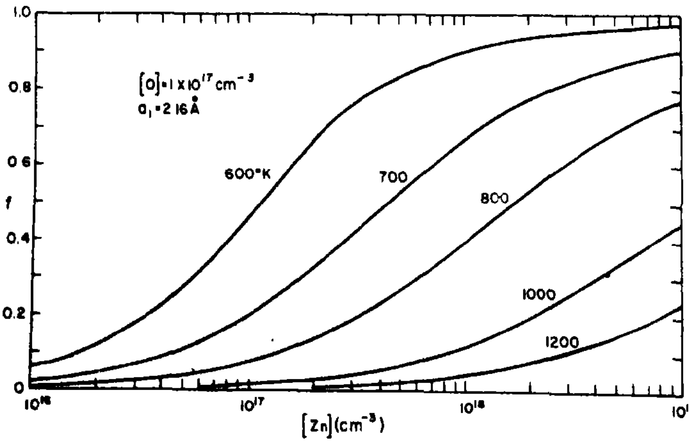

Fig. 1. The fraction f of oxygen donors which are bound as nearest-neighbor pairs with Zn acceptors as a function of the Zn concentration [Zn]. These curves were calculated for an oxygen concentration of $[O] = 10^{17}$ cm^{-3} and a Zn^-–O^+ nearest-neighbor separation of 2·16 Å.

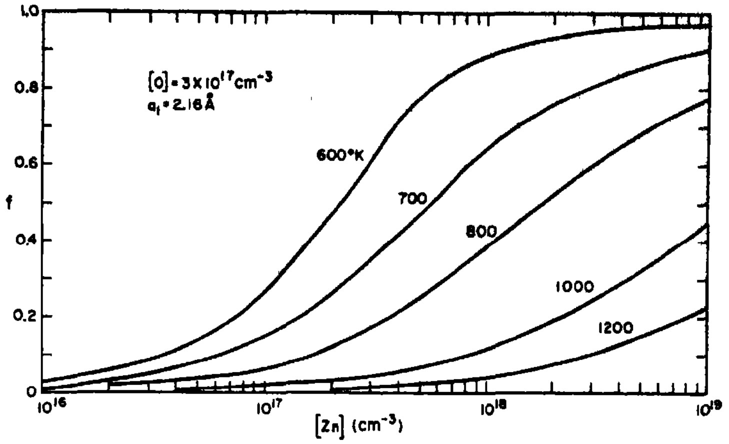

Fig. 2. A plot similar to Fig. 1 but calculated for [O] = 3×10^{17} cm^{-3}.

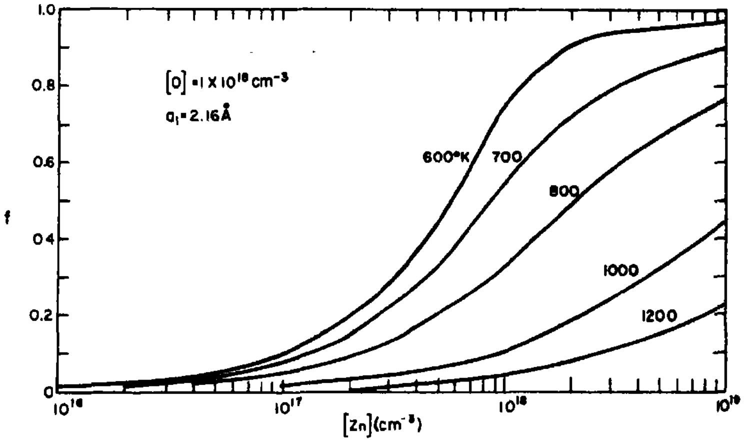

Fig. 3. A plot similar to Fig. 1 but calculated for [O] = 10^{18} cm^{-3}.

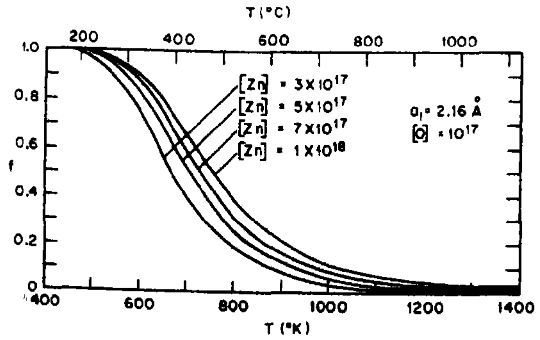

Fig. 4. The temperature dependence of f for [O] = 10^{17} cm^{-3}, $a_1 = 2{\cdot}16$ Å, and four values of [Zn].

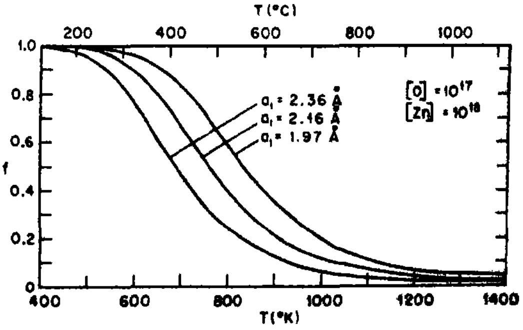

Fig. 5. A plot of f vs. T showing the effect of changing the nearest-neighbor separation. These curves were calculated for [O] = 10^{17} cm^{-3} and [Zn] = 10^{18} cm^{-3}.

necessary to include the constraint $\beta < N_D$ in the calculation explicitly since there is no danger of these conditions being violated. This is illustrated in Table 2 where values are plotted for γ as a function of T for various values of m. It will be recalled [See equations (21) and (22)] that γ is the ratio of *all* pairs to *first neighbor* pairs. Thus if $\gamma > 1$ and $P_1 \approx 1$ one is in danger of violating the above-mentioned constraint. It is seen from Table 2 that this never occurs. Only at very high temperatures does γ become $\gg 1$ and at these temperatures P_1 is $\ll 1$. Problems of over-pairing would only arise if one included a much greater number of shells in the explicit pairing.

Table 2. Values of γ for various values of m and T. By definition [See equations (19) and (21)] γ is the ratio of all pairs to first-neighbor pairs

m (No. of shells paired)	Temperature 600	(°K) 1000	1400	∞
1	1	1	1	1
2	1·006	1·08	1·26	4
3	1·007	1·11	1·41	7
4	1·008	1·14	1·56	11
5	1·01	1·18	1·73	17
6	1·01	1·20	1·80	20

4. COMPARISON BETWEEN THE DISCRETE AND FLUID MODELS FOR ION PAIRING IN SEMICONDUCTORS

In the fluid model for ion pairing[1, 8–11] it is assumed that the host lattice can be approximated by a homogeneous continuum of dielectric constant ϵ and that donors and acceptors can occupy arbitrary positions within the host. In order to avoid complications of higher-order clustering (such as dipole–dipole interactions among mobile pairs) it is assumed that one of the impurity species is immobile and distributed randomly throughout the host. One can then choose an origin at one of the immobile ions and proceed to calculate the probability, $g(r)\mathrm{d}r$, that the nearest oppositely charged, unpaired ion is in a spherical shell of thickness $\mathrm{d}r$ and radius r. In the absence of any interactions, the ions would all be distributed randomly with the average separation (peak of the distribution curve) being determined by the concentration. If there are N particles per unit volume, each particle occupies a volume $v \approx 1/N$. Setting $v = \frac{4}{3}\pi r_0^3$ gives $r_0 \approx (\frac{3}{4}\pi N)^{1/3}$ for the average separation. For $N \approx 10^{17}\ \mathrm{cm}^{-3}$, $r_0 \approx 135$ Å.

If one assumes an attractive interaction of the form

$$V(r) = \begin{cases} \infty & r < a \\ -\dfrac{e^2}{\epsilon r} & r \geq a, \end{cases} \tag{24}$$

where a is a hard-core distance of closest approach, the distribution of nearest-pair separations is given by

$$g(r) = 4\pi r^2 h \exp(-4/3\pi r^3 N)\exp(e^2/\epsilon kTr), \qquad r > a \tag{25}$$

where N is the number of mobile ions per unit volume, and h is a normalization parameter determined by requiring

$$\int_a^\infty g(r)\,\mathrm{d}r = 1. \tag{26}$$

From equation (25) it can be seen that $g(r)$ has an exponential peak at $r = a$ caused by the Coulomb attractions and a broad peak at large r (near r_0) which is simply a concentration effect. These two peaks are separated by a minimum at $r \approx e^2/2\epsilon kT \equiv b$. The existence of this minimum in the distribution function provides a natural distinction between paired and unpaired ions. Thus in the fluid model the fraction of donors paired is taken to be

$$\frac{P}{N_D} = \int_a^b g(r, N_A)\,\mathrm{d}r, \tag{27}$$

where it is assumed that $g(r, N_A)$ has been properly normalized [equation (26)]. (Note that N_A and N_D can be interchanged but *one* species is assumed immobile). Because of the difficulty of repeated numerical integrations of equations (26) and (27), considerable effort has gone into devising approximate solutions of the fluid model. The most successful of these[1, 9] gives a result analogous to equation (8) of Section 1:

$$\frac{P}{(N_A-P)(N_D-P)} = \Omega(\epsilon, a, T), \qquad (28)$$

where Ω is calculated from Tables in Ref. [1].

Equation (28) has been applied to the system GaP(Zn, O) with $a = a_1 = 2{\cdot}16$ Å for comparison with the discrete model. The results are shown in Figs. 6 and 7 where $f = P_1[\mathrm{O}]$ (discrete model) and $f = P/[\mathrm{O}]$ (fluid model) are plotted as functions of [Zn] and T. It is seen that *the discrete model predicts more pairing at all temperatures and concentrations* (i.e., it predicts a larger equilibrium constant). This is perhaps surprising since, by definition, P includes pairs at separations $a \leqslant r \leqslant b$ whereas P_1 includes only pairs at separations $r = a_1 = a$. Thus the fluid model does not simply redistribute the separations of a few near-lying shells of pairs as one might expect; it places a substantially greater fraction of the ions into the category 'unpaired'. There are two primary reasons for this: (1) The fluid model overestimates the 'volume' available to the ions and thereby (in effect) overestimates the entropy of the unpaired ions. This has the effect of reducing the pairing. (2) The fluid model overestimates the electrostatic interaction of the unpaired ions by ignoring screening effects which become important at large separations. This also reduces the pairing. The first point is easiest to understand if one considers the simple example of substitutional pairing in the absence of interactions (i.e., accidental or random pairing). If the ions are unrestricted in the sense that they can substitute on any of the $2N$ lattice sites in the crystal then the probability that a given donor has an acceptor as its nearest-neighbor is $N_A Z_1/2N$. This would be the case, for example, in Ge or Si. If the ions are required to substitute on opposite sublattices, however, the corresponding probability is $N_A Z_1/N$. Thus the probability of DA pair formation is automatically enhanced by a factor of two when the ions are restricted to opposite sublattices. This argument is easily verified by explicit calculation in the case of the discrete model (the Ω_i for the case of Ge mentioned above turn out to be half as large as those for GaP). The fluid model cannot easily accommodate such refinements as restricted substitutional pairing but one can heuristically justify a simple doubling of the Ω values calculated from Ref. [1]. This brings

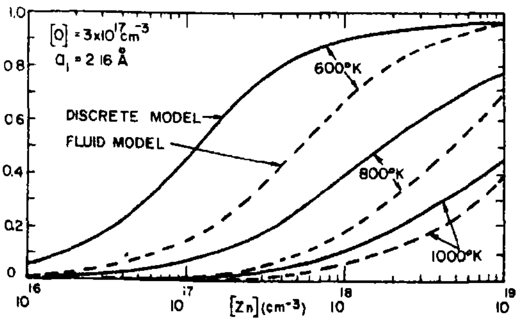

Fig. 6. A comparison of the [Zn] concentration dependence of f as predicted by the discrete and fluid models of ion pairing.

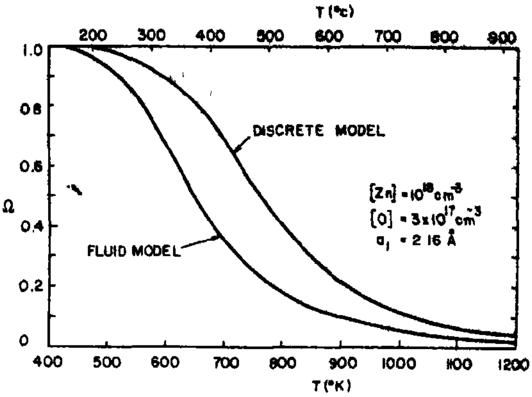

Fig. 7. A comparison of the temperature dependence of f as predicted by the discrete and fluid models of ion pairing.

the predicted pairing into much closer agreement with the discrete model.

In order to see how the fluid model overestimates the electrostatic interaction of unpaired ions it is necessary to refer to the fundamental equations of the model [equations (25–27)] rather than the commonly-used approximation [equation (28)]. The integral of $g(r)\,dr$ between a and b is certainly insensitive to any screening effects because of the small r values involved. It is through the *normalization parameter*, h, that screening becomes important. From equations (25) and (26) it is seen that

$$h^{-1} = \int_a^{\infty} 4\pi r^2 \exp\left(-\frac{4}{3}\pi r^3 N\right) \exp\left(e^2/\epsilon kTr\right) \mathrm{d}r. \tag{29}$$

If screening were included it would cause the integrand to fall off more rapidly with r and would hence increase h and increase P/N_D. When this effect is taken into account along with the doubling of Ω described above, the fluid model is nearly in agreement with the discrete model but it is still roughly 10–15 per cent low for intermediate states of pairing ($0{\cdot}1 < f < 0{\cdot}9$). Thus, while it is gratifying that the disagreement between the two models can be resolved, the resolution seems clearly to favor the discrete model for simplicity and reliability.

Acknowledgements—It is a pleasure to acknowledge numerous helpful discussions with M. DiDomenico, Jr. I have also benefitted from discussions with R. A. Faulkner, R. M. Martin and J. C. Phillips.

REFERENCES

1. REISS H., FULLER C. S. and MORIN F. J., *Bell Syst. Tech. J.* **35**, 535 (1956).
2. PRENER J. S. and WILLIAMS F. W., *Phys. Rev.* **101**, 1427 (1956).
3. HARDY J. R. and BULLOUGH R., *Phil. Mag.* **15**, 237 (1967). *Ibid* **16**, 405 (1967).
4. FLOCKEN J. W., *Phys. Rev. B* **1**, 435 (1970).
5. WILLIAMS F., *Phys. Status Solidi* **25**, 493 (1968).
6. DEAN P. J., *Junction Electroluminescence*, in *Applied Solid State Science*, Vol. 1, (Edited by R. Wolfe) Academic Press, New York, 1969.
7. CASEY H. C. and TRUMBORE F. A., *Mater. Sci. Eng.* **6**, 69 (1970).
8. BJERRUM N., *Kgl Danske Vidensk. Selskab.* 7, No. 9 (1926).
9. FUOSS R. M., *Trans. Faraday Soc.* **30**, 967 (1934).
10. FOWLER R. H. and GUGGENHEIM E. A., *Statistical Thermodynamics*, Chap. IX, Cambridge University Press, Cambridge (1939).
11. REISS H., *J. chem. Phys.* **25**, 400 (1956); *ibid* **25**, 408 (1956).
12. PRENER J. S., *J. chem. Phys.* **25**, 1294 (1956).
13. LIDIARD A. B., *Phys. Rev.* **94**, 29 (1954).
14. PATRICK L., *Phys. Rev. Lett.* **21**, 1685 (1968).
15. PATRICK L., *Phys. Rev.* **180**, 794 (1969).
16. SRINIVASAN G., *Phys. Rev.* **178**, 1244 (1969).
17. VAN VECHTEN J. A. and PHILLIPS J. C., *Phys. Rev. B* **2**, 2160 (1970).
18. PAULING L., *The Nature of the Chemical Bond* Third Edition Cornell Univ. Press, New York (1960).
19. PHILLIPS J. C., *Phys. Rev. B* **2**, 2147 (1970).
20. PHILLIPS J. C., (private communications).
21. DIDOMENICO M., Jr. (private communication).
22. We are interested only in temperatures at which one or more of the impurity species has sufficient mobility for the pairing to proceed. At lower temperatures the pair distribution becomes frozen.
23. WILEY J. D. and SEMAN J. A., *Bell Syst. Tech. J.* **49**, 355 (1969).
24. DEBYE P. and HÜCKEL E., *Phys. Z.* **24**, 195 (1923).
25. Strictly speaking, one should minimize F with respect to the P_j's subject to the constraint that $\beta < N_D$. This insures that the total number of pairs doesn't exceed the number of donors (we have already assumed $N_D < N_A$). As will become clear shortly, however, it is not necessary to impose this constraint explicitly.
26. By setting $K = 0$ and $m = 2$ equations (16–18) reduce to those given by PRENER J. S. and WILLIAMS F. E., *Phys. Rev.* **101**, 1427 (1956).
27. These calculations had already been performed using Pauling's radii (Ref. [18]) before the revised values of Van Vechten and Phillips (Ref. [17]) were published. The differences are small and will not be important for present purposes, however.

J. Phys. Chem. Solids Pergamon Press 1971. Vol. 32, pp. 2063–2074. Printed in Great Britain.

ELECTRONIC BAND STRUCTURE OF ScN

P. WEINBERGER, K. SCHWARZ* and A. NECKEL
Institute of Physical Chemistry, University of Vienna, Austria

(*Received* 5 *October* 1970; *in revised form* 7 *December* 1970)

Abstract—Proceeding from the self-consistent HFS-potentials[1] of the ions Sc^+ and N^-, a quasi-selfconsistent calculation of the band structure of ScN was carried out via the APW-method. The energy eigenvalues and the wave functions for an equivalent of 256 k-points in the first Brillouin zone were calculated using the full Slater exchange potential. According to these calculations, ScN is a semiconductor with a band gap of about 0·1 eV and possesses a partially ionic character.

1. INTRODUCTION

A NON-self-consistent calculation[2] of the band structure of ScN, starting with the atomic HFS-potentials[1], showed that the charge within the N-sphere is 1·1 electronic charges greater than the charge within the same sphere of the free atom. This result suggests that ScN has a partially ionic character. Therefore, it was decided to carry out a quasi-self-consistent APW-calculation of the band structure, based on HFS-potentials of the free ions Sc^+ and N^-.

The quasi-self-consistent APW-method was used for the first time in 1966 by Switendick[3]. Meanwhile papers have been published, not only on metals[4–7] but also on ionic crystals[8] and refractory phases[9].

2. METHOD OF COMPUTATION

ScN crystallizes in the NaCl-structure. The cubic parameter a is $a = 4{\cdot}45$ Å (10).

The traditional 'muffin-tin'-form[11] was used for the construction of the crystal potential. The starting potential was constructed by superposing the self-consistent HFS-potentials of the ions Sc^+ $(1s^22s^22p^63s^23p^63d4s)$ and N^- $(1s^22s^22p^4)$† according to the α-expansion method of Löwdin[12].

The crossing point of the superposed spherically averaged potential curves of the ions in the (100) direction determines the atomic-sphere radii. These radii, which are held constant during the self-consistency iterations, have the values of 2·191000 a.u. for Sc and of 2·013450 a.u. for N.

The crystal wave functions for the equivalent of 256 k-points within the first Brillouin zone were calculated for each iteration step. All vectors $\mathbf{k}_i = \mathbf{k} + \mathbf{K}_i$ ($\mathbf{K}_i$ being a reciprocal lattice vector) with $|\mathbf{k}_i| = (\pi/a)\sqrt{80}$ were included‡ in the wave functions. The expansion in spherical harmonics was taken up to $l = 12$. A spherically averaged radial charge density $\sigma_p{}^{\nu}(r)$[11] (r is the radius measured from the centre of the atomic sphere) was calculated for each atomic sphere p from the crystal wave functions of the valence electrons. For the first six iterations a frozen core approximation was used for all states below the Sc-3d and N-2s bands. Because the Sc-3s and Sc-3p wave functions extend beyond the APW-sphere, it was necessary to use Löwdin's α-expansion technique[12] to obtain the contributions from these states to the core charge density $\sigma_p^c(r)$ in each sphere. For the further iterations the states corresponding to the atomic Sc-3s and 3p states were treated as bands, i.e. not only were the valence states but also the above mentioned states included in the APW-calculation. These states will be referred to as 'semi-core-levels' throughout this paper, and the radial charge density corresponding to them will be denoted as $\sigma_p^{sc}(r)$. The radial charge density of the remaining core states, however, will be denoted as $\sigma_p^c(r)$. For the first six iterations the total radial charge density $\sigma_p(r)$ within the p-th sphere was obtained by adding the superposed radial charge density $\sigma_p^c(r)$ of the core states to $\sigma_p^v(r)$. For the further iterations $\sigma_p(r)$ was obtained by adding $\sigma_p^c(r)$ and $\sigma_p^{sc}(r)$ to $\sigma_p^v(r)$.

---

*Present Address: Quantum Theory Project, University of Florida, Gainesville, U.S.A.

†In order to obtain convergent wave functions for N^-, we did not follow the procedure for the calculation of the wave functions of anions proposed by Watson[13] or Paschalis and Weiss[14]. Instead, the coefficient of the Slater exchange potential was made larger than the unity quoted in the programme of Herman and Skillman[1]. The smallest value of this coefficient for which a localized $2p$-state could be obtained was 1·185, which was the value used to obtain the starting potential for the ScN calculation. However, in view of the quasi-self-consistency of the band structure calculation, this approximation should not affect the final result.

‡For a few low symmetry points we had to use a smaller value, because we could handle only 50 symmetrized APW's with our facilities.

By solving Poisson's differential equation, the Coulomb-potential $V_{Cp}(r)$ within the p-th atomic sphere is obtained with the exception of an additive constant C_p.

$$V_{Cp}(r) = -\frac{2Z_p}{r} + \frac{2}{r}\int_0^r \sigma_p(r')\,\mathrm{d}r' + 2\int_r^{R_p} \frac{\sigma_p(r')}{r'}\,\mathrm{d}r' + C_p. \tag{1}$$

Z_p is the atomic number.

$\sigma_p(r)$ also permits the calculation of the exchange potentials $V_{Xp}(r)$ within the atomic spheres, according to Slater's free electron approximation

$$V_{Xp}(r) = -6[3\sigma_p(r)/32\pi^2 r^2]^{1/3}. \tag{2}$$

A constant charge density $\bar{\rho}$ is assumed between the spheres; it is defined in such a way that the unit cell is electrically neutral.

A charge distribution consisting of spherically symmetric charge densities within the APW-spheres and a constant charge density between the APW-spheres leads to a potential outside the spheres which is equal to that of a charge distribution of fictitious point charges Q_p

$$Q_p = Z_p - \int_0^{R_p} \sigma_p(r)\,\mathrm{d}r + \frac{4\pi}{3} R_p^3\,\bar{\rho} \tag{3}$$

at the atomic sites and a uniform charge density $\bar{\rho}$ throughout the unit cell. This charge distribution permits the application of Ewald's method[15, 16] to calculate the spherically averaged mean value $V_{Ep}(R_p)$ of the Ewald potential at the surface of the p-th APW-sphere and the mean value V_{EC} of the Coulomb potential between the spheres.

The Ewald potential has the following spherical averages

$$V_{E1}(r) = Q_1\phi_1(r) + Q_2\phi_2(r) \qquad \text{in sphere 1,}$$

$$V_{E2}(r) = Q_2\phi_1(r) + Q_1\phi_2(r) \qquad \text{in sphere 2,}$$

$$\text{where } \phi_1(r) = 2\left(\frac{1}{r} + \frac{8\pi}{3a^3}r^2 - \frac{4{\cdot}584850}{a}\right)$$

$$\text{and} \qquad \phi_2(r) = 2\left(\frac{8\pi}{3a^3}r^2 - \frac{1{\cdot}089730}{a}\right). \tag{4}$$

for the NaCl-structure.

The spherically averaged mean value V_{Ep} of the Ewald potential at the sphere radius R_p is set equal to the Coulomb potential $V_{Cp}(r)$ to determine the constant C_p

$$V_{Cp}(R_p) = -\frac{2Z_p}{R_p} + \frac{2}{R_p}\int_0^{R_p} \sigma_p(r')\,\mathrm{d}r' + C_p$$

$$= V_{Ep}(R_p). \tag{5}$$

Since the average value of the Ewald

potential over the unit cell is zero, equation (6)

$$4\pi \sum_{p=1}^{2} \int_0^{R_p} V_{Ep}(r) r^2 \, \mathrm{d}r + V_{Ec}\Omega_c = 0 \qquad (6)$$

determines the average value V_{Ec} of the Ewald potential outside the spheres. Ω_c is the volume between the spheres in the unit cell.

From the constant charge density $\bar{\rho}$ the constant exchange potential V_{Xc} between the APW-spheres can be obtained according to Slater's approximation:

$$V_{Xc} = -6(3\bar{\rho}/8\pi)^{1/3}. \qquad (7)$$

The potential in the p-th sphere, referred to the constant potential between the APW-spheres, can therefore be written in the following way by combining equations (1) to (7):

$$\begin{aligned} V_p(r) = &-\frac{2Z_p}{r} + \frac{2}{r}\int_0^r \sigma_p(r')\,\mathrm{d}r' \\ &+ 2\int_r^{R_p} \frac{\sigma_p(r')}{r'}\,\mathrm{d}r' + \frac{2}{R_p}\left\{Z_p - \int_0^{R_p} \sigma_p(r')\,\mathrm{d}r'\right\} \\ &+ V_{Ep}(R_p) - V_{Ec} + V_{Xp}(r) - V_{Xc}. \qquad (8) \end{aligned}$$

The wave function of the state μ in the p-th atomic sphere can be expressed in the following form:

$$\Psi_p^{\mu}(r) = \sum_l \sum_m C^{\mu}_{p,lm} R_{pl}(r) Y_{lm}(\vartheta, \varphi).$$

($R_{pl}(r)$ is the radial wave function; $Y_{lm}(\vartheta, \varphi)$ are the spherical harmonics; r, ϑ, φ are the spherical coordinates of point r, with respect to the centre of the sphere p). From this wave function a quantity $q_{p,nl}(E_\mu)$ can be calculated [2, 17], which represents the number of electronic charges with nl-character* of the state μ with energy $E_\mu(\mathbf{k})$ in the p-th sphere. Adding these $q_{p,nl}(E_\mu)$-values, each properly weighted according to symmetry and degeneracy over the occupied states, leads to the total charge $\bar{q}_{p,nl}$ with nl-character within the p-the atomic sphere.

3. CONVERGENCE

In the present calculation six iterations have been performed applying the frozen core approximation. Using the potential obtained in the fifth iteration, an APW-calculation for the semi-core-states was made. The sixth iteration step was now repeated using a potential, which was calculated from a total radial charge density $\sigma_p(r)$, consisting of $\sigma_p{}^c(r)$, $\sigma_p{}^{sc}(r)$ and $\sigma_p{}^v(r)$. For the further three iteration steps the semi-core-states were always included in the APW-calculation.

In order to obtain a rather stable and rapid convergence, a method was used[11], in which the input charge density $[\sigma_p(r)]^i_{\text{in}}$ for the i-th iteration step was composed of the input and output charge densities of the $(i-1)$-th step, by using a constant factor $f = 0{\cdot}75$

$$[\sigma_p(r)]^i_{\text{in}} = f[\sigma_p(r)]^{i-1}_{\text{in}} + (1-f)[\sigma_p(r)]^{i-1}_{\text{out}}.$$

In order to check the convergence of the iteration process, various criteria can be applied. An appropriate criterion seems to be the change of the nl-like charge $\bar{q}_{p,nl}$ of the valence electrons within the p-th atomic sphere. In Fig. 1 the charge with $2p$-character $\bar{q}_{N,2p}$, within the N-sphere and the charge with $3d$-character $\bar{q}_{\text{Sc},3d}$ within the Sc-sphere are plotted vs. the number of iterations. The discontinuity at the sixth iteration is due to the fact that for the first six iterations the frozen core approximation was used, while for the following iterations the semi-core-states were treated as bands. It can be seen that the charges $\bar{q}_{N,2p}$ and $\bar{q}_{\text{Sc},3d}$ vary only slightly (by 0·013 and 0·012 electronic charges, respectively) between the ninth and the eighth iteration step. It is apparant from Fig. 1 that a significant charge transfer be-

---

*Following the atomic notation, the states are labelled according to l and the number n of $V(n-l-1)$ nodes in the radial part of the wave function in a given sphere.

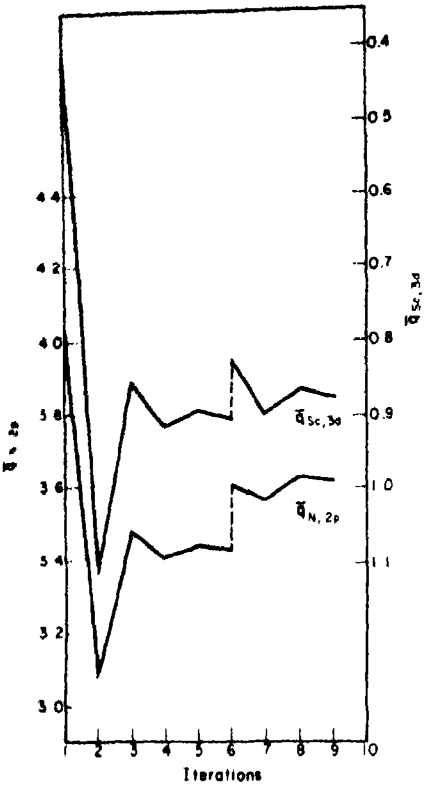

Fig. 1. Change of the charges $q_{Sc,3d}$ and $q_{N,2p}$ in the course of the iteration process.

tween p-like charge in the N-sphere and d-like charge in the Sc-sphere occurs in the initial iterations towards self-consistency. The self-consistency, therefore, is to a large extent an adjustment of this charge distribution from the initial estimate to the final value appropriate to the solid.

The change of the energy eigenvalues ($\Delta E_\mu(\mathbf{k})$) is approximately 0·002 Ryd for p-states and 0·006 for d-states between the last iteration and the preceding one.

The maximum difference between the input and output values of $rV(r)$ for the final (9th) iteration is 0·015 Ryd × a.u. (at $r = 0{\cdot}997$ a.u.) for the Sc-sphere and 0·013 Ryd × a.u. (at $r = 1{\cdot}380$ a.u.) for the N-sphere.

Considering the various other assumptions in the APW-method in the present form, the convergence can be regarded as sufficient.

4. RESULTS AND DISCUSSION

The quasi-self-consistent potential referred to the constant potential between the APW-spheres as zero is given in Table 1. The energies of the quasi-self-consistent calculation are listed in Table 2. An accurate density of states was obtained from these selfconsistent energies by an LCAO-interpolation scheme, following Slater and Koster[17]. Connolly has developed a computer programme[18], which first performs a least squares fit to the set of energy bands obtained by the APW-method, using the LCAO interaction integrals as parameters. The 3d orbitals of Sc and the 2s and 2p orbitals of N were used as basis functions. The LCAO interaction integrals obtained are given in the Appendix. With these optimized parameters, interpolated energies are obtained at a large number of points in the Brillouin-zone. (In the present calculation we used 131 072 equivalent points). Finally a histogram-technique was used with $\Delta E = 0{\cdot}0085$ Ryd to get the density of states (Fig. 2). The integral of the density of states leads to the Fermi energy of 0·4908 Ryd, referred to the constant potential between the spheres.

The $q_{p,nl}(E_\mu)$ values for some selected k-points are given in Table 3*.

In analogy to the density of states, a nl-character density $\chi_{nl}(E)$ can be defined[2]. $\chi_{nl}(E)$ indicates the number of electrons with a nl-like charge within the atomic spheres per unit energy range (Fig. 3).†

The band structure of ScN (Fig. 4) shows a low lying 2s-band (Figs. 2 and 3), which contains a slight admixture of 3d- and 4p-states. The 2s-band is separated from the three valence bands with predominant 2p-character by an energy gap of 7·8 eV.

The analysis of the nl-character of these bands (Fig. 3) shows that they contain only

---

*The authors are prepared to provide the $q_{p,nl}(E_\mu)$ values for all states indicated in Table 2 on request.

†This was done only for the 256-grid, because $\chi_{nl}(E)$ did not fit into the interpolation scheme for the density of states.

Table 1. Quasi-self-consistent potentials $V(r)$ in the Sc-sphere and in the N-sphere, referred to the constant potential between the APW-spheres as zero (V in Ryd, r in a.u.)

r	$-rV(r)$	r	$-rV(r)$	r	$-rV(r)$
Scandium-sphere					
0·00080	41·90286	0·11552	29·81886	0·66106	11·04669
0·00160	41·80495	0·12194	29·33009	0·68673	10·66149
0·00241	41·70621	0·12836	28·85799	0·71240	10·29301
0·00321	41·60667	0·13478	28·40117	0·73807	9·93920
0·00481	41·40561	0·14120	27·95886	0·76374	9·59825
0·00642	41·20320	0·14761	27·52983	0·78942	9·26918
0·00802	40·99904	0·15403	27·11331	0·81509	8·95092
0·00963	40·79396	0·16045	26·70836	0·84076	8·64305
0·01123	40·58829	0·16687	26·31432	0·86643	8·34486
0·01284	40·38235	0·17329	25·93053	0·89211	8·05620
0·01444	40·17642	0·17970	25·55644	0·91778	7·77652
0·01605	39·97083	0·18612	25·19162	0·94345	7·50579
0·01755	39·76581	0·19254	24·83565	0·96912	7·24352
0·01925	39·56151	0·19896	24·48820	0·99479	6·98960
0·02086	39·35809	0·20538	24·14896	1·04614	6·50559
0·02246	39·15579	0·21179	23·81766	1·09748	6·05197
0·02407	38·95459	0·21821	23·49397	1·14882	5·62501
0·02567	38·75468	0·22463	23·17776	1·20017	5·22579
0·02728	38·55612	0·23747	22·56668	1·25151	4·84920
0·02888	38·35899	0·25030	21·98280	1·30286	4·49408
0·03049	38·16333	0·26314	21·42409	1·35420	4·15886
0·03209	37·96916	0·27598	20·88907	1·40555	3·84171
0·03530	37·58546	0·28881	20·37599	1·45689	3·54150
0·03851	37·20808	0·30165	19·88329	1·50823	3·25677
0·04172	36·83694	0·31448	19·40948	1·55958	2·98692
0·04493	36·47209	0·32732	18·95305	1·61092	2·73105
0·04814	36·11342	0·34016	18·51280	1·66227	2·48880
0·05134	35·76076	0·35299	18·08740	1·71361	2·25993
0·05455	35·41403	0·36583	17·67596	1·76496	2·04414
0·05776	35·07303	0·37866	17·27734	1·81630	1·84168
0·06097	34·73767	0·39150	16·89107	1·86765	1·65231
0·06418	34·40765	0·40434	16·51616	1·91899	1·47658
0·06739	34·08321	0·41717	16·15242	1·97033	1·31417
0·07060	33·76393	0·43001	15·79923	2·02168	1·16551
0·07381	33·44986	0·44284	15·45651	2·07302	1·03017
0·07702	33·14095	0·45568	15·12389	2·12436	0·90873
0·08023	32·83711	0·46852	14·80150	2·17571	0·80018
0·08343	32·53827	0·48135	14·48891	2·22705	0·70511
0·08664	32·24448	0·50702	13·89418	2·27840	0·62247
0·08985	31·95560	0·53270	13·33741	2·32974	0·55253
0·09306	31·67178	0·55837	12·81853	2·38109	0·49438
0·09627	31·39275	0·58404	12·33312	2·43243	0·44860
0·10269	30·84941	0·60971	11·87906	2·48377	0·42379
0·10911	30·32484	0·63538	11·45130	2·53512	0·39178
Nitrogen-sphere					
0·00116	13·97515	0·14810	10·68672	0·80531	3·80983
0·00231	13·95012	0·15736	10·51062	0·84233	3·60149
0·00347	13·92491	0·16661	10·33863	0·87936	3·40167
0·00463	13·89952	0·17587	10·17053	0·91638	3·21029
0·00694	13·84812	0·18513	10·00615	0·95341	3·02706
0·00926	13·79613	0·19438	9·84527	0·99043	2·85194
0·01157	13·74352	0·20364	9·68774	1·02745	2·68467

Table 1 *(cont.)*

r	$-rV(r)$	r	$-rV(r)$	r	$-rV(r)$
0·01388	13·69037	0·21290	9·53334	1·06448	2·52518
0·01620	13·63675	0·22215	9·38197	1·10151	2·37321
0·01851	13·58271	0·23141	9·23342	1·13854	2·22865
0·02083	13·52830	0·24067	9·08764	1·17556	2·09124
0·02314	13·47358	0·24992	8·94445	1·21259	1·96085
0·02546	13·41860	0·25918	8·80380	1·24961	1·83720
0·02777	13·36339	0·26844	8·66558	1·28664	1·72018
0·03008	13·30801	0·27769	8·52977	1·32366	1·50947
0·03240	13·25247	0·28695	8·39628	1·36069	1·50496
0·03471	13·19681	0·29620	8·26511	1·39771	1·40636
0·03703	13·14108	0·30546	8·13621	1·43474	1·31359
0·03934	13·08530	0·31472	8·00960	1·47176	1·22630
0·04165	13·02954	0·32397	7·88522	1·50879	1·14447
0·04397	12·97616	0·34249	7·64346	1·54582	1·06776
0·04628	12·91803	0·36100	7·41067	1·58284	0·99616
0·05091	12·80680	0·37951	7·18727	1·61987	0·92936
0·05554	12·69598	0·39802	6·97292	1·65689	0·86736
0 05017	12·58571	0·41654	6·76792	1·69392	0·80985
0·06479	12·47616	0·43505	6·57177	1·73094	0·75690
0·06942	12·36741	0·45356	6·38436	1·76797	0·70819
0·07405	12·25956	0·47208	6·20505	1·80499	0·66387
0·07858	12·15270	0·49059	6·03344	1·84202	0·62360
0·08331	12·04687	0·50910	5·86879	1·87905	0·58758
0·08794	11·94212	0·52761	5·71058	1·91607	0·55552
0·09256	11·83852	0·54613	5·55810	1·95310	0·52762
0·09719	11·73604	0·56464	5·41085	1·99012	0·50368
0·10182	11·63476	0·58315	5·26826	2·02715	0·48392
0·10645	11·53466	0·60167	5·12990	2·06417	0·46822
0·11108	11·43575	0·62018	4·99536	2·10120	0·45677
0·11570	11·33804	0·63869	4·86432	2·13823	0·44958
0·12033	11·24152	0·65720	4·73650	2·17525	0·44697
0·12496	11·14618	0·67572	4·61167	2·21228	0·44887
0·12959	11·05201	0·69423	4·48965	2·24930	0·45575
0·13422	10·95899	0·73125	4·25344	2·28633	0·46184
0·13885	10·86711	0·76828	4·02706	2·32335	0·49321

about 15 per cent 3*d*-states. The result for ScN differs from that for the compounds ScC and TiC, but also for TiN (2, 9, 19). The 2*p*-bands of the latter compounds contain a considerable portion of 3*d*-states. Because of the strong interaction between metal 3*d*-states and nonmetal 2*p*-states, one can conclude that strong covalent bonds exist in these substances. As compared to ScC or TiC, ScN exhibits a less covalent character.

The conduction bands of ScN have predominantly 3*d*-character unlike ScC and TiC, whose conduction bands are mixtures of 2*p*- and 3*d*-states.

While the non self-consistent calculation[2] of the energy bands of ScN led to an energy gap of about 0·6 eV between the highest occupied valence band and the lowest conduction band, the present calculation yields an energy gap of about 0·1 eV (0·0071 Ryd). It should, however, be noted that the relative position of the valence and conduction bands may depend considerably on the chosen exchange potential.

Based on an empirical relation, which permits the estimation of the energy gaps of III–V semiconductors, Sclar[20] predicts a value of 2·6 eV for the energy gap in ScN. For the compounds DyN, ErN and HoN Sclar's estimations are in agreement with his

*Table 2. Energy eigenvalues E(**k**) in Ryd, referred to the constant potential between the APW-spheres as zero*

k	Irred. Rep	$E(\mathbf{k})$	**k**	Irred. Rep.	$E(\mathbf{k})$
(000)	Γ_1	−0·5409	(130)	G	0·8356
		0·9755			0·9168
	Γ_{15}	0·4908		UG	0·3644
	Γ_{12}	0·7250			0·6082
	$\Gamma_{25'}$	0·6501			0·8174
(010)	Δ_1	−0·5212	(140)	Z_1	−0·4623
		0·3766			0·3644
		0·8103			0·8323
		1·0518			0·8855
	Δ_2	0·7344		Z_2	0·8246
	$\Delta_{2'}$	0·6233		Z_3	0·2860
	Δ_5	0·4612			0·8039
		0·7058	(140)	Z_4	0·3608
(020)	Δ_1	−0·4854			0·5981
		0·2658	(220)	Σ_1	−0·4446
		0·8732			0·2223
	Δ_2	0·7551			0·7810
	$\Delta_{2'}$	0·5653			0·8524
	Δ_5	0·4315		Σ_2	0·7416
		0·7845		Σ_3	0·3340
(030)	Δ_1	−0·4717			0·7626
		0·2575		Σ_4	0·3190
		0·8853			0·9994
	Δ_2	0·7776	(230)	G	−0·4436
	$\Delta_{2'}$	0·5167			0·2479
	Δ_5	0·4264			0·3276
		0·8211			0·7437
(040)	X_1	−0·4735			0·8665
		0·8693			0·9552
	X_2	0·7870		UG	0·3118
	X_3	0·4979			0·7305
	$X_{4'}$	0·2818			0·8117
	X_5	0·8249	(240)	W_1	−0·4504
	$X_{5'}$	0·4290			0·8488
(110)	Σ_1	−0·5026		W_2	0·8239
		0·3420		$W_{2'}$	0·3122
		0·7270			0·9170
		0·7829		W_3	0·3071
	Σ_2	0·6775			0·7251
	Σ_3	0·4247	(330)	K_1	−0·4521
		0·6925			0·2899
	Σ_4	0·3872			0·6435
		0·8760			0·8778
(120)	G	−0·4694		K_2	0·8014
		0·2534		K_3	0·2904
		0·3637			0·8106
		0·7775		K_4	0·3616
		0·8209			0·9003
		0·9325	(111)	Λ_1	−0·4849
	UG	0·3830			0·2976
		0·6410			0·7144
		0·7736		Λ_3	0·3727
(130)	G	−0·4591			0·7141
		0·2543			0·8818
		0·3647	(121)	G	−0·4545
		0·8008			0·2280

Table 2 (cont.)

k	Irred. Rep.	$E(\mathbf{k})$	**k**	Irred. Rep.	$E(\mathbf{k})$
(121)	G	0·3311	(231)	Q_1	−0·4354
		0·6813			0·3067
		0·7896			0·7382
		0·9494			0·9172
	UG	0·3561		Q_2	0·2127
		0·7733	(231)	Q_2	0·3236
		0·8919			0·7589
(131)	G	−0·4475			0·8091
		0·2386			0·9637
		0·3158	(222)	L_1	−0·4199
		0·6539		$L_{2'}$	0·1566
		0·8138			0·8071
		0·9217		$L_{3'}$	0·3043
	UG	0·3567			0·7832
		0·8004			1·0020
		0·8973			
(221)	G	−0·4326			
		0·1894			
		0·3195			
		0·7629			
		0·7967			
		0·9307			
	UG	0·3108			
		0·7603			
		0·9983			

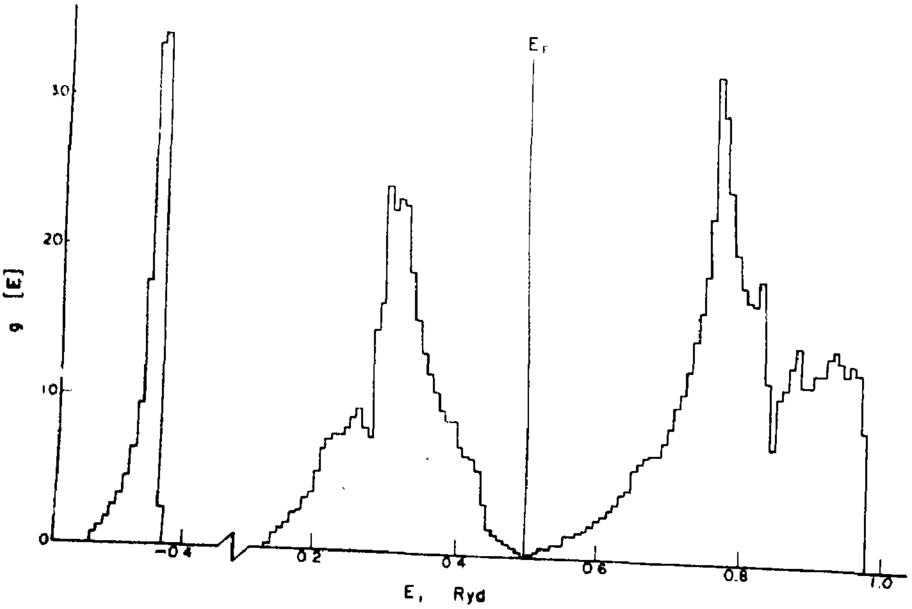

Fig. 2. Density of states histogram (spin included) for ScN in electrons per primitive cell × Rydberg. $\Delta E = 0·0085$ Ryd.

Table 3. Analysis of the charge ($q_{p,nl}(E_\mu)$ values) in the APW-spheres (in per cent) for some selected energy states

		Nitrogen-sphere					Scandium-sphere				
k	Irred. Rep.	$2s$	$3s$	$2p$	$3d$	$4f$	$4s$	$4p$	$3d$	$4f$	$E(\mathbf{k})$
(000)	Γ_1	75·95					5·58				−0·5409
	Γ_{15}			86·71				1·46		1·84	0·4908
	Γ_{12}				4·75				85·52		0·7250
	$\Gamma_{25'}$				2·90				77·23		0·6501
(040)	X_1	83·24					0·61		5·33		−0·4735
	X_1		9·70		0·18		0·01		85·16		0·8693
	X_2				3·78				90·38		0·7870
	X_3				4·23				60·25		0·4979
	$X_{4'}$			60·85		0·07		9·78			0·2818
	X_5				0·02				93·00		0·8249
	$X_{5'}$			79·22		0·03		4·52		1·08	0·4290
(240)	W_1	84·13			0·01			1·71	4·15	0·16	−0·4504
	W_1		7·21		1·13	0·02		0·01	86·56	0·07	0·8488
	W_2					0·02			93·10		0·8239
	$W_{2'}$			64·19		0·04	2·65		15·64	0·44	0·3122
	$W_{2'}$			12·93	2·16	0·33	2·03		76·90	0·13	0·9170
	W_3			56·63	0·44	0·06		6·84	8·12	0·10	0·3071
	W_3			16·84	1·27	0·27		0·19	65·91	0·46	0·7251
(222)	L_1	84·29			0·02			5·32		0·46	−0·4199
	$L_{2'}$			48·51		0·08	6·88		10·69		0·1566
	$L_{2'}$			20·88		0·45	0·84		69·06		0·8071
	$L_{3'}$			59·19		0·12			25·34		0·3043
	$L_{3'}$			2·27		0·65			87·85		0·7832
	$L_{3'}$			28·39		0·49			69·00		1·0020
(330)	K_1	83·92		0·05		0·01	0·12	1·65	4·09	0·15	−0·4521
	K_1	0·17		55·13	0·53	0·02	2·60	2·78	12·02	0·28	0·2899
	K_1		0·42	15·18	2·29	0·23	0·44	0·01	59·13	0·49	0·6435
	K_1		6·72	3·89	0·80	0·12	0·46	0·15	82·46	0·06	0·8778
	K_2				0·18	0·20			90·75	0·07	0·8014
	K_3			58·30	0·17	0·07		8·08	4·83	0·02	0·2904
	K_3			10·52	0·17	0·13		0·10	80·71	0·15	0·8106
	K_4			66·99	0·11	0·04		2·18	15·48	0·47	0·3616
	K_4			15·23	2·05	0·28		0·85	77·01	0·18	0·9003

measurements of the absorption edges in the optical transmission curves[21]. In the case of ScN, however, Sclar[21] did not find a distinct absorption edge. From nuclear magnetic resonance studies, Kume[22] concludes that ScN is semi-metallic. The electrical resistivity, measured by Sclar[21] and Lyutaya and Samsonov[23], increases linearly with temperature. The observed metallic-type conductivity, however, is no clear proof of the metallic character of stoichiometric ScN. As the examined samples were nitrogen-deficient, the metallic conductivity might be due to nonstoichiometry.

Very informative is a comparison of the charges within the APW-spheres in the crystal with the charges obtained by superposition of the charge densities of the free ions Sc^+ and N^- and those obtained by superposition of the charge densities of the free atoms. The superposition is made according to the α-expansion technique of Löwdin[12]. Such a comparison is given in Table 4. The same table also shows a comparison of the charges $\bar{q}_{p,nl}$ of the core-, semi-core and valence states in the crystal with the corresponding charges in the free ions and in the free atoms.

In the Sc-sphere the charge with $4s$-character decreases by about 0·1 electrons. On the other hand, there are 0·2 electrons with

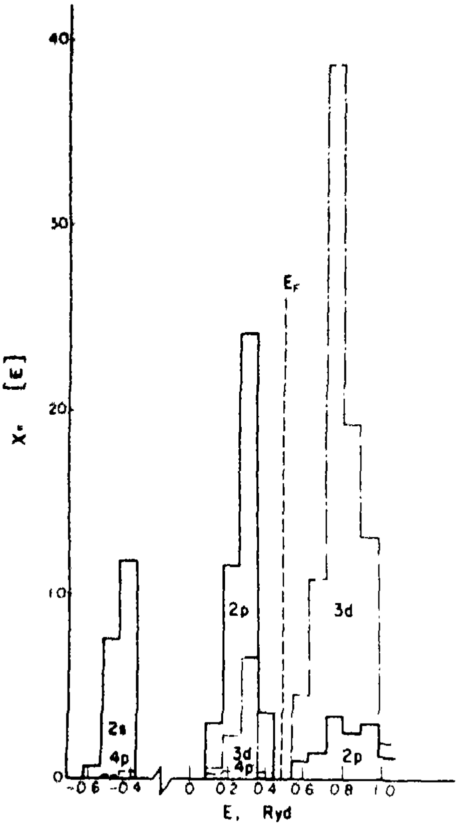

Fig. 3. nl-Character $\chi_{nl}(E)$ for ScN in electrons in the APW-spheres per primitive cell × Ryd. ΔE = 0·085 Ryd.

4p-symmetry. The 3d-charge is only slightly increased in comparison with the free atom. In the N-sphere the 2p-charge increases by about 1·2 electrons, whilst the charge with the 2s-character decreases by about 0·1 electrons.

The treatment of the states which correspond to the atomic 3s and 3p levels of Sc as bands leads to wave functions which have a more diffuse character than the atomic functions. Thus, an increase of the semi-core charge in the N-sphere is effected as well as a decrease of the semi-core charge in the Sc-sphere in comparison with the charges obtained by superposition of the atomic charge densities.

The comparison of the total charges in the APW-spheres with the charges obtained by superposition of the charge densities of the free ions and the free atoms respectively, leads to the following result:

The charge in the N-sphere is more negative by about 0·2 electrons, the charge in the Sc-sphere is more positive by about 0·2 electrons than the charges obtained by superposition of the charge densities of the free ions. This result leads to the conclusion that the charge of the particles in solid ScN is larger than unity.

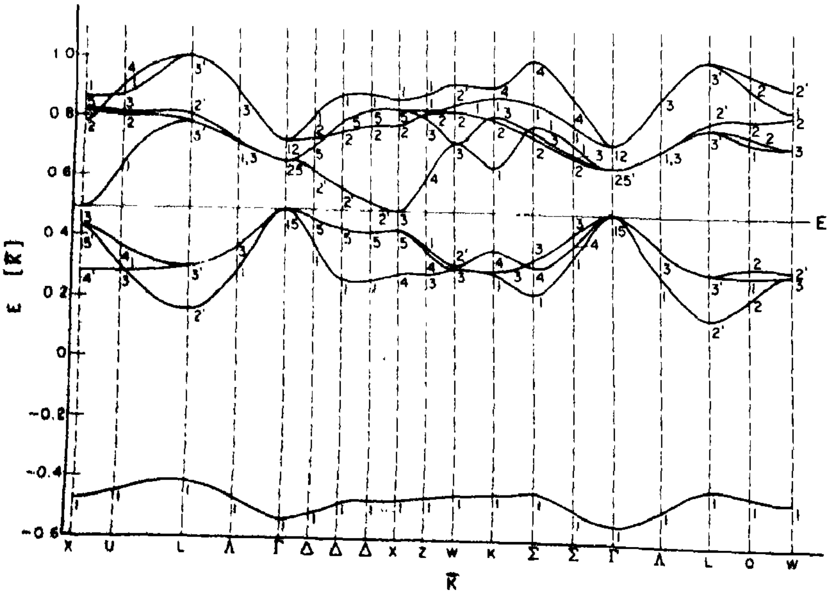

Fig. 4. Band structure of ScN.

Table 4. Electronic charges $q_{p,nl}$ in the APW-spheres and in the intermediate region in the Wigner-Seitz cell.

'Bands' refer to the self consistent charge distribution given by the average of the occupied states at the 256 k-points in the full Brillouin zone. 'Ionic (superposed)' refers to the charge obtained by superposition of the charge densities of the ions Sc^+ and N^-, using the α-expansion technique of Löwdin[12]. 'Atomic (superposed)' refers to the charge obtained by superposing the charge densities of the free atoms Sc and N via the α-expansion technique. 'Ionic (free ion)' or 'Atomic (free atom)' resp., refers to the charge of the free ion or free atom resp., in the same spherical volume.

State		Bands	Ionic (superposed)	Atomic (superposed)	Ionic (free ion)	Atomic (free atom)
			Scandium-sphere			
Valence states	3*d*	0·8768				
	4*s*	0·0976				
	4*p*	0·1977				
	4*f*	0·0255				
	total	1·2043	1·3904	1·4889	0·9710	1·0442
Semi core states	total	7·7651	7·8189	7·8130	7·8187	7·8128
Core states	total	10·0000	10·0000	10·0000	10·0000	10·0000
Total charge in APW-sphere		18·9694	19·2093	19·3019	18·7897	18·8570
			Nitrogen-sphere			
Valence states	2*s*	1·6579				
	2*p*	3·6161				
	3*d*	0·0139				
	4*f*	0·0032				
	total	5·2935	5·0922	4·7335	4·7810	4·2126
Semi core states	total	0·0500	0·0258	0·0269		
Core states	total	2·0000	2·0000	2·0000	2·0000	2·0000
Total charge in APW-sphere		7·3435	7·1180	6·7604	6·7810	6·2126

Charge between the APW-spheres	
Valence states	1·5030
Semi core states	0·1832
Total charge between the APW-spheres	1·6862

Therefore, ScN is assumed to have a more distinct ionic character than ScC; with the latter compound the charge in the Sc-sphere increases by 0·5 electrons and the charge in the *C*-sphere increases by 0·4 electrons when forming the compound. This result might be modified by a self-consistent calculation, but its essential features will be retained. While ScC hardly possesses ionic character, a transfer of charge from the Sc-nucleus to the N-nucleus must be assumed in ScN.

Because of the filled valence bands, one might expect that ScN is a considerably more stable compound than ScC. As a matter of fact, the observed deviations from the stoichiometry in the case of ScN are considerably smaller than in the case of ScC. Thus, samples with a composition $ScN_{0\cdot97}$ could be prepared [23]. ScC, on the other hand, whose Fermi-level lies in the range of high density of states, only exists with a high carbon deficiency as $ScC_{0\cdot3-0\cdot5}$[24, 25].

Acknowledgements—The authors wish to express their thanks to the Jubiläumsfonds der österreichischen Nationalbank for their partial financial support. They are greatly indebted to Professor Dr. Hans Nowotny for the encouragement and the continuous support he gave throughout this work. They also wish to express their appreciation to Dr. John W. D. Connolly for the density of states programme and to Mr. P. Rastl for his valuable assistance. The computations were performed using the facilities of the University of Vienna Computing Centre (Statistisches Institut der Universität Wien).

REFERENCES

1. HERMAN F. and SKILLMAN S., *Atomic Structure Calculations*, Prentice-Hall, Englewood Cliffs, New Jersey (1963).
2. SCHWARZ K., WEINBERGER P. and NECKEL A., *Theor. Chim Acta* **15**, 149 (1969).
3. SWITENDICK A. C., *J. appl. Phys.* **37**, 1022 (1966).
4. SNOW E. C. and WABER J. T., *Phys Rev.* **157**, 570 (1967).
5. SNOW E. C., *Phys Rev.* **171**, 785 (1968)
6. SNOW E. C., *Phys. Rev.* **172**, 708 (1968).
7. RUDGE W. E., *Phys Rev.* **181**, 1024 (1969).
8. DECICCO P. D., *Phys. Rev.* **153**, 931 (1967).
9. CONKLIN J. B. and SILVERSMITH D. J., *Int. J. Quant. Chem.* **2**, 243 (1968)
10. BECKER K. and EBERT F., *Z. Phys.* **31**, 268 (1925).
11. MATTHEISS L. F., WOOD J. H. and SWITENDICK A. C., *Methods in Computational Physics* Vol. 8, p. 63, (Edited by B. Alder, S. Fernbach and H. Rotenberg), Academic Press, New York (1968).
12. LÖWDIN P. O., *Adv. Phys* **5**, 96 (1956).
13. WATSON R. E., *Phys Rev.* **111**, 1108 (1958).
14. PASCHALIS E. and WEISS A., *Theor. Chim Acta* **13**, 381 (1969).
15. EWALD P. P., *Ann. Phys.* **64**, 253 (1921).
16. SLATER J. C. and DECICCO P. D., *Quantum Theory of Molecules and Solids*, Vol. III, App. 4, p. 310, McGraw-Hill, New York, (1967).
17. SLATER J. C. and KOSTER F. G., *Phys. Rev.* **94**, 1498 (1954).
18. CONNOLLY J. W. D., Proceedings of the Electronic Density of States Conference, New York, Nov. 3–6, 1969 (to be published).
19. ERN V. and SWITENDICK A. C., *Phys. Rev.* **137A**, 1927 (1965).
20. SCLAR N., *J. appl. Phys.* **33**, 2999 (1962).
21. SCLAR N., *J. appl. Phys.* **35**, 1534 (1964).
22. KUME K., *J. phys. Soc. Japan* **19**, 414 (1964).
23. LYUTAYA M. D. and SAMSONOV G. V., *Redkie i Redkozem. Elementy v Tekhn., Akad. Nauk Ukr. SSR, Inst- Probl. Materialoved* 118 (1964).
24. RASSAERTS H., NOWOTNY H., VINEK G. and BENESOVSKY F., *Monatsh. Chem.* **98**, 460 (1967).
25. AUER-WELSBACH H. and NOWOTNY H., *Monatsh. Chem.* **92**, 198 (1961).

APPENDIX

Optimized LCAO interaction integrals (Ryd). (For notation see Slater and Koster[17]).

$E_{xy,xy}(000)$	0·70820	$E_{xy,xz}(011)$	0·00762
$E_{xy,xy}(110)$	−0·03258	$E_{xy,3z^2-r^2}(110)$	−0·00927
$E_{xy,xy}(011)$	0·00958	$E_{x,y}(110)$	0·02231
$E_{3z^2-r^2,3z^2-r^2}(000)$	0·78618	$E_{x,xy}(111)$	−0·00211
$E_{3z^2-r^2,3z^2-r^2}(110)$	−0·00369	$E_{x,x^2-y^2}(111)$	−0·00058
$E_{x^2-y^2,x^2-y^2}(110)$	−0·00616	$E_{x,yz}(111)$	0·00036
$E_{x,x}(000)$	0·41773	$E_{s,s}(000)$	−0·43457
$E_{x,x}(011)$	−0·00641	$E_{s,s}(110)$	−0·00833
$E_{x,x}(110)$	0·01300	$E_{s,3z^2-r^2}(001)$	0·06760
$E_{x,xy}(010)$	0·05959	$E_{s,x}(110)$	−0·00183
$E_{z,3z^2-r^2}(001)$	0·12170	$E_{s,xy}(111)$	−0·01183

J. Phys. Chem. Solids **Pergamon Press 1971. Vol. 32, pp. 2075–2090. Printed in Great Britain.**

SPIN COMPONENT OF THE HALL EFFECT AND TRANSVERSE MAGNETORESISTANCE IN DILUTE ALLOYS CONTAINING MAGNETIC SOLUTES

J. E. A. ALDERSON and C. M. HURD
National Research Council of Canada, Ottawa, Canada

(*Received* 16 *October* 1970; *in revised form* 7 *December* 1970)

Abstract—The influence is considered of the high field/low field transition upon the interpretation of the transverse magnetoresistance and the Hall effect in dilute polycrystalline alloys containing a magnetic solute. It is shown that when the experiment encompasses such a transition the usual method for calculating the temperature-independent positive contribution to the magnetoresistance can lead to appreciable systematic error. In the case of the Hall effect, on the other hand, when allowance is made for the above transition the interpretation leads to the separation of a spin component which saturates in an external field of a few kilogauss. It is shown that this contribution is probably due to the presence of superparamagnetic clusters which, being ferromagnetic particles, shown an anomalous Hall effect on a microscopic scale. In the presence of an external field these individual components are added constructively to give the observed macroscopic spin contribution. Evidence is shown of clustering in very dilute alloys of the AuFe, CuFe, CuMn and AgMn systems.

1. INTRODUCTION

THIS paper is concerned with the interpretation of results of measurements of the transverse magnetoresistance and the Hall effect in polycrystalline alloys where the experiment encompasses the transition between the high and low-field conditions. We have considered elsewhere[1] this problem when applied to the Hall effect in polycrystalline samples of the pure group 1*B* metals, and this extended here to the case of noble metal based alloys containing magnetic impurities in dilute concentrations. When a magnetic field is applied to such a sample it produces a component in the total electrical resistance of the sample which is of opposite sign to the normal increase resulting from the effect of the Lorentz force. This is known as the *spin contribution*, or *negative magnetoresistance*, and we shall show that there is a corresponding *spin contribution* in the Hall effect.

It is the method used to extract this spin contribution from the measured values of the total Hall and magnetoresistance effects which is the subject of this paper. We try to show, using a combination of empirical examples and assumptions based upon them, that to ignore the transition between the above conditions is to risk systematic error in the determination of the spin contribution. Furthermore, we show that this error is probably quite significant in the usual procedure employed by previous workers to determine the spin component of the transverse magnetoresistance of some low temperature systems exhibiting a Kondo effect.

The work has involved the measurement of the field dependence at 4·2°K (in the range up to 15·17 kG) of the Hall effect and the transverse magnetoresistance in polycrystalline samples of Cu, Ag or Au containing one of In, Cd, Sb, Pd, Fe or Mn in concentrations up to about 6000 atomic ppm. In some cases the temperature dependence (in the range 4·2–77°K) of the transverse magnetoresistance at 15·17 kG was also determined. The results and their discussion for the measurements of the magnetoresistance and Hall effects are considered separately in Sections 3 and 4 respectively.

2. EXPERIMENTAL METHOD

The measurements of the magnetoresistance and the Hall effect were made upon the same sample and in identical experimental conditions. (We have already reported[2] Hall effect results obtained during this work for systems containing non-magnetic solutes.) The samples were therefore in the form of flat plates with the shape described previously[3] and into which pointed potential probes were pressed. These were aligned along the longitudinal axis of the sample with a separation of about 3 cm. The shape of the samples was consequently far from the optimum for accurate absolute magnetoresistance measurements, but we find that the precision of our data is sufficient to illustrate the points under consideration. The precision of the magnetoresistance (i.e. the ordinate of Figs. 1–3) is estimated between 0·2–4 per cent, with the maximum imprecision occurring at the lowest field strength. The error in the Hall resistivity is estimated to amount to about ± 0·007 vm amp^{-1}, so that the uncertainty in the differences plotted as ordinate in Figs. 6–8 is about twice this amount. All measurements were made with a dc potentiometric arrangement[1, 3] having a resolution of 1×10^{-8}v. Field strengths up to 15·17 kG were available. The voltages arising from the Hall and magnetoresistance effects were determined from the mean of results obtained from the four permutations of applied electric and magnetic field directions

The Consolidated Mining and Smelting Company supplied the Ag, Au, Cd, Sn and Sb starting materials of 6*N* grade, together with the In of 5*N* grade The American Smelting and Refining Company supplied the Cu of 6*N* grade. The Mn of 99·99 per cent purity was supplied by King Products, while the Fe of equivalent purity had been obtained privately from the Batelle Memorial Institute. The details of the sample preparation are exactly as described previously[1–3] Before measurement, each sample was annealed in vacuum for a minimum of 24 hr. at 550°C to assist homogenisation and the the relief of internal strain. The concentrations are everywhere quoted in atomic ppm (see the relevant figures) and were determined by the Analysis Section of *NRCC* using the method of atomic absorption. As a check upon the metallurgical state, we verified wherever possible for each alloy series that the $RRR(= R_{273°K}/R_{4.2°K})$ showed a linear dependence upon the chemical concentration.

3. TRANSVERSE MAGNETORESISTANCE

3.1 *Introduction*

In the low-field condition the topology of the Fermi surface has no direct influence upon the electronic motion and the standard theory [4] predicts that the transverse magnetoresistance ($\Delta\rho/\rho_{H=0}$, where $\Delta\rho$ is the change in electrical resistance ρ produced by the field H) will vary as H^2, as is observed experimentally. In the high-field condition an ideal polycrystalline sample of an uncompensated metal with an open Fermi surface consists of randomly oriented crystallites in which $\Delta\rho/\rho_{H=0}$ is either saturated or varying as H^2. Those crystallites in which $\Delta\rho/\rho_{H=0}$ remains large are short-circuited by those in which it has saturated, and it appears from experiment that the net result of the averaging over a large number of crystallites is an essentially linear dependence of $\Delta\rho/\rho_{H=0}$ upon H. Ziman [4] suggests that this arises from the reduction with increasing H in the number of effectively open orbits, since at lower fields a very extended orbit can appear to be open. But to derive the linear field dependence from first principles is a difficult problem in the general case, and the most recent attempt is probably that by Stachowiak[5] to which the interested reader is referred. Consequently if the conditions are changed from the high to the low-field state, the dependence of $\Delta\rho/\rho_{H=0}$ upon H will change correspondingly from a linear to a quadratic behaviour. An example of this for some Ag-based alloys is shown in Fig. 1 in the form of a Kohler plot.

We are concerned with the significance of this transition in measurements of $\Delta\rho$ made upon very dilute alloys where the end result is a *difference* between the value obtained for the pure solvent and that obtained for the alloy. For example, the negative magnetoresistance of dilute alloys containing magnetic impurities is of interest in the study of the Kondo effect. It has usually been obtained (as in, for example, Monod[6] and Daybell and Steyert[7]) from the total magnetoresistance of a dilute alloy at low temperatures (which is generally typical of the low or intermediate field condition) by subtraction of a temperature-independent positive contribution obtained for the sample at a relatively high temperature where the negative contribution is negligible. Such a procedure will be shown to imply that the latter measurement is typical of the high-field condition (since it implies a linear variation of $\Delta\rho$ with H), and it is the systematic error incurred in this assumption and in subtracting a high-field result from that representative of a low or intermediate-field condition which is the subject of the following.

3.2 *Transverse magnetoresistance results and their discussion*

Figure 1 shows in a Kohler plot the field dependence of $\Delta\rho/\rho_{H=0}$ measured at 4·2°K for Ag containing In, Cd and Sb in the concentrations indicated, as well as the corresponding temperature dependence of $\Delta\rho/\rho_{H=0}$ found at 15·17 kG for the pure Ag sample. The isothermal results show the transition from the linear field dependence in the predominantly high-field condition to the quadratic behaviour of the low-field condition. Note that the temperature dependence of $\Delta\rho/\rho_{H=0}$ retains the linear field dependence

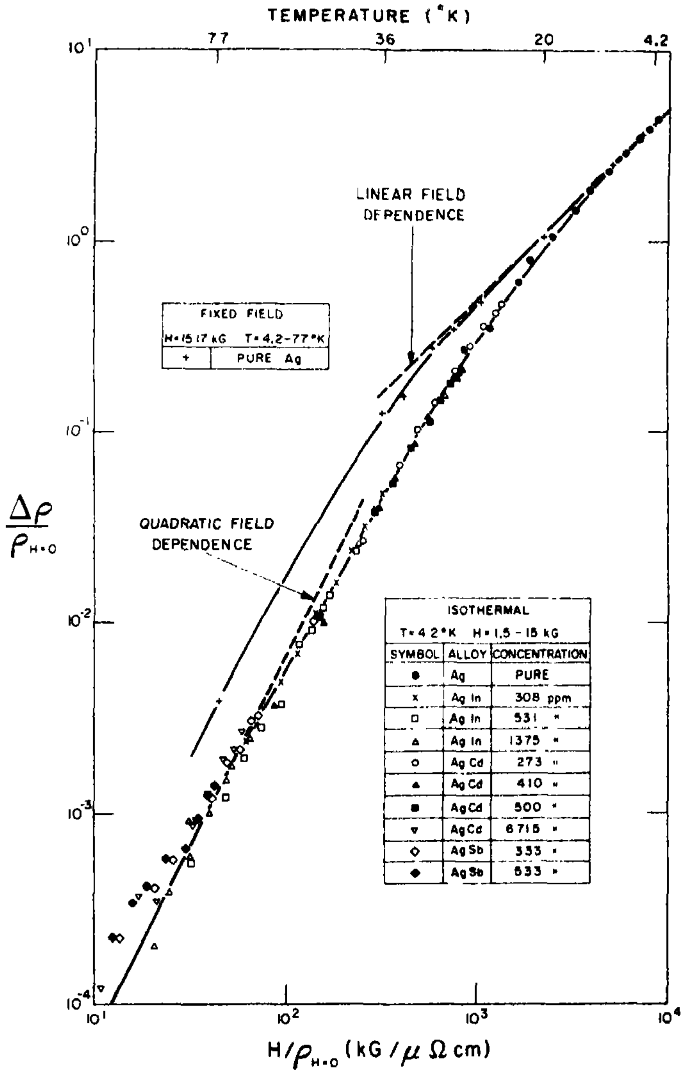

Fig. 1. A Kohler plot showing the field dependence of the transverse magnetoresistance measured at 4·2°K for the polycrystalline samples indicated. The solute concentrations are in atomic ppm. Also shown is the corresponding temperature dependence at 15·17 kG found for pure Ag.

characteristic of the high-field condition to lower values of $H/\rho_{H=0}$ than the isothermal field dependence.

This has also been observed by Saeger and Lück[8] in measurements upon Cu, and it presumably reflects the relatively greater effect upon the open orbits of scattering by non-magnetic impurities than that by low temperature phonons. The latter are known to give anisotropic scattering and to be most effective in scattering electrons located in neck states (since Umklapp processes from belly states are frozen out at low temperatures), while the impurities under consideration give predominantly s-type scattering and involve therefore predominantly electrons in belly states. Furthermore, qualitatively speaking, an open orbit is seen in general to involve a longer segment upon the belly surface than upon a neck, and this will tend to emphasize the importance of s-type scattering in bringing about the transition of an open orbit to the low-field condition as the total amount of scattering is increased.

An intermediate case between the scattering effects of phonons and the above polyvalent impurities is provided by a transition metal impurity which has a large d-component in its scattering potential. Since, according to band structure calculations[9, 10] for Cu and Ag at least, there is a strong d admixture of the wave functions along the $\langle 110 \rangle$ directions (although it is weakest in the case of Ag), the implication is that electrons in states on these areas of the Fermi surface will be subjected to strong scattering by such an impurity. Ni in Cu has been cited as an example of this[11], and Fig. 2 shows some results for the apparently equivalent example of Pd in Ag. Comparison of the transition from the high-field behaviour shown in Figs 1 and 2 illustrates the point under consideration; as $H/\rho_{H=0}$ is reduced, the high-field behaviour is maintained by the AgPd samples to a degree intermediate between the extreme cases provided by scattering by the low temperature phonons and by the charged s-type impurities. This is thought to reflect the fact that since some of the open orbits (for example, those lying in bands with their axes along either the $\langle 110 \rangle$ or $\langle 111 \rangle$ directions) traverse the regions of the Fermi surface for which there is a high admixture of d-wave functions, they consequently experience the intensive scattering in these regions due to the presence of the transition metal solute. While there are other open orbits (analogous, for example, to those directed along the $\langle 100 \rangle$ directions in Cu[12]) which do not directly traverse these regions and which are consequently less affected by the d-wave scattering. Our experiments indicate that the net effect of all this is somewhere between that seen for low temperature phonons and for s-type impurities, but such a view must remain speculative until further data are available.

The situation when the impurity has a localized magnetic moment and therefore contributes a negative component to the transverse magnetoresistance is illustrated in Fig. 3 for the case of some AgMn alloys. In these experiments the negative component in samples containing ≤ 100 ppm solute was too small to be detected, and the resulting positive magnetoresistance shows the smooth transition between the quadratic and linear dependence which is typical of a non-magnetic solute. In this case the transition is between the low-field region, where $\Delta\rho/\rho_{H=0}$ is determined by the anisotropy of the electron scattering by the Mn ions, toward the high-field region where the galvanomagnetic properties are independent of the nature of the scattering process. This is the 'background' variation of $\Delta\rho/\rho_{H=0}$ observed when the spin component is vanishingly small. It is therefore the normal Coulombic contribution arising from the Mn ion. The negative component is superimposed upon this background in Fig. 3 and its value at any given abscissa should therefore be obtained as the difference between the total $\Delta\rho/\rho_{H=0}$ and the corresponding positive value obtained from the background field dependence. Note that

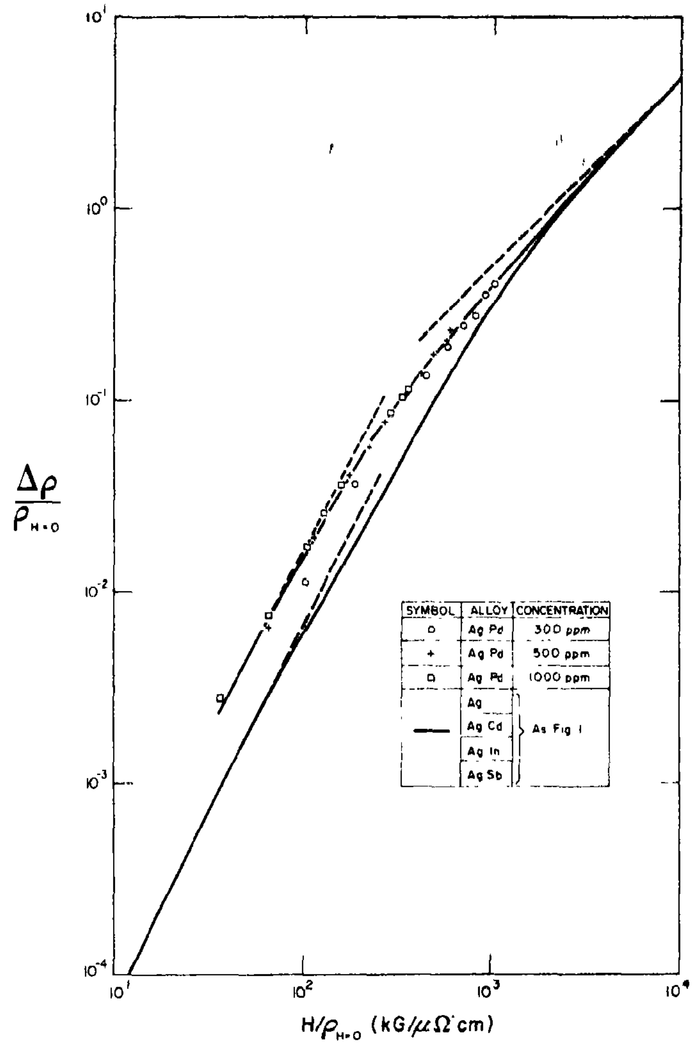

Fig. 2. A Kohler plot showing the field dependence of the transverse magnetoresistance measured at 4·2°K for the polycrystalline samples indicated. The solute concentrations are in atomic ppm. The quadratic and linear field dependences appropriate to the low- and high-field conditions are shown by the dashed lines.

we have made no assumptions about the nature of the spins giving rise to the negative component; they may be individual and localised or they may arise from clusters of solute ions. This is relevant since it appears from our Hall effect results in Section 4 that some clustering may occur in the alloys we have studied.

In order to obtain the negative component from measurements of the total magnetoresistance made in the intermediate field condition, it is clearly incorrect in principle to subtract a positive contribution which has been obtained by extrapolation from data appropriate to either the low or high-field conditions. To illustrate this point, the insert in Fig. 3 represents schematically the procedure carried out by, for example, Monod

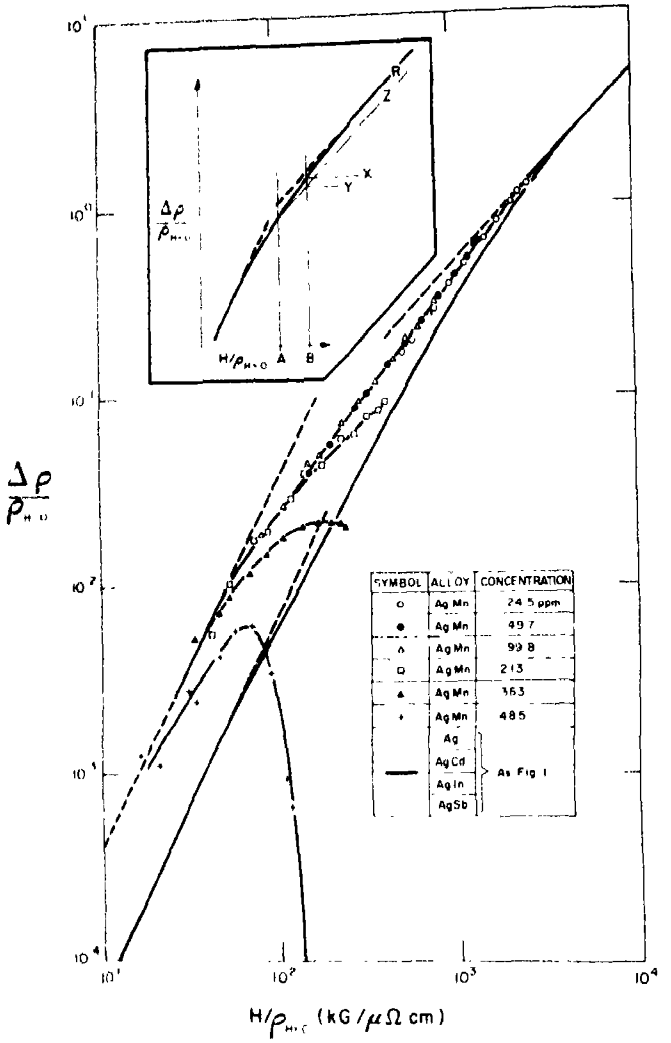

Fig. 3 A Kohler plot showing the field dependence of the transverse magnetoresistance measured at 4·2°K for polycrystalline samples of AgMn. The solute concentrations are in atomic ppm. The solid line shows for comparison the equivalent results for the non-magnetic solutes of Fig. 1, and the dashed lines indicate the quadratic and linear field dependences appropriate to the low- and high-field conditions. The insert shows a stylised view of the temperature dependence of the positive component of the transverse magnetoresistance of the system. This is used in the text to illustrate how a systematic error can be incurred in the determination of the negative component from the data.

[6] and Daybell and Steyert[7] in their study of magnetoresistance in low temperature Kondo systems. It represents in a Kohler plot the temperature dependence of the positive component of the total magnetoresistance in an alloy containing an insignificant amount of magnetic impurity. The procedure used by the above workers involves the determination of a positive contribution in the range 15–20°K, and this is systematically subtracted

from the total magnetoresistance measured at low temperature. The result is taken to be the negative component. The above temperature range is chosen since in it any negative component due to a magnetic solute was small in the fields available, and the scattering by phonons was taken to be negligible.

But a sample containing 28–75 ppm solute [6, 7] subjected to tens of kilogauss in this temperature range is not in the high-field condition and, since the negative component is negligible in this case, the corresponding value of $H/\rho_{H=0}$ can be represented by A in the insert to Fig. 3. The procedure used by the above workers then assumes that the positive contribution so obtained remains independent of temperature down to the lowest temperatures. This is equivalent to assuming a linear dependence of $\Delta\rho$ upon H (such is observed in any case in the high-field condition) and in the Kohler plot of Fig. 3 (insert) this is represented by the solid line of unit gradient and labelled Z. The procedure used is therefore an extrapolation of a high-field dependence into an intermediate-field regime, and the error arises from the difference between the assumed variation Z and the real one represented by R. For a value of $H/\rho_{H=0} = B$ in the figure (such as would be produced by lowering the temperature of the sample), the error in the positive contribution calculated by this procedure is represented by the difference between the ordinates X and Y.

The important question is whether the above method can give rise to a *significant* source of error in the measurements. To answer this each case must be considered separately, since the magnitude of the error depends upon how close A of Fig. 3 (insert) is to the high-field condition and this in turn is a function of the applied field strength, the temperature, and the purity of the sample. (This is why, for example, Monod [6] found empirically for a 17 ppm CuMn alloy that $\Delta\rho$ apparently varied linearly with H for sufficiently high fields in the range 1·4–20°K. Our point is that it is incorrect to therefore assume that a similar relationship is valid in the results for the 75 ppm alloy which formed the main part of his letter.) We can obtain some idea of how significant is the error which arises in Ag-based alloys from a consideration of our data shown in Figs. 1–3, and especially the temperature dependence of $\Delta\rho/\rho_{H=0}$ obtained for pure Ag at 15 kG (clearly comparable with the range 10–26 kG used in the work cited above) and shown in Fig. 1.

When the sample has a value of $H/\rho_{H=0}$ in the approximate range $5\times10^2 - 10^3$, which corresponds roughly to the situations existing in the work by Monod[6] and Daybell and Steyert[7], the error in $\Delta\rho/\rho_{H=0}$ produced by the procedure outlined above (which is given by the separation XY of Fig. 3) would be about 0·03. If we then take for illustration the specific case of Ag+99·8 ppm Mn at 15 kG, since this corresponds closely to the case of the slightly less concentrated CuMn sample studied by Monod at slightly higher field strengths, the appropriate value of $H/\rho_{H=0}$ (i.e. B of the insert to Fig. 3) is 790 kG/$\mu\Omega$cm. $\rho_{H=0}$ in this case was found to be 0·019 $\mu\Omega$cm, so that the error in the estimated positive component of $\Delta\rho$ could be about 0·6 $n\Omega$cm. Since the total negative component of $\Delta\rho$ in such dilute, noble metal based alloys amounts typically to about[6] 0–6 $n\Omega$cm, we see that an error of about 10 per cent could be incurred by this procedure. Furthermore, it is clear from the insert in Fig. 3 that the error always *reduces* the apparent magnitude of the negative component. It is interesting to note in this connection that Monod[6], in footnote 10 of his letter, refers to a correction of a few per cent increase which was made to his measured value of the negative component of $\Delta\rho$ in order to account for an evident systematic error arising from his procedure.

It follows from the above that such a single, temperature-independent correction cannot in principle be valid if it is to correct for the error arising from the separation XY in Fig. 3 (insert), since this is a function of the field, the temperature, and the solute concentration in the sample. It seems to us that in such measurements where some part of the experiment is conducted in the intermediate-field condition, the only method for the determination of the negative part of $\Delta\rho$ which is correct in principle is to make a Kohler plot such as Fig. 3. The negative part can then be obtained for a given abscissa as the difference between the ordinate value obtained for the alloy and that corresponding to the 'background' curve obtained for samples effectively free of magnetic impurity. Since the latter will be displaced with varying temperature, this procedure should strictly speaking be carried out at each temperature of measurement, although in measurements made only in the residual resistance temperature range it may be found in practice that this is unnecessary.

Note that we cannot estimate from the above the uncertainty in Monod's values of the exchange parameters caused by his erroneous analysis. This would require a knowledge of the effective moment of the scattering spin (see equation (1) of [6]) and, although Monod assumes they are individual localised moments, we show in the following that there is probably significant clustering in the alloys we have studied and therefore such an assumption is not well founded.

Rohrer's study[13] of magnetoresistance in relatively concentrated alloys (0·11–1·2 at.%) could also be mentioned in this context. However, his procedure did not consider either of the principal points of this paper: the possibility of clustering effects, and the influence of the high-field/low-field transition upon the positive contribution.

4. HALL EFFECT

4.1 *Introduction*

The appearance of a Hall field E_H in a sample carrying a current density J can be characterised by the Hall resistivity ρ_H given by

$$\rho_H = E_H/J_x = R_H H \tag{1}$$

J_x is the longitudinal component of J, H is the applied magnetic field and R_H is the Hall coefficient defined at $H = H'$ by

$$R_H(H') = \frac{1}{J}\left(\frac{\delta E_H}{\delta H}\right)_{H=H'}. \tag{2}$$

It is convenient to introduce the argument by anticipating our experimental results by means of a schematic representation of the field dependence expected for the quantities defined in (1) and (2).

Figure 4 shows an exaggerated (for clarity) and idealised representation of the dependence of R_H and ρ_H upon H expected for a fixed, low temperature as the conditions are made to vary between the high and low-field limits. The sketch is for an arbitrary material, in either a single crystal or poly-crystalline form (although we are concerned throughout principally with the polycrystalline case), containing a variable concentration of some scattering source, which in this case we shall take to be a non-magnetic solute element. The behaviour shown in the figure is idealised in that we have assumed there to be no evident effects of either a solute-solute interaction or any change in the solvent metal's band structure as the solute is added.

In the low-field condition E_H (and hence ρ_H) is a linear function of H. R_H is therefore field-independent and, as is well known[11], its value is determined from the magnitude at each point on the Fermi surface of the electron's mass, velocity, and (anisotropic) relaxation time associated with the dominant scattering mechanism; the topology of the Fermi surface has no direct influence upon the galvanomagnetic effects. In the high-field limit ρ_H is again a linear function of H but the gradient of this function is now determined solely by the geometrical details of the Fermi surface of the solvent metal and by its state of

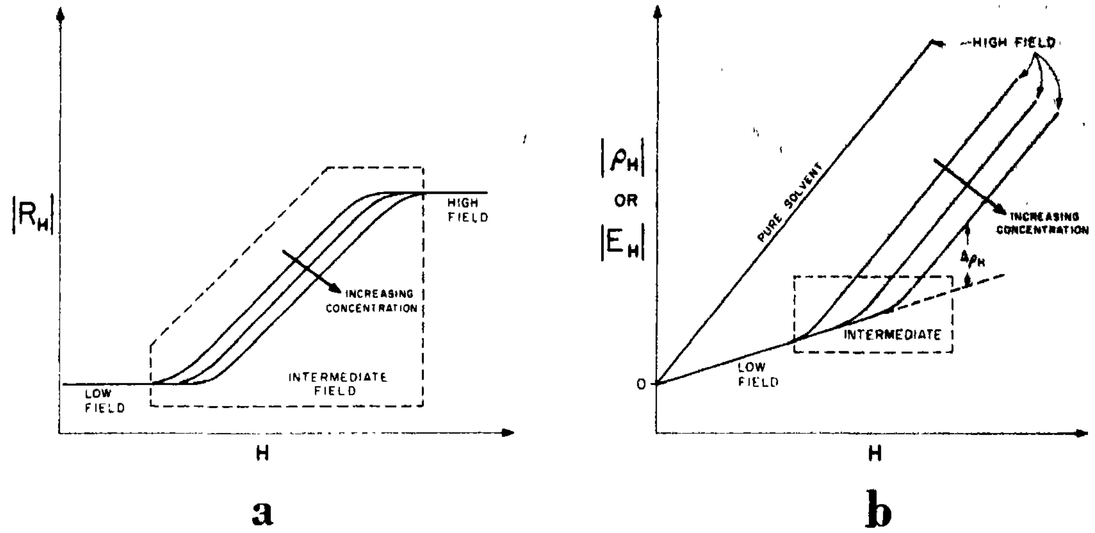

Fig. 4 An idealised representation of the isothermal, low temperature field dependence of (a) the Hall coefficient and (b) the Hall resistivity (or field) which is observed when the experiment encompasses the high-field/low-field transition. The example represents an alloy system containing various dilute concentrations of a non-magnetic solute.

compensation; the nature of the dominant electron scattering process is irrelevant. (Several examples of the behaviour illustrated in Fig. 4(a) can be found in the literature. We have previously shown[1] the effect in Cu-based alloys, while the case of Al is particularly striking since it involves[14] a change in the sign of R_H.)

Note that at low temperatures the *ideally* pure solvent metal is taken to be necessarily in the high-field condition for all values of H, where by 'pure' we mean a sample in which the electron's mean free path is not significantly limited by impurities or by lattice imperfections. This is justifiable since, in terms of the scale we envisage for Fig. 4(b), for all practical purposes the pure solvent undergoes the transition to the high-field condition at the zero-field value. This has an important bearing upon the interpretation of the data: at a fixed H, the difference between ρ_H for the alloy and that for the pure solvent might appear to give the contribution to ρ_H due to the solute addition. But, as Fig. 4(b) shows, when the alloy is measured in the low-field condition this procedure will clearly give an erroneous field dependence for the solute's contribution to ρ_H since it will reflect the difference between the field dependences characteristic of the high and low-field conditions, and this should not be confused with any intrinsic contribution from the solute atom.

The preceding has been concerned with the case when the solute atom possesses no magnetic moment, while in Fig. 5(a) we show schematically by means of the solid lines the corresponding behaviour observed when the solute is magnetic. [The dashed lines represent for comparison the non-magnetic case and are identical to the behaviour shown in Fig. 4(b).] The sketch shows the presence in the low-field condition of a contribution which appears to saturate with increasing field strength. This we shall refer to as a *spin contribution*. As the field is increased above the saturation of this component, ρ_H varies linearly with H up to the transition to the high-field condition. For a sufficiently dilute alloy the spin contribution becomes too small to be detectable and the field dependence of ρ_H is then identical to the case for a non-magnetic solute.

Since we wish to discuss the spin contribution to the Hall effect, and to avoid the erroneous component of the field dependence to which we referred above, we have chosen to present our data and their discussion in terms of $\Delta\rho_H$ defined as shown in Fig. 5(a). For a fixed value of H, this represents the difference between ρ_H and its value extrapolated from the low-field condition for an alloy with a negligible amount of magnetic solute, [as indicated by the dash-dot line of Fig. 5(a)]. Experimentally the establishment of this extrapolation presents no problem when the data follow the idealised behaviour shown in Fig. 5(a), since it is known that the linear extrapolation must pass through the origin and also be parallel to the low-field dependence upon H observed when the magnetic component is saturated. But in less well behaved systems (of which AgMn is found to be an example) the extrapolation is considerably more uncertain and it can lead in those cases to significant systematic error in $\Delta\rho_H$. It is seen from the behaviours illustrated in Figs. 4(b) and 5(a) that three possible field dependences can be expected for $\Delta\rho_H$. These are illustrated in Fig. 5(b); curves A and B represent the behaviour of $\Delta\rho_H$ in a sample which contains an appreciable amount of respectively a non-magnetic and a magnetic solute, and which undergoes the transition to the high-field condition at X. The difference between these two curves in the low-field condition therefore represents the spin contribution to the Hall effect. Curve C, on the other hand, represents an exaggerated case of B in which the conditions are such that the experiment does not encompass the high-field/low-field transition in the range of fields available. Examples of each of these behaviours can be seen in the following results.

4.2 *Hall effect results*

Figure 6 shows the field dependence of $\Delta\rho_H$ obtained at 4·2°K for some polycrystalline alloys of the AuFe system. At the lowest

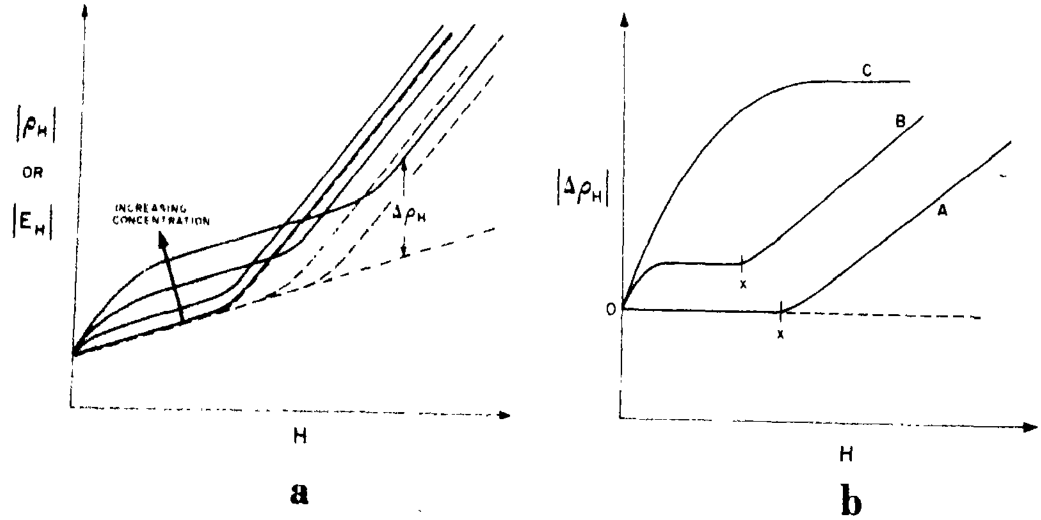

Fig. 5. (a) An idealised representation of the isothermal field dependence of the Hall resistivity (or field) observed for a dilute alloy containing a magnetic solute when the experiment encompasses the high-field/low-field transition. The dashed lines represent the corresponding behaviour [Fig. 4(b)] observed with a non-magnetic solute. Our experimental results are discussed in terms of the spin contribution $\Delta\rho_H$. (b) Types of field dependence which can be expected for $\Delta\rho_H$ defined in Figs. 4(b) and 5(a).

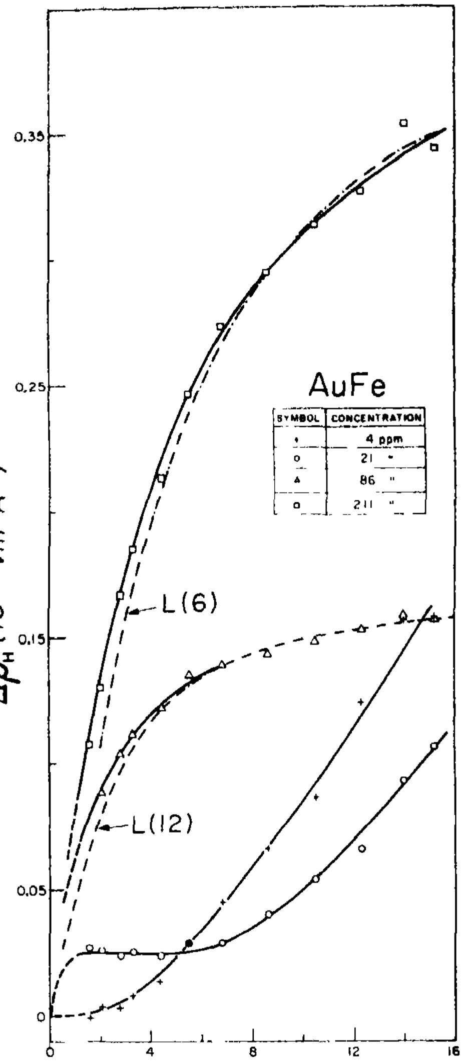

Fig. 6. Field dependence at 4·2°K of $\Delta\rho_H$ [Fig. 5(b)] for polycrystalline AuFe samples. Here, and in Figs. 7 and 8, the accuracy of $\Delta\rho_H$ at any value of H is approximately $\pm 0{\cdot}014 \times 10^{-10}$ vmA^{-1}. The dash-dot lines are the Langevin function [(3) of the text] obtained for the arguments indicated. These correspond to approximately 7 and 14 atoms per cluster for the $L(6)$ and $L(12)$ functions respectively.

solute concentration (4 ppm) the spin contribution is not detectable, and $\Delta\rho_H$ shows a field dependence of Type A [refer throughout to Fig. 5(b)] with a transition X to the high-field condition occurring in the range 2–4 kG. The spin contribution becomes detectable, however, when the concentration is increased to 21 ppm, and $\Delta\rho_H$ then shows a field dependence of Type B; X in this case lies in the range 6–10 kG. For the remaining examples shown in Fig. 6 the concentration is large enough that with the fields available we are unable either to produce the transition to the high-field condition or to saturate the spin contribution. Consequently they can be classified as Type C.

Figure 7 shows a similar set of data obtained for alloys of the AgMn system. In the case of the two most dilute samples (24 and 50 ppm Mn) there is no detectable spin contribution and their behaviour is Type A. For the rest there is evidence of a small spin contribution at low field strengths but its saturation is obscured by a component which leaves the total $\Delta\rho_H$ relatively independent of concentration. This cannot represent the transition to the high-field condition (since it is independent of concentration) but comparison with the results of Fig. 3 shows that it is correlated with the onset of the detectable negative component in the transverse magnetoresistance. We shall see that it is therefore thought to arise from the progressive alignment of the localised moments upon the individual Mn atoms as the field strength is increased.

Figure 8 shows corresponding results for alloys of the CuFe and CuMn systems. These have been included to show the behaviour observed for two systems having widely separated Kondo temperatures (T_K). It is seen that even so there are qualitative similarities in each case: the two samples of lowest concentrations show a field dependence of Type A, while Cu + 111 ppm Mn and Cu + 48 ppm Fe show a spin contribution which apparently saturates at fields of a few kilogauss. The most concentrated alloys in each system are in the low-field condition throughout the experiment (although in the case of Cu + 308 ppm Mn $\Delta\rho_H$ shows a non-linear dependence upon H because at higher fields

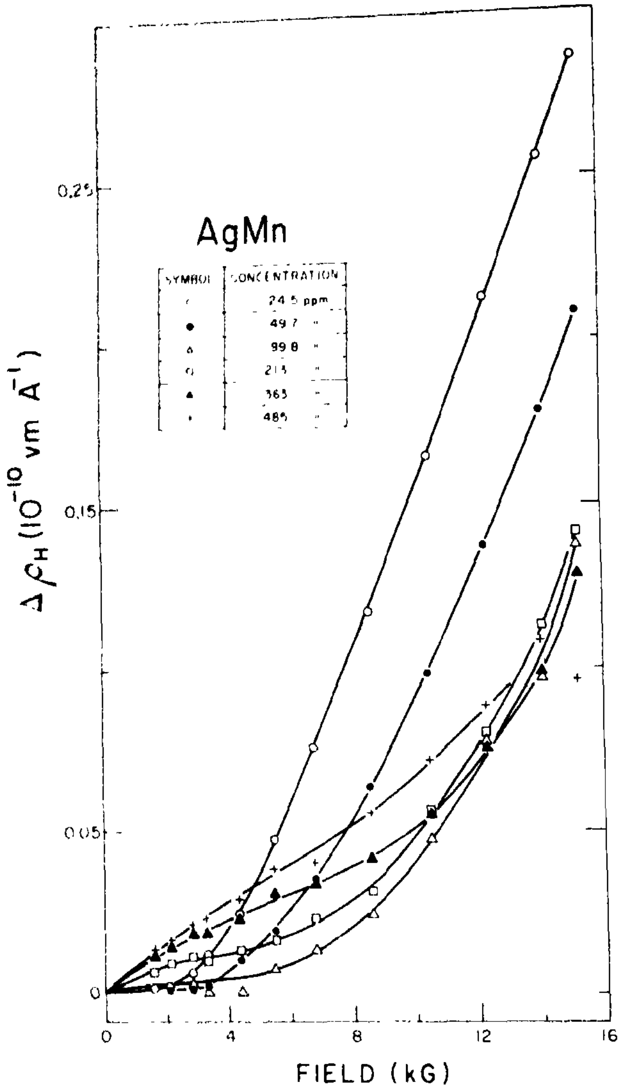

Fig. 7. Field dependence at 4·2°K of $\Delta\rho_H$ [Fig. 5(b)] for polycrystalline AgMn alloys. These results show an apparently concentration-independent component at higher concentrations and fields which correlates with the appearance of a negative magnetoresistance component in the corresponding data of Fig. 3.

it contains that component which correlates with the negative magnetoresistance, and which was referred to above in connection with the AgMn system).

4.3 *Discussion of the Hall effect results*

The results shown in Fig. 6 have several features which are quite unexpected in terms of what is known of this system from theory and experiment. But before we discuss these, we would like to draw attention to a similarity between these results and those obtained earlier by Gaidukov[15] for a somewhat impure sample of Au (which is generally

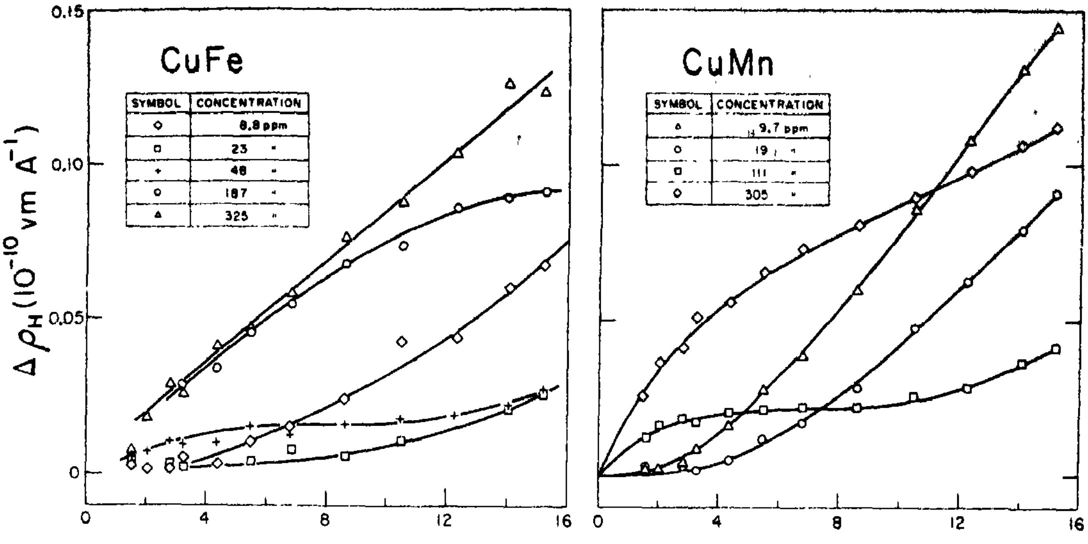

Fig. 8. Field dependence at 4·2°K of $\Delta\rho_H$ [Fig. 5(b)] for polycrystalline CuFe and CuMn alloys.

assumed to have contained traces of Fe since it showed the resistance minimum effect). Specifically we refer to the field dependence of the Hall voltage (measured in the range 0–20 kG and at temperatures between 0.07 and 295°K) shown in Fig. 1 of that paper. At the lower temperatures E_H shows an abrupt change between two separate, linear field dependences. Close scrutiny shows that as the temperature is raised this change occurs at correspondingly higher values of the applied field. At 295°K there is no such change, and E_H is a single, linear function of H over the whole range of fields studied. As we have already pointed out[1], here is a manifestation of the high-field/low-field transition, and we can now see a direct comparison between Fig. 1 of[15] and the behaviour shown in Fig. 5(b).

At room temperature the scattering by phonons was sufficient to maintain the low-field condition throughout Gaidukov's experiment (hence the single, linear field dependence observed for E_H), but at lower temperatures the experiment encompassed the high-field/low-field transition with the resultant change in slope of the field dependence of E_H. The sample in Gaidukov's experiment was nominally pure, and the concentration of the magnetic impurity was evidently small enough that no spin component in E_H was observable. His data therefore fall into the category Type A of Fig. 5(b) and are qualitatively equivalent to our results for Au + 4 ppm Fe shown in Fig. 6. The anomalous 'step' in the field dependence of R_H found by Gaidukov (and which in any case is made more abrupt by his erroneous method of calculating R_H from E_H) is therefore not an intrinsic property of Fe in Au, and it was incorrectly cited as such by More[16] in connection with some previous theoretical results.

Probably the most obvious supposition relating to Fig. 6 is that the spin component arises from the effect upon spin-flip scattering of the alignment of the individual localised moments as the external field is increased. This effect is thought to be a principal cause of the negative magnetoresistance[17] in the low-field regime, and it has already been considered to give rise to an anomalous field dependence of R_H in Kondo systems[18].

Briefly, the physical picture is that[17, 18] the itinerant electrons can be treated by a two-band model, each band containing electrons of a given spin direction. With no external field the electrons in each band are identical except for their spin configuration, but as the strength of the applied field is increased a difference appears between the relaxation times associated with each band, and this appears directly as a field-dependent contribution to R_H. The difference between the relaxation times arises because only the lowest Zeeman levels of the magnetic ion are occupied in the higher applied fields, whereas all levels are involved in the spin scattering at zero applied field. A spin-flip process which can only lead to a final, total energy for the electron which lies in the already occupied energy range is forbidden by the exclusion principle, and for a given initial spin direction these processes become[17] an increasingly greater fraction of the total number of spin-flips as the external field is increased. Hence the origin of the increasing difference between the relaxation times of electrons of different initial spin configurations.

The above processes are expected to make an important contribution to the low-field Hall effect[18] at least until all the ionic moments are aligned in the external field, and this will occur at about[17] $g\mu_B H/k_B T \doteqdot 4$. ($g$ is here the g-value of the magnetic ion, μ_B is the Bohr magneton and k_B is Boltzmann's constant.) Taking for simplicity $g = 2$, saturation at 4·2°K is expected to occur at about 120 kG – a vastly higher field than the few kilogauss at which we observe saturation in Fig. 6. Clearly, this suggests that the observed spin component does not arise from the alignment of the ionic spins. This is further supported by the apparent lack of correlation between the negative magnetoresistance and the saturating spin component in the Hall effect. For example, the corresponding magnetoresistance results for the samples described in Fig. 6 show a qualitative behaviour identical to that illustrated in Fig. 1 (it seems unnecessary to reproduce them here). The only evident negative component is found to be small and to occur for the two most concentrated samples and at the highest values of $H/\rho_{H\to 0}$, whereas the spin component in the Hall effect is evident in all but the most dilute sample. A clearer illustration of this lack of correlation is obtained from the comparison between Figs. 3 and 7, to which we have referred in Section 4.2.

Our experiments show no evident correlation between the presence of a spin component and the value of the Kondo temperature T_K for the system. T_K varies over about three decades between the systems we have considered[19] and yet a comparison of Figs. 6–8 shows that qualitatively the same behaviour is observed for the spin component in each case. We therefore conclude that the spin component is not intimately connected with either the Kondo effect or the formation of the compensated Nagaoka state.

But the qualitative behaviour shown in Fig. 6 is reminiscent of an observation first made by Daybell and Steyert[20] in the study of the low temperature ($T \ll 1$°K) magnetic susceptibility of very dilute CuFe alloys. They observed a field-dependent component which saturated above about 1 kG to a temperature-independent value. Later work established a corresponding component in NMR experiments[21] and in measurements of the magnetisation[22]. Although the origin of this component has not been conclusively established, there is considerable evidence [19, 21] that it arises from the superparamagnetism of clusters of precipitated solute atoms. It is envisaged that these clusters (containing perhaps 20–100 solute atoms) are precipitated during the fabrication of the sample; each is imagined to be a single-domain ferromagnetic particle having a correspondingly large total moment. Provided the thermal relaxation of their moment to the surrounding lattice is fast enough, the magnetisation of the body will be determined by the Langevin function

$$L(x) = \coth(x) - 1/x. \qquad (3)$$

Here $x = \mu H/k_B T$, where μ is the total moment of the cluster.

We believe that this effect also provides a plausible explanation of the observed spin component in R_H. An itinerant electron travelling in the ferromagnetic cluster experiences the spin-orbit coupling and the consequent skew scattering which is known (see, for example, Maranzana[23]) to give rise to the so-called anomalous Hall effect in a ferromagnetic metal. It is well known that in such a metal the effect of this interaction is to produce an anomalous Hall component in each domain. But with no external field applied, the net effect when averaged over a large number of domains is zero; it is only when an external field is applied to align the direction of magnetisation of the domains that the anomalous effect becomes obvious on a macroscopic scale. That situation is therefore equivalent to the one under consideration, except that here the ferromagnetic domains are separated by the diamagnetic host. As the external field is increased, the moments of the clusters become increasingly aligned and their anomalous contributions to the Hall effect constructively interfere to produce an effect which is evident on a macroscopic scale. We expect, by analogy with the theoretical[24] and phenomenological[25] behaviour of the corresponding ferromagnetic case, that the spin component of ρ_H will therefore vary directly with the intensity of magnetisation in the sample. This contrasts with the behaviour expected from the effect of individual spin alignment upon the spin-flip scattering processes (referred to above); in that case the theory predicts[18] a spin component of ρ_H which varies with the square of the magnetisation.

The dash-dot lines in Fig. 6 show that a rough fit of the Langevin function can be made to the data for the two most concentrated AuFe alloys. Of the two, the results for the Au + 86 ppm Fe sample are probably the most representative of the spin component since this sample showed only a very small negative magnetoresistance effect at the higher field values, and the data therefore contain none of the high-field component in $\Delta\rho_H$ (which is most obvious in the AgMn series of Fig. 7) due to the change in spin-flip scattering brought about by the alignment of the individual solute atom spins. The data for this sample are fitted by $x = 12$ which, taking a value of $3{\cdot}68\,\mu_B$ for an individual solute atom spin[26], leads to an estimate of approximately 14 atoms per cluster; $x = 6$ clearly leads to half this value. There is independent evidence for the existence of superparamagnetic clusters in AuFe both from Mössbauer [27] and bulk magnetisation measurements [28, 29], and it is interesting to note that the latter led to estimates of 10 and 50 atoms per cluster.

5. CONCLUSIONS

We have presented evidence in Sections 3 and 4 to show that in dilute alloys of the systems under consideration it is important to allow for the effects of the high-field/low-field transition in the interpretation of the transverse magnetoresistance and the Hall effects. In the case of the latter the treatment leads to a spin contribution which is composite: it consists of a component which is relatively easily saturated and which is thought to arise from the presence of superparamagnetic clusters, together with a component which correlates with the appearance of a negative magnetoresistance. This component is therefore thought to arise from the modification of electron spin-flip scattering by the external field but, since we are limited to a maximum field of 15 kG, we have not been able to test this hypothesis over a sufficiently wide range of fields.

If it is correct to attribute the principal spin component in the Hall effect to clustering, then our results show that there is appreciable clustering in our alloys of the AuFe, AgMn, CuMn and CuFe systems. It is most noticeable in AuFe, and from these data we estimate a cluster to contain roughly 14 solute atoms; it is a small effect in AgMn (and obscured by the secondary effect referred to above), while in the CuFe and CuMn systems it is also a small effect and one which saturates in our samples at about 2-3 kG. Assuming that our method of sample preparation is no more conducive to the formation of clusters than that of other workers in this field, we can expect to see manifestations of the effect in other results. We have commented above on existing evidence for clustering in CuFe [19-22] and in AuFe[27-29] (although it is not all unequivocal [30, 31]), and we note that the field dependence of the thermopower observed in very dilute AuFe alloys at low temperatures by Huntley and Walker[32] contains an unexplained field-dependent component which disappeared above about 3 kG in their experiment. It seems that here too the possibility that clustering effects are significant should have been considered. In fact, perhaps the most important conclusion from our work is that in a subject for which the theory is developed in terms of an idealised system of independent, non-interacting solute atoms, the interference from metallurgical effects such as clustering in measurements upon real systems should not be disregarded. It appears that for some typical systems at least, the Hall effect can provide useful supporting evidence of clustering effects.

Acknowledgements—It is a pleasure to thank P. Tymchuk, E. C. Goodhue and J. A. Desaulniers of the Analytical Section, and F. Turner of Materials Preparation for the work they have done on our behalf

REFERENCES

1. ALDERSON J. E. A., FARRELL T. and HURD C. M., *Phys. Rev.* **B1**, 3904 (1970).
2. ALDERSON J. E. A. and HURD C. M., *Can. J. Phys.* **48**, 2162 (1970).
3. ALDERSON J. E. A., FARRELL T. and HURD C. M., *Phys. Rev.* **174**, 729 (1968).
4. ZIMAN J. M., Electrons and Phonons, Oxford University Press, Oxford (1960).
5. STACHOWIAK H., *Physica* **45**, 481 (1970).
6. MONOD P., *Phys. Rev. Lett.* **19**, 1113 (1967).
7. DAYBELL M. D. and STEYERT W. A., *Phys. Rev. Lett.* **20**, 195 (1968).
8. SAEGER K. E. and LÜCK R., *Phys. Kond. Mater.* **9**, 91 (1969).
9. SEGALL B., *Phys. Rev.* **125**, 109 (1962).
10. BHATNAGAR S., *Phys. Rev.* **183**, 657 (1969).
11. DUGDALE J. S. and FIRTH L. D., *J. Phys. C. (Solid State)* **2**, 1272 (1969).
12. DATARS W. R., *Phys. Lett.* **29A**, 700 (1969).
13. ROHRER H., *Phys. Rev.* **174**, 583 (1968).
14. FORSVOLL K. and HOLWECH I., *Phil. Mag.* **10**, 921 (1964).
15. GAIDUKOV Yu. P., *Zh. eksp. teor. Fiz.* **34**, 836 (1958). [English translation: *Soviet Phys. JETP* **34**, 577 (1958)].
16. MORE R. M., *Solid State Commun.* **7**, 237 (1969).
17. BÉAL-MONOD M.-T. and WEINER R. A., *Phys. Rev.* **170**, 552 (1968).
18. BÉAL-MONOD M.-T. and WEINER R. A., *Phys. Rev.* **B3**, 145 (1971).
19. HEEGER A. J., *Solid State Phys.* **23**, 283 (1969).
20. DAYBELL M. D and STEYERT W. A., *Phys. Rev.* **167**, 536 (1968).
21. GOLIBERSUCH D. C. and HEEGER A. J., *Phys. Rev.* **182**, 584 (1969).
22. HEDGCOCK F. T., MUIR W. B., RAUDORF T. and SZMIDT R., *Phys. Rev. Lett.* **26**, 457 (1968).
23. MARANZANA F. E., *Phys. Rev.* **160**, 421 (1967).
24. KONDO J., *Prog. theor. Phys.* **27**, 772 (1962).
25. RHYNE J. J., *Phys. Rev.* **172**, 523 (1968).
26. HURD C. M., *J. Phys. Chem. Solids* **28**, 1345 (1967).
27. JAIN A. P. and CRANSHAW T. E., *Phys. Lett.* **25A**, 425 (1967).
28. TOURNIER R. and ISHIKAWA Y., *Phys. Lett.* **11**, 280 (1964).
29. CRANGLE J. and SCOTT W. R., *J. appl. Phys.* **36**, 921 (1965).
30. CRAIG P. P. and STEYERT W. A., *Phys. Rev. Lett.* **13**, 802 (1964).
31. BORG R. J., *Phys. Rev.* **B1**, 349 (1970).
32. HUNTLEY D. J. and WALKER C. W. E., *Can. J. Phys.* **47**, 805 (1969).

J. Phys. Chem. Solids Pergamon Press 1971. Vol. 32, pp. 2091–2100. Printed in Great Britain.

Fe^{2+} IMPURITIES, ISOLATED AND IN PAIRS, IN ZnS AND CdS STUDIED BY THE MÖSSBAUER EFFECT

A. GERARD*, P. IMBERT†, H. PRANGE‡, F. VARRET† and M. WINTENBERGER§

(*Received* 14 *August* 1970; *in revised form* 3 *December* 1970)

Abstract—Mössbauer effect studies of divalent iron impurities substituting the metal ion at tetrahedral sites in cubic ZnS and hexagonal ZnS and CdS were performed. No indication of a static Jahn-Teller distortion for the isolated Fe^{2+} ions was found. For the case when one next metal neighbor is also replaced by Fe^{2+} or by another impurity a strong quadrupole splitting was visible already at room temperature.

IN A CUBIC tetrahedral crystalline environment the ground state of the $3d^6$ electronic configuration of the Fe^{2+} ion is a degenerate orbital doublet of symmetry E_g. Goodenough [1] has discussed the possibility of static Jahn–Teller distortions in this case. He pointed out that the anisotropy energy associated with an isolated tetrahedral complex is considerably smaller than that associated with an isolated octahedral complex containing for example Cu^{2+}. As a consequence in a crystal long range elastic coupling between sites occupied by Jahn–Teller ions would influence much more strongly the manifestation of static Jahn–Teller distortions in the case of tetrahedral site Fe^{2+} ions.

The Mössbauer effect in ^{57}Fe represents an appropriate method to detect possible localized static distortions from cubic symmetry. We present here results of an investigation of the quadrupole interaction in Fe^{2+} as a substitutional impurity on tetrahedral sites in ZnS and CdS. Samples with different concentrations allowed us to detect effects produced by adjacent impurity sites. These effects were also present when the neighboring impurity of Fe^{2+} was another metallic but non Jahn–Teller ion.

ZnS and CdS crystallize in the cubic blende as well as the hexagonal wurtzite structure [2, 3]. In blende the metal ions are located in a purely cubic crystal field whereas in wurtzite an additional small trigonal component is present[4].

Two earlier investigations of Fe^{2+} in ZnS by Mössbauer spectroscopy have led to apparently contradictory results: Marfunin and Mkrtchyan[5] have found a quadrupole splitting of 0·80 mm/s at room temperature and of about 2·05 mm/s at 80°K in natural crystals of blende and wurtzite. This splitting is attributed by them to a possible Jahn–Teller distortion; on the other hand Belozerskii *et al.*[6] using ZnS wurtzite containing ^{57}Co as source did not observe any splitting but only a broadening of the Mössbauer line at 78°K.

Slack *et al.*[7, 8] have measured the optical absorption of Fe^{2+} impurities in cubic ZnS in the near and far infrared. Their results are in satisfactory agreement with the predictions of crystal field theory for Fe^{2+} at cubic tetrahedral lattice sites; however, in their sample with the highest concentration of iron a number of Fe^{2+} ions did not seem to behave as isolated ions. The value they obtained for the spin-orbit splitting in the E_g ground state seems to indicate that it is not appreciably

---

*Institut de Physique, Université de Liège, Belgium.
†SPSRM, Centre d'Etudes Nucléaires de Saclay, France.
‡Institut für Technische Kernphysik der TH Darmstadt, Germany (Fed. Rep.).
§Laboratoire d'Electrostatique et de Physique du Métal, BP 319, Grenoble, France.

reduced by a dynamic Jahn–Teller mechanism as described by Ham[9].

Samples and experimental features

Synthetic powder samples of ZnS blende and wurtzite and CdS wurtzite containing different concentrations of iron (enriched in ^{57}Fe) and in some cases of additional impurities (Cd^{2+} in ZnS and Zn^{2+} in CdS) have been prepared by mixing the sulfides and by firing at appropriate temperatures*. The structure was established by X-ray analysis at room temperature.

Measurements of the gamma resonance absorption were performed with a ^{57}Co source in copper, moved by a linear velocity transducer (symmetrical triangular velocity signal). The linearity and calibration of the velocity scale were carefully checked by using metallic iron and Fe_2O_3 absorbers as references, and experimental line widths were less than 0·25 mm/s.

The sample temperature was controlled with germanium thermometers or thermocouples during the experiments, and was kept constant with an accuracy better than ± 0·1°K.

Mössbauer spectra of Fe^{2+} *in* ZnS *and* CdS

The iron concentration of the absorber samples, investigated in the temperature range from 1·4°K to room temperature, was varied between 0·2 and 31 at.%.

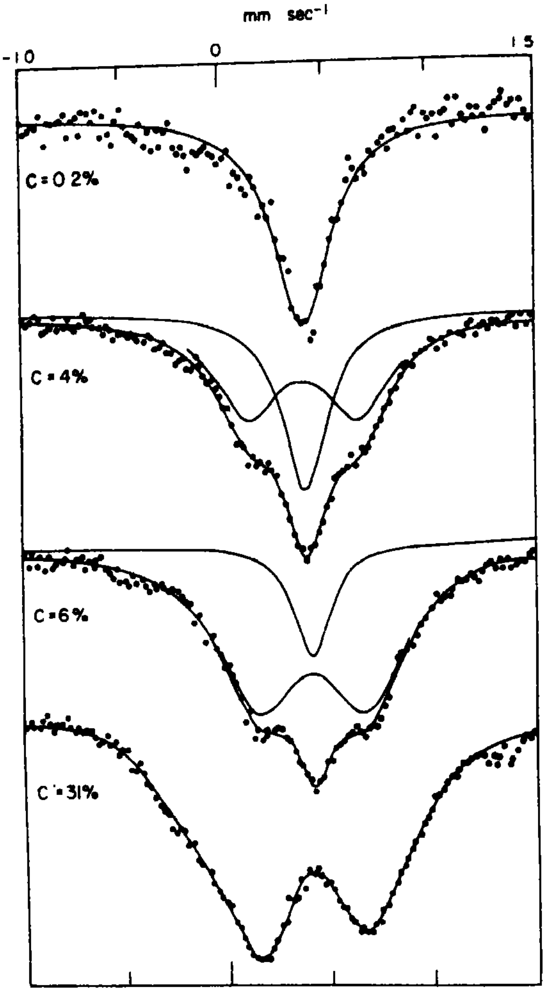

Fig. 1. ZnS wurtzite: Mössbauer spectra at room temperature for different iron concentrations *c* in atomic per cent.

Apart from slight variations in the line widths no noticeable difference could be found in the spectra for the two ZnS modifications. The spectra could be explained by a superposition of one central line not split at room temperature and of a doublet with identical isomer shifts characteristic of Fe^{2+}. The relative intensities of these contributions are independent of temperature but change with iron concentration (Fig. 1): being suppressed at very low concentration the doublet becomes dominant when 6 per cent of the metal atoms in the host lattice are replaced by iron. This could explain the differences between the results of Ref. [5] and [6]. The splitting of the doublet is concentration independent; however, if the concentration exceeds 10 per cent a certain line broadening is noticed, particularly near 77°K.

At very low temperature (Fig. 2) the separation ΔE_0 of the two lines in the doublet is about 3 mm/s, 3·19 mm/s for ZnS and 2·86 mm/s for CdS at 4·2°K. On the other hand the central part of the spectra is strongly con-

---

*The samples were partly prepared by Mme Saint-James and Mme Carcaillet (SPSRM–CEN de Saclay).

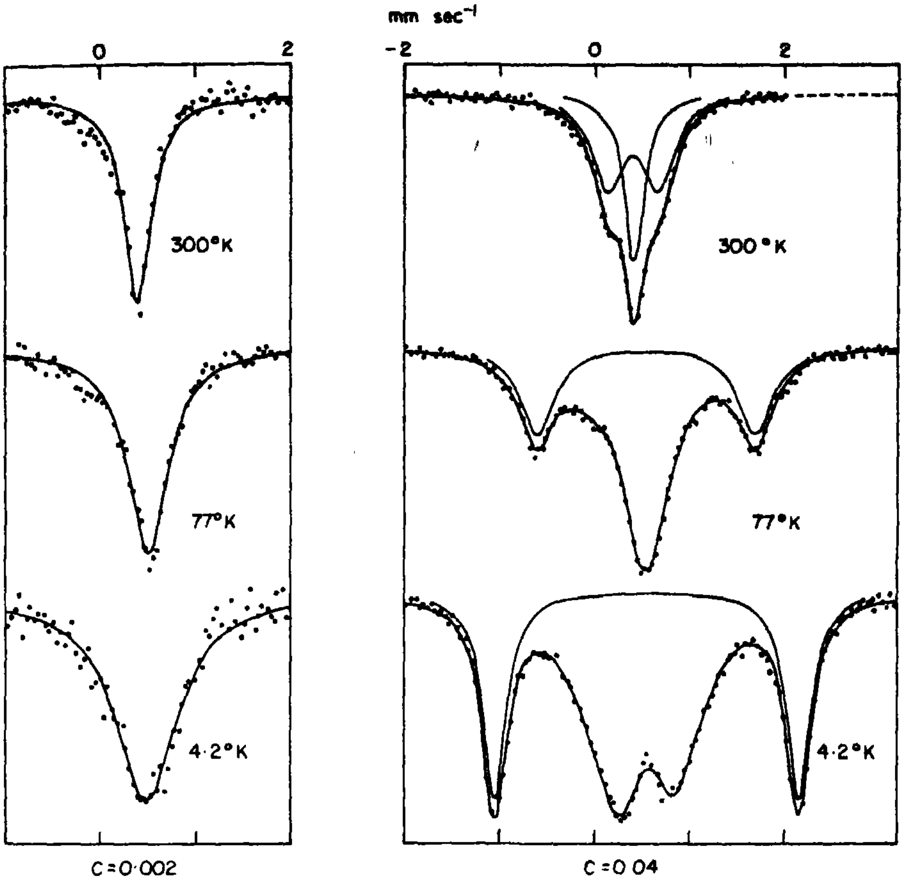

Fig. 2. ZnS wurtzite: Mössbauer spectra at different temperatures for iron concentrations $c = 0{\cdot}2$ and 4 per cent.

centration dependent; at low temperatures it broadens the more the higher the concentration is and changes from a single line at lower concentration to a broad, doubly peaked absorption region at concentrations of some per cent*.

Our experimental results may be reasonably explained by distinguishing between two kinds of impurity sites: those having no other impurity atom amongst their 12 nearest metal neighbors, and those which have at least one of the 12 next metal neighbors replaced by another Fe^{2+} ion. We shall call the former ones 'isolated' ions.

The fraction of isolated ions depends on concentration. If all impurity atoms are substitutionally incorporated and randomly distributed in the host lattice, it is given by the curve 1 in Fig. 3[10]. Within the experimental error the measured relative intensity of the central line varies according to this statistical distribution curve for the isolated ions (Fig. 3). Hence the doublet corresponds to Fe^{2+} having one or more iron ions among the 12 nearest metal neighbors. For concentrations $c < 5$ per cent the doublet represents mainly the contribution of ions associated in

---

*A slight disymmetry in some spectra originates from the presence of very small amounts of Fe^{3+} ions.

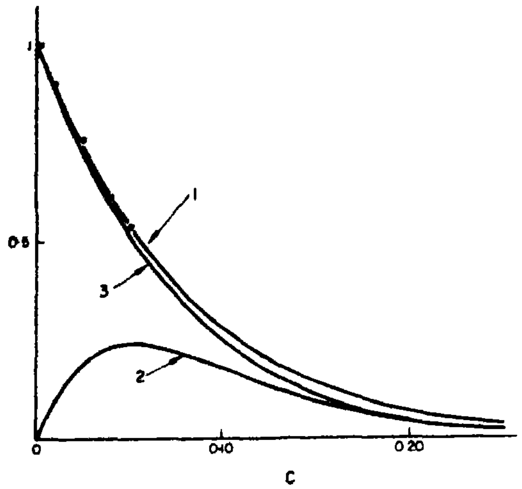

Fig. 3. Fraction of isolated Fe^{2+} ions (curve 1) and of pairs (curve 2) statistically distributed in ZnS as a function of impurity concentration (atomic per cent). The experimental points represent the area of the central part relative to the total absorption in the Mössbauer spectra as fitted with a computer. Curve 3 presents the fraction of paired ions relative to the total number of non-isolated impurities.

pairs as is reflected by curve 3 in Fig. 3. At higher concentrations accumulations of 3 and more iron impurities become more frequent and, dominating the pairs, they cause a noticeable line broadening of the doublet lines in the Mössbauer spectrum.

Interpretation of results for isolated Fe^{2+}

The trigonal component in the crystal field in wurtzite cannot split the orbitally two-fold degenerate E_g ground state. The wave functions depend on the parameter Θ (Fig. 4) connected with the splitting δ_t in a trigonal field of the T_{2g} state by [11]

$$\sin\Theta \simeq \frac{1}{\sqrt{3}}\left(1+\frac{2}{3}\frac{\delta_t}{\Delta}\right) \text{ where}$$

Δ is the cubic field splitting. The axial electric field gradient created by the $3d^6$ electron configuration in presence of a trigonal field is identical for the two wave functions subtending E_g and equals

$$V_{zz} = \frac{2}{21}|e|\,\langle r^{-3}\rangle_{3d}\,\langle 3L_z^2 - L(L+1)\rangle =$$
$$= \frac{4}{7}|e|\,\langle r^{-3}\rangle_{3d}\frac{2}{3}\frac{\delta_t}{\Delta}.$$

This corresponds to a temperature independent quadrupole splitting of

$$\Delta E_t \simeq \Delta E_0 \frac{2}{3}\frac{\delta_t}{\Delta}, \text{ with } \Delta E_0 \simeq 3 \text{ mm/s}.$$

Taking the experimental line width measured in the most diluted samples of ZnS and CdS

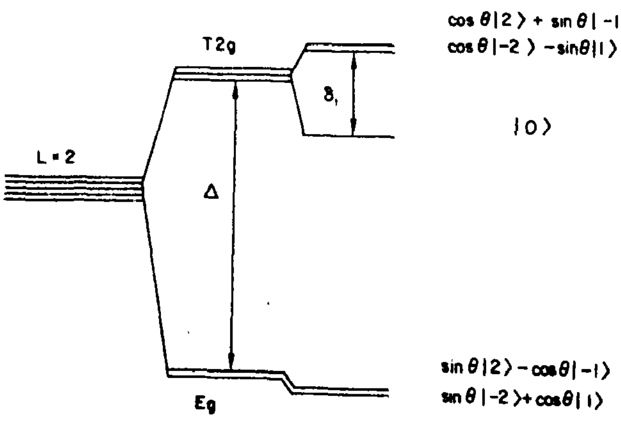

Fig. 4. Scheme of orbital electronic levels of $Fe^{2+}(^5D)$ in tetrahedral cubic environment in presence of a small trigonal distortion.

wurtzite at room-temperature one can establish an upper limit of 0·06 mm/s for ΔE_t leading to a value of δ_t/Δ smaller than 3 per cent. The effect on the wave functions of such a small trigonal crystal field is negligible. We may therefore assume a cubic crystal field in blende as well as in wurtzite unless additional distortions must be taken into account. The orbital doublet E_g is consequently affected only by a second order spin-orbit interaction. This causes a splitting into 5 equally spaced levels[12] which lead to zero electric field gradient each.

The absence of localized static Jahn–Teller distortions in the environment of very diluted isolated Fe^{3+} ions in the blende and wurtzite structure is confirmed by the missing or very small quadrupole interaction (spectra for $c = 0{\cdot}002$ in Fig. 2). This result is not surprising if one takes account of the weak Jahn–Teller anisotropy associated with an isolated tetrahedral complex containing Fe^{2+} as calculated by Goodenough[1]. Insufficient for being attributed to static Jahn–Teller distortions, the line broadening observed at very low temperatures and originating in quadrupole interaction reflects the influence of local strain. These strains lead to small splittings δ of the orbital doublet E_g, varying from one lattice site to the other. This assumption is supported by the following observations:

(a) The broadening of the central part of the spectrum increases with iron concentration, in other words with the number of impurities present in the neighborhood beyond the shell of nearest metal neighbors. Now the impurities are likely to introduce strains into the lattice. At equal concentrations the line broadening is more pronounced in CdS than in ZnS, probably due to the fact that the ionic radius of Fe^{2+} differs more from that of Cd^{2+} than from that of Zn^{2+}.

(b) The strains produced artificially by using an adhesive cement (like araldite) generate a considerable broadening at low temperature; so a kind of splitting similar to that observed at 4·2°K for $c = 0{\cdot}04$ (Fig. 2) is induced on samples with a much lower iron concentration.

(c) Simple calculations of quadrupolar interactions assuming only tetragonal distortions[13] are consistent with the broadening observed at low temperature in the central part of the Mössbauer spectra, if we suppose that the tetragonal field splitting δ of the orbital ground state E_g ranges between zero and

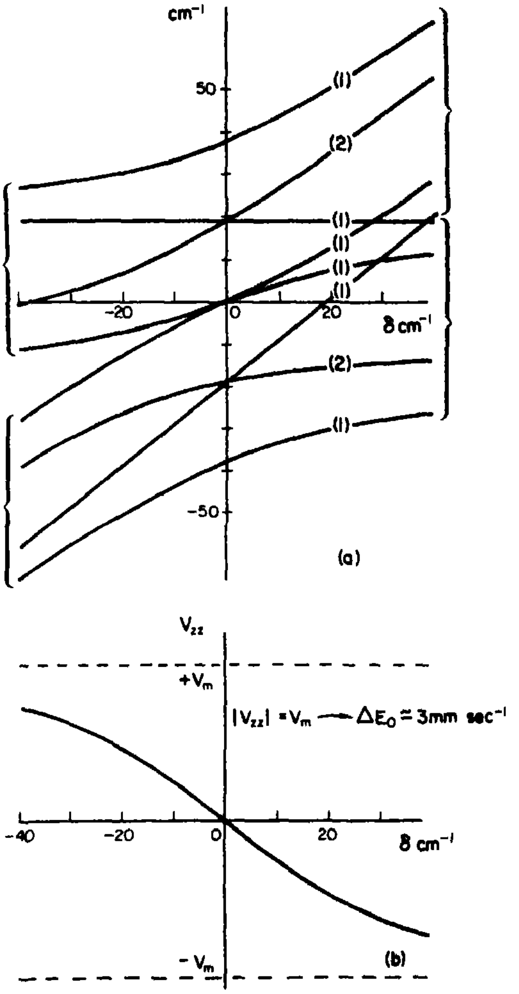

Fig. 5. Change of spin-orbit levels of E_g (5a) and of the principal component V_{zz} of the EFG produced by the lowest lying level (5b) as a function of splitting δ induced by a tetragonal field. The order of degeneracy of each level is indicated by the number in parenthesis.

some 10 cm^{-1}: the Fig. 5a shows the variation of the spin-orbit levels of E_g calculated vs. δ, and the Fig. 5b gives the corresponding component V_{zz} of the electric field gradient calculated for the lowest level which, practically, is the only one populated at 4·2°K [in these calculations the spin-orbit splitting in a cubic field, $2D = 6((\lambda^2/\Delta)+\rho)$[11] ($\lambda$ being the spin-orbit coupling and ρ the spin-spin interaction) was taken to be 19 cm^{-1}; the positive sign of δ in Fig. 5 corresponds to the case where the ground state orbital function is $L_z = 0$]. For small values of $|\delta|$ ($|\delta| \leq 15\ \mathrm{cm}^{-1}$) V_{zz} is found to be almost proportional to δ leading to a quadrupole splitting ΔE_0 of the order of 0·75 mm/s for $|\delta| = 10\ \mathrm{cm}^{-1}$. These values can be regarded as an estimate of the average effects produced by strains which the isolated Fe^{2+} ions are 'feeling' in ZnS wurtzite with a 4 per cent iron admixture (spectra in Fig. 2). In addition Fig. 5a shows that the existence of an orbital level splitting $|\delta|$ of this order of magnitude does not disturb the spin-orbit levels of E_g in a manner inconsistent with the optical absorption spectra obtained by Slack *et al.* in cubic ZnS[8]. On the other hand a splitting of this size could account for the line broadening observed in their spectrum for the sample which had the biggest iron content. Finally,

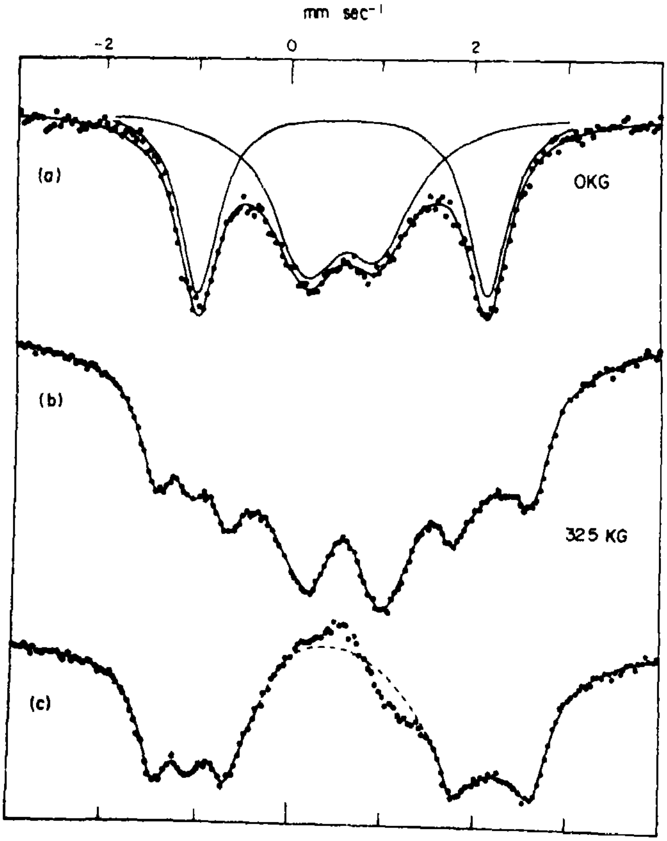

Fig. 6. ZnS würtzite: iron concentration $c = 5\%$. Mössbauer spectra at 4·2°K without external field (a), with a longitudinal magnetic field of 32·5 kOe (b). (c) is deduced from (b) by subtracting the central part of (a).

no change of the Mössbauer spectrum could be found between 4·2 and 1·4°K obviously excluding any hypothesis of low frequency vibrations responsible for line broadening at low temperature.

Fundamentals of interpretation concerning the results for Fe^{2+} *ion pairs*

The observed quadrupole interaction in the case of Fe^{2+} ion pairs implies that the orbital degeneracy of the doublet E_g is lifted. As long as the energy separation δ between the electronic orbital singlets is small relative to the cubic field splitting Δ the wave function of the ground state can be written in the form

$$|L_z\rangle = \cos\varphi\,|0\rangle + \sin\varphi\,\frac{|2\rangle + |-2\rangle}{\sqrt{2}}$$

with the quantization axis chosen parallel to a twofold axis of the tetrahedron.

The calculation shows that, neglecting spin-orbit coupling, the quadrupole splitting ΔE originating in the EFG due to the $3d$ electrons is independent of the parameter φ and depends on temperature according to

$$\Delta E \simeq \left(\frac{e^2Q}{2h}\right)\cdot\frac{4}{7}\langle r^{-3}\rangle \tanh\frac{\delta}{2kT}$$

(where Q is the quadrupolar moment of the 14·4 keV state of ^{57}Fe)

$$= \Delta E_0 \tanh\frac{\delta}{2kT} \quad (\Delta E_0 \simeq 3\ \mathrm{mm/s})$$

and that the asymmetry parameter η of the EFG is given by

$$|\eta| = \sqrt{3}\,|\tan 2\varphi|.$$

In Table 1 the isomer shifts and the values ΔE of the quadrupole splitting are given for different temperatures at low iron concentrations for which the doublet is mainly to be attributed to Fe^{2+} ion pairs. The corresponding values for δ derived from the previous equation are respectively 105 ± 5 cm^{-1} for Fe^{2+} in ZnS blende or wurtzite and 67 ± 10 cm^{-1} for Fe^{2+} in CdS wurtzite. These values are not much larger than the spin-orbit splitting and can only be considered as an order of magnitude estimate due to the approximations made in the calculation.

The observation of the Mössbauer spectra of polycrystalline samples in an external magnetic field enables us to determine the sign of the principal component of the EFG as well as an order of magnitude estimate of

Table 1. *Results for pairs of impurities in* ZnS *and* CdS

Host lattice and type of pairs	Isomer shift [mm/s] at 300°K. Source: ^{57}Co in copper	Quadrupole splitting of the doublet ΔE [mm/s]			Orbital splitting* of E_g $\delta[cm^{-1}]$
		300°K	77°K	4·2°K	
ZnS blende: $C_{Fe} = 1$ to 5% (pairs Fe–Fe)	+0·43 ± 0·03	0·60 ± 0·10	2·40 ± 0·05	3·19 ± 0·05	105 ± 5
ZnS wurtzite: $C_{Fe} = 1$ to 5% (pairs Fe–Fe)	+0·46 ± 0·03	0·56 ± 0·10	2·38 ± 0·05	3·19 ± 0·05	105 ± 5
CdS wurtzite: $C_{Fe} = 1$ to 5% (pairs Fe–Fe)	+0·48 ± 0·03	0·57 ± 0·10	1·60 ± 0·20	2·86 ± 0·10	67 ± 10
ZnS wurtzite $C_{Fe} = 0·5\%$, $C_{Cd} = 5\%$ (pairs Fe–Cd)	+0·44 ± 0·03	1·15 ± 0·05	2·90 ± 0·05	3·24 ± 0·05	156 ± 5
CdS wurtzite $C_{Fe} = 0·5\%$, $C_{Zn} = 5\%$ (pairs Fe–Zn)	+0·50 ± 0·03	0·85 ± 0·05	2·70 ± 0·05	3·12 ± 0·05	139 ± 5

*δ has been calculated by the approximation formula $\Delta E = \Delta E_0 \tanh(\delta/2kT)$.

the asymmetry parameter η[14]. Such a measurement has been performed at 4·2°K in ZnS blende and wurtzite. An analysis, however, was not possible in the case of CdS because of the modest separation between the two superimposed parts of the spectra. The results obtained for Fe^{2+} ion pairs in ZnS are the following:

(a) V_{zz} is positive in ZnS blende and wurtzite.

(b) One can establish an upper limit of about 0·5 for η in ZnS wurtzite. Because of the lower resolution it is difficult to fix such a limit in the case of blende.

(c) No internal magnetic field induced by an external field of 30 kOe at 4·2°K can be detected by the technique used here. This demonstrates the smallness or absence of susceptibility effects under these conditions.

As first approach let us assume $\eta = 0$. This corresponds to a tetragonal distortion of the environment of the Fe^{2+} pairs. The orbital ground state is $|L_z\rangle = (1/\sqrt{2})(|2\rangle + |-2\rangle)$ as in FeV_2O_4[15]. Within the spin Hamiltonian concept such a situation would lead to $\mathscr{H}_s = D S_z^2$ with $D < 0$ and $|D| \approx 10$ cm^{-1}, favoring an axial magnetic anisotropy. Hence the ground state should be magnetic $(S_z = \pm 2)$ and induce, under the previous experimental conditions, an internal magnetic field. At all sites where the external magnetic field is parallel to the z axis this field would be almost saturated at 4·2°K ranging about 100 kOe as in FeV_2O_4 and in $ZnCr_2O_4$ or $MgCr_2O_4$ with Fe^{2+} incorporated substitutionally[16]. The non-existence of susceptibility effects in the present case is probably due to an antiferromagnetic exchange coupling between the two ions forming pairs as for Mn^{2+} pairs in ZnS and CdS[17, 18].

In Fig. 7 the arrangements of the ion pairs in the lattice of ZnS of CdS are shown. It appears that there is one atom of the two tetrahedrons of sulphur neighbors in common. In the blende structure (Fig. 7a) the two tetrahedrons result from each other by translation. In wurtzite exist two different arrangements, that of Fig. 7a and that of Fig. 7b. The configuration of Fig. 7b corresponds to iron ions associated in pairs but not in the same plane perpendicular to a trigonal axis as in Fig. 7a. In this case the tetrahedrons can be transformed in each other by translation followed by a rotation of 60° about the trigonal axis through the common corner. The configuration of Fig. 7a contains an axis of

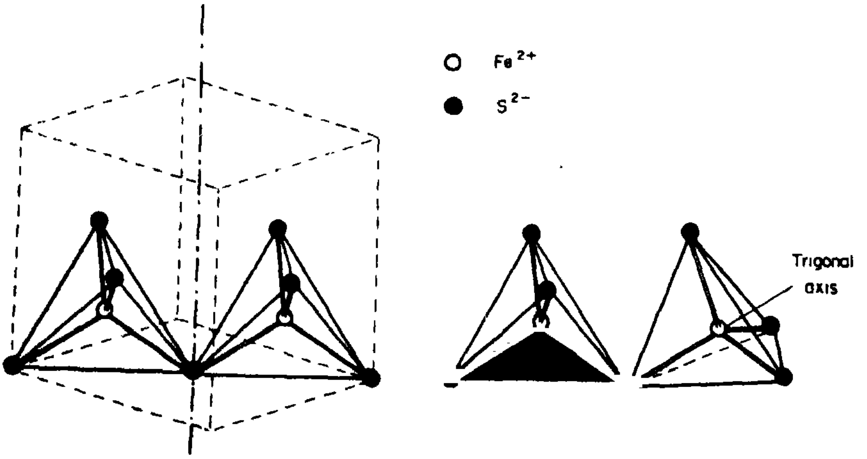

(a) (b)

Fig. 7. Arrangement of pairs in the blende and wurtzite structures. (blende: 7a; wurtzite: 7a and 7b).

symmetry of order 2 parallel to an axis of order 4 of the cubic lattice. This could constitute a direction of quadratic distortion common to each iron in the pair. Such an axis does not exist in Fig. 7b.

At present status of experimental work it is difficult to make any conclusions concerning the role played by the Jahn–Teller effect. The origin of local distortions, which have been deduced from the Mössbauer spectra in the case of ion pairs is not cleared. A theoretical investigation of vibrations of the complex formed by such pairs and their environment has to our knowledge not yet been performed. On the other hand we have observed an electronic splitting of about 150 cm^{-1} in the Fe^{2+} ion ground state when the pairs were formed by Fe^{2+} and another impurity as partner not being a Jahn–Teller ion (Cd^{2+} in ZnS or Zn^{2+} in CdS). The compounds $(Zn_{0\cdot945}Cd_{0\cdot05}Fe_{0\cdot005})S$ and $(Cd_{0\cdot945}Zn_{0\cdot05}Fe_{0\cdot005})S$ have been prepared to study the pairs Fe–Cd in ZnS and Fe–Zn in CdS. The results are given in Table 1. One realizes that a local distortion from cubic symmetry cannot be excluded even in absence of a Jahn–Teller effect, if a second impurity is replacing a next metal neighbor of the host lattice. At first glance one would expect a simple volume effect. This, however, does not seem to be the only possible effect, since the pairs Fe–Fe and Fe–Zn in the CdS lattice show considerably different splitting values δ (67 and 139 cm^{-1}) although the ionic radii of Zn^{2+} and Fe^{2+} are almost equal compared to the very different radius of Cd^{2+}. The weakness of Mössbauer absorption (because they are very diluted in iron) in the two compounds containing the mixed pairs Fe–Zn and Fe–Cd has as yet not permitted their study in an external magnetic field.

Finally let us mention briefly the study we have performed with a ^{57}Co source in cubic ZnS. Room temperature spectrum exhibits a narrow line the isomer shift of which is the same as for Fe^{2+} in ZnS absorbers. At 78°K the line becomes broad ($\Gamma_{exp} \simeq 1$ mm/s) as observed in hexagonal ZnS[6]; at lower temperature such as 4·2°K we obtained a very broad doubly peaked absorption with some lateral wings, indicating a spread of δ values up to several tens of cm^{-1} probably connected with strains or defects in our sample.

Conclusions and suggestions

The Mössbauer study of highly diluted iron impurities in ZnS and CdS lattices has failed to reveal any static Jahn–Teller distortion of the tetrahedral surroundings of the Fe^{2+} ions. On the other hand vicinity effects between one Fe^{2+} ion and another impurity have been observed. These effects manifest themselves very differently on Fe^{2+} when the two atoms are or are not next nearest metallic neighbours. The related electronic splittings δ are typically of the order of 100 cm^{-1} in the first and 10 cm^{-1} in the second case. In the first situation only there is a common anion to the two tetrahedral sites of impurities, and thus this common anion S^{2-} seems to be of primordial importance for the appearance of the strong local distortions observed around Fe^{2+} paired with another impurity in ZnS and CdS.

It would be interesting to test if the above conclusions hold for Fe^{2+} impurities incorporated into tetrahedral cubic sites in other host lattices, such as spinels for example. As for diluted Fe^{2+} impurities in *A* sites of normal cubic spinels, some results suggest also the absence of local static Jahn–Teller effect: $ZnCr_2O_4$ and $MgCr_2O_4$ doped with 3% Fe^{2+} exhibit only a broadened Mössbauer line near 20°K, above their Néel temperatures ($T_N \simeq$ 10–14°K)[16], and preliminary results we have obtained with Fe^{2+} doped $ZnAl_2O_4$ samples indicate a spread of the electronic splitting δ in the range 0–20 cm^{-1}[19]. In synthetic samples of Fe^{2+} doped $MgAl_2O_4$ however, Ono *et al.*[20] have observed a large quadrupolar interaction, as in $FeAl_2O_4$. But one must point out that a small degree of inversion in the spinel host lattice in expected to give drastic quadrupolar effects on Fe^{2+} ions in *A* sites, because the charge defects which occur in the cation distribution; such an assumption, which is evoked [21, 22] to account for the large quadrupolar splitting observed in cubic $FeAl_2O_4$[20, 23], might well be also responsible for the same behaviour of Fe^{2+} impurities in synthetic $MgAl_2O_4$; further a better normality in the cation distribution could explain the different behaviour of natural $MgAl_2O_4$ samples[24].

It may be mentioned that, contrary to the blende and wurtzite structures, adjacent tetrahedral surroundings do not have an anion in common in the spinel lattice. So it would be useful to check if Fe^{2+} pairs located at adjacent *A* sites in cubic spinels give a quadrupolar interaction considerably lower than in ZnS or CdS.

Acknowledgement – We would like to express our gratitude to Mme F. Hartmann-Boutron for many comments and discussions which were very useful for us in the course of this work.

REFERENCES

1. GOODENOUGH J. B., *J. Phys. Chem. Solids* **25**, 151 (1964).
2. WYCKOFF R. W. G., *Crystal Structures*, Ed. 2, p. 108 Interscience Publ New York (1963).
3. BIRMAN J. L., *Phys. Rev.* **109**, 810 (1958)
4. MORIGAKI K., *J. phys. Soc. Japan* **19**, 187 (1964).
5. MARFUNIN A. S. and MKRTCHYAN A. R., *Geokhimya* **10**, 1094 (1967) and BORSHAGOVSKII B. V. *et al.*, *Izv. akad. nauk. SSSR. Ser. Khim.* 1267 (1968).
6. BELOZERSKII G. N., NEMILOV Y. A., TOMILOV S. B. and SHEDCHJKOV A. V., *Soviet Phys. Solid State* **8**, 485 (1966).
7. SLACK G. A., HAM F. S. and CHRENKO R. M., *Phys. Rev.* **152**, 376 (1966).
8. SLACK G. A., ROBERTS S. and HAM F. S., *Phys. Rev.* **155**, 170 (1967).
9. HAM F. S., *Phys. Rev.* **138**, A1727 (1965).
10. KREITMAN M. M. and BARNETT D. L., *J. chem. Phys.* **43**, 364 (1965).
11. VARRET F. and HARTMANN-BOUTRON F., *Ann. Phys.* **3**, 157 (1968).
12. LOW W. and WEGER M., *Phys. Rev.* **118**, 1119 (1960).
13. HARTMANN-BOUTRON F., Private communication.
14. COLLINS R. L. and TRAVIS J. C., *Mössbauer Effect Methodology* (Edited by I. J. Gruverman) Vol. 3, p. 123, Plenum Press, New York (1967).
15. HARTMANN-BOUTRON F. and IMBERT P., *J. appl. Phys.* **39**, 775 (1968).
16. VARRET F., GERARD A., HARTMANN-BOUTRON F., IMBERT P. and KLEINBERGER R., *Proc. Conf. Appl. Mössbauer Effect*, Tihany 1969; to be published.
17. BRUMAGE W. H., YARGER C. R. and LIN C. C., *Phys. Rev.* **133**, A765 (1964).
18. KREITMAN M. M., MILFORD F. J., KENAN R. P. and DAUNT J. G., *Phys. Rev.* **144**, 367 (1966).
19. GERARD A., IMBERT P., PRANGE H. and VARRET F. To be published.
20. ONO K., ITO A. and SYONO Y., *Phys. Lett.* **19**, 620 (1966).
21. TANAKA M., TOKORO T. and AIYAMA Y., *J. phys. Soc. Japan* **21**, 262 (1966).
22. MATHUR H. B., SINHA A P. B. and YAGNIK C. M., *Indian J. Pure appl. Phys.* **5**, 155 (1967).
23. ROSSITER M. J., *J Phys. Chem. Solids* **26**, 775 (1965).
24. ONO K., CHANDLER L. and ITO A., *Phys. Lett.* **24A**, 273 (1967).

J. Phys. Chem. Solids Pergamon Press 1971. Vol. 32, pp. 2101–2104. Printed in Great Britain.

RESISTIVITY OF SUPERCONDUCTING ALLOYS IN THE MIXED STATE IN A WEAK FIELD

J. GILCHRIST and P. MONCEAU
Centre de Recherches sur les Très Basses Températures, C.N.R.S., Cedex 166,
Grenoble-Gare, France

(*Received* 16 *November* 1970)

Abstract—We have determined the resistivity of lead-indium alloys in the mixed state as a function of temperature T in different magnetic fields, H_0. The temperature variation confirms previous experimental and theoretical results but we find that $\rho_f/\rho_n \approx H_0/1{\cdot}2H_{c2}$ as $T \to 0$, differing from the empirical law of Kim *et al.*

IN THEIR study of high Ginzburg–Landau parameter ($\kappa \gg 1$) alloys in the mixed state, Kim *et al.*[1] found that the differential resistivity, ρ_f, in a weak field $H_0(\ll H_{c2})$ had a minimum at some non-zero temperature, T_m. T_m depended somewhat on H_0, being less for higher field. They also formulated the empirical law

$$\rho_f/\rho_n = H_0/H_{c2} \qquad (1)$$

for $T \to 0$, in which ρ_n is the normal state resistivity and H_{c2} the Ginzburg–Landau upper critical field, and for which κ was not necessarily very large.

To explain the minimum, Clem[2] found that the motion of fluxoids is opposed by a viscous drag having a thermal component in addition to the usual isothermal eddy-current term. For T well below the critical temperature T_c, the thermal viscosity is an increasing function of temperature so that $\rho_f(T)$ initially decreases. Clem explicitly neglects lattice thermal conductivity and finds that the effect would be the more marked, the more the material is impure. In fact it seems fair to neglect lattice conduction, even though macroscopically it may be predominant, since energy transfer is between electrons over a distance of the order of their mean free paths.

Axt and Joiner[3] studied Pb–Tl alloys and found that the minimum of $\rho_f(T)$ was more pronounced for the dirtier alloy $Pb_{60}Tl_{40}$, since for $Pb_{95}Tl_5$ there was no minimum at all. Literal application of Clem's theory gave $T_m \approx 0{\cdot}3T_c$, but it is remarkable that Clem's expression for the thermal viscosity term has a maximum near $0{\cdot}55T_c$, just where Axt and Joiner found the minimum of $\rho_f(T)$. If the isothermal viscosity in weak field had been assumed to be temperature independent (and not to vary like $H_{c2}(T)$), T_m would have been correctly predicted.

More recently Chow[4] added a term to expression (1) due to interaction between fluxoids and suggested

$$\rho_f/\rho_n = H_0/H_{c2}(0)\,[1+\gamma H_0/H_{c2}(T)] \qquad (2)$$

where γ is a nearly-constant coefficient of the order 10^{-1} to 1, and T is not necessarily zero. Associated with Clem's thermal viscosity calculation, Chow's result provides[5] an explanation for the field dependence of T_m and implies that as $H_0 \to 0$ the isothermal viscosity is independent of temperature, so that T_m would be $0{\cdot}55T_c$.

We studied the resistivity of Pb–In alloys[6] by measuring the surface resistance by a resonance method at 2·4 GHz where the conductivity is static because $\hbar\omega/\epsilon_0(t) \ll 1$,

($\hbar\omega$ is the microwave energy and $\epsilon_0(t)$ the intrinsic pair-breaking energy[7]) and by a limited number of differential resistance measurements. Some 2·4 GHz results are shown in Figs. (1a) and (b). In temperature dependence we find the principal features of the previous results, a more pronounced minimum for the dirtier alloy and T_m lower for higher field. For the lowest fields T_m lies between $0{\cdot}55T_c$ and $0{\cdot}67T_c$. Owing to its moderate κ (2·95) and incomplete demagnetising coefficient, the flux density B in the $Pb_{90}In_{10}$ was not strictly proportional to H_0 and had to be calculated, knowing the magnetisation curves at various temperatures. It would seem in this case that ρ_f would depend on B rather than on H_0.

Two remarks can be made, arising from the different experimental method we used. Firstly, since the measurements were made at 2·4 GHz the effect is not due to a macroscopic temperature gradient across the specimen. (This may result from doing the experiment at d.c. but is certainly not a necessary cause of the resistance minimum.) The additional viscous drag has its explanation on the scale of the fluxoid lattice. Secondly, the current densities induced in our specimens were weaker than would have been needed at d.c., and so less energy was dissipated. It was convenient to have the specimen in He exchange gas rather than immersed in liquid, and so naturally there was no anomaly at T_λ, such as was reported in Refs. [1] and [2].

A further remark concerns the general level of resistivity at low fields as exemplified by the extrapolation to $T = 0$. The extrapolations of ρ_f/ρ_n are shown in Fig. 1 where it has been noted that according to Clem's expression $\partial\rho_f/\partial T = 0$ at $T = 0$. At $T = 0$ we find

$$\rho_f/\rho_n = H_0/aH_{c2}(0) \tag{3}$$

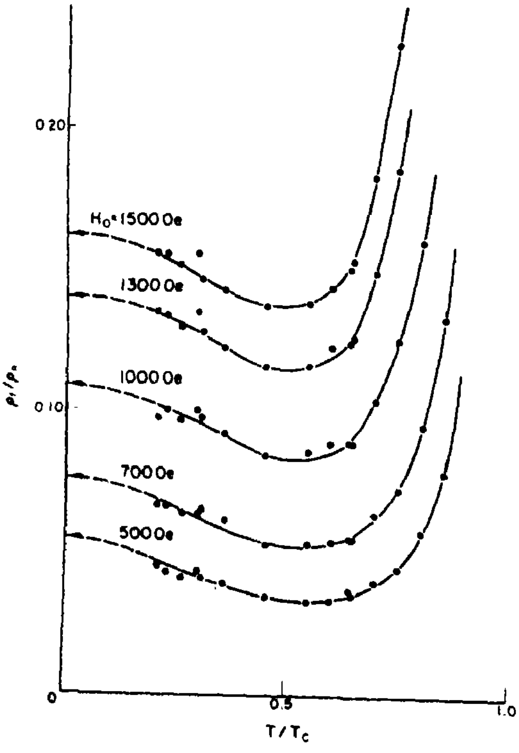

Fig. 1(a)

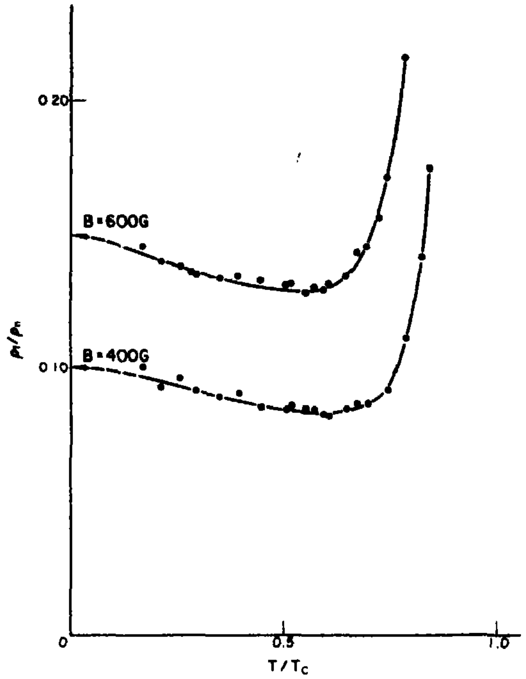

Fig. 1(b)

Fig. 1. Normalised resistivity of (a) $Pb_{50}In_{50}$, (b) $Pb_{90}In_{10}$ as a function of reduced temperature in various fields. For the two specimens $T_c = 6{\cdot}48$, $7{\cdot}02$ K respectively and $\rho_n = 21{\cdot}3\ \mu\Omega$ cm, $7{\cdot}95\ \mu\Omega$ cm.

with a not necessarily equal to 1·0 and with B/μ_0 instead of H_0 where different. We extrapolated our $H_{c2}(T)$ data to $T = 0$ by fitting them to the curve $[1-(T/T_c)^2]$ and to $[1-(T/T_c)^2]/[1+(T/T_c)^2]$. For $Pb_{50}In_{50}$ this gave $H_{c2}(0) = 7520$ Oe, 7660 Oe respectively while $H_0\rho_n/\rho_f(0) = 9300 \pm 200$ Oe. For $Pb_{90}In_{10}$ the respective figures are 3500 Oe, 3620 Oe and 4000 ± 100 Oe so that for $Pb_{50}In_{50}$, $a = 1{\cdot}22 \pm 0{\cdot}04$ and for $Pb_{90}In_{10}$, $a = 1{\cdot}13 \pm 0{\cdot}05$.

It seems that expression (1) has at best a qualitative theoretical justification in that the fraction $H_0/H_{c2}(0)$ represents the volume fraction occupied by normal cores of fluxoids. We may alternatively try to guess the probable extrapolation downwards from H_0 near H_{c2}. Caroli and Maki[8], Thompson[9] and Ebisawa and Takayama[10] calculated the resistivity of dirty superconductors near H_{c2} and found

$$\rho_f/\rho_n = 1-\alpha[1-H_0/H_{c2}(T)] \tag{4}$$

where $\alpha = 4\kappa_1^2(0)/[1{\cdot}16(2\kappa_2^2(T)-1)+1]$ according to (7) and differs from this only when $T \neq 0$ according to [9, 10]; κ_1 and κ_2 are the generalised κ's and total demagnetising effect is assumed. At $T = 0$, $\alpha \approx 1{\cdot}7$, and although experimental data has sometimes been interpreted as supporting the contention that at $T = 0$, $\alpha = 1{\cdot}0$[11] we are inclined to believe that the sum of existing data can more reasonably be extrapolated to 1·7[7, 12]. On this assumption, we have sketched in Fig. 2 two possible variations of ρ_f/ρ_n at $T = 0$. If (1) is accurate in low fields then ρ_f/ρ_n must have an inflection as in (2)(a), but if (3) is true then there may be a more natural looking curve like (2)(b). Our data from sur-

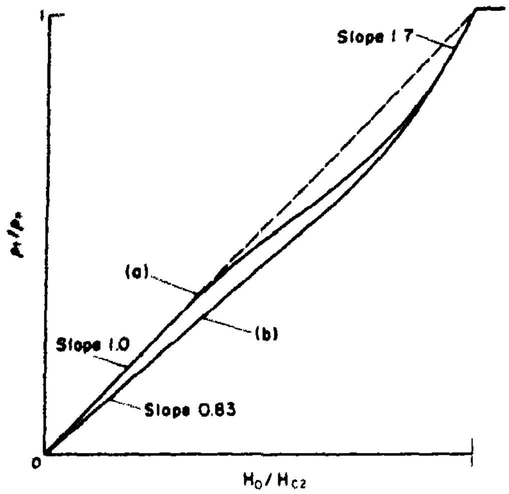

Fig. 2. Two possible forms of the resistivity curve as a function of field as $T \rightarrow 0$.

face resistance are all of the type (2)(b) but the measurements we took by the four-contact method were like (2)(a). More precisely, the raw differential-resistance data were like expression (1) but after we had applied a correction which was intended to remove the error due to joule heating we found curves like (2)(a). We conclude that there is a discrepancy within our own data at low fields but we place more reliance on the 2·4 GHz results where we are sure pinning is ineffective and which suggest expression (3) with $a \approx 1{\cdot}2$.

REFERENCES

1. KIM Y. B., HEMPSTEAD C. F. and STRAND A. R., *Phys. Rev.* **139**, A 1163 (1965).
2. CLEM J. R., *Phys. Rev. Lett.* **20**, 735 (1968).
3. AXT C. J. and JOINER W. C. H., *Phys. Rev. Lett.* **21**, 1168 (1968).
4. CHOW W. S., *Phys. Rev.* **188**, 783 (1969).
5. CHOW W. S., *Phys. Rev. B* **1**, 2130 (1970).
6. GILCHRIST J. le G. and MONCEAU P., *J. Phys. C London* **3**, 1399 (1970).
7. FISCHER G., McCONNELL R. D., MONCEAU P. and MAKI K., *Phys. Rev. B* **1**, 2134 (1970) and *Phys. Rev.* **B2**, 2817 (1970).
8. CAROLI C. and MAKI K., *Phys. Rev.* **164**, 591 (1967).
9. THOMPSON R. S., *Phys. Rev. B* **1**, 327 (1970).
10. EBISAWA H. and TAKAYAMA H., *Proceedings of the 12° International Conference on the Low Temperature Physics*, Kyoto, Japan (Sept. 1970).
11. AXT C. J. and JOINER W. C. H., *Phys. Rev.* **171**, 461 (1968).
12. MUTO Y., MORI K. and NOTO K., *Proceedings of the International Conference on the Science of Superconductivity*, STANFORD, Aug. 1969 (to be published in *Physica*).

J. Phys. Chem. Solids Pergamon Press 1971. Vol. 32, pp. 2105–2110. Printed in Great Britain.

VIBRATIONAL ENTROPIES OF HYDROGEN IN PALLADIUM-SILVER-HYDROGEN ALLOYS BY THE ISOTOPIC SOLUBILITY RATIO METHOD

P. T. GALLAGHER* and W. A. OATES
Metallurgy Department, University of Newcastle, N.S.W. 2308. Australia

(*Received* 2 *November* 1970)

Abstract—The solubilities of hydrogen and deuterium in Pd-Ag alloys containing 10, 20, 30 and 40 wt. % Ag were measured at 125°C by the Sieverts' technique using Pd black as the transference catalyst. The results obtained were analysed in terms of the isotopic solubility ratio theory. In the Pd-10Ag-H, Pd-20Ag-H and Pd-30Ag-H alloy systems, there was no significant change in the partial vibrational entropy of hydrogen S_H^V in the range of hydrogen contents H/M from 0·025 to 0·325, nor was there any marked difference between these systems. However in the Pd-40Ag-H system, S_H^V decreased markedly with increasing hydrogen concentration in the range of H/M from 0·050 to 0·150.

1. INTRODUCTION

In the infinitely dilute solutions of hydrogen in metals, the partial excess entropy of solution of hydrogen S_H^{XS} depends markedly upon the lattice structure of the host metal and seems to be related to the partial heat of solution of hydrogen in the metal, ΔH_H[1]. Since the configurational entropy can be assumed to be ideal in the infinitely dilute solution region, the partial excess entropy of solution of hydrogen S_H^{XS} is identical with the partial non-configurational entropy of solution of hydrogen S_H^{NC}. From the data available it also appears that the non-configurational entropy can be interpreted as being principally given by the vibrational entropy S_H^V and that electronic or magnetic contributions to the non-configurational entropy are relatively insignificant[1].

When attention is focussed on a particular metal–hydrogen system it is clear that, in general, the configurational entropies will not be ideal in the concentrated solutions[2] and thus the excess entropy can no longer be identified with the non-configurational entropy. It is usual in statistical treatments to assume that the non-configurational entropy is independent of hydrogen concentration but there is little evidence to justify or reject this assumption. With the lattice expansion that takes place on the introduction of interstitial solutes it might be expected that the vibration frequency of the solute atom would decrease at higher concentration levels and hence the vibrational entropy would increase as the hydrogen concentration increases. On the other hand, from the suggested correlation between the excess entropy and the heat of solution for infinitely dilute solutions of hydrogen in metals[1], little variation of the non-configurational entropy might be expected in a particular system since the heat of solution does not seem to vary by more than one or two kcals as the hydrogen concentration is varied. For example, in the Nb-H system, where the heat of solution varies from −8·44 kcals./g.at.H for $NbH_{r\to 0}$ to −10·98 for $NbH_{0\cdot 84}$ (3), the change in the excess entropy is expected to be only 0·25 eu.

There are two methods available to measure experimentally any variation of the vibrational contribution to the non-configurational entropy with hydrogen concentration. Hydrogen vibration frequencies may be obtained directly by neutron scattering techniques[4–10] although this method has not yet been used to study systematically the influence of hydrogen concentration. Vibrational entropies may also be obtained by measuring the relative solubilities of hydrogen and deuterium in a metal at a particular temperature[11–14].

---

*Present Address: Central Research Laboratory, John Lysaght (Australia) Limited, Newcastle, N.S.W. 2300, Australia.

Fowler and Smithells[15] first pointed out that a comparative study of the solubilities of hydrogen and deuterium in a metal could provide important checks on the accuracy of any theory proposed to interpret the experimental results. On this basis, the difference in the solubilities of hydrogen and deuterium in the dilute solution region in Pd was interpreted as being due to the difference in the masses of the two isotopes[16]. More recently the isotopic solubility ratio method has been used to elucidate non-configurational effects in metal–hydrogen solutions[13, 14, 17].

In this method it is assumed that the non-configurational entropy is wholly vibrational and that, because of the large mass ratio of the metal and hydrogen atoms, all the optical modes have the same frequency. Taking the reference energy level to be that of free atoms of hydrogen and deuterium at rest and using a method similar to that of Ebisuzaki, Kass and O'Keeffe[13], it can be readily shown[18] that for a particular concentration of hydrogen or deuterium in the metal, the ratio of the individual gas pressures is a measure of the characteristic temperature of vibration of the hydrogen atoms, θ, related to the vibration frequency ν by $\theta = h\nu/k$, viz;

$$\begin{aligned} RT \ln (p_{D_2}/p_{H_2})^{1/2} &\\ = (F_D - F_H) - \tfrac{1}{2}\{(G_T - H_0)_D - (G_T - H_0)_H\} &\\ + \tfrac{1}{2}(D_D - D_H) + \tfrac{3}{2}Nh(\nu_D - \nu_H) & \end{aligned}$$

where F_D and F_H are the thermal free energies of the dissolved deuterium and hydrogen atoms; $(G_T - H_0)_D$ and $(G_T - H_0)_H$ are the thermal free energies of the diatomic gases, deuterium and hydrogen respectively, which can be obtained from standard thermodynamic tables; D_D and D_H are the dissociation energies per mole of the diatomic gases deuterium and hydrogen at 0°K and ν_D and ν_H are the vibration frequencies of the dissolved deuterium and hydrogen atoms.

In the Einstein oscillator assumption $\nu_H = \sqrt{2}\nu_D$ and as $(D_D - D_H) = 1810$ cals[19], the above equation can be written in the form

$$\log (p_{D_2}/p_{H_2})^{1/2} = \frac{F_D - F_H}{4{\cdot}575\,T} - \frac{\Delta(G_T - H_0)_{D-H} - 1810}{9{\cdot}15\,T} - 0{\cdot}191(\theta/T) \qquad -(1)$$

where F_D and F_H, functions of $(\theta/\sqrt{2}T)$ and (θ/T) respectively can be read from tables (20) or calculated from the following equations

$$F_D = 3RT \ln (1 - \exp.(-\theta/\sqrt{2}T))$$

$$F_H = 3RT \ln (1 - \exp. (-\theta/T)).$$

Using equation (1), plots of $\log (p_{D_2}/p_{H_2})$ vs. $1/T$ can be drawn for various values of θ. In the Sieverts' law region $\log (p_{D_2}/p_{H_2})^{1/2}$ at constant composition $(X_H = X_D)$ can be replaced by $\log (X_H/X_D)$ at constant gas pressure and it is in this form that equation (1) has been used and presented in graphical form by Ebisuzaki, Kass and O'Keeffe[13].

By plotting equation (1) in an alternative form, Fig. 1, it can be seen that the isotopic solubility ratio method should be a particularly suitable way of measuring any variations in the characteristic temperature of vibration, θ, with hydrogen concentration, especially if the experimental temperature is kept low. With this in mind the solubilities of hydrogen and deuterium in Pd–Ag alloys were measured to this purpose. As well as being most pronounced at low temperatures, the isotopic effect is also more pronounced on systems having a low hydrogen atom vibration frequency, as is expected to be the case in these and other f.c.c. alloy systems[1].

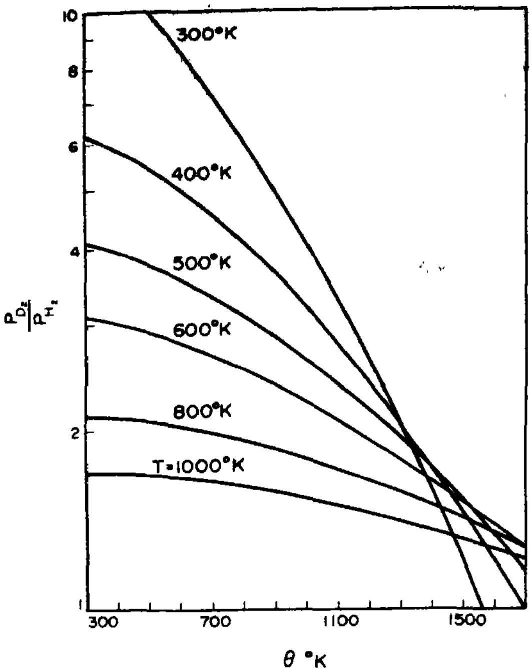

Fig. 1. Isotopic solubility ratio as a function of θ at various temperatures.

2. EXPERIMENTAL

The solubilities of hydrogen and deuterium in the pressure range 10–760 torr were measured in Pd–Ag alloys (nominal composition 10, 20, 30 and 40 wt. % Ag) at 125°C using palladium black as the transference catalyst[21]. The one gram samples of each alloy prepared from 99·99% Pd and 99·99% Ag were in the form of 0·007" foil that had been degassed for at least 12 hr at 600°C in a vacuum of better than 10^{-5} torr. Chemical analysis of the samples gave silver contents of 9·65, 19·95, 29·80 and 39·80 wt. % for the nominal 10, 20, 30 and 40 wt. % Ag alloys.

After abrading each sample with a fine emery paper, a thin coating of palladium black (less than 0·01 gram, usually 0·005 gram) was deposited onto the sample at a current density of 100–200 ma/cm² for 1–3 min. from a Pd plating solution prepared in the manner described by Hills and Ives[22].

The solubilities were measured by the Sieverts' technique in an apparatus very similar to that described by Humbert and Elliott [23]. The system 'hot' volume was calibrated using helium.

During the experimental runs, temperature control was better than ± 1°C while the pressures were measured to within ±0·005 cm using a cathetometer.

The concentrations of hydrogen (or deuterium) in the metal alloy are given in terms of the atomic ratio $r = H/(\text{Pd}+\text{Ag})$(or $D/(\text{Pd}+\text{Ag})$) and it is estimated that this ratio is measured to better than ±0·005 over the entire composition range in each alloy. In the calculation of r no allowance has been made for the amount of hydrogen (or deuterium) dissolved in the Pd black, as in most cases it was found that this would result in an error in r of less than 0·001, and at the most 0·003 for hydrogen pressures approaching one atmosphere[24].

3. RESULTS AND DISCUSSION

The isothermal data for the solubilities of hydrogen and deuterium in the Pd–Ag alloys at 125°C are given in Figs. 2 to 5. For each alloy-gas system the results presented were obtained from at least two experimental absorption–desorption runs. Most of the results shown were obtained during absorption, only occasional checks being made during desorption to ensure that the results represent true equilibrium in the hydrogen–metal and deuterium–metal reactions. In each Fig. the dashed line represents the data of Brodowsky and Poeschel[25] for the solubility of hydrogen in the same alloys at 125°C.

Reading the equilibrium hydrogen and deuterium pressures from the smoothed curves drawn through the experimental points in Figs. 2–5, the values of θ at varying hydrogen concentrations in the alloys were obtained from Fig. 1, the results being given in Table 1.

Before discussing these results an estimate should be made of the possible errors in these values of θ arising from the experimental errors in obtaining the solubility isotherms for each alloy. It would appear that the possible

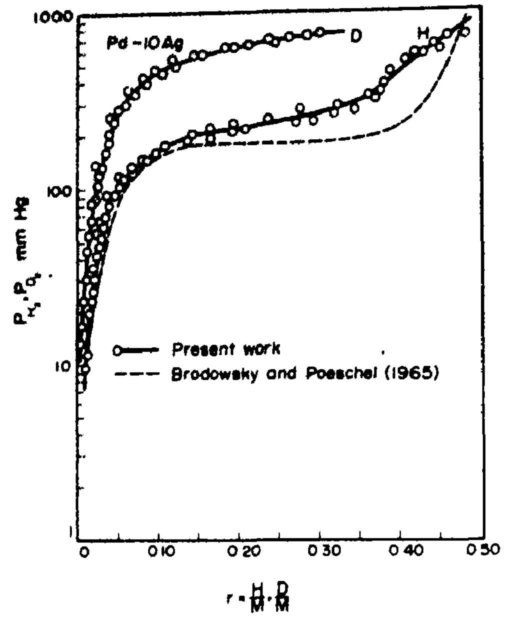

Fig. 2. Solubilities of hydrogen and deuterium in Pd–10Ag at 125°C

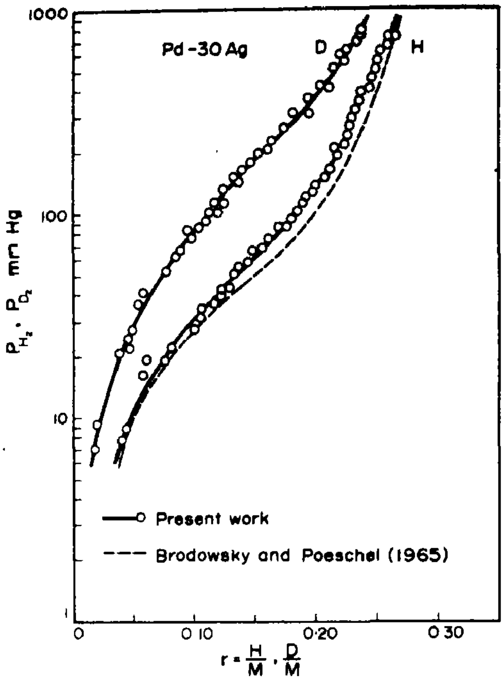

Fig. 4 Solubilities of hydrogen and deuterium in Pd–30Ag at 125°C

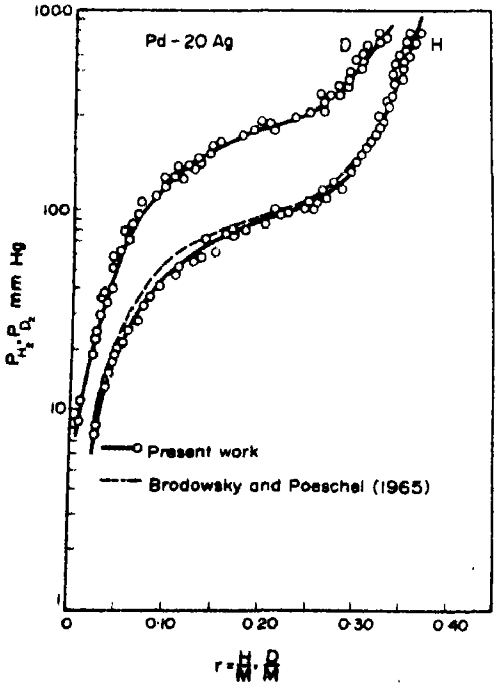

Fig. 3. Solubilities of hydrogen and deuterium in Pd–20Ag at 125°C.

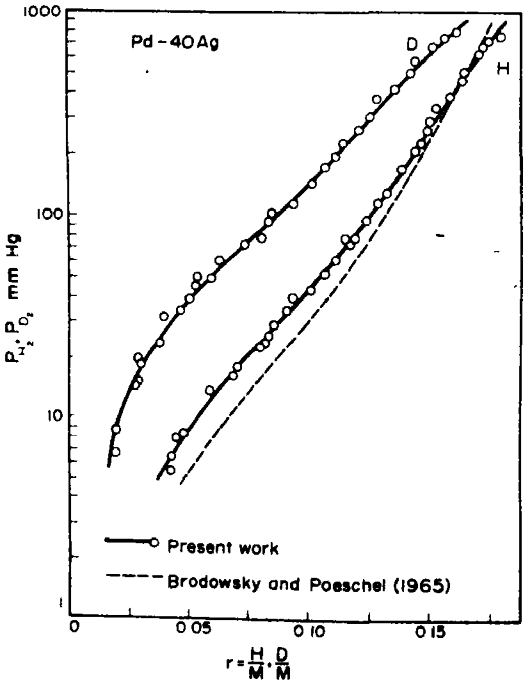

Fig. 5. Solubilities of hydrogen and deuterium in Pd–40Ag at 125°C.

Table 1. *Values of θ and S_H^V obtained from isotopic solubility ratio analysis of results*

$r = H/M$	p_{D_2}/p_{H_2}	Pd-10Ag θ	S_H^V eu	p_{D_2}/p_{H_2}	Pd-20Ag θ	S_H^V eu
0·025	2·67	1130	1·41	3·06	1030	1·72
0·050	2·57	1150	1·35	3·03	1040	1·68
0·075	2·73	1110	1·47	2·97	1060	1·62
0·100	2·82	1090	1·52	3·01	1050	1·65
0·125	2·85	1080	1·55	2·96	1060	1·65
0·150	2·85	1080	1·55	2·94	1060	1·65
0·175	2·86	1080	1·55	2·91	1070	1·59
0·200	2·95	1060	1·62	2·81	1090	1·52
0·225	2·96	1060	1·62	2·76	1100	1·49
0·250	2·96	1060	1·62	2·83	1090	1·52
0·275	2·91	1070	1·59	2·93	1070	1·59
0·300	2·81	1090	1·52	2·97	1060	1·65
0·325				2·77	1100	1·49
Average		1090 ±30	1·53 ±0·08		1070 ±20	1·60 ±0·08
		Pd-30Ag			Pd-40Ag	
0·050	2·62	1140	1·38	4·64	680	3·44
0·075	2·53	1160	1·34	3·80	860	2·41
0·100	2·75	1110	1·47	3·26	990	1·86
0·125	2·86	1080	1·55	2·97	1060	1·62
0·150	2·98	1050	1·65	2·33	1220	1·20
0·175	2·93	1070	1·59			
0·200	2·81	1090	1·52			
0·225	2·61	1140	1·38			
Average		1105 ±40	1·49 ±0·11			

errors in the atomic ratio measurements are much greater than the possible errors in measuring the equilibrium pressures and also that the possible errors in measuring the isotopic solubility ratio would be much greater in the steeper sections of the isotherms than in the slowly ascending sections of these isotherms. As the systematic errors would be common to both the hydrogen and deuterium isotherms of each alloy, only the random errors in the atomic ratio measurements were considered to be important in the measurement of the isotopic solubility ratio and these were estimated from the experimental isotherms. Consequently it is expected that for the Pd-10Ag-H, Pd-20Ag-H, and Pd-30Ag-H systems the reported values of θ are correct to within ± 50°, while for the Pd-40Ag-H system, in which the isotherms are much steeper than in the other alloys investigated, the variation is of the order of ± 100°.

In the range of compositions studied there was no significant variation of θ with hydrogen concentration for the Pd-10Ag-H, Pd-20Ag-H and Pd-30Ag-H alloy systems, nor was there any marked variation between these systems. However for the Pd-40Ag-H system the values of θ increased considerably with increasing hydrogen concentration, suggesting that on the Pd–Ag–H ternary diagram lines of equal θ are converging rapidly at this alloy composition. It should be noted that this compositional variation of θ is in the opposite direction to that expected from lattice-strain considerations.

From the values of θ for each alloy at each hydrogen concentration of interest it is possible to calculate the partial vibrational entropy of solution of hydrogen S_H^V for the assumed Einstein oscillator, these results also being included in Table 1. The variation of S_H^V with hydrogen concentration is also small for the Pd-10Ag-H, Pd-20Ag-H and Pd-30Ag-H systems, while for the Pd-40Ag-H system S_H^V decreases markedly as the hydrogen concentration increases.

It is hoped that a more detailed picture of the variation of the hydrogen atom vibration frequency spectrum with increasing hydrogen concentration will be obtained by cold neutron spectroscopy studies on the same alloy systems as more results by this valuable technique become available.

Acknowledgement—This research was supported by a grant from the Australian Institute of Nuclear Science and Engineering.

REFERENCES

1. GALLAGHER P. T. and OATES W. A., *Trans. Met. Soc. AIME* **245**, 179 (1969).
2. OATES W. A., LAMBERT J. A. and GALLAGHER P. T., *Trans. Met. Soc. AIME* **245**, 47 (1969).
3. VELECKIS E. and EDWARDS R. K., *J. Phys. Chem.* **73**, 683 (1969)
4. BERGSMA J. and GOEDKOOP J. A., *Physica* **26**, 744 (1960).
5. SAKAMOTO M., *J. phys. Soc. Japan* **19**, 1862 (1964).
6. RUBIN R., KLEY W. and PERETTI J., *Euratom Report*., EUR 1643 e, 163 (1964).
7. KLEY W., PERETTI J., RUBIN R. and VERDAN G., *Proc. Symp. Inelastic Scattering Neutrons Condensed Matter*, Brookhaven National Laboratory, BNL-940 (C-45), 105 (1965).
8. RUBIN R., PERETTI J., VERDAN G. and KLEY W., *Phys. Lett.* **14**, 100, (1965).
9. KLEY W., PERETTI J., RUBIN R. and VERDAN G., *J. Phys. (Paris)* **28**C1, 26 (1967).
10. RUSH J. J. and FLOTOW H. E., *J. chem. Phys.* **48**, 3795 (1968).
11. EICHENAUER W., *Mem. Sci. Rev. Met.* **57**, 943 (1960).
12. EICHENAUER W., LOSER W. and WITTE H., *Z. Metallk.* **56**, 287 (1965).
13. EBISUZAKI Y., KASS W. J. and O'KEEFFE M., *J. chem. Phys.* **46**, 1373 (1967).
14. McQUILLAN A. D., In *Phase Stability in Metals and Alloys*, (Edited by P. S. Rudman, J. Stringer and R. I. Jaffee), pp. 375, McGraw-Hill, New York (1967).
15. FOWLER R. H. and SMITHELLS C. J., *Proc. R. Soc. (London) Ser. A* **160**, 37 (1937)
16. LACHER J. R., *Proc. R. Soc. (London), Ser. A*. **161**, 525 (1937).
17. EBISUZAKI Y., KASS W. J. and O'KEEFFE M., *J chem. Phys.* **49**, 3329 (1968).
18. GALLAGHER P. T. and OATES W. A. To be published
19. ROSSINI F. S., WAGMAN D. D., EVANS W. H., LEVINE S. and JAFFEE I., *Nat. Bur. Std. (U.S.)* Circ No. 500, Pt. 1 (1961).
20. FURUKUWA G. T. and DOUGLAS T. B., in *American Institute of Physics Handbook*, (Edited by D. E. Gray), pp. 4–47 to 4–63, McGraw-Hill, New York, 2nd Ed. (1963)
21. BRODOWSKY H. and WICKE E., *Engelhard Ind. Tech. Bull.* 7, 41 (1966).
22. HILLS G. J. and IVES D. J. G., in *Reference Electrodes* (Edited by D. J. G. Ives and G. J. Danz) Academic Press, New York, pp. 111 (1961).
23. HUMBERT J. C. and ELLIOTT J. F., *Trans. Met. Soc. AIME* **218**, 1076 (1960).
24. BRODOWSKY H., *Z. Phys. Chem. NF* **44**, 129 (1965)
25. BRODOWSKY H. and POESCHEL E., *Z. Phys. Chem. NF* **44**, 143 (1965).

J. Phys. Chem. Solids Pergamon Press 1971. Vol. 32, pp. 2111–2122. Printed in Great Britain.

PERSISTENCE OF VACANCY MOTION IN HARD SPHERE CRYSTALS

C. H. BENNETT*
Division of Engineering and Applied Physics, Harvard University, Cambridge, Mass. 02138, U.S.A.

and

B. J. ALDER
Lawrence Radiation Laboratory, University of California Livermore, Calif. 94550, U.S.A.

(*Received* 1 *November* 1970)

Abstract—It was found that for a period of about 20 mean collision times monovacancies had an enhanced probability of moving directly (0°) and 60° forward, however, the effect on the self-diffusion coefficient is negligible at the normal melting point of the hard sphere crystal. For divacancies a stronger and longer lasting persistence of jump direction leads to a significant change from the random correlation factor of 0·458 to the correlated one of 0·515 at the normal melting point. A crude analysis leads to the conclusion that the jumping particle has roughly thermal velocity.

1. INTRODUCTION

TREATMENTS of solid state diffusion by the vacancy mechanism have generally assumed that the path of a vacancy is a random walk whose successive steps are uncorrelated in direction or time[1]. This assumption is only justified when the lattice surrounding the vacancy relaxes to its equilibrium state in a time short compared to the time between jumps. This paper describes an investigation of the deviations from random walk behavior for monovacancies and divacancies found by a molecular dynamics study of the f.c.c. crystal phase of a classical system of several hundred hard spheres.

A previous brief note[2] pointed out that monovacancies had a relaxation time of about twenty collisions per particle during which the vacancy had an enhanced probability of moving directly forward, or forward with a 60° deviation relative to the direction of the previous jump. The investigation has now been extended to divacancies. The method by which vacancy motion is detected in a molecular dynamics system is described in the next section. The following section presents and discusses the results. The final section explores the effects of persistence on diffusion, and in particular, on the ratio of macroscopic to microscopic self-diffusion and on the isotope effect in tracer diffusion. The latter study was carried out by means of a Monte Carlo calculation which incidentally yielded a more accurate value for the random walk correlation factor for divacancy diffusion on an f.c.c. lattice, as described in an Appendix.

2. METHOD

The present discussion will be mainly concerned with the method of detecting vacancy motion and with the problems arising from the different ways in which the jump event may be defined. The system used for the monovacancy runs consisted of 107 hard sphere particles initially placed on a 108 site f.c.c. lattice with periodic boundary conditions. For the divacancy study 254 particles were placed on a 256 site lattice. Random initial velocities were assigned to the particles, and their simultaneous equations of motion were solved rigorously, i.e., without reference to the lattice. However, to keep track of the vacancy, each particle was considered as belonging to one of the lattice sites. A particle was said to have exchanged with a vacancy whenever it was found inside a small cubic region (edge = 0·33 of the f.c.c. lattice constant) around the vacant site: the vacancy and jump-detection region were thereupon reassigned to the site formerly belonging to that particle. In the 2-vacancy runs, each of the vacancies had its own detection region. No vacancy was ever observed to exchange except with one of its nearest neighbor particles. Examinations of the detection regions were carried out every hundred system collisions, i.e., every 1.9 mean collision times for the 1-vacancy system and every 0·8 mean collision times for the 2-vacancy system.

---

*In partial fulfillment of the requirements for the degree of doctor of philosophy.

In order to study the sensitivity of the results to the size of the detection region, two larger concentric cubic regions, with edges 0·39 and 0·45 f.c.c. lattice constants, were simultaneously monitored (see Fig. 1). Entry of a particle into either of these regions was recorded, but was not counted as a jump, and did not cause reassignment of the regions to another site. At $V/V_0 = 1{\cdot}47$, approximately the lowest density at which a small crystal is stable against melting[3], about 96 per cent of the particles which entered the 0·45 region continued as far as the 0·39 region, and about 97 per cent of these continued to the 0·33 region and were counted as jumps. At higher densities, the number of unsuccessful attempts was reduced; e.g., at $V/V_0 = 1{\cdot}3448$, approximately the thermodynamic melting point, about 98 per cent of particles entering the 0·49 region later entered the 0·33 region. As Table 1 shows the time spent going from the outermost to the innermost region was generally around 3 mean collision times. This indicates that the jumping particle travels roughly with thermal velocity. The time required to traverse the distance between the outermost and innermost region by a particle with velocity $\sqrt{kT/m}$ in the jump direction varies from 2·84 mean collision times at $V/V_0 = 1{\cdot}47$ to 4·22 mean collision times at $V/V_0 = 1{\cdot}25$, the collision frequency being higher at higher density.

The above data makes it evident that, de-

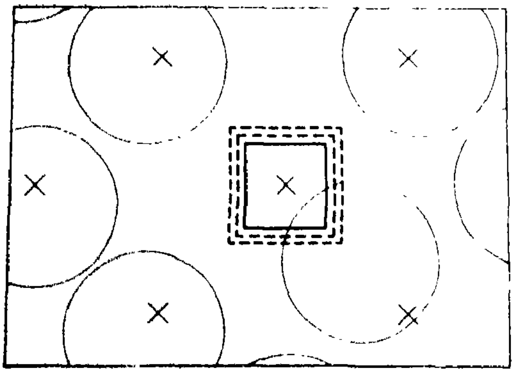

Fig. 1. Typical configuration of the particles surrounding a vacancy showing the three concentric cubic test regions around the vacancy of edge size 0·45, 0·39, and 0·33 f.c.c. lattice constants.

Table 1. Velocity of jumping particle deduced from the distribution of times to travel a given distance

Time*	$V/V_0 = 1{\cdot}47$†	$V/V_0 = 1{\cdot}3448$
0–1	4_2	6_2
1–2	51_8	47_7
2–3	15_4	34_6
3–4	6_3	5_2
4–5	9_4	4_2
5–10	11_4	4_2
10–20	4_2	0
>20	0	0

*Time for jumping particle to traverse the distance between two cubes of edge 0·45 and 0·33 f.c.c. lattice constants centered at the vacancy. The unit of time corresponds to 1·87 mean collision times, the frequency with which the test was conducted.

†Per cent of the events that required the indicated time to traverse the given distance. The small number indicates the uncertainty in the last significant number.

pending on the criterion chosen to define a successful jump event, there will be an uncertainty of a few collision times as to when a jump occurs, and, even the number of jumps detected will depend on the jump criterion. The extra jumps which would have been detected had the detection region been larger would have consisted of exchange-reexchange pairs, i.e., pairs of jumps in opposite directions which produce no net vacancy or particle displacement. If the detection region were made very small (smaller than the Lennard-Jones-Devonshire free volume per site) another ambiguity arises—a jump might not be detected until long after it had subjectively happened, and a backlog of undetected jumps would be built up which, when finally detected, would be perceived as occurring simultaneously. The choice of the 0·33 detection region size was based on the idea that the reexchange frequency ought to be about one twelfth, the value it would have if the vacancies executed a random walk. The ambiguities with this gate size are small since, as stated above, the number of reexchanges does not depend strongly on gate size and, as Table 1 shows, the uncertainty in the time of the jumps is small since almost all particles that entered the outermost region proceeded within a few collision times all the way to the innermost region. The few cases where a long time was required for the particle to go from the outer to the inner region could involve a recrossing of the outer region before reentry into both the outer and inner region at a later time. The program did not record departure from the outer region explicitly; departure could only be inferred from the later entry of another particle.

These ambiguities do not affect the diffusion coefficient. The ambiguous reexchanges modify the jump frequency, Γ, and in a reciprocal way the Bardeen–Herring correlation factor f—both are somewhat ill-defined, yet their product, the diffusion coefficient, remains well defined. The reciprocal ambiguity of Γ and f may either be accepted, or some convention may be adopted which eliminates it, e.g. by formally eliminating all reexchange pairs from the vacancy trajectory. This formalism is explored in the thesis of C. H. Bennett.

3. RESULTS

Figure 2 illustrates the persistence observed for monovacancies at $V/V_0 = 1{\cdot}47$. The observed jumps are classified according to their direction relative to the preceeding jump. The fraction of jumps in each category ($\cos\theta = -1, -\frac{1}{2}, 0, +\frac{1}{2}$, and $+1$) is plotted as a function of time elapsed since the preceeding jump. $\cos\theta = -1$ corresponds to a reexchange; $+1$ to a jump in the same direction as the preceeding one, If the vacancy executed an ideal random walk, the jumps would be distributed among the five categories in the ratios 1:4:2:4:1. Indeed the distribution follows these ratios for jumps occurring more than about 30 collision times after the previous jump. In Table 2 the same data are given in terms of the actual numbers of jumps observed. Underlining indicates statistically significant deviations from the 1:4:2:4:1 ratios. The results at $V/V_0 = 1{\cdot}42$ are qualitatively in agreement with those displayed in Fig. 2. The data for the $V/V_0 = 1{\cdot}3448$ system although insufficient to permit drawing a graph, agree with those at the other densities in having a significant excess of jumps in the 60° forward ($+\frac{1}{2}$) direction for short time delays between jumps. The last two columns of the table compare the observed distribution of the total number of jumps for a given time delay with the declining exponential distribution which would obtain if the jump times were uncorrelated.

Several deductions about the persistence phenomenon can be made from these data. First of all, a time-decaying enhancement of the jump probability for the $+\frac{1}{2}$ direction at all these densities is noticeable. This is accompanied by a corresponding time-decaying suppression of jumps in the backward (-1) and 120° ($-\frac{1}{2}$) directions. The relaxation

Table 2. Observed numbers of jumps of monovacancies classified by the direction cosines relative to the preceeding jump as a function of the time since the preceeding jump

t^*	cos θ† −1	$-\frac{1}{2}$	0	$\frac{1}{2}$	1	$N(t)$‡	$N_0(t)$§
$V/V_0 = 1{\cdot}47$							
0	—	7	7	49	32	95	26
1·9–7·5	0	5	28	75	20	128	193
9·3–17	3	26	43	65	15	152	202
19–35	29	87	71	117	31	335	302
> 37	66	193	98	228	54	639	626
Total	98	318	247	534	152	1349	1349
$V/V_0 = 1{\cdot}42$							
0	—	0	1	5	3	9	7
1·9–7·5	0	0	5	25	4	34	51
9·3–17	2	3	19	25	5	54	58
19–35	10	29	22	26	7	94	100
> 37	39	165	90	140	36	470	445
Total	51	197	137	221	55	661	661
$V/V_0 = 1{\cdot}3448$							
0	—	0	0	0	0	0	0·3
1·9–35	0	0	1	4	0	5	10·3
37–∞	12	38	24	45	8	127	121·4

Time elapsed since preceeding jump, in mean collision times

†Cosine of the angle between present and preceeding jump directions. If successive jumps were uncorrelated their occurrence would be in the ratio of 1:4:2:4:1 for $\cos\theta = -1, -\frac{1}{2}, 0, \frac{1}{2}, 1$ respectively

‡Total number of jumps occurring in all directions during the given time interval.

§Total number of jumps during interval if jump times had been uncorrelated, $\propto \exp(-t/\langle t\rangle)$, where $\langle t\rangle$, the mean time between jumps is 47·5 at $V/V_0 = 1{\cdot}47$, 92·5 at $V/V_0 = 1{\cdot}42$ and 432 at $V/V_0 = 1{\cdot}3448$

time for both the enhancement and the suppression is about 20 collisions per particle, namely the approximate time for a particle to travel the distance between two adjacent sites moving at thermal velocity.

At $V/V_0 = 1{\cdot}47$ a particularly strong straight-ahead persistence is observed for jumps separated by little or no time delay. This can be explained in terms of nearly simultaneous colinear sliding of two adjacent particles or a row of particles, since a number of simultaneous triple jumps and even one quadruple jump were observed. This phenomenon has previously been observed in perfect crystals near melting. The effect dropped off rapidly with increasing density away from the melting point. Thus, at $V/V_0 = 1{\cdot}47$ the straight-ahead frequency is 10 times larger than that given by the random walk while at $V/V_0 = 1{\cdot}42$ the enhancement is much less significant. Some preliminary short runs were made on an 869-particle, 870-site two-dimensional hard disk system near its thermodynamic melting point ($A/A_0 \approx 1{\cdot}27$). Though only a few jumps occurred, a preference for the forward and 60° directions was also evident (see Table 3).

In studying the persistence in divacancy motion account must be taken of the fact that a divacancy can jump in only eight directions on an f.c.c. lattice without becoming dis-

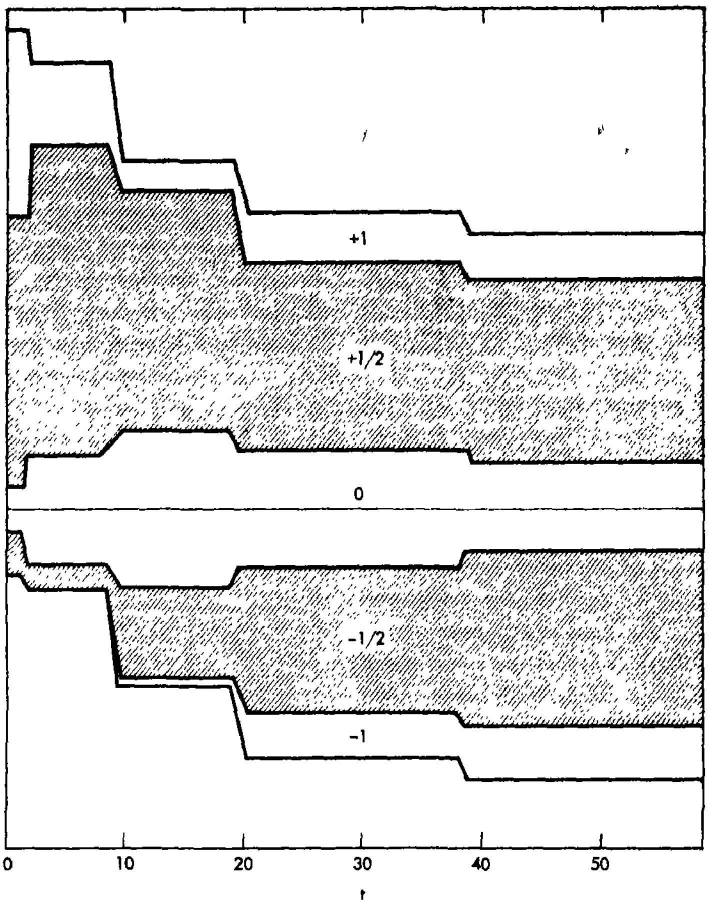

Fig. 2. The fraction of successive jumps having the direction cosines indicated as a function of the time between successive jumps measured in terms of mean collision times at $V/V_0 = 1{\cdot}47$.

Table 3. Distribution of jump directions relative to previous jump for disks near the melting density

	cos θ*			
A/A_0	-1	$-\frac{1}{2}$	$\frac{1}{2}$	1
1·27	0	0	9	2
1·26	2	8	19	11
1·25	0	1	4	3

*If successive jumps were uncorrelated their occurrence would be in the ratio of 1:2:2:1 for $\cos\theta = -1, -\frac{1}{2}, \frac{1}{2}, 1$, respectively.

sociated. Among those eight, four involve successive jumps of the same member(s) of the vacancy having $\cos\theta$ values of $-1s$, $-\frac{1}{2}s$, $0s$, and $\frac{1}{2}s$, while the remaining four with $\cos\theta$ values of $-\frac{1}{2}d$, $0d$, $\frac{1}{2}d$, and $1d$ involve successive jumps of different members (d). All these jumps have equal probability for a divacancy executing a random walk. Table 4, analogous to Table 2, classifies the observed successive jumps according to direction cosine and time delay in order to show the statistically significant deviations from the random walk distribution (underlined).

Table 4. Observed number of jumps of divacancies classified by the direction cosine relative to the previous jump as a function of the time since the preceeding jump

$V/V_0 = 1{\cdot}3448$	cos θ†									
t*	$-1s$	$-\frac{1}{2}s$	$-\frac{1}{2}d$	$0s$	$0d$	$\frac{1}{2}s$	$\frac{1}{2}d$	$1d$	$N(t)$‡	$N_0(t)$§
0–15	0	0	0	0	0	4	1	1	6	9
16–39	1	1	1	0	1	2	0	4	10	11
40–79	2	3	2	1	1	3	3	1	16	11
>80	3	3	1	2	0	1	2	2	14	15
Total	6	7	4	3	2	10	6	8	46	46
av‖	1·04	1·22	0·69	0·52	0·35	1·74	1·04	1·39		
$V/V_0 = 1{\cdot}30$										
0–15	0	0	0	0	0	3	0	0	3	6
16–39	1	1	1	0	1	5	1	2	12	7
40–79	1	1	1	0	0	1	3	1	8	10
>80	1	3	1	4	1	6	2	2	20	20
Total	3	5	3	4	2	15	6	5	43	43
av.‖	0·56	0·93	0·56	0·74	0·37	2·80	1·12	0·94		
$V/V_0 = 1{\cdot}25$										
0–15	0	0	0	0	0	0	0	0		
16–39	0	0	0	0	0	0	1	0		
40–79	0	0	0	0	0	2	0	0		
>80	1	0	0	0	1	1	2	3		
Total	1	0	0	0	1	3	3	3		

*Time elapsed since preceeding jump, in mean collision times.

†Cosine of the angle between present and preceeding jump direction for same vacancy (s) and different vacancy (d). If successive jumps were uncorrelated they would all have equal probability of occurrence.

‡Total number of jumps occurring in all directions during the given time interval.

§Total number of jumps during interval if jump times had been uncorrelated, $\propto \exp(-t/\langle t\rangle)$, where $\langle t\rangle$, the mean collision time between jumps, is 73 for $V/V_0 = 1{\cdot}3448$, 109 for $V/V_0 = 1{\cdot}30$ and 158 for $V/V_0 = 1{\cdot}25$

‖Normalized frequencies averaged over all times.

As with monovacancies an enhanced jump probability in forward directions is observed, particularly for the 60° direction of the same vacancy motion. A corresponding suppression of jumps in other directions follows, which is particularly strong for $0d$. A long time decay is observed for these persistence effects, increasing from about 30 mean collision time at $V/V_0 = 1{\cdot}3448$ to over 100 at $V/V_0 = 1{\cdot}25$ Because of this long time decay, the influence of persistence on divacancy diffusion would increase with increased density, rather than decrease as with monovacancies. While the 20 collision relaxation time for monovacancy persistence can be explained in terms of the necessary local anisotropy of the vacancy environment during the time required to complete a jump at thermal velocity, the relaxation time for divacancy persistence implies that divacancy motion at high density is accompanied by a long-lasting, and hence presumably long-range, fluctuation. The participation of a similar fluctuation in monovacancy movement at high density cannot at present be ruled out, because the monovacancy jump frequency is too low at high densities to allow significant persistence data to be gathered in a reasonable amount of computer time.

Several divacancy runs were carried out at $V/V_0 = 1{\cdot}42$ and 1·45, but the divacancy dissociated so often that most of the jumps occurred while the vacancies were apart. In these runs the main effect on each vacancy of having another vacancy present, was to increase the jump probability in the $+\frac{1}{2}$ direction over what it would have been in a one-vacancy crystal at the same density. This is shown in Table 5, where the distribution in direction cosines for all successive jumps regardless of the time delay are compared for the monovacancy and divacancy systems. For the divacancy system each vacancy was treated as if the other vacancy was not present.

Table 5. Comparison of the direction cosines for monovacancy jumps in monovacancy and divacancy systems

	$\cos\theta$*					
	-1	$-\frac{1}{2}$	0	$\frac{1}{2}$	1	$\langle\cos\theta\rangle$†
107–1·47	$0{\cdot}87_{9}$	$0{\cdot}71_{4}$	$1{\cdot}10_{6}$	$1{\cdot}19_{5}$	$1{\cdot}36_{12}$	$0{\cdot}120_{16}$
107–1·42	$0{\cdot}93_{13}$	$0{\cdot}90_{6}$	$1{\cdot}24_{15}$	$1{\cdot}00_{7}$	$1{\cdot}00_{13}$	$0{\cdot}024_{22}$
254–1·45	0·89	0·71	1·08	1·60	1·33	$0{\cdot}117_{13}$
254–1·42	0·96	0·77	1·14	1·11	1·33	$0{\cdot}086_{22}$

*Weighted average for all jumps. The small numbers indicate the uncertainty in the last significant figures given.

†Average value of the direction cosine.

4. DIFFUSION

If the vacancies executed a random walk their diffusion coefficient would be simply $\Gamma/6a^2$; the product of the mean jump rate and the square of the distance traveled per jump, namely the nearest neighbor lattice spacing. This vacancy diffusion coefficient when multiplied by the vacancy concentration leads to the macroscopic diffusion coefficient, that is the diffusion coefficient for indistinguishable particles. The random walk of vacancies leads, however, to a nonrandom walk of distinguishable particles[4]. This is because successive jumps of the same particle tend to be in opposite directions, because any particle which has just jumped is next to the vacancy located at the site it formerly occupied. The mean direction cosine between successive jumps of the same particle on a f.c.c. lattice has thus been shown[5] not to be zero but $\langle\cos\theta_p\rangle = -0{\cdot}12267$.

For a general non-zero mean value of the direction cosine between the i'th and $(i+k)$'th jump the diffusion coefficient has to be multiplied by a correlation factor given by $f = 1 + 2\sum_{k=1}^{\infty}\langle\cos\theta_{i,i+k}\rangle$. For a random walk in which the diffusing species has an axis of 2 fold symmetry about the jump direction $\langle\cos\theta_{i,i+k}\rangle = \langle\cos\theta_{i,i+1}\rangle^k$ so that $f = 1 + \langle\cos\theta\rangle/1 - \langle\cos\theta\rangle$. Thus for a random vacancy walk the particle diffusion or microscopic self diffusion coefficient is smaller (by $f_p = 0{\cdot}78146$) than the macroscopic diffusion coefficient, $(f_v = 1)$. The former diffusion coefficient can be deduced from N.M.R. measurements or isotopic tracer experiments. For non-dissociating divacancies a random walk leads to a correlation factor of $f_v = \frac{1}{2}$, while for distinguishable particles $f_p = 0{\cdot}458$, as shown in an Appendix.

The effect of persistence is to cause the correlation factors to deviate from their random walk values. As mentioned earlier, the value of the correlation factor is somewhat dependent on what definition one uses for the jump event. However, the product Γf remains well defined, as does the ratio f_p/f_v. Persistence, if memory effects extended over more than successive jumps, could also cause deviations from the average value of the direction cosine of k jumps being equal to the k'th power of the average value of the direction cosine between successive jumps, but no such deviations were observed. Thus f_v was computed from the above formula in the presence of persistence using the time average distribution of $\langle\cos\theta_V\rangle$ as given in Table 5.

To calculate f_p in the presence of persistence, on might first calculate $\langle\cos\theta_p\rangle$ via a difficult summation of probabilities of all vacancy trajectories which return to the origin. However, in the present work a straight forward Monte-Carlo calculation was carried out instead. A vacancy was placed in a 4000-site periodic f.c.c. lattice and a random number generator was employed to choose jumps with frequencies weighted according to the angle made with the previous jump, using the angular distribution data given in Table 5. The net particle displacements were squared and summed for each of about one-hundred 4000-step trajectories, yielding a direct measurement of the particle diffusion coefficient implied by the chosen angular distribution. To check the method, a run was made using equal jump probabilities in all directions; the resulting f_p value was 0·7813 ± 0·0011 in agreement with the accepted value. The values of f_p for monovacancies in the presence of persistence at V/V_0 = 1·47 and 1·42, as well as the values for f_v and f_p/f_v, are compiled in Table 6. It can be seen that persistence depresses the ratio of the microscopic to macroscopic selfdiffusion by about 3 per cent from the random walk value at V/V_0 = 1·42 and by about 18 per cent at V/V_0 = 1·47; the difference at 1·3448 from the random walk value is not significant.

Due to the lack of symmetry about the jump direction for divacancies, the above simplifications in the calculation for f do not hold for either the particle or vacancy trajectories. The value of f_p for divacancies was hence calculated by a Monte-Carlo scheme similar to that used for monovacancies with the jump probabilities in the eight allowed directions weighted according to the observed distribution given in Table 4. The results are given in Table 6. Also given there are the values of f_v for divacancies calculated on the basis of $\langle \cos \theta_{i\ i+k} \rangle$ values obtained for each k separately from a weighted random walk with a one step memory, using a matrix method described in an Appendix. Summation over the first 10 k values converged to an accuracy of one part in 10^6 for f_v.

Persistence increases both the value of f_v and f_p for monovacancies and divacancies. For monovacancies the increase is larger for f_v than for f_p so that the ratio is depressed from the random walk value. For divacancies the ratio may be either raised or lowered from its random walk value. In practice, however, the random walk is a good model for monovacancy motion and hence diffusion for a hard sphere crystal at the melting point and higher densities, since divacancy motion is relatively unimportant[6] and monovacancy correlation factors have nearly the random value. For real materials persistence effects might be important near the melting point if they have relatively high vacancy jump frequencies, for example f.c.c. gold and particularly many b.c.c. substances such as sodium. Persistence might also be detected in materials with significant divacancy contributions to diffusion, e.g. copper[7,8], even if monovacancies moved without persistence.

The mass-dependence of the tracer diffusion coefficient has often been measured in hopes of ascertaining the diffusion mechanism[9], by use of the relation[10, 11]

$$((D_\alpha/D_\beta)-1)/((m_\alpha/m_\beta)^{-1/2}-1) = f.\,\Delta K,$$

Table 6. Correlation factor for vacancy and particle diffusion

	Monovacancies			Divacancies		
	no*	V/V_0 = 1·47	1·42	no	1·3448	1·30
f_p	0·7815	$0{\cdot}820_2$	$0{\cdot}798_1$	$0{\cdot}458_1$	$0{\cdot}515_2$	$0{\cdot}626_4$
f_v	1·000	1·273	1·050	0·500	0·587	0·637
f_p/f_v	0·7815	$0{\cdot}644_8$	$0{\cdot}760_1$	$0{\cdot}916_2$	$0{\cdot}878_3$	$0{\cdot}984_8$

*No persistence. The small numbers indicate the uncertainty in the last significant figure given.

where D_α and D_β are the diffusion coefficients of two tracer isotopes, m_α and m_β are their respective masses, and f is taken to be the random walk microscopic correlation factor (e.g. 0·7815 for monovacancies, and 0·458 for divacancies on the f.c.c. lattice). The factor ΔK, whose value may be between zero and one, was introduced[12, 13] to take account of collective motion at the time of the jump, which would cause the effective mass of the jumping atom to be between its true mass and that of the host atoms. Persistence, a manifestation of collective motion occurring after the jump, complicates the interpretation of isotope effect experiments by suggesting that the isotope effect quotient may be either greater or less than the random walk value of f. A quantitative treatment of the effect of persistence on the isotope effect will not be attempted here.

The observed persistence is also a clue to the kind of collective motion involved in particle jumps. The zero-delay straight-ahead persistence observed for monovacancies at low density suggests that the collective motion accompanying the jump event is a relatively long-wavelength longitudinal wave, involving a concerted colinear sliding in the jump direction of the jumping atom and a row of atoms behind it, which are therefore predisposed to jump in the same direction. The 60-degree persistence observed at higher density suggests a shorter-wavelength mode with some transverse character, since consecutive jumps take place in different directions.

Acknowledgement – We wish to thank Professor D. Turnbull and A. Bienenstock for constant advice, encouragement and inspiration, and Mary Ann Mansigh for her skillful performance of the intricate programming. The project was partially supported through N.S.F. contract GP2174 and GP7022. The work was also carried out under the auspices of the U.S. Atomic Energy Commission.

REFERENCES

1. BARDEEN J. and HERRING C., *Imperfections in Nearly Perfect Crystals*, J. Wiley, New York (1952).
2. BENNETT C. H. and ALDER B. J., *Solid State Commun.* **6**, 785 (1968).
3. ALDER B. J., HOOVER W. G. and YOUNG D. A., *J. Chem. Phys.* **49**, 3688 (1968).
4. BARDEEN J. and HERRING C., *Atom Movements, Am. Soc. Metals*, Cleveland (1951).
5. COMPAAN K. and HAVEN Y., *Trans. Faraday Soc.* **52**, 786 (1956).
6. BENNETT C. H. and ALDER B. J., to be published.
7. ROTHMAN S. J. and PETERSON N. L., *Phys. Status Solidi* **35**, 305 (1969).
8. MEHRER H. and SEEGER A., *Phys. Status Solidi* **35**, 313 (1969).
9. PETERSON N. L., *Solid State Physics* (Edited by F. Seitz and D. Turnbull). Academic Press, New York (1968).
10. SCHOEN A. H., *Phys. Rev. Lett.* **1**, 138 (1958).
11. THARMALINGAM K. and LIDIARD A. B., *Phil. Mag.* **4**, 899 (1959).
12. MULLEN J. G., *Phys. Rev.* **121**, 1649 (1961).
13. LeCLAIRE A. D., *Phil. Mag.* **14**, 1271 (1966).
14. HOWARD R. E., *Phys. Rev.* **144**, 650 (1966).

APPENDIX

The jump of a vacancy in the several allowed directions has been shown to depend on the vacancy's previous history. The simplest model for such a correlated walk is one in which the vacancy 'remembers' only one previous step. This model has been found to give an adequate statistical description of the monovacancy and divacancy trajectories observed in the dynamics experiments. This section describes in detail how microscopic and macroscopic correlation factors may be calculated for monovacancy and divacancy walks having a one-step memory.

Microscopic correlation factor

Microscopic correlation factors (i.e. for diffusion of distinguishable particles) were calculated by a Monte-Carlo method. A defect (monovacancy or divacancy) was introduced into a periodic crystal of several thousand particles and allowed to make jumps, the direction for each jump being chosen from a weighted probability distribution depending on the previous jump direction. The implied particle displacements were monitored on an infinite lattice consisting of the original lattice plus all its periodic images. After several thousand jumps, the net displacements of the particles were squared and summed, and then divided by the number of jumps to get an estimate of the correlation factor, which is defined as this ratio in the limit of an infinite number of vacancy jumps on an infinite lattice. Too small a lattice and too few jumps both lead to overestimation of the correlation factor; the former because in a periodic lattice of length L, the vacancy, once it has moved a distance $L/2$ from a site, has effectively escaped from that site and is equally likely to return from any direction; the latter because even on a finite lattice the available return paths cannot be adequately sampled unless the vacancy makes more than about L^3 steps.

Trajectories of 4000 steps on a 4000-site lattice appeared adequate to give the monovacancy correlation factor with about 0·1 per cent accuracy. As an example, for a random walk, the average value of f_p over several hundred such trajectories was found to be $0{\cdot}7813 \pm 0{\cdot}0011$, in agreement with the accepted value[5], 0·78146. The divacancy correlation factor, on the other hand, was not known very accurately even in the random walk case[14]. Hence, a number of divacancy runs, on different sized lattices, were made using equal jump probabilities in all directions with results listed in Table 7. For $N \gg 4000$ the finite-lattice error is evidently negligible compared to the statistical uncertainty. The best value for the divacancy correlation factor may be taken as 0·458 ± 0·001; this is in agreement with the previous value of 0·475 ± 0·024.

The microscopic correlation factors f_p listed in Table 6 for nonrandom walks were obtained by the above procedure from the consecutive jump correlations observed in the monovacancy and divacancy dynamics runs (see Tables 4 and 5). Each value is an average of 20 or more trajectories of at least 4000 steps on a lattice of at least 4000 sites.

Table 7. Monte-Carlo calculations of the microscopic correlation factor for a divacancy random walk on an f.c.c. lattice

Number of sites	Number of steps per trajectory	Number of trajectories averaged	Correlation factor f_p
32	999	135	$0{\cdot}494_7$
108	1001	312	$0{\cdot}467_1$
108	1728	285	$0{\cdot}468_1$
256	1002	312	$0{\cdot}462_2$
256	3999	132	$0{\cdot}461_2$
500	8000	245	$0{\cdot}4595_{12}$
1372	10976	61	$0{\cdot}4590_{17}$
4000	16000	41	$0{\cdot}4576_{13}$
4000	32000	20	$0{\cdot}4580_{18}$
4000	64000	10	$0{\cdot}4560_{18}$
13500	8000	10	$0{\cdot}4592_{15}$
	14000	102	$0{\cdot}4583_8$
	108000	60	$0{\cdot}4581_5$

A number of other Monte-Carlo runs were made to explore the effect on the correlation factor of an arbitrary variation in the jump probability distribution about the isotropic distribution. For monovacancy motion with a one-step memory, the correlation has four variational degrees of freedom, since the probabilities in the $-1, -\frac{1}{2}, 0, +\frac{1}{2}$, and $+1$ directions are independently variable, subject to the constraint that they sum to unity. Since a one-step memory cannot distinguish among, say, the four $+\frac{1}{2}$ jumps, they must remain equiprobable. Table 8 shows the response of the monovacancy microscopic correlation factor to four different orthogonal perturbations of the consecutive-jump correlation. The correlation factor depends mainly on the probabilities in the -1 and $-\frac{1}{2}$ directions. Unexpectedly, f_p is decreased slightly by a large shift of probability from the $+\frac{1}{2}$ to the $+1$ direction, even though this perturbation would increase f_v (by increasing $\langle\cos\theta_i\rangle$). The last column in Table 8 gives the response coefficient, i.e. the ratio of the change in f_p to the magnitude of the perturbation, λ. For small λ's, the response to each perturbation should be linear, and thus the set of response coefficients would enable one to calculate f_p for an arbitrary weakly-correlated walk with one-step memory. In spite of the obvious nonlinearity of the response to the perturbations in the last 2 cases given in Table 8, the linear approximation gave values for f_p within 0·01 of the correct ones using the jump probabilities observed in the dynamics runs.

Table 9 shows the response of the divacancy values for f_p to seven orthogonal perturbations of the consecutive-jump correlation. As for monovacancies, the strongest response is to alteration of the simple reexchange frequency. Response was fairly linear to those perturbations for which linearity was tested, although it might not be for the others. For divacancies also, the linear response hypothesis gave values within 0·01 of the correlation factors directly calculated on the basis of the dynamics data.

Table 8. Response of the monovacancy microscopic correlation factor to four perturbations from an isotropic distribution of jump probabilities

		$\cos\theta_p$					
-1	$-\frac{1}{2}$	0	$\frac{1}{2}$	1	λ	f_p	$(f_p-0{\cdot}7815)/\lambda$
1	1	1	1	1	0	0·78146	0
$(1-\lambda)$	$(1+\frac{1}{11}\lambda)$	$(1+\frac{1}{11}\lambda)$	$(1+\frac{1}{11}\lambda)$	$(1+\frac{1}{11}\lambda)$	$+1$	$0{\cdot}938_2$	$+0{\cdot}156_2$
					$\frac{1}{3}$	$0{\cdot}833_2$	$+0{\cdot}154_6$
1	$(1-\lambda)$	$(1+\frac{4}{7}\lambda)$	$(1+\frac{4}{7}\lambda)$	$(1+\frac{4}{7}\lambda)$	$+1$	$0{\cdot}819_3$	$+0{\cdot}038_2$
					$+\frac{1}{2}$	$0{\cdot}807_2$	$+0{\cdot}055_4$
1	1	$(1-\lambda)$	$(1+\frac{2}{5}\lambda)$	$(1+\frac{2}{5}\lambda)$	$+1$	$0{\cdot}782_1$	$+0{\cdot}001_1$
					-1	$0{\cdot}770_2$	$+0{\cdot}012_2$
1	1	1	$(1-\lambda)$	$(1+4\lambda)$	$+1$	$0{\cdot}762_2$	$-0{\cdot}014_2$
					$+\frac{1}{2}$	$0{\cdot}780_2$	$-0{\cdot}004_3$

Macroscopic correlation factor

It is a trivial problem to calculate the correlation factor

Table 9. Response of the divacancy microscopic correlation factor to seven perturbations from an isotropic distribution of jump probabilities

			cos θ_r					
	-1	$-\frac{1}{2}$	0	$\frac{1}{2}$	1	λ	f_p	$(f_p-0\cdot458)/\lambda$
S:	1	1	1	1	—	0	$0\cdot458_1$	0
D:	—	1	1	1	1			
S:	$(1-\lambda)$	$\left(1+\frac{\lambda}{3}\right)$	$\left(1+\frac{\lambda}{3}\right)$	$\left(1+\frac{\lambda}{3}\right)$	—	$1\cdot0$	$0\cdot625_2$	$0\cdot167_3$
D:	—	1	1	1	1	$0\cdot6$	$0\cdot552_2$	$0\cdot157_4$
S:	1	$(1-\lambda)$	$\left(1+\frac{\lambda}{2}\right)$	$\left(1+\frac{\lambda}{2}\right)$	—	$1\cdot0$	$0\cdot496_2$	$0\cdot038_3$
D:	—	1	1	1	1			
S:	1	1	$(1-\lambda)$	$(1+\lambda)$	—	$1\cdot0$	$0\cdot471_3$	$0\cdot013_3$
D:	—	1	1	1	1			
S:	1	1	1	1	—	$1\cdot0$	$0\cdot551_3$	$0\cdot093_3$
D:	—	$(1-\lambda)$	$\left(1+\frac{\lambda}{3}\right)$	$\left(1+\frac{\lambda}{3}\right)$	$\left(1+\frac{\lambda}{3}\right)$			
S	1	1	1	1	—	$1\cdot0$	$0\cdot504_2$	$0\cdot046_3$
D:	—	1	$(1-\lambda)$	$\left(1+\frac{\lambda}{2}\right)$	$\left(1+\frac{\lambda}{2}\right)$			
S.	1	1	1	1	—	$1\cdot0$	$0\cdot473_3$	$0\cdot015_3$
D:	—	1	1	$(1-\lambda)$	$(1+\lambda)$			
S:		all $(1-\lambda/4)$				-2	$0\cdot4086_{25}$	$0\cdot025_1$
D:		all $(1+\lambda/4)$				-1	$0\cdot4384_{20}$	$0\cdot020_3$
						$+1\cdot2$	$0\cdot4768_{22}$	$0\cdot016_3$
						$+2\cdot4$	$0\cdot4928_{24}$	$0\cdot014_1$

f_r for monovacancies moving with one-step memory from the average cosines, as explained in the main text. For a divacancy walk with one step memory, each of the terms in the summation must be calculated separately:

$$2f_r = 1 + 2\sum_{k=1}^{\infty} \langle \cos_{i,i+k} \rangle .$$

This is done for a given set of probabilities $\{p(\sigma)\}$ for the eight allowed types of divacancy jumps by the following method. The divacancy is represented in a moving co-ordinate system (ξ, η, ζ) such that the vector connecting the two (distinguishable) members of the vacancy is always $(-\sqrt{\frac{1}{2}}, \sqrt{\frac{1}{2}}, 0)$ and the most recent jump vector is $(\sqrt{\frac{1}{2}}, 0, \sqrt{\frac{1}{2}})$. As the divacancy moves, the (ξ, η, ζ) co-ordinate system may change from right-handed to left-handed, but at any instant each of its axes will be either parallel or antiparallel to one of the cubic crystal axes. Each of the eight allowed jumps, σ, may be represented by a simple matrix $M(\sigma)$ relating the (ξ, η, ζ) coordinate system after the jump to that before the jump; the matrices are given in Table 10.

If the divacancy makes $k+1$ consecutive jumps, of types $\sigma_1, \sigma_2 \ldots \sigma_{k+1}$, respectively, then the cosine of the angle between the first and last jumps will be

$$\cos\theta_{1,k+1} = (\sqrt{\tfrac{1}{2}}, 0, \sqrt{\tfrac{1}{2}})M(\sigma_1)M(\sigma_2)\ldots M(\sigma_k)\begin{pmatrix}\sqrt{\frac{1}{2}}\\ 0\\ \sqrt{\frac{1}{2}}\end{pmatrix}.$$

Table 10. Matrices used in the calculation of the divacancy macroscopic correlation factor

$-1S$	$-\frac{1}{2}S$	$0S$	$+\frac{1}{2}S$
$\begin{pmatrix}0&0&-1\\0&1&0\\-1&0&0\end{pmatrix}$	$\begin{pmatrix}0&0&-1\\-1&0&0\\0&1&0\end{pmatrix}$	$\begin{pmatrix}0&0&1\\0&1&0\\-1&0&0\end{pmatrix}$	$\begin{pmatrix}0&0&1\\-1&0&0\\0&1&0\end{pmatrix}$
$-\frac{1}{2}D$	$0D$	$+\frac{1}{2}D$	$+1D$
$\begin{pmatrix}0&0&-1\\1&0&0\\0&-1&0\end{pmatrix}$	$\begin{pmatrix}0&0&-1\\0&-1&0\\1&0&0\end{pmatrix}$	$\begin{pmatrix}0&0&1\\1&0&0\\0&-1&0\end{pmatrix}$	$\begin{pmatrix}0&0&1\\0&-1&0\\1&0&0\end{pmatrix}$

where the product of M-matrices performs the appropriate transformation between the initial and final coordinate systems. The average cosine for all k-step trajectories will be

$$\langle\cos\theta_{1,k+1}\rangle = (\sqrt{\tfrac{1}{2}}, 0, \sqrt{\tfrac{1}{2}})\Big[\sum_{\sigma_1} p(\sigma_1) \sum_{\sigma_2} p(\sigma_2) \ldots \sum_{\sigma_k} p(\sigma_k)\Big](M(\sigma_1)M(\sigma_2)\ldots M(\sigma_k))\begin{pmatrix}\sqrt{\tfrac{1}{2}}\\ 0\\ \sqrt{\tfrac{1}{2}}\end{pmatrix}.$$

Although the M-matrices don't commute with each other they do commute with the scalar probability factors, hence the above reduces to

$$\langle\cos\theta_{1,k+1}\rangle = (\sqrt{\tfrac{1}{2}}, 0, \sqrt{\tfrac{1}{2}})\Big[\sum_{\sigma_1} p(\sigma_1)M(\sigma_1) \sum_{\sigma_2} p(\sigma_2)M(\sigma_2) \ldots \sum_{\sigma k} p(\sigma_k)M(\sigma_k)\Big]\begin{pmatrix}\sqrt{\tfrac{1}{2}}\\ 0\\ \sqrt{\tfrac{1}{2}}\end{pmatrix}$$

$$= (\sqrt{2}, 0, \sqrt{2})\Big[\sum_{\sigma} p(\sigma)M(\sigma)\Big]^k\begin{pmatrix}\sqrt{2}\\ 0\\ \sqrt{2}\end{pmatrix},$$

where $\sum_{\sigma} p(\sigma)M(\sigma)$ is simply a weighted sum of the eight matrices in Table 8. If the $p(\sigma)$ are all equal, the sum is zero and f_M assumes its no-memory value of $\tfrac{1}{2}$. This method was used to calculate the divacancy macroscopic correlation factors exhibited in Table 6.

J. Phys. Chem. Solids Pergamon Press 1971. Vol. 32, pp. 2123–2128. Printed in Great Britain.

ISOLATED SINGLE VACANCY IN DIAMOND–II. JAHN–TELLER EFFECT

F. P. LARKINS*
Mathematical Institute, Oxford, England

(*Received* 23 *July* 1970)

Abstract—The Jahn-Teller splittings for the lowest degenerate electronic states of the single isolated vacancy in diamond in the single positive, neutral and negatively ionized charged states have been calculated to first order. The magnitude of the linear coupling force terms is largely independent of the choice of atomic functions to represent the orbitals on the carbon atoms in the two cases considered, but it is sensitive to the extent of configuration interaction between electronic states of the same symmetry. The results demonstrate that it is necessary to include terms involving the derivatives of the overlap integrals in any such calculations. In some cases the predicted splittings are very large. Reasons for including higher-order terms in a more detailed calculation are discussed.

1. INTRODUCTION

THE INVESTIGATIONS of the electronic behaviour of the various charge states of the diamond vacancy by a molecular orbital approach which has been reported[1], hereafter referred to as Paper I, predicted that the ground and low-lying excited states of the centres are in some cases orbitally degenerate. Jahn and Teller[2] have shown that with the exception of linear molecules a geometrical configuration in which the electronic state is orbitally degenerate cannot be the stable state of the system. There is a nuclear configuration of lower symmetry in which the system has a lower energy. In this paper we shall be concerned with the static effect and calculate the magnitude of the Jahn–Teller splittings and the associated distortions of the nuclear framework for the defect centres investigated in Paper I. A recent paper by Hagston[3] on the dynamical Jahn–Teller effect for defects in diamond is unsatisfactory because of the incorrect formulation of the adiabatic approximation. The many-electron vibronic function has been expressed in terms of a product of one electron vibronic functions instead of a product of a many-electron electronic and vibrational function. As a consequence, cross-terms in the wave function are ignored.

The general theory developed by Van Vleck[4] and Öpik and Pryce[5] has previously been applied to the vacancy problem in diamond by Friedel *et al.*[6]. The perturbation-type approach incorporates a rigid-atom model proposed by Lidiard and Stoneham[7] which allows the atomic orbitals which make up the l.c.a.o. molecular function to move rigidly with the nucleus and core electrons on the atoms nearest the vacancy. There are however serious limitations in the numerical calculations reported by Friedel *et al.* These workers have neglected the overlap integral between hybrid orbitals on the atoms neighbouring the vacancy. This overlap integral, denoted S_{ab}, has a value of 0·165 or 0·242 depending upon whether Slater or Clementi-type atomic functions are chosen to represent the $2s$ and $2p$ orbitals on these atoms. Because of the neglect of the overlap the expressions for the derivatives of the molecular integrals required in the evaluation of the Jahn–Teller forces do not contain terms involving the derivative of the overlap integrals. In addition normalisation constants for the single-electron molecular orbitals will be considerably in error. It has also been assumed that the eigenvectors for the symmetry states from the various configurations contributing to a particular electronic level may be obtained from a molecular orbital calculation using the unmodified value for the one-centre Coulomb Integral[8]. We believe that these assumptions are not justified and therefore reduce the validity of the calculation.

---

*Present Address: Chemistry Department, Monash University, Clayton, Victoria 3168, Australia.

The calculations reported here investigate the use of the first-order perturbation theory approach coupled with the rigid-atom method to determine the Jahn–Teller splittings of the electronic levels for the various centres based upon the results of Paper I.

2. THEORETICAL CONSIDERATIONS

A detailed account of the theory of the static Jahn–Teller effect has previously been given[4–6]. All spin and spin-orbit coupling effects are neglected in the present treatment. It is also assumed that the electronic levels are sufficiently well separated from one another that interlevel coupling effects may be ignored. These effects have recently been discussed in general terms[9]. The model assumes that only the nearest neighbours to the vacancy contribute to its interaction with lattice distortions. The displacements of the four atoms nearest the defect may be described in terms of 12 normal co-ordinates[10]. In the first-order theory we are concerned only with the coupling between the degenerate electronic states and the normal modes of E and T_2 symmetry. Any coupling of the electronic states to the symmetric mode is a second-order contribution and therefore neglected in this treatment. A tetragonal distortion of the system results from coupling with the Q_ϵ and Q_θ, E modes, while interaction with the Q_ξ, Q_η and Q_ζ, T_2 modes causes a trigonal distortion of the system.

For a two-fold degenerate E level comprising the two states $|\theta\rangle$ and $|\epsilon\rangle$ which transform like $2x^2-y^2-z^2$ and y^2-z^2 respectively and are degenerate in the undistorted environment with electronic energy E^0, the only possible distortion of the nuclear framework will result from coupling with the E modes. The vibronic Hamiltonian for the E manifold may be written as:

$$\mathscr{H}_E = \left[E^0 + \sum_\alpha \left\{-\frac{h^2}{2M}\frac{\partial^2}{\partial Q_\alpha^2} + \frac{1}{2}M\omega_\alpha Q_\alpha^2\right\}\right] \times \begin{pmatrix}1 & 0\\ 0 & 1\end{pmatrix} + I_{EE}Q_\theta\begin{pmatrix}-1 & 0\\ 0 & 1\end{pmatrix} + I_{EE}Q_\epsilon\begin{pmatrix}0 & 1\\ 1 & 0\end{pmatrix}.$$

The first term gives the electronic energy for zero Q_α, the nuclear kinetic energy and the quasi-elastic energy term. M is the mass of the carbon atom and ω_α is the response frequency for the α mode. The latter terms in the expression which depend on I_{EE} are responsible for the Jahn–Teller effect. Within the rigid-atom approximation

$$I_{EE} = \left(\frac{\partial}{\partial Q_\theta}\langle\theta|H|\theta\rangle\right)_0.$$

For finite values of I_{EE} the ground-state energy is reduced by

$$\Delta E_{EE} = \frac{I_{EE}^2}{2M\omega_E^2}.$$

The new equilibrium configuration cannot be determined unambiguously without including higher-order terms in the Hamiltonian. Öpik and Pryce[5] have shown that for a crystal with cubic symmetry there are three possible equivalent tetragonal distortions which represent the energy minima. The configurations for these distortions have symmetry axes along the x, y and z directions. For a tetragonal distortion along the x axis Q_ϵ is zero and

$$|Q_\theta| = |I_{EE}|/M\omega_E^2.$$

The sign of Q_θ can only be determined by a detailed knowledge of the higher order terms. Equivalent results hold for the y and z directions.

For the three-fold degenerate state the results are formally the same irrespective of whether the state has T_1 or T_2 symmetry. When all the Q_α modes are zero the three electronic states $|\xi\rangle$, $|\eta\rangle$ and $|\zeta\rangle$ belonging to the T representation are degenerate. These states transform like x, y, z or yz, zx, xy. The vibronic Hamiltonian for such a state is more complicated than previously because there are terms linear in Q_ϵ, Q_θ, Q_ξ, Q_η and Q_ζ. The vibronic Hamiltonian for the T_1 manifold may be written as follows:

$$\mathscr{H}_T=\left[E^0+\sum_\alpha\left\{\frac{h^2}{2M}\frac{\partial^2}{\partial Q_\alpha^2}+\frac{1}{2}M\omega_\alpha^2Q_\alpha^2\right\}\right]$$

$$\times\begin{pmatrix}1&0&0\\0&1&0\\0&0&1\end{pmatrix}+\frac{I_{TE}}{6}\begin{pmatrix}2Q_\theta&\cdot&\cdot\\\cdot&-Q_\theta+\sqrt{3}Q_\epsilon&\cdot\\\cdot&\cdot&-Q_\theta-\sqrt{3}Q_\epsilon\end{pmatrix}$$

$$+I_{TT}\begin{pmatrix}\cdot&Q_\zeta&Q_\eta\\Q_\zeta&\cdot&Q_\xi\\Q_\eta&Q_\xi&\cdot\end{pmatrix}.$$

I_{TE} and I_{TT} may be defined as

$$I_{TE}=2\sqrt{3}\left(\frac{\partial}{\partial Q_\epsilon}\langle\eta|H|\eta\rangle\right)_0$$

$$I_{TT}=\left(\frac{\partial}{\partial Q_\xi}\langle\eta|H|\zeta\rangle\right)_0.$$

The terms involving I_{TE} and I_{TT} are responsible for the Jahn–Teller effect. The configuration which now results in an energy minimum for the system may either be tetragonally or trigonally distorted. The energy reduction for the tetragonal distortion is

$$\Delta E_{TE}=\frac{I}{9}I_{TE}^2/2M\omega_E^2$$

while for a trigonal distortion the energy lowering is given by

$$\Delta E_{TT}=\frac{4}{3}I_{TT}^2/2M\omega_T^2.$$

The stable configuration for the distorted system is determined by the larger of ΔE_{TE} and ΔE_{TT}. For intralevel coupling only, mixed distortions do not occur[9]. For a trigonally distorted system there are four equivalent configurations with symmetry axes along the $\langle\bar{1},1,1\rangle$, $\langle1,\bar{1},1\rangle$, $\langle1,1,\bar{1}\rangle$ and $\langle\bar{1},\bar{1},\bar{1}\rangle$ directions. The equilibrium distortion configuration for the various equivalent symmetry directions are as defined in Table 1 of Ref.[5] with Q_1, Q_2, Q_4, Q_5 and Q_6 replaced by Q_θ, Q_ϵ, Q_ξ, Q_η and Q_ζ respectively. The distortions considered in this study are defined in terms of q_E and q_T where

$$q_E=I_{TE}/12M\omega_E^2=1/12\,q_1$$

$$q_T=2I_{TT}3M\omega_T^2=2/3\,q_3.$$

3. RESULTS

On the basis of the results shown in Figs. 2, 3 and 4 of Paper I the Jahn–Teller splittings for the following degenerate levels have been determined

V^+ : ${}^2T_2$

V^0 : ${}^1E, {}^3T_1, {}^1T_2$

V^- : ${}^2T_1, {}^2T_2, {}^2E$.

The I_{EE}, I_{TE} and I_{TT} terms necessary for the calculations are evaluated by a similar method and numerical procedure to that outlined in Paper I for the F_α terms. The values for the derivatives of the molecular integrals necessary for the determination of the trigonal force terms are given in Table 1 for the two alternative choices of atomic functions from Paper I. The derivatives of the molecular integrals used to evaluate the tetragonal force terms are listed in Table 2. The expressions for the derivatives, shown in Table 2, include terms involving the derivative of the overlap integral. In particular, because of the inclusion of these terms the derivative

$$\left(\frac{\partial}{\partial Q_\epsilon}\langle y|H^0|y\rangle\right)_0$$

Table 1. *Derivatives of molecular integrals for trigonal distortion terms*

$\frac{d}{dQ_t}$ (integral)	Clementi functions	Slater functions
$\langle y\|H^0\|z\rangle$ $\langle v\|H^0\|x\rangle$	−12·8235* −16·7565	−11·7702 −16·7369
$\langle vv\|\frac{1}{r_{12}}\|yz\rangle$	1·1817	1·1210
$\langle vx\|\frac{1}{r_{12}}\|yy\rangle$	−1·0882	−1·0749
$\langle vv\|\frac{1}{r_{12}}\|vx\rangle$	4·0695	4·2085
$\langle vy\|\frac{1}{r_{12}}\|xy\rangle$	2·4284	2·5462
$\langle xy\|\frac{1}{r_{12}}\|xz\rangle$	2·3005	1·7870
$\langle vx\|\frac{1}{r_{12}}\|xx\rangle$	5·1366	4·9964
$\langle yy\|\frac{1}{r_{12}}\|yz\rangle$	3·8278	3·3737
$\langle vy\|\frac{1}{r_{12}}\|vz\rangle$	2·2648	1·8086
$\langle xx\|\frac{1}{r_{12}}\|yz\rangle$	1·0021	1·0306

*All derivatives in eV/A.

depends strongly upon the value chosen for the self-penetration integral P as shown in the table.

The values of the linear response frequencies calculated by Larkins and Stoneham[10] allowing for complete relaxation of all the atoms in the crystal, i.e. adiabatic approximation, are $\omega_E = 1·13 . 10^{14}$ rad/sec and $\omega_T = 0·98 . 10^4$ rad/sec. These values are smaller than the values predicted previously using a restricted relaxation model[7], i.e. sudden approximation, where $\omega_E = 2·02 . 10^4$ rad/sec and $\omega_T = 1·43 . 10^{14}$ rad/sec. In this study, as in Paper I, we use the latter values to include some contribution from higher order terms; however, the required values for the Jahn–Teller energy and distortion terms using the estimates from Ref. [10] may be readily calculated from the results in Tables 3–5 by multiplying the tetragonal terms by 3·20 and the trigonal ones by 2·13.

Using the information given in Tables 1 and 2 to calculate the I terms and the effective frequencies the Jahn–Teller splittings and the corresponding distortions for the various levels may be determined. The results for the degenerate electronic levels of the V^+, V^0 and V^- centres considered are presented in Tables 3, 4 and 5 respectively.

Table 2. *Derivatives of molecular integrals for tetragonal distortion terms*

$\frac{d}{dQ_\epsilon}$ (integral)	Clementi functions	Slater functions
$\langle y\|H^0\|y\rangle$	−8·1787* −3·8432†	−7·4022 −4·2221
$\langle vy\|\frac{1}{r_{12}}\|vy\rangle$	0·4648	0·5070
$\langle vv\|\frac{1}{r_{12}}\|yy\rangle$	1·2779	1·3758
$\langle vx\|\frac{1}{r_{12}}\|vz\rangle$	−0·8300	−0·8875
$\langle xv\|\frac{1}{r_{12}}\|xv\rangle$	0·7279	0·6415
$\langle vy\|\frac{1}{r_{12}}\|yy\rangle$	1·9287	1·7287
$\langle xx\|\frac{1}{r_{12}}\|yy\rangle$	−0·1560	−0·2777

*Case 1.
†Case 2.

4. DISCUSSION

Several general features emerge which underlie all the calculations. From the tables it is apparent that the magnitude of the splitting is not very sensitive to whether Slater or Clementi functions are chosen to represent the wave functions for the 2s and 2p orbitals on the carbon atoms. This finding is contrary to what had previously been conjectured[11]. The uncertainty in the calculations, as represented by the values for case 1 and case 2 with a particular basis set, is much greater than the difference due to an alternative choice of functions. It is also clear that the magnitude of the effect depends upon the extent of configuration interaction. This is most easily seen from the variation of the trigonal force terms, because here the values of the derivatives of the molecular integrals are the same in both cases.

For the tetragonal cases the variation from case 1 to case 2 is much larger. This is due partly to the change in the values of the eigenvectors, but more importantly, to changes in the value of the one-electron term which arise through inclusion of terms involving the derivative of the overlap integral, as discussed in the previous section. In Paper I it was shown that delocalisation of electronic charge away from the vacancy does not cause changes in the relative ordering of the lowest electronic levels; however, this effect does result in a change in the extent of configurational mixing which will effect the values obtained for the Jahn-Teller splittings, especially for the trigonally distorted case. This effect remains to be fully investigated once some of the centres have been positively identified.

Unfortunately, no definite experimental results are yet available for the magnitude of the Jahn-Teller effect for the electronic levels of the single vacancy in diamond. To extrapolate from the results on silicon is rather unsatisfactory, because of the different response characteristics of the two lattices [10]; therefore, such a comparison has not been made.

For the lowest $^2T_2$ level of the V^+ centre the value predicted for the Jahn-Teller splitting is unreasonably large. The results, which show very good agreement between the values obtained using Slater and Clementi functions, favour a trigonal distortion of the lattice in order to remove the orbital degeneracy. This result is different from that obtained by Friedel *et al.*[6], for in their study a small tetragonal distortion of the nuclear framework was favoured for the $^2T_2$ level.

Table 3. Jahn-Teller terms for positive vacancy: $^2T_2$ level

Function	I_{TE} eV/Å	ΔE_{TE} eV	I_{TT} eV/Å	ΔE_{TT} eV
Slater: Case 1	−23·28	0·50	−11·50	2·36
Slater: Case 2	−10·45	0·10	−12·25	2·67
Clementi: Case 1	−26·37	0·63	−11·52	2·36
Clementi: Case 2	−8·43	0·06	−12·43	2·76

Values of q_E and q_T may be determined from the relationships given in the footnote of Table 4.

The results for the lowest levels of the neutral vacancy are given in Table 4. All the calculations predict that the Jahn-Teller splitting of the $^3T_1$ level results from a trigonal distortion of the vacancy system. Again the calculated magnitude of the splitting is very large, especially in the case 1 approximation. We are inclined to think that such a large effect would be most unlikely for the diamond system. For the lowest ^1E level the Jahn-Teller splitting is less than for the $^3T_1$ level such that if the undistorted electronic levels were corrected by these splittings the $^3T_1$ level would be predicted as the ground state level in all four cases con-

Table 4. Jahn-Teller terms for neutral vacancy: $^3T_1$, $^1T_2$, ^1E levels

Function	I_{TE} eV/Å	ΔE_{TE} eV	I_{TT} eV/Å	ΔE_{TT} eV
1. $^3T_1$ Level				
Slater: Case 1	21·58	0·43	8·64	1·34
Slater: Case 2	8·42	0·06	6·86	0·84
Clementi: Case 1	24·67	0·56	8·37	1·25
Clementi: Case 2	6·26	0·04	5·29	0·50
2. $^1T_2$ Level				
Slater: Case 1	21·44	0·42	−5·18	0·48
Slater: Case 2	8·91	0·07	−4·20	0·31
Clementi: Case 1	24·00	0·52	−5·03	0·46
Clementi: Case 2	6·83	0·05	−3·39	0·21
	I_{EE} eV/Å	ΔE_{EE} eV		
3. ^1E Level				
Slater: Case 1	6·96	0·41		
Slater: Case 2	2·82	0·06		
Clementi: Case 1	7·92	0·51		
Clementi: Case 2	2·09	0·04		

Values of q_E, q_T and $|Q_\theta|$ may be determined from the following relationships: $q_E = 3\Delta E_{TE}/2I_{TE}$; $q_T = \Delta E_{TT}/I_{TT}$ and $|Q_\theta| = 2\Delta E_{EE}/I_{EE}$.

sidered for the neutral vacancy. The change in the value of ΔE_{EE} for the ${}^1E$ level from case 1 to case 2 indicates the extent of uncertainty in the calculation. With the case 1 approximation using Clementi-type functions a tetragonal distortion associated with the ${}^2T_2$ level is predicted; however, in the alternative approximation a trigonal distortion of the system is favoured for this level. A more accurate knowledge of the parameters involved is needed to resolve such conflicting results. The results obtained by Lannoo and co-workers[6, 11] predict a trigonally distorted system associated with the Jahn–Teller splitting of the ${}^3T_1$ and ${}^1T_2$ levels. These results are in more qualitative agreement with the present findings.

Table 5. Jahn–Teller terms for negative vacancy: ${}^2T_2, {}^2T_1, {}^2E$ levels

Function	l_{TE} eV/A	ΔE_{TE} eV	l_{TT} eV/Å	ΔE_{TT} eV
1. ${}^2T_2$ Level				
Slater: Case 1	-0·89	1×10^{-3}	-3·09	0·18
Slater: Case 2	1·91	4×10^{-3}	−2·05	0·07
Clementi: Case 1	1·19	1×10^{-3}	-3·12	0·18
Clementi: Case 2	-2·27	5×10^{-4}	−1·47	0·04
2. ${}^2T_1$ Level				
Slater: Case 1	-1·01	1×10^{-3}	−0·24	1×10^{-4}
Slater: Case 2	−0·65	4×10^{-4}	-1·03	0·02
Clementi: Case 1	0·90	7×10^{-3}	−0·26	1×10^{-3}
Clementi: Case 2	−0·40	1×10^{-4}	−1·55	0·04
	l_{EE} eV/Å	ΔE_{EE} eV		
3. ${}^2E$ Level				
Slater: Case 1	0·91	0·007		
Slater: Case 2	1·19	0·01		
Clementi: Case 1	0·62	0·002		
Clementi: Case 2	0·95	0·007		

Values of q_E, q_T and $|Q_\theta|$ may be determined from the relationships given in the footnote of Table 4.

For the ${}^2T_2$, ${}^2T_1$ and ${}^2E$ electronic levels of the negatively charged vacancy the predicted Jahn–Teller splittings are all small with the possible exception of the results for case 1 of the ${}^2T_2$ level. Correction of the energy levels shown in Fig. 4 of Paper I for these splittings results in no change in the relative ordering of these levels. A trigonally distorted equilibrium configuration of the nuclear framework is predicted for the ${}^2T_2$ level. For the ${}^2T_1$ level the situation is more uncertain, although a trigonal distortion of the system is favoured in the majority of the calculations.

5. CONCLUSION

These calculations demonstrate that the magnitude of the Jahn–Teller splittings is largely independent of the choice of atomic functions in the two cases considered, but is sensitive to the extent of configuration interaction for a particular level and to the inclusion of overlap derivatives. The unreasonably large values obtained for the ${}^2T_2$ level of the V^+ centre and the ${}^3T_1$ level of V^0 even when using modified effective frequencies demonstrate that the first-order theory with only linear coupling terms is inadequate for this system. In particular, if the system has a large symmetric relaxation then second-order terms of the kind $Q_a Q_\alpha$ may be very important. Interlevel coupling effects are considered to be small for the systems investigated.

Acknowledgements—I would like to thank Professor C. A. Coulson and Drs A. B. Lidiard and A. M. Stoneham for helpful discussions. I also thank the Rhodes Trust for the award of the Victorian Rhodes Scholarship and Wadham College, Oxford for a Senior Scholarship.

REFERENCES

1. COULSON C. A. and LARKINS F. P., previous paper
2. JAHN H. A. and TELLER E., *Proc. R. Soc.* **A161**, 220 (1937).
3. HAGSTON W. E., *J Phys. C.* 3, 791 (1970).
4. VAN VLECK J. H., *J. chem. Phys.* 7, 72 (1939).
5. ÖPIK U. and PRYCE M. H. L., *Proc. R Soc.* **A238**, 425 (1957).
6. FRIEDEL J., LANNOO M. and LEMAN G., *Phys. Rev.* **164**, 1056 (1967).
7. LIDIARD A. B. and STONEHAM A. M., *Science and Technology of Industrial Diamonds* 1, 1, Industrial Diamond Information Bureau, London (1967).
8. LANNOO M., *Theses du Troisieme Cycle*, Orsay (1966).
9. STONEHAM A. M. and LANNOO M., *J. Phys. Chem. Solids* **30**, 1769 (1969).
10. LARKINS F. P. and STONEHAM A. M., *J. Phys.* C (to be published).
11. LANNOO M. and STONEHAM A. M., *J. Phys. Chem. Solids* **29**, 1987 (1968).

J. Phys. Chem. Solids Pergamon Press 1971. Vol. 32, pp. 2129-2133. Printed in Great Britain.

HELIUM DIFFUSION IN LiH*

J. B. HOLT, M. Y. ALMASSY and R. W. CRAWFORD
Lawrence Radiation Laboratory, University of California, Livermore, Calif. 94550, U.S.A.

(*Received* 21 *January* 1971)

Abstract – Helium diffusion was studied in single crystals of LiH. The helium was introduced into the material by the nuclear reaction $Li^6(n, \alpha)H^3$. In the temperature range from 200–520°C, the apparent diffusion coefficient is given by:

$$D_A = 2{\cdot}04 \exp(-28{,}200/RT).$$

The results appear to be independent of radiation does from 10^{15}–10^{17} nvt, and of magnesium content up to 2300 ppm. The most plausible mechanism is the diffusion of helium atoms via interstitial sites as they are continually trapped at unspecified lattice defects.

1. INTRODUCTION

INERT GAS diffusion has been studied in various solids such as reactor fuel elements, minerals, rocks, and glasses[1]. Unfortunately, the mechanism of diffusion in these materials is often obscured by undetermined parameters such as grain boundaries, thermal gradients, variable composition, etc. For this reason, mainly in the past few years, inert gas diffusion measurements have been made in simple ionic compounds which might serve as models for the more complex materials. By now, a fairly extensive volume of diffusion data has been accumulated on the alkali halides[2].

Nearly all of these studies deal with radioactive isotopes of inert gases, either produced by neutron activation of ions in the lattice or inserted by ion implantation. Usually, the availability of radioactive isotopes simplifies experimental equipment. Thus, one probable reason for the scarcity of helium diffusion data in ionic compounds is the lack of a suitable radioactive isotope. For the experiments to be described, equipment was designed to accurately measure small amounts of helium (10^9 atoms) (see Ref. [3]) produced in LiH by the nuclear reaction $Li^6(n, He^4)H^3$.

2. MATERIALS

Single crystals of LiH were synthesized by reacting 99·999 per cent pure hydrogen gas with molten lithium metal contained in stainless steel reactors with iron liners. The reactors were pressurized to 60 psi hydrogen and held at 730°C for 2 hr, or until there was no further decrease in pressure. When the reaction was complete, the temperature was decreased 1·5 deg/hr until 600°C was reached, and then maintained at that temperature for 24–48 hr. After this anneal, the reactors were cooled to room temperature at a rate of 6 deg/hr.

Usually, the crystals were light blue in color due to the presence of excess lithium. Some crystals were later annealed in 60 psi hydrogen at 550°C for over 120 hr. This second anneal produced clear, colorless crystals with no visible imperfections except a few subgrain boundaries. Both annealed and unannealed crystals were used in the diffusion experiments with similar results. An analysis of a typical crystal showed the following impurities: Al, 10 ppm; Ca, 10 ppm; Cu, 7 ppm; Fe, 7 ppm; Mg, 30 ppm; Na, 70 ppm; and Si, 30 ppm.

3. EXPERIMENTAL PROCEDURE

LiH is an extremely hydroscopic material, so all experimental work was carried out in a dry, oxygen-free atmosphere. A sample showing signs of contamination at any point in the experiment was immediately rejected from further consideration.

---

*Work performed under the auspices of the U.S. Atomic Energy Commission.

Diffusion samples, approximately 1·0 cm × 1·0 cm × 0·06 cm, were cleaved from large single crystals. These were individually sealed in quartz tubes and then enclosed in aluminum cans prior to neutron irradiation in the Livermore Pool Type Reactor. Helium atoms were produced throughout each sample using the $Li^6(n, He^4)H^3$ nuclear reaction. Homogeneity was insured since the neutron mean free path of ~ 1 cm[4] was much larger than the thickness of the sample, ~ 0·06 cm.

The flux was $5{\cdot}0 \times 10^{12}$ neutrons/cm^2 sec for thermal neutrons, and $5{\cdot}0 \times 10^{11}$ neutrons/cm^2 sec for fast neutrons. Irradiation times varied from 3 min to 5·5 hr, which produced thermal neutron doses from ~ 10^{15} neutrons/cm^2 to ~ 10^{17} neutrons/cm^2. This dose range corresponds to $3{\cdot}8 \times 10^{15}$ helium atoms/cm^3 of LiH to $4{\cdot}2 \times 10^{7}$ helium atoms/cm^3 of LiH with the natural abundance of Li^6. Upon completion of irradiation, the crystals were removed from the quartz tubes in an argon dry-box and visually examined for signs of contamination or mechanical damage.

For the diffusion runs, a sample was placed into a stainless steel chamber which in turn was inserted into the automatic helium diffusion apparatus. The complete system, including the sample chamber, was pumped down to less than 5×10^{-9} torr. After being isolated from the rest of the system by a pneumatic valve, the sample chamber was pressurized to 12 torr of hydrogen. This pressure is much higher than the dissociation pressure of LiH in the experimental temperature range of 200–500°C[5].

The samples were heated rapidly (3–6 min) to the diffusion temperature with a small resistance furnace and held at constant temperature to within ±5°C for 2–64 hr. At selected time intervals (10 min to several hr), the gas content of the sample chamber was expanded into a titanium sublimation pump where the hydrogen was gettered. Within 3 sec a new hydrogen atmosphere was introduced into the sample chamber. The partial pressure of helium was measured by a high sensitivity, low-resolution partial-pressure gauge. The amount of helium was determined by comparison of the partial pressure to measurements on known mixtures of hydrogen and helium.

At the end of each run, the temperature of the crystal was raised to the melting point of LiH to release the remaining helium. From these isothermal experiments the data was obtained for fractional release (F) as a function of time. Two samples containing MgH_2 were also measured to determine the effect of introducing cation vacancies. The MgH_2 is expected to be in solid solution for the concentrations utilized[6].

4. EXPERIMENTAL RESULTS

One solution to Fick's second law for diffusion out of a slab of thickness h is given by equation (1) for the boundary conditions, $c(0, t) = c(h, t) = 0$ for $t > 0$, and $c(x, 0) = c_0$ for $0 \leq x \leq h$[7],

$$\frac{\bar{c}}{c_0} = 1 - 2\left(\frac{4Dt}{h^2}\right)^{1/2} \left\{\pi^{-1/2} + 2\sum_{n=1}^{\infty} (-1)^n \operatorname{ierfc}\frac{nh}{2(Dt)^{1/2}}\right\} \quad (1)$$

The average concentration, $\bar{c}$, is defined as $(c_0 - c_t)/c_0$, where c_0 is the initial helium concentration in the solid, and c_t is the concentration of helium released from the solid in time t. The fractional release (F) is equivalent to c_t/c_0 so that $\bar{c}$ is also equal to $1 - F$. A computer program was written which fits the experimental data to equation (1) and solves for D as an adjustable parameter. Figure 1 shows the data from a typical sample. The circles are experimental points, while the solid curve is generated from the computer fit to the data. The fit is very good over the duration of the run and is representative of all samples.

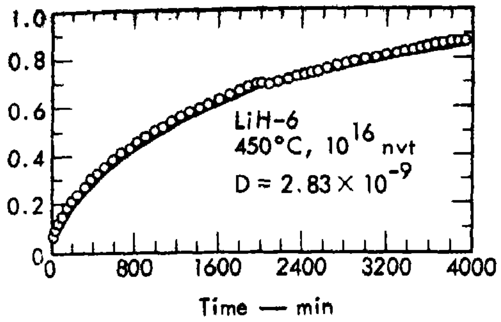

Fig. 1. Isothermal plot showing the fractional release vs. time for a typical sample at 450°C. The open circles are the experimental points while the solid line is the solution to equation (1) for $D_A = 2{\cdot}83 \times 10^{-9}$ cm²/sec.

An approximation to equation (1), which should be valid at short times, is given by equation (2).

$$F^2 = \frac{16Dt}{\pi h^2}. \qquad (2)$$

Figure 2 shows the same data as shown in Fig. 1, but here it is plotted according to the form of equation (2). The linearity is good for short times and does not deviate until $F \simeq 0{\cdot}65$. The D value computed from the initial slope of Fig. 2 differs from that calculated from equation (1) by less than 10 per cent. Thus, it is possible to obtain correct values for D by use of the approximate equation without resorting to the complexities of computer calculations.

In these experiments the values for D were derived by solving equation (1), and a least-squares analysis gives the apparent diffusion coefficient, D_A, as

$$D_A = 2{\cdot}04 \exp(-28{,}200/RT). \qquad (3)$$

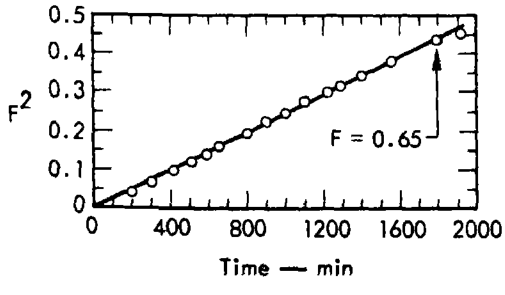

Fig. 2. F^2 vs. time plot for the same data as shown in Fig. 1. The value of the apparent diffusion coefficient is $D_A = 2{\cdot}9 \times 10^{-9}$ cm²/sec.

The individual D_A values are listed in Table 1 and plotted in Fig. 3 along with the line calculated from equation (3). The plot contains measurements on samples whose neutron dose varied from 10^{15} to 10^{17} nvt. Within experimental error, in this range the diffusion coefficients are independent of dose. Included in Fig. 3 are the results from two samples containing 2300 ppm by weight of magnesium. The purpose of adding magnesium was to introduce cation vacancies into the lattice in order to determine their effect on the diffusion coefficients. Since the amount of magnesium is greater by an order of magnitude than the sum of all other divalent cation impurities, any influence of additional

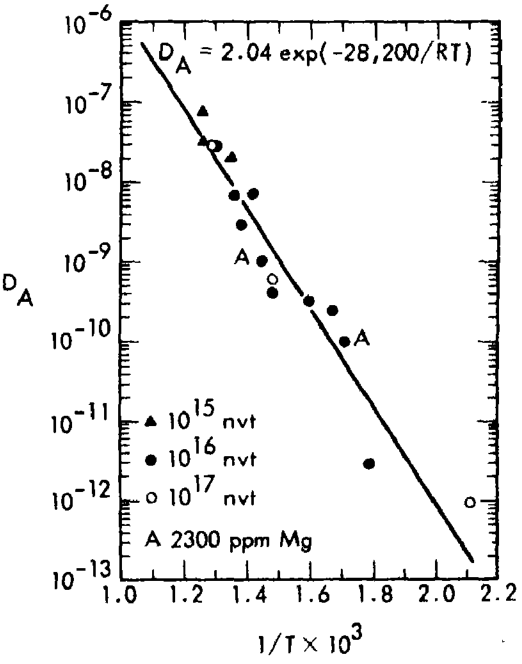

Fig. 3. An Arrhenius plot of all data points including two containing 2300 ppm Mg(A) and doses from 10^{15} to 10^{17} nvt. The line is a least-squares fit to the points.

Table 1. List of experimental diffusion coefficients at different temperatures

Sample No.	Dose (nvt)	Temperature (°C)	Diffusion coefficient
LiH-2a	10^{16}	350	$3{\cdot}3 \times 10^{-10}$
LiH-2b	10^{16}	430	$7{\cdot}3 \times 10^{-9}$
LiH-3	10^{16}	400	$4{\cdot}0 \times 10^{-10}$
LiH-4a	10^{17}	200	$9{\cdot}8 \times 10^{-13}$
LiH-5a	10^{17}	400	$6{\cdot}0 \times 10^{-10}$
LiH-6a	10^{16}	285	$2{\cdot}8 \times 10^{-12}$
LiH-6b	10^{16}	450	$2{\cdot}8 \times 10^{-9}$
LiH-7	10^{16}	495	$2{\cdot}8 \times 10^{-9}$
LiH-9	10^{15}	520	$7{\cdot}4 \times 10^{-8}$
LiH-10	10^{15}	468	$2{\cdot}0 \times 10^{-8}$
LiH-11	10^{15}	520	$3{\cdot}1 \times 10^{-8}$
LiH-13	10^{16}	462	$6{\cdot}9 \times 10^{-9}$
LiH-14	10^{16}	325	$2{\cdot}4 \times 10^{-10}$
LiH-15*	10^{16}	420	$1{\cdot}0 \times 10^{-9}$
LiH-16*	10^{16}	310	$1{\cdot}0 \times 10^{-10}$

*Mg Impurity

vacancies should be easily observed. No second phase precipitates were found in the LiH samples containing magnesium by X-ray analysis, as expected[6].

5. DISCUSSION

Recently, Jaswal and Streifler[8], Wilson and Johnson[9], Harrison and Fischer[10] and Dellin *et al.*[11] published theoretical calculations of the activation energy for helium migrating interstitially in LiH. The calculations gave very similar values: 13·8 kcal/mole[8], 15·9 kcal/mole[9], 12·4 kcal/mole[10], and 13·8 kcal/mole[11]. However, these values are much lower than our experimental energy of 28·3 kcal/mole. This disagreement between theoretical and experimental energies suggests that a simple interstitial model is inadequate to describe helium transport in LiH.

If the helium were to diffuse by a vacancy mechanism, the observed activation energy should be similar to that for self-diffusion of one of the ionic components. Experimental activation energies for self-diffusion are: 34·6 kcal/mole[12] and 22·0 kcal/mole for the H^- ion, and 29·0 kcal/mole for the Li^+ ion [13]. These energies are close to our experimental activation energy. However, helium diffusion by a vacancy mechanism is unlikely when the apparent diffusion coefficients of the samples containing magnesium are considered.

When Mg^{2+} is added to LiH, one cation vacancy is created for each Mg^{2+} ion, assuming complete solid solution and intrinsic Schottky-type disorder. The concentrations of cation and anion vacancies are determined by electroneutrality considerations and the mass action equation,

$$K = (V_{Li^+})(V_{H^-}) \tag{4}$$

where (V_{Li^+}) is the concentration of lithium ion vacancies and (V_{H^-}) is the concentration of hydrogen-ion vacancies. At a selected temperature, an increase in the concentration of cation vacancies introduced by magnesium will cause a proportional decrease in the concentration of anion vacancies[14].

The self-diffusion coefficient may be defined as

$$D = D_V C_V \tag{5}$$

where D_V is the vacancy-diffusion coefficient and C_V is the concentration of vacancies. For the case of helium diffusion in LiH containing Mg^{2+}, the diffusion coefficients should be enhanced if a cation vacancy mechanism predominates, or be diminished if anion vacancies are involved. As can be seen in Fig. 3, the addition of magnesium seems to have no effect of the diffusion of helium in LiH.

The most plausible explanation for these experimental results is that helium atoms diffuse via interstitial sites, but are continually trapped in some type of lattice defect. Such traps might include radiation-induced clusters, cation vacancies, anion vacancies or vacancy pairs. Since the apparent diffusion coefficients in Fig. 3 appear to be independent of dose in the range from 10^{15} to 10^{17} nvt, then radiation-induced clusters are probably not important as traps.

If the trapping mechanism does apply, the activation energy from Fig. 3 is [15]

$$E = (E_m + B_T - H_f) \qquad (6)$$

where E_m is the energy for mobility through interstitial sites, B_T is the binding energy of the helium atom to the trap, and H_f is the enthalpy of formation for vacancies. For LiH, $H_f \simeq 43$ kcal/mole [8] and $E_m \simeq 14$ kcal/mole, so that $B_T \sim 57$ kcal/mole. From our experimental data, it is not possible to select the trap involved, and no theoretical calculations for trapping energies of helium in different lattice defects are available for comparison. Therefore, the nature of the traps remains unspecified at this time.

Some mention should be made about the possible influence of bubble formation on the diffusion and trapping of helium. There is evidence for the occurrence of gaseous helium [16] and also bubble formation [17] in irradiated LiH. Bubbles which probably contain helium have also been found in neutronirradiated LiF [18]. However, the effect of bubble formation (if any) on these experiments is unknown and remains an area for further experimental investigation.

Acknowledgements—The authors wish to express their appreciation to Clyde Griffith for preparation of the single crystals, and to H. Leider, A. Rothman, and W. D. Wilson for helpful discussions and review of the manuscript.

REFERENCES

1. See for example: (a) WHAPHAM A. D., *Nucl. Appl.* **2**, 123 (1966). (b) ROGERS W. A., BURITZ R. S. and ALPERT D., *J. appl. Phys.* **25**, 868 (1954). (c) REYNOLDS J. H., *Geo. Cosmochim. Acta* **20**, 101 (1960). (d) ALTEMORE V. O., *J. appl. Phys.* **32**, 1309 (1961).
2. See for example: (a) FELIX F. W., *Phys. Status Solidi* **27**, 529 (1968). (b) FELIX F. W., *Proc. Brit. Ceram. Soc.* **15**, 273 (1967). (c) BANNASCH W. and SCHMELING P., *J. Phys. Chem. Solids* **26**, 1999 (1965). (d) KALBITZER S., *Z. Naturf.* **17A**, 1071 (1962). (e) SCHMELING P., *J. Phys. Chem. Solids* **28**, 1185 (1967). (f) MATZKE H., *Z. Naturf.* **22A**, 507 (1967). (g) SCHMELING P., *Phys. Status Solidi* **21**, 175 (1965). (h) ELLEMAN T. S., *Annual Progress Report,* Contract AT-(40-1)-3508;d (to be published).
3. CRAWFORD R. W., FRAZER J. and HOLT J. B., *Rev. scient. Instrum.* **42**, 674 (1971).
4. ZWEIFEL D. F., *Nucleonics* **18**, 174 (1960).
5. HEUMANN F. K. and SALMON O. N., *KAPL*-1667 (1956).
6. PRETZEL F. E. and RUSHING C. C., *J. Phys. Chem. Solids* **17**, 232 (1961).
7. CRANK J., *Mathematics of Diffusion*, Clarendon Press, Oxford (1956).
8. JASWAL S. S. and STREIFLER M. F., *Bull. Am. Phys. Soc.* **16**, 438 (1969).
9. WILSON W. D. and JOHNSON R. A., *Phys. Rev.* **31**, 3510 (1970).
10. HARRISON S. W. and FISCHER C. R., *Bull. Am. Phys. Soc.* **14**, 612 (1969); HARRISON S. W., *Ph.D. Thesis*, CUNY (1970).
11. DELLIN T. A., DIENES G. J., FISCHER C. R., HATCHER R. D. and WILSON W. D., *Phys. Rev.* **131**, 3510 (1970).
12. PRETZEL F. E., GRITTON G. V. and RUSHING C. C., *LA*-2463 (1963).
13. FUNKE K. and RICHTERING H., *Ber. Buns. Phys. Chem.* **72**, 619 (1968).
14. LAURANCE N., *Phys. Rev.* **120**, 57 (1960).
15. NORGETT M. J. and LIDIARD A. B., *Radiation Damage in Reactor Materials*, Vol. 1, Intern. At. Energy Agency, Vienna (1969); *Phil. Mag.* **18**, 1193 (1968).
16. PRETZEL F. E., VIER D. T., SzKLARZ E. G. and LEWIS W. B.; SOUERS P. C., JOLLY T. A. and CLINE C. F., *J. Phys. Chem. Solids* **28**, 1717 (1967).
17. IMAI T., *Phil. Mag.* **21**, 281 (1970).
18. (a) SENIO I., *Science* **126**, 208 (1957). (b) SMALLMAN R. E. and WILLIS B. T. M., *Phil. Mag.* **2**, 1018 (1957). (c) GILMAN J. J. and JOHNSTON W. G., *J. appl. Phys.* **29**, 877 (1958). (d) LAMBERT M. and GUINIER A., *Compt. Rend.* **224**, 2791 (1957). (e) MANNAMI M., AKISUE Q. and TANAKA K., *Japan J. appl. Phys.* **6**, 283 (1967).

J. Phys. Chem. Solids Pergamon Press 1971. Vol. 32, pp. 2135–2143. Printed in Great Britain.

VACANCY FLOW EFFECT ON ELECTROMIGRATION IN SILVER

NGUYEN VAN DOAN
Section de Recherches de Métallurgie Physique, Commissariat a l'Energie Atomique,
Centre d'Etudes Nucléaires de Saclay, France

(*Received* 8 *May* 1970; *in revised form* 28 *December* 1970)

Abstract—The 'apparent effective valence Z^{**}, deduced from experiments on electromigration using tracer atoms, differs from the true 'effective valence' Z^* by the 'vacancy flow term', previously introduced by Howard and Lidiard and by Manning in ionic crystals. This corrective term could explain the small values obtained for Z^{**} of the transitional tracers: ^{54}Mn, ^{59}Fe, ^{58}Co and ^{63}Ni in Silver.

An experiment has been carried out with ^{59}Fe in copper to confirm this hypothesis.

1. INTRODUCTION

IN ORDER to study the electronic structure of ions at the saddle point, i.e. ions halfway between two vacancies during a jump, we have investigated the electromigration of some solutes in Silver[1, 2]: ^{110}Ag, ^{109}Cd, ^{114m}In, ^{113}Sn and ^{124}Sb. In fact, many such experiments have been performed in recent years [3–8], but the results vary over a wide range according to the authors and to the experimental procedures. For the saddle point investigation, it is necessary to undertake the experiments in the same laboratory. For this reason, to supplement the above mentioned solutes, we have been interested in the behaviour of transition elements.

The choice of the iron group is governed by the well-known variation of the excess resistivity of ions distributed homogeneously at the lattice site in a noble metal matrix[9]. This variation is thoroughly explained by the virtual bound states model introduced by Friedel[10–13]. It would be interesting to examine to what extent the model can be used to describe the electronic structure of transitional ions at the saddle point.

For the time being we will limit ourselves to the presentation of the preliminary experimental results. We will see that they are very unusual. In fact, they could be explained by the presence of the vacancy flow effect. In Section 2 we show by means of the Thermodynamics of Irreversible Processes how this effect is introduced. In Section 3, we point out its importance in the explanation of the small values obtained for the apparent effective valences.

2. VACANCY FLOW EFFECT

In the previous paper[1], we have neglected the term $(L_{AB}/L_{BB})(z_A - z_A^*/z_B - z_B^*)$ in the expression of the flux of ^{124}Sb in silver. It will be shown that this term can become important in some cases, especially for the tracer atoms investigated in the present work.

In a metallic alloy where the diffusion occurs by a vacancy mechanism, the flux **J** of the components *A* and *B* can be written in the following form[1]:

$$\mathbf{J}_A = -\frac{L_{AA}}{T}\frac{\mathrm{d}}{\mathrm{d}x}(\tilde{\mu}_A - \tilde{\mu}_L) - \frac{L_{AB}}{T}\frac{\mathrm{d}}{\mathrm{d}x}(\tilde{\mu}_B - \tilde{\mu}_L) - \frac{L_{Ae}}{T}\frac{\mathrm{d}}{\mathrm{d}x}\tilde{\mu}_e \quad (1)$$

$$\mathbf{J}_B = -\frac{L_{BA}}{T}\frac{\mathrm{d}}{\mathrm{d}x}(\tilde{\mu}_A - \tilde{\mu}_L) - \frac{L_{BB}}{T}\frac{\mathrm{d}}{\mathrm{d}x}(\tilde{\mu}_B - \tilde{\mu}_L) - \frac{L_{Be}}{T}\frac{\mathrm{d}}{\mathrm{d}x}\tilde{\mu}_e \quad (2)$$

where $\tilde{\mu}_i$ are the potentials from which the thermodynamic forces are derived:

$$\tilde{\mu}_A = \mu_A + z_A e\phi$$
$$\tilde{\mu}_B = \mu_B + z_B e\phi$$
$$\tilde{\mu}_L = \mu_L$$
$$\tilde{\mu}_e = E_F - e\phi$$

and $\mathbf{E} = -(d\phi/dx)$ is the electric field.

These fluxes are measured with respect to the lattice reference, defined by a thin layer of $\mathrm{Hf}^{181}\mathrm{O}_2$ tracer or simply by the initial interface of welding (revealed by chemical etching). The phenomenological coefficients L_{AA}, L_{BB} are related respectively to the self- and hetero-diffusion coefficients $D^A_{A^*}$, $D^A_{B^*}$. The cross-term $L_{AB} = L_{BA}$ describes the coupling between fluxes of atoms A and B. The coefficients L_{Ae}, L_{Be} originate from the interaction of atoms A and B with the charge carriers.

Let $z_A^* eE$ and $z_B^* eE$ be the friction forces due to charge carriers on atoms A and B, averaged over a jump path:

$$L_{Ae} = L_{AA} z_A^* + L_{AB} z_B^* \tag{3}$$

$$L_{Be} = L_{BA} z_A^* + L_{BB} z_B^* . \tag{4}$$

For dilute solutions ($n_B \ll n_A$), equation (2) reduces to:

$$\mathbf{J}_B = -D^A_{B^*} \frac{\partial n_B}{\partial x} + \frac{n_B D^A_{B^*}}{kT} \times \left[(z_B - z_B^*) + \frac{L_{BA}}{L_{BB}} (z_A - z_A^*) \right] e\mathbf{E}. \tag{2'}$$

It follows that, in our tracer diffusion experiments, the drift velocity $\mathbf{v}_B$ resulting from the electric field is given by:

$$\mathbf{v}_B = \frac{D^A_{B^*}}{kT} \left[(z_B - z_B^*) + \frac{L_{BA}}{L_{BB}} (z_A - z_A^*) \right] e\mathbf{E}. \tag{5}$$

This expression may be compared to the Nernst–Einstein's relation which states that:

$$\mathbf{v}_B{}^0 = \frac{D^A_{B^*}}{kT} (z_B - z_B^*) e\mathbf{E}. \tag{6}$$

It means that this relation is valid only when the fluxes are independent. On the other hand, it is important to note that the correction term L_{BA}/L_{BB} is identical to the 'vacancy flow effect' introduced by Howard and Lidiard[14] in the ionic crystals and calculated by Manning[15] in a more complete kinetic analysis.

At this stage, in order to avoid confusion with previous notations[1, 2] we will define the various valences as following:

z_A, z_B are valences of the matrix and of the tracer atom;

z_A^*, z_B^* are valences relative to the friction forces;

$Z_A^* = z_A - z_A^*$, $Z_B^* = z_B - z_B^*$ are effective valences which are to be compared with theoretical expression[16–18];

Z_A^{**}, Z_B^{**} are apparent effective valences measured in our experiments and related to the true effective valences by the relations (10) and (11).

Let us consider two following cases:

(1) *Self-diffusion $B = A^*$*

Equation (5) becomes:

$$\mathbf{v}_{A^*} = \frac{D^A_{A^*}}{kT} (z_A - z_A^*) \left(1 + \frac{L_{A^*A}}{L_{A^*A^*}} \right) e\mathbf{E}$$

where[19]:

$$1 + \frac{L_{A^*A}}{L_{A^*A^*}} = \frac{1}{f_A}$$

f_A being the correlation factor, equal to 0·78 for f.c.c. lattice.

Therefore:

$$\mathbf{v}_{A^*} = \frac{D^A_{A^*} Z_A^* e\mathbf{E}}{f_A kT} \tag{7}$$

where: D^A_A / f_A is the uncorrelated self-diffusion coefficient. Hence, in the case of self-diffusion, the vacancy flow effect compensates exactly the correlation effect. This result is not surprising, for in a vacancy mechanism, the flux of solvent atoms is equal and opposite to the flux of vacancies whose jumps are not correlated[1], [20], [21].

(2) *Heterodiffusion* $B = B^*$

Here:

$$v_{B^*} = \frac{D_{B^*}^A}{kT}\left[Z_B^* + \frac{L_{BA}}{L_{BB}} Z_A^*\right] e\mathbf{E}. \qquad (8)$$

We can therefore write (7) and (8) in the Nernst–Einstein's form:

$$v_i = \frac{D_i^A Z_i^{**} e\mathbf{E}}{kT} \qquad (i = A^* \text{ or } B^*) \qquad (9)$$

where:

$$Z_A^{**} = Z_A^*/f_A \qquad (10)$$

$$Z_B^{**} = Z_B^*\left[1 + \frac{L_{BA}}{L_{BB}}\frac{Z_A^*}{Z_B^*}\right]. \qquad (11)$$

If L_{BA}/L_{BB} is small (for example ^{124}Sb in Ag):

$$Z_B^{**} \simeq Z_B^*.$$

But it should be mentioned that L_{BA}/L_{BB} could be negative and approach the limiting value -2; that is, instead of accelerating the diffusion of the tracer $B(L_{BA}/L_{BB} > 0)$, the vacancy flow effect can in certain cases slow it down considerably $(L_{BA}/L_{BB} < 0)$. This can be seen by using Howard and Lidiard's expressions for L_{BA} and L_{BB}[22]:

$$\frac{L_{BA}}{L_{BB}} = \frac{-2 + 3(W_3/W_1)}{1 + \frac{7}{2}(W_3/W_1)} \qquad (12)$$

where W_i's are standard vacancy jump frequencies.

$$\text{When: } \frac{W_3}{W_1} \to 0, \lim \frac{L_{BA}}{L_{BB}} \to -2.$$

On the other hand, Manning has derived a more general expression[23] for the vacancy flow effect:

$$2\langle n_p\rangle = \frac{L_{BA}}{L_{BB}}$$

namely:

$$\langle n_p\rangle = \frac{3W_3 - 2W_1 + (W_3/W_4)(W_0 - W_4)7(1-F)}{2W_1 + 7FW_3} \qquad (13)$$

or:

$$\boxed{\langle n_p\rangle = \frac{-2+\varphi r}{2+7Fr}} \qquad (14)$$

where: $r = W_3/W_1$

$$\varphi = 3 + 7(1-F)(W_0/W_4 - 1) \qquad (15)$$

$7F$ and φ are plotted as a function of W_0/W_4 [23, 24] in Fig. 1. The Fig. 2 represents $\langle n_p\rangle$ vs. the ratio r for various values of W_0/W_4. In particular, for $W_0 = W_4$, $2\langle n_p\rangle$ is approximately given by equation (12).

To determine the true effective valences Z_B^* from experiments, one therefore need to know these ratios W_0/W_4 and W_3/W_1, which can be deduced from both the isotope effect measurement and the solute-enhanced self-diffusion [25]. Unfortunately, there are at present only a few cases where the data are available.

3. EXPERIMENTAL RESULTS AND DISCUSSION

The experimental techniques are destribed in [1, 2]. A thin layer of radioisotopes is deposited between two cylinders of Ag metal. The isotopes are obtained from the Département des Radioéléments at Saclay in the form of chlorides. The plating bath consists of a saturated ammonium oxalate solution whose pH is reduced to 4 by addition of oxalic acid [26]. The welding of the two cylinders and of the whole specimen to electrodes is carried out at the same time, in a vacuum of 10^{-6} mm Hg, at 750°C during 1 hr[1]. In order to avoid the evaporation of silver, the anneal is made under a purified argon atmosphere for periods

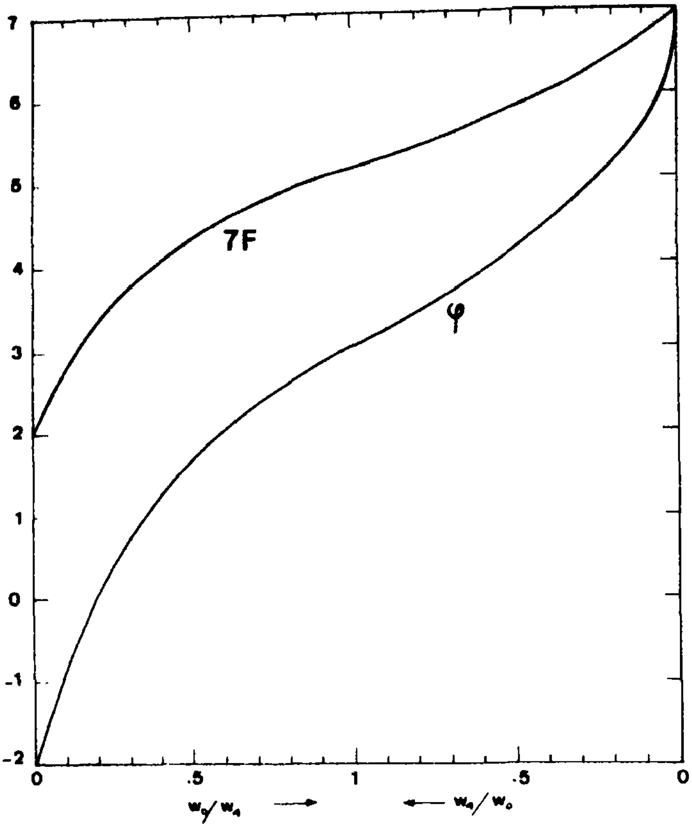

Fig. 1. $7F$ and φ as a function of W_0/W_4 and W_4W_0.

of 2 to 3 weeks depending on the tracer. After the experiment, the tracer has diffused according to a gaussian distribution with its maximum shifted to the anode from the original welding interface by a quantity x_m. The following tracers have been investigated: ^{54}Mn, ^{59}Fe, ^{58}Co and ^{63}Ni (Table 1). Typical curves obtained are shown in Fig. 3(a, b, c). The Fig. 4 shows the plots of Ln (specific activity) vs. the square of $x - x_m$ (distance from the maximum).

The apparent effective valence is related to x_m by:

$$Z_B^{**} = \frac{4pkTx_m}{e\rho_0 J} \qquad (16)$$

where: $\rho_0 J = E$ and p is the slope of the plots in Fig. 4.

The temperature is determined by using values of Q and D_0 from the literature[26–29]. In general the temperature thus obtained does not differ by more than 10°C from that indicated by two insulated thermocouples placed at 2·5 mm from the isotope layer, excepting the case of ^{58}Co where the calculated temperature is 20 to 40°C higher than that of the thermocouples. On the other hand, the recent diffusion data for this tracer[30] are consistent with observed temperatures given in Table 1.

In order to show the importance of the vacancy flow effect, let us consider first the case where it is neglected:

$$Z_B^{*} = Z_B^{**} \qquad (17)$$

and we will see that the results are quite

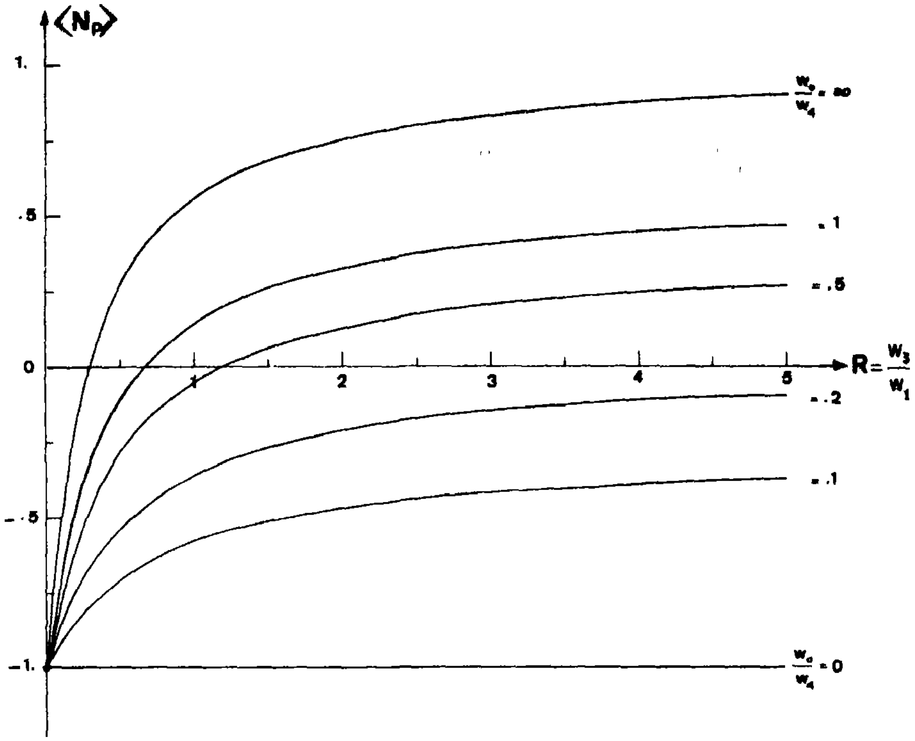

Fig. 2. Vacancy flow term $\langle n_p \rangle$ as a function of W_3/W_1 for some values of W_0/W_4.

anomalous. From (16) and (17), one can calculate the sum of the excess resistivities due to the ion at the stable position and at the saddle point, using Bosvieux and Friedel's model[18]:

$$\Sigma_B \equiv \Delta\rho^{(\text{stable})} + \Delta\rho^{(\text{saddle})}$$

$$= (1 + f_0 - 2Z_B^*)\rho_0/100 \qquad (18)$$

f_0 is equal to $-2{\cdot}5$ in Silver. The results are given in Table 2. It can be noticed that the two last columns show almost the same values, namely:

$$\Sigma_B \simeq \Delta\rho_{\text{Linde}} \quad (\text{in Ag or Au}). \qquad (19)$$

The case of ^{63}Ni is questionable in view of the

Table 1. Electromigration of transitional tracers in silver

Tracer	t (sec)10^6	D (cm^2/sec) 10^{-9}	ρ_0 ($\mu\Omega$-cm)	J (amp/cm^2)	x_m (μ)	Z_B^**	$\pm\Delta Z_B^*$*
^{54}Mn	0·7293	3·17	7·53	4062	70	−9·83	3·2
	1·4211	2·95	7·50	5170	200	−12·21	2·3
^{59}Fe	1·2354	1·212	7·55	4194	250	−52·41	3·8
	*1·3644	1·69	8·82	3904	365	−51·74	4·4
^{58}Co	1·6344	1·022	7·55	4549	250	−43·32	4·6
	1·3948	1·011	7·55	4847	200	−38·53	5·2
^{63}Ni	2·088	0·826	7·52	5468	150	−20·97	9·2

*Experiment performed in copper.

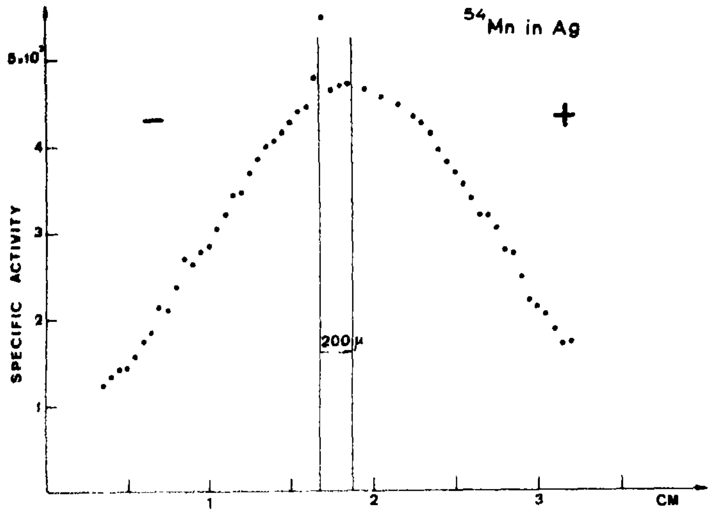

Fig. 3(a).

large experimental error for this run. For the sake of simplification, let us assume that $\Delta\rho^{(\mathrm{stable})}$ is comparable to the value of the resistivity given by Linde[9] for corresponding substitutional impurities in Au (excepting Mn). This assumption implies further that:

(a) the contribution to $\Delta\rho_{\mathrm{Linde}}$ from lattice relaxation around the impurity atom is neglected;

(b) $\Delta\rho^{(\mathrm{stable})}$ does not include the contribution from the vacancy adjacent to the jumping atom, for it arises only from the momentum transferred to the latter.

From equation (19), this would mean that the excess resistivity of the ion at the saddle point would be very small for all these tracers. Physically this is very surprising, for one would expect $\Delta\rho^{(\mathrm{saddle})}$ to be at least of the

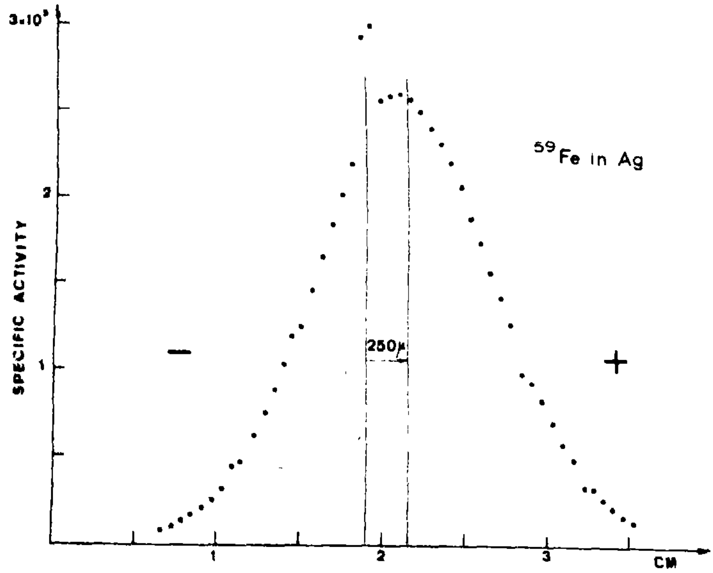

Fig. 3(b).

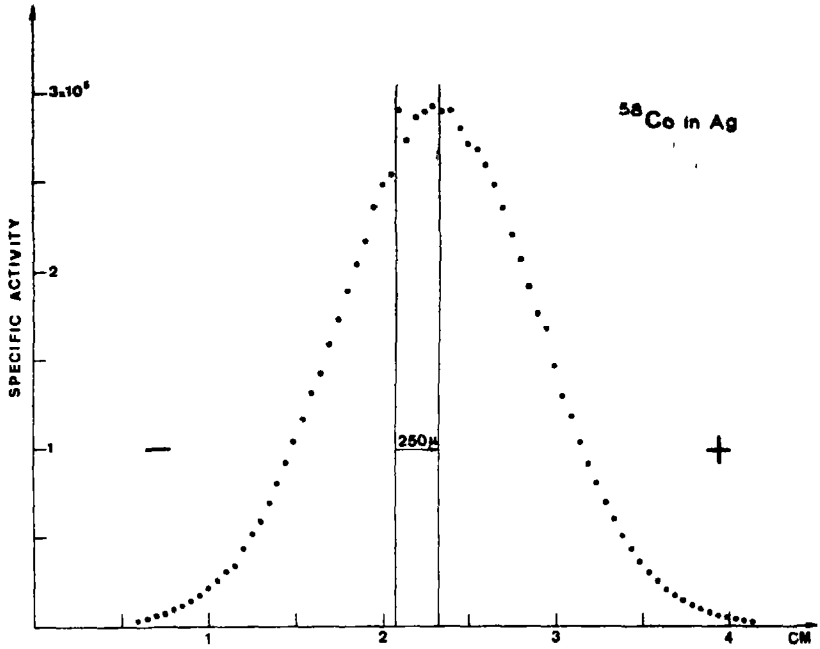

Fig. 3(c). Typical curves of electromigration in Silver (a) ^{54}Mn; (b) ^{59}Fe; (c) ^{58}Co.

same order of magnitude as $\Delta\rho^{(\mathrm{stable})}$.

A tentative explanation to this unexpected result can be given by taking into account the vacancy flow effect. Z_B^* is no longer equal to Z_B^{**}, but it is given by equation (11):

$$Z_B^* = Z_B^{**} - 2\langle n_p \rangle Z_A^*. \qquad (11')$$

Therefore if $\langle n_p \rangle$ is negative, the absolute value $|Z_B^*|$ would be much greater than $|Z_B^{**}|$. Unfortunately, the data necessary to the $\langle n_p \rangle$ calculation for the tracers of interest in Silver, namely the ratios W_0/W_4 and W_3/W_1 are not available. For this reason, we have carried out an experiment with ^{59}Fe in Copper (see Table 1) where at 980°C we have[31]:

$$\frac{W_3}{W_1} = 0{\cdot}04 \quad \text{and} \quad \frac{W_4}{W_0} = 0{\cdot}15$$

Hence: $\langle n_p \rangle = -0{\cdot}789$

with: $Z_{\mathrm{Cu}}^* = -18$[32–34] and $Z_{\mathrm{Fe}}^{**} = -51{\cdot}8$, the equations (11′) and (18) give respectively:

$$Z_{\mathrm{Fe}}^* = -80{\cdot}2$$

$$\Sigma_{\mathrm{Fe}} = 14{,}2\ \mu\Omega\text{-cm/at. \%. (in copper)}$$

Table 2. Comparison between resistivities deduced from the present work and from Linde's measurement ($\mu\Omega$-cm/at. %)

Tracer	N°	T (°C)	$Z_B^* \approx Z_B^{**}$	Σ_B	$\Delta\rho_{\mathrm{Linde}}$ (Ag)	$\Delta\rho_{\mathrm{Linde}}$ (Au)	$\Delta\rho_{\mathrm{Linde}}$ (Cu)
^{54}Mn	1	877	−9·8	1·37	1·60	2·41	2·83
	2	873	−12·2	1·72			
^{59}Fe	1	880	−52·4	7·80	—	7·66	9·3
	2*	994	−51·8	9·14			
^{58}Co	1	882	−43·3	6·43	—	6·1	6·4
	2	880	−38·5	5·71			
^{63}Ni	1	876	−20·9	3·04	—	1·0	1·25

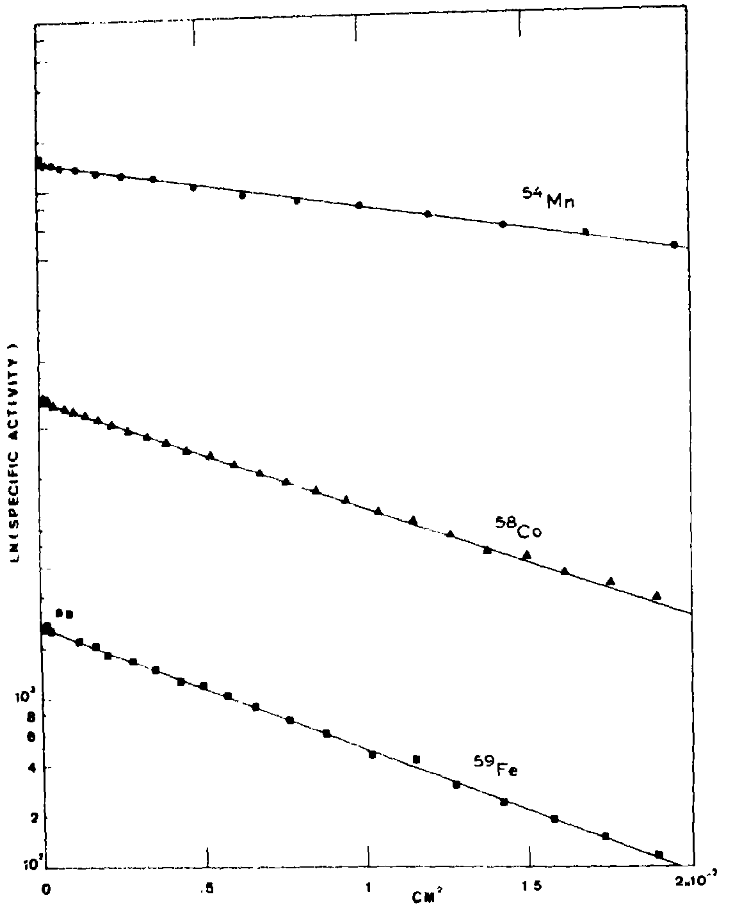

Fig. 4. Ln (specific activity) versus the square of $x-x_m$ (distance from the maximum).

In the same system, Kuz'menko[35] has given for Z^*_{Fe} results varying from −28 to −65·7, but they have to be divided by 0·78 to give exact values of Z^{**}_{Fe}.

In the same way, if one assumes the same value of $\langle n_p \rangle$ for ^{59}Fe in Silver where $Z^*_{Ag} = -12{\cdot}5$[1], one would obtain:

$$Z^*_{Fe} = -71{\cdot}2$$

$$\Sigma_{Fe} = 10{\cdot}8\,\mu\Omega\text{cm/at.}\ \%. \quad \text{(in Silver)}$$

Therefore these values of Σ_{Fe} are more reasonable in view of Linde's data.

In conclusion, the small values of $|Z^{**}_B|$ in Table 2 suggest that for all transitional tracers investigated in the present work the vacancy flow term $\langle n_p \rangle$ is negative and plays an important role in the interpretation of the experimental results. Considerations on the relative magnitude of $\Delta\rho^{(\text{stable})}$ and $\Delta\rho^{(\text{saddle})}$, for example $\Delta\rho^{(\text{saddle})} \geqslant \Delta\rho^{(\text{stable})}$, would enable us to predict an upper limit of the ratio W_3/W_1 for a given W_0/W_4. On the other hand, it would be very interesting to take into account this vacancy flow effect for results in Ref. [2]. However, the correction in this case is thought to be less important[36], for the term $\langle n_p \rangle$ would be small in view of estimated vacancy jump frequency ratios[25]. This is also, to a certain extent, supported by the reasonable experimental values obtained for the different excess resistivities considered.

Acknowledgements—We are grateful to Dr Y. Adda and G. Brebec of this laboratory for their interest and encouragement, to Professor H. B. Huntington and Professor J. Friedel for helpful correspondence and discussions. We are also very pleased to thank Dr. J. R. Manning for his interesting comments.

REFERENCES

1. NGUYEN VAN DOAN et BREGEC G., *J. Phys. Chem. Solids* **31**, 475 (1970).
2. NGUYEN VAN DOAN, *J. Phys. Chem. Solids* **31**, 2079 (1970).
3. KUBASCHEWSKI O., unpublished work.
4. GILDER H. M. and LAZARUS D., *Phys. Rev.* **145**, 508 (1966).
5. ARCHIPOVA N. K., KLOTSMAN S. M., TIMOFEEV A. N. and TRAKHTENBERG I. Sh., *Phys. Status Solidi* **16**, 729 (1966); **18**, 847 (1966).
6. HEHENKAMP Th., *Habilitationsschrift Münster* (1966).
7. STEPPER H. J. and WEVER H., *J. Phys. Chem. Solids* **28**, 1103 (1967).
8. HEHENKAMP Th., HERZIG Ch., HEUMANN Th., *Jülich Conf.*, **1**, 69 (1968).
9. LINDE J. O., *Ann. Phys.* **15**, 219 (1932).
10. FRIEDEL J., *Can. J. Phys.* **34**, 1190 (1956).
11. DE FAGET DE CASTELJAU P. and FRIEDEL J., *J. Phys. Radium* **17**, 27 (1956).
12. BLANDIN A. and FRIEDEL J., *J. Phys. Rad.* **20**, 160 (1959).
13. DANIEL E., *J. Phys. Chem. Solids* **23**, 975 (1962).
14. HOWARD R. E. and LIDIARD A. B., *J. phys. Soc. Japan, Suppl.* **18**, 197 (1963).
15. MANNING J. R., *Diffusion Kinetics for Atoms in Crystals*, Van Nostrand, New-York (1968).
16. FIKS V. B., *Fiz. tverd. Tela* **1**, 16 (1959); *Soviet Phys. solid State* **1**, 16 (1959).
17. HUNTINGTON H. B. and GRÖNE A. R., *J. Phys. Chem. Solids* **20**, 76 (1961).
18. BOSVIEUX C. and FRIEDEL J., *J. Phys. Chem. Solids* **23**, 123 (1962).
19. ADDA Y. et PHILIBERT J., *La Diffusion dans les Solides*, P.U.F. Paris (1966).
20. HUNTINGTON H. B., *Trans. TMS-AIME* **245**, 2571 (1969).
21. HEHENKAMP Th., *Vacancies and Interstitials in metals*, North-Holland, Amsterdam, 19 (1969).
22. HOWARD R. E. and LIDIARD A. B., *Reports on progress in Physics*, **XXVII**, 161 (1964).
23. MANNING J. R., *Phys. Rev.* **139**, A2027 (1965).
24. MANNING J. R., *Phys. Rev.* **136**, A1759 (1964).
25. MANNING J. R., *Phys. Rev.* **154**, 561 (1967).
26. MULLEN J. G., *Phys. Rev.* **121**, 1649 (1961).
27. LEVY J. and NIESSEN P., *J. Mat. Sci.* **5**, 96 (1970).
28. HIRONE T. and YAMAMOTO H., *J. phys. Soc. Japan* **16**, 455 (1961).
29. HIRONE T., MIURA S., SUZUOKA T., *J. phys. Soc. Japan* **16**, 2456 (1961).
30. BERNARDINI J., *Scripta Metall.* (to be published).
31. BOCQUET J. L., private communication.
32. KHAR'KOV E. I. and KUZ'MENKO P. P., *Ukr. Fiz. Zhur.*, **5**, 428 (1960).
33. WEVER H., *Z. Elektrochem.* **60**, 1170 (1956).
34. GRÖNE A. R., *J. Phys. Chem. Solids* **20**, 88 (1961).
35. KUZ'MENKO P. P., OSTROVSKII L. F. and KOVAL'CHUK V. S., *Soviet Phys. solid State* **4**, 356 (1962).
36. NGUYEN VAN DOAN, *Thesis*, Orsay (1970).

J. Phys. Chem. Solids Pergamon Press 1971. Vol. 32, pp. 2145–2149. Printed in Great Britain.

SPIN–SPIN RELAXATION NEAR THE CURIE POINT*

D. L. HUBER
Department of Physics, University of Wisconsin, Madison, Wisc. 53706, U.S.A.

(*Received* 18 *December* 1970)

Abstract—The electronic spin–spin relaxation time, T_2, is calculated for Heisenberg ferromagnets in the region immediately above the Curie point. The calculation, which pertains to zero field, predicts that $1/T_2$ diverges as $\chi_T^{3/4}$ where χ_T is the isothermal susceptibility. The relative efficiencies of the dipolar spin–spin relaxation and exchange induced spin diffusion are compared. For systems with parameters comparable to EuO spin–spin relaxation dominates for temperatures such that the ratio of the correlation length to lattice parameter is greater than two. In systems having the parameters of iron dipolar effects are much less important.

1. INTRODUCTION

THE PURPOSE of this paper is to examine the effects of the dipolar interaction on the relaxation of the fluctuations in the magnetization in a ferromagnet in which special emphasis is placed on the region immediately above the Curie point. Our objective is to calculate the spin–spin relaxation time and to compare the efficiency of dipolar induced spin–spin relaxation with the more familiar exchange-induced spin diffusion.

The stimulus for this paper comes from recent neutron scattering experiments which have been carried out in the critical region in a variety of ferromagnetic and antiferromagnetic materials[1–3]. Above the critical temperature the inelastic scattering measurements which are taken at small momentum transfer directly probe the decay rates of the long wavelength spin fluctuations. In the conventional interpretation of these experiments the decay rate for cubic systems is written Dq^2 in the long wavelength limit, with D being the spin diffusion constant and q the wave vector of the fluctuation. The dependence on q^2 reflects the fact that the operator for the total magnetization commutes with the Heisenberg (isotropic) exchange interaction. If only the exchange interaction is present the long wavelength fluctuations decay slowly with a rate which goes to zero in the small q limit.

When in addition to the exchange interaction dipolar terms are included in the Hamiltonian the total magnetization is no longer a constant of the motion. As a consequence there exists a second decay rate associated with the dipolar interaction which does not go to zero in the long wavelength limit. We wish to determine the range of wave vector and temperature for which this rate dominates the decay of the fluctuations.

It should be noted that calculations of the spin–spin relaxation time in zero field for purely dipolar systems were reported by Broer[4] nearly thirty years ago. Wright, in a later paper, examined the decay rates in systems where both dipolar and exchange interactions were present[5]. An analysis of T_2 which is closer in spirit to the present calculation has also been given by Kubo and Tomita[6]. However the calculations in all of these papers were limited (for the most part) to temperatures far above the Curie point where it was legitimate to use the infinite temperature approximation in the evaluation of various statistical averages.

The calculation of the spin–spin relaxation time also has many points in common with the calculation of the electron paramagnetic resonance linewidth. There is a difference however in that the EPR calculation pertains to a magnetic system in a finite magnetic field. Since the second order phase transition is present only at zero field it is expected that differences between finite and zero field relaxation times may be especially significant near the Curie temperature, T_c.

---

*Research supported by the National Science Foundation.

Kawasaki in a recent paper, has investigated the EPR width near T_c[7]. He concludes that at small fields it diverges as $\chi_T^{3/4}$, where χ_T is the isothermal susceptibility. We also find the $\chi_T^{3/4}$ behavior. In addition we are able to obtain a numerical estimate for T_2.

2. CALCULATION

We write the Hamiltonian for the magnetic system in the form

$$\mathscr{H} = -\sum_{(i,j)} 2J_{ij}\mathbf{S}_i\,.\,\mathbf{S}_j + g^2\mu^2 \sum_{(i,j)} (1/r_{ij})^3 \times (\mathbf{S}_i\,.\,\mathbf{S}_j - 3(\mathbf{r}_{ij}\,.\,\mathbf{S}_j)(\mathbf{r}_{ij}\,.\,\mathbf{S}_i)r_{ij}^{-2}). \quad (1)$$

The first term in (1) is the exchange interaction and the second represents the dipolar coupling. The symbol g denotes the g-factor, μ is the Bohr magneton, and the sum is over pairs of spins (i,j) whose separation is $\mathbf{r}_{ij}$. We also exclude crystal field effects.

In order to study the dynamics of the system we introduce the relaxation function for the operator A, $(A(t),A)$, by

$$(A(t),A) = \int_0^\beta d\lambda\, \langle \exp[(\lambda + it/\hbar)\mathscr{H}]A \times \exp[-(\lambda + it/\hbar)\mathscr{H}]A^+\rangle - \beta\langle A\rangle\langle A^+\rangle, \quad (2)$$

where $\beta = 1/KT$ and the brackets denote a statistical average.

As shown by Mori and Kawasaki[8] when the decay rate of $(\dot{A}(t),\dot{A})$ is much faster than the decay rate of $(A(t),A)$ then $(A(t),A)$ can be approximated by $(A,A)\exp[-\Gamma_{AA}t]$ where

$$\Gamma_{AA} = (A,A)^{-1}\int_0^\infty (\dot{A}(t),\dot{A})\,dt, \quad (3)$$

with $\dot{A} = (i\hbar)^{-1}[A,\mathscr{H}]$.

In our calculation we take the operator A to be the z component of the magnetization

$$M_z = g\mu \sum_i S_{zi}, \quad (4)$$

and identify Γ with the inverse of the spin–spin relaxation time $1/T_2$.

Evaluating the commutator $[M_z, \mathscr{H}]$ where $\mathscr{H}$ is given by equation (1) leads to the result

$$\dot{M}_z = -3g^3\frac{\mu^3}{\hbar}\sum_{i,j} (\mathbf{r}_{ij}\times\mathbf{S}_i)_z(\mathbf{r}_{ij}\,.\,\mathbf{S}_j)(r_{ij})^{-5}, \quad (5)$$

where the sum is over both i and j $(i \neq j)$.

Thus, formally, the spin–spin relaxation time is given by

$$1/T_2 = \chi_T^{-1}\int_0^\infty dt(\dot{M}_z(t),\dot{M}_z) \quad (6)$$

where $\dot{M}_z$ is given by equation (5) and χ_T by

$$\chi_T = (M_z, M_z). \quad (7)$$

Equation (6) is a general expression for the relaxation time which is valid at arbitrary temperatures above T_c. To evaluate T_2 near T_c we will use approximation methods developed for the calculation of the spin diffusion constant in the critical region[9, 10]. We begin by expanding the spin operators in a Fourier series

$$S_{\alpha l} = \frac{1}{N}\sum_{\mathbf{q}} e^{i\mathbf{q}\cdot\mathbf{r}_l}S_\alpha(\mathbf{q}), \quad (8)$$

where $\alpha = x$, y, or z. N is the number of spins, and the sum is over the Brillouin zone. The dipolar interaction is likewise expanded in terms of the dipolar sums $U_{\alpha\beta}(\mathbf{q})$:

$$(3(\mathbf{r}_{ij})_\alpha(\mathbf{r}_{ij})_\beta - \delta_{\alpha\beta}(r_{ij})^2)(r_{ij})^{-5} = \frac{1}{N}\sum_{\mathbf{q}} \times e^{i\mathbf{q}\cdot\mathbf{r}_{ij}}U_{\alpha\beta}(\mathbf{q}); \quad (9)$$

the equation for $\dot{M}_z$ is then rewritten in terms of $S_\alpha(\mathbf{q})$ and $U_{\alpha\beta}(\mathbf{q})$. It is apparent from equation (5) that $(\dot{M}_z(t), \dot{M}_z)$ is a four-spin relaxation function. We replace this function by its value obtained in the Random Phase Approximation (RPA), i.e.

$$\begin{aligned}&(S_\alpha(\mathbf{q}_1,t)S_\beta(\mathbf{q}_2,t), S_\gamma(\mathbf{p}_1)S_\delta(\mathbf{p}_2)) \xrightarrow[\text{RPA}]{}\\ &KT[\delta_{\alpha\gamma}\delta_{\beta\delta}\delta_{\mathbf{q}_1\mathbf{p}_1}\delta_{\mathbf{q}_2\mathbf{p}_2}\\ &+\delta_{\alpha\delta}\delta_{\beta\gamma}\delta_{\mathbf{q}_1\mathbf{p}_2}\delta_{\mathbf{q}_2\mathbf{p}_1}]\times(S(\mathbf{q}_1,t)S(\mathbf{q}_1)) \, . \, (S(\mathbf{q}_2,t),\\ &S(\mathbf{q}_2))\end{aligned} \qquad (10)$$

where we have made use of the fact that $(S_\sigma(\mathbf{q},t), S_\alpha(\mathbf{q}))$ is independent of α above T_c.

In the RPA $1/T_2$ is written

$$\begin{aligned}1/T_2 = KTg^6\mu^6\hbar^{-2}\chi_T^{-1}\frac{1}{N^2}\Sigma_{\mathbf{q}}[(U_{xx}(\mathbf{q})\\ -U_{yy}(\mathbf{q}))^2+4U_{xy}(\mathbf{q})^2+U_{xz}(\mathbf{q})^2\\ +U_{yz}(\mathbf{q})^2]\int_0^\infty \mathrm{d}t(S(\mathbf{q},t),S(\mathbf{q}))^2.\end{aligned} \qquad (11)$$

To evaluate the integral we take $(S(\mathbf{q},t), S(\mathbf{q}))$ to be of the form

$$g^2\mu^2(S(\mathbf{q},t),S(\mathbf{q})) = \frac{\chi_T e^{-\Gamma_{\mathbf{q}}t}}{1+q^2\xi^2}, \qquad (12)$$

where ξ is the correlation length and Γ is a function of q and ξ which for cubic systems is given by

$$\Gamma_{\mathbf{q}} = Dq^2(1+A(q\xi)^2+\cdots), \qquad (13)$$

where D is the spin diffusion constant and A is on the order of unity. In taking this form for $\Gamma_{\mathbf{q}}$ we neglect the contribution of the dipolar coupling for finite q. This approximation should be sufficient for the purpose of obtaining an estimate of T_2.

The behavior of the functions $U_{\alpha\beta}(\mathbf{q})$ has been discussed by Cohen and Keffer[11]. In order to simplify the calculation we will again postulate cubic symmetry in which case

$$U_{\alpha\beta}(\mathbf{q}) = \frac{-4\pi q_\alpha q_\beta}{q^2 v}+\frac{4\pi}{3}\frac{\delta_{\alpha\beta}}{v}, \qquad (14)$$

where v is the volume per spin. As discussed in Ref. [11] equation (14) is valid for $10/R \ll q \ll 1/a$, where R is the sample size and a is the lattice parameter. Introducing equations (12), (13) and (14) into equation (11) leads to the result

$$1/T_2 = \frac{\pi KT_c\chi_T g^2\mu^2}{2Dv\xi\hbar^2 N}, \qquad (15)$$

where we have set $A = 1$ and have neglected the higher terms in the expansion of $\Gamma_{\mathbf{q}}$ in powers of $(q\xi)^2$, an approximation which is valid since the integrand falls off as $(q\xi)^{-6}$ for $q\xi \gg 1$.

Equation (15) is the principal result of the section. Its significance will be discussed in Section 3.

3. DISCUSSION

According to our current understanding of second order phase transitions in systems with Heisenberg exchange interactions we have (approximately)[7].

$$\chi_T \sim \xi^2,$$

$$D \sim \xi^{-1/2}.$$

As a consequence $1/T_2$ is predicted to diverge as $\chi_T^{3/4}$ near T_c. In order to obtain an estimate of the magnitude of T_2 we need to calculate ξ and D. For the former we make use of the approximate expression (static RPA).

$$\xi^2 = \lim_{q\to 0} 2(\chi_T/g^2\mu^2)(J(0)-J(\mathbf{q}))/q^2N, \qquad (16)$$

which has been shown to yield nearly the correct correlation length in antiferromagnets near the Neel point when χ_T is replaced by the staggered susceptibility[12].

For cubic lattices with nearest neighbor interactions (16) reduces to

$$\xi^2 = 2(\chi_T/g^2\mu^2)Ja^2N^{-1}, \tag{17}$$

where a is the lattice parameter. It is convenient to rewrite ξ^2 in terms of the dimensionless parameter

$$\Delta = 3KT_c\chi_T/g^2\mu^2S(S+1)N, \tag{18}$$

and then use an approximate version of the Rushbrooke–Wood equation to relate J to T_c[13]:

$$KT_c \approx \frac{ZJS(S+1)}{2}, \tag{19}$$

where Z is the number of nearest neighbors.

With the help of (18) and (19) we can rewrite (17) to read

$$\xi^2 = \frac{4\Delta a^2}{3Z}. \tag{20}$$

Comparison between experiment and theory has indicated that the self-consistent model of Bennett and Martin[9] and Kawasaki[10] provides a rather accurate (within a factor of two) estimate of the spin diffusion constant near T_c[14]. In our notation their formalism leads to the result

$$D = 0{\cdot}15Z^{3/4}\hbar^{-1}[S(S+1)]^{1/2} \times Ja^2\left(\frac{v}{a^3}\right)^{1/2}\Delta^{-1/4}, \tag{21}$$

where we have made use of equations (18) and (20).

With the help of equations (20) and (21) we can rewrite $1/T_2$ in the form

$$\frac{\hbar}{T_2} = 3[S(S+1)]^{1/2}\left(\frac{g^4\mu^4}{Ja^6}\right)\frac{\Delta^{3/4}}{Z^{1/4}}\left(\frac{a^3}{v}\right)^{3/2}. \tag{22}$$

It should be noted that the expression for T_2 given above is similar to the relaxation time obtained at high temperature in the exchange narrowing limit[6] except that it is enhanced by a dimensionless factor proportional to $\Delta^{3/4}$. This enhancement reflects both the increase in range of the static correlations and the thermodynamic slowing down of the spin fluctuations.

As we have noted for sufficiently small wave vectors the dipolar mechanism will dominate the decay of the spin fluctuations. Since the diffusive behavior is restricted to the region $q \leqslant \xi^{-1}$ spin diffusion will be unimportant for values of Δ which exceed a characteristic Δ^* obtained by equating $D\xi^{-2}$ to $\hbar/T_2$. We find

$$\Delta^* = 0{\cdot}2Z\left(\frac{v}{a^3}\right)\frac{Ja^3}{g^2\mu^2}. \tag{23}$$

As an example we consider EuO for which $J = 1{\cdot}1 \times 10^{-16}$ ergs[15] $a = 5{\cdot}1$ Å, $g = 2$, $Z = 12$ and $v = a^3/4$. We have

$$\Delta^* \simeq 26, \qquad \text{(EuO)}$$

which indicates that the decay of the long wavelength fluctuations ($q < \xi^{-1}$) is dominated by dipolar processes for temperatures such that the correlation length is greater than 10 Å. On the other hand for iron $J = 1{\cdot}4 \times 10^{-14}$ ergs[14], $Z = 8$, $a = 2{\cdot}9$ Å, $g = 2{\cdot}15$ and $v = a^3/2$ from which we obtain

$$\Delta^* \simeq 700, \qquad \text{(Fe)}$$

indicating a much weaker effect.

The principal conclusion of this paper is that dipolar interactions can have a very pronounced effect on the decay of the long wavelength spin fluctuations near the Curie point. Because of this considerable care must be exercised in the interpretation of neutron scattering data in this region, particularly for systems where $\Delta^* \leqslant 10^2$.

With regard to the approximations introduced in the calculation we make the following comments. First, although we can not make a precise estimate of the errors associated with the RPA we have reason to believe that they will not significantly affect our results. Calculations embodying basically the same approximations have led to estimates of the decay rates of the fluctuations in the staggered magnetization in antiferromagnets which are in agreement with experiment to better than a factor of two[16, 17]. Second we must emphasize that our calculation is not appropriate for temperature such that $\Delta > \Delta^*$. In this region one must handle the dipolar and exchange interactions on an equal footing and include the contribution of the former to the decay of $(S(\mathbf{q}, t), S(\mathbf{q}))$ in equation (11). Third, although calculations have been carried out for cubic systems the $\chi_T^{3/4}$ divergence in $1/T_2$ is a result which is independent of the lattice symmetry as long as the exchange interaction is isotropic and crystal field terms can be neglected.

Our final point concerns the effects of dipolar interactions in Heisenberg antiferromagnets. An analysis similar to that outlined here indicates that their contribution to the decay of the fluctuations in the total magnetization may be much smaller than in ferromagnets. The reason for this difference appears in equation (11). In evaluating the sum over $\mathbf{q}$ near the Néel point it is necessary to examine the contributions from $\mathbf{q} \approx 0$ and $\mathbf{q} \approx \mathbf{K}_0$, where $\mathbf{K}_0$ is the reciprocal lattice vector in the ordered state. Near T_N the uniform field susceptibility is slowly varying while the diffusion constant is predicted to diverge as $\xi^{1/2}$[7]. Consequently the contribution from the small $\mathbf{q}$ region goes to zero at T_N. The magnitude of the contributions from $\mathbf{q} \approx \mathbf{K}_0$ is more difficult to estimate. For simple and body centered cubic lattices the functions $U_{xx}(\mathbf{q}) - U_{yy}(\mathbf{q})$, $U_{xy}(\mathbf{q})$, $U_{xz}(\mathbf{q})$, and $U_{yz}(\mathbf{q})$ vanish for $\mathbf{q} = \mathbf{K}_0$[11]. Because of this the summation is not dominated by the contributions from the critical fluctuations and hence $1/T_2$ is predicted to be non-divergent near T_N. For lattices where these functions are not zero $1/T_2$ is predicted to diverge as $\xi^{5/2}$ as the Néel point is approached from above. The $\xi^{5/2}$ divergence is similar to the behavior predicted for the EPR linewidth in the small field limit[7].

REFERENCES

1. COLLINS M. F., MINKIEWICZ V. J., NATHANS R., PASSELL L. and SHIRANE G., *Phys. Rev.* **179**, 417 (1969).
2. LAU H. Y., CORLISS L. M., DELAPALME A., HASTINGS J. M., NATHANS R. and TUCCIARONE A., *Phys. Rev. Lett.* **23**, 1225 (1969).
3. SCHULHOF M. P., HELLER P., NATHANS R. and LINZ A., *Phys. Rev. Lett.* **24**, 1184 (1970).
4. BROER L. J. F., *Physica* **10**, 801 (1943).
5. WRIGHT A., *Phys. Rev.* **76**, 1826 (1949).
6. KUBO R. and TOMITA K., *J. phys. Soc. Japan* **9**, 888 (1954).
7. KAWASAKI K., *Prog. theor. Phys.* **39**, 285 (1968).
8. MORI H. and KAWASAKI K., *Prog. theor. Phys.* **27**, 529 (1962).
9. BENNETT H. S. and MARTIN P. C., *Phys. Rev.* **138**, A608 (1965).
10. KAWASAKI K., *J. Phys. Chem. Solids* **28**, 1277 (1967).
11. COHEN M. H. and Keffer F., *Phys. Rev.* **99**, 1128 (1955).
12. TUCCIARONE A., CORLISS L. M. and HASTINGS J. M., *J. appl. phys.* **42**, 1378 (1971).
13. RUSHBROOKE G. S. and WOOD P. J., *Mol. Phys.* **1**, 257 (1958).
14. KRUEGER D. A. and HUBER D. L., *Solid State Commun.* **6**, 869 (1968). The theoretical curves in this paper are to be compared with recent measurements reported by Bourdonnay *et al.* (*Phys. Lett.* **31A**, 561 (1970)).
15. McGUIRE T. R., ARGYLE B. F., SHAFER M. W. and SMART J. S., *J. appl. phys.* **34**, 1345 (1963).
16. HUBER D. L. and KRUEGER D. A., *Phys. Rev. Lett.* **24**, 111 (1970).
17. RIEDEL E. and WEGNER F., *Phys. Lett.* **32A**, 273 (1970).

J. Phys. Chem. Solids Pergamon Press 1971. Vol. 32, pp. 2151–2161. Printed in Great Britain.

IMPACT IONIZATION IN *p*-TYPE InSb

C. L. DICK, Jr. and B. ANCKER-JOHNSON
Boeing Scientific Research Laboratories and University of Washington,* Seattle,
Wash. 98124, U.S.A.

(*Received* 14 *December* 1970)

Abstract – Impact ionization in *p*-InSb is shown to be initiated by injected electrons. At sufficiently high average electric field strengths, $\gtrsim 1$ kV/cm, impact ionization begins next to the cathode. An impact ionization wavefront forms there and propagates along the sample with a velocity $v_{it} = 3{\cdot}2 \times 10^8$ cm/sec at 77 K. At moderate field strengths an impact ionization wavefront is initiated at some plane between the cathode and anode. Before its initiation in such a case, injected electrons exclusively propagate in a well defined front at 10^7 cm/sec, then when the field ahead of the injected front reaches ~ 490 V/cm, impact ionization is initiated and the impact ionization wavefront propagates to the anode with v_{it}. After the impact ionization wavefront reaches the anode, carrier density grows exponentially to a steady-state magnitude. The growth rate dependence on field strength is best expressed by $g(E) \propto \exp(0{\cdot}8 \times 10^6/E^2)$. Thus the energy dependence of the electrons during impact ionization in *p*-InSb at 77 K appears to be Maxwellian.

1. INTRODUCTION

IMPACT ionization in *p*-InSb is initiated by an entirely different mechanism than impact ionization in *n*-InSb. Carrier multiplication in *p*-type is initiated by injected electrons engaging in ionizing collisions[1]. The resulting impact ionization wavefront propagates along the sample length leaving in its wake a high density electron-hole plasma. In *n*-type the thermal equilibrium electrons initiate impact ionization when they are sufficiently accelerated.

Since the injection of nonequilibrium electrons plays such an important role in the impact ionization process in *p*-InSb, injection is briefly reviewed first. Then the physical mechanism responsible for ionization in *p*-InSb is described and experimental verification presented. Finally, the first estimates of the impact ionization generation rate in *p*-InSb are given.

2. INJECTION PRECEDING IMPACT IONIZATION

Electric field strengths from a few V/cm to ~ 500 V/cm in *p*-InSb produce copious injection of approximately equal densities of electrons and holes[2, 3]. The subject of dynamic and steady-state injection of electrons and holes in *p*-InSb is treated in detail in a recent paper[4]. It is shown that excess electrons are injected at the cathode and propagate to the anode behind a well-defined leading edge, or front, with an ambipolar velocity that depends on field intensity. After the front reaches the anode, the excess carrier density grows exponentially with time to the nonequilibrium steady-state. The agreement between theory[4–6] and experiment[4, 6] is good.

In the present work, injection properties are studied at high field strengths, namely just below the threshold for impact ionization in *p*-InSb, E_{itp}, a threshold that is considerably higher than in *n*-InSb, $E_{itp} > E_{itn}$, as will be shown. This study necessarily involves measuring conduction characteristics on shorter time scales than used previously[4], since the characteristic times associated with injection decrease with increasing field intensities.

An example of excess carrier conductivity, σ_{ex}, and electric field strength, both as functions of time and of distance along the current axis of the sample, x, are shown in

---

*Research on plasmas in semiconductors in the Department of Electrical Engineering is partially supported by the National Science Foundation.

Fig. 1 for a moderate applied voltage.* The measurement technique has been described [7]. This method has a resolution of ~ 10 μm in space and ~ 1 nsec in time, and the absolute conductivity and electric field strength measurements are accurate to within ~ 15 per cent. The current, I, and field strength averaged over the sample length, E, for the same applied voltage as used to obtain the data of Fig. 1 are displayed in Fig. 2 as functions of time. For $t \leq 35$ nsec, E is constant to within ±6 per cent, but decreases as I begins to increase significantly. It is necessary to allow E to decrease in order to prevent the sample from conducting a destructively high current.

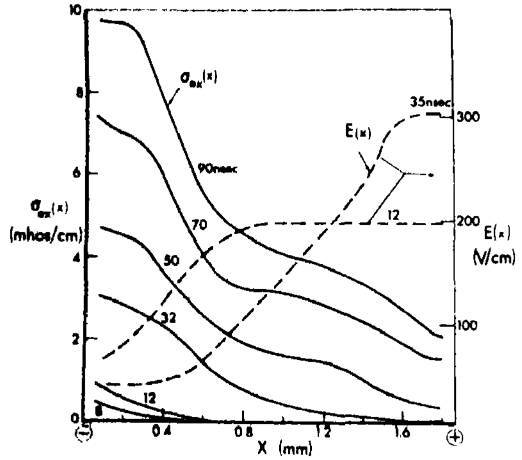

Fig. 1. Excess carrier conductivity (left hand ordinate) and field strength (right hand ordinate) in p-InSb as functions of distance between cathode and anode and as a function of time, for a moderate average field of 170 V/cm. By 12 nsec a considerable nonuniformity in E has developed and this nonuniformity is even more pronounced by 32 nsec.

The observed properties of $\sigma_{ex}(x, t)$ and $E(x, t)$ in Fig. 1, along with those of $E(t)$ in Fig. 2, $t \leq 90$ nsec, yield the following information:

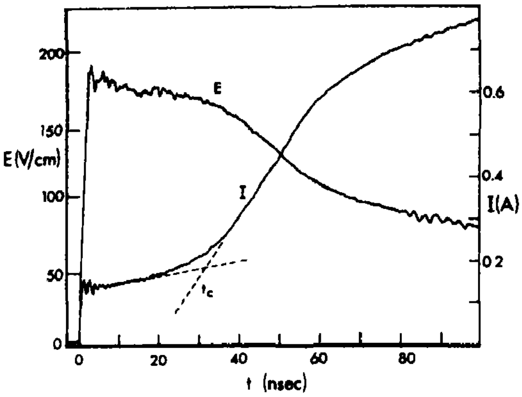

Fig. 2. Current and average field strength as functions of time corresponding to the conductivity data of Fig. 1.

1. A front of injected carriers propagates from cathode to anode in 32 nsec under the influence of a field $E = 170$ V/cm.
2. The propagating front results in a spatially nonuniform increase in injected carrier density, both before and after the front arrives at the anode in a time $t_c = 32$ nsec.
3. The arrival of the conductivity front at the anode, as determined by laborious spatial measurements, Fig. 1, coincides with t_c, simply obtained from $I(t)$ in Fig. 2.
4. An average velocity for the front is defined by the total sample length divided by t_c; it is $5{\cdot}6 \times 10^6$ cm/sec in this example.
5. Within the sample, $E(x)$ decreases behind the front and increases ahead of it, as $E(x)$ for 12 nsec (constant voltage conditions) and 32 nsec (non-constant voltage) in Fig. 1 illustrate.

These results are in agreement with those obtained at lowered applied voltages [4].

This example of excess conduction resulting from injection leads to the following model of impact ionization in p-InSb.

3. THE ORIGIN OF IMPACT IONIZATION IN p-InSb

Impact ionization in p-InSb at 77 K is accompanied by a very nonuniform $E(x)$ distribution. A low field region has been observed [8, 9] to propagate a 5 mm length between cathode and anode in typically 3

---

*Data for samples cut from three single crystals appear in this paper. The crystals are identified in each figure and the thermal equilibrium properties of each crystal are included in the figures.

Fig. 1 for a moderate applied voltage.* The measurement technique has been described [7]. This method has a resolution of ~ 10 μm in space and ~ 1 nsec in time, and the absolute conductivity and electric field strength measurements are accurate to within ~ 15 per cent. The current, I, and field strength averaged over the sample length, E, for the same applied voltage as used to obtain the data of Fig. 1 are displayed in Fig. 2 as functions of time. For $t \leq 35$ nsec, E is constant to within ±6 per cent, but decreases as I begins to increase significantly. It is necessary to allow E to decrease in order to prevent the sample from conducting a destructively high current.

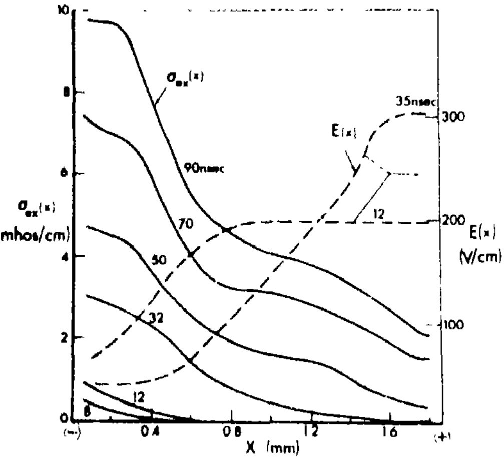

Fig. 1. Excess carrier conductivity (left hand ordinate) and field strength (right hand ordinate) in p-InSb as functions of distance between cathode and anode and as a function of time, for a moderate average field of 170 V/cm. By 12 nsec a considerable nonuniformity in E has developed and this nonuniformity is even more pronounced by 32 nsec.

The observed properties of $\sigma_{ex}(x, t)$ and $E(x, t)$ in Fig. 1, along with those of $E(t)$ in Fig. 2, $t \leq 90$ nsec, yield the following information:

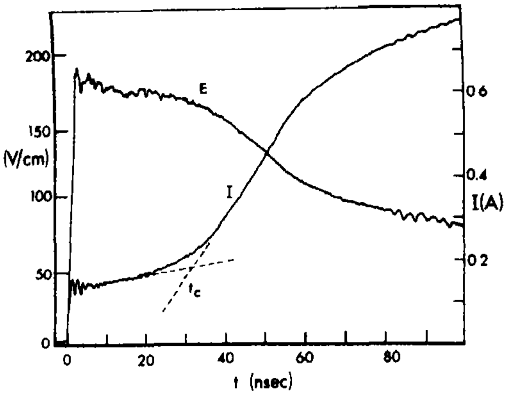

Fig. 2. Current and average field strength as functions of time corresponding to the conductivity data of Fig. 1.

1. A front of injected carriers propagates from cathode to anode in 32 nsec under the influence of a field $E = 170$ V/cm.

2. The propagating front results in a spatially nonuniform increase in injected carrier density, both before and after the front arrives at the anode in a time $t_c = 32$ nsec.

3. The arrival of the conductivity front at the anode, as determined by laborious spatial measurements, Fig. 1, coincides with t_c, simply obtained from $I(t)$ in Fig. 2.

4. An average velocity for the front is defined by the total sample length divided by t_c; it is $5 \cdot 6 \times 10^6$ cm/sec in this example.

5. Within the sample, $E(x)$ decreases behind the front and increases ahead of it, as $E(x)$ for 12 nsec (constant voltage conditions) and 32 nsec (non-constant voltage) in Fig. 1 illustrate.

These results are in agreement with those obtained at lowered applied voltages [4].

This example of excess conduction resulting from injection leads to the following model of impact ionization in p-InSb.

3. THE ORIGIN OF IMPACT IONIZATION IN p-InSb

Impact ionization in p-InSb at 77 K is accompanied by a very nonuniform $E(x)$ distribution. A low field region has been observed [8, 9] to propagate a 5 mm length between cathode and anode in typically 3 nsec when very high average fields, ⩾ 700 V/cm, are applied. In *n*-InSb, fields in excess of $E_{itn} \approx 250$ V/cm impact ionize in a much shorter time, < 0·5 nsec[9]. Furthermore, the time required for the establishment of a steady-state condition of impact ionization depends on the sample length in *p*-InSb, but is independent of length in *n*-InSb[9]. It is proposed, therefore, that neither the equilibrium electrons nor holes initiate impact ionization, presumably because the former are too few ($\sim 10^5$ cm^{-3})* to start an avalanche and the latter are too massive ($m_h^*/m_e^* \approx 30$)† to acquire the requisite energy for ionizing collisions in such short times at the applied fields (< 2500 V/cm). Rather, injected electrons are required to initiate the observed impact ionization in *p*-InSb. As will be shown in the next section, the following model accounts for the observed conduction characteristics associated with impact ionization in *p*-InSb.

---

*Data for samples cut from three single crystals appear in this paper. The crystals are identified in each figure and the thermal equilibrium properties of each crystal are included in the figures.

When electrons are injected by fields greatly exceeding E_{itp}, e.g. $E = 1200$ V/cm, they initiate an avalanche process once they penetrate the sample a short distance, too short to measure with existing techniques but probably ~ 10 μm, the best estimate of the mean free path for impact ionization in InSb [13]. (If the average drift velocity of electrons is $\sim 10^8$ cm/sec in fields large enough to cause impact ionization[14], they drift ~ 10 μm in a time of the same order as their mean free time, $\sim 10^{-11}$ sec.) After the injected electrons produce impact ionization in a thin layer at the cathode, the field there drops and increases elsewhere in the sample because the source impedance is much less than the sample impedance. This is true even when $E(t)$ is not constant (compare the 32 nsec curve in Fig. 1). The newly produced electrons at the front of this thin layer then acquire drift velocities even greater than the injected electrons had (although the enhancement may not be very large because of the hot electron effect[14]) and cause impact ionization in an adjacent layer of the sample. Thus an impact ionization front, initiated adjacent to the cathode, propagates along the length of the sample to the anode.

If the applied voltage results in fields less then 1200 V/cm, the injected electrons will penetrate more than a mean free path for impact ionization into the sample before an impact ionization wavefront is initiated. If the applied voltage establishes an average field of less than ~ 300 V/cm, a wavefront composed of injected electrons only will traverse the sample.

This proposed model for impact ionization in *p*-InSb is expected to pertain to any *p*-type semiconductor in which the hole/electron mass ratio is large and the thermal equilibrium electron density is small. The next section presents experimental verification of this model.

4. EXPERIMENTAL VERIFICATION OF THE IMPACT IONIZATION WAVEFRONT

Measurements of conductivity and field strength as functions of distance, and measurements of field strength and current as functions of time, coupled with measurements of the injection and impact ionization wavefront velocities are discussed below and compared with the model for impact ionization in *p*-InSb that was proposed in the preceding section.

4.1 *Conductivity measurements*

By adjusting the magnitude of the voltage applied to *p*-InSb it is possible to create excess carrier conduction in one of three characteristic modes:

1. Injection only as discussed in Section 2. Everywhere within the sample during this mode $E(x) < E_{itp}$.

2. 'Mixed' conduction. This mode occurs at intermediate applied voltages that produce

---

*Calculated from $n_i^2 \simeq n_0 p_0 \approx 10^{19}$ cm^{-6} and $p_0 \approx 10^{14}$ cm^{-3}. The value of n_i^2 comes from an extrapolation of calculations previously reported[10].

†The hole effective mass is 0·45 m_e[11] and the electron effective mass is 0·015 m_e[12].

injection only until $E(x)$ ahead of the injected plasma front rises sufficiently to allow the electrons at the leading edge to produce impact ionization.

3. Impact ionization immediately following injection of electrons a very short distance into the sample. In this mode $E(x) > E_{IIp}$ during the entire pulse duration.

Figure 3 shows $\sigma_{ex}(x)$ parametric in time for the three different modes of conduction described. Figure 3(a) includes some of the same data as Fig. 2 but contains more detail at early times.

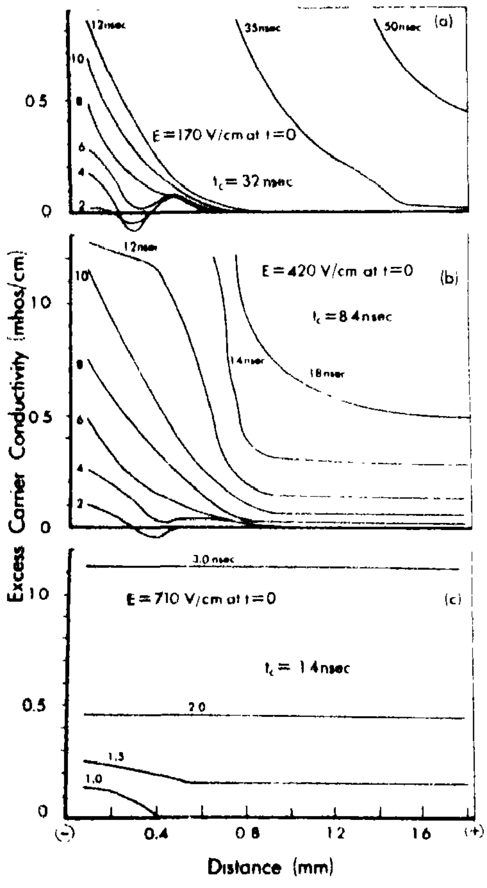

Fig. 3. Excess carrier conductivity as a function of distance for: (a) An applied voltage small enough to produce injection only. (These curves are from the same set of measurements as those in Fig. 2.) (b) An applied voltage magnitude that produces conduction caused by both injected carriers and carriers resulting from impact ionization. (c) An applied voltage so high that the conduction is predominantly the result of impact ionization.

In Fig. 3(a) $E(x)$ is everywhere less than E_{IIp}, hence injection only is seen. The resulting σ_{ex} profile is shown for $2 \leqslant t \leqslant 12$ nsec after the application of power, for a time (35 nsec) shortly after the front arrives at the anode ($t_c = 32$ nsec), and for a time during the exponential growth of carrier density (50 nsec). The depletion layer, previously reported[4], is seen at the earliest times.

Figure 3(b) shows injection only for 6 nsec, followed by impact ionization after the injected front has propagated 0·9 mm from the cathode toward the anode (compare the 6 and 8 nsec curves). Impact ionization begins in this case when the field ahead of the front has increased to 490 V/cm, as shown by Figs. 4 and 5(a) for $6 \leqslant t \leqslant 8$ nsec. Figure 5(a) shows E(x), corresponding to the applied voltage conditions of Fig. 3(b), for two times; just before the impact ionization wavefront is launched (6 nsec) and just after (8 nsec).

Once the ionization front is formed, it travels so fast through the remainder of the sample that, with advancing time, a uniformly

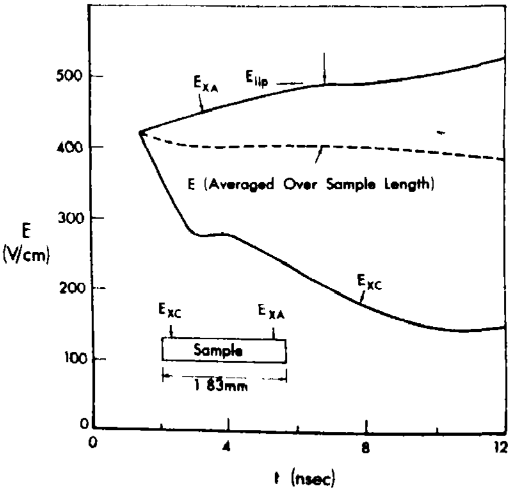

Fig. 4. Electric field intensity as a function of time for both $\bar{E}$, averaged over the sample length, and two specific $E(x)$, one near the cathode, E_{XC}, and the other near the anode, E_{XA}. These data are associated with the conductivity data of Fig. 3(b).

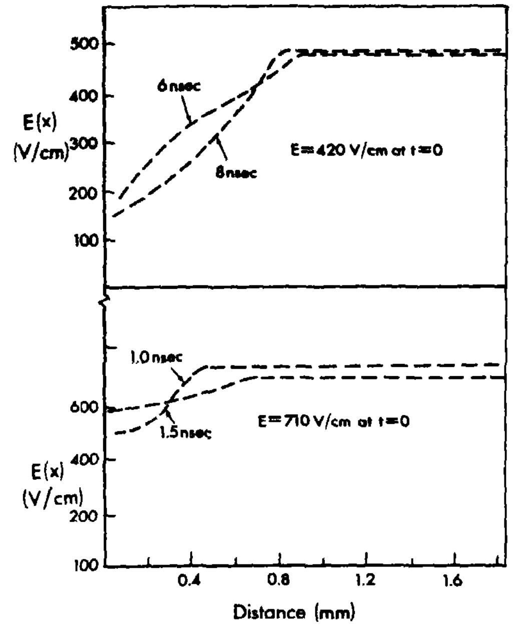

Fig. 5. Electric field strength as a function of distance for two different applied voltages: (a) corresponding to the conditions of Fig. 3(b); and (b) corresponding to the conditions of Fig. 3(c).

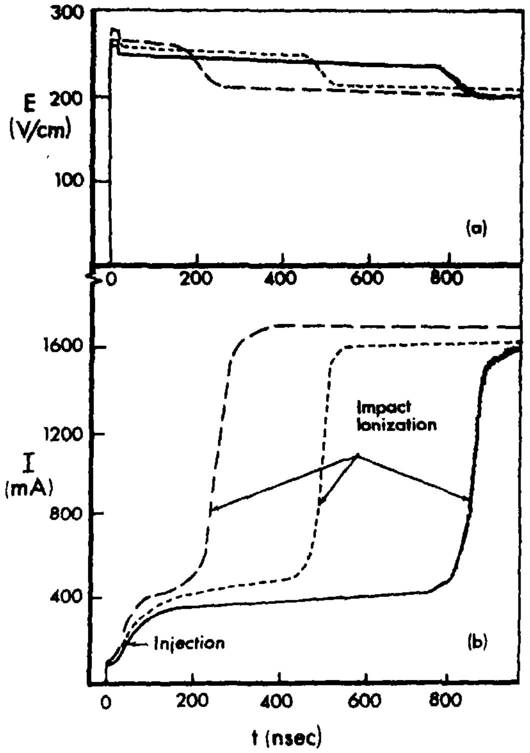

Fig. 6. (a) Electric field strength and (b) current, as functions of time for a case of conduction involving injection, then impact ionization, and finally in the nonequilibrium steady-state injection only. Sample length is 1·0 mm.

distributed, growing conductivity is observed in the anode half of the sample, Fig. 3(b). Figures 4 and 6 show more information about this mixed mode of conduction; the third mode, Fig. 3(c), is discussed after Figs. 4 and 6 are explained.

Figure 4 demonstrates that, during the injection front transit time, the field behind the front and near the cathode, E_{XC}, decreases and the field ahead of the front, near the anode, E_{XA}, increases. After the impact ionization front is launched, for this particular case at 7 nsec, the field near the cathode levels off, whereas the field near the anode continues to increase as it did during the injection phase of conduction. In both cases, the increase is caused by the nonuniform filling of the sample with excess carriers.

It is even possible for impact ionization to be initiated long after an injected front has passed completely through the sample. Indeed, even after the apparent establishment of a nonequilibrium steady-state, the initiation of impact ionization can occur, as illustrated by the lowest current curve and associated field intensity curve in Fig. 6. This phenomenon is a result of the nonuniform distribution of field strength. As previously shown[4] for relatively long samples, e.g. 1 cm, large fields exist adjacent to the anode due to a nonuniform distribution of the excess carriers. This nonuniform distribution is also exhibited by the ~ 2 mm sample in the moderate field case of Fig. 1. In this latter case, the $E(x)$ at later times, approaching steady-state (not shown in Fig. 1), are still higher adjacent to the anode than shown in the figures, while in the central 80 per cent of the sample the field is quite low and essentially uniform[4, 7]. These high fields near the anode are responsible, it is argued below, for the results in Fig. 6.

The curves of $E(t)$ and $I(t)$ for the lowest applied voltage in Fig. 6 show the following properties: An initial $E = 260$ V/cm decreases at ~ 10 nsec to 250 V/cm. This happens when the injected front reaches the anode, as is apparent from the sharp increase in I commencing also at ~ 10 nsec. The injected density thereafter grows exponentially, a characteristic previously observed[4–6], until $t \approx 150$ nsec. Beyond this time, until 800 nsec, there is little change in I because $\sigma_{ex}(x)$ is increasing very slowly. At ~ 800 nsec, the excess carriers are distributed such that the field adjacent to the anode is large enough to initiate impact ionization in this narrow region of the sample. Since there is then a large quantity of excess carriers adjacent to the anode, whereas at $t < 800$ nsec this was the region of least density, the current can increase rapidly until a new, much more uniform, distribution of excess carriers is attained. Upon establishment of the new distribution, it is probable that $E(x)$ everywhere drops below that value necessary to sustain impact ionization, and hence, injection only is needed to maintain the nonequilibrium steady-state conduction. A slight increase in the applied voltage, as the other two sets of curves in Fig. 6 show, results in the critical field for impact ionization in the high field region adjacent to the anode being reached earlier in time. Further increases in applied voltage result in the initiation of impact ionization before the injected front reaches the anode, as is discussed above and illustrated in Fig. 3(b).

The third characteristic process by which impact ionization occurs in p-InSb is demontrated by Fig. 3(c). When the applied voltage is high, so that, for example, $E = 710$ V/cm, very little injection has time to occur before an impact ionization front is initiated. In the example of Fig. 3(c), enough injection has occurred, by little more than 1·0 nsec after the onset of the applied power pulse, to trigger impact ionization at the leading edge ($x = 0{\cdot}45$ mm) of the injection front where $E(x)$ is 740 V/cm, Fig. 5(b). Figure 5(b) shows $E(x)$ corresponding to the applied voltage condition of Fig. 3(c) for two times, just before the impact ionization wavefront is launched (1 nsec) and shortly after (1·5 nsec). Once the injected electrons begin suffering ionizing collisions, there are many electrons available for more ionizing collisions because the generation rate is so high (see Section 5 below). The electrons just produced by the ionizing collisions are quickly accelerated to ionization energies because of their very low inertia, and so impact ionization is produced in a layer adjacent to the injected front. This process continues, so forming an impact ionization wavefront that propagates the remaining length of the sample.

From the data of Figs. 3(b) and (c), and 4 and 5, it is apparent that the threshold fields, E_{tip}, necessary to initiate impact ionization in p-InSb and the requisite times are quite different from the threshold field in n-InSb, $E_{tin} \approx 250$ V/cm, and the formation time, $< 0{\cdot}5$ nsec. In p-type for the examples given here, a field of 710 to 740 V/cm exists for ~ 1 nsec before impact ionization is evident, and with a lower applied voltage a field of 420 to 490 V/cm persists for ~ 7 nsec without producing impact ionization.

The lowest measured value of E_{tip} is 490 V/cm, Figs. 4 and 5(a). It is possible that impact ionization in p-InSb is produced at a somewhat lower field strength, but even at long times, e.g. μsec, slightly in excess of 400 V/cm are required[2, 3].

The fact that $E_{tip} > E_{tin}$ is a result of excess electrons being responsible for the initiation of impact ionization in p-InSb. There must be a combination of the presence of enough excess electrons to saturate the electron traps (this is discussed in Section 5 below), enough time for the trap saturation to take place, and enough field available to compensate for losses to the traps. Furthermore, E_{tip} is not a constant of the materials as is E_{tin}; the latter depends only on energy band structure since an adequate supply of carriers capable of producing ionization is readily available. This non-constancy of E_{iip} is traceable to the fact that conditions at the initiation of impact ionization differ widely in *p*-InSb, in contrast to the conditions in *n*-InSb. The differing conditions are the results of injection and the attendant distributions in space and time of the excess electrons and, therefore, in $E(x, t)$. Since the probability of an ionizing collision occurring depends not only on the magnitude of E, but also on the density of accelerated carriers, E_{iip} varies with injection conditions.

4.2 *Wavefront velocity measurements*

For the three conduction cases of Fig. 3 the values of the front transit times, t_r, determined from $I(t)$ as illustrated in Fig. 2, agree very well with front arrival times obtained from $\sigma_{ex}(x, t)$ data. This agreement was also found at lower applied voltages [4, 6].

Average front-velocity curves are shown in Figs. 7 and 8. These are generated by dividing the sample length by the observed t_r. The three modes of conduction shown in Fig. 3 can be seen also in Figs. 7 and 8. The velocity curves exhibit two saturation levels, most clearly seen in Fig. 8, dashed curve. The lower level at ~ 10^7 cm/sec is the maximum ambipolar drift velocity that the injected electrons can attain, in agreement with earlier experimental work [6, 15]. At higher fields than those responsible for ambipolar drift, the conduction becomes mixed. Thus, the measured velocity is an average of the injected-front velocity and the velocity of the impact-ionization front. Since the latter is initiated progressively earlier in time and nearer the cathode as the field is increased, the average velocity, Figs. 7 and 8, increases with E until the ionization starts next to the cathode. The higher saturation level, $3{\cdot}2 \times 10^8$ cm/sec, corresponds to the impact-ionization front-velocity, v_{ii}: electrons immediately upon injection produce impact ionization adjacent to the cathode and this excess conductivity region propagates to the anode.

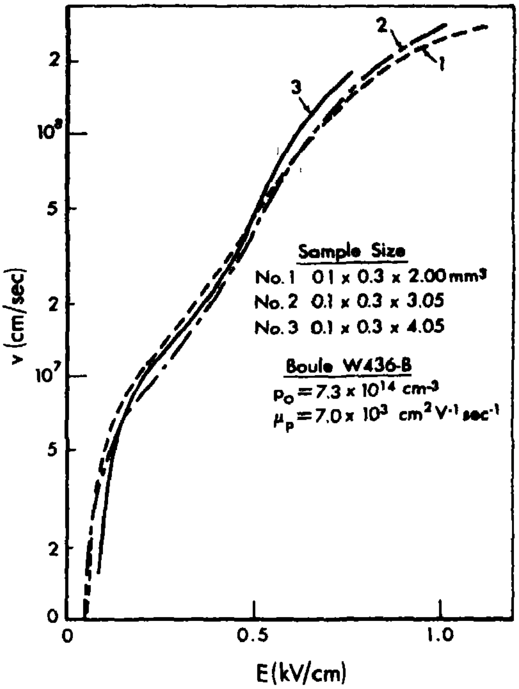

Fig. 7. Average front velocity as a function of average electric field strength, demonstrating that the velocity is independent of sample length.

A value of v_{ii} may also be obtained from conductivity data such as that recorded in Fig. 3(c). In this example, during ~ 0·4 nsec an ionization front propagates ~ 1·4 mm, in good agreement with the $3{\cdot}2 \times 10^8$ cm/sec determined from the $I(t)$ characteristics, Fig. 8.

Figure 7 demonstrates that the velocity measurements are independent of the sample length, hence a genuine transit time is measured. (The requirements of constant E and the maximum available pulse power prevented extending all of these curves to the same maximum E.)

The impact-ionization wavefront velocity and the maximum injected-front velocity are independent of the nature of the contacts, Fig. 8. Above 500 V/cm, a given field produces the same velocity, whereas when $E \leqslant 500$

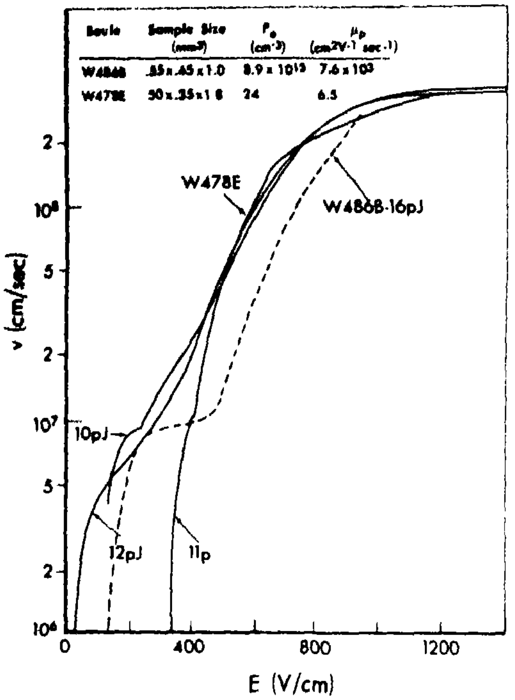

Fig. 8. Front velocity as a function of average electric field strength, showing the saturated ambipolar drift velocity (~ 10^7 cm/sec) and the impact-ionization front velocity ($3{\cdot}2 \times 10^8$ cm/sec) The effects of contacts on the velocity are also illustrated.

V/cm in samples of the same boule but with different contacts, a given average front velocity corresponds to very different fields. These results are as expected from the model: The three samples made from boule W478E have three different types of current-carrying contacts: 12*pJ* has good injectors, 10*pJ* has moderate injectors, 11*p* has very poor injectors. The resulting $v(E)$ dependencies below 500 V/cm, the field range dominated by injection, reflect the dissimilarity in the contacts. The ionization front velocity, however, is independent of the nature of the contacts, as expected, because only a relatively small number of injected electrons is necessary for its initiation.

The velocity of the impact-ionization front is independent of the equilibrium hole density, p_0, Fig. 9, over the limited range tested. This is as expected since the holes play no role in the impact ionization process according to the proposed model. Figure 9 also shows that v_{II} decreases with decreasing lattice temperature, T_l, for $T_l \leq 90$ K. This qualitative dependence is to be expected from the well known[16] dependence of electron mobility on T_l, i.e., the electron mobility also decreases for $T_l \leq 90$ K.

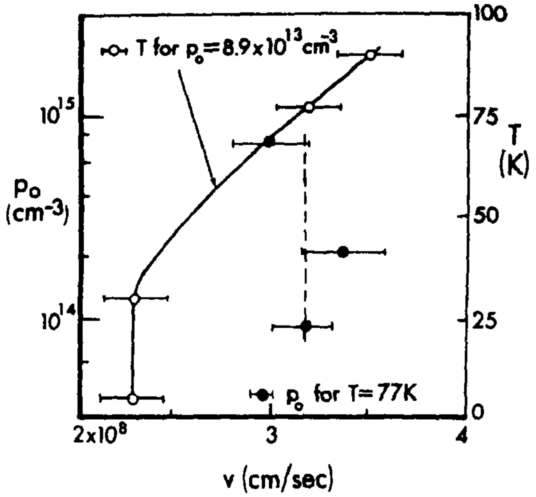

Fig 9 Impact-ionization front velocity as a function of temperature and equilibrium hole density.

The impact ionization front velocity is higher than any electron drift velocity yet reported (9×10^7 cm/sec) in InSb[14]. It is physically reasonable that the front velocity can somewhat exceed an average particle velocity; indeed there are many examples in physics of a disturbance propagating somewhat faster than the average particle in the disturbance.

The existence of an impact ionization wavefront in *p*-InSb and its high velocity suggest some possible device applications, as has been suggested[17]. One such application is a subnanosecond sequential switch. Side probes located as desired along the length of a bar of *p*-InSb may monitor either the potential or resistance, whichever is preferred. When the plasma front passes the probe location both these quantities drastically decrease. Probes displaced by, e.g. 1 mm, will be activated 0·3 nsec apart, thus the impact ionization wave may be utilized as a fast sequential switch.

5. GENERATION RATE MEASUREMENTS

The McGroddy–Nathan measurement technique[18] used to determine $g(E)$ in n-InSb must be modified slightly before it can be applied to measure $g(E)$ in p-InSb because of the existence of electron traps in this material. Laff and Fan[19] and more recently Hollis *et al.*[20] have shown that in p-InSb electron trapping times are $\sim 10^{-9}$ sec. The electron traps must be saturated before true generation rates can be determined. In Fig. 3(c), shortly after t_c, the excess carriers fill the sample uniformly and exponential growth occurs throughout the sample. Once exponential growth is observed, the electron traps are essentially saturated and an approximate $g(E)$ measurement can be made using this relation:

$$g(E) = \frac{1}{I'}\frac{dI}{dt}\bigg|_{t=t_c}, \qquad (1)$$

where I' is defined as I at $t = t_c$. An example of a measurement of I' and dI/dt is illustrated in Fig. 10. The applied voltage is constant to within 10 per cent during the determination of dI/dt. The results of the measurement of $g(E)$ in one p-InSb sample are shown in Fig. 11.

The generation data are plotted in Fig. 11 in a form suitable for comparison with the theory of generation by impact ionization at high E. At such E it is usual to assume (first by Wolff [21]) a symmetric or Maxwellian energy distribution function of the electrons. This assumption results in essentially all the carriers gaining the same amount of energy in the same time period. The general equation is then

$$g(E) = v_{\text{drift}} \times f_1(E) \times \exp(-C_H/E^2). \qquad (2)$$

The function f_1 depends so weakly on E that it is usually neglected. The constant C_H is defined[22, 23] so

$$C_H = \frac{3\epsilon_i\epsilon_H}{e^2\lambda_H^2}. \qquad (3)$$

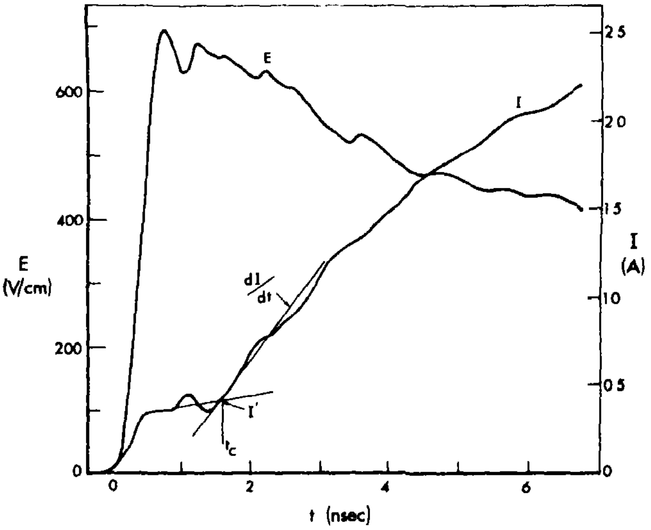

Fig. 10. Current (right hand ordinate) and average electric field strength (left hand ordinate), as functions of time, illustrating a typical $g(E)$ measurement in p-InSb.

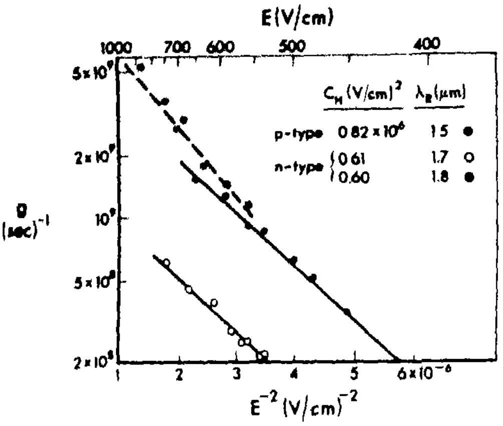

Fig. 11. Generation rate data plotted for comparison with an exp $(-C_H/E^2)$ dependency.

where ϵ_i is the ionization energy, ϵ_R is the optical ponon energy, e the electronic charge and λ_R the mean free path for optical phonon collisions. Also assumed in equation (2) is an isotropic scattering probability for optical phonon collisions and no electron–electron collisions.

The agreement between the functional dependence of $g(E)$ in the p-type sample and in the two n-type samples of Fig. 11 is very good. The resulting magnitudes of λ_R are given in Fig. 11, assuming[24] $\epsilon_i = 1{\cdot}1$, $\epsilon_{\text{gap}} = 0{\cdot}25$ eV and a value[25] of $\epsilon_R = 0{\cdot}0244$ eV. The absolute magnitude of $g(E)$ for the p-InSb sample compares well with that of the n-InSb samples. Thus, at these high E the assumptions of a symmetric energy distribution function and isotropic polar-optical scattering appear valid. Furthermore, the assumption of no recombination during the dI/dt measurement $(0{\cdot}9 < t < 3{\cdot}8$ nsec) appears to be confirmed.

6. CONCLUSIONS

Injected electrons are responsible for the initiation of impact ionization in p-InSb. The ionization process occurs along the length of a sample at the leading edge of an impact ionization wavefront. The wavefront velocity is $3{\cdot}2 \times 10^8$ cm/sec at 77 K, independent of thermal equilibrium hole density. The threshold field for impact ionization in p-InSb is much higher than the threshold field in n-InSb and depends on the injected electron density magnitude and spatial distribution, and on time. The impact ionization generation rate in p-InSb is 10^9 pairs/sec at $E = 550$ V/cm and depends on E as given by this expression: $\exp(0{\cdot}8 \times 10^6/E^2)$. As a result of this work the impact ionization process in bulk p-InSb is now well understood.

REFERENCES

1. ANCKER-JOHNSON B. and DICK C. L. Jr., *Solid State Commun.* **9**, 125 (1971) and DICK C. L. Jr and ANCKER-JOHNSON B., *Bull. Am Phys. Soc.* **14**, 746 (1969)
2. ANCKER-JOHNSON B., COHEN R. W. and GLICKSMAN M., *Phys. Rev.* **124**, 1745 (1961).
3. ANCKER-JOHNSON B., In *Semiconductors and Semimetals*, (Edited by R. C. Willardson and A. C. Beer), Vol. 1, p. 379, Academic Press, New York (1966).
4. ANCKER-JOHNSON B. and ROBBINS W. P., *J. appl. Phys* **42**, 762 (1971).
5. DEAN R. H., *J. appl Phys.* **40**, 596 (1969).
6. ANCKER-JOHNSON B., ROBBINS W. P. and CHANG D. B., *Appl. Phys. Lett.* **16**, 377 (1970).
7. ANCKER-JOHNSON B. and DICK C. L., Jr., *Appl. Phys. Lett.* **15**, 141 (1969).
8. ANCKER-JOHNSON B., *J. phys. Soc. Japan* **21 Suppl.**, 694 (1966).
9. ANCKER-JOHNSON B., *J. phys. Soc. Japan* **22**, 1156 (1967)
10. LANDSBERG P. T., *Proc. Phys. Soc. Lond.* **B70**, 282 (1957)
11. MOORADIAN A. and FAN H. Y., *Phys. Rev.* **148**, 873 (1966).
12. BURSTEIN E., PICUS G. S. and GEBBIE H. A., *Phys. Rev* **103**, 825 (1956)
13. DUMKE W. P., *Phys. Rev.* **167**, 783 (1968).
14. GLICKSMAN M. and HICENBOTHEM W. A., Jr., *Phys. Rev.* **129**, 1572 (1963).
15. ANCKER-JOHNSON B., *Proc. Intl Conf. on Physics of Semiconductors*, p. 813, Nauka, Moscow (1968)
16. HILSUM C. and ROSE-INNES A. C., *Semiconducting III-V Compounds*, p. 126, New York, Pergamon Press (1961).
17. DICK C. L. Jr. and ANCKER-JOHNSON B., IEEE Device Research Conference, June 29, 1970, Seattle, Paper No. II-B-8
18. McGRODDY J. C. and NATHAN M. I., *J. phys. Soc Japan* **21 Suppl.**, 437 (1966).
19. LAFF R. A. and FAN H. Y., *Phys. Rev.* **121**, 53 (1961).
20. HOLLIS J. E. L., CHOO S. C. and HEASELL E. L., *J. appl. Phys.* **38**, 1626 (1967)

21. WOLFF P. A., *Phys. Rev.* **95**, 1415 (1954).
22. SHOCKLEY W., *Solid State Electron.* **2**, 35 (1961).
23. MOLL J. L. and MAYER N., *Solid State Electron.* **3**, 155 (1961); MOLL J. L. and VAN OVERSTRAETEN R., *Solid State Electron.* **6**, 147 (1963); BARTELINK D. J., MOLL J. L. and MEYER N. I., *Phys. Rev.* **130**, 972 (1963).
24. POROWSKI S. A., PAUL W., McGRODDY J. C., NATHAN M. I. and SMITH J. E., Jr., *Solid State Commun.* **7**, 905 (1969).
25. NASLEDOV D. N., POPOV Yu. G. and SMETANNIKOVA Yu. S., *Fiz. tverd. Tela* **6**, 3728 (1964) [English Transl. *Soviet Phys.-solid State* **6**, 2989 (1965)].

J. Phys. Chem. Solids Pergamon Press 1971. Vol. 32, pp. 2163–2171. Printed in Great Britain.

A STUDY OF THE CRYSTAL FIELD PARAMETERS IN THULIUM GARNETS

PAUL H. E. MEIJER
Catholic University of America, Washington, D.C. 20017, U.S.A.
and
Naval Ordnance Laboratory, Silver Spring, Md. 20910, U.S.A.

(*Received* 14 *December* 1970)

Abstract – The crystal field parameters for non-Kramers ions are usually not very well known. Thulium garnets are no exception. We discuss the pros and cons of the parameters reported in the literature. Their correctness is tested against the susceptibility measurements. We propose a method to determine these crystal field parameters from the susceptibility. A table, to facilitate the use of this method, has been computed. From the first moment we conclude that Koningsteins V_{20} parameter is correct. From the second moment, which gives a bilinear combination of V parameters, we conclude that one of the higher order parameters probably has the wrong sign.

1. INTRODUCTION

THE RARE earth ion in Garnets is located at the c-site in the structure; space group 0_h^{10}. The ion is surrounded by eight oxygen ions located exactly at, but near to the corners of a cube. These ions, as well as others further away, produce an electric field. This field, usually called the crystal field, produces a splitting of the 'free' ground state of the ion which results in the quenching of the $(2J+1)$-fold degeneracy of the ground state. For low J values of the angular momentum, as is the case in the transition metals as well as in a few rare earths one can guess these parameters, and subsequently adapt them to the experimental values of these quantities that follow from the eigenvalues and eigen functions of the spin Hamiltonian. If one deals with a highly symmetric crystal field and low angular momentum, the ratio of these parameters is determined by the symmetry of the crystal field. Often one has to assume only one proportionality factor. In the case of the heavy rare earths one is not that fortunate. Even if one assumes that the field has pure cubic symmetry, which is not even true for nearest neighbors only, one deals with an undetermined parameter: the ratio between the fourth order and the sixth order contribution to the cubic field. This ratio can be expressed in two different ways. One uses for the crystalline potential, expressed in operator polynomials $\mathcal{O}$, either[1]:

$$V_{er} = V_4\{\beta[\mathcal{O}_4^0 - 5\mathcal{O}_4^4] + q\gamma[\mathcal{O}_6^0 + 21\mathcal{O}_6^4]\} \tag{1a}$$

where the quotient $q = V_6/V_4$, or [2]

$$V_{cr} = W\left\{\frac{x}{F(4)}\left[\mathcal{O}_4^0 - 5\mathcal{O}_4^4\right] + \frac{(1-|x|)}{F(6)}[\mathcal{O}_6^0 + 21\mathcal{O}_6^4]\right\}. \tag{1b}$$

The coefficients V_6 and V_4 are related to the extension of the orbit of the ion in question. The coefficients $F(4)$, $F(6)$, are F_{40} and F_{60}. For these and the Stevens factors see Table 1.

Using the Hamiltonian from Ref.[2] with $x = 0{\cdot}6$ Schieber, Lin and Van Vleck[3] calculated the susceptibility of the system. This value of the parameter x corresponds to $q = -0{\cdot}1541$ and leads to a spectrum with a singlet ground state followed by two triplet excited states at about 100 and 200 cm^{-1}

Table 1. *Basic data for Thulium*

$J = 6$	$g = 7/6$		
$F_{20} = 3$	$F_{22} = 1$		$\alpha = 0{\cdot}010101$
$F_{40} = 60$	$F_{42} = 3$	$F_{44} = 12$	$\beta = 0{\cdot}16325\ 10^{-3}$
$F_{60} = 7560$	$F_{62} = 72$	$F_{64} = 180$	$\gamma = 0{\cdot}56061\ 10^{-5}$

above the ground state, all other levels lying much higher up. Note that the spectrum in the tables of Lea, Leask and Wolf is upside down since V_4 is actually negative. We deduced that Schieber, Lin and Van Vleck seem to have used a V_4 of about $-215\,\text{cm}^{-1}$. The sing of the Y_4^4 and Y_6^4 is opposite of the spin Hamiltonian as tabulated by Hutchings [4] on account of the $\pi/4$ rotation from local to crystal system, but that does not affect the energy levels in zero field.

Little has been done to see how the spectra behaves in a magnetic field, even for the simplest case where the crystal field is purely cubic. The earliest paper, by White and Andelin[5], takes $q = 0$, which is much too restrictive. Schieber, Lin and Van Vleck calculate the susceptibility (at zero field) which is of questionable use for the Iron garnets, since they have a large internal field.

The most condemning evidence against the use of a purely cubic field, attractive as it may be for a first orientation, comes from paramagnetic resonance experiments. They show clearly that the g-factors are anisotropic, which cannot result from cubic fields.

2. CRYSTAL FIELD POTENTIAL

Although the exact crystal field potential for Thulium in T ALG or TIG will be an open question for some time, one can make a number of reasonable assumptions using related garnets and hope that the magnetic properties are not too sensitive to the choice of these quantities. The most direct piece of information comes from spectra on (diluted) Thulium garnets. Measurements were done by Pearson, Hermann and Buchanan[6] and by Koningstein[7]. The latter gives the analysis of his data in terms of the crystal field parameters. His parameters are in the zero field Hamiltonian: $\mathscr{H}_0 = \sum_{n,m} \theta_n V_n^m \mathscr{O}_n^m$ are:

$$V_2^0 = 270; \quad V_2^2 = 95; \quad V_4^0 = -170;$$
$$V_4^2 = -140; \quad V_4^4 = 1020; \quad V_6^6 = 30;$$
$$V_6^2 = 115; \quad V_6^4 = -475;$$

all in cm^{-1}. Thulium was the doping agent in the YAIG-host.

$$\theta_2 \equiv \alpha; \theta_4 \equiv \beta; \theta_6 \equiv \gamma; (B_n^m = \theta_n V_n^m).$$

The fit of the eigenvalues of the spin-Hamiltonian based on his parameters with his spectra is not too good. Moreover, the cirterium proposed by Buchanan *et al.*[9] to recognize the group theoretical characterization of the lines has not been applied.

For the sake of comparison, and in order to get a general impression about the relative positions and degeneracies of the levels, we computed the zero field energy levels for several sets of parameters. (See Fig. 1.)

This was done as follows. We took the values of V_n^m from the different papers, multiplied them with the Stevens factors and the $J = 6$ matrix elements from Hutchings[4] Tables. In a later version of the program we generated the operator polynomials of Stevens. From this we construct the $(2J+1)$ dimensional Hamiltonian, which on account of the future use with a magnetic field in arbitrary direction, is written in complex notation. The eigenvalues and eigenfunctions were calculated by Jacobi's method. The functions are at this moment not yet needed but stored for computation of the magnetic moment as a function of the temperature.

The general form of the zero field spectrum is probably quite different from the Schieber–Lin–Van Vleck (a) values. Whether it is of the form Koningstein (b) has proposed remains to be seen, but the simple fact they have in common in the non-magnetic ground state. This is directly confirmed by the experimental result: the susceptibility levels off to

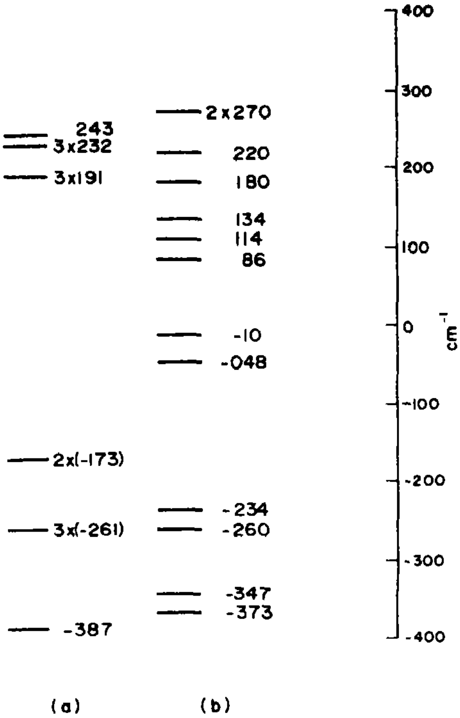

Fig. 1. Level spectrum for zero magnetic field computed with: (a) the parameters of Schieber, Lin and Van Vleck: (b) the parameters of Koningstein.

a constant value at $T=0$, compare Fig. 2 rather than follow a pseudo Curie law.

We also tried a third level structure using some unpublished parameters. The fit was quite bad which was not surprising since the parameters were held in doubt by their originators. The conclusion from these calculations is however that it is unlikely that the ground state is degenerate.

What else can be deduced from the magnetization curve, besides the simple fact that it always lies below the free spin value? In order to find out what the overall splitting is one can plot the magnetic moment M vs. $1/T$, for fixed H. At the origin the value is equal to the free spin values as shown below.

If we look upon Curie's law as a high temperature expansion of the magnetic moment for a free spin there is only one term. For a spin in a crystal field we have

$$
\begin{aligned}
(2J+1)\langle \mathbf{M}\rangle &= kT\frac{\partial}{\partial H}\ln(\exp(\beta\mathscr{H}))\\
&= \frac{\partial}{\partial H}\sum\frac{(-\beta)^{n-1}}{n!}M_n \qquad (2)
\end{aligned}
$$

where $\beta = 1/kT$ and M_n the nth semi invariant [10]. Using the Hamiltonian

$$\mathscr{H}=\mathscr{H}_0+\mathbf{M}\cdot\mathbf{H}$$

we find for the first two terms:

$$
\begin{aligned}
(\partial/\partial H)M_1 &= \langle \mathbf{M}\rangle = 0\\
(\partial/\partial H)M_2 &= (\partial/\partial H)(\langle\mathscr{H}^2\rangle-\langle\mathscr{H}\rangle^2)\\
&= 2H\langle \mathbf{M}^2\rangle = \tfrac{2}{3}HJ(J+1).
\end{aligned}
$$

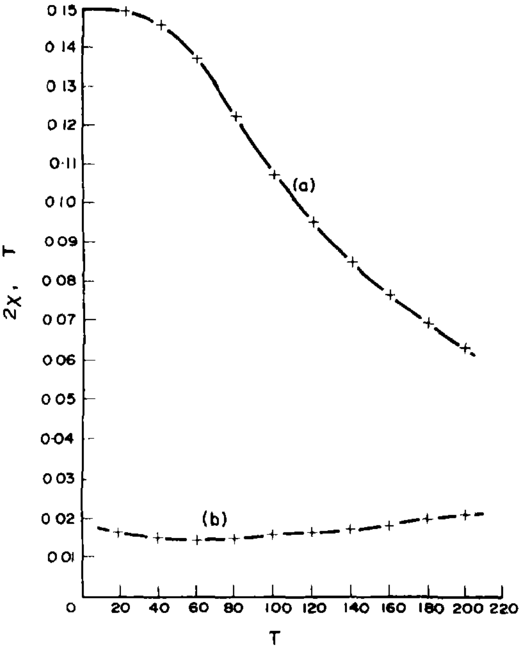

Fig. 2. The susceptibility in c.g.s. units as a function of the temperature computed with the parameters of: (a) Van Vleck: (b) Koningstein. The measured values follow the curve (a) which is no coincidence, since the Van Vleck parameters were deducted from the experiment. The temperature is in degrees K.

We have used $\langle \mathbf{M}.\mathscr{H}_0\rangle = 0$, since the magnetic tensor is antisymmetric and the crystal field is symmetric with respect to the secondary diagonal of the matrix. Also $\langle\mathcal{H}_0\rangle = 0$ since the Stevens operators are traceless. The second moment leads to Curie's law.

The first term of interest in the above expansion is the term in β^2, which contains the third moment. The only non zero contribution is the trace of $\mathcal{H}_0 M^2$. Note that although $\mathcal{H}_0$ and M do not commute, all three arrangements of these two operators lead to the same quantum mechanical average. The result is that this term will give us a weighted average of the diagonal elements and as such, determines a linear combination of the coefficients O_n^0. ($n = 2, 4, 6$). However the sums

$$\Sigma J_z^2 O_n^0 = 0 \text{ for } n = 4, 6$$

hence we only deal with B_2^0. This is not surprising since J_z^2 is proportional to O_2^0, apart from a constant and O_4^0 and O_6^0 are orthogonal to both O_2^0 and the constant. Consequently we have

$$\begin{aligned}\langle\mathcal{H}_0 J_z^2\rangle &= (2J+1)^{-1}\Sigma\, \mathcal{H}_0 J_z^2\\ &= B_2^0 J(J+1)(2J-1)(2J+3)/15.\end{aligned}$$

This result is obtained assuming that the magnetic field was along the z-axis in the local coordinate system. The influence of the direction of the field will be considered later.

Using this idea we plotted both the numerical results obtained with the V's of Koningstein and of Van Vleck together with the experimental data from Schieber, Lin and Van Vleck. (Fig. 2). The result is quite interesting, particularly if we consider Fig. 3, a plot which is adapted to the expansion[2]. This enables us (ideally) to separate the different terms in the expansion. For very high temperatures the points seem to follow the Koningstein curve. The figure shows at one hand that his cylindrical field parameter is quite reasonable. At the other hand that the Van Vleck Hamiltonian is completely incorrect near the origin of the figure. This is no surprise since Van Vleck's assumption of a purely cubic field is definitely untenable in the light of the well known deformation of the cube. This deformation is known from the work of Geller and Gilleo[11]. Hutchings and Wolf showed, for Ytterbium Iron Garnets[12], via extensive point charge calculations and comparison with experimental data that the crystal field is definitely not cubic or nearly cubic.

For somewhat lower temperatures the data points start to shift over to the Van Vleck curve. For large values of the inverted tem-

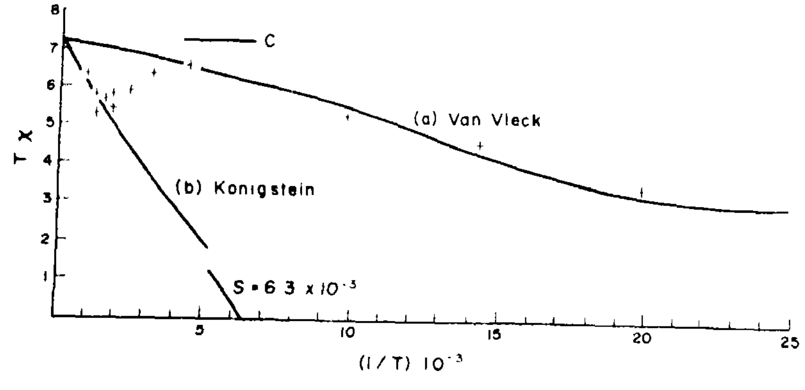

Fig. 3. Susceptibility times temperature vs. inverse temperature. The units are the same as in Fig. 2. The horizontal bar gives the value of the Curie constant C for a $J = 6$ spin. The intercept of curve (b) is indicated by S. Its slope is $-C/S$. This is also the approximate slope of the experimental data. The experimental values are indicated by +. Again curve (a) is Van Vleck parameters, (b) Koningstein's parameters

peratures the susceptibility of the ion is the result of the composition of the ground state wave function i.e. the linear combination of the basis wave functions and it is clear, in particular for Fig. 2, that the Koningstein parameters do not give the correct wave functions.

Second order coefficient (third moment)

In this and the next sections we take a more detailed view of the high temperature expansion.

First the influence of the angle. If the external field is along the 100 direction with respect to the crystal, the field makes an angle of 45° with the z-axis in each of the six of the local coordinate systems. In each system the term we considered above will have the form

$$\Sigma \mathscr{H} \, (H_z J_z \cos \Theta + H_x J_x \sin \Theta)^2$$

for the sake of convenience we considered the field in the zox plane. This gives rise to two non zero terms in the trace, one due to the diagonal part of $\mathscr{H}_0$ and the other due to the elements that are two steps removed from the main diagonal. The cross terms have trace zero. The second set of terms are indicated in the second column of Table 2.

To obtain the direction dependence of the second susceptibility coefficient (that is the coefficient in β^2) one has to add the six sublattice contributions. In order to do this each has to be transformed from its own local coordinates to the coordinate system with z-axis along the field. This leads to a linear combination of the tabulated values. Each coefficient is a product of the strength constant B of the crystal field and a trigonometrical factor.

Second let us determine V_2^0 from the experiment. From equation (2) we find the ratio between the $n = 3$ and $n = 2$ coefficients:

$$-V_2^0 \theta_2 \mathrm{Tr}\,(\mathcal{O}_2^0 J_z^2)/\mathrm{Tr}\,(J_z^2) =$$
$$-\tfrac{3}{5}\,(2J-1)(2J+3)\,V_2^0 \Theta_2.$$

(the factorials cancel against the binomial coefficient). Using the slope of the experimental data we find $V_2^0 \sim 300\ \mathrm{cm}^{-1}$, somewhat higher than the parameter of Koningstein.

Third order coefficient (fourth moment)

The minimum in the experimental points in Fig. 3 is determined by the ratio of the second order coefficient to twice the third order coefficient, provided the fourth order coefficient is not too large yet at that temperature. This enables us to determine, or may be only to estimate, the third order coefficient. This coefficient represents a more elaborate combination of spin Hamiltonian parameters. In order to make use of this information we constructed a table of the following averages:

$$(J_z^2 \mathcal{O}_\mu^\lambda \mathcal{O}_{\mu'}^{\lambda'}) \text{ and } (J_+^2 \mathcal{O}_\mu^\lambda \mathcal{O}_{\mu'}^{\lambda'})$$

The values are listed in Table 3 for $J = 6$. There are similar 'selection rules' as in the previous case, which are evident from the table.

The evaluation of the above traces can also be accomplished in algebraic fashion. This is considered in Appendix A.

From the table it can be seen that the traces which are not zero on account of a selection rule, are of the order of 10^6 to 10^{13}. This gives a certain selectivity but unfortunately not very much. We had hoped that certain contributions would be dominant so that one could obtain an idea about a few coefficients.

Table 2. Coefficients necessary to determine the second order terms

λ	$\Sigma J_z^2 \mathcal{O}_0^\lambda$	$\Sigma J_+^2 \mathcal{O}_2^\lambda$
2	6006	5854
4	0	−17820
6	0	28046090

It is only possible, however, to give a certain limitation to the coefficients. This is done by summing all traces, multiplied by the crystal

Table 3. *Coefficients necessary to determine the third order terms*

	20	40	60	22	42	62	44	64	66
20	383526	21003840	0	0	0	0	0	0	0
	0	0	0	−135857	4609314	−23950123	0	0	0
40		4608115200	123070750720	0	0	0	0	0	0
		0	0	3488659	−531473252	16349557760	0	0	0
60			2629717458944	0	0	0	0	0	0
			0	−14968791	10286286592	−6795473792	0	0	0
22				36704	1286865	−17297211	0	0	0
				0	0	0	3429147	−9979224	0
42					132532770	946753936	0	0	0
					0	0	−40955651	3314001280	0
62						150524063744	0	0	0
						0	126645172	−11683827584	0
44							48067048	772934312	0
							0	0	3396556320
64								121103927296	0
								0	−19410449152
66									73047734272
									0

field parameters $V_n{}^m$ and the Stevens factors and comparing this with the experimental data. The result is between 0·6 and $9{\cdot}4\times 10^6$ $(\mathrm{cm}^{-1})^2$ depending on whose parameters were used. In this calculation the fourth moment was used. This quantity is determined by the difference between

$$\langle \mathcal{O}_n{}^m \mathcal{O}_{n'}^{m'} J_z{}^2\rangle - \langle \mathcal{O}_n{}^m \mathcal{O}_{n}^{m'}\rangle\langle J_z{}^2\rangle .$$

As before the order in which the operators appear is irrelevant since J_z is diagonal. This is no longer the case for arbitrary field directions.

From Fig. 3 we estimate the following series for the susceptibility χ:

$$T\chi = C(1-0{\cdot}148\,x+0{\cdot}047\,x^2+\ldots)$$
$$\times\,(x=(1/T)10^{-3}).$$

Using this, and the conversion factor from degrees to cm^{-1} we find for the ratio r between the third coefficient and the second coefficient: $r = 231\ \mathrm{cm}^{-1}$. To compare this ratio with the crystal field parameters calculation we used Koningstein's value for $V_2{}^0$ in the denominator, which seems to be in accordance with the magnetization experiment (Van Vleck's parameters would give $r=\infty$).

The result is

$$r = \frac{1}{2}\left\{\sum_{mnm'n'}\sum B_n{}^m B_{n'}^{m'}\,\theta_n\theta_{n'}\left\{\left\langle \mathcal{O}_n{}^m \mathcal{O}_{n'}^{m'} J_z{}^2\right\rangle\right.\right.$$
$$\left.\left. -\left\langle \mathcal{O}_n{}^m \mathcal{O}_{n'}^{m'}\right\rangle\left\langle J_z{}^2\right\rangle\right]\right\}\Big/\left\{B_{20}\theta_2\left\langle \mathcal{O}_{20} J_z{}^2\right\rangle\right\} =$$
$$-41{\cdot}4\ \mathrm{cm}^{-1}.$$

Although we obtain the right order of magnitude, ignoring the sign, the result is far from satisfactory. We speculate that the sign of the V_{42} parameter may be wrong, but that is only so if V_{66} remains zero, which it may not be.

Comparing the proposed crystal field parameters with the susceptibility measurements leads to the following conclusions. The parameters of Van Vleck do not give the proper high temperature behavior; i.e. absence of the dip near the origin of Fig. 3. The parameters of Koningstein do give the proper high temperature behavior, which in turn leads to believe that his $V_2{}^0$ parameter is about correct, but fails to give the correct low temperature behavior. Judging from the energy spectrum (Fig. 1) this is due to the lack of degenerate levels. The reason that Van Vleck's parameters give such good fit to the low temperature data is mostly due to the presence of a three fold level about $100\ \mathrm{cm}^{-1}$ above the ground state.

In conclusion I would like to stress that very accurate susceptibility measurements would be valuable for the exploration of crystal field parameters, where direct observaon is difficult.

APPENDIX A

We want to determine the coefficients B in

$$\mathcal{O}_\lambda{}^\mu(J)\mathcal{O}_{\lambda'}^{\mu'}(J) = \sum B_{\lambda\lambda'\lambda''}^{\mu\mu'\mu''}\mathcal{O}_{\lambda}^{\mu''}(J). \tag{A1}$$

The symbol J stands for J_z, J_+ and J_-. We take $\mu=\mu'=\mu''=0$ to begin with; the other values can be generated by step-up and step-down operators. This problem can be solved in different manners.

The simplest way is the direct evaluation, in which the coefficients B are solved by comparing the coefficients of the polynomials in J_z at each side of the equation. This process is limited to $\lambda''\leqslant 6$ since the $\mathcal{O}$'s are not further tabulated.

A somewhat more general method to determine the B's is to use the orthogonality property of the $\mathcal{O}$'s. This leads to

$$T[\mathcal{O}_\lambda{}^\mu(J)\mathcal{O}_{\lambda'}^{\mu'}(J)\mathcal{O}_{\lambda''}^{\mu''}(J)] = \sum B_{\lambda\lambda'\lambda''}^{\mu\mu'\mu''}T_r[\mathcal{O}_{\lambda''}^{\mu''}\mathcal{O}_{\lambda''}^{\mu''}]. \tag{A2}$$

Unfortunately the $\mathcal{O}$'s are not normalized, hence both sides have to be evaluated. The calculation of traces is rather tedious. There is some literature available on the value of traces, but all proved to be incomplete for our purpose. We calculated traces $\Sigma J_z{}^n$ for $n = 1$ to 14, as function of J. (Table 4).

By far the most elegant method is to make use of the relation between the $\mathcal{O}$'s and the Tensor Operators$\langle|T|\rangle$. Using the notation of de Shalit and Talmi[13] (Ref. *S-T*) we have

$$\langle J, M|T_\mu{}^\lambda|J\,M'\rangle = (-1)^{J-M}\begin{pmatrix} J & \lambda & J\\ M & \mu & M'\end{pmatrix}(J\|T^\lambda\|J) \tag{A3}$$

with $(J\|T^\lambda\|J) = (J\|1\|J) = \sqrt{2J+1}$. We want to find the proportionality factor $P(J)$ between the Stevens opera-

Table 4. Sums required to decompose the product of the two Stevens operators

$$A_k = \sum_{1}^{n} P^k;\ n(n+1) = m;\ A_k = (2n+1)\, m\, P_k(m)$$

$$A_1 = \tfrac{1}{2} m$$
$$A_2 = (2n+1)(2n+1)m/6$$
$$A_3 = m^2/4$$
$$A_4 = (2n+1)\, m\, (3m-1)/30$$
$$A_5 = m^2 (2m-1)/12$$
$$P_6 = (3m^2 - 3m + 1)/42$$
$$P_8 = (5m^3 - 10m^2 + 9m^2 + 9m - 3)/90$$
$$P_{10} = (3m^4 - 10m^3 + 17m^2 - 15m + 5)/66$$
$$P_{12} = (105m^5 - 525m^4 + 1435m^3 - 2360m^2 + 2073m - 691)/2730$$
$$P_{14} = (12m^6 - 84m^5 + 336m^4 - 880m^3 + 1436m^2 - 1260m + 420)/360$$

tors C and tensor operators T·

$$PC_\mu^\lambda = T_\mu^\lambda \qquad \text{(A4)}$$

the factor P depends on the basis chosen. By comparison we find

$$P(J) = (-1)^{J-M} \sqrt{\frac{(2J-\lambda)!}{(2J+\lambda+1)!}}\, C_\lambda \qquad \text{(A5)}$$

with $C_\lambda = 2, 2, 4$ for $\lambda = 2, 4, 6$.

Using Ref. *S-T* we find, from the equation at the top of p. 518, after multiplication with

$$\sum_{j_3 m_3} \begin{pmatrix} l_1 & l_2 & j_3 \\ m_1'' & m_2'' & m_3 \end{pmatrix}$$

and using the orthogonality property (p. 515) for the special case that $l_1 = l_2 = l_3 = J$ and $j_i = \lambda_i$, $i = 1, 2, 3$ in conjunction with $m_i = \mu_i$, $m_i' = M_i$ for the same i values, the following expression for the coupling of two Clebsch–Gordan coefficients

$$\sum_{M_3} (-1)^{3J+M_1+M_2+M_3} \begin{pmatrix} J & \lambda_1 & J \\ -M_3 & \mu_1 & M_2 \end{pmatrix} \begin{pmatrix} J & \lambda_2 & J \\ M_1 & \mu_2 & M_3 \end{pmatrix}$$

$$= \sum_{\lambda_3 \mu_3} (2\lambda_3+1) \begin{pmatrix} \lambda_1 & \lambda_2 & \lambda_3 \\ \mu_1 & \mu_2 & \mu_3 \end{pmatrix} \begin{pmatrix} J & \lambda_3 & J \\ M_2 & \mu_3 & M_1 \end{pmatrix} \begin{Bmatrix} \lambda_1 & \lambda_2 & \lambda_3 \\ J & J & J \end{Bmatrix}. \qquad \text{(A6)}$$

If we replace Clebsch–Gordan coefficients by the Stevens operators

$$\begin{pmatrix} J & \lambda & J \\ M & \mu & M' \end{pmatrix} = (-1)^{J-M} \sqrt{\frac{(2J-\lambda)!}{(2J+\lambda+1)!}}\, C_\lambda \langle |\mathcal{O}_\lambda^\mu| \rangle \qquad \text{(A7)}$$

in the previous expression, then we find, for the case that all M's and N's are zero, the following expression:

$$(-1)^{3J} \sqrt{\frac{(2J-\lambda_1)!\,(2J-\lambda_2)!}{(2J+\lambda_1+1)!\,(2J+\lambda_2+1)!}}$$

$$C_{\lambda_1} C_{\lambda_2} \langle |\mathcal{O}_{\lambda_1}^0| \rangle \langle |\mathcal{O}_{\lambda_2}^0| \rangle = \sum (2\lambda_3+1) \times$$

$$\begin{pmatrix} \lambda_1 & \lambda_2 & \lambda_3 \\ 0 & 0 & 0 \end{pmatrix} \begin{Bmatrix} \lambda_1 & \lambda_2 & \lambda_3 \\ J & J & J \end{Bmatrix} \sqrt{\frac{(2J-\lambda_3)!}{(2J+\lambda_3+1)!}}\, C_{\lambda_3} \langle |\mathcal{O}_{\lambda_3}^0| \rangle. \qquad \text{(A8)}$$

In order to evaluate B in equation (A1) we need to know the Clebsch–Gordan coefficient and the Racah coefficient on the right hand side of the equation. The first is (note that in our case we always deal with even λ's and $\lambda_3 = 2$:

$$5 \begin{pmatrix} \lambda_1 & \lambda_2 & 2 \\ 0 & 0 & 0 \end{pmatrix}$$

$$= 5 \left[\frac{(2\lambda_1 - 2\lambda_2 + 4)!\,(2\lambda_2 - 2\lambda_1 + 4)!\,(2\lambda_1 + 2\lambda_2 - 4)!}{(2\lambda_1 + 2\lambda_2 + 5)!} \right]^{1/2}$$

$$\cdot \frac{(\lambda_1 + \lambda_2 + 2)!}{(\lambda_1 - \lambda_2 + 2)!\,(\lambda_2 - \lambda_1 + 2)!\,(\lambda_1 + \lambda_2 - 2)!}.$$

The second is a special case of the Racah coefficient containing the value 2. These are listed in Edmonds (Table 5) we need ($c' = c, c-1, c-2$):

$$\begin{Bmatrix} a & b & c \\ 2 & c' & b \end{Bmatrix} = \begin{Bmatrix} 2 & c' & c \\ a & b & b \end{Bmatrix} = (-1)^{a+b+c} \frac{P}{\sqrt{Q}}$$

for $a = b\ (=J)$. From the table we find

$$Q = (2b-1)(2b)(2b+1)(2b+2)(2b+3) \cdot (2c'-1)(2c'+1)(2c'+2)(2c'+3).$$

and for P the three following expressions.

(1) if $c' = c\ (=\lambda)$
$$P = 2c(c+1)[3c(c+1) - 4a(a+1)]$$

(2) if $c' = c-1\ (=\lambda-1)$
$$P = (1-c^2)\, c\, [6(2a+c+1)(2a-c+1)]^{1/2}$$

(3) if $c' = c-2\ (=\lambda-2)$
$$P = c[6(c-1)(2a+c+1)(2a-c+1)(2a-c+2)]^{1/2}.$$

From this we can deduct the algebraic expressions for the coefficients B.

REFERENCES

1. VAN VLECK J. M., *J. chem. Phys. Solids* **27**, 1047 (1966)
2. LEA K. R., LEASK M. J. M. and WOLF W. P., *J. chem Phys. Solids* **23**, 1381 (1962).
3. SCHIEBER M. M., LIN C. C. and VAN VLECK J. M., *J. chem. Phys. Solids* **27**, 1041 (1966).
4. HUTCHINGS M. T., *Solid State Physics* **16**, 227 (1964).
5. WHITE R. L. and ANDELIN J. P., *Phys. Rev.* **115**, 1435 (1959).
6. PEARSON J. J., HERRMANN G. F. and BUCHANAN R. A., *J. appl. Phys* **39**, 980, 1968.
7. KONINGSTEIN J. A. *Theoret. Chim. Acta (Berlin)* **5**, 327 (1966).
8. KONINGSTEIN J. A., in *Optical Properties of Ions in Crystals* (Edited by H. M. Crosswhite), p. 105, Interscience Publishers (1967).

9. BUCHANAN R. A., PEARSON J. J. and HERMANN G. F., *Solid State Commun.* 7, 195 (1969).
10. CRAMER H., *Mathematical Methods of Statistics*, Princeton University Press, Princeton 1945. Also extensively used by HORWITZ G. and CALLEN H. B., *Phys. Rev.* **124**, 1757 (1961).
11. GILLEO M. S. and GELLER S., *J. chem. Phys. Solids* 3, 30 (1957).
12. HUTCHINGS M. T. and WOLF W. P., *J. chem. Phys.* **41**, 617 (1964).
13. de SHALIT A. and TALMI I., *Nuclear Shell Theory*, New York Academic Press (1963).

J. Phys. Chem. Solids Pergamon Press 1971. Vol. 32, pp. 2173–2179. Printed in Great Britain.

ELECTRONIC ENERGY LEVELS IN FERROMAGNETIC Eu_3P_2 AND Eu_3As_2

G. BUSCH, M. CAMPAGNA, F. HULLIGER and H. C. SIEGMANN*

(*Received* 14 *December* 1970)

Abstract – Electronic energy levels are determined for the ferromagnetic semiconductors Eu_3P_2 and Eu_3As_2 by means of spin-polarization measurements of photoemitted electrons. The $4f^7$-levels of the Eu^{2+}-ion are located near the upper edge of the valence band. The band structure is very similar to the one observed in EuS and EuSe and, as in the case of the chalcogenides, magnetically interacting impurity states are detected within the band gap. Significant changes in the spin-polarized levels occur on disordering the lattice.

1. INTRODUCTION

THE CLASSICAL methods for investigating the density of states in solids are often insufficient to assign to the observed peaks specific electronic energy levels. In ferromagnets it is important to locate the electronic states which make up the magnetic moment due to alignment of electron spins at temperatures below the Curie point T_c. These magnetic levels are characterized by a certain degree of electronic spin polarization. Since spin polarization is at least partly conserved in photoemission[1], the magnetic levels can be detected by a measurement of the spin polarization of photoemitted electrons.

The europium pnictides Eu_3P_2 and Eu_3As_2 have recently been synthesized and were found to be ferromagnetic semiconductors with Curie temperatures of 25 and 18 K, respectively[2, 3]. They both crystallize in the cubic Ba_3P_2-structure in which the cations are coordinated by a distorted octahedron of anions[3]. The interest in these compounds arises from their similarity with the europium monochalcogenides EuO, EuS and EuSe. These rocksalt-type chalcogenides have been extensively studied the last 10 yr and unusual phenomena have been disclosed. It is hoped that from a study of the pnictides, which turned out to have a band structure very similar with the chalcogenides, new information is obtained on the origin of the unique properties of certain ferromagnetic semiconductors.

2. EXPERIMENTAL

There are three parts to the experiment: (i) electron emission from the photocathode, (ii) extraction of electrons from the magnetic field applied at the photocathode to align the Weiss domains and formation of an electron beam, (iii) the measurement of the electron spin polarization (ESP) in the polarization analyzer. Details of the apparatus are described in [1, 4]. The photocathode is a thin film evaporated in situ by electron bombardment of bulk samples of Eu_3P_2 and Eu_3As_2. During film preparation the pressure in the apparatus was 10^{-8} to 10^{-9} torr but almost immediately after film deposition it decreased to $\sim 10^{-10}$ torr, at which pressure the measurements were carried out. Heating of the substrate from 4·2 to ~400 K was employed for changing the structural order in the samples. During the measurements the substrate was kept at 4·2 K; this is well below the Curie point T_c for both compounds. Additional cryopumping allowed the annealing and cooling of the films without any detectable amount of surface contamination.

---

*Eidgenössische Technische Hochschule Zürich, Laboratorium für Festkörperphysik, CH-8049 Zürich, Hönggerberg, Switzerland.

3. RESULTS AND DISCUSSION

Both compounds are efficient photoemitters with work function ϕ around 2·5 eV. The number of photoemitted electrons per incident photon, the photoelectric yield Y, was $\simeq 10^{-3}$ at the photon energy $h\nu = 5$ eV. Near threshold energy we found

$$Y^3 = h\nu + \phi.$$

ϕ was evaluated using this equation.

The ESP is a vector quantity whose components are defined as the expectation values of the Pauli matrices:

$$\mathbf{P} = \{\langle\sigma_x\rangle, \langle\sigma_y\rangle, \langle\sigma_z\rangle\}.$$

In our experiments a magnetic field **B** sufficient to align the Weiss domains is applied in z-direction perpendicular to the film surface. Therefore, $\langle\sigma_x\rangle = \langle\sigma_y\rangle = 0$ and $|\mathbf{P}| = \langle\sigma_z\rangle$. The expectation value of the spin direction is given by

$$\langle\sigma_z\rangle = \frac{N\uparrow - N\downarrow}{N\uparrow + N\downarrow}$$

where $N\uparrow$ and $N\downarrow$ are the numbers of electrons with spin parallel and antiparallel to the z-direction.

Figures 1 and 3 show the ESP data for Eu_3P_2 and Eu_3As_2 films, respectively. To interpret the results we make use of the summation rule for the degrees of polarization. The total beam of photoelectrons with observed ESP $P(h\nu)$ is composed of electron beams emitted from states n with intensities $I_n(h\nu)$ and ESP $P_n(h\nu)$. Therefore

$$P(h\nu) = \frac{\sum_n I_n(h\nu) P_n(h\nu)}{\sum_n I_n(h\nu)}.$$

We have $I_n(h\nu) = 0$ for $h\nu \leqq E_n$; E_n is the energy difference between the level n and the vacuum level E_∞; we define $E_\infty = 0$. For $h\nu > E_n$, the function $I_n(h\nu)$ increases rapidly due to the escape function which accounts for the electron losses by migration to the surface and escape over the surface barrier potential. When an electron level n with $P_n \neq P_{n-1}$ is admixed, a kink is observed in the otherwise smooth $P(h\nu)$-curve. The photon energy at which the kink occurs yields E_n.

Eu_3P_2.

We consider first the results on Eu_3P_2-films prepared on a substrate at 380 K. Similar results were obtained with films evaporated on a cold substrate and subsequently annealed. This type of film has a comparatively high degree of crystallinity and will be denoted by Eu_3P_2(I).

Magnetization measurements [3] yield the number of Bohr magnetons for Eu^{2+} and it follows that the electrons in the $4f^7$-shell are completely polarized at 4·2 K: $P_{4f^7} = 100$ per cent. Therefore, the sharp increase of the ESP at $h\nu \geqq 3{\cdot}1$ eV in Fig. 1 for Eu_3P_2(I) locates these states. The sharp decrease which is observed at $h\nu \geqq 4{\cdot}1$ eV must arise from electrons in valence-band states formed by the anions since these are known to be essentially unpolarized. Near threshold we have initially in Eu_3P_2(I) an ESP of 15 per cent which decreases before the onset of emission from the $4f$-states. We suggest that the highest-lying occupied states are impurity states that are polarized via exchange interaction with the $4f^7$-states.

The decrease of ESP for $2{\cdot}5 \leqq h\nu \leqq 3$ eV is attributed to a tail of valence-band states, that extends into the band gap. The tail can be generated by the special crystal structure or by a certain amount of disorder in the lattice. However, the decrease of ESP might also be due to a second type of impurities which experiences no exchange interaction with the $4f^7$-states.

These results are summarized by an energy-level diagram in Fig. 2. It is not appropriate to show the $4f^7$-levels in a band scheme, because these levels are known to be highly localized

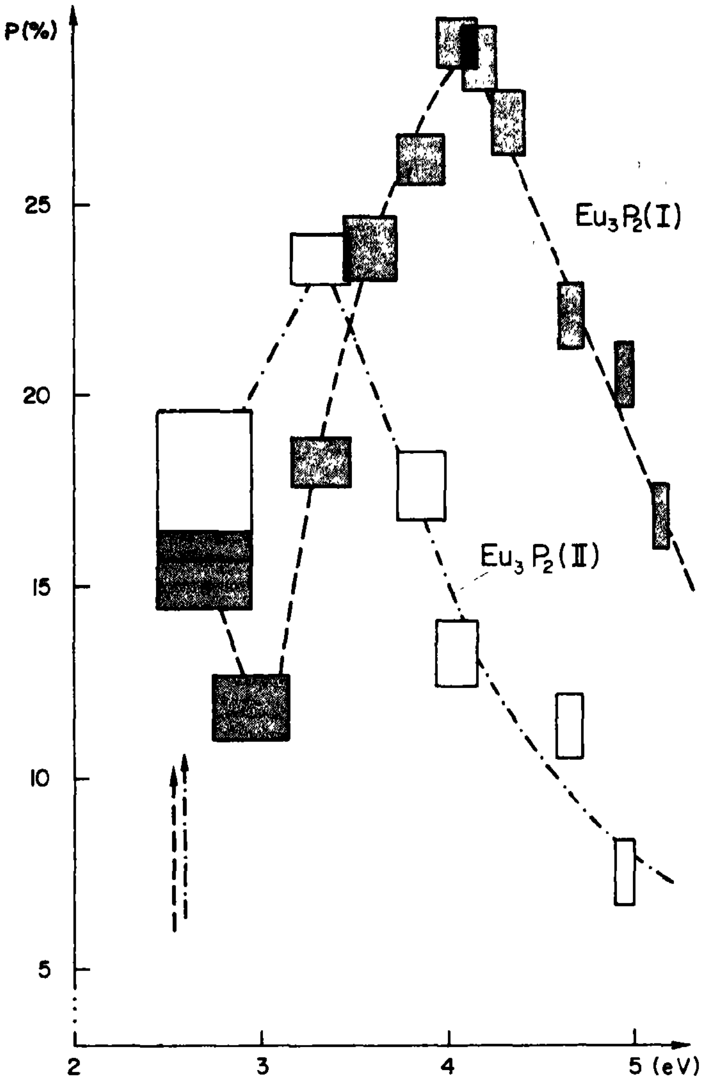

Fig. 1. The dependence of photo-ESP on photon energy $h\nu$ for ordered (I) and disordered (II) films of Eu_3P_2 at $B = 22{\cdot}8$ kG. Arrows indicate work functions obtained by plotting Y^{3}vs. $h\nu$.

and therefore the one-electron approximation breaks down: If one electron is excited out of the $^8S_{7/2}$ configuration, the remaining 6 electrons form a ^7F_J state which is split into a multiplet, $J = 0,1 \ldots,6$, because of the spin-orbit interaction. The energy for the multiplet splitting is supplied by the photoexcitation process. The $4f^7$-level appears as a peak with a minimum linewidth of 0·6 eV. We have chosen to indicate energy differences between $4f^7$ and $4f^6$ configurations, and the energy required to excite one of the $4f^7$-electrons can directly be visualized from Fig. 2.

The optical absorption edge was reported to be 1·2 eV[3] and is interpreted by transitions from $4f$- to the nearest unoccupied states, which are assumed to be conduction band states. With this further assignment

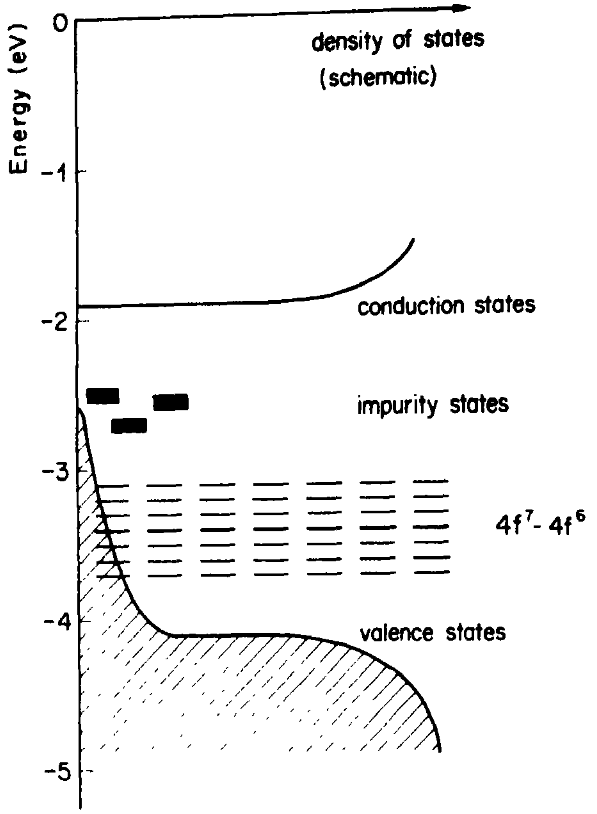

Fig. 2. Energy-level diagram for Eu_3P_2 from analysis of photo-ESP. The position of the conduction states was taken from optical absorption (3, 4).

the energy-level diagram is consistent with the other observations made on films of Eu_3P_2 [5]: Electrical-resistivity measurements reveal carriers with an activation energy of 0·6 eV, and the optical absorption shows a low-energy peak which is explained by transitions from impurity to conducting states and/or from the tail of the valence band to conduction band states. The general features of the energy-level diagram for the europium pnictides and chalcogenides are the same; in the pnictides, the magnitude of the gap between valence and conduction band is smaller, which is expected since the ionicity is lower.

The polarized type of impurity states must be located at Eu-atoms in order to experience the indirect exchange interaction. If excess Eu is present in a monovalent state it acts as a donor and we suggest that this is the origin of the impurity states. This view is supported by an observation of von Molnar[6] that in EuO excess Eu also causes impurity levels lying 0·5 eV below the conduction band.

Next consider the results on Eu_3P_2 (II). These films were prepared on a substrate at 4·2 K, which means that a certain amount of structural disorder is introduced in the lattice. The sharp decrease of the ESP occurs with these films for $h\nu \geqq 3{\cdot}3$ eV and indicates that the density of states in the 'tail' of the valence-band states has increased on disordering. Furthermore, the $4f^7$-states are shifted to higher energies, since at 3·3 eV the ESP is higher for disordered than for ordered films.

Similar effects on disordering the lattice have been observed in the ferromagnetic semiconductor EuS[7]. According to present theories[8] the density of states in ordered and disordered systems is roughly the same, but there exists a 'tailing' of the band edges into the gap, which explains the first observation. Disordering induces a lowering of the vacuum level with respect to the atomlike $4f^7$-state also in EuS. Eu_3P_2 seems to be particularly suited for studying the effects of disordering on ferromagnetism, since the relatively complicated crystal structure makes the disordered state quite different from the ordered one.

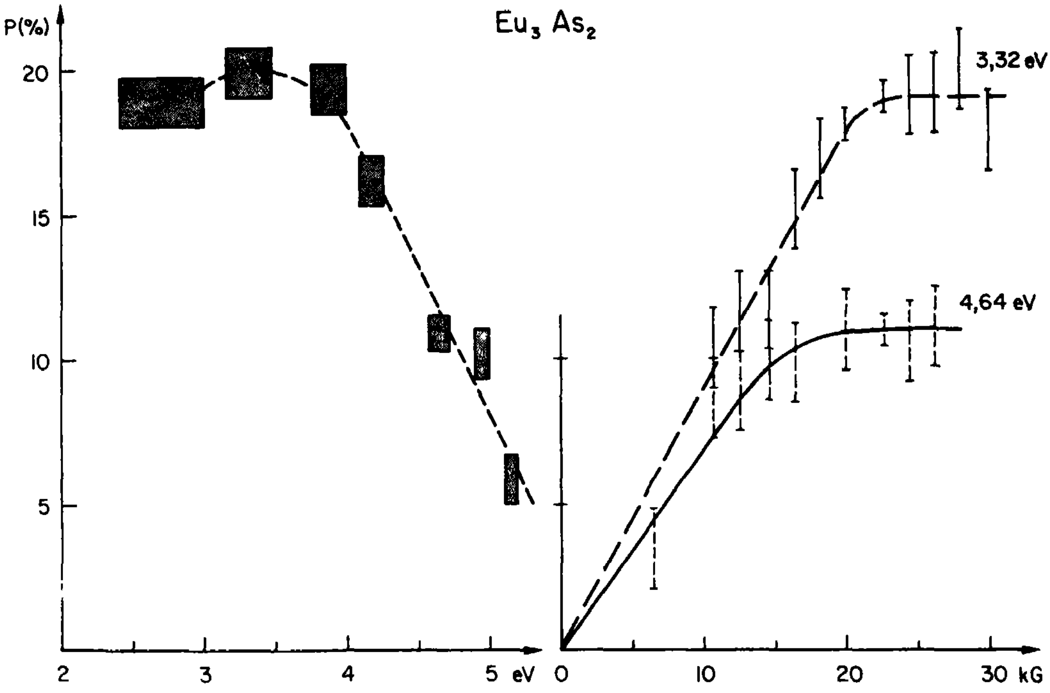

Fig. 3. The dependence of photo-ESP on photon energy at $B = 22{\cdot}8$ kG (left) and on the magnetic field strength at two photon energies (right) for ordered films of Eu_3As_2.

Eu_3As_2.

On the left-hand side of Fig. 3 the dependence of the ESP on photon energy is shown for a constant magnetic field of 22·8 kG and for Eu_3As_2-films prepared on substrates at 390 K. The maximum ESP is 20 per cent only and at 5 eV it is smaller by a factor of 3 compared to Eu_3P_2(I). This indicates that the $4f^7$-states merge to a large extent into the valence-band states. The number of impurity states above the $4f^7$-levels is significantly smaller in Eu_3As_2 since the ESP reaches already a maximum value near the threshold energy.

On the right-hand side of Fig. 3 the dependence of ESP on the magnetic field strength is shown for ordered Eu_3As_2-films. These dependences show the shape of magnetization curves which indicates the presence of ferromagnetic ordering in our samples at the temperature of the measurement (Corresponding curves were obtained for Eu_3P_2). The magnitude of the saturation-ESP depends on photon energy which follows from the left-hand side of Fig. 3. The saturation field $B \approx 20$ kG is large because of the large demagnetizing field for **B** perpendicular to the film surface.

The impurity levels are spin-polarized and this is a direct experimental evidence for the existence of an exchange interaction with the 4*f*-states. Yanase and Kasuya[9] and Nagaev [10] have treated the effects of such 'magnetic impurity states' on the properties of ferromagnetic semiconductors. This theory was applied for explaining the increase of T_c observed in doped europium chalcogenides. From the postulate of an exchange interaction of the carriers with the 4*f*-shell one can also deduce an anomalous peak of the electrical resistivity at T_c by spin-disorder scattering [11, 12].

In Fig. 4 we show the temperature dependence of the resistivity in arbitrary units for a bulk sample of Eu_3As_2. Spot welding of platinum contacts obviously introduced a large amount of carriers as it lowered the resistance of the samples by two or three orders of magnitude. At 18 K (this is T_c for *pure* material) the resistivity has a sharp anomaly whose shape is very similar to the one observed by von Molnar and Kasuya [13] in EuS doped with Gd, except that in EuS the position of the peak depends strongly on the carrier concentration. In EuS, the gross features of this behavior were found to be relatively insensitive to the nature of the dopant but very dependent on dopant concentration[6]. With Eu_3As_2, measurements on different samples have shown that the position of the peak is independent of carrier concentration. This means that there must be different conditions for the occurrence of critical scattering and for the enhancement of T_c that have not been recognized so far. It should be noted, that the pnictides do not show a red shift of the absorption edge on cooling below T_c that is comparable in magnitude with the one observed in the chalcogenides[5]. We suggest that the character of the conducting states is different for pnictides and chalcogenides.

4. CONCLUSIONS

The measurement of photo-ESP proves to

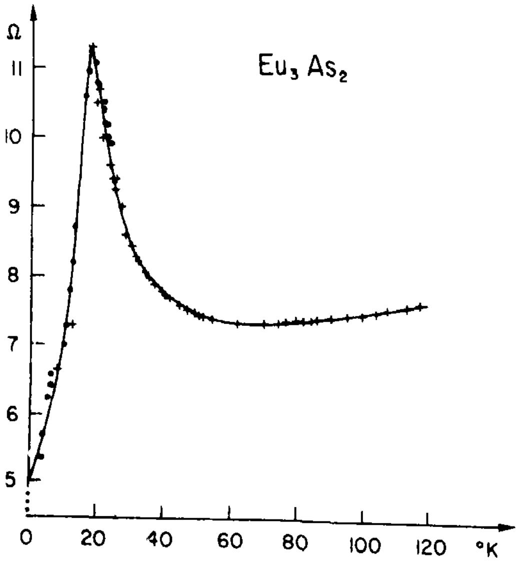

Fig. 4. The temperature dependence of the electrical resistivity in arbitrary units for a bulk sample of Eu_3As_2 with spot-welded platinum contacts.

be a powerful tool for determining the energy-level diagram in ferromagnetic semiconductors. Using this technique, an assignment and location of spin-polarized electron states is given for the ferromagnetic semiconductors Eu_3P_2 and Eu_3As_2. The differences between these substances and the europium monochalcogenides do not arise from a difference, that can be attributed to a band structure scheme. More refined conditions for the occurrence of some unusual phenomena must be formulated. The final explanation should take into account the local surroundings of the Eu^{2+}, the different crystal fields and the altered wave functions of the anions. The crystal structure of the pnictides is not simple. This leads to drastic effects on the electronic energy levels if disorder is introduced in the lattice.

Acknowledgement—This work has received financial support from the Schweizerischer Nationalfonds and the Verein zur Förderung der Festkörperphysik an der ETH.

REFERENCES

1. BUSCH G., CAMPAGNA M. and SIEGMANN H. C., *J. appl. Phys.* **41**, 1044 (1970).
2. JUNOD P., MENTH A. and VOGT O., *Phys. kondens. Mater.* **8**, 323 (1969).
3. HULLIGER F. and VOGT O., *Solid State Commun.* **8**, 771 (1970).
4. BUSCH G., CAMPAGNA M., COTTI P. and SIEGMANN H. C., *Phys. Rev. Lett.* **22**, 597 (1969).
5. BUSCH G., HULLIGER F., STREIT P., WACHTER P. and WULLSCHLEGER J., *Conférence Internationale de Magnétisme*, Grenoble (1970).
6. VON MOLNAR S., *IBM J. Res. Dev.* **14**, 269 (1970).
7. BUSCH G., CAMPAGNA M. and SIEGMANN H. C., 16th Annual Conf. on Magnetism and Magnetic Materials, Miami, Fla, (1970).
8. MOTT N. F., *Phil. Mag.* **22**, 175 (1970), and ref. cited therein.
9. YANASE A. and KASUYA T., *J. phys. Soc. Japan* **25**, 1025 (1968).
10. NAGAEV E. L., *Soviet Phys.-solid State* **11**, 2886 (1970).
11. HAAS C., *Phys. Rev.* **168**, 531 (1968).
12. WOOLSEY R. B. and WHITE R. M., *Phys. Rev.* **B1**, 4474 (1970).
13. VON MOLNAR S. and KASUYA T., *Phys. Rev. Lett.* **21**, 1757 (1968).

J. Phys. Chem. Solids Pergamon Press 1971. Vol. 32, pp. 2181–2191. Printed in Great Britain.

CATION MIGRATION, CATION VALENCIES AND THE CUBIC-TETRAGONAL TRANSITION IN $Mn_xFe_{3-x}O_4$

V. A. M. BRABERS
Department of Physics, Eindhoven University of Technology, Eindhoven, Netherlands

(*Received* 4 *December* 1970)

Abstract—Thermal expansion measurements of polycrystalline, single crystalline and textured specimens $Mn_xFe_{3-x}O_4$ are reported. The experimental data are interpreted in terms of two cation migration processes, namely the cation exchange between the octahedral and tetrahedral sublattices, and an octahedral Mn^{3+} clustering. The changes in the crystal structure of cubic $Mn_{1\cdot9}Fe_{1\cdot1}O_4$ in the temperature range of 250–350°C indicate a shift in the cation distribution of 0·15–0·20 ions per unit AB_2O_4, which is stabilised by the macroscopic tetragonal distortion of the lattice. The tetragonal distortions of the specimens $x = 1\cdot9$ in combination with electrical conductivity measurements on $x = 2\cdot0$ reveals unequivocally that in the spinel structure octahedral Mn^{3+} and Fe^{2+} are the stable cation valencies at low temperatures.

1. INTRODUCTION

In the $Mn_xFe_{3-x}O_4$ system two crystal structures exist at room temperature, namely the cubic spinel structure, if the manganese content $x < 1\cdot9$ and the tetragonally deformed spinel structure for $x > 1\cdot9$[1]. Dunitz *et al.*[2] pointed out that the tetragonal distortion originates from the Jahn–Teller effect of the transition metal cations which have an orbitally degenerate electronic state. The cubic-tetragonal transition in the $Mn_xFe_{3-x}O_4$ system is now supposed to be caused by a cooperative phenomenon of orientation of the tetragonally distorted $Mn^{3+}O_6^{2-}$ octahedra [3, 4], so that at a critical concentration of octahedral Mn^{3+} ions the spinel structure becomes tetragonal just at room temperature. Robbrecht *et al.*[5] completed the theory of the transition for the case of an ion exchange between the sublattices. The critical concentration of octahedral Mn^{3+} ions depends also on the kind of the other cations which are present on the octahedral and tetrahedral sublattices, as was experimentally shown by Blasse[6]. Consequently, the valency and the distribution of the cations among the tetrahedral and octahedral sites will influence the cubic-tetragonal transition of the lattice.

Several authors[7–10] studied the cation distribution of manganese ferrites by means of neutron or X-ray diffraction, and the results show that the manganese ions in these materials have a slight preference to be located on the tetrahedral sites as Mn^{2+} ions. The cation distribution in $Mn_xFe_{3-x}O_4$ can be represented by the formula

$$\underset{x-y}{Mn^{II}}\ \underset{1-x+y}{Fe^{III}}(Mn_yFe_{2-y})O_4. \qquad (1)$$

The cations inside the brackets occupy octahedral sites, those before the brackets tetrahedral sites. As is indicated in formula (1), the tetrahedral Mn ions are bivalent and the tetrahedral Fe ions are trivalent. So $1-x+y$ octahedral ions per unit AB_2O_4 must be bivalent because of the electro-neutrality of the system. Between the bivalent and trivalent octahedral ions there will be an equilibrium according to the equation:

$$Mn^{2+}+Fe^{3+} \rightleftarrows Mn^{3+}+Fe^{2+}. \qquad (2)$$

For a long time disagreement about this equilibrium has existed in the literature. From the fact that the magnetic moment of $MnFe_2O_4$ appeared to be 4·5–4·6 μ_B[7], Harrison *et al.*

[11] concluded that Mn^{3+} and Fe^{2+} ions form the stable configuration at low temperatures. However, this conclusion is only justifiable so far as the Néel coupling scheme with an antiparallel arrangement of the magnetisation of A and B sublattices is valid for $MnFe_2O_4$. Another explanation of the low magnetic moment was given by Lotgering[12] and Sawatzky *et al.*[13] by taking spin canting into consideration. In this explanation the octahedral Mn^{2+} and Fe^{3+} ions occur simultaneously at low temperatures.

From the semiconducting properties of the materials $Mn_xFe_{3-x}O_4$, no decisive answer to the question of the octahedral cations can be obtained either, as follows from a comparison between Lotgering's[14] and Šimša's [15] papers. Neither can the NMR detection of an Mn^{3+} signal in $MnFe_2O_4$ by Kubo *et al.* [16] be used to decide about the situation of the equilibrium, because in a more recent paper the authors reported the sample which was used in the measurements to have an excess of manganese ($x = 1\cdot03$)[17]. In a previous article[18], we concluded from the i.r. spectra of the cubic manganese ferrites that at low temperatures Mn^{2+} and Fe^{3+} ions coexist on the octahedral sites. However, Kanturek and Šimša[19] found in their i.r. spectra indications of the coexistence of octahedral Mn^{3+} and Fe^{2+} ions. Miller[20] used a crystallographic criterion to elucidate the valencies of octahedral manganese and iron ions in the spinel structure. Previous investigations of numerous systems[21] had shown that at room temperature, tetragonal distortions from cubic symmetry are observed in spinels where more than about 60 per cent of the B sites are occupied by Mn^{3+} ions. Miller supposed that this critical value of 60 per cent also holds for the system $Zn_{1-0.5t}Ge_{0.5t}Fe_tMn_{2-t}O_4$. From the combination of this critical value with the experimental observation that the crystal structure is tetragonal in the composition range $0 \leq t \leq 0\cdot8$, Miller inferred that Mn^{3+} and Fe^{2+} ions are the stable co-existing valency states on octahedral sites. However, his experimental results are in disagreement with the results of O'Keeffe[22], who found the tetragonal structure in the range $0 \leq t \leq 0\cdot5$ only. Moreover, the assumption that the value of 60 per cent for the critical Mn^{3+} concentration holds also for the system mentioned above is disputable, because high valency ions like Ge^{4+} may change the critical Mn^{3+} concentration substantially[6].

The aim of the present work is to determine the valencies of the octahedral cations in the $Mn_xFe_{3-x}O_4$ system, using the cubic-tetragonal transition in the manganese ferrite system itself as a criterion. For a correct interpretation of the experiments, an investigation of the possible cation migration processes is also carried out.

2. EXPERIMENTAL

Polycrystalline $Mn_xFe_{3-x}O_4$ materials were prepared with the usual ceramic technique. Mixtures of analytically pure α-Fe_2O_3 and $MnCO_3$ were prefired for 3 hr at 1100°C in carbon dioxide for compositions $x \leq 1\cdot0$ and in air for compositions $x > 1\cdot0$. The products were ground and from the powder obtained bars were pressed and sintered The compositions $x = 0\cdot8$, $1\cdot0$ and $1\cdot4$ were sintered for 3 hr in a mixture of 99% N_2 and 1% O_2 at temperatures of 1365, 1340 and 1295°C, respectively. The specimens $x = 1\cdot9$, $1\cdot95$, $2\cdot0$, $2\cdot10$ and $2\cdot25$ were sintered for 5 hr in air at temperatures of 1380, 1375, 1365, 1350 and 1315°C, respectively.

All the sintered specimens were cooled to room temperature in 45 min in a controlled atmosphere to avoid oxidation of the samples. The tetragonal materials $x > 1\cdot9$ were subsequently annealed for 3 hr at 900°C under vacuum in sealed silica tubes and quenched to room temperature X-ray diffraction proved that in this way homogeneous spinels without any second phase were obtained. Chemical analysis showed that the oxygen stoichiometry of the samples was within 2/10 mol%.

Cubic ⟨100⟩ oriented spinel single crystals ($x \leq 1\cdot90$) were grown by a floating zone technique[23]. After the preparation, the crystals were heat treated for 70 hr to improve the oxygen stoichiometry and the mechanical properties The annealing conditions were the same as the sintering conditions.

Textured specimens of the tetragonal spinels with compositions $1\cdot90 < x \leq 2\cdot25$ were prepared in air by a zone-melting process of polycrystalline bars; as seed-crystals ⟨100⟩ oriented cubic spinel crystals of the compositions $x = 1\cdot9$ were used. In the zone-melting process a cubic ⟨100⟩ oriented spinel crystal was formed from the melt, which transformed into a tetragonal textured specimen on cooling to room temperature. At the cubic-tetragonal transition temperature, reorientation of the tetragonal *c*-axis occurred in certain regions of the crystal in any of three perpendicular directions. The zone-melted specimens were annealed at 900°C for 24 hr in a sealed silica tube under vacuum to improve the homogeneity and quenched to room temperature. By etching at 105°C for 10 hr with a mixture of nitric acid, acetic acid and water (volume parts 1 : 1 : 3), it turned out that in the specimens obtained the *c*-axis was predominantly oriented perpendicularly on the length of the samples[24]. It was also possible by annealing at 900°C, followed by a slow cooling process, to align the *c*-axes in the textured specimens with compositions $1{\cdot}9 < x \leq 2{\cdot}10$ and to obtain large tetragonal single crystals[25].

The cation diffusion and the tetragonal-cubic transition was studied by combining X-ray diffraction and thermal expansion measurements on polycrystalline and textured tetragonal specimens (compositions $x = 1{\cdot}95$, 2·00, 2·10 and 2·25) and on ⟨100⟩ oriented cubic spinel crystals (compositions $x = 0{\cdot}8$, 1·0, 1·4 and 1·9). The dimensions of the samples were $50 \times 2 \times 2$ mm. The measurements were carried out in argon to avoid oxidation. More details about the dilatometer have been described elsewhere[24].

3. THE CATION EXCHANGE BETWEEN THE OCTAHEDRAL AND TETRAHEDRAL SUBLATTICES IN THE CUBIC SPINELS $Mn_xFe_{3-x}O_4$

Until now, many papers have been devoted to the temperature dependence of the ionic distribution in spinels. Néel[26] was the first to present an expression for ionic distribution at equilibrium for the simple case of a binary cubic spinel. An extension of the case of ternary systems was given by Smart[27]; a statistico-thermodynamic approach of this problem was made by Men *et al.*[28, 29]. An extended migration law for tetragonal spinels was set up by Mănăilă for octahedrally distorted spinels by taking the alignment of local Jahn–Teller distortions into account[30].

Experimental data on the temperature dependence of the cation distribution in the $Mn_xFe_{3-x}O_4$ system are rare. Hastings and Corliss[7] did not find any temperature dependent cation distribution in quenched $MnFe_2O_4$ samples. However, Driessens[10] reported a temperature dependence which was proved by the difference of the cation distribution in samples quenched from various temperatures; at lower temperatures, the manganese ions showed a preference to be located on tetrahedral sites. In a previous paper, the author[31] concluded from conductivity measurements that in Mn–Fe spinels a reversible cation exchange between octahedral and tetrahedral sites occurs already at 300°C which had also been shown by Yasuoka *et al.*[32] with NMR measurements. Thermal expansion measurements on cubic single crystals, which are reported in the present article, confirm that this cation exchange really occurs.

By relating the lattice parameter of the cubic spinels as a function of the total Mn content with the cation distributions reported in the literature[1, 10], it can be concluded that the lattice parameter of these spinels increases with the tetrahedral Mn^{2+} concentration and that a change of the tetrahedral Mn^{2+} concentration will result in an anomalous thermal dilatation. Figure 1 shows that in addition to the magnetic anomaly at 290°C, anomalous behaviour at 400°C appears in the thermal expansion of a single crystal of $Mn_{1{\cdot}0}Fe_{2{\cdot}0}O_4$. Samples quenched from 600°C show a sudden increase in the thermal expansion near 400°C, followed by a decrease in the thermal expansion coefficient to nearly half its original value. Slowly cooled specimens exhibit only a slowly

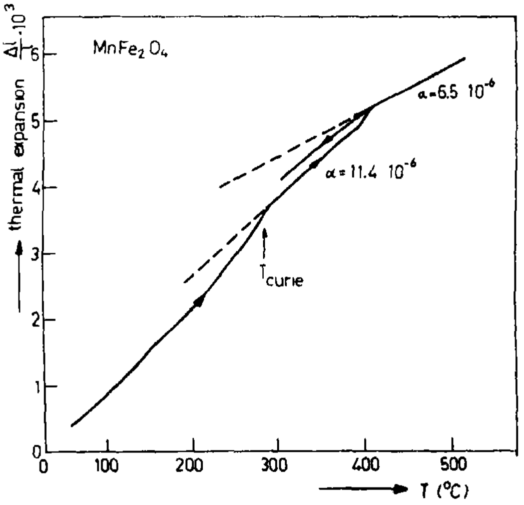

Fig. 1. Thermal expansion of single crystalline $MnFe_2O_4$, measured in the ⟨100⟩ direction.

diminishing expansion coefficient with rising temperature. Further, at temperatures below 350°C a difference in length of about 0·025 per cent between quenched and slowly cooled samples is observed which consists with the variation of the lattice constant observed before by X-ray diffraction on heat treated $Mn_{1\cdot1}Fe_{1\cdot9}O_4$ single crystals[31]. After repeating the annealing and quenching procedure at 600°C, the same dilatation curves were invariably obtained, which proves that oxidation of the specimens during the measurements did not affect the results.

This anomalous behaviour can be interpreted in terms of temperature dependent cation distribution between the octahedral (B) and tetrahedral (A) sublattices: $Mn_A + Fe_B \rightleftarrows Mn_B + Fe_A$. Below 400°C it is supposed that the cation exchange is too slow to achieve the equilibrium distribution. By quenching from 600°C, too many manganese ions are frozen on octahedral sites. So there is a shortage of manganese ions on tetrahedral sites, which results in a smaller lattice parameter. When increasing the temperature, equilibrium is attained at about 400°C and the excess octahedral manganese ions will diffuse to tetrahedral sites. Consequently, the thermal dilatation of the quenched sample will display a sudden increase near this temperature. A further increase in the temperature will cause manganese ions to diffuse back to octahedral sites as a result of the shifting of the equilibrium distribution, and the thermal expansion coefficient diminishes. The observation that for slowly cooled specimens only the slope of the dilatation curve diminishes gradually with increasing temperature round 400°C is also in agreement with the assumptions regarding the cation exchange between the sublattices.

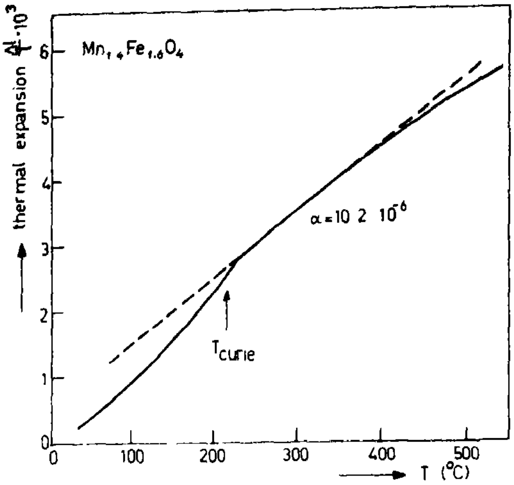

Fig. 2. Thermal expansion of single crystalline $Mn_{1\cdot4}$-$Fe_{1\cdot6}O_4$ measured in the ⟨100⟩ direction.

The anomaly in the linear expansion caused by the cation exchange was also detected in single crystals $x = 0\cdot8$ and $x = 1\cdot4$. Figure 2 represents the thermal expansion of a crystal $x = 1\cdot4$, which was slowly cooled from 600°C to room temperature. Measurements on $x = 0\cdot8$ did not reveal clear information on the cation exchange, since the Curie temperature of this material is very close to the temperature region where the cation exchange becomes noticeable.

4. Mn^{3+} CLUSTERING ON THE OCTAHEDRAL SUBLATTICE

In addition to the cation exchange between the two sublattices another cation diffusion process in the Mn–Fe spinel system is possible, namely a clustering of octahedral Mn^{3+} ions. The physical reason for the formation of these clusters has been sought in the Jahn–Teller effect of the Mn^{3+} ions. In a cubic lattice these ions tend to distort their environment, which increases the elastic energy of the crystal. A reduction of the elastic energy is possible by grouping the distorting ions into clusters in which then parallel alignment of the distorted octahedra occurs.

Recently, Červinka *et al.*[33] observed local inhomogeneities by means of X-ray diffraction in $Mn_{1\cdot9}Fe_{1\cdot1}O_4$, slowly cooled from 900°C in air. Naturally, the inhomogeneity may well be occasioned by oxidation of their samples during the cooling process, since even a segregation of a second phase of

α-$(Fe,Mn)_2O_3$ was observed in one of the samples. However, the existence of a two-phase region in the manganese-rich part of the $Mn_xFe_{3-x}O_4$ system indicates that Mn^{3+} clustering is an intrinsic process without any interference of oxidation [24, 34].

In a paper mentioned before [1], the author investigated the lattice parameters of the tetragonal Mn–Fe spinels, of which the results are given in Fig. 3. The samples prepared with the usual ceramic techniques showed broadened X-ray diffraction lines. It was observed that the linewidth decreased with increasing Mn content and that for pure Mn_3O_4 the broadening did not occur, which points to the possibility of chemical inhomogeneities, like Mn^{3+} clustering, as the cause of the line-broadening. By annealing the sintered specimens in vacuum the line-broadening disappeared and in addition to this effect also a decrease in the c/a ratio was observed, which was suggested to be caused by migration of manganese ions from octahedral to tetrahedral sites during the annealing process. However, the alterations in linewidth and in c/a ratio appear simultaneously, and it seems that both these phenomena are connected with the clustering of octahedral Mn^{3+} ions. Since the largest variation in c/a ratio and linewidth were observed with $x = 2{\cdot}0$, we investigated the influence of thermal treatments on these phenomena further on specimens $x = 2{\cdot}0$. Table 1 summarises the results.

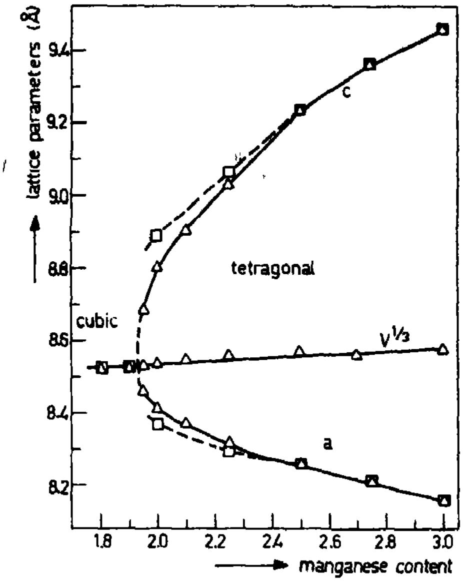

Fig. 3. Lattice parameters of tetragonal $Mn_xFe_{3-x}O_4$ (1). □ samples sintered at temperatures between 1175 and 1400°C and cooled to room temperature in 45 min. △ samples annealed in silica tubes under vacuum for 3 hr at 900°C, 16 hr at 600°C and 3 hr at 300°C.

From these experiments it follows that for the compositions $x = 2{\cdot}0$ the changes in linewidth and c/a ratio go on during the slow cooling between 300 and 200°C and that both

Table 1. Influence of thermal treatments on the structure at room temperature of tetragonal Mn_2FeO_4 *specimens*

Thermal treatment	c/a	Line-broadening
A. Specimen sintered in air at 1360°C and cooled in 1½ hr	1·064	++
B. Specimen sintered in air at 1360°C and quenched	1·045	—
C. Sample *A*, annealed in vacuum for 3 hr 900°C, 15 hr 600°C and 3 hr 300°C	1·045	—
D. Sample *B*, annealed in vacuum for 3 hr 900°C, 15 hr 600°C and 3 hr 300°C	1·045	—
E. Sample *B*, annealed for 48 hr at 200°C in vacuum	1·060	+
F. Sample *B*, annealed for 48 hr at 200°C in air	1·060	+

these changes are simultaneous. If one supposes the manganese ions to have, at low temperatures, a preference for the tetrahedral sites, the c/a ratio for samples annealed at 200°C would be unchanged or smaller. Which of these two possibilities occurs, depends on the electron distribution over the octahedral ions (See equation (2)). The experimental results given in Table 1 contradict the proposed cation exchange between the sublattices because an increase in the c/a ratio was observed. The conclusion that octahedral Mn^{3+} clustering is the only process active during these annealing experiments seems justified, since oxidation is also ruled out by the identical result of the experiments *E* and *F*. In Section 6 of this paper, however, it will be shown that the octahedral manganese concentration is not a function monotonously increasing with temperature, but that certain peculiarities appear near the tetragonal-cubic transition temperature, by which cation migration between the sublattices during our annealing experiments at 200°C cannot be ruled out. How far the observed variations of the c/a ratio will be due to a change in the cation distribution or to Mn^{3+} clustering is hard to say, and consequently no decisive answer to the question of the electron distribution over the octahedral cations can be given with the experiments reported so far. But the identical results for the annealing of the specimens $x = 2{\cdot}0$ at 200°C in air and in vacuum prove that the Mn^{3+} clustering is an intrinsic process of the $Mn_xFe_{3-x}O_4$ system and is not only caused by oxidation.

To get an idea about the influence of the oxidation on Mn^{3+} clustering, the thermal dilatation of homogeneous polycrystalline specimens $x = 2{\cdot}0$ was measured in air and in argon (c/a = 1·045); the results are displayed in Fig. 4. At 127°C the magnetic anomaly occurs and near 200°C a small increase in the thermal expansion coefficient goes on, which is caused by the tetragonal-cubic transition (See Section 5). Above 250°C, the measurements in air differ substantially from those in argon. In air two peaks in the thermal expansion coefficient are found at about 300 and 400°C, respectively. A sample quenched to room temperature after the measurements in air up to 320°C turned out to be a single phase, although a considerable line-broadening in the X-ray diagram was observed. After the measurements in air up to 450°C segregation into a cubic spinel phase and a tetragonal γ-$(Mn,Fe)_2O_3$ phase was observed. The X-ray diffraction lines of the spinel as well as the lines of the γ-$(Mn,Fe)_2O_3$ phase displayed substantial broadening. These results indicate that oxidation of the sample substantially increases the octahedral Mn^{3+}-clustering, which is obvious, because oxidation increases the cation mobility by creating cation vacancies. From the results of the measurement in argon it appears that the Mn^{3+} clustering without interference of the oxidation process is too slow to go on during the heating of the sample (2°C/min).

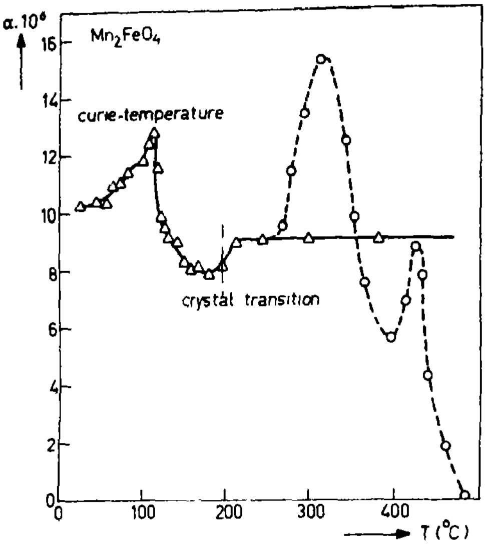

Fig 4. Thermal expansion of polycrystalline Mn_2FeO_4. △ measurements in argon. ○ measurements in air.

5. THE CUBIC-TETRAGONAL TRANSITION TEMPERATURE

No precise data of the cubic-tetragonal transition temperature of homogeneous

$Mn_xFe_{3-x}O_4$ materials are available in the literature, which is a consequence of the phase segregation accompanying the transition. From the investigation of the two-phase region by McMurdie *et al.*[34] and by Van Hook *et al.*[35] some approximated values can be deduced. Measurements of the thermal dilatation of homogeneous tetragonal specimens can be used to determine the transition temperature of these materials. As is shown by Fig. 4 the effect in the expansion coefficient at the transition temperature is very small for polycrystalline samples, which is the outcome of the fact, that for polycrystalline materials only changes of the crystal volume are detected and no linear alterations of the crystal axes. With the purpose of enlarging the effect at the transition temperature, the dilatation measurements were carried out on textured specimens, in which the crystallites were ordered in such a way that in the length of the sample the *a*-orientation of the crystallites dominates. Consequently, a strong dilatation will be observed at the transition temperature. Figure 5 displays the results of the measurements on samples $x = 1{\cdot}95$, 2·0, 2·10 and 2·25. From these curves it can be seen that for the specimens $x = 1{\cdot}95$ and 2·0 an abrupt dilatation occurs at 72 and 198°C, respectively, and that for the specimen $x = 2{\cdot}10$ a transition region from 350–360°C enters the measurements. The sudden expansion of the specimens $x = 1{\cdot}95$ and 2·0 indicates the first order type of the transition. With the measurement on $x = 2{\cdot}25$ and more or less also with the measurement on 2·10, the octahedral Mn^{3+} clustering interferes with the crystal transition, which could be concluded from the large X-ray line-broadening observed on a specimen $x = 2{\cdot}25$ after the measurements up to 700°C. During measuring the material becomes inhomogeneous with respect to the octahedral Mn^{3+} concentration, which causes a transition region to be observed instead of a sharp transition temperature. This transition region is not in contradiction with the first order type of the transition as was pointed out theoretically by Haas[36].

Irani *et al.*[37] found for a large number of tetragonally distorted oxygen-spinels one linear relation between the transition temperature and the $(c/a)_{T=0}$ ratio. This linear dependence is to be expected if one makes the assumption that the interaction energy between distorted polyhedra is proportional to the c/a ratio[37]. In Fig. 6 the transition temperature of homogeneous $Mn_xFe_{3-x}O_4$ specimens obtained from our dilatation measurements is plotted against the value of the c/a ratio at room temperature. The data for pure Mn_3O_4 reported by McMurdie [38] are also included. The linearity of the curve agrees very well with the relation given by Irani; only the c/a ratio of the specimen $x = 1{\cdot}95$ is somewhat too low, which may be due to the fact that this ratio was determined very close to the transition temperature $(T \approx 0{\cdot}85T_{tr})$ [3].

In the composition range $2{\cdot}10 < x < 3{\cdot}0$ it is difficult to find accurate values of the transition temperature because of the two-phase region. In order to get more information about the tetragonal distortions in this intermediate region, a number of specimens $x = 2{\cdot}66$ were prepared by sintering in air at 1235°C, followed by annealing for 100 hr at various temperatures between 700 and 1235°C in a controlled atmosphere and subsequent quenching to room temperature. In the X-ray diagram all the samples showed line-broadening, which increased when the annealing temperature approached 900°C. The sample annealed at 890°C even decomposed into two phases, which were tetragonal at room temperature with c/a ratios of 1·136 and 1·110, respectively. The results of these annealing experiments denote that the transition temperature of a homogeneous specimen $x = 2{\cdot}66$ is close to 890°C and that the room temperature value of the c/a ratio lies between 1·136 and 1·110. From the plotted values of Fig. 6 it can be concluded that the relation between the transition

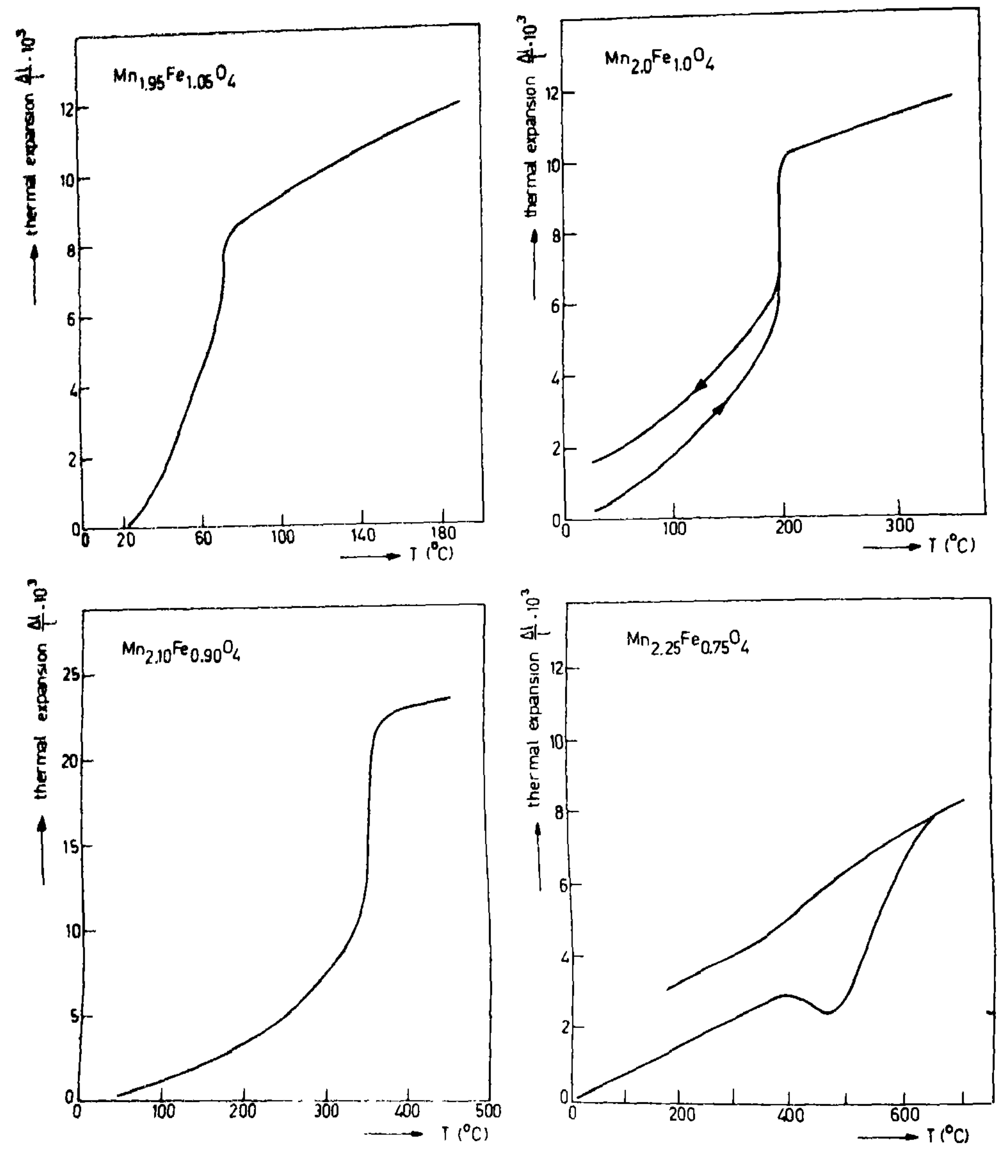

Fig. 5. Thermal dilatation curves of textured tetragonal $Mn_xFe_{3-x}O_4$ specimens.

temperature and the c/a ratio at room temperature is in first approximation linear for the whole $Mn_xFe_{3-x}O_4$ system.

6. THE OCTAHEDRAL CATION VALENCIES IN THE $Mn_xFe_{3-x}O_4$ SYSTEM

Recently, O'Bryan and Levinstein[39] reported the structure of slowly cooled $Mn_{1.88}Fe_{1.12}O_4$ to be tetragonal at 300°K, while fast cooled specimens were cubic. The c/a ratio of the tetragonal specimen was 1·005 and the transition temperature 260°C, which deviates strongly from our results given in Section 5. O'Bryan *et al.* supposed that at low temperatures manganese ions in this material have an energetic preference for

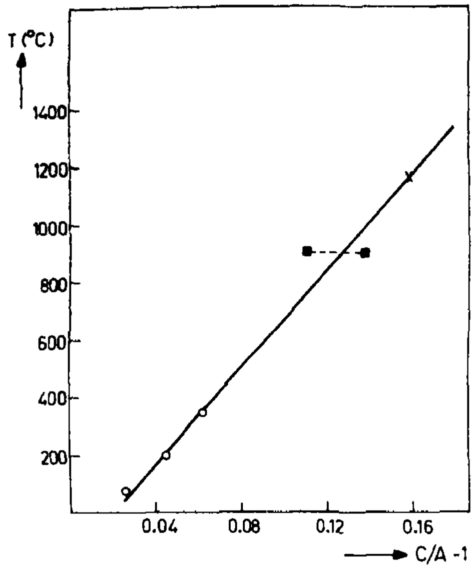

Fig. 6. The tetragonal-cubic transition temperature plotted against the tetragonal c/a ratio at 20°C. ○ values obtained from thermal expansion measurements. ■ values from annealing experiments on $Mn_{2.66}Fe_{0.34}O_4$. × high temperature X-ray diffraction[38].

octahedral sites; consequently, higher temperatures tend to randomise the distribution of the manganese ions, and material quenched from high temperatures will contain fewer octahedral manganese ions and will have lower transition temperatures than slowly cooled material. However, this is only true, if Mn^{3+} in presence of Fe^{2+} ions form the stable configuration on the octahedral sites at low temperatures. Moreover, the supposition that manganese ions in the manganese iron spinels have at low temperatures a preference for the octahedral sites is in contradiction with the cation distributions observed in these spinels [7-10].

To investigate this problem further, we measured the thermal expansion in the temperature range of 20–700°C on a number of cubic ⟨100⟩ oriented single crystals $x = 1{\cdot}9$, which composition is comparable with that used by O'Bryan. In Fig. 7 a typical dilatation curve is represented. After the measurement up to 450°C the specimen was quenched to room temperature and then turned out to be cubic. Only slight line-broadening was observed. Another specimen which was measured up to 320°C, displayed the same shrinkage near 300°C, but after quenching to room temperature it appeared to be tetragonal with c/a ratio 1·052. The X-ray diffraction lines of this specimen were also a little broadened.

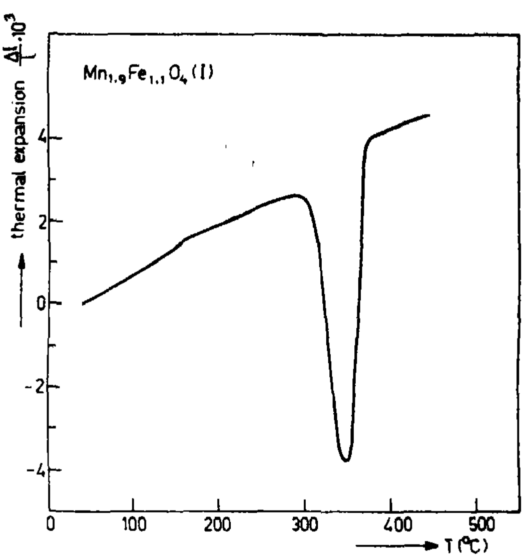

Fig. 7. Thermal expansion of cubic $Mn_{1.9}Fe_{1.1}O_4$ single crystal annealed at 1340°C in 0·20 atm oxygen and cooled to room temperature in 45 min.

The observed phenomena can be interpreted by supposing that near 300°C a cation migration between tetrahedral and octahedral sublattices becomes possible according to the equation

$$Mn_A^{II} + 2Fe_B^{III} \rightleftarrows Mn_B^{III} + Fe_B^{II} + Fe_A^{III}. \qquad (a)$$

Here, Mn_A^{II} means a bivalent Mn ion in a tetrahedral site, etc. A macroscopic distortion of the lattice may cause the equilibrium (a) to shift towards the right, because the transition from the cubic to the tetragonal structure is an exothermic process[40], and because at low temperatures the equilibrium (a) lies to the left. Thus, the shifting of a number of tetrahedral Mn^{2+} ions to the octahedral sublattice can be stabilised by a macroscopic distortion of the lattice; consequently, octahedral Mn^{3+} ions in the presence of Fe^{2+} ions cannot but be stable in the tetragonal spinel structure at low temperatures. Near 300°C such a shift of the manganese ions really takes place and the cubic structure changes into a tetragonal one. The cubic ⟨100⟩ oriented single crystal transforms into a tetragonal textured specimen, in which the a-axes or the c-axes of the crystallites may dominate in the direction of the length of the sample. If the a-axes prevails, a strong shrinkage will occur, which is also displayed in Fig. 7. Near 360°C the tetragonal structure becomes again cubic, which results in a steep increase in the dilatation till about the original value is reached. The cubic structure of the specimen quenched from 450°C indicates that at this temperature the shift in the cation distribution which was stabilised below 360°C by the macroscopic distortion no longer exists. The cubic structure of this specimen also rules out the influence of oxidation during the measurements. From the c/a ratio of 1·052 observed on the sample quenched from 320°C the number of migrating manganese ions can be estimated to be 0·15–0·20 per unit AB_2O_4.

In Fig. 8 is represented the thermal dilatation of a cubic ⟨100⟩ oriented single crystal $x = 1{\cdot}9$, which was annealed under more oxidising conditions (1225°C, 1 atm oxygen). The cation shift in this specimen already appeared near 270°C, which can be understood as the result of higher cation mobility caused by the increased cation vacancy concentration. Another peculiarity of this measurement is that strong dilatation is observed before shrinkage occurs near 350°C. Thus, in this case the c-axis prevails in the direction of the length of the specimen.

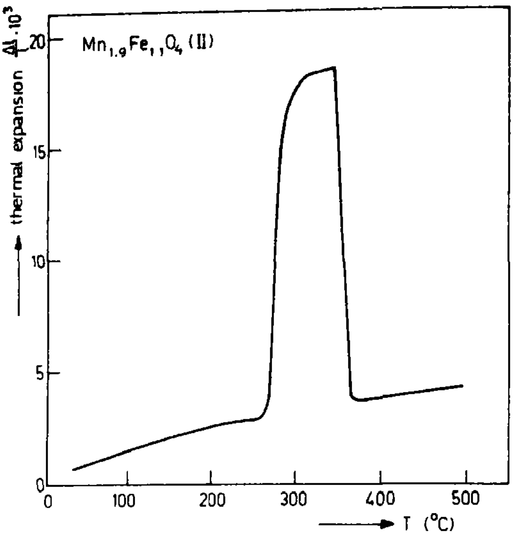

Fig. 8. Thermal expansion of a cubic $Mn_{1.9}Fe_{1.1}O_4$ single crystal annealed at 1225°C in 1 atm oxygen and cooled to room temperature in 45 min.

From the reported thermal expansion measurements on single-crystalline $Mn_{1.9}Fe_{1.1}O_4$ one must conclude that in the tetragonal structure Fe^{2+} and Mn^{3+} are the stable valencies on the octahedral sites. For the interpretation of the electrical conductivity phenomena in the cubic Mn–Fe spinels Šimša[15] introduced the hypothesis that Mn^{3+} and Fe^{2+} form a pair stabilised by Jahn–Teller effects and that this pair acts as donor for the electrical conduction. Electrical conductivity measurements which were carried out in our laboratory on single crystals Mn_2FeO_4 revealed no anisotropy for the tetragonal structure and no change of the activation energy at the tetragonal-cubic transition ($E = 0{\cdot}47$ eV; $T = 198$°C)[24]. This implies that also in the cubic spinel structure the Mn^{3+}-Fe^{2+} pairs form the stable configuration at low temperatures.

7. CONCLUSIONS

The combined thermal dilatation and X-ray measurements show that two types of cation migration take place in the $Mn_xFe_{3-x}O_4$ system. The cation exchange between the octahedral and tetrahedral sublattices occurs in the entire system and already appears at temperatures of the order of 200°C; the octahedral Mn^{3+} clustering occurs only in that part of the system rich in manganese. The measurements on the cubic single crystals

$x = 1\cdot9$ show that in the temperature range of 250–350°C a shift in the cation distribution is induced and stabilised by the macroscopic tetragonal distortion of the lattice. From this distortion it follows that at low temperatures the equilibrium of the electron distribution among the octahedral cations according the equation

$$Mn^{2+} + Fe^{3+} \rightleftarrows Mn^{3+} + Fe^{2+}$$

must for the tetragonal structure be placed on the right-hand side. Electrical conductivity measurements on Mn_2FeO_4 prove that this statement also holds for the cubic spinel structure.

Acknowledgement—The author would like to thank Mr. M Heijligers for his careful help with the preparations of the samples.

REFERENCES

1. BRABERS V. A. M., *Phys. Status Solidi* **33**, 563 (1969).
2. DUNITZ J. D. and ORGEL L. E., *J. Phys. Chem. Solids* **3**, 20 (1957).
3. WOJTOWICZ P. J., *Phys. Rev.* **116**, 32 (1959).
4. KANAMORI J., *J. appl. Phys. Suppl.* **31**, 35 (1961)
5. ROBBRECHT G. G. and DE CLERCK E. F., *Physica* **31**, 1033 (1965).
6. BLASSE G., *Philips Res. Rep.* **20**, 528 (1965).
7. HASTINGS J. M. and CORLISS L. M., *Phys. Rev.* **104**, 328 (1956).
8. YAMZIN I. I., BELOV N. V. and NOZIK YU. Z., *J phys. Soc. Japan* **17**, B-III, 55 (1962).
9. BOUCHER R., BUHL R. and PERRIN M., *J. appl. Phys.* **40**, 1126 (1969).
10. DRIESSENS F. C. M. and RIECK G. D., *Acta crystallogr.* **20**, 521 (1966).
11. HARRISON F. W., OSMOND W. P. and TEALE R. W., *Phys. Rev.* **106**, 865 (1957).
12. LOTGERING F. K., *Philips Res. Rep.* **20**, 320 (1965).
13. SAWATZKY G. A., VAN DER WOUDE F. and MORRISH H., *Phys. Rev.* **187**, 747 (1969).
14. LOTGERING F. K., *J. Phys. Chem. Solids* **25**, 95 (1964).
15. ŠIMŠA Z., *Czech. J. Phys.* **B15**, 435 (1965).
16. KUBO T., ABE H. and HIRAI A., *J. phys. Soc. Japan* **23**, 124 (1967).
17. KUBO T., HIRAI A., and ABE H., *J. phys. Soc. Japan* **26**, 1094 (1969).
18. BRABERS V. A. M. and DEKKER P., *Phys. Status Solidi* **29**, K73 (1968).
19. KANTUREK J. and ŠIMŠA Z., *Phys. Status Solidi* **36**, K47 (1969).
20. MILLER A., *J. appl. Phys. Suppl.* **31**, 261 (1960).
21. WICKHAM D. G. and CROFT W. J., *J. Phys. Chem. Solids* **7**, 351 (1958).
22. O'KEEFFE M., *J. Phys. Chem. Solids* **21**, 172 (1961).
23. KOOY C. and COUWENBERG H. J. N., *Philips tech. Rev.* **23**, 161 (1962).
24. BRABERS V. A. M., Thesis Eindhoven University of Technology (1970).
25. BRABERS V. A. M., *J. Cryst. Growth* **8**, 26 (1971).
26. NÉEL L., *C. r. hebd. Séanc. Acad. Sci., Paris* **230**, 190 (1950).
27. SMART J. S., *Phys. Rev.* **94**, 847 (1954).
28. MEN A. N., KURUSHIN YU. N., ZHURAVLEVA M. G. and CHUFAROV G. I., *Dokl. Akad. Nauk. SSSR* **176**, 594 (1967).
29. MEN A. N., KURUSHIN YU. N., ZHURAVLEVA M. G. and CHUFAROV G. I., *Dokl. Akad. Nauk. SSSR* **175**, 132 (1967).
30. MĂNĂILĂ R., *J. Phys. Chem. Solids* **28**, 2335 (1967).
31. BRABERS V. A. M., *Ber. dt. keram. Ges.* **47**, 648 (1970).
32. YASUOKA H., HIRAI A., SHINJO T., KIYAMA M., BANDO Y. and TAKADA T., *J. phys. Soc. Japan* **22**, 174 (1967).
33. ČERVINKA L., HOSEMANN R. and VOGEL W., *Acta crystallogr.* **A26**, 277 (1970).
34. MCMURDIE H. F., SULLIVAN B. M., MAUER F. A., *J. Res. NBS* **45**, 35 (1950).
35. VAN HOOK H. J. and KEITH M. L., *Am. Miner.* **43**, 69 (1958).
36. HAAS C., *J. Phys. Chem. Solids* **26**, 1225 (1965).
37. IRANI K. S., SINHA A. P. B. and BISWAS A. B., *J. Phys. Chem. Solids* **23**, 711 (1962).
38. MCMURDIE H. F. and GOLOVATO E., *J. Res. NBS* **41**, 589 (1948).
39. O'BRYAN H. M. and LEVINSTEIN H. J., *J. Phys. Chem. Solids* **30**, 1719 (1969).
40. SCHMAHL N. G. and HENNINGS, *Arch. Eisenhütten Wes.* **40**, 395 (1969).

J. Phys. Chem. Solids Pergamon Press 1971. Vol. 32, pp. 2193–2199. Printed in Great Britain.

SPONTANEOUS AND STIMULATED EMISSION FROM CdSe AT HIGH EXCITATION LEVELS

I. FILINSKI*
Chemical Laboratory B, Technical University of Denmark, Lyngby, Denmark

and

B. WOJTOWICZ-NATANSON
Institute of Experimental Physics, University of Warsaw, Warsaw, Poland

and

J. M. HVAM
Physics Laboratory III, Technical University of Denmark, Lyngby, Denmark

(*Received* 6 *June* 1969; *in revised form* 23 *November* 1970)

Abstract—Luminescence of CdSe single crystals excited by high intensity light pulses has been investigated in the temperature region 4·2–77°K. The rate of increase of the intensity of several free and bound exciton lines as a function of excitation intensity has been determined. The line with the highest rate of increase has been interpreted as being due to interaction of two free excitons. Electron-beam pumped laser emission from this line has been obtained at low temperatures and its contribution to the laser emission at higher temperatures is discussed.

1. INTRODUCTION

ALTHOUGH lasing transitions have been observed in several II–VI compounds the mechanism giving rise to the lasing lines is still not wholly understood. In a recent paper C. Benoit a la Guillaume *et al.*[1] have shown that at least three different processes can lead to laser effects in CdS. Some significant changes occurring in the luminescence of CdSe when the intensity of exciting light is greatly increased haved been reported in the last few years[2–5]. From measurements of the dependence of the intensity of luminescence on the intensity of excitation interesting information may be obtained concerning the nature of recombination centers and the mechanism of luminescence and laser action. This paper reports more detailed studies of these effects in CdSe in the region of exciton lines.

2. EXPERIMENTAL

Thin CdSe platelets were used in the measurements. The luminescence was excited by high intensity pulses from a Xenon flash tube (20 p.p.s., 0·2 Joule per flash). Calibrated neutral filters were used for attenuation of the excitation intensity. The recombination radiation was analyzed by a SPM-2 grating monochromator (with 20 Å/mm dispersion) or with a PGS-2 spectrograph (with 7·8 Å/mm dispersion in the investigated spectral region) and was recorded by a photo-multiplier. Spectra were taken with a PAR boxcar integrator followed by a logarithmic converter. The lowest temperature was obtained by immersing crystals in liquid Helium. Carbon and Platinum resistors were used for temperature measurements.

The laser emission was obtained by pulsed electron-beam excitation (200 nsec., 50 Hz). The beam energy was 30 keV and currents up to 40 mA were used. Platelets that were cleaved to form a cavity perpendicular to the electron-beam (laser geometry) were mounted on a copper cold finger in a Helium dewar. In spontaneous emission measurements the light emitted directly from the bombarded face was detected. The output from the photomultiplier was led to a sampling oscilloscope, sampling on the leading edge of the pulse in order to avoid the influence of heating during the pulse.

---

*On leave from the University of Warsaw.

3. RESULTS AND DISCUSSION

The dependence of the intensity of the most prominent lines in the exciton spectrum on the intensity of exciting light was measured at 4·2°K. This dependence can be expressed by the formula

$$I_{\text{lum}} = I^{\alpha}_{\text{exc}} \tag{1}$$

where I_{lum} is the intensity of luminescence and I_{exc} the intensity of exciting light. The values of the power α are given in Table 1.

As the temperature was increased from 4·2 to 77°K the spectrum shifted towards longer wavelengths due to the variation of the band gap. The positions of the maxima in this temperature range are shown in Fig. 1. The shifts of the phonon lines A_1–LO and A_1–2LO are seen to be weaker corresponding to shifts of 1·5 and 0·5 kT respectively towards higher energies relative to the band gap in agreement with the results from Ref. [6]. With the change of temperature a significant change of spectral distribution of emitted intensity is observed (Fig. 2).

The intensity of the recombination radiation of the free exciton A_1 is nearly a linear function of the excitation intensity, as should be expected for high excitation intensities at 4·2°K (at very high excitation intensity, however, this function can become sublinear [4,7]), at which the number of free excitons should be proportional to the number of created pairs of carriers.

The I_2 line is ascribed to the radiative recombination of an exciton bound to a neutral donor[8]. The binding energy of this complex measured from the spectrum as the distance on energy scale between this line and the A_1 line is 4 meV. With increasing temperature the intensity of the I_2 line diminishes rapidly, because of the small binding energy of the complex. The dependence on the excitation intensity is linear, as could be expected if the number of these shallow neutral donors is independent of the excitation intensity. (The number of free excitons increases linearly with the number of incident photons).

The dependence of the intensity of the

Table 1. *Positions of some of the exciton lines in* CdSe *at* 4·2°K *and the respective values of* α *obtained by photoexcitation*

Symbol	Exciton complex	Wavelength	Energy	α*
		Å	eV	
A_1	free exciton Γ_9–Γ_7 in state $n = 1$	6789	1·826	1·1
I_2	exciton bound to neutral donor	6803	1·822	1·0
I_1	exciton bound to neutral acceptor	6823	1·817	1·6
P	?	6847	1·811	1·9
A_1-LO	free exciton with emission of 1 phonon	6889	1·799	> 1
I_1-LO	exciton bound to neutral acceptor with emission of 1 phonon	6924	1·790	> 1
A_1-2LO	free exciton with emission of 2 phonons	6993	1·773	

*Because of some overlapping of the peaks and of a strong background the accuracy of α is about 20 per cent.

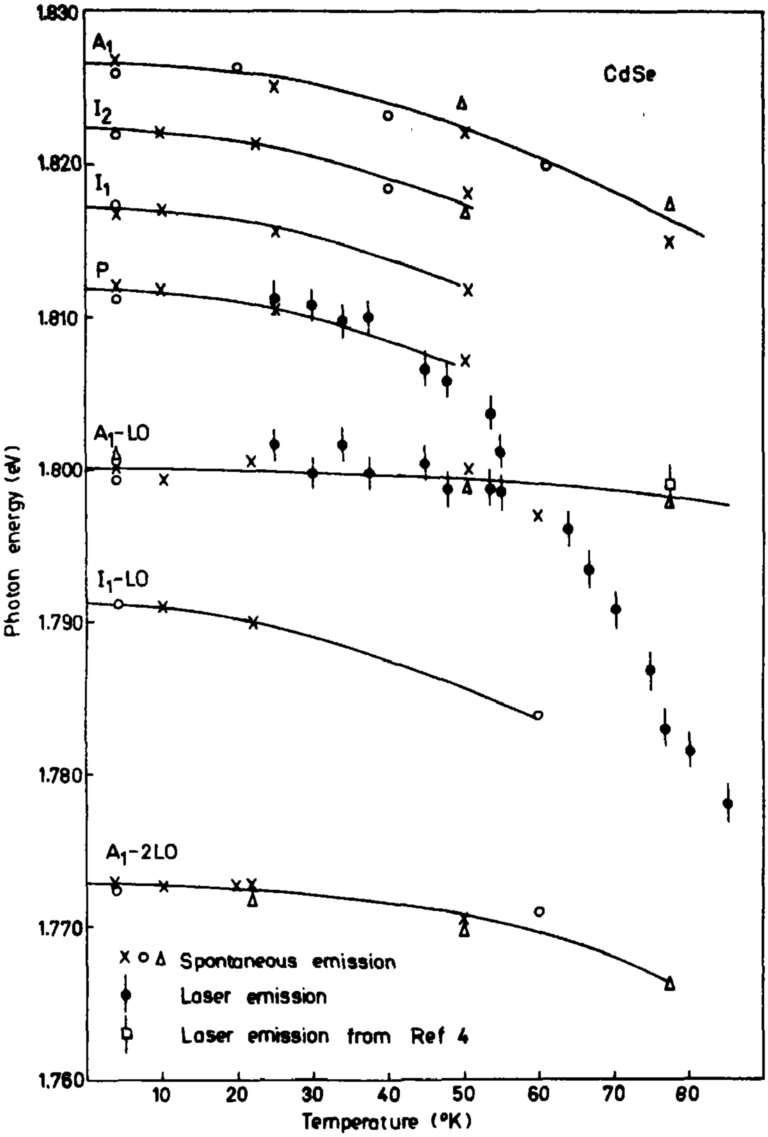

Fig. 1. Position of spontaneous and stimulated emission lines vs. temperature. The spontaneous emission was excited by a flash lamp. The laser emission was electron-beam excited with a beam energy of 30 keV and beam currents of 1–5 mA.

I_1 line on excitation is superlinear with $\alpha = 1{\cdot}6$. One may expect this value of power since this line is due to recombination of excitons bound to neutral acceptors[8]. Its intensity should therefore be proportional to both the concentration of free excitons and of neutral acceptors. As CdSe is always *n*-type, acceptors will tend to be ionized in unexcited samples. Hence, far from saturation, the concentration of neutral acceptors should be proportional to the number of free holes generated by the light. The concentration of free holes, on the other hand, will increase as the square root of the excitation

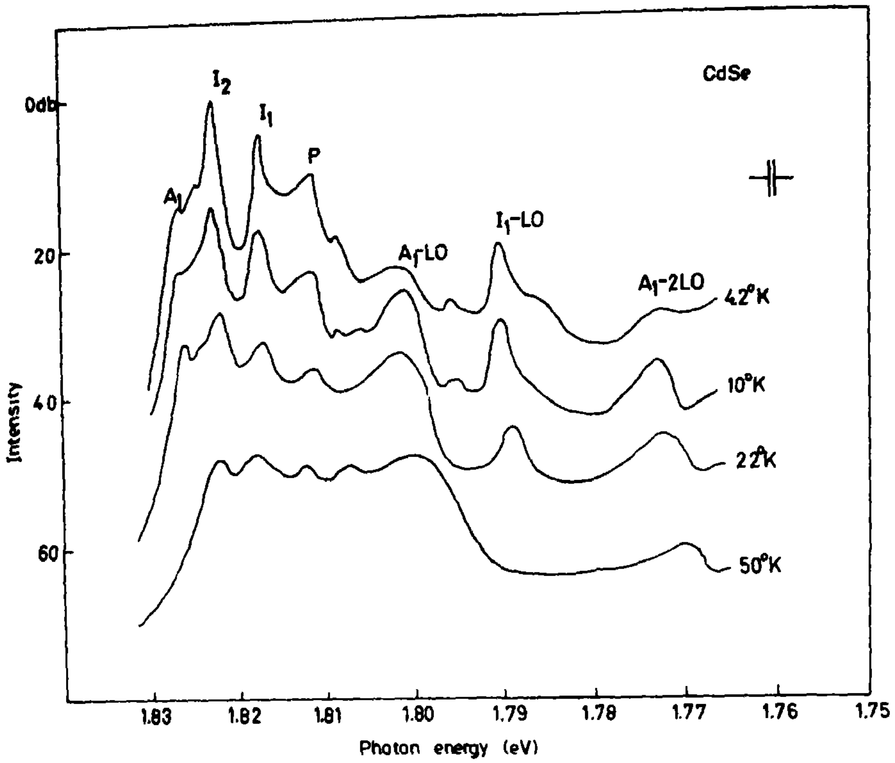

Fig. 2. Photoexcited luminescence spectra at different temperatures

intensity, as can be seen from the following argument. The number of free excitons which is proportional to the product $n \cdot p$ of electron and hole concentrations is observed to increase almost linearly with light intensity. Assuming $n = p$ (low temperature) one gets a square root dependence for the hole concentration. With values $\alpha = 1$ for free excitons and $\alpha = 0{\cdot}5$ for neutral acceptors one should expect $\alpha = 1{\cdot}5$ for the I_1 line.

For the P line we have found $\alpha = 1{\cdot}9$, i.e. a value higher than that for the I_1 line. In the previous paper [2] the P line was tentatively ascribed to the recombination of free excitons in the excited state $n = 2$ with simultaneous emission of a longitudinal optical phonon. It should be noted, however, that the P line is separated from the free exciton A_1 line by 15 meV, i.e. by the value equal to the free exciton binding energy. Haynes[9] has observed in Si a line the intensity of which increases as the square of the intensity of exciting light and the position of which is shifted from the free exciton line by the exciton binding energy. This line was explained by Haynes as arising from the decay of excitonic molecules. The binding energy of the excitonic molecule is expected to be very small[9] (in case of CdSe it could be estimated as $E_b < 3$ meV), and one should not expect to observe this line at elevated temperatures. As the P line persists even to 50°K (see Fig. 2) we think that in our case a collision of two excitons resulting in dissociation of one of them into a free electron and a free hole and a radiative recombination of the other is a more probable process than the mechanism proposed by Haynes. The $h\nu$ of emitted photons would then be about $E_g - 2E_x$, where E_x is the binding energy of a free exciton and E_g the energy gap. Assuming such an exciton–exciton collision process one can expect that the intensity of the P line should increase as the square of that of the exciting light.

This interpretation of the origin of the P line is the same as was first proposed by C. Benoit a la Guillaume *et al.* for one of the three processes leading to laser transitions in CdS[1, 10, 11]. A new luminescence line observed in ZnO, CdS and CdSe at low temperatures and high excitation was ascribed the same recombination mechanism[12]. In all the three materials this line is separated by the exciton binding energy from the A_1 line.

We have obtained electron-beam pumped laser emission in CdSe in the temperature range from 25 up to above 100°K. The laser lines were relatively broad containing several unresolved modes. The number of modes was increasing drastically with increasing excitation. Hence the spectra were recorded as close to the threshold as possible. Fig. 3 shows spontaneous and stimulated emission spectra corresponding to a sample temperature of 35°K. In the spontaneous spectrum the I_2 line is dominant which was typical for the samples used in the laser measurements (Cd-rich compared to the optically excited samples). In the laser geometry we observed stimulated emission at wavelengths close to the P line as well as the A_1-LO line (but not in between). Whether laser emission was obtained in one band or the other or in both bands simultaneously was dependent on sample, position on sample, and excitation in a nonsystematic way. In the actual recordings of Fig. 3 the laser emission in the A_1-LO band had a somewhat higher threshold than in the P band.

With increasing temperature the two laser lines approached each other and above 60°K we only observed laser emission in one band

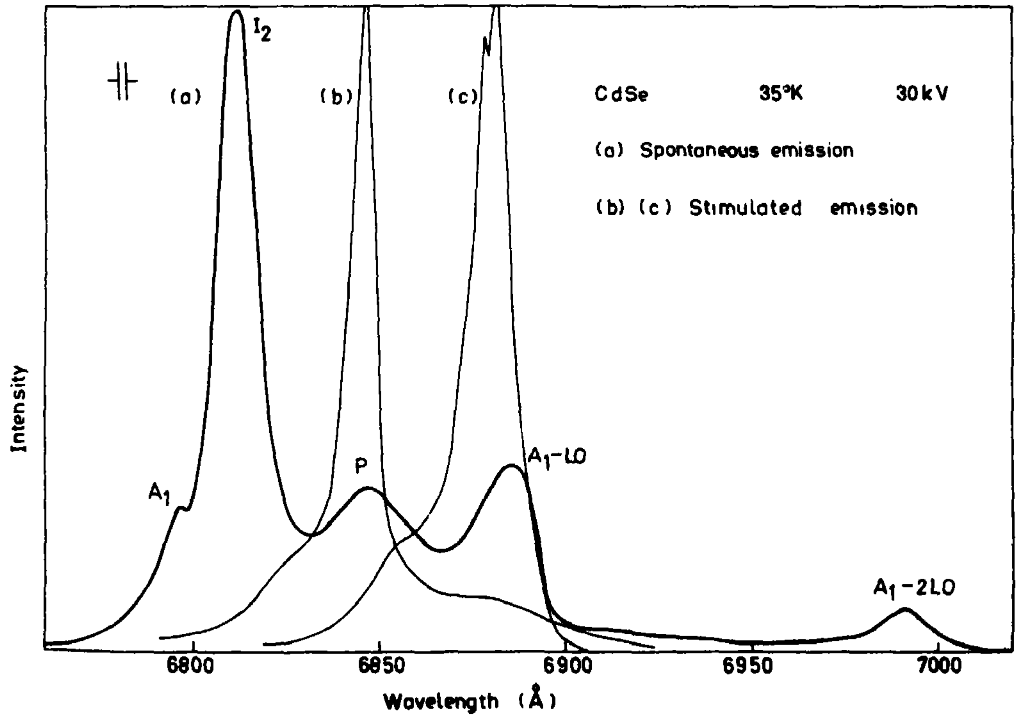

Fig. 3. Electron-beam excited emission spectra at 35°K. The intensity of the laser lines have been reduced by a factor of about 50. Beam currents 1 mA in (a) and (b) and 4 mA in (c).

which on the other hand exhibits a shift that is considerably larger than the shift of the band gap, here represented by the A_1 line (see Fig. 1). At 80°K the shift relative to the band gap is about 20 meV. The threshold for laser action did not increase appreciably from Helium temperature up to above 100°K, the threshold current being 1–2 mA in this temperature range. Our results at the lower temperatures are consistent with the laser emission that has earlier been observed in CdSe[4, 5]. At 77°K, however, Ref. [4] reports laser emission in the A_1-LO band which we have not been able to obtain. The threshold for laser action from the A_1-LO process has been calculated[13] to rise exponentially with temperature at higher temperatures due to the growth in phonon population.

The peak position of neither the A_1-LO line[13] nor the exciton–exciton line[11] is expected to be shifted drastically with temperature increase. However, the large shift of the position of the laser line only requires that the maximum net gain shifts accordingly, which may as well be caused by the temperature and wavelength dependent absorption tail that has been observed below the lowest exciton energy in several II–VI compounds[14, 15]. This absorption (described by the empirical Urbach's rule) has recently been shown[16] to be able to explain a similar temperature shift of the laser line in CdS assuming a relatively broad gain curve following the band gap, and with an extended low energy tail. One would expect the exciton–exciton line to be broad and with a low energy tail in contrast to the A_1-LO line[13]. We therefore suggest that the laser emission at elevated temperatures is due to the same process as the low temperature laser action on the P-line, namely the exciton–exciton collision process. This is also supported by the continuous and smooth shift of the laser line.

We have observed a similar shift of the laser line at elevated temperatures in CdS and ZnO[17] and the contribution of the absorption tail to this shift is under investigation to appear in a later publication.

4. CONCLUSION

The measured excitation dependences of the different exciton lines are in agreement with the identifications of the lines. The near quadratic dependence of the P line together with its position an exciton binding energy below the A_1 line strongly suggest this line to be due to an exciton–exciton collision process. At low temperatures we have obtained laser action from the P line as well as the A_1-LO line. The continuous shift of the laser line with increasing temperature in connection with the slow rise in threshold current points towards a recombination process with a low energy tail in photon energy and with no inverse absorption process connected to it. These conditions are apparently met by the exciton–exciton collision process although the exact lineshape has not been evaluated for this process at finite temperatures. The position of the laser line is probably largely determined by the onset of the background absorption.

Acknowledgements—We would like to thank Professor L. Sosnowski and Dr. T. Skettrup for stimulating discussions and for their interest in this work. We are also indebted to Professor N. I. Meyer, Professor R. W. Asmussen, Dr. J. Mycielski, Dr. W. Wardzynski and Professor I. Balslev for critical discussions of the results. One of us (B.W-N.) wishes to express her gratitude to Professor R. W. Asmussen for his kind permission to execute a part of this work in his laboratory.

REFERENCES

1. BENOIT A LA GUILLAUME C., DEBEVER J. M. and SALVAN F., *Phys. Rev.* **177**, 567 (1969).
2. RAZBIRIN B. S., FILINSKI I. and WOJTOWICZ-NATANSON B., *Phys Status Solidi* **18**, K37 (1966).
3. GRUN J. B., MYSYROWICZ A., RAGA F., BIVAS A., LEVY R. and NIKITINE S., *Phys. Status Solidi* **22**, K155 (1967).
4. PACKARD J R., CAMPBELL D. A. and TAIT W. C., *J. appl. Phys.* **38**, 5255 (1967).
5. HURWITZ C. E., II–VI *Semiconducting Compounds*-1967 *Int. Conf.*, p. 682. W. A. Benjamin, New York (1967).
6. SEGALL B. and MAHAN G. D., *Phys. Rev.* **171**, 935 (1968).

7. MYSYROWICZ A., GRUN J. B., BIVAS A., LEVY R. and NIKITINE S., *Phys. Lett.* **25A**, 286 (1967).
8. GROSS E. F., RAZBIRIN B. S., FEDOROV V. P. and NAUMOV Yu.P., *Phys. Status Solidi* **30**, 485 (1968).
9. HAYNES J. R., *Phys. Rev. Lett.* **17**, 860 (1966).
10. BENOIT A LA GUILLAUME C., DEBEVER J. M. and SALVAN F., II–VI *Semiconducting Compounds*-1967 *Int. Conf.* p. 669. W. A. Benjamin, New York (1967).
11. BENOIT A LA GUILLAUME C., DEBEVER J. M. and SALVAN F., IX *Int. Conf. Semiconductor Physics*, p. 581. Moscow, 'Nauka', Leningrad (1968).
12. MAGDE D., MAHR H., *Phys. Rev. Lett.* **24**, 890 (1970).
13. HAUG H., *J. appl. Phys.* **39**, 4687 (1968).
14. SEGALL B., *Phys. Rev.* **163**, 769 (1967).
15. GNATENKO Yu.P. and KURIK M. V., *Soviet Phys-Solid State* **12**, 892 (1970).
16. LEHENY, R. F., SHAKLEE K. L., IPPEN E. P., NAHORY R. E. and SHAY J. L., *Appl. Phys. Lett.* **17**, 494 (1970).
17. HVAM J. M., *Proceedings of the Tenth International Conference on the Physics of Semiconductors*, U.S.A.E.C. 1970, p. 71, Cambridge, Mass. (1970).

J. Phys. Chem. Solids Pergamon Press 1971. Vol. 32, pp. 2201–2209. Printed in Great Britain.

A HIGH TEMPERATURE STUDY OF NATIVE DEFECTS IN ZnTe*

F. T. J. SMITH
Lincoln Laboratory, Massachusetts Institute of Technology, Lexington, Mass. 02173, U.S.A.

(*Received* 19 *November* 1970)

Abstract—Hall coefficient and resistivity measurements have been made on undoped ZnTe single crystals at temperatures up to 1000°C under controlled partial pressures of either zinc or tellurium. All samples are *p*-type. The Hall mobility of holes has been measured, and the equilibrium hole concentrations along both the zinc-rich and tellurium-rich solidus curves have been determined. At compositions close to the zinc-rich solidus, the dependence of hole concentration on Zn(g) partial pressure supports the conclusion of Thomas and Sadowski that the hole concentration is controlled by the presence of a doubly ionized native acceptor defect. At compositions close to the tellurium-rich solidus the situation is apparently more complicated. The dependence of the hole concentration on Te_2(g) partial pressure is considerably weaker than expected if the only defect of importance were the acceptor defect found close to zinc saturation. At high temperatures in this composition region there are appreciable concentrations of a neutral defect which precipitates on cooling to room temperature. We suggest that the acceptor defect is a zinc vacancy, as proposed by Thomas and Sadowski, and that the neutral defect is a tellurium interstitial. Evidence has been obtained for the association of the acceptor with a donor during slow cooling of tellurium-saturated specimens.

1. INTRODUCTION

ZINC telluride unless intentionally doped is always *p*-type and exhibits retrograde solubility for tellurium. Its homogeneity range is therefore usually assumed to lie entirely on the tellurium-rich side of the stoichiometric composition. Conductivity measurements made on crystals of ZnTe in zinc vapor at 700–950°C by Thomas and Sadowski[1] have shown that at compositions close to zinc saturation the hole concentration is controlled by the presence of a doubly ionized native acceptor defect.

The initial objectives of the present study were to determine whether this native defect also controls the hole concentration at compositions close to tellurium saturation and to measure the defect concentrations along the zinc-rich and tellurium-rich solidus lines. In order to do this we have made both Hall coefficient (R_H) and resistivity (ρ) measurements on undoped single crystals of ZnTe at temperatures up to 1000°C while controlling either the zinc or tellurium partial pressure. For zinc pressures close to saturation the results are in good agreement with those of Thomas and Sadowski[1]. In the region close to tellurium saturation, where high temperature measurements have not previously been made, the results indicate the presence of an appreciable concentration of a second native defect.

2. EXPERIMENTAL

Some of the crystals used had been grown[2] by the temperature gradient solution zoning method from a Te-rich solution. Others were obtained by an open tube vapor transport method in which helium was used as the carrier gas. Specimens cut from these crystals were annealed in a large excess of molten zinc at 1000°C for 4 days. This treatment served to purify them by the solvent extraction process[3] and also to remove precipitates, presumed to be tellurium, which could be seen in the crystals grown from Te-rich solution. Mass spectrographic analyses of

---

*This work was sponsored by the Department of the Air Force.

samples after this process showed concentrations of probable foreign donors and acceptors at the level of $10^{17}\,cm^{-3}$. No increase in impurity content was found when the analysis was repeated after a series of high temperature electrical measurements lasting up to 2 weeks.

The apparatus used for high temperature measurements has been described previously [4]. The desired zinc or tellurium partial pressure was maintained by controlling the temperature of a reservoir containing either pure zinc or tellurium (Cominco Grade 69, nominally 99·9999 per cent pure), using published vapor pressure data[5]. The zinc and tellurium pressures were restricted to values within a factor of about 100 below the respective saturation pressures. This restriction was found to be necessary to prevent appreciable sublimation of the specimen during a run. Resistivity and Hall coefficient measurements were made by the van der Pauw method. The specimen, which was in the form of a square plate approximately 8 × 8 × 1 mm, was contacted by four spring-loaded graphite knife edges, two on one edge of the specimen and two on the opposite edge. The contacts were found to be ohmic down to room temperature once the specimen holder assembly had been heated to 650°C or above for a few minutes. Measurements were made with a d.c. magnetic field of 5·3 kOe and either d.c. or a.c. sample currents of less than 10 ma. The sample voltages were detected by a d.c. microvolt amplifier or by a lock-in amplifier, respectively. The a.c. system gave improved sensitivity, which was useful at the higher temperatures.

Equilibrium measurements were made with a zinc reservoir at sample temperatures between 635 and 1000°C. The resistivities observed at 950°C are in good agreement with those of Thomas and Sadowski[1], but at the lowest temperatures our values are about a factor of two higher than theirs. Values of the hole concentration for a particular combination of sample temperature and zinc pressure (p_{Zn}) varied by less than ±20 per cent between specimens. This reproducibility indicates that impurities present at the level of $10^{17}\,cm^{-1}$ did not have a significant effect on the carrier concentration, since the impurity concentrations determined by mass spectrographic analysis were in this range but varied appreciably between specimens, especially those from crystals obtained by the two different growth methods.

3. RESULTS

All measured values of the Hall coefficient were positive, indicating p-type conductivity. The Hall mobility (R_H/ρ) for holes at any fixed temperature within the range studied (300–1300°K) was found to be independent of hole concentration between 1×10^{15} and $5 \times 10^{18}\,cm^{-3}$ and was reproducible to about ±10 per cent between specimens. This indicates that the observed mobilities were limited by lattice scattering. Values for a typical specimen are plotted as a function of temperature in Fig. 1. The room temperature value is $92 \pm 5\,cm^2/V\text{-sec}$, in agreement with previous results[1, 5]. At high temperatures the values are somewhat below those used by Thomas and Sadowski[1] to convert their measured conductivities to hole concentrations. For example, at 1000°K our measured value is

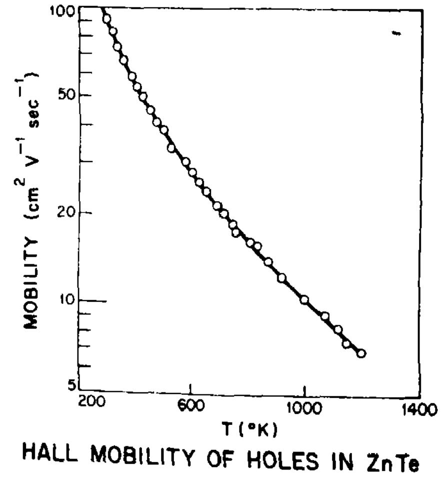

Fig. 1. Hall mobility of holes in a typical ZnTe specimen.

10 ± 1 cm^2/V-sec, compared with the value of 16 cm^2/V-sec which they obtained by extrapolation from lower temperature data.

Figure 2 shows equilibrium values of the hole concentration ($=1/R_He$) for a typical specimen at a number of temperatures between 635 and 953°C, plotted as a function of p_{Zn} for pressures close to zinc saturation. At each temperature the concentration varies as p_{Zn}^m, where $m = -(0{\cdot}34 \pm 0{\cdot}02)$. This zinc pressure dependence is in excellent agreement with the observations of Thomas and Sadowski[1]. As discussed below, this is the pressure dependence expected if the holes are due to the presence of a native acceptor defect which is doubly ionized over the temperature range in which the equilibrium measurements were made.

Values of the hole concentration (p) at fixed values of p_{Zn} were determined as a function of temperature by interpolation from concentration vs. p_{Zn} isotherms like those in Fig. 2. Plots of $\log p$ vs. $1/T$ based on these interpolated values are straight lines, as illustrated by the lower line in Fig. 3, which gives the results for $p_{Zn} = 100$ Torr. The apparent enthalpy of formation (ΔH_f) of the acceptor defect can be found from the slopes of these lines, which are equal to $-(\Delta H_f/3kT)$ [6]. From the lines for several pressures between 40 and 200 Torr, we obtain $\Delta H_f = 4{\cdot}8 \pm 0{\cdot}3$ eV, compared with the value 3·95 eV found in a similar manner by Thomas and Sadowski[1]. Thus according to our data the hole concentration in ZnTe close to zinc saturation at high temperatures is given by

$$p = p_0 (p_{Zn})^{-1/3} \exp(-4{\cdot}80/3kT) \qquad (1)$$

where $p_0 = 1{\cdot}46 \times 10^{24}$ cm^{-3} atm$^{1/3}$, p is in cm^{-3} and p_{Zn} is in atm.

Equilibrium measurements were made with a tellurium reservoir at sample temperatures between 750 and 1060°C. Values of the hole concentration for a particular combination of sample temperature and tellurium pressure (p_{Te_2}) varied by less than ±10 per cent between specimens, again showing that impurities present at the level of 10^{17} cm^{-3} did not have a significant effect on the carrier concentration.

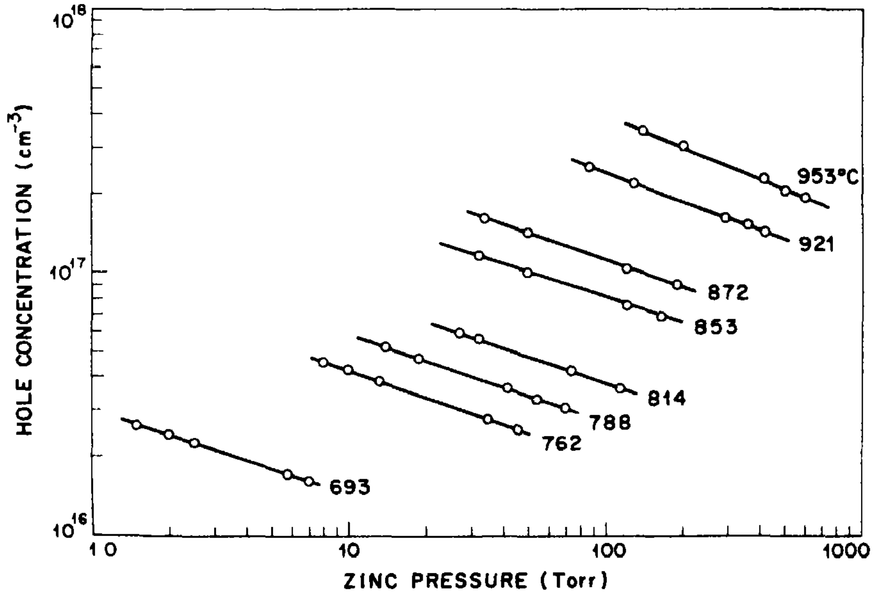

Fig. 2. Isotherms of hole concentration vs. zinc partial pressure for zinc partial pressures close to saturation.

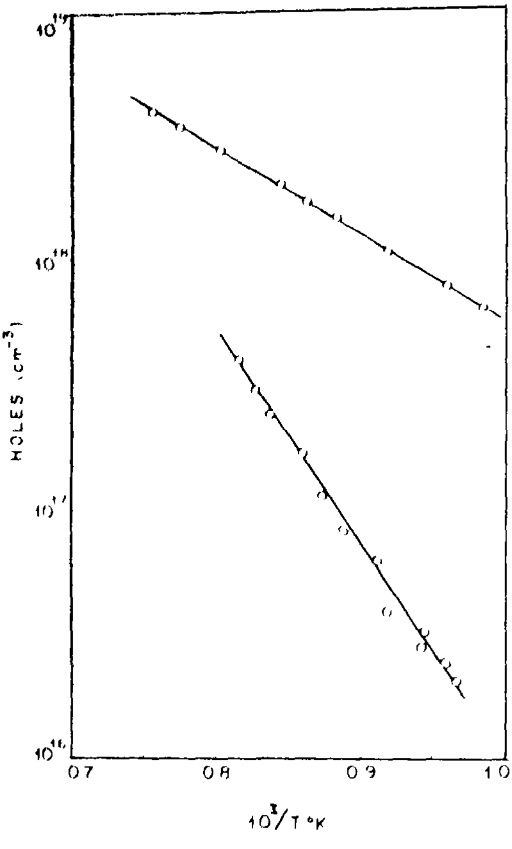

Fig. 3. Hole concentration as a function of temperature at a constant zinc pressure of 100 Torr (lower curve) and a constant tellurium pressure of 100 Torr (upper curve).

Figure 4 shows the equilibrium values of the hole concentration at four temperatures for the specimen of Fig. 2, plotted as a function of p_{Te_2} for pressures close to tellurium saturation. No data for this pressure region have been reported previously. At each temperature the concentration varies as $p^m_{Te_2}$, where m increases from about 0·05 at 750°C to 0·10 at 1050°C.

Values of the hole concentration (p) at fixed values of p_{Te_2} were determined as a function of temperature by interpolation from isotherms like those shown in Fig. 4. Plots of $\log p$ vs. $1/T$ based on these interpolated values are straight lines, as shown by the lower line in Fig. 3, which gives the results for $p_{Te_2} = 100$ Torr. The slopes of these lines are considerably less than those for the analogous lines at fixed values of P_{Zn} close to zinc saturation.

To obtain the hole concentrations at the zinc-rich limit of the ZnTe homogeneity range, carrier concentration isotherms like those in Fig. 2 were extrapolated to the values of p_{Zn} in equilibrium with zinc-saturated material. Only a short extrapolation was required, since the highest zinc pressure used at each temperature was close to the saturation pressure. The hole concentrations along the tellurium-rich solidus were found in a similar way by extrapolating isotherms like those of Fig. 4. The

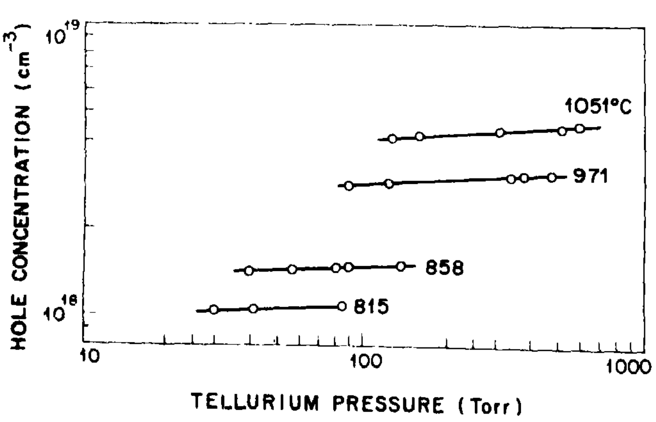

Fig. 4. Isotherms of hole concentration vs. tellurium partial pressure for tellurium partial pressures close to saturation.

concentrations obtained in this manner by using the zinc and tellurium saturation pressures measured by Brebrick[7] are listed in Table 1 and plotted on a logarithmic scale against $1/T$ in Fig. 5. The data are well represented by two straight lines with similar slopes. In both cases the carrier concentration decreases with decreasing temperature.

The concentration isotherms obtained with a zinc reservoir (Fig. 2) were also extrapolated to the zinc pressures over tellurium-saturated ZnTe. These pressures, which were calculated from Brebrick's values[7] for the tellurium saturation pressures and for the equilibrium constant $K_g = 4(p_{Zn})^2 p_{Te_2}$, are so small that an extrapolation over approximately 8 orders of magnitude in zinc pressure is necessary. The hole concentrations obtained in this way are also given in Table 1. At the highest temperatures these concentrations are close to those obtained by extrapolating the tellurium pressure isotherms of Fig. 4, but at lower temperatures they are systematically higher.

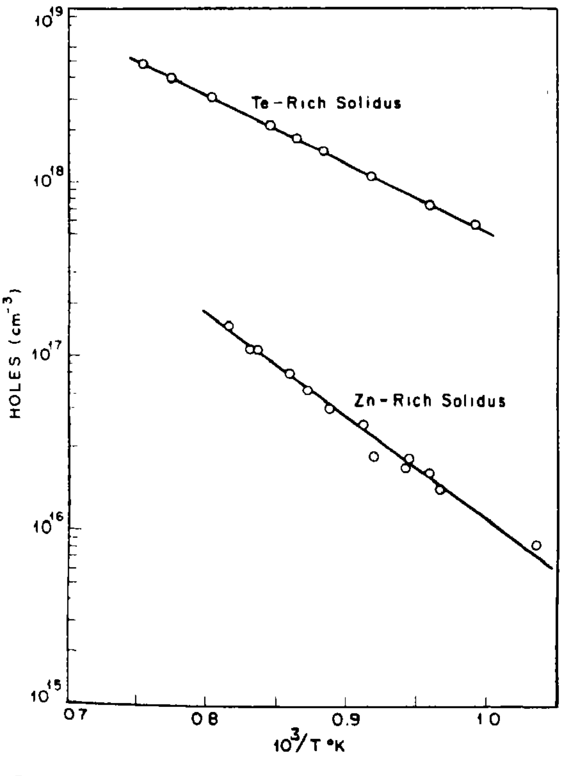

Fig. 5. Equilibrium hole concentration as a function of temperature for zinc saturated (lower line) and tellurium saturated (upper line) zinc telluride.

Table 1. Hole concentrations along the solidus for both zinc and tellurium saturated compositions

T(°K)	Zinc saturation (cm^{-3})	Tellurium saturation (cm^{-3}) (a)	(b)
1330	—	$5{\cdot}0\times10^{18}$	$5{\cdot}0\times10^{18}$
1250	$1{\cdot}8\times10^{17}$	$3{\cdot}3\times10^{18}$	$3{\cdot}0\times10^{18}$
1124	$5{\cdot}2\times10^{16}$	$1{\cdot}5\times10^{18}$	$1{\cdot}3\times10^{18}$
1020	$1{\cdot}5\times10^{16}$	$6{\cdot}0\times10^{17}$	$5{\cdot}0\times10^{17}$

(a) Values obtained by extrapolation of isotherms measured in zinc vapor using equation (1).

(b) Values obtained by extrapolation of isotherms measured in tellurium vapor close to saturation.

The hole concentrations reported so far were based on the results of measurements made at fixed temperatures on samples which were in equilibrium with the surrounding vapor. In a number of other experiments, resistivity and Hall coefficient measurements were made as samples were cooled to room temperature. Two different cooling rates were used, one of about 5°C/min which was obtained by turning the furnace power off, and the other of about 5°C/*h* obtained by programming the furnace temperature controller. For samples which were initially equilibrated with zinc vapor near saturation at temperatures up to 650°C and then rapidly cooled, the initial carrier concentration was retained down to approximately 310°C, as shown by the lower curve in Fig. 6. Thus the electrically active defect concentration characteristic of the initial equilibrium temperature was quenched in, and changes in p_{Zn} during cooling had no effect on the electrical properties. On further cooling the hole concentration decreased exponentially with $1/T$, probably due to the de-ionization of the second level of the acceptor defect. The slope in this region

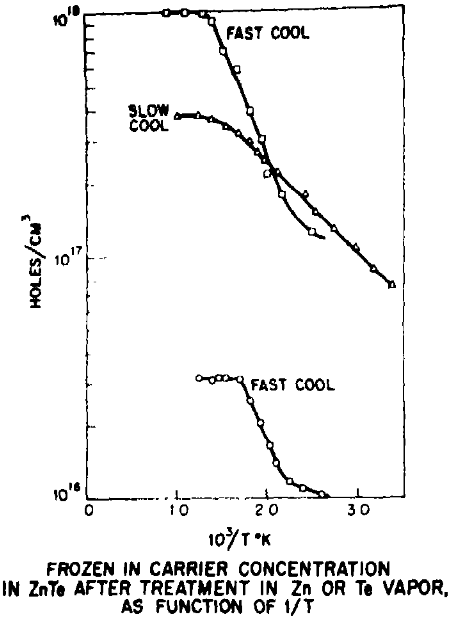

Fig. 6. Hole concentrations as a function of temperature observed during cooling to room temperature from zinc saturated (lower curve) and tellurium saturated conditions (upper two curves).

corresponds to an activation energy of 0·20 eV. This value is appreciably greater than the value of 0·13–0·16 eV previously estimated[8] for this level from low temperature electrical measurements. At the lowest temperatures, the slope of the curve decreased, indicating that de-ionization of the second level of the defect was almost complete at room temperature. (The fact that de-ionization of the second level decreased the hole concentration by more than a factor of two results from partial compensation of the lower level by donor impurities.) When the specimen was re-heated at about 5°C/min to the initial equilibration temperature, the hole concentration vs. temperature curve was retraced with no hysteresis, and was not affected by changes in reservoir temperature during heating.

A similar dependence of hole concentration on temperature, as shown by the upper curve in Fig. 6, was observed for specimens cooled rapidly after initial equilibration with tellurium vapor near saturation. Because of the slower kinetics in this composition range, the electrically defect concentration could be quenched in for initial equilibrium temperatures up to 750°C. At temperatures between 500 and 100°C, the hole concentration again decreased exponentially with an activation energy of about 0·20 eV. As in the case of zinc saturated specimens, the hole concentration vs. temperature curve was retraced with no hysteresis on heating at about 5°C/min, and the tellurium pressure had no effect on the electrical properties.

In other cooling experiments, specimens equilibrated at high temperatures with zinc or tellurium vapor were cooled to room temperature at the slower rate of about 5°C/*h*. The variation of carrier concentration with temperature in a typical experiment, performed on a sample initially equilibrated at a tellurium pressure close to saturation, is shown by the curve in Fig. 6 marked 'slow cooling'. As in the fast cooling experiments, the carrier concentration at first remained constant with decreasing temperature and then decreased exponentially with $1/T$. In this case, however, the slope of the straight line corresponds to an activation energy of only about 0·07 eV, rather than 0·20 eV.

4. DISCUSSION

We shall now attempt to interpret the experimental results in terms of specific models for the native defects in ZnTe.

For compositions close to the zinc-rich limit of the homogeneity range, we observe the same pressure dependence of the hole concentration as that reported by Thomas and Sadowski[1] on the basis of their high temperature conductivity measurements. The observation that the carrier concentration is dependent on pressure strongly suggests that the hole concentration is controlled by native defects rather than impurities. In addition the specific form of the dependence can be understood easily if the predominant defect is a doubly-ionized acceptor (A'')

formed by the reaction

$$O = A'' + 2h + \mathrm{Zn}(g) \qquad (2)$$

where h is a hole and Zn(g) is a zinc atom in the gas phase. The equilibrium constant for this reaction is

$$K = [A'']p^2 p_{\mathrm{Zn}} \qquad (3)$$

where $[A'']$ is the concentration of the defects and p is the hole concentration (frequently represented by $[h]$.) Since $[A] = p/2$. $K = 1/2\, p^3 p_{\mathrm{Zn}}$, and solving for p yields the observed pressure dependence

$$p = (2K)^{1/3}(p_{\mathrm{Zn}})^{-1/3}. \qquad (4)$$

The defect concentration obtained from the carrier concentration along the Zn-rich solidus (Fig. 5) increases from 5×10^{15} cm^{-3} at 1000°K to 9×10^{16} cm^{-3} at 1250°K.

The simplest point defects in ZnTe that would be associated with an excess of Te and might be expected to behave as acceptors are the zinc vacancy and the tellurium interstitial[9]. Formation of either would be consistent with the equilibrium constant given by equation (3). A probable identification is suggested by the results of the cooling experiments and of the equilibrium measurements for compositions close to tellurium saturation.

The similarity in shape between the $\log p$ vs. $1/T$ curves (Fig. 6) obtained in the fast cooling (~5°C/min) experiments with zinc and tellurium reservoirs, and particularly the agreement between the activation energies for the linear portions of the two curves, indicates that the same acceptor defect is responsible for the holes present in ZnTe at both extremes of the homogeneity range. The formation of precipitates during fast cooling, but only in the experiments with a tellurium reservoir, indicates that samples sufficiently close to tellurium saturation contain an additional defect, whose solubility decreases with decreasing temperature. This defect is electrically inactive, since its precipitation does not affect the carrier concentration, and it diffuses more rapidly than the acceptor, since the latter also exhibits retrograde solubility (see Fig. 5) and would therefore precipitate on cooling if it were sufficiently mobile. (Precipitation due to the retrograde solubility of tellurium has been observed for acceptor defects in HgTe[10] and PbTe[11, 12].)

The results of tellurium self-diffusion experiments[12] on ZnTe indicate that the diffusing species is the tellurium interstitial, although they do not establish its electrical activity. In addition, data on the pressure dependence of chalcogen self-diffusion in the II–VI compounds, which are available for all these materials except ZnS, can be most simply explained by the diffusion of neutral chalcogen interstitials[13]. Therefore we suggest that the mobile, electrically inactive defect present in ZnTe is the tellurium interstitial. If this is the case, then by elimination the doubly-ionizable acceptor defect is probably the zinc vacancy.

The carrier concentration data obtained in equilibrium measurements on ZnTe specimens with compositions close to tellurium saturation cannot be simply interpreted in terms of doubly ionized acceptor and electrically inactive defects. If there is no interaction between the two types of defects, then according to the mass action law the carrier concentration in such samples should vary with p_{Zn} in the manner given by equation (1), just as it does for samples close to zinc saturation. There are significant deviations from equation (1), however. The carrier concentrations along the Te-rich solidus predicted by this equation (Col. a, Table 1) are appreciably higher than those obtained by extrapolating the isotherms observed in experiments with a tellurium reservoir (Col. b, Table 1), particularly at the lower temperatures. In addition, since $(p_{\mathrm{Zn}})^2 p_{\mathrm{Te}_2} = K_g/4$ for the vapor in equilibrium with solid ZnTe, equation (1) predicts that the carrier concentration should increase as $(p_{Te_2})^{1/6}$. The exponents of p_{Te_2} observed in the experiments with a tellurium reservoir are only 0·05–0·10, values significantly less than 1/6.

Deviations from the simple mass action relationship given by equation (1) would result if the activity coefficients of the free holes or the acceptor defects differed from unity. The measured hole concentrations were always less than 10 per cent of the distribution function for holes, so that the activity coefficient for holes can probably be taken as unity through the concentration range[14]. The coulombic repulsive interaction between the doubly charged acceptors would tend to increase their activity coefficient and reduce their concentration. However, the average separation between the acceptors is 65 Å even for the highest concentration observed ($3 \cdot 5 \times 10^{18}$ cm^{-3}). Since the static dielectric constant is about 10 (Ref. [8]), for this separation the screened coulombic interaction term[15] is only about $kT/10$ at 1250°K, which is too small to have an appreciable affect on the activity coefficient.

Deviations from the pressure dependence given by equation (1) could also result if interactions between the doubly ionized acceptors and the electrically inactive defects increased the acceptor activity coefficient. Such interactions would become more probable with increasing tellurium partial pressure, as the concentrations of both types of defects increase. Although the possibility of some such interaction cannot be eliminated, on the basis of the present data it is unlikely that the two defects form a bound complex. Since the binding energy of such a complex would probably not exceed 1 eV (Ref. [6]), its concentration would be expected to change rapidly due to dissociation over the temperature range investigated, and there would be a correspondingly rapid change in the pressure dependence of the carrier concentration. The observed change in the slopes of the isotherms in Fig. 4 is quite gradual, however. Thus we have been unable to formulate a defect model which adequately explains the equilibrium data for ZnTe with compositions close to tellurium saturation.

In slow cooling (5°C/h) experiments on specimens in this composition range, the carrier concentration at first remained constant and then decreased with an activation energy of 0·07 eV. Since the acceptor defect was initially present in these samples, failure to observe the 0·20 eV level must be due to the formation of an associate involving the acceptor in such a way as to remove or displace this level. The most probable such associate would be with an oppositely charged species. An associate between a doubly ionizable acceptor and a singly ionizable donor would be expected[6] to have a single acceptor level somewhat deeper than the lower level of the isolated acceptor, which is about 0·05 eV[8]. Evidence for associates of this type in tellurium-saturated ZnTe has been obtained by Title, Mandel, and Morehead[16] in paramagnetic resonance experiments. In the resonance experiments the associate concentration was greatly reduced by zinc saturating the specimens. In agreement with this finding, in slow cooling experiments on crystals close to zinc saturation we have observed only the 0·20 eV level.

Acknowledgements—The author is grateful to A. J. Strauss for many helpful discussions and to J. Steininger for supplying some of the crystals used.

REFERENCES

1. THOMAS D. G. and SADOWSKI E. A., *J. Phys. Chem. Solids* **25**, 395 (1964).
2. STEININGER J. and ENGLAND R. E., *Trans. A.I.M.E.* **242**, 444 (1968).
3. AVEN M. and WOODBURY H. H., *Appl. Phys. Lett.* **1**, 53 (1962).
4. SMITH F. T. J., *Met. Trans.* **1**, 617 (1970).
5. NESMEYANOV AN. N., *Vapor Pressures of the Elements*, p. 190, 337. Academic Press, New York (1963).
6. KROGER F. A., *The Chemistry of Imperfect Crystals*, p. 277, Ch. 9. North Holland, Amsterdam (1964).

7. BREBRICK R. F., *J. electrochem. Soc.* **116**, 1274 (1969).
8. AVEN M. and SEGALL B., *Phys. Rev.* **131**, 81 (1963).
9. BREBRICK R. F., *Progress in Solid State Chemistry* (Edited by H. Reiss), Vol. 3, p. 213. Pergamon Press, New York (1966).
10. STRAUSS A. J. and BREBRICK R. F., *J. Phys. Chem. Solids* **31**, 2293 (1970).
11. SCANLON W. W., *Phys. Rev.* **126**, 509 (1962).
12. REYNOLDS R. A. and STEVENSON D. A., *J. Phys. Chem. Solids* **30**, 139 (1969).
13. WOODBURY H. H., *II-VI Semiconducting Compounds* (Edited by D. G. Thomas), p. 244. W. A. Benjamin, New York (1967).
14. ROSENBERG A. J., *J. Phys. Chem. Solids* **21**, 665 (1960).
15. FUOSS R. M., *Chem. Revs.* **17**, 27 (1935).
16. TITLE R. S., MANDEL G. and MOREHEAD F. F., *Phys. Rev.* **136**, A300 (1964).

J. Phys. Chem. Solids Pergamon Press 1971. Vol. 32, pp. 2211–2215. Printed in Great Britain.

DELAYED ELASTICITY RESULTING FROM PERIODIC STRESS-INDUCED ATOMIC DIFFUSION

R. H. DOREMUS
General Electric Research and Development Center, Schenectady, N.Y.

(*Received* 16 *November* 1970)

Abstract – The internal friction resulting from bulk redistribution of atoms in a periodic stress gradient is derived. The calculated internal friction peak agrees well with data on hydrogen in vanadium and niobium and deuterium in vanadium. The resulting diffusion parameters are different from these calculated previously with the assumption of a single relaxation time.

1. INTRODUCTION

ATOMS of different size in solid solution redistribute in a stress gradient, giving rise to delayed elasticity, the rate of recovery being determined by diffusion of the atoms. Gorsky described this elastic after-effect and studied it in ordered copper–gold alloys[1]. Recently the diffusion of hydrogen and deuterium in niobium and vanadium was determined from analysis of strain relaxation[2, 3] and internal friction[4, 5] experiments. Alefeld *et al.*[6] solved the diffusion equation for strain relaxation and internal friction; solutions were presented with a series of terms with different relaxation times, but only a single relaxation time was used in analysis of the experiments cited above.

In this paper the diffusion equation is solved in closed form for the redistribution of atoms in a periodic stress gradient in a different way, and the internal friction resulting from this redistribution is derived. A peak occurs in the internal friction at constant temperatures as a function of frequency, and this peak is broader than the one usually derived for a single relaxation time. The peak shape agrees well with that measured experimentally[4, 5], and this agreement explains the apparent decrease at low temperatures in the diffusion coefficient calculated by assuming a single relaxation time[4, 5]. The absolute value of the diffusion coefficient and the activation energy for diffusion calculated from the present equations and the data of Cantelli *et al.*[4, 5] are different than the values calculated with the assumption of a single relaxation time.

2. DERIVATION OF EQUATIONS

The diffusion equation is solved for a single diffusing species, with a uniform stress gradient $\partial P/\partial x$ imposed in one direction, for example, by bending a thin sheet or a bar. The flux J of diffusing atoms per unit area in the x-direction is

$$J = -D\left(\frac{\partial c}{\partial x} + \frac{cv^*}{RT}\frac{\partial P}{\partial x}\right) \qquad (1)$$

where D is the diffusion coefficient of the atoms, $c(x, t)$ is their concentration at position x and time t, P is the pressure or stress, R is the gas constant, T the absolute temperature, and v^* is an activation volume. It is possible to relate v^* to the elastic coefficients of the matrix and the strain fields of the particles [6]. In using equation (1) it is assumed that the activity coefficient of the diffusing atoms is constant with concentration.

The differential equation for diffusion results when the flux of equation (1) is substituted into the equation of continuity. It is assumed that the excess concentration built up by the stress gradient over the initial uniform concentration is small. The excess concentration ratio s is defined as $s = (c/c_0) - 1$, where c_0 is the uniform initial concentration, so that $s \ll 1$. It is also assumed that $\partial P/\partial x$ is constant with distance x. Then

$$\frac{\partial c}{\partial t} = \frac{\partial(-J)}{\partial x} = D\frac{\partial^2 c}{\partial x^2}, \text{or} \frac{\partial s}{\partial t} = D\frac{\partial^2 s}{\partial x^2}. \quad (2)$$

A solution of this equation with a periodic pressure difference $\Delta P e^{i\omega t}$ of frequency $f = \omega/2\pi$ imposed across the slab of thickness L is desired, since internal friction is conveniently measured with a periodic stress. It is assumed that the solution has the form $s = s_0 e^{i\omega t}$ where s_0 is a function of distance but not time. Then

$$\frac{d^2 s_0}{dx^2} = \frac{i\omega s_0}{D}$$

and the solution for s is

$$s = \gamma(e^{-hx} - e^{hx}) = 2\gamma \sinh(hx) \quad (3)$$

where

$$h = (i\omega/D)^{1/2} = (1+i)(\omega/D)^{1/2}.$$

The factor $e^{i\omega t}$ is included in the integration coefficient γ. Only one arbitrary coefficient is included in equation (3), because it is assumed as a boundary condition that the mass of solute is preserved in the slab. Then s integrated over the slab is zero, and the concentration gradient is symmetrical about the center of the slab ($x = 0$).

Another boundary condition is that no solute flux passes through the slab surfaces at $x = -L/2$ and $L/2$, from which the coefficient γ is determined. If $P' = \Delta P e^{i\omega t}/L$ is the periodic stress gradient, equation (1) is

$$-\frac{J}{Dc_0} = \frac{\partial s}{\partial x} + \frac{v^* P'}{RT}$$

and at $x = -L/2$

$$-\left(\frac{\partial s}{\partial x}\right) = 2\gamma h \cosh\frac{hL}{2} = \frac{v^* P'}{RT}, \quad (4)$$

since $J(-L/2) = 0$. With this value of γ, equation (3) becomes

$$s = -\frac{v^* P'}{RTh}\frac{\sinh(hx)}{\cosh(hL/2)}. \quad (5)$$

The relationship between this concentration distribution and the delayed elasticity results from the assumption that there is an incremental deformation in the sample that is proportional to the excess concentration $c_0 s$. Equation (21) of Alefeld *et al.*[6] is based on the same assumption. The total elastic deformation in a body under periodic applied stress $\Delta P e^{i\omega t}$ results from both the normal instantaneous deformation determined by the 'relaxed' modulus M_R and the delayed deformation resulting from the redistribution of solute atoms. It is assumed that other delayed elastic deformations are negligible. Then the deformation d at the sample surface $x = -L/2$ is

$$\mathrm{d} = \frac{\Delta P e^{i\omega t}}{M_R} + \zeta c_0 s(-L/2) \quad (6)$$

where ζ gives the incremental deformation that results from unit excess concentration. Again ζ can be related to the elastic coefficients and strain fields of the particles[6]. The complex modulus M^* is given by [7]

$$M^* = \frac{\Delta P e^{i\omega t}}{\mathrm{d}} = M_R(1 + i\tan\delta) \quad (7)$$

where $\tan\delta$ is the internal friction. If $\tan\delta \ll 1$, equations (6) and (7) give

$$\tan\delta = \frac{M_R \zeta c_0}{\Delta P e^{i\omega t}} \operatorname{Imag}[s(-L/2)] \quad (8)$$

then

$$\tan\delta = \frac{4M_R\zeta c_0 v^*}{RT\beta}\left[\frac{\tan\beta\,(1 - \tanh^2\beta) - \tanh\beta\,(1 + \tan^2\beta)}{1 + (\tan\beta\tan\beta)^2}\right] \quad (9)$$

with $\beta = (\omega/2D)^{1/2}(L/2)$.

The internal friction as a function of frequency at constant temperature, derived from this equation, is shown in Fig. 1. The peak is compared to the one derived for a single relaxation time $\tau = \pi^2 L^2/D$:

$$\frac{\tan\delta}{(\tan\delta)_{\max}} = \frac{2\omega\tau}{1+(\omega\tau)^2}. \tag{10}$$

At frequencies lower than maximum the two curves are closely similar, both decreasing as the frequency decreases at frequencies much lower than the maximum. However, on the high frequency side the present peak of equation (9) decays more slowly than the normal one. At frequencies much higher than maximum equation (9) decreases with the inverse square root of frequency, whereas equation (10) decreases in inverse proportionality to the frequency.

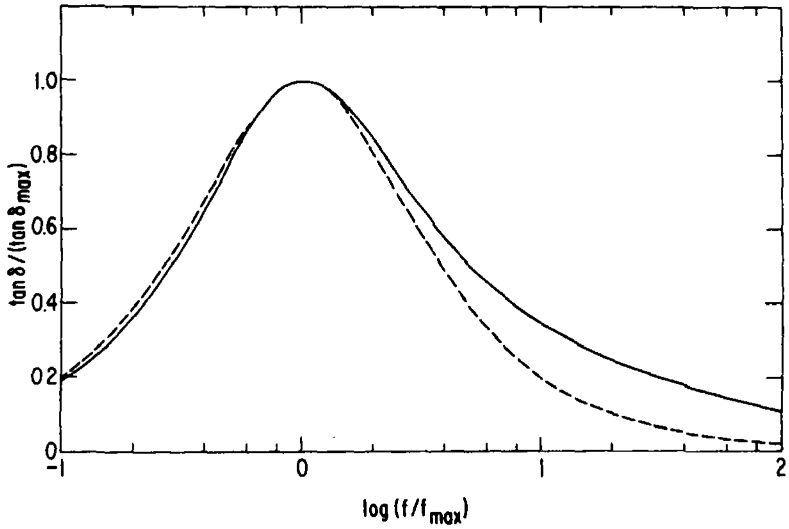

Fig. 1. The relative internal friction as a function of frequency, calculated from equation (9) (line) and the usual loss equation, equation (10) (dashed line).

3. COMPARISON WITH EXPERIMENTAL RESULTS

The peak maximum occurs at $\beta^2 = 1\cdot19$, or the frequency $f_m = 1\cdot18\,(8)\,D/2\pi L = 1\cdot50 D/L^2$, from which the absolute value of the diffusion coefficient can be calculated. Thus it is not necessary to know values of M_R, c_0, α, or v^* to calculate the diffusion coefficient; these factors determine the height of the internal friction peak, not its position. This relation is close to that of $f_m = \pi D/2L^2 = 1\cdot57\, D/L^2$ found from equation (10).

The internal friction is usually measured at a constant frequency over a range of temperatures. The shape of the resulting internal friction vs. temperature curve can be calculated from equation (9) by assuming the diffusion coefficient D varies with temperature as $D = D_0 \exp(-Q/RT)$, where D_0 and Q, the activation energy, are independent of temperature. The wider the internal friction peak the lower the activation energy. Thus the activation energy for diffusion can be determined from a fit of such calculated curves with experimental data.

The data of Cantelli *et al.*[5] for the internal friction of deuterium in vanadium are compared with the calculated peak in Fig. 2, using an activation energy of 0·10 eV. The fit is good over the entire temperature range, supporting the functional form of equation (9).

In the three systems listed in Table 1 Cantelli *et al.* reported deviations from exponential temperature dependence of the diffusion coefficient at low temperatures [4, 5]. However, equation (9) fits their data for each of these systems, implying that the deviations arise because they assumed equation (10) to hold.

The activation energies Q calculated from their data by matching them with the internal friction peak of equation (9) are given in Table 1. For hydrogen and deuterium in vanadium the Q values from equation (9) are higher than those calculated by the previous workers, but are similar for hydrogen in niobium. The diffusion coefficients at the temperatures of maximum internal friction were calculated from the relation given above for f_m, and the D_0 values in Table 1 were calculated from these coefficients and the Q values. The values of D at maximum internal friction were somewhat higher than those calculated by the previous workers. The

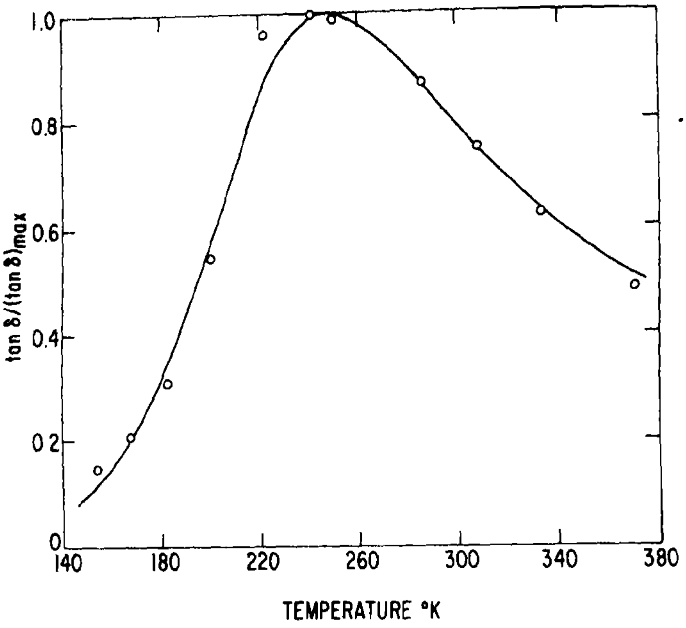

Fig. 2. The smoothed data of Cantelli *et al.*[5] for the internal friction of deuterium in vanadium as a function of temperature (circles), compared to the internal friction calculated from equation (9) (line).

Table 1. Activation energy Q and pre-exponential factor D_0 for diffusion, calculated from internal friction

System	Q, eV	$D_0 \times 10^3$, cm²/sec	Reference
H_2 in V	0·078	2·4	This paper, 5
	0·059	0·44	5
	0·050	0·35	3
D_2 in V	0·10	2·3	This paper, 5
	0·073	0·31	5
	0·080	0·35	3
H_2 in Nb	0·117	1·2	This paper, 4
	0·110	0·54	2
	0·109	0·54	4

experimental results for hydrogen in niobium are less reliable than those for vanadium, because in niobium a large oxygen peak in the region of maximum internal friction from hydrogen diffusion makes the peak position and activation energy for the latter more difficult to determine.

The comparison with experimental data indicates that equation (9) describes the internal friction resulting from the redistribution of atoms in a stress gradient, and that the conventional loss equation with a single relaxation time is less satisfactory.

Acknowledgement – Discussions with W. G. Johnston were most helpful.

REFERENCES

1. GORSKY W. S., *Phys. Zeits. Sow.* **8**, 562 (1935).
2. SCHAUMANN G., VOLKL J. and ALEFELD G., *Phys. Rev. Lett.* **21**, 841 (1968).
3. VOLKL J., SCHAUMANN G. and ALEFELD G., *J. Phys. Chem. Solids* **31**, 1805 (1970).
4. CANTELLI R., MAZZOLAI F. M. and NUOVO M., *Phys. Status Solidi* **34**, 597 (1969).
5. CANTELLI R., MAZZOLAI F. M. and NUOVO M., *J. Phys. Chem. Solids* **31**, 1811 (1970).
6. ALEFELD G., VOLKL J. and SCHAUMANN G., *Phys. Status Solidi* **37**, 337 (1970).
7. ZENER C., *Elasticity and Anelasticity of Metals*, p. 61, University of Chicago Press (1948).

J. Phys. Chem. Solids Pergamon Press 1971. Vol. 32, pp. 2217–2221. Printed in Great Britain.

ANISOTROPY IN THE RESISTIVITY OF $NbSe_2$

J. EDWARDS and R. F. FRINDT
Department of Physics, Simon Fraser University, Burnaby, British Columbia, Canada

(*Received* 12 *November* 1970)

Abstract—The resistivity of the metallic layer structure $NbSe_2$ has been measured across the layers ($\|c$) by a four probe technique which could be used for other layer structures. The temperature dependent part of the resistivity $\rho'_{\|c}$ was found to be linear in T from 300 to 80°K, and had a T^3 dependence below 60°K. The ratio of the resistivities $\rho'_{\|c}/\rho'_{\perp c}$ was constant at 31 : 1 from 300 to 80°K and then fell linearly with temperature.

1. INTRODUCTION

$NbSe_2$ is a metallic compound that crystallises into a hexagonal layer structure[1]: each layer consists of a Se–Nb–Se sheet, either two or four layers making up one unit cell. The details of the crystallography of $NbSe_2$ and related layer structures may be found in the reviews by Hulliger[2] and Wilson and Yoffe[3].

The bonds between Nb and Se within a layer are covalent, while bonds between layers are of the weak van der Waals type. As a result, many of the properties of $NbSe_2$ should show anisotropic behaviour. Measurements of the resistivity of $NbSe_2$ along the layers ($\perp c$) have been made[4, 5], but in spite of recent interest in layer structures, no data has yet been published on the anisotropy in resistivity of a metallic layer structure such as $NbSe_2$.

This work presents the results of resistivity measurements on the two layer modification of $NbSe_2$ by a method that may also be extended to semiconducting layer structures.

2. EXPERIMENTAL

Single crystals of $NbSe_2$ were prepared by generally following the method described by Kershaw *et al.* [4]. Chemical vapour transport, using iodine as the carrier, was employed with charge and growth-zone temperatures of 750 and 700°C for all samples. The purity of the elements used was 99·93 per cent for the Nb and 99·999 per cent for the Se. The resulting crystal platelets were of all sizes up to 2 cm × 2 cm × 0·4 mm thick. The resistivity measurements were taken on as-grown samples, both parallel and perpendicular to the c-axis.

The method for obtaining a four-terminal configuration for measurements parallel to the c-axis in layer structures is shown in Fig. 1. The voltage probes were partially cleaved from the body of the crystal. The connecting wires were attached using a conducting silver paste.

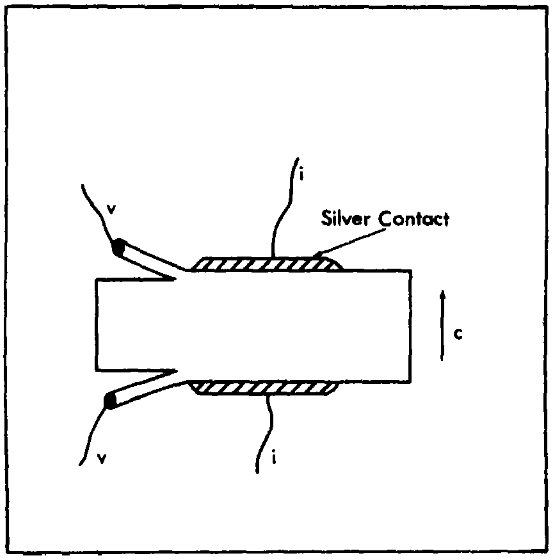

Fig. 1. Arrangement of leads for resistivity measurements on layer structures parallel to the c-axis. (Thickness is exaggerated for clarity).

Typical sample dimensions were 5 mm × 5 mm × 0·1 mm thick; the current contact area was about 1 mm^2 and the voltage contacts were about 0·005 mm thick.

Resistivity measurements were made perpendicular to the c-axis on some crystals, using either a conventional four-probe geometry or the van der Pauw method.

Temperatures below 77°K were measured using a gold–iron–silver normal thermocouple [6]: above 77°K standard freezing mixtures were used.

3. RESULTS

Measurements parallel to c were taken on nine samples, including a series of six made by successive cleaving of one of the thicker single crystals. The thickness of these nine ranged from 0·007 to 0·08 cm.

For a typical current contact area (A) of 1 mm^2 the measured resistivity (RA/t) of the samples was independent of thickness (t) for thicknesses less than 0·02 cm, but above this thickness, the measured resistivity was reduced (Fig. 2). Results similar to those in Fig. 2 were obtained by a two-dimensional analogue method, showing that shape effects were detectable for $l/t \leqslant 10$, L being the contact length. This corresponds in our samples to $t \geqslant 0{\cdot}01$ cm. One crystal (#1 in Fig. 2) was measured, first with a small current contact (~ 30 per cent of crystal area) and secondly with a larger contact (~ 80 per cent of crystal area). Results were obtained that were consistent with the sample resistance being a function of the contact area, not the crystal area.

Figure 3 shows the resistivity parallel to

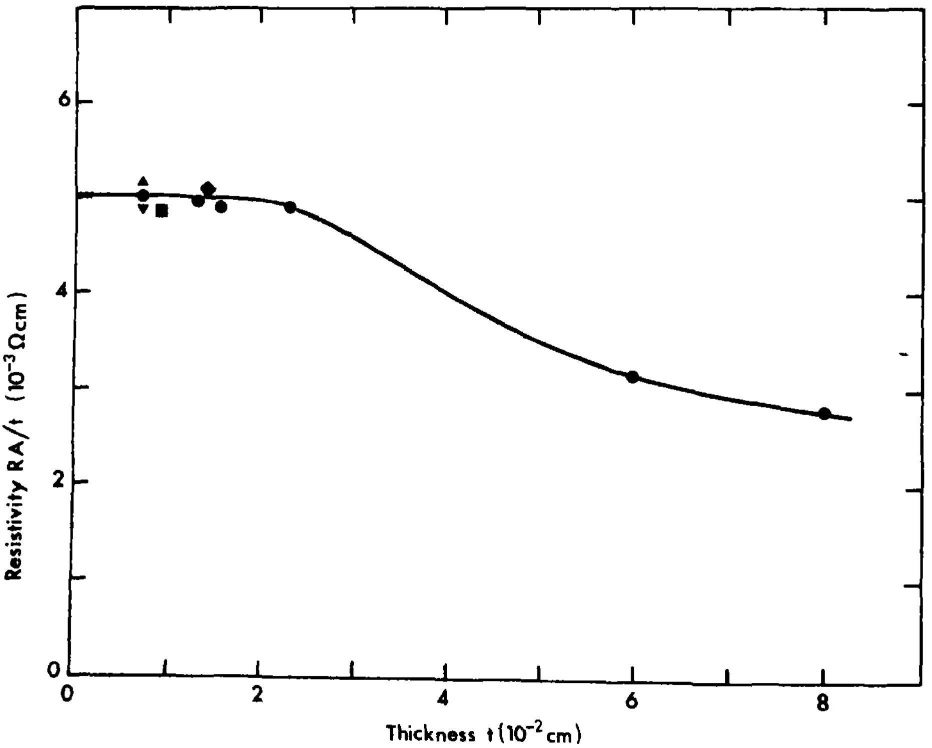

Fig. 2. Plot of resistivity of NbSe$_2$ parallel to c-axis against thickness for various crystals at room temperature. ▲, crystal #1 with small contact; ▼, crystal #1 with large contact; ■, crystal #3; ◆, crystal #4; ●, successive cleavings from crystal #5.

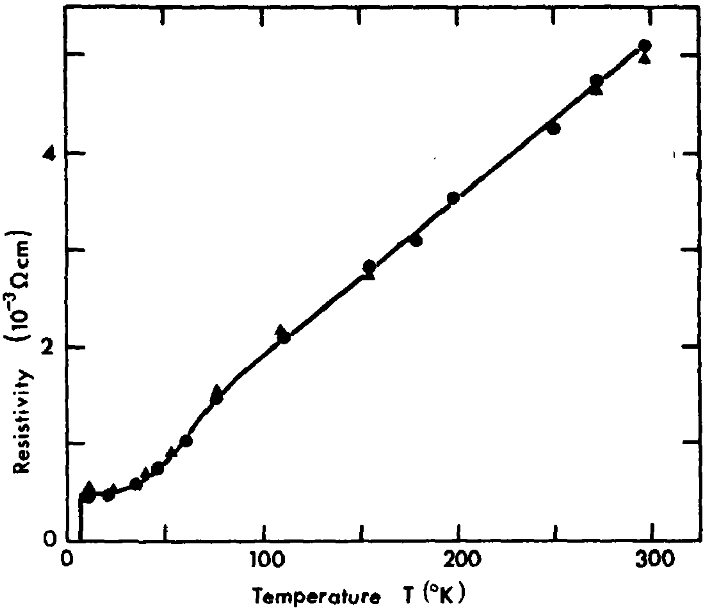

Fig. 3. Plot of resistivity parallel to c-axis against temperature for two $NbSe_2$ crystals.

c obtained for two crystals as a function of temperature. These results were typical of those obtained with all seven crystals of thickness less than 0·02 cm.

A logarithmic plot of the ideal resistivity $\rho'(T)$ both parallel and perpendicular to c is shown in Fig. 4. Because of the superconducting transition at 7°, there is an uncertainty in the value of the residual resistivity $\rho(0)$. The value for $\rho(0)$ was taken to be $\rho(7°)$, and $\rho'(T)$ was consequently given by $\rho'(T) = \rho(T) - \rho(7°)$. Our results for $\rho'_{\perp c}$ are in good agreement with the results of Lee *et al.*[5], also shown in Fig. 4. The resistivity $\rho'_{\| c}$ has a T^3 temperature dependence below approximately 60°K, while $\rho'_{\perp c}$ follows a T^2 law below 45°K. The error in the exponents is estimated to be $\pm 0{\cdot}2$. We feel that the data is not accurate enough to specify the temperature dependence below about 20°K. Our value for $\rho(7°)_{\perp c}$ was 10×10^{-6} Ω cm.

The ratio of ideal resistivities $\rho'_{\| c}/\rho'_{\perp c}$ is plotted in Fig. 5 as a function of temperature. The error bars in Fig. 5 mainly reflect the error in the estimates of $\rho(0)$ and the crystal dimensions.

The superconducting transition temperature was measured to be 7·0°K with current parallel or perpendicular to c. The measurements showed that any departures of the $NbSe_2$ from stoichiometry were small since it has been shown[7] that T_c is very sensitive to minor variations in niobium concentration.

4. DISCUSSION

The anisotropic behaviour of $NbSe_2$ shows itself in the ratio $\rho'_{\| c}/\rho'_{\perp c}$ being considerably greater than one, and also in the ratio being a function of temperature.

The ideal resistivities $\rho'_{\| c}$ and $\rho'_{\perp c}$ are both linear in T at temperatures above 100°K (Fig. 4). Since $\theta_D = 210$°K for $NbSe_2$[8], this behaviour is typical of most metals[9].

A full explanation of the low temperature observations that $\rho'_{\| c} \sim T^3$ and $\rho'_{\perp c} \sim T^2$ will require a knowledge of both the Fermi surface and the phonon spectrum of $NbSe_2$.

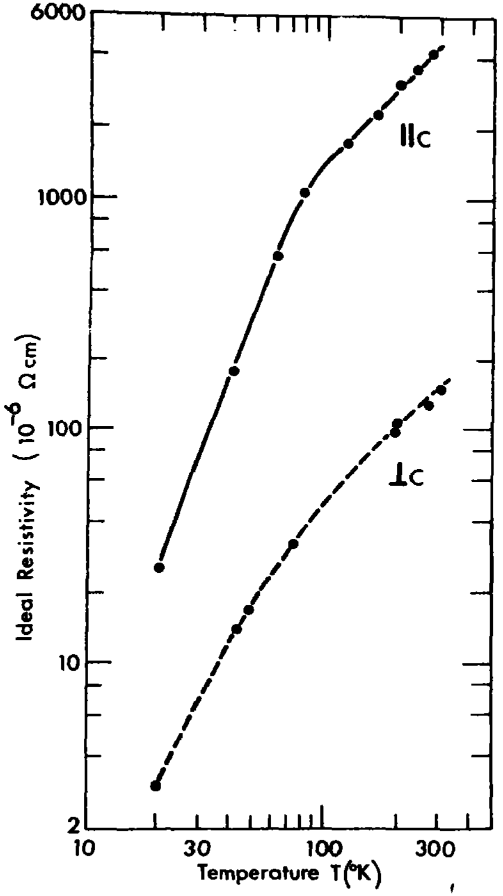

Fig. 4. Logarithmic plot of ideal resistivities $\rho'_{\parallel c}$ and $\rho'_{\perp c}$ of $NbSe_2$ against temperature. ● this work; -+- – Lee *et al.*[5].

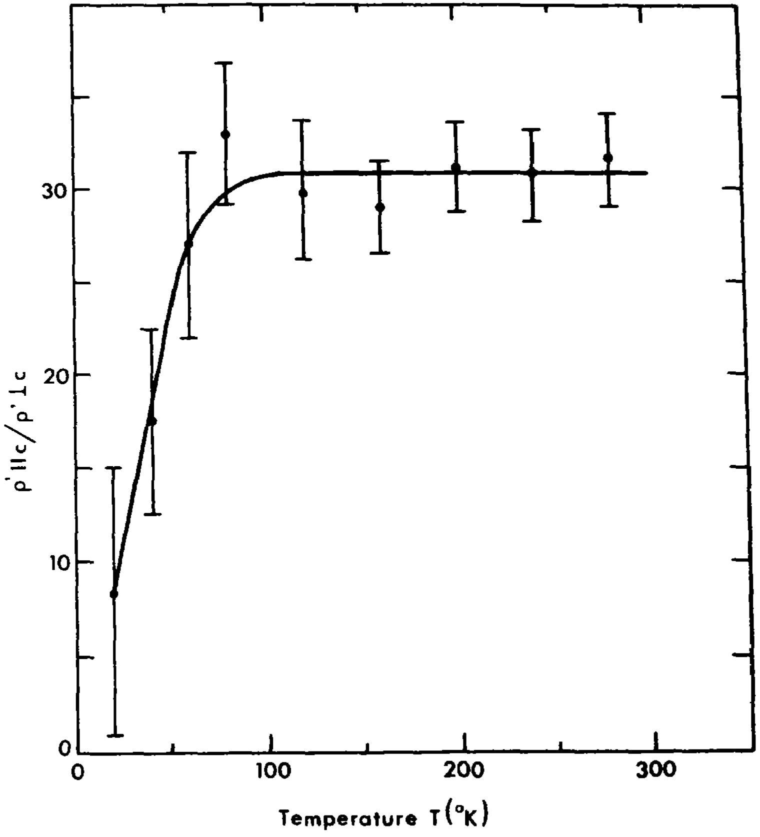

Fig. 5. Plot of the ratio of ideal resistivities $\rho'_{\parallel c}/\rho'_{\perp c}$ for $NbSe_2$ against temperature.

Some conjectures about the Fermi surface have been made [3] but, as yet, there have been no experimental determinations carried out. With regard to the phonon spectrum, it has been suggested by Krumhansl and Brooks [10] in the case of graphite, and for layer structures in general by Newell[11] that at the lowest temperatures the phonon spectrum resembles that of an anisotropic three-dimensional Debye solid, while at higher temperatures, the spectrum will, to a good approximation, resemble that of a two-dimensional Debye solid. Experimental confirmations of the theory given by [10] and [11] have been provided by the low-temperature specific heat of graphite[12, 13]. A T^3 dependence has been observed for the lattice specific heat of $NbSe_2$ and other related layer structures below 10°K[8], so that $NbSe_2$ may resemble a two-dimensional Debye solid in some temperature range above 10°K.

The Hall coefficient for $NbSe_2$ for current $\perp c$ is observed to change sign at 26°K, the samples going from p-type to n-type on cooling[5]. It would be of interest to see if similar behaviour is observed for current parallel to the c-axis.

Acknowledgements—We thank Dr. D. J. Huntley and Dr. S. Gygax for helpful comments and acknowledge the financial support of the National Research Council of Canada.

REFERENCES

1. REVOLINSKY E., SPIERING G. A. and BEERNTSEN D. J., *J. Phys. Chem. Solids* **26**, 1029 (1965).
2. HULLIGER F., In *Structure and Bonding* (Edited by C. Jorgenson) Vol. 4, p. 83. Springer Verlag, Berlin (1968).
3. WILSON J. A. and YOFFE A. D., *Adv. Phys.* **18**, 193 (1969).
4. KERSHAW R., VLASSE M. and WOLD A., *Inorg. Chem.* **6**, 1599 (1967).
5. LEE H. N. S., MCKENZIE H., TANNHAUSER D. S. and WOLD A., *J. appl. Phys.* **40**, 602 (1969).
6. BERMAN R., BROCK J. C. F. and HUNTLEY D. J., *Cryogenics* **4**, 233 (1964).
7. ANTONOVA E. A., MEDEEV C. A. and SHEBALIN I. Yu., *Zh. eks. teor. Fiz.* **57** (2), 329 (1969).
8. VAN MAAREN M. H. and HARLAND H. B., *Phys. Lett.* **29A**, 571 (1969).
9. MEADEN G. T., In *Electrical Resistance of Metals*, p. 59, Plenum Press, New York (1965).
10. KRUMHANSL J. A. and BROOKS H., *J. chem. Phys.* **21**, 1663 (1954).
11. NEWELL G. F., *J. chem. Phys* **23**, 2431 (1955).
12. DE SORBO W. J. and TYLER W. W., *J. chem. Phys.* **21**, 1660 (1954).
13. DE SORBO W. J. and NICHOLS G. E., *J. Phys. Chem. Solids* **6**, 352 (1958).

J. Phys. Chem. Solids Pergamon Press 1971. Vol. 32, pp. 2223–2229. Printed in Great Britain.

THERMAL CONDUCTIVITY OF CUBIC SODIUM TUNGSTEN BRONZES

A. E. WHITEMAN, J. J. MARTIN
Department of Physics, Oklahoma State University, Stillwater, Oklahoma

and

H. R. SHANKS
Institute for Atomic Research and Department of Physics, Iowa State University, Ames, Iowa

(*Received* 8 *September* 1970; *in revised form* 27 *October* 1970)

Abstract—The thermal conductivities of a series of metallic cubic sodium tungsten bronzes with $0.51 \leqslant x \leqslant 0.86$ have been measured from liquid helium to room temperature. The apparent Lorenz ratios for the samples have a peak at low temperatures caused by lattice conduction. At high temperatures the apparent Lorenz ratio is constant for each sample and approaches L_0 as x increases. The lattice conductivity was calculated for sodium vacancy scattering using the Debye approximation to the Callaway theory. At low temperatures this calculated lattice conductivity correlated well with that obtained by subtracting $L_0\sigma T$ from the measured thermal conductivity. Large deviations occurred at high temperature indicating that the high temperature Lorenz ratio for the lower x samples is considerably larger than L_0, but approaches L_0 at low temperatures. The $x = 0.75$ ordering of the Na atoms enhances the low temperature lattice conductivity, and at high temperatures the ordering causes a peak in L/L_0 at $x = 0.75$.

1. INTRODUCTION

THE NONSTOICHIOMETRIC compounds M_xWO_3 (where M represents a metal ion) are commonly called the tungsten bronzes. Although other tungsten bronzes have been investigated most of the work has been done on the alkali tungsten bronzes and, in particular, on sodium tungsten bronze, Na_xWO_3. The sodium tungsten bronzes are metallic over the range $x = 0.25$ to 1.0 and have the cubic Perovskite structure above $x = 0.48$. The sodium atoms occupy their lattice sites at random except at $x = 0.75$ where a partial ordering occurs. Atoji and Rundle[1] have observed this partial ordering of the sodium atoms by neutron diffraction studies.

The metallic properties of Na_xWO_3 arise from the contribution of a free electron from each sodium atom to a conduction band formed by tungsten and oxygen orbitals. Feinleib, Scouler and Ferretti[2] have summarized the present models for the tungsten bronzes and related materials such as ReO_3 which is also metallic. The model proposed by Goodenough[3] which consists of a conduction band formed by π bonded oxygen and tungsten $5d$ (t_{2g}) states is consistent with most transport property data. The authors are not aware of any band structure calculations for Na_xWO_3. However, the band structure would probably be similar to the band structure calculated by Matheiss[4] for ReO_3.

The electrical transport properties of metallic sodium tungsten bronzes have been reviewed by Muhlestein and Danielson[5, 6]. In addition, they have reported new results on electrically homogeneous crystals. Their electrical resistivity data versus sodium concentration show a change of slope at $x = 0.75$ where the sodium ions are thought to order. Their Hall effect and Seebeck effect data also show an anomaly near $x = 0.75$. They interpreted this result in terms of the addition of a second band above $x = 0.75$ which displays hole conductivity. This interpretation agrees with the band model proposed by Goodenough[3] for metallic sodium tungsten bronzes.

Measurements of the thermal conductivity should be interesting since it is possible to change the free electron concentration in these materials without changing the lattice symmetry and because of the $x = 0{\cdot}75$ ordering of the sodium atoms. Since the Lorenz ratio should have the theoretical value at low temperatures it should be possible to determine the lattice thermal conductivity at low temperatures. The only other known thermal conductivity results are those of Shanks and Redin[7] who measured several samples at temperatures above 300 K.

2. EXPERIMENTAL PROCEDURE

The thermal conductivity measurements were made with a steady-state heat-flow apparatus of conventional design. Electrical resistivity measurements were made on the same samples. Below 50 K the sample temperature and temperature difference were measured with Cu vs. Au + 0·07 at.% Fe thermocouples. Above 50 K, Cu vs. constantan thermocouples were used. The thermocouples were fastened to the sample with small Cu clamps that were coated with In. The clamp separation was determined from the room temperature electrical resistivity, which was measured independently. Therefore, the same geometrical factor applied to the thermal conductivity and to the electrical resistivity. The power input to the sample was calculated from the voltage and current that were applied to a heater clamped to one end of the sample. Thermal conductivity and electrical resistivity data were taken from liquid helium temperature to room temperature. Radiative heat losses make the thermal conductivity results inaccurate above 200 K.

The samples were cut from single crystals of Na_xWO_3 grown by electrolytic reduction of a melt of Na_2WO_4 and WO_3 as described by Shanks, Sidles and Danielson[8]. The x-values were determined from the known relationships between lattice constant and sodium concentration [9]. The samples were approximately 3 mm square by 15 mm long. Each sample was annealed for 24 hr at 700°C. The room temperature electrical resistivity was checked both for magnitude and for homogeneity along the sample before any thermal measurements were made. The room temperature resistivities are in good agreement with those reported by Muhlestein and Danielson[5]. Table 1 gives the room temperature and liquid helium temperature resistivities of our samples.

3. RESULTS AND DISCUSSION

The thermal conductivity results are shown in Fig. 1. For clarity we have omitted data on additional samples with x values of 0·86, 0·75 and 0·51. The results for these additional samples are in excellent agreement with the data shown in Fig. 1. The $x = 0{\cdot}84$ sample was not measured at liquid helium temperatures; this sample was used to check the variation of the Lorenz ratio as a function of x at the higher temperatures. Our $x = 0{\cdot}51$ sample is in good agreement with the data of Shanks and Redin[7] on a similar sample. The temperature dependence of the thermal conductivity is similar to that of an impure metal or an alloy. The small upturn below 50 K in the lower x samples is caused by lattice conduction. Our electrical resistivity results, which were measured at the same time as the thermal conductivity, are in excellent agreement with those of Muhlestein and Danielson[5].

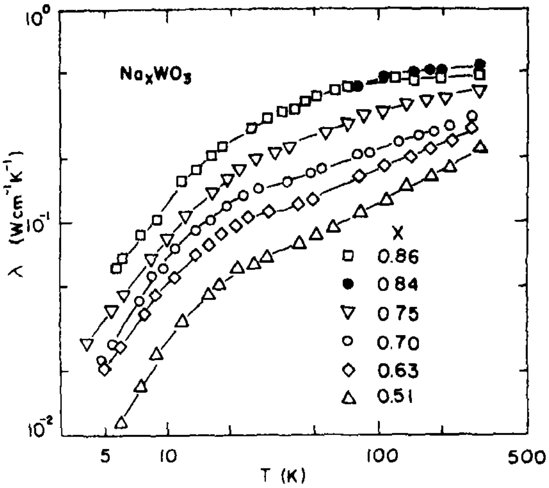

Fig. 1. Thermal conductivities of Na_xWO_3 as functions of the temperature from 5 to 300 K.

The thermal conductivity of metals has been reviewed by Klemems[10] and by Mendels-

Table 1. Sample resistivities

X	$\rho_{300}(10^{-6}$ ohm–cm)	$\rho_{4.2}(10^{-6}$ ohm–cm)
0·86	15·4	3·42
0·86	16·8	3·92
0·84	17·1	4·93
0·75	22·9	7·88
0·75	21·1	7·61
0·70	27·6	10·9
0·63	37·0	19·3
0·51	54·8	30·5

sohn and Rosenberg[11]. In metals the electronic thermal conductivity is related to the electrical resistivity by the Wiedemann-Franz-Lorenz (WFL) rule.

$$\lambda_e = LT\rho^{-1}, \tag{1}$$

where λ_e is the electronic thermal conductivity, L the Lorenz ratio, T the absolute temperature, and ρ the electrical resistivity. The WFL rule should be valid for high temperatures, where nearly elastic phonon-electron scattering dominates, and at very low temperatures, where impurity scattering dominates. For both cases, $L = L_0 = (\pi^2/3)(k/e)^2 = 2{\cdot}45 \times 10^{-8}$ V^2/K^2, where k is Boltzmann's constant and e is the electronic charge. At intermediate temperatures the WFL rule breaks down, and L shows a minimum because inelastic phonon-electron scattering limits the thermal conductivity much more than it limits the electrical conductivity.

Figure 2 shows the apparent Lorenz ratios that were calculated from our measured thermal conductivities and electrical resistivities. At the higher temperatures only the low x samples show large deviations from L_0. There is no evidence of a minimum in the apparent Lorenz ratio that would be caused by inelastic phonon-electron scattering. The large peaks at low temperatures are caused by lattice conduction.

The measured thermal conductivity is the sum of the electronic and lattice contributions. At low temperatures the electronic contribution should be given by equation (1) with $L = L_0$. Since Na vacancy scattering causes the large residual electrical resistivity of the tungsten bronzes, the dip in L caused by inelastic phonon-electron normally seen in metals should be masked by the elastic Na vacancy scattering. Then if we assume $L = L_0$ up to 40 or 50 K we can determine the lattice thermal conductivity λ_G, from

$$\lambda_G = \lambda - L_0 T\rho^{-1}. \tag{2}$$

Figure 3 shows the lattice conductivity calculated from equation (2). At low temperatures the lattice conductivity shows a temperature dependence slightly less than the T^2 dependence which is characteristic of electron-phonon scattering in metals. Crystal defects such as dislocations also show a similar temperature dependence, while more complex

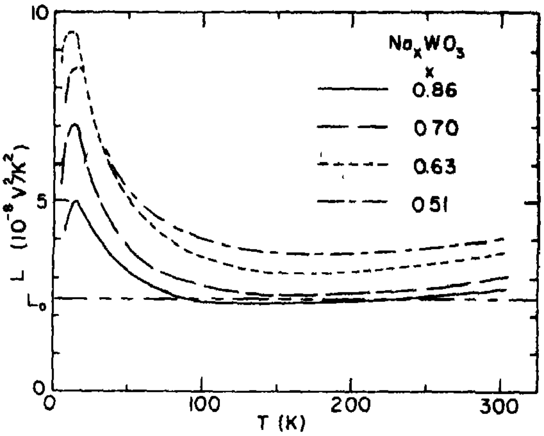

Fig. 2. Apparent Lorenz ratios of Na_xWO_3 as functions of the temperature from 5 to 300 K. The peaks at low temperatures are caused by lattice conduction.

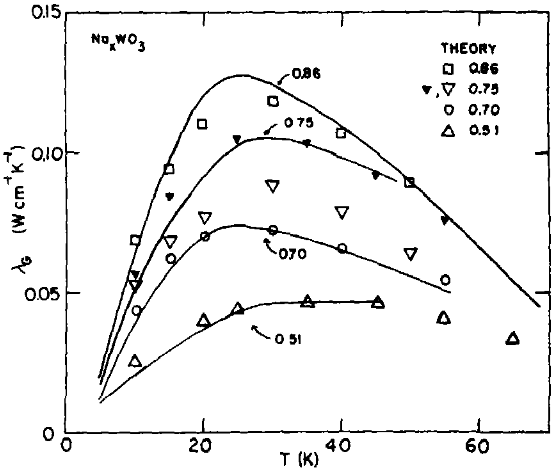

Fig. 3. Lattice components of the thermal conductivity of Na_xWO_3 as functions of the temperature from 5 to 60 K. The solid curves show the lattice conductivity obtained by subtracting $L_0\sigma T$ from the measured thermal conductivity. The plotted points for the respective samples were calculated for sodium vacancy scattering using the Debye approximation to the Callaway theory.

defects such as slip planes would produce a temperature dependence less than T^2. At higher temperatures the lattice conductivity decreases as the temperature increases which is characteristic of point defect scattering and phonon–phonon scattering. The lattice conductivity increases as x increases. If we treat the sodium vacancies as point defects then we would expect the lattice conductivity to increase as the number of sodium vacancies decreases; that is as x increases since there are $(1-x)$ sodium vacancies. It should be noted that the crystal lattice expands very slowly as x increases[9], and this expansion should not significantly alter the lattice conductivity.

For the samples with $x \geqslant 0{\cdot}70$ the lattice conductivity decreases approximately as T^{-1} as the temperature increases. The apparent Lorenz ratio approaches L_0 for these samples at temperature above 100 K, so that the lattice conductivity becomes a very small part of the total thermal conductivity except, perhaps, at $x = 0{\cdot}75$ which we will discuss later. Now we need to consider the low x samples. If we assume that $L = L_0$ at the higher temperatures for the $x = 0{\cdot}51$ sample, then the lattice conductivity given by the curve in Fig. 3 would continue to rise to a value of about 0·065 W/cmK at 200 K. That is it would become larger than the lattice conductivity for the high x samples. Alternatively, the Lorenz ratio rises above L_0 for the $x = 0{\cdot}51$ sample, and the lattice conductivity decreases with temperature as it should if the lattice conductivity is limited by point defects (Na vacancies) and phonon–phonon scattering. This last possibility should not be ruled out because large deviations from L_0 have been observed in transition metals at high temperatures where the lattice conductivity is small[12–14].

In order to check this last possibility, we have attempted to fit the lattice conductivity with the aid of the Debye approximation to the Callaway theory[15]. In this approximation the lattice conductivity, λ_G, can be expressed as

$$\lambda_G = \frac{k}{2\pi^2 c}\left(\frac{kT}{\hbar}\right)^3 \int_0^{\theta/T} \tau_c \frac{y^4 3_y}{(e^y - 1)^2}\, dy, \quad (3)$$

where c is an average sound velocity, θ is the Debye temperature, $y = \hbar\omega/kT$, where ω is the phonon angular frequency, and τ_c is a combined relaxation time found by the reciprocal addition of the relaxation times for the scattering processes present.

For τ_c we used

$$\tau_c^{-1} = c/D + A\omega^4 + E\omega/T + B\omega^2 T^3 \exp(-\theta/aT). \quad (4)$$

The first term represents scattering by the crystal boundaries and was left in only to insure convergence of the computer program for small values of y. The second term represents point defect scattering. Klemens [16] has derived an expression for A for the case of mass difference scattering. The largest mass defects present are the Na vacancies, if we ignore any isotope or impurity mass effects, Klemens' expression becomes

$$A = \frac{V}{4\pi c^3}(1-x), \quad (5)$$

where V is the molecular volume and $(1-x)$ is the number of Na vacancies per molecule randomly distributed throughout the crystal. The third term was used to represent the electron-phonon scattering which dominates the lattice conductivity at low temperatures. For ordinary metals this term should be $E\omega$ which gives a T^2 dependence. However, if the phonon wavelength is longer than the electron mean free path the adiabatic approximation breaks down; Pippard[17] has treated this case and finds a term $E\omega^2$ when the phonon wavelength is much longer than the electron mean free path. The last term represents phonon–phonon scattering.

A sound velocity of 4×10^5 cm/sec[18] and a Debye temperature of 500 K[19] was used in equation (3) to calculate the lattice conductivity. The initial fit was made for the $x = 0{\cdot}86$ sample. The phonon–phonon scattering parameters B and a were adjusted to fit the lattice conductivity near 60 K. The parameter a changes the slope of λ vs. T in this range. The point defect parameter A was then adjusted to give a fit near the thermal conductivity maximum and E adjust for a low temperature fit. The point defect term was then scaled as $(1-x)$ to calculate the lattice conductivity for the other samples with the phonon–phonon term held constant. We found $E = 4 \times 10^{-4}$ K, $B = 3{\cdot}5 \times 10^{-22}$ sec K^{-2}, $a = 5$ and the point defect term $A = 9{\cdot}3 \times 10^{-41}$ $x\ (1-x)$ sec^3 gave a good fit to the lattice conductivity on all but the $x = 0{\cdot}75$ samples. The results of the calculation are shown as the points in Fig. 3. Equation (5) gives $A = 7{\cdot}2 \times 10^{-41}\ (1-x)$; considering the approximations involved the agreement is excellent. Both the ω and ω^2 forms for electron–phonon scattering were tried in equation (4). Neither form would fit the low temperature data. The $E\omega/T$ term was finally used since it seemed to fit the measured λ_G fairly well. Evidently, the electron–phonon scattering cuts off as the temperature increases. The term used in equation (4) probably should not be interpreted as representing the actual electron–phonon scattering rate. E had a negligible effect on the results above 30 K. We see that the Na vacancy term gives good agreement with the measured lattice conductivity except at $x = 0{\cdot}75$.

For $x = 0{\cdot}75$ the measured lattice conductivity (from equation (2) with $L = L_0$) is much higher than the conductivity calculated from equation (3) for Na vacancy scattering. The point defect term, $A\omega^4$, requires that the defects are randomly distributed throughout the crystal. At $x = 0{\cdot}75$ the Na ions are ordered[1], and, therefore, the thermal conductivity should be much higher than the result for random vacancies. The solid points shown in Fig. 3 are the curve calculated for the $x = 0{\cdot}75$ sample with A adjusted to $1{\cdot}5 \times 10^{-41}$ sec^3 rather than the value of $2{\cdot}3 \times 10^{-41}$ sec^3 which scales with the values used for other x values.

At low temperatures lattice conduction is as much as 50 per cent of the total thermal conductivity. We can use equation (3) with (4) to extrapolate the lattice conductivity to higher temperatures. For the $x = 0{\cdot}51$ sample the lattice conductivity decreases to a value of $6{\cdot}5 \times 10^{-3}$ W/cm-K at 200 K which is less than 4 per cent of the total thermal conductivity. Similar results hold for the other samples. Therefore, we conclude that the large Lorenz ratios at high temperature for the low x samples are an electronic effect and are not caused by the lattice thermal conductivity. By subtracting the theoretical lattice conductivity calculated from equation (3) from the total thermal conductivity we can estimate the electronic contribution and then calculate a Lorenz ratio that contains only the electronic contribution. Figure 4 shows L/L_0 vs. T for the $x = 0{\cdot}51$ sample. The increase of L/L_0 at high temperatures is much smaller for the higher x samples. Figure 5 gives a plot of L/L_0 vs. x at 200 K.

Klemens[20] has pointed out that L is not only a consequence of the equivalence of the elastic relaxation times for electrical and

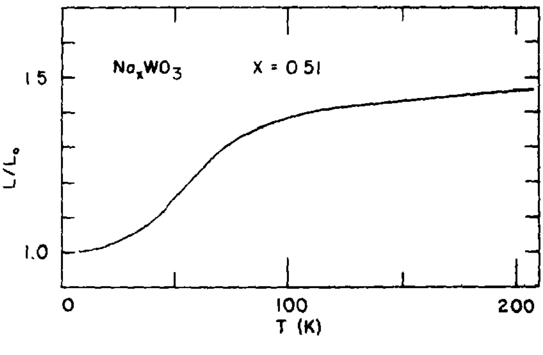

Fig. 4. Ratio of the calculated Lorenz ratio to the theoretical Lorenz ratio for $x = 0{\cdot}51$ as a function of the temperature from 5 to 200 K. The calculated Lorenz ratio was found by assuming that the difference between the experimental total thermal conductivity and the theoretical lattice conductivity was the electronic component of the thermal conductivity.

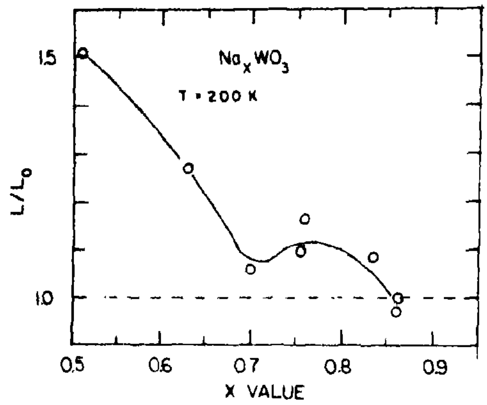

Fig. 5. Ratio of the calculated Lorenz ratio of Na_xWO_3 to the theoretical Lorenz ratio as a function of x at 200 K. At this high temperature the lattice conductivity is very small compared to the electronic conductivity so that the calculated Lorenz ratio can be obtained using the experimental thermal conductivity.

thermal conduction but that it also includes the energy dependence of the density of states and scattering processes within a few kT of the Fermi surface. Since the band structure of the transition metals and transition metal compounds is complex, one would expect significant deviations of L from L_0. Such deviations have been observed in Th[12], Cr [13], and Ti and Hf[14]. The deviations of L from L_0 can be related to the ratio of the Fermi energy, E_f, to kT with the deviations becoming larger as kT approaches E_f, that is, as the temperature increases. Recently, Goff[13] has discussed the Lorenz ratio of Cr in these terms. Detailed models of the band structure and Fermi surface of the tungsten bronzes are not yet available[2]; however, the conduction bands are thought to have a narrow d-like character[3]. For our lower x samples the Fermi energy is reduced, $E_f \alpha x^{2/3}$, and the deviation of L from L_0 should be larger for the low x samples.

Figure 5 also shows a small peak in L/L_0 near $x = 0.75$ where the Na atoms are ordered[1]. Muhlestein and Danielson[5, 6] have observed anomalies in the electrical conductivity, the Seebeck coefficient and in the Hall coefficient in the vicinity of the $x = 0.75$ ordering. They have interpreted their results in terms of the formation of a super zone at $x = 0.75$ which cuts the original Brillouin zone in half. Our electrical resistivity results are in excellent agreement with those of Muhlestein and Danielson. The low temperature lattice conductivity was enhanced for the $x = 0.75$ samples, so that the peak in L/L_0 may be the result of incorrectly subtracting the lattice term. However, if the lattice term for the $x = 0.75$ samples decreases as the temperature increases at the same rate as it does for the other samples the lattice contribution then accounts for less than half of the peak in L/L_0. The Hall coefficient, as measured by Muhlestein and Danielson, varies less rapidly with x in the vicinity of $x = 0.75$ than it would if only one kind of carrier were present. They interpreted their result in terms of a second band which displayed hole conduction. This interpretation is consistent with the band model of Goodenough which has a second conduction band for $0.75 \leqslant x \leqslant 0.86$.

Gallo[21] has discussed the Lorenz ratio for metals when there are two kinds of carriers. He obtains an increase in L that is caused by the separate diffusion of the electrons and holes. The result is similar to the well known bipolar diffusion in semiconductors; but it is, of course, much smaller since an energy gap does not enhance the thermal transport. Therefore, at least part of the peak in L/L_0 near $x = 0.75$ is caused by the electronic thermal conductivity.

4. SUMMARY

The thermal conductivity of a series of cubic sodium tungsten bronze samples with $0.51 < x < 0.86$ has been measured from liquid helium temperature to room temperature. At low temperatures the lattice conductivity is a significant part of the total thermal conductivity. The lattice conductivity was analyzed in terms of the Callaway[15] theory. For all samples, except $x = 0.75$ samples, the point defect term agreed with Klemens' expression for mass defect scattering and went as $1-x$; this result indicated that Na vacancy scattering was the dominant scattering mechanism. The lattice conductivity decreases as the temperature increases and it becomes a very small part of the total thermal conductivity. The result is that the electronic contribution at the higher temperatures for low x samples is larger than that predicted by the theoretical WFL rule and L rises above L_0 at high temperatures for the low x samples. This result can be qualitatively understood in terms of the narrow d-like character of the conduction band. The $x = 0{\cdot}75$ ordering of the Na atoms shows up in the low temperature lattice conductivity, and at high temperatures the ordering causes a peak in L/L_0 at $x = 0{\cdot}75$.

Acknowledgements—The authors would like to thank the Oklahoma State University Research Foundation for their support. The transport measurements were made at the Oklahoma State University. The crystal preparation and x-value analysis was performed in the Ames Laboratory, U.S. Atomic Energy Commission. We would also like to thank Joe A. Miller for his help with the data taking.

REFERENCES

1. ATOJI M. and RUNDLE R. E., *J. chem. Phys.* **32**, 627 (1960).
2. FEINLEIB J., SCOULER W. J. and FERRETTI A., *Phys. Rev.* **165**, 765 (1968).
3. GOODENOUGH J. B., *Bull. Soc. Chim. France* **4**, 1200 (1965).
4. MATHEISS L. F., *Phys. Rev.* **181**, 987 (1969).
5. MUHLESTEIN L. D. and DANIELSON G. C., *Phys. Rev.* **158**, 825 (1967).
6. MUHLESTEIN L. D. and DANIELSON G. C., *Phys. Rev.* **160**, 562 (1967).
7. SHANKS H. R. and REDIN R. D., *J. Phys. Chem. Solids* **27**, 75 (1966).
8. SHANKS H. R., SIDDES P. H. and DANIELSON G. C., *Advances in Chemistry Series*, No. **39**, 237 (1963).
9. REULAND R. J. and VOIGT H. R., *Anal. Chem.* **35**, 1263 (1963).
10. KLEMENS P. G., in *Handbuch der Physik*, Vol. 14, p. 198, (Edited by S. Flugge), Springer-Verlag, Berlin (1956).
11. MENDELSSOHN K. and ROSENBERG H. M., *Solid State Phys.* **12**, 223 (1960).
12. SCHETTLER H. G., MARTIN J. J., SCHMIDT F. A. and DANIELSON G. C., *Phys. Rev.* **187**, 801 (1969).
13. GOFF J. F., *Phys. Rev.* **B1**, 1351 (1970).
14. WHITE G. K. and WOODS S. B., *Phil. Trans. R. Soc. London* **A251**, 273 (1959).
15. CALLAWAY J., *Phys. Rev.* **113**, 1046 (1959).
16. KLEMENS P. G., *Solid State Phys.* **7**, 1 (1958).
17. PIPPARD A. B., *Phil. Mag.* **46**, 1104 (1955).
18. SHANKS H. R. (private communication).
19. VEST R. W., GRIFFEL M. and SMITH J. F., *J. chem. Phys.* **28**, 293 (1958).
20. KLEMENS P. G. in *Thermal Conductivity* Vol. 1, p. 1. (Edited by R. P. Rye), Academic Press, New York (1969).
21. GALLO C. F., *J. appl. Phys.* **36**, 3410 (1965).

J. Phys. Chem. Solids Pergamon Press 1971. Vol. 32, pp. 2231–2243. Printed in Great Britain.

THEORY OF LOCAL OSCILLATION OF SUBSTITUTIONAL DEFECTS NEAR A FREE SURFACE

U. T. HÖCHLI
IBM Research Laboratory, Zurich, Switzerland*

(*Received* 13 *October* 1970)

Abstract—An impurity atom substituting for a host atom near the surface of a discrete semiinfinite lattice can give rise to local oscillation. In general the conditions for local oscillation are low defect mass and strong binding of the impurity to its ligands. Results have been computed for a monatomic cubic crystal for both impurity atoms at and near the surface and are shown in Figs. 3, 4 and 5, of the text. Rotational invariance requires that force constants at the surface be different from bulk force constants. These surface forces give rise to surface waves, even where they have been reported absent in monatomic cubic crystals with nearest-neighbor forces only. These forces also influence the dynamics of local modes of surface impurities. It is shown that surface forces can be taken into account quantitatively as a perturbation of an ideal semiinfinite crystal if the eigenfrequency of the local mode is large enough, say twice the lattice frequency. For very large frequencies and small impurity mass the limit of the Einstein model is reached.

An infrared absorption experiment is proposed to detect local oscillation of surface impurities.

1. INTRODUCTION

STATIONARY vibrations which extend over a small part of a solid arise either from defects or geometrical termination of the solid. Such vibrations, called local modes, are characterized by an amplitude which decreases exponentially with the distance from the defect, or the surface, edge or corner, respectively.

Local modes at defects have been predicted by Lifshitz[1] and coworkers and independently by Montroll and Potts[2]. The first experimental evidence was given by Schäfer [3] who found an infrared absorption peak of *H* and *D* in KCl and was able to identify it as arising from a local mode due to its isotope effect.

The theory of elastic surface modes dates back to 1887 when Lord Rayleigh[4] found solutions of the wave equations for an isotropic semiinfinite medium which indicated waves propagating along the surface with an amplitude decreasing exponentially with the distance from the surface. Such waves, seismic and water waves, have of course been known before. Crystalline surface waves also exist; Wallis[5] has shown that surfaces of all dimensions less than 3 give rise to oscillation in diatomic crystals but fail to do so in monatomic crystals with only nearest-neighbor forces. Crystalline surface waves are generated by digital acoustic transducers [6].

Since a defect can give rise to local oscillations in a solid, one suspects that it can do so when placed near the surface or even at the surface. One can guess further that the local mode frequency depends on the site of the defect, and reaches its bulk value far enough away from the surface. Of all the vibrational properties of defects, the local modes are the easiest to detect. A vast amount of *H*, *D*, Li^6 and Li^7 substitutional ions have been observed in ionic crystals by infrared spectroscopy. This work as well as theoretical work on defects in solids has been reviewed by Maradudin *et al.*[7].

Isolated defects at surfaces have received relatively little attention in the past, presumably because it is very hard to produce and reproduce ideal surfaces. They are, however, of considerable technical interest, e.g.:

---

*Part of this work was performed while the author was at Battelle Institute, Carouge, Switzerland.

1. Adsorption and desorption are now used to obtain ultrahigh vacuum[8].
2. Surface catalysis[9] may be caused by irregularities and impurities on solid surfaces.
3. Crystal growth[10] results from adsorption of particles from the vapor phase on a surface, and is an instance where surface defects are detrimental.
4. Vacancies are attracted by boundaries and dislocation lines. This probably leads to growth of cavities and finally to creep and fatigue failures of metals[11]. One can hope to explain these phenomena better and even control the processes involved, once the role of the adsorbed atom at a surface is understood.

This paper sets out to predict the behavior of local modes of defects located anywhere in a semiinfinite crystal. The model is essentially the same as for bulk defects except that the vibrational states of the unperturbed crystal are adjusted to the loss of translational symmetry in one direction. Our model does predict local oscillation of adsorbed atoms under conditions which should be easily satisfied in nature. Thus it is felt that the same techniques that have been used to detect *U* centers should also prove successful for the detection of adatoms.

The remainder of this work is divided into the following parts: The next section describes a model involving forces between ions of a semiinfinite lattice and forces between a defect and its surroundings. Lattice Green's function technique is used to calculate the eigenfrequencies of this model. Section 3 is devoted to the relative stability of defects near a surface. In Section 4 the validity of the model is investigated and a comparison to more and less accurate models is made. Finally, a short section is devoted to experimental consequences of local oscillation of surface defects.

2. DYNAMICS OF DEFECTS IN A SEMI-INFINITE LATTICE

(a) *Model Hamiltonian, outline of solution*

The Hamiltonian describing the motion of ionic point charges in a simple cubic lattice is given by

$$H = \sum_{mi} (p_i^2(m)/2M_m) + \frac{1}{2}\sum_{mim'j} \phi_{ij}(m,m')u_i(m)u_j(m'). \quad (1)$$

Here i and j denote Cartesian directions x, y, z; and m indicate lattice points. The defect shall have the index $m = m_d$ and a mass $M(m_d) = m_0$, whereas the bulk masses $M_m = M$, $m \neq m_d$. The force constants Φ around the defect have only point symmetry of the defect, whereas outside this region and away from the surface, they have translational symmetry, i.e., they depend only on $m - m'$. In order to restrict the lattice to the one half space below the surface, one postulates $\Phi(m, m') = 0$ if m and m' denote sites in different half spaces.

The equations of motion deduced from this Hamiltonian are

$$M_m \ddot{u}_i(k) = -\sum_{m'j} \Phi_{ij}(m,m')u_j(m'). \quad (2)$$

If the equation for harmonic motion

$$u_i = u_{i0}\exp i\omega t \quad (3)$$

is inserted in (2) then one finds

$$\sum_{j,m} \{M_m\omega^2\delta_{mm'} - \Phi_{ij}(m,m')\}\, u_j(m) = 0 \quad (4)$$

which leads to the consistency equation

$$\det(M_m\omega^2\delta_{mm'} - \Phi_{ij}(m,m')) = 0. \quad (5)$$

Equation (5) determines the eigenfrequencies of the system, whereas the eigenvectors are obtained from (4) after insertion of ω.

In order to solve (5) it is advantageous to take recourse in the known properties of an ideal lattice having no defects. Lifshitz[1], and later Montroll and Potts[2] introduced this method in their search for local oscillation of defects in different models. We sketch an outline of how the method works; details are to be found in Ref. [7]. If (4) is written in compact form,

$$Ru = 0, \tag{6}$$

where R stands for

$$R_{ij}(m, m') \ldots M_m \omega^2 \delta_{mm'} - \Phi_{ij}(m, m'), \tag{7}$$

then we can put $R = L - D$ where L contains only forces and masses of the ideal lattice, whereas D accounts for changes thereof due to the introduction of defects. Formally one can multiply (7) by L^{-1} from the left to get

$$L^{-1}(L-D)u = (1 - L^{-1}D)u = 0. \tag{8}$$

This leads to the consistency relation[12]

$$\det(L^{-1}D - 1) = 0. \tag{9}$$

$L^{-1} = G$ is called the lattice Green's function. Both L^{-1} and D depend on ω. Equation (9) therefore is a condition that can serve to determine the parameter ω. Equation (9) is of order $3(N+1)$ where N is the number of atoms interacting direct with the defect due to a change of force constants. The original equation (5) is equivalent to (9) but of infinite order. The price to be paid for this drastic reduction of order is the evaluation of $3(N+1)$ matrix elements of the lattice Green's function.

The only three-dimensional lattices where Green's functions have been evaluated are the simple cubic infinite and semiinfinite lattices with nearest-neighbor interactions only. This determines the choice of the force constants Φ_{ij} entering equations (1) through (9). The model of simple cubic lattice with nearest-neighbor interaction has been introduced by Rosenstock and Newell[13]. Each ion is bound to its nearest-neighbor by a central force α and a noncentral force β. Thus the force matrices for the ideal lattice are diagonal in the cartesian coordination

$$\Phi_L = \Phi_{ij}(m_x, m_y, m_z, m_x \pm 1, m_y, m_z) = -\begin{pmatrix} \alpha & 0 & 0 \\ 0 & \beta & 0 \\ 0 & 0 & \beta \end{pmatrix} \tag{10}$$

for all $m_z \geq 0$ and similarly for neighbors in the y and z direction. All other force constants are put at zero except the self force which is determined by the criterion that the Hamiltonian be translationally invariant[7],

$$\Phi(m, m) = \Phi_0 = (2\alpha + 4\beta)\,1, \tag{11}$$

1 being the unit matrix.

A surface in the $x-y$ plane at $m_z = -\frac{1}{2}$ puts the force constants

$$\Phi(m_x, m_y, 0; m_x, m_y, -1) = 0. \tag{12}$$

The self-forces at the surface are thus

$$\Phi(m_x, m_y, 0; m_x, m_y, 0) = \begin{pmatrix} 2\alpha + 3\beta & 0 & 0 \\ 0 & 2\alpha + 3\beta & 0 \\ 0 & 0 & \alpha + 4\beta \end{pmatrix}. \tag{13}$$

Figure 1 shows a schematic view of the surface region. An impurity atom can occupy a site $m_z = 0$ as shown (surface defect), $m_z \geq 1$ (bulk defect) or $M_z = -1$ (adatom). In the case of an adatom we shall relocate the defect to the site $m_z = 0$ and consider all bonds except to $m_z = 1$ as non-existent. This leaves all force constants in the defect region unchanged.

Wallis has shown that in such a semiinfinite lattice no coupling exists between displacements of any atoms in different cartesian coordinates. This follows from the fact that all force matrices are diagonal. Consequently

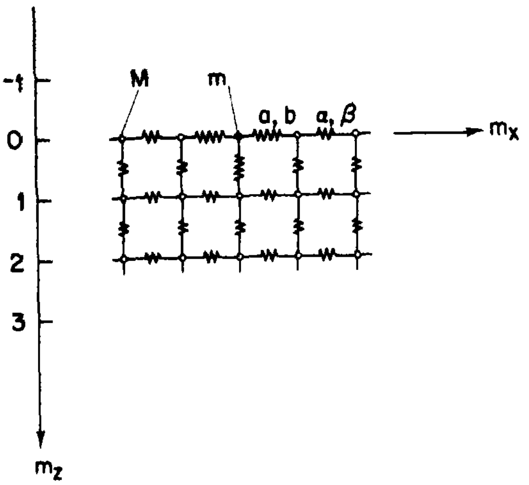

Fig. 1. Defect site at the surface in the Rosenstock-Newell model.

there can be no surface modes. On the other hand, cubic crystals with continuous mass distribution do exhibit surface waves[13]. Thus the Rosenstock-Newell model gives incorrect results in the continuous limit.

Ludwig and Lengeler[14] have pointed out that this discrepancy arises from the fact that the Hamiltonian based on equations (10) through (13) does not have rotational invariance. They also showed that rotational invariance can be restored by introducing additional coupling constants S between surface atoms. Their forces destroy the R-N symmetry of the semiinfinite lattice by coupling different components of displacements. The inclusion of off-diagonal terms in the force matrices gives rise to considerable mathematical complication. In order to benefit from (9) it is advantageous to define an ideal lattice L given by (10) through (13) and take the surface forces S into account as a perturbation. The consequences of these off-diagonal terms will be treated in more detail in Section 4.

The defect matrix is given by the difference between the real forces in the defect region and the lattice forces. Neglecting surface forces in the R-N model, both are diagonal and can be written as a direct sum

$$D = D_{xx} + D_{yy} + D_{zz} \tag{14}$$

where, for example, D_{xx} connects all displacements in the x-direction of the defect and its ligands.

In a vector space, given by the displacements of the atoms $(0\,0\,m_z)$, $(1\,0\,m_z)$, $(-1\,0\,m_z)$, $(0\,1\,m_z)$, $(0\,-1\,m_z)$, $(0\,0\,m_z+1)$, $(0\,0\,m_z-1)$, in the k-direction, the D matrices read as follows:

$$D = L - R = \begin{pmatrix} d_0 & d_1 & d_2 & d_3 & d_4 & d_5 & d_6 \\ d_1 & -d_1 & & & 0 & & \\ d_2 & & -d_2 & & & & \\ d_3 & & & -d_3 & & & \\ d_4 & & & & -d_4 & & \\ d_5 & & 0 & & & -d_5 & \\ d_6 & & & & & & -d_6 \end{pmatrix} \tag{15}$$

The matrix elements d_k are given explicitly in Table 1.

Now we proceed to the evaluation of the Green's functions (10). Green's functions of an eigenvalue problem such as (4) are given by[15]

$$G(\omega) = \sum_\lambda \frac{u_\lambda u_\lambda^*}{\omega - \omega_\lambda} \tag{16}$$

where ω_λ and u_λ are the eigenvalues and eigenvectors of (4). In the case of continuous spectra such as provided by an infinite ideal lattice the sum over k becomes an integral which in three dimension reads

$$G_0(m_1, m_2, m_3) = \pi^{-3} \int \mathrm{d}\varphi_1 \mathrm{d}\varphi_2 \mathrm{d}\varphi_3 \frac{\cos m_1\varphi_1 \cos m_2\varphi_2 \cos m_3\varphi_3}{M\omega^2 - 2\beta(1-\cos\varphi_1) - 2\beta(1-\cos\varphi_2) - 2\alpha(1-\cos\varphi_3)} \tag{17}$$

G_0 depends only on the difference vector m between two lattice points, reflecting translational symmetry. Some of these Green's functions have been evaluated numerically [16] and we shall reproduce here the largest ones in Fig. 2 to note that they decrease with

Table 1.

Site	m_z	Matrix	Elements						
			d_0	d_1	d_2	d_3	d_4	d_5	d_6
Bulk	$\geqslant 1$	D_{zz}	$\epsilon f^2+2\delta+4\eta$	$-\eta$	$-\eta$	$-\eta$	$-\eta$	$-\delta$	$-\delta$
Surface	0	D_{zz}	$\epsilon f^2+\delta+4\eta$	$-\eta$	$-\eta$	$-\eta$	$-\eta$	0	$-\delta$
Adatom	-1	D_{zz}	$\epsilon f^2+\delta-4\beta$	β	β	β	β	0	$-\delta$
Bulk	$\geqslant 1$	D_{xx}	$\epsilon f^2+2\delta+4\eta$	$-\delta$	$-\delta$	$-\eta$	$-\eta$	$-\eta$	$-\eta$
Surface	0	D_{xx}	$\epsilon f^2+2\delta+3\eta$	$-\delta$	$-\delta$	$-\eta$	$-\eta$	0	$-\eta$
Adatom	-1	D_{xx}	$\epsilon f^2-2\alpha-3\beta+b$	α	α	β	β	0	$-\eta$

All matrix elements are in units of $M\omega_L{}^2$

$f=\omega/\omega_L$

a = central force constant between defect and nearest neighbor

b = noncentral force constant between defect and nearest neighbor

$\delta=a-\alpha$

$\eta=b-\beta$

$f^2=\omega^2/\omega_L{}^2$

$\epsilon=(M-m_0)/M$.

increasing frequency and with increasing lattice vector. The numbering of the basis vectors m is the same as that of (15).

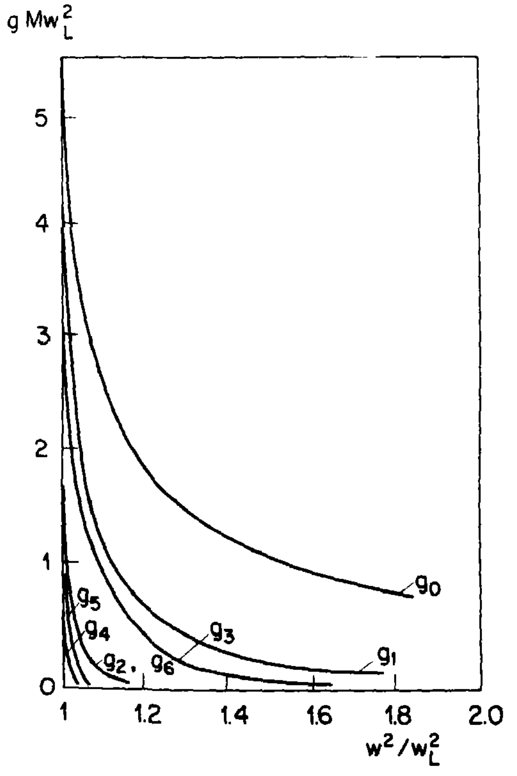

Fig. 2. Coupled displacements at a surface derived from a rotationally invariant Hamiltonian involving nearest-neighbor interaction only.

The Green's functions for the semiinfinite lattice have also been derived by Montroll and Potts[2]. If the lattice is to fill the positive half-space with free surface atoms at $m_z=0$, the eigenvectors satisfying the boundary condition are

$$(m)=(2/N)^{1/2} \times\cos\left[(2m+1)\pi j/2N\right]\exp i(kx+ly) \quad (18)$$

with eigenvalues

$$\lambda_j=M\omega^2-2\gamma(1-\cos\pi_j/N) \qquad j=0,1,\ldots N-1. \quad (19)$$

These eigenvectors and eigenvalues inserted in (16) yield the Green's functions G for the semiinfinite lattice in terms of the Green's function for the infinite lattice, G_0,

$$G(m_x,m_y,m_z)=G_0(m_x,m_y,m_z) +G_0(m_x,m_y,2m_z+1)+0(1/N). \quad (20)$$

This result has also been derived by Dobrzynski and Mills[17] who use it to determine properties of absorbed layers. The term of order $1/N$ is of no practical importance. The Green's functions for the R–N semiinfinite lattice can also be written as a direct product of cartesian components

$$G = G_{xx} + G_{yy} + G_{zz}. \qquad (21)$$

Since both G and D are expressed as direct sums of their diagonal coordinates, the consistency equation (9) factorizes:

$$\det(GD-1) = \det(G_{xx}D_{xx}-1)$$
$$\times \det(G_{yy}D_{yy}-1)\det(G_{zz}D_{zz}-1) = 0. \qquad (22)$$

Each of the three terms gives rise to equations of order 7. Equation (22) can be factorized further by taking into account C_{4v} point symmetry of the Hamiltonian. The displacements of the defect and its nearest neighbors transform according to the irreducible representations of the C_{4v} group, namely,

$$u \sim 5\Gamma_1 + \Gamma_2 + 2\Gamma_3 + \Gamma_4 + 6\Gamma_6. \qquad (23)$$

Thus equations of order 5, 1, 2, 1, 6 are to be solved. In the present case the reduction in dimension from 7 to 6 or less is insufficient to justify the trouble of performing it. Local mode frequencies will be evaluated using the consistency relation in the form of (22).

(b) *Eigenfrequencies*

For particle motion perpendicular to the surface the third factor of the left-hand side of (22) is relevant. In order to facilitate numerical computation, (22) is written as an eigenvalue equation

$$\det(G_{zz}D_{zz} - \lambda) = 0. \qquad (24)$$

Solutions of (24) have been computed on an IBM 360 computer and the defect parameters entering G and D have been varied until solutions $\lambda = 1$ were found. Equation (24) depends on the parameters ω, α/β, a, b and m, and gives one relation between them. By specifying the substrate, one parameter, namely, α/β can be fixed. The substrate which most resembles a monatomic lattice is KCl with α/β very large. Tabulated Green's functions exist for $\alpha/\beta = 2^N$ up to 16, thus we chose $\alpha/\beta = 16$. Since it can be expected that a/b is also large we neglected any change in b and put $b = \beta$. This enabled us to determine the eigenfrequency as a function of the defect mass and the central binding force and present it in the form of graphs.

Figure 3 shows the eigenfrequency as a function of defect mass for defects in the interior of the lattice. Curves are given for $a/\alpha = 1$ and 1·5. The case $m_z = \infty$ represents a bulk defect in the absence of a surface, since according to (20), $G = G_0$ for large arguments m_z.

In the case of $a/\alpha = 1$ our result corresponds to that by Maradudin. The substitutional defect situated just below the surface, at $m_z = 1$, shows almost the same properties as the bulk defect. Evidently the presence of a surface is not felt very far in the interior of a crystal if only nearest-neighbor forces are considered. Note that a finite amount of defect mass or defect force is required for local oscillation.

Figure 4 shows a similar plot for substitutional surface atoms and adatoms. These defects have quite different eigenfrequencies than bulk defects, due to the fact that they are bound to the substrate with one central force instead of two. Local oscillation takes place if either the mass defect exceeds 0·25 or if the force defect exceeds 0·5.

The adatom has almost the same eigenfrequencies as the surface atoms since they differ only by shear forces. If the ratio of defect mass to lattice mass is made arbitrarily small, the local mode frequency approaches the Einstein frequency, which is obtained assuming all atoms fixed except the adatom. This is a check of the present theory in the limit of large frequencies. Figure 5 shows the Einstein frequency of the surface atom, $\omega = (a+4b)^{+1/2}/M^{+1/2}$, and local mode frequencies as a function of mass defect and force defect.

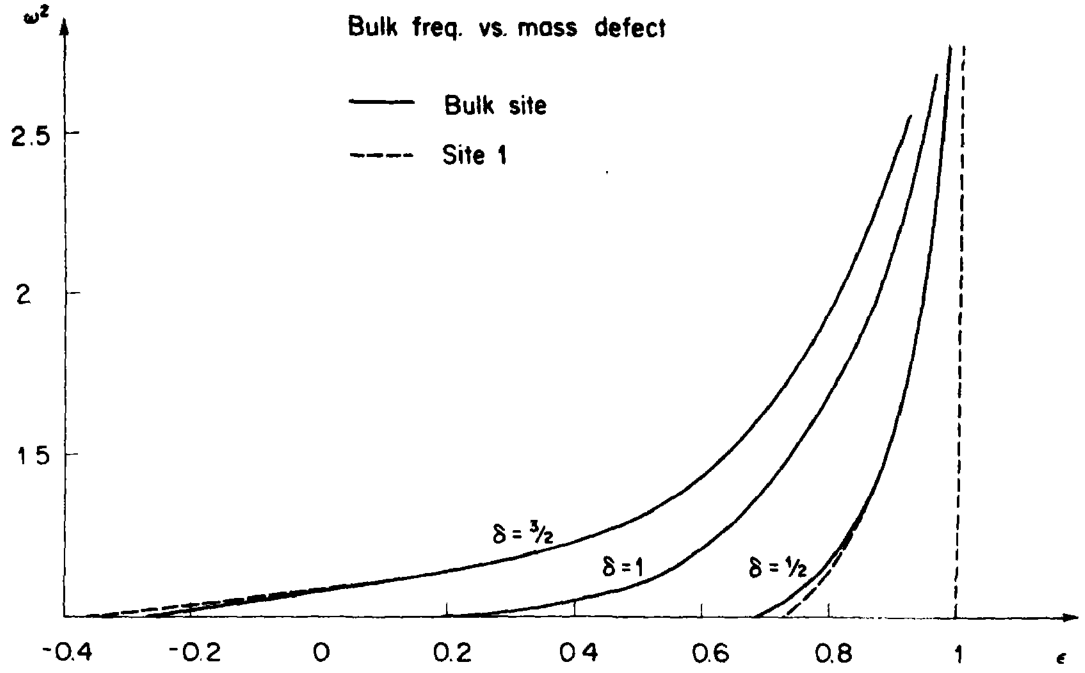

Fig. 3. Some Green's functions for the simple cubic lattice.

(c) *Oscillation parallel to the surface*

For bulk defects removed from the surface, oscillations in all three directions are degenerate due to cubic symmetry. At the surface the oscillation frequency changes by an amount of $0(\beta)$ since only one shear constant is removed. It will become evident in Section 4 that within the accuracy of our treatment, parallel local oscillation frequencies are the same as those of bulk modes.

3. STABILITY OF DEFECTS AT THE SURFACE

Montroll and Potts have observed that attractive and repulsive forces exist between a surface and an isotopic defect. We wish to generalize their results for all impurities in order to determine which sites can be stable. The zero point energy of a harmonic crystal is given by

$$E = \frac{\hbar}{2} \sum_k \omega_k \tag{25}$$

where the sum includes all eigenfrequencies of a crystal. The difference of energy due to the introduction of a defect is

$$\Delta E = \frac{\hbar}{2} \sum (\omega_k - \omega_{k0}) \tag{26}$$

where ω_{k0} are the eigenfrequencies of an unperturbed lattice. According to Montroll and Potts[2] this sum can be expressed in terms of the defect formalism

$$\Delta E = -\frac{\hbar}{2\pi} \int^{\infty} \omega \frac{\mathrm{d}}{\mathrm{d}\omega} [\log \det G(i\omega) D(i\omega) - 1] \mathrm{d}\omega. \tag{27}$$

This can be simplified considerably if it is assumed that both mass defect and force defect are small compared to unity. Then for $\epsilon \ll 1, \delta \ll 1$,

$$\Delta E = -\frac{\hbar}{2\pi} \int_0^{\infty} \omega \frac{\mathrm{d}}{\mathrm{d}\omega} \left(\sum_m^k G_{mm}(\omega) D_{mm}(\omega) \right) \mathrm{d}\omega \tag{28}$$

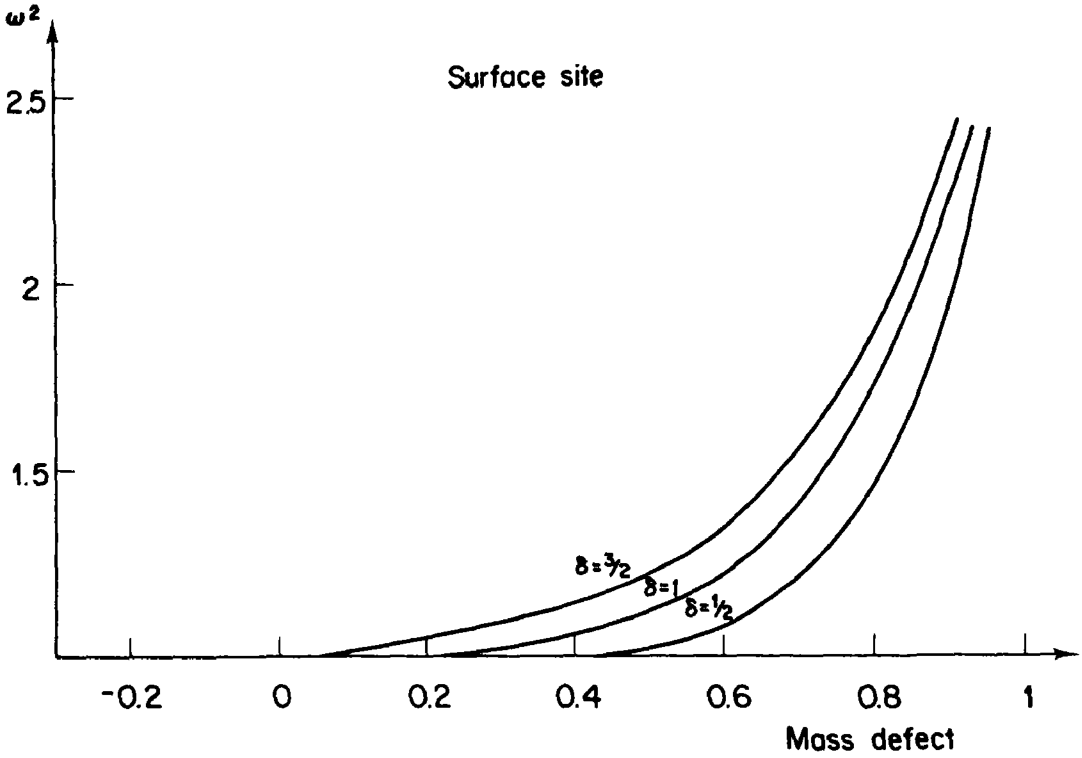

Fig. 4. Local oscillation frequency of defects near the surface as a function of impurity mass and force.

where m denotes all the lattice points of the defect region. Montroll and Potts have evaluated (27) and (28) for the limit $\beta \to 0$ for the isotopic defect. For $\delta = 0$ the zero energy becomes

$$\Delta E = \frac{1}{2}\hbar\omega_L\left\{-1+(1-\epsilon^2)^{1/2}\left(1+\frac{2}{\pi}\arc\sin\epsilon\right)\right\}. \tag{29}$$

It is straightforward to include the defect force $\delta = (a-\alpha)/\alpha$ as long as $\delta \ll 1$. To first order in ϵ and δ,

$$E = \frac{h\omega_L}{2\pi}\left(\frac{\delta}{2}+\epsilon\right) \tag{30}$$

for defects in the infinite lattice, and

$$\Delta E = \frac{h\omega_L}{2\pi}\left(\frac{\delta}{2}+\epsilon\right)(1-1/16m_z^2) \tag{31}$$

for the defects at a distance m_z from a surface.

For surface sites,

$$\Delta E = \frac{h\omega_L}{2\pi}\left(\frac{\delta'}{4}+\epsilon\right) \tag{32}$$

where δ' is the binding force of the surface atom which is not necessarily the same as δ. Both are taken in units of $M\omega_L^2$. The zero point energy for the different sites is shown in Fig. 6. Surface defects are stable with respect to diffusion if $\delta' \geq 2\delta$, i.e., for strongly adsorbed atoms. Thus atoms which occupy a stable surface site should exhibit local modes if their mass is smaller than that of the substrate. It should be borne in mind that these equations are valid for δ and $\epsilon \ll 1$, and that in the more interesting cases $\delta \sim 1$. Equations (30), (31) and (32) give only the first term of an infinite series in δ and ϵ. Qual-

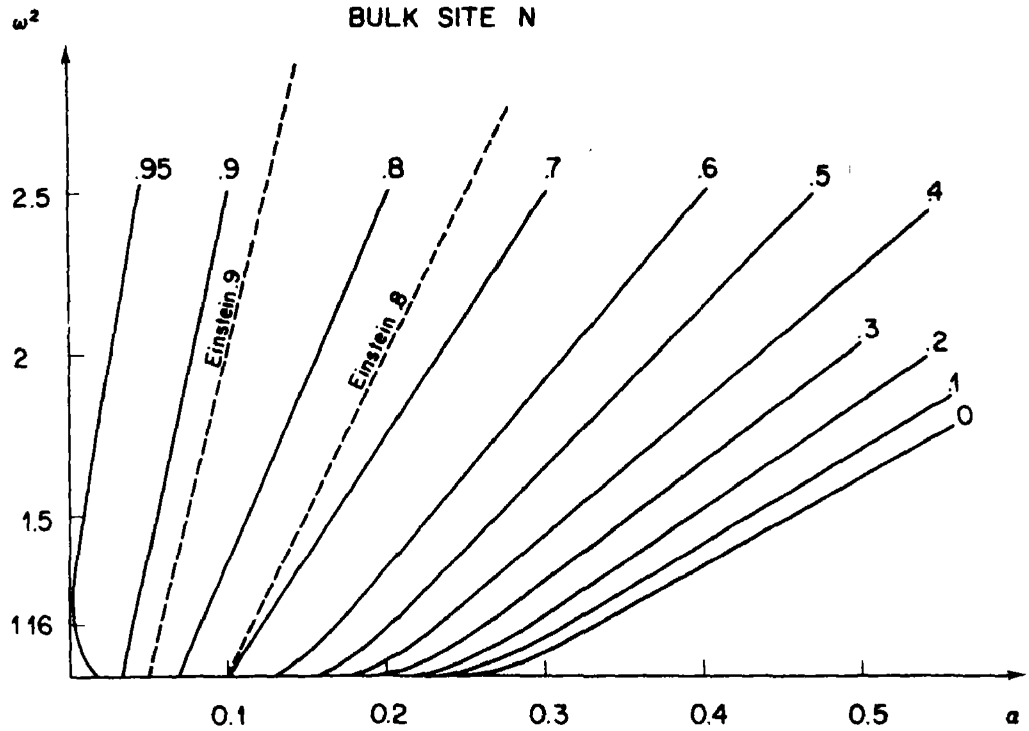

Fig. 5. Local oscillation frequency of surface impurities and absorbed atoms as a function of impurity mass and force.

itatively the above conclusion should still hold for larger δ and ϵ, since the zero point energy is a monotonous function of both defect mass and force.

4. EFFECT OF ROTATIONALLY INVARIANT SURFACE FORCES ON AN R-N MODEL

Consider the site (0,0,0) of an R–N semi-infinite lattice with all atoms at the equilibrium position. An infinitesimal rotation ω_y about the y axis through the origin displaces the atoms at $\pm 1,0,0$ by $\pm d\omega_y$ and the atom at 0,0,1 by $d\omega_y$, where d is the lattice distance.

The force on the atom at the origin after rotation is given by

$$\begin{aligned} F\{u'(0,0,0)\} &= \beta\{u'(0,0,1)-u'(0,0,0)\} \\ &+\beta\{u'(1,0,0)-u'(-1,0,0)-2u'(0,0,0)\} \\ &=(\beta d\omega_y,0,0). \end{aligned} \tag{33}$$

Thus a force of magnitude $\beta d\omega_y$ acts in the x-direction. Obviously, before rotation

$$F\{u(0,0,0)\}=0. \tag{34}$$

This is clearly a violation of the principle that forces between lattice points should be invariant against rigid body rotation.

As Ludwig and Lengeler[14] have shown, the R–N model can be made rotationally invariant by the introduction of surface forces between nearest neighbors at the surface,

$$S(000,\pm 100)=\beta/2\begin{pmatrix} 0 & 0 & \pm 1 \\ 0 & 0 & 0 \\ \mp 1 & 0 & 0 \end{pmatrix} \tag{35a}$$

$$S(000,0\pm 10)=\beta/2\begin{pmatrix} 0 & 0 & 0 \\ 0 & 0 & \pm 1 \\ 0 & \mp 1 & 0 \end{pmatrix}. \tag{35b}$$

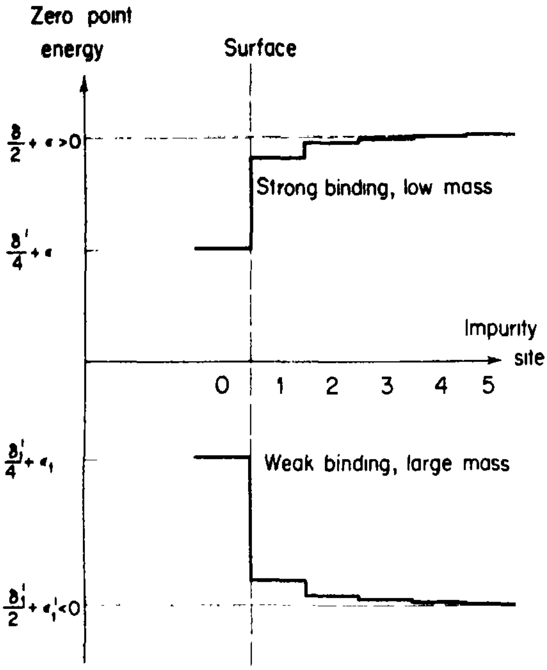
Zero point energy
Surface
$\frac{\delta}{2}+\epsilon>0$
$\frac{\delta'}{4}+\epsilon$
Strong binding, low mass
Impurity site
0
1
2
3
4
5
$\frac{\delta_1'}{4}+\epsilon_1$
Weak binding, large mass
$\frac{\delta_1'}{2}+\epsilon_1'<0$

Fig. 6. Comparison of local mode frequencies and Einstein frequencies in the limit of small defect mass.

These force constants couple displacements as shown in Fig. 7. If atom 0 is displaced at an angle of 45° with respect to the surface, both neighboring atoms are displaced at ±90° to the original atom by the action of the surface force. These displacements extend over the whole surface, giving rise to static warping. Since they depend linearly on the lattice constant d they are absent in the continuous limit d → 0[18]. It is intuitively clear that these warping forces give rise to surface waves in the harmonic approximation and we shall show that these forces give rise to new eigenfrequencies not covered by bulk modes.

Starting with the force matrix for the uncorrected semiinfinite lattice L, one can introduce the surface correction S and obtain a rotationally invariant Green's function

$$G_{r.i.} = (L+S)^{-1}. \tag{36}$$

Since all elements of S are of order β, the Dyson series

$$G_{r.i} = G - GSG + GSGSG - \cdots \tag{37}$$

converges and can be terminated after the second term, i.e., linear in β. The rotationally invariant Green's function is obviously no longer diagonal in the cartesian coordinates but of the form

$$G_{r.i.} = \begin{pmatrix} (G_{xx}) & (0) & (G_{xz}) \\ 0 & (G_{zz}) & (G_{yz}) \\ (-G_{xz}) & (-G_{yz}) & (G_{zz}) \end{pmatrix} \tag{38}$$

where (G_{xx}) is the matrix defined by (18), (20) and (21), and

$$G_{xz}(m,n) = \sum_{k,l} G_x(m,k)S_{xz}(k,l)G_z(l,n). \tag{39}$$

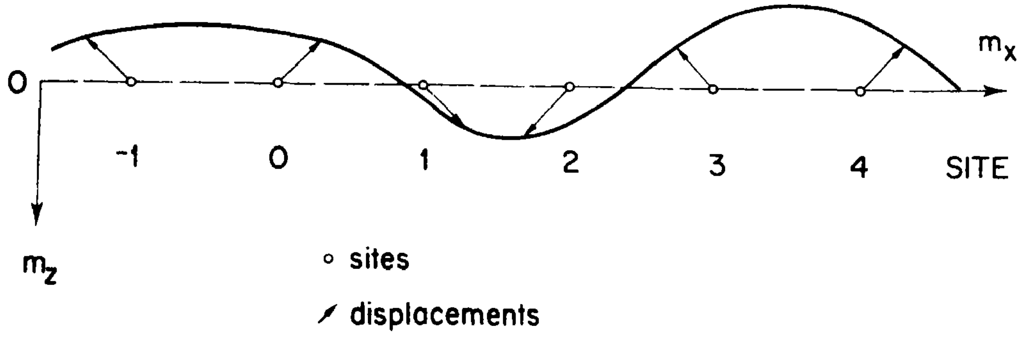

Fig. 7. Relative stability of defects near a surface.

With the use of (35) this becomes

$$G_{xz}(m,0,0;m,0,0) = (\beta/2)(G_0(0) - G(m,0,0))(G_0 - G(0,0,m)), \quad (40)$$

$$G_{xz}(m,0,0;n,0,0) = (\beta/2)G(0,0,m) \times (G_0(0) - G(0,0,n)), \quad (41)$$

if $m \neq n$, and 0 if m_y or $m_z \neq 0$. Thus $G_{r.i.}$ differs from G by terms of order $\beta/2$.

Similarly, the rotationally invariant lattice matrix

$$L_{r.i.} = L(1+GS) \quad (42)$$

contains the surface correction S. The solutions of

$$L_{r.i.}u = 0 \quad (43)$$

imply

$$\det L_{r.i.} = \det L \det(1+GS) = 0. \quad (44)$$

The first term determines the bulk frequencies, whereas the second term can vanish if G is of order $1/\beta$. This is above the band covered by bulk frequencies and shows that the surface forces restore the transition between crystalline surface waves and Rayleigh waves.[*]

The defect matrix of an adatom in a rotationally invariant model will also contain the projection of the S matrices, but with opposite sign, thus the consistency equation becomes

$$\det[(G-GSG)(D-S)+1] = 0. \quad (45)$$

It differs from the original equation (9) in terms of order β and higher. For $\omega > 2\omega_L$ all Green's functions are bound by

$$G_m < k_m/\omega.$$

Thus the frequencies solving (45) are in error by an amount of $0(\beta)$ or less.

The consequences of the lack of rotational invariance are thus two-fold:

(1) The band of surface modes extending into the forbidden region $M\omega_L^2 > 4\alpha+8\beta$ by an amount of $0(\beta)$ is neglected.

(2) Local mode frequencies computed in

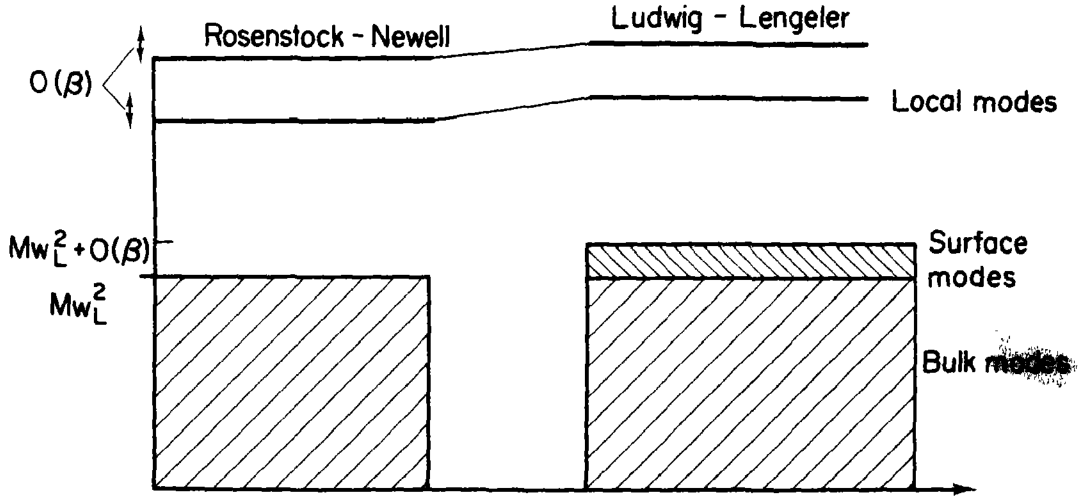

Fig. 8. Bands in a rotationally invariant Rosenstock–Newell model.

---

[*] The analog of Rayleigh waves in discrete lattice theory are low velocity waves localized at the surface. Their eigenfrequency has to exceed the lattice frequency for reasons of orthogonality to the bulk waves. In continuous matter theory no distinction exists between frequency bands of localized and bulk modes since the dispersion relation is linear and the frequencies are not bound.

the forbidden region are in error by an amount of $O(\beta)$.

Figure 8 shows a schematic representation of these findings.

The R–N model should therefore give approximately correct answers for situations found in surface chemistry, namely, adatoms whose mass is an order of magnitude smaller than those of the substrate and whose binding force is comparable to those of the substrate.

A comparison among the different force models in use is made in Table 2. For each model the internal consistency is given, and practical aspects, like availability of Green's functions and the dimension of the characteristic matrix, are given. The last two entries indicate how the characteristic matrix can be decomposed using the specific symmetry of the model and the point symmetry of the defect plus substrate.

5. PROPOSAL FOR EXPERIMENTAL DETECTION OF LOCAL OSCILLATION

Adsorbed atoms are involved in a number of chemical processes, yet little experimental data are available on the detection of isolated adsorbed atoms. Field ion microscopy[19] can detect single surface atoms, but it is not specific to adatoms. Occasionally it reveals the presence of an impurity among a multitude of surface host atoms. Paramagnetic resonance [20] has been applied for the study of isolated broken bonds on Si surfaces but it is restricted to the relatively rare cases of an unpaired spin at a surface.

The only experimental work on infrared

Table 2. Consistency of force models

Model	Consistency	Green's functions available	Dimension of matrix $GD+1$	Reduction due to RN condition	Number of C_{4v} representation of displacements				
					Γ_1	Γ_2	Γ_3	Γ_4	Γ_5
Nearest-neighbor central forces	Lattice unstable	Analytical	3	1+1+1	1				2
Nearest-neighbor central and non-central forces	Consistent	Tabulated	21	7+7+7	5	1	2	1	6
Same as above 100 surface	No rotational invariance	Sum of tabulated Green's function	21	7+7+7	5	1	2	1	6
This model for 100 surface	Consistent	As above, approximation only	21	21 (7+7+7 in crude approximation)	5	1	2	1	6
Nearest and next nearest-neighbor central forces	Consistent	Not available	57	57	9	6	6	6	15

detection of local modes seems to be that of Pliskin and Eischens[21]. These authors were able to derive the observed infrared absorption from vibration modes by measuring an isotope shift of 1·39 between deuterium and hydrogen. Unfortunately the substrate was polycrystalline and the vacuum was not such as to exclude contamination with other material. Furthermore the partial H_2 pressure was sufficiently high to allow formation of a monolayer of hydrogen on the substrate. Whereas it is beyond doubt that Pliskin and Eischens did observe a vibration mode involving hydrogen, the question remains whether it was a molecular vibration involving some other adatoms or a local mode. This question could be answered in an experiment on single-crystal material using present-day ultrahigh vacuum technology.

We therefore propose that light should be focused and sent between two parallel slabs of single-crystal material containing isolated adsorbed atoms. It is reflected many times to make the effective surface large. The amount of infrared absorption from local surface modes may be estimated in terms of the corresponding absorption from bulk modes. A surface typically contains 10^{15} sites/cm^2, it may be occupied by 10^{13} defects isolated from one another by ten lattice constants. The light beam can be made ten times as intense as for bulk transmission technique, since it is focused into a narrow gap between two surfaces of cm^2 size.

The light absorption found this way corresponds to that of bulk defects in a 10^{-2} cm^3 sample with a defect concentration of 10^{16} cm^3. This is slightly less than one usually likes to have in infrared absorption spectroscopy but it should be detectable.

Infrared absorption should be a useful tool for detection of absorbed atoms and may eventually be applied to determine various steps in chemical reaction on solid surfaces.

Acknowledgements—It is my pleasure to acknowledge valuable contributions by Professor H. Thomas. I also benefitted from discussions with Drs. M. Boon, A. Steinemann and P. E. Chan from Battelle Institute.

REFERENCES

1. LIFSHITS E. M., *Nuovo Cim. Suppl.* **4**, 716 (1956).
2. MONTROLL E. W. and POTTS R. B., *Phys. Rev.* **100**, 525 (1955); **102**, 72 (1956).
3. SCHAEFER G., *J. Phys. Chem. Solids* **12**, 233 (1960).
4. RAYLEIGH LORD, *Proc. Lond. Math. Soc.* **17**, 4 (1885).
5. WALLIS R. F., *Phys. Rev.* **116**, 302 (1959).
6. CARR P. H., *IEEE Trans. Microwave Theory and Techniques* **MTT 17**, 845 (1969), and other work in the same special issue.
7. MARADUDIN A. A., MONTROLL E. W. and WEISS G. H., In *Solid State Physics Suppl.* (Edited by F. Seitz and D. Turnbull) Vol. 3, Academic Press London (1963); MARADUDIN A. A., *ibid.* Vol. 18, p. 273 (1966); *ibid.* Vol. 19, p. 1 (1966).
8. WUTZ M., In *Theorie und Praxis der Vakuumtechnik*, p. 206. Vieweg, Braunschweig (1965).
9. EMMETT P. H., In *Catalysis* (Edited by P. H. Emmett), Reinhold, New York (1955).
10. KAISCHEW R. and BUDEVSKI E., *Contemporary Phys. (GB)* **8**, 489 (1967).
11. MACHLIN E. S., *Trans. AIME* **206**, 106 (1956).
12. There is some formal ambiguity in the sign of $L^{-1}D$ in (10). Since one can as well define the ideal lattice by $-L$, the equation $\det(-L^{-1}D-1)=0$ is just as valid, but then the Green's functions have opposite sign. The present definition of D agrees with Ref. [7].
13. ROSENSTOCK H. B. and NEWELL G. F., *J. Chem. Phys.* **21**, 1607 (1953).
14. LUDWIG W. and LENGELER B., *Solid State Commun.* **2**, 83 (1964).
15. KOSTER G. F and SLATER J. C., *Phys. Rev.* **95**, 1167 (1954).
16. MARADUDIN A. A., MONTROLL E. W., WEISS G. H., HERMAN R. and MILNES H. W., *Mem. Acad. Roy. Belg.* **14**, 1709 (1960).
17. DOBRZYNSKI L. and MILLS D. L., *J. Phys. Chem. Solids* **30**, 1043 (1969).
18. STONELEY R., *Proc. R. Soc.* **A232**, 447 (1955).
19. MUELLER E. W., PANITZ J. A. and McLANE S. B., *Rev. scient Instrum.* **39**, 83 (1968).
20. MUELLER K. A., CHAN P., KLEINER R., OVENALL D. W. and SPARNAAY M. J., *J. appl. Phys.* **35**, 2254 (1964).
21. PLISKIN, W. A. and EISCHENS, R. P., *Z. Phys. Chem. (Frankfurt)* **24**, 11 (1960).

J. Phys. Chem. Solids Pergamon Press 1971. Vol. 32, pp. 2245–2257. Printed in Great Britain.

ISOLATED SINGLE VACANCY IN DIAMOND–I. ELECTRONIC STRUCTURE

C. A. COULSON and F. P. LARKINS*
Mathematical Institute, Oxford, England

(*Received* 23 *July* 1970)

Abstract—Some of the assumptions underlying the molecular approach to the determination of the electronic properties of the vacancy in diamond have been examined. The ordering of the lowest electronic levels of the neutral and single negatively charged states of the vacancy is sensitive to the choice of atomic functions to represent the $2s$ and $2p$ orbitals on the atoms nearest the defect as well as to the symmetric relaxation of these atoms. However, for limited delocalisation of electronic charge from the vacancy there is no change in the ordering of the lowest levels. The ${}^3T_1$ electronic state is predicted as the ground state of the neutral vacancy if the atoms nearest the defect relax towards its centre as implied by the molecular model; however, for a symmetric relaxation of the nearest neighbours away from the centre of the vacancy the ${}^1E$ level is more likely to be the lowest level. Present experimental knowledge of the vacancy in diamond does not resolve this uncertainty.

1. INTRODUCTION

THE THEORETICAL investigations of the electronic structure of the isolated vacancy[1, 2] and the isolated neutral divacancy[3] in diamond using a molecular approach, which have been previously reported, are based upon an undistorted model for the defect. In addition, simple nodeless Slater functions with orbital exponent 1·595 have been used to represent the $2s$ and $2p$ orbitals on the atoms nearest the defect in the crystal. The calculation for the isolated vacancy[1] predicted that the GR1 absorption band observed in irradiated diamonds between 1·65 and 2·4 eV resulted from an electronic transition between the ${}^1E$ and ${}^1T_2$ levels of the neutral vacancy. In this paper we investigate in more detail than previously the calculated electronic properties of the isolated vacancy in its single positive, V^+, neutral, V^0, and single negative, V^-, charge states, in order to determine the sensitivity of the electronic energy levels to some of the assumptions underlying the model.

Firstly, we choose an alternative set of functions to represent the $2s$ and $2p$ orbitals on the atoms nearest the defect. This is of interest because when using nodeless Slater-type functions the $2s$ function is not orthogonal to the $1s$ function; therefore, the values obtained for the one-centre kinetic and potential energy integrals are in error. We have considered the self-consistent atomic functions proposed by Clementi[4] adequate alternatives for this purpose. It has also been necessary to repeat the previous calculations on the vacancy using Slater-type functions because of a numerical error in the semi-empirical estimate of the one-centre Coulomb integral. Secondly, we have considered the effect on the energies of the various electronic states of choosing single-electron molecular orbital wave functions which allow for some delocalisation of the electronic charge away from the vacancy on to next-nearest neighbour atoms. Finally, we investigate the sensitivity of the various levels to the symmetric relaxation forces which arise from the rearrangement of the vacancy electrons when forming molecular orbitals.

2. MOLECULAR APPROACH TO THE VACANCY PROBLEM

A detailed discussion of the molecular approach to the isolated vacancy in diamond may be found in the original paper by Coulson and Kearsley[1]. The basis of the defect molecule method is to assume that the electronic behaviour of the system in the immediate neighbourhood of the vacancy is only dependent upon the n electrons which are assumed to be localized within the undistorted defect. All exchange and polarisation effects with non-vacancy electrons are ignored. It is then possible to use the well-established techniques of molecular orbital theory to simplify the calculation.

---

*Present Address: Chemistry Department, Monash University, Victoria, 3168, Australia.

In a field of T_d symmetry, as for the vacancy electrons, the single-electron molecular orbitals belong to the a_1 and t_2 irreducible representations. In this problem the neighbours to the vacancy A, B, C and D are assigned co-ordinates $(\bar{1},1,1)$, $(1,\bar{1},1)$, $(1,1,\bar{1})$ and $(\bar{1},\bar{1},\bar{1})$ respectively, in units of $a/4$, where a is the cell constant, as shown in Fig. 1. We assume that the vacancy electrons are initially in tetrahedral hybrid orbitals $a-d$ associated with these atoms which are directed towards the centre of the defect. A suitable set of real non-localized single-electron wave functions which are mutually orthogonal and correspond to these irreducible representations is as follows

$$\begin{aligned} v &= N_1(a+b+c+d) \quad \subset a_1 \\ t_x &= N_2(-a+b+c-d) \\ t_y &= N_2(a-b+c-d) \\ t_z &= N_2(a+b-c-d) \end{aligned} \left.\vphantom{\begin{aligned} t_x \\ t_y \\ t_z \end{aligned}}\right\} \subset t_2$$

where $N_1 = 0{\cdot}5(1+3S_{ab})^{-1/2}$, $N_2 = 0{\cdot}5(1-S_{ab})^{-1/2}$ and S_{ab} is the overlap integral between two hybrids on neighbouring atoms to the vacancy. It should be noted that this is not the set chosen by Coulson and Kearsley, but will prove more versatile in the calculations to follow. The symmetry states of the wave functions belonging to the configurations $a_1{}^p t_2{}^{n-p}$, where $p = 0$, 1 or 2 and n is the number of vacancy electrons, may now be determined and the corresponding determinantal wave functions, $\psi(R)$, expressed in terms of the single-electron molecular orbitals. In the present problem we have $n = 3$, 4 or 5 depending upon whether we are considering the single positive, neutral or single negative charge state of the vacancy.

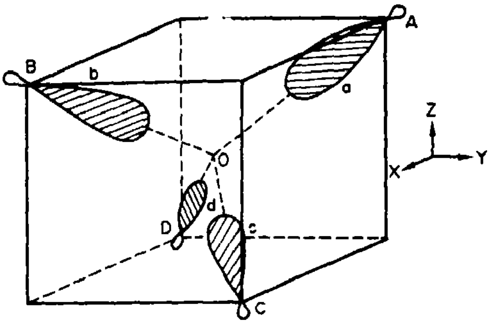

Fig. 1. Defect molecule for isolated vacancy: T_d symmetry.

The spin-independent Hamiltonian for the vacancy system, excluding exchange with non-vacancy electrons, may be written as follows,

$$H = \sum_{i=1}^{n} (T_i + V_i) + \sum_{i>j}^{n} \frac{1}{r_{ij}}$$

where T_i denotes the kinetic energy operator for the ith electron and V_i represents the potential energy of interaction of the vacancy electron i with the nuclei, the K shell electrons surrounding the vacancy atoms, and with the bonded valence electrons on these atoms. Now,

$$V_i = \sum_{K} V_{Ki}$$

where $K = A$, B, C, D and V_{Ki} is evaluated using the Goeppert-Mayer and Sklar approximation[5]. The energy of the various symmetry states, R, belonging to each configuration before configuration interaction may now be determined using the expression

$$E(R) = \frac{\int \psi^*(R) H \psi(R)\, d\tau}{\int \psi^*(R) \psi(R)\, d\tau}$$

once a suitable choice is made for the 2s and

$2p$ functions. The energy $E(R)$ may be expressed in terms of molecular integrals, $A-K$, defined in Ref. [1]. The formal expressions for the energy levels of the V^0 and V^- systems are given by Yamaguchi[2]. These energies are of no great value in themselves, because we must allow for interaction between configurations of the same orbital symmetry and spin-multiplicity in order to obtain results which may be usefully compared with experiment. This configurational mixing is the final step in the basic calculation.

3. RESULTS AND DISCUSSION OF UNDISTORTED VACANCY CALCULATIONS

We have chosen to consider only the findings obtained using an approach in which the intra-atomic Coulomb integral, Q, is modified in a semi-empirical manner. Corresponding to the semi-empirical values for Q it is possible to obtain two estimates for the self-penetration integral, P. These integrals are defined as

$$Q=\int a^*(1)a^*(2)\frac{1}{r_{12}}a(1)a(2)\,\mathrm{d}\tau$$

and

$$P=\int a^*(1)\{T_1+V_{A1}\}a(1)\,\mathrm{d}\tau$$

where 'a' is the tetrahedrally hybridized orbital on atom A directed towards the centre of the vacancy. It is believed that the results obtained by such an approach are more physically reasonable[1]. Upon checking the previous calculation for Q it was discovered that an error had occurred in the numerical evaluation, although the basic formulae were correct. The value we obtained for Q was 12·856 eV compared with the previous estimate of 13·293 eV. It was therefore necessary to repeat the calculations using Slater-type functions with orbital exponent 1·595 to compare these findings with those obtained using the Clementi-type functions[4]. As previously, we have considered two cases for each choice of function with Q = 12·856 eV. Case 1 involves using the value for P obtained with the analytical wave functions, while in the case 2 approximations P has the value − 16·42 eV. This value is the negative of the ionisation potential of an electron from a tetrahedral hybrid in the sp^3 valence state of the atom.

Table 1. Molecular integrals required for the vacancy calculation: modified cases

Integral	Slater functions	Clementi functions
A*	−38·132‡	−38·315
B*	−27·972	−26·475
A†	−43·764	−43·694
B†	−38·069	−38·726
C	9·820	9·808
D	8·722	8·765
E	9·422	9·487
F	8·332	8·020
G	1·790	1·953
J	0·677	0·474
K	−1·232	−1·217

*Case 1.
†Case 2.
‡All energies in electron volts.
§Integrals $A-K$ are defined in Ref. [1].

It is significant that even though large differences of 6 to 7 eV were obtained between the values of the one-centre kinetic and potential energy integrals for the different choices of atomic wave functions, the value of P, the integral of primary importance, does not differ very much for the two studies. We obtain for the case 1 approximation, P (Clementi) = −7·13 eV, while P (Slater) = −8·00 eV. The numerical values of the basic molecular integrals, $A-K$, which form the central part of the calculation are given in Table 1. The values of the one- and two-centre integrals required in the calculation were obtained using a version of the Diatomic Molecular Integral program[6, 7], while the Mulliken approximation[8] was used to obtain estimates of the three- and four-centre terms. The predicted electronic structure for V^+, V^0 and V^- for both choices of functions are shown in Figs. 2–4 respectively. From Table 1 it is apparent that the values for the integrals agree fairly well in most cases for both the choices of functions. The most significant changes are for the B, J and F integrals. The general feature of all the calculations is the strong dependence of the levels on configuration interaction effects which in some cases are very large and cause the inversion of the energy levels. It is also significant, especially for the cases using Clementi-type functions, that several levels show a marked dependence on the value of P. The most important are the $^5A_2$ level of V^0 and the ^2E and $^2T_2$ levels of V . As in the previous work the electronic levels are much more compressed in the case 2 study.

When we compared the results using Slater functions and the corrected value of Q with those obtained by Coulson and Kearsley we observe that even though there are fairly large changes in the numerical values of some of the molecular integrals, $A-K$, and in the energies of the electronic levels (~ 5 eV), there are only small changes in the general features of the calculations.

In the present study the electronic properties predicted for the V^+ centre (Fig. 2) show good agreement for both sets of functions with the $^2T_2$ level lowest at least 2 eV below the $^4T_1$ level. It is interesting that the electronic structure of the positively ionised vacancy was previously not examined using the modified theory because it was considered to be very much less stable than either V^0 or V^-. However, the present calculation suggests that this is not necessarily true. From Figs. 2–4 it is apparent that for the case 1 studies the $^2T_2$ ground state of V^+ is within 3 eV of the ground state of V^0 and over 2 eV lower than the lowest level for V^-. Admittedly, the situation is less favorable when case 2 is examined. Of course, we cannot really conclude anything definite about the relative stability of the various defect centres because of the further inadequacies in the model when applied to charged states. Nevertheless, these calculations do demonstrate that the possible non-existence of V^+ should not be argued on the basis of the unmodified calculation by Coulson and Kearsley as has been previously suggested[9]. If the $^2T_2$ electronic level is the ground state of this centre, then the centre should exhibit paramagnetic resonance and be Jahn–Teller distorted because of the degeneracy of the lowest level. In view of the large separation of the levels, it seems unlikely that there would be an observable electronic transition associated with this centre.

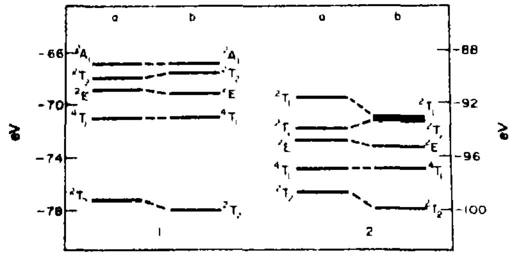

Fig. 2a. Electronic structure of positive vacancy in diamond: Slater functions (a) before configuration interaction, (b), after configuration interaction 1, $P = -8.00$ eV, 2. $P = -16.42$ eV.

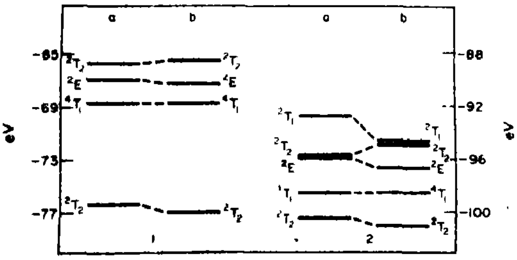

(b)

Fig. 2b. Electronic structure of positive vacancy in diamond: Clementi functions (a), before configuration interaction, (b), after configuration interaction 1. $P = -7.13$ eV, 2. $P = -16.42$ eV.

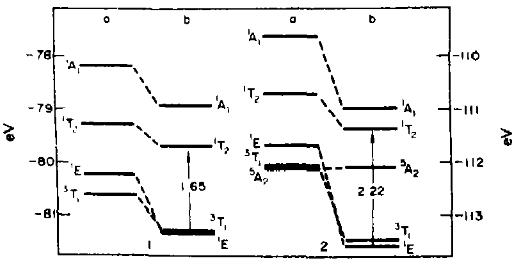

Fig. 3a. Electronic structure of neutral vacancy in diamond. Slater functions (a), before configuration interaction, (b), after configuration interaction 1. $P = -8.00$ eV, 2. $P = -16.42$ eV.

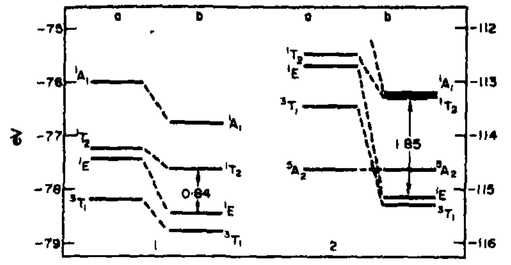

(b)

Fig. 3b. Electronic structure of neutral vacancy in diamond: Clementi functions (a). before configuration interaction, (b). after configuration interaction 1. $P = -7{\cdot}13$ eV, 2. $P = -16.42$ eV.

For the neutral vacancy, the calculation using Clementi-type functions predicts that in both limits the $^3T_1$ level is lowest, being 0·31 eV below the ^1E level in case 1 and 0·13 eV below this level in case 2. This is in contrast to the Slater calculation where the $^3T_1$ level is 0·04 and 0·09 eV above the ^1E level in case 1 and 2 respectively. The relative ordering of the other levels of interest is the same in both calculations. It is also interesting that for the unmodified case using Clementi-type functions with $Q = 17{\cdot}81$ eV the ^1E level is lowest 0·48 eV below the $^3T_1$ level and with a separation of 7·18 eV between the ^1E and $^1T_2$ levels. Hence the ordering of the $^3T_1$ and ^1E levels is sensitive to the choice of the value for Q. In the Slater case while there is not a change in order with decreasing Q values the energy difference between the ^1E and $^3T_1$ levels does also decrease. Formally, the energy difference between the $^3T_1$ and ^1E states arising from the configuration $a_1{}^2t_2{}^2$ before configuration interaction is $D - F$. Now, this difference has increased from 0·39 eV with Slater-type functions to 0·74 eV with Clementi-type functions. The interactions with states of the same symmetry from higher configurations are no longer sufficient to invert these two levels in the latter case.

The difference in energy between the lowest ^1E and $^1T_2$ states before configuration interaction is formally $F - D + 2J$. Using the values in Table 1 this difference has decreased from 0·96 eV (Slater) to 0·21 eV (Clementi) such that the final energy separations are 0·84 eV (case 1) and 1·85 eV (case 2) using Clementi-type functions, compared with 1·65 eV (case 1) and 2·22 eV (case 2) using Slater-type functions.

If the separations obtained using Clementi-type functions are reliable then the spin- and orbitally-allowed transition between the ^1E and $^1T_2$ levels would not be observable at room temperature. However, in view of the small energy differences between the lowest two levels, we cannot make any reliable prediction as to the ground state of this centre without further examination of some of the assumptions inherent in the model. These assumptions are considered more fully in the following sections.

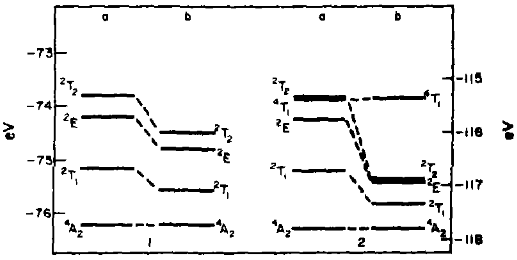

Fig. 4a. Electronic structure of single negative vacancy in diamond: Slater functions (a). before configuration interaction, (b). after configuration interaction 1. $P = -8{\cdot}00$ eV, 2. $P = -16{\cdot}42$ eV.

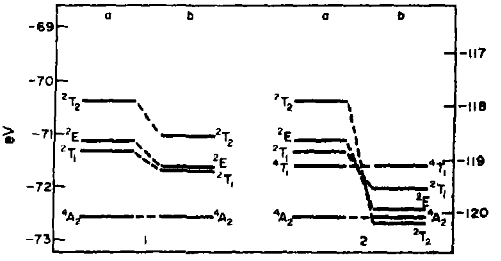

(b)

Fig. 4b. Electronic structure of single negative vacancy in diamond: Clementi functions (a). before configuration interaction, (b). after configuration interaction 1. $P = -7{\cdot}13$ eV, 2. $P = -16{\cdot}42$ eV.

For the V^- centre, both Slater- and Clementi-type functions give similar predictions for case 1; however, the energy levels from the latter study show a significant dependence on the value of P, as shown in Fig. 4. Using Slater-type functions the calculation predicts that the $^4A_2$ level is lowest with the $^2T_1$ level 0·67 eV (case 1) to 0·45 eV (case 2) above this ground state. The changes in the ordering of the energy levels for case 2 using Clementi-type functions are due largely to the increased configuration interaction with higher states. This arises because the modification in B, the one-electron molecular integral, between case 1 and 2 is 10·10 eV using Slater-type functions, whereas it is 12·25 eV in the Clementi study. As a consequence the higher states make a relatively larger contribution to the lowest levels in the latter case. Hence, for example, in case 2 the $^2T_2$ level is lowered 2·29 eV to become the lowest level, compared with 1·54 eV in the study using Slater-type functions. Whereas case 1 of the investigation with Clementi-type functions predicts that the $^4A_2$ level is lowest, 0·88 eV below the $^2T_1$ level with the ^2E level 0·08 eV above this level, the case 2 approximation predicts that the $^2T_2$ level is lowest, 0·12 eV below the $^4A_2$ level and 0·28 eV below the ^2E level. It is again necessary to investigate more closely some of the assumptions involved in the model before we can draw any conclusion from this particular study. In the next section we examine the effect of delocalisation of the electrons away from the vacancy, while in the following section we consider the response of the various energy levels to the symmetric displacements of the atoms nearest the defect.

4. DELOCALISATION OF THE ELECTRONIC CHARGE FROM THE VACANCY

One of the main assumptions of the defect-molecule method is that the vacancy electrons are located entirely within the defect and do not diffuse into the rest of the crystal. This approximation to the real situation would appear to be reasonable in most cases, as in few electron spin resonance studies on defect centres in irradiated diamonds has there been any appreciable hyperfine structure observed; however, the experiments by Baldwin[10], which still await confirmation, suggest that the delocalisation of the electronic charge from the vacancy in diamond may be of the order of 10 per cent. Therefore a more realistic initial wave function for the vacancy electron which may be used in the present calculation has the form

$$a' = \lambda a + \mu(p+q+r)$$

where a is the original tetrahedral hybrid orbital on atom A directed towards the centre of the vacancy and p, q and r represent tetrahedral hybrid orbitals on atoms P, Q and R, which are nearest neighbour atoms to atom A, directed along **PA**, **QA** and **RA** respectively. A similar kind of wave function has been used for a calculation on the methane molecule[11]. λ and μ are parameters which determine the extent of delocalisation. The relation between λ and μ is determined by the requirement that the delocalised wave function a' is normalized and that $\mu = 0$ when $\lambda = 1$. In a similar way the original tetrahedral hybrids b, c and d may be replaced by the delocalised functions b', c' and d'. We again neglect all exchange and polarisation effects with other bonded valence electrons in this initial study.

Estimates for the energy levels of the various centres may now be obtained by using these new functions to evaluate the integrals involved in the energy expressions. Expansion of these modified integrals containing the wave functions a', b', c' and d' yield formulae which may be expressed in terms of the atomic hybrid integrals multiplied by various powers of λ and μ. In all the expressions except those obtained by modifying the one-centre kinetic and potential energy integrals terms of order μ^2 and above were neglected. This is a reasonable approximation because μ is always small in the cases considered. To obtain values for the new integrals the basic one- and two-electron integrals must be evaluated at four internuclear distances. Namely, 2·918, 4·766, 5·586 and 7·343 a.u. Having evaluated the modified integrals it is fairly straightforward to determine the energy level scheme for various values of λ.

We have considered three cases with values of 0·95, 0·90 and 0·85 for λ. These correspond respectively to approximately 10, 19 and 28 per cent delocalisation of the wave function for the vacancy electron away from the defect. We have observed that as λ decreases the overlap term $\langle a'|b'\rangle$ first increases relative to the value for $\lambda = 1$ and reaches a maximum near $\lambda = 0{\cdot}95$. For values of $\lambda > 0{\cdot}80$ it is larger than the initial value. The additional term in the overlap expression arising from the interaction between the orbital '*a*' and the hybrids *p*′, *q*′, *r*′ on the nearest neighbours to atom *B* is sufficient, for small decreases in λ, to compensate for the diminished overlap contribution from within the vacancy. The current approach is considered to be adequate because we are primarily interested in the trends which result in the relative ordering of the energy levels with increased delocalisation. A more detailed account of these calculations is given elsewhere[12].

For the neutral vacancy we find in all cases no change in the ordering of the lowest levels with increasing delocalisation. Figure 5 shows the results for the case 1 studies. The ^1E level is initially lowered in energy relative to the $^3T_1$ level as λ decreases, but for values of λ less than 0·95 it increases again. For $\lambda = 0{\cdot}95$ the ^1E level is 0·16 eV below the $^3T_1$ level (Slater case 1), while for the study with Clementi-type functions it is within 0·12 eV of the $^3T_1$ ground state. Also the $^1E - {}^1T_2$ separation increases to a maximum near $\lambda = 0{\cdot}95$ then decreases again. For $\lambda = 0{\cdot}95$ these separations for the various cases are as follows:

Slater:	case 1, 2·41 eV; case 2, 2·90 eV
Clementi:	case 1, 1·85 eV; case 2, 2·80 eV.

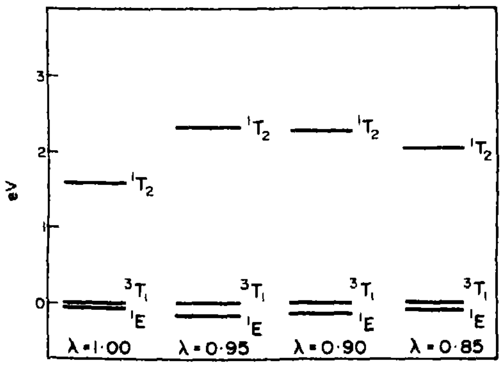

Fig. 5a. Electronic structure of neutral vacancy in diamond. Delocalisation study using Slater functions: Case 1.

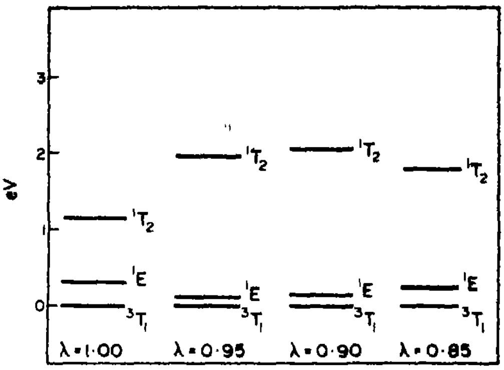

Fig. 5b. Electronic structure of neutral vacancy in diamond. Delocalisation study using Clementi functions: Case 1.

It is again possible to relate these changes to variations in the *D*, *F* and *J* integrals. In the Clementi study, for limited delocalisation the ^1E level is closer to the $^3T_1$ lowest level; therefore the probability of an observable $^1E \rightarrow {}^1T_2$ transition is enhanced.

In the V^- centre, the most important finding characteristic of all the studies is that the $^4A_2$ level is reinforced as the lowest in energy at least 0·5 eV below the next lowest level in every case where delocalisation is incorporated. The energy of the lowest ^2E and $^2T_2$ levels relative to the $^4A_2$ level increases as λ decreases, reaching a maximum near $\lambda = 0{\cdot}90$ approximately 1 to 2 eV above the ground state. The separation between the $^4A_2$ and $^2T_1$ levels is much less sensitive to the extent of delocalisation. The relative ordering of the lowest levels of the V^+ centre is not changed by delocalisation. In all cases the $^2T_2$ level is lowest in energy, at least 2 eV below the $^4T_1$ level.

5. COUPLING OF THE ELECTRONIC STATES TO THE SYMMETRIC MODE

The displacement of the four atoms nearest the vacancy may be described in terms of 12 normal co-ordinates[13]. Three of these co-ordinates represent translations and three rotations which are of no interest to us in this problem. The six remaining co-ordinates (Q_a, Q_ϵ, Q_θ, Q_ξ, Q_η, Q_ζ) are classified as follows. Q_a represents the symmetric mode of A_1 symmetry; Q_ϵ and Q_θ are modes of E symmetry, while the Q_ξ, Q_η and Q_ζ modes belong to the T_2 representation of the T_d group. All electronic states of the vacancy system may couple with the Q_a mode, whereas only degenerate states may interact with the E or T_2 modes of lower symmetry giving rise to the Jahn–Teller effect.

To first order it is assumed that there is no coupling between the various normal modes. We may therefore consider the interaction between the electronic states and the symmetric mode independently of the Jahn–Teller problem. We have assumed that the energy lowerings due to the symmetric relaxation are more important in determining the relative ordering of the lowest levels than the Jahn–Teller splittings, and concentrated on this effect. The Jahn–Teller problem is considered in the following paper[14].

The change in energy of a particular electronic state for a given distortion Q_a of the atoms nearest the vacancy, including only linear coupling terms, may be represented within the harmonic approximation as follows:

$$E(Q_a) = E_0 - F_aQ_a + \tfrac{1}{2}M\omega_a^2Q_a^2$$

where F_a is the constant applied symmetric force on the atoms neighbouring the defect which results in a distortion Q_a. E_0 is the energy of electronic state for zero distortion. The last term represents the change in total potential energy of the system for a distortion Q_a of the nearest neighbour atoms to the vacancy, M is the mass of the carbon atom and ω_a is the effective or response frequency of the lattice for the A_1 mode. A discussion of the limitations of using such an expression may be found elsewhere[13]. Now, the static equilibrium distortion is given by

$$\frac{\partial E}{\partial Q_a} = -F_a + M\omega_a^2Q_a = 0.$$

Therefore

$$Q_a = \frac{F_a}{M\omega_a^2}$$

and the corresponding relaxation energy is

$$\Delta E_a = E - E_0 = -\frac{F_a^2}{2M\omega_a^2}.$$

For a system of vacancy electrons in a molecular orbital represented by the configuration interaction wave function, $\Psi(R)$, the symmetric force term, F_a, may be defined as

$$F_a = -\left(\frac{\partial}{\partial Q_a}\langle\Psi(R)|H|\Psi(R)\rangle\right)_0$$

using the rigid atom model suggested by Lidiard and Stoneham[15]. This is not the definition used by Friedel *et al.*[16]. Terms involving the repulsion between the atoms neighbouring the vacancy are already implicitly included in the potential energy term when determining the effective frequency ω_a.

To determine the value of F_a, $\Psi(R)$ is expressed in terms of the wave functions, $\psi_j(R)$, for the various configurations with suitable coefficients c_j. That is,

$$\Psi(R) = \sum_j c_j\psi_j(R)$$

and

$$F_a = -\left(\frac{\partial}{\partial Q_a}\left(\sum_{ij} c_ic_j\langle\psi_i|H|\psi_j\rangle\right)\right)_0.$$

This expression reduces to a sum of terms involving the derivatives of the molecular integrals shown in Table 2, and additional terms involving the derivatives of the coefficients. These latter first-order terms make only a small contribution to F_a in most cases, but have been included in this investigation. The derivatives of the molecular integrals are expressed in terms of the derivatives of atomic-hybrid integrals which are then evaluated using the following numerical procedure. The integral whose derivative is required is evaluated at the internuclear distances r_0+h and r_0-h, where $r_0 = 2{\cdot}52$ Å and $h = 0{\cdot}10$ Å. Then the required derivative $f'(r)$ at r_0 is given by

$$f'(r_0) = \frac{df}{dr}\bigg/_{r=r_0} = \frac{f(r_0+h)-f(r_0-h)}{2h}.$$

This formula is equivalent to fitting a parabola through the points $f(r_0)$, $f(r_0+h)$ and $f(r_0-h)$ and determining the slope of the tangent to the curve at the point corresponding to $f(r_0)$. The values obtained for the derivatives of the molecular integrals for the two choices of atomic functions are given in Table 2. The different values obtained for the derivatives of the one-electron integrals in the case 1 and 2 approximations result from different factors multiplying the derivative of the overlap integral. Using this information F_a for each electronic level may be determined and then the corresponding values for Q_a and ΔE_a for a suitable choice of ω_a.

Table 2. Derivatives of the molecular integrals used in the calculation of the symmetric relaxation terms

$\frac{d}{dQ_a}$(Integral)	Slater function	Clementi function
$\langle v\|H^0\|v\rangle$	8·3089*‡ 7·0976†	7·9303* 6·9067†
$\langle x\|H^0\|x\rangle$	2·4168* 3·7150†	2·4466* 4·2166†
$\left\langle vv\left\|\frac{1}{r_{12}}\right\|vv\right\rangle$	−1·6522	−1·4866
$\left\langle xx\left\|\frac{1}{r_{12}}\right\|xx\right\rangle$	−0·9796	−1·0528
$\left\langle vx\left\|\frac{1}{r_{12}}\right\|vx\right\rangle$	−1·4949	−1·4189
$\left\langle xy\left\|\frac{1}{r_{12}}\right\|xy\right\rangle$	−0·3154	−0·0201
$\left\langle vz\left\|\frac{1}{r_{12}}\right\|zv\right\rangle$	−0·0558	−0·0710
$\left\langle xy\left\|\frac{1}{r_{12}}\right\|yx\right\rangle$	1·0355	1·1000
$\left\langle vx\left\|\frac{1}{r_{12}}\right\|vz\right\rangle$	−0·4866	−0·5072

*Case 1.
†Case 2.
‡All derivatives in eV/Å.

Recently,[13] a dynamic relaxation procedure has been used to determine the adiabatic linear response frequencies. These are the ones required in the calculation of first order static distortion terms. The magnitude of these frequencies was found to be much smaller than the Raman frequency (2·49 . 10^{14} rad/sec) and the linear response frequencies calculated previously[15, 16]. This latter calculation used a sudden approximation in which only the four nearest neighbours to the vacancy were allowed to move under the externally applied forces. The adiabatic symmetric mode frequency ω_a has a value 0·95 . 10^{14} rad/sec. With this frequency and the forces determined as above the first-order contribution to the symmetric relaxation energy is predicted to be large (2·4–6·7 eV)[13]. Non-linear terms must therefore be important. In order to avoid the more difficult calculation involving these terms which is unreliable with the wave function available it is possible to choose an effective linear response frequency ω_a' which will give reasonable distortions[13]. This approach is adequate since we are primarily interested in the sensitivity of the ordering of the lowest electronic levels to symmetric relaxation terms. In fact, our calculations show that the order of the lowest levels is not very sensitive to the value chosen for ω_a'. For convenience we choose $\omega_a' = 2{\cdot}02 \,.\, 10^{14}$ rad/sec, the value estimated by Lidiard and Stoneham [15] for the tetragonal response frequency using the sudden approximation. The magnitude of the energy and distortion terms using the adiabatic frequency may be readily obtained by multiplying the results given in Tables 3 and 4 by 4·52.

6. DISCUSSION OF RESULTS AND RELATION TO EXPERIMENT

The results obtained for the lowest levels of V^0 and V^- centres are given in Tables 3 and 4 respectively. For most levels the total energy change – electronic and elastic – for the system is 1 to 2 eV. The lowering in the energy of a particular electronic level will be twice this energy. Because the symmetric force term F_a is not constant for all the electronic levels of a particular centre it will be important to consider the symmetric relaxation when determining the relative ordering of these levels. This result also suggests that the calculation by Lannoo and Stoneham [17] on the Huang–Rhys factor and the band moments of the GR1 band in diamond is inadequate, since their work assumes that F_a is the same for the ^1E and $^1T_2$ electronic states of the neutral vacancy.

For all levels the symmetric relaxation of the atoms nearest the defect is predicted to be inwards towards the centre of the vacancy. This is an inevitable result, because the defect molecule approach assumes that the atoms neighbouring the vacancy remain sp^3-hybridised after removal of the vacancy atom. As a consequence of this assumption certain force terms are neglected. If the covalent bonds between nearest neighbour atoms in the perfect crystal were in 'tension' then on the breaking of a bond we should expect an atom to experience a net force and so be displaced from its previous equilibrium position. We believe, however, that this contribution to the force would be small because the C–C bond length in diamond is only 0·007 Å longer than the average single C–C bond length in saturated hydrocarbons [18]. The more important contribution to the force which has been neglected results from a possible change in hybridisation of the atom nearest the defect. For example, it is well known that while the methane molecule has a tetrahedral structure the methyl radical is planar. We should expect a similar effect for the atoms adjacent to the vacancy, resulting in a displacement of these atoms away from the centre of the vacancy. In the discussion which follows we denote this symmetric force by f_a. It follows that the resultant displacement of the atoms will depend upon the relative magnitudes of f_a and F_a. Unfortunately there appears to be no simple way of obtaining reliable values of f_a for the various electronic levels.

Table 3. Symmetric term for the $^3T_1$, $^1T_2$, ^1E and $^5A_2$ levels of the neutral vacancy

Function	F_a eV/Å	ΔE_a eV	Function	F_a eV/Å	ΔE_a eV
1. $^3T_1$ Level			3. $^1T_2$ Level		
Slater: case 1	−12·13	−1·45	Slater: case 1	−14·34	−2·03
Slater: case 2	−10·88	−1·17	Slater: case 2	−14·39	−2·04
Clementi: case 1	−12·17	−1·46	Clementi: case 1	−14·55	−2·09
Clementi: case 2	−11·97	−1·41	Clementi: case 2	−13·78	−1·87
2. ^1E Level			4. $^5A_2$ Level		
Slater: case 1	−11·01	−1·20	Slater: case 1	−7·19	−0·51
Slater: case 2	−10·95	−1·19	Slater: case 2	−9·87	−0·96
Clementi: case 1	−10·97	−1·14	Clementi: case 1	−7·87	−0·61
Clementi: case 2	−12·13	−1·45	Clementi: case 2	−12·15	−1·46

Values of Q_a may be obtained from the relationship. $Q_a = 2\Delta E_a/F_a$.

In the extreme case given by the defect-molecule approach f_a will be zero. If the electronic energy levels for the neutral vacancy are corrected for symmetric relaxation effects using the results in Table 3 then in case 1 using Slater functions and both cases with Clementi functions the $^3T_1$ level is predicted to be the ground state of the system. Alternatively, if we assume f_a is constant for all electronic levels of a particular charge state of the vacancy then it is possible in a qualitative way to examine further the changes in the ordering of the energy levels. For all values of F_a greater than f_a the investigation using Clementi-type functions predicts that the $^3T_1$ level is the ground state for the neutral vacancy. In the Slater study it is not possible to decide whether the $^3T_1$ or ^1E level will be lowest in energy for the general case. Also since F_a for the $^1T_2$ level is larger than the corresponding force for the ^1E level the separation between these two levels will decrease as Q_a becomes more negative (larger inward displacement). Under these conditions there is unlikely to be a $^1E \rightarrow {}^1T_2$ transition which could be associated with the GR1 band observed in irradiated diamonds. For f_a greater than F_a, but again equal for all levels, Q_a will be positive. Now, the ^1E level will be lowered in energy more than the $^3T_1$ or $^1T_2$ levels for a given value of Q_a, such that it could be predicted as the ground-state even in the studies with Clementi-type functions. Since the separation between the ^1E and $^1T_2$ levels would also be increased it is possible that the predicted energy for the $^1E \rightarrow {}^1T_2$ transition in the Clementi case would correspond to that observed for the GR1 band (1·65–2·4 eV). However, it seems likely that the Slater studies would then predict somewhat higher values for this transition.

Unfortunately, the experimental information available is too limited to provide a definite answer. The preliminary work by Baldwin [10], believed to be on the V^+ centre, does suggest that the hyperfine interaction data is consistent with the atoms nearest the defect being relaxed away from the centre of the vacancy; however, this work must be confirmed before we can have confidence in these findings. The interpretation of the stress splitting data on the GR1 band also seems more consistent with relaxation of atoms away from the centre of the vacancy [17].

For the negatively charged vacancy the same difficulty arises. If the electronic energy levels shown in Fig. 4 are modified for the equilibrium symmetric relaxations given in Table 4 (i.e. by $-F_aQ_a$), then in the cases using Slater-type functions the $^4A_2$ level remains lowest in energy, 0·31 eV below the ^2E

Table 4. Symmetric term for the $^2T_2$, $^2T_1$, ^2E and $^4A_2$ levels of the negatively charged vacancy

Function	F_a eV/Å	ΔE_a eV	Function	F_a eV/Å	ΔE_a eV
1. $^2T_2$ Level			3. ^2E level		
Slater: case 1	−11·43	−1·29	Slater: case 1	−12·00	−1·42
Slater: case 2	−12·48	−1·53	Slater: case 2	−11·29	−1·26
Clementi: case 1	−11·98	−1·42	Clementi: case 1	−12·88	−1·64
Clementi: case 2	−15·04	−2·23	Clementi: case 2	−13·54	−1·81
2. $^2T_1$ Level			4. $^4A_2$ Level		
Slater: case 1	−9·32	−0·86	Slater: case 1	−9·36	−0·86
Slater: case 2	−10·63	−1·11	Slater: case 2	−10·83	−1·16
Clementi: case 1	−9·76	−0·93	Clementi: case 1	−10·05	−1·00
Clementi: case 2	−12·84	−1·63	Clementi: case 2	−13·32	−1·74

Values of Q_a may be obtained from the relationship, $Q_a = 2\Delta E_a/F_a$.

level (case 1) and 0·14 eV below the $^2T_2$ level (case 2). When the Clementi results are modified the ^2E level is lowest in energy in the case 1 study, 0·32 eV below the $^4A_2$ level with $^2E-{}^2T_2$ and $^2E-{}^2T_1$ separations of 1·00 and 1·34 eV respectively; however, for case 2, the $^2T_2$ level remains lowest with the $^4A_2$, ^2E and $^2T_1$ levels 1·10, 1·12 and 1·84 eV respectively above this level. For smaller negative values of Q_a it is possible that all studies would predict either a ^2E or $^2T_2$ ground state for the system. However, if we consider the cases where $f_a > F_a$ (Q_a positive) then all studies would probably favour a $^4A_2$ ground state. It is unlikely that the GR1 band could be associated with an electronic transition involving the electrons of the negative vacancy system; however, in view of further inadequacies in the model when applied to charge states this possibility cannot be definitely eliminated. For the negative vacancy interlevel coupling effects may also be important[19].

7. CONCLUSION

With an undistorted model for the vacancy system the calculations demonstrate that the predicted electronic structure for the V^0 and V^- system depends upon the choice of functions which represent the s and p orbitals on the atoms nearest the defect. The most significant result is that the order of the lowest $^3T_1$ and ^1E levels of the neutral vacancy system are inverted when Clementi-type functions are used rather than Slater-type functions. A simple model shows that for limited delocalisation the ^1E level of V^0 is lowered more in energy than the $^3T_1$ level, but not enough to cause inversion of these two levels. The relative order of these two levels also depends upon the value chosen for the one-centre Coulomb integral. It has been demonstrated that the symmetric forces estimated within the framework of the harmonic model using a rigid-atom approximation are different for the various electronic states of a particular centre. In order to determine the relative order of the lowest levels it is therefore necessary to include this symmetric relaxation energy contribution. For a negative value of Q_a (relaxation inwards) the $^3T_1$ level is predicted as the most probable ground state of the neutral vacancy, whereas for Q_a positive the ^1E level is the most probable ground state with an allowed transition to a $^1T_2$ level which may be related to the GR1 band observed in irradiated diamonds.

The calculations for the V^+ centre do suggest that the $^2T_2$ electronic state is most likely to be the ground state of this system. Although we are unable to calculate the relative stabilities of the various charge states of the vacancy in any precise manner, the findings of this work do demonstrate that the V^+ centre will not necessarily be less stable than the V^0 or V^- centres. The ordering of the lowest levels in the V^- centre are also sensitive to the extent of symmetric relaxation. A more detailed study which allows for flexible hybrid orbitals on the atoms nearest the defect and includes relaxation as an integral part of the problem may be necessary to resolve some of these uncertainties.

Acknowledgements – We have had several helpful discussions with Drs A. B. Lidiard and A. M. Stoneham throughout the course of this work. Some of the calculations reported here were made using facilities generously provided by the Atomic Energy Research Establishment, Harwell. One of us (F.P.L.) would like to thank the Rhodes Trustees for the award of the Rhodes Scholarship for Victoria and Wadham College, Oxford, for a Senior Scholarship

REFERENCES

1. COULSON C. A. and KEARSLEY M. J., *Proc. R. Soc.* **241A**, 433 (1957).
2. YAMAGUCHI T., *J. phys. Soc. Japan* **17**, 1359 (1962).
3. COULSON C. A. and LARKINS F. P., *J. Phys. Chem. Solids* **30**, 1963 (1969).
4. CLEMENTI E., *Suppl. IBM J. Res. Dev.* **9**, 2, Table 1-03 (1965).
5. GOEPPERT-MAYER M. and SKLAR A. L., *J. chem. Phys.* **6**, 645 (1938).
6. CORBATO F. J. and SWITENDICK A. C., *Methods of Computational Physics* (Edited by Alder, Fernbach and Rotemberg), Vol. 2, Academic Press, New York (1963).
7. HOPGOOD F. R. A., *Midiat on Atlas*, Atlas Computing Laboratory publication (August 1966).

8. MULLIKEN R. S., *J. Chim. Phys.* **46**, 500 (1949).
9. OWEN J., in *Physical Properties of Diamond* (Edited by R. Berman), p. 274, O.U.P., London (1965).
10. BALDWIN J. A., *Phys. Rev. Lett.* **10**, 220 (1963).
11. COULSON C. A., *Trans. Faraday Soc.* **33**, 388 (1937).
12. LARKINS F. P., *D. Phil. Thesis*, Oxford (1969).
13. LARKINS F. P. and STONEHAM A. M., *J. Physics C* (to be published).
14. LARKINS F. P., *J. Phys. Chem. Solids* (1971).
15. LIDIARD A. B. and STONEHAM A. M., *Science and Technology of Industrial Diamonds* **1**, 1. Industrial Diamond Information Bureau, London (1967).
16. FRIEDEL J., LANNOO M. and LEMAN G., *Phys. Rev.* **164**, 1056 (1967).
17. LANNOO M. and STONEHAM A. M., *J. Phys. Chem. Solids* **29**, 1987 (1968).
18. SUTTON L. E., *Interatomic Distances* (Ed.) Suppl. Chem. Soc. Special Publication No. 18 (1965).
19. STONEHAM A. M. and LANNOO M., *J. Phys. Chem. Solids* **30**, 1769 (1969).

J. Phys. Chem. Solids Pergamon Press 1971. Vol. 32, pp. 2259–2262. Printed in Great Britain.

TECHNICAL NOTES

Estimation of bonding parameters and overlap integrals in octahedral iron group complexes from magnetic susceptibility and anisotropy data

(*Received* 26 *August* 1970; *in revised form* 14 *January* 1971)

INTERPRETATION of the magnetic behaviours of the iron group complexes in terms of anisotropic ligand field theory follows a procedure in which consistent values of certain parameters are evaluated from the magnetic anisotropy and susceptibility data at different temperatures. Comparison of the theoretical expressions of magnetic susceptibility and anisotropy with the experimental results furnishes, in particular, valuable information regarding the covalency parameters. It is generally found that in all complexes of the iron group the orbital moment and S.O. coupling constant are reduced from their respective free ion values due to the covalency effect. The covalency parameters referred to above are the reduction factors for the orbital moment and S.O. coupling constant and these will be explicitly defined in course of the discussion that follows. The reduction factors can be expressed in terms of bonding parameters and some overlap integrals. These expressions along with the knowledge of the above two reduction factors obtained from magnetic data enable one to estimate the bonding parameters and overlap integrals.

The molecular orbitals in an octahedral complex are quoted elsewhere. Tinkham's work[1] may be referred for the purpose. We do not reproduce them again but simply note that for antibonding molecular orbitals which describe the motion of magentic electrons in the complex the bonding parameters η_π and η_σ of Tinkham's expressions should be conveniently replaced by $-\eta_\pi$ and $-\eta_\sigma$, where η_π and η_σ are now implied to be positive. The orbital reduction factors are given by,

$$k_i(\pi\pi) = \frac{\langle\phi_m(t_{2g})|l_i|\phi_n(t_{2g})\rangle}{\langle\psi_m(t_{2g})|l_i|\psi_n(t_{2g})\rangle} \qquad (1)$$

$$k_i(\pi\sigma) = \frac{\langle\phi_m(t_{2g})|l_i|\phi_n(e_g)\rangle}{\langle\psi_m(t_{2g})|l_i|\psi_n(e_v)\rangle} \qquad (2)$$

where $i = x, y, z$, ϕ_j is the molecular orbital corresponding to the atomic $3d$ orbital ψ_j. In case of pure O_h symmetry, $k_x = k_y = k_z = k$(say), and following Stevens[2] and Tinkham[1] we have

$$k(\pi\pi) = 1-\tfrac{1}{2}\eta_\pi{}^2N_\pi{}^2 \qquad (3)$$

$$k(\pi\sigma) = N_\pi N_\sigma\Big[1-2(\eta_\pi s_\pi+\eta_\sigma s_\sigma) - \tfrac{1}{2}\eta_\pi\eta_{p_\sigma} - \tfrac{1}{2}\eta_\pi\eta_s a\Big\langle p_z\Big|\frac{\partial}{\partial z}\Big|s\Big\rangle\Big] \qquad (4)$$

where,

$$N_\sigma{}^{-2} = 1-4\eta_\sigma S_\sigma+\eta_\sigma{}^2 \qquad (5)$$

$$N_\pi{}^{-2} = 1-4\eta_\pi S_\pi+\eta_\pi{}^2 \qquad (6)$$

and the parameters η_π, η_σ, η_{p_σ}, η_s and overlap integrals S_σ, S_π have been defined by Tinkham[1].

The reduction factor for the spin orbit coupling constant is given by expressions analogous to (1) and (2) with the simple change that l_i should be replaced by $\zeta(f)\cdot l_i$ where $\zeta(f)$ is the S.O. coupling constant for the free ion. Following Tinkham[1] these reduction factors denoted by the symbol R, are given by

$$R(\pi\pi) = N_{\pi}^{2} \tag{7}$$

$$R(\pi\sigma) = N_{\pi}N_{\sigma}. \tag{8}$$

Armed with the expressions for k's and R's we set out to evaluate the bonding parameters η's and overlap integrals S's in the octahedral iron group complexes. Often reduction factors k's and R's are assumed to partake of the symmetry of the complex which is usually considered to be a distorted octahedron. The distortion being small we shall make an approximation by taking the mean values of k's and R's and use these mean values in the expressions (3), (4), (7), (8) for the octahedral case.

(a) [Ti^{3+}, $6H_2O$]: Magnetic measurements on susceptibility at different temperatures give the following parameters in the case of $TiCs(SO_4)_2 . 12H_2O$ alum[3]:

$k_{\parallel}(\pi\pi) = 0{\cdot}80$ $\quad$ $k_{\perp}(\pi\pi) = 0{\cdot}58$

$\zeta_{\parallel} = 142{\cdot}6\ \text{cm}^{-1}$ $\quad$ $\zeta_{\perp} = 151{\cdot}4\ \text{cm}^{-1}$

Henceforth we shall omit the index $(\pi\pi)$ unless it is necessary to avoid confusion. The average value of $k = \frac{1}{3}(k_z + k_x + k_y) = \frac{1}{3}(k_{\parallel} + 2k_{\perp}) = 0{\cdot}65$; and average $\zeta = \frac{1}{3}(\zeta_{\parallel} + 2\zeta_{\perp}) = 148{\cdot}5\ \text{cm}^{-1}$. $\zeta(f)$ (free ion) being $154\ \text{cm}^{-1}$, $R(\pi\pi) = 148{\cdot}5/154{\cdot}0 = 0{\cdot}96$.

With these values of k and R, equations (3), (6) and (7) give $\eta_{\pi} = 0{\cdot}85$, $S_{\pi} = 0{\cdot}20$.

(b) [V^{3+}, $6H_2O$]: Bose *et al.*[4] obtained the following parameters from magnetic data in the case of $V(NH_4)(SO_4)_2 . 12H_2O$ alum:

$\alpha_{\parallel}k_{\parallel} = 0{\cdot}99$ $\quad$ $\alpha_{\perp}k_{\perp} = 0{\cdot}945$

$\alpha_{\parallel}\zeta_{\parallel} = 66\ \text{cm}^{-1}$ $\quad$ $\alpha_{\perp}\zeta_{\perp} = 87{\cdot}75\ \text{cm}^{-1}$

where $\alpha_{\parallel}$ and $\alpha_{\perp}$ are the effective orbital Lande factors introduced by Abragam & Pryce[5], and for pure O_h case $\alpha_{\parallel} = \alpha_{\perp} = \alpha = \frac{3}{2}$. On the assumption of O_h approximation taking average values

$$\alpha k = \tfrac{1}{3}(\alpha_{\parallel}k_{\parallel} + 2\alpha_{\perp}k_{\perp}) = 0{\cdot}96$$

Hence $k = \frac{2}{3}(0{\cdot}96) = 0{\cdot}64$.

Similarly, mean $\zeta = 53{\cdot}67\ \text{cm}^{-1}$. $\zeta(f)$ being $102\ \text{cm}^{-1}$ $R = 53{\cdot}67/102 = 0{\cdot}53$.

With these values of k and R we get as before,

$$\eta_{\pi} = 1{\cdot}16, \qquad S_{\pi} = 0{\cdot}10.$$

(c) [Fe^{2+}, $6H_2O$]: Study of magnetic properties of $Fe(NH_4)_2(SO_4)_2 . 6H_2O$ by Mrs. D. Pal in our laboratory (Unpublished) gives the following values of reduction factors

$k_{\parallel} = 0{\cdot}90$ $\quad$ $k_{\perp} = 0{\cdot}80$

$R_{\parallel} = 0{\cdot}85$ $\quad$ $R_{\perp} = 0{\cdot}78$.

We proceed in the same way as in the case of Ti^{3+} and get the following results:

Average $k = 0{\cdot}83$, average $R = 0{\cdot}80$, $\eta_{\pi} = 0{\cdot}65$ and $S_{\pi} = 0{\cdot}065$

(d) [Co^{2+}, $6H_2O$]: The following values of the parameters have been obtained from magnetic data in the case of $Co(NH_4)_2(SO_4)_2 . 6H_2O$[6].

$\alpha_{\parallel}k_{\parallel} = 1{\cdot}20$ $\quad$ $\alpha_{\perp}k_{\perp} = 1{\cdot}096$

$\alpha_{\parallel}\zeta_{\parallel} = -194{\cdot}4\ \text{cm}^{-1}$ $\quad$ $\alpha_{\perp}\zeta_{\perp} = -230{\cdot}0\ \text{cm}^{-1}$

$$[\zeta(f) = -180\ \text{cm}^{-1}].$$

Assuming O_h approximation and proceeding as in the case of V^{3+}, we get the following results

Mean $k = 0{\cdot}75$, mean $R = 0{\cdot}81$

$\eta_{\pi} = 0{\cdot}78$ and $S_{\pi} = 0{\cdot}12$.

(e) [Ni^{2+}, $6H_2O$]: Magnetic measurements of Bhattacharya and Majumdar[7] on $NiSiF_6$, $6H_2O$ give the following values of the reduction factors:

$k_{\parallel} = 0{\cdot}786$ $\quad$ $k_{\perp} = 0{\cdot}825$

$R_{\parallel} = 0{\cdot}910$ $\quad$ $R_{\perp} = 0{\cdot}955$.

Taking mean values, $k = 0\cdot 81$, $R = 0\cdot 94$. In this case the reduction factors which are obtained from the magnetic data are $k(\pi\sigma)$, $R(\pi\sigma)$ and not $k(\pi\pi)$, $R(\pi\pi)$. Further when both σ and π parameters are involved in the expressions for the reduction factors (vide equations (4) and (8)) we neglect the weaker π-bonding in comparison with the usually stronger σ-bonding. Thus neglecting π-bonding

$$k = N_\sigma(1 - 2\eta_\sigma S_\sigma), \qquad R = N_\sigma.$$

Putting the mean values of k and R, we get, $\eta_\sigma = 0\cdot 64$, $S_\sigma = 0\cdot 11$

(f) [Cu^{2+}, $6H_2O$]: From the magnetic anisotropy data of Bose *et al.*[8] and the results of mean susceptibility at different temperatures measured accurately in our laboratory on $CuK_2(SO_4)_2 . 6H_2O$, we have evaluated the covalency reduction factors. These reduction factors have been evaluated by fitting the theoretically calculated values with the experimental results as close as possible, and the closest fit is shown in Table 1. The theoretical expressions for the gramme-ionic susceptibilties are

$$K_\parallel = \frac{N\beta^2}{4KT} g_\parallel^2 + 8N\beta^2 \frac{k_\parallel^2}{E(B_{2g}) - E(B_{1g})}$$

$$K_\perp = \frac{N\beta^2}{4KT} g_\perp^2 + 2N\beta^2 \frac{k_\perp^2}{E(E_g) - E(B_{1g})}$$

where K = Boltzmann constant.

$$g_\parallel = 2\left[1 - \frac{4R_\parallel k_\parallel \zeta(f)}{E(B_{2g}) - E(B_{1g})}\right]$$

$$g_\perp = 2\left[1 - \frac{R_\perp k_\perp \zeta(f)}{E(E_g) - E(B_{1g})}\right]$$

and the other symbols have their usual significance. Optical absorption experiment of Mukherjee and Chhonkar[9] on undiluted crystals of $Cu\,K_2\,(SO_4)_2 . 6H_2O$ shows only one broad band at 12400 cm^{-1} without any clear fine structure. Further works[10] on aqueous solution and diluted crystals indicate that the separation between the fine structure components should be only a few hundred cm^{-1}, and hence in Table 1 we approximately put $[E(B_{2g}) - E(B_{1g})] \approx [E(E_g) - E(B_{1g})] \approx 12400\ cm^{-1}$. Table 1 gives the following values of the reduction factors.

Table 1. $k_\parallel = 0\cdot 80$, $k_\perp = 0\cdot 60$, $R_\parallel = 0\cdot 96$, $R_\perp = 0\cdot 75$, $\zeta(f) = -828\ cm^{-1}$ $[E(B_{2g}) - E(B_{1g})] \approx [E(E_g) - E(B_{1g})] \approx 12400\ cm^{-1}$ $g_\parallel = 2\cdot 41 (2\cdot 43)$ [12], $g_\perp = 2\cdot 06 (2\cdot 05)$ [12]

Temperature °K	Anisotropy $(K_\parallel - K_\perp) \times 10^6$		Mean susceptibility $\bar{K} \times 10^6$	
300	581	(572)	1536	(1551)
250	679	(677)	1833	(1845)
200	830	(830)	2282	(2301)
150	1070	(1087)	3026	(3045)
100	1559	(1573)	4516	(4497)

Experimental values are indicated within parentheses.

$$k_\parallel = 0\cdot 80 \qquad k_\perp = 0\cdot 60$$

$$R_\parallel = 0\cdot 96 \qquad R_\perp = 0\cdot 75.$$

Taking mean values, $k = 0\cdot 67$, $R = 0\cdot 82$. As in the case of Ni^{2+}, reduction factors of interest are $k(\pi\sigma)$, $R(\pi\sigma)$ and neglecting π-bonding we finally get $\eta_\sigma = 0\cdot 75$ and $S_\sigma = 0\cdot 12$.

The only unsatisfactory value of bonding parameter occurs in the case of $V(NH_4)(SO_4)_2 . 12H_2O$. The bonding parameter η_π is found to be greater than unity indicating that orbitals of the magnetic electrons are more of ligand type. Probably the error lies in the magnetic data themselves or in the evaluation of the reduction factors from these data. Further, in the case of $Cu\,K_2\,(SO_4)_2 . 6H_2O$ magnetic data indicate considerable anisotropy in the covalency reduction factors and neglect of π-bonding renders them isotropic even under D_{4h} symmetry[11].

Thus, it is probably an over simplification of the state of affairs, when we assume a pure O_h approximation and neglect π-bonding in this particular case.

It is to be noted that magnetic anisotropy and susceptibility experiments at different temperatures furnish enough data for accurate evaluation of the covalency reduction factors and e.p.r. g-values, where available, not only provide an additional check on these parameters but also greatly facilitate their determination. These parameters, in turn, give useful information regarding the degree of covalency and overlap integrals as has been demonstrated above. The mean susceptibility data alone may, of course, be utilized to evaluate the covalency reduction factors. Indeed this has been done in the case of Titanium and Vanadium alums as magnetic anisotropy cannot be measured in the case of cubic crystals. However, use of the additional magnetic data on anisotropy, if it can be measured, enables one to evaluate more accurately and reliably all the ligand field parameters including the reduction factors because magnetic anisotropy is much more sensitive than mean susceptibility to these parameters[13]. Moreover, the accuracy of magnetic anisotropy experiments is higher than that of mean susceptibility; and when the results of these two measurements are combined with e.p.r. data, if available, it would considerably reduce the confidence limits on the parameters that are determined in the ligand field treatment of magnetic behaviours. However, even in absence of e.p.r. results, it is possible to evaluate these parameters from a careful analysis of susceptibility and anisotropy data.

The importance of magnetic susceptibility and anisotropy measurements in providing a simple but efficient method to determine not only the degree of covalency but also overlap integrals in octahedral iron group complexes is obvious from the above discussion.

Acknowledgement – The authors express their sincere thanks to Professor A. Bose, D.Sc, F.N.I., for valuable criticism of the work.

Magnetism Department,
Indian Association for the Cultivation of Science,
Calcutta – 32.
India

C. BASU
U. S. GHOSH

REFERENCES

1. TINKHAM M., *Proc. R. Soc.* **A236**, 549 (1956).
2. STEVENS K. W. H., *Proc. R. Soc.* **A219**, 542 (1953).
3. BOSE A., CHAKRAVARTY A. S. and CHATTERJEE R., *Proc. R. Soc.* **A255**, 145 (1960).
4. BOSE A., CHATTERJEE R. and RAI R., *Proc. Phys. Soc.* **83**, 959 (1964).
5. ABRAGAM A. and PRYCE M. H. L., *Proc. R. Soc.* **A205**, 135 (1951).
6. GHOSH D., *D. Phil. Thesis*, Calcutta University (1969).
7. BHATTACHARYA B. D. and MAJUMDAR M., *Ind. J. Phys.* **40**, 549 (1966).
8. BOSE A., MITRA S. C and DUTTA S. K., *Proc. R. Soc.* **A239**, 165 (1957).
9. MOOKHERJI A. and CHHONKAR N. S., *Ind. J. Phys.* **33**, 74 (1959).
10. MATHUR S. C. and SURI P. R., *J. Phys. Chem. Solids* **29**, 2068 (1968).
11. MAJUMDAR D. and GHOSH U.S., *Ind. J. Phys.*, in press.
12. BLEANEY B., PENROSE R. P. and PLUMPTON BETTY I., *Proc. R. Soc.* **A198**, 406 (1949).
13. GREGSON A. K. and MITRA S., *Chem. Phys. Lett.* **3**, 528 (1969).

J. Phys. Chem. Solids Vol. 32, pp. 2262–2265.

Harmonic mixing and energy relaxation of warm electrons in n-GaAs at low temperatures

(*Received* 8 *September* 1970; *in revised form* 1 *November* 1970)

1. INTRODUCTION

THE ENERGY relaxation time τ_ϵ of elemental semiconductors like Ge, Si and Te has been studied in considerable detail[1–6]. A number of papers have also been devoted to the non-ohmic transport and energy loss processes in III–IV compounds like InSb[7–11], InAs[12] and GaAs[13, 14], at liquid helium temperatures where energy dissipation by acoustic phonon scattering via the deformation potential and the piezoelectric potential are the dominant mechanisms. It is the purpose of the present paper to report measurements of the microwave harmonic mixing d.c. signal of n-type GaAs in the temperature range between 30 and 80°K where polar optical scattering is expected to be the predominant energy loss process[13]. Warm electron energy relaxation times τ_ϵ are deduced from these data and compared with calculated values including polar optical, piezoelectric and deformation potential scattering. A comment in a recent paper of Krishnamurthy *et al.*[15] on a previous publication dealing with the energy relaxation in p-Te[5] is shown to be not correct.

2. EXPERIMENTAL

The experimental setup to determine the energy relaxation time from the phase dependent harmonic mixing signal has been described extensively in Refs.[4] and[5]. The 1kHz modulated fundamental wave $E_1 \cos(\omega t + \varphi)$ at 9·375 GHz is fed via a phase shifter into one of the arms of a single-ridged double-Tee junction, the second harmonic $E_2 \cos(2\omega t)$ at 18·75 GHz to the other arm. Both waves are mixed in the GaAs – sample and produce a 1 kHz modulated d.c. signal, which is picked up by a resonance amplifier. The average X-band microwave field strength at the position of the sample was varied in the range between 2 and 20 V/cm, the average K-band microwave field strength was approximately 2V/cm. The ridged waveguide with the sample mounted between the broad walls was inserted into a liquid helium cryostat to obtain temperatures between 4·2 and 300°K. The temperature increase of the sample and the surrounding waveguide from 20 to 80°K took a time of about two hours and therefore allowed reasonably accurate measurements at different temperatures. A reference sample in the waveguide system was held at room temperature and permitted a continuous observation of the phase differences between the incident fundamental wave and the second harmonic wave. A detailed description of the experimental procedure including the calibration of the system was given in Ref.[5]. In the case of the present measurements with GaAs a calibration of the waveguide system with samples of other materials with known energy relaxation times was not necessary since the contribution of the energy relaxation to the phase shift in n-GaAs was negligible at temperatures higher than 80°K. Above this temperature the position of the phase shifter where the mixing signal vanished, remained constant with increasing temperature. All values of the phase difference due to the energy relaxation between 30 and 80°K were based on this constant phase above 80°K.

The unoriented samples were cut from bulk single crystal n-type GaAs with a Hall mobility of 3600 cm^2/Vs at 77°K which increased to 6200 cm^2/Vs at 30°K. The carrier concentration was 5×10^{14} cm^{-3} at 77°K and remained constant down to 20°K. Indium contacts were alloyed to the samples.

3. RESULTS

Measured values of the relative phase shift ψ between fundamental and second harmonic wave due to the energy relaxation are plotted vs. temperature in Fig. 1. The phase shift has a constant value of 45° below 30°K and decreases with increasing temperature to a constant value of 0° at approximately 80°K. The relation between ψ and the energy

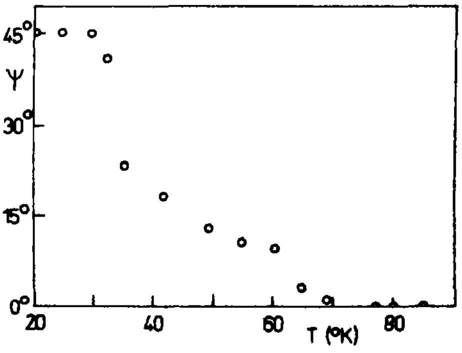

Fig. 1. Relative phase shift ψ vs. temperature.

relaxation time τ_ϵ is given by[16]

$$\tan 2\psi = \frac{2y^3+6y^3x^2-4y^3x^4-y^2x-9y^2x^3-2yx^4-2x^3}{1+3y^2+2y^3x+10y^3x^3+9y^2x^2-2y^2x^4+3yx^3+yx+3x^2} \qquad (1)$$

where $x = \omega\tau_m$, $y = \omega\tau_\epsilon$, τ_m being the momentum relaxation time and $\omega = 5{\cdot}9\times 10^{10}$ rad/s the frequency of the fundamental wave. In the limit of $x = 0$ this equation reduces to equation (2) of Ref.[4]. From equation (1) and values of τ_m calculated from the mobility μ and the relation $\tau_m = \mu m^*/e$, data of τ_ϵ were obtained which are plotted vs. temperature in Fig. 2 (open circles).

4. DISCUSSION

The product $\omega\tau_m$ which enters equation (1) in our case has its maximum value of $1{\cdot}35\times 10^{-2}$ at 30°K. With this value of $x = \omega\tau$ the quantity ψ is smaller by 0·5° than for $x = 0$. This difference is smaller than the accuracy of measurement which is ±1°. Therefore momentum relaxation can be neglected. According to a theory by Paranjape[17] the average rate of energy loss was calculated for the case of polar optical scattering in the approximation $T_e - T \ll T$, T_e being the electron temperature, and T the lattice temperature, respectively. The velocity distribution of the carriers is assumed to be the Maxwell–Boltzmann one at T_e which is only a rough approximation in the warm carrier range. This leads to the expression

$$\tau_\epsilon = \frac{3}{2\sqrt{2}\,eE_0}(\pi m^* k_B T)^{1/2}(T/\theta)^2 \frac{\exp(\theta/T)-1}{\exp(\theta/2T)\,K_0(\theta/2T)} \qquad (2)$$

where $E_0 = 5950$ V/cm is the coupling field, $m^* = 0{\cdot}064\, m_0$ is the effective mass and $\theta = 418$°K is the Debye temperature of n-type GaAs[18]. k_B denotes Boltzmann's constant and K_0 a modified Bessel function. The result of the calculation is plotted in Fig. 2 (curve a).

For comparison, the temperature dependences of the energy relaxation times due to energy loss via piezoelectric and deformation potential scattering are included in Fig. 2. The theoretical expressions for τ_ϵ in these cases were first derived by Kogan[19]. Curve b of Fig. 2 is calculated for piezoelectric energy loss with a coupling parameter $e_{14}^2 = 1\times 10^{10}$ dyn/cm². This value is obtained from the elastic and dielectric constants of GaAs tabulated by Willardson and Beer[20]. Curve c of Fig. 2 is computed for deformation potential scattering with[21] $E_1 = 7$ eV. Obviously the energy loss is dominated by

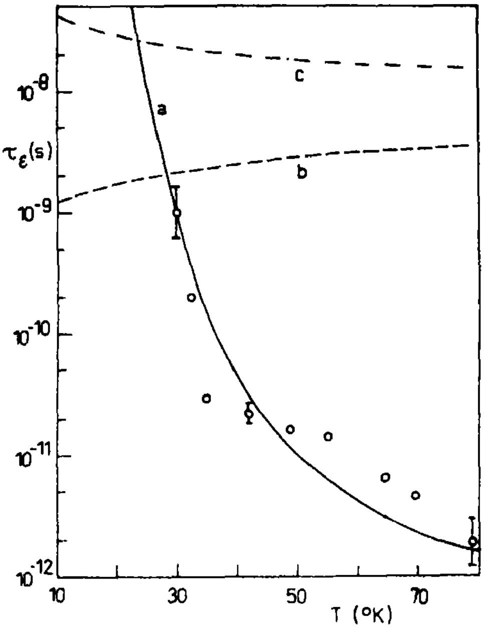

Fig. 2. Energy-relaxation time of n-type GaAs vs. temperature: (o) Experimental values. (a) Theoretical curve for polar optical scattering. (b) Theoretical curve for piezoelectric scattering. (c) Theoretical curve for deformation potential scattering.

polar optical scattering alone and there is good agreement between experiment and theory in the temperature range investigated.

APPENDIX

In a recent paper of Krishnamurthy *et al.*[15] it was pointed out that τ_m would affect the conclusions of our work on energy relaxation in *p*-Tellurium[5]. Despite the fact that equation (12) of Ref. [15] is not correct[16], the value of $\omega\tau_m$ was $1{\cdot}3 \times 10^{-2}$ at 150°K corresponding to a mobility of 2560 cm²/Vs at this temperature, and an effective mass $m^* = 0{\cdot}15\, m_0$. The influence of $\omega\tau_m$ calculated with equation (1) yields a contribution to $\tan 2\psi$ of 4 per cent or 0·05° in ψ, which is well below the accuracy of measurement. Thus our conclusions on energy relaxation in *p*-Te are not influenced by momentum relaxation.

Acknowledgements—Thanks are due to Professor K. Seeger for suggesting this work and for many helpful discussions. We are indebted to Dr. F. Seifert for kindly supplying the crystal.

REFERENCES

1. GIBSON A. E., GRANVILLE J. W. and PAIGE E. G. S, *J. Phys. Chem. Solids* **19**, 198 (1961).
2. MORGAN T. N. and KELLY C. E., *Phys. Rev.* **137**, A 1573 (1965).
3. SEEGER K., *Z. Phys.* **172**, 68 (1963).
4. HESS K. and SEEGER K., *Z. Phys.* **218**, 431 (1969).
5. KAHLERT H., HESS K. and SEEGER K., *Solid State Commun.* **7**, 1149 (1969).
6. HOLM-KENNEDY J. W. and CHAMPLIN K. S. *Appl. Phys. Lett.* **15**, 382 (1969).
7. SLADEK R. J. *Phys. Rev.* **120**, 1589 (1960).
8. LIFTSHITS T. M., OLEINIKOV A. Ya. and SHULMAN A. Ya. *Phys. Status Solidi.* **14**, 511 (1966).
9. KINCH M. A., *Proc. Phys. Soc.* **90**, 819 (1967).
10. MANEVAL J. P., ZYLBERSZTEJN A. and BUDD H. F., *Phys. Rev. Lett.* **23**, 848 (1969).
11. WHALEN J. J. and WESTGATE C. R., *Appl. Phys. Lett.* **15**, 292 (1969).
12. BAUER G. and KAHLERT H., Proceedings of the 10th Int. *Conf. Phys. Semicond.* p. 65, Cambridge (1970).
13. OLIVER D. J., *Phys. Rev.* **127**, 1045 (1962).
14. CRANDALL R. S., *Phys. Rev.* **B1**, 730 (1970).
15. KRISHNAMURTHY B. S. and PARANJAPE V. V., *Solid State Commun.* **8**, 713 (1970).
16. SEEGER K. and HESS K., *Z. Phys.* **237**, 252 (1970).
17. PARANJAPE B. V., *Rep. Br. elect. Ind. Res. Ass.* L/T 285 (1953).
18. CONWELL E. M., *High Field Transport in Semiconductors*, p. 252, Academic Press, New York and London (1967).
19. KOGAN Sh. M., *Fiz. tverd. Tela* **4**, 2474 (1962). *Soviet. Phys. Solid State* **4**, 1813 (1963).
20. WILLARDSON R. K. and BEER A. C., *Physics of III-V Compounds*, Vol. 2, p. 110, Vol. 3, p. 14, Academic Press, New York (1967).
21. EHRENREICH H., *Phys. Rev.* **120**, 1951 (1960).

Ludwig Boltzmann – Institüt für Festkörperphysik und Institüt für Angewandte Physik der Universitat Wien, Austria

K. HESS
H. KAHLERT

J. Phys. Chem. Solids, 1971, Vol. 32, pp. 2267–2274. Pergamon Press. Printed in Great Britain

FAR INFRARED FREE-CARRIER ABSORPTION IN *n*-TYPE GALLIUM ARSENIDE*

S. PERKOWITZ
Physics Department, Emory University, Atlanta, Georgia 30322, U.S.A.

(*Received* 30 *November* 1970; *in revised form* 29 *March* 1971)

Abstract – The far i.r. absorption between 20 and 200 cm^{-1} has been measured at 300 and 77°K in one high resistivity and three doped samples of *n*-type gallium arsenide. The doped samples had carrier concentrations of $2{\cdot}6 \times 10^{15}$, $5{\cdot}0 \times 10^{15}$ and $1{\cdot}5 \times 10^{16}$ cm^{-3}. As was predicted in an earlier paper, in the limit $(\omega\tau)^2 \gg 1$ the free-carrier absorption in the far i.r. approaches the Drude form with frequency dependence ω^{-2}. The absorption data were fitted to the Drude equation to yield values of carrier concentration and mobility which agreed fairly well with the Hall values at room temperature. Some deviations from the predictions of the Drude theory were noted. The data were taken using a Fourier transform spectrometer and a Golay detector and some comments on the suitability of this system for far i.r. measurements in doped semiconductors are given.

1. INTRODUCTION

THE OPTICAL absorption of gallium arsenide has been thoroughly examined[1–4] in the middle i.r. region 200 to 2000 cm^{-1}. While the lattice behavior has been found to be describable by the usual single-oscillator model[5,6], the free-carrier absorption has required a more complicated theory. This absorption is certainly not described by the Drude model in the middle i.r. since, in the limit $\omega\tau \gg 1$ (where ω is the optical frequency and τ is the electron scattering time) the absorption has the dependence ω^{-3} rather than the predicted dependence ω^{-2}. Spitzer and Whelan[1] and others [2–4] have observed this inverse cube dependence for *n*-type samples with carrier concentrations between $1{\cdot}5 \times 10^{16}$ and 9×10^{18} cm^{-3} at frequencies between 500 and 2000 cm^{-1}. These results were explained by the quantum mechanical calculations of Visvanathan[7], Dumke[8] and especially Haga and Kimura[9]. The latter calculated the total absorption as the sum of an acoustic mode contribution with frequency dependence ω^{-2}, an optical mode contribution with dependence $\omega^{-2{\cdot}4}$ and an ionized impurity term with dependence $\omega^{-3{\cdot}3}$.

In his calculation, Dumke had noted that the quantum theoretical result for absorption approaches the classical result for photon energies much less than the carrier energies. In a recent paper[10] this criterion was used together with the Haga–Kimura results to show that the free-carrier absorption in *n*-type gallium arsenide should show nearly classical behavior for frequencies below 200 cm^{-1}, carrier concentrations above 1×10^{17} cm^{-3} and temperatures between 77 and 300°K. This paper reports the results of far i.r. absorption measurements between 20 and 200 cm^{-1} at 300 and 77°K in one high resistivity and three doped samples of *n*-type gallium arsenide. The doped samples had carrier concentrations well below the predicted lower limit, but it was found that the bulk of the absorption data could be described by the simple Drude model. Far i.r. absorption measurements have been reported previously in high resistivity gallium arsenide[6, 11] as well as in lightly doped samples[12, 13]. Both of the latter measurements were made at 4·2°K and the emphasis was on shallow donor absorption rather than on free-carrier absorption.

---

*Work supported by grants from the Alfred P. Sloan Foundation and the Research Corporation.

2. EXPERIMENTAL DETAILS

The single crystal samples were obtained from the Bayside Laboratories of General Telephone and Electronics, Inc. Details of sample dimensions and room temperature mobilities and carrier concentrations are given in Table 1. The sample diameters are quoted to give an idea of the sample size which can be successfully examined by the techniques described below. The carrier concentration and mobility values were obtained by Hall and resistivity measurements using the van der Pauw geometry and were calculated assuming a scattering factor of unity. All the samples were mechanically polished on both faces to a smooth mirror finish.

The far i.r. transmission data were obtained by Fourier transform spectroscopy, a technique which has been fully described elsewhere[14]. A commercial system, the Grubb Parsons Mark II Cube interferometer, was used almost exactly as supplied. Most of the data were obtained using a 12·5 micron Mylar beamsplitter which gave a usable signal level over the range 20 to 200 cm^{-1}. Data were taken with a resolution of either 4 or 8 cm^{-1}, corresponding to running times of 40 or 20 min. The lower resolution gave a noticeable improvement in the signal-to-noise ratio and was adequate to resolve most of the structure seen in the transmission curves. The transmission coefficient was obtained by a sample in-sample out method.

The transmitted radiation was detected by means of a Unicam Golay cell. This type of detector is less sensitive than any of several types of cooled detector, but its simplicity and ease of operation are most attractive. The Golay cell was sufficiently sensitive to permit the use of samples as small as those described in Table 1, samples so small that the necessary masking reduced the useful light intensity 90 to 98 per cent. However, it was clear that the detector was being operated near the limit of its useful range. In all cases it was necessary to average over several runs to obtain a completely satisfactory signal-to-noise figure. In an attempt to measure transmission in a sample with a carrier concentration of 1×10^{17} cm^{-3} and of the same general size and thickness as those described here, it was found that the interferogram maximum could not be distinguished from the noise except after averaging over eight runs; even then, the signal-to-noise ratio was too low to be useful. To use a Golay cell to examine semiconductor samples with concentrations above the mid-10^{16} range, it would be necessary to use samples of larger lateral dimension, though these may not be available in single-crystal form; or to use thinner samples, though thicknesses less than 0·05 cm would require careful handling. One advantage of the use of small samples is that it reduces the convergence error in the Grubb Parsons instrument which was recently discussed by Fleming [15]. The error in the calculated absorption coefficients due to this convergence effect was calculated and found to be less than 5 per cent for the fairly large absorptions obtained at room temperature, and less than 10 per cent for the smaller absorptions measured at 77°K.

3. RESULTS AND DISCUSSION

Figures 1 and 2 show the absorption coefficient vs. frequency curves for all four samples at 300 and 77°K, respectively. The absorption coefficient α was obtained from the transmission data by means of the relation

$$T = \frac{(1-R)^2 e^{-\alpha x}}{1 - R^2 e^{-2\alpha x}} \tag{1}$$

where T is the transmission coefficient, R is the reflectivity and x is the sample thickness. Since a separate measurement of the reflectivity was not made, R was calculated from the expression $R = (n-1)^2/(n+1)^2$ where n is the real part of the refractive index. This expression has been simplified by assuming that $n^2 \gg k^2$ where k is the imaginary part of the refractive index. A second simplification

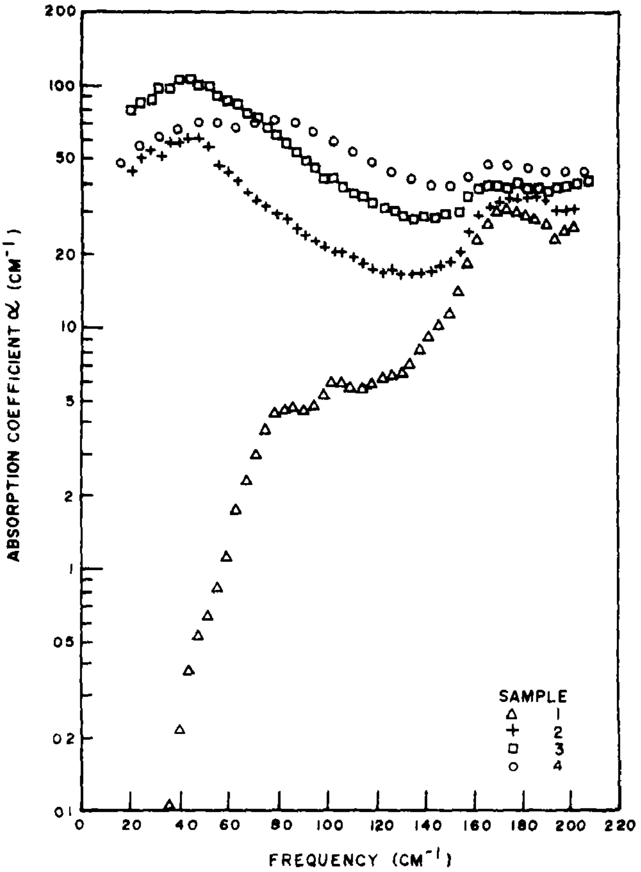

Fig. 1 Absorption coefficient at 300°K as a function of frequency for the four samples listed in Table 1.

was made by assuming that the free-carrier contribution to the real part of the dielectric constant was negligible. This approximation, together with the condition $n^2 \gg k^2$, means that n is given by the pure lattice expression

$$n^2 = \epsilon_\infty + \frac{(\epsilon_s - \epsilon_\infty)}{1 - \left(\dfrac{\omega}{\omega_T}\right)^2} \qquad (2)$$

where ϵ_s and ϵ_∞ are the static and high frequency dielectric constants respectively, ω_T is the transverse optical frequency and where a damping term has been omitted because it is unimportant for frequencies much below ω_T. For the carrier concentrations and absorptions encountered here, the simplifying assumptions introduce a negligible error into the calculation of α from equation (1) for frequencies above about 25 cm^{-1}. However, equation (2) as written is a good approximation to n only for frequencies above about 40 cm^{-1}. The numerical values of the lattice parameters were taken as $\epsilon_\infty = 11{\cdot}10$, $\epsilon_s - \epsilon_\infty = 1{\cdot}95$ and $f_T = \omega_T/2\pi c = 268{\cdot}2$ cm^{-1} as given by Iwasa *et al.*[16], at both 300 and 77°K.

The most obvious feature of the data shown in Figs. 1 and 2 is the distinct difference in shape and large difference in magnitude between the curve for the high-resistivity sample 1 on the one hand and the curves for the doped samples on the other. These differences are

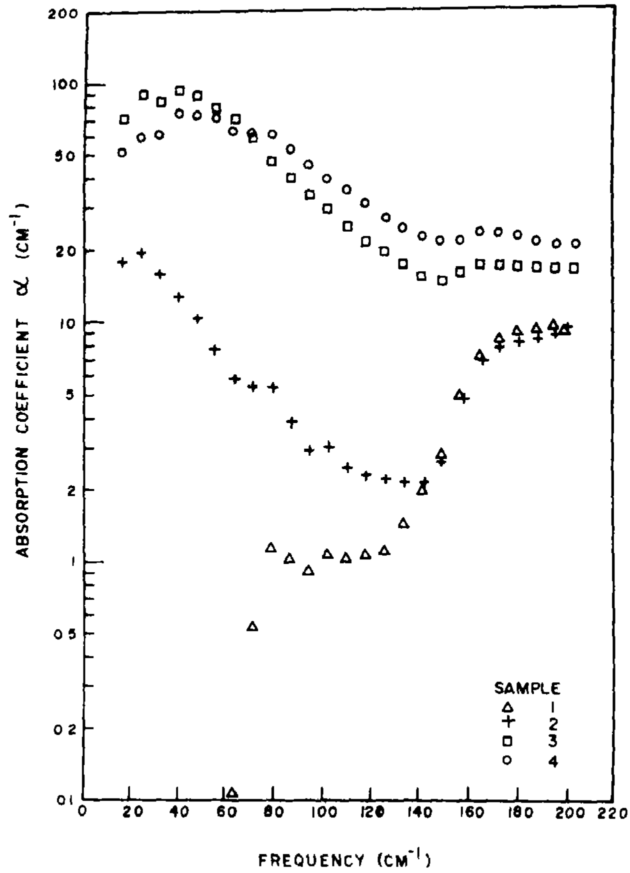

Fig 2 Absorption coefficient at 77°K as a function of frequency for the four samples listed in Table 1

Table 1. Summary of dimensions, electrical and optical results for carrier concentration and mobility, and frequency dependence of the reduced absorption α' *for the gallium arsenide samples used in the absorption measurements. The quantity* p *is defined by the relation* $\alpha' \infty \omega^{-p}$

Sample	Diameter (cm)	Thickness (cm)	Temperature (°K)	p	Carrier concentration (cm $^{-3}$) Electrical	Optical	Mobility (cm^2/volt-sec) Electrical	Optical
1 [a]	0·4	0·1095						
2	0·3	0·0540	300	1·9	2 6(10^{15})	2·9(10^{15})	[b]	4400
			77	1·8–2·3	[b]	[c]	[b]	[c]
3	0·6	0·0462	300	1·9	5·0(10^{15})	7·1(10^{15})	4300	4800
			77	2·1	[b]	3·6(10^{15})	[b]	3000
4	0·6	0·0758	300	2·0	15·0(10^{15})	9·5(10^{15})	5600	4000
			77	1·9	[b]	7·5(10^{15})	[b]	4800

[a] High resistivity sample.
[b] Data not available.
[c] Fit not made to optical data.

due to free-carrier absorption. It is apparent that in the far i.r., this absorption is large compared to the lattice contribution even for low carrier concentrations. The data for the high-resistivity sample shows some structure which appears as additional onsets of absorption at about 60 and 150 cm^{-1} and as two small peaks between 80 and 100 cm^{-1}. Stolen[11] has observed similar structure in high-resistivity gallium arsenide and has ascribed it to multiphonon effects.

To analyze the free-carrier absorption, it is useful to assume that the total absorption can be written as the sum of a lattice term and a free-carrier term. The analysis will show that this assumption is justified. Since the absorption measured in sample 1 should represent lattice effects only, the subtraction of this data from the absorption for the doped samples should yield the desired free-carrier term. The subtraction was carried out for all the doped samples at both temperatures and the resulting reduced absorption α' was plotted against frequency on a log–log scale. Typical curves are shown in Fig. 3. In all cases, it was possible to fit the data over a large frequency range by a straight line. A least-squares fit was made to the linear region of each curve. The slopes of these best-fit lines are given in Table 1 and it can be seen that except for sample 2 at 77°K, the reduced absorption varies as $\omega^{-(2\pm0.1)}$ in all cases. The scatter in the low-temperature data for sample 2 was too great to allow an unambiguous straight-line portion to be defined and the slope could be fixed only between the limits shown.

The approximate inverse quadratic dependence on frequency suggests immediately that the Drude theory is valid to describe the free-carrier absorption, provided the condition $(\omega\tau)^2 \gg 1$ is met. We will analyze the reduced absorption in terms of the Drude theory, first showing that with a certain approximation the absorption can be separated into lattice and free-carrier parts and then discussing the frequency dependence and magnitude of the absorption. From the standard development, the total absorption is given by

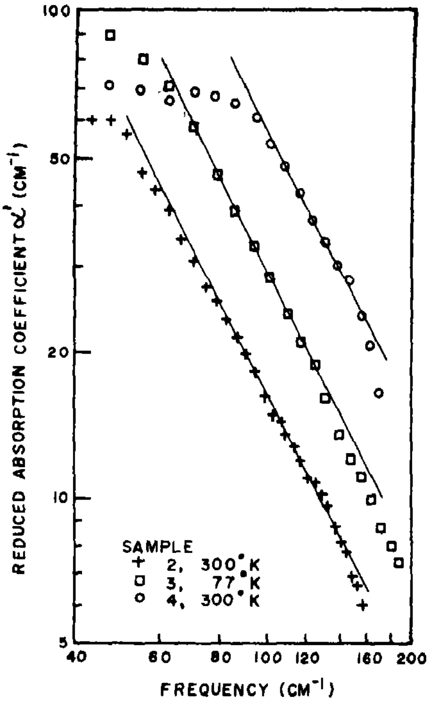

Fig. 3. Reduced absorption coefficient as a function of frequency for two of the doped samples at 300°K and one doped sample at 77°K. The solid lines are drawn with a slope of −2.

$$\alpha = \frac{\omega}{nc}\left(\epsilon_i^{lat} + \frac{\omega_p^2\tau}{\omega(1+\omega^2\tau^2)}\right) \qquad (3)$$

where ϵ_i^{lat} depends on lattice parameters only and where ω_p is the plasma frequency. This latter quantity is defined by the relation $\omega_p^2 = 4\pi Ne^2/m^*$ where N is the free-carrier concentration and m^* is the effective mass. The quantity n in the denominator of equation (3) in general contains both free-carrier and lattice parameters so that the total absorption cannot be written as the sum of a lattice term and a free-carrier term. However, for the samples considered here, n is given by equation (2) and contains only lattice parameters. With this simplification it is possible to define a pure lattice absorption term $\omega\epsilon_i^{lat}/nc$ and, after subtracting this term from the total absorption, to obtain a 'free-carrier' absorption

$$\alpha_{fc} = \frac{\omega_p{}^2\tau}{nc(1+\omega^2\tau^2)}. \qquad (4)$$

This result is to be compared to the reduced absorption α' for frequencies above 40 cm^{-1}.

The frequency dependence of α_{fc} is given almost wholly by the term $(1+\omega^2\tau^2)^{-1}$ since, as can be determined from equation (2), n is almost independent of frequency in the far i.r. Over the range 40 to 200 cm^{-1} n changes by less than 9 per cent. Thus in the limit $(\omega\tau)^2 \gg 1$ the free-carrier absorption exhibits the inverse-square dependence. As the frequency becomes so low that $\omega\tau \leq 1$ the term $(1+\omega^2\tau^2)$ becomes less sensitive to frequency and the free-carrier absorption curve flattens out. The transition between the two limits $(\omega\tau)^2 \ll 1$ and $(\omega\tau)^2 \gg 1$ has been observed by Ellis and Moss[17] in silicon carbide. In that material the Hall mobilities are much lower than in gallium arsenide and $\omega\tau = 1$ at middle i.r. frequencies near 700 cm^{-1}. For all three of the present samples the Hall mobilities are such that $\omega\tau = 1$ at about 30 cm^{-1}. Both the inverse square dependence and the flattening out of the absorption curve are apparent in Fig. 3. The inverse square behavior occurs at frequencies consistent with the condition $(\omega\tau)^2 \gg 1$ for all three samples. The flattening out of the curve appears to begin at about the right frequency for samples 2 and 3 but for sample 4 starts at far too high a frequency.

To further test the validity of equation (4) to describe the data, a least-squares fit was carried out. The data can be fitted to the equation to obtain 'optical' values of ω_p and τ, which can be used to calculate the carrier concentration N and drift mobility $\mu = e\tau/m^*$. The fit is made most easily by noting that if n is taken as a constant, a plot of $(\alpha')^{-1}$ vs. ω^2 should yield a straight line of slope $nc\tau/\omega_p{}^2$ and y-intercept $nc/\omega_p{}^2\tau$. Such a fit was made to each set of data, except for the set describing sample 2 at 77°K, at frequencies above 40 cm^{-1}. For sample 2 at 300°K and for sample 3 at 300 and 77°K the fit was satisfactory. For sample 3 at both temperatures, the fit was reasonably satisfactory only for frequencies above 80 cm^{-1} and ω_p and τ were calculated using only the corresponding portion of the data. In all cases N and μ were found by using the value $m^*/m_0 = 0{\cdot}072$[18] and by taking n as a constant equal to its average value over the frequency range. The optical values are compared to the electrical results in Table 1. The agreement at 300°K is fair overall, with differences of 12 to 42 per cent in the concentration and mobility values. Since there are no electrical data at 77°K, an exact comparison cannot be made. One would not expect the carrier concentration to change drastically between 300 and 77°K so the optical results for N are probably of the right order of magnitude. However, judging from typical values for gallium arsenide Hall mobilities at 77°K, the optical mobility values appear to be far too small.

Though the Drude theory has been fairly successful in describing much of the free-carrier data, there are some aspects of the results which are inconsistent with the Drude model. One such anomaly, previously mentioned, is the premature flattening out of the absorption curve for sample 4. This behavior seems to be part of a general effect occurring in all the doped samples. As Figs. 1 and 2 show, the absorption curves for all three samples exhibit a maximum at frequencies ranging from 25 to 70 cm^{-1}. The Drude theory does in fact predict the presence of a low frequency maximum if the carrier concentration is low but, as will be seen, the predicted and observed positions of the maxima are in poor agreement. It is not obvious that the Drude theory leads to such low-frequency maxima. The derivation is not difficult but is algebraically complicated and we will only sketch its outline here. At very low frequencies the lattice absorption becomes completely negligible compared to the free-carrier term for the carrier concentrations used here and the total absorption is very nearly just α_{fc}. A consideration of equation (4) shows that if the frequency is so low that $(\omega\tau)^2 \ll 1$, then α_{fc} has a maximum approximately where n has a minimum. At such low frequencies it is no longer valid to omit the free-carrier contribution to the real part of the dielectric constant or to take $n^2 \gg k^2$ so that equation (2) is not even approximately correct. In a full development for n, it can be shown that n has a minimum and that therefore α has a maximum at a frequency which depends on ω_p and τ in a complicated way. The positions of the maxima for samples 2, 3 and 4 at 300°K were calculated as 10, 14 and 21 cm^{-1} respectively. The observed positions are all shifted to much higher frequencies, namely, about 40, 40 and 70 cm^{-1} respectively. A second anomaly, which is perhaps related to the shift in the positions of the maxima, arises from the fact that the absorption curves for samples 3 and 4 intersect at about 70 cm^{-1} at both 300 and 77°K. Such an intersection cannot be explained by the Drude theory if the quoted values of the free-carrier parameters, even with reasonable error estimates, are used.

4. CONCLUSIONS

The main portion of the present results confirms the prediction that for far i.r. frequencies such that $(\omega\tau)^2 \gg 1$, the free-carrier absorption in gallium arsenide varies as ω^{-2}. This behavior was observed for carrier concentrations much less than the estimated lower limit of 1×10^{17} cm^{-3}. The error in the estimate seems to lie in the previous analysis [10] of the optical mode contribution to the total absorption. This contribution is expected to dominate at the carrier concentrations and temperatures used here. A reconsideration of the optical mode term suggests that the conditions $\omega_l > \omega$ and $kT \gg \hbar\omega$, where T is the temperature and ω_l is the longitudinal optical frequency, are sufficient to obtain classical behavior for nondegenerate samples. The present samples are distinctly nondegenerate at both 300 and 77°K and the condition $\omega_l > \omega$ is met in the far i.r. The condition $kT \gg \hbar\omega$ is met for frequencies below 200 cm^{-1} at 300°K but requires frequencies below 50 cm^{-1} at 77°K and so is not satisfied over much of the frequency range at the lower temperature. Therefore, although the new criteria eliminate the prediction of a lower limit in carrier concentration, they do not explain why classical behavior is observed at 77°K.

The anomalous behavior of the absorption peaks for samples 2 and 3 occurs at frequencies such that $\omega\tau \cong 1$. The connection between the quantum and classical absorption theories is clear-cut only for $(\omega\tau)^2 \gg 1$ and it perhaps should not be surprising that the low-frequency results deviate from the Drude theory. This is definitely not the case for sample 4, however, where the anomalous behavior is seen at frequencies such that $(\omega\tau)^2 \gg 1$ and there is no obvious explanation for the relatively large disagreement with the Drude theory.

A large part of the discrepancy between the optical and electrical values for N and μ can be ascribed to measurement errors in the absorption coefficients and in the electrical data. Such errors account for deviations of 20 to 25 per cent. An additional deviation of perhaps 10 per cent may be due to the differences between the Hall mobility and the drift mobility though not all the discrepancies are in the right direction. All these deviations are not quite large enough to completely explain discrepancies of the order of 40 per cent. This disagreement probably represents some departure from the Drude theory even in the region where a reasonable fit can be made to equation (4).

Much of the interest in any future far i.r. semiconductor measurements should lie in further exploration of the very low frequency region, and in the comparison of optical and electrical values for the free-carrier parameters as a means of obtaining scattering information.

Acknowledgements—The author is grateful to J. Black and C. J. Summers of the Bayside Laboratories of General Telephone and Electronics, Inc. for supplying

samples. Discussions with A. McSweeney, of the Georgia Institute of Technology Electronics Research Center, were most helpful.

Note added in proof: While this paper was in proof the author was made aware of the work of H. Sobotta [*Phys. Lett.* **32A**, 4 (1970)] who measured absorption between 70 and 250 cm^{-1} at 300°K in n-GaAs. His results for carrier concentrations of $3{\cdot}0\times10^{16}$ and $1{\cdot}1\times10^{17}$ cm^{-3} could be generally described by the Drude theory but there were large discrepancies between the electrical and optical mobilities.

REFERENCES

1. SPITZER W. G. and WHELAN J. M., *Phys. Rev* **114**, 59 (1959).
2. MILVIDSKII M. G., OSVENSKII V. B., RASHEVSKAYA E. P and YUGOVA T G, *Soviet Phys. solid State* **7**, 2784 (1966).
3. VAKULENKO O. V. and LISITSA M. P., *Soviet Phys. solid State* **9**, 769 (1967).
4. RASHEVSKAYA E P. and FISTUL V. I., *Soviet Phys. solid State* **9**, 1443 (1967); **9**, 2849 (1968).
5. HASS M and HENVIS B W., *J. Phys. Chem. Solids* **23**, 1099 (1962).
6. JOHNSON C. J., SHERMAN G. H. and WEIL R., *Appl. Opt.* **8**, 1667 (1969).
7. VISVANATHAN S., *Phys. Rev.* **120**, 376 (1960); **120**, 379 (1960).
8. DUMKE W. P., *Phys. Rev.* **124**, 1813 (1961).
9. HAGA E. and KIMURA H., *J. phys. Soc. Japan* **18**, 777 (1963); **19**, 658 (1964).
10. PERKOWITZ S., *J. appl. Phys.* **40**, 3751 (1969).
11. STOLEN R. H., *Appl. Phys. Lett.* **15**, 74 (1969).
12. BOSOMWORTH D. R., CRANDALL R. S. and ENSTROM R. E., *Phys. Lett.* **28A**, 320 (1968).
13. SUMMERS C. J., DINGLE R. and HILL D. E., *Phys. Rev.* **1B**, 1603 (1970).
14. See, for example, RICHARDS P. L., in *Spectroscopic Techniques* (Edited by D. H. Martin), p. 33, John Wiley, New York (1967).
15. FLEMING J. W., *Infrared Physics* **10**, 57 (1970).
16. IWASA S., BALSLEV I. and BURSTEIN E., in *Proceedings of the International Conference on the Physics of Semiconductors*, Paris, 1964 (Dunod, Paris, 1964), p. 1077.
17. ELLIS B. and MOSS T S., *Proc. R. Soc.* **299A**, 393 (1967).
18. EHRENREICH H., *Phys. Rev.* **120**, 1951 (1960).

J. Phys. Chem. Solids, 1971, Vol. 32, pp. 2275–2284. Pergamon Press. Printed in Great Britain

OPTICAL SPECTRA, RELAXATION, AND ENERGY TRANSFER OF Eu^{3+} AND Cr^{3+} IN A EUROPIUM PHOSPHATE GLASS

M. J. WEBER*
Raytheon Research Division, Waltham, Mass. 02154, U.S.A.

and

E. J. SHARP and J. E. MILLER
Night Vision Laboratory, Ft. Belvoir, Va. 22060, U.S.A.

(*Received* 11 *February* 1971)

Abstract – Optical absorption and emission spectra and relaxation of Eu^{3+} ions and of Cr^{3+} impurities in a $Eu(PO_3)_3$ glass are reported. Europium fluorescence occurs from the $^5D_0$ state with near-unity quantum efficiency at low emperatures. The Cr^{3+} fluorescence occurs in the form of a broadband emission in the near-infrared which is attributed to Stokes-shifted $^4T_2 \rightarrow {}^4A_2$ transitions. The Eu^{3+} emission overlaps the Cr^{3+} absorption bands and both radiative and nonradiative $Eu^{3+} \rightarrow Cr^{3+}$ energy transfer were observed. To investigate the transfer processes, the Eu^{3+} fluorescence decays were measured as a function of temperature and chromium concentration. The results indicate that non-radiative energy transfer involves a combination of energy migration through the Eu^{3+} system and transfer to fast-relaxing Cr^{3+} ions which act as quenching centers.

1. INTRODUCTION

THE OPTICAL absorption and emission spectra of europium metaphosphate glass have been investigated and are found to be similar to those reported for Eu^{3+} ions in other glasses [1-3]. In undoped $Eu(PO_3)_3$ glass, the Eu^{3+} fluorescence occurs with near-unity radiative quantum efficiency at low temperatures. This is in contrast to the behavior of Eu^{3+} ions in many crystals where at high europium concentrations self-quenching of fluorescence due to multiple-ion interactions is frequently observed[4, 5]. Although the Eu^{3+}-Eu^{3+} coupling in $Eu(PO_3)_3$ is insufficient for self-quenching, resonant energy transfer is still possible. While this does not result in net relaxation of the excited Eu^{3+} system, it can lead to energy migration and subsequent transfer to other quenching centers. Migration of excitation to energy sinks has been invoked previously to account for the relaxation of rare-earth ions present as impurities in other glasses[6, 7]. Here these processes are studied in a 100 per cent rare-earth glass.

Investigation of the energy level scheme and decay properties of Cr^{3+} ions in $Eu(PO_3)_3$ glass reveals that they are well suited to serve as fast-relaxing sinks for Eu^{3+} excitation. Europium-to-chromium energy transfer in an europium aluminum borate ($EuAl_3B_4O_{12}$) doped with chromium impurities has been reported by Blasse and Bril and was attributed to long-range electric multipole coupling between Eu^{3+} and Cr^{3+} ions[8]. Such interactions are active in $Eu(PO_3)_3$:Cr^{3+} glass. The observed characteristics of the Eu^{3+} decay and its dependence on temperature and chromium concentration indicate, in addition, that energy migration through the Eu^{3+} system to Cr^{3+} impurities also pays an important role in the relaxation of Eu^{3+} ions.

Measurements and interpretation of the absorption and emission spectra of Eu^{3+} and Cr^{3+} ions in $Eu(PO_3)_3$ glass are presented below together with studies of the fluorescence

---

*Research supported in part by the Night Vision Laboratory, Ft. Belvoir, Va., U.S.A.

kinetics following pulsed selective excitation. Calculations of the radiative contribution to the excited state lifetimes are made to determine the quantum efficiencies in the absence of energy transfer. Pulsed and steady-state experiments are then employed to establish the existence and nature of radiative and nonradiative Eu^{3+}-to-Cr^{3+} energy transfer. The dependences of the energy transfer on chromium concentration and on temperature are also examined. A detailed elaboration of the theory and interpretation of the processes active in the nonradiative transfer is presented in a separate paper[9].

2. EXPERIMENTAL PROCEDURES

Samples of chromium-doped $Eu(PO_3)_3$ glasses were prepared at the National Bureau of Standards. The starting materials consisted of reagent grade ammonia phosphate, europium oxide, and chromium oxide of 99·99 per cent purity. The batch ingredients were fired for 4 hr at 850°C in a Vycor crucible and were then transferred to a platinum crucible where they were melted at 1450°C for approximately 2 hr. The charge was then poured on a heated plate, placed in an annealing furnace at 600°C, and cooled over a period of about 8 hr. Undoped samples of $Eu(PO_3)_3$ had a very pale peach coloration; the chromium-doped samples were green. The measured density of the europium metaphosphate glass was 3·48 gm/cm^3; the refractive index at 643·8 nm was 1·585. A spectrochemical analysis of the impurities in the undoped $Eu(PO_3)_3$ glass is given in Table 1.

Table 1. Spectrochemical analysis of impurities in undoped $Eu(PO_3)_3$ *glass*

Element	Concentration (wt. %)
Ca, V, Mn	0·01–0·001
B, Mg, Al Si, Fe, Cu	0·001–0·0001
Cr	0·0001
Rare earths (other than Eu)	Not detected

Absorption spectra were recorded using a Cary 14 spectrophotometer. Fluorescence studies were performed using a 0·5 m grating monochromator equipped with a cooled S-1 photomultiplier detector; the excitation source was a high-pressure xenon arc lamp. For recording excitation spectra, another grating monochromator was introduced between the source and the sample. The sample was contained in a quartz dewar through which flowed dry nitrogen gas. By a combination of a liquid nitrogen heat exchanger and a nichrome wire heater, the gas temperature could be varied continuously from 77 to 700°K. The sample temperature was measured with a thermocouple.

Pulsed selective excitation and fluorescence decay studies were performed in the above optical arrangement by replacing the xenon arc lamp with a xenon flashlamp, the total flashlamp pulse duration of $\approx 5 \mu$sec. Fluorescence decay signals were displayed directly on an oscilloscope and photographed.

3. OPTICAL PROPERTIES OF EUROPIUM

Spectra

The observed optical absorption and emission spectra of $Eu(PO_3)_3$ are characteristic of transitions between the lower energy levels of the $4f^6$ configuration of trivalent europium. The absorption spectrum recorded at room temperature is given in Fig. 1. The absorption bands at approximately 580–600, 525, 465, 415, and 390 nm are identified as transitions from $^7F_0$ and $^7F_1$ levels to the $^5D_0$, $^5D_1$, $^5D_2$, $^5D_3$, and other ^5D, ^5G, ^5L states of Eu^{3+}, respectively. The wavelengths, intensities, and widths of these $4f$–$4f$ transitions are in general similar to those observed for Eu^{3+} ions in other glasses[1–3].

Fluorescence was observed from the $^5D_0$ level at 17,280 cm^{-1} to levels of the ^7F ground multiplet. No fluorescence from $^5D_1$ or higher excited states of Eu^{3+} was observed. This is not unexpected since at high europium concentrations these states are usually quenched by ion–ion interactions and $^5D_0$ is the only

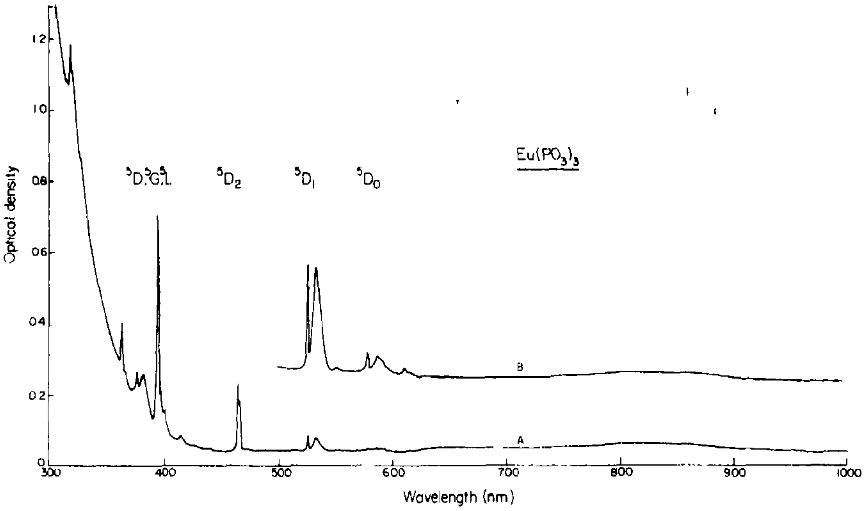

Fig. 1. Absorption spectrum of $Eu(PO_3)_3$ glass at 295°K. Sample thickness: $A = 0{\cdot}056$ cm, $B = 0{\cdot}465$ cm.

metastable state. The $^5D_0 \rightarrow {}^7F_J$ spectra recorded at 77 and 600°K are shown in Fig. 2 (the transitions to $^7F_5$ and $^7F_6$ are very weak and are not included). The wavelengths and relative intensities of the various transitions are given in Table 2. The energy level scheme derived from the absorption and fluorescence spectra is illustrated in Fig. 3.

Divalent europium, which may be formed by electron transfer, can give rise to strong emission in the near-ultraviolet[10]. A search was made for the characteristic fluorescence expected from Eu^{2+} but none was found.

The $^5D_0 \rightarrow {}^7F_1$ fluorescence lines of Eu^{3+} are magnetic-dipole allowed transitions; the other fluorescence lines arise from forced electric-dipole transitions. The large ratio of the fluorescence intensities for the $^5D_0 \rightarrow {}^7F_2$ and $^5D_0 \rightarrow {}^7F_1$ transitions implies a low symmetry field at the europium site[2]. Robinson and Fournier[11], from optical absorption and emission studies of Yb^{3+}, have suggested that the Yb^{3+} ions are located at sites of near octahedral symmetry in rare-earth (RE) metaphosphate glasses having approximate compositions $RE(PO_3)_3$. In the present glass, the splitting of the $^5D_0 \rightarrow {}^7F_1$ transition into three resolvable lines (complete removal of the J-degeneracy) indicates that the symmetry at the Eu^{3+} site is not only non-cubic but lower

Table 2. *Wavelengths and relative intensities of* $^5D_0 \rightarrow {}^7F$ *fluorescence transitions of* Eu^{3+} *in* $Eu(PO_3)_3$ *glass*

Terminal state	Relative intensity	Peak wavelengths (nm)
$^7F_0$	0·8	578·7
$^7F_1$	13·8	588·0, 592·3, 596·8
$^7F_2$	67·7	611·4, 615·2, 619·2, 622·9
$^7F_3$	3·4	653·4, 661·2
$^7F_4$	12·8	690·4, 710·9
$^7F_5$	0·4	≈ 746
$^7F_6$	1·1	≈ 810

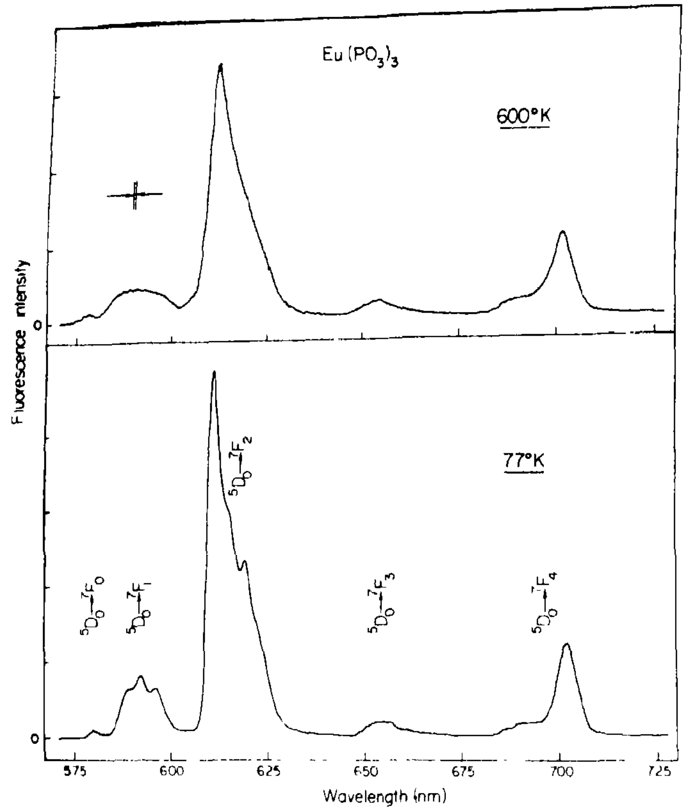

Fig. 2. $^5D_0 \rightarrow {}^7F$ fluorescence spectra of Eu(PO$_3$)$_3$ glass. The gain for 600°K spectrum was increased by $\approx X5$.

than axial symmetry. Also, unlike Yb^{3+} where the J-manifolds are well separated, significant J-mixing between the ^7F_J states of Eu^{3+} is probably present which can further reduce the selection rules for radiative and nonradiative transitions.

The Eu^{3+} absorption and emission lines in Figs. 1 and 2 are broad even at low temperatures as is typical for rare-earth ions in glasses. Although the structure observed in the optical spectra indicates distinct symmetry at the Eu^{3+} site, the width and asymmetry of the lines indicate site-to-site variations in the crystal field. The width of the $^7F_0 \rightleftarrows {}^5D_0$ transition, which is least sensitive to local fields, is $\approx 60\,\text{cm}^{-1}$. This is much greater than would be expected if the sites were all equivalent. The observed broadening can arise from the existence of non-uniform, non-identical ligand fields caused by a variety of local site symmetries and by different ranges of rare earth–oxygen bond distances. Recently a model for the rare-earth ion site in phosphate glasses has been proposed[12, 13]; it involves coordination by three PO$_4$ tetrahedra and associated distortions which reproduce many of the features of the observed Yb^{3+} line-shapes. A similar model may be apropos for the present glass.

At elevated temperatures the spectra become broadening due to thermal vibrations. This thermal broadening eventually becomes comparable to the inhomogeneous broadening due to the unequivalent sites and accounts for the loss of structure in the spectra seen from Fig. 2.

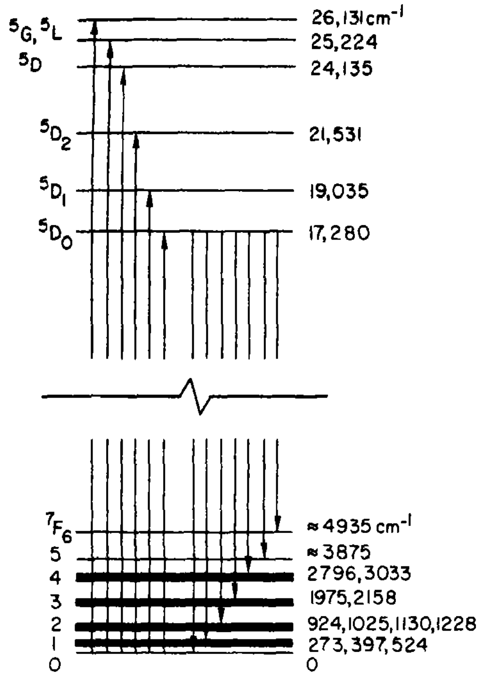

Fig. 3. Lower energy levels of Eu^{3+} in Eu $(PO_3)_3$ glass; individual Stark levels are not shown. Energies are in cm^{-1}.

Fluorescence kinetics

The Eu^{3+} fluorescence kinetics were examined after exciting an undoped $Eu(PO_3)_3$ sample with radiation from a xenon flashlamp. The risetime of the europium $^5D_0$ fluorescence following selective excitation at 466 or 395 nm was $< 5\,\mu$sec, thus indicating rapid decay from the higher excited Eu^{3+} states to $^5D_0$. The $^5D_0$ fluorescence exhibited a simple exponential decay with a characteristic lifetime of 2.1 msec at 77°K. The observation that the decay can be fitted by a single exponential indicates that site-to-site variations are not so large as to cause greatly differing decay rates. The temperature dependence of the lifetime is shown in Fig. 4 and is discussed later.

The radiative contribution to the $^5D_0$ lifetime was found from the Einstein relationship between the integrated absorption coefficient $k(\nu)$ and the spontaneous emission lifetime τ[14]. For electric-dipole transitions of frequency ν_{ij} between levels i and j having degeneracies g_i and g_j,

$$\tau_{ji} \int k_{ij}(\nu)\, \mathrm{d}\nu = \frac{g_j}{g_i} \frac{c^2 N_i}{8\pi n^2 \nu_{ij}^2}, \tag{1}$$

where N_i is the number of Eu^{3+} ions per cm^3 in level i, n is the refractive index, and c is the velocity of light. The three peaks in the 580–620 nm region labeled $^5D_0$ in Fig. 1 correspond to transitions to $^5D_0$ from the $^7F_0$ ground state and thermally populated levels of the $^7F_1$ and $^7F_2$ excited states. The integrated absorption coefficients of these lines together with the Boltzmann populations N_i for the initial level i were used in equation (1) to find the spontaneous emission probabilities τ_{ij}^{-1} from $^5D_0$ to $^7F_1$ and $^7F_2$. The results were in good agreement with the corresponding relative fluorescence intensities in Table 2. The total radiative decay rate was determined by summing the probabilities from $^5D_0$ to all levels of ^7F, that is,

$$\frac{1}{\tau_j} = \sum_i \frac{1}{\tau_{ji}}. \tag{2}$$

The τ_{ji} values were found from the above results and the relative fluorescence intensities in Table 2. Using equation (2), the total calculated radiative lifetime was 2·3 msec; the uncertainty was estimated to be ± 10 per cent. This agrees, within the estimated error, with the measured $^5D_0$ lifetime in Fig. 4 extrapolated to low temperatures. Therefore the $^5D_0$ decay in undoped $Eu(PO_3)_3$ has near-unity quantum efficiency at low temperatures.

This result may seem surprising since quenching of europium fluorescence by multiple-ion interactions is frequently observed[4, 5] at Eu^{3+} ion densities such as that present in $Eu(PO_3)_3$ glass. However, because of the site-to-site crystal field variations in glasses, and the large average separation between Eu^{3+} ions, the probability for these processes is reduced and thereby the quenching. No concentration quenching of Eu^{3+} fluorescence in the borates $Y_{1-x}Eu_xAl_3B_4O_{12}$ [8] and $Gd_{1-x}Eu_xAl_3B_4O_{12}$ for $0 < x \leqq 1$ has also been reported[15]. The absence of quenching in these compounds, which have the huntite structure, is probably associated with the large distance between neighboring rare-earth ions (5·9 Å) and the presence of intervening BO_3 groups which reduce possible exchange coupling.

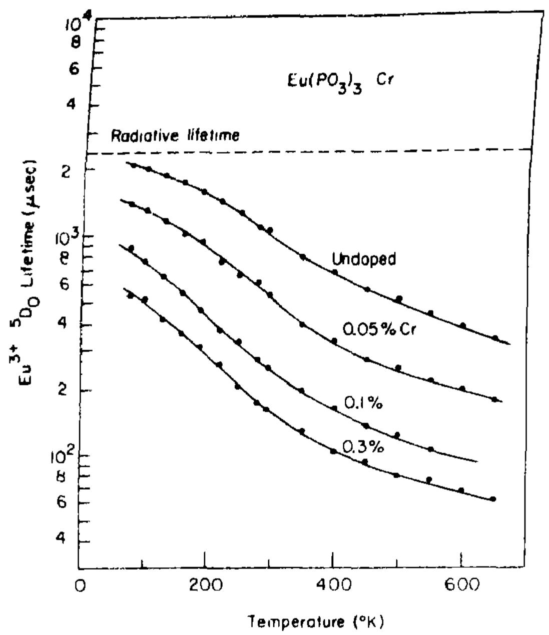

Fig. 4. Temperature dependence of the Eu^{3+} ($^5D_0$) fluorescence lifetime for an undoped (see text) and three chromium doped $Eu(PO_3)_3$ samples.

4. OPTICAL PROPERTIES OF CHROMIUM

Spectra

The absorption spectra of trivalent chromium impurities in glasses have been studied extensively[16–18]. Tischer[18], in particular, has investigated and analyzed the spectral properties of Cr^{3+} in several different phosphate glasses. Landry, Fournier and Young [17], from optical and spin resonance studies, have proposed a model in which Cr^{3+} ions in phosphate glass are octahedrally coordinated by O^{2-} ligands in a locally well-defined complex. The spectra, therefore, are attributed to ions residing in a crystal potential of predominantly cubic symmetry.

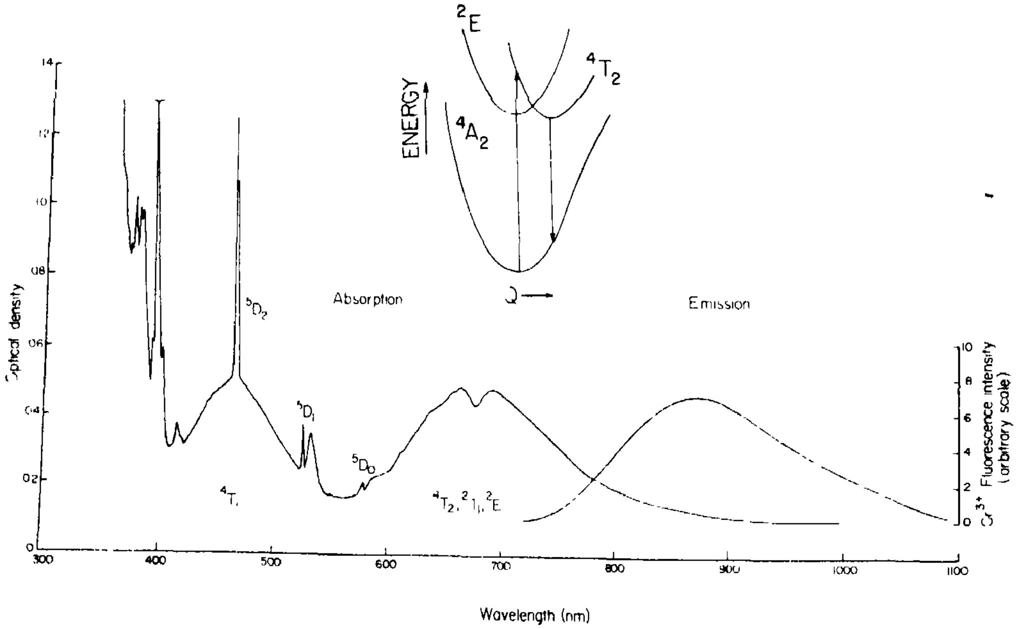

Fig. 5. Absorption and Cr^{3+} emission spectra at 295°K of $Eu(PO_3)_3$ glass containing 0·3 per cent Cr. Sample thickness: 0·22 cm.

The absorption spectrum of $Eu(PO_3)_3$ glass doped with chromium is shown in Fig. 5. The broad Cr^{3+} bands are evident from a comparison of Figs. 1 and 5. The peaks in the Cr^{3+} absorption spectrum, following Tischer's assignments[18], are: $^2E(^2G) - 14450\,cm^{-1}$, $^2T_1(^2G) - 15020\,cm^{-1}$, $^4T_2(^4F) - 15630\,cm^{-1}$, $^2T_2(^2G) - \approx 20600\,cm^{-1}$, $^4T_1(^4F) - 21800\,cm^{-1}$. Assuming simple octahedral coordination of the oxygen ligands, the spectrum can be interpreted using a crystal-field strength $Dq = 1560\,cm^{-1}$ and a Racah parameter $B = 620\,cm^{-1}$. These values are in reasonable agreement with those found by Tischer for other chromium-doped phosphate glasses.

Fluorescence was observed from chromium-doped $Eu(PO_3)_3$ in the form of a broad emission band centered at approximately 900 nm. This fluorescence band is included in Fig. 5. The emission was similar to that observed by us from Cr^{3+} impurities in an $AlMg_2(PO_3)_3$ glass and attributed to Stokes-shifted $^4T_2 \rightarrow {}^4A_2$ transitions[19]. The origin of the emission band can be understood from the schematic configuration coordinate diagram for Cr^{3+} included in Fig. 5. Depending upon the relative location of the minima of the excited ^2E and ^4T bands and the distance of the minima from the crossing point of the two potential energy curves, emission may arise from either $^2E \rightarrow {}^4A_2$ (R-line fluorescence) or $^4T_2 \rightarrow {}^4A_2$ transitions. The latter, being spin-allowed, are more probable and have been observed from several Cr-doped crystals[20] and chromium complexes[21] where the $^4T_2$ minima were sufficiently low. The minimum of the $^4T_2$ band of Cr^{3+} in $Eu(PO_3)_3$ glass appears to be located such that $^4T_2 \rightarrow {}^4A_2$ emission predominates even at 77°K.

Fluorescence kinetics

The decay of the Cr^{3+} emission, when excited at wavelengths greater than 600 nm so that only Cr^{3+} ions are excited, was only approximately exponential and fast: ~15–25 μsec at room temperature and 25–50 μsec at 77°K. To account for this relaxation, we consider the probability for radiative decay. Because of the large Stoke shift between the $^4A_2 \rightleftarrows {}^4T_2$ absorption and emission bands, a generalized Einstein relationship[22] must be used in place of equation (1). This is given by

$$\tau_{ji} \int k_{ij}(\nu)\,\mathrm{d}\nu = \left[\frac{E_{eff}(\nu_{ij})}{E_{eff}(\nu_{ji})}\right]^2 \frac{Nc^2}{8\pi n(\nu_{ij}) n(\nu_{ji})} \times \frac{\nu_{ij}}{\nu_{ji}{}^3} \frac{g_j}{g_i} \frac{\delta_\gamma{}^\Sigma |\langle \mathbf{r}_{\gamma\delta} \rangle|^2}{\delta_\gamma{}^\Sigma |\langle \mathbf{r}_{\delta\gamma} \rangle|^2} \tag{3}$$

where E_{eff} is the effective field at the emitting center, N is the density of the chromium ions, and $\langle r_{\gamma\delta} \rangle$ is the electric-dipole matrix element between component states γ and δ of levels i and j. For broad bands, the frequencies ν_{ij} and ν_{ji} are some suitably averaged absorption and emission frequencies; here these are taken simply to be the band peaks. In applying equation (3) to find the radiative lifetime τ for the $^4T_2$ band, it is necessary to subtract from the broad absorption bands in the 600–800 nm region of Fig. 5 contributions arising from $^4A_2 \rightarrow {}^2E$ and $^4A_2 \rightarrow {}^2T_1$ transitions. A decomposition of these bands was attempted in Ref. [18] assuming Gaussian-shaped bands; the results indicated that about 80–90 per cent of the absorption intensity in this spectral region originated from $^4A_2 \rightarrow {}^4T_2$ transitions and we shall assume this is also true in the present glass. A large uncertainty exists in the choice of the electric-dipole matrix elements because, depending upon the nature of the emitting center, they may differ significantly for transitions involving absorption or emission. Taking the matrix elements to be equal and using the integrated absorption coefficient at 295°K, we find a τ of 26 μsec. This is within a factor of two of the measured lifetime. In view of the approximations made and the fact that the radiative quantum efficiency is not known, this result is consistent with the hypothesis that the Cr^{3+} emission originates from the $^4T_2$ state.

5. ENERGY TRANSFER

Energy transfer from excited Eu^{3+} ions in $Eu(PO_3)_3$ glass to Cr^{3+} impurities is energetically possible. Comparing Figs. 2 and 5, one sees that lines in the $^5D_0 \rightarrow {}^7F$ fluorescence spectrum of Eu^{3+} occur in the region of the $^4A_2 \rightarrow {}^2E$, $^2T_1$, $^4T_2$ absorption bands of Cr^{3+}. This spectral overlap is essential for either radiative or nonradiative energy transfer. In addition, at all temperatures investigated the Cr^{3+} fluorescence lifetime was very much less than that of the $^5D_0$ state of Eu^{3+}, hence Cr^{3+} impurities can serve as fast relaxing energy sinks for excited Eu^{3+} ions. Energy transfer from trivalent rare earths to Cr^{3+} has been reported previously in other compounds[8, 23].

The existence of $Eu^{3+} \rightarrow Cr^{3+}$ energy transfer was established from the presence of Eu^{3+} lines in the excitation spectrum of the Cr^{3+} emission. In Fig. 6 the excitation spectra of the Eu^{3+} fluorescence and the Cr^{3+} fluorescence are shown. Comparison of the two reveals that both Eu^{3+} and Cr^{3+} absorption bands are present in the latter spectrum.

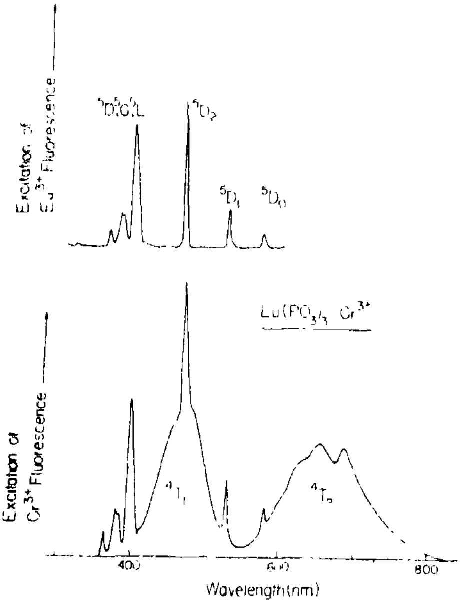

Fig. 6. Comparison of the excitation spectra of the $^4T_2 \rightarrow {}^4A_2$ fluorescence of Cr^{3+} (bottom) and the $^5D_0 \rightarrow {}^7F$ fluorescence of Eu^{3+} (top) for $Eu(PO_3)_3{:}Cr^{3+}$ (0·1 per cent) at 77°K.

The kinetics of the transfer were studied using pulsed selective excitation techniques. The decay of the broadband Cr^{3+} emission was found to be dependent upon the excitation wavelength used. When excited at wavelengths greater than 600 nm, corresponding to the Cr^{3+} absorption bands, the decay was fast, ~ 15 μsec at room temperature. When excited via the Eu^{3+} absorption lines, however, the Cr^{3+} fluorescence exhibited an additional longer decay component characteristic of the Eu^{3+} $^5D_0$ lifetime. This indicates that the Eu^{3+} excitation first decays to the $^5D_0$ state before being transferred to Cr^{3+}.

The appearance of Eu^{3+} lines in the Cr^{3+} excitation spectrum and the transient experiments above both demonstrate the existence of $Eu^{3+} \rightarrow Cr^{3+}$ energy transfer via the $^5D_0$ excited state but do not establish whether this transfer is radiative or nonradiative. Radiative transfer was evident from observed changes in the relative intensities of Eu^{3+} emission lines for samples having different chromium doping levels. Note that Eu^{3+} transitions from $^5D_0$ to $^7F_4$ occur at wavelengths near the peak of the Cr^{3+} absorption and thus would be more strongly absorbed than, for example, transitions to $^7F_2$ or $^7F_1$. The ratio of the $^5D_0 \rightarrow {}^7F_2$ to $^5D_0 \rightarrow {}^7F_4$ fluorescence intensities was measured and found to increase with increasing Cr^{3+} content, thereby confirming the presence of radiative energy transfer.

Energy transfer may also occur nonradiatively by direct interaction of an excited Eu^{3+} ion with a nearby Cr^{3+} ion and/or by energy migration through the Eu^{3+} system to Cr^{3+} quenching centers. The importance of these processes is dependent upon the Cr^{3+} concentration and, in contrast to radiative transfer, will be reflected by a change in the Eu^{3+} decay time. The decay of the $^5D_0$ fluorescence of Eu^{3+} was therefore measured for an undoped and three different chromium-doped $Eu(PO_3)_3$ samples[24] and for temperature ranges from 77 to 650°K. The transient decays of the undoped sample were exponential. The initial portion of the decays of the Cr^{3+}-doped samples, on the other hand, were nonexponential; the final portion of these decays, however, could be fitted by an exponential law. The characteristic time for this latter decay is plotted in Fig. 4 and is seen to decrease with both increasing Cr content and temperature.

The complex decay behavior observed for the chromium-doped samples and its dependence on concentration and temperature are consistent with a model of diffusion-limited relaxation[9]. The relaxation, in such cases, is composed of an initial nonexponential portion arising from donors which interact directly with acceptors via multipolar or exchange forces and a final exponential portion arising from more distant donors which relax by diffusion and by intrinsic processes. As the concentration of quenching centers is increased, the average distance the donor excitation must migrate to reach a center is reduced. This accounts for the shorter lifetimes at higher Cr^{3+} concentrations in Fig. 4. The temperature dependence of the relaxation time can arise from changes in the diffusion coefficient or from the increased probability of additional relaxation processes. As shown elsewhere, the predicted temperature dependence of the diffusion coefficient agrees with the observed lifetime behavior[9]. Thus the model for the nonradiative Eu^{3+}-to-Cr^{3+} energy transfer in $Eu(PO_3)_3$: Cr is one involving a combination of energy migration through the Eu^{3+} system and transfer to fast-relaxing Cr^{3+} ions which act as quenching centers.

Further experiments

Two series of additional measurements were made to study the process of energy transfer to Cr^{3+} impurities. In the first series, the room temperature excitation spectrum of the Cr^{3+} emission was recorded for samples containing 0·05, 0·1, 0·3 per cent Cr. It was found that the intensities of the Cr^{3+} excitation bands increased relative to those of the Eu^{3+} excitation bands with increasing Cr content. In the second series, the excitation spectrum of a 0·1 per cent Cr-doped sample was recorded at 77, 295, and 400°K[25]. In the latter experiment, it was found that the Eu^{3+} band intensities increased relative to the Cr^{3+} bands with increasing temperature.

The above results, together with the Eu^{3+} lifetime data in Fig. 4, are consistent with the hypothesis that the dominant Eu^{3+} relaxation in the samples studied occurs via Cr^{3+} impurities which act as quenching centers. To see this, consider a simplified model in which excited Eu^{3+} ions in the $^5D_0$ state decay at an intrinsic rate $1/\tau_0$, due to radiative and nonradiative processes, and at an effective transfer rate $1/\tau_T$ due to energy migration and transfer to Cr^{3+} impurities. Since both excited Eu^{3+} ions and excited Cr^{3+} ions decay rapidly to their metastable $^5D_0$ and $^4T_2$ levels, we can, for the present purposes, treat both ions as essentially two-level systems; that is, the effective transitions for Eu^{3+} are $^5D_0 \rightleftharpoons {}^7F$, and for Cr^{3+}, $^4T_2 \rightleftharpoons {}^4A_2$. The rate equations for the excited state populations n^*_{Cr} and n^*_{Eu} are

$$\frac{dn^*_{Cr}}{dt} = -\left(\frac{1}{\tau_{Cr}} + P_{Cr}\right)n^*_{Cr} + P_{Cr}n_{Cr} + \frac{1}{\tau_T}n^*_{Eu}, \qquad (4)$$

and

$$\frac{dn^*_{Eu}}{dt} = -\left(\frac{1}{\tau_0} + \frac{1}{\tau_T} + P_{Eu}\right)n^*_{Eu} + P_{Eu}n_{Eu}, \qquad (5)$$

where P_{Cr} and P_{Eu} are the optical pumping rates per ion. The intensity I of the Cr^{3+} fluorescence is proportional to the excited Cr^{3+} ion population. In a steady-state experiment, we have, from equations (4) and (5),

$$n^*_{Cr} = \frac{\tau_{Cr}P_{Cr}N_{Cr}}{1+\tau_{Cr}P_{Cr}} + \frac{\tau_{Cr}\tau_{Eu}P_{Eu}N_{Eu}}{\tau_T(1+\tau_{Cr}P_{Cr})(1+\tau_{Eu}P_{Eu})}.$$

For the usual limit of weak pumping (i.e., $\tau P \ll 1$),

$$n^*_{Cr} \approx \tau_{Cr}P_{Cr}N_{Cr} + \tau_{Cr}\tau_{Eu}P_{Eu}N_{Eu}/\tau_T. \qquad (7)$$

In equation (7), $1/\tau_{Eu} = 1/\tau_0 + 1/\tau_T$ and N_{Cr} and N_{Eu} are the total numbers of Cr^{3+} and Eu^{3+} ions, respectively.

We now examine two regions of the Cr^{3+} excitation spectrum: one at a frequency ν_1 where only Eu^{3+} ions are initially excited and therefore $P_{Cr}(\nu_1) = 0$, and a second at a frequency ν_2 where only Cr^{3+} ions are excited. The ratio of the Cr^{3+} fluorescence intensities for the two excitation bands is, from equation (7),

$$\frac{I(\nu_1)}{I(\nu_2)} = \frac{P_{Eu}(\nu_1)}{P_{Cr}(\nu_2)} \frac{N_{Eu}}{N_{Cr}} \frac{\tau_{Eu}}{\tau_T}. \tag{8}$$

The appearance of Eu^{3+} bands in the Cr^{3+} excitation spectrum requires, as expected, a finite transfer time τ_T. At the other extreme, if the $Eu^{3+} \rightarrow Cr^{3+}$ energy transfer is the predominant cause of Eu^{3+} relaxation, τ_{Eu} will be approximately equal to τ_T and the relaxation times drop out of equation (8). In this case the Cr^{3+} bands should increase relative to the Eu^{3+} bands in proportion to N_{Cr}, which is in qualitative agreement with the above observations.

The explicit change in the ratio in equation (8) with temperature is more difficult to predict because the P's and τ's may both vary with temperature. At high temperatures and high Cr concentrations, where $\tau_{Eu} \simeq \tau_T$, the largest change with temperature is probably the increase in the total pumping probability P_{Eu} as the $^7F_1$ and $^7F_2$ levels, with their larger absorption cross sections, become populated. Thus the simple model used here would also account qualitatively for the observed variations in the excitation spectrum with temperature.

Acknowledgements—The glass samples used in these experiments were prepared at the National Bureau of Standards by G. Cleek and D. Blackburn: we are very grateful to them for preparing the glasses and for measuring the density and refractive index. The experimental assistance of T. Varitimos throughout all phases of the spectroscopic measurements was especially appreciated.

REFERENCES

1. KURKJIAN C. R., GALLAGHER P. K., SINCLAIR W. R. and SIGETY E. A., *Phys. Chem. Glasses* **4**, 239 (1963).
2. GALLAGHER P. K., KURKJIAN C. R. and BRIDENBAUGH P. M., *Phys. Chem. Glasses* **6**, 95 (1965).
3. MACKAY J. H. and NAHUM J., *Phys. Chem. Glasses* **9**, 52 (1968).
4. VAN UITERT L. G. and IIDA S., *J. chem. Phys.* **37**, 986 (1962).
5. VAN UITERT L. G. and JOHNSON L. F., *J. chem. Phys.* **44**, 3514 (1966).
6. PEARSON A. D. and PETERSON G. E., *Appl. Phys. Lett.* **8**, 210 (1966).
7. PEARSON A. D., PETERSON G. E. and NORTHOVER W. R., *J. appl. Phys.* **37**, 729 (1966).
8. BLASSE G and BRIL A., *Phys. Status Solidi* **20**, 551 (1967).
9. WEBER M. J. *Phys. Rev. B* (in press).
10. RINDONE G. E. in *Luminescence of Inorganic Solids* (Edited by P. Goldberg), p. 419. Academic Press, New York (1966).
11. ROBINSON C. C. and FOURNIER J. T., *Chem Phys. Lett* **3**, 517 (1969).
12. ROBINSON C. C. and FOURNIER J. T., *J. chem. Phys. Solids* **31**, 895 (1970).
13. FOURNIER J. T. and BARTRAN R. H. *J. chem. Phys. Solids* **31**, 2615 (1970).
14. RINCK B., *Z. Naturforsch.* **3**, 406 (1948).
15. BLASSE G., *J. chem. Phys.* **46**, 2583 (1967).
16. BATES T and DOUGLAS R. W., *J. Soc. Glass Technol.* **43**, 289 (1959).
17. LANDRY R. J., FOURNIER J. T. and YOUNG C. G., *J. chem. Phys.* **46**, 1285 (1967).
18. TISCHER R. E., *J. chem. Phys.* **48**, 4291 (1968).
19. SHARP E. J., MILLER J. E. and WEBER M. J., *Phys. Lett* **30A**, 142 (1969).
20. GLASS A. M., *J. chem. Phys.* **50**, 1501 (1969) and references cited therein.
21. SCHLAFER H. L., GAUSMANN H. and WITZKE H., *J. chem. Phys.* **46**, 1423 (1967).
22. FOWLER W. B. and DEXTER D. L., *Phys. Rev.* **128**, 2154 (1962); *J. chem. Phys.* **43**, 1768 (1965).
23. BLASSE G. and BRIL A., *Phys. Lett.* **25A**, 29 (1967).
24. Nominal mole per cent Cr values are given.
25. The signal-to-noise ratio decreased rapidly at higher temperatures, thus making additional measurements impractical.

J. Phys. Chem. Solids, 1971, Vol. 32, pp. 2285–2300. Pergamon Press. Printed in Great Britain

THE MAGNETO-QUANTUM-ELECTRIC EFFECT*

W. SALANECK†, Y. SAWADA‡ and E. BURSTEIN

Department of Physics and Laboratory for Research on the Structure of Matter, University of Pennsylvania, Philadelphia, Penna. 19104, U.S.A.

(*Received* 27 *November* 1970; *in revised form* 8 *February* 1971)

Abstract—We report the results of an investigation of the magneto-quantum-electric effect associated with the absorption of phonons or photons by charge carriers (electrons or holes) in solid state plasmas in the presence of a static magnetic field $\mathbf{H}_0$. The effect is based on the lateral displacement (in a direction perpendicular to both $\mathbf{q}$ and $\mathbf{H}_0$) of the centers of the cyclotron orbits of the charge carriers upon absorption of quanta with a component of wave vector $\mathbf{q}$ in the plane of the real-space orbits. Simple theoretical arguments are used to show that: (a) for spherical energy surfaces, this displacement occurs for $\mathbf{q} \perp \mathbf{H}_0$ when quanta are absorbed in cyclotron ($\Delta n = \pm 1$) transitions, and (b) for ellipsoidal energy surfaces, the absorption of quanta leads to a displacement which is perpendicular to $\mathbf{q}$ and to the normal to the plane of the orbit in either cyclotron ($\Delta n = \pm 1$) or Landau ($\Delta n = 0$) transitions. In both cases, the lateral translation due to continuous quanta absorption constitutes a 'd.c.' current. This current sets up a surface charge density on the lateral boundaries of the sample, and thus, a d.c. electric field appears across the sample. A comparison is made of the *MQE* effect with several similar and/or related effects. The *MQE* fields associated with the giant-quantum-absorption of longitudinal phonons in bismuth are observed and are shown to be in excellent agreement with the predictions of the theory.

1. INTRODUCTION

We have investigated the magneto-quantum-electric (*MQE*) effect[1, 2], which is associated with the absorption of phonons or photons by electrons or holes in solid state plasmas under the influence of a static magnetic field $\mathbf{H}_0$. This *MQE* effect is based on the lateral displacement of the centers of the cyclotron orbits of charge carriers, in a direction perpendicular to both $\mathbf{q}$ and $\mathbf{H}_0$, upon absorption of quanta with a component of wave vector $\mathbf{q}$ in the plane of the real-space orbits. For spherical energy surfaces, the effect occurs in the Voigt configuration ($\mathbf{q} \perp \mathbf{H}_0$) when quanta are absorbed in cyclotron ($\Delta n = \pm 1$) transitions. In the ellipsoidal case, the effect occurs for both Voigt and Faraday ($\mathbf{q} // \mathbf{H}_0$) configurations and the absorption of quanta leads to a displacement which is perpendicular to $\mathbf{q}$ and to the normal to the plane of the orbit in either cyclotron ($\Delta n = \pm 1$) or Landau ($\Delta n = 0$) transitions. In both cases, the lateral translation due to the continuous absorption of quanta constitutes a 'd.c. current'. In a sample of finite size, this current sets up a surface charge density Σ on the lateral boundaries, and thus a d.c. electric field, $E^{MQ} = 4\pi\Sigma$ (hereafter designated as the Magneto-Quantum-Electric (*MQE*) field) appears across the sample.

Presented here are the theoretical foundations of the *MQE* effect, comparisons with other similar and/or related effects, and the observation of *MQE* fields associated with the $\Delta n = 0$ giant-quantum-attenuation (*GQA*) of longitudinal sound waves in bismuth. Transverse fields associated with the Hall effect of the acousto-electric current accompanying lower frequency sound waves in bismuth have been observed as a somewhat similar configuration by Yamada[3, 4]. The differences between this acousto-magneto-electric (*AME*) effect and the *MQE* effects are also discussed.

---

*Work supported in part by the Advanced Research Projects Agency and the U.S. Office of Naval Research.

†Present Address: Xerox Corporation, Research Laboratories Department, Rochester, New York 14603, U.S.A.

‡Present Address: Osaka University, Physics Department, Osaka, Japan.

2. THEORY

In solid state plasmas, the interaction of electrons and holes with a flux of photons or phonons (quanta) takes place via the electric field of the photons or, in the case of phonons via the electric field associated with induction effects (metals and semimetals), deformation potentials (semimetals and semiconductors), and/or piezoelectric effects (semiconductors). When the mean-free-path of the carriers l is large such that $ql > 1$, the interaction of the carriers with the quanta of frequency ω and wave vector $\mathbf{q}$ can be viewed in terms of elementary processes in which photons and phonons are absorbed as quanta with well defined energy $\hbar\omega$ and momenta $\hbar\mathbf{q}$ and the carriers are excited from an initial state $\epsilon_n(\mathbf{k})$ to a final state $\epsilon'_n(\mathbf{k}')$, with $\epsilon'_n - \epsilon_n = \hbar\omega$ and $\mathbf{k}' - \mathbf{k} = \mathbf{q}$. The interaction of the plasma with a flux of quanta is studied either by observing the attenuation of the flux or by observing the changes in the constants of the motion of the system in the presence of the flux. The latter corresponds to observable changes in transport phenomena uniquely related to the quanta-plasma interactions.

In the standard semiclassical approach, the flux is represented by a vector-potential $\mathbf{A}(\omega, \mathbf{q})$. The associated fields are given by $\mathbf{E}(\omega, \mathbf{q}) = (i/c)\partial\mathbf{A}(\omega, \mathbf{q})/\partial t$ and $\mathbf{H}(\omega, \mathbf{q}) = \nabla \times \mathbf{A}(\omega, \mathbf{q})$. For a plane propagating wave of frequency ω and wave vector $\mathbf{q}$.

$$\mathbf{A}(\omega, \mathbf{k}) = \mathbf{A} \exp\left[i(\mathbf{q} \cdot \mathbf{r} - \omega t)\right], \tag{1}$$

where $\mathbf{A}$ represents the magnitude and polarization direction of the wave. The Hamiltonian for the single-particle energy states of the plasma is written as

$$\mathscr{H}_0 = \frac{\hbar^2}{2m_0} \mathbf{k} \cdot \boldsymbol{\alpha} \cdot \mathbf{k} \tag{2}$$

where $\boldsymbol{\alpha}$ is the inverse mass tensor in units of the free electron mass m_0.

Spherical energy surfaces

In the simple case of spherical energy surfaces, the inverse mass tensor is diagonal with all non-zero components equal to some α_0. The Hamiltonian and the wavefunctions are given by

$$\begin{gathered} \mathscr{H}_0 = \frac{\hbar^2}{2m^*} \mathbf{k} \cdot \mathbf{k} \\ \psi_j = F_j(\mathbf{r}) U_j(\mathbf{r}) = \exp\left[i(\mathbf{k} \cdot \mathbf{r})\right] U_j(\mathbf{r}) \end{gathered} \tag{3}$$

where the effective mass is $m^* = m_0/\alpha_0$, and $U_j(\mathbf{r})$ is the Bloch function of the jth energy band. $F_j(\mathbf{r}) = \exp\left[i(\mathbf{k} \cdot \mathbf{r})\right]$ is the free electron wavefunction. The constants of the motion, those quantities that commute with the Hamiltonian, are $\mathscr{H}_0$ itself, and the 'momentum' components k_x, k_y and k_z. In the presence of flux of quanta, the Hamiltonian takes the form

$$\mathscr{H} = \frac{1}{2m^*}\left[\hbar\mathbf{k} + \frac{e}{c}\mathbf{A}\right] \cdot \left[\hbar\mathbf{k} + \frac{e}{c}\mathbf{A}\right] \tag{4}$$

for a carrier charge $-e$. With propagation in the z-direction ($\mathbf{q} // \mathbf{z}$), and to terms of first order in $\mathbf{A}$, the Hamiltonian can be expressed in the form $\mathscr{H} = \mathscr{H}_0 + \mathscr{H}'$ where

$$\begin{gathered} \mathscr{H}' = \mathscr{H}_1 \exp\left[i(qz - \omega t)\right] \text{ and} \\ \mathscr{H}_1 = \frac{e\hbar}{m^* c} \mathbf{A} \cdot \mathbf{k}. \end{gathered} \tag{5}$$

In the presence of the flux, $\mathscr{H}_0$ and the components of $\mathbf{k}$ are no longer constants of the motion. The time rates of change of these quantities are obtained from the commutator with the Hamiltonian

$$\begin{gathered} \dot{\mathscr{H}}_0 = i\hbar k \equiv \hbar q \mathscr{H}'/m^* \text{ and} \\ \dot{k} = (0, 0, i\hbar q \mathscr{H}'). \end{gathered} \tag{6}$$

The expectation value of the operator $\dot{\mathscr{H}}_0$ is the quantity $d\epsilon/dt$ and is given by

$$\langle \dot{\mathscr{H}}_0 \rangle = w \cdot \Delta\epsilon, \tag{7}$$

where w is the rate at which quanta are absorbed and $\Delta\epsilon = \epsilon'_n(\mathbf{k}') - \epsilon_n(\mathbf{k}) = \hbar\omega = \hbar q k_z/m^*$ is the energy change of the electron upon absorption of a quantum of frequency ω wave vector $\mathbf{q}$. The expectation value of the momentum is similarly given by

$$\langle \dot{k}_z \rangle = dk_z/dt = w \cdot q. \tag{8}$$

The rate of quanta absorption, w, is given by the 'golden rule',

$$w = \frac{2\pi}{\hbar} \sum_{nn'} |\langle n|\mathscr{H}_1|n'\rangle|^2 \{f(\epsilon_n) - f(\epsilon_{n'})\} \times \delta(\epsilon_n - \epsilon_{n'} - \hbar\omega) \tag{9}$$

where $f(\epsilon_n)$ and $f(\epsilon_{n'})$ are the Fermi functions for the initial and final states of the electrons. This energy transfer corresponds to an acoustoelectric effect[5,6] in the case of a phonon flux, and a radiation pressure effect in the case of photons.

When a static magnetic field, $\mathbf{H}_0$, is applied to the system, the situation is slightly different. The conduction electron energy states are quantized into Landau sub-bands labeled by the quantum number n. Upon the absorption of a quantum of energy $\hbar\omega$ and momentum $\hbar\mathbf{q}$, an electron makes a transition from an energy state $\epsilon_n(\mathbf{k})$ to state $\epsilon_{n'}(\mathbf{k}')$ and experiences a change in momentum $\Delta\mathbf{k} = \mathbf{k}' - \mathbf{k} = \mathbf{q}$. The Hamiltonian, in the presence of the magnetic field, becomes

$$\mathscr{H}_0 = \frac{1}{2m^*} \boldsymbol{\pi} \cdot \boldsymbol{\pi} \tag{10}$$

where $\boldsymbol{\pi} = \hbar\mathbf{k} + (e/c)\mathbf{A}_0$ is the kinetic momentum[7] for a carrier of negative charge and $\mathbf{A}_0$ is defined by $\mathbf{H}_0 = \nabla \times \mathbf{A}_0$. The components of $\boldsymbol{\pi}$ obey the commutation rule

$$(\boldsymbol{\pi} \times \boldsymbol{\pi})\, \zeta = -(ie\hbar\mathbf{H}_0/c)\, \zeta \tag{11}$$

where ζ is any scalar function.

With $\mathbf{H}_0 // \mathbf{y}$, i.e., the Voigt configuration, $\mathbf{H}_0 \perp \mathbf{q}$, constants of the motion are the Hamiltonian itself and the quantities

$$\begin{aligned} X_0 &= x + \pi_z/m^*\omega_c \\ Z_0 &= z - \pi_x/m^*\omega_c \text{ and} \\ \pi_y &= \hbar k_y \end{aligned} \tag{12}$$

where $\omega_c = eH_0/(m^*c)$ is the cyclotron frequency. The (X_0, Z_0) are the coordinates of the center of the cyclotron orbit of the electron. In the presence of a flux of quanta, the time rate of change of $\mathscr{H}_0$, X_0, Z_0 and k_y is given by

$$\begin{aligned} \dot{\mathscr{H}}_0 &= i\hbar k_z q \mathscr{H}'/m^* \\ \dot{X}_0 &= icq\mathscr{H}'/(eH_0) = (i\mathscr{H}'/\hbar)\delta X_0 \\ \dot{Z}_0 &= 0 \\ \dot{k}_y &= q \end{aligned} \tag{13}$$

where $\delta X_0 = \hbar qc/(eH_0)$ is the change in the x-coordinate of the center of the cyclotron orbit of the carrier. This displacement is proportional to the quantum of momentum $\Delta\mathbf{k} = \mathbf{q}$ absorbed by the electron.

The equations (12) and (13) are gauge independent. Dropping the band index j from equation (3), the wave functions have the general form

$$\psi_n(\mathbf{r}) = F_n(\mathbf{r}) U_n(\mathbf{r}), \tag{14}$$

where the index n now labels the Landau sub-bands of the band j. In the Landau assymmetric gauge, $\mathbf{A}_0 = (0, 0, -H_0 x)$, the electron wave functions, $F_n(\mathbf{r})$, are product wavefunctions of plane waves of y- and z-arguments, and a one dimensional simple-harmonic-oscillator wavefunction, H_n, of argument $x - X_0$. The wavefunctions are given by

$$F_n(\mathbf{r}) = \exp\,[i(k_y y + k_z z - \omega t)]\, H_n(x - X_0) \tag{15}$$

Thus, the X_0 appears explicitly in $F_n(\mathbf{r})$, and is given by $X_0 = c\hbar k_z/(eH_0)$. It is then obvious that the carrier absorbs momentum in the z-direction of an amount $\Delta k_z = q$, the orbit shift is $\delta X_0 = c\hbar q/(eH_0)$. In the other assymetric gauge, $\mathbf{A}_0 = (H_0 x, 0, 0)$, the $Z_0 = -c\hbar k_x/(eH_0)$ appears explicitly in $H_n(\mathbf{r})$. In this latter case, it can be seen explicitly how a change of momentum in the x-direction by an amount $\Delta k_x = q$ results in an orbit shift in the z-direction by an amount $\delta Z_0 = c\hbar q/(eH_0)$. The δX_0 and δZ_0 can be computed, however, for any arbitrary gauge as illustrated in the preceeding paragraphs.

If a dipole moment operator is defined by $\boldsymbol{\mu} = e\mathbf{r}_0$, where $\mathbf{r}_0$ is the position vector of the center of the cyclotron orbit, then the components of the time derivative of $\boldsymbol{\mu}$ correspond to a 'polarization current' $\mathbf{J}^p = N\dot{\boldsymbol{\mu}}$ where N is the density of carriers. From equation (13)

$$J_z^p = N\langle\dot{\mu}_z\rangle = 0, \text{ and}$$
$$J_x^p = N\langle\dot{\mu}_x\rangle = Ne\langle\delta\dot{X}_0\rangle = New\delta X_0. \qquad (16)$$

Thus in the Voigt ($\mathbf{q} \perp \mathbf{H}_0$) configuration, when quanta are absorbed continuously in $\Delta n = \pm 1$ (cyclotron) transitions[8], such that energy and momentum are conserved, the lateral displacement of the center of the orbit constitutes a current which flows in a direction mutually perpendicular to $\mathbf{q}$ and $\mathbf{H}_0$ as illustrated in Fig. 1. In the Faraday configuration ($\mathbf{q} // \mathbf{H}_0 // y$), on the other hand, neither $\Delta n = 0$ transitions (which can be induced by longitudinal phonons) nor $\Delta n = \pm 1$ transition (which can be induced by photons or transverse phonons) leads to an orbit shift when the energy surface is spherical, i.e., X_0 (and Z_0) are independent of the change in the component of the momentum of the electron. Such transitions do, however, lead to orbit shifts in the Faraday configuration when the energy lands are ellipsoidal.

For a plasma of N electrons/cm^3 and a quanta flux of ϕ cm^{-2} sec^{-1}, the attenuation constant is given by $\Gamma = Nw/\phi$, and the *MQE* polarization current density corresponding to equations (16) is

$$J_x^p = N\langle\dot{\mu}_x\rangle = \Gamma\phi c\hbar q/H_0. \qquad (17)$$

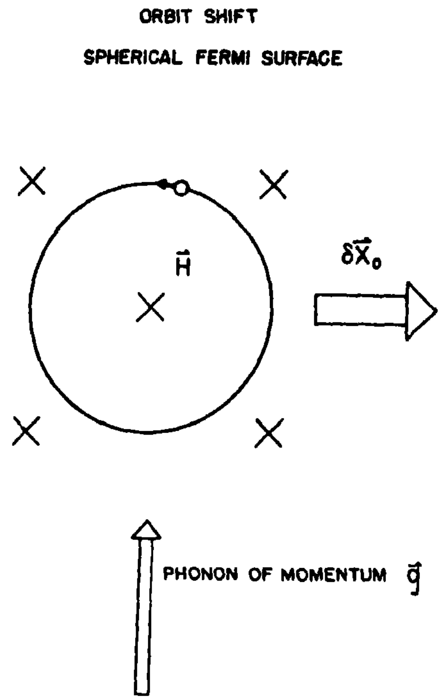

Fig. 1. Orbit shift for spherical energy surfaces. The direction of the magnetic field is into the paper and $\delta\mathbf{X}_0$ is perpendicular to both $\mathbf{q}$ and $\mathbf{H}_0$.

It is conceptually important at this point to notice some of the simularities of the *MQE* effect with the photoemission of electrons from a solid (photoelectric, *PE*, effect). When an electron in a solid absorbs a photon of energy $\hbar\omega$ such that $\hbar\omega > \Phi$, where Φ is the work function of the material, the electron can be 'photo-emitted' from the solid. Because of the quantum properties of the incident radiation, the following four characteristics of the emission are observed: (1) the photoelectric current, $\mathbf{J}^{PE}$, is proportional to the intensity of the radiation (number of photons/sec), (2) photoemission occurs even for very low photon intensity, so long as the photon energy is larger than the work function ($\hbar\omega > \Phi$) (3) the maximum energy of the emitted electrons is independent of the intensity and (4) the maximum energy after emission is proportional to the energy of the photon, $\hbar\omega$.

The *MQE* polarization current, $\mathbf{J}^P$, has four analogous characteristics because of the quantum properties of the wave vector $\mathbf{q}$ associated with a normal vibrational mode of the crystal lattice: (1) The *MQE* current, $\mathbf{J}^P$, is proportional to the phonon flux ϕ, (the number of phonons per cm^2 per sec), (2) the orbit translation occurs even for low acoustic intensity, (3) the magnitude of δX_0 is independent of the acoustic intensity, and (4) the magnitude of δX_0 is proportional to the wave vector $\mathbf{q}$ associated with the phonon. The *MQE* effect depends upon the discrete amount of momentum, $\hbar\mathbf{q}$, carried by the acoustic wave just as the *PE* effect depends upon discrete amount of energy, $\hbar\omega$, of the electromagnetic wave. Also, as implied above, there exists an energy threshold for the *PE* effect but not for the *MQE* effect. However, an observational threshold for the *MQE* effect is that $ql > 1$. Although individual photons (or rather photo-excited electrons) can be detected in the *PE* effect, individual phonons in the *MQE* effect cannot. In principle, individual orbit shifts occur, but only the d.c. fields associated with continuous phonon absorption are detected.

Ellipsoidal energy surfaces

When ellipsoidal energy surfaces are involved, the situation is slightly more complex. These effects are illustrated by considering an energy ellipsoid with only one principle axis coincident with the x, y, z coordinate system. With the x-direction coincident with one principle axis of the ellipsoid and the other two principle axes rotated by an angle θ in the y-z plane, the off diagonal components of the inverse mass tensor reduce to $\alpha_{xy} = \alpha_{zx} = \alpha_{xz} = \alpha_{yx} = 0$ and $\alpha_{yz} = \alpha_{zy} \neq 0$. Equation (2) becomes

$$\mathscr{H} = \hbar^2(\alpha_{xx}k_x{}^2 + \alpha_{yy}k_y{}^2 + \alpha_{zz}k_z{}^2 + 2\alpha_{yz}k_yk_z)/(2m_0). \quad (18)$$

With a magnetic field in the y-direction ($\mathbf{H}_0 // \mathbf{y}$), the constants of the motion are $\mathscr{H}_0$ and

$$X_0 = x + \pi_z/(m_c^* \omega_c),$$
$$Z_0 = z - \pi_x/(m_c^* \omega_c), \text{ and} \quad (19)$$
$$\pi_y = \hbar k_y$$

where the effective cyclotron mass is $m_c^* = (\hbar^2/2\pi)\partial a_\perp/\partial\epsilon$ and $a_\perp$ is the ellipsoid cross-sectional area perpendicular to the magnetic field. Using the assymetric gauge $\mathbf{A}_0 = (0, 0, -H_0x)$ for simplicity, the first of equations (19) becomes

$$X_0 = (k_z + k_y a_{yz}/\alpha_{zz})\hbar c/(eH_0). \quad (20)$$

The wavefunctions in the presence of $\mathbf{H}_0$ are again given by

$$\psi_n(\mathbf{r}) = \exp[i(k_y y + k_z z)]\, H_n(x - X_0) U_n(\mathbf{r}). \quad (21)$$

As in the spherical case, absorption of quanta of wave vector $\mathbf{q} // \mathbf{z}$ (Voigt configuration) leads to a change in the x-coordinate of the center of the cyclotron orbit by an amount $\delta X_0 = c\hbar q/(eH_0)$. However, in this ellipsoidal case, absorption of quanta with $\mathbf{q} // \mathbf{H}_0 // \mathbf{y}$ also results in an orbit displacement as illustrated in Fig. 2. The magnitude of the displacement is

$$\delta X_0 = c\hbar q \alpha_{yz}/(\alpha_{zz} e H_0) \quad (22)$$

and is proportional to the off-diagonal terms of the inverse tensor. This result indicates that the magnitude of δX_0 depends upon the 'tilt' of the principle axis with respect to the magnetic field. As in the spherical case, the corresponding polarization current density is given by $J_x{}^P = e\Gamma\phi\delta X_0$.

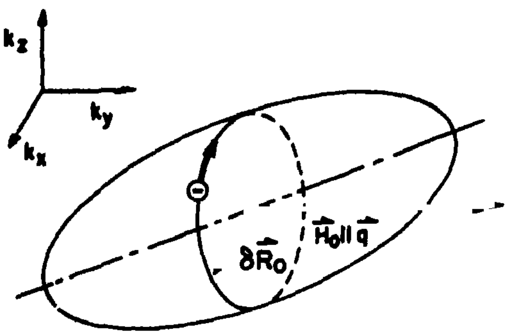

Fig. 2. Orbit shift for ellipsoidal energy surfaces. The shift is always in a direction perpendicular to both the magnetic field direction and the quantum propagation direction. When $\mathbf{H}_0 // \mathbf{q}$, the magnitude of the orbit shift depends upon the angle between $\mathbf{H}_0$ and the principle axes of the ellipsoid.

Selection rules

The selection rules governing the nature of the transitions for each configuration can be determined by considering the initial state wavefunctions $|n\rangle = \psi_n(\mathbf{r})$ and the final state wavefunctions

$$\psi_n(\mathbf{r}+\delta\mathbf{r}_0) = \psi_n(\mathbf{r}) + 2n\lambda\delta\mathbf{r}_0\psi_{n-1}(\mathbf{r}), \quad (23)$$

where $\lambda = (m^*\omega_c/\hbar)^{1/2}$ and $H_n(x)$ is the nth Hermite polynomial of argument λx. The gauge $\mathbf{A}_0 = (0, 0, -H_0 x)$ is used. From ordinary time-dependent perturbation theory [9]

$$\psi_n(\mathbf{r}, t) = a(t)\psi_n(\mathbf{r}) + \sum_{n'} b_{nn'}(t) \times \exp(-i\omega_{nn'}t)\psi_n(\mathbf{r}+\delta\mathbf{r}_0) \quad (24)$$

where $\omega_{nn'} = \hbar^{-1}(\epsilon_{n'} - \epsilon_n)$. Under the condition $\omega_c\tau > 1$, where τ^{-1} is an effective collision frequency of the carriers, transitions occur only for $\omega \sim \omega_{nn'}$, and the 'polarization current' corresponds to

$$\begin{aligned}\langle\dot{\boldsymbol{\mu}}\rangle = i\frac{cq}{H_0}\sum_{nn'}\{&\langle n|\mathscr{H}'(t)|n\rangle \\ &+ \langle n|\mathscr{H}'(t)|n'\rangle\, b_{nn'}(t)\exp(-i\omega_{nn'}t) \quad (25)\\ &+ \langle n'|\mathscr{H}'(t)|n\rangle\, b^*_{nn'}(t)\exp(i\omega_{nn'}t) + \cdots\}.\end{aligned}$$

The first term on the right in equation (25) corresponds to Landau ($\Delta n = 0$) transitions and is nonzero in the Faraday ($\mathbf{q} // \mathbf{H}_0$) configuration only for quanta with longitudinal field as in Longitudinal acoustic phonons. The second and third terms correspond to cyclotron ($\Delta n = \pm 1$) transitions which occur for transverse polarization for photons and transverse polarized phonons in both the Faraday and Voigt configurations. The interaction Hamiltonian $\mathscr{H}'(t)$ yields nonzero matrix elements connecting the states n and n' only for particular relationships among the phonon (or photon) polarization, Fermi surface geometry and direction of the applied magnetic field as discussed above[10].

In order that the energy associated with the quanta flux be absorbed as an elementary excitation, the Landau sub-band separation must be large compared with the collision broadening of the levels. This condition can be written as $\omega_c\tau > 1$. It is also necessary that the magnitude of the displacement δX_0 be larger than the uncertainty in the position of the orbit. This restriction leads to the condition $ql > 1$, where l is the mean-free-path of the electron. This is just the condition that the electron feel several oscillations of the wave before being scattered.

The magneto-quantum-electric field

In the presence of a flux of quanta, ϕ, (cm^{-2} sec^{-1}), the lateral displacements δX_0, of the center of the cyclotron orbits of the carriers, which results from the continuous absorption of quanta, leads to a polarization current density,

$$J^P = Nwe\,\delta X_0 = \Gamma\phi c\hbar q/H_0, \quad (26)$$

where Γ(cm^{-1}) is the attenuation constant. When the flux fills the volume of the sample, in the form of a parallelopiped, the lateral displacements of the carriers sets up a polarization surface charge density, Σ, on the surfaces whose normals have a component parallel to δX_0. The corresponding electric field which appears across the sample between these surfaces, $E = 4\pi\Sigma$, is the magneto-quantum-electric (*MQE*) field, $\mathbf{E}^{MQ}$. The free carriers not participating in the quanta absorption are also subject to the influence of $\mathbf{E}^{MQ}$, setting up a 'screening' current of opposite sign to that of the orbital displacement 'polarization' current, $\mathbf{J}^P$. This screening current, $\mathbf{J}^S$, leads to a decrease in the net surface charge density. $\mathbf{J}^S$ is itself acted on by the external static magnetic field, $\mathbf{H}_0$, in such a way as to set up a Hall current in a direction perpendicular to both $\delta\mathbf{X}_0$ and $\mathbf{H}_0$. In an open circuit condition, no net flow occurs into or out of the crystal. Accordingly $\mathbf{J}^P + \mathbf{J}^S = 0$.

Consider the simple case of spherical energy surfaces with $\mathbf{H}_0$ in the y-direction and the flux of quanta propagating in the z-direction. Under these conditions, the displacement of the cyclotron orbits are along $\hat{x}$ and $J_x{}^P = -J_x{}^S$, while $J_y{}^P = J_z{}^P = J_y{}^S = 0$. The electric fields which are set up by these displacements are given by

$$\begin{aligned} E_x &= \rho_{xx} J_x{}^P = -\rho_{xx} J_x{}^S \\ E_y &= 0 \\ E_z &= -\rho_{zx} J_x{}^P = \rho_{zx} J_x{}^S \end{aligned} \tag{27}$$

where $\rho_{xx} = \rho_{yy} = \rho_{zz}$ and $\rho_{xz} = \rho_{zx}$ are the nonzero components of the magnetic field dependent resistivity tensor. The E_x is the *MQE* field, E^{MQ}. The E_z is the Hall field, $E^{MQ,H}$, which is set up by the action of $\mathbf{H}_0$ on the screening current, $\mathbf{J}^S$. Using the expression for $J_x{}^P$ from equation (17) and setting $S = \hbar\omega\phi$, the energy flux of the quanta, the fields, in the case of an electron plasma, are given by

$$\begin{aligned} E_x &= E^{MQ} = -\rho_{xx}\frac{cq\Gamma S}{H_0\omega} \\ E_z &= E^{MQ,H} = \rho_{zx}\frac{cq\Gamma S}{H_0\omega}. \end{aligned} \tag{28}$$

The ratio of the magnitudes of the *MQE* field to the *MQ,H* (Hall) field is given by $E^{MQ}/E^{MQ,H} = \rho_{xx}/\rho_{zx}$. The magnitude of ρ_{xx} (and therefore E^{MQ}) will depend upon whether the plasma is compensated or uncompensated. The magnitude of ρ_{zx} (and therefore $E^{MQ,H}$), however, will not depend upon whether or not the plasma is compensated. Under quanta absorption conditions, $E^{MQ,H}$ is proportional to $\omega_c\tau$ for both compensated and uncompensated plasmas. $\omega_c = eH_0/m_c^*$ is the cyclotron frequency and τ^{-1} is some effective scattering frequency of carriers at the Fermi energy. In the case of an uncompensated plasma, ρ_{xx} (and E^{MQ}) will be proportional to $(\omega_c\tau)^2$. Thus E^{MQ} will be larger than $E^{MQ,H}$ by a factor of $\omega_c\tau$. Accordingly, in solids with uncompensated plasmas, it will be advantageous to measure $E^{MQ,H}$, and in solids with compensated plasmas, it will be more advantageous to measure E^{MQ}. The $\omega_c\tau$ dependence of the various ρ_{ij} are discussed in more detail in Section 3.

In the case of ellipsoidal energy bands, the absorption of quanta in the Voigt configuration ($\mathbf{q}\,//\,\mathbf{z}$ and $\mathbf{H}_0\,//\,\mathbf{y}$) leads to an 'orbit displacement' polarization current similar to that for spherical energy surfaces. The expressions for E^{MQ} and $E^{MQ,H}$ given in equation (28) is therefore also applicable in the Voigt configuration.

The absorption of quanta in the Faraday configuration ($\mathbf{H}_0\,//\,\mathbf{q}\,//\,\mathbf{y}$), when the principle axes of the ellipsoidal energy surface are tilted with respect to the magnetic field direction, also leads to an 'orbit displacement' polarization current. For the case when the principle axes are tilted in the y-z plane about the x-axis, the cyclotron orbits are displaced along $\hat{x}$. The orbit displacement polarization current, the *MQE* field, and the *MQH* field are given by

$$J_x{}^P = Nwe\,\delta X_0 = \frac{cq\Gamma S}{H_0}\left(\frac{\alpha_{yz}}{\alpha_{zz}}\right)\rho_{xx}$$

$$E^{MQ} = E_x = -\frac{cq\Gamma S}{H_0\omega}\left(\rho_{xx}\frac{\alpha_{yz}}{\alpha_{zz}}\right)$$

$$E^{MQ,H} = E_z = \frac{cq\Gamma S}{H_0\omega}\left(\rho_{zx} \frac{\alpha_{yz}}{\alpha_{zz}}\right). \tag{29}$$

The ratio of E^{MQ} to $E^{MQ,H}$ is again equal to ρ_{xx}/ρ_{zx}.

3. COMPARISON WITH OTHER EFFECTS

Acoustoelectric and optoelectric effects

Acoustic (A) waves and electromagnetic waves (photons) also produce other effects in solid state plasmas. The propagation of A waves sets up a longitudinal acousto-electric (AE) current[5, 6] and the corresponding propagation of electromagnetic waves sets up a longitudinal radiation pressure or optoelectric (OE) current. Under 'open circuit conditions', these currents lead to the accumulation of surface charges at the front and back faces of the sample and thereby lead to longitudinal electric fields. In addition, in the presence of a transverse magnetic field ($\mathbf{H}_0 \perp \mathbf{q}$), the longitudinal AE and OE currents lead to Hall fields in a direction transverse to both that of the wave and the magnetic field. The Hall field of the AE current is known as the Acousto-Magneto-Electric (AME) effect. Yamada has observed[3] 'oscillations' in the AME fields in bismuth. These oscillations were not observed under quanta absorption conditions and were caused by magnetic field dependent oscillations in the collision frequency, τ, of carriers at the Fermi surface as discussed in Section 4. In the specific case of ellipsoidal energy bands where principle axes are tilted relative to $\mathbf{q}$, the AE and OE currents can also exhibit a Planar Hall Effect[11].

Under the conditions $ql \ll 1$ and $\mathbf{H}_0 = 0$, AE and OE effects can only be observed in materials with uncompensated plasmas. Under the above conditions, the electrons and holes are moved in the same direction and their effects cancel in compensated materials. In the presence of a transverse magnetic field, however, both compensated and uncompensated plasmas will exhibit AE and OE fields.

When $ql \gg 1$ and $\mathbf{H}_0 \neq 0$, the situation is different. Under these conditions, the energy and momentum conservation relations for the absorption of quanta by the carriers are only satisfied for certain discrete values of the magnetic field strength. Since, in general, there is a different discrete set of values for electrons and for holes, the longitudinal AE and OE effects can also occur in materials with compensated plasmas.

As shown by Weinreich[6], the longitudinal AE field, $\mathbf{E}^{AE}$, set up by a flux of phonons propagating in the z-direction is given by

$$E^{AE} = \Gamma \frac{Sq}{Ne}. \tag{30}$$

A similar expression holds for the OE field. From equations (28) and (30) it is evident that the ratio of the MQE field and the AE field is

$$E^{MQ}/E^{AE} = Nec\,\rho_{xx}/H_0. \tag{31}$$

In the case of uncompensated plasmas, $Nec/H_0 \approx 1/\rho_{xz}$, and therefore the ratio of the fields is approximately equal to ρ_{xx}/ρ_{xz}.

For the ellipsoidal energy surface with the principle axes tilted in the y-z plane, and under the conditions $\mathbf{q} // \mathbf{H}_0 // \mathbf{y}$ and $ql \gg 1$, the fields are given in general, by

$$\begin{aligned} E_x &= \rho_{xx}J_x{}^{MQ} + \rho_{xy}J_y{}^{AE} + \rho_{xz}J_z, \\ E_y &= \rho_{yx}J_x{}^{MQ} + \rho_{yy}J_y{}^{AE} + \rho_{yz}J_z \quad \text{and} \\ E_z &= \rho_{zx}J_x{}^{MQ} + \rho_{zy}J_y{}^{AE} + \rho_{zz}J_z. \end{aligned} \tag{32}$$

The currents are given by $J_z = 0$, $J_y = J^{AE}$ and $J_x = -J_x{}^P = J^S$. The components of the magnetic field dependent resistivity tensor refer to the entire compensated plasma and can be written as

$$\rho_{xx} = \rho_{xx}^0 + \rho_{xx}^1(\omega_c{}^2\tau^2) \tag{33a}$$

$$\rho_{xy} = \rho_{xx}(\omega_c\tau) \tag{33b}$$

$$\rho_{yy} = \rho^{0}_{yy} + \rho^{1}_{yy}(\omega_c{}^2\tau^2) \tag{33c}$$

$$\rho_{zy} = \rho^{0}_{zy} + \rho^{1}_{zy}(\omega_c{}^2\tau^2) \tag{33d}$$

$$\rho_{zx} = \rho_{zx}(\omega_c\tau) \tag{33e}$$

where again $\omega_c = eH_0/m_c^*$ is the cyclotron frequency and τ^{-1} is some effective scattering frequency of carriers at the Fermi energy. Component (33b) corresponds to the Hall field of the *AE* current when $\mathbf{H}_0$ has a nonzero component in the *x*-direction. Component (33d) is due to crystal anisotropy, and component (33e) corresponds to the Hall field of the screening current $J_x{}^S$. For spherical energy surfaces in the Faraday configuration ($\mathbf{q}\,//\,\mathbf{H}_0\,//\,\mathbf{y}$) these equations reduce to $J_y = J^{AE}$ and $\rho_{yy} = \rho_{xy} = \rho_{zy} = 0$. There is no *MQE* effect. For the Voigt configuration ($\mathbf{q}\,//\,\mathbf{y}, \mathbf{H}_0\,//\,\mathbf{z}$), however, $J^{MQ} = J_x \neq 0$ and $J^{AE} = J_y \neq 0$. The only nonzero off-diagonal components of the resistivity tensor and $\rho_{xy} = \rho_{yx}$ and

$$\begin{aligned} E_x &= \rho_{xx}J_x{}^{MQ} + \rho_{xy}J^{AE} \\ E_y &= \rho_{yx}J_x{}^{MQ} + \rho_{yy}J^{AE} \\ E_z &= 0. \end{aligned} \tag{34}$$

The Hall effect of the *AE* current competes with the *MQE* current in the *x*-direction and the Hall effect of the screening current of J^{MQ} competes with the *AE* field in the quanta propagation direction, $\hat{y}$.

Phonon generation and amplification

The flux of phonons as a function of distance travelled in the material is related to the attenuation constant, Γ, such that $\phi(x) = \phi(0)\exp(-\Gamma x)$. Thus far this attenuation constant has been assumed to be electric field independent. Acoustic flux amplification can, however, take place in crossed electric and magnetic fields[12]. This amplification corresponds to an electric field dependent $\Gamma(E)$. When $\Gamma(E) < 0$, the flux density grows with increasing *x*. The electric field dependent attenuation constant can be derived[13] by incorporating the appropriate field dependent wave functions into equation (9).

$$\Gamma(E) = \Gamma(0)\{1 - E/E^c\} \tag{35}$$

where the critical field is $E^c = \omega H_0/(qc)$. For $E > E^c$ the drift applied to the electrons shifts the population in momentum space such that phonon emission is more probable than phonon absorption[14]. Thus, the influence of the *MQE* field on the attenuation constant must be considered in the derivation of equation (28). Equation (35) must be solved simultaneously with equation (28) for the *MQE* field.

$$E^{MQ} = \rho_{xx}\Gamma(E^{MQ})\frac{qcS}{H_0\omega}. \tag{36}$$

The self consistant field and attenuation constant are then given by

$$\begin{aligned} E^{MQ} &= \frac{\beta}{(1+\beta)}E^c \text{ and} \\ \Gamma(E^{MQ}) &= \frac{1}{(1+\beta)}\Gamma(0) \end{aligned} \tag{37}$$

where $\beta = S\Gamma(0)\,(cq/H_0\omega)^2\rho_{xx}$ is a nonlinear (in H_0) parameter. For $\beta \gg 1$, the *MQE* field is on the order of the critical field, but can never be larger than E^c. In this case the attenuation constant is small compared to its zero-field value, $\Gamma(E) = \beta^{-1}\Gamma(0)$. For $\beta \ll 1$, however, the *MQE* field is small compared to the critical field, but the attenuation constant assumes its zero-field value, $\Gamma(E) = \Gamma(0)$.

It should be noted here that the *MQE* effect has a counter part in what is sometimes called the Esaki 'kink' effect[15]. Whereas in the *MQE* effect, the quanta-absorption-induced displacement of the centers of the cyclotron orbits of charge carriers results in an electric field appearing across a sample of finite size, the Esaki 'kink' effect corresponds to induced phonon emission such that energy and momentum are conserved when the translation of the centers of the cyclotron orbits of charge carriers is caused by the application of an external d.c. electric field. With an external magnetic field $\mathbf{H}_0$ in the y-direction, an applied electric field in the x-direction, $\mathbf{E}^{EX}$, will add an electrostatic energy term, exE^{EX}, to the Hamiltonian equation (10). Then the energy absorbed by an electron in going from at state $\epsilon_n(\mathbf{k})$ to $\epsilon_n(\mathbf{k}')$ is $\Delta\epsilon = \epsilon_n(\mathbf{k}) - \epsilon_n(\mathbf{k}')$ and is given by

$$\Delta\epsilon = \hbar\omega - eE^{EX}\,\delta X_0 \qquad (38)$$

where δX_0 is again equal to $c\hbar q/(eH_0)$. Setting $\Delta\epsilon = 0$ defines the critical external electric field, $E^c = v_s H_0/c$, for negative energy transfer, where $v_s = \omega/q$ is the sound velocity in the z-direction of the crystal. This critical field is the same as that for sound wave amplification that appears in equation (35). The condition $\Delta\epsilon < 0$ corresponds to energy transfer from the electron plasma to the phonon population. Experimentally, it is found that for $\mathbf{H}_0 \perp \mathbf{E}^{EX}$, the current $\mathbf{J}$ is small until $E^{EX} = E^c$, after which the current increases dramatically. The E^c thus determined is linear in the magnitude of $\mathbf{H}_0$ and corresponds to the velocity of sound in the direction mutually perpendicular to both $\mathbf{E}^{EX}$ and $\mathbf{H}_0$.

4. EXPERIMENT

GQA in bismuth

It is convenient to observe the *MQE* fields directly in a compensated crystal such as bismuth. The results of the study of *GQA* [16] of sound waves in bismuth for several different experimental configurations can be found in the literature[17–19]. The electron Fermi surface for bismuth can be represented by three ellipsoids as shown in Fig. 3. It is also convenient that during the giant-quantum-attenuation (*GQA*) of longitudinally polarized phonons propagating in the bisectrix, or y-direction, of bismuth[18], the sound wave couples only to the ellipsoid labeled I in Fig. 3. Thus for $\mathbf{q} // \mathbf{y}$, the relevant portion of the Fermi surface consists of one ellipsoid whose major axes are tilted with respect to the propagation direction. The equation of the surface in the k-space is given by[20]

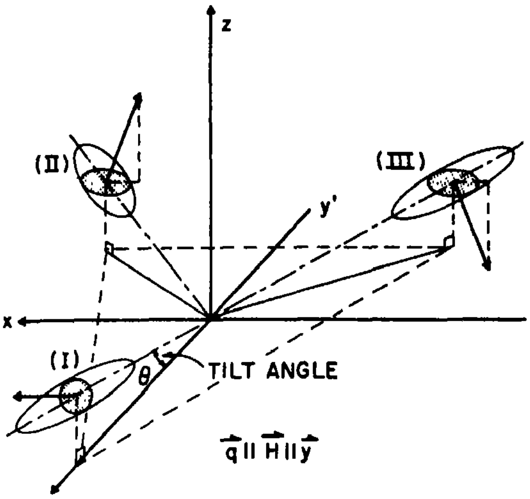

Fig 3 A representation of the electron Fermi surface of bismuth. The solid arrows indicate the direction of the orbit shift associated with each ellipsoid when $\mathbf{q} // \mathbf{H}_0 // \mathbf{y}$. See for example, ABELES B. and MEIBOOM S., *Phys. Rev.* **101**, 544 (1956).

$$\epsilon_F(1 + \epsilon_F/\epsilon_g) = \epsilon'_F = (\alpha_{xx}k_x{}^2 + \alpha_{yy}k_y{}^2 + \alpha_{xx}k_z{}^2 + 2\alpha_{yz}k_yk_z)\hbar^2/2m_0) \qquad (39)$$

which corresponds to equation (18) and the tilted ellipsoid configuration discussed in Sections 2 and 3. The magnitudes of the components of the inverse mass tensor for this ellipsoid given by[18, 20] $\alpha_{xx} = 187$, $\alpha_{yy} = 1{\cdot}64$, $\alpha_{zz} = 81{\cdot}1$, and $\alpha_{yz} = 9{\cdot}41$. Thus, the ellipsoid is tilted by $\sim 6°$ about the k_x-axis and the long axis lies in the k_y-k_z plane. In addition, in our bismuth crystals having a resistance ratio of $R(300°\text{K})/R(4°\text{K}) \geq 400$, the condition $ql > 1$ and $\omega_c\tau > 1$ is satisfied at $T = 4{\cdot}2°\text{K}$ and $H_0 \sim 10^3$ Oe for phonon frequencies greater than about 100 MHz. The $\Delta n = 0$ giant-quantum-attenuation (*GQA*) of longitudinal phonons with ($\mathbf{q}//\mathbf{y}$) by the electrons of this ellipsoid results in a characteristic magnetic field dependence of the attenuation of the flux. Thus characteristic magnetic field dependence will be observed in the corresponding *MQE* fields. Such that the essential conceptual connection between the *MQE* and *GQA* effects can be made, a brief discussion of the $\Delta n = 0$ *GQA* associated with this ellipsoid follows.

In the presence of an externally applied magnetic field $\mathbf{H}_0$, the energy levels of the electrons consist of Landau sub-bands of spacing $\hbar\omega_c$ and are labeled by the index n. With $\mathbf{H}_0//\mathbf{y}$ and using the Landau assymetrical gauge $\mathbf{A}_0 = (0, 0, -H_0 x)$, the energy levels and wave functions of the electrons (neglecting spin) are given by

$$\epsilon'_n(k_y) = (n+\tfrac{1}{2})\hbar\omega_c + (\alpha_{yy} + \alpha_{yz}/\alpha_{zz})\hbar^2 k_y^2/(2m_0) \quad (40)$$

$$\psi_n(\mathbf{r}) = \exp\,[i(k_y y + k_z z)]\, H_n(x - X_0) U_n(\mathbf{r})$$

where $n = 0, 1, 2, \ldots$ with $\omega_c = eH_0(\alpha_{xx}\alpha_{yy})^{1/2}/(m_0 c)$ and $U_n(\mathbf{r})$ is the Bloch function. The $H_n(x - X_0)$ is the nth Hermite polynomial of argument $(eH_0/c\hbar)^{1/2}(x - X_0)$ and $X_0 = -e\hbar(k_y + k_z\alpha_{yz}/\alpha_{zz})/(cH_0)$. The $\Delta n = 0$ *GQA* corresponds to a Landau excitation, that is, an electron makes an 'intra-sub-band' transition from an initial state $\epsilon_n(\mathbf{k})$ to a final state $\epsilon_n(\mathbf{k}')$ absorbing a quantum (phonon) of energy $\hbar\omega$ and momentum $\hbar\mathbf{q}$. The changes in energy and momentum of the electron are given by

$$\Delta\epsilon = (\alpha_{yy} + \alpha_{yz}/\alpha_{zz})\hbar^2(k_y'^2 - k_y^2)/(2m_0) = \hbar\omega$$

and (41)

$$\Delta k_y = k_y' - k_y = q.$$

The relevant parameters must satisfy the condition[16] $ql(\hbar\omega_c/\epsilon_F)^{1/2} > 1$, where l is the mean-free path of the electrons at the Fermi energy ϵ_F.

Upon defining k_0 as the average of k_y' and k_y, that is $k_0 = \tfrac{1}{2}(k_y + k_y')$, the condition for a $\Delta n = 0$ *GQA* transition is that $\omega/q = \hbar k_0(\alpha_{yy} + \alpha_{yz}/\alpha_{zz})/m_0$, i.e. the 'phase' velocity of the electron on a given Landau sub-band, $\hbar k_0(\alpha_{yy} + \alpha_{yz}/\alpha_{zz})/m_0$, is equal to the velocity of the phonon as shown in Fig. 4. Transitions will only occur within a given sub-band when the corresponding $\mathbf{k}_0$ is 'at' the Fermi level, allowing electrons to go from an initially occupied state below the Fermi energy to an initially unoccupied state above the Fermi energy. As a function of the magnitude of $\mathbf{H}_0$, the phonon attenuation will exhibit a series of peaks whose period is reciprocal in the magnitude of $\mathbf{H}_0$. The Fermi 'group' velocity for a given sub-band is given by

$$v_F(n) = 2(\alpha_{yy} + \alpha_{yz}/\alpha_{zz})/m_0)(\epsilon_F' - n\hbar\omega_c) \quad (42)$$

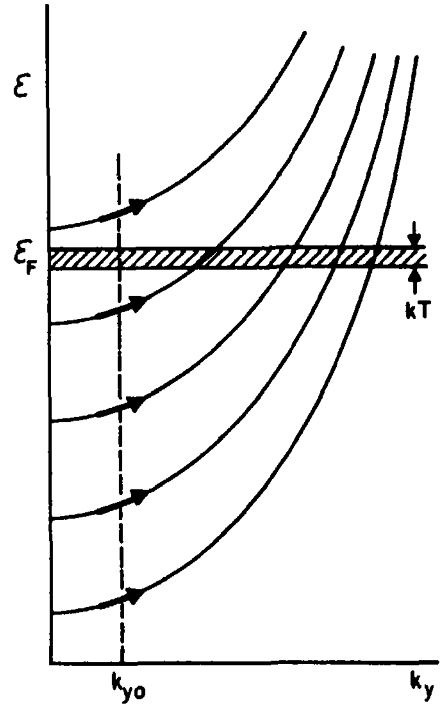

Fig. 4. A representation of giant-quantum-attenuation for longitudinal sound waves. $\mathbf{q}//\mathbf{y}$. The solid arrows indicate the energy and momentum conserving transition for each Landau level. Each transition occurs only when the arrow is at the Fermi level such that the electron can go from an occupied to an unoccupied state. The spacing between Landau levels is proportional to the magnitude of the magnetic field.

from which one obtains the *GQA* period

$$\Delta\left(\frac{1}{H_0}\right) = \frac{2e\hbar/m^*c}{(v_F{}^2 - v_s{}^2)} \qquad (43)$$

where $v_s = \omega/q$ is the sound velocity and $m^* = m_0/(\alpha_{xx} + \alpha_{yz}/\alpha_{zz})$. In case where $v_s \ll v_F$, equation (43) reduces to the period of de-Haas–van Alphen effect in the magnetic susceptibility. For arbitrary direction of $\mathbf{H}_0$ and $v_s \ll v_F$, equation (43) becomes

$$\Delta\left(\frac{1}{H_0}\right) = 2\pi e\hbar c a_\perp \qquad (44)$$

where $a_\perp$ is the cross-sectional area of the ellipsoid whose normal is parallel to $\mathbf{H}_0$. As $\mathbf{H}_0$ is rotated away from the y-direction but within the x-y plane, the magnitude of the component of $\mathbf{q}$ along $\mathbf{H}_0$ decreases as the cosine of the angle between $\mathbf{q}$ and $\mathbf{H}_0$, and the perpendicular cross-sectional area $a_\perp$, increases. Thus the amplitude and the $\Delta(1/H_0)$ period of the attenuation peaks decreases as the configuration goes from $\mathbf{H}_0 // \mathbf{y}$ to $\mathbf{H}_0 // \mathbf{x}$. The *MQE* fields should have the same dependence upon $\mathbf{H}_0$. Note however the *GQA* is independent the sign of $\mathbf{H}_0$, but the *MQE* fields change sign upon field reversal.

Experimental techniques

Conventional acoustic pulse echo techniques at frequencies of in the range 220 to 330 MHz were employed. The voltage detection scheme was designed to simulate continuous wave (*CW*) conditions. Number 40 enamelcoated, copper wires were spot welded to the binary (**x**) and trigonal (**z**) faces of bismuth single crystal cubes approximately 5mm on a side. A 20 MHz fundamental x-cut quartz transducer was bonded to one bisectrix (**y**) face, and driven at its 11th harmonic or higher. The geometry is illustrated in Fig. 5. The sample was immersed in liquid He at 4·2°K. As the phonon pulse was passing the voltage detection point, the difference voltages across the binary faces ΔV_x and across the trigonal faces ΔV_z were detected via a differential amplifier whose output was fed to a gated integrator. The phonon pulses were ~ 1μ-sec long, but the gate was open only ~ 0·1μ-sec during the time the pulse was passing the pickup points. All data was independent of gate position as long as the gate was open during some part of the time the phonon pulse was passing. At a repetition rate of ~ 300 Hz, the integrated ΔV_x and ΔV_z were recorded as a function of the magnitude of $\mathbf{H}_0$ for various angles θ, where θ is the angle between $\mathbf{q}$ and $\mathbf{H}_0$ in the x-y plane.

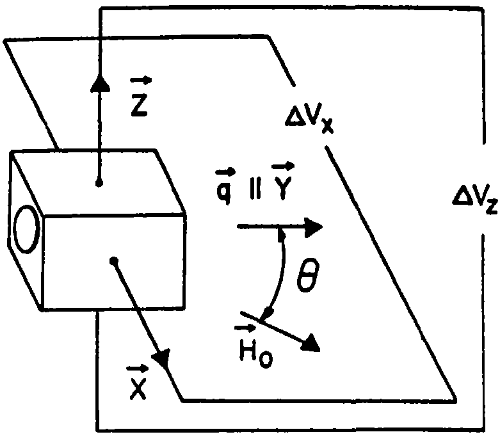

Fig. 5 Sample electrode configuration. The circle represents the transducer.

Analysis of MQE data

The $\Delta n = 0$ giant-quantum-attenuation of longitudinal sound waves in bismuth has been carried out at liquid helium temperatures and is discussed in Ref. [18], and at different frequencies in Refs. [17] and [19]. The attenuation data associated with ellipsoid 1 is shown in Fig. 6. For $\mathbf{H}_0 // \mathbf{q} // \mathbf{y}$ and at 292 MHz. Only one period of oscillations reciprocal in $\mathbf{H}_0$ is observed. Spin splitting of the peaks, which has not been discussed here, is observable on the last attenuation peak[18, 20]. The last peak corresponds to the so called quantum limit attenuation the so called quantum limit, where the $n = 0$

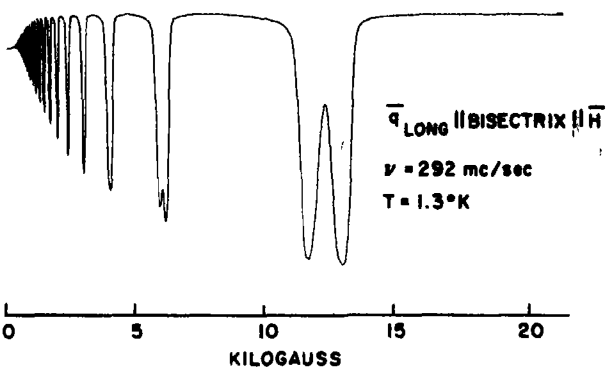

Fig. 6. *GQA* data for longitudinal phonons propagating in the *y*-direction (bisectrix) in bismuth when $H_0 // y$. SAWADA Y., BURSTEIN E. and TESTARDI L., *J. phys. Soc. Japan* **21**, (Suppl.), 760 (1966).

Landau sub-band is passing through the Fermi level ($\frac{1}{2}\hbar\omega_c \approx \epsilon_F$).

The entire discussion, in Sections 2 and 3, concerning a tilted ellipsoidal energy surface for electrons in a compensated material, applies to bismuth when $\mathbf{q} // \mathbf{y}$. The voltages corresponding to the transverse electric fields associated with these *GQA* oscillations are shown in Figs. 7 and 8. In Fig. 7, the voltage appearing across the *x*-faces of the sample, ΔV_x, is shown for $\mathbf{q} // \mathbf{y}$ and various magnetic field directions, where θ is the angle between $\mathbf{q}$ and $\mathbf{H}_0$, in the *x*-*y* plane. The ΔV_x exhibits the same $\Delta(1/H_0)$ periods as the *GQA* data for each value of θ. The experimentally determined zero-field attenuation at 220 MHz is about 20 db/cm corresponding to $\Gamma(0) \approx 10^{-2}\,\text{cm}^{-1}$ for $\mathbf{q}//\mathbf{y}$ at $T = 4{\cdot}2°\text{K}$. With an acoustical energy flux of $S = 1$ Watt/cm^2, the nonlinear coupling parameter of equation (37) is small compared to unity, $\beta \lesssim 10^{-3}$. Therefore, the *MQE* field is not large enough to alter the zero-field attenuation constant, $\Gamma(E)$, and equation (29) for the *MQE* field holds. The calculated value of $\mathbf{E}^{MQ}$ at a magnetic field strength corresponding to $\sim 1{\cdot}5 \times 10^4$ G is approximately 3×10^{-3} V/cm. From Fig. 7, the magnitude of ΔV_x associated with the last *GQA* peak, which occurs at $\sim 1{\cdot}5 \times 10^4$ G for $\theta = 0°$, is $\sim 10^{-3}$ V.

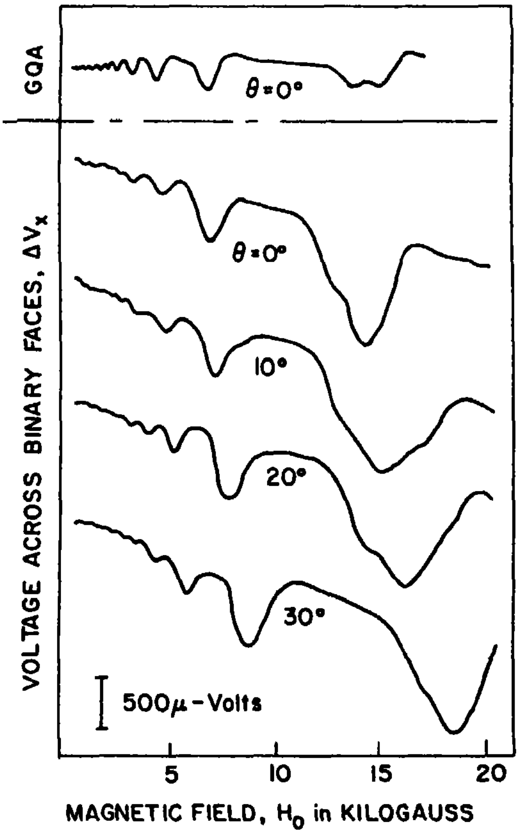

Fig. 7. The voltage across the *x*-faces of the sample corresponds to the *MQE* effect for longitudinal phonon propagation in the *y*-direction. *GQA* data for $\theta = 0$ is also shown. θ is the angle between the *y*-direction and $\mathbf{H}_0$ with $\mathbf{H}_0$ in the *x*-*y* plane.

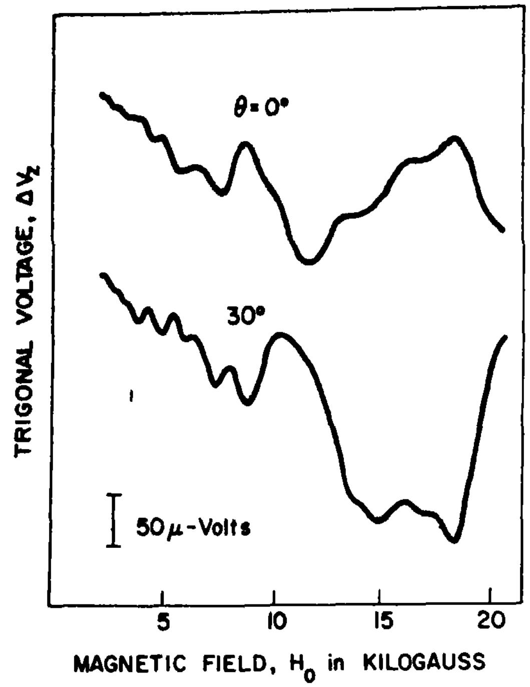

Fig. 8. The voltage across the x-faces (trigonal direction) corresponds to the Hall effect of the screening current associated with *MQE* field in the x-direction. Longitudinal phonon propagation is in the y-direction. θ is the angle between the y-direction and $\mathbf{H}_0$ with $\mathbf{H}_0$ in the x-y plane.

Table 1.

Parameter	Value[a]	Source
$\Gamma(0)$	10^{-2} cm^{-1}	*b*
E^{MQ}	$\sim 3\times10^{-3}$ V/cm	*b*
$E^{MQ,H}$	$\sim 2\times10^{-4}$ V/cm	*b*
β	$\leq 10^{-3}$	*b*
ρ_{xx}	3×10^{-2} Ω-cm	*c*
ρ_{xz}	2×10^{-3} Ω-cm	*c*

a: at a field of ~ 1·5 × 10⁴ G.
b: experimental.
c: MASE S., *et al.*, *Phys. Rev.* **127**, 1030 (1962).

This corresponds to a field (*MQE*) of 2×10^{-3} V/cm. Also, reversing the direction of $\mathbf{H}_0$ for any given θ was found to change the sign (±) of the voltage, ΔV_x, consistant with equation (29). In addition, the *MQE* voltage depends linearly upon the thickness of the sample in the x-direction. These values are summarized in Table 1.

The voltage appearing across the z-faces of the samples, ΔV_z, was also observed for the same values of θ. As illustrated in Fig. 8, the ΔV_z has a different 'oscillatory' dependence upon the magnitude of $\mathbf{H}_0$. The magnitude of these 'oscillations' in ΔV_z are roughly on the order of one tenth of ΔV_x. Referring to equation (29), the ratio of $E^{MQ,H}$ to E^{MQ} should be on the order of ρ_{xz}/ρ_{xx}. Using the values of the components of the resistivity tensor in bismuth at $\sim 10^4$ G, taken from the literature[21] $\rho_{xx} \approx 3\times10^{-2}$ Ω-cm and $\rho_{xz} \approx 2\times10^{-3}$ Ω-cm, and $\rho_{xz}/\rho_{xx} \approx 0{\cdot}07$, in reasonable agreement with the observations. For $\mathbf{H}_0$ not along symmetry directions, generally three sets of oscillations periodic in $1/H_0$ could be found in ΔV_z. But ΔV_z is the voltage associated with several effects: the Hall effect of the screening current flowing in response to the *MQE* current in the x-direction, a field due to crystal anisotropy (ρ_{zy}), and the Hall effect of the acoustic-electric current flowing parallel to the phonon propagation direction (when $\mathbf{q} \perp \mathbf{H}_0$). The off-diagonal terms of the magnetic field dependent resistivity tensor can be used to calculate these contributions to ΔV_z. The resistivity tensor components, however, are affected by the presence of all three electron ellipsoids. If a τ is defined such that τ^{-1} is some effective scattering frequency for all carriers at the Fermi energy, for all sections of the Fermi surface[22], τ will in general exhibit three sets of 'oscillations', each periodic in $1/H_0$. The number of carriers at the Fermi surface of each ellipsoid is increased when a given Landau sub-band passes through the Fermi surface. This increase in carrier density results in an increase in the scattering frequency. The discrete set of values of the magnitude of $\mathbf{H}_0$ for which these carrier density maximuma occur, are generally different for each ellipsoid (for arbitrary direction of $\mathbf{H}_0$). Because each ρ_{ij} is some function of $\omega_c\tau$, these 'Shubnikov–de Haas' oscillations[22] are observed in ΔV_z. These considerations were discussed above in connection with equations (32) and (33).

In connection with considerations of the variations in $\omega_c\tau$ producing 'oscillatory' effects in the various ρ_{ij}, an experiment was performed where the phonon flux was replaced by a d.c. current, $\mathbf{J}^{DC}$. The d.c. current would effectively take the place of the acoustoelectric current produced by the flux in the y-direction. With a current of 10 to 100 mamp flowing in the y-direction of a bismuth crystal, the difference voltages ΔV_x and ΔV_z were again recorded as a function of magnetic field for various directions of $\mathbf{H}_0$ in the x-y plane. Oscillations, periodic in $1/H_0$, are evident in both ΔV_x and ΔV_z for all directions of $\mathbf{H}_0$. It is found that the oscillatory behavior of ΔV_z is essentially the same for the d.c. current as for the phonon flux ($\mathbf{q}//\mathbf{y}$) for all directions of $\mathbf{H}_0$. Except for symmetry directions, three sets of 'oscillations' periodic in $1/H_0$ were observed. The angular dependence of the magnetic field strength at which a given peak appears in ΔV_z for the acoustic case is shown in Fig. 9. The ΔV_z data for the d.c. current case are quite similar to ΔV_z in the phonon experiment.

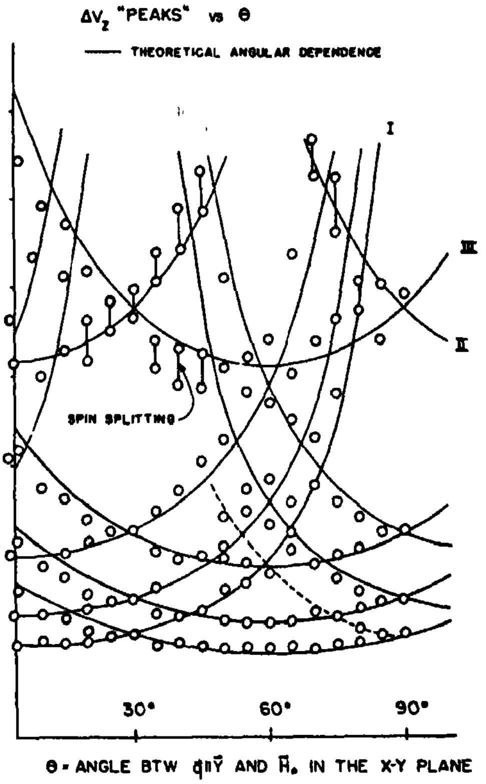

Fig. 9. The peaks in the trigonal voltage correspond to variations in electron density at the Fermi surface as a function of magnetic field. The density variations are periodic in $1/H_0$ and correspond to the cross-sectional area perpendicular to the direction of $\mathbf{H}_0$ of the particular electron ellipsoid. The solid lines are based upon calculated cross-sectional areas of ellipsoids I, II, and III. The magnetic field scale is arbitrary.

The voltage across the x-faces of the sample in the d.c. current case ($\mathbf{J}^{DC}//\mathbf{y}$) is quite different, however, from the ΔV_x with the acoustic flux. Except for symmetry directions, three sets of 'oscillations' periodic in $1/H_0$ were observed in ΔV_x in the d.c. current case, whereas only one set was observed when the phonon flux was used. Thus, referring to equations (32), the dominate term in the equation for E_x is $\rho_{xx}J_x{}^{MQ}$, and the planar Hall term, $\rho_{xy}J_y{}^{AE}$ is small. Careful examination of the data revealed an apparent 10 per cent modulation of the ΔV_x, in the acoustic case, by another oscillatory function. The ratio of the calculated $\rho_{xy}J_y{}^{AE}$ to $\rho_{xx}J_x{}^{MQ}$ is in agreement with this observation. In addition, reversing the direction of the magnetic field when the d.c. current was flowing left the ΔV_x curves unaltered, i.e. peaks remained peaks, and minima remained minima as a function of the magnitude of $\mathbf{H}_0$. In the acoustic case, however, the *MQE* fields reversed sign upon field reversal ($\mathbf{H}_0 \rightarrow -\mathbf{H}_0$).

5. SUMMARY

Quanta-absorption-induced lateral displacements of the centers of cyclotron orbits of charge carriers in solid state plasmas in a magnetic field are shown to produce transverse electric fields. The conditions for the observation of the *MQE* fields are $\omega_c\tau \gg 1$ and $ql \gg 1$, the same as for the observation of well defined *GQA* oscillations. In addition, the observation of *GQA* requires $ql(\hbar\omega_c/$

$\epsilon_F)^{1/2} > 1$. The *MQE* fields are found to be too small to influence the rate of quanta absorption, at least in the case of acoustical phonon absorption. In materials with spherical Fermi surfaces, the *MQE* fields appear for $\mathbf{q} \perp \mathbf{H}_0$ in a direction mutually perpendicular to both $\mathbf{q}$ and $\mathbf{H}_0$. This is essentially the Hall effect configuration and care must be taken in separating the Hall field (*AME*) and the *MQE* field. In materials with ellipsoidal energy surfaces, however, the *MQE* fields can appear transverse to $\mathbf{q}$ and $\mathbf{H}_0$ for $\mathbf{q} // \mathbf{H}_0$, when $\mathbf{q}$ is not parallel to any of the principle axes of the ellipsoid. The magnitude and magnetic field dependence of the *MQE* fields are indicative of the shape of the Fermi surface, energy band structure, and the electron–phonon (or photon) coupling in the plasma. A consideration of the effect has shown that the *MQE* effect can be observed in both compensated and uncompensated materials. In uncompensated materials, however, it may be advantageous to measure the Hall effect of the screening current of the *MQE* current, rather than the *MQE* fields themselves. Data on the observation of the *MQE* fields and other transverse electric fields associated with the $\Delta n = 0$ giant-quantum-attenuation of longitudinally polarized acoustic waves in bismuth are presented. All aspects of the data are in excellent agreement with the theory.

Acknowledgements—The authors wish to acknowledge helpful discussions with L. Testardi, R. G. Chambers and V. L. Gurevich and the technical assistance of P. C. Corden.

REFERENCES

1. SAWANDA Y., BURSTEIN E., SALANECK W. and TESTARDI L., *Phys. Rev. Lett.* **19**, 776 (1967).
2. SALANECK W., SAWANDA Y. and BURSTEIN E., *Phys. Rev. Lett.* **19**, 779 (1967).
3. YAMADA T., *J. phys. Soc. Japan* **20**, 1424 (1965).
4. EPSHTEIN E. and GULYAEV Y., *Soviet Phys.-Solid State* **9**, 288 (1967).
5. PARMENTER R., *Phys. Rev.* **89**, 990 (1953).
6. WEINREICH G., *Phys. Rev.* **104**, 321 (1956) and *Phys. Rev.* **107**, 317 (1957).
7. JOHNSON M. and LIPPMAR B., *Phys. Rev.* **76**, 828 (1949).
8. Note that $\Delta n = 0$ Landau type transitions for spherical energy surfaces with Voigt configuration only occur in the presence of spatial dispersion effects. For reference, see McWORTER A. and WALPOLE J., *Phys. Rev.* **158**, 719 (1967).
9. SCHIFF L., McGraw Hill, New York (1955).
10. In metals where the skin depth is small, higher order terms in equation (25) may be important.
11. GOLDBERG C. and DAVIS R., *Phys. Rev.* **94**, 1121 (1954) and PEARSON G. and SUHL H., *Phys. Rev.* **83**, 768 (1951).
12. Reference [6] and HUTSON A. R., *J. appl. Phys.* **32**, 2287 (1961).
13. KAZARINOV R. F. and SKOBOV V. G., *Soviet Phys.-JETP* **16**, 1057 (1963), and AKHIEZER, A. I., KAGANOV M. I. and LIUBARSKII G. Ia., *Soviet Phys.-JETP* **5**, 1164 (1957).
14. McFEE J. H., *Physical Acoustics*, Vol. IV, Part A, Chap. 1, Academic Press, New York and London (1966).
15. ESAKI L., *Phys. Rev. Lett.* **8**, 4 (1962).
16. See for example, GUREVICH V., SKOBOV V. and FIRSOV Yu., *Soviet Phys.-JETP* **13**, 552 (1961).
17. TOXEN A. and NSAH S. T., *Bull. Am. phys. Soc.* **9**, 264 (1964) and *Phys. Rev.* **137**, A211 (1963).
18. SAWADA Y., BURSTEIN E. and TESTARDI L., *J. phys. Soc Japan* **21**, (suppl.), (1966).
19. MASE S., FUJIMORI Y. and MORI H., *J. phys. Soc. Japan* **9**, 1744 (1966).
20. LAX B., MAVROIDES J., ZEIGER H. and KEYES R., *Phys. Rev. Lett.* **5**, 241 (1960).
21. See for example LAX B., BUTTON K., ZEIGLER H. and ROTH L., *Phys. Rev.* **102**, 715 (1956) and MASE S., VON MOLNAR S. and LAWSON A., *Phys. Rev.* **127**, 1030 (1962).
22. SMITH G., BARAFF G. and ROWELL J., *Phys. Rev.* **135**, A1118 (1964).

J. Phys. Chem. Solids, 1971, Vol. 32, pp. 2301–2304. Pergamon Press. Printed in Great Britain

EFFECT OF PRESSURE ON THE MELTING OF CESIUM CHLORIDE*

S. N. VAIDYA and G. C. KENNEDY

Institute of Geophysics and Planetary Physics, University of California, Los Angeles, Calif. 90024, U.S.A.

(*Received* 19 *January* 1971)

Abstract—Melting curve of cesium chloride has been determined to 50 kbar in a single-stage piston-cylinder apparatus. Our results agree with Clark's experimental data which extend up to 15 kbar. We have also found that the melting temperature of cesium chloride changes linearly with its specific volume up to 45 kbar in contrast to the behavior of other recently studied ionic compounds.

1. INTRODUCTION

THE EFFECT of pressure on the melting of ionic compounds has recently been discussed by Kennedy and Vaidya[1]. They note that when melting temperatures are plotted against the isothermal compression of Van der Waals solids, melting curves concave to the temperature axis results. They also note that when melting curves are plotted for metals, melting temperatures are linear with the volume of the melting solid and that when melting curves are plotted for ionic compounds, resulting curves appear to be concave toward the volume axis of the plot. This relationship has been explored to compressions of as much as 30 per cent in the case of the Van der Waals solids, helium and methane, and to compressions of as much as 40 per cent in the case of the metals, rubidium and potassium. Unfortunately, no highly compressible ionic compound has been examined. A casual search of the literature suggested that cesium chloride was one of the most compressible of ionic compounds and that its fusion curve had a very steep initial slope. Thus, we elected to examine the melting of cesium chloride to the highest pressures and temperatures readily attainable with precision.

The melting curves and phase diagrams of sodium, potassium, rubidium, silver, cuprous and thallous halides have recently been determined, by methods of differential thermal analysis, to pressures of circa 50 kbar[2–10]. Melting curves of the lithium and cesium halides have not been examined over this pressure range.

Cesium chloride, CsCl, undergoes a phase change to a new polymorph with NaCl structure at about 469°C[11] at 1 atmosphere. Its melting point at atmospheric pressure is approximately 645°C. The melting of CsCl, to pressures of approximately 15 kbar, has been investigated by Clark[2]. He finds a triple point between two polymorphs and liquid at approximately 1 kbar and 665°C. The initial slope of the melting curve of CsCl above the triple point is 42°C/kbar. This is the steepest melting curve of any substance which has come to our attention. Further, the cesium halides are the most compressible of the metal halides. Recent data on a density as a function of pressure are available[12].

2. EXPERIMENTAL METHOD

Cesium chloride of 99·5 per cent stated purity was supplied by Research Organic and Inorganic Chemical Co. This is the same stock we recently used in compressibility measurements[12]. The powdered material was dried for 48 hr at 200°C and then tightly packed in a niobium metal capsule with a reentrant thermocouple well. A boron nitride sleeve insulated the niobium capsule from the graphite furnace tube. Molten pyrex glass served as the pressure transmitting medium. Further experimental details are given by Akella *et al.*[4] and by Williams and Kennedy[13].

---

*Publication #889 Institute of Geophysics and Planetary Physics, University of California, Los Angeles, Calif. 90024, U.S.A.

CsCl melts at temperatures in excess of 1800°C at 50 kbar. Consequently thermocouples stable to very high temperatures are required. We have found that Pt/Pt-10Rh thermocouples deteriorate rapidly at temperatures much above 1500°C and the W-3Re/W-25Re thermocouples are stable to at least 2000°C. The behavior of Englehart premium grade W-3Re/W-25Re thermocouple in high pressure differential thermal analysis assemblies has been extensively studied by Williams and Kennedy[13]. Because of the mechanical and chemical stability of these thermocouples, they were selected for use in this study.

Determinations of the melting temperature were made by differential thermal analysis on both compression and decompression cycles. In a particular experiment, lasting nearly 10 hr, a large number of DTA points could be determined over a 20–25 kbar range. Most of the experiments were terminated owing to capsule failure and consequent loss of sample. Capsules of tantalum and molybdenum were tried, but niobium capsules seemed to serve best at the highest temperatures and pressures.

3. RESULTS

Our measurements of the melting temperature of CsCl along with Clark's results[2] are shown in Fig. 1. A smooth curve through the 116 data points was drawn by use of a polynomial regression fit

$$T_m = T_m{}^0 + b_1P + b_2P^2.$$

Davis and England[14] and Williams and Kennedy[13] have intercompared W-3Re/W-25 Re and *Pt*/Pt-10Rh thermocouples at high temperatures and pressures. Differences in the apparent temperatures indicated by these thermocouple pairs at high temperatures and high pressures is attributed to the difference in the effect of pressure on the ther-

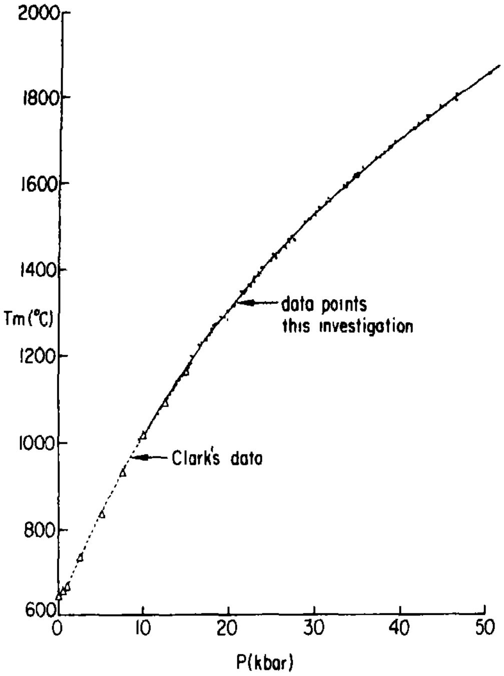

Fig. 1. CsCl melting data. Curve from least squares fit.

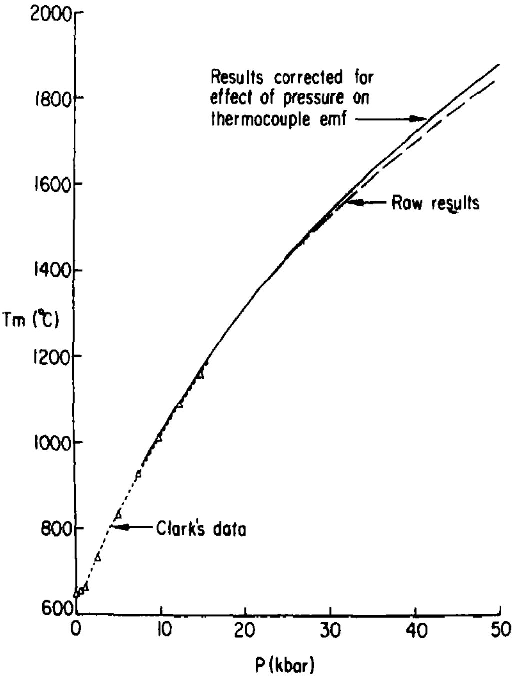

Fig. 2. CsCl melting curves.

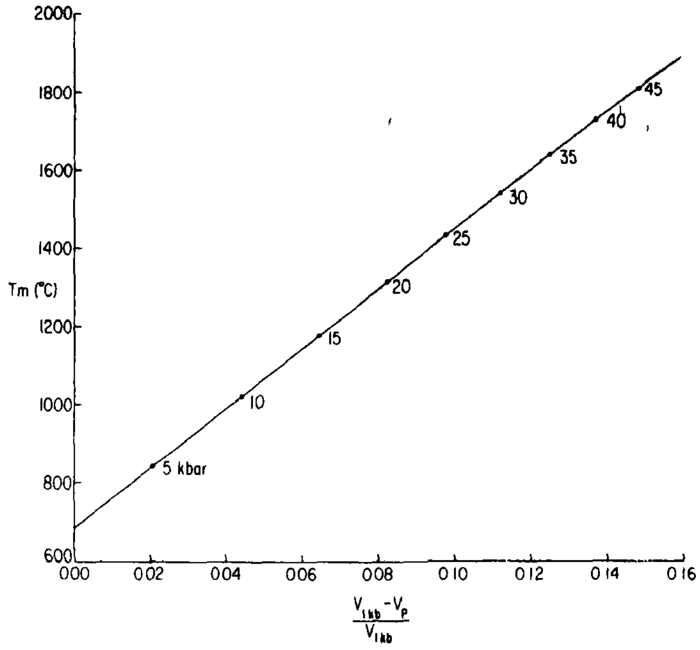

Fig. 3. Melting temperature of CsCl vs. volume compressions of the solid at ambient temperature.

mal emf of the two sets of material. Intercomparison experiments can only be made through the useful range of the Pt/Pt-10Rh thermocouples. Further, Getting and Kennedy's experiments[15] on the effect of pressure on Pt/Pt-10Rh wires extend only to 35 kbar and 1000°C. Thus large extrapolations are necessary in order to estimate the correction for the effect of pressure on W-3Re/W-25Re wires at the highest pressures and temperatures of the present experiment. The accuracy of our measurements is thus substantially less than the precision of the measurements, owing to uncertainties in extrapolation of the corrections and also owing to uncertainties involved in the calibration of individual pairs of wires[16]. The precision of our measurements at the highest temperatures and pressures is approximately ±5°C; however, the accuracy is certainly no better than ±10°C. Figure 2 shows the curve through the raw data points and the curve after applying extrapolated corrections for the effect of pressure on thermo-e.m.f. We also show the results from Clark's studies to 15 kbar. At 50 kbar the corrections to our raw data amounts to approximately 34°C. The results are also tabulated at regular pressure intervals. (Table 1).

Figure 3 is a plot of the temperature of melting vs. the room temperature compression of the solid. In this plot the recent compressibility data on the simple cubic phase above 1 kbar[12] is used. To our surprise the plot is exactly linear to within the precision of the measurements. In this respect CsCl behaves like a metal and does not show the slight curvature toward the volume axis as is shown by other studied ionic compounds[1]. Vaidya and Gopal[17] have suggested that substances melt in accordance with an equation

$$T_m = T_m^{0'} \cdot \left[1+2(\gamma-\tfrac{1}{3}) \cdot \left|\frac{V_0'-V}{V_0'}\right|\right]$$

where $T_m^{0'}$ and V_0' are the melting temperatures and specific volumes at the reference pressure.

Table 1. Melting data for Cesium Chloride. Melting temperatures, T_m, computed from the relation $T_m = 642{\cdot}55 + 42{\cdot}436P - 0{\cdot}53741P^2 + 0{\cdot}00341P^3$, where P is pressure in kbar. Standard deviation, 5°C

P (kbar)	Clark[1] T_m, °C Corrected for the effect of pressure on Pt/Pt-10Rh thermocouples	This Work T_m, °C Uncorrected for the effect of pressure on thermocouples	T_m, °C Corrected for the effect of pressure on W-3Re/W-25Re thermocouples
0	645		
5	841	842	843
10	1015	1017	1018
15	1160	1170	1173
20		1304	1308
25		1421	1428
30		1524	1535
35		1616	1631
40		1698	1719
45		1774	1802
50		1847	1881

The Gruneisen parameter, γ, estimated from the slope of the line in Fig. 3 is 4·29. The γ thus obtained is much too great. Vaidya and Gopal[17] have suggested these large values of γ result because the melting temperature is plotted against the room temperature specific volume of the solid and not against the specific volume of the solid along the melting curve. If corrections of the kind outlined by Vaidya and Gopal are made[4, 6, 17], γ reduces to 2·78. This is in fair agreement with the thermal value of γ for CsCl which is 2·02.

Acknowledgements – Our thanks are due to Miss Sharon Bailey for excellent help with the data processing. This research has been partially supported by NSF Grant GA 25,404.

REFERENCES

1. KENNEDY G. C. and VAIDYA S. N., *J. geophys. Res.* **75**, 1019 (1970).
2. CLARK S. P., Jr., *J. chem. Phys.* **31**, 1526 (1959).
3. PISTORIUS C. W. F. T., *J. chem. Phys.* **45**, 3513 (1966).
4. AKELLA J., VAIDYA S. N. and KENNEDY G. C., *Phys. Rev.* **185**, 1135 (1969).
5. PISTORIUS C. W. F. T., *J. chem. Phys.* **43**, 1557 (1965).
6. AKELLA J., VAIDYA S. N. and KENNEDY G. C., *J. appl. Phys.* **40**, 2800 (1969).
7. RAPOPORT E. and PISTORIUS C. W. F. T., *Phys. Rev.* **172**, 838 (1968).
8. PISTORIUS C. W. F. T. and CLARK J. B., *Phys. Rev.* **173**, 692 (1968).
9. PISTORIUS C. W. F. T., *J. Phys. Chem. Solids* **25**, 1477 (1964); **26**, 1003 (1965).
10. DARNELL A. J. and McCOLLUM, *J. Phys. Chem Solids* **31**, 805 (1970).
11. MENARY J. W., UBBELOHDE A. R. and WOODWARD I., *Proc. R. Soc.* London A **208**, 158 (1951).
12. VAIDYA S. N. and KENNEDY G. C., *J. Phys. Chem. Solids* (in press).
13. WILLIAMS D. W. and KENNEDY G. C., *J. geophys. Res.* **74**, 4359 (1969).
14. DAVIS B. T. C. and ENGLAND J. L., *J. geophys. Res.* **69**, 1113 (1964).
15. GETTING I. C. and KENNEDY G. C., *J. appl. Phys.* **41**, 4552 (1970).
16. ZYSK E. D and TOENSHOFF D. A., *21st Annual Conf. Instr. Soc. Am.* 1966.
17. VAIDYA S. N. and RAJA GOPAL E. S., *J. Phys. Chem. Solids* **28**, 1074 (1966).

J. Phys. Chem. Solids, 1971, Vol. 32, pp. 2305–2310. Pergamon Press. Printed in Great Britain

A STUDY ON SOME Co–Te COMPOSITIONS BY MÖSSBAUER SPECTROSCOPY

V. FANO
Laboratorio MASPEC del C.N.R. Parme, Italy

and

I. ORTALLI
Istituto di Fisica, Università Parma, Italy
Gruppo Nazionale Struttura della Materia, Parma, Italy

(*Received* 23 *November* 1970; *in revised form* 16 *January* 1971)

Abstract—The binary systems formed by sixth group elements with transition elements show large homogeneity ranges in the vicinity of stoichiometric compositions. In order to interpret physical measurements, it is necessary to study the type of ordering of the vacancies, which may vary with the system considered. In this work, a Mössbauer study has been made on some Co–Te composition ranges with the NiAs structure. Mossbauer absorption spectra on ^{57}Co diffused into the samples are examined. The results are· (a) over the entire γ-phase range there are but two types of Co with different electronic configuration corresponding to two different crystallographic sites ($Q_{\rm I}$ and $Q_{\rm II}$). (b) For the composition $Co_{0.67}Te$, the absorption values are quite different from those for other compositions: the intensity of the two peaks in the Mössbauer absorption spectra and the quadrupole splitting of $Q_{\rm I}$ are much larger than for the other γ-phase compositions. (c) We can confirm that the stoichiometric composition CoTe does not exist

1. INTRODUCTION

THE Co–Te system has been subject to deep study[1–6]. Nevertheless some basic questions about the system with NiAs and related structures are unresolved. It is not clear, for instance, whether the γ-phase, which, by subtraction of Co atoms from the (0, 0, 1/2) planes, passes from the NiAs to the $Cd(OH)_2$ structure with compositions ranging from $CoTe_{1.2}$ to $CoTe_{1.8}$ at 600°C, includes particular compounds with ordered defects. The magnetic, X-ray and density measurements, are contradictory[8, 9]. The existence of variously ionized Co atoms has not yet been experimentally verified. Some authors have concluded that the γ-phase range does not include the stoichiometric composition CoTe and that this compound does not exist, but this conclusion is not universally accepted [10, 11].

With Mössbauer spectroscopy we attempt to clarify the previously mentioned doubts. We have obtained spectra of $Co_{1-x}Te$ of fixed composition doped with ^{57}Co. ^{57}Co introduced into a $Co_{1-x}Te$ host in microquantity is chemically indistinct from the other Co that constitutes the host, provided there is complete homogeneity. Its distribution among the crystallographic sites, revealable by Mössbauer spectroscopy, gives unique information about the crystallographic sites that are filled (or emptied) at a given composition. ^{57}Fe, produced by electron-capture decay of ^{57}Co diffused into the sample, remains at the same sites as the ^{57}Co because the recoil energy is too small to displace it. The eventual various bond situations that ^{57}Co may have are 'felt' by the ^{57}Fe. In fact, iron and cobalt can crystallize together with tellurium in both the NiAs and its derived $Cd(OH)_2$ structure.

2. EXPERIMENTAL PROCEDURE

The examined undoped samples were single crystals spontaneously grown in the melt. They were synthetized by direct combination of Co and Te at 99,999 per cent and further purified with oxygen in the desired stoichiometric ratios (12): $Co_{1\cdot15}Te$, $Co_{1\cdot00}Te$, $Co_{0\cdot85}Te$, $Co_{0\cdot75}Te$, $Co_{0\cdot67}Te$, $Co_{0\cdot54}Te$. $^{57}CoCl_2$ in hydrochloric acid solution was deposited directly on a face of our samples (0·3 mm thickness), and then dried. The divalent ^{57}Co was reduced to elementary ^{57}Co by an atmosphere of H_2 in a quartz tube that had been previously washed with HF and outgassed. In this way the presence of various valence states of ^{57}Co cannot be ascribed to partial oxidation of the diffused Co. The reduction and subsequent diffusion of ^{57}Co was at 500°C. At this temperature, stoichiometric variations caused by Te evaporation were negligible at normal pressure. The samples were kept at 500°C until the ^{57}Co was distributed throughout the whole volume ($\geqslant$ 3 hr). This was tested by the spectrum intensity of the sample side on which was deposed the $^{57}CoCl_2$ with the spectrum intensity of the opposite side. ^{57}Co was considered distributed throughout the whole sample when the two intensities were equal. The sample with composition $Co_{0\cdot54}Te$ has the same structure as the γ-phase after a thermal treatment of only a few hours at 500°C; partial transformation from the γ-phase to the marcasite structure is detectable for much longer annealing times at 500°C. After thermal treatment, the samples were quenched in H_2O and were thinned by lapping off 0·05 mm of thickness from the surface where there was the $^{57}CoCl_2$ deposit in order to remove the sporious products of the reaction.

The Mössbauer apparatus used was of electromagnetic type working at constant acceleration. $Na_4Fe(CN)_6 \cdot 10H_2O$ (0·10 mg $^{57}Fe/cm^2$) was used as absorber: this material displays a single absorption line, whose FWHM is 0·27 mm/s, with a ^{57}Co-in-Pd source. A proportional counter was used as detector.

3. RESULTS AND DISCUSSION

The results of the Mössbauer measurements are summarized in Tables 1 and 2 and are shown in Figs. 1–3. The positions and widths of the peaks were determined in the usual way that is, by fitting the experimental data with Lorentzian shape curves.

Table 1. *Mössbauer isomer shifts (I.S.) and quadrupole splittings (Q.S.) in mm/s at room temperature. The shifts are relative to* $Na_4Fe(CN)_6 \cdot 10H_2O$ *absorber*

	Q_I		Magnetic splitting		
	I.S.	*Q.S*	*I.S.*	*Q.S.*	H(KG)
$Co_{1\cdot15}Te$	−(0·68 ± 0·10)	0·34 ± 0·10	−(0·06 ± 0·04)	0·17 ± 0·06	326 ± 6
$Co_{1\cdot00}Te$	−(0·65 ± 0·04)	0·35 ± 0·04	(0·00 ± 0·10)	0·16 ± 0·06	332 ± 5

Table 2.

	Q_I		Q_{II}	
	I.S.	*Q.S.*	*I.S.*	*Q.S.*
$Co_{0\cdot85}Te$	−(0·61 ± 0·03)	0·38 ± 0·04	−(0·70 ± 0·03)	0·13 ± 0·04
$Co_{0\cdot75}Te$	−(0·59 ± 0·04)	0·37 ± 0·06	−(0·68 ± 0·04)	0·11 ± 0·06
$Co_{0\cdot67}Te$	−(0·60 ± 0·04)	0·74 ± 0·06	−(0·71 ± 0·04)	0·09 ± 0·06
$Co_{0\cdot54}Te$	−(0·60 ± 0·03)	0·43 ± 0·04	−(0·70 ± 0·03)	0·11 ± 0·03

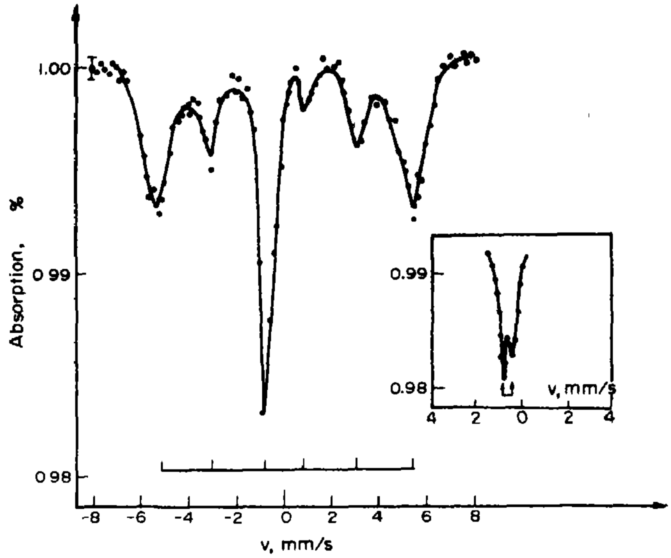

Fig. 1. Absorption Mossbauer experimental spectrum of ^{57}Co diffused in $Co_{1.15}Te$ at room temperature. In the square appear the central peak with a double resolution.

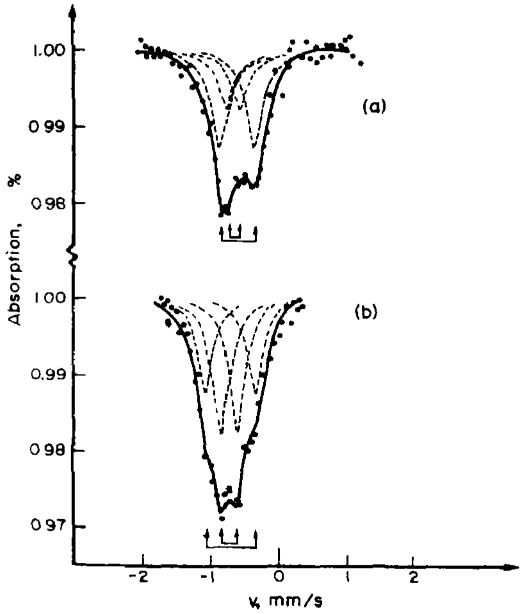

Fig. 2. Absorption Mössbauer experimental spectra of ^{57}Co diffused in (a) $Co_{0.85}Te$, (b) $Co_{0.67}Te$ and (c) $Co_{0.54}Te$ at room temperature.

A qualitative interpretation of the bonding situation in the Co–Te system is made in a reflected way from the ^{57}Fe. By Mössbauer spectroscopy, we may detect a large variety of iron valence states[13]. For compositions more rich in Co than $Co_{0.85}Te$, the absorption spectra reveal the presence of a single quadrupole coupling caused by substitutional ^{57}Fe that is, in a crystalline environment of the NiAs type (Fig. 1). for these compositions we also note a magnetic hyperfine structure corresponding to ^{57}Fe in a metallic cobalt host[14] (the value of the induction at the iron nuclei is typically 330 KG) (Table 1). The presence of these Co precipitates for the stoichiometric composition CoTe and for the next nearest composition confirm that the compound CoTe does not exist and does not belong to the γ-phase.

At the composition $Co_{0.85}Te$, the presence of metallic Co is not yet detectable; we note however, another quadrupole coupling (Q_{II}). The absorption spectrum obtained at this composition may be considered as composed of two parts: Q_I, having the same characteristics, as the quadrupole coupling found at compositions more rich in Co, and Q_{II}. Whenever, there are three or more peaks ascribed to iron valence states, doubt arises

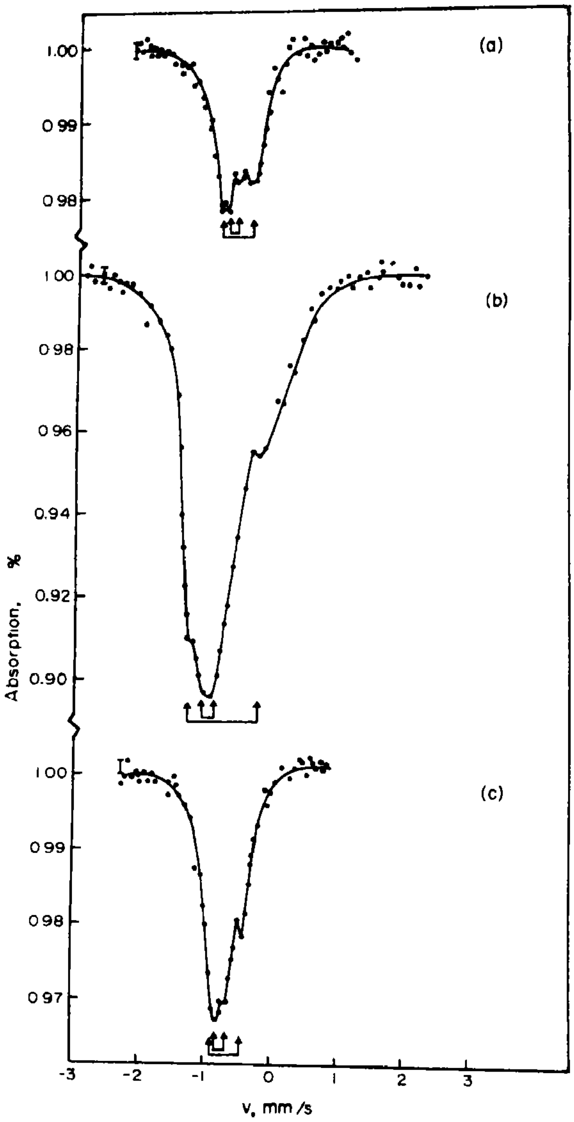

Fig 3. Absorption Mössbauer theoretical spectrum of ^{57}Co diffused in $Co_{0.85}Te$: (a) room temperature, (b) liquid nitrogen temperature. The solid line indicates the fit by a sum of four Lorentzian curves.

as to whether the multiply ionized atoms are caused by an Auger effect[15, 16]. In fact, the γ-phase of the Co–Te system is a medium of the same nature as are compositions more rich in cobalt, where one notes only an electric field gradient as a consequence of symmetry far from octahedral. The isomer shifts of the two iron types ($\delta_1 = -0{\cdot}6$ mm/s, $\delta_2 = -0{\cdot}7$ mm/s) fall in a region not distinct in valence type. The value of the shifts is in agreement with formation of hybrid orbitals d^2sp^3. All through the γ-phase range we note always only these two Fe types. However, the second Fe type may be considered an ion in a crystalline environment of the $Cd(OH)_2$ type, which differs from the other in that the two transition element atoms immediately above and below are lacking.

The fact that the second Fe ($\delta_2 = -0{\cdot}7$ mm/s) belongs to a different crystallographic site is confirmed by the increase of the central doublet intensity at liquid nitrogen temperature (Fig. 3), where the solid line indicate the fit by a sum of four Lorentzian-like functions resolved in two quadrupole doublets. We deduce that the two Fe ions have a different ionization degree by studying the quadrupole moments Q_{I} and Q_{II} as a function of temperature. For the composition $Co_{0{\cdot}85}Te$ at liquid nitrogen temperature, Q_{II} does not vary; the small Q_{II} value and its behaviour as a function of temperature are characteristic of Fe^{3+} ($3d^5$). On the other hand the quadrupole coupling Q_{I}, which is larger than the preceding one, becomes double (from 0·4 mm/s to 0·7 mm/s). This is in agreement with the $3d$ population variation as a function of temperature, a variation noticed in Fe^{2+} ($3d^6$) compounds. The possibility that the Q_{I} increase at liquid nitrogen temperature may be caused by structural variation must be excluded. In fact, the structure changes should affect the Mössbauer parameters of the other iron type.

The intensity of the two absorption peaks for $Co_2Te_3(Co_{0{\cdot}67}Te)$ is greater than for the other compositions examined (Fig. 2). This can be understood if we suppose the existence of a superstructure. Such a hypothesis is confirmed by the fact that at room temperature only at this composition does the external quadrupole coupling (Q_{I}) increase from $\simeq 0{\cdot}4$ to 0·74, corresponding to a highly determined divalent state. Usually, [17, 18] in going from NiAs to $Cd(OH)_2$ structure, we expect to find ordered structures. In fact the composition Co_2Te_3 differs from the others in other properties: its susceptibility varies with temperature in different ways depending on composition[4]. The Curie–Weiss law is completely satisfied only for the stoichiometric composition Co_2Te_3. Moreover, Co_2Te_3 single crystals, which show a resistivity one third lower perpendicular to the c-axis, than parallel to it, are grown by vapour phase transport under different growing conditions [19]. All through the γ-phase range, increasing the tellurium concentration increases the central peak intensity, than is, the number of neighboring sites of the $Cd(OH)_2$ type increases.

In a preceding work [12] Mössbauer absorption spectra were observed on some γ-phase compositions (relative to a ^{125}Te source). That case is easier: we see only a quadrupole coupling (relative to Te) whose quadrupole splitting decreases when the Te content increases. The presence of a single quadrupole coupling is a consequence of the undirectional character of the tellurium bond.

The small decrease of the quadrupole splitting as the Co-atom vacancies in the (0, 0, 1/2) planes increase may be caused by a variation in the polarization state of the tellurium.

REFERENCES

1. TENGNER S., *Z. anorg. Chem.* **239**, 126 (1938).
2. KOSTER W. and HORN E., *Z. Metallk.* **43**, 333 (1952).
3. GALPERIN F. M. and PEREKALINA T. M., *Dokl. Akad. Nauk. SSSR* **69**, 19 (1949).
4. HARALDSEN H., GRØNVOLD F. and HURLEN T., *Z. anorg. Chem.* **283**, 143 (1956).
5. DUDKIN L. D. and DIUL'DINA K. A., *Zh. neorg. Khim.* **4**, 2313 (1959).
6. GHEIDERIKH V. A., GHERASSIMOV YA. I., MATLASIEVICH O. B., *Khimiceskaja sbiass V. Kristallokh. Nayka i Tekhnika* p. 292, MINSK (1969).
7. UCHIDA E., *J. phys. Soc. Japan* **10**, 517 (1955).
8. UCHIDA E., *J. phys. Soc. Japan* **11**, 465 (1956).
9. ARIYA S. M., KOLBINA E. M. and APURINA M. S., *Zh. neorg. Khim.* **2**, 24 (1957).
10. ALBERS W. and HAAS C., Phys. Semicond. (Conf. Paris, 1964), p. 1261, Dunod, Paris (1964).
11. ARKHAROV V. I., KLOTSMAN S. M., TIMOFEEV and TRAKHTEMBERG I. H., *Phys. Metals Metallogr.* **14**, 68 (1962).
12. ORTALLI I., FANO V. and GIBART P., *Proceedings of XVI Colloque Ampère Bucarest* 1970.
13. INGALLS R. and DEPASQUALI G., *Phys. Lett.* **15**, 262 (1965).
14. QAIM S. M., *Proc. Phys. Soc.* **90**, 1065 (1967).
15. WERTHEIM G. K., *Phys. Rev.* **124**, 764 (1961).

16. CAVANAGH J. F., *Phys. Status Solidi* **36**, 657 (1969).
17. BERTAUT E. F., *Acta crystallogr.* **6**, 557 (1953).
18. JELLINEK F., *Öst. Chem Ztg* **60**, 311 (1959).
19. GIBART P. and VACHERAND C., *J. cryst. Growth* **5**, 111 (1969).

J. Phys. Chem. Solids, 1971, Vol. 32, pp. 2311–2330. Pergamon Press. Printed in Great Britain.

SHOCK-WAVE COMPRESSION OF SAPPHIRE FROM 15 TO 420 KBAR. THE EFFECTS OF LARGE ANISOTROPIC COMPRESSIONS*

R. A. GRAHAM and W. P. BROOKS
Sandia Laboratories, Albuquerque, New Mexico

(*Received* 14 *January* 1971)

Abstract—Under shock compression, sapphire (crystalline Al_2O_3) exhibits Hugoniot elastic limit, HEL, values of from 120–210 kbar; the largest values observed for any solid. Because of the large HEL, the stress configuration of the shock-loaded sample is highly anisotropic. A critical examination of the effects of large anisotropic stresses on the compression of solids is accomplished with shock experiments on sapphire in three crystallographic directions at stress values within the elastic range to stress values up to twice the HEL. The maximum shear strengths observed range from 4·9 to 5·6 per cent of the shear modulus. When stresses in excess of the HEL are achieved, sapphire is observed to undergo a catastropic loss of shear strength; in contrast to the yield behavior observed for metals. The results are compared to observations on high density polycrystalline Al_2O_3 and other solids with large HEL values. The behavior of sapphire is found to be analogous to that previously observed for crystalline SiO_2. Data in the elastic range show a third order elastic constant $C_{111} \approx C_{333} = -(3{\cdot}6 \pm 0{\cdot}4) \times 10^{13}$ dyne/cm^2. Analytical methods are developed to determine the shear stress offset independent of the hydrostatic data.

1. INTRODUCTION

COMPRESSION measurements for hydrostatic pressures greater than a few tens of kbars are difficult to accomplish and limited in accuracy [1]. Ultrasonic measurements of compressibility and its pressure derivative can be precisely determined but are limited to modest pressures [2]. Consequently, shock-wave compression measurements, which may be accomplished at very high pressures, are frequently employed to provide data which may be used to calculate high pressure isothermal compression curves [3] or to test extrapolation of ultrasonic data to very high pressure [2]. Unfortunately, data from shock compression experiments are not directly comparable to either ultrasonic data or static high pressure isothermal data. The experimental conditions of the shock experiment not only include heating due to the rapid compression but also include a potentially large shear stress component which is an inherent property depending upon the shear strength of the solid. Early shock compression workers usually assumed that the shear strength of solids was negligible so that the shock compression was isotropic and the calculation of an isothermal compression curve from the shock data was concerned only with thermodynamics of the shock heating and the equation-of-state of the solid [4]. It is now widely recognized that the effect of shear strength of the solid must be evaluated before hydrostatic and shock compression data can be directly compared. Unfortunately, the shear strengths of solids under shock-wave compression have not received as much study as thermodynamic effects and are not well enough understood to evaluate their effects unequivocally.

The object of the present paper is to evaluate shear strength effects in solids which exhibit unusually large shear strengths with correspondingly large anisotropic compressions. After introducing basic concepts of the stress configurations imposed by shock-loading and the shear strength, the existing models for the effects of shear strength of solids on the compressions experienced in a shock compression experiment will be reviewed. Following this, an experimental study of the shock compression of sapphire (single crystal Al_2O_3) will be described and the results will be presented and examined for shear strength effects. A determination of several higher-order elastic constants will also be presented. The results of the present investigation will then be used along with the other data in the literature to assess the present understanding of shear strength effects in solids under shock compression.

---

*Work supported by the U.S. Atomic Energy Commission.

2. BACKGROUND

(a) *Shear strength of solids*

Shock loading a sample with the detonation of a high explosive[5], the impact of a projectile[6, 7], or the rapid deposition of radiant energy[8] produces an inertial response with pressures and pressure-time histories which depend upon the compressional properties of the sample. When the sample is loaded over a large planar area the compression is uniaxial, i.e., a state of uniaxial strain is achieved for times less than that required for unloading pulses to arrive in the test area. If the sample has a finite, i.e., non-zero, shear strength, the stress configuration is not isotropic since the resulting inertial stress components normal to the shock compression direction are less than the stress component in the shock propagation, or axial, direction. The shock experiment measures only the stress component in the axial direction while the lateral stress components can only be inferred by indirect means. Moreover, the axial component of stress will be larger than the isotropic pressure at the same compression to an extent depending upon the magnitude of the shear component of stress. The relation between the isotropic and anisotropic compressions must be known before the shock data can be converted to equivalent isotropic compression conditions.

The magnitude of the shear may be expressed in terms of the stress component, σ_x, measured in the shock experiment and a mean pressure value by considering an anisotropic stress configuration and defining a mean pressure, $\bar{P}$, as

$$\bar{P} \equiv \tfrac{1}{3}(\sigma_x+\sigma_y+\sigma_z). \qquad (1)$$

If a solid is laterally isotropic the lateral stress components are equal, i.e., $\sigma_y=\sigma_z$. Equation (1) may then be rearranged such that

$$\bar{P} = \sigma_x - \tfrac{2}{3}(\sigma_x-\sigma_z). \qquad (2)$$

The maximum value of the shear stress, $\tau_{\max}$, is

$$\tau_{\max} = \tfrac{1}{2}(\sigma_x-\sigma_z), \qquad (3)$$

thus,

$$\bar{P} = \sigma_x - \tfrac{4}{3}\tau_{\max}. \qquad (4)$$

It will be convenient in what follows to refer to the difference between σ_x and $\bar{P}$ as the *shear stress offset* defined as

$$\sigma_\tau \equiv \sigma_x - \bar{P}. \qquad (5)$$

The determination of differences between longitudinal shock compression stresses, σ_x, and hydrostatic pressures, P, at the same volume could provide an experimental measure of the shear stress offset. However, as previously indicated, measurements of both σ_x and P are normally not available in the same high pressure range and it is desirable to evaluate σ_τ independently so that measurements of σ_x may be used to compute $\bar{P}$.

Since the strain configuration is known to be uniaxial and since solids are frequently observed to behave elastically up to a yield stress value in shock compression called the Hugoniot elastic limit, HEL, the shear stress value at the HEL can be computed assuming that Hooke's law is valid. In this case

$$\tau^* = \tfrac{1}{2}[(1-2\nu)/(1-\nu)]\sigma_H \qquad (6)$$

where τ^* is the limiting shear imposed by the shear strength of the solid as computed from the measured HEL, σ_H, and ν is Poisson's ratio for the solid. It is convenient to define a *shear strength offset*

$$\sigma^* \equiv \tfrac{4}{3}\tau^* \tag{7}$$

in a like manner to the shear stress offset σ_τ.

In this paper the high pressure region above the HEL will be examined to determine the magnitude of the *shear stress offset*, σ_τ, and its relation to the *shear strength offset*, σ^*. Previous theoretical and experimental studies have indicated the basis for two radically different relations between σ_τ and σ^*. These relations are developed for *elastic-plastic solids* and what will be called *elastic-isotropic solids*.

(b) *The elastic–plastic solid*

The theory of plasticity has been adapted to the uniaxial strain configuration in studies by Wood[9] and Fowles[10]. One result which may be extracted from this work is that under ideally plastic deformation

$$\sigma_\tau = \sigma^*, \qquad \sigma_\tau > \sigma_H; \tag{8}$$

that is, the shear stress offset is independent of pressure and equals the shear strength offset which is a fixed property of the solid. For the elastic–plastic solid the magnitude of the shear stress has no inherent effect on the properties of the solid and the solid can be characterized as having a constant shear strength.

The elastic–plastic solid has very attractive features since it is particularly simple in concept both theoretically and phenomenologically and the numerous static studies of plastic flow and deformation can be used as a guide for the shock deformation. Furthermore, the microscopic theories of dislocation motion in solids have been successful in explaining many aspects of plastic flow under static conditions and similar dislocation theories have been successfully pursued under shock loading. This provides a fundamental basis for understanding the response of solids to large anisotropic compressions and second-order effects involving small changes in σ_τ. In addition, rate effects observed in shock experiments may be described in terms of the dislocation theory.

Since the initial experimental confirmation of elastic-plastic response of aluminum by Fowles[10] in 1961, several experimental investigations have demonstrated that a number of metals respond to shock loading as elastic–plastic solids[11–18]. In addition a recent examination of the fixed point phase transition pressures measured under hydrostatic and shock conditions indicated that the elastic–plastic model correctly correlated the shock and static results for a number of metals [19]. Although numerous deviations to the elastic–plastic response of metals have been noted, such as different HEL values than predicted from static measurements[20, 21] and unloading paths[22] not predicted by elastic plastic response, it appears likely that they can be explained in terms of modifications to the basic theory.

Confirmation of the elastic plastic model is particularly gratifying since HEL values can be routinely measured experimentally and the HEL value can be used to calculate σ_τ if elastic–plastic response correctly describes the solid. Furthermore a recent survey of HEL values[20] indicates that shear strength effects are not negligible in many instances.

Unaware of the simplicity of the elastic-plastic response, crystalline quartz chooses to respond to anisotropic compressions in a radically different fashion, thereby raising questions as to the generality of the elastic–plastic response, and the calculation of σ_τ from the measured HEL values.

(c) *The elastic–isotropic solid*

Shock experiments on single crystal quartz revealed an unexpected and dramatically different response than that observed for metals. Neilson and Benedick[23] conducted experiments in which X-cut quartz was shock-loaded at high pressures and the resulting piezoelectric outputs were measured. Interpretation of these piezoelectric outputs required that quartz exhibit an unusually large HEL and a state of zero piezoelectric polarization in the high pressure region above the HEL. The piezoelectric response of quartz to isotropic compression is zero; hence, zero polarization requires $\sigma_\tau = 0$. This observation led Wackerle[24] and Fowles[25] to perform shock compression measurements on crystalline quartz which, when compared with Bridgman's hydrostatic data, showed that even though σ^* was unusually large, that $\sigma_\tau = 0$ for stresses greater than the HEL. The manner in which quartz suffers this loss of shear strength seems inexplicable within the theory of plasticity and classical dislocation mechanics. Unlike the elastic–plastic solid which has a fixed characteristic shear strength, the elastic–isotropic solid suffers a catastropic loss of shear strength when a critical shear stress is exceeded. The magnitude of the shear stress alters the shear properties of the solid.

The phenomenological difference between the elastic–plastic solid and the elastic–isotropic solid is demonstrated in Fig. 1. Unlike the elastic–plastic response which shows a constant offset from the isotropic compression curve above the HEL, the elastic–isotropic response shows no offset. If the process by which the loss of shear strength occurs does not alter properties of the solid, the hydrostatic compression curve and shock compression curve will be the same in regions where the shock heating is negligible.

In contrast to the situation for metals, the generality of the loss of shear strength has not been systematically explored. It has been suggested[26, 27] that the elastic–isotropic response may be typical of 'brittle' solids but little systematic attempt has been made to verify this characterization.

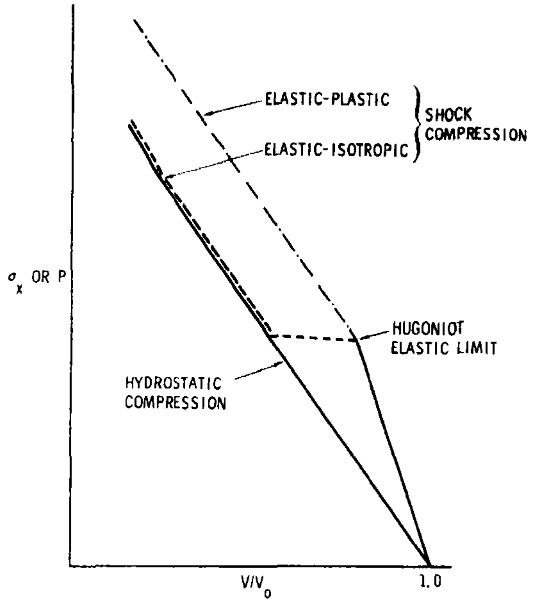

Fig. 1. Principal features of the two simplest models for the compressional behavior of solids under shock compression. The elastic–plastic solid exhibits a constant shear stress offset from the hydrostatic curve for stresses greater than the HEL. On the other hand, the elastic–isotropic solid exhibits no shear stress offset. Unlike the elastic–plastic solid, the shear strength of the elastic–isotropic solid is irreversibly reduced by the shear stress accompanying uniaxial strain.

Recently, Ahrens *et al.*[28], reported shock-compression measurements on a high-density polycrystalline Al_2O_3 and concluded that Al_2O_3 responded as an elastic–plastic solid. This was subsequently confirmed by Munson[29]. Since polycrystalline Al_2O_3 is a brittle solid this observation is not consistent with the early predictions of the response of brittle solids. Further complicating the question, McWhan[30] reported static compression measurements on quartz with X-ray techniques and found that the shock data and the high pressure static data showed a small, 1 per cent offset in volume. Thus, at the present time we have no consistent basis for predicting the shear stress offsets of solids other than metals and are faced with a fundamental unknown in the mechanical response of solids to large anisotropic compressions.

The present study of the shock compression of single crystal Al_2O_3, sapphire, was undertaken to examine further the effects of large anisotropic compressions resulting from large values of the HEL[31]. Analytical methods developed in the discussion section give an explicit basis for identification of the loss of shear strength under shock loading. Sapphire is an excellent material for further study because it has similar characteristics to quartz. Both crystals are oxides, both crystals are trigonal; however, sapphire has much larger values for elastic constants. Furthermore, the shear strength effects for sapphire are larger than thermal effects thus affording an uncoupling between mechanical and thermal effects.

Even though the principal interest of this investigation is in the high pressure region above the HEL, measurements were accomplished both below and above the HEL. The measurements below the HEL permit an examination of several elastic constants at compressions an order of magnitude larger than those previously employed and help to guide the extrapolation of the ultrasonic data to the high pressure region.

3. EXPERIMENTAL ARRANGEMENTS

The experiments were of two basic types; those which determined the high pressure response above the Hugoniot elastic limit, HEL, and those which determined the elastic response below the HEL. The high pressure experiments utilized shock-loading with plane wave high explosive techniques, while the elastic response was determined in experiments which utilized projectile impact loading techniques.

The high pressure experiments were accomplished by generating explosively driven plane shock-waves into the samples and monitoring their response with an optical technique similar to that employed by Wackerle[24]. A schematic of this experimental arrangement is shown in Fig. 2. The high explosive plane-wave generators and explosive pads send a shock wave from the detonation through an intermediate driver plate of 2024 aluminum and into the disk-shaped sample. Various pressures are then achieved by the choice of different high explosive materials. The various explosive and impact configurations are described in Table 1.

During the experiment the position of the wire and its image are viewed through appropriate lenses through a 0·1 mm observation slit in the camera and recorded on film as a function of time as the shock wave enters the sample and reflects from the free surface. As the shock enters the sample, the reflectivity of the input surface plating is destroyed and the background light intensity is abruptly changed. An alternate transit time measurement with quartz pins was necessary because of the unreliable nature of the change in reflectivity as the shock entered the sample. The sharp extinction in background light was not always achieved.

After arrival of the second wave the image was sometimes optically distorted as shown in Fig. 2 by the opening of minute scratches on the polished surface. In these cases, however, the scratches themselves or the edge of reflecting surface follow the surface motion directly and their motion was used to obtain second-wave free-surface velocity measurements.

The calibrations of displacement and time are particularly simplified in this technique. The position of the wire above the free surface is measured before shot time to one part in 10^4. The displacement magnitude is then indicated directly on the film by the distance between the wire and its image before shock arrival at the free surface. The rotation speed of the rotating mirror in the camera was measured at shot-time with a resulting sweep rate accurate to $\pm\frac{1}{2}$ per cent. Consideration of all the possible experimental errors in measurements and data reduction gives estimated errors of ±1 to 2 per cent in shock velocity and ±3 per cent in free-surface velocity.

The samples used in the high pressure experiments were cut from single crystal boules of sapphire grown by the Verneuil technique

Table 1. Shock loading configurations

Designation	Configuration	Measurements
H	Gun-symmetric impact	impact velocity electrical response
HQ	Gun-quartz gauge	impact velocity quartz gauge signals
B	*P*-40(a) + 25 mm Baratol(b) plus 12 mm 2024 aluminum alloy	free surface velocity (optical) shock velocity (optical/and/or quartz pins)
T	*P*-40(a) + 25 mm TNT plus 12 mm 2024 aluminum alloy	"
C	*P*-40(a) + 25 mm Composition B plus 12 mm 2024 aluminum alloy	"
H	*P*-40(a) + 25 mm PBX 9404 plus 12 mm 2024 aluminum alloy	"

(a) Designation for 10 cm dia. plane wave explosive lens as described in Ref. [5].
(b) Explosive compositions are further described in Ref. [5].

by the Linde Co. The samples were cut, crystallographically oriented, and polished by the Valpey Corporation. The disks were nominally 31 mm in diameter and 6, 10 or 13 mm in thickness. The material was clean and free of defects to the unaided eye. Crystallographic orientations investigated were the natural growth direction of 60°, the optical orientation 0° as well as the 90° orientation.*

Experiments below the HEL were accomplished utilizing the symmetrical projectile impact and electrical response technique previously discussed in some detail[32]. The sample disk is mounted on the impact face of a high velocity compressed gas gun and impacted with a projectile faced with another sample disk. Because of the symmetry of the impacting samples. the particle velocity imparted to the sample is precisely one-half the measured impact velocity. The shock-wave velocity at various particle velocities is measured by observing the electrical response of the sample which is initially charged to a high voltage. The transit time of the shock is clearly indicated on the electrical response records. This experiment is especially useful for determining the shock compression in the elastic range. Experiments beginning at low stress levels and increasing in stress amplitude help to insure the proper identification of the elastic-wave in the high pressure experiments.

One critical projectile impact experiment was performed with Sandia quartz shock-wave stress gauges[33] in which both the impact surface response and back surface response is precisely monitored in time. This type of experiment which has been previously described[34] provides superior time-resolution of the stress profiles in the sample.

4. RESULTS

Measurements and data analysis for shock compression experiments are concerned with the description of the stress vs. time or stress vs. position profiles which result when one surface of a plane sample is subjected to various transient high pressure loadings The characteristics of these profiles can be shown to be directly related to the stress vs. com-

---

*The crystallographic orientation of the 0° axis is [0001], for the 90° axis is $[\bar{1}2\bar{1}0]$ and for the 60° axis is $[11\bar{2}3]$.

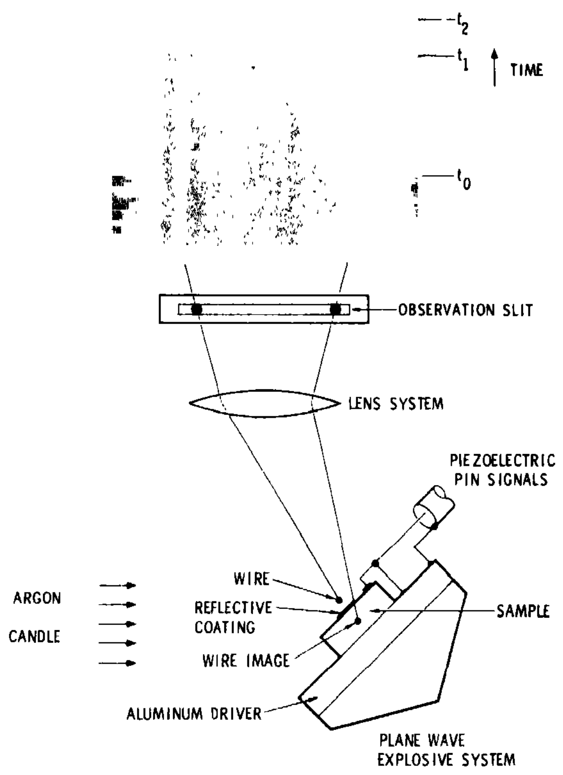

Fig. 2. Experimental technique used in the high pressure experiments. The displacement vs time response of the free surface of the sample to high explosive loading is monitored with a high speed streak camera which follows the motion of a 0·1 mm dia. wire and its image as reflected from the surface of the sample. The high speed camera was a Beckman and Whitley Model 770 with a maximum writing speed of 16·7 mm/μsec. Shock arrival times of the first waves are also monitored with piezoelectric pins. The typical record shows the extinction of background light when the shock enters the sample at time t_0. The arrival time of the first wave at the free surface is t_1 and the arrival time of the second wave is at t_2. For the experimental record shown, the time difference $t_1 - t_0$ is 1·077 μsec and the height of the wire above the sample is 1·610 mm.

pression curve for the sample material. In the present paper two characteristically different wave profiles are observed in the various stress ranges. These are (1) a single elastic compressive wave of stress less than the HEL and (2) a two-shock front profile consisting of an elastic wave, whose amplitude is the HEL, and a slower moving higher pressure wave. Since different assumptions are employed in the data reduction in each of the two cases the method of data reduction for each experiment will be described.

The stress vs. compression states for each experiment are calculated assuming steady wave conditions and applying the conservation of mass and momentum conditions across each shock front. Thus, from the conservation of mass

$$\frac{\Delta V}{V_0} \equiv \eta = \frac{\Delta u}{U - u_i}, \tag{9}$$

and from the conservation of momentum

$$\Delta\sigma = \rho_0(U - u_i)\Delta u, \tag{10}$$

where V_0 is the specific volume ahead of a shock front, ΔV is the magnitude of the change in specific volume imparted by the shock front, η is the strain or compression, Δu is the change in particle velocity, u_i is the particle velocity ahead of the shock front, $\Delta\sigma$ is the change in stress imparted by the shock front in a direction normal to the shock front. All velocities are in laboratory coordinates.

(a) *Elastic range experiments*

Experiments conducted within the elastic range were accomplished with the symmetrical impact configuration. Under these conditions a single shock front propagates with amplitude equal to the input particle velocity and travels with a fixed shock propagation velocity. In the experiment the particle velocity is measured with an accuracy of ±0·3 per cent while the shock velocity is measured with an accuracy of ±1 to 1–½ per cent. These values should be contrasted to the explosively driven experiments which produce multiple shock fronts whose free-surface velocities are measured with an accuracy of ±3 per cent while the shock propagation velocities are measured with an accuracy of 1 to 2 per cent.

The shock velocity and particle velocity values observed are shown in Table 2 along with the computed stress and compression data. The experiments in the elastic range are conducted over a range of stress from 15 to 100 kbar with measurements in three crystallographic orientations. Typical records from which these data are obtained have been previously shown[32]. Increased shock velocity is observed with increasing particle velocity in all crystallographic orientations. This behavior will be compared to ultrasonic determinations of higher order elastic constants in the discussion section.

One special experiment was conducted on a 60° orientation sample. This crystallographic orientation is the natural growth direction of the artificially grown sapphire boules. For this reason, the availability, low cost and high quality of the material in the large diameters required for this work, make the 60° orientation more desirable than other orientations. On the other hand, this crystallographic orientation is apparently not a 'specific direction,' that is, a longitudinal motion applied along the disk axis may produce both a quasi-longitudinal and a quasi-shear wave[35]. However, even though sapphire has trigonal symmetry the elastic stiffnesses do not vary significantly with orientation. For example, the longitudinal wave speeds in the 0° and 90° orientations differ by only ½ per cent. Hence, the nonsymmetric response would be expected to be small if not insignificant.

To determine the extent of the effect, a 60° orientation sample was impacted at 28 kbar with a quartz gauge which precisely measures the input stress to the sample. This same experiment also included a quartz gauge measurement of the resulting shock wave profile after propagation through a distance of

Table 2. *Shock compression data for sapphire*

					$\rho_0 = 3{\cdot}986$ g cm^{-3}						
		Sample	First wave				Second wave				
Shot no.	Configuration	thickness	u_1	U_1	σ_1	V_1/V_0	u_2	$\bar{U}_2$	U_2	σ_2	V_2/V_0
		mm	mm μsec^{-1}	mm μsec^{-1}	kbar		mm μsec^{-1}	mm μsec^{-1}	mm μsec^{-1}	kbar	
					0° orientation						
H298	*H*	2·54	0·0333	11·29	15·2	0·9970					
H221	*H*	5·11	0·0401	11·2	17·9	0·9964					
H305	*H*	2·56	0·0463	11·1	21·3	0·9958					
H297	*H*	2·57	0·0810	11·25	36·7	0·9929					
H216	*H*	5·11	0·0943	11·2	42·1	0·9916					
H299	*H*	2·54	0·1122	11·3	50·4	0·9901					
132-65	*B*	10·89	0·38	11·65	175	0·9674	Second wave not observed				
134-66	*B*	10·90	0·34	(11·6)[a]	157	0·9707	Second wave not observed				
357-67	*B*	6·450	0·31	(11·5)[a]	142	0·9730	0·49	8·05	7·56	196	0·9488
331-65	*T*	12·70	0·30	11·55	138	0·9740	0·69	8·88	8·61	271	0·9283
379-67	*T*	6·400	0·32	11·6-11·4	148	0·9722	0·71	8·76	8·49	262	0·9258
330-65	*C*	10·86	0·33	11·55-11·6	150	0·9715	0·86	9·12	8·91	337	0·9114
663-66	*C*	6·401	0·37	11·5-11·4	170	0·9677	0·83	8·55	8·24	319	0·9111
160-65	*H*	12·68	0·41	11·77	195	0·9652	1·08	8·82	8·52	419	0·8855
380-67	*H*	6·400	0·46	11·64	210	0·9605	0·94	8·91	8·67	370	0·9029
					0° orientation						
H317	*H*	2·59	0·1213	11·2	52·6	0·9892					
H318	*H*	2·58	0·1477	11·2	64·1	0·9868					
178-66	*B*	10·86	0·342	11·39	155	0·9700	0·474	6·90	5·97	186	0·9472
546-65	*T*	10·89	0·291	11·57	134	0·9748	0·69	8·63	8·25	264	0·9259
545-65	*H*	10·80	0·381	11·76	179	0·9676	0·98	8·72	8·44	378	0·8957
					60° orientation						
H245	*H*	3·21	0·0370	11·1	16·1	0·9967					
H267	*HQ*		0·0653		28·2	0·9943					
		12·67		11·16	28·5						
H248	*H*	3·21	0·0703	11·2	31·3	0·9937					
H246	*H*	3·19	0·0780	11·1	34·5	0·9930					
H250	*H*	3·20	0·1268	11·1	55·7	0·9886					
H211	*H*	3·15	0·225	11·2	102	0·9796					
192-64	*B*	12·832	0·267	11·23	120	0·9762	0·456	8·07	7·60	177	0·9510
257-64	*C*	12·750	0·374	11·38	170	0·9671	0·895	8·62	8·34	341	0·9034
219-66	*C*	12·800	0·35	11·43-11·40	160	0·9694	0·83	8·53	8·14	314	0·9097
188-64	*H*	12·817	0·282	11·54	130	0·9756	0·99	9·39	9·18	388	0·8980

[a] Not measured due to partial experimental failure. Values shown are those assumed to calculate first wave parameters.

12 mm. The result is shown in Table 2 as shot No. H267. The input and output measurement agreed to within 1 per cent and the shock profile showed no dispersion in time. Thus, on the basis of this measurement the 60° orientation samples can be considered as exhibiting pure longitudinal wave propagation without detectable error in measurements or calculations.

(b) *High pressure experiments*

Analysis of the explosively-driven shock profile measurements requires a number of additional assumptions due to the reflection of the shocks from the free surface of the samples and the subsequent interaction of the reflected elastic wave with the slower moving high pressure wave. The arrival of the shock waves at the free-surface causes a complete reflection of the incident wave back into the bulk of the sample. If this reflection occurs symmetrically, the resulting free surface velocity is twice the incident particle velocity. This free-surface velocity assumption has been applied to compute the incident particle velocity from the measured free surface velocity. The interaction of this reflected elastic wave with the high pressure wave causes a detectable effect on the data analysis.

The high pressure wave is perturbed before it arrives at the measuring station; thus, the principal problem is to deduce the unperturbed second wave shock velocity from the measurements at the free surface. This interaction is a more important problem than that experienced in experiments on metals because of the possibility of the irreversible loss of shear strength at high pressures. A detailed and graphical description of the problem is given by Ahrens *et al.*[28] and is discussed for the similar situation in quartz by Wackerle [24] and Fowles [25].

Following Wackerle [24] the second wave propagation velocity, U_2, is calculated from the relation:

$$U_2 = \bar{U}_2\left[1 - \frac{\Delta t}{t_1}\left\{\frac{(U_3-2u_1)(U_1-2u_1)t_2 - U_1^2 t_1}{U_1(U_3-2u_1)t_2 + U_1^2 t_1}\right\}\right] \tag{11}$$

where $\bar{U}_2$ is the nominal shock velocity taken as the original thickness, l, divided by the arrival time, t_2, of the second wave at the free surface, Δt is the difference in arrival times between the first and second waves, t_1 is the arrival time of the first wave, the u's are the particle velocities of the various waves as indicated by the subscripts, U_3 is the shock velocity of the reflected elastic wave after interaction with the second wave, and U_1 is the shock velocity of the first wave.

In the stress range just above the HEL the calculated value of U_2 is sensitive to the choice of a value for U_3 which is not measured in the experiment. However, even though U_2 cannot always be calculated unequivocally the uncertainty in U_3 is not sufficient to change any conclusions and only in the experiments 178-66, 357-67 and 192-64 does it affect the U_2 values significantly. In the data shown in Table 2 the value of U_3 is chosen to be U_1+2u_1, in accordance with the view that the material can be elastically reduced to zero stress and subsequently restressed to support the same HEL value. This assumption was found to lead to no inconsistencies among the data and among comparisons to other investigators data.

In order to examine the possibility of nonsteady material response accompanying the transition from elastic compression to inelastic compression, experiments were conducted at three sample thicknesses and for four different explosive driving pressures. Although no unequivocal evidence of stress relaxation was observed behind the elastic wave, the amplitude of the elastic wave, HEL, summarized in Table 3 shows both a thickness dependence and a driving pressure dependence which is characteristic of nonsteady behavior of the elastic wave. It is probable that small stress relaxation could occur and not be detected by the displacement-time measurements which are inherently

Table 3. Hugoniot elastic limits of sapphire

Driver	0° orientation	90° orientation	60° orientation
Sample thickness			
Baratol			
13 mm	—	—	120
11 mm	165*	155	—
6 mm	140	—	—
TNT			
13 mm	140	—	—
11 mm	—	135	—
6 mm	150	—	—
Comp B			
13 mm	—	—	—
11 mm	150	—	165*
6 mm	170	—	—
9404			
13 mm	195	—	130
11 mm	—	180	—
6 mm	210	—	—

*mean value of two experiments.

limited by poor resolution of rapid changes in velocity.

The values observed range from 120 to 210 kbar. Thus sapphire exhibits the largest HEL value ever observed for any material. There is considerable scatter in the HEL data. Examination of similar sapphire samples in polarized light indicated considerable internal strain in many samples and it appears that the scatter in HEL values results from the extent of the internal strain in the samples.

5. DISCUSSION

Because of the very large HEL values, the shock compression response for sapphire is well suited for use in studying the effects of large anisotropic compressions on solids. From the data in the elastic range, values for several third order elastic constants will be computed at substantially larger compressions than previously employed. From the data in the high pressure region above the HEL the shear stress configuration will be determined and conclusions drawn concerning the effect of shear on compressional behavior of solids. Finally, the HEL values themselves will be analyzed to provide a basis for predicting the conditions under which large values of HEL are observed. As indicated in the introduction the present understanding of these questions for solids other than the metals is inadequate even though these questions are important to our determinations of high pressure equations of state, physical property measurements under shock compressions, and a general theory of plasticity of solids.

This section will first compare the data in the elastic range to extrapolations of ultrasonic measurements of elastic constants. Following this, the high pressure data above the HEL will be examined for evidence of shear stress components and compared to the amplitudes of the HEL and to values for other solids.

(a) *Elastic range data*

The compressions achieved in the elastic range are an order of magnitude larger than those achieved in the recent ultrasonic measurements of Gieske and Barsch[36].

Unlike shock compression data at stresses greater than the HEL, uncertain effects of the stress configuration are minimal and interpretation of the data is more direct. Even though ultrasonic measurements are far more precise than shock compression techniques, the larger compressions of the shock experiment enhance higher order effects sufficiently to be observable.

Fowles [25] has recently demonstrated that Thurston's finite strain theory can be adapted so that shock compression data in the elastic range can be used along with ultrasonic data to determine higher order elastic constants. Fowles [25] developed an explicit stress vs. compression relation involving higher order elastic constants for large uniaxial elastic compression which we will use to interpret the shock compression data. In order to test the adequacy of the usual second order elastic constant description of sapphire at large compressions, the data of Gieske and Barsch are used to calculate the stress-volume relations from Fowles' finite strain development. The results of the calculations are shown in Fig. 3 along with the shock compression data. At the smaller compressions the different crystallographic orientations cannot be distinguished between at the scale of the figure and the differences at the largest compressions are less than the experimental error. Recent shock compression data of Barker *et al.*[37] on 0° sapphire are also included in the figure.

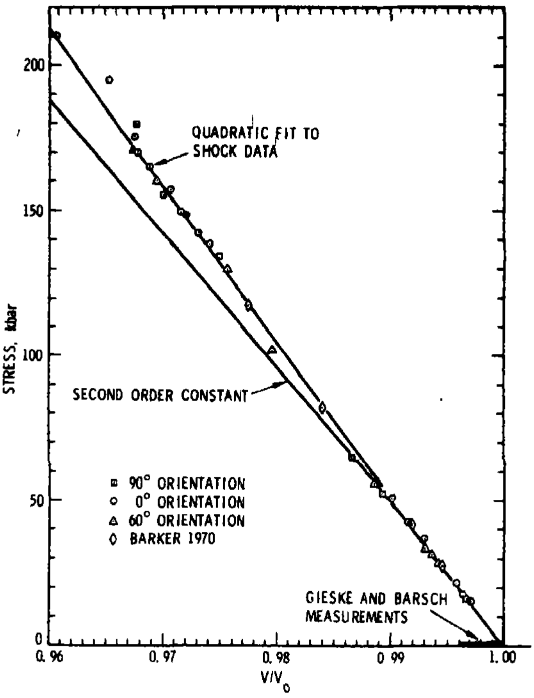

Fig. 3. Shock compression of sapphire in the elastic range. The second-order elastic constants of Gieske and Barsch are used in Fowles' finite strain equations to predict the large strain results in the 0° and 90° orientations indicated by the second order constant line. The slight negative curvature of the second order constant line is a result of finite strain theory. The difference between the shock results, as fit by a quadratic, and the finite strain values predicted from the usual second-order constant predictions allow third order elastic constants to be computed. Recent shock data of Barker are also included. To the scale used in the figure the compressions in the various crystallographic orientations cannot be distinguished between. The compression range of the hydrostatic pressure measurements of Gieske and Barsch are indicated along the abscissa.

Examination of the extrapolated ultrasonic data in Fig. 3 shows a systematic deviation between the compression computed from second order constants and the observed shock compressions. The value of the third order elastic constant which gives the best fit to the shock data is obtained by determining the difference between the stress compression curve calculated from the second order constants and the observed shock compression data. Within the accuracy of the data, $C_{111} \approx C_{333} = -(3{\cdot}6 \pm 0{\cdot}4) \times 10^{13}$ dyne/cm^2.

Because third order elastic constants give sufficiently good description to the shock data, extrapolation of the ultrasonically measured bulk modulus and its pressure derivative should provide an accurate estimate of the isotropic compression curve for comparison with the shock compression data above the HEL.*

(b) *High pressure response*

The unusually large HEL values observed for sapphire cause large deviations in stress-volume relations from the isotropic compressions achieved in hydrostatic experiments. Furthermore the large shear stresses which are a consequence of the large HEL values cause concern that the shear itself may cause irreversible changes in the properties of the solid. Although it is possible to compare shock data directly with hydrostatic data as one method for determination of shear stress offset in the high pressure region, it is advantageous to develop techniques for determining shear strength from the shock data itself, independent of the hydrostatic data. Conclusions based on the study of the shock data alone impose no *a priori* assumptions concerning the equivalence of the shock and hydrostatic compressions and from a pragmatic point of view the conclusions are not susceptible to changes in the static data or uncertainties concerning the equation of state. Accordingly, we will delay comparing shock and static data until the shock data has been examined for evidence of shear stress offset.

---

*Note added in proof (See p. 2330).

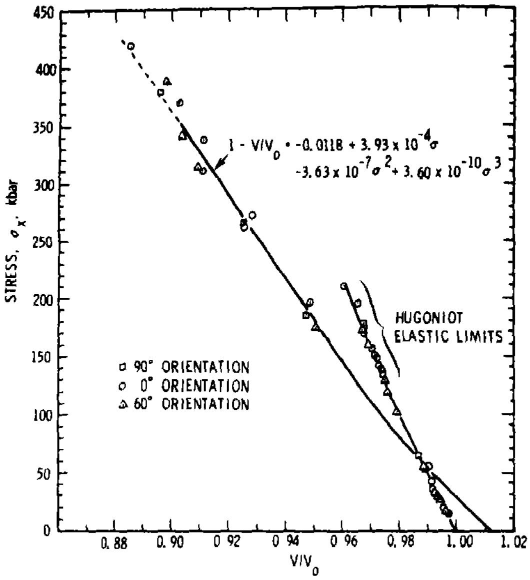

Fig. 4. Stress-volume relations for sapphire under shock-wave compression. The experimental points for the present investigation are fit with the cubic polynomial relation shown. All high pressure points show a common compression curve in spite of the fact that various Hugoniot elastic limits are observed depending upon the crystallographic orientation and driving pressure. For stresses above 350 kbar the data are not as accurately fit by the cubic polynomial.

(c) *Compression observations*

One of the most obvious and striking features of the data shown in Fig. 4 is that all the high pressure compression states fall on a common compression curve. The common compression curve is observed even though HEL values ranging from 120 to 210 kbar were observed for the different crystallographic orientations, sample thicknesses and driving pressures. According to the elastic–plastic model each high pressure experiment should exhibit a shear stress offset equal to the shear strength offset which is proportional to the HEL. Thus, different high pressure compression curves should be observed for different HEL values. The common compression curve indicates the constant shear strength model will not describe the response of sapphire. Although the value of the shear stress offset cannot be obtained from the observation of a common compression curve it is possible to conclude that sapphire experiences a substantial loss of shear strength and a collapse *toward* the isotropic compression curve. The common compression curve, which is an explicit demonstration of a significant loss of shear strength, was also observed for shock-loaded crystalline quartz [24].

(d) *Shock velocity values*

The stress-volume conditions in the immediate vicinity of the HEL are a sensitive indication of changes in the shear strength in the high pressure region. This can be demonstrated by considering equation (5) which relates the longitudinal stress, σ_x, measured in the shock experiment to the mean pressure, $\bar{P}$, and the shear stress offset, σ_τ. The shock compressibility may be obtained from derivatives of equation (5) with volume such that

$$\frac{d\sigma_x}{dV} = \frac{d\bar{P}}{dV} + \frac{d\sigma_\tau}{dV}. \qquad (12)$$

A constant shear stress immediately above the HEL requires $d\sigma_\tau/dV = 0$. In this case the shock compressibility and isotropic compressibility are equal and a disturbance will travel with the bulk sound speed. On the other hand a significant change in σ_τ requires $d\sigma_\tau/dV \neq 0$ and a change in shock compressibility will result. If the shear strength is reduced the shock compressibility will be less than the isotropic compressibility and a disturbance will travel with a velocity less than bulk sound speed. In the absence of a phase transition this 'slow second-wave' is an explicit indication of large decreases in shear strength.

One of the experiments was conducted at a pressure just above the HEL. The second-wave shock velocity on experiment 178-66 is calculated to 6·0 mm/μsec compared to the bulk sound speed of 8·0 mm/μsec. Two other experiments (192-64 and 357-67) also showed shock velocities substantially less than bulk sound speed. The method of data reduction is admittedly subject to error because of the interaction of the first and second waves. However, the reduced data in experiment 178 cannot be changed sufficiently by various assumptions in the data analysis to obtain a shock velocity as large as the bulk sound speed. Thus, the slow second wave velocity data give a positive indication of the loss of shear strength for pressures just above the HEL.

Wackerle's shock compression study of crystalline quartz[24] also showed one experiment in which the shock velocity was substantially less than bulk sound speed. Although Wackerle did not comment on this observation, it is now evident that both sapphire and quartz show similarities in their compressional behaviors in the immediate vicinity of the HEL. Recent piezoelectric response measurements confirm the slow second wave behavior for quartz[38].

(e) *Determination of shear offset*

Although it is not common to do so, the high pressure shock data can be used to give an explicit measure of the shear offset. Under the assumption that all high pressure data points have a constant offset from the isotropic compression curve and that no phase changes have occurred, the high pressure data can be extrapolated to zero stress and the observed offset in relative volume between the extrapolation and the initial relative volume can be used to compute the shear stress offset. By so doing the high pressure shock data may be used as an independent measure of the offset of an anisotropic curve without prejudice as to the nature of the high pressure response. This then provides for an independent comparison of shock data and static data. A schematic of the method for doing this is shown in Fig. 5.

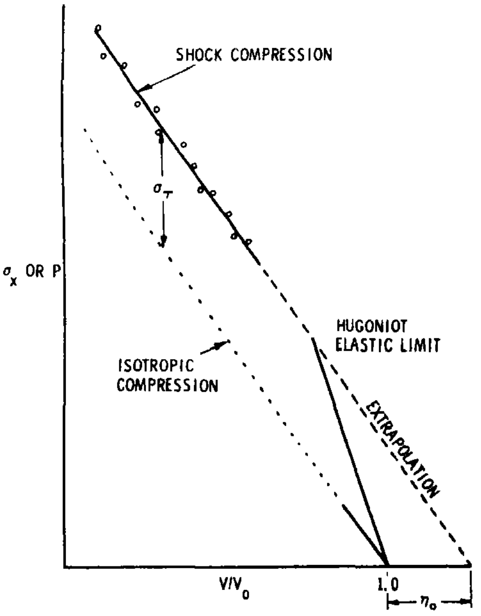

Fig. 5. Extrapolation of high pressure shock data to zero stress may be used to obtain an independent measure of the offset between shock data and the isotropic compression curve. The volume offset at zero stress is a direct measure of the volume offset and the stress offset may be computed as described in the text. The solid depicted responds as an elastic-plastic solid such that $\sigma_\tau = \sigma^*$. The extrapolation does not involve any *a priori* assumptions concerning shear strength and thus may be used as an independent measure of stress offsets.

Assuming that the shear stress offset, σ_τ, is constant for all data above the HEL it can be shown that

$$\sigma_\tau = B\eta_0 \qquad (12)$$

where B is the bulk modulus, η_0 is the magnitude of the zero-stress relative volume offset measured from the extrapolation of the high pressure shock data. The bulk modulus must be known but may be determined from data at atmospheric pressure. The change in bulk modulus with pressure will not seriously affect the calculation since only the change in modulus for compressions up to a value equal to the volume offset will affect the calculation.

The zero stress relative volume offset for sapphire is determined from the shock data above the HEL with a cubic polynomial fit to the data. A cubic polynomial expansion about the initial volume, V_0, shows that:

$$1-\frac{V}{V_0} = -\eta_0 + A\sigma - B\sigma^2 + C\sigma^3, \qquad (13)$$

where $A = 1/B_0$ and B_0 is the atmospheric pressure bulk modulus. If the bulk modulus is assumed to be linear in pressure: [2]$B = (1+B_0')/2B_0{}^2$ and $C = (1+3B_0'+2(B_0')^2)/6B_0{}^3$, where B_0' is the first pressure derivative of the bulk modulus. The adequacy of the cubic polynomial to represent incompressible solids like sapphire in this pressure range has been discussed by Anderson[2].

The best fit for the zero stress volume offset was judged by requiring the first linear term of the polynomial to agree with the ultrasonic measurement of compressibility. The volume offset so obtained is the initial point of a high pressure compression curve fit to the shock data with initial slope in agreement with the ultrasonic data. Iterations are performed in which a volume offset is assumed and fit to the data until agreement with the adiabatic compressibility is obtained. This technique was found to give a volume offset to three significant figures with the present data. Since the coefficient of the second term is related to the pressure derivative of the bulk modulus, B_0', this value is also obtained from the polynomial fit. The values derived for the present shock data are: $\eta_0 = 0{\cdot}0118$, $B_0 = 2{\cdot}542\times10^3$ kbar, and $B' = 3{\cdot}69$. Because the compressions are relatively small, these values are representative of adiabatic compressions.

Using a bulk modulus value of $2{\cdot}542\times10^3$ kbar[36], the shear stress offset of $\sigma_\tau = 30$ kbar is obtained from equation (12); whereas, the calculated shear strength offset, σ^* from equation (7) has values which range from 55 to 110 kbar.*

From another point of view, the relative volume offset can be used to calculate an HEL value consistent with the elastic–plastic theory and this value can be compared to the measured HEL values. Assuming constant values for bulk modulus, B, and the appropriate one-dimensional strain elastic constant, C, up to compressions to the HEL, it can be shown that if the solid responds as an elastic–plastic solid that:

$$\sigma_\eta = B\eta_0(1-B/C)^{-1} \qquad (14)$$

where σ_η is the computed HEL consistent with the observed volume offset and the elastic–plastic model.

The calculated HEL from equation (13) is 60 kbar. This value should be compared to the measured HEL values which range from 120 to 210 kbar. The discrepancy between the HEL predicted from the elastic–plastic theory and the measured values indicates that the elastic–plastic model will not describe the compression of sapphire.

(f) *Summary of shear strength observations*

In summary, it is clear that there are three

---

*All calculations involving elastic constants in this paper use the data of Gieske and Barsch, Ref. [36]. Their paper also contains an excellent summary of other elastic constant data on Al_2O_3. For the single crystal τ^* was calculated from: $\tau^* = \frac{1}{2}(1-C_{xz}/C_{xx})\sigma_{//}$, where x is the shock propagation direction and z is the lateral direction and the C's are the elastic stiffness constants.

different interpretations of the shock data which show a substantial loss of shear strength when sapphire is shocked above the HEL. These are:

1. a common high pressure compression curve, independent of the HEL values,
2. shock-velocity values substantially less than local bulk sound speed,
3. and measurements of the volume offset obtained when the high pressure data are extrapolated to zero pressure.

These same criteria are generally applicable to other materials in investigating shear strength effects.

(g) *Comparison with static data*

To this point the conclusions concerning the shear stress offset are based entirely upon the shock data. There are two static pressure measurements which can be used for an independent determination of the high pressure isotropic compression curve. Both of these are shown in Fig. 6.

The compression measurements of Hart and Drickamer[39] were accomplished with X-ray techniques in a high pressure anvil apparatus. Although the measurements show a large experimental error they can be used as a nominal guide to compressions at high pressure.

The most accurate measurements are the ultrasonic wave velocity measurements of Gieske and Barsch[36] to 10 kbar. Although these data must be extrapolated to significantly higher compressions, the determination of higher-order elastic constants in the elastic range show that the bulk modulus and its pressure derivative should give an accurate description of the compression to values used in the present experiments. The comparison of ultrasonic extrapolation and X-ray data show an appreciable difference but the difference is probably within the experimental error of the X-ray measurement.

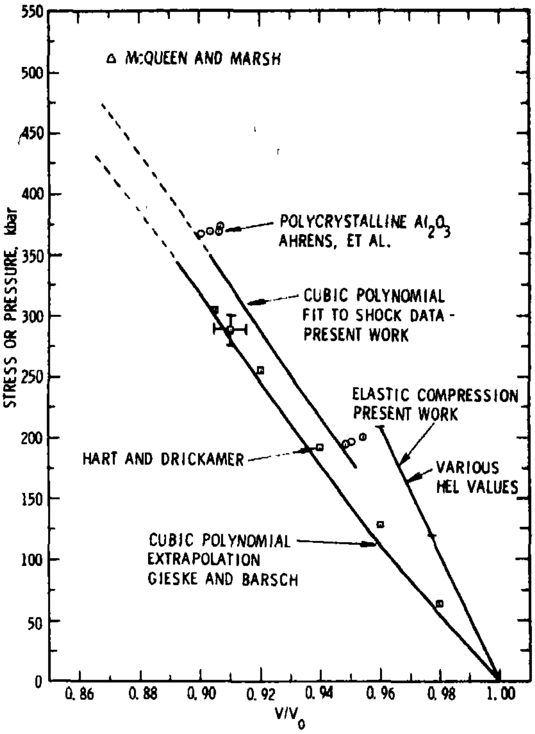

Fig. 6. Compression data for Al_2O_3 derived from various sources. The data obtained in the present investigation is shown by the various polynomial statistical fits. The data of Hart and Drickamer were obtained from lattice parameter determinations. Estimates of their experimental error are shown on one experimental point. The ultrasonic data of Gieske and Barsch measured to 10 kbar are extrapolated with a cubic polynomial to compare to the shock data. The point of McQueen and Marsh for single crystal Al_2O_3 is reported in Ref. [2]. The shock data on a high density Al_2O_3 is shown for comparison with the single crystal data. The cubic polynomial fails to give an accurate representation above a stress of 350 kbar and is shown by a dotted line for comparative purposes only. A logarithmic equation such as a Murnaghan equation gives an excellent correspondence between the data of the present work and that of McQueen and Marsh.

The temperature rise due to shock compression of sapphire is not appreciable because of the relatively small compressions involved. Accordingly, the thermal pressure correction computed from conservation of energy is not significant; amounting to about a 6 kbar correction at 400 kbar and about a 1 kbar correction at 150 kbar. These thermal pressure corrections are less than the experimental scatter and small compared to the offset between the static and shock data; hence, the correction has not been applied to the shock data.

The stress offset observed between the extrapolated ultrasonic data and the best fit to the shock data range from 38 to 43 kbar depending upon the pressure range where the comparisons are accomplished. Likewise the volume offsets are observed to range from 1·1 to 1·3 per cent. Similar offsets to the data of Hart *et al.* are 0·75 to 1·0 per cent and 25 to 38 kbar. These values for stress and volume offsets are in excellent agreement with the values derived from the shock data alone, yet grossly different from values predicted from the elastic–plastic theory and the measured HEL values. Thus, the direct comparison of the static and shock data also demonstrates that when sapphire is shocked to pressures greater than the HEL that a substantial loss of shear strength is observed.

A striking feature of both sapphire and quartz is that both materials show about a 1 per cent volume offset to the isotropic compression curve after a substantial loss of shear strength is experienced. Thus there may be some similarities to the condition of these materials after the loss of shear strength.

Because of the unusual character of the loss of shear strength it is not implausible that the thermodynamic treatment of the yield is inadequate. Unlike yield under elastic–plastic conditions which is analogous to a second order phase transition, the loss of shear strength is analogous to a first-order phase transition. For example, the shear strain elastic energy for sapphire at 200 kbar is 12 cal/g. The loss of shear strength on the time scale of the shock experiments will cause this energy to appear as thermal pressure with an average value of about 6 kbar. Although this pressure is about a factor of five too small to account for the observed difference between static and shock results, the possibility of severe local inhomogeneities due to failure along specific crystallographic planes might cause sufficient complications to cause concern as to the proper treatment of these thermal effects. In any event it appears that more detailed study of possible thermodynamic effects is warranted.

(h) *Hugoniot elastic limit values*

The unusually large HEL values observed for sapphire and the equally unusual loss of shear strength in the high pressure region suggest fundamentally different shear-failure mechanisms than observed for metals. It is, therefore, instructive to compare the maximum shear stress supported by sapphire to predictions of the theoretical shear strength, i.e., the inherent shear strength of the perfect crystal. Present capability for calculating the theoretical shear strength are not sufficiently realistic to give accurate estimates[40, 41]. However, most calculations give a lower bound to the shear strength of about 0·03 G, where G is the appropriate shear modulus. Experimental measurements of values for theoretical shear strength are limited to Brenner's measurements[42] on metallic whiskers which gave values of 0·027 G for Cu, 0·036 G for Au and 0·052 for Fe.

The largest HEL value observed in sapphire was 210 kbar which corresponds to a maximum shear stress of 83 kbar based on the atmospheric pressure elastic constants. This maximum shear stress value is 0·056 C_{44}; large enough to approach estimates of the theoretical shear strengths. The case for quartz is even more noteworthy since the highest HEL observed is 0·11 C_{44}. Thus, both sapphire and quartz exhibit shear strengths under shock compression which could reasonably be theoretical shear strengths and both sapphire and quartz lose shear strength and collapse toward an isotropic compression curve when shocked above the HEL.

On the basis of the limited data it is premature to suggest a general model for the loss of shear strength; however, it is worthwhile to examine the existing shock-compression literature for evidence of large HEL values and shear stress offsets. These data are collected in Table 4. There are reasonably complete

Table 4. Shear strengths of shock loaded crystals

Crystal	Structure	$\tau_{\max}$[a] kbar	C_{44} kbar	$\tau_{\max}/C_{44}$	Loss of shear strength
SiO_2	Trigonal		579		
Z-cut[24][b]		62		0·108	Yes
X-cut[38]		33		0·057	Yes
Al_2O_3	Trigonal		1472		
0° orientation		83		0·056	Yes
90° orientation		72		0·049	Yes
60° orientation		68		0·046	Yes
MgO[46]	Cubic		1559		Yes? limited
[100]		25		0·016	shock data
TiO_2[47]	Cubic		1239		
[001]		33		0·027	?
[100]		12		0·0096	?
Si[44]	Cubic		796		
[100]		28		0·035	?Yes, possible transition
[111]		12		0·015	No
Ge[111][43]	Cubic	10	672	0·015	No
NaCl[45]	Cubic		128		
[111]		2·3		0·018	Yes? one experiment
[110]		0·28		0·0022	No
[100]		0·09		0·0007	No

[a] $\tau_{\max}$ is taken to be the maximum observed value of $\frac{1}{2}(\sigma_x - \sigma_y)$, where σ_x is the maximum observed HEL value and σ_y is the minimum lateral stress computed from atmospheric pressure elastic constants. The rationale for taking maximum values is based on the likelihood that the lower values are caused by samples of inferior quality due to internal strains or other defects. In anisotropic crystals lateral stresses may vary due to lateral anisotropy. Because of non steady effects these maximum values may relax to lower stress values.

[b] Reference numbers following the various materials indicate the source for the HEL values used to compute $\tau_{\max}$.

data for SiO_2, Al_2O_3, Ge[43], and Si[44] with limited information available for NaCl[45], MgO[27, 46] and TiO_2[27, 47]. One immediate conclusion that can be drawn from an examination of the existing data is that not all solids which are brittle at room temperature and atmospheric pressure exhibit loss of shear strength under shock loading. Furthermore, as previously stated, polycrystalline Al_2O_3, a brittle solid, responds as an elastic–plastic solid. On the other hand, crystalline Al_2O_3 and SiO_2 exhibit a substantial loss of shear strength.

Thus the experimental evidence indicates that a general model proposing that brittle materials lose their shear strength when shocked above the HEL is not suitable to predict material response. Definitions of brittle materials as ordinarily posed are based on crack propagation at stresses less than that necessary to cause slip and inelastic deformation. The large isotropic pressure component of shock experiments will not permit crack propagation; hence, in contrast to static experiments, materials cannot fail by crack propagation and inherent strength properties may be observed in bulk materials.

It appears possible that different shear-failure mechanisms may be encountered in a given crystal shock loaded along different crystallographic axes. If loading is accomplished in a direction which causes no shear on the slip plane, failure cannot be expected by conventional slip mechanisms. Experimental evidence for this is shown in Table 4 where large HEL values are observed in [100] Si and [111] NaCl, while much lower values are observed in other directions. There is some evidence, admittedly inconclusive, for loss of shear strength in both cases. The [111] NaCl investigation shows one experiment with a wave velocity lower than bulk sound speed. The high pressure [100] Si data show velocities less than bulk sound speed; however, this observation is inconclusive because of the possibility of a phase transition. In any event, the possibility of preferential loss of shear strength in various crystallographic directions in a given crystal should not be overlooked. In fact, it would be highly desirable if various crystals were studied in detail for experimental evidence to examine this question.

The shock compression data[28] on high density polycrystalline Al_2O_3 indicate elastic–plastic response and no loss of shear strength. Although at first glance this seems inconsistent with the results of the present investigation, there is no reason that the yield mechanisms of the polycrystal and single crystal should be the same. In fact, the HEL values for various polycrystalline Al_2O_3 samples as shown in Table 5, show a marked dependence on porosity of the sample. This indicates that the HEL is governed by grain boundary and intergrannular effects and that the shear strength of intergrannular material is apparently less than that required to exceed the shear strength of the crystallite.

Table 5. Hugoniot elastic limits of polycrystalline Al_2O_3

Density g cm^{-3}	HEL kbar	Reference
3·98	112 ± 13	28
3·969	70 -- 136	29
3·92	140	49
3·81	83 ± 5	28
3·76	58 – 72	20
3·72	80	49

The elastic–plastic response of polycrystalline Al_2O_3 and the elastic–isotropic response of single crystal Al_2O_3 support the view that a critical shear stress must be exceeded before a loss of shear strength occurs. Furthermore, this observation indicates that shear strength effects at high pressure are different for polycrystalline and single solids of the same chemical composition.

It seems clear that if slip cannot occur under shock-loading due to an insufficient number of mobile dislocations or due to shear stress of insufficient magnitude on the slip plane, that failure must occur by different mechanisms than ordinarily encountered. The shock data indicate that as the shear stress values approach the theoretical shear stress estimates, substantial loss of shear strength is observed in the high pressure phase. If solids are observed to sustain shear strengths under shock loading which approach or are greater than 0·03 G, a loss of shear strength should be anticipated.

It is perhaps noteworthy that all of the oxides investigated support maximum stress values in excess of 25 kbar and that both of the materials which are known to lose their shear strength are oxides. Since the oxides are known to have elastic properties dependent principally upon the oxygen ion framework [36, 48] the critical shear stress observed for oxides may be a property of the oxygen framework and single crystal oxides are good candidates for materials with large HEL's and a corresponding loss of shear strength.

6. SUMMARY AND CONCLUSIONS

The shock compression data for sapphire show that the compressional behavior of sapphire is analogous to quartz in that both solids exhibit large HEL values and both exhibit a substantial loss of shear strength when shocked above the HEL. Sapphire and quartz are best characterized as elastic–isotropic solids and not elastic–plastic solids. These conclusions are based upon observations of: (1) common high pressure compression curves for various HEL values, (2) high pressure shock velocities less than local bulk sound speed, and (3) the volume offset when the high pressure data are extrapolated to zero pressure.

Comparison of hydrostatic and shock compression curves for both sapphire and quartz show differences in volume at a given pressure of about 1 per cent. The reason for this is not understood.

The present theoretical and experimental descriptions of yield mechanisms in solids and shear strength effects at high pressure are inadequate to characterize solids other than metals. Brittle material classifications under static conditions do not adequately characterize those materials which are known to respond as elastic–plastic or elastic–isotropic. There is evidence for different shear-failure mechanisms and different shear strength effects between single crystals and polycrystals and for crystals shocked in various crystallographic directions.

When the shear strengths of solids approach the theoretical shear strength values under shock loading, elastic–isotropic response and changes in shear sensitive properties should be anticipated. It is central to our understanding of the compressional behavior of solids under large anisotropic compressions to accomplish further detailed investigations of HEL values and compression curves for stresses immediately above the Hugoniot elastic limit.

Acknowledgement—The authors are pleased to acknowledge many useful discussions with their Sandia Laboratories colleagues, the assistance in the experiments by C. W. Huddle and G. E. Ingram, discussions on elastic-plastic response with R. W. Rohde and J. N. Johnson and methods for statistical fits to the data with A. R. Champion.

REFERENCES

1. DRICKAMER H. G., LYNCH R. W., CLENDENEN R. L. and PEREZ-ALBUERNE E. A., In *Solid State Physics* (Edited by F. Seitz and D. Turnbull). Vol. 19, Academic Press, New York (1966).
2. ANDERSON O. L., *J. Phys. Chem. Solids* **27**, 547 (1966).
3. MCQUEEN R. G. and MARSH S. P., *J. appl. Phys.* **31**, 1253 (1960).
4. RICE M. H., MCQUEEN R. G. and WALSH J. M., In *Solid State Physics* (Edited by F. Seitz and D. Turnbull). Vol. 6. Academic Press. New York (1958).
5. DEAL W. E. JR., In *Modern Very High Pressure Techniques* (Edited by R. H. Wentorf, Jr.). Butterworths, Washington (1962).
6. KARNES C. H., In *Mechanical Behavior of Materials Under Dynamic Loads* (Edited by U. S. Lindholm). Springer-Verlag, New York (1968).
7. GRAHAM R. A., *J. bas. Engng* **89**, 911 (1967).
8. GRAHAM R. A. and HUTCHISON R. E., *Appl. Phys. Lett.* **11**, 69 (1967).
9. WOOD. D. S., *J. appl. Mech.* **19**, 521 (1952).
10. FOWLES G. R., *J. appl. Phys.* **32**, 1475 (1961).
11. LUNDERGAN C. D. and HERRMANN W., *J. appl. Phys.* **34**, 2046 (1963).
12. BARKER L. M., LUNDERGAN C. D. and HERRMANN W., *J. appl. Phys.* **35**, 1203 (1964).
13. BUTCHER B. M. and CANNON J. R., *AIAA Journal* **2**, 2174 (1964).
14. BUTCHER B. M. and MUNSON D. E., In *Proceedings Fourth Symposium on Detonation* ACR-126, Office of Naval Research, U.S. Government Printing Office (1965).
15. BUTCHER B. M. and KARNES C. H., *J. appl. Phys.* **37**, 402 (1966).
16. MUNSON D. E. and BARKER L. M., *J. appl. Phys.* **37**, 1652 (1966).
17. GRAHAM R. A., ANDERSON D. H. and HOLLAND J. R., *J. appl. Phys.* **38**, 223 (1967).
18. HERRMANN W., In *Wave Propagation in Solids*, American Society of Mechanical Engineers, New York (1970).
19. JONES O. E. and GRAHAM R. A., In *Accurate Characterization of the High-Pressure Environment* (Edited by E. C. Lloyd), National Bureau of Standards Special Publication 326, March 1971.
20. See a recent comprehensive summary in GRAHAM R. A. and JONES O. E., Sandia Laboratories Report SC-R-68-1857 (Oct. 1968).
21. JONES O. E., NEILSON F. W. and BENEDICK W. B., *J. appl. Phys.* **33**, 3232 (1962).
22. VAN THIEL M. and KUSUBOV A., In *Accurate Characterization of the High-Pressure Environment* (Edited by E. C. Lloyd), National Bureau of Standards Special Publication 326, March 1971.
23. NEILSON F. W. and BENEDICK W. B., *Bull. Am. phys. Soc.* **5**, 511 (1960); also Sandia Laboratories Report SCR-502 (April 1962).
24. WACKERLE J., *J. appl. Phys.* **33**, 922 (1962).
25. FOWLES G. R., Poulter Laboratories Technical Report 003-61, Stanford Research Institute (1961); also *J. geophys. Res.* **72**, 5729 (1967).
26. DUVALL G. E. and FOWLES G. R., In *High Pressure Physics and Chemistry* (Edited by R. S. Bradley), Vol. 2, Academic Press, New York (1963).
27. AHRENS T. J. and LINDE R. K., In *Behavior of Dense Media Under High Dynamic Pressures*, Gordon and Breach, New York (1968).
28. AHRENS, T. J., GUST W. H. and ROYCE E. B., *J. appl. Phys.* **39**, 4610 (1968).
29. MUNSON D. E., Sandia Laboratories Report SC-RR-69-803 (Jan. 1970).

30. MCWHAN D. B., *J. appl. Phys.* **38**, 347 (1967).
31. BROOKS, W. P. and GRAHAM R. A., *Bull. Am. phys. Soc.* **11**, 414 (1966).
32. GRAHAM R. A. and INGRAM G. E., In *Behavior of Dense Media Under High Dynamic Pressures*. Gordon and Breach, New York (1968).
33. GRAHAM R. A., NEILSON F. W. and BENEDICK W. B., *J. appl. Phys.* **36**, 1775 (1965).
34. INGRAM G. E. and GRAHAM R. A., to be published in *Proceedings Fifth Symposium on Detonation*, Pasadena, Calif. (Aug. 18–21, 1970).
35. HEARMON R. F. S., *An Introduction to Applied Anisotropic Elasticity*. Oxford University Press (1961).
36. GIESKE J. H and BARSCH G. R., *Phys. Status Solidi* **29**, 121 (1968).
37. BARKER L. M. and HOLLENBACH R. E., *J. appl. Phys.* **41**, 4208 (1970).
38. GRAHAM, R. A and INGRAM G. E., *Bull. Am. phys. Soc.* **14**, 1163 (1969).
39. HART H. V. and DRICKAMER H. G., *J. chem. Phys.* **43**, 2265 (1965).
40. COTTRELL A. H., *Dislocations and Plastic Flow in Crystals*, Oxford at the Clarendon Press (1958).
41. KELLY A. H., *Strong Solids*, Clarendon Press, Oxford (1966).
42. BRENNER S. S., *J. appl. Phys.* **27**, 1484 (1956), see values given in Ref. [41].
43. GRAHAM R. A., JONES O. E and HOLLAND J. R., *J. Phys. Chem. Solids* **27**, 151 (1966).
44. GUST W. H. and ROYCE E. B., *J. appl. Phys.* **42**, 1897 (1971).
45. MURRI W. J. and ANDERSON G. D., *J. appl. Phys.* **41**, 3521 (1970).
46. AHRENS T. J., *J. appl. Phys.* **37**, 2532 (1966).
47. LINDE R. K. and DECARLI P. S., *J. chem. Phys.* **50**, 319 (1969).
48. ANDERSON O. L., In *Physical Acoustics* (Edited by W. P. Mason), Vol. III-B, Academic Press, New York (1965).
49. GUST W. H. and ROYCE E. B., *Bull. Am. phys. Soc.* **13**, 901 (1968).

The reviewer called our attention to static compression measurements of C_{111} and C_{333} reported by R. E. Hankey and D. E. Schuele, *J. Acoust. Soc. Am.* **48**, 190 (1970). These authors also report values obtained by J. H. Gieske in a Ph.D. thesis at Penna. State University. The various values are shown below.

Comparison of third-order constants[a]

	Gieske	Hankey *et al.*	Present Work
C_{111}	−3·92	−3·87	−3·6
C_{333}	−3·10	−3·34	−3·6

[a] All units are 10^{13} dyne cm^{-2}

Differences between the static and shock compression may involve fourth-order constant contributions.

J. Phys. Chem. Solids, 1971, Vol. 32, pp. 2331–2344. Pergamon Press. Printed in Great Britain

THE EFFECT OF HYDROGEN ON THE LOW TEMPERATURE INTERNAL FRICTION OF A NIOBIUM SINGLE CRYSTAL

O. BUCK and D. O. THOMPSON
North American Rockwell Science Center, Thousand Oaks, Calif. 91360, U.S.A.

and

C. A. WERT
Department of Metallurgy and Mining Engineering, and Materials Research Laboratory University of Illinois at Urbana-Champaign, Ill. 61801, U.S.A.

(*Received* 14 *January* 1971)

Abstract—The internal friction and Young's modulus of a hydrogen doped niobium single crystal were measured in the temperature range 20 to 370°K. Nucleation of niobium hydrides is indicated by the growth of an internal friction maximum. The height of the internal friction maximum is proportional to the hydrogen concentration and it shifts progressively to higher temperatures with increasing hydrogen concentration. The activation energy of the peak was found to be about 0·27 eV. From the experimental correlation between temperature and hydrogen concentration at which the peak forms it is possible to deduce the $\alpha/\alpha+\beta$ solvus. The solvus yields a heat of solution of about 0·12 eV, in agreement with other measurements. Deuterium doped niobium did not yield significantly different results from the ones obtained with hydrogen.

1. INTRODUCTION

THE EFFECTS of hydrogen upon the mechanical properties of pure and alloyed metals have been of interest for many years. Most of the interest in these effects arises from the fact that hydrogen affects adversely the engineering properties of many metal systems; of these, the effects of hydrogen in producing embrittlement and loss of ductility are probably the most important. Westlake[1] has recently given a summary of many investigations in this area. Internal friction measurements constitute a powerful additional tool which provides a correlation between the metallurgical effects of hydrogen in metals and the physical mechanisms by which such effects are generated[2–11]. These measurements are sensitive to atomistic events as well as to the more gross material properties. It was the purpose of this work to study the effects of hydrogen in niobium single crystals using internal friction techniques and to identify possible physical mechanisms which contribute to embrittlement in this material. The work is reported in two papers; in this paper the experimental results are reported and in the second an interpretative discussion of the results will be given.

2. EXPERIMENTAL TECHNIQUES

The experiments described in this paper were all performed on a ⟨110⟩ niobium single crystal 6 mm in dia. and 12·5 cm long. It had an initial resistivity ratio of about 400[12]. The measurements reported here were made in an apparatus which has been described in detail earlier[13] operating over a temperature range from about 20 to 370°K. The crystal was mounted with three set screws at its center of gravity and was free at both ends; its resonant frequency in the fundamental mode was about 13 kHz. All measurements were made at a constant strain amplitude of about 1×10^{-7}.

Hydrogenation of the sample was accomplished by heating it to about 750°C in a micro-

Sieverts apparatus[14] similar to the one described by Albrecht *et al.*[15]. In this way, hydrogen charges of 100, 633, 3460, 17700 and 91000 at. ppm were successively placed in the sample. After each of these chargings, a complete set of temperature dependent internal friction and modulus data was obtained from about 20 to 370°K. Thereafter the crystal was outgassed and the measurements repeated using the same procedure. It was then recharged successively to 2910 at. ppm hydrogen and 2660 at. ppm deuterium and again the measurement cycle was repeated.

Aging behavior of the hydrogen-charged crystal during measurement required adoption of a rather complicated measurement procedure. Even at low hydrogen concentrations hysteretic effects were introduced into the decrement and modulus data by low temperature aging, i.e., cooling and warming between room temperature and 20°K yielded different results. To obtain some understanding of the source of this large hysteretic behavior and to determine its temperature dependence, a scheme of experimentation was adopted which would permit the establishment of temperature ranges within which the hysteretic phenomenon could be observed to occur at the various hydrogen concentrations. A standard sequence was developed in which the crystal with the various hydrogen concentrations was cooled successively from room temperature to 240, 160, 80 and 20°K and held for about 20 hr. Measurements were made during the temperature descent as well as during temperature ascent back to room temperature. Cooling and heating rates of about 0·3°K/min were used. Length change measurements were also made with a standard vernier gauge as a function of hydrogen concentration.

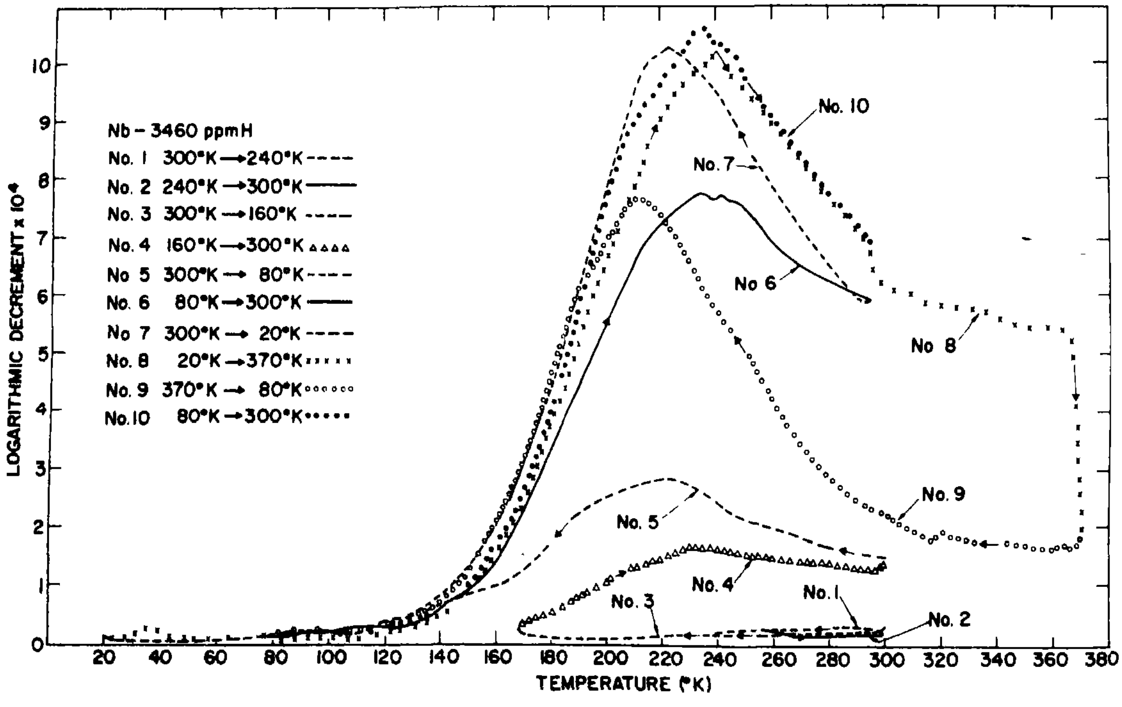

Fig. 1. Logarithmic decrement of Nb-3460 at. ppm H as a function of temperature.

3. RESULTS

The results obtained for the logarithmic decrement after charging the sample to 3460 at. ppm H are shown in Fig. 1. The large hysteretic effects which result in the internal friction maximum at 240°K (in this case) are clearly evident. Curve No. 1 represents the results obtained in the initial cooldown from room temperature to about 240°K. The decrement is very low ($\sim 3\times 10^{-5}$) and remains small during the retrace to room temperature at this concentration (curve No. 2), i.e., no appreciable hysteresis and peak structure has been developed as a result of aging at 240°K. Curve No. 3 retraces curves No. 1 and 2 down as far as 240°K, and then continues to 160°K for a second low temperature aging cycle. On the retrace to room temperature (curve No. 4) the formation of the peak structure has commenced. The aging continues with a subsequent descent to 80°K, curve No. 5. Note that the maximum in curve No. 5 is larger than that in curve No. 4, suggesting that the mechanism which creates the internal friction maximum continues at room temperature after being nucleated at the lower temperature. Curves No. 6 through 8 show the continued aging as the lowest temperature attained is reduced to 20°K. The sample was then heated to about 370°K for 24 hr. During this isothermal anneal the maximum in the decrement was reduced somewhat (curve No. 9), but following another aging period at 80°K, curve No. 10 reproduced the results found in curves No. 7 and 8.

Results obtained with a hydrogen concentration of 17,700 at. ppm are shown in Fig. 2. They are qualitatively the same as those obtained for smaller hydrogen concentrations, but the aging cycle is shifted upwards in temperature. At this concentration, peak growth occurs in the first curve at 240°K, whereas in Fig. 1 (3460 at. ppm) it did not commence until the sample was cooled to 160°K. Note that the maximum value of the decrement is larger than for the smaller con-

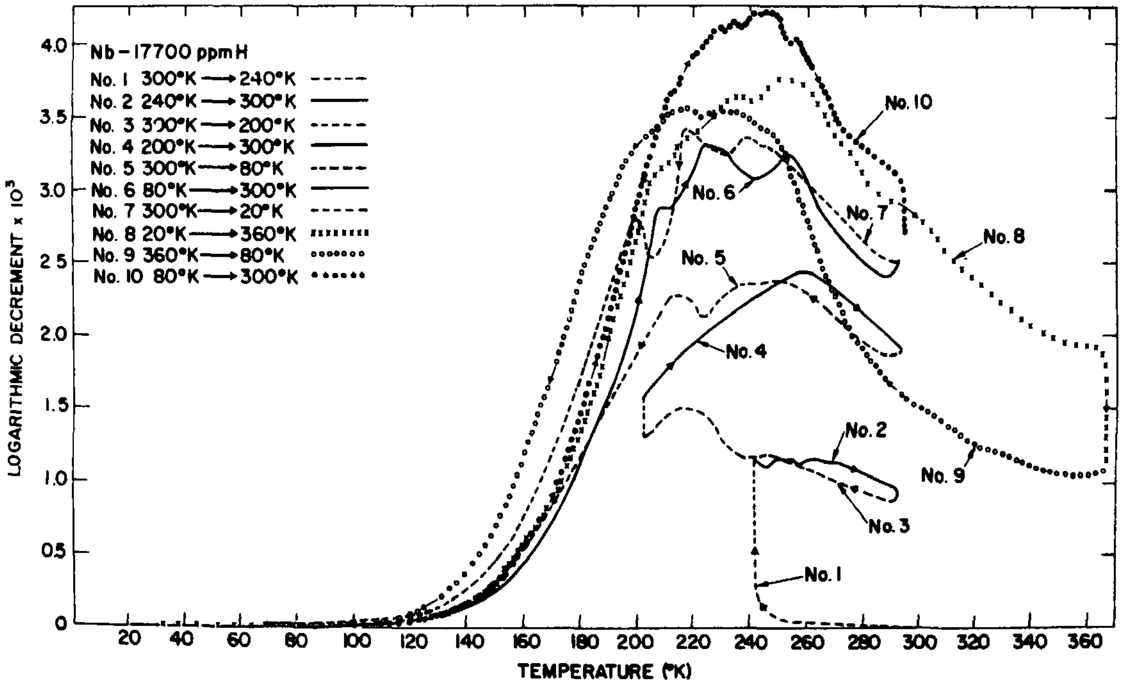

Fig. 2. Logarithmic decrement of Nb-17700 at. ppm H as a function of temperature.

centration and that the same general annealing features are observed at 370°K.

Changes in Young's modulus for the specimen containing 17,700 at. ppm are shown in Fig. 3; the numbering scheme in this plot is the same as that used for the corresponding decrement curves given in Fig. 2. Generally, the modulus results are completely complementary to the decrement results shown in Fig. 2 in the sense that the aging mechanism which produces the internal friction growth simultaneously lowers the modulus. Thus curve No. 10 shows a minimum modulus value in the 250°K region corresponding to the maximum decrement in this same region. Curve No. 8 also shows that the annealing process at 370°K produces a recovery of the modulus, again in concert with the decrement results shown earlier. The irregularity in the modulus curve in the range 70–80°K is independent of the hydrogen concentration, and is apparently a property of the niobium itself.

Examples of the isothermal growth of the decrement and decay of the modulus at a hydrogen concentration of 17,700 at. ppm with time at 241·5°K are shown in Fig. 4a (these are the transitions between curves No. 1 and 2 in Figs. 2 and 3). Fig. 4b shows the results obtained during an anneal at 366°K. At this temperature the decrement decays and the modulus grows (transitions between curves 8 and 9 in Figs 2 and 3). Note that the time required to achieve 50 per cent of the property changes is smaller at 241·5°K than it is at 366°K. This result indicates that the kinetics of formation and decay of the internal friction maximum are significantly different.

A summary of the decrement results obtained during the warming cycle from 20°K to room temperature (equivalent to curve No. 8 of Figs. 1 and 2), is given in Fig. 5 for the various hydrogen concentrations studied. These concentrations and the curve identifications are given in the legend on the figure. A semilogarithmic plot is used to display these results because of the large variation of peak heights even though such a plot does not show the peaks as clearly as do linear plots (see the corresponding curves No. 8 of Figs. 1 and 2). Details below 90°K are omitted; no effects were observed in this region attributable to

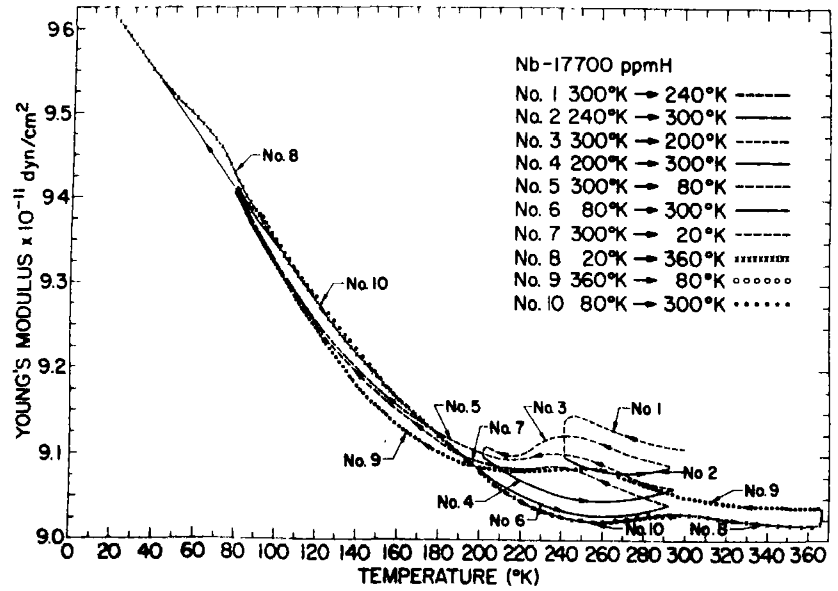

Fig. 3. Youngs' modulus of Nb-17700 at. ppm H as a function of temperature.

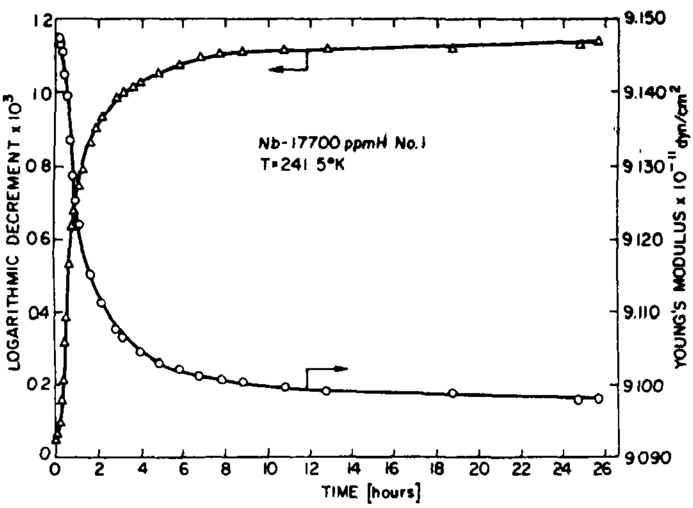

Fig. 4(a). Isothermal change of the logarithmic decrement and Young's modulus of Nb-17700 at. ppm H at 241·5°K.

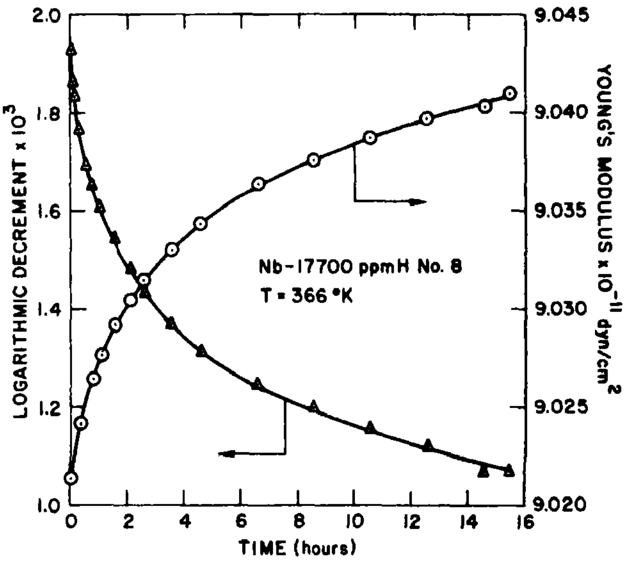

Fig. 4(b). Isothermal change of the logarithmic decrement and Young's modulus of Nb-17700 at. ppm H at 366°K.

the presence of hydrogen in this crystal.

Two essential features are to be noted in this summary of results. They are these: (1) with the exception of the first doping to 100 at. ppm hydrogen, the maximum amplitude of the peak increases monotonically with hydrogen concentration, and (2) the center temperature of the decrement maximum moves to higher temperatures as the concentration is increased. Additionally, there are some other features to be noted. In the virgin crystal (0 at. ppm hydrogen), two peaks were observed, one at 195°K and an exceptionally narrow one at 232°K. These have been

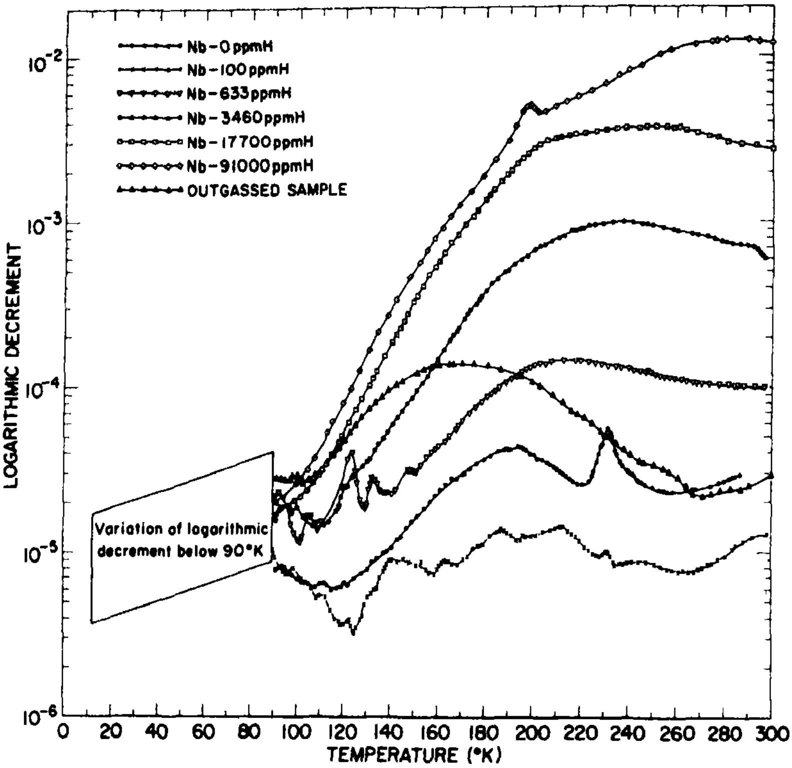

Fig. 5. Logarithmic decrement of hydrogen doped Nb after aging at 20°K.

observed before[11]; it is seen, however, that the 232°K 'spike' in this crystal was found in the 0 at. ppm data, only slightly in the 100 at. ppm results, and hardly, if at all, in the higher concentration experiments. It is also seen that the first hydrogen addition (to 100 at. ppm) suppressed the decrement below the initial level. Whether this is a true effect of hydrogen is not known with certainty at this time, but this reduction may be associated with dislocation pinning. The final curve in this series, i.e., the 'outgassed' sample shown by filled triangles (▲), shows decrement values which are considerably larger than those found in the initial, or 0 at. ppm hydrogen, curve. The peak value is about the same as that found in the 633 at. ppm results, but its center is located at 175 instead of 220°K.

A logarithmic plot of the peak values of the logarithmic decrement as a function of hydrogen concentration is given in Fig. 6. These decrement values are obtained from the results shown in Fig. 5 which, as will be recalled, are the results obtained in the final warmup from 20°K to room temperature. The temperature given in parentheses beside each point is the temperature at which the maximum decrement occurred for each concentration. Two features are apparent in this curve. The maximum value of the decrement is approximately proportional to the concentration (the line is drawn through the points with a slope of unity) and the temperature of the maximum increases monotonically with concentration.

A summary of the modulus data which correspond to the decrement results of Fig. 5 is shown in Fig. 7. Generally, the modulus increases as a function of hydrogen concentration at any temperature, it should be kept in mind, however, that the room temperature

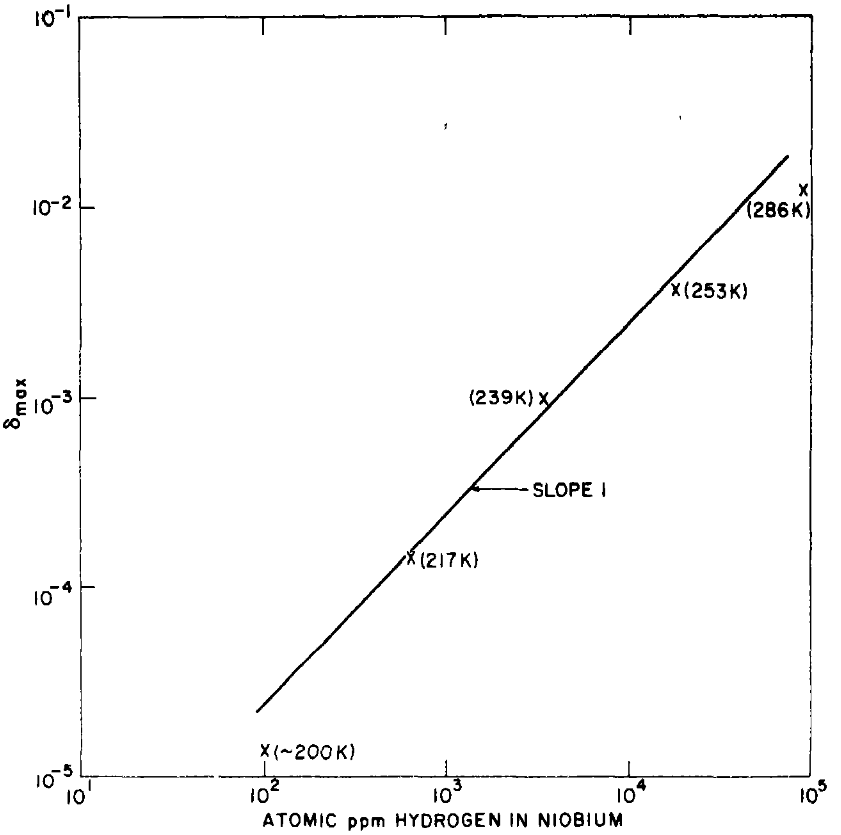

Fig. 6. The height of the precipitation peak after aging at 20°K as a function of hydrogen concentration (numbers give the temperature of the peak).

values of the modulus after low temperature aging are not as large as that measured for the initial condition at room temperature (c.f. Fig. 3). The modulus shows an irregular behavior for all alloys near 80°K, as noted earlier. This irregularity does not seem to depend upon the hydrogen content, nor is there any consistent decrement maximum in this region which would suggest that the irregularity is a modulus defect. There are some modulus steps, however, which clearly should be interpreted as modulus defects which accompany the measured internal friction phenomena. One of these occurs at 195°K in the as-received condition. Apparently this defect accompanies the decrement maximum at this same temperature shown in Fig. 5. Another clearly defined step occurs at about 190°K in the 91,000 at. ppm results which apparently accompanies the maximum in the decrement at 195°K shown in Fig. 5 for this concentration. In all cases, the temperature dependence of the modulus diminishes toward room temperature, and in fact, becomes positive for a ways above room temperature. This flattening has been observed before [16, 17], and in this case, makes a positive identification of modulus defect structure somewhat difficult. This point will be pursued further in the discussion.

Decrement and modulus results are given in Figs. 8 and 9 at two different frequencies (approximately 13 and 39 kHz) for both hydrogen and deuterium charged conditions.

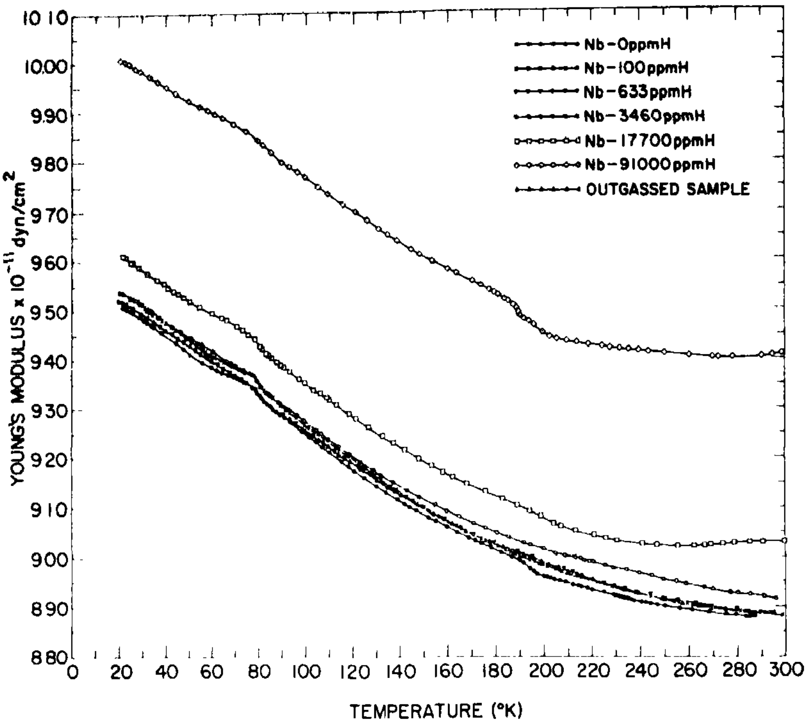

Fig. 7. Young's modulus of hydrogen doped Nb after aging at 20°K.

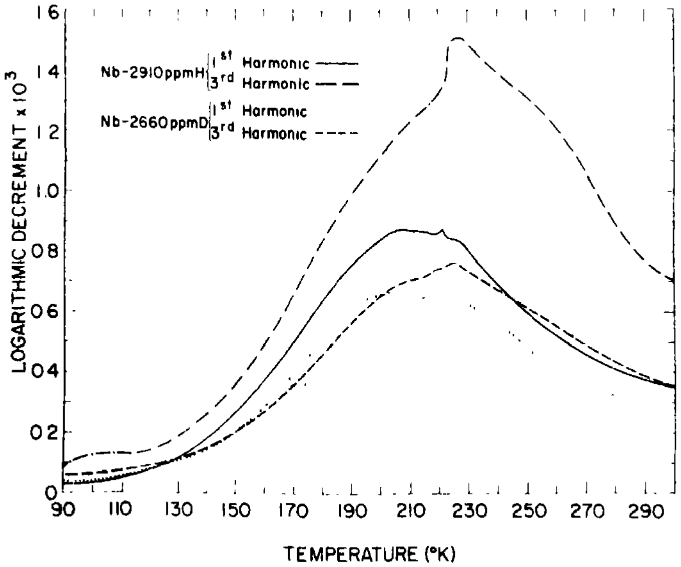

Fig. 8. Logarithmic decrement at 13 and 39 kHz of Nb-2910 at. ppm H and Nb-2660 at. ppm D as a function of temperature.

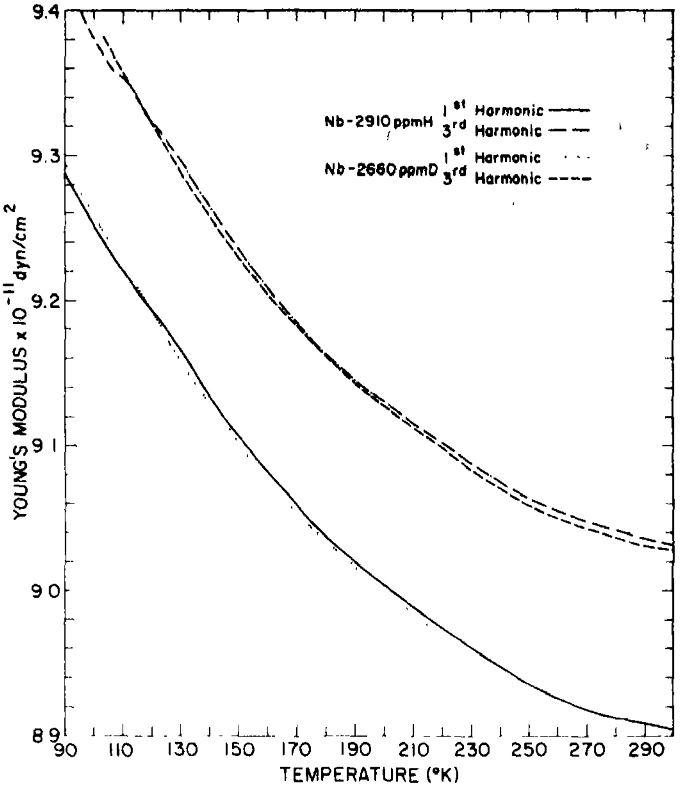

Fig. 9. Young's modulus at 13 and 39 kHz of Nb-2910 at. ppm H and Nb-2660 at. ppm D as a function of temperature.

The hydrogen charge (~ 2900 at. ppm) was introduced after the sample had been doped to 91000 at. ppm and outgassed, and the deuterium charge (~ 2600 at. ppm) after removal of the 2900 at. ppm hydrogen charge. Both of the third harmonic curves are shifted to higher temperatures from their respective fundamental curves. This result is consistent with the expectations of a thermally activated loss mechanism and yields an activation energy of 0·27 ± 0·05 eV. On the other hand, corresponding curves for hydrogen and deuterium exhibit very little temperature shift. The peak amplitudes of three of these curves fit nicely on the plot given in Fig. 6 for these charge conditions; an exception is the unexpected departure of the third harmonic curve for hydrogen. In all of these data there is some evidence of the '230°K spike' discussed earlier. The corresponding modulus curves (Fig. 9) for these same conditions show that for both hydrogen and deuterium the modulus values derived from the third harmonic mode are significantly larger than those obtained from the fundamental mode. No explanation for this difference is available at present.

4. DISCUSSION OF RESULTS

The apparent complexity of the internal friction maximum observed in this work seems to preclude a detailed description of the dissipation mechanism. At least three well-known models might be used to interpret the results. These possibilities will be discussed briefly, but a final selection of a model and its comparison with the experimental results will be deferred to a later paper. The principal part of the discussion is therefore concerned with the internal friction and modulus changes which occur during precipitation of the hydride.

The mechanism which generates the internal friction maximum observed in this work is associated with the formation of niobium hydride. In fact, the temperature at which the first logarithmic decrement changes occur appears to define a point on the phase boundary for each composition. These points fit well on the phase diagram established from earlier work and reproduced in Fig. 10. Here are plotted (1) part of the phase diagram according to Walter and Chandler[18], (2) a solvus line established by Westlake[19] from resistometric measurements and (3) points derived from the present investigation. The agreement is excellent. These same data plotted logarithmically as a function of $1/T$ as shown in Fig. 11, all yield values for the heat of solution in the range 0·11–0·12 eV. The 'temperature windows' from the present work are plotted as error bars at the appropriate concentrations. Although this technique is very inaccurate, especially at low temperatures, a best fit yields 0·11 eV. Temperature variation of the onset of brittle fracture with composition of hydrogen also yields a value of about this magnitude, i.e. 0·13 eV[20]. This agreement implies, as Westlake earlier proposed, that the onset of hydrogen embrittlement and precipitation of a hydride are correlated phenomena.

At least three well-known acoustical loss mechanisms might be used to account for the 'precipitation' internal friction maximum observed in this work: The first of the mechanisms is a dislocation-interstitial drag mechanism which results in a relaxation known as the cold-work peak; it has been described theoretically by Schoeck[21]. Although no dislocations have been deliberately introduced by external cold-work, precipitates in other systems have been observed to produce dislocations which result in a cold-work peak[22]. Punched-out dislocations about hydride-precipitates in niobium have also been observed[23]. These dislocations could, together with a dilute hydrogen atmosphere, be responsible for this damping peak. A second possibility is that of a stress-

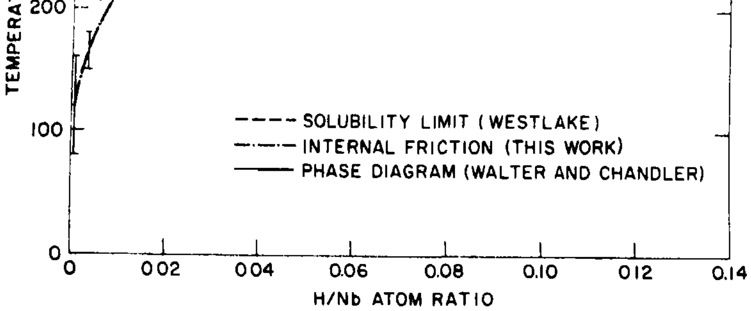

Fig. 10. The Nb-H phase diagram at low hydrogen concentrations (after Westlake[19], Walter and Chandler[18], and this work).

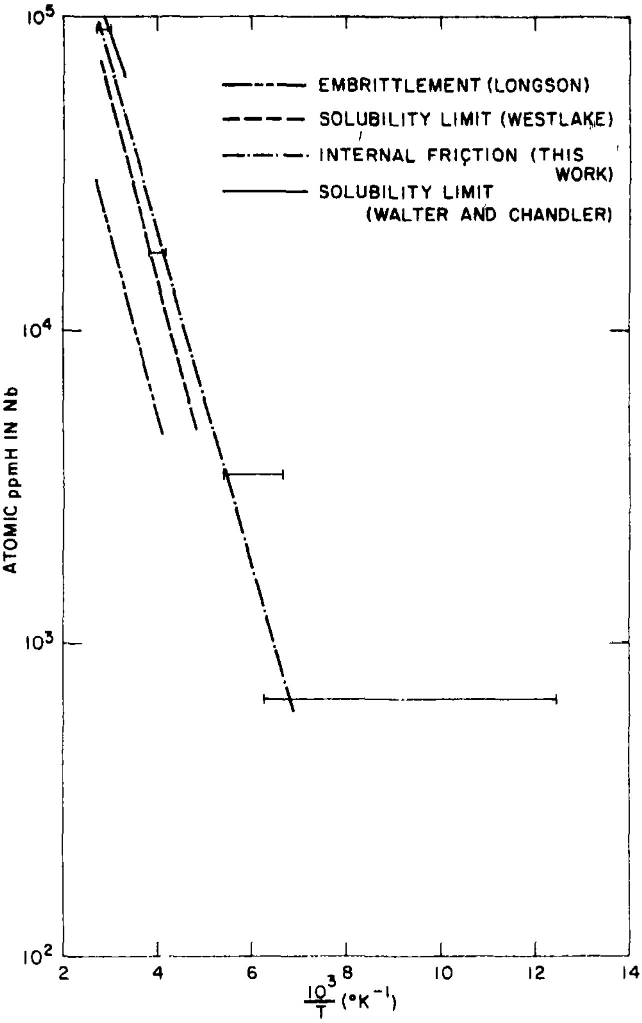

Fig. 11. A comparison of solvus curves (after Westlake[19] and this work) and an embrittlement curve (after Longson[20]).

induced reorientation of the hydride precipitate[8]. This mechanism requires rather long range diffusion of hydrogen through the hydride such as is characteristic of the Gorsky mechanism[3]; in this case the 'boundaries' or diffusion lengths are determined by the size of the hydride precipitate. A third possibility is suggested by the observed energy (about 0·27 eV) for the 'precipitation' peak and the observation that punched-out dislocation loops surround the hydride precipitate [23, 24]. It has been found that the well-known α-peak in niobium is characterized by an activation energy of 0·25 eV[25–28] and its origin has been associated with the thermal generation of kinks on dislocations as described by Seeger *et al.*[29]. It is appealing to suggest that the 'precipitation' peak is due to thermal kink generation in the dislocations punched out by the hydride precipitate.

The narrow spike-like peak near 230°K cannot be a thermally activated peak. It does not shift in position as the frequency is varied, having been observed by Viswanadham at virtually the same temperature at frequencies near 1 Hz[30]. Viswanadham also found a small temperature arrest at this point during heating of a Nb-H specimen through this range, indicating that a phase-change occurs at that temperature. These observations are strikingly similar to observations of internal friction in Ta-H alloys made by Kofstad and Butera[31]. They found a similar sharp, spike-like peak at about 310°K. This temperature corresponds to loss of long range order of H atoms in Ta_2H[32, 33]. The strong similarity of the internal friction curves of Kofstad and Butera to those of the present work suggests

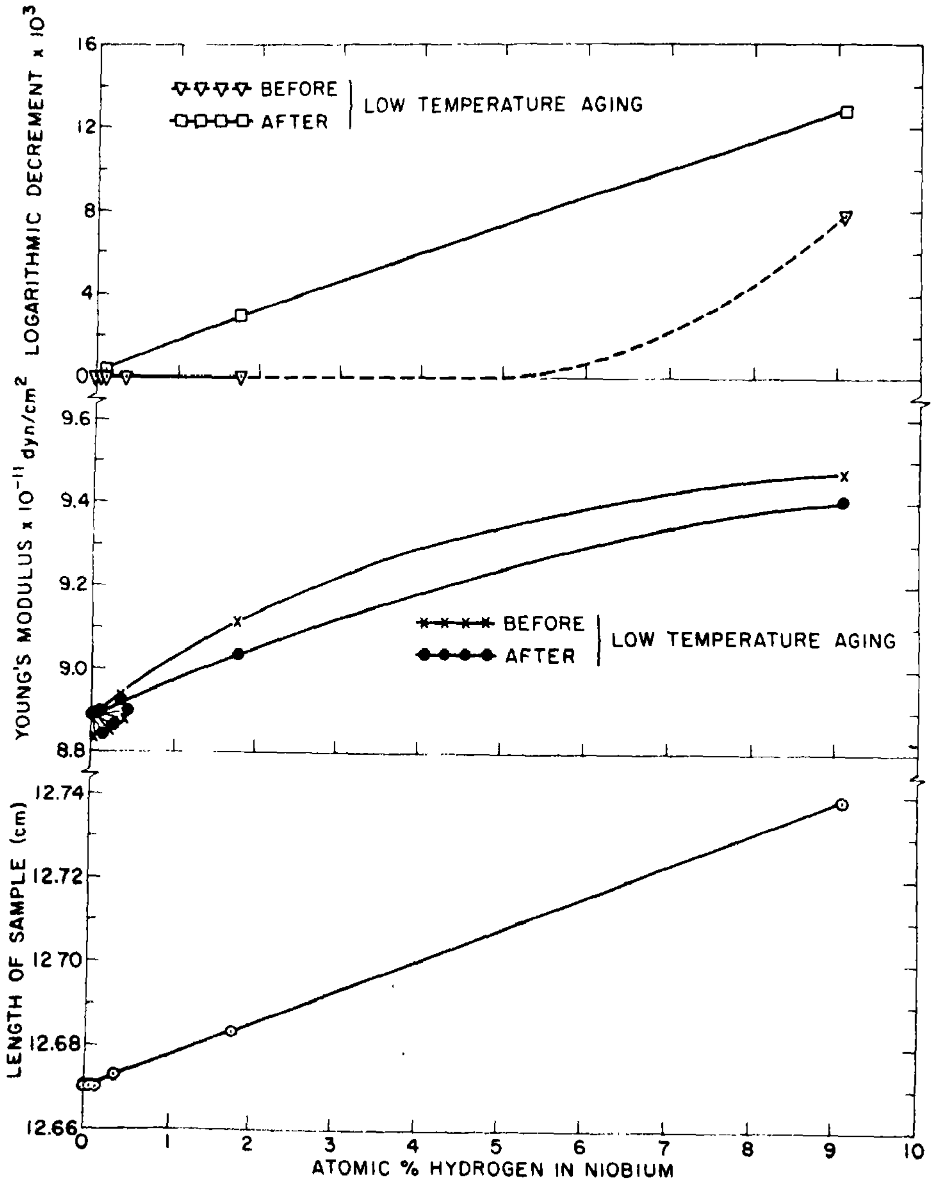

Fig. 12. Room temperature values of the sample length, Logarithmic decrement and Young's modulus of Nb doped with hydrogen before and after low temperature aging.

that a similar phase may be present in the two cases.

In Fig. 12 are summarized the effects of dissolved hydrogen upon the sample length, logarithmic decrement, and Young's modulus at room temperature as a function of hydrogen concentration. The length (bottom plot) and decrement (top plot) data were obtained prior and after low temperature cycling. Two sets of data are shown for the modulus-crosses (X) indicate the values obtained at 300°K prior to any cooling of the sample, and solid points (●) give the values at the same temperature after full low temperature aging. There are two items of particular interest in these results. It is clear from the decrement data that the initial value of the decrement is large when the hydrogen concentration is sufficiently large so that the hydride phase is present at room temperature. This result is consistent with the temperature-cycled data presented earlier which resulted in the formation of the 'precipitation' peak. Secondly, it is interesting to compare the variations in length and modulus change in this concentration range. The variation in length is linear (within an experimental accuracy of ±0·01 cm) across the concentration range investigated and can be described by the relation

$$\frac{\Delta l}{l} = 6\times 10^{-4}\ \text{per at.\% H.}$$

in which l is the sample length. This coefficient is about the average of those found by Walter and Chandler[18] and Albrecht, *et al.*[34]. On the other hand, the change in modulus is neither linear in concentration across this range nor is it describable by the same coefficient as the length change. It is apparent that the modulus is lower when the hydride is present than it would have been had the hydrogen been retained in solution. From the before-cooling modulus data and for concentrations up to 2 at.%, the modulus coefficient is

$$\frac{\Delta E}{E} = 1{\cdot}5\times 10^{-2}\ \text{per at.\% H.}$$

It is surprising to find this coefficient so much larger than that obtained from the length change measurements. Although no explanation can be offered with any certainty at this time, the comparison may suggest that the contribution of the hydrogen to the modulus change is principally electronic[35].

5. SUMMARY AND CONCLUSIONS

The Young's modulus and logarithmic decrement of a niobium single crystal have been measured as a function of hydrogen concentration over a temperature range from 20 to 370°K. It has been found that:

(1) An internal friction maximum is created by the formation of hydrides. This maximum is thermally activated and is characterized by an activation energy of about 0·27 eV.

(2) A comparison of the present results with those of Westlake[19] (resistivity) and Longson[20] (embrittlement) suggests that all these property changes are due to the formation of the hydride. These three experiments yield a heat of solution of about 0·12 eV. Whether the hydride formation per se or some consequence of it (such as punched-out dislocations around the hydride) is responsible for the property changes is not known at the present time.

(3) The fractional change in the modulus of the doped crystal per atom percent of hydrogen is about 25 times greater than the corresponding change in length coefficient.

Acknowledgement—The authors would like to thank Dr. R. E. Reed, Solid State Division, Oak Ridge National Laboratory, for the gift of the niobium single crystal and Dr. B. S. Hickman and D. H. Leslie of the Science Center for hydrogenation of the crystal. One author (C.A.W.) wishes to acknowledge support of the U.S. Atomic Energy Commission, Contract #AT (11-1)-1198.

REFERENCES

1. WESTLAKE D. G., *Trans. ASME* **62**, 1000 (1969).
2. CANNELLI G. and VERDINI L., *Ricerca scient.* **36**, 98 (1966).
3. SCHAUMANN G., VÖLKL F. and ALEFELD G. *Phys. Rev. Lett.* **21**, 891 (1968).
4. SCHAUMANN G., VÖLKL F. and ALEFELD G. Int. Conf. Vacancies and Interstitials in Metals, Jülich, p. 881 (1968).

5. CANTELLI R., MAZZOLAI F. M. and NUOVO M., *Phys. Status Solidi* **34**, 597 (1969).
6. MAZZOLAI F. M. and NUOVO M., *Solid State Commun.* 7, 103 (1969).
7. STURGES C. M. and MIODOWNIK A. P., *Acta Metall.* **17**, 1197 (1969).
8. CANNELLI G. and MAZZOLAI F. M., *Nuovo Cim. X* **64B**, 171 (1969).
9. CANTELLI R., MAZZOLAI F. M. and NUOVO M., *J. Phys. Chem. Solids* **31**, 1811 (1970).
10. CANNELLI G. and MAZZOLAI F. M., *J. Phys. Chem. Solids* **31**, 1913 (1970).
11. WERT C. A., THOMPSON D. O. and BUCK O., *J. Phys. Chem. Solids* **31**, 1793 (1970).
12. The authors are indebted to Dr. R. E. Reed, Solid State Division, Oak Ridge National Lab., who prepared the crystal.
13. THOMPSON D. O. and GLASS F. M., *Rev. scient. Instrum.* **29**, 1034 (1958).
14. The authors are indebted to Dr. B. S. Hickman and D. H. Leslie, of this laboratory, who charged the samples with H and D, respectively.
15. ALBRECHT W. M., MALLET M. W. and GOODE W. D., *J. electrochem. Soc.* **105**, 219 (1958).
16. WESTLAKE D. G., *Phil. Mag.* **16**, 905 (1967).
17. SMITH R. E. and BOLEF D. I., *Phys. Rev. Lett* **22**, 183 (1969).
18. WALTER R. F. and CHANDLER W. T., *Trans AIME* **233**, 762 (1965).
19. WESTLAKE D. G., *Trans AIME* **245**, 287 (1969).
20. LONGSON B., *The Hydrogen Embrittlement of Niobium*, TRG Report No. 1035c (1966).
21. SCHOECK G., *Acta Metall.* **11**, 617 (1963).
22. DAHLSTROM N. A., DOLLINS C. C. and WERT C. A., to be published.
23. PATON N. E., of this laboratory, unpublished results.
24. ASHBY M. F. and JOHNSON L., *Phil. Mag.* **20**, 1009 (1969).
25. CHAMBERS R. H. and SCHULTZ J., *Acta Metall.* **8**, 585 (1960).
26. BRUNER L. J., *Phys. Rev.* **118**, 399 (1960).
27. BORDONI P. B., NUOVO M. and VERDINI L., *Phys. Rev.* **123**, 1204 (1961).
28. AMATEAU M. F., MITCHELL T. E. and GIBALA R., *Phys. Status Solidi* **36**, 407 (1969).
29. SEEGER A., DONTH H. and PFAFF F., *Disc. Faraday Soc.* **23**, 19 (1957).
30. VISWANADHAM R. K., Thesis, Univ. of Illinois, Urbana-Champaign, 1970.
31. KOFSTAD P. and BUTERA R. A., *J. appl. Phys.* **34**, 1517 (1963).
32. SABA W. G., WALLACE W. E., SANDMO H. and CRAIG R. S., *J. chem. Phys.* **35**, 2148 (1961).
33. WALLACE W. E., *J. chem. Phys.* **35**, 2156 (1961).
34. ALBRECHT W. M., GOODE W. D. and MALLET M. W., *J. electrochem. Soc.* **106**, 981 (1959).
35. DUCASTELLE F., CANDRON R. and COSTA P., Presented at the 3rd Int. Conf. on Solid Compounds of Transition Elements, Oslo (16–20 June 1969).

J. Phys. Chem. Solids, 1971, Vol. 32, pp. 2345–2350. **Pergamon Press. Printed in Great Britain**

SUPERCONDUCTIVITY IN THE K, Rb, AND Cs TUNGSTEN FLUOROXIDE BRONZES

F. F. HUBBLE, JOAN M. GULICK and W. G. MOULTON
Florida State University, Tallahassee, Florida 32306, U.S.A.

(*Received* 12 *January* 1971)

Abstract—Tungsten fluoroxide bronzes are compounds of the general formula $M_xWO_{3-z}F_z$, where for this investigation M is an alkali metal and $z = x$. These compounds form dark blue or black hexagonal crystals for $0{\cdot}08 < x < 0{\cdot}30$. It has recently been demonstrated that Li dissolves in this crystal matrix to give compounds of the formula $M_xLi_yWO_{3-z}F_z$, where $z = x+y$ for this investigation. We have performed magnetization experiments on 24 of the above compounds which show they are superconductors with transition temperatures generally between 0·8 and 4·5K. The transition temperatures, T_c, upper critical fields, H_{c2}, and magnetization curves have been measured for powder samples using the alkali metals K, Rb, and Cs, and empirical relationships between x and y and T_c and H_{c2} have been established. The Abrikosov–Ginzburg and Gor'kov relations between H_{c2} and t provide a good fit to the Rb and Cs data respectively.

1. INTRODUCTION

THE TUNGSTEN bronzes are nonstoichiometric compounds of the general formula M_xWO_3 where M is a metal, usually an alkali metal. For K, Rb and Cs and $0{\cdot}27 \leq x \leq 0{\cdot}32$ these compounds form hexagonal dark blue or black crystals in which the alkali metal is an interstitial dopant and lies in the open hexagonal channels[1]. The theoretical upper limit for x is 0·33.

Superconductivity was first observed in a tetragonal sodium bronze by Raub *et al.*[2] Sweedler *et al.*[3] subsequently investigated the superconducting transition temperature in a series of Na, K, Rb, and Cs bronzes. All samples having either the tetragonal I ($a = 12{\cdot}1$ Å, $c = 3{\cdot}75$ Å) or hexagonal symmetry were found to be superconducting with transition temperatures ranging from 0·50 to 1·98 K. Remeika *et al.*[4] were able to raise the transition temperature of some of the hexagonal bronzes to above 6 K by leaching out some of the alkali metal while maintaining the hexagonal structure. The transition temperature is an inverse function of alkali metal content over the range studied.

Gulick and Sienko have substituted fluorine for some of the oxygen in the bronzes to yield compounds of the formula $K_xWO_{3-x}F_x$[5]. These compounds exhibit the hexagonal structure down to $x = 0{\cdot}09$ and it is thus possible to investigate the dependence of the superconducting transition temperature on alkali metal concentration or conducting electron concentration over a wider range than possible with the nonfluorinated bronzes.

Recently Li has been found to readily dissolve in the hexagonal phase of K_xWO_3, and it has been proposed that the Li atoms occupy sites at the centers of polyhedra defined by triangles formed by three corner sharing WO_3 octahedra. The general formula for such a solution is $M_xLi_yWO_3$ with a theoretical upper limit on y of 0·66[6]. We have used K, Rb, and Cs and made compounds with the nominal composition $M_xWO_{3-x}F_x$ and $M_xLi_yWO_{3-x-y}F_{x+y}$ and have investigated some of their superconducting properties.

---

*Research sponsored by the Air Force Office of Scientific Research, Office of Aerospace Research, USAF, under Grant No. AFOSR-928-67. The United States Government authorized to reproduce and distribute reprints for Governmental purposes notwithstanding any copyright notation hereon.

2. EXPERIMENTAL

Proper proportions of W, WO_3, and MF to yield compounds of the formula $M_xWO_{3-x}F_x$, where M is the appropriate alkali metal, were ground together in a porcelain mortar. For the Li doped fluoroxide bronzes LiF was added to the above mixture to give compounds of the formula $M_xLi_yWO_{3-x-y}F_{x+y}$. Alfa Inorganics standard reagent grade laboratory chemicals were used throughout, except for LiF which was 'ultrapure'.

The mixtures were placed in platinum tubes which were sealed by crimping the ends. The tubes were heated in a furnace from room temperatures to 800°C in 1½ hr, held at 800°C for 24 hr, then heated to 1000°C, and held for 72 hr. The samples cooled to room temperature in 3 hr in the open furnace.

Powder diffraction patterns of the compounds were obtained with a Debye–Scherrer powder camera using Ni-filtered copper Kα radiation. The X-ray patterns were assigned with a good degree of success to a hexagonal unit cell plus a tetragonal unit cell. A few low intensity lines at low angles could not be assigned. The Rb and Cs series X-rays showed no tetragonal lines for $x \not> 0{\cdot}125$ and only a few weak tetragonal lines for $x > 0{\cdot}08$. The $x = 0{\cdot}08$ samples however had much stronger tetragonal lines and efforts to make hexagonal samples for $x < 0{\cdot}08$ produced only the tetragonal phase or only a small portion of the sample in the hexagonal phase. It has been reported that $x = 0{\cdot}13$ is the lower limit for the hexagonal phase of the alkali metal bronzes (M_xWO_3)[6] however, the hexagonal fluoroxide Rb and Cs bronzes ($M_xWO_{3-x}F_x$) appear to be stabilized to metal concentration as low as $x \approx 0{\cdot}09$.

The X-ray patterns of the K bronzes showed no tetragonal phase only for $x = 0{\cdot}30$. For $0{\cdot}08 \leq x \leq 0{\cdot}125$ the patterns show a set of tetragonal lines of intensity comparable to the hexagonal set. Thus for K, the substitution of fluorine for some of the oxygen atoms does not stabilize the hexagonal phase for $x \leq 0{\cdot}13$ as it does for the Rb and Cs bronzes.

The X-ray films of the Rb- and Cs-Li doped bronzes ($M_xLi_yWO_{3-x-y}F_{x+y}$) for $0{\cdot}00 \leq y \leq 0{\cdot}10$ showed a few low intensity tetragonal lines indicating a small admixture of the tetragonal phase. The K-Li doped samples however yielded X-ray patterns with more intense and a more complete set of tetragonal lines. Attempts to make the hexagonal Li doped bronzes with $y > 0{\cdot}10$ were unsuccessful due to the appearance of a red substance and grey clumps mixed in appreciable amounts with the lustrous blue–black hexagonal crystals.

The dependence of the superconducting transition temperature, T_c and the upper critical field, H_{c2}, was measured with a stable high frequency (800 KHz) oscillator[7]. The sample in a 2 ml. vial serves as the core of a coil whose inductance determines the frequency of the oscillator. The inductance of the coil is proportional to the volume within the coil available for magnetic flux occupation, and upon the onset of superconductivity the flux is excluded from the sample due to the Meissner effect, thus changing the coil inductance and the frequency of the oscillator. The coil and sample were located at the end of a long (127 cm) probe in a helium magnet dewar, such that both coil and sample were submerged in the liquid helium. The superconducting transition temperature was determined by the temperature dependence of the oscillator frequency, and the percentage of the sample becoming superconducting was determined by the magnitude of the frequency shift. The upper critical field was measured by observing the oscillator frequency as a function of an applied magnetic field produced by a Magnion standard laboratory magnet, and the fields were measured with a rotating coil gaussmeter. The frequencies were measured with a Hewlett-Packard 5245L frequency counter fed to a digital to analogue converter and the output displayed on an x–y recorder. For the measurements in a magnetic field, the output of the rotating coil gaussmeter was fed to the x-axis of the recorder giving a direct frequency shift vs. field plot.

Temperature was measured with a germanium resistance thermometer calibrated to ±0·01 K.

3. DISCUSSION

The dependence of the superconducting transition temperature on alkali metal concentration is shown in Figs. 1 and 2, and in Table 1. The transitions in general are quite broad, of the order of 0·5–1·0 K. Much of this transition breadth can be accounted for by the temperature dependence of the penetration depth

$$\lambda = \lambda_0(1-t^4)^{-1/2}. \qquad (1)$$

The samples are powders and have a large surface area, and a small change in the penetration depth causes an appreciable change in the frequency of the oscillator making the transition broader on the low side of the transition temperature. The transition on the high temperature side is much sharper and the rounding here is due primarily to sample inhomogeneity, strains in the crystal, and impurities. The transitions were all measured by decreasing the temperature of the helium bath by pumping and observing the frequency shift of the oscillator. A check for hysteresis in T_c for several samples was made by traversing the transition via increasing temperature and no hysteresis was observed within experimental limits.

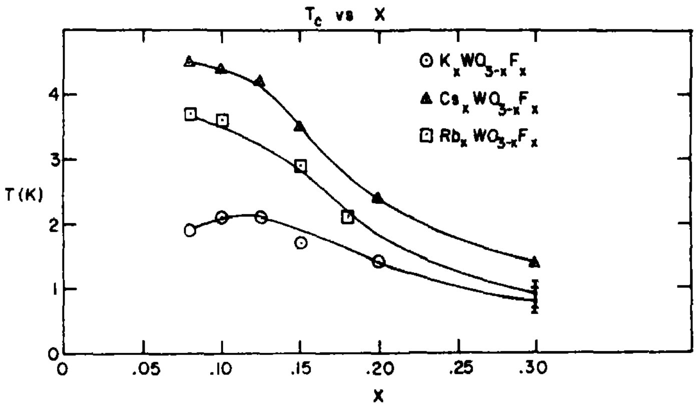

Fig. 1. T_c vs. alkali metal concentration, x.

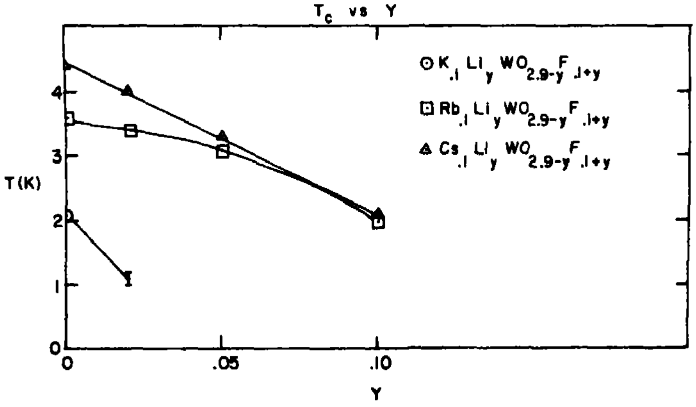

Fig. 2. T_c vs. Li concentration, y with constant $x = 0·10$.

Table 1.

Sample		T_c	$H_{c2}(0)$	% of Sample superconducting
K	0·08	1·9		
K	0·10	2·1		
K	0·125	2·1		
K	0·15	1·7		
K	0·20	1·4		
K	0·30	0·8 ± 0·2		
Rb	0·08	3·7	8·0	50
Rb	0·10	3·6	9·4	100
Rb	0·15	2·9	9·0	80
Rb	0·18	2·1	5·9	60
Rb	0·30	0·9 ± 0·2		
Cs	0·08	4·5	9·0	75
Cs	0·10	4·4	8·5	100
Cs	0·125	4·2	7·7	100
Cs	0·15	3·5	8·2	100
Cs	0·20	2·4	7·0	100
Cs	0·30	1·4	4·0	

It has been established that each alkali metal atom, including Li, contributes one electron to an otherwise empty conduction band in the WO_3 matrix, and studies by Gulick and Sienko indicate that fluorine substitution has the effect of adding one conduction electron per fluorine[5]. The transition temperatures of the two series studied decrease with increasing electron concentration, and electrons contributed by the Li and the Rb and Cs atoms appear to be equally effective in lowering T_c.

The magnetization of the samples was computed from the oscillator frequency dependence on increasing magnetic field. The frequency of the oscillator is given by

$$\nu(H) = 1{\cdot}517 \times 10^4 L^{-1/2} \pm 0{\cdot}05\% \qquad (2)$$

where $\nu(H)$ is in hertz and L is in henries. The inductance is proportional to the volume in the coil available for flux occupation, and this volume may be divided into that occupied by the sample, $V(H)$, and that outside the sample, V

$$L = K(V + V(H)) \qquad (3)$$

where K is a constant. Substituting into 2 and solving for $V(H)$ yields

$$V(H) - V + \frac{2{\cdot}291 \times 10^8}{K\nu^2(H)}. \qquad (4)$$

The magnetization of the sample is given by

$$M = \frac{(B-H)}{4\pi(1-\epsilon)} \qquad (5)$$

where ϵ is the demagnetization factor and B, the average field inside the sample, is dependent on H, the applied field, and is given by

$$B = pH \qquad (6)$$

where

$$p = \frac{V(0) - V(H)}{V(0) - V(H_{c2})}. \qquad (7)$$

Inserting 4, 6, and 7 into 5 we get

$$M = \frac{-H}{4\pi(1-\epsilon)}\left[\frac{\nu^2(0)(\nu^2(H_{c2}) - \nu^2(H))}{\nu^2(H)(\nu^2(H_{c2}) - \nu^2(0))}\right]. \qquad (8)$$

The samples consisted of hexagonal crystals, irregularly shaped and broken crystals, and clumps of crystals and therefore it was impossible to determine the lower critical field, H_{C1}, from the magnetization data since the demagnetization factor could not be calculated. The upper field is shape independent and was measured from the magnetization curves [8]. Before each magnetization measurement the sample temperature was raised above the transition temperature and then brought to thermal equilibrium in a field not greater than 3 G to eliminate hysteresis. The field was swept from 0 G to well above H_{c2} and back to -50 G at sweep rates of 100–400 G/min. Hysteresis was present in all samples, but in most cases its magnitude was small.

The values of H_{c2} shown in Table 1 were determined from the calculated magnetization curves. The Rb and the Li doped Rb fluoroxide bronze data (Fig. 3) followed closely the Abrikosov–Ginzburg relation [9]

$$H_{c2}(t) = H_{c2}(0)\,\frac{1-t^2}{1+t^2} \tag{9}$$

which was used to calculate $H_{c2}(0)$ for these compounds. The Cs and Li-doped Cs bronzes (Figs. 4 and 5) followed Gor'kov's relation [10]

$$H_{c2}(t) = H_{c2}(0)\,[1-1{\cdot}24t^2+0{\cdot}28t^4-0{\cdot}04t^6] \tag{10}$$

and this formula was used to calculate $H_{c2}(0)$ for these compounds. $H_{c2}(0)$ could not be found experimentally by extrapolating the $H_{c2}(t)$ data to $t = 0$ because in these experiments t was always greater than 0·3 and it was felt that the extrapolation could not yield accurate values. No attempt was made to measure $H_{c2}(0)$ for the K bronzes due to their low transition temperatures.

4. CONCLUSIONS

The data thus far collected is obviously preliminary in nature. As in the bronzes which do not contain fluorine, T_c is an inverse function of conduction electron concentration. For those compounds which can be

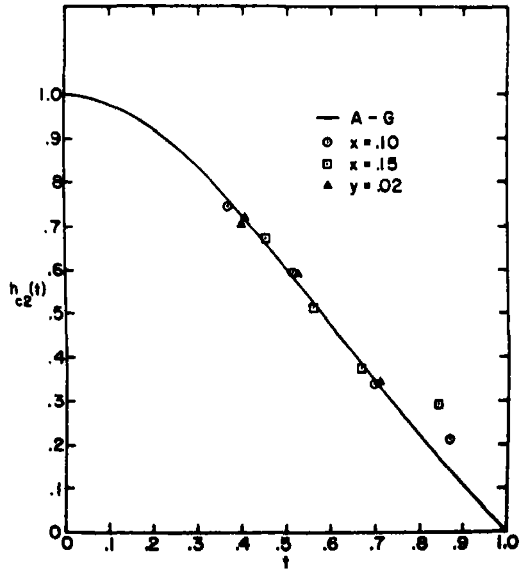

Fig. 3. Reduced upper critical field, $h_{c2}(t) = H_{c2}(t)/H_{c2}(0)$ vs. reduced temperature, $t = T/T_c$ for $Rb_xWo_{3-x}F_x$ and $Rb_{0\cdot1}Li_yWo_{2\cdot9-y}F_{0\cdot1+y}$.

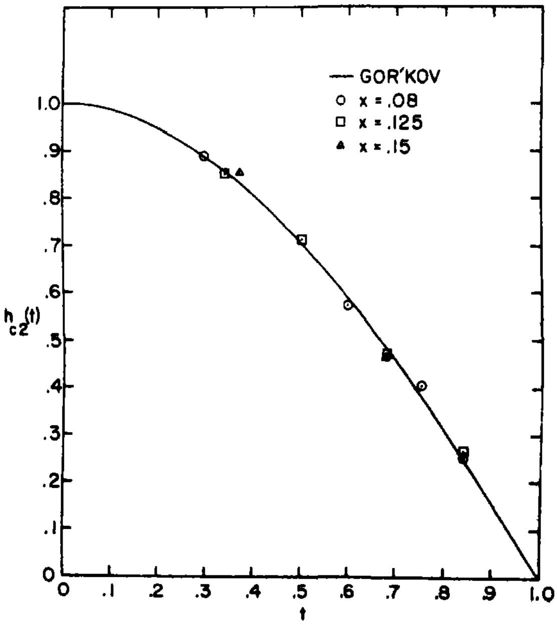

Fig. 4. $h_{c2}(t)$ vs. t for $C_{sx}Wo_{3-x}F_x$

Table 2.

Sample				T_c	$H_{c1}(0)$	% of Sample superconducting
K	0·1	Li	0·02	1·1 ± 0·1		
Rb	0·1	Li	0·02	3·4	6·9	80
		Li	0·05	3·1	5·7	80
		Li	0·10	2·0	4·3	80
Cs	0·1	Li	0·02	4·0	6·2	100
		Li	0·05	3·3	5·2	60
		Li	0·10	2·1	4·8	80

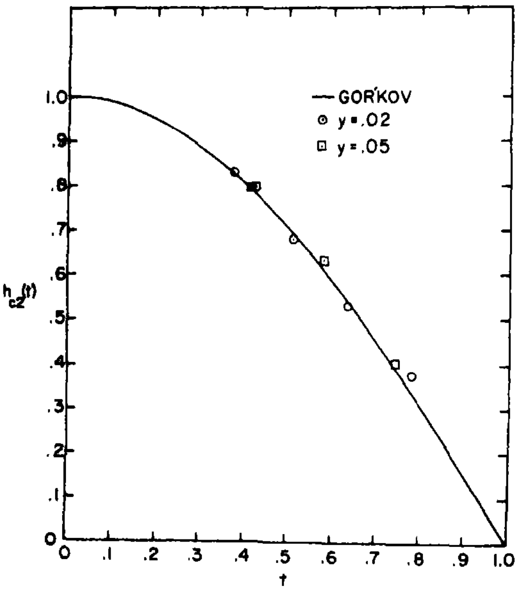

Fig. 5. $h_{c2}(t)$ vs. t for $\mathrm{Li}_y\mathrm{Wo}_{2\cdot 9-y}F_{0\cdot 1+y}$.

compared with previously published data, T_c for the fluoride doped compounds is in all cases higher than for the nondoped compounds with the same nominal electron concentration. There appears to be no difference in the trend with respect to the use of LiF rather than the other alkali fluorides as the source of conduction electrons.

In all of the samples studies here the hexagonal phase has been the predominant phase and it has been assumed that this is the superconducting phase. However it is possible that the tetragonal phase is also superconducting with a transition temperature different from that of the hexagonal phase. If this were the case one would expect to observe a broadened transition when the T_c's were only slightly different.

Experiments are now in progress to measure T_1 in both the superconducting and normal states. Elemental analysis and reducing power determinations will be carried out on all samples when these are completed, and further correlations may be possible at that time.

REFERENCES

1. MAGNELI A., *Acta chem. scand.* 7, 315 (1953).
2. RAUB CH. J., SWEEDLER A R., JENSEN M. A., BROADSTON S. and MATTHIAS B. T., *Phys. Lett.* **13**, 746 (1964).
3. SWEEDLER A. R., RAUB C J. and MATTHIAS B. T., *Phys. Lett.* **15**, 108 (1965).
4. REMEIKA J P., GEBALLE T. H., MATTHIAS B. T., COOPER A. S., HALL G. W. and KELLEY E. M., *Phys. Lett.* **24A**, 565 (1967).
5. GULICK J. C. and SIENKO M. J., *J. Solid State Chem.* **1**, 195 (1970).
6. BANKS E. and GOLDSTEIN A., *Inorg. Chem.* 7, 966 (1968).
7. SCHAWLOW A. L. and DEVLIN G. E., *Phys. Rev.* **113**, 120 (1959).
8. LYNTON E. A., *Superconductivity*, Chapter 3, John Wiley, New York (1962).
9. TINKHAM M., *Phys. Rev.* **129**, 2413 (1963).
10. GOR'KOV L. P. and EKSPERIM Z. H., *i theor. Fiz.* **37**, 835 (1959). [English Translation: *Soviet Phys. JETP* **10**, 593 (1960).]

J. Phys. Chem. Solids, 1971, Vol. 32, pp. 2351–2356. Pergamon Press. Printed in Great Britain

ELASTIC MODULI OF THULIUM AND YTTERBIUM FROM 4·2 TO 300°K

M. ROSEN

Nuclear Research Centre, Negev, P.O.B. 9001, Beer-Sheva, Israel

(*Received* 5 *January* 1971)

Abstract—The longitudinal and transverse acoustic velocities of high-purity polycrystalline thulium and ytterbium have been measured by a pulse technique at a frequency of 10 MHz between 4·2 and 300°K. The variation with temperature of the Young moduli E, shear moduli G, adiabatic compressibilities K_S, and Debye temperature θ_D have been determined. The anomalies in the elastic properties observed in thulium were correlated with the magnetic changes known to occur in this metal at low temperatures. The shape of the compressibility curve suggests that the transition from the antiferromagnetic to the ferromagnetic state in thulium is a gradual process, extending over a temperature interval. No anomalies were observed in the elastic properties of the nonmagnetic ytterbium. The limiting values of the Debye temperatures (at 0°K) of thulium and ytterbium are 200 and 117·5°K, respectively.

1. INTRODUCTION

THE LOW-TEMPERATURE behavior of the 'heavy' rare-earth metals, from gadolinium to lutetium, has extensively been investigated from both theoretical[1] and experimental[2] standpoints. Most of these metals display complex magnetic spin structures with strong dependence on temperature. The magnetic contribution to the total energy in the vicinity of the transition points generally affects the elastic moduli since they are the second derivatives of the thermodynamic potential of the lattice with respect to strain.

The present paper is concerned with the temperature dependence of the elastic moduli, adiabatic compressibility, and Debye temperature of polycrystalline thulium and ytterbium. The elastic properties of the other 'heavy' rare-earth metals in polycrystalline form (gadolinium, terbium dysprosium, holmium and erbium) have previously been reported in detail[3]. The elasticity and anelasticity of the 'light' rare-earth metals, with the exception of lanthanum, have also been presented in a series of papers[4–6].

2. EXPERIMENTAL DETAILS

The high-purity (99·9%) polycrystalline specimens, supplied by Leytess Metal and Chemical Corp., New York, were in the form of flat disks 6 mm in dia. by about 5 mm thick. The specimens were hand-lapped to a parallelism of faces of better than 2 parts in 10^4. The thickness of the disks was measured by means of a calibrated indicator stand to within 5×10^{-4} mm. Room temperature densities (Table 1) were determined to $\pm 0{\cdot}003$ g cm^{-3} by a fluid-displacement method using monobromobenzene. The temperature variation of the acoustical path lengths of the specimens was calculated by using the average coefficients of thermal expansion given by Gschneidner[7] and listed in Table 1.

The elastic moduli, adiabatic compressibilities and Debye temperatures were determined from the experimentally measured longitudinal and transverse sound-velocities. An ultrasonic pulse technique was employed at a frequency of 10 MHz. Experimental details and method of data analysis were described elsewhere[3]. The estimated error

Table 1. Average room-temperature densities and thermal expansion coefficients of the specimens

Element	Density ($g\,cm^{-3}$)	Average linear coefficient of thermal expansion ($°K^{-1}$)
Tm	9·288	$13{\cdot}3\times10^{-6}$
Yb	6·991	$24{\cdot}96\times10^{-6}$

in the absolute values of the elastic moduli is 0·4 per cent. The relative, point to point, precision is better by a factor of 4.

3. RESULTS AND DISCUSSION

3.1 *Thulium*

Neutron diffraction measurements[8] indicate that thulium is paramagnetic above 56°K and sinusoidally-modulated antiferromagnetic between 56 and 38°K. Below 38°K the metal has a *ferrimagnetic-type antiphase domain* structure with a net moment parallel to the hexagonal *c* axis. In the ferromagnetic region, below 22°K, the magnetic layers are parallel to the *c* axis. The structure is in the form of 4 layers with spins up followed by three layers with spins down. Magnetization data[9, 10] are in qualitative agreement with neutron diffraction measurements. The transition point from the paramagnetic to antiferromagnetic state, at about 56°K, is clearly displayed in various transport properties[11–14], as well as in the temperature dependence of the specific heat[15]. However, no unusual behavior was observed at the ferromagnetic transition point, in the vicinity of 22°K.

The temperature variation of the Young (E) and shear (G) moduli of polycrystalline thulium is shown in Fig. 1. With decreasing temperature, from the ambient down to about 200°K, both moduli increase in the normal manner. Below this temperature E and G exhibit a very small temperature dependence followed by a minimum at T_N (55°K). With decreasing temperature, in the antiferromagnetic region, the elastic moduli of polycrystalline thulium increase abruptly by 5 per cent of their values over a rather limited temperature interval of about 20°K. The sharp increase of the moduli with decreasing temperature is halted at about 35°K where the sinusoidally modulated antiferromagnetic structure changes to the ferrimagnetic-type structure[8].

The ferromagnetic transition point is not clearly displayed in the temperature variation of the elastic moduli, Fig. 1. However, a shallow minimum, followed by a well-defined dip were observed at 25 and 13°K, respectively. But neither of these two temperatures coincides with the Curie point of 22°K, as determined from neutron diffraction data[8].

The temperature dependence of the adiabatic compressibility K_S, of thulium is shown in Fig. 2. The normal decrease of the compressibility with decreasing temperature, in the range between 300 and 200°K, is followed by a shallow change, and subsequently by a sharp maximum at the Néel temperature (55°K). At lower temperatures the behavior of the adiabatic compressibility is consistent with that of the elastic moduli, displaying two maxima at 25 and 13°K. The shape of the broad maximum in the compressibility, peaked at 25°K would suggest that the transition from the antiferromagnetic to the ferromagnetic state in thulium is not a usual second-order type cooperative phenomenon. It appears that the low-temperature transition in thulium has a gradual character and extends over a wide temperature range. This is apparently the reason why the Curie point of thulium is indiscernible in various transport properties of this metal[10–14].

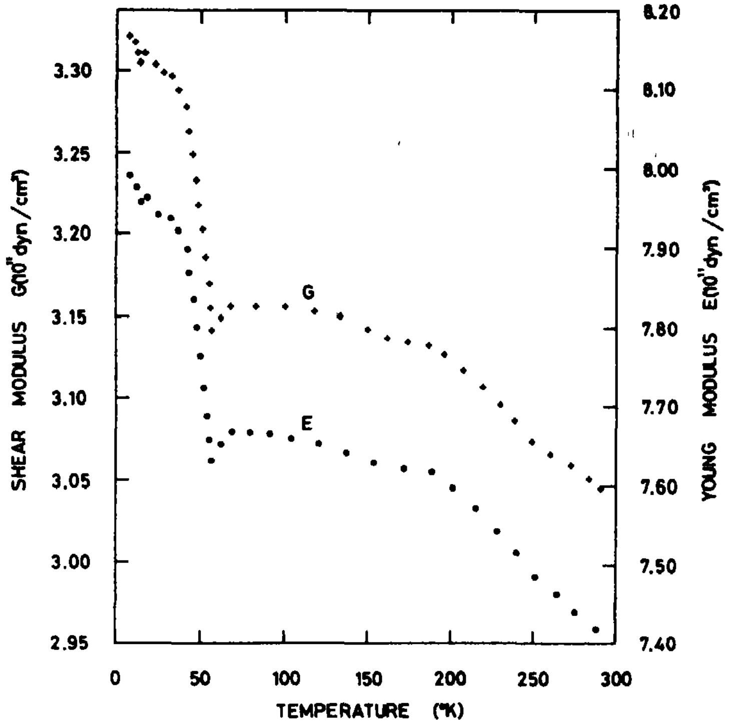

Fig. 1. Temperature variation of the Young (E) and shear (G) moduli of polycrystalline thulium.

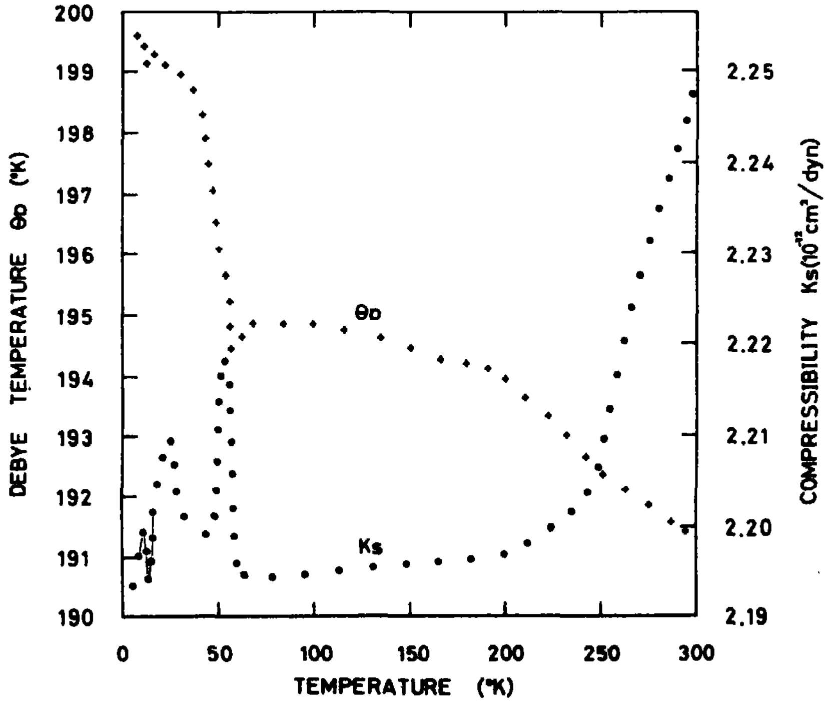

Fig. 2. Temperature variation of the adiabatic compressibility (K_S) and the Debye temperature (θ_D) of polycrystalline thulium.

The temperature dependence of the Debye temperature, θ_D, is shown in Fig. 2. It is very similar to the variation of the elastic moduli, Fig. 1. The limiting value of θ_D, extrapolated to 0°K, is 200°K. This value is significantly higher than 167°K obtained from specific heat measurements[15].

3.2 *Ytterbium*

Ytterbium metal is different from the other rare-earths in several respects. Contrary to the other metals of the series which have an h.c.p. structure at room temperature, ytterbium (and also europium) is f.c.c. Furthermore, ytterbium is divalent in contrast to most rare-earth metals whose properties in the metallic state can be explained in terms of a trivalent model for the ion cores. The 4*f* shell in ytterbium is full, leaving only two electrons for conduction processes. Therefore, the physical properties of this metal are markedly different from the other rare-earths. Lock[16] found that ytterbium metal is paramagnetic with a Curie constant of 56×10^{-6} e.m.u. g^{-1}. But recent magnetization data[17] suggest that very pure ytterbium may be diamagnetic. Magnetoresistance measurements[18] show that ytterbium is a compensated metal with a closed Fermi surface. No low-temperature anomalies were observed in the electrical resistivity[19,20], thermoelectric power[12], and specific heat measurements. The density of ytterbium is much lower than that of its neighbor thulium, Table 1.

The Young (E) and shear (G) moduli of polycrystalline ytterbium are shown in Fig. 3. The absolute values of the moduli of this metal are significantly lower compared with those of thulium. The temperature variation of the elastic moduli of ytterbium, Fig. 3, is smooth and well-behaved as would be expected from a metal that does not possess any

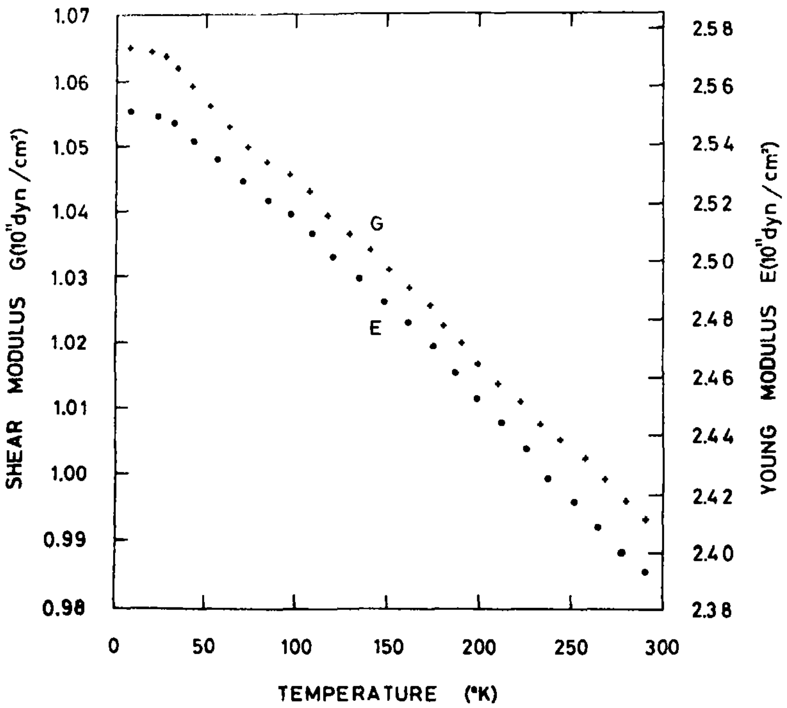

Fig. 3. Temperature variation of the Young (E) and shear (G) moduli of polycrystalline ytterbium.

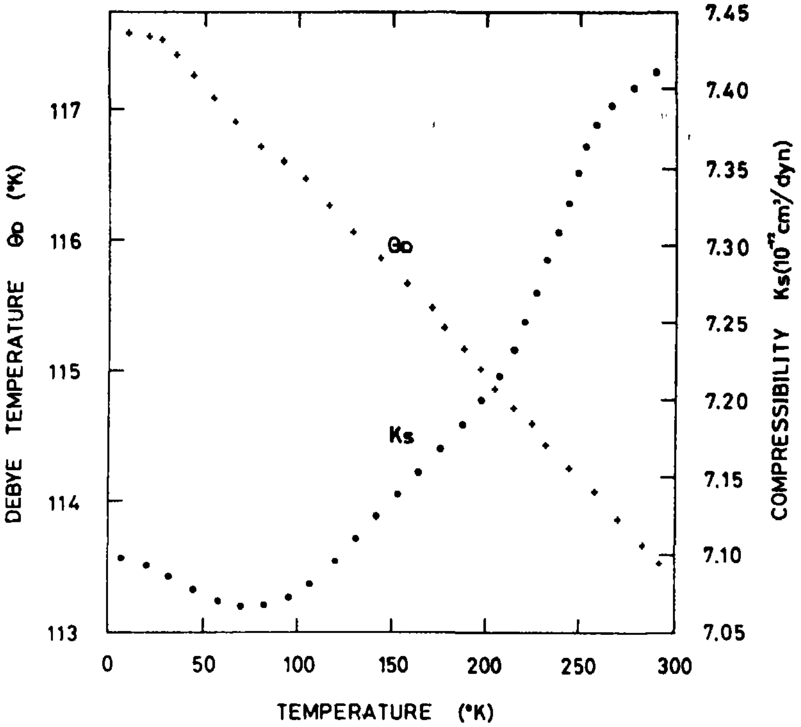

Fig. 4. Temperature variation of the adiabatic compressibility (K_S) and the Debye temperature (θ_D) of polycrystalline ytterbium.

magnetic transitions at low temperatures. The compressibility of ytterbium is rather high, therefore it is not surprising that the elastic moduli E and G increase by about 8 per cent with decreasing temperature from the ambient to 4·2°K.

The temperature dependence of the adiabatic compressibility, K_S, of ytterbium is shown in Fig. 4. From the ambient down to about 100°K, K_S decreases smoothly, then levels off with decreasing temperature. According to the third law of thermodynamics, the compressibility should meet with zero temperature. However, the reason for the slight increase in K_S (Fig. 4) at temperature below 80°K is not clear.

The limiting Debye temperature, extrapolated to 0°K, is 117·5°K, Fig. 4. This value is in good agreement with 118°K as determined from low-temperature specific heat measurements [21]. It should be noted that the temperature dependence of θ_D, as displayed in Fig. 4, does not exhibit the reported [21] minimum at 14°K, as was calculated from heat capacity data.

Acknowledgements—The author wishes to express his gratitude to A. Halwany, D. Kalir and B. Cohen for their assistance in the various phases of this work.

REFERENCES

1. YOSIDA K., in *Progress in Low Temperature Physics* (Edited by C. J. Gorter), Vol. 4, p. 265, North-Holland, Amsterdam (1964).
2. BELOV K. P., LEVITIN R. Z. and NIKITIN S. A., *Usp. fiz. Nauk* **82**, 449 (1964) [English transl.: *Soviet Phys. Ups.* 7, 179 (1964)].
3. ROSEN M., *Phys. Rev.* **174**, 504 (1968).
4. ROSEN M., *Phys. Rev.* **166**, 561 (1968).
5. ROSEN M., *Phys. Rev.* **180**, 540 (1969).
6. ROSEN M., *Phys. Rev.* **181**, 932 (1969).
7. GSCHNEIDNER K. A., *Solid State Phys.* **16**, 275 (1964).
8. KOEHLER W. C., CABLE J. W., WOLLAN E. O. and WILKINSON M. K., *Phys. Rev.* **126**, 1672 (1962).

9. RHODES B. L., LEGVOLD S. and SPEDDING F. H., *Phys. Rev.* **109**, 1547 (1958).
10. FONER M., SCHEIBER M. and McNIFF E. J., *Phys. Lett.* **25A**, 321 (1967); RICHARDS D. B. and LEGVOLD S., *Phys. Rev.* **186**, 508 (1969).
11. COLVIN R. V., LEGVOLD S. and SPEDDING F. H., *Phys. Rev.* **120**, 741 (1960).
12. BORN H. J., LEGVOLD S. and SPEDDING F. H., *J. Appl. Phys.* **32**, 2543 (1961).
13. ALIEV N. G. and VOLKENSHTEIN N. V., *Zh. eksp. teor. Fiz.* **49**, 1450 (1966).
14. EDWARDS L. R. and LEGVOLD S., *Phys. Rev.* **176**, 753 (1968).
15. JENNINGS L. D., HILL E. D. and SPEDDING F. H., *J. chem. Phys.* **34**, 2082 (1961).
16. LOCK J. M., *Proc. Phys. Soc. London* **B70**, 476 (1957).
17. SCHIEBER M., FONER S., DOCLO R. and McNIFF E. D., *J. appl. Phys.* **39**, 885 (1968).
18. DATARS W. R. and TANNUMA S., *Phys. Lett.* **27A**, 182 (1968).
19. CURRY M. A., LEGVOLD S. and SPEDDING F. H., *Phys. Rev.* **117**, 953 (1960).
20. VOLKENSHTEIN N. V. and STARTSEV V. E., *Soviet Phys. JETP* **19**, 308 (1964).
21. LOUNASMAA O. V., *Phys. Rev.* **129**, 2460 (1963).

J. Phys. Chem. Solids, 1971, Vol. 32, pp. 2357–2362. Pergamon Press. Printed in Great Britain

LATTICE-ION INTERACTIONS OF Fe^{2+} ION IN A TETRAHEDRAL ENVIRONMENT

B. D. BHATTACHARYYA*

Department of Magnetism, Indian Association for the Cultivation of Science, Jadavpur, Calcutta 32, India

(*Received* 17 *November* 1970)

Abstract—The theoretical expressions for magnetic susceptibility of Fe^{2+} ion in a tetrahedral environment have been derived on the basis of the more general molecular orbital method of Van Vleck, Stevens and Bose *et al.*, considering quantum-mechanical tunneling which links the equivalent vibronic states of the Jahn–Teller ions. Attempts have been made to fit the experimental results of optical absorption, and magnetic susceptibility with a unique set of values of parameters in the theoretical expressions at all temperatures. From this an estimate of the parameters which describe the Jahn–Teller potential is made.

1. INTRODUCTION

IRON (II) forms a series of isomorphous coordination compounds having the general formula R_2FeX_4, where X is a halide or pseudohalide and R is of the quaternary ammonium or phosphonium type radical [1, 2]. X-ray studies [3] of the series of isomorphous organometallic halides of Ni^{2+} and Fe^{2+} indicate that the 3*d* ions in all these compounds are tetrahedrally coordinated. The absorption spectrum of the Fe^{2+} tetrahedral complex $[FeCl_4]^{2-}$ consists of only one ligand field band with a maximum in the region around 4000 cm^{-1} [2, 4]. Such a band is undoubtedly due to the $^5E \rightarrow {}^5T_2$ transition originated from the splitting of the free-ion ground term $(3d^6, {}^5D)$ under a ligand field of symmetry T_d. The Mössbauer spectra studies [5] on tetrahedral Fe^{2+} ion have however indicated the presence of a small distortion from the cubic tetrahedral symmetry. A reduction of symmetry ($T_d \rightarrow c_{3v}$) of the ligand field causing a further splitting of the orbital triplet $^5T_2$ into $A_1 + E$ appears from the i.r. studies [6]. The ground state orbital doublet (^5E), however, remains unsplit under this field of lower symmetry.

The present work deals with the theory of magnetic susceptibility and anisotropy of the tetrahedral unit $[FeCl_4]^{2-}$ present in the complex R_2FeX_4, taking into consideration the covalency overlap of the central paramagnetic ion with the ligands as well as the quantum-mechanical tunneling between the three vibrationally coupled equivalent asymmetric configurations. Attempts have been made to fit the theory with the experimental results [1, 5, 7, 8] measured at different temperatures, consistent with the available optical data [2, 4, 5]. Finally, in fitting the magnetic and optical data, we estimate the lattice-ion coupling parameter for the tetrahedral complex.

2. THEORY

High-spin tetrahedral Fe^{2+} ions can be considered as systems originally consisting of four-unpaired electrons or holes having the electronic configuration $3d^6\,{}^5D$ with several states $^5E, {}^3T_2, {}^3E, {}^5T_2$ (in order of energy) arising out of $[t_2{}^3 . e^3]$, and $[t_2{}^4 . e^2]$ configurations under the cubic field. The determinantal wave functions for the ground doublet ^5E state and the excited triplet $^5T_2$ state can be written as [9]

---

*Present Address: Department of Physics, St. Xavier's College, Calcutta 16, India.

$$[t_2{}^3\,.\,e^3]:|{}^5E_\epsilon\rangle = |-\overset{+}{(yz)}\overset{+}{(xz)}\overset{+}{(xy)}\overset{+}{(z^2)} \times \overset{+}{(x^2-y^2)}\overset{-}{(x^2-y^2)}|,$$

$$|{}^5E_\theta\rangle = |\overset{+}{(yz)}\overset{+}{(xz)}\overset{+}{(xy)}\overset{+}{(z^2)}\overset{-}{(z^2)}\overset{+}{(x^2-y^2)}|,$$

$$[t_2{}^4\,.\,e^2]:$$

$$|{}^5T_2\xi\rangle = |\overset{+}{(yz)}\overset{-}{(yz)}\overset{+}{(xz)}\overset{+}{(xy)}\overset{+}{(z^2)}\overset{+}{(x^2-y^2)}|,$$

$$|{}^5T_2\eta\rangle = |-\overset{+}{(yz)}\overset{+}{(xz)}\overset{-}{(xz)}\overset{+}{(xy)}\overset{+}{(z^2)}\overset{+}{(x^2-y^2)}|,$$

$$|{}^5T_2\zeta\rangle = |\overset{+}{(yz)}\overset{+}{(xz)}\overset{+}{(xy)}\overset{-}{(xy)}\overset{+}{(z^2)}\overset{+}{(x^2-y^2)}|, \qquad (1)$$

which are inclusive of the overlap of the surrounding s- and p- orbitals with the central metal d-orbitals as given by[10]:

$$(yz) = N\Big[dyz + \frac{\lambda}{2}(\sigma_1 + \sigma_3 - \sigma_2 - \sigma_4) + \frac{\lambda}{4}\{(\pi x_4 + \pi x_2 - \pi x_1 - \pi x_3) + \sqrt{3}(\pi y_4 + \pi y_2 - \pi y_1 - \pi y_3)\}\Big].$$

$$(xz) = N\Big[dxz + \frac{\lambda}{2}(\sigma_1 + \sigma_2 - \sigma_3 - \sigma_4) + \frac{\lambda}{4}\{(\pi x_1 + \pi x_2 - \pi x_3 - \pi x_4)\}\Big].$$

$$(xy) = N\Big[dxy + \frac{\lambda}{2}(\sigma_1 + \sigma_4 - \sigma_2 - \sigma_3) + \frac{\lambda}{4}\{(\pi x_3 + \pi x_2 - \pi x_1 - \pi x_4) + \sqrt{3}(\pi y_1 + \pi y_4 - \pi y_2 - \pi y_3)\}\Big].$$

$$(x^2-y^2) = N'\Big[d_{x^2-y^2} + \frac{\lambda'}{4}\{(\pi y_1 + \pi y_2 + \pi y_3 + \pi y_4) + \sqrt{3}(\pi x_1 + \pi x_2 + \pi x_3 + \pi x_4)\}\Big] \qquad (2)$$

$$(z^2) = N'\Big[d_{3z^2-r^2} + \frac{\lambda'}{4}\{(\pi x_1 + \pi x_2 + \pi x_3 + \pi x_4) - \sqrt{3}(\pi y_1 + \pi y_2 + \pi y_3 + \pi y_4)\}\Big].$$

The N's are normalising constants and the λ's are the amount of admixture of the s- and p-orbitals with the d-orbitals.

3. JAHN-TELLER PROBLEM

The system we wish to consider thus consists of a ground state orbital doublet ${}^5E$ interacting with the vibrations of the ligands. We shall assume that this interaction is linear in displacements of the ligands relative to the Fe^{2+} ion. It is convenient to choose these displacements to transform according to irreducible representations of the cubic group. As $[E\times E]_{\text{sym}} = A_1 + E$, it means that we need only retain the E modes (Q_2, Q_3). The symmetric mode A_1 produces no splitting and need not be considered in the interaction term responsible for distortion from cubic symmetry. Thus the first-order vibronic Hamiltonian[11–13] is:

$$\mathscr{H}_{\text{vib}} = \mathscr{H}_0\mathscr{I} + A(U_2Q_2 + U_3Q_3), \qquad (3)$$

with

$$\mathscr{H}_0 = \epsilon_0 + \tfrac{1}{2}\mu\omega^2(Q_2{}^2 + Q_3{}^2) + \frac{1}{2\mu}(p_2{}^2 + p_3{}^2), \qquad (4)$$

where μ and ω are the effective mass and angular frequency of the vibrating tetrahedron; P_2 and P_3 are the momenta conjugate to Q_2 and Q_3 respectively. ϵ_0 is the electronic energy in the degenerate symmetrical configuration; and A is a measure of the strength of electron lattice coupling. $\mathscr{I}$, U_2, and U_3 are Hermitian electronic operators having matrix elements between the states $|{}^5E_\theta\rangle$, $|{}^5E_\epsilon\rangle$, and defined by Ham[13] as

$$U_2 = \begin{pmatrix} 0 & 1 \\ 1 & 0 \end{pmatrix}, \qquad U_3 = \begin{pmatrix} -1 & 0 \\ 0 & 1 \end{pmatrix}. \qquad (5)$$

If the nuclei are regarded as 'fixed' on the lower-branch of the potential surface, the electronic eigenstate of the potential-energy operator in equations (3) and (4) has the form

$$\psi_{\text{electronic}} = |{}^5E_\theta\rangle \cos\tfrac{1}{2}\varphi - |{}^5E_\epsilon\rangle \sin\tfrac{1}{2}\varphi. \quad (6)$$

where the relations

$$Q_2 = \rho \sin\varphi, \qquad Q_3 = \rho\cos\varphi, \quad (7)$$

are used. Now the vibronic Hamiltonian $\mathscr{H}_{\text{vib}}$ is to be solved. The vibronic eigenfunction for the complex may be written in the form of simple Born–Oppeheimer product of the electronic wave function and two-dimensional harmonic-oscillator wave functions. As the oscillator mean positions depend upon the electronic functions, it is necessary to label the vibrational wave function as

$$\chi_i = \chi(\rho-\rho_0)\chi(\varphi - j\pi/3), \quad (8)$$

where $i = x, y, z$; $j = 2, 4, 0$, and $\rho_0 = |A|/\mu\omega^2$. The total vibronic zero order wave functions describing the decoupled stable equilibrium states are

$$\Phi^{(X)} = \psi_x\chi_x, \quad \Phi^{(Y)} = \psi_y\chi_y, \quad \Phi^{(Z)} = \psi_z\chi_z, \quad (9)$$

where $\psi_x\chi_x$ is the vibronic wave function for the valley corresponding to distortion in the x-direction, $\psi_y\chi_y$ and $\psi_z\chi_z$ correspond to distortion in the y- and z- directions, respectively. It is evident that three vibrational functions of φ are not strictly orthogonal, and a small but finite overlap integral γ between different functions exists. The three vibronic wave functions in equation (9) of equal energy are also coupled together by the off-diagonal matrix elements

$$\Gamma = \langle\Phi^{(X)}|\mathscr{H}_n|\Phi^{(Y)}\rangle = \langle\Phi^{(Y)}|\mathscr{H}_n|\Phi^{(Z)}\rangle$$
$$= \langle\Phi^{(Z)}|\mathscr{H}_n|\Phi^{(X)}\rangle. \quad (10)$$

The perturbation Hamiltonian $\mathscr{H}_n$ in equation (10) is given by

$$\mathscr{H}_n = \frac{1}{2\mu}(P_2^2 + P_3^2). \quad (11)$$

We now consider overlap between pairs of wave functions and symmetrize them. The result is:
a singlet

$$\Psi_A = (3+3\gamma)^{-1/2}(\Phi^{(X)} + \Phi^{(Y)} + \Phi^{(Z)}),$$

at

$$E_g = 2\Gamma;$$

and a doublet

$$\Psi_\theta = (6-6\gamma)^{-1/2}(2\Phi^{(Z)} - \Phi^{(X)} - \Phi^{(Y)}), \quad (12)$$

$$\Psi_\epsilon = (2-2\gamma)^{-1/2}(\Phi^{(X)} - \Phi^{(Y)}),$$

at

$$E_\theta = E_\epsilon = -\Gamma.$$

The energy difference 3Γ is the tunnel splitting. Γ is taken to be positive, so that the 'symmetric' singlet state ΨA lies above the 'antisymmetric' doublet state Ψ_θ, Ψ_ϵ.

4. CALCULATION OF SUSCEPTIBILITY

For magnetic susceptibility we consider the perturbation Hamiltonian as:

$$\mathscr{H}' = \zeta R_i\mathbf{L}\,.\,\mathbf{S} + \beta\mathbf{H}(\chi_i\mathbf{L} + 2\mathbf{S}), \quad (13)$$

where χ_i's and R_i's are the orbital reduction and the s-O coupling reduction factors, respectively, arising from the overlap of $3d$ charge clouds of Fe^{2+} ion with the s- p-charge clouds of the ligands [14], ζ is the s-O coupling parameter of the free ion. The first term (s-o coupling term) in the above equation is large compared with the second term (Zeeman term), but has no effect within the ground manifold. To include the effect of s-O coupling (as the s-O interaction admixes some triplet wave functions to the ground wave functions), we correct our orbitals as:

$$|^5E_\theta M_s'\rangle = |^5E_\theta M_s\rangle - \sum_\sigma \alpha_i\langle\sigma|\mathbf{L}\,.\,\mathbf{S}|^5E_\theta M_s\rangle\,\sigma, \tag{14}$$

$$|^5E_\epsilon M_s'\rangle = |^5E_\epsilon M_s\rangle - \sum_\sigma \alpha_i\langle\sigma|\mathbf{L}\,.\,\mathbf{S}|^5E_\epsilon M_s\rangle\,\sigma,$$

where M_s refers to the azimuthal spin quantum number and σ denotes the components of the excited $^5T_2$ state; α_i $(=\zeta R_i/10\,Dq)$ is a measure of the s-O mixing into the ^5E term of the $^5T_2$ term with a separation $10\,Dq$ between them. In our construction of the corrected orbitals we disregard the small trigonal separation in comparison to the cubic field separation, $10\,Dq$.

Finally, the magnetic susceptibility up to second order is determined by [15]

$$K_i = N\frac{\sum\limits_{n,m}[(E^{\textcircled{1}}_{nm})^2/kT - 2E^{\textcircled{2}}_{nm}]\exp(-E_n^{(0)}/kT)}{\sum\limits_n \exp(-E_n^{(0)}/kT)} \tag{15}$$

$$(i = \|\ \text{or}\ \perp)$$

where N is the Avogardro number and k the Boltzmann constant; $E^{\textcircled{1}}_{nm}$, $^{\textcircled{2}}_{nm}$ are the first- and second-order Zeeman energy terms respectively; these two terms are obtained by the application of the Zeeman operator

$$Z_i = \beta(x_i\mathbf{L} + 2\mathbf{S}), \qquad (i = \|\ \text{or}\ \perp). \tag{16}$$

Performing the outlined calculations up to second order, one finally obtains the expressions for the principal gm-ionic magnetic susceptibility as:

$$K_i = \frac{N\beta^2}{kW}\left[\frac{1}{T}\left\{G^\theta_{1j} + G^\epsilon_{1j} + G^A_{1j}\exp\left(\frac{-3\Gamma}{kT}\right)\right\}\right.$$
$$\left. + 2k\left\{G^\theta_{2j} + G^\epsilon_{2j} + G^A_{2j}\exp\left(\frac{-3\Gamma}{kT}\right)\right\}\right], \tag{17}$$

$$(i = \|\ \text{or}\ \perp, \quad j = z\ \text{or}\ x),$$

where

$$w = 10 + 5\exp(-3\Gamma/kT); \tag{18}$$

and

$$G^\theta_{1z} = 2\{|\langle\Psi_\theta 2|z_\||\Psi_\theta 2\rangle|^2 + |\langle\Psi_\theta 1|z_\||\Psi_\theta 1\rangle|^2\}$$
$$= 10(2 - 2\alpha_\|\chi_\| - 4\gamma\alpha_\| x_\| + 7/3\gamma)^2,$$
$$G^\epsilon_{1z} = 2\{|\langle\Psi_A 2|z_\||\Psi_\epsilon 2\rangle|^2 + |\langle\Psi_\epsilon 1|z_\||\Psi_\epsilon 1\rangle|^2\}$$
$$= 10(2 - 6\alpha_\|\chi_\| + \gamma)^2,$$
$$G^A_{1z} = 2\{|\langle\Psi_A 2|z_\||\Psi_A 2\rangle|^2 + |\langle\Psi_A 1|z_\||\Psi_A 1\rangle|^2\}$$
$$= 10(2 - 4\alpha_\|\chi_\| - 4/3\gamma)^2,$$
$$G^\theta_{2z} = \frac{2}{3\Gamma}(s_0^2 + s_1^2), \quad G^\epsilon_{2z} = \frac{2}{3\Gamma}(s_2^2 + s_3^2),$$
$$G^A = -\frac{2}{3\Gamma}(s_0^2 + s_1^2 + s_2^2 + s_3^2);$$
$$G^\theta_{1x} = 2\{|\langle\Psi_\theta \pm 2|z_\perp|\Psi_\theta \pm 1\rangle|^2 + |\langle\Psi_\theta 0|z_\perp|$$
$$\times\Psi_\theta \pm 1\rangle|^2\} = 10(2 - 5\alpha_\perp\chi_\perp - 9\gamma\alpha_\perp\chi_\perp$$
$$+ 7/3\gamma)^2,$$
$$G^\epsilon_{1x} = 2\{|\langle\Psi_\epsilon \pm 2|z_\perp|\Psi_\epsilon \pm 1\rangle|^2 + |\Psi_\epsilon 0|z_\perp|$$
$$\times\Psi_\epsilon \pm 1\rangle|^2\} = 10(2 - 3\alpha_\perp\chi_\perp - 3\gamma\alpha_\perp\chi_\perp$$
$$+ \gamma)^2,$$
$$G^A_{1x} = 2\{|\langle\Psi_A \pm 2|z_\perp|\Psi_A \pm 1\rangle|^2 + |\langle\Psi_A 0|z_\perp|$$
$$\times\Psi_A \pm 1\rangle|^2\} = 10(2 - 4\alpha_\perp\chi_\perp + 8\xi\alpha_\perp\chi_\perp$$
$$- 8/3\gamma); \tag{19}$$

$$G^\theta_{2x} = \frac{4}{3\Gamma}(U_0^2 + U_1^2), G^\epsilon_{2x} = \frac{4}{3\Gamma}(U_2^2 + U_3^2),$$
$$G^A_{2x} = -\frac{4}{3\Gamma}(U_0^2 + U_1^2 + U_2^2 + U_3^2);$$

with

$$s_0 = \langle\Psi_\theta 2|z_\||\Psi_A 2\rangle$$
$$= \sqrt{2}(4\alpha_\|\chi_\| + 4\gamma\alpha_\|\chi_\| - \tfrac{2}{3}\gamma),$$
$$s_1 = \langle\Psi_\theta 1|z_\||\Psi_A 1\rangle$$
$$= \sqrt{2}(2\alpha_\|\chi_\| + 2\gamma\alpha_\|\chi_\| - \gamma/3),$$
$$s_2 = \langle\Psi_\epsilon 2|z_\||\Psi_A 2\rangle$$
$$= 2\sqrt{\tfrac{2}{3}}\gamma = 2s_3 = \langle\Psi_\epsilon 1|z_\||\Psi_A 1\rangle;$$

$$
\begin{aligned}
U_0 &= \langle \Psi_\theta 0 | z_\perp | \Psi_A \pm 1 \rangle \\
&= \frac{1}{\sqrt{3}}(3\alpha_\perp\chi_\perp - 3\gamma\alpha_\perp\chi_\perp + \gamma), \qquad (20) \\
U_1 &= \langle \Psi_\theta \pm 2 | z_\perp | \Psi_A \pm 1 \rangle \\
&= \sqrt{2}(\alpha_\perp\chi_\perp - \gamma\alpha_\perp\chi_\perp + \gamma/3), \\
U_2 &= \langle \Psi_\epsilon 0 | z_\perp | \Psi_A \pm 1 \rangle \\
&= (3\alpha_\perp\chi_\perp - 3\gamma\alpha_\perp\chi_\perp + \gamma), \\
U_3 &= \langle \Psi_\epsilon \pm 2 | z_\perp | \Psi_A \pm 1 \rangle = \frac{2}{\sqrt{6}} U_2.
\end{aligned}
$$

Since each state in equation (12) is fivefold degenerate in spin the azimuthal spin quantum numbers ±2, ±1, 0 are associated to these states i.e. they become $|\Psi_\theta \pm 2\rangle$, $|\Psi_\theta \pm 1\rangle$ etc. in the equations (19) and (20).

In performing the above calculations, terms involving γ^2, α_i^2 ($i = \|$ or $\perp$) are disregarded as their contributions are very small.

5. INTERPRETATION OF EXPERIMENTAL RESULTS

The numerical results of our calculations are conveniently presented in terms of the effective magnetic moments $P_\|$ and $P_\perp$. The moments P_i ($i = \|$ or $\perp$) are related to K_i by

$$P_i^2 = \frac{3k}{N\beta^2} K_i T. \qquad (21)$$

The theoretical parameters appearing in the expression for magnetic susceptibilities and energy values of the ligand field levels (in optical spectra) are, the cubic field splitting parameter 10 Dq, the 'Jahn–Teller energy' parameter ΔE_{JT} $(= A^2/2\mu\omega^2)$, the tunnel splitting parameter 3Γ, the nuclear vibrational overlap integral γ, the orbital reduction and the s-O coupling reduction factors χ_i, and R_i ($i = \|$ or $\perp$) along and perpendicular to the principal axis of the complex. The cubic field energy separation is typically of the order of 4000 cm^{-1} in these compounds[2], which is considerably lower than that found in octahedrally coordinated Fe^{2+} complexes.

In tetrahedral Fe^{2+} complexes Jahn–Teller effects in the ^{5}E ground state turn out, however, to be weak. Values of Jahn–Teller energy parameter ΔE_{JT} were found[13] for the excited $^5T_2$ state for tetrahedral Fe^{2+} in cubic ZnS, CdTe, and MgAl$_2$O$_4$ as ~535, 255 and 945 cm^{-1} respectively. For the ^5E ground state it is much less. The magnitude of ΔE_{JT} for the ^5E ground state in the case of tetrahedral Fe^{2+} complexes is readily furnished by the recent experimental data for the quadrupole splitting[5]. For (NEt$_4$)$_2$FeCl$_4$ the value of $\Delta E_{JT} =$ 135 cm^{-1} and for (NMe$_4$)$_2$FeCl$_4$, $\Delta E_{JT} = 125$ cm^{-1}. The tunnel splitting parameter is estimated to be 8 cm^{-1}[16].

Having fixed the values of the parameters 10 Dq, ΔE_{JT} and 3Γ, the remaining parameters viz. χ_i, R_i ($i = \|$ or $\perp$) and γ are then adjusted by trial so as to fit the experimental results as closely as possible. The parameters best suited to fit the theory with the experimental results are shown in Table 1. For the tetrahedral complexes, the values of the reduction factors $\chi_\| = 0{\cdot}82$, $\chi_\perp = 0{\cdot}80$, $R_\| = R_\perp = 0{\cdot}80$ give reasonable fit at all temperatures. The result indicates an appreciable anisotropic covalency overlap of the ligand charges with the charge cloud of the central metal atom. The orbital moment in a direction parallel to the principal axis is reduced by 18 per cent and s-o coupling coefficient by 20 per cent, due to covalency effect, from the free ion value, while in the perpendicular direction they are reduced by 20 per cent. In fitting the experimental results for different temperatures, 10 Dq, ΔE_{JT}, 3Γ, χ_i, R_i ($i = \|$ or $\perp$) are assumed to remain invariant with temperature. The parameter that is most likely to vary is γ, and we make use of the fact, that γ decreases with temperature.

6. CONCLUSION

Using the harmonic approximation $\gamma = \exp(-3\Delta E_{JT}/2\hbar\omega)$, and $\Delta E_{JT} = 125$ cm^{-1}, $\gamma = 0{\cdot}35$ we can estimate the angular frequency of the vibrating tetrahedron $\omega \approx 288$ cm^{-1} at 343°K. The variation of the overlap γ

Table 1

Ligand field parameters and mean moments for Fe^{2+} *tetrahedral complexes*

$10Dq = 4000\,\mathrm{cm}^{-1}$ $\chi_{\parallel} = 0{\cdot}82,\ \chi_{\perp} = 0{\cdot}80$

$\Delta E_{JT} = 125\,\mathrm{cm}^{-1}$ [for $(NMe_4)_2FeCl_4$] $R_{\parallel} = R_{\perp} \approx 0{\cdot}80$

$= 135\,\mathrm{cm}^{-1}$ [for $(NEt_4)_2FeCl_4$]

$3\Gamma = 8\,\mathrm{cm}^{-1}$ $\zeta = -104\,\mathrm{cm}^{-1}$ (free ion value).

$(NMe_4)_2FeCl_4$ complex				$(NEt_4)_2FeCl_4$ complex			
		P_i^2				P_i^2	
Temp. °K	γ	(theoretical)	experimental	Temp. °K	γ	theoretical	experimental
343	0·35	29·16	29·16	300	0·33	28·92	28·92
195	0·30	28·60	28·84	200	0·29	28·67	28·64
100	0·20	28·20	28·25	150	0·25	28·60	28·59
4	0·009	15·26	15·17	100	0·20	28·47	28·50

with temperature indicates the possibility of variation of the Jahn–Teller energy with temperature. As $\Delta E_{JT} = A^2/2\mu\omega^2$, the lattice-ion coupling parameter A, also changes with temperature. This parameter may also be evaluated using crystal field theory and is found to have the value

$$A = \frac{2\sqrt{3}}{7}\frac{|e|}{b^2}q\left[3\frac{\langle\bar{\gamma}^2\rangle}{b^2} - \frac{25}{9}\frac{\langle\bar{\gamma}^4\rangle}{b^4}\right]. \quad (23)$$

Change in the value of b, the average Fe^{2+}-ligand distance, with temperature may be attributed as due to thermal changes in the anisotropic part of the ligand field, as also observed by earlier workers of this laboratory on many salts of the iron group[17, 18].

Acknowledgement—I would like to express my gratitude to Prof. A. Bose D. Sc., F.N.I., for helpful discussions.

REFERENCES

1. GILL N. S., *J. chem. Soc.* 3512 (1961); 426 (1962).
2. FORSTER D. and GOODGAME D. M. L., *J. chem. Soc.* 262, 268, 454 (1965).
3. PAULING P. *Inorg. Chem.* **5**, 1498 (1966).
4. FURLANI C., CERVONE E. and VALENTI V., *J. inorg. nucl. Chem.* **25**, 159 (1963).
5. EDWARDS P. R., JOHNSON C. E. and WILLIAMS R. J. P., *J. chem. Phys.* **40**, 2074 (1967).
6. BURBRIDGE C. D. and GOODGAME D. M. L., *J. chem. Soc.* (*A*), 1074 (1968).
7. CLARK R. J. H., NYHOLM R. S. and TAYLOR F. B., *J. chem. Soc.* (*A*), 1802 (1967).
8. CLARK R. J. H. and DUN T. M., *J. chem. Soc.*, 1198 (1963).
9. BHATTACHARAYYA B. D., *Phys. Status Solidi* **38**, K157 (1970).
10. BALLHAUSEN C. J. and GRAY H. B., *Molecular Orbital Theory*, W. A. Benjamin, New York (1964).
11. MOFFITT W. and THORSON W., *Phys. Rev.* **108**, 1251 (1957).
12. LONGUET-HIGGINS H. C., OPIK U., PRYCE M. H. L. and SACK R. A., *Proc. R. Soc.* **A244**, 1 (1958).
13. HAM F. S., *Phys. Rev.* **166**, 307 (1968); **152**, 376 (1966).
14. STEVENS K. W. H., *Proc. R. Soc.* **A219**, 542 (1953).
15. VAN VLECK J. H., *The Theory of Electric and Magnetic Susceptibilities*, Oxford University Press (1932).
16. HOCHLI U. T., *Phys. Rev.* **162**, 262 (1967).
17. BOSE A., CHAKRAVARTY A. S., CHATTERJEE R., *Proc. R. Soc.* **A261**, 43 (1961).
18. BOSE A., MITRA S. and DATTA S. K., *Proc. R. Soc.* **A230**, 165 (1957); **A248**, 158 (1958).

J. Phys. Chem. Solids, 1971, Vol. 32, pp. 2363–2372. Pergamon Press. Printed in Great Britain

THE PRESSURE DEPENDENCE OF THE ELASTIC CONSTANTS OF THE ALKALI CHLORIDES*

W. N. POTTER, R. A. BARTELS and R. W. WATSON
Physics Department, Trinity University, San Antonio, Texas 78212, U.S.A

(*Received* 25 *May* 1970; *in revised form* 10 *August* 1970)

Abstract—The pressure derivatives of the elastic stiffness constants of LiCl and RbCl have been measured using the ultrasonic pulse-echo technique. The values at room temperature and zero pressure are:

	dB/dP	dC_{44}/dP	dC'/dP
LiCl	5·41	1·63	3·63
RbCl	5·39	−0·64	5·53

where the notation $B = (C_{11}+2C_{12})/3$ and $C' = (C_{11}-C_{12})/2$ has been used. These results in combination with previous results for NaCl and KCl allow for a systematic study of the elastic properties of all alkali chlorides having the NaCl structure. Such a study has been made using a Born model with the cohesive energy consisting of two parts, a Coulomb interaction between all ions and a short-range repulsive interaction between nearest neighbors only. In most cases the experimental results are predicted within 10 per cent, the exceptions being associated with the shear constant C_{44} and its pressure derivative. The model is least successful for LiCl, and it is shown that the addition of next-nearest-neighbor interactions can improve the situation for LiCl but not for the other three materials.

1. INTRODUCTION

THE BORN model has long been used to explain the binding energy of the alkali halides. The model has been widely accepted because of its simplicity as well as its success in predicting the cohesive energy for simple ionic compounds. In the Born model the attraction energy is accounted for by a coulomb interaction between point-like ionic charges, and the repulsion energy by less understood interactions which are short range and two-body in character. The elastic constants and their pressure derivatives are valuable tools for investigating this model as they are strong indicators of the short range contributions to the binding energy.

The present study was undertaken to obtain elastic data for a complete series of the alkali halides and then to test the Born model by systematically applying it to all members of the series. The series chosen contains the four alkali chlorides having the NaCl structure: namely, LiCl, NaCl, KCl, and RbCl. To this end the elastic constants and their pressure dependence were measured for LiCl and RbCl. These data were combined with previous results for NaCl and KCl[1], thus giving the complete experimental data needed for the systematic study.

These compounds represent a series with fixed anion size but with a large variation in cation size: the ratio of cation/anion radius varies from 0·33 for LiCl to 0·82 for RbCl. LiCl is unique in this group since it has next-nearest-neighbor (NNN) contact (or 'double repulsion'). Nearest-neighbor (NN) contact determines the ionic separation in the other three materials (see Fig. 1). The simplest form of the Born model ignores NNN interactions and should thus have varying success in dealing with this series of alkali chlorides.

In this work, the importance of NNN repulsion and the feasibility of adding other interactions to the Born model in order to improve its success in predicting experimental

---

*Supported by the Robert A. Welch Foundation, Houston, Texas.

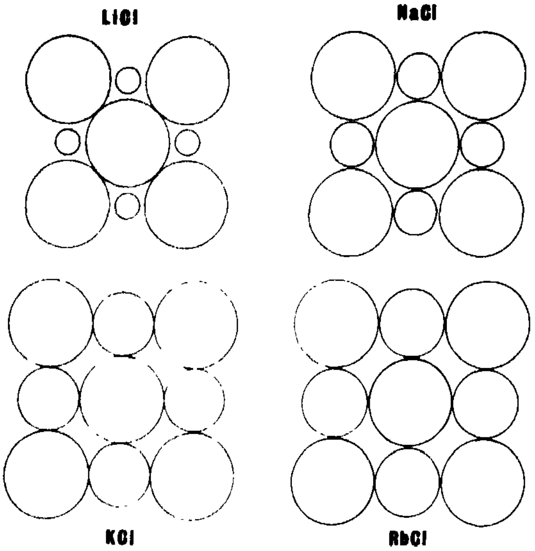

Fig. 1. The arrangement of ions in the cube-face layers of the alkali chlorides with the sodium chloride structure. The drawings are scaled according to the lattice dimensions of the compounds and according to the ionic radii of Pauling[3].

results are investigated. Particular emphasis is given to the elastic constant C_{44} and its pressure derivative. This shear constant is a sensitive indicator of NNN interactions (the NN and NNN contributions to C_{44} are of opposite sign) and should also be sensitive to non-central forces that may be present in the chemical bonds. In applying the Born model to the elastic properties of LiF and NaF, Miller and Smith[2] encountered the most difficulty with the shear constant C_{44}.

During the course of this investigation we became aware of the work by Roberts and Smith on the pressure dependence of the elastic constants of the sodium and potassium[4] and of the rubidium[5] halides. They also conducted a systematic study of alkali halide series using the Born model. Their work and ours are somewhat complementary in the following ways. Their approach in studying a series was to look at the four halides of a given metal whereas our approach is to vary the metal ion for a given halogen (Cl). They were chiefly interested in the equations of state and thus were most concerned with the bulk modulus; we deal extensively with the success of the Born model in predicting the shear constants. In order to apply the Born model they made the complete thermal corrections necessary to render their data applicable to the room temperature static lattice; we use the less correct procedure of applying the Born model to the room temperature adiabatic elastic constants without thermal corrections. A comparison of the results of these two methods can then be made.

2. EXPERIMENTAL PROCEDURE

Single crystals of RbCl and LiCl were purchased from Semi-Elements, Inc. All samples were in the form of right circular cylinders and two specimens of each material were used in the measurements, a one inch long sample oriented at [100] ± 1° and a ¾ in. long sample oriented at [110] ± 2°. The end faces were parallel to within ± 0·001 in.

The method used for the elastic stiffness measurements was the ultrasonic pulse-echo technique[6]. The details of experimental procedure described by Bartels and Schuele [1] were closely followed with the exception that a gas (nitrogen) pressure system and Bourdon tube pressure gauge were used.

The buffer rod method was employed to obtain the elastic constants at zero (atmospheric) pressure; that is, in order to simplify the detailed interpretation of the echo structure, a long aluminum or silica rod was placed between the quartz transducer and the sample. For pressure runs the transducers were cemented directly to the crystals using Nonaq stopcock grease enriched with *d*-mannitol.

The pressure dependence of the elastic constants was obtained by recording the change in arrival time for an echo at different pressures. The technique involved observing on an oscilloscope screen the n^{th} echo with arrival time T_n. The change in arrival time ΔT_n was then recorded for pressures up to 30,000 psi. A typical data plot is shown in Fig. 2.

3. RESULTS

For the crystals and orientations used in this work the adiabatic elastic constants are related to experimental values by

$$\begin{aligned} C_{44} &= \rho v_1^2 = \rho v_5^2, \\ C' &= (C_{11}-C_{12})/2 = \rho v_2^2, \\ C'_{11} &= (C_{11}+C_{12}+2C_{44})/2 = \rho v_3^2, \\ C_{11} &= \rho v_4^2, \end{aligned} \qquad (1)$$

where v_1 and v_2 are the velocities of the transverse waves in the [110] direction with

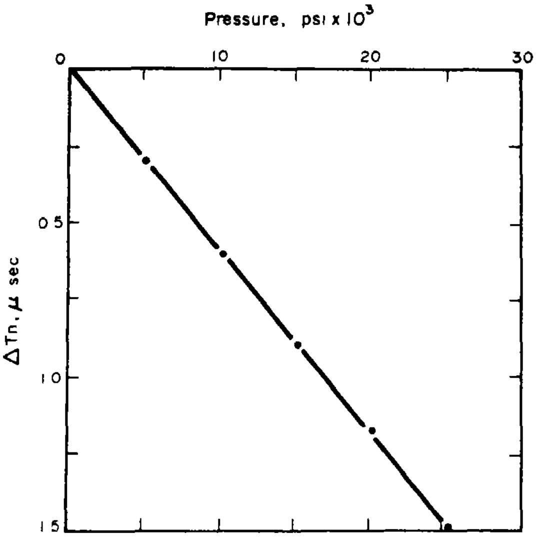

Fig. 2. A typical data plot of change in arrival time with pressure. These data are for the 5th echo of the longitudinal wave propagating in the [110] direction in RbCl.

particle displacement in the [001] and [$\bar{1}$10] directions respectively; v_3 and v_4 are the velocities of the longitudinal waves in the [110] and [100] directions respectively; and v_5 is the velocity of a transverse wave in the [100] direction; ρ is the density of the material. These measured elastic constants as well as the adiabatic bulk modulus $B_S = (C_{11} + 2C_{12})/3$ are given in Table 1.

Table 1. *The adiabatic elastic constants of* LiCl *and* RbCl *in units of Mbars* (1 *Mbar* = 10^{12} *dyne* cm^{-2})

	LiCl	RbCl
C_{44}	0·2489	0·0468
C'	0·1338	0·1518
C'_{11}	0·6050	0·2612
B_S	0·3115	0·1638

This method of using two crystals of [110] and [100] orientations for each compound allows for internal checks. The values of C_{11} and C_{44} obtained from the two crystals agree within 0·5 per cent for LiCl and within 0·1 per cent for RbCl. The values shown in Table 1 are based on measurements from the [110] sample. The single crystal elastic constants of LiCl and RbCl have been measured by Haussühl[7] and by Marshall, Pederson, and Dorris[8]. Our RbCl results are within about 1 per cent of those given in both of these papers. Our LiCl values agree with Haussühl's to about 1 per cent but disagree as much as 10 per cent with those of Marshall, Pederson, and Dorris.

In order to determine the pressure derivatives of the elastic constants, the arrival time T_n for the n^{th} echo was measured with change in pressure. Since T_n is linear with pressure

Table 2. *The basic data used in the present investigation for the alkali chlorides at* 299°*K*

Data	LiCl	NaCl	KCl	RbCl
Lattice constant (Å) [9]	5·1398	5·6402	6·2932	6·5807
X-ray density (gms/cm^3)	2·0736	2·1634	1·9868	2·8182
Molecular volume (10^{-24} cm^3)	33·945	44·856	62·309	71·245
Linear coefficient of thermal expansion (10^{-4} deg^{-1})	0·448[8]	0·400[1]	0·369[1]	0·346[5]
Specific heat, C_p (cal mole^{-1} deg^{-1})	11·5[8]	11·9[1]	12·2[1]	12·3[5]
Isothermal bulk modulus (Mbar)	0·2906	0·2332	0·1727	0·1569
Specific heat ratio (C_p/C_v)	1·072	1·058	1·049	1·044

for the range under investigation (see Fig. 2), the slope, dT_n/dP, was calculated by the linear least squares technique. The fractional change in arrival time per change in pressure is thus given by

$$\frac{d\ln T}{dP} = \frac{1}{nT}\frac{dT_n}{dP} \qquad (2)$$

where T is the zero pressure transit time and n is the number of the echo under study. The fractional change in elastic constant per unit change in pressure is then found from

$$\frac{d\ln C}{dP} = \frac{1}{3B_T} - \frac{2d\ln T}{dP}. \qquad (3)$$

The $1/3B_T$ term corrects for the change of length and density with pressure.

Table 3 gives the values of dC/dP, $d\ln C/dP$, and $d\ln C/d\ln r = -3B_T d\ln C/dP$ for the bulk modulus and the two shear constants C_{44} and $C' = (C_{11} - C_{12})/2$. These data are from measurements on the [110] crystal and each result is based on from two to six separate measurements. The NaCl and KCl results from Bartels and Schuele[1] are included here for comparison and because they will be employed in the later analysis. As in the case of the elastic constants themselves, the use of the two differently oriented crystals allows for internal checks in the pressure results and, as before, the results were more consistent for RbCl than for LiCl. The values of dC_{11}/dP differ by 1·2 per cent for RbCl and by 4·9 per cent for LiCl; for dC_{44}/dP the respective differences are 1·6 per cent and 3·1 per cent. We assign an accuracy of ± 1 per cent to the measurements of the elastic constants and ± 5 per cent to their pressure derivatives. We feel that this estimate may be conservative for RbCl but somewhat optimistic for LiCl. In general the results for RbCl were more reproducible than for LiCl.

In the series of alkali chlorides from LiCl to RbCl, Table 3 shows that there is very little variation in dB/dP. It is interesting to note that values of dB/dP for fourteen different alkali halides taken from this work, from Miller and Smith[2] and from Roberts and Smith[4, 5] show less than a 10 per cent variation and have a mean value of 5·36 with a standard deviation of 0·11. dC_{44}/dP, on the other hand, changes considerably for the four alkali chlorides and even undergoes a change in sign. For KCl and RbCl, dC_{44}/dP is negative, indicating a decrease of C_{44} with an increase in pressure.

4. DISCUSSION

A simple Born model for the binding energy of ionic crystals consists of two parts: a coulomb interaction over the entire crystal and a short range repulsion interaction over nearest neighbor ions only. The approach used in this investigation has been to consider the experimental elastic constants C_{exp} as composed of two parts: a coulomb contribu-

Table 3. The experimental results of the pressure dependence of the adiabatic elastic constants of the alkali chlorides. The elastic constants are taken as B, C_{44}, and C'. dC/dP, $d\ln C/dP$ (in units of $Mbar^{-1}$) and $d\ln C/d\ln r$ are shown. $d\ln C/d\ln r$ represents the fractional change in elastic constant per fractional change in ionic spacing (r)

	$\frac{dB}{dP}$	$\frac{dC_{44}}{dP}$	$\frac{dC'}{dP}$	$\frac{d\ln B}{dP}$	$\frac{d\ln C_{44}}{dP}$	$\frac{d\ln C'}{dP}$	$\frac{d\ln B}{d\ln r}$	$\frac{d\ln C_{44}}{d\ln r}$	$\frac{d\ln C'}{d\ln r}$
LiCl	5·41	1·63	3·63	17·4	6·5	27·1	−15·1	−5·7	−23·6
NaCl	5·27	0·37	4·79	21·3	2·9	26·3	−14·9	−2·0	−18·5
KCl	5·34	−0·39	5·61	29·4	−6·1	33·5	−15·3	3·2	−17·4
RbCl	5·39	−0·64	5·53	32·9	−13·7	36·7	−15·5	6·4	−17·3

tion to the elastic constants C_C, which is easily calculated, and a short range contribution given by

$$C_{SR} = C_{\text{exp}} - C_C. \tag{4}$$

The coulomb contributions to the elastic constants are given by Huntington [10] as

$$\begin{aligned} \Omega B_C &= -0{\cdot}777e^2/r, \\ \Omega C_{44_C} &= 1{\cdot}278e^2/r, \\ \Omega C'_C &= -1{\cdot}335e^2/r, \end{aligned} \tag{5}$$

where Ω is the molecular volume, e is the electron charge and r is the nearest neighbor separation. The coulomb contribution to the hydrostatic strain derivative $\Omega \mathrm{d}C/\mathrm{d}\ln r$ is given by

$$(\Omega \mathrm{d}C/\mathrm{d}\ln r)_C = -4\Omega C_C. \tag{6}$$

The contributions to ΩC and $\Omega \mathrm{d}C/\mathrm{d}\ln r$ are presented in Table 4 according to the scheme of equation (4): i.e., we are subtracting the coulomb contributions from the experimental values and designating the remainder as the short range contribution.

The energy of one ion, using a simple Born model, is

$$u(r) = -\alpha e^2/r + 6I(r) \tag{7}$$

where e^2/r is the traditional coulomb energy between two charged bodies, α is the Madelung constant which accounts for the summation of the coulomb potential over the entire crystal, and $I(r)$ is the short range interaction between the six nearest neighbors only. A mole of alkali halide contains twice Avogadro's number, N_0, of ions. In summing over all $2N_0$ ions to obtain the energy per mole, each interaction is counted twice and the energy per mole is given by

$$U(r) = 2N_0u(r)/2 = N_0u(r) = -N_0\alpha e^2/r + 6N_0I(r). \tag{8}$$

Since the net force on the ions must be zero when they are in equilibrium position d, we have

$$\frac{\mathrm{d}U}{\mathrm{d}r}(r = \mathrm{d}) = 0 \tag{9}$$

or

$$\alpha e^2/\mathrm{d}^2 + 6I'(r = \mathrm{d}) = 0$$

where primes indicate derivatives with respect to r.

Table 4. The partitioning of the elastic constants and their pressure derivatives into the calculated coulomb contribution and the remainder (designated as the experimental short range contribution). The units are 10^{-12} *ergs/molecule*

		ΩC_{exp}	$= \Omega C_{\text{coul}}$	$+ \Omega C_{SR}$
	B	10·6	−7·0	17·6
	C_{44}	8·5	11·5	−3·0
LiCl	C'	4·5	−12·0	16·5
	$\mathrm{d}B/\mathrm{d}\ln r$	−160·0	27·9	−187·9
	$\mathrm{d}C_{44}/\mathrm{d}\ln r$	−48·2	−45·9	−2·3
	$\mathrm{d}C'/\mathrm{d}\ln r$	−107·6	47·9	−155·5
	B	11·0	−6·4	17·4
	C_{44}	5·8	10·5	−4·7
NaCl	C'	8·3	−10·9	19·2
	$\mathrm{d}B/\mathrm{d}\ln r$	−165·0	25·6	−190·6
	$\mathrm{d}C_{44}/\mathrm{d}\ln r$	−11·7	42·0	−53·7
	$\mathrm{d}C'/\mathrm{d}\ln r$	−151·0	43·6	−194·6
	B	11·3	−5·7	17·0
	C_{44}	3·9	9·4	−5·5
KCl	C'	10·4	−9·8	20·2
	$\mathrm{d}B/\mathrm{d}\ln r$	−173·0	22·8	−195·8
	$\mathrm{d}C_{44}/\mathrm{d}\ln r$	12·5	−37·5	50·0
	$\mathrm{d}C'/\mathrm{d}\ln r$	−182·0	39·2	−221·2
	B	11·7	−5·5	17·2
	C_{44}	3·3	9·0	−5·7
RbCl	C'	10·8	−9·4	20·2
	$\mathrm{d}B/\mathrm{d}\ln r$	−180·8	21·8	−202·6
	$\mathrm{d}C_{44}/\mathrm{d}\ln r$	21·4	−35·8	57·2
	$\mathrm{d}C'/\mathrm{d}\ln r$	−185·3	37·4	−222·7

The short range contributions to the elastic constants and hydrostatic strain derivatives are given by [2, 6]

$$\begin{aligned} \Omega B_{SR} &= \tfrac{2}{3}(r^2I'' - 2rI'), \\ \Omega C_{44_{SR}} &= 2rI', \\ \Omega C'_{SR} &= r^2I'' + rI', \\ \Omega \mathrm{d}B_{SR}/\mathrm{d}\ln r &= \tfrac{2}{3}(r^3I''' - 3r^2I'' + 4rI'), \end{aligned} \tag{10}$$

$$\Omega \mathrm{d}C_{44_{SR}}/\mathrm{d}\ln r = 2(r^2 I'' - 2rI'),$$
$$\Omega \mathrm{d}C'_{SR}/\mathrm{d}\ln r = r^3 I''' - 2rI',$$

evaluated at $r = \mathrm{d}$.

In the simple Born model, I is usually taken as $I = B\exp(-\delta r/\mathrm{d})$ (or some equivalent exponential form) or as $I = Ar^{-n}$. Used in equations (10), these two forms of the repulsive term yield identical results in all calculations except for $\mathrm{d}B_{SR}/\mathrm{d}\ln r$ and $\mathrm{d}C'_{SR}/\mathrm{d}\ln r$. Using $I = B\exp(-\delta r/\mathrm{d})$ in equation (9) and equations (10) the following seven equations in two inknowns can be obtained:

$$\begin{aligned} \delta I &= \alpha e^2/6\mathrm{d}, \\ \Omega B_{SR} &= \tfrac{2}{3}(\delta+2)\delta I, \\ \Omega C_{44_{SR}} &= -2\delta I, \\ \Omega C'_{SR} &= (\delta-1)\delta I, \\ \Omega \mathrm{d}B_{SR}/\mathrm{d}\ln r &= -2(\delta^2+3\delta+4)\delta I, \\ \Omega \mathrm{d}C_{44_{SR}}/\mathrm{d}\ln r &= 2(\delta+2)\delta I, \\ \Omega \mathrm{d}C'_{SR}/\mathrm{d}\ln r &= -(\delta^2-2)\delta I. \end{aligned} \qquad (11)$$

This model then provides seven equations involving seven independent experimental values and only two unknowns, δ and δI.

The first two equations of the set immediately above were used to calculate values of δ and δI; these values were then employed in the remaining five equations to obtain theoretical short range contributions. In Table 5 the measured values have been separated into three parts: the Coulomb contributions according to equations (5, 6), the theoretical short range contributions from equations (11), and the amount left unaccounted for by this simple model: i.e., the "not accounted for" column would be zero if the model fit the data perfectly. We show here the relative magnitudes of the three parts. When it makes a difference, results obtained using a power law form of the repulsive energy are included in parentheses in Table 5. In considering the 'per cent not accounted for" column, it should be noted that the experimental values used to determine these contributions possibly contained inaccuracies of 1 per cent for the elastic constants and 5 per cent for their pressure derivatives.

Table 5. The per cent contributions to the elastic constants and their hydrostatic strain derivatives obtained by employing an exponential repulsive term in a simple Born model. Similar calculations were also made using a power function; where these latter results differ from those obtained using the exponential form, the values are shown in parentheses

		Per cent Coulomb	Per cent short range	Per cent not accounted for
	ΩB	28	72	0
	ΩC_{44}	60	28	12
	$\Omega C'$	37	57	6
LiCl	$\Omega \mathrm{d}B/\mathrm{d}\ln r$	13(13)	75(82)	12(5)
	$\Omega \mathrm{d}C_{44}/\mathrm{d}\ln r$	30	34	36
	$\Omega \mathrm{d}C'/\mathrm{d}\ln r$	22(18)	74(70)	4(12)
	ΩB	27	73	0
	ΩC_{44}	68	32	0
	$\Omega C'$	36	63	1
NaCl	$\Omega \mathrm{d}B/\mathrm{d}\ln r$	12(12)	81(88)	7(0)
	$\Omega \mathrm{d}C_{44}/\mathrm{d}\ln r$	36	45	19
	$\Omega \mathrm{d}C'/\mathrm{d}\ln r$	18(16)	78(79)	4(5)
	ΩB	25	75	0
	ΩC_{44}	63	29	8
	$\Omega C'$	33	63	4
KCl	$\Omega \mathrm{d}B/\mathrm{d}\ln r$	10(10)	87(87)	3(3)
	$\Omega \mathrm{d}C_{44}/\mathrm{d}\ln r$	42	57	1
	$\Omega \mathrm{d}C'/\mathrm{d}\ln r$	15(14)	79(83)	6(3)
	ΩB	24	76	0
	ΩC_{44}	61	28	11
	$\Omega C'$	32	66	2
RbCl	$\Omega \mathrm{d}B/\mathrm{d}\ln r$	10(9)	89(86)	1(5)
	$\Omega \mathrm{d}C_{44}/\mathrm{d}\ln r$	39	55	6
	$\Omega \mathrm{d}C'/\mathrm{d}\ln r$	14(12)	85(80)	1(8)

Since the short range value for ΩB was employed to determine the unknowns, it is completely accounted for. In the case of the shear constants (C_{44} and C' in Table 5), one notices that the model is quite successful for C', but with the exception of NaCl, the model shows relatively large failures in predicting C_{44}.

The hydrostatic strain derivatives of the elastic constants are more strongly dependent upon the short range interaction. For these quantities (rows four, five, and six for each crystal in Table 5) the per cent not accounted for by this model is generally larger. Particularly large failures are seen in LiCl and NaCl, again associated with the shear constant C_{44}. If one takes into account that C_{44} is the elastic constant which is most sensitive to NNN and to non-central forces and that these forces are not considered in the present model, it would be expected that a larger unaccounted-for contribution would result. LiCl, which has NNN ion contact, displays the largest unaccounted for term (36 per cent) in $\mathrm{d}C_{44}/\mathrm{d}\ln r$. On the whole, however, this Born model, while a simple one, does explain the elastic properties of these alkali chlorides relatively well.

The values of δ calculated from the first two equations (11) are plotted in Fig. 3 vs. the NN separation (one half the lattice constant): the result is a remarkably linear relationship. In looking at a series of halides of a given metal, Roberts and Smith[4, 5] found similar results. In contrast to our work, they used repulsive parameters calculated from thermally corrected values of the isothermal bulk modulus and of the equilibrium condition. For comparison we have also included their values in Fig. 3. The thermal corrections apparently boost the repulsive parameter by about 10 per cent. It might be worth noting that the use of the adiabatic, rather than the isothermal, bulk modulus somewhat compensates for the neglect of the thermal corrections.

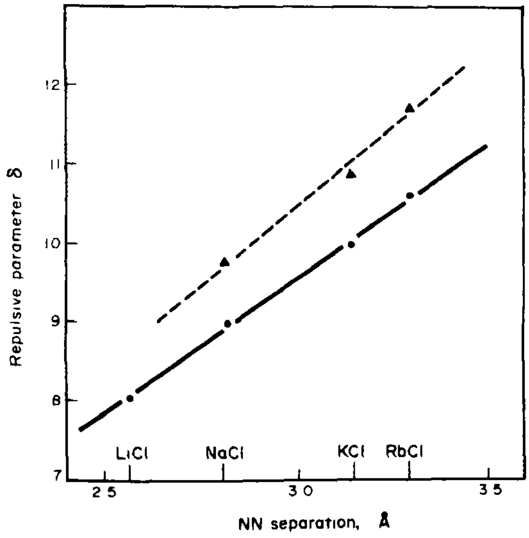

Fig. 3. The repulsive parameter δ from a simple Born model vs. NN separation (solid line). The broken line is from thermally corrected data of Roberts and Smith [4, 5]. If a r^{-n} repulsive potential is used, δ and n are related by $\delta = n+1$.

As previously noted, a model with only NN repulsion does not adequately explain the experimental elastic results for LiCl. Since LiCl is the only crystal in the series with NNN contact, a model to account for the experimental results of LiCl should include NNN as well as NN interactions. The energy per ion for such a model can be written

$$\begin{aligned} & u(r) = -\alpha e^2/r + 6I(r) + 6W(r), \\ \text{where}\quad & I(r) = A\exp(-\delta r/\mathrm{d}), \qquad (12) \\ \text{and}\quad & W(r) = B\exp(-p\sqrt{2}r/\mathrm{d}). \end{aligned}$$

I has the same meaning as before and W is the interaction of an ion with the 12 next nearest neighbors. The resulting equations for the equilibrium condition and short range contributions are

$$\begin{aligned} \alpha e^2/6\mathrm{d} &= \delta I + pW, \\ \Omega B_{SR} &= \tfrac{2}{3}[(\delta+2)\delta I + (p+2)pW], \\ \Omega C_{44_{SR}} &= -2\delta I + \tfrac{1}{2}(p-3)pW, \\ \Omega C'_{SR} &= (\delta-1)\delta I + \tfrac{1}{4}(p-7)pW, \qquad (13) \\ \Omega \mathrm{d}B_{SR}/\mathrm{d}\ln r &= -\tfrac{2}{3}[(\delta^2+3\delta+4)\delta I \\ &\quad + (p^2+3p+4)pW], \\ \Omega \mathrm{d}C_{44SR}/\mathrm{d}\ln r &= 2(\delta+2)\delta I - \tfrac{1}{2}(p^2-2p-6)pW, \\ \Omega \mathrm{d}C'_{SR}/\mathrm{d}\ln r &= -(\delta^2-2)\delta I - \tfrac{1}{4}(p^2-6p \\ &\quad -14)pW. \end{aligned}$$

These equations were handled in the following manner; various amounts of NNN interaction were added by systematically varying the ratio $pW/\delta I$ and using the first three of equations (13) to calculate δ, δI, and p; these parameters were then used in the last four of equations (13) to see if agreement between theory and experiment was improved over that using NN interactions only. Only the agreement for LiCl was improved with this procedure; and, even in this case, the 'per cent not accounted for' increased for some quantities and decreased for others. The best overall agreement occured at $pW/\delta I = 0{\cdot}08$ for LiCl, a value very close to that found by Miller and Smith[2] for LiF.

A linear theoretical relationship between $(-C_{44}/B)_{SR}$ and $(C'/B)_{SR}$ can be obtained from equations (11). This relation is plotted as a solid line in Fig. 4. The experimental value for NaCl lies quite close to the theoretical line. The points for the other three crystals, however, do not agree well with theory: LiCl lies below the nearest neighbor line whereas KCl and RbCl lie above the line. Employing the equations of the model with both NN and NNN repulsion, and making the assumption $\delta = p$, the new theoretical relationship between $(-C_{44}/B)_{SR}$ and $(C'/B)_{SR}$ is obtained (again a linear relationship). For a ratio of $W/I = 0{\cdot}18$ this relation is displayed as the broken line in Fig. 4, indicating that the elastic constants of LiCl can be explained by a model which considers both NN and NNN interactions. The value of $W/I = 0{\cdot}18$ is not in itself particularly significant; it was chosen because it is the value which forces the line through the LiCl point. What is significant is that any positive value of W/I results in a NNN + NN line that lies below the NN-only line. The main conclusion reached in considering Fig. 4 is that a NNN short range repulsive interaction does not affect the elastic constants in the right direction to correct for KCl and RbCl.

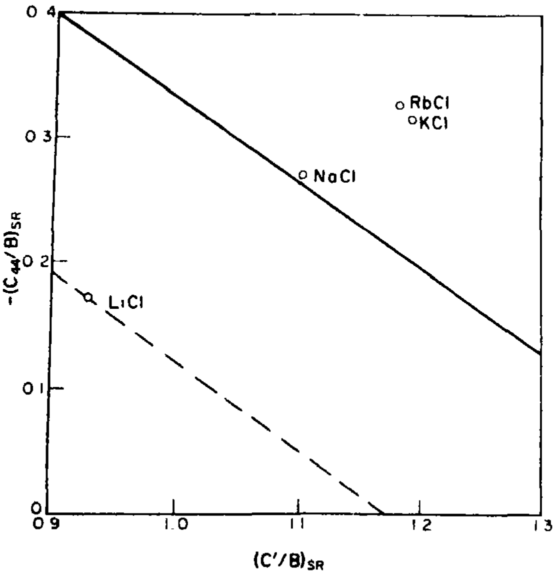

Fig. 4. A plot of short range stiffness ratios $-(C_{44}/B)$ vs (C'/B). The data for the experimental points are from Table 6. The solid line is a theoretical relation obtained from considering only NN interactions, and the broken line indicates the theoretical relationship when NNN interactions are added.

The physically important point is the following: the simple nearest neighbor model predicts a $C_{44_{SR}}$ which is not sufficiently negative for KCl and RbCl; therefore the addition of a positive term from a NNN repulsion energy cannot remedy the situation. It is clear that any modification of the simple nearest neighbor theory which is to account for the experimental results of KCl and RbCl must supply an additional negative contribution to $C_{44_{SR}}$. A Van der Waal's dipole–dipole attractive potential seems to be a correction in the right direction for KCl and RbCl.

It is also reasonable to suggest that the bond may not be 100 per cent ionic, but partially covalent in character. We have made calculations by varying the charge on the ions, but this procedure did not significantly improve the agreement between theory and experiment.

5. CONCLUSION

A simple Born model which includes coulomb and nearest neighbor interactions does a reasonably good job of predicting the elastic properties of the alkali chlorides. For the elastic constants of NaCl, the predictions are within experimental error. For the other three crystals, the failure of the model to account for the elastic constants C' was on the order of 5 per cent. The amount of C_{44} not accounted for is on the order of 10 per cent, which is not surprising since C_{44} is a strong indicator of NNN and non-central forces, two interactions which are undoubtably present but not included in the model. The 'unaccounted for' terms predicted for $dB/d\ln r$ and $dC'/d\ln r$ for all four crystals and $dC_{44}/d\ln r$ for RbCl and KCl were within experimental accuracy. However, for NaCl and LiCl, the per cent of $dC_{44}/d\ln r$ which was not accounted for by the model was quite large (19 and 36 per cent, respectively).

An interesting and unexpected result was that the Born repulsive parameter δ was found to be a linear function of the NN separation distance.

It is clear that the Born model for LiCl can be improved by the addition of NNN interactions, a result similar to that found by Miller and Smith[3] for LiF. A model for KCl and RbCl cannot be improved by the addition of a nearest neighbor attraction, but instead an interaction which leads to a greater negative contribution to C_{44} is required.

Acknowledgement—We wish to thank Dr. Charles S. Smith of the University of North Carolina for helpful discussions and for preprints of his work.

REFERENCES

1. BARTELS R. A. and SCHUELE D. E., *J. Phys. Chem. Solids*, **26**, 537 (1965).
2. MILLER R. A. and SMITH C. S., *J. Phys. Chem. Solids*, **25**, 1279 (1964).
3. PAULING L., *The Nature of the Chemical Bond*, 3rd ed., Sec. 13.2, Cornell University Press, Ithaca (1960).
4. ROBERTS R. W. and SMITH C. S., *J. Phys. Chem. Solids* **31**, 619 (1970).
5. ROBERTS R. W. and SMITH C. S., *J. Phys. Chem. Solids* **31**, 2397 (1970).
6. DANIEL S. W. B. and SMITH C. S., *The Physics and Chemistry of High Pressure*, p. 50, *Soc. of Chem. Indus.*, London (1963).
7. HAUSSÜHL S., *Z. Phys.*, **159**, 223 (1960).
8. MARSHALL B. J., PEDERSON D. O. and DORRIS G. G., *J. Phys. Chem. Solids* **28**, 1061 (1967).
9. National Bureau of Standards Circular 539.
10. HUNTINGTON H. B., *Solid State Physics* (Edited by F. Seitz and D. Turnbull), Vol. 7, p. 279, Academic Press, New York (1958).
11. KITTEL C., *Introduction to Solid State Physics*, 3rd ed., p. 118, John Wiley, New York (1966).

APPENDIX

Adiabatic and isothermal elastic stiffnesses and compliances

Table 1(a) gives the adiabatic and isothermal elastic stiffnesses and compliances for LiCl and RbCl at 299°K. These values were calculated using the standard relations [11] and the values of Tables 1 and 2, along with the thermodynamic relation

$$\frac{B_S}{B_T} = 1 + \frac{TV\beta^2 B_S}{C_p} \tag{1A}$$

where β is the volume coefficient of thermal expansion, T is the absolute temperature, C_p is the heat capacity at constant pressure, and V is the volume.

Temperature dependence of the elastic constants

The temperature coefficients of the elastic constants $(d\ln C/dT)_p$ can be thought of as comprised of two parts: one part arises from the explicit (constant volume) temperature dependence and the other from an implicit dependence arising from volume changes of the crystal due to temperature. The pressure dependence measurements allow for these two effects to be separated using the relationship

$$(d\ln C/dT)_p = (d\ln C/dT)_V + \alpha(d\ln C/d\ln r)_T \tag{2A}$$

where α is the linear coefficient of thermal expansion. Table 2(a) presents the different components for the temperature coefficients.

Table 1(a). *The adiabatic and isothermal stiffnesses C and compliances S for* LiCl *and* RbCl. *The units for C are Mbar and for S (Mbar)$^{-1}$*

	C_{11}	C_{12}	C_{44}	S_{11}	S_{12}	S_{44}
LiCl						
adiabatic	0·4899	0·2223	0·2489	2·848	−0·889	4·018
isothermal	0·4690	0·2014	0·2489	2·874	−0·863	4·018
RbCl						
adiabatic	0·3662	0·0626	0·0468	2·874	−0·420	21·37
isothermal	0·3593	0·0557	0·0468	2·904	−0·390	21·37

Table 2(a). *The constituent parts of the temperature derivatives of the elastic constants of the alkali chlorides. Units are* 10^{-4} *deg*$^{-1}$

		$(d\ln C/dT)_p =$	$(d\ln C/dT)_V$	$+\alpha(d\ln C/d\ln r)_T$
LiCl	C_{44}	−4·2	−1·7	−2·5
	C'	−16·4	−5·8	−10·6
	B	−5·6	+1·2	−6·8
NaCl	C_{44}	−2·7	−1·9	−0·8
	C'	−11·3	−3·9	−7·4
	B	−5·1	+0·8	−5·9
KCl	C_{44}	−2·1	−3·3	+1·2
	C'	−11·3	−4·9	−6·4
	B	−5·2	+0·4	−5·6
RbCl	C_{44}	−2·4	−4·6	+2·2
	C'	−11·8	−5·9	−5·9
	B	−5·2	+0·2	−5·4

Haussühl[7] gives values for $(d\ln C/dT)_p$ for these four compounds at 273°K. His values are used after correcting them to 299°K by assuming that dC/dT is the same throughout this temperature range. As found in other studies with alkali halides[1, 2], the constant volume temperature derivative is always negative for the shear constants and positive for the adiabatic bulk modulus.

J. Phys. Chem. Solids, 1971, Vol. 32, pp. 2373–2383. Pergamon Press. Printed in Great Britain

VACUUM ULTRAVIOLET ABSORPTION IN ALKALI DOPED FUSED SILICA AND SILICATE GLASSES*

G. H. SIGEL, Jr.
U.S. Naval Research Laboratory, Washington, D.C. 20390, U.S.A.

(*Received* 17 *August* 1970; *in revised form* 16 *February* 1971)

Abstract—Optical absorption and reflectance spectra of quartz, alkali doped fused silica, and several simple silicate glasses of high purity were measured in the region extending from 5 to 14 eV. The doping of lithium, sodium and potassium into SiO_2 was observed to introduce optical absorption whose effect was to shift the u.v. edge of the glass to lower energies by several eV. This absorption accounts for the poor transmission of high purity silicate glasses in the far u.v. relative to SiO_2. The simultaneous introduction of aluminum with the alkali was effective in eliminating most of this absorption. These observations were consistent with the hypothesis that the breakup of the Si—O—Si bonding network is related to the increased u.v. absorption of silicate glasses At higher energies beyond the u.v. edge, several strong reflectance bands were observed and these have been tentatively assigned to exciton and band-to-band transitions. The data are discussed qualitatively in terms of both molecular orbital and valence bond theories, taking into consideration the increased ionic character of the Si–O bond in the alkali silicate glasses.

1. INTRODUCTION

PREVIOUS investigations have indicated that the u.v. absorption spectra of silicate glasses may be dependent both on the glass composition[1–3] and its method of preparation[4, 5]. Recent work[6] has established that in sufficiently pure alkali silicate glasses, the position of the u.v. absorption edge is independent of the atmosphere employed during melting. This was achieved by the elimination of traces of transition metal and rare earth impurities whose various oxidation states contribute significantly to the u.v. absorption. However, even in silicate glasses free of impurity-induced u.v. absorption, the absorption edge was observed to lie several eV lower than that for SiO_2. These pure materials provided an excellent opportunity to study the nature of alkali-induced u.v. absorption in silicate glasses.

Stevels[7] has suggested that the intrinsic absorption edge of an oxide glass corresponds to the transition of a valence electron of an oxygen ion in the glass network to an excited state. In the absence of impurities, the shift in the absorption edge of silicate glasses relative to SiO_2 might then result from the excitation of valence electrons of singly bonded (nonbridging) oxygen ions which arise from the introduction of network modifying alkali ions into the SiO_2 structure. One could then discuss the location of the ultraviolet edge of oxide glasses in terms of the strength of the Si—O—Si bridging in the network as suggested by Scholze[8]. McSwain *et al.*[3] have observed such a shift in alkali borate glasses. With the assumption that the absorption edge and the first absorption maximum coincide, Stevels[7] predicted that the u.v. absorption of glasses should increase in the order of phosphate, silicate, borate glass. This prediction does not correlate with the experimental data. The discrepancy was attributed to the presence of non-bridging oxygens. However, the covalent aspects of the bonding were not considered in Stevel's treatment. In SiO_2 and silicates in general, rather than a valence band characteristic of the ionic states, one expects strong

---

*Research supported by the Advanced Research Projects Agency.

mixing between valence orbitals of Si and O. For example, one can consider four sp^3 tetrahedral orbitals on each Si which are directed toward neighboring oxygens. The fundamental optical absorption of SiO_2 may result from both the excitation of electrons in bonding and anti-bonding levels formed from these hybridized states as well as the atomic states of oxygen.

The object of the present work was to determine the effect of alkali modifiers on the ultraviolet absorption of silicates and to explore the electronic processes which underlie the fundamental optical absorption of both SiO_2 and simple silicate glasses. The u.v. absorption resulting from the introduction of small amounts of Na, Li, and K into fused silica has been measured in the wavelength range 150 to 250 nm. Also, the fundamental optical properties of several simple alkali silicate glasses have been studied by means of vacuum u.v. reflectance spectra at wavelengths between 90 and 170 nm. These data have been compared with the fundamental optical absorption of pure SiO_2 which had been measured previously by Loh[9] and Phillip[10]. Mechanisms which might be responsible for the structure in the ultraviolet absorption of alkali silicates are suggested and discussed, taking into account both the covalent and the ionic character of the bonding.

2. EXPERIMENTAL METHODS

Materials preparation

The alkali-doped fused silica samples were prepared by doping, fusing, and sintering techniques previously described by Lell[11]. Since considerable loss of alkali may occur during preparation, flame photometric determinations of the alkali content of samples were made. These results are given in Table 1. Samples containing equivalent amounts of aluminum and alkali were also prepared. Samples were cut, ground, and polished into thicknesses ranging from 2 to 0·1 mm depending on the concentration of alkali present.

Table 1. Alkali concentrations in doped fused silica samples

Sample no.	Initial doping level (mole %)	Flame photometric Determination in (mole %)
101	0·05 Li	0·006 Li
102	0·2 Li	0·018 Li
104	0·03 Na	0·015 Na
105	0·2 Na	0·05 Na
106	0·5 Na	0·12 Na
107	0·05 K	0·01 K
108	0·2 K	0·035 K
111	0·5 Na + 0·5 Al	0·32 Na, 0·29 Al
115	0·2 K + 0·2 Al	0·165 K, 0·13 Al
118	0·2 Al	0·11 Al
119	0·5 Al	0·20 Al
120	Undoped	0·001 Li

The alkali silicate glasses were prepared at NRL using high purity SiO_2, Al_2O_3, and alkali carbonates. The SiO_2 was prepared by fractionally distilling ethyl silicate which was in turn hydrolyzed in an ethyl alcohol solution with water and NH_4OH. It was dried and ignited at 1160°C in fused silica beakers. This produced SiO_2 with transition metal content of less than 0·5 ppm. Carbonates were prepared by starting with reagent grade materials and purifying them by fractional precipitation. EPR, colormetric analysis, and mass spectrographic analysis were then used to select batches of the purest materials. The dry mixed materials were melted in platinum crucibles at 1400°C for 16 hr. Both conventional furnaces employing silicon carbide heating elements as well as a vacuum furnace with *r–f* crucible heating were used.

High purity ultraviolet grade crystalline quartz and fused silica were obtained from commercial suppliers. The crystal quartz was supplied by Sawyer Research Products, Inc., and the fused silica was Corning 7940 UV grade.

Measurements

A McPherson model 235 monochromator of the Seya Namioka[12] type was used for transmittance measurements in the region 140 to 250 nm. The light source was a Hinteregger[13] type discharge lamp with a flow-through hydrogen gas system. The detector consisted of a vacuum mounting with a sodium salicylate coated window and an 1P21 phototube. Per cent transmittance as a function of wavelength was obtained by taking the ratio of the light intensity measured with the sample in the beam to that measured with the sample removed.

Reflectance measurements in the range 90 to 200 nm were taken on a McPherson model 225 1 meter normal incidence type spectrophotometer which had an NRL-designed[14] reflectometer mounted at the exit slit. The light source and detection system were similar to that described above. The reflection measurements were confined to normal incidence. To prevent scattering of the incident light in normal incidence reflectivity measurements, irregularities in the surface should not be higher than $\lambda/16$ to obtain a good specular reflection[15]. Irregularities of 20 to 50A in height can be expected on optically polished glass surfaces. Since the reflectance measurements were made in the 900 to 1700A region, some surface scattering might be expected here especially for glasses which are slightly hygroscopic. In order to investigate the effects of surface polishing, the reflectance spectra of a sodium silicate and a lithium silicate glass were measured three times after separate grinding and polishing operations. The variation in the reflectance values of these glasses in the regions of peak reflectivity was about 20 per cent. However the absorption bands did not shift by a measurable amount.

3. RESULTS AND DISCUSSION

Fundamental absorption of SiO_2

Crystalline quartz and fused silica become opaque to electro-magnetic radiation at wavelengths below 145 nm as shown in Fig. 1. At shorter wavelengths, the fundamental absorption of bulk samples can be studied by means of reflectance measurements. Strong reflectance bands correspond to regions of strong absorption. This can be concluded by the inspection of the expressions for normal

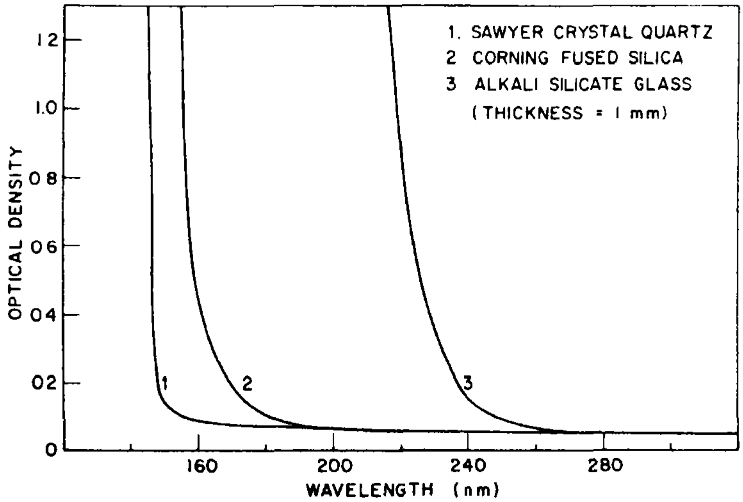

Fig. 1. Position of u.v. absorption edges of high purity (1) crystalline quartz, (2) fused silica and (3) NRL $2SiO_2$-$1Na_2O$ glass (samples of 1 mm thickness).

incidence reflectivity and optical absorption in a dielectric medium of complex index $\hat{n} = n - i\kappa$ where n is the index of refraction and κ is the extinction coefficient. The attenuation of light beam in such a medium is given by the expression

$$I = I_0 e\left(\frac{4\pi\kappa}{\lambda}\right) d = e^{-kd} \qquad (1)$$

where d is the thickness λ is the incident wavelength, I_0 is the incident intensity, and k is the absorption coefficient. The reflectivity, R, at normal incidence at the first surface, is given by the expression

$$R = \frac{(n-1)^2 + \kappa^2}{(n+1)^2 + \kappa^2}. \qquad (2)$$

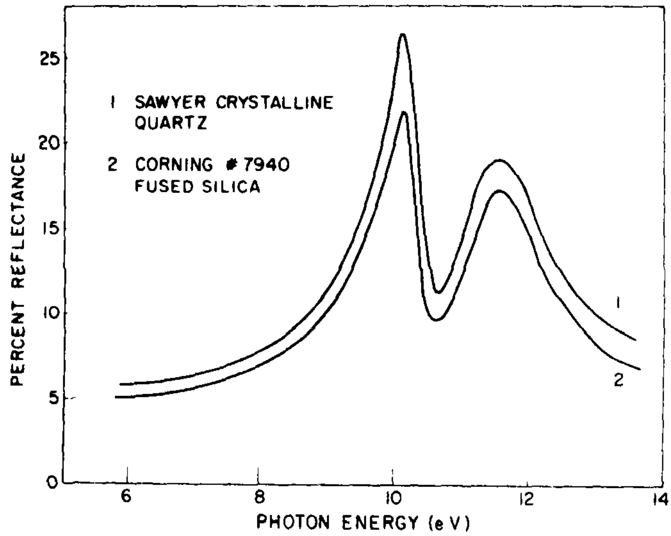

Fig. 2. Vacuum u.v. reflectance of high purity (1) crystalline quartz and (2) fused silica showing the two lowest energy peaks at 10·2 and 11·5 eV.

For large values of κ relative to n, i.e., in regions of high absorption, κ dominates equation (2) and $R \rightarrow 1$. Thus strong reflection peaks normally indicate regions of high optical absorption. In pure SiO_2 this is certainly the case since Phillip's data[10] indicate less than 0·1 eV shift between reflection and absorption maxima. Figure 2 shows the reflectance spectra taken in our laboratory of high purity α-crystal quartz and fused silica. The similarity of the reflectance of the crystalline and glassy SiO_2 indicate that the absorption bands are not strongly dependent on the long range periodicity of the network. This suggests that the absorption may arise from electronic transitions characteristic of the SiO_4 tetrahedron. The first absorption peak in SiO_2 does not occur until 120 nm (10·2 eV) although the transmission cut off occurs at lower energy (8·2 eV). Fused silica and crystal α-quartz both consist of Si atoms tetrahedrally bonded to four O atoms, each O atom being common to (bridging) two such SiO_4 tetrahedra. The Si—O bond distance is roughly 1·6A in both materials. The Si—O—Si bond angle in crystal α-quartz is 144°, while in the amorphous fused silica Bell and Dean[16] found that a distribution of bond angles with a mean value of 150° was obtained when a model was constructed, allowing for the proper constraints such as density, entropy, stoichiometry and bonding.

Recent X-ray diffraction data on vitreous silica by Mozzi and Warren[17] indicate the Si—O—Si bond angle varies from 120° to 180° with a maximum at 144°.

A band structure calculation for SiO_2 has not been performed to date. However, there are two recent theoretical approaches which have been used in an effort to interpret the spectra of SiO_2. These are a valence bond calculation of Ruffa[18] and a molecular orbital approach of Reilly[19]. There is not universal agreement at this time with regard to the electronic transitions involved. Loh[9] has proposed that the 10·2 eV band is an exciton (i.e., a bound electron-hole pair) of the Si—O antibonding level and the 11·5 eV peak represented an interband transition. This tentative assignment was made by the comparison of the SiO_2 spectra with that of other semiconductors and insulators on the assumption that in general exciton transitions result in sharp peaks while interband transitions manifest themselves as either broad peaks or absorption edges. Ruffa's calculation gives general support of this interpretation. Ruffa identified the sharp (120 nm) 10·2 eV peak with a Wannier exciton formed by the breaking of a single Si—O bond. The next broad peak at 108 nm (11·5 eV) was attributed to band-to-band transitions. He proposed that the silicon $3p$ electron freed by the breaking of the Si—O bond would go into a relatively large radius orbit about the silicon atom. If this were true, one might then expect the excited state to correspond to a Wannier exciton. The exciton binding energy was calculated to be 1·27 eV provided that the electron-hole reduced mass μ was assumed to be 0·5 and a dielectric constant of K of 2·31 was used. The observed separation of the two lowest-energy reflection peaks is 1·3 eV, but the calculated energy is quite sensitive to one's choice of μ and K.

Reilly[19] employed a molecular orbital approach to interpret the valence levels of SiO_2, using hybrid orbitals of a Si—O—Si molecule. He observed that the highest filled valence band of SiO_2 was probably associated with the oxygen $2p$ valence electrons which do not participate in the Si—O bond, which is in agreement with the earlier work of O'Brien [20] and Mackey *et al.*[21]. Since the similarity of the absorption of crystalline and amorphous forms of SiO_2 requires transitions which are insensitive to the Si—O—Si bond angle, Reilly proposed that the 10·2 eV peak arose from a transition to an exciton state with the hole orbital corresponding to the oxygen $2p_x$ orbital (i.e., the non-bonding oxygen orbital orthogonal to the SiO bonding orbital) and the electron orbital resembling the oxygen $3s$. Possible explanations given for the 11·5 eV peak were that it corresponded to a transition from the non-bonding oxygen p levels to the antibonding level or that it corresponded to the oxygen $2p$–$3d$ transition which is roughly 11 eV in the oxygen atom. It would seem, however, that such atomic-like transitions might be questionable since the $3s$, $3d$, and $4s$ levels of oxygen are rather close and may well be mixed in a solid. For example, the fundamental absorption of GeO_2 [22], which is structurally isomorphic to SiO_2 and for which the above arguments should apply, differs significantly from that of SiO_2.

Effects of the introduction of alkali into SiO_2

The introduction of small amounts (0·05 to 0·5 mole %) Na, Li, or K into SiO_2 produced a significant shifting of the u.v. edge to longer wavelengths. For example, the effects of sodium doping on the u.v. absorption is shown in Fig. 3. A plot of the optical density vs. the measured alkali concentrations (see Table 1) revealed that the induced absorption was directly proportional to the alkali concentration. The concentration dependence of the optical density at a wavelength of 180 nm is given in Fig. 4 for a series of Na doped samples. The optical absorption was observed to increase linearly with the addition of Li or K to the SiO_2. The intensity of the absorption increased in the order Li, Na, K for a given alkali concentration. It was not possible to

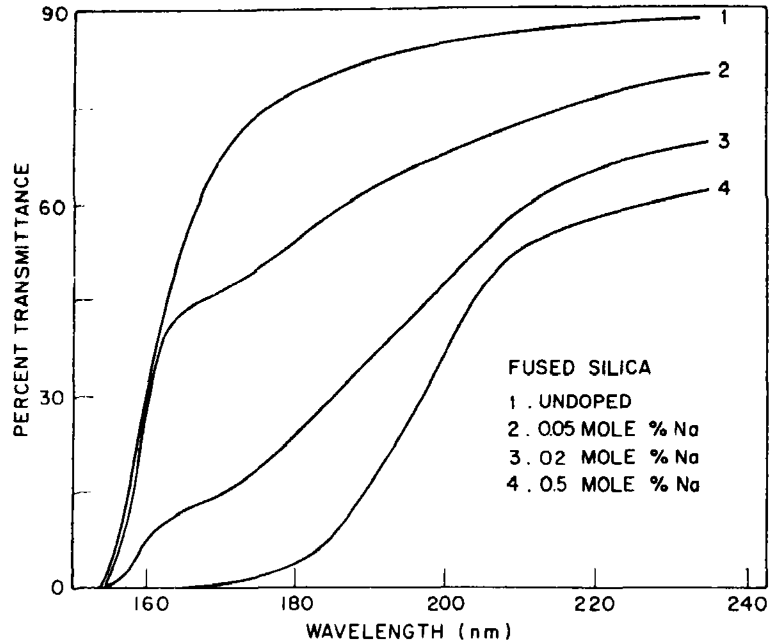

Fig. 3. Effect of the addition of sodium on the u.v. absorption of SiO_2. Nominal doping levels are (1) 0·05 mole%, (2) 0·2 mole% Na, (3) 0·5 mole% Na. (Table I contains actual concentrations of sodium remaining in the fused samples).

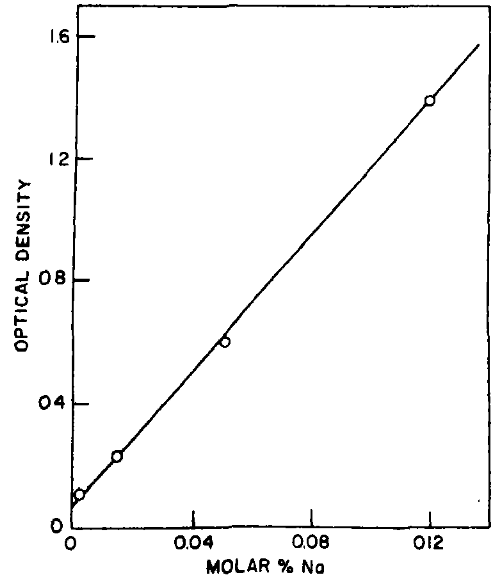

Fig. 4. The relation between the optical density and the concentration of sodium in the fused silica. This data was taken for $\lambda = 180$ nm. The undoped material contained 0·002 mole% Na.

determine for these samples whether the absorption was the result of the broadening or shifting of the 10·2 eV peak of pure SiO_2, or whether a new band was growing in at lower energies.

Alkali and aluminum doped fused silica

Samples were also co-doped with equal amounts of aluminum and alkali. The u.v. transmittance of these samples was significantly greater than those with alkali alone, as illustrated in Fig. 5. There was evidence in some samples, especially those containing aluminum, of absorption near 195 nm. This absorption may arise from the presence of divalent iron impurities in the samples [6].

The reduction of the ultraviolet absorption in lightly doped SiO_2 by the addition of aluminum may be evidence for the existence of alkali–aluminum pairing in the glass [23, 24]. By coordinating with four oxygens, aluminum can enter substitutionally for silicon

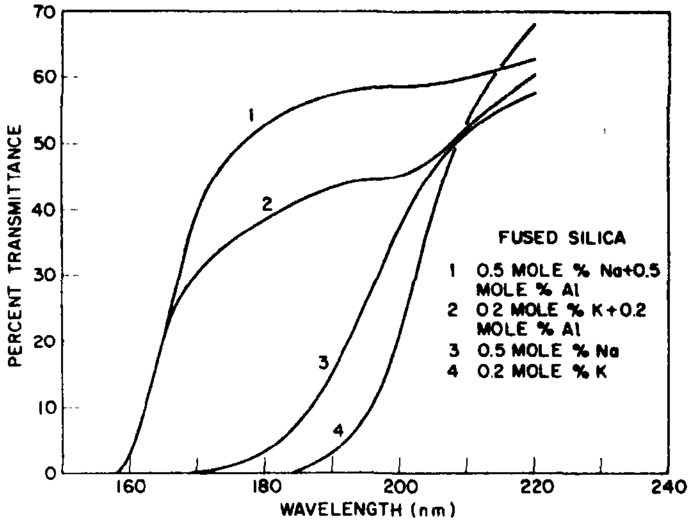

Fig. 5. The effect of aluminum on the u.v. absorption of alkali doped SiO_2. Samples co-doped with alkali + aluminum exhibit much weaker u.v. absorption than those doped with alkali alone.

in the glass network, and local charge neutrality can be maintained if an alkali ion remains in close priximity to the aluminum. In this manner the glass network can remain intact without the creation of non-bridging oxygens as shown schematically in Fig. 6.

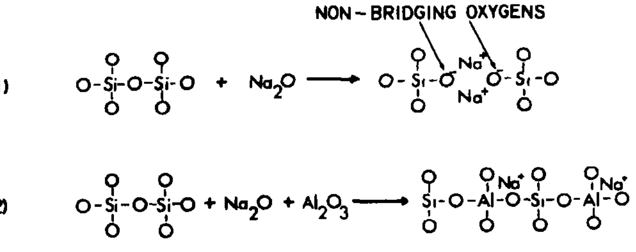
NON-BRIDGING OXYGENS
(1)
O-Si-O-Si-O + Na2O → O-Si-O⁻ Na⁺ Na⁺ O⁻-Si-O
(2)
O-Si-O-Si-O + Na2O + Al2O3 → Si-O-Al-O-Si-O-Al-O
(ALL BRIDGING OXYGENS)

Fig. 6. Schematic representation in two dimensions of (1) the creation of non-bridging oxygens by the introduction of Na into the SiO_2 network and (2) the ability of aluminum to restore the bridging in spite of the presence of alkali.

These measurements are consistent with the hypothesis that the presence of singly bonded oxygens is related to the increase in absorption in the 6–8 eV range.

The transmittance measurements on the alkali doped SiO_2 established that (1) the u.v. absorption in the 150–200 nm region was proportional to the alkali content, (2) at a given concentration the absorption edge shifted for different alkalis, and (3) the simultaneous doping of aluminum and alkali reduced the u.v. absorption. These observations suggested that non-bridging oxygens were involved with the absorption mechanism.

Reflectance measurements at shorter wavelengths were required to establish the extent of the network modifier induced absorption. The reflection spectra of several simple alkali silicate glasses were studied in order to clarify the nature of the alkali-induced absorption.

Reflection spectra of silicate glasses

The reflectance spectra of several high purity NRL silicate glasses have been measured in the wavelength region of 90 to 170 nm. Significant changes relative to the SiO_2 reflectance were evident in all of the glasses. The spectra of the glasses were characterized by three reflection peaks at approximately 145 nm (8·5 eV), 130 nm (9·3 eV) and 108 nm (11·5 eV). The reflectance of two simple alkali silicate glasses is shown in Fig. 7. The glasses. It appears that the absorption measured in the alkali doped fused silica results from this band. Since no reflectance measurements were possible on the alkali-doped fused silica samples due to size limitations, commercial fused silica with poor u.v. transmission (Infrasil) was used for the reflectance measurements. This material showed evidence of a weak 8·5 eV absorption band. Recently Plazoder[25] has shown reflectance data for what was apparently impure α-quartz which also shows evidence of the 8·5 eV band (peak labeled *A* in his Fig. 1), although he did not associate it with an alkali impurity or non-bridging oxygen absorption.

Table 2 summarizes the reflectance data for the SiO_2 and silicate glasses which have been measured in the present work. All of the silicate glasses exhibited an absorption band near 8·5 eV. The type of network modifier, including both alkali and alkaline earth metals, did not appear to influence the position of this band as much as it did the halfwidth. This

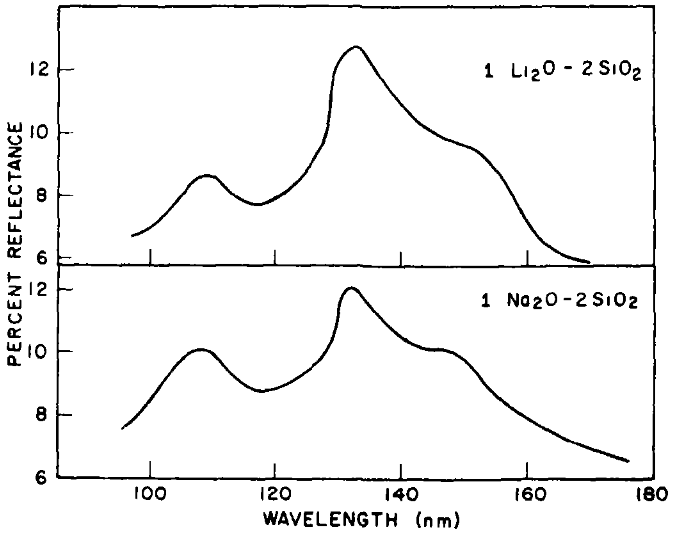

Fig. 7. Reflectance spectra of two simple binary silicate glasses. (upper) 1 Li_2O–$2SiO_2$ (lower curve) 1 Na_2O–$2SiO_2$. This data shows the similarity of the spectra regardless of the type of network modifier as well as the tailing of the low energy band.

reflectance spectra of a soda lime glass and an alkali aluminosilicate glass are given in Fig. 8 along with that for SiO_2 for purposes of comparison. This data indicate that the new band which arises at 145 nm (8·5 eV) is responsible for the shift in the u.v. edge of alkali silicate

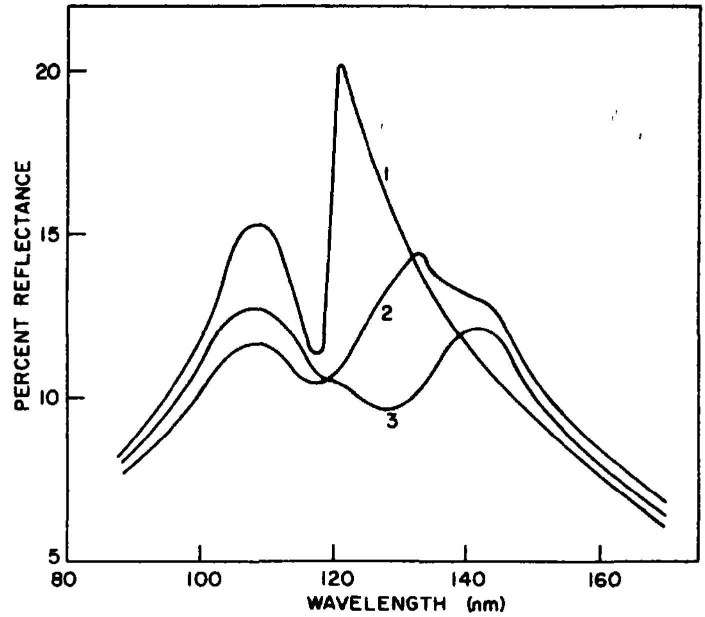

Fig. 8. Reflectance spectra of (1) SiO_2, (glassy) $1Na_2O$-$1CaO$-$5SiO_2$ and (3) $1Na_2O$-$1Al_2O_3$-$3SiO_2$ glasses showing the growth of new low energy band at 145 nm (8.5 eV) as well as the unchanged 108 nm (11.5 eV) band. Both bands were observed in all alkali silicate glasses regardless of composition.

Table 2. Energies of reflection peaks in silicate glasses

Glass type	Location of reflection peaks (eV)			
SiO_2 (crystal)	—	—	10·2	11·5
SiO_2 (glassy)	—	—	10·2	11·5
1 Li_2O—$2SiO_2$	8·5	9·3	—	11·5
1 Na_2O—$2SiO_2$	8·5	9·3	—	11·5
1 Na_2O—$3SiO_2$	8·5	9·3	—	11·5
1 Na_2O—$6SiO_2$	—	9·0*	—	11·5
1 Na_2O—1CaO—$5SiO_2$	8·5	9·3	—	11·5
1 Na_2O—1Al_2O—$3SiO_2$	8·5	—	10·2	11·5

*This broad peak appears to result from contributions from 8·5 and 9·3 eV peaks. The high viscosity of this glass during melting tends to produce a non-homogeneous melt.

is evident in Fig. 7 in which the tail of sodium silicate glass extends to higher wavelengths than the lithium glass.

The 8·5 eV band arises when network modifiers are introduced into the SiO_2. The creation of non-bridging O^- ions which occurs simultaneously with the addition of M^+ or M^{2+} cations will increase the ionic character of the bonding. Since the position of the band is not particularly sensitive to the type of cation added, the large shift relative to SiO_2 (8·5 vs. 10·2 eV) seems to result from the presence of the non-bridging oxygen ions. This conclusion is supported by the results on the alkali and aluminum doped fused silica samples.

It would be desirable to have a calculation on the magnitude of the alkali–oxygen interaction in the silicate system and the degree to which the charge density of the Si—O bond is changed when the oxygen becomes non-bridging and a neighboring alkali is introduced. If the Si—O bond were sufficiently weakened by such an interaction one could predict the existence of a lower energy absorption such as observed here. One should probably also consider excitation of the alkali-oxygen bond as another possible contribution to the optical absorption. Such a calculation would be difficult since the exact positions of the alkali ions in the glass are not known.

The movement of the absorption edge of Li_2O—Na_2O- and K_2O silicate glasses to longer wavelengths with increasing cation size could arise from a broadening of the spectra with ion size. The radii of the alkali ions are by no means small compared to the interatomic distance. Tha alkali ions will sit near the O^- in order to provide charge compensation. The larger modifier ions may tend to distort the SiO_4 tetrahedra whereas the smaller ions may not. The greater local disorder present for the large ions might account for the broader spectra which they exhibit.

In the silicate glasses the addition of large but equal parts of Al_2O_3 and Na_2O to SiO_2 did not quench the 8·5 eV band. This is not surprising since a fraction of a mole % of unpaired network modifiers is sufficient to produce a strong 8·5 eV absorption in the lightly doped SiO_2. Nevertheless, the aluminosilicate glasses showed the highest reflectance in the 11·5 eV band which is thought to be characteristic of the bridging Si—O network. They also exhibited a weak 10·2 eV band. This does seem to indicate that aluminum is able to enhance the bridging in the glasses.

The 11·5 eV (108 nm) reflectance peak which is found in SiO_2 was observed in all of the silicate glasses. This observation suggests two possibilities: (1) there is still a sufficient number of SiO_4 tetrahedra remaining in the glasses to produce the absorption characteristic of the bridging network, or (2) the 11·5 eV band arises from transitions involving atomic levels unperturbed by the addition of alkali. The first of these suggestions seems more probable. As the alkali content is increased more and more non-bridging oxygens are formed until the material consists of groups of isolated SiO_4 tetrahedra linked by ionic M^+—O^- bonds. It is apparently these isolated tetrahedra which still contribute to the 11·5 eV band.

However, if the Si—O—Si network remains partially intact, the question arises as to why the 10·2 eV band of SiO_2 does not also appear in the spectra of silicate glasses. These glasses exhibit a peak near 130 nm (9·3 eV). In shape it is similar to the 10·2 eV peak of SiO_2 although it is not as sharp. If the 10·2 eV peak is a Wannier exciton of the 11·5 eV band, as suggested by Loh[9] and Ruffa[18], the change in the effective dielectric constant of the glass relative to SiO_2 could shift the band. The lack of periodicity in a glass could also effect the value of the reduced mass of the exciton. The energy of the bound electron hole pair in the Wannier model is given by

$$E_W = E_G - \frac{\mu(e^2/K)^2}{2\hbar^2} \tag{3}$$

where E_G is the band gap energy μ is the reduced electron-hole mass and K is the dielectric constant.

There is perhaps some question with regard to the use of the term 'exciton' in a non-periodic system. In an amorphous system, it is clear that excitonic motion cannot be characterized by a unique wave vector. However, Dexter and Knox[27] have stated that to the extent that the exciton concept is valid in ionic crystals, it is probably valid in glasses and liquids. A Wannier exciton in a glass can be thought of as a localized electron-hole pair of large radius experiencing a hydrogenic-like potential dependent on the square of the dielectric constant of the material. If the Wannier model is assumed to apply in silicate glasses, the experimental value for E_G–E_W would be about 2·2 eV vs. the 1·3 eV observed in SiO_2. To account for the observed 0·9 eV shift would require an index change of 0·035 in the silicate glass which is quite reasonable. However such a change should also affect the band to band transition at 11·5 eV. Another possibility is that the energy band changes which accompany the onset of disorder modify the value of the reduced mass in equation (3). Further progress in the interpretation of these spectra would seem to hinge largely on the availability of a band structure calculation for SiO_2 which might serve as a basis for the extension to more complex silicate glasses.

3. CONCLUSIONS

The introduction of alkali oxide into SiO_2 introduces an optical absorption band at 8·5 eV which shifts the fundamental edge to longer wavelengths. The ability of aluminum to suppress this absorption band in low concentrations suggests that the breakup of Si—O—Si bonding with the production of non-bridging oxygens is responsible for this lower energy transition. The next highest band near 9·3 eV in silicate glasses has been interpreted in terms of the Wannier model employed for fused silica, taking into account the shift of position produced by the change of index of refraction. The 11·5 eV band in alkali silicate glasses appears to be identical with that observed in SiO_2, i.e. a bonding to antibonding level transition, characteristic of the SiO_4 tetrahedron.

Acknowledgements—The author is indebted to Mr. R. J. Ginther of the Naval Research Laboratory for the preparation of the high purity alkali silicate glasses and to Dr. E. Lell of Bausch and Lomb, Inc., Rochester, New York for the preparation of the doped fused silica samples. The author also wishes to thank Dr. M. H. Reilly and Dr. M. N. Kabler for their constructive comments with regard to this work.

REFERENCES

1. BISHAY A. M., *Phys. Chem. Glass.* **2**, 26 (1961).
2. SMITH H. L. and COHEN A. J., *J. Am. ceram. Soc.* **47**, 564 (1964).
3. MCSWAIN B. D., BORELLI N. F. and SU G.-J., *Phys. Chem. Glass.* **4**, 1 (1963).
4. SMITH H. L. and COHEN A. J., *Phys. Chem. Glass.* **4**, 173 (1963).
5. HENSLER J. R., *Sixth International Congress on Glass*, Washington, D.C. (1962).
6. SIGEL G. H. and GINTHER R. J., *Glass Technol.* **9**, (1968).
7. STEVELS J. M., *Proceedings 11th International Congress on Pure and Applied Chemistry* **5**, 519 (1953).
8. SCHOLZE H., *Glastech. Ber.* **32**, 81 (1959).
9. LOH E., *Solid State Commun.* **2**, 269 (1964).
10. PHILLIPP H. R., *Solid State Commun.* **4**, 73 (1966).
11. LELL E., *J. Am. ceram. Soc.* **43**, 422 (1960).
12. NAMIOKA T., *J. opt. Soc. Am.* **49**, 951 (1959).
13. SAMSON J. A. R., *Techniques of Vacuum Ultraviolet Spectroscopy*, J. Wiley, New York (1967).
14. BERNING P. H., HASS G. and MADDEN R. P., *J. opt. Soc. Am.* **50**, 586 (1960).
15. HOLLAND L., *The Properties of Glass Surfaces* Chap. 2, J. Wiley, New York (1964).
16. BELL R. J. and DEAN P., *Nature Lond.* **212**, 1354 (1966).
18. RUFFA A. R., *Phys. Status Solidi* **29**, 605 (1968).
19. REILLY M. H., *J. Phys. Chem. Solids* **31**, 1041 (1970).
20. OBRIEN M. C. M., *Proc. R. Soc. Lond.* **A231**, 404 (1955).
21. MACKEY J. H., SMITH H. L. and HALPERIN A., *J. Phys. Chem. Solids* **27**, 1759 (1966).
22. PAJASOVA L. *Czech. J. Phys.* **B19**, 1265 (1969).
23. LELL E., *Phys. Chem. Glass.* **3**, 84 (1962).
24. KATS A., and STEVELS J. M. *Phillips Res. Rep.* **11**, 115 (1956).
25. PLATZODER K., *Phys. Status Solidi* **29**, K63 (1968).
26. PAULING L., *The Nature of the Chemical Bond*, Cornell Univ. Press, Ithaca, New York (1960).
27. DEXTER D. L., and KNOX R. S., *Excitons*, Interscience Publishers, New York (1965).

J. Phys. Chem. Solids, 1971, Vol. 32, pp. 2385–2391. Pergamon Press. Printed in Great Britain

THEORETICAL ENERGY LEVELS AND g VALUES FOR THE ^{4}I TERMS OF Nd^{3+} AND Er^{3+} IN $LiYF_4$

N. KARAYIANIS
Harry Diamond Laboratories, Washington, D.C. 20438, U.S.A.

(*Received* 29 *January* 1971)

Abstract – An analysis is made of previously reported spectra of Nd^{3+} and Er^{3+} in lithium yttrium fluoride. The parameters of the Hamiltonian $\mathbf{H} = \sum_n \lambda(\mathbf{L}\cdot\mathbf{S})^n + \sum_{km} B^{\dagger}_{km}\mathbf{C}_{km}$, diagonalized in the ^{4}I ground terms of these ions, are varied to reproduce reported energy levels and ground state g values. The resultant spin-orbit (λ_n) and crystal-field (B_{km}) parameters are compared with those reported previously for calcium tungstate, and are used to predict as yet unreported energy levels and excited state g values.

1. INTRODUCTION

IN RECENT articles fluorescence spectra to the $J = 9/2$ and $11/2$ ground multiplets of Nd^{3+} in $LiYF_4$[1] and fluorescence and absorption spectra to the ground term of Er^{3+} in $LiYF_4$ [2] have been reported. We have analyzed the ^{4}I ground terms of these complementary ions by diagonalizing the hamiltonian

$$\mathbf{H} = \mathbf{H}_E + \mathbf{H}_x \qquad (1)$$

in a Russell–Saunders basis for ^{4}I where $\mathbf{H}_E$, the effective spin orbit hamiltonian[3] and $\mathbf{H}_x$, the crystal field hamiltonian[3, 4] are given by

$$\mathbf{H}_E = \sum_{n=1}^{3} \lambda_n (\mathbf{L}\cdot\mathbf{S})^n \qquad (2)$$

and

$$\mathbf{H}_x = \sum_{km} B^{\dagger}_{km}\mathbf{C}_{km}. \qquad (3)$$

The parameters λ_n and B_{km} were varied to obtain a least squares fit between reported energy levels and g values for the ground states. The g values were reported for Nd^{3+} and Er^{3+} by Sattler and Nemarich[5] and for Er^{3+} by Brown, Roots and Shand[2]. In the fitting procedure, S_4 symmetry was assumed for the Stark field at the ion site which limits the allowed values of (k,m) in equation (3) to (2,0), (4,0), (6,0), (4,4) and (6,4), with all B_{km} real except for B_{64}.

For Nd^{3+}, where only two of the four multiplets were reported, only one spin-orbit parameter is needed to accommodate the splitting between the two multiplets. Therefore, only λ_1 was allowed to vary, and λ_2 and λ_3 were kept fixed at those values found by Karayianis and Farrar[4] for Nd^{3+} in $CaWO_4$. Even at that, only a very small change in λ_1 (from 294·651 to 294·733 cm^{-1}) was necessary to fit the 10 reported doublets to better than 1 cm^{-1} r.m.s. deviation and the ground state $g_{\parallel}$ to one part in 2000. The symmetry assignments and energy spacings of Nd^{3+} in $LiYF_4$ are remarkably similar to those in $CaWO_4$.

For the case of Er^{3+}, whereas Brown *et al.* [2] reported levels in all four multiplets of the ground term, they did not report polarization measurements. We therefore assigned symmetries to mimic those given by Wortman[6] for Er^{3+} in $CaWO_4$. Owing to the similarity of the Nd^{3+} spectra in $LiYF_4$ and $CaWO_4$, one might well expect a similar result for Er^{3+}, thus justifying this choice. However, as pointed out by Wortman and Brown *et al.*, most lines appear both in the σ and π spectra for Er^{3+}, and the symmetry assignments are not as unambiguous as they appear to be in

Nd^{3+}. The theoretical analysis is helpful in making assignments, but again caution is required as the relatively large r.m.s. deviations between theoretical and experimental energies that remain after fitting—18 cm^{-1} for Er^{3+}: $CaWO_4$ and 14 cm^{-1} for Er^{3+}: $LiYF_4$—suggest that either some erroneous assignments have been made or effects neglected in the theory* are significant. Future refinements to the theory of the effective spin-orbit hamiltonian are expected to shed light on this point.

The purpose of the analysis reported below is twofold. First, spin-orbit and crystal-field parameters are obtained for Nd^{3+} and Er^{3+} in $LiYF_4$ and compared with similar parameters obtained in $CaWO_4$. This comparison leads to approximate ratios of the radial integrals $\langle r^k \rangle$ and of the lattice-dependent parameters A_{km} under the assumption

$$B_{km} = \langle r^k \rangle A_{km}.$$

Second, the analysis predicts excited state g values and energy levels where measurements are as yet unreported. Future measurements of these properties are needed to corroborate the assignments made for Er^{3+} and to test the method of using spin-orbit parameters obtained for an ion in one lattice to predict energy levels in a different lattice as applied here to Nd^{3+}.

2. NEODYMIUM

Symmetry assignments for the lowest two multiplets of the ^4I ground term and for the two $^4F_{3/2}$ levels of Nd^{3+} in $LiYF_4$ can be deduced from polarization data of Harmer *et al.* given in Fig. 9 of their paper.† Since the $^4I_{9/2}$ multiplet reduces to $2\Gamma_{5,6} + 3\Gamma_{7,8}$, then the fact that 3 pure σ transitions are observed from the lower of the $^4F_{3/2}$ levels indicates this level (at 11,538 cm^{-1}) is a $\Gamma_{7,8}$. The level at 11,597 cm^{-1} is therefore a $\Gamma_{5,6}$, similar to the assignments for Nd^{3+} in $CaWO_4$[7].

From these assignments, the polarization data unambiguously determine the symmetries of the two ground multiplets according to Table 1, with the exception of a level at 2,042 cm^{-1} in the $^4I_{11/2}$ multiplet (which, incidently, is the terminal laser level). Transitions to this level are observed both in the σ and π spectra from each of the $^4F_{3/2}$ levels. Only four other levels in the $^4I_{11/2}$ multiplet are observed, $2\Gamma_{5,6}$ and $2\Gamma_{7,8}$. It is reasonable to assume, therefore, that the level at 2042 cm^{-1} is an accidentally degenerate (or at least an unresolved or mixed) pair of doublets, one $\Gamma_{5,6}$ and one $\Gamma_{7,8}$.

To test this assumption and to obtain a theoretical fit to the known levels, the level at 2042 cm^{-1} arbitrarily was assigned as a $\Gamma_{5,6}$. Then, λ_1 and the B_{km} parameters were varied to fit to the 5 levels of $^4I_{9/2}$ and 5 levels in $^4I_{11/2}$. The sixth level in $^4I_{11/2}$ (a $\Gamma_{7,8}$) was left free to see if fitting 10 out of 11 levels would place the free level near 2042 cm^{-1}. The parameters λ_2 and λ_3 were kept fixed during this procedure at values found previously for Nd^{3+} in $CaWO_4$[4]. Simultaneously, it was required that the ground state $g_\parallel$ equal the value measured by Sattler and Nemarich[5]. The spin-orbit and crystal field parameters (given in Table 2) obtained in this manner result in a fit to the 10 energy levels within an r.m.s. deviation of 0·82 cm^{-1} and result in theoretical values of $g_\parallel = +1{\cdot}988$‡ and $g_\perp = 2{\cdot}609$ compared with measured values of $g_\parallel = 1{\cdot}987$ and $g_\perp = 2{\cdot}554$. The complete set of theoretical energy levels and g values is given in Table 1.

The theoretical energy of the free $\Gamma_{7,8}$ level for the best fit parameters of Table 2 is 2037 cm^{-1}. This value is sufficiently close to 2042 cm^{-1} to reinforce the assumption of near degeneracy and to suggest that there may be a 'satellite' line to the transition to the level at

---

*See Section 8 of Ref. [3] for a discussion of this point.

†See Ref. [1], p. 1488.

‡For a magnetic field applied in the positive z direction, a depressed Γ_6 or Γ_8 level is defined as a positive $g_\parallel$.

Table 1. *Experimental energy levels and theoretical energy levels in* cm^{-1} *and g values for the* ^4I *ground terms of triply-ionized neodymium* (f^3) *and erbium* (f^{11}) *in* LiYF$_4$

		Nd^{3+} : LiYF$_4$				Er^{3+} : LiYF$_4$			
Multiplet	Γ	Experimental[a] cm^{-1}	Theoretical[b] cm^{-1}	$g_\parallel$	$g_\perp$	Experimental[c] cm^{-1}	Theoretical[d] cm^{-1}	$g_\parallel$	$g_\perp$
$^4I_{9/2}$	7,8	0	−1	+1·988	2·609	12660	12648	+1·000	2·653
	7,8	132	133	−2·104	1·832	12565	12567	−1·035	1·879
	5,6	182	181	+2·639	2·456	12537	12535	+3·025	1·988
	5,6	249	250	−1·353	2·594	12466	12488	−1·621	2·003
	7,8	528	528	+2·355	2·769	12360	12352	+2·270	2·838
$^4I_{11/2}$	7,8	1998	1998	+7·297	1·390	10315	10320	+5·613	3·325
	7,8	—	2037	−5·930	1·285	10289	10288	−3·987	3·098
	5,6	2042	2042	−4·861	2·586	10283	10293	−5·577	2·448
	5,6	2079	2079	+2·239	0·559	10235	10256	+0·966	0·607
	5,6	2228	2227	−5·805	1·817	10222	10185	−4·042	2·909
	7,8	2264	2265	+1·439	5·544	—	10168	+1·225	5·535
$^4I_{13/2}$	5,6		3949	−9·625	0·727	6714	6698	−9·354	1·860
	7,8		3976	+8·453	2·229	6699	6682	+7·132	4·233
	5,6		3993	+9·073	0·224	6671	6664	+9·480	1·240
	7,8		4026	−7·129	1·976	6648	6638	−5·367	3·936
	5,6		4205	−8·542	4·072	6554	6564	+5·571	5·386
	5,6		4229	−3·497	4·435	6514	6534	−1·239	5·984
	7,8		4238	+1·837	7·405	6511	6532	+1·543	7·425
$^4I_{15/2}$	5,6		5862	+8·331	5·301	280	295	+10·579	3·901
	5,6		5924	−7·136	5·030	261	266	−8·768	3·681
	7,8		5952	−12·277	0·517	240	238	−12·034	1·852
	7,8		6032	+9·241	0·968	208	201	+7·888	1·069
	7,8		6307	+2·737	8·280	55	48	+0·809	5·165
	5,6		6344	−1·115	7·535	28	28	−0·370	7·984
	7,8		6370	−13·907	0·227	17	15	−11·058	2·586
	5,6		6423	+4·570	7·887	0	−5	+3·350	8·214
	r.m.s. deviation (10 levels) 0·82						(25 levels) 13·70		

[a] Ref. [1]. [b] Calculated using Nd^{3+} : LiYF$_4$ parameters in Table 2. [c] Ref. [2]. [d] Calculated using Er^{3+} : LiYF$_4$ parameters in Table 2.

2042 cm^{-1} in LiYF$_4$, much as Johnson[8] found for the laser level of Nd^{3+} in CaWO$_4$.

Levels that belong to different irreducible representations of a point group and that are almost degenerate are capable of being mixed by a small, symmetry-destroying perturbation that otherwise may be ignored. Such an effect can explain the observed σ, π polarizations of the level at 2042 cm^{-1} even though it may not be exactly degenerate with a neighboring level. Under these conditions it is not possible to assign a given irreducible representation to these levels. The facts that theory predicts them so close and that experiment shows the polarizations to be mixed lend credence to an assumption that such mixing obtains for these levels.

A previously reported calculation[9] that is based on the same data of Harmer *et al.* but that neglects J-mixing was not successful in obtaining an adequate fit to the few energy levels involved (r.m.s. of 9 or 10 cm^{-1}). Although these authors neglected J-mixing for this case, they obtained an equally poor fit for the lowest two multiplets of Nd^{3+} in CaWO$_4$ by including J-mixing[10]. It is surprising that better fits were not obtained since they used intermediate coupled wavefunctions for the free Nd^{3+} ion as basis functions. Ostensibly J-mixing from the $J = 13/2$ and $15/2$ multiplets that was not included in their calculations in either case, while small, is sufficient to prevent a better fit. But it would seem that for a system where only 8 energy differences are specified* and where six independent free parameters (the B_{km}) are available, a better fit would be possible, and neglected effects would manifest themselves as inaccuracies in the crystal field parameters. From this point of view, the practice of using intermediate coupled, free ion wavefunctions to analyze crystal field data for the lanthanides is open to some question. For the price of dealing with the complexity of these wavefunctions† apparently one does not buy too much.

Besides being very simple to apply, the method here of using pure Russell–Saunders wavefunctions as a basis in which to diagonalise **H** automatically includes full J-mixing by $\mathbf{H}_x$ of the levels in the given term. While fitting just some of the levels, one obtains consistent theoretical energy levels and excited state g values for the whole term which can be compared with future measurements. In the case of Nd^{3+} in $LiYF_4$, future absorption measurements to the $J = 13/2$ and $15/2$ multiplets and excited state g value measurements will serve to test both the accuracy of the parameters reported here and the validity of the spin-orbit hamiltonian method of analyzing spectra.

3. ERBIUM

Energy levels for Er^{3+} in $LiYF_4$ given in Table 1 were taken from the measurements of Brown *et al.*[2] who did not report polarizations. We therefore assigned symmetries to the levels similar to those reported by Wortman[6] for Er^{3+} in $CaWO_4$. In this way it was possible to obtain a fit within an r.m.s. of 14 cm^{-1} to 25 (out of 26) levels of the ground ^4I term. The spin-orbit and crystal field parameters obtained are listed in Table 2, and the set of theoretical energy levels and g values are given in Table 1. From Table 1, the theoretical ground state g values are $g_\parallel = +3{\cdot}350$ and $g_\perp = 8{\cdot}214$ whereas Brown *et al.*[2] report $g_\parallel = 3{\cdot}32$ and $g_\perp = 8{\cdot}09$. In a very dilute sample, Sattler and Nemarich[5] measured $g_\parallel = 3{\cdot}137$ and $g_\perp = 8{\cdot}105$.

Brown *et al.* calculated crystal field parameters based on splittings of 'the 8|SLJ> states' (presumably, the 8 doublets of the ground $^4I_{15/2}$ multiplet), assuming D_{2d} symmetry which differs from S_4 in that B_{64} is also real. They found two possible sets of parameters that fit their data, one with positive and the other with negative B_{20}. We reduced their parameters to the B_{km} defined by (3) and listed them in columns B and C of Table 3 for comparison with our results given in column A. Referring to their crystal field parameters as b_{km}, the relationships we assume to our B_{km} are‡

$$\begin{aligned} &B_{20} = 2b_{20}, \\ &B_{40} = 8b_{40}, \quad B_{44} = -(8/\sqrt{70})\,b_{44} \qquad (4) \\ &B_{60} = 16b_{60}, \quad B_{64} = -(8\sqrt{14}/21)\,b_{64}. \end{aligned}$$

Brown *et al.* discarded the set with positive B_{20} (column B, Table 3) for several reasons, one of which was their belief that B_{20} is negative at the Y^{3+} site. On the other hand, preliminary lattice summations of Brown and Morrison[11] using extrapolated neutron diffraction data of $CaWO_4$ for the lattice con-

---

*Remember the sixth level in $^4I_{11/2}$ was not reported, and that only the energy differences in each multiplet (4 in each multiplet) are independent.

†For the actinides, where the spin-orbit interaction is much stronger than in the lanthanides, these basis functions may be unavoidable. A reference for this case is the work on Np^{4+} by SHARMA K. K. and ARTMAN J. O., *J. chem. Phys.* **50**, 1241 (1969).

‡These relationships assume the b_{km} of Brown *et al.* are equal to the $\langle r^k \rangle A_{km}$ of Wybourne. In Table 6-1 of his book, *Spectroscopic Properties of Rare Earths*, p. 165, *Interscience, New York* (1964), Wybourne has errors, some of which are corrected by Eremin *et al.*, *Soviet Phys. solid State* **11**, 1697 (February 1970).

Table 2. *Phenomenological spin-orbit and crystal-field parameters in* cm^{-1} *and ground state g values for the* ^4I *terms of* Nd^{3+} *and* Er^{3+} *in* CaWO$_4$ *and* LiYF$_4$

	Nd^{3+}		Er^{3+}	
	CaWO$_4$	LiYF$_4$	CaWO$_4$	LiYF$_4$
λ_1	294·651	294·733	−613	−616·677
λ_2	−2·41864	−2·4186	−19·3	−19·1123
λ_3	0·04172	0·0417	−0·499	−0·4819
B_{20}	548·81	502·22	404	346·77
B_{40}	−942·41	−964·49	−685	−570·54
B_{44}	1004·66	1104·94	728	726·66
B_{60}	−17·12	−27·40	12·4	−65·42
$R\ B_{64}$	946·84	1019·20	452	510·06
$I\ B_{64}$	1·34	34·77	164	121·58
r.m.s. deviation	4·33[a]	0·82[b]	18[c]	13·70[d]
Ground state				
Theoretical $g_{\parallel}$	+2·029	+1·988	+1·265	+3·350
$g_{\perp}$	2·587	2·609	8·487	8·214
Experimental $g_{\parallel}$	2·034[12]	1·987[5]	1·251[13]	3·137[5]
$g_{\perp}$	2·538	2·554	8·401	8·105

[a] For 26 levels, see Ref. [4]. [b] For 10 levels, this work. [c] for 26 levels, see Ref. [6] [d] For 25 levels, this work.

stants of LiYF$_4$ give a positive B_{20}. Our empirical results (column *A*, Table 3) also give a positive B_{20}. Owing to the similarity in the spectra* of Nd^{3+} and Er^{3+} in CaWO$_4$ and LiYF$_4$, and the relatively good theoretical fits obtained for Er^{3+} with positive B_{20}, we feel that a negative B_{20} is unlikely. The agreement between theoretical and experimental *g* values for the gound state reinforces this view. On the other hand, the factor-of-four worse r.m.s. fit $(18/4{\cdot}33 = 4{\cdot}2)$ obtained for Er^{3+} with respect to Nd^{3+} in CaWO$_4$ detracts from this view although deficiencies in the theory proportional to $(\zeta/F_2)^2$ may explain this discrepancy. The ratio of this quantity for Er^{3+} with respect to Nd^{3+} is 4·07, using $\zeta = 890$, $F_2 = 328$ for Nd^{3+} and $\zeta = 2380$, $F_2 = 435$ cm^{-1} for Er^{3+}. It is hoped that a future implementation of these corrections will allow for an equally good fit to the Er^{3+} spectra and result in more accurate phenomenological parameters.

4. COMPARISON OF THE B_{km}

Besides noting that the four spectra involving Nd^{3+} and Er^{3+} in CaWO$_4$ and LiYF$_4$ are remarkably similar if the erbium ^{4}I levels are inverted, a further, more quantitative, comparison can be made by considering

Table 3. *Crystal-field parameters in* cm^{-1} *for the* ^4I *term of* Er^{3+} *in* LiYF$_4$

	A[a]	B[b]	C[a]
B_{20}	347	190	−230
B_{40}	−571	−1184	−1368
B_{44}	727	858	632
B_{60}	−65	−45	408
$R(B_{64})$	510	295	239
$I(B_{64})$	122	0	0

[a] From Table 2 of this paper. [b] From Brown *et al.* (see Ref. [2]).

---

*Invert the Er^{3+} ^{4}I levels to compare them with Nd^{3+} as in Table 1.

crystal field parameters. If one neglects interconfigurational mixing of the impurity ion levels and if the interaction between the impurity ion and the host material can furthermore be characterized as an effective electrostatic field dependent only on the host, the B_{km} can be factored as*

$$B_{km} = \langle r^k \rangle A_{km}. \tag{5}$$

The A_{km} depend only on the host material under these assumptions, and the expectation values of r^k depend only on the impurity ion.

Ratios of the B_{km} for different ions in the same crystal give values for ratios of the radial integrals as in the following example,

$$B_{km}(Er)/B_{km}(Nd)|_{\mathrm{CaWO_4}} = \langle r^k \rangle_{Er} / \langle r^k \rangle_{Nd}. \tag{6}$$

On the other hand, ratios of the B_{km} for the same ion taken in different crystals give the relationship between the electrostatic field components of the two hosts. For example,

$$B_{km}(\mathrm{LiYF_4})/B_{km}(\mathrm{CaWO_4})|_{Er} = A_{km}(\mathrm{LiYF_4})/A_{km}(\mathrm{CaWO_4}). \tag{7}$$

Ratios of the type given by (6) are expected to be independent of m for a given k and independent of the host material, whereas ratios of the type given by (7) are expected to be independent of the impurity ion. Deviations from these rules indicate, first of all, inaccuracies in the determination of the B_{km}, but, more fundamentally, they indicate violations in the assumptions under which factorizations of the B_{km} obtain according to equation (5).

The above ratios were calculated from the parameters of Table 2 and are given in Table 4. Ratios involving B_{60} are seen to be significantly out of line—probably as a result of the accidentally small values for these parameters which amplify any errors.

Average ratios in the fourth column of Table 4 are compared with ratios of radial integrals obtained by Freeman and Watson[14] given in the fifth column. For each k-fold field the F–W values are smaller by ratios of 0·933, 0·693 and 0·628 for $k = 2, 4$, and 6. This, qualitatively, is what one might expect on the basis of the nephelauxetic effect[15].

Regarding the host-intrinsic, electrostatic field ratios (columns 6–8 of Table 4), the average values can be summarized as follows. The A_{km} of $\mathrm{LiYF_4}$ are, for $k = 2$, 4 and 6, respectively, 0·89, 0·99† and 1·08 times as big

Table 4. *Ratios of phenomenological crystal-field parameters for the* ^4I *terms of* $\mathrm{Nd^{3+}}$ *and* $\mathrm{Er^{3+}}$ *in* $\mathrm{CaWO_4}$ *and* $\mathrm{LiYF_4}$

	$\lvert B_{km}(Er)/B_{km}(\mathrm{Nd})\rvert$			$\langle r^k \rangle_{Er}/\langle r^k \rangle_{\mathrm{Nd}}$	$\lvert B_{km}(\mathrm{LiYF_4})/B_{km}(\mathrm{CaWO_4})\rvert$		
k,m	$\mathrm{CaWO_4}$	$\mathrm{LiFY_4}$	Average	F–W[b]	Nd	Er	Average
2,0	0·736	0·691	0·713	0·665	0·914	0·859	0·886
4·0	0·727	0·592	0·676	0·469	1·025	0·833	0·929
4,4	0·725	0·658			1·099	0·999	1·049
6,0[a]	−0·706	2·410			1·587	−5·405	—
6,4	0·508	0·514	0·511	0·321	1·078	1·091	1·084

[a] The B_{60} are on the order of 30 cm⁻¹ whereas all other B_{km} are in the 400 to 1000 cm⁻¹ area (see Table 2). Any errors in the B_{60} therefore result in relatively huge variations in their ratios. [b] FREEMAN A. J. and WATSON R. E., *Phys. Rev.* **127**, 2058 (1962). These ratios become 0·680, 0·515, and 0·373, closer to our average values, if the $\langle r^k \rangle$ are used for Nd as calculated by SYNEK M. and GROSSGUT P., *Phys. Rev.* **A1**, 1(1970).

---

*We have neglected crystal field shielding corrections that enter as a factor of $(1 - \sigma_k)$ on the right-hand side of (5), but that tend to cancel when ratios of B_{km} are taken. See, for example, STERNHEIMER R. M., BLUME M. and PEIERLS R. F., *Phys. Rev.* **173**, 376 (1968).

†There is no obvious reason for the $k,m = 4,0$ ratio to equal the $k,m = 4,4$ ratio here. An average was taken as an approximate, convenient way of presenting the results

as those of $CaWO_4$. It will be interesting to see if similar results are obtained for other ions as new measurements are reported.

Acknowledgement—The author would like to thank A. L. Harmer, A. Linz, D. R. Gabbe, M. R. Brown, K. G. Roots and W. A. Shand without whose data this paper and any light it may shed on the problems discussed would not have been possible. He also gives special thanks to H. F. Gibson, C. A. Morrison, and D. E. Wortman for their continued interest.

REFERENCES

1. HARMER A. L., LINZ A. and GABBE D. R., *J. Phys. Chem. Solids* **30**, 1483 (1969).
2. BROWN M. R., ROOTS K. G. and SHAND W. A., *J. Phys. C.* (*Solid State Phys.*) **2**, 593 (1969).
3. KARAYIANIS N., *J. chem. Phys.* **53**, 2460 (1970).
4. KARAYIANIS N. and FARRAR R. T., *J. chem. Phys.* **53**, 3436 (1970).
5. SATTLER J. P. and NEMARICH J., *Phys. Rev.* **B4**, 1 (1971).
6. WORTMAN D. E., *J. chem. Phys.* **54**, 314 (1971).
7. FARRAR R. T., *Optical Spectra of Rare Earths I. Neodymium in* $CaWO_4$. HDL Report No. TR-1309 (1965).
8. JOHNSON L. F., *Quant. Electron* **2**, 1021 (1964).
9. SENGUPTA D. and ARTMAN J. O., *J. chem. Phys.* **53**, 838 (1970).
10. SENGUPTA D. and ARTMAN J. O., *J. chem. Phys.* **50**, 5308 (1969).
11. BROWN E. A., MORRISON C. A. (private communication).
12. RANON U., *Phys. Lett.* **8**, 154 (1964).
13. ANTIPIN A. A. KATYSHEV A. N., KURKIN I. N. and SHEKUN L. Ya., *Soviet Phys. Solid State* **10**, 468 (1968).
14. FREEMAN A. J. and WATSON R. E., *Phys. Rev.* **127**, 2058 (1962).
15. JORGENSEN C. K., *Orbitals in Atoms and Molecules*, Academic Press, New York (1962).

J. Phys. Chem. Solids, 1971, Vol. 32, pp. 2393–2401. Pergamon Press. Printed in Great Britain

PHASE CHANGES OF THE DISORDERED In-Mg AND Al-Mg ALLOYS

M. KOGACHI
Department of Physics, University of Osaka Prefecture, Sakai, Osaka, Japan

and

Y. MATSUO
Department of Physics, Faculty of Science, Nara Women's University, Nara, Japan

(*Received* 28 *January* 1971)

Abstract—Phase changes of disordered alloys with composition in the binary systems of In-Mg and Al-Mg are discussed in terms of the structure-dependent energy of conduction electrons. The energy expression is given by using the mean pseudopotential of alloy, under approximations for volume, valence and screening effects. The 'q_0-effect' can explain qualitatively the observed phase changes for both the systems, except for an appearance of the complex intermediate phases in the Al-Mg system. The energies are calculated for several compositions and also for lattice distortions, which supports the interpretation following the q_0-effect.

1. INTRODUCTION

THE STABILITY and the change of phase in a binary alloy system have been discussed by many investigators. Mott and Jones[1] discussed the phase boundaries from thermodynamical points of view and pointed out that the characteristic of phase change should be based on the internal energy of the system at the absolute zero temperature. The structure-dependent internal energy, U, can be devided conveniently into two terms; one is an energy due to the interaction between ions and the other is an energy of conduction electrons. The latter is recognized as rather important in the determination of crystal structure. Among the various treatments as to the contribution of conduction electrons to U, the theory of 'Brillouin zone effect' introduced by Jones[2] and Goodenough[3] is in particular famous. The Hume–Rothery rule of phase change was explained by adopting this theory. Massalski and his co-workers[4] applied it to interprete their experimental results on the h.c.p. ζ-, ϵ- and η-phases of binary systems. The variation of axial ratio c/a of them with composition was inclusively explained in terms of electron-to-atom ratio e/A of the system. Yonemitsu[5] and Preece and King[6] also dealt with the phase changes of In-rich binary alloys from the same standpoint and showed that the phase boundaries occurred at the definite values of e/A.

However, as pointed out by Massalski and Pops[7], the theory of Brillouin zone effect has some difficulties in its application. For example, a peculiar change of the axial ratio of Cd-Mg alloy with composition[8] cannot be explained, if consideration is restricted to the effect of electron-to-atom ratio. Furthermore, this treatment is based essentially on the rigid band approximation and thus removes the characters of constituent atoms other than their valences. Therefore, it may be desirable to introduce some physical quantities of constituent atoms into the energy expression in order to discuss the phase change of an alloy system.

Recently, the total energy expression for a binary alloy system was made following the pseudopotential theory[9, 10]. Hayes *et al.* [11] obtained the energy expression, at constant volume, for a binary alloy with an arbitrary degree of order and calculated the ordering energy for stoichiometric LiMg.

Inglesfield[12] discussed the feature of alloying behavior in terms of a single alloying potential and explained the ordering and the narrow range of homogeneity in the intermediate phases of HgMg and Hg_2Mg. The application of his treatment is restricted to an alloy in which the components have the same valence and approximately the same atomic volume. Unfortunately, a large number of alloy systems are beyond the restriction. An extension of the treatment for such alloys will be tried rather roughly in this paper.

In Section 2, the potential and energy of an alloy system is given by using atomic bare pseudopotentials. The approximations for volume difference and valence difference and for screening effect introduced into the evaluation of electronic energy are briefly discussed. In Section 3, the results of Section 2 are applied to the In–Mg and Al–Mg systems. The observed phase changes for both the systems are interpreted qualitatively by means of the 'q_0-effect'.

2. ENERGY EXPRESSION FOR CONDUCTION ELECTRONS

Let us build an A–B binary alloy up from $(1-c)N$ atoms of type A with atomic bare potential $w_A{}^b(\mathfrak{r})$, atomic volume Ω_A and valence z_A, and cN atoms of type B, with $w_B{}^b(\mathfrak{r})$, Ω_B and z_B. The atomic potentials, $w_A{}^b(\mathfrak{r})$ and $w_B{}^b(\mathfrak{r})$, are thought to be localized nearly spherically around each nucleus. The atomic volume Ω of the A–B alloy is taken to be equal to the weighted average of Ω_A and Ω_B with composition. The volume change due to alloying gives rise to some modifications of the potential and other physical quantities of constituent atoms. If the volume of alloy varies with composition obeying the Vegard's law, however, the electronic structure may not be directly affected by this. Then, the form of atomic potential of the component is treated as the same as in its pure metal. In addition, the density of conduction electrons is assumed to be uniform throughout crystal. The number of electrons per atom, z, of an alloy system is thus evaluated to vary linearly with composition. The treatment is just the same as that in the Brillouin zone effect. In order to deal with electron density rigorously, the reduction of it inside ion cores due to orthogonality hole effect[10] should be taken into account. Because of the approximations mentioned above, the present approach should be more or less obscure.

The total potential, $W(\mathfrak{r})$, of the A–B alloy system, acting on each conduction electron, is expressed by

$$W(\mathfrak{r}) = W^b(\mathfrak{r}) + W^{SC}(\mathfrak{r}), \tag{1}$$

where the first term is

$$W^b(\mathfrak{r}) = \sum_A w_A{}^b(\mathfrak{r}-\mathfrak{r}_A) + \sum_B w_B{}^b(\mathfrak{r}-\mathfrak{r}_B), \tag{2}$$

and each sum is taken over all the sites occupied by A or B atoms, respectively, which are called the A-site or B-site. The second term is a screening potential resulting from interaction between conduction electrons. In order to obtain the structure-dependent energy per atom, U_e, of conduction electrons, the second-order perturbation theory is used. The crystal potential $W(\mathfrak{r})$ is treated as the perturbed Hamiltonian. This is probably a good approximation, if the atomic pseudopotentials are used as in equation (2)[9, 10]. By analogy with the usual way, U_e is given by*

$$U_e = \sum_{\mathfrak{q}}{}' \, |\langle \mathfrak{k}|W^b(\mathfrak{r})|\mathfrak{k}+\mathfrak{q}\rangle|^2 f(q)/\epsilon(q), \tag{3}$$

where

$$f(q) = \frac{1}{N}\sum_{k<k_F} \frac{1}{\frac{1}{2}(k^2-|\mathfrak{k}+\mathfrak{q}|^2)}$$

$$= -\frac{\Omega k_F}{4\pi^2}\left(1+\frac{4k_F{}^2-q^2}{4k_F q}\ln\left|\frac{q+2k_F}{q-2k_F}\right|\right), \tag{3a}$$

---

*Throughout the present work, atomic units are used for all quantities except for energy, which is in rydbergs.

$$\epsilon(q) = 1-\frac{8\pi}{\Omega q^2}f(q), \tag{3b}$$

$$k_F = (3\pi^2 z/\Omega)^{1/3}, \tag{3c}$$

$$\Omega = (1-c)\Omega_A + c\Omega_B \tag{3d}$$

and

$$z = (1-c)z_A + cz_B. \tag{3e}$$

In the course of derivation of equation (3) from equation (1), a rough assumption is introduced into the treatment for screening potential $W^{SC}(\mathfrak{r})$. It is difficult to clarify the screening effect straightforwardly, in particular, when the constituent atoms have different valences. The screening potential is treated here by analogy to the procedure of Harrison for simple metals[9], in which the electron is thought to interact with each other through the Hartree potential only. The resulting expression differs from that obtained by Hayes *et al.*[11], who dealt with this effect rigorously, in the following respects; the latter has the two quantities, $|a_0(\mathfrak{k})|^2$ and $B(\mathfrak{k},\mathfrak{q})$, whereas in the former $|a_0(\mathfrak{k})|^2$ is set equal to unity and $B(\mathfrak{k},\mathfrak{q})$ is omitted. According to them, for the system LiMg, $|a_0(\mathfrak{k})|^2$ increases the matrix element of the screening potential by 6 to 8 per cent for important values of $\mathfrak{q}$. The term resulting from $B(\mathfrak{k},\mathfrak{q})$ decreases the screening potential matrix elements by about 0·5 per cent for $q = 0{\cdot}25$ a.u. and by 20 to 30 per cent for $q = 1{\cdot}50$ a.u. Therefore, the combined effect of the two corrections tends to redistribute the screening potential in $\mathfrak{q}$-space, which is neglected in the present work.

The matrix element $\langle\mathfrak{k}|W^b(\mathfrak{r})|\mathfrak{k}+\mathfrak{q}\rangle$ in equation (3) is written, using equation (2), as

$$\langle\mathfrak{k}|W^b(\mathfrak{r})|\mathfrak{k}+\mathfrak{q}\rangle = \bar{v}^b(q)S(\mathfrak{q}) + c(1-c)\Delta v^b(q)(S_A(\mathfrak{q})-S_B(\mathfrak{q})), \tag{4}$$

where

$$\bar{v}^b(q) = (1-c)v_A{}^b(q) + cv_B{}^b(q), \tag{4a}$$

$$\Delta v^b(q) = v_A{}^b(q) - v_B{}^b(q), \tag{4b}$$

$$v_A{}^b(q) = \Omega^{-1}\int w_A{}^b(\mathfrak{r})\,\mathrm{e}^{-i\mathfrak{q}\cdot\mathfrak{r}}\,\mathrm{d}V, \tag{4c}$$

$$S(\mathfrak{q}) = N^{-1}\sum_i \mathrm{e}^{-i\mathfrak{q}\cdot\mathfrak{r}_i} = (1-c)S_A(q) + cS_B(\mathfrak{q}) \tag{4d}$$

and

$$S_A(\mathfrak{q}) = \{(1-c)N\}^{-1}\sum_A \mathrm{e}^{-i\mathfrak{q}\cdot\mathfrak{r}_A}. \tag{4e}$$

$v_B{}^b(q)$ and $S_B(\mathfrak{q})$ have similar forms as equations (4c) and (4e), respectively. Taking the square of equation (4), there appears two cross terms which vanish only when the crystal in question can be built up from a primitive lattice. For example, these do not vanish for h.c.p. structure. If only a perfect disordered alloy is concerned, however, they disappear even for h.c.p. structure (see Appendix). The structure factor $S(\mathfrak{q})$ vanishes unless the wave vector $\mathfrak{q}$ is a reciprocal lattice vector $\mathfrak{g}_n$, which is usually called the normal reflection in the X-ray crystallography. Then, the structure-dependent energy U_e of conduction electrons becomes

$$U_e = \bar{U}_e + \Delta U_e, \tag{5}$$

$$\bar{U}_e = \sum_{\mathfrak{g}_n}{}' |S(\mathfrak{g}_n)|^2|\bar{v}^b(g_n)|^2 f(g_n)/\epsilon(g_n), \tag{5a}$$

$$\Delta U_e = \sum_{\mathfrak{q}}{}' |c(1-c)(S_A(\mathfrak{q})-S_B(\mathfrak{q}))|^2 \times |\Delta v^b(q)|^2 f(q)/\epsilon(q). \tag{5b}$$

These differ from those given by Inglesfield [12] in the expressions of atomic potential and screening effect. The first term $\bar{U}_e$ depends on the basic structure of alloy and the average potential $\bar{v}^b(q)$. The second term ΔU_e depends on the configuration of A or B atoms on the particular sites and also the difference potential $\Delta v^b(q)$. This term plays an important role in the problem, for example, on order-disorder transition of alloy. For a perfect disordered alloy, however, ΔU_e is reduced to a quantity depending on the composition but not on the structure[12]. Thus, $\bar{U}_e$ of equation (5a) is a basic expression for discussion on phase changes at the disordered state. The energy $\bar{U}_e$ is equivalent to that for the virtual crystal model.

According to the pseudopotential theory [9, 10], the contribution of interaction between ion cores to U is expressed as an electrostatic energy of the lattice of positive point ions in a uniform negative background. The effect of this term is to favor the structure with high symmetry such as f.c.c., b.c.c. and h.c.p. The energy of them is small, negligible in fact, but it appears to increase rapidly with any distortion of them[1, 13]. Therefore, this term is necessary to be taken into account when a distortion is concerned.

3. APPLICATION TO THE In-Mg AND Al-Mg SYSTEMS

In order to interprete qualitatively the behavior of phase changes, it is very useful to introduce the concept given by Heine and Weaire[13]. The mean energy $\bar{U}_e$ is rewritten as

$$\bar{U}_e = \sum_{g_n}{}' W(g_n)F(g_n), \tag{6}$$

where

$$W(g_n) = \sum_{|\mathbf{g}_n| = g_n} |S(\mathbf{g}_n)|^2 \tag{6a}$$

and

$$F(q) = |\bar{v}^b(q)|^2 f(q)/\epsilon(q). \tag{6b}$$

Here $W(g_n)$ is the structural weight of a set

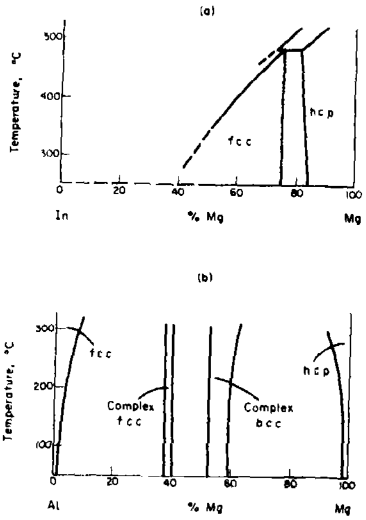

Fig. 1. Schematic phase diagrams for (a) In-Mg and (b) Al-Mg systems. Ordered phases are omitted. No data is given by Hansen[14] for the region of 0–50 per cent Mg in In-Mg alloy.

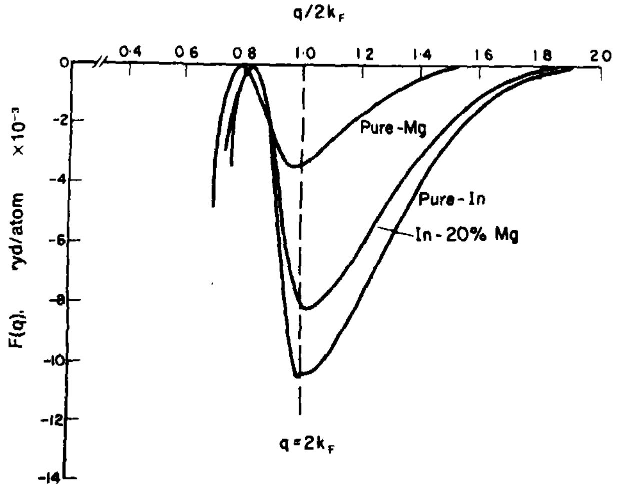

Fig. 2. $F(q)$ curves for pure In, pure Mg and In-20 per cent Mg.

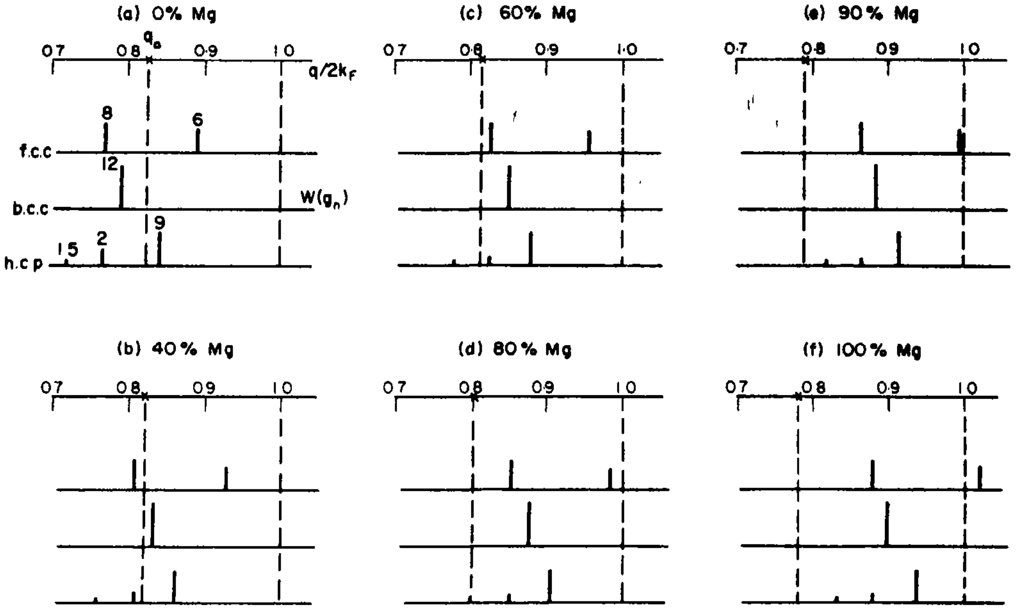

(a) 0% Mg (c) 60% Mg (e) 90% Mg

(b) 40% Mg (d) 80% Mg (f) 100% Mg

Fig. 3. Positions of q_0 and structural weights $W(g_n)$ of the first few reciprocal lattice vectors for the f.c.c., b.c.c. and h.c.p. structures for In-Mg system.

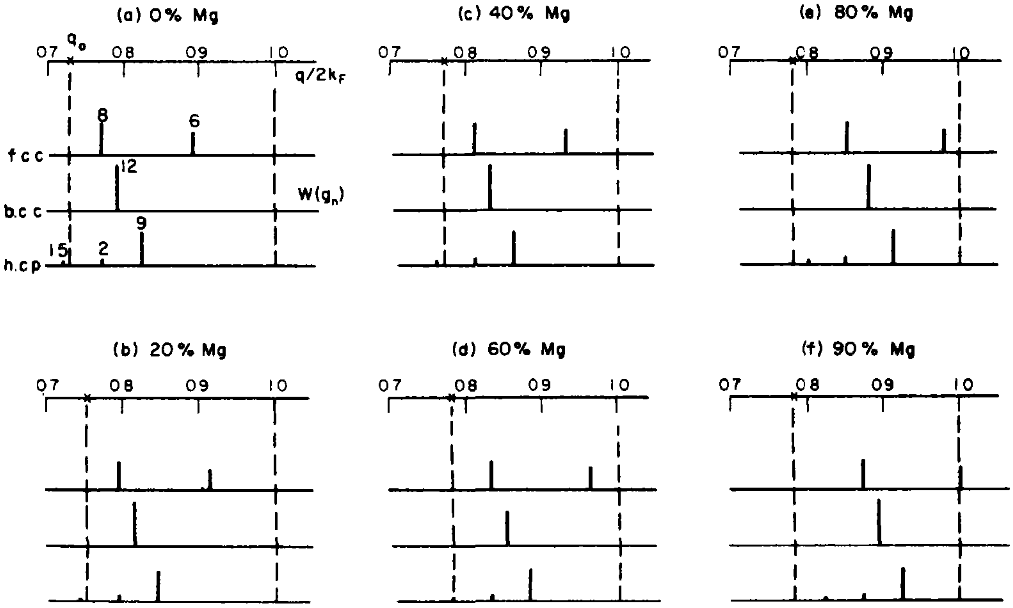

(a) 0% Mg (c) 40% Mg (e) 80% Mg

(b) 20% Mg (d) 60% Mg (f) 90% Mg

Fig. 4. Positions of q_0 and structural weights $W(g_n)$ of the first few reciprocal lattice vectors for the f.c.c., b.c.c. and h.c.p. structures for Al-Mg system.

of the reciprocal lattice vectors $\mathfrak{g}_n$. The function $F(q)$ is the energy-wave-number characteristic for the mean energy and its curve has a strong convexity near q_0, which is the first zero value of $F(q)$. The effect of q_0 is to favor the structure for which the first few reciprocal lattice vectors avoid it. The present analysis is based on this 'q_0-effect'.

The phase diagrams of the In-Mg and Al-Mg systems[14] are shown in Fig. 1, where ordered phases are omitted. The atomic volume varies with composition nearly obeying the Vegard's law in both the systems [15]. The values of atomic volume for In, Al and Mg are 176·5, 112·1 and 156·9 a.u., respectively, from which the mean atomic volume Ω of alloy were calculated by equation (3d). The values of $v^b_{\text{In}}(q)$, $v^b_{\text{Al}}(q)$ and $v^b_{\text{Mg}}(q)$ which appear in equation (4a) were obtained from the model potentials $v(q)$ for them[16] by the relation of

$$v_A{}^b(q) = (\Omega_A/\Omega)\epsilon_A(q)v_A(q) \qquad (7)$$

where $\epsilon_A(q)$ is the dielectric constant for A metal. For In-Mg and Al-Mg alloys, $F(q)$ were calculated with various compositions and some of them are shown in Fig. 2. The positions of q_0 obtained are shown in Fig. 3 for In-Mg alloys and in Fig. 4 for Al-Mg alloys together with the structural weights $W(g_n)$ of the first few reciprocal lattice vectors for the f.c.c., b.c.c. and h.c.p. (with ideal c/a) structures. All the wave number scales in the figures are normalized by $2k_F$, k_F being a radius of the Fermi sphere of each alloy (equation (3c)).

The structures of pure In, Al and Mg were discussed by Heine and Weaire[13] and Weaire[17]. As seen from Fig. 3, the simple structure with lowest energy for pure In is clearly f.c.c. However, even for f.c.c. both $g\{111\}$ and $g\{200\}$ lie near q_0, and $\bar{U}_e$ favors more complicated structures, which have a distribution of structural weight avoiding q_0. Thus, a tetragonal distortion resulting from splitting of $g\{200\}$ is realized in pure In (c/a = 1·08). As Mg is dissolved into In, q_0 shifts slightly to smaller q, but $W(g_n)$ shift

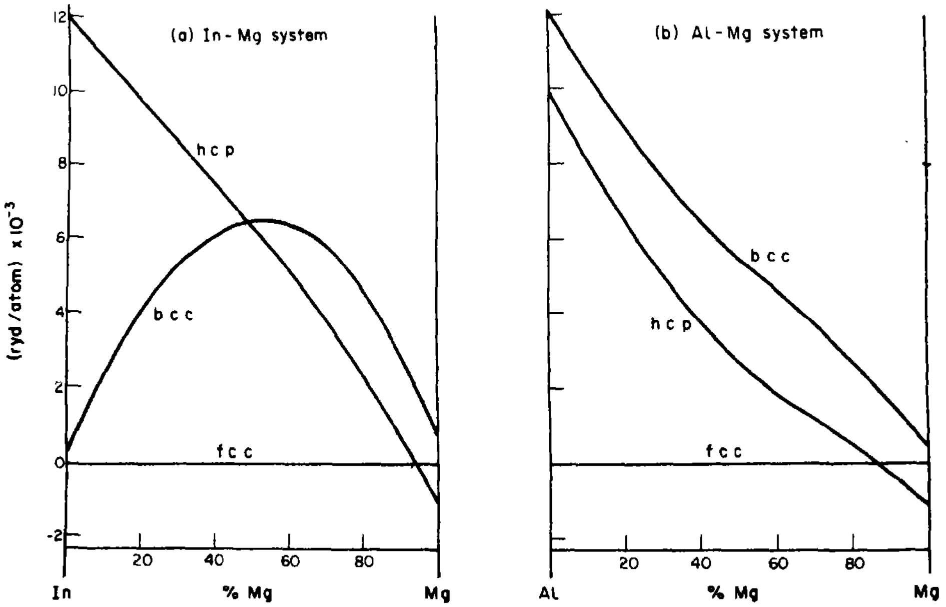

Fig. 5. Variations of the mean energy $\bar{U}_e$ with composition for b.c.c. and h.c.p., relative to that for f.c.c. (a) In-Mg system, (b) Al-Mg system.

appreciably to the opposite direction. Throughout this variation in the region from pure In to about 80 per cent Mg, the f.c.c. structure associated with the tetragonal distortion remains most stable among the three basic structures. A degree of the distortion, however, is expected to decrease with increasing Mg content and the f.c.c. structure may be realized at a certain content of Mg, because $g\{200\}$ approaches to $q = 2k_F$ and then the effect of its splitting becomes less significant. Unfortunately, the observed phase diagram exhibits nothing for 0–50 per cent Mg region, saying only that the disordered f.c.c. phase is believed to extend to 100 per cent In, merging into the tetragonal structure of In at higher In concentration[14]. The set $g\{200\}$ for f.c.c. lies on the position of $q = 2k_F$ at 90 per cent Mg and passes over it for higher concentration of Mg. Thus, in this region the h.c.p. structure becomes more favorable than the others, since the main structural weight

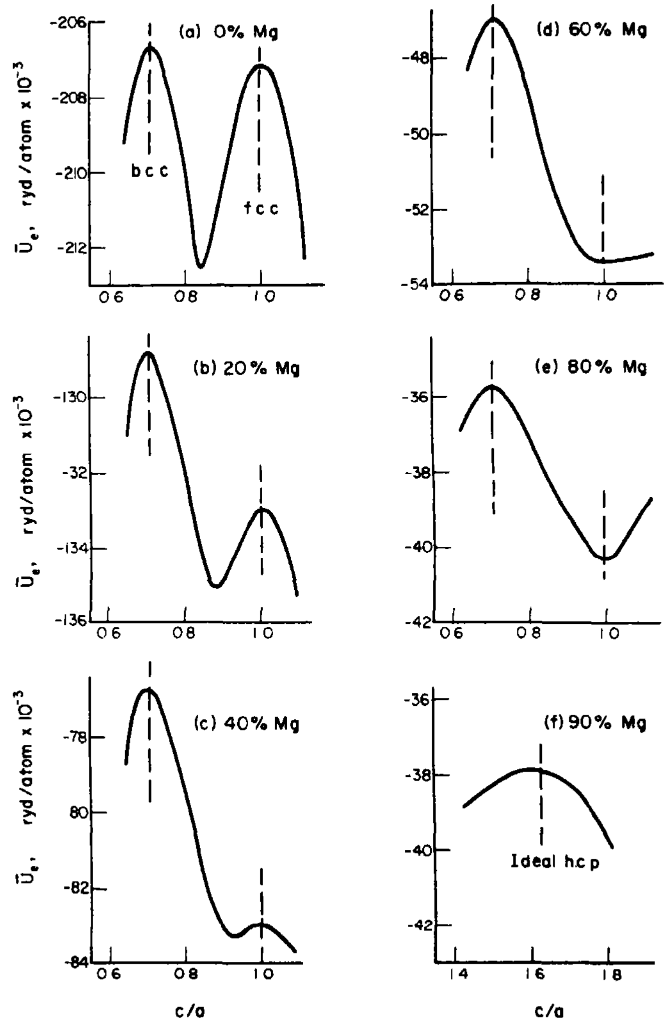

Fig. 6. Variations of the mean energy $\bar{U}_e$ for In-Mg system with tetragonal distortion (a)–(e), and distortion from ideal h.c.p. (f).

for h.c.p. falls farthest away from q_0.

For the Al-Mg system, the situation differs from the In-Mg system in that all the main reciprocal lattice vectors for the three basic structures lie in $q > q_0$ for a whole range of composition. It is expected from Fig. 4 that the f.c.c. structure is more favorable than the others in the region from pure Al to 80 per cent Mg, beyond which the h.c.p. structure has lowest energy from the same reason as in the case of In-Mg alloys. Complex intermediate phases observed in this system cannot be reproduced by the present inspection.

The above qualitative interpretation of phase changes by means of the q_0-effect will be supported by the energy calculation according to equation (5a). In Fig. 5, the variations of $\bar{U}_e$ with composition are shown for the In-Mg and Al-Mg systems, calculated for the other two basic structures relative to $\bar{U}_e$ for the f.c.c. structure. These show the phase changes consistent to those expected from the q_0-effect mentioned above. Figs. 6 and 7 illustrate the $\bar{U}_e$ changes with lattice distortion for both the systems, respectively. It may be understood from Fig. 6 that the instability of f.c.c. for In-rich alloys in the In-Mg system decreases in its degree with increasing Mg content and the f.c.c. phase appears beyond about 40 per cent Mg, taking the contribution of the ion core energy term into account. The $\bar{U}_e$ curve is fairly flat with respect to c/a change of h.c.p. structure in Mg-rich In-Mg alloys (Fig. 6(*f*)). Thus, their axial ratio is expected to be very close to the ideal value[18]. For the Al-Mg system, no lattice distortion from f.c.c. cannot be expected for a wide range of 0–80 per cent Mg (Fig. 7).

4. CONCLUSION

The structure-dependent energy of conduction electrons is expressed by using the bare pseudopotential of an alloy, in which the components have different valence and different volume. Approximations for the valence, volume and screening effects are crude and rather convenient. An estimation of error due to the treatment is difficult. However, Heine

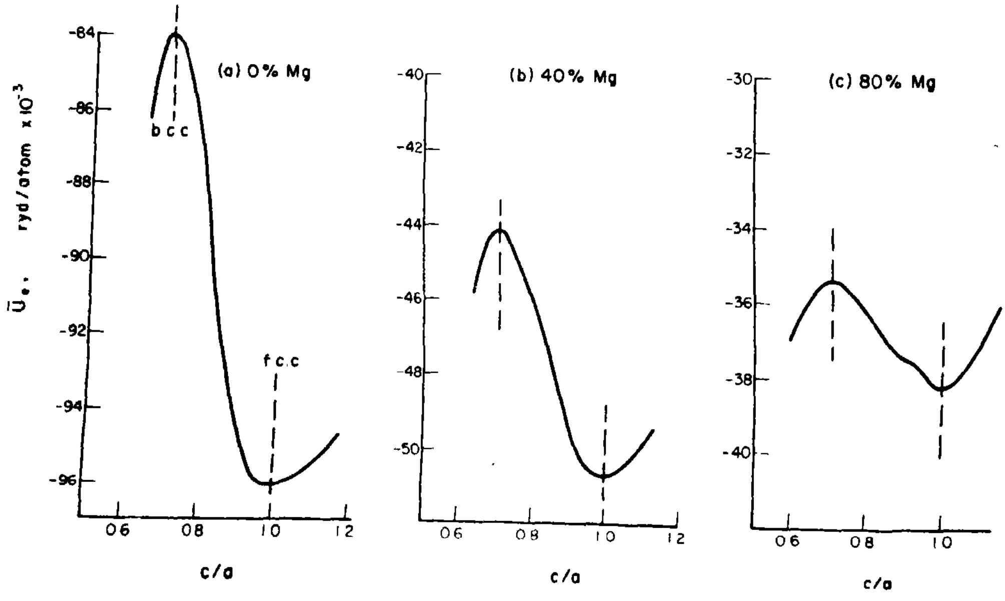

Fig. 7. Variations of the mean energy $\bar{U}_e$ with tetragonal distortion for Al-Mg system.

and Weaire[19] suggest that a volume difference seems unlikely to introduce very great errors undoubtedly and that a valence difference of one may not be enough to invalidate a perturbation theory of the conduction electron energy. Their suggestion may be supported by the present application of the treatment to the In-Mg and Al-Mg systems.

REFERENCES

1. MOTT N. F. and JONES H., *The Theory of the Properties of Metals and Alloys*, Clarendon Press, Oxford (1936).
2. JONES H., *Proc. R. Soc.* **A147**, 396 (1934).
3. GOODENOUGH J. B., *Phys. Rev.* **89**, 282 (1953).
4. For example; RAYNOR G. V. and MASSALSKI T. B., *Acta Metall.* **3**, 480 (1955). MASSALSKI T. B. and KING H. W., *Acta Metall.* **10**, 1171 (1962). KING H. W., MASSALSKI T. B. and ISAACS L. L., *Acta Metall.* **11**, 1355 (1963).
5. YONEMITSU K., *J. phys. Soc. Japan* **21**, 1231 (1966).
6. PREECE G. M. and KING H. W., *Acta Metall.* **17**, 21 (1969).
7. MASSALSKI T. B. and POPS H., *Acta Metall.* **18**, 961 (1970).
8. HUME-ROTHERY W. and RAYNOR G. V., *Proc. R. Soc.* **A174**, 471 (1940).
9. HARRISON W. A., *Pseudopotentials in the Theory of Metals*. W. A. Benjamin, New York (1966).
10. HEINE V., *The Physics of Metals—I. Electrons* (Edited by J. M. Ziman), Cambridge University Press, London (1968).
11. HAYES T. M., BROOKS H. and BIENESTOCK A., *Phys. Rev.* **175**, 699 (1968).
12. INGLESFIELD J. E., *J. Phys. C* **2**, 1285, 1293 (1969).
13. HEINE V. and WEAIRE D., *Phys. Rev.* **152**, 603 (1966).
14. HANSEN M., *Constitution of Binary Alloys*, McGraw-Hill, New York (1958).
15. PEARSON W. B., *Handbook of Lattice Spacings and Structures of Metals and Alloys*, Pergamon Press, London (1958).
16. ANIMALU A. and HEINE V., *Phil. Mag.* **12**, 1249 (1965).
17. WEAIRE D., *J. Phys. C* **1**, 210 (1968).
18. RAYNOR G. V., *Proc. R. Soc.* **A180**, 107 (1942).
19. HEINE V. and WEAIRE D., *Solid State Physics* (Edited by F. Seitz, D. Turnbull and H. Ehrenreich), Vol. 24, pp. 445, 447, Academic Press, New York (1970).

APPENDIX

The main part, denoting by $G(\mathfrak{q})$, of a cross term in the square of (4) is

$$G(\mathfrak{q}) = S^*(\mathfrak{q})(S_A(\mathfrak{q}) - S_B(\mathfrak{q})). \tag{A1}$$

The structure factor $S(\mathfrak{q})$ for h.c.p. lattice is given by

$$S(\mathfrak{q}) = \tfrac{1}{2}(1+\epsilon)\delta\mathfrak{q}, \mathfrak{g}_n, \tag{A2}$$

where

$$\delta\mathfrak{q}, \mathfrak{g}_n = \begin{cases} 1 \text{ when } \mathfrak{q} = \mathfrak{g}_n, \\ 0 \text{ when } \mathfrak{q} \neq \mathfrak{g}_n \end{cases} \tag{A3}$$

and

$$\epsilon = e^{-i((2/3)q_1+(1/3)q_2+(1/2)q_3)}. \tag{A4}$$

Substituting (A2) into (A1) and using (4d), $G(\mathfrak{q})$ is

$$G(\mathfrak{q}) = \frac{1+\epsilon^*}{2c}\left\{S_A(\mathfrak{g}_n) - \frac{1}{2}(1+\epsilon)\right\}\delta\mathfrak{q}, \mathfrak{g}_n. \tag{A5}$$

The quantity $S_A(\mathfrak{g}_n)$ in (A5) can be rewritten as

$$\begin{aligned} S_A(\mathfrak{g}_n) &= \frac{1}{(1-c)N}\sum_A e^{-i\mathfrak{g}_n\cdot\mathfrak{r}_A} \\ &= \frac{1}{(1-c)N}\{p(1-c)N + (1-p)(1-c)N\epsilon\} \\ &= p + (1-p)\epsilon. \end{aligned} \tag{A6}$$

Whence,

$$G(\mathfrak{q}) = \frac{1}{2c}(1+\epsilon^*)(1-\epsilon)\left(p-\frac{1}{2}\right)\delta\mathfrak{q}, \mathfrak{g}_n. \tag{A7}$$

Thus, $G(\mathfrak{g}_n)$ does not vanish generally. However, if the structure in question has a perfectly disordered arrangement of A and B atoms, p is thought to be equal to $\frac{1}{2}$ so that $G(\mathfrak{g}_n)$ vanishes.

Note added in proof: The phase diagram of In–Mg for 0–50% Mg region is found in Constitution of Binary Alloys, First Supplement, McGraw-Hill, New York (1965). It shows that the f.c.c. phase appears beyond about 40% Mg, as suggested in Section 3.

J. Phys. Chem. Solids, 1971, Vol. 32, pp. 2403–2407. Pergamon Press. Printed in Great Britain

DETERMINATION OF LONGITUDINAL OPTICAL MODE FREQUENCIES BY POLARIZED SPECULAR REFLECTANCE INFRARED SPECTROSCOPY*

J. B. BATES and M. H. BROOKER†
Oak Ridge National Laboratory, Oak Ridge, Tenn. 37830, U.S.A.

(*Received* 19 *October* 1970; *in revised form* 17 *January* 1970)

Abstract – Accurate longitudinal optical mode frequencies have been determined for a variety of polycrystalline inorganic materials employing simple specular reflectance techniques with polarized i.r. radiation. Longitudinal optical and transverse optical frequencies determined for ZnO, CaO, MgO, $NaNO_3$ and $NaClO_3$ are in excellent agreement with literature values. The methods employed should be generally applicable to polycrystalline inorganic and organic materials.

1. INTRODUCTION

POLARIZED i.r. reflectance spectra measured at near normal incidence have been used in this laboratory to determine the polarization characteristics of strong i.r. transitions in single crystals of materials such as $NaBF_4$[1] and $KClO_3$[2]. It was shown in these studies that, by limiting the maximum deviation from normal incidence of the i.r. beam to about 15°, the observed frequencies agreed within experimental error ($\pm 1\ cm^{-1}$) with those measured by transmission which were taken to be the transverse optical (TO) modes of the internal crystal vibrations. In a classic paper by Berreman[3], it was shown that longitudinal optical (LO) modes could be observed in polarized i.r. absorption or reflectance measurements on thin films of LiF using oblique angles of incidence. We attempted to extend our polarized specular reflectance (PSR) studies to include evaporated thin films and mechanically deposited surfaces of various crystalline inorganic materials.

Our initial PSR measurements using angles of incidence varying between 40 and 75° were made on thin films of alkali-metal carbonates [4] which had been evaporated onto stainless steel substrates. The PSR spectra recorded qualitatively resembled the polarized absorption and reflectance spectra of LiF inasmuch as reflection maxima were obtained at frequencies which corresponded to the LO mode frequencies determined by other techniques. To verify our apparent observations of LO modes in PSR spectra of the carbonates, we have subsequently investigated the spectra of polycrystalline surfaces of various metal oxides, nitrates, and chlorates. The utility of PSR spectra in determining LO mode frequencies will be illustrated by discussing the spectra of those materials for which the LO modes of certain crystal vibrations have been determined by different means in independent studies.

2. EXPERIMENTAL AND RESULTS

Polycrystalline surfaces of ZnO, CaO, MgO, $NaClO_3$ and $NaNO_3$ were prepared by simply spreading each finely divided powdered material onto a stainless steel plate. For some samples, it was convenient to mix the powder with a small amount of water and then spread the resulting paste onto the surface of the plate. The water was removed by heating the sample for several hours at about 180°C. Irregularities were removed by smoothing the

---

*Research supported by the U.S. Atomic Energy Commission under contract with the Union Carbide Corporation.

†Holder of National Research Council of Canada Postdoctoral Fellowship.

surface with a spatula. For Na_2CO_3 and Li_2CO_3, best results were obtained by evaporating thin films of these materials from aqueous solution on a steel plate and drying the resulting surface at 180°C. Identical results were obtained from surfaces of the same material that were prepared by different methods indicating that the effects of particle size, if any, are minimal. The results of our measurements of the carbonate PSR spectra will be presented elsewhere[4].

Polarized specular reflectance spectra and multiple internal reflectance spectra were measured on a Perkin–Elmer 621 i.r. spectrophotometer equipped with a AgBr polarizer. The steel plate with the deposited smooth, dried sample was mounted on the optical bench of a Wilks model 9 MIR attachment. The angle of incidence as measured from the normal to the surface could be varied from between 15 and 75° by moving both the sample and the mirrors. Although bands due to LO modes could be observed with incident angles as small as 30° from the normal, an incident angle of 75° was employed throughout these measurements in order to obtain a maximum intensity from the LO modes. Reflectance spectra were measured with the polarizer set at 0 and 90° with respect to the plane of incidence. These two polarizations will be denoted by p and s, respectively. Multiple internal reflectance spectra were obtained

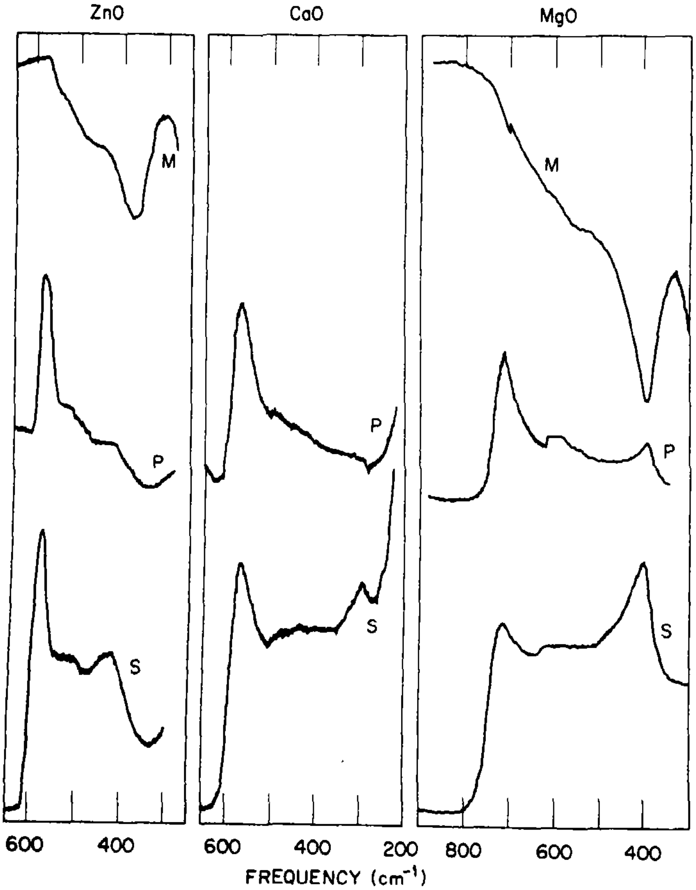

Fig. 1. MIR (M) and p and s polarized specular i.r. reflectance spectra of ZnO, CaO and MgO polycrystalline surfaces.

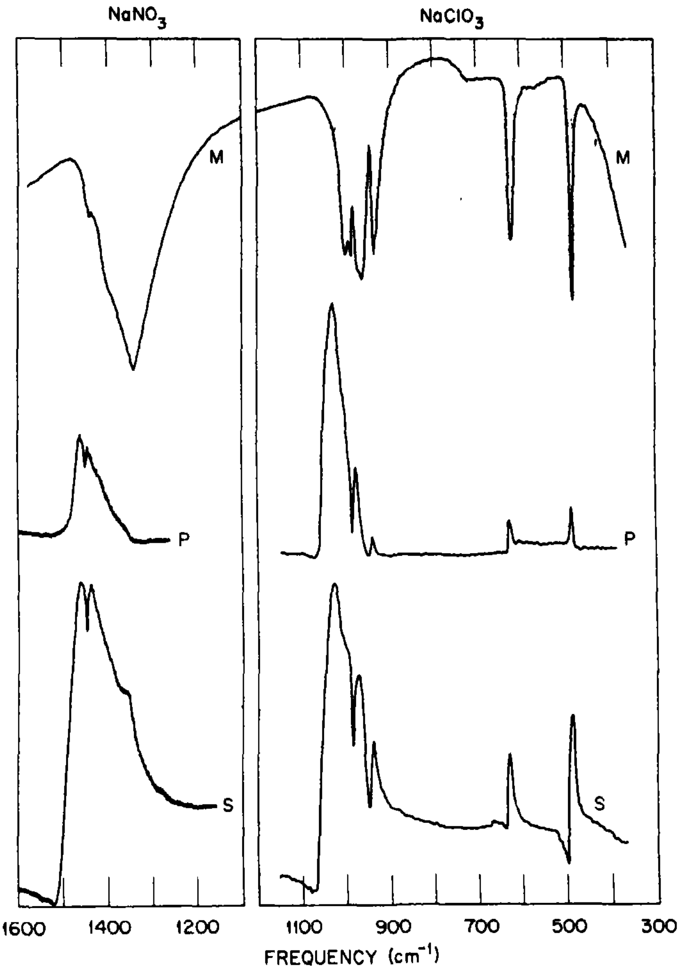

Fig. 2. MIR (M) and *p* and *s* polarized specular i.r. reflectance spectra of NaNO$_3$ and NaClO$_3$ polycrystalline surfaces.

from finely powdered samples pressed against the surface of a KRS-5 prism with face angle of 60°, placed in the Wilks model 9 MIR attachment. Peak frequencies measured from the MIR and PSR spectra are accurate to ± 2 cm^{-1}.

The *s* and *p* polarized reflectance spectra and the MIR spectra of ZnO, CaO and MgO and of NaNO$_3$ and NaClO$_3$ measured at 300°K are shown in Figs. 1 and 2, respectively. The results from these measurements are collected in Table 1 along with the LO and TO mode frequencies for the specified transitions previously reported. The LO mode frequencies for CaO and MgO reported by Wilkinson[5] were determined by noting the position at which the real part of the dielectric constant vanished (Drudes' method[3]) as derived from reflection spectra; the frequencies and assignments for the optical modes of ZnO and NaClO$_3$ were based on single crystal Raman data of Arguello *et al.*[6] and Hartwig *et al.*[7], respectively, and the LO and TO modes of the ν_3 vibration in NaNO$_3$ were

Table 1. LO and TO mode frequencies as measured by PSR and MIR compared with the frequencies and assignments previously reported. All measurements reported at 300°K

Material	Frequencies (cm^{-1})				Assignment
	PSR		MIR	Other	
	p	*s*			
ZnO	585	585	—	585[a]	LO, Quasi A_1, E_1
	—	413	—	413	TO, E_1
	—	—	385	380	TO, A_1
CaO	575	568	—	577[b]	LO
		290	[c]	286	TO
MgO	725	718	—	717[b]	LO
		402	396	403	TO
$NaNO_3$	1458	1458	—	1450[a]	LO $\nu_3(E_u)$
		1355	1350	1353	TO
$NaClO_3$	1030	1025	—	1030[a]	LO $\nu_3{}^a(F)$
	—	—	995	—	$2\nu_4$
	—	—	988	988	TO $\nu_3{}^a(F)$
	978	—	—	983	LO $\nu_3{}^b(F)$
	—	970	970	—	?
			962	965	TO $\nu_3{}^b(F)$
	939	938	—	940	LO ν_1
	—	—	936	936	TO ν_1
	629	626		629	LO ν_2
	—	—	623	623	TO ν_2
	486	—	—	490	LO ν_4
	—	483	482	489	TO ν_4

[a]Polarized Raman; [b]Analysis of i.r. reflection spectra. [c] TO mode of CaO below the low frequency limit of MIR measurements.

determined from analysis of single crystal reflection data of Ketelaar *et al.* [8].

3. DISCUSSION

As described by Berreman [3], at the time of his publication there were four methods employed to measure LO modes in crystals: (1) Measurement of ω_t (TO mode frequency), ϵ_0, and ϵ_∞ (ϵ dielectric constant) and use of the Lyddane–Sachs–Teller relation; (2) varying ω_e (LO mode frequency) to obtain the best fit to reststrahlen reflectance data; (3) determination (by reflectance) of the frequency at which the real part of ϵ vanishes; (4) inelastic neutron scattering experiments. A fifth method, polarized Raman spectra of single crystals, must be added to this list. Methods 1–4 are difficult and often subject to large errors or uncertainties in the frequencies obtained. LO modes can be accurately determined from polarized Raman experiments, but this technique is limited to the modes that are both i.r. and Raman active in acentric crystals, and the measurements should be made on single crystals. Finally, Berreman's demonstration that the LO mode can be observed in absorption or polarized reflectance measurements on thin films of LiF using oblique angles of incidence [3] indicated that this additional technique might be generally applied to other crystals.

The data collected in Table 1 show remarkable agreement between the LO modes measured in our PSR spectra and the LO modes observed by other techniques. In the case of CaO, MgO, and $NaNO_3$, we believe that our measurements are more accurate than those previously reported. For materials such as $NaClO_3$ or ZnO in which several LO and TO modes occur in close proximity, an unambiguous assignment of the observed bands could not be made from PRS data alone. However, for crystals which have only one optical mode (CaO and MgO) or in which the optical modes occur in isolated spectral regions ($NaNO_3$), the results of our measurements show that the PSR technique provides a simple method for determining LO mode frequencies. We also measured the PSR spectra of both evaporated thin films and pressed surfaces of LiF. Our results qualitatively agreed with those of Berreman[3] although the peak position of the LO mode appeared to shift upward to a maximum of 684 cm^{-1} as the angle of incidence was increased from 45 to about 60°. The frequency reported by Berreman was 669 cm^{-1} for an incident angle of 34°[3].

The *p* and *s* polarized spectra (Figs. 1 and 2 and Table 1) exhibited the characteristics expected from the previous work on LiF[3]. The LO modes appear predominantly in the *p* polarized spectra while the TO modes are stronger in the *s* polarized spectra. The LO mode frequencies were observed to be slightly displaced toward the lower TO frequencies in the *s* polarized spectra (Table 1). The *s* polarized reflectance spectrum of $NaClO_3$ shown in Fig. 2 is nearly identical with the reflectance spectrum obtained from a single crystal of this material reported by Andermann and Dows[9]. We found, in general, for all of the materials studied, the *s* polarized spectra resembled the reflectance spectra previously reported, exhibiting the high frequency reflection minima which have formerly been cited as characteristic of all reflection spectra. The *p* polarized spectra, however, did not exhibit these minima as the spectra in Figs. 1 and 2 show. The reflectance spectra recorded with the polarizer removed always resembled the *s* polarized spectra.

The MIR spectra measured for the materials listed in Table 1 gave no evidence of absorption due to the LO components. Weak absorption around 500 cm^{-1} is mostly due to the KRS-5 prism (Figs. 1 and 2). It has been previously demonstrated[10] that the MIR technique is a superior method for measuring i.r. TO mode frequencies. This contention is further supported by the results of the present investigations and from recent studies of crystalline carbonates[4]. It thus appears that a combination of PSR and MIR measurements provide simple and convenient means for determining LO and TO mode frequencies in polycrystalline materials.

REFERENCES

1. BATES J. B., *J. chem. Phys.* **54**, (1971).
2. BATES J. B., *ibid.* **54**, (1971).
3. BERREMAN D. W., *Phys. Rev.* **130**, 2193 (1963).
4. BROOKER M. H. and BATES J. B., *J. chem. Phys.* **54**, 4788 (1971).
5. WILKINSON G. R. in *Molecular Spectroscopy*, Proceedings of a Conference held at Brighton, England, 7–19 April 1968, (Edited by P. Hepple) The Institute of Petroleum, London (1968).
6. ARGUELLO C. A., ROUSSEAU D. L. and PORTO S. P. S., *Phys. Rev.* **181**, 1351 (1969).
7. HARTWIG C. M., Rousseau D. L. and PORTO S. P. S., *Phys. Rev.* **188**, 1328 (1969).
8. KETELLAAR J. A. A., HAAS C. and FAHRENFORT J., *Physica* **20**, 1259 (1954).
9. ANDERMANN G. and DOWS D. A., *J. Phys. Chem. Solids* **28**, 1307 (1967).
10. BROOKER M. H., *J. chem. Phys.* **53**, 4100 (1970).

J. Phys. Chem. Solids, 1971, Vol. 32, pp. 2409–2413. Pergamon Press. Printed in Great Britain

LOW TEMPERATURE 'EDGE EMISSION' OF CdSe

I. FILINSKI*
Chemical Laboratory B, Technical University of Denmark, Lyngby, Denmark

and

B. WOJTOWICZ-NATANSON
Institute of Experimental Physics, University of Warsaw, Warsaw, Poland

(*Received* 6 *June* 1969; *in revised form* 7 *December* 1970)

Abstract—The time resolved spectra and the dependence on the excitation intensity of the phonon assisted edge emission of CdSe single crystals have been measured in the temperature range 4·2–77°K. It is concluded that at 4·2°K this emission is mainly due to the electronic transitions between donor-acceptor pairs, while at higher temperatures the contribution of free to bound transitions may become dominant. Values of the ionization energies of donor and acceptor involved have been obtained.

1. INTRODUCTION

THE BROAD emission band or so called 'edge emission' consisting of a series of maxima spaced by the longitudinal optical phonon energy appears in the luminescence of several II–VI compounds. Often two or sometimes more series separated by a few hundredth of an eV are observed. The relative intensities of these series depend upon the crystal, the intensity of excitation and the temperature. The high energy series (HES) is usually attributed to recombination of free electrons with holes bound to acceptors ('free to bound' recombination) while the low energy series (LES) is interpreted as being due to donor-acceptor pair-recombination or 'bound to bound' recombination.

The best proof that LES is due to pair recombination involves the observation and identification of sharp lines due to transitions at close pairs. Such lines have been observed in several semiconductors[1–6] including direct band gap semiconductors ZnSe[7] and CdS[8]. The other characteristic properties of pair recombination exhibited by LES are, long nonexponential time decay, displacement of the band maxima to lower energies with time and shift of maxima to higher energies as the excitation intensity is increased[1–9].

These properties can be used for identification of the origin of the 'edge emission' bands when the discrete lines of the pair spectrum are not seen.

These 'pair lines' have not been observed in CdSe. In order to obtain some information on the origin of the edge emission in CdSe we have studied: the time resolved spectra in the temperature range between 4·2 and 77°K, and the dependence of luminescence intensity on the level of excitation.

2. EXPERIMENTAL

The luminescence of CdSe single crystals (thin platelets) was excited by high intensity pulsed light from a Xenon flash tube (20 p.p.s., 0·2 Joule per flash) and was analysed by a SPM-2 grating monochromator (with 15 Å/mm dispersion in the investigated spectral region). Spectra were taken with a PAR boxcar integrator followed by a logarithmic converter.

3. RESULTS AND DISCUSSION

The time resolved spectra at 4·2°K with different retardations in respect to the excitation pulse are shown in Fig. 1. The

---

*On leave from the University of Warsaw.

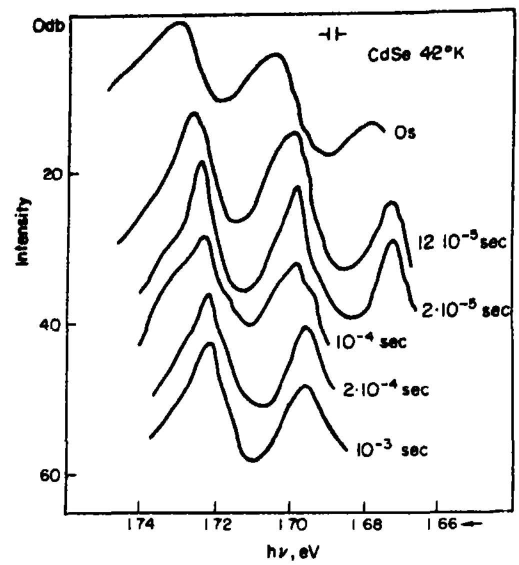

Fig. 1. Time resolved spectra of the edge emission at 4·2°K. The intensity of emission is in Logarithmic scale.

positions of maxima shift with time towards lower energies. The halfwidths of maxima diminish significantly with time (from 16 meV at 0 μs to 3 meV at 20 μs). For longer times however, this tendency is stopped and after 1 ms the maxima are somewhat broadened. A similar effect was observed for GaP[5]. Considering the shape of the high energy side of curves taken at 12 μs and at 20 μs one can detect a second hand, shifted approximately by 10 meV towards higher energies.

As can be seen from Fig. 2 the high energy series—HES, which was hardly noticeable at 4·2°K becomes as strong as the low energy series—LES at 20°K. At higher temperatures LES diminishes and at 60°K it is not seen any more.

The position and the halfwidth of the LES is also influenced by the intensity of the exciting light (Fig. 3). Pronounced broadening and shift of maxima towards higher energies for increasing intensity of excitation is clearly seen.

It is difficult to establish the exact position of the HES as a function of temperature and of the time after excitation because of the strong contribution of the LES at the lowest temperatures. It seems however, that there

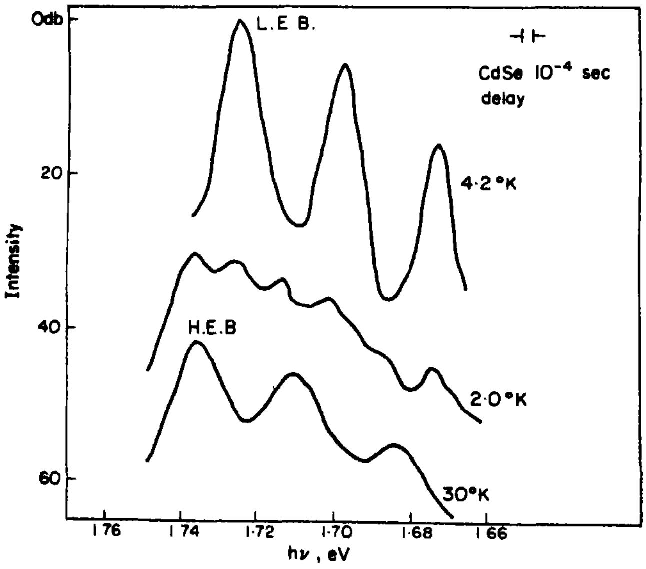

Fig. 2. Time resolved spectra of the edge emission at 100 μs after excitation for various temperatures (a) 4·2°K. (b) 20°K, (c) 30°K. Logarithmic scale.

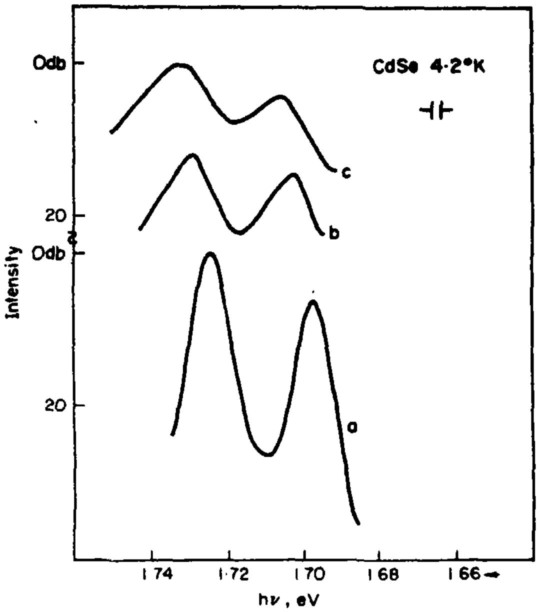

Fig. 3 Edge emission spectra taken at 4·2°K (a) in a.c. method and in pulse method (b and c). The excitation intensity for (c) is 7 times as strong as for (b). Logarithmic scale.

is no appreciable time shift of the HES. Taking this into account and the similarity to CdS we assume that the HES is due to the free to bound transitions (recombination of free electrons with holes trapped on acceptors) as was suggested earlier[10]. Extrapolating the position of the first (no-phonon) maximum of the HES to 4·2°K we can estimate the transition energy as 1·736 eV. The band gap at 4·2°K is 1·841 eV[11] so the ionization energy of the acceptor E_a is about 105 meV.

The observed effects in the edge emission of CdSe are very similar to those in CdS. The shift of the LES with time after excitation and with the change in the excitation intensity is easily explained by assuming that the radiation arises from bound to bound transitions i.e. from recombination of electrons trapped on donors with holes trapped on distant acceptors. It is of course of interest to find the values of binding energies of these donors and acceptors although their nature remains still unknown.

It is known that in II–VI compounds the discrete levels in the forbidden gap are connected with crystal defects as well as impurities. These defects act also as binding centers for excitons. At 4·2°K the bound exciton lines I_2 (exciton bound to neutral donor) and I_1 (exciton bound to neutral acceptor) are the most prominent in the exciton spectrum. It seems reasonable to connect the pair spectra with these donors and acceptors[8]. Their ionization energies may be estimated from the positions[11–12] of the respective exciton lines by application of the 'Haynes rule'[13] for acceptors and the 'Halsted and Aven rule'[14] for donors (as in CdSe $m_e/m_h \ll 1$). In this way we get 20 meV for the donor and 90 meV for the acceptor ionization energies. This method gives, however, only rough estimates.

There are only few data concerning shallow donors in CdSe. The donor ionization energy estimated from transport phenomena is in the range 14–30 meV[11]. Calculations by Trylski[15] and by Gorzkowski and Suffczynski[16] give the value as 16·6 and 17·65 meV, respectively. Taking into account the above mentioned values and the value of 20 meV from the bound exciton position, it seems reasonable to estimate the donor ionization energy in CdSe as being 18 (± 2 meV).

With the known energy gap and the donor ionization energy the ionization energy of the acceptor involved in the 'bound to bound' transition may be found. For sufficiently distant pairs separated by **r** the energy of emitted photons is given by

$$h\nu = E_g - E_a - E_d + E_c \qquad (1)$$

where E_g is the band gap energy, E_a and E_d are, respectively, acceptor and donor binding energies and

$$E_c = e^2/\epsilon r \qquad (2)$$

is the Coulomb attraction between the hole and the electron, where ϵ is the static dielectric constant of the material.

In case of no-phonon emission of pair recombination the assumption of a random distribution of donors and acceptors and of much higher concentration of donors than of acceptors (CdSe is always *n*-type) leads to the following formula giving the intensities of emitted light as a function of energy at time t[5, 6]:

$$I_{E_c}(t) = I_0 E_c^{-4} \exp\left\{-\frac{4E_d}{E_c} - W_0 t \exp\left(-\frac{4E_d}{E_c}\right)\right\}. \tag{3}$$

Here W_0 is the reaction constant and E_c defined by equation (2) is the Coulomb energy. In this formula the zero of energy was taken at $E_g - E_a - E_d$. The position of the maxima at a given time may be obtained by taken the derivative of the expression (3) with respect to E_c and setting it equal to zero. This leads to the formula for W_0:

$$\ln W_0 = \frac{4E_d}{E_{c\,\max}} + \ln\left(1 - \frac{E_{c\,\max}}{E_d}\right) - \ln t \tag{4}$$

where $E_{c\,max}$ is the Coulomb energy found from the position of the emission peak at time t.

The energy gap E_g in CdSe at 4·2°K (obtained from the exciton spectrum[11] is 1·841 eV.

Assuming $E_d = 18$ meV, the difference $(E_a - E_{c\,\max})$ at various times were calculated from equation (1), using for $h\nu(t)$ the experimentally measured positions of the first (no-phonon) maximum of the LES at 4·2°K. Figure 4 shows $(E_a - E_{c\,\max})$ as a function of time. From this curve the value of $E_{c\,\max}$ at various times were obtained. Setting these values of $E_{c\,\max}$ into formula (4) the reaction constant W_0 was calculated. The best constancy of W_0 with time was obtained for $E_a = 109$ meV. On the other hand taking for the ionization energy of the acceptor the value of 105 meV obtained from the HES spectra and applying the same procedure as above, but now with respect to E_d we get for the ionization energy of the donor $E_d = 22$ meV.

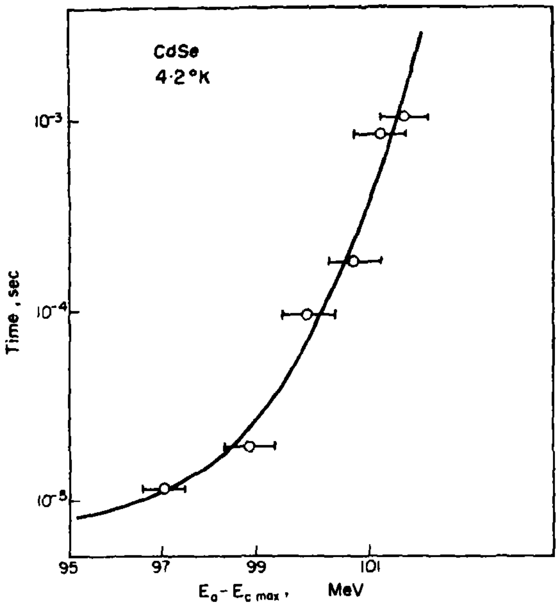

Fig. 4. The difference between the acceptor ionization energy (E_a) and the Coulomb energy ($E_{c\,\max}$) as a function of time after excitation ($E_g = 1·841$ eV, $E_d = 0·018$ eV).

The bound to bound reaction constant. calculated from equation (4) is $W_0 = 1·45 \times 10^7 s^{-1}$. In the limiting case of $r = \infty$ we get 1·714 eV as the recombination radiation energy. Calculating the average separation of pairs for different times atter excitation (taking for dielectric constant $\epsilon \doteq 10$ and for E_c value obtained from the diagram in Fig. 4) we get $r = 100$ Å at 10^{-5}s and $r = 180$ Å at 10^{-3}s. The mean spacing between pairs, calculated from $(4\pi/3)r^3 = 1/N$, is $\langle r\rangle = 189$ Å at concentration 3×10^{16} cm^{-3}. Such pairs will recombine after a few milliseconds. The low value of E_d and the fact that CdSe is a direct band semiconductor are the causes of the fast recombination rate.

4. CONCLUSIONS

From the time resolved spectra in the temperature range 4·2 to 77°K it is concluded that in CdSe, as in other II–VI compounds, there are two edge emission series. The low energy band due to the bound transitions while the high energy band is ascribed to free to bound transitions.

The calculated bound to bound reaction constant for CdSe $W_0 = 1{\cdot}4 \times 10^7\ \mathrm{s}^{-1}$ is smaller than for CdS ($4 \times 10^8\ \mathrm{s}^{-1}$)[3].

The derivation of the donor and acceptor ionization energies, executed in three different ways (from exciton binding energies, from HES and from LES spectra) are consistent, giving $E_d \approx 18$–22 meV and $E_a \approx 90$–109 meV.

Acknowledgements – We would like to thank Dr. W. Wardzynski for stimulating discussions and for his interest in this work. We are also indebted to Professors N. I. Meyer and R. W. Asmussen, Drs. J. Mycielski, T. Skettrup and I. Balslev for critical discussions of the results. One of us (B.W-N.) wishes to express her gratitude to Professor R. W. Asmussen for his kind permission to execute a part of this work in his Laboratory.

REFERENCES

1. THOMAS D. G., HOPFIELD J. J. and GERSHENZON M., *Phys. Rev. Lett.* **10**, 162 (1963).
2. THOMAS D. G., GERSHENZON M. and TRUMBORE F. A., *Phys. Rev.* **133**, A269 (1964).
3. THOMAS D. G., HOPFIELD J. J. and COLBOW K., *Proc. Int. Symposium on Radiative Recombination*, p. 67. Dunod, Paris (1964).
4. TRUMBORE F. A. and THOMAS D. G., *Phys. Rev.* **137**, A1030 (1965).
5. THOMAS D. G., HOPFIELD J. J. and AUGUSTYNIAK W. M., *Phys. Rev.* **140**, A202 (1965).
6. WARDZYNSKI W., WOJAKOWSKI A. and ZDANOWICZ W., *Phys. Lett.* **29A**, 547 (1969).
7. DEAN P. J. and MERZ J. L., *Phys. Rev.* **178**, 1310 (1969).
8. HENRY C. H., FAULKNER R. A. and NASSAU K., *Phys. Rev.* **183**, 798 (1969).
9. COLBOW K., *Phys. Rev.* **141**, 742 (1966).
10. WARDZYNSKI W. and WOJTOWICZ-NATANSON B., *Proc. Int. Symposium Radiative Recombination*, p. 287. Dunod, Paris (1964).
11. *Physics and Chemistry of* II–VI *Compounds*, pp. 344, 402, 403, 588, (Edited by M. Aven) North-Holland, Amsterdam (1967).
12. FILINSKI I. and WOJTOWICZ-NATANSON B., *J. Phys. Chem. Solids*, to be published.
13. HAYNES J. R., *Phys. Rev. Lett.* **4**, 361 (1960).
14. HALSTED R. E. and AVEN M., *Phys. Rev. Lett.* **14**, 64 (1965).
15. TRYLSKI J., *Phys. status solidi* **21**, K53 (1967).
16. GORZKOWSKI W. and SUFFCZYNSKI M., *Phys. Lett.* **29A**, 550 (1969).

J. Phys. Chem. Solids, 1971, Vol. 32, pp. 2415–2421. Pergamon Press. Printed in Great Britain

NUCLEAR MAGNETIC RESONANCE KNIGHT SHIFTS AND QUADRUPOLE EFFECTS IN TRANSITION METAL DIBORIDES

G. C. CARTER
Institute for Materials Research, National Bureau of Standards, Gaithersburg, Md. 20760, U.S.A.
and
J. C. SWARTZ
Edgar C. Bain Laboratory For Fundamental Research, United States Steel Corporation Research Center, Monroeville, Penna. 15146, U.S.A.

(*Received* 30 *November* 1970)

Abstract—Nuclear magnetic resonance data for ScB_2, YB_2 and MnB_2 are presented. These data together with earlier NMR data provide a complete picture of the 3*d* and 4*d* transition metal diborides: ScB_2 through MnB_2 and YB_2 through MoB_2. The Knight shifts, electric quadrupole coupling constants, and linewidths of the central resonance of the ^{45}Sc and ^{11}B nuclei in ScB_2 are essentially temperature independent in the range 4–300°K. The boron Knight shifts $\mathscr{K}(B)$ are 0·00(1)%, −0·004(10)% and −0·05(2)% in ScB_2, YB_2 and MnB_2, respectively. $\mathscr{K}(Sc) = 0{\cdot}07(1)\%$ and $\mathscr{K}(Y) = 0{\cdot}20(3)\%$ in the respective diborides. The difference between these values and the higher values for metallic Sc and Y is attributed primarily to reduced orbital and Pauli contributions. For the 3*d* series ScB_2 to MnB_2, the Knight shifts, electronic specific heats, magnetic susceptibilities and transport properties indicate increasing *d*-electron character with increasing group number. The quadrupole coupling constant of ^{11}B across both 3*d* and 4*d* series does not correlate with the *c*/*a* ratio or unit cell volume. This may indicate deviation of the boron atoms from a planar configuration.

1. INTRODUCTION

To obtain information on the electronic structure of the transition metal diborides, we have observed nuclear magnetic resonance (NMR) spectra of the diborides of groups III–VII transition elements. Our results[1] for TiB_2, VB_2, CrB_2 and NbB_2 are approximately the same as those already reported by Silver and Kushida[2]. This communication reports NMR results on ScB_2, YB_2 and MnB_2 and collates these with previous information on the 3*d* and 4*d* diboride series.

The diborides have the hexagonal AlB_2-type (C32) structure, with the transition atoms at sites with hexagonal symmetry (6/mmm) and the boron atoms at sites with trigonal symmetry $(\bar{6}/m2)$[3]. Thus, for both sites, axial Knight shifts and electric quadrupole effects are expected to occur. The spacing of the transition atoms in both *a* and *c* directions is almost the same as that in the pure transition metals[3]. The boron atoms are in interstitial planes where hyperfine effects of the *d* electrons can be anticipated. Various other data giving evidence of *d* electron effects are reviewed in the Discussion Section.

2. EXPERIMENTAL

The samples were prepared by pulse heating compacted stoichiometric mixtures of the powdered elements in an argon atmosphere.* Three samples of ScB_2 were studied. As initially prepared, the first sample contained some unreacted scandium metal (detected by NMR) and some other unidentified phases (detected by X-ray diffraction). After crushing and reheating this sample to the reaction temperature, the pure scandium NMR signal was not evident and only one weak unidentified line remained in the X-ray pattern. The

---

* Most of the samples were obtained from Cerac Co., Butler, Wisconsin, U.S.A.; the remaining samples were prepared at the National Bureau of Standards by D. P. Fickle.

NMR and X-ray results on the other samples indicated that the second sample was similar to the reheated first sample and the third sample was somewhat superior. Two samples each of YB_2 and MnB_2 were studied. X-ray analyses showed some second phases in all four of these samples.

The NMR spectra were obtained with a Varian wide-line spectrometer. Time averaging techniques were used to build up sufficient signal-to-noise ratios. The quoted results were obtained by averaging the results of increasing and decreasing field sweeps.

3. RESULTS

ScB₂

Typical spectra of ^{45}Sc are shown in Fig. 1. As shown in Table 1, the value for the quadrupole coupling constant, e^2qQ/h, as deduced from the 3 pairs of satellites is the same as that derived from the central resonance, using second order quadrupole theory[5]. The linewidth between the two main central peaks varied inversely with frequency between $\nu = 4$ and 16 MHz (i.e., pure 2nd order quadrupole broadening). No axial Knight shift pattern was apparent from the observed spectra. From the central resonance, the value for ν_0 could be found[5] from which the isotropic Knight shift listed in Table 1 was obtained.

The boron spectrum is similar to that of other diborides[1, 2]. The central line ($m = \frac{1}{2} \rightleftarrows m = -\frac{1}{2}$) shows a little structure in the middle* which does not disappear as one goes to higher frequencies (up to 21·5 MHz). We attribute much of this structure to boron in the probe itself, as a narrow resonance of the empty probe occurs at that position.

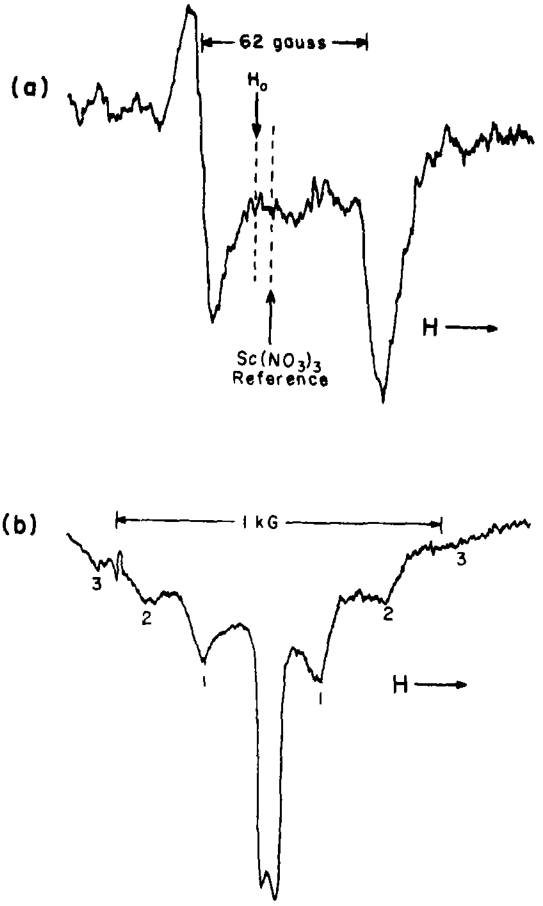

Fig. 1. ^{45}Sc resonance at 8 MHz and room temperature. (a) The central resonance as split due to second order quadrupole effect. The resonance was taken in the absorption mode averaging 304 scans. (b) The total resonance taken in the dispersion mode. This spectrum represents the average of 292 scans. The signal on top of the third satellite on the low field side is due to Al in the probe.

The ^{11}B quadrupole satellite lines were somewhat lower in intensity with respect to the central resonance for samples No. 1 and No. 2 than for sample No. 3. Differing local environmental conditions at the boron sites are the most likely cause of this low intensity of the satellites[6], although the reheating of the first sample did not increase the satellite intensity noticeably. The ^{11}B central resonance is affected only little by varying local environmental conditions due to the small hyperfine coupling constant. This is reflected in the constancy of the linewidth for the three samples.

---

*Central structure in the spectrum of CrB_2 has been noted previously[2].

Table 1. *Numerical results of NMR. The estimated error in the last decimal is indicated in brackets beside each number*

		^{45}Sc in ScB_2			^{11}B in ScB_2		^{89}Y in YB_2	^{11}B in YB_2	^{11}B in MnB_2
	300°K	77°K	4°K	300°K	77°K	4°K	300°K	300°K	300°K
$\mathscr{K}$, %	+0·07(1)[a]	+0·07(2)[a]	+0·07(2)[a]	0·00(1)[b]	0·00(1)[b]	−0·006(8)[b,c]	0·20(3)[d]	−0·004(10)	−0·05(2)
$\frac{e^2qQ}{h}$, MHz[e] (from 2nd order central structure)	6·2(2)	6·1(2)	6·1(3)	—	—	—	—	—	—
$\frac{e^2qQ}{h}$, MHz (from quadrupole satellites)	6·1(2)[e]	6·2(2)[e]	6·2(3)[e]	0·52(2)[f]	0·53(7)[f]	0·50(6)[f]	—[g]	0·34(2)[e]	(see text)
peak to peak width, in gauss (10^{-4} Weber/m²)	38(3)	40(3)	40(3)	12(1)	12(2)	12(1)	12(2), abs. 20(3), disp.	8(1)	30(5)
		at 16 MHz			field indep.		at 2·7 MHz	4–16 MHz	8–16 MHz

[a] ^{45}Sc with respect to a concentrated solution of $Sc(NO_3)_3$.

[b] ^{11}B with respect to triethyl borate. Measurement hampered by boron signal of probe. The indicated room temperature value includes a set of small, negative values measured with three Varian probes at 4, 8 and 16 MHz and a small, positive value measured with a Varian probe at 21·5 MHz.

[c] Some saturation effects.

[d] Measured at 2·7258 MHz and compared with the ^{14}N resonance of HNO_3 at 4·0115 MHz, using $\nu^{14}/\nu^{89} = 1{\cdot}47462$ (Ref. [4]) to calculate $(\nu_{metal} - \nu_{salt})/\nu_{salt}$.

[e] Using $\gamma = 1{\cdot}3660$ kHz/G.

[f] Using $\gamma = 1{\cdot}0344$ kHz/G.

[g] ^{89}Y has spin ½ – no quadrupole effects present.

YB_2

The NMR spectra of the two samples were similar and from these the values for the ^{89}Y and ^{11}B Knight shifts listed in the table were determined. The ^{89}Y lineshape showed some asymmetry probably due to the second phase.

MnB_2

Barnes and Creel[7] have reported e^2qQ/h and $\mathscr{K}_{ax}$ values for ^{11}B but there seems to be no report of $\mathscr{K}_{iso}$(B) values. Our measurements between 8–21 MHz determine the value listed in the table. The lineshape of the central resonance of ^{11}B was rather symmetric and relatively broad. The quadrupole satellites were poorly defined indicating inferior quality of our samples to the one employed by Barnes and Creel. The ^{55}Mn resonance was not observed.

4. DISCUSSION

Knight shifts

The present results together with some earlier data for the diborides are displayed in Figs. 2 and 3 as a function of the transition atom group. The electronic specific heat coefficient. γ_{el}, shown in Fig. 2(a), suggests (neglecting electron–phonon effects) that the d-electrons in ScB_2 and TiB_2 do not contribute significantly to the density of states at the Fermi surface, $N_\gamma(E_F)$. At VB_2 there is some d-electron influence, which increases substantially for CrB_2 and a (Cr–Mn)B_2 alloy, and then decreases rather sharply again for MnB_2. The room temperature magnetic susceptibility, χ, is shown in Fig. 2(b). The χ behavior generally follows the γ_{el} curve rather well, including the slight dip in magnitude near TiB_2 before becoming substantially larger for CrB_2 and MnB_2. Both of the latter compounds exhibit magnetic order: CrB_2 has a Néel transition near 86°K[7, 8], and MnB_2 has a Curie transition near 145°K [7, 10, 11]. The electrical resistivities of ScB_2 and TiB_2 are much lower than those of VB_2 and CrB_2[14, 15]. TiB_2 has a large negative Hall coefficient whereas VB_2 and CrB_2 have near zero Hall coefficients[14, 15]. Such transport properties suggest the onset of a d-like band between TiB_2 and VB_2 in this series. Therefore, the electronic specific heat, magnetic and transport properties all suggest that d electron effects are negligible for ScB_2 and TiB_2 and become

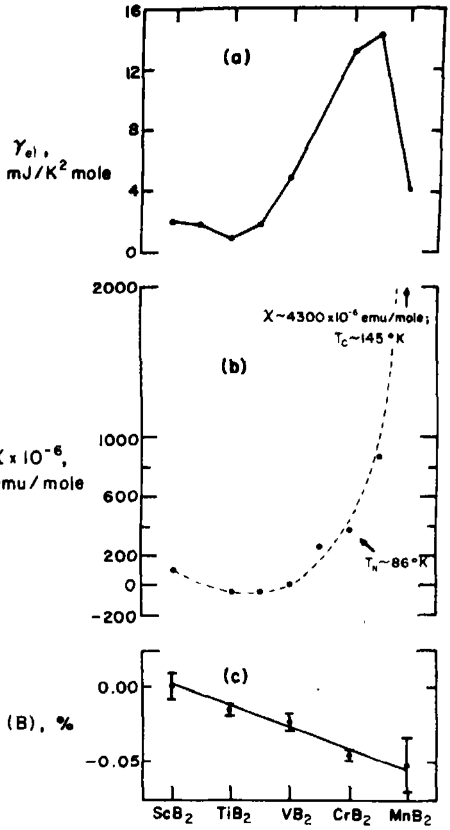

Fig. 2. Properties of the diborides ScB_2. TiB_2. VB_2. CrB_2 and MnB_2 as a function of position of the transition metal in the periodic tables. (a) Electronic specific heat coefficient. γ_{el}. from Ref. [8]. The points midway between (ScB_2. TiB_2). (TiB_2, VB_2) and (CrB_2. MnB_2) are for the compounds $(Sc_{0.5}, Ti_{0.5})B_2$. $(Ti_{0.5}, V_{0.5})B_2$ and $(Cr_{0.5}, Mn_{0.5})B_2$. (b) Room temperature magnetic susceptibility. χ: ScB_2 from Ref. [9]; TiB_2 up to $(Cr_{0.5}Mn_{0.5})B_2$ from Ref. [8]; MnB_2 data from Refs. [7.10 and 11]. (c) Knight shifts of the boron resonance: ScB_2 and MnB_2—present results; TiB_2, VB_2 and CrB_2 from Refs. [1] and [2]

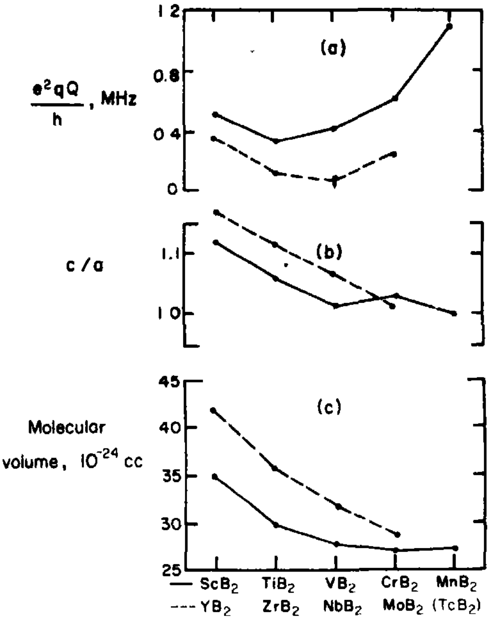

Fig. 3. (a) Electric quadrupole coupling constants at the boron sites. For TB_2 of the 3*d* transition metal series, points are connected with a solid line; for the 4*d* series points are connected with a dashed line: ScB_2—present results; TiB_2 from Refs. [1] and [2]; VB_2 and CrB_2 from Ref. [2]; MnB_2 from Ref. [7]; YB_2 present results; ZrB_2, NbB_2, MoB_2 from Ref. [2]. (b) c/a values: ScB_2 and MnB_2 from Ref. [3]: TiB_2, VB_2, CrB_2 from Refs. [3] and [12]; YB_2 from Ref. [13], ZrB_2, NbB_2, MoB_2 from Ref. [2]. (c) Molecular volume: ScB_2 and MnB_2 from Ref. [3]; TiB_2, VB_2 and CrB_2 from Refs. [3] and [12]; YB_2 from Ref. [13]; ZrB_2, NbB_2 and MoB_2 from Ref. [2].

significant for VB_2 and the later diborides.[*]

Figure 2(c) shows the Knight shifts of boron in the 3*d* diborides.[†] There is an obvious trend of increasingly negative values with group number. Since the intra-atomic contributions to $\mathscr{K}$(B) (viz. the Pauli term and the core polarization from the valence 2*p* electron) are if anything positive[17], the existence of negative $\mathscr{K}$(B) values must be attributed to inter-atomic effects. The observation of negative Knight shifts at non-magnetic sites in compounds containing a magnetic component is not unusual[18–21]. The case of silicon in V_3Si is similar to that of boron in the present compounds in that the atomic hyperfine field is positive[17] yet $\mathscr{K}$(Si) in V_3Si is negative[18]. Moreover, the $\mathscr{K}$ vs. χ plot shows that the negative hyperfine field at Si is associated with the *d* electron paramagnetism[22]. These results have recently been ascribed to inter-atomic conduction electron polarization[17] and a similar model may apply to the diborides as well. Regardless of the model details, Fig. 2(c) clearly indicates inter-atomic *d* polarization effects which increase with increasing group number. The positive contributions to $\mathscr{K}$(B) are expected to be small because the hyperfine coupling constant of boron is quite small. In the case of ScB_2 the low density of *d* electrons noted previously suggests insignificant *d* polarization, so that the zero value of $\mathscr{K}$(B) signifies an absence of hyperfine effects rather than the cancellation of appreciable positive and negative contributions.

Knight shifts of the transition atoms sites in TB_2 are available for $T = $ Sc, Y and V. In all cases the shifts are substantially reduced from the pure metal values. The values 0·07 and 0·20% for ScB_2 and YB_2 compare with 0·25 and 0·37 per cent respectively for pure Sc and Y[23]. $\mathscr{K}$(V) is +0·58 per cent in pure vanadium[24] and −0·3 per cent in the diboride[1, 2, 8]. It has been established that the dominant contribution to $\mathscr{K}$(V) in pure V arises from orbital paramagnetism [25]. The anticipated orbital shift for pure Sc and Y is smaller but still may be the dominant contribution to the observed shift. The still lower values for $\mathscr{K}$(Sc) and $\mathscr{K}$(Y) for the diborides could result from a decrease in the positive shift contributions (orbital and Pauli) or from an increase in the magnitude of the negative contributions. A $\mathscr{K}$ vs. χ plot would distinguish these possibilities but unfortunately this is ill-determined because neither $\mathscr{K}$ nor χ has much temperature dependence. In view of the absence of d character in ScB_2 indicated by the data in Fig. 2, the reduction in $\mathscr{K}$(Sc) between the metal and diboride must be primarily a reduction in the positive terms, the largest of which may be the orbital term. Suppression of the orbital term in $\mathscr{K}$(V) of VB_2 would help to account for the large reduction from the pure metal value in this case also.*

---

[*] Recent band calculations of McAlister[16] for ScB_2 through CrB_2 indicate a trend of increasing density of states with group number, which is consistent with the experimental picture.

[†] A similar plot for the 4*d* diborides using the present data and those reported by Silver and Kushida[2] shows a strong trend toward negative $\mathscr{K}$(B) between YB_2 and ZrB_2 followed by small negative values for NbB_2 and MoB_2.

Sufficient electronic specific heat and magnetization data are not available for detailed comparisons.

Electric quadrupole interaction

Figure 3 compares the boron quadrupole coupling constants for the 3d and 4d diborides with the c/a ratios and the unit cell volumes. While the latter two quantities decrease almost monotonicly with increasing transition group number, the coupling constants first decrease and then increase. Evidently the electric field gradient (EFG) at the boron sites is not a simple function of the volume or tetragonality of the space available at these sites.

One factor which has not been mentioned in previous discussions of the EFG is pleating or puckering of the hexagonal boron rings [26]. The symmetry of the AlB_2 space group [27] does not require the boron atoms of each ring to be co-planar; alternate atoms may be situated δ above and below the central plane of the ring. Such pleating of the boron rings would increase the B–B spacings and decrease the B–T spacings. Since the threefold symmetry at the boron sites would still prevail, the asymmetry parameter of the NMR pattern, $\eta = (\partial^2V/\partial x^2 - \partial^2V/\partial y^2)/(\partial^2V/\partial z^2)$, would remain zero, and the spectrum would not reveal the pleating. Nevertheless, the lack of correlation between the observed EFG and the unit cell parameters in Fig. 3 indicates the importance of other varying factors, one of which may be the degree of pleating.

5. CONCLUSION

A review of existing data on electronic specific heat, magnetic and transport properties of the 3d diborides has suggested negligible d electron effects in ScB_2 and TiB_2 and obvious d effects commencing with VB_2. Qualitatively consistent with this picture, the boron Knight shift is zero in ScB_2 and becomes increasingly negative (indicative of inter-atomic d polarization) in the subsequent 3d diborides. In view of the lack of d character in ScB_2, the smaller Knight shift of Sc in ScB_2 than in pure Sc is ascribed to smaller Pauli or orbital shift contributions rather than to greater d polarization. The smaller values of $\mathscr{K}$(V) in VB_2 relative to that in pure V may result from both weaker orbital and stronger d polarization effect in the diboride. Although there is less information on the 4d diborides, the Knight shift data suggest qualitative similarities with the 3d diborides.

The lack of correlation of the EFG at the boron site with the volume or tetragonality of the unit cell has suggested that the magnitude of pleating of the boron ring structure is an important factor. As yet there is no quantitative information on the pleating magnitude with which to test this hypothesis.

Finally it should be noted that previous investigations of more metal-rich borides (T_2B and TB) have suggested a rigid-band correlation with the band structures of the pure transition elements[28, 29]. Such a correlation for the diborides is not obvious. A recent NMR study of the various vanadium borides[30], shows that $\mathscr{K}$(V) varies systematically with the number and configuration of adjacent boron atoms. Further studies of this sort would aid in developing correlations between the electronic structures of the diborides and the pure transition metals.

---

*Here again, the lack of any strong temperature dependence of $\mathscr{K}$(V) or χ for VB_2[8] precludes the application of a $\mathscr{K}$-χ plot to identify the d contribution to $\mathscr{K}$(V).

Acknowledgements—Helpful discussions with L. H. Bennett, R. E. Watson, and F. L. Carter, X-ray analyses by C. J. Bechtoldt, and laboratory assistance by R. L. Parke are gratefully acknowledged.

REFERENCES

1. CARTER G. C. and SWARTZ J. C., National Bureau of Standards, unpublished research (1969).
2. SILVER A. H. and KUSHIDA T., *J. chem. Phys.* **38**, 865 (1963).
3. PEARSON W. B., *Handbook of Lattice Spacings and Structures of Metals*, Vol. 2, Pergamon Press, New York (1967).
4. FULLER G. H. and COHEN V. W., Nuclear Data Tables, Vol. 5, Academic Press (1969).
5. ROWLAND T. J., *Prog. Math. Sci.* **9**, pp. 31–32 (1961).
6. See for example, McCART B. R. and BARNES R. G., *J. chem. Phys.* **48**, 127 (1968).
7. BARNES R. G. and CREEL R. B., *Phys. Lett.* **29A**, 203 (1969).
8. CASTAING J., CAUDRON R., TOUPANCE G. and COSTA P., *Solid State Commun.* **7**, 1453 (1969).
9. PESHEV P., ETOURNEAU J. and NASLAIN R., *Mat. Res. Bull.* **5**, 319 (1970).
10. CADEVILLE M. C., *J. Phys. Chem. Solids* **27**, 667 (1966).
11. ANDERSSON L., DELLBY B. and MYERS H. P., *Solid State Commun.* **4**, 77 (1966).
12. ARONSSON B., a chapter in *Modern Materials*, Vol. 2 (Edited by H. Hausner), Academic Press, New York (1960).
13. ELLIOTT R. P., *Constitution of Binary Alloys, First Supplement*, p. 143, McGraw-Hill, New York (1965).
14. JURETSCHKE H. J. and STEINITZ R., *J. Phys. Chem. Solids* **4**, 118 (1958).
15. WILLIAMS W. S. and DOLLOFF R. T., *Bull. Am. phys. Soc.* **4**, 228 (1959).
16. McALISTER A. J., National Bureau of Standards, unpublished computations (1970).
17. BENNETT L. H., WATSON R. E. and CARTER G. C., *J. Res. Natn. Bur. Stand.* **74A**, 569 (1970).
18. SHULMAN R. G., WYLUDA B. J. and MATTHIAS B. T., *Phys. Rev. Lett.* **1**, 278 (1958); BLUMBERG W. E., EISINGER J., JACCARINO V. and MATTHIAS B. T., *Phys. Rev. Lett.* **5**, 149 (1960).
19. JACCARINO V., *J. appl. Phys.* **32S**, 102 (1961); JONES E. D. and BUDNICK J. I., *J. appl. Phys.* **37**, 1250 (1966).
20. JONES E. D., *J. appl. Phys.* **39**, 1090 (1968) and *Phys. Rev.* **180**, 455 (1969).
21. SAJI H., YAMADAYA T. and ASANUMA M., *J. phys. Soc. Japan* **21**, 255 (1966).
22. CLOGSTON A. M. and JACCARINO V., *Phys. Rev.* **121**, 1357 (1961).
23. BARNES R. G., BORSA F., SEGEL S. L. and TORGESON D. R., *Phys. Rev.* **137**, A1828 (1965).
24. DRAIN L. E., *Proc. phys. Soc.* **83**, 755 (1964).
25. CLOGSTON A. M., GOSSARD A. C., JACCARINO V. and YAFET Y., *Rev. mod. Phys.* **36**, 170 (1964); BUTTERWORTH J., *Proc. phys. Soc.* **83**, 71 (1964).
26. GOLDSCHMIDT H. J., *Interstitial Alloys*, pp. 265–266, Plenum Press, New York (1967).
27. *International Tables for X-ray Crystallography*, Vol. 1, The Kynoch Press, England (1952).
28. LUNDQUIST N. and MYERS H. P., *Arch. Phys.* **20**, 463 (1961); CADEVILLE M. C. and MEYER A. J. P., *Compt. Rend.* **255**, 3391 (1962); CADEVILLE M. C., DANIEL E. and MEYER A. J. P., Colloques Internationaux du Centre National de la Recherche Scientifique, Orsay #157, p. 361 (1965); CADEVILLE M. C. and DANIEL E., *J. Physique* **27**, 449 (1966); CADEVILLE M. C., JESSER R. and SCHWAB A., 2nd International Conference on Solid Compounds of Transition Elements, Enschede (1967)
29. TYAN Y. S., TOTH L. E. and CHANG Y. A., *J. Phys. Chem. Solids* **30**, 785 (1969).
30. BARNES R. G., CREEL R. C. and TORGESON D. R., *Solid State Commun.* **8**, 1411 (1970).

J. Phys. Chem. Solids, 1971, Vol. 32, pp. 2423–2427. Pergamon Press. Printed in Great Britain

ACCURATE NUMERICAL METHOD FOR CALCULATING SPECTRA IN SOLIDS–IV. EXTENSION TO TRIGONAL CRYSTALS*

E. FINKMAN†, Z. KAM, E. COHEN and G. GILAT
Department of Physics, Technion-Israel Institute of Technology, Haifa, Israel

(*Received* 23 *November* 1970)

Abstract—The extrapolation method of calculating frequency distribution functions is extended to trigonal crystals. The generalization of this method for the calculation of spectral functions can be conveniently accomplished by filling the volume of integration in wave-vector space, by rectangular prisms only, in an exhaustive manner. This is achieved at the cost of using a zone larger than the irreducible Brillouin zone. The way by which the Brillouin zone is transformed into a 'practical' zone is described.

1. INTRODUCTION

THE EXTRAPOLATION method[1–4] for calculating frequency distribution functions has been extensively used in recent years, and has proved to be an accurate and rapidly converging technique of calculating densities of states and derived properties. Its generalization to the calculation of spectra in solids, which takes into account transition probabilities (i.e., matrix elements) has recently been accomplished for the imaginary[5] and real parts[6]. In order to perform a computation of spectral functions in solids one is in general in need of a model which gives simultaneously the dispersion relations in q-space (i.e., $\omega=\omega_j(\mathbf{q})$) and the q-dependence of the transition probabilities (i.e., $F_j(\mathbf{q},\omega)$ according to the notation of Refs. [5] and [6] or $|<j'|M(\mathbf{q})|j>|^2$). Given such a model one should be able, in principle to calculate various spectra (i.e., intensities $I(\omega)$ vs. energy $\hbar\omega$) to a high degree of resolution and compare them with experiment. The present method enables one to extract in a reliable manner fine features inherent to the model, which might otherwise be completely obscured by cruder computations. With the aid of electronic computers the computational resolution of $I(\omega)$ can easily match and even exceed current experimental resolutions and can therefore serve in comparison with experiment as a dependable test of the validity of a given theoretical model. Examples of such experiments are the current-voltage (I–V) characteristics of tunneling experiment in superconductors, phonon or magnon assisted optical transitions between electronic states, localized modes due to impurities observed in i.r. spectra, and other examples. Typical resolution in such experiments is of the order of $0{\cdot}1\ \mathrm{cm}^{-1}$ or less. In other words, if ω_m denotes the range of the spectrum and $\Delta\omega$ is an estimate of the experimental resolution, then $\omega_m/\Delta\omega$ is typically of the order of 10^3–10^4. The extrapolation method can readily match and exceed the above estimates.

The extrapolation method has already been worked out for cubic[1–2] hexagonal[3] and tetragonal[4] systems. The motivation for the present extension to the trigonal system is the recently measured[7] optical side bands due to magnons in antiferromagnetic $FeCl_2$, a crystal which has trigonal symmetry. In the present article we present only the method of extension of the extrapolation method to trigonal crystals. Its actual application will be

---

*Supported in part by Volkswagen Foundation.

†In partial fulfillment of the requirements for the D.Sc. degree in the Department of Physics at the Technion.

published[7] together with the experimental data.

In essence, the extrapolation method is a technique of integration over a specified volume in reciprocal space, which yields in an exhaustive manner all the normal modes of vibrations or other elementary excitations such as spin waves dispersion relations, electronic band structure, etc. This integration is usually accomplished by filling this volume, which in many cases is just the irreducible part of the first Brillouin zone (IBZ), with simply shaped small volumes such as rectangular and triangular prisms. In all cases so far[1–4], except for the hexagonal crystals, it was found possible to fill the IBZ with only rectangular prisms. The rectangular prisms are more easily accessible to computation than the triangular prisms[3] are. Moreover, it was found that if matrix elements are to be included in the calculation for the purpose of computing spectral functions other than mere densities of states, it may be even more difficult to treat the triangular prisms.

In this study we develop a method which enables us to calculate densities of states and spectral functions for hexagonal and trigonal crystals. This is achieved in two stages: First it is shown that it is possible to reconstruct the trigonal IBZ from six hexagonal IBZ's. The connection between the two different lattices is demonstrated by choosing a new hexagonal unit cell, which has three times as many atoms in comparison with the original trigonal primitive cell. Secondly we demonstrate that by enlarging the hexagonal IBZ it can be filled with rectangular prisms only.

2. EXTENSION TO TRIGONAL LATTICES

The trigonal lattice (Fig. 1) can be constructed from three primitive translations that form basis vectors for a rhombohedral unit cell. The elementary translations are given by

$$\begin{aligned}\mathbf{a}_1 &= (s, 0, r),\\ \mathbf{a}_2 &= (-s/2, \sqrt{3}\, s/2, r),\\ \mathbf{a}_3 &= (-s/2, -\sqrt{3}\, s/2, r),\end{aligned} \qquad (1)$$

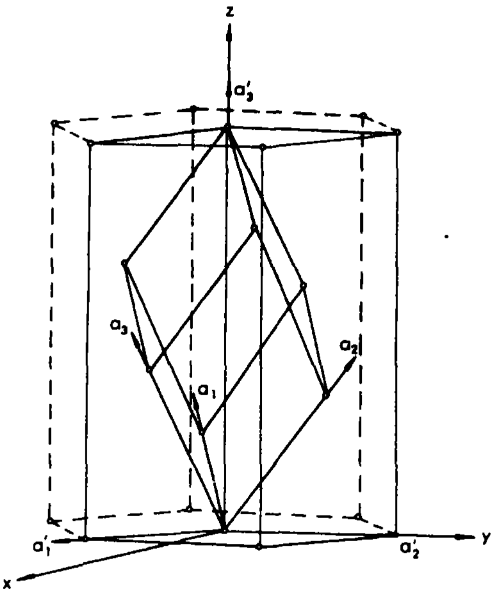

Fig. 1. Trigonal lattice, and basis vectors for trigonal ($\mathbf{a}_1, \mathbf{a}_2, \mathbf{a}_3$) and hexagonal ($\mathbf{a}'_1, \mathbf{a}'_2, \mathbf{a}'_3$) symmetries.

where r and s are given by the hexagonal lattice parameters a and c using the relations

$$s = a/\sqrt{3}; r = c/3, \qquad (2)$$

and the volume of the primitive rhombohedron is $3\sqrt{3}s^2r/2$. Examples of crystals with a trigonal lattice are $CdCl_2$, $NiCl_2$ $CdBr_2$ and $FeCl_2$, with one chemical unit per primitive cell. For instance, in the case of $FeCl_2$ the Fe atom is located at (000), and the two Cl atoms are at $(00 \pm u)$ respectively, with u close to $0.25\,c$.

Next we define a new basis, namely

$$\begin{aligned}\mathbf{a}'_1 &= (3s/2, -\sqrt{3}\, s/2, 0),\\ \mathbf{a}'_2 &= (0, \sqrt{3}\, s, 0),\\ \mathbf{a}'_3 &= (0, 0, 3r)\end{aligned} \qquad (3)$$

and we obtain a unit cell which contains three equivalent primitive trigonal cells. Its volume is $(g\sqrt{3}s^2r/2)$. The symmetry of the new lattice generated by these translations is hexagonal. Evidently the hexagonal lattice is simpler than the trigonal one, and moreover, the problem of obtaining phonon densites of states for *hcp* crystal has already been treated[3]. This is the main reason for using the transformation of equation (3). On the other hand, by so doing we increase the number of atoms per unit cell by a factor of 3. The apparent consequence of this would be to raise by the same factor the dimensionality of the phonon dynamical matrix, or the Hamiltonian matrix for the magnons. This, however, can be avoided, as we presently show.

Starting with the trigonal basis vectors $\mathbf{a}_i$ in real space, as given by equation (1) we form the reciprocal lattice vectors $\mathbf{b}_k$ given by the usual relation

$$\mathbf{b}_k = \frac{\mathbf{a}_i \times \mathbf{a}_j}{3\sqrt{3}\,s^2 r/2} \tag{4}$$

where i, j and k form a cyclic triade. Specifically, the $\mathbf{b}_k$ are given by

$$\begin{aligned} \mathbf{b}_1 &= (2/3\,s, 0, 1/3\,r), \\ \mathbf{b}_2 &= (-1/3s, \sqrt{3}/3s, 1/3r) \\ \mathbf{b}_3 &= (-1/3s, -\sqrt{3}/3s, 1/3r), \end{aligned} \tag{5}$$

and the trigonal first Brillouin zone is shown in Fig. 2.

In a similar way, the reciprocal lattice vectors for the hexagonal symmetry, namely $\mathbf{b}'_k$ can be constructed by using the direct space basis given in equation (3). The $\mathbf{b}'_k$ are given by

$$\begin{aligned} \mathbf{b}'_1 &= (1/3s, 0, 0), \\ \mathbf{b}'_2 &= (1/3s, \sqrt{3}/3s, 0), \\ \mathbf{b}'_3 &= (0, 0, 1/3r), \end{aligned} \tag{6}$$

and the first Brillouin zone is shown in Fig. 3. Its volume is 1/3 of the volume of the trigonal Brillouin zone. It can be shown by using symmetry arguments that the irreducible Brillouin zone (IBZ) of the trigonal lattice is 1/12 of the full zone. This is exemplified in Fig. 4. Likewise, the IBZ for the hexagonal case is 1/24 of the full zone. Taking this into account and bearing in mind that the number of atoms per unit cell has been multiplied by three, the hexagonal IBZ is contained exactly six times in the trigonal IBZ. By applying suitable manipulations based on symmetry operation, one can reconstruct the trigonal IBZ so that it includes exactly six hexagonal IBZ. Although these manipulations are quite elementary, it is not easy to describe them literarily in detail. For the purpose of the present discussion it is sufficient, perhaps, to say that these manipulations consist mainly of symmetry operations which remove parts of

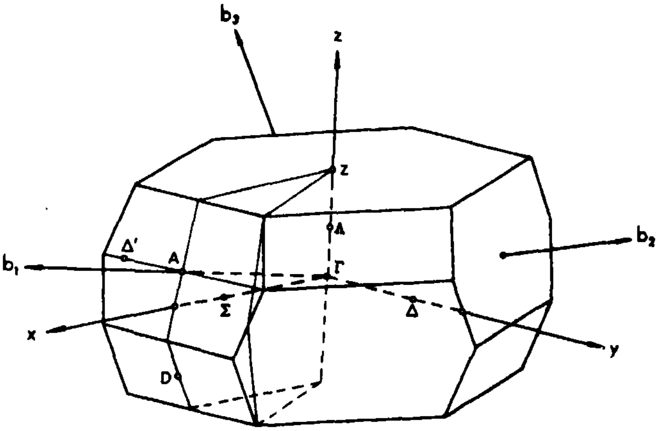

Fig. 2. Trigonal first Brillouin zone (for $r < s/\sqrt{2}$). The labels of points of high symmetry follow Koster (Ref. [9]).

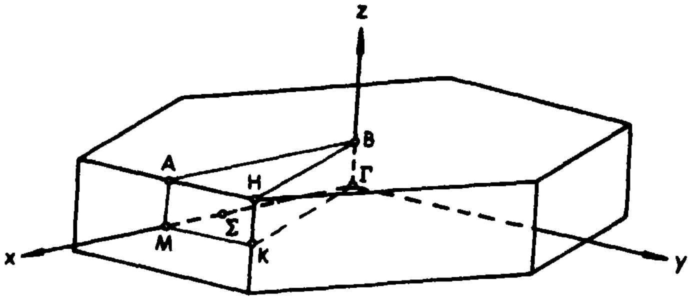

Fig. 3. Scheme of hexagonal first Brillouin zone

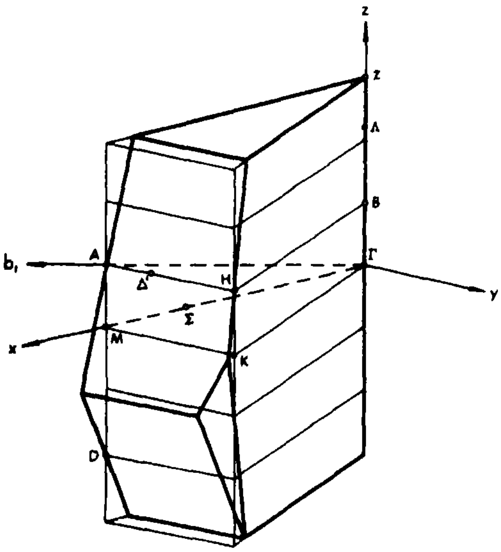

Fig. 4. Trigonal IBZ is represented by solid lines. The thin lines represent the edges of the trigonal practical zone (TPZ), which is equivalent to six hexagonal IBZ.

the shape of the trigonal IBZ shown in Fig. 4. and replace them by adding equivalent parts from outside the trigonal IBZ. The zone which is thus generated is to be referred to as the trigonal 'practical' zone (TPZ) and it includes all and only non-equivalent points. For example we demonstrate one of these manipulations. The line Δ' in Fig. 4, which is a 2-fold axis, can be used to transform by rotation a part of the extra volume between $q_z = -1/3r$ and $q_z = 1/3r$ into the missing part between the planes $q_z = 1/3r$ and $q_z = 1/r$. It should be emphasized that the practical zone is certainly not contained in the first trigonal IBZ, although it is equivalent to it in all other respects.

This construction enables us to carry out density of states computations for the entire trigonal IBZ by using only one of the six hexagonal IBZ shown in Fig. 4. This can be performed by using the method described by Raubenheimer and Gilat[3]. The advantage of this is mainly in transforming the problem of computing densities of states for trigonal lattices into an already solved problem. This is done at the apparent cost of increasing the size of the phonon dynamical matrix (or the magnetic Hamiltonian) by a factor of three. This, however, is avoidable, because as a matter of fact we know beforehand how to express the dynamical matrix appropriate to the primitive trigonal crystal.

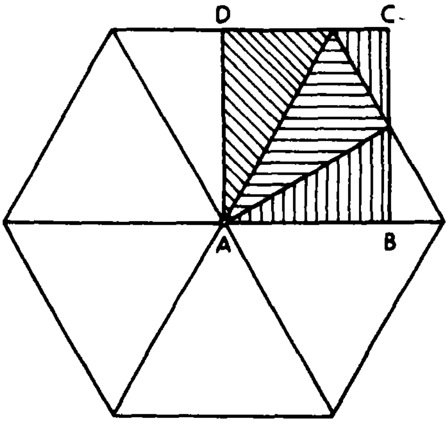

Fig. 5. Three hexagonal irreducible zones are joined into a practical zone for the purpose of calculating spectral functions.

In other words, we can define two wave-vector $\mathbf{q}_t$ and $\mathbf{q}_h$, where $\mathbf{q}_t$ varies over the TPZ and q_h over the hexagonal IBZ. $\mathbf{q}_t$ and $\mathbf{q}_h$ are related by

$$\mathbf{q}_t = \mathbf{q}_h + \{(l-4)/3r\}\mathbf{e}_z \qquad (7)$$

where $\mathbf{e}_z$ is a unit vector along the z-axis, and l is an integer which labels the different hexagonal IBZ in Fig. 4 and satisfies the condition $1 \leq l \leq 6$. It is obvious that by expressing the phonon dynamical matrix, (or the magnetic Hamiltonian) as a function of $\mathbf{q}_t$ rather than of $\mathbf{q}_h$, one is able to retain the original (trigonal) relative simplicity for these expressions.

Another source of complications is brought about by employing triangular prisms (wedges) as zones of integration without the restriction that the gradients lie in the hypothenum plane (HBΓK in Fig. 3). With this restriction the analytical formulae for the integration in wedges were written for the hexagonal case. As the hypothenum plane is not a mirror plane in the triangular lattice, the wedges used in the hexagonal case cannot be used for the trigonal IBZ. A brute force method of avoiding these shapes is to enlarge the hexagonal IBZ by a factor of three[10], as shown schematically in Fig. 5. The advantage of this enlargement is especially significant when one is interested in computing spectral functions $I(\omega)$ derived from transition probabilities[5]. Recently, Dalton[8] proposed a general method for obtaining the expressions of Gilat and Kam[5] required for the calculations of spectral functions from the earlier expressions of Gilat and Raubenheimer [2, 3] for the calculations of density of states. Dalton also extended the analytical formulae of integration for wedges without the restriction on the direction of the gradient. As a result of his work triangular prisms have become more accessible for computations.

Acknowledgement—We would like to express our gratitude to Prof. J. Zak and Dr. Norris W. Dalton for helpful discussions.

REFERENCES

1. GILAT G. and DOLLING G., *Phys. Lett.* **8**, 304 (1964).
2. GILAT G. and RAUBENHEIMER L. J., *Phys. Rev.* **144**, 390 (1966).
3. RAUBENHEIMER L. J. and GILAT G., *Phys. Rev.* **157**, 586 (1967).
4. KAM Z. and GILAT G., *Phys. Rev.* **175**, 1156 (1968). There is a small error in the footnote included in Ref. [6]. The label of the plan should be MAHΓ instead of MABX. The same correction applied to the text in the same page.
5. GILAT G. and KAM Z., *Phys. Rev. Lett.* **22**, 715 (1969).
6. GILAT G. and BOHLIN L., *Solid State Commun.* **7**, 1727 (1969).
7. FINKMAN E. and COHEN E., to be published.
8. DALTON N. L., private communication (to be published).
9. KOSTER G. F., in *Solid State Physics* (Edited by F. Seitz and D. Turnbull), Academic Press, New York (1957).
10. The suggestion is due to Dr. L. J. Raubenheimer, private communication.

J. Phys. Chem. Solids, 1971, Vol. 32, pp. 2429–2437. **Pergamon Press. Printed in Great Britain**

PROPRIETES ET STRUCTURE MAGNETIQUE DE Mn_3O_4

B. BOUCHER, R. BUHL* et M. PERRIN*
Service de Physique du Solide et de Résonance Magnétique, Centre d'Etudes Nucléaires de Saclay,
BP n° 2, 91, Gif-sur-Yvette, France

(*Received* 30 *April* 1970; *in revised form* 28 *September* 1970)

Resumé—Après un exposé des propriétés cristallographiques et magnétiques de Mn_3O_4, on montre que la structure magnétique à 4,2°K déterminée par diffraction de neutrons est composée de 8 sous-réseaux répartis sur une maille double de la maille chimique. L'étude de l'évolution thermique du motif a permis de mettre en évidence un point de transition à 33°K correspondant à un brusque réarrangement des moments dans la maille.

Abstract—After a survey of cristallographic and magnetic properties of Mn_3O_4, we show that the magnetic structure at 4·2°K determined by neutron diffraction measurements is divided into 8 sub-lattices in a cell the volume of which is twice the chemical one. The study of thermal variations allows to show a transition point at 33°K corresponding to a rearrangement of moments in the cell.

1. PREPARATION ET PROPRIETES CRISTALLOGRAPHIQUES

LA PRÉPARATION de Mn_3O_4 sous forme polycristalline a déjà été décrite par l'un d'entre nous [1]. Rappelons seulement que ce corps, qu'il soit trempé ou refroidi lentement jusqu'à la température ambiante, possède toujours les mêmes propriétés cristallographiques (dimensions de la maille, groupe d'espace, paramètres de l'oxygène) et magnétiques (intensité d'aimantation à 4,2°K, température de Curie).

Il cristallise dans le système quadratique; des spectres de rayons X à 300°, 77° et 4,2°K ont montré que la maille varie peu avec la température comme le montre le Tableau 1 [2]. Les valeurs trouvées sont en bon accord avec celles que donne la littérature à ce sujet [3].

Tableau 1. *Paramètres de la maille de* Mn_3O_4 *à* $T = 300,77,4.2°K$

T(°K)	a(Å)	c(Å)	c/a
300	5,763	9,456	1,64
77	5,756	9,439	1,64
4,2	5,756	9,439	1,64

Le groupe d'espace est D_{4h}^{19} (I 4_1/amd). Il s'agit d'un spinelle déformé dont les ions oxygène sont en position 16 h (coordonnées réduites 0, x, z) et les ions manganèse en position 4a et 8d. Un premier spectre de diffraction neutronique a été fait à la température ambiante (soit au-dessus de la température d'ordre magnétique). Un calcul par la méthode des moindres carrés portant sur les treize premières raies mesurées correspondant à 25 réflexions a permis de préciser les paramètres de l'oxygène: le facteur d'agitation thermique ayant été pris isotrope, les valeurs trouvées sont $x = 0,227$ et $z = 0,383$. Le Tableau 2 donne la comparaison entre les valeurs expérimentales et calculées; le facteur de confiance $R = \Sigma|I_{cal} - I_{obs}|/\Sigma I_{cal}$ est de 5 pour cent.

2. PROPRIETES MAGNETIQUES

La courbe $1/\chi(T)$ représentant l'inverse de la susceptibilité en fonction de la température (Fig. 1) est caractéristique d'un composé ferrimagnétique [4]. La température de Curie

---

*Laboratoire de Magnétisme, Faculté des Sciences de Paris, Tour 22, 11, Quai St Bernard, Paris 5ème.

Tableau 2. Intensités nucléaires expérimentales et calculées (température ambiante) $JF^2/(\sin\theta \sin 2\theta) \exp(-2B(\sin^2\theta)/\lambda^2)$ en barns par maille (a, a, c)

hkl	$I_{exp.}$	$I_{cal.}$	*hkl*	$I_{exp.}$	$I_{cal.}$
101	24	106	312	196	194
112	204	184	303	1000	998
200	78	78	321 224 215	410	536
103	620	698			
211 202 004	13024	12744	116 314 400 323	292	388
220 213	1698	1816			
301	264	206	411 206 402 305	3018	3304
204 105	140	116			

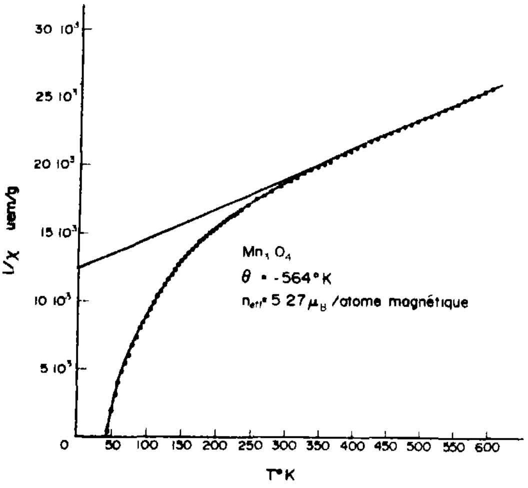

Fig. 1. Variation de l'inverse de la susceptibilité en fonction de la température.

est de 42,5°K, valeur en parfait accord avec d'autres mesures[5]. Pour $T > 400$°K, $1/\chi$ est une fonction linéaire de T et son extrapolation donne une température de Curie asymptotique de −564°K traduisant l'existence de fortes interactions antiferromagnétiques; le moment paramagnétique exprimé en magnétons de Bohr par atome magnétique déduit de la pente de l'asymptote (5,27 μ_B) correspond à celui calculé avec la formule ionique $Mn^{2+}Mn^{3+}Mn^{3+}O_4^-$ en prenant pour valeurs de moments celles correspondants aux spins seuls ($n_{eff.} = 5,24\,\mu_B$).

Au-dessous de 42,5°K, Mn_3O_4 est ferrimagnétique et la courbe de première aimantation à 4,2°K obtenue en champs pulsés[4] (Fig. 2) montre que:

(a) l'anisotropie magnétocristalline est importante, la partie linéaire de la courbe n'étant atteinte qu'avec des champs supérieurs à 50 kOe;

(b) aucune saturation n'est obtenue à 200 kOe;

(c) l'extrapolation à champ nul donne une aimantation spontanée de 1,65 μ_B/molécule.

Ces résultats en champs pulsés sont semblables à ceux obtenus par Jacobs[6] qui avait alors démontré que les moments en site *B* devaient prendre une configuration non colinéaire et dont la résultante devait être plus petite que celle des moments en site *A*.

Dwight et Menyuk[7] ont mesuré sur monocristal une aimantation spontanée de 1,85 μ_B/molécule; celle-ci est dirigée suivant un axe [100]. L'anisotropie dans le plan (010)

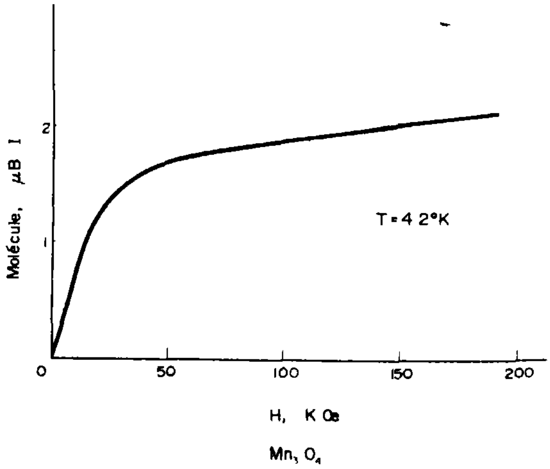

Fig. 2. Variation de l'aimantation en fonction du champ à $T = 4,2$°K.

est considérable: ils trouvent dans l'expression de l'énergie d'anisotropie ($E_c = K_c \sin^2\theta$) $K_c = 10^7$ ergs/cm³. Dans le plan (001), des champs relativement petits sont capables d'orienter l'aimantation du corps suivant les différentes directions de facile aimantation [100] et [010] (quelques kOe suffisent).

3. STRUCTURE MAGNETIQUE A 4,2°K

Deux spectres de diffraction de neutrons ($\lambda = 1{,}140$ Å) ont été faits sur poudre à 4,2°K, l'un avec champ magnétique de 15 kOe dirigé suivant le vecteur diffusion et l'autre sans champ (Fig. 3 et 4). Par comparaison avec le spectre à température ambiante, on remarque un certain nombre de raies nouvelles d'origine purement magnétique qui s'indexent toutes dans une maille double de la maille chimique (le sens du doublement étant dirigé suivant l'axe [010]; doublement étant dirigé suivant l'axe **a** ou **b**) [8]. Dans la suite nous admettrons que la maille est doublée suivant l'axe [010]; les indices des réflexions seront donc exprimés dans la maille a, 2a, c.

L'examen des deux spectres conduit aux constatations suivantes:

(A) Les raies 010, 001, 011, 100, 020 sont nulles. On en déduit alors que le motif magnétique à 4,2°K est composé de 8 sous-réseaux répartis comme suit (les coordonnées et les translations sont notées dans la maille chimique a, a, c).

(1) Dans le site tétraédrique 4a, deux sous-réseaux porteurs de moments $\mathbf{T}_1$ et $\mathbf{T}_2$ correspondant aux positions (0, 0, 0 (+ $\frac{1}{2}$ $\frac{1}{2}$ $\frac{1}{2}$)) (+010) et (0, $\frac{1}{2}$, $\frac{1}{4}$ (+$\frac{1}{2}$$\frac{1}{2}$$\frac{1}{2}$)) (+010).

(2) Dans le site octaédrique 8d

(a) Deux sous-réseaux de moments $\mathbf{R}_1$ et $\mathbf{R}_2$ en position (0, $\frac{1}{4}$, $\frac{5}{8}$ (+$\frac{1}{2}$$\frac{1}{2}$$\frac{1}{2}$)) (+010) et ($\frac{1}{2}$, $\frac{1}{4}$, $\frac{1}{8}$ (+$\frac{1}{2}$$\frac{1}{2}$$\frac{1}{2}$) (+010).

(b) Quatre sous-réseaux de moments $\mathbf{S}_1$, $\mathbf{S}_2$, $\mathbf{S}_3$ et $\mathbf{S}_4$; $\mathbf{S}_1$ correspond aux positions ($\frac{1}{4}$, 0, $\frac{3}{8}$) et ($\frac{3}{4}$, $\frac{1}{2}$, $\frac{7}{8}$); $\mathbf{S}_3$ aux positions ($\frac{1}{4}$, $\frac{1}{2}$, $\frac{7}{8}$) et ($\frac{1}{4}$, 0, $\frac{3}{8}$) (la translation $\frac{1}{2}$ $\frac{1}{2}$ $\frac{1}{2}$ n'étant pas une opération de symétrie pour les moments magnétiques). Les positions de $\mathbf{S}_2$ et $\mathbf{S}_4$ se déduisent respec-

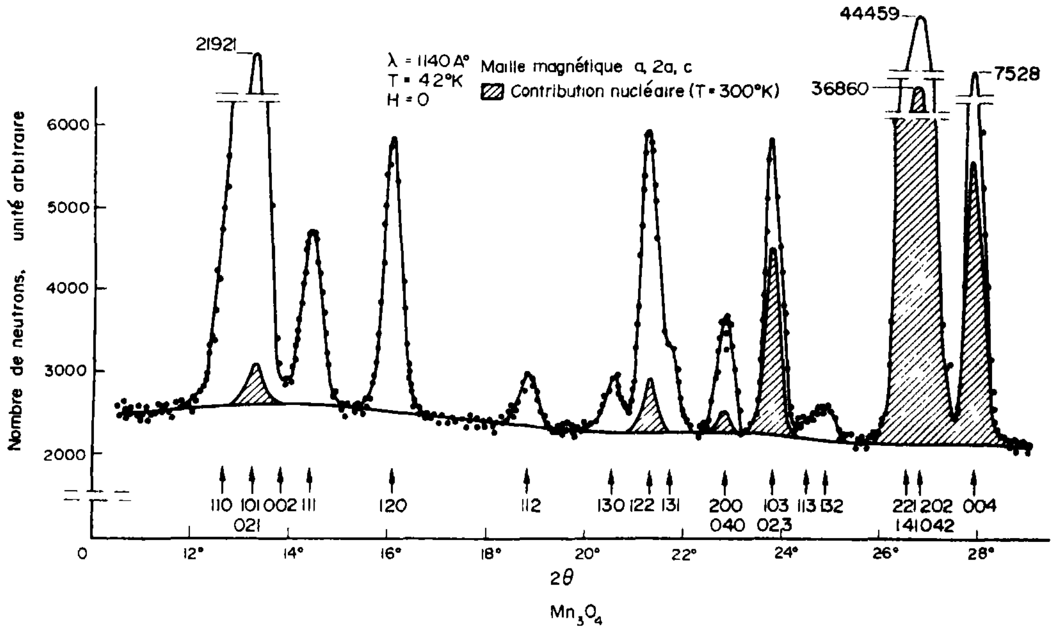

Fig 3. Spectre de diffraction de neutrons à 4,2°K $\lambda = 1{,}140$ Å $- H = 0$, les zones hachurées représentent les raies nucléaires.

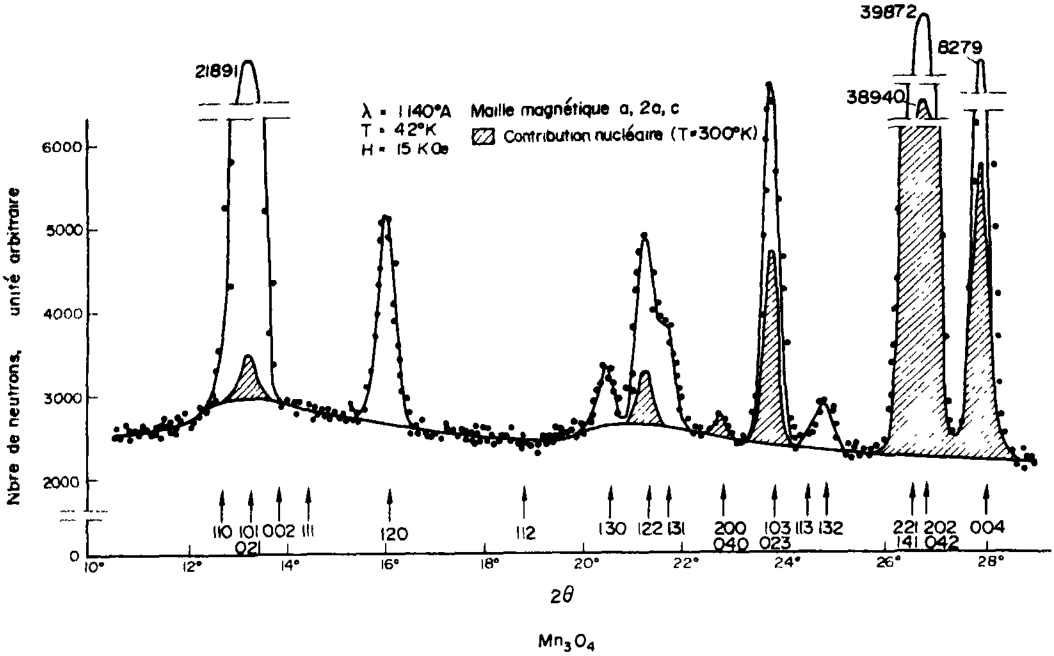

Fig. 4. Spectre de diffraction de neutrons à 4,2°K $\lambda = 1{,}140$ Å, $H = 15$ kOe, les zones hachurées représentent les raies nucléaires.

tivement de celles de S_1 et S_3 par la translation $+\mathbf{b}(|\mathbf{b}| = a)$. Ce sont ces quatre sous-réseaux qui doublent la maille suivant *b*.

(3) les moments $\mathbf{T}_1+\mathbf{T}_2$, $\mathbf{R}_1+\mathbf{R}_2$, $\mathbf{S}_1+\mathbf{S}_2+\mathbf{S}_3+\mathbf{S}_4$ et l'aimantation résultante sont dirigés suivant l'axe [010].

(B) La raie 101–021 est particulièrement intéressante en raison de sa forte intensité magnétique; les 2 réflexions, quoique confondues sur les spectres, peuvent être connues séparément. En effet, considérons un cristallite en position de réflexion et dont la maille est doublée suivant l'axe **b**.

(a) Si un champ magnétique est appliqué suivant la direction [021], l'aimantation ne change pratiquement pas de direction en raison de la très forte anisotropie existante dans tout plan passant par **c**[7] et l'intensité de la réflexion 021 reste donc inaltérée.

(b) Si le champ est maintenant appliqué suivant la direction [101], l'aimantation tourne pour venir se placer au voisinage de l'axe **a** (direction de facile aimantation la plus proche de celle du champ); la maille est doublée alors suivant cet axe et ce phénomène s'accompagne d'une réarrangement des moments magnétiques $\mathbf{S}_i$ et $\mathbf{R}_i$ respectant la symétrie d'ordre 4 du cristal. Il s'ensuit que la réflexion notée 101 (maille a, 2a, c) sur le spectre sans champ devient une réflexion 201 (maille 2a, a, c) sur le spectre avec champ. Les intensités des réflexions 201 (maille 2a, a, c) et 021 (maille a, 2a, c) étant égales, on a dans le cas du spectre avec champ l'égalité $I_{101-021} = 2I_{021}$.

Si on admet que dans cette nouvelle position, l'orientation du motif magnétique et la disposition relative des moments sont indépendants de la valeur du champ extérieur (au moins tant que celui-ci reste inférieur à 15 kOe), la relation précédente donne l'intensité de la réflexion 021 sur le spectre sans champ et par voie de conséquence l'intensité de la réflexion 101.

(C) Dans le spectre avec champ, la contribution magnétique de la raie 200–040 est nulle; par un raisonnement analogue au précédent on en déduit alors que la réflexion 040 dans le spectre sans champ a une intensité nulle.

Ces différentes constatations jointes aux valeurs des intensités magnétiques des raies, permettent alors de déterminer la disposition et les grandeurs des moments des sous-réseaux. Nous admettrons que $\mathbf{T}_1$ et $\mathbf{T}_2$ ont même module, cette hypothèse étant faite aussi pour $\mathbf{R}_1$, $\mathbf{R}_2$ d'une part, $\mathbf{S}_1\mathbf{S}_2\mathbf{S}_3\mathbf{S}_4$ d'autre part.

$\mathbf{T}_1$ et $\mathbf{T}_2$ (comme $\mathbf{R}_1$ et $\mathbf{R}_2$) sont dans un plan (100); ils admettent la direction [010] comme axe de symétrie ($\mathbf{T}_1+\mathbf{T}_2$ est antiparallèle à $\mathbf{R}_1+\mathbf{R}_2$). $\mathbf{S}_1$, $\mathbf{S}_2$, $\mathbf{S}_3$ et $\mathbf{S}_4$ se répartissent sur un cône d'axe [010]. Ils sont symétriquement disposés par rapport aux plans (100) et (001) ($\mathbf{S}_1+\mathbf{S}_2+\mathbf{S}_3+\mathbf{S}_4$ étant parallèle à $\mathbf{R}_1+\mathbf{R}_2$).

La structure est représentée schématiquement sur la Fig. 5.

4. RESULTATS NUMERIQUES

Mn_3O_4 est quadratique et la distorsion de sa maille est dûe à l'ion Mn^{3+} qui, par effet Jahn-Teller, déforme le site octaédrique. Ainsi qu'on l'a montré par ailleurs[1], pour obtenir un effet Jahn-Teller coopératif, il faut que la concentration d'ions Mn^{3+} en site octaédrique soit grande; la forte valeur du rapport *c*/*a* conduit à penser que la 'formule ionique est Mn^{2+} $[Mn^{3+}Mn^{3+}]O_4$. Il s'agit donc là d'un spinelle 'normal', chaque site étant peuplé d'un seul type d'ion.

Les composantes des moments magnétiques sur chacun des sites ont été calculées à partir des intensités magnétiques observées et de la valeur de l'aimantation résultante[7] par une méthode d'essais successifs en cherchant à minimiser les écarts entre les intensités expérimentales et calculées des 12 raies les plus significatives. Les résultats sont les suivants:

(a) Dans le site tétraédrique, le moment de l'ion Mn^{2+} est de 4,65 μ_B et fait un angle de 13°30′ avec l'axe 010. Ce faible angle est peu significatif car il n'apporte qu'une légère améllioration aux intensités calculées com-

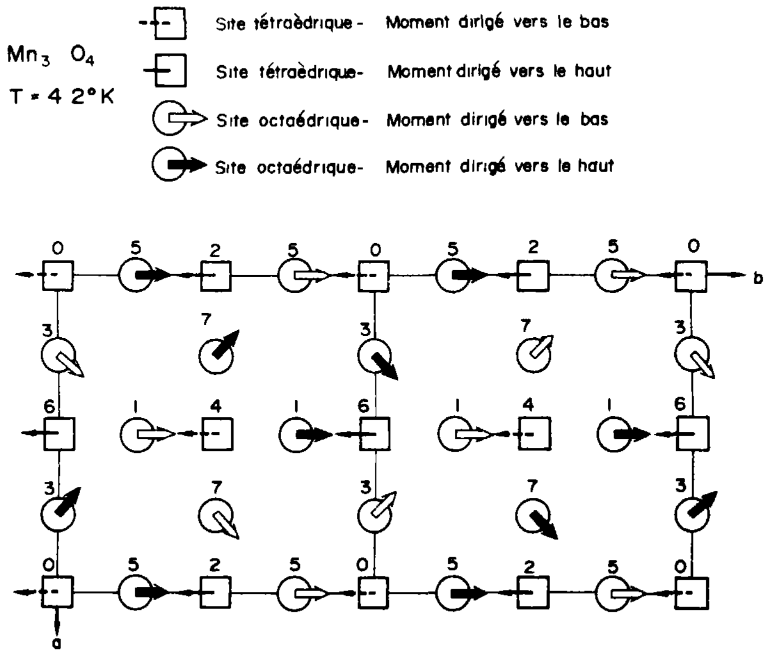
Mn3 O4
T = 4 2°K
Site tétraèdrique - Moment dirigé vers le bas
Site tétraèdrique - Moment dirigé vers le haut
Site octaédrique - Moment dirigé vers le bas
Site octaédrique - Moment dirigé vers le haut
0 5 2 5 0 5 2 5 0
b
3 7 3 7 3
6 1 4 1 6 1 4 1 6
3 7 3 7 3
0 5 2 5 0 5 2 5 0
a

Fig. 5. Schéma de la structure magnétique à 4,2°K. Les chiffres donnent les cotes en ⅛ des différents ion magnétiques.

parées aux intensités expérimentales. La valeur du moment obtenu est plus faible que celle du spin seul (5 μ_B).

(b) Dans le site octaédrique, les moments $\mathbf{R}_i$ et $\mathbf{S}_i$ ont le même module, soit 3,55 μ_B (la valeur du spin seul de Mn^{3+} étant de 4 μ_B). $\mathbf{R}_1$ et $\mathbf{R}_2$ font un angle de 69°30 avec l'axe [010]. Le cône sur lequel se disposent les moments $\mathbf{S}_i$ a un demi-angle au sommet de 66°10′, les composantes Sx, Sy, Sz sur les axes **a** **b** et **c** étant de 1,29 μ_B, 1,43 μ_B et 2,98 μ_B respectivement.

Le moment résultant est de 1,85 μ_B/molécule. Le Tableau 3 donne la comparaison entre les intensités magnétiques des raies observées et calculées dans le cas du modèle décrit ci-dessus.

5. EVOLUTION DE LA STRUCTURE EN FONCTION DE LA DIRECTION DU CHAMP A 4,2°K

Le spectre avec champ montre que les raies 110, 111 et 112 sont nulles; ceci s'explique par le fait qu'un champ dirigé suivant l'une de ces directions fait tourner l'aimantation d'un angle tel, que la maille se trouve alors doublée suivant la direction [100], les directions liées à ces raies ne correspondant plus à un noeud du réseau réciproque, il n'y a plus réflexion. Il faut donc admettre que lorsqu'on fait tourner le motif autour de l'axe [001] sous l'action d'un champ, de manière à passer d'une direction de facile aimantation [010] à la suivante [100] il y a ré'arrangement des moments constituant le motif magnétique, réarrangement qui doit en particulier respecter la symétrie

Tableau 3. Intensités magnétiques expérimentales et calculées à 4,2°K en μ_B^2/maille (a, 2a, c) $Jq^2F_M^2$ pour $H = 0$ avec $q = \sin(\mathbf{F}, \mathbf{K})$

hkl	$I_{exp.}$	I_{cal}	*hkl*	$I_{exp.}$	I_{cal}
010	0	0	200 040	2848	2840
001	0	0	210	0	0
011	0	0			
100	0	0	103 023 041 041 201	4000 ± 800	3904
020	0	0			
110	1140 ± 100	1136	113 211 132	1840 ± 350	2176
021 101	12336 ± 240	12412			
002	0	4	140	0	0
111	1752 ± 40	1752	220	0	0
012	0	0	123 141 221 042 033 212	27900 ± 18000	11744
120	3344 ± 70	3336			
030	0	0			
121	0	0			
102	0	0	004	10100 ± 6000	6618
022	0	0	014	0	0
031	0	0	050	0	0
112	1012 ± 90	1038	230	0	0
130	1140 ± 100	1136			
003	0	0			
122	5936 ± 120	5936			
013	0	0			
131	2088 ± 100	2040			
032	0	0			

quadratique du cristal. L'axe d'ordre 4 faisant correspondre les sous-réseaux $\mathbf{R}_i$ aux $\mathbf{S}_i$, $\mathbf{R}_1$ et $\mathbf{R}_2$ se subdivisent donc, après rotation du motif, en quatre sous-réseaux; réciproquement les quatre sousréseaux $\mathbf{S}_i$ se réduiront à deux après cette même rotation. Le nouveau motif obtenu devra avoir une structure semblable à celle du motif initial mais avec un arrangement différent des moments du site octaédrique. Ce 'flipping' se reproduira à chaque fois que la direction de facile aimantation tournera de 90°.

Dans tout plan passant par l'axe **c**, les champs usuels ne permettent pas de suivre l'évolution de la structure en raison de la trop grande anisotropie; signalons à titre d'exemple qu'un champ de 15 kOe appliqué suivant la direction [131] n'écarte le motif du plan de base que de 6°.

6. EVOLUTION THERMIQUE DE LA STRUCTURE

Les raies les plus intenses et par là même les plus significatives ont été étudiées en fonction de la température.

L'intensité de la raie de surstructure 111 s'annule à 33°K très brutalement (Fig. 6a); on a vérifié qu'il en est de même pour les autres raies *hkl* où *k* est impair. A cette température, il y a transition, les mailles magnétique et chimique devenant identiques.

Les raies 101, 021, 120 et 122 (Figs. 6b, c et d) ont permis de suivre l'évolution de la structure entre 4,2°K et le point de transition. Les variations des différents paramètres en fonction de la température sont indiquées Fig. 10. On constate en particulier qu'à 33°K la composante suivant **a** des $\mathbf{S}_i$ s'annule alors que les deux autres composantes gardent une valeur finie; les raies de surstructures étant

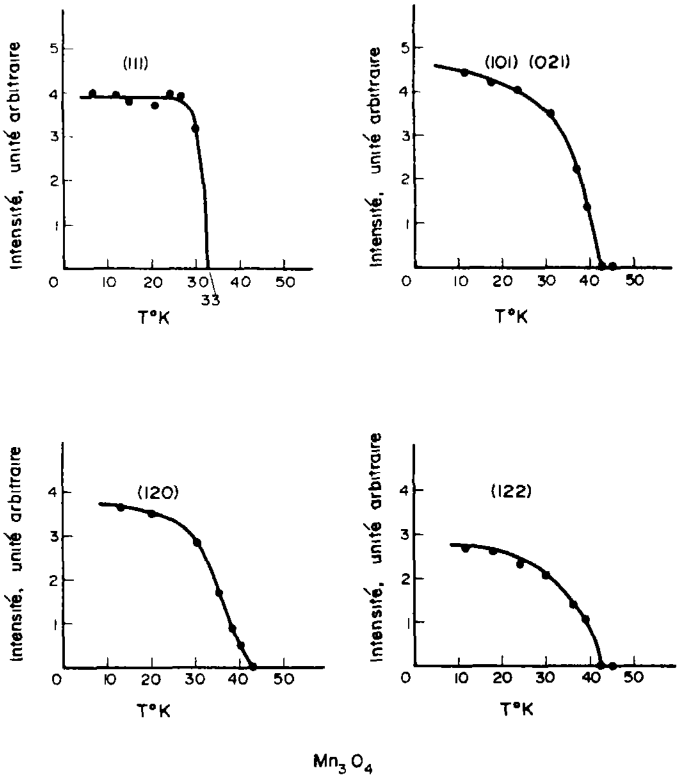

Fig. 6. Variations de l'intensité magnétique en fonction de la température des raies: (a) 111, (b) 101–021, (c) 120, (d) 122.

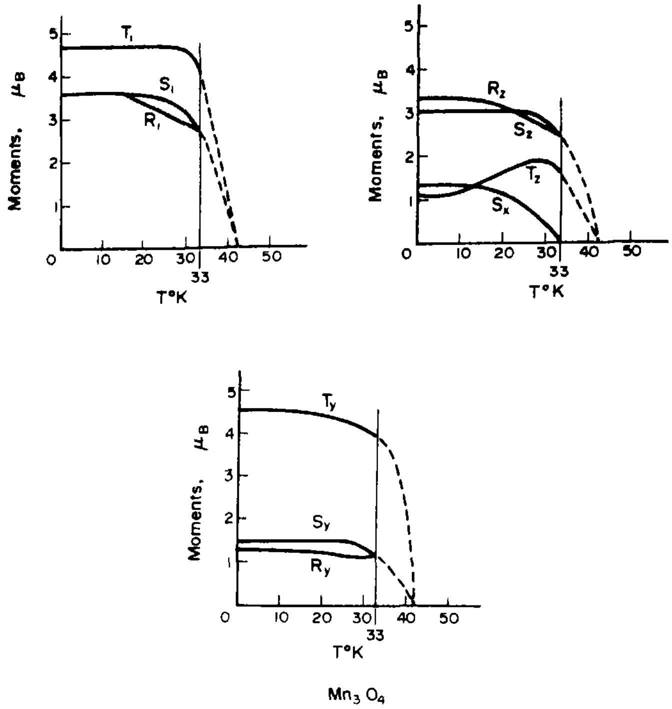

Fig. 7. Variation des moments et de leurs composante's en fonction de la température.

les seules à subir une discontinuité au passage du point de transition, on déduit que les moments S_i se réarrangent brusquement à 33°K, les valeurs absolues de leurs composantes suivant **b** et **c** restant inchangées. En d'autres termes, deux sous-réseaux S_i sur les quatre verront leur composante suivant **c** changer simplement de signe, ce qui ramène la maille magnétique aux dimensions de la maille chimique. *A* 33°K, la structure n'est pas colinéaire et au-delà de cette température il devient difficile de suivre l'évolution des différents paramètres définissant le motif magnétique en raison de l'imprécision sur les intensités des raies.

Remarque. Il est intéressant de noter que variations thermiques des moments $\mathbf{R}_i$ et $\mathbf{S}_i$ (Fig. 7) ne sont pas identiques; si, à 4,2°K ces moments ont sensiblement même valeur absolue, on remarque qu'à température supérieure, ils diffèrent notablement (bien qu'il s'agisse du même type d'ion Mn^{3+}). Au point de transition (33°K), $\mathbf{R}_i$ et $\mathbf{S}_i$ semblent être égaux, ils font le même angle avec l'axe [010] et il est probable que cette propriété se conserve jusqu'à la température de Curie.

7. CONCLUSION

La structure trouvée à 4,2°K ne peut trouver son explication par la seule considération d'échange isotrope. Ainsi que nous l'avons déjà remarqué dans certains manganites [9, 10], l'anisotropie (qu'elle soit locale ou d'échange) semble jouer un rôle déterminant; en particulier, elle pourrait expliquer l'inégalité des moments $\mathbf{R}_i$ et $\mathbf{S}_i$ entre 4,2 et 33°K.

Remerciements—Nous remercions M. le Prof. Herpin et M. Meriel pour l'intérêt qu'ils ont témoigné lors de la réalisation de ce travail.

Nous remercions aussi les chercheurs cités ainsi que

MM. de Gunsbourg, Denis et Teyrol pour l'aide qu'ils nous ont apportée par leurs mesures d'aimantation et de paramagnétisme.

Nous tenons à remercier aussi MM. Sougi et Piesvaux pour leur collaboration aux mesures de diffraction de neutrons.

REFERENCES

1. BUHL R., *J. Phys. Chem. Solids* **30**, 805 (1969).
2. *Mesures effectuées* par JEHANNO M., Dph-SRM-Saclay.
3. SINHA A. P. B., SANJANA N. R. et BISWAS A. B., *Acta crystallogr.* **10**, 439 (1957).
4. *Mesures effectuées* chez ALLAIN M., DPh-SRM-Saclay.
5. PERTHEL R. et RAHN H., *Phys. Status Solidi* **5**, 563 (1964); BOROVIK-ROMANOV A. S. et ORLOVA M. P., *JETP* **5**, 1023 (1967).
6. JACOBS I. S., *J. Phys. Chem. Solids* **11**, 1 (1959).
7. DWIGHT K. et MENYUK N., *Phys. Rev.* **119**, 1470 (1960).
8. KASPER J. S., *Bull. Am. Phys. Soc.* **4**, 178 (1959).
9. BOUCHER B., BUHL R. et PERRIN M., *J. Phys. Chem. Solids* **32**, 1471 (1971).
10. BOUCHER B., BUHL R. et PERRIN M., *J. Phys. Chem. Solids* (à paraître).

J. Phys. Chem. Solids, 1971, Vol. 32, pp. 2439–2447. Pergamon Press. Printed in Great Britain

SUPERCONDUCTORS WITH MAGNETIC IMPURITIES IN A SINGLET GROUND STATE

H. CAPELLMANN

Department of Physics, University of Pennsylvania, Philadelphia, Penna. 19104, U.S.A.

(*Received* 4 *May* 1970)

Abstract—The effect of magnetic impurities (Pr and Tm) on the superconductors Th, La Pb_3 and La Sn_3 is discussed. Due to crystal field splitting the impurities have a nonmagnetic ground state and low lying excited states. In particular the case of Pr in La Pb_3 is discussed. Interband mixing of 4*f* and conduction electrons leads to a dynamical electron–electron interaction due to exchange of virtual excitations of the impurities. This leads to a lowering of the superconducting transition temperature T_c.

1. INTRODUCTION

RECENTLY Bucher *et al.*[1] studied superconductors with small amounts of magnetic ions undergoing crystal field splitting and exhibiting a non-magnetic ground state. They restricted their studies to Pr^{3+} and Tm^{3+} in superconductors of cubic symmetry, Th, $LaTl_3$, $LaPb_3$ and $LaSn_3$. Bucher and Coworkers observed a depression in the superconducting transition temperature T_c which cannot be explained by spin disorder scattering due to ions thermally excited from their non-magnetic ground state to some magnetic excited state.

We examine the effective electron–electron interaction due to exchange of virtual excitations of the magnetic impurities. For the specific cases we examine this dynamical interaction leads to a lowering of the superconducting transition temperature and thus may explain the results of Bucher *et al.* There are several ways in which a conduction electron could interact with the impurity and which could give rise to an effective electron-electron interaction due to exchange of virtual excitations of the impurity. There is the Heisenberg exchange interaction giving rise to an interaction Hamiltonian of the form $H_{HEX} \sim J.s$. Furthermore aspherical Coulomb scattering can take place. In addition there is a further exchangelike interaction due to interband mixing of conduction and 4*f* electrons. The first two types of interaction have been discussed by Fulde *et al.*[2]. They find that, in case the Heisenberg exchange contributes, it will lower the superconducting transition temperature T_c, whereas the aspherical Coulomb scattering will raise T_c. They neglected interband mixing.

The most experimental information is available for the case of Pr being dissolved in $LaPb_3$. Specific heat measurements by Bucher and coworkers are consistent within 1 per cent with the first excited state of the Pr^{3+} being a doublet, all other excited states lying much higher in energy. Lea *et al.*[3] calculated the level system of Pr^{3+} in cubic symmetry. Praseodymium has two electrons in the 4*f* shell which couple to a total $J = 4$. If we denote the state of z-component of total angular momentum being M by $|M\rangle$, Lea and coworkers give the ground state in cubic symmetry as:

$$|a\rangle = \alpha_0|4\rangle + \beta_0|0\rangle + \alpha_0|-4\rangle. \tag{1}$$

There is only one doublet possible, the wave functions being

$$\begin{aligned} |b_1\rangle &= \alpha_l|4\rangle + \beta_l|0\rangle + \alpha_l|-4\rangle \\ |b_2\rangle &= \gamma_l|2\rangle + \gamma_l|-2\rangle \end{aligned} \tag{2}$$

and where

$$\begin{aligned} &\alpha_0 = 0{\cdot}4564, \quad \beta_0 = 0{\cdot}7638 \\ &\alpha_l = 0{\cdot}501, \quad \beta_l = -0{\cdot}6455 \\ &\gamma_l = 0{\cdot}7071. \end{aligned} \tag{3}$$

Both states $|b_1\rangle$ and $|b_2\rangle$ are nonmagnetic, i.e.: $\langle J\rangle = 0$. We see that an interaction Hamiltonian $J.s$ due to Heisenberg exchange does not couple the ground state to the first excited states.

Interband mixing and aspherical Coulomb scattering do give a coupling between the states $|a\rangle$ and $|b_i\rangle$. We show that the interband mixing of $4f$ and conduction electrons does indeed lead to a lowering of T_c. The experimentally found depression of T_c thus might be explained by an interaction whose dominating part is due to interband mixing. Further experimental investigations are necessary, however, to clarify this point.

2. THE INTERACTION HAMILTONIAN DUE TO INTERBAND MIXING

Pr and Tm have two electrons and two holes in the $4f$ shell respectively which couple to a total $J = 4$ in Pr and a total $J = 6$ in Tm.

First we want to concentrate on Pr. To treat the mixing of conduction and impurity wave functions, we work with conduction states which are partial waves about the impurity. (The following is analogous to the treatment of Ce in [4]. Only the $l = 3$ states of the impurity are of interest and furthermore—for the conduction impurity mixing potential being mainly spherically symmetric—only $l = 3$ conduction electron partial waves will enter the problem. Again like in [4] we make up spin orbit eigenstates from these partial waves so that we work only with states of definite angular momentum. c_{kM}^+ and c_{kM} are creation and destruction operators for electrons of wave number k, total angular momentum $\frac{5}{2}$ and z-component M $(=\pm\frac{1}{2}, \pm\frac{3}{2}, \pm\frac{5}{2})$. $c_{M'}^+$ and $c_{M'}$ create and destroy electrons on the impurity with angular momentum $\frac{5}{2}$ and z-component M'. (Spin orbit eigenstates with angular momentum $\frac{7}{2}$ are much higher in energy and are of no interest here). We start with an interaction Hamiltonian

$$H_1 = \sum_{k,M} \left[V_k c_{kM}^+ c_M + V_k^* c_M{}^+ c_{kM} \right]. \qquad (4)$$

Following [5] we can replace H_1 by an interaction H_2 given by

$$H_2 = \tfrac{1}{2} \sum_{a,b,c} \langle b|H_1|c\rangle\langle c|H_1|a\rangle \left\{ \frac{1}{e_a - e_c} + \frac{1}{e_b - e_c} \right\} \qquad (5)$$

$|a\rangle$ and $|b\rangle$ are the initial and final states and e_a and e_b their energies. The $|c\rangle$'s are the possible intermediate states, there are two sets:

$$|c_1\rangle = c_{kM}^+ c_{k'M'}^+ c_{M''}^+ |vac\rangle \qquad (6)$$

$$|c_2\rangle = c_M{}^+ c_{M'}^+ c_{M''}^+ |vac\rangle. \qquad (7)$$

The e_c's are their energies, probably of the order of several eV.

Using (6) and (7) as intermediate sets in (5) is only an approximation. To be correct we would have to use the exact wave functions corresponding to having three (or 1) electrons on the impurity. If, however, the splitting in energy inside a set of states is small and can be neglected with respect to e_{c_1} (or e_{c_2}), their average, then we can use any complete set of functions as intermediate states, (6) and (7) being the simplest and most useful [6]. Furthermore (5) corresponds to second order perturbation theory. In order to be able to neglect higher order terms H_1/e_c must be small, which is the case for the situation we are dealing with. For the $|a\rangle$'s and $|b\rangle$'s we use the model based upon the calculation of the level system of Pr^{3+} in cubic symmetries by Lea *et al.*[3], e.g. the ground state of Pr^{3+} is given by

$$|a\rangle = \alpha_0|4\rangle + \beta_0|0\rangle + \alpha_0|-4\rangle \qquad (8)$$

where

$$|4\rangle = c_{5/2}^+ c_{3/2}^+ |vac\rangle \qquad (9)$$

and the other $|i\rangle$'s are obtained by successive applications of the angular momentum lowering operator. The states $|a\rangle$ and $|b\rangle$ are best labeled by $|I_i, kM\rangle$ where I_i describes the states of the impurity, the kM describes the conduction electron involved in the scattering process.

We define the operator K_i^+ by

$$|I_i, kM\rangle = c^+_{kM} K_i^+ |vac\rangle \tag{10}$$

e.g. for the ground state of the impurity K_0^+ has the form:

$$K_0^+ = \alpha_0\{c^+_{5/2}c^+_{3/2} + c^+_{-3/2}c^+_{-5/2}\} + \frac{1}{\sqrt{14}}\beta_0\{2c^+_{1/2}c^+_{-1/2} + 3c^+_{3/2}c^+_{-3/2} + c^+_{5/2}c^+_{-5/2}\}. \tag{11}$$

With this notation the interaction Hamiltonian takes the form:

$$H_2 = \sum g^{ji}_{k'M',kM} c^+_{k'M'} K_j^+ K_i c_{kM}. \tag{12}$$

The g's are explicitly given by

$$g^{ji}_{k'M',kM} = \tfrac{1}{2}\sum_c \langle k'M',I_j|H_1|c\rangle\langle c|H_1|kM,I_i\rangle \times\left\{\frac{1}{e^{(i)}_{kM} - e_c} + \frac{1}{e^{(j)}_{k'M'} - e_c}\right\} \tag{13}$$

where $e^{(i)}_{kM}$ is the energy of the state $|kM,I_i\rangle$. The matrix elements are calculated in a straightforward way and are given in Appendix 1.

3. SUPERCONDUCTING PROPERTIES

To calculate the superconducting properties we use the Nambu formalism[7]. We introduce the two component electron field operators

$$\psi = \begin{pmatrix} c_{pjM} \\ c^+_{pj-M} \end{pmatrix} \qquad \psi^+ = (c^+_{pjM} c_{pj-M}). \tag{14}$$

Furthermore it will be convenient to define the operator $C_j^+ = K_j^+ K_0$. For the purpose of superconductivity only the part of H_2 which involves scattering processes taking the impurity from the ground state to an excited state or vice versa will be important.

We therefore can write the total Hamiltonian in the form

$$H = \sum_p \epsilon_p \psi_p^+ . \tilde{\tau}_3 . \psi_p + \sum_i E_i C_i^+ C_i + H_2 + H_H + H_{AC} + H_{ph} \tag{15}$$

where $\bar{H}_2$ takes the form

$$H_2 = \sum_{j\neq 0} \tfrac{1}{2} g^{j0}_{p'p}\{(C_j^+ + C_j)\psi^+_p . \tilde{\tau}_3 . \psi_p + (C_j^+ - C_j)\psi^+_{p'} . \psi_p\}. \tag{16}$$

Here the symmetry

$$g^{ji}_{p'M'pM} = g^{ji}_{p'-M'p-M} \tag{17}$$

was used.

$\tilde{\tau}_3$ is the Pauli matrix $\begin{pmatrix} 1 & 0 \\ 0 & -1 \end{pmatrix}$.

H_{ph} is the part of the Hamiltonian describing the phonons and the electron–phonon interaction. H_H and H_{AC} describe the Heisenberg exchange and the aspherical Coulomb scattering respectively. The commutation relations for the operators C_j^+ and C_j are neither purely Fermi-like nor purely Bose-like. This, normally, prevents the straightforward application of many body theory, because Wick's theorem does not hold. In the following we shall make the approximation of treating the C_j^+ and C_j as Boson-creation and annihilation operators. Thus we introduce unphysical states into the problem. The physical states are only those where either no boson or only one boson is present, all other states are unphysical. If, however, the expectation value for $n_j = C_j^+ C_j$ is a very small number $\alpha \ll 1$, then the unphysical states will enter the problem with a weight of α^2 or smaller. In Appendix 2 we show that, for the low temperatures we are interested in, this is indeed the case because of the weakness of the coupling which produces the virtual excitations. Therefore the approximation of treating the C's as boson operators is a valid one.

We now want to discuss the specific case of Pr^{3+} in $LaPb_3$. As mentioned before, the Heisenberg exchange Hamiltonian does not couple the ground state and the first excited states, a doublet (equation (2)), and is therefore neglected. For the aspherical Coulomb scattering we use the interaction Hamiltonian given in [2]. In the representation we use it as the form:

$$H_{AC} = \sum I_2(k',k)\frac{Q_2}{R}(C_2{}^{+}+C_2)g_{\mathbf{k}'\mathbf{k}}\psi^{+}_{\mathbf{k}'}\cdot\tilde{\tau}_3\cdot\psi_{\mathbf{k}}$$

where

$$I_2(k',k) = \frac{4\pi}{5}\int_0^\infty \mathrm{d}r_1\int_0^\infty \mathrm{d}r_2\frac{e^2}{r_>}\left(\frac{r_<}{r_>}\right)^2[R_{4f}(r_2)]^2$$
$$\times R_{k's}(r_1)R_{kd}(r_1) \qquad (19)$$

$R(r)/r$ is the radical part of a given wave function. Q_2 is the quadrupole moment of the $4f$ shell. [8] gives $Q_2 = 0{\cdot}294$.

R is a constant given by

$$R = \left(\frac{6\pi}{5}\right)^{1/2}\frac{2\sqrt{7}\alpha_0\gamma_l+3\sqrt{10}\beta_0\gamma_l}{28}.$$

The nonvanishing coupling constants are given by:

$$\hat{g}_{k'1/2\,1/2k5/2\,5/2} = 1 \qquad \hat{g}_{k1/2\,1/2k5/2-3/2} = 1/\sqrt{5} \qquad (20a)$$

$$\hat{g}_{k'1/2\,1/2k3/2-3/2} = -\sqrt{\tfrac{4}{5}} \qquad \hat{g}_{k'1/2-1/2k5/2\,3/2} = 1/\sqrt{5} \qquad (20b)$$

$$\hat{g}_{k'1/2-1/2k3/2\,3/2} = \sqrt{\tfrac{4}{5}} \qquad \hat{g}_{k'1/2-1/2k5/2-5/2} = 1. \qquad (20c)$$

Furthermore

$$\hat{g}_{\mathbf{k}'\mathbf{k}} = \hat{g}_{\mathbf{k}\mathbf{k}'}. \qquad (20d)$$

All other coupling constants are zero.

In our following discussions we shall treat the effects of the impurity scattering on the macroscopic properties of the system as a perturbation. For low impurity concentration linear perturbation theory should be adequate. We use the standard definitions for the finite temperature Green's function $\tilde{G}$ and the self energy $\tilde{\Sigma}$. (The ~ indicates that the quantity discussed is a matrix):

$$\tilde{G}^{-1}(\mathbf{p},i\omega) = i\omega-\epsilon_p\cdot\tilde{\tau}_3-\tilde{\Sigma}(\mathbf{p},i\omega). \qquad (21)$$

The equation, we shall obtain for $\tilde{\Sigma}$, will contain three separate parts resulting from the electron–phonon interaction, the impurity scattering due to interband mixing and the aspherical Coulomb scattering. Interband mixing and aspherical Coulomb scattering do not couple the same conduction electron states; the interband mixing only couples $j = \frac{5}{2}$ states to $j = \frac{3}{2}$ states, whereas the aspherical Coulomb scattering only couples states with $\Delta j = \pm 1,2$. Therefore there will be no interference between the two phenomena. In the equation for $\tilde{\Sigma}$ the contributions from interband mixing and aspherical Coulomb scattering will be additive and can be treated separately.

First we discuss the interband mixing, we call its contribution to the self-energy $\tilde{\Sigma}_I$. Although the impurity scattering due to interband mixing involves only the $j = \frac{5}{2}$ electrons directly, the electron–phonon interaction will spread the effect of the impurity scattering to all j, thus creating a single superconducting transition temperature T_c. Therefore the quantity of physical interest will be $\tilde{\Sigma}$ averaged over all angular momenta, which then will only depend on the wave number p. To lowest order for the impurities we get the following equation for $\tilde{\Sigma}_I(p_F,i\omega_n)$:

$$\sum_I(p_F,i\omega_n) = \frac{-n_I}{2\beta}n(3,\tfrac{5}{2})\sum_{\substack{p',n',j\\M,M'}}$$
$$\times\{\tilde{\tau}_3\cdot\tilde{G}(p',i\omega_{n'})\cdot\tilde{\tau}_3[g^j_{MM'}g^j_{M'M}+(g^j_{MM'})^2]$$
$$+\tilde{G}(p',i\omega_{n'})[-g^j_{MM'}g^j_{M'M}+(g^j_{MM'})^2]\}$$
$$\times D_j(i\omega_n-i\omega_{n'}) \qquad (22)$$

where $n(l,j)$ is the density of states of electrons with orbital angular momentum l and total angular momentum j at the Fermi surface divided by the total density of states $N(0)$ at the Fermi surface. n_I is the concentration of the impurities,

$$\beta = \frac{1}{k_BT};\quad \omega_n = \frac{(2n+1)\pi}{\beta}$$

$$D_j(i\omega) = \frac{1}{i\omega-E_j}-\frac{1}{i\omega+E_j} \qquad (23)$$

$g^j_{MM'}$ is an abbreviation for $g^{j0}_{p_F,5/2,M\,p'\,5/2,M'}$.

Actually we evaluate g^j_{MM} for $p' = p_F$, too, and neglect the p' dependence. The justification is that due to the rapid p' dependence in G only those p' close to the Fermi surface will contribute to the integral (22). The argument used here is the same as the one used in strong phonon coupling theory[9]. Incidentally, equation (22) does not contain terms proportional to $\tilde{\tau}_3 . \tilde{G}$ and $\tilde{G} . \tilde{\tau}_3$ because of the averaging. $\tilde{\Sigma}_I(p,J,M,\omega)$ does contain terms proportional to $\tilde{\tau}_3 . \tilde{G}$ and $\tilde{G} . \tilde{\tau}_3$, they vanish when averaged over J and M, however.

We call the contribution to the self-energy due to aspherical Coulomb scattering $\tilde{\Sigma}_{AC}$. We get the following equation:

$$\tilde{\sum_{AC}} (p_F,i\omega_n) = -\frac{4n_I}{\beta}\left(I_2(p_F,p_F)\,\frac{Q_2}{R}\right)^2 \times \sum_{\substack{J,M,n'\\ p',j',M'}} (\hat{q}_{p_I j'M' p_I JM})^2 n(J\pm\tfrac{1}{2},j) \times \tilde{\tau}_3 . \tilde{G}(p',i\omega_{n'}) . \tilde{\tau}_3 D_2(i\omega_n - i\omega_{n'}) \tag{24}$$

where

$$n(j\pm\tfrac{1}{2},j) = \begin{cases} n(2,j) \text{ for } j = \tfrac{3}{2},\tfrac{5}{2} \\ n(0,j) \text{ for } j = \tfrac{1}{2}. \end{cases} \tag{25}$$

In the evaluation of (22) and (24) we closely follow the method developed in [9] for strong phonon coupling theory and the details of the calculation can be looked up there.

For simplicity we neglect retardation effects in the phonon-induced interactions and we take that part of the effective electron-electron interaction to be instantaneous.

Making the ansatz:

$$\tilde{\Sigma}(p_F,\omega) = [1-Z(\omega)]\omega + Z(\omega)\Delta(\omega) . \tilde{\tau}_1. \tag{26}$$

We get the following two equations for the superconducting transition temperature T_c:

$$[1-Z(\omega)]\omega = -N(0) . n_I \int_0^\infty \mathrm{d}\omega' (S_I + S_{AC}) \times \tanh(\tfrac{1}{2}\beta_c\omega') \times \left(\frac{1}{\omega'+\omega+E+i\delta} - \frac{1}{\omega'-\omega+E-i\delta}\right) \tag{27}$$

and

$$Z(\omega)\Delta(\omega) = N(0)\int_0^\infty \frac{\mathrm{d}\omega'}{\omega'}\Delta(\omega')\tanh(\tfrac{1}{2}\beta_c\omega') \times \left\{V^{(ph)}_{\omega\omega'} + n_I(\tilde{S}_I + S_{AC}) \times \left(\frac{1}{\omega'+\omega+E+i\delta} + \frac{1}{\omega'-\omega+E-i\delta}\right)\right\} \tag{28}$$

where E is the excitation energy of the impurity doublet and

$$S_I = \sum_{M,M',j} [n(3,\tfrac{5}{2}) g^j_{MM'}]^2 \tag{29a}$$

$$\tilde{S}_I = \sum_{M,M',j} n^2(3,\tfrac{5}{2}) g^j_{MM'} g^j_{M'M} \tag{29b}$$

$$S_{AC} = \sum_{\substack{j',M'\\ j,M}} (g_{k_F j'M' k_F jM})^2 n(j'\pm\tfrac{1}{2},j') n(j\pm\tfrac{1}{2},j) \times \left(\frac{4I_2Q_2}{R}\right)^2 \tag{29c}$$

$V^{ph}_{\omega\omega'}$ represents the phonon interaction which we take to be a constant for ω, $\omega' < \omega_D$, the Debye frequency, and zero beyond.

From equation (28) we see that the effect of the impurities upon the transition temperature T_c will be determined by the quantity $S_I + S_{AC}$. S_{AC} is positive. In terms of the quantities defined in equations (5), (6), (7) we get the following result for $\tilde{S}_I$:

$$\tilde{S}_I = -|V_{k_F}|^4 . 0{\cdot}284\left\{\frac{1}{e_a - e_{c_1}} + \frac{1}{e_b - e_{c_1}} + \frac{1}{e_a - e_{c_2}} + \frac{1}{e_b - e_{c_2}}\right\}^2 + |V_{k_F}|^4 . 0{\cdot}141\left\{\frac{1}{e_a - e_{c_1}} + \frac{1}{e_b - e_{c_1}}\right\}^2. \tag{30}$$

For e_{c_1}, $e_{c_2} > e_a$, e_b (which is the case for the physical situation we are discussing $\tilde{S}_I$ is negative.

Appendix 3 shows the perturbation scheme we used to calculate the transition temperature T_c.

With

$$T_c = T_c^{(0)} + T_c^{(1)};\quad Z(\omega) = 1 + Z_I(\omega) \tag{31}$$

(where T_c^0 is the transition temperature for zero impurity concentration) and with Ω_c being of the order of β_c we get

$$\begin{aligned}
&\frac{1}{\log(1{\cdot}14\beta_c^{(0)}\Omega_c) - T_c^{(1)}/T_c^{(0)}}\\
&\quad = \frac{N(0)V_{ph}}{1 - N(0)V_{ph}\log\omega_D/\Omega_c}\\
&\quad + N(0)n_I\left\{\int_{\Omega_c}^{\omega_D}\frac{d\omega'}{\omega'}(\tilde{S}_I + S_{AC})\left(\frac{1}{\omega'+E}\right.\right.\\
&\quad \left.+\frac{1}{-\omega'+E}\right)\frac{N(0)V_{ph}}{1 - N(0)V_{ph}\log\omega_D/\Omega_c}\\
&\quad + \int_{\Omega_c}^{\omega_D}\frac{d\omega'}{\omega'}N(0)V_{ph}(\tilde{S}_I + S_{AC})\frac{2}{\omega'+E}\\
&\quad - Z_I(0)V_{ph} + \frac{2(\tilde{S}_I + S_{AC})}{E}\\
&\quad + A\int_{\Omega_c}^{\omega_D}\frac{d\omega''}{\omega''}\int_{\Omega_c}^{\omega_D}\frac{d\omega'}{\omega'}N(0)V_{ph}(\tilde{S}_I + S_{AC})\\
&\quad \times\left(\frac{1}{\omega'+\omega''+E} + \frac{1}{\omega'-\omega''+E}\right)\\
&\quad \left. - A\int_{\Omega_c}^{\omega_D}\frac{d\omega'}{\omega'}Z_I(\omega')V_{ph}\right\}
\end{aligned} \tag{32}$$

where

$$A = \frac{2N(0)V_{ph} + (N(0)V_{ph})^2\log\omega_D/\Omega_c}{[1 - N(0)V_{ph}\log\omega_D/\Omega_c]^2}. \tag{33}$$

After carrying out the integrals we get

$$\frac{T_c^{(1)}}{T_c^{(0)}} \approx -\frac{N(0)n_I}{E}(19S_I - 42{\cdot}3\tilde{S}_I - 23{\cdot}3S_{AC}) \tag{34}$$

4. CONCLUSION

From equation (34) we see that the aspherical Coulomb scattering will tend to enhance T_c (as was pointed out by Fulde *et al.* in [2]), whereas the effect of interband mixing will be to lower T_c. Due to the particular form of ground state and first excited states of the Pr^{3+} impurity in the case we discussed, the Heisenberg exchange interaction $J.s$ did not contribute to the coupling between the two. As pointed out in [2], the coupling due to Heisenberg exchange between the ground state and higher excited states contributes to the depression in T_c.

The Hamiltonian used to describe the interband mixing contains some quantities which are not yet known from experiment: The mixing potential V_k and the energies e_{c_1} and e_{c_2} corresponding to having three or one $4f$ electrons on the Pr impurity. An experimental investigation of these quantities will be helpful to establish the relative strength of interband mixing and Heisenberg exchange.

Acknowledgement—I am grateful to Professor J. Robert Schrieffer for suggesting the problem and for many helpful discussions.

REFERENCES

1. BUCHER E., ANDRES K., MAITA J. P. and HULL G. W., Jr., *Helv. Phys. Acta* **41**, 723 (1968).
2. FULDE P., HIRST L. L. and LUTHER A., *Z. Phys.* **230**, 155 (1970).
3. LEA K. R., LEASK M. J. M. and WOLF W. P., *J. Phys. Chem. Solids* **23**, 1381 (1962).
4. COQBLIN B., SCHRIEFFER J. R., *Phys. Rev.* **185**, 849 (1969).
5. SCHRIEFFER J. R., *J. appl. Phys.* **38**, 1143 (1967).
6. WATSON R. E., KOIDE S., PETER M. and FREEMANN E. J., *Phys. Rev.* **139**, 648 (1966).
7. NAMBU Y., *Phys. Rev.* **117**, 648 (1960).
8. TRAMMEL G. T. and SEIDEL E. R., *Proc. Intl. Conf. of Rare Earths* (Grenoble).
9. SCALAPINO D. J., SCHRIEFFER J. R. and WILKINS J. W., *Phys. Rev.* **148**, 263 (1966).

APPENDIX 1

Calculation of coupling constants

There are two types of matrix elements we want to calculate, corresponding to the two sets (6) and (7) of intermediate states in the scattering process:

$$\mathcal{M}^{(1)} = \sum_{M''} \langle k'M',I_j|V_k^* c_M^+ c_{kM}|c_{M''}^+ c_{k'M'}^+ c_{kM}^+\rangle$$

$$\times \langle c_{kM} c_{k'M} c_{M''}|V_{k'} c_{k'M'}^+ c_{M'}|kM,I_0\rangle \qquad (1.1a)$$

$$\mathcal{M}^{(2)} = \sum_{M''} \langle k'M',I_j|V_{k'} c_{k'M'}^+ c_{M'}\,|c_{M''}^+ c_{M'}^+ c_M^+\rangle$$

$$\times \langle c_M c_{M'} c_{M''}|V_k^* c_M^+ c_{kM}|kM,I_0\rangle. \qquad (1.1b)$$

Here the states $|kM\,I_i\rangle$ are given by:

$$|kM,I_0\rangle = \alpha_0 c_{kM}^+\{c_{5/2}^+ c_{3/2}^+ + c_{-3/2}^+ c_{-5/2}^+\}|vac\rangle$$

$$+\frac{1}{\sqrt{14}}\beta_0 c_{kM}^+\{2c_{1/2}^+ c_{-1/2}^+ + 3c_{3/2}^+ c_{-3/2}^+ + c_{5/2}^+ c_{-5/2}\}|vac\rangle. \qquad (1.2a)$$

This describes the ground state of the impurity. The two excited states we consider are given by:

$$|kM,I_1\rangle = \alpha_I c_{kM}^+\{c_{5/2}^+ c_{3/2}^+ + c_{-3/2}^+ c_{-5/2}^+\}|vac\rangle$$

$$+\frac{1}{\sqrt{14}}\beta_I c_{kM}^+\{2c_{1/2}^+ c_{-1/2}^+ + 3c_{3/2}^+ c_{-3/2}^+ + c_{5/2}^+ c_{-5/2}^+\}|vac\rangle$$

$$|kM,I_2\rangle = \gamma_I \frac{1}{\sqrt{14}} c_{kM}^+\{\sqrt{5}c_{3/2}^+ c_{1/2}^+ + 3c_{5/2}^+ c_{-1/2}^+$$

$$+\sqrt{5}c_{-1/2}^+ c_{-3/2}^+ + 3c_{1/2}^+ c_{-5/2}^+\}|vac\rangle. \qquad (1.2c)$$

The constant α, β, γ are obtained from [3] and are given by

$$\alpha_0 = 0{\cdot}4564, \qquad \beta_0 = 0{\cdot}7638$$

$$\alpha_I = 0{\cdot}501, \qquad \beta_I = -0{\cdot}6455 \qquad \gamma_I = 0{\cdot}7071. \qquad (1.3)$$

The calculation of the matrix elements is straightforward. In the following results the index j in $\mathcal{M}^{(i)j}_{M',M}$ indicates into which excited state the impurity is scattered. $j = 1$ corresponds to the state $|I_1\rangle$, $j = 2$ to the state $|I_2\rangle$.

$$\text{(a)}\quad \mathcal{M}^{(1)1}_{-3/2,5/2} = \left(-\frac{1}{\sqrt{14}}\alpha_0\beta_I + \frac{3}{\sqrt{14}}\beta_0\alpha_I\right).|V_{k_F}|^2 = \mathcal{M}^{(1)1}_{3/2,-5/2}$$

$$\text{(b)}\quad \mathcal{M}^{(1)1}_{5/2,5/2} = \left(-\alpha_0\alpha_I - \frac{1}{\sqrt{14}}\beta_0\beta_I\right)|V_{k_F}|^2 = \mathcal{M}^{(1)1}_{-5/2,-5/2}$$

$$\text{(c)}\quad \mathcal{M}^{(1)1}_{-5/2,3/2} = \left(\frac{3}{\sqrt{14}}\alpha_0\beta_I - \frac{1}{\sqrt{14}}\beta_0\alpha_I\right)|V_{k_I}|^2 = \mathcal{M}^{(1)1}_{5/2,-3/2}$$

$$\text{(d)}\quad \mathcal{M}^{(1)1}_{3/2,3/2} = (-\alpha_0\alpha_I - \tfrac{9}{14}\beta_0\beta_I)|V_{k_F}|^2 = \mathcal{M}^{(1)1}_{-3/2,-3/2}$$

$$\text{(e)}\quad \mathcal{M}^{(1)1}_{1/2,1/2} = -\tfrac{2}{7}\beta_0\beta_I|V_{k_F}|^2 = \mathcal{M}^{(1)1}_{-1/2,-1/2}. \qquad (1.4)$$

All other matrix elements $\mathcal{M}^{(1)1}_{M',M}$ vanish. The matrix elements (1.4) involve the impurity being scattered into the excited state $|I_1\rangle$. For scattering into the state $|I_2\rangle$ we get the results:

$$\text{(a)}\quad \mathcal{M}^{(1)2}_{1/2,5/2} = -\tfrac{3}{7}\beta_0\gamma_I|V_{k_F}|^2 = \mathcal{M}^{(1)2}_{-1/2,-5/2}$$

$$\text{(b)}\quad \mathcal{M}^{(1)2}_{-1/2,3/2} = \frac{\sqrt{5}}{7}\beta_0\gamma_I|V_{k_F}|^2 = \mathcal{M}^{(1)2}_{1/2,-3/2}$$

$$\text{(c)}\quad \mathcal{M}^{(1)2}_{5/2,1/2} = (-\tfrac{3}{14}\beta_0\gamma_I + \sqrt{\tfrac{5}{14}}\alpha_0\gamma_I)|V_{k_F}|^2 = \mathcal{M}^{(1)2}_{-5/2,-1/2}$$

$$\text{(d)}\quad \mathcal{M}^{(1)2}_{-3/2,1/2} = \left(\frac{3}{\sqrt{14}}\alpha_0\gamma_I + \frac{3\sqrt{5}}{14}\beta_0\gamma_I\right)|V_{k_F}|^2 = \mathcal{M}^{(1)2}_{3/2,-1/2}. \qquad (1.5)$$

All other $\mathcal{M}^{(1)2}_{M',M}$ vanish.

For the matrix elements $\mathcal{M}^{(2)}$ we get

$$\mathcal{M}^{(2)j}_{M'M} = \mathcal{M}^{(1)j}_{M'M} \text{ for } M' \neq M \qquad (1.6)$$

All $\mathcal{M}^{(2)j}_{MM}$ vanish.

APPENDIX 2

In Section 3 we made the approximation of treating the operators C_j^+, C_j as Boson-operators. To show that this is a meaningful approximation we have to show that the expectation value of $n_j = C_j^+ C_j$ is small.

We neglect effects of temperature. We are interested in the occupation number for the 'Boson' at T_c, temperature effects will be of the order of $e^{-E_I/kT_c} < 10^{-2}$ and are neglected.

We only want to get an idea about the order of magnitude of $\langle n_j\rangle$, we therefore only discuss the effects of interband mixing, neglecting aspherical Coulomb scattering. We use the Hamiltonian in its conventional form:

$$H_1 = \sum g^{i0}_{kmk'M'} c_{kM}^+ c_{k'M'} C_i^+ + h.c. \qquad (2.1)$$

The c's are electron operators, the C's the defined 'Boson' operators.

To lowest order the Boson self energy is given by:

$$\pi_j(\omega) = i\tfrac{1}{2}\int (g^{j0}_{kMk'M'}\, g^{0j}_{k'M'kM} + g^{j0}_{k'M'kM} g^{0j}_{kMk'M'})$$

$$\times G_{kM}(\omega')G_{k'M'}(\omega+\omega'). \qquad (2.2)$$

To lowest order in the g's we can use G^0's instead of G's. (In our description for the phonon interaction G^0 is not influenced by phonons.) The real part of π_i will have no significant influence upon the Boson occupation number, its only effect will be to shift the energy slightly.

For the imaginary part we get:

$$\mathcal{T}_m\pi_i(\omega) = \pi\Sigma f_p(1-f_q)[\delta(\omega-\epsilon_q+\epsilon_p)$$

$$+\delta(\omega+\epsilon_q-\epsilon_p)] \times S_i^{(i)} \qquad (2.3)$$

$\epsilon_p = P^2/2m$ is the electron energy, f_P is the Fermi function. For the mixing potential V_k we use the following model: V_k is a constant equal to V_{kF} for ϵ_k within a range ϵ of the Fermi energy, and it vanishes for k outside this region. The order of magnitude of the Boson occupation number should not depend crucially upon the detailed behavior of V_k. Carrying out the integral yields the following result:

$$\mathscr{T}_m\pi_l(\omega) = \begin{Bmatrix} |\omega| \text{ for } |\omega| < \epsilon \\ 2\epsilon - |\omega| \text{ for } \epsilon < |\omega| < 2\epsilon \\ 0 \text{ for } 2\epsilon < |\omega| \end{Bmatrix} \times \pi N^2(0) \,.\, S_l^{(l)} \tag{2.4}$$

where

$$S_l^{(l)} = \sum_{M,M'} (g_{MM'}^{(l)} \,.\, n(2,\tfrac{1}{2}))^2. \tag{2.5}$$

The occupation number is given by the integral:

$$n = i \int_{-\infty}^{+\infty} \frac{e^{i\delta\omega}}{\omega - E_l + i\delta - i\mathscr{T}in\pi_l(\omega)} \mathrm{d}\omega \tag{2.6}$$

δ is a number infinitesimally small and positive.

Doing the integral gives a number of the order of $\pi N^2(0) S_l^{(l)}$. The density of states can be obtained from measurements of the electronic specific heat at low temperatures[1]. $S_l^{(l)}$ is estimated from equation (34). This yields a Boson occupation number of the order of $< 10^{-2}$. Therefore unphysical states characterized by the presence of more than one boson will enter only with a weight of 10^{-4} and do not contribute significantly.

APPENDIX III

We develop the perturbation scheme, we used to calculate the effect of the impurity scattering upon the transition temperature T_c. We have an equation of the form:

$$Z(\omega)\Delta(\omega) = N(0) \int_0^{\infty} \frac{\mathrm{d}\omega'}{\omega'} \Delta(\omega') K(\omega,\omega') \tanh(\tfrac{1}{2}\beta_c\omega')$$

$$\left(\beta_c = \frac{1}{k_B T_c}\right) \tag{3.1}$$

where

$$K(\omega,\omega') = K_0(\omega,\omega') + K_1(\omega,\omega') \tag{3.2a}$$

and

$$Z(\omega) = Z_0(\omega) + Z_1(\omega) \tag{3.2b}$$

We treat $K_1(\omega,\omega')$ and $Z_1(\omega)$ as a perturbation. Assuming that the kernel $K(\omega,\omega')$ varies in ω or ω' on the scale of the order of the Debye frequency, we split the integral over ω' in (3.1) into two intervals. An integral from 0 to Ω_c and one from Ω_c to ∞ where we take Ω_c of the order of $k_B T_c$. In the first interval we neglect the variation of the kernel with ω' and we get the following result:

$$\int_{-\infty}^{+\infty} \mathrm{d}\omega' [\langle\omega|\mathscr{Z}|\omega'\rangle - \langle\omega|\mathscr{K}|\omega'\rangle]\Delta(\omega') =$$

$$N(0)K(\omega,0)\Delta(0)\log(1\ 14\beta_c\Omega_c). \tag{3.3}$$

There we introduced the operators $\mathscr{Z}$ and $\mathscr{K}$ which are defined by their matrix elements:

$$\langle\omega|\mathscr{F}|\omega'\rangle = Z(\omega)\delta(\omega-\omega') \tag{3.4}$$

$$\langle\omega|\mathscr{K}|\omega'\rangle = \begin{cases} \dfrac{N(0)K(\omega,\omega')}{\omega'} \text{ for } \omega' > \Omega_c \\ 0 \text{ for } \omega' < \Omega_c. \end{cases} \tag{3.5}$$

Inverting equation (3.3) we get

$$\frac{1}{\log(1 \cdot 14\,\beta_c\Omega_c)} = N(0) \int_{-\infty}^{+\infty} \langle 0|[\mathscr{Z} - \mathscr{K}]^{-1}|\omega'\rangle K(\omega',0)\,\mathrm{d}\omega'. \tag{3.6}$$

Perturbation theory to first order gives

$$\begin{aligned} \frac{1}{\log(1 \cdot 14\,\beta_c\Omega_c)} = {} & N(0)\int \langle 0|[\mathscr{Z}_0 - \mathscr{K}_0]^{-1}|\omega'\rangle K_0(\omega',0)\,\mathrm{d}\omega' \\ & + N(0) \int \langle 0|[\mathscr{Z}_0 - \mathscr{K}_0]^{-1}|\omega'\rangle K_1(\omega',0)\,\mathrm{d}\omega' \\ & + N(0) \int \langle 0|[\mathscr{Z}_0 - \mathscr{K}_0]^{-2}|\omega''\rangle \langle\omega''|\mathscr{K}_1 - \mathscr{Z}_1|\omega'\rangle \\ & \qquad K_0(\omega',0)\,\mathrm{d}\omega'\mathrm{d}\omega''. \end{aligned} \tag{3.7}$$

To use this perturbation scheme we must be able to calculate the inverse of $\mathscr{Z}_0 - \mathscr{K}_0$. We give a method of how to determine this inverse for the case that $(\mathscr{K}_0)_{\omega\omega'} \equiv \langle\omega|\mathscr{K}_0|\omega'\rangle$ consists of a sum of separable terms.

$$(\mathscr{K}_0)_{\omega\omega'} = \sum_{l=1}^{N} A_l(\omega) B_l(\omega') \tag{3.8}$$

$\mathscr{L}$ shall be the inverse to $\mathscr{Z}_0 - \mathscr{K}_0$, its matrix elements $\mathscr{L}'_{\omega\omega'}$:

$$\sum_{\omega''} (\mathscr{Z}_0 - \mathscr{K}_0)_{\omega\omega''} \mathscr{L}_{\omega''\omega'} = \delta(\omega - \omega') \tag{3.9}$$

or more explicitly:

$$\mathscr{L}'_{\omega\omega'} = \frac{1}{Z(\omega)}\delta(\omega-\omega') + \sum_{l=1}^{N} \frac{A_l(\omega)}{Z(\omega)} I_l(\omega') \tag{3.10}$$

where

$$I_l(\omega') = \sum_{\omega} B_l(\omega'')\mathscr{L}'_{\omega''\omega'}. \tag{3.11}$$

The I_l's are determined from the system of equations we get by multiplying (3.10) by $B_1(\omega), B_2(\omega), \ldots\ldots B_N(\omega)$ successively and summing over ω.

With the definitions:

$$c_{ij} = \sum_{\omega} \frac{1}{Z(\omega)} B_i(\omega) A_j(\omega) \tag{3.12}$$

we get:

$$\begin{aligned} & I_1(\omega)[c_{11} - 1] + I_2(\omega)c_{12} + \cdots + I_N(\omega)c_{1N} = \frac{B_1(\omega)}{Z(\omega)} \\ & I_1(\omega)c_{21} + I_2(\omega)[c_{22} - 1] + \cdots \qquad = \frac{B_2(\omega)}{Z(\omega)} \\ & \quad \vdots \qquad\qquad \ddots \\ & I_1(\omega)c_{N1} + \cdots\cdots \qquad + I_N(\omega)[c_{NN} - 1] = \frac{B_N(\omega)}{Z(\omega)}. \end{aligned} \tag{3.13}$$

We can solve for the I_i's and putting them back into (3.10) yields $\mathscr{L}_{\omega\omega'}$. For the case we are interested in in this paper we have

$$\langle\omega|\mathscr{Z}_0|\omega'\rangle = \delta(\omega-\omega') \tag{3.14}$$

$$\langle\omega|\mathscr{K}_0|\omega'\rangle = \frac{N(0)V_{ph}}{\omega'}\Theta(\omega)\Theta(\omega_D-\omega)\,\Theta(\omega'-\Omega_0)\,\Theta(\omega_D-\omega') \tag{3.15}$$

where

$$\Theta(\omega) = \begin{cases} 0 \text{ for } \omega < 0 \\ 1 \text{ for } \omega > 0. \end{cases} \tag{3.16}$$

For the inverse of $\mathscr{Z}_0-\mathscr{K}_0$ we get:

$$\langle\omega|[\mathscr{Z}_0-\mathscr{K}_0]^{-1}|\omega'\rangle = \delta(\omega-\omega') + \frac{N(0)V_{ph}}{1-N(0)V_{ph}\log\dfrac{\omega_D}{\Omega_c}}\;\frac{\Theta(\omega)\Theta(\omega_D-\omega)\Theta(\omega'-\Omega_c)\Theta(\omega_D-\omega')}{\omega'} \tag{3.17}$$

J. Phys. Chem. Solids, 1971, Vol. 32, pp. 2449–2451. Pergamon Press. Printed in Great Britain

TECHNICAL NOTES

Phonon density of states for MgF^2*

(*Received* 1 *March* 1971)

A PHONON density of states, $G(\nu)$, for MgF_2 has been calculated by the linear interpolation method of Gilat and Raubenheimer[1, 2], using an axially symmetric rigid ion model for the lattice dynamics[3, 4]. It is shown in Fig. 1. Because of the limited amount of experimental data available at this time and the complexity of the rutile structure, the details of the density of states are not expected to be very accurate. However, there are reasons to believe that the gross features of $G(\nu)$ are given correctly in the present calculation. In TiO_2, for example, Traylor *et al.*[5] have measured the phonon dispersion curves by neutron scattering. They found that neither a rigid ion model nor a fairly sophisticated shell model could adequately fit all of their experimental data, although the shell model gave generally better agreement. Nevertheless, the overall structure of $G(\nu)$ predicted by the two models was not greatly different. Also, the one-phonon spectrum for optical absorption by the $M(C_{2h})$ center in MgF_2[6] exhibits structure that may be correlated in a qualitative way with the present results for $G(\nu)$, as shown in Fig. 2.

In real space, the rutile structure is primitive tetragonal, with equivalent but differently oriented, triatomic molecules at the corner and body center of the unit cell. The reciprocal cell is also tetragonal, and can be generated by symmetry operators from a 45-degree wedge containing one-sixteenth of the total volume [7]. In order to calculate $G(\nu)$ by the Gilat–Raubenheimer method, this wedge is broken

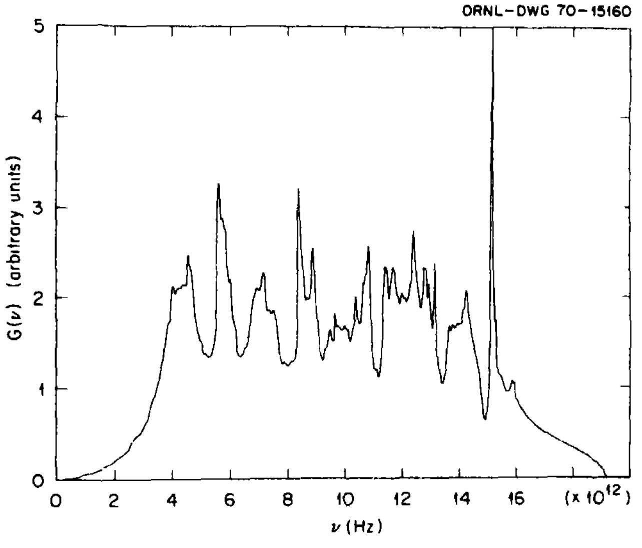

Fig. 1. Density of states for MgF_2.

---

*Research sponsored by the U.S. Atomic Energy Commission under contract with Union Carbide Corporation.

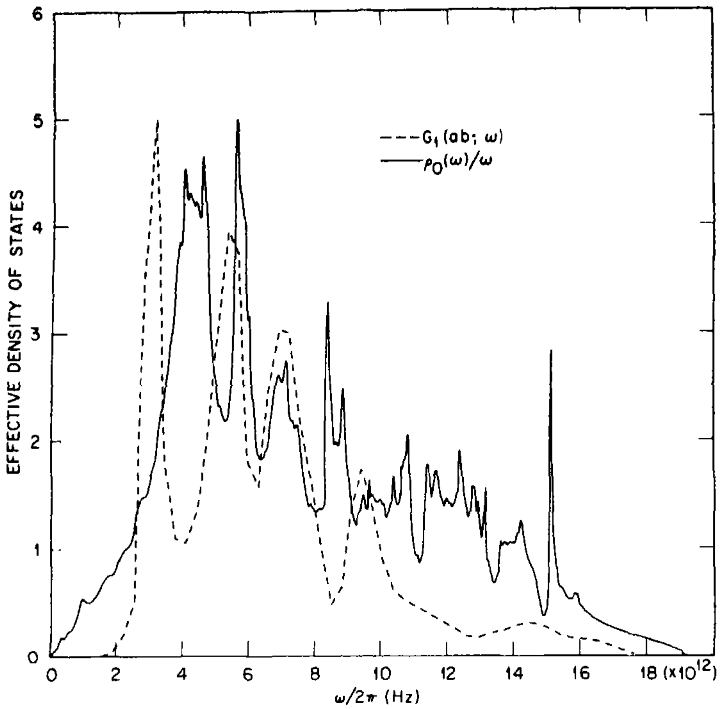

Fig. 2. A comparison of $G(\nu)/\nu = \rho_0(\omega)/\omega$ with the one-phonon spectrum for optical absorption by the $M(C_{2h})$ center in MgF_2, from Ref. [6].

down into smaller volumes surrounding a mesh of points at which the phonon frequancies $\nu_j(q)$ and their gradients $\nabla_{-q}\nu_j(q)$ are determined, and this information is used to sweep across the smaller volumes to fill the histogram bins. The wedge can be wholly filled with full or half rectangular parallelopipeds, and since the reciprocal cell contains (110) mirror planes, the contributions of wedge-shaped smaller volumes along the diagonal face of the irreducible segment of the zone can be determined by sweeping over a full parallelopiped and weighting the result by a factor of one-half.

For the present calculation the axially symmetric rigid ion model parameters were taken from the work of Katiyar[4]. These parameters were determined primarily from Raman and infrared data, and they give fair agreement with measured elastic constants and fragmentary neutron scattering results. In their work on TiO_2, however, Traylor *et al.*[5] found that the rigid ion model could not fit all branches of the spectrum. In particular, the rigid ion model failed to predict the correct zone boundary degeneracies, even when tensor forces were included; only a shell model with tensor forces gave agreement with all of the qualitative features of the data. We would therefore expect the details of the curve in Fig. 1 to change as more experimental information and better theoretical models become available.

The major computational problem for crystals having the rutile structure is that there are six atoms per unit cell and thus 18 different branches of the dispersion curves. This complicates considerably the problem of obtaining an adequate least squares fit with any model containing a reasonable number of parameters. Furthermore, even after a model has been chosen, the computations required to find $G(\nu)$ by the linear interpolation method prohibit the use of very fine meshes. For the calculation reported here, the number of mesh points used was 154, $G(\nu)$ was sorted into roughly 1000 bins, and the computer time necessary was approximately 12 min on an IBM 360-91.

Acknowledgement—The author wishes particularly to thank Dr. J. G. Traylor for providing his programs for the calculation of phonon dispersion curves in the rutile structure and for many helpful discussions.

Solid State Divison,
Oak Ridge National Laboratory,
Oak Ridge,
Tennessee 37830,
U.S.A.

M. MOSTOLLER

REFERENCES

1. GILAT G. and RAUBENHEIMER L. J., *Phys. Rev.* **144**, 390 (1966).
2. RAUBENHEIMER L. J. and GILAT G., *Phys. Rev.* **157**, 586 (1967).
3. KATIYAR R. S. and KRISHNAN R. S., *Can. J. Phys.* **45**, 3079 (1967).
4. KATIYAR R. S., *J. Phys. C. Solid State Phys.* **3**, 1693 (1970).
5. TRAYLOR J. G., SMITH H. G., NICKLOW R. M. and WILKINSON M. K., *Phys. Rev.* **83**, 3457 (1971).
6. MOSTOLLER M., SIBLEY W. A., HENDERSON B. and WOOD R. F., *Phys. Rev.*, to be published.
7. SLATER J. C., *Quantum Theory of Molecules and Solids* Vol. 2, p. 430. McGraw-Hill (1965).

J. Phys. Chem. Solids, Vol. 32, pp. 2451–2454.

The sorption of light paraffins in linde 5A zeolite

(*Received* 8 *September* 1970; *in revised form* 11 *November* 1970)

IN RECENT years it has been shown, principally by Dubinin and other Russian workers [1, 2], that a simple extension of the Polanyi potential theory can provide a valuable means of correlating equilibrium data for the sorption of gases in microporous solids such as zeolites. This theory, which is referred to as the Dubinin–Polanyi theory of pore volume filling, predicts that, for any particular sorbate–sorbent system, the equilibrium data may be represented by a unique, temperature independent, characteristic curve of volume sorbed ($W = aV_m$) plotted against adsorption potential ϵ where:

$$\epsilon = \mu_z - \mu_l = RT \ln\left(\frac{f}{f_s}\right) \qquad (1)$$

μ_z = Chemical potential of sorbed species
μ_l = Chemical potential of pure saturated liquid sorbate at same temperature
T = Absolute temperature
f = Equilibrium fugacity of sorbed species (= equilibrium pressure)
f_s = Equilibrium fugacity for saturated liquid sorbate at same temperature
a = Sorbate concentration
V_m = molar volume of sorbed species (= molar volume of saturated liquid sorbate at same temperature).

For a series of different sorbates and a single sorbent the characteristic curves will in general have different shapes, but the limiting adsorption volume W_0, obtained by extrapolation from the characteristic curves, should be constant and approximately equal to the specific micropore volume of the sorbent. In the present note experimental data are presented for the sorption of light paraffins in 5A zeolite. It is shown that the Dubinin–Polanyi theory gives a satisfactory correlation of the data and, by using the critical temperature as the scaling factor, a single generalized curve is obtained which gives an approximate representation of the data for all sorbates over the entire range of temperature and concentration studied.

EXPERIMENTAL

Equilibrium adsorption isotherms were determined gravimetrically using a Cahn vacuum microbalance system to measure the weight of a sample of zeolite when subjected to a range of hydrocarbon pressures. Full details are given elsewhere[3]. The hang down tube of the balance could be immersed in a Dewar vessel, a liquid thermostat or, for preconditioning, an electric furnace. Prior to the experimental measurements the zeolite was preconditioned at 375°C for a period of 50 hr under a vacuum of 10^{-6} torr. A dosing system was used to change the pressure in the system by the introduction or removal of fixed volumes of hydrocarbon vapour. The adsorptive properties of zeolites are quite sensitive to the presence of trace impurities in the system, particularly moisture and to obtain reliable and consistent data it was found necessary to exercise care both in the preconditioning of the zeolite and in the drying of the hydrocarbon gas. Matheson bottled gas (Research Grade) was used and a drying tube of 4A molecular sieve was included in the line to the system. Measurements were carried out using both Linde pelleted 5A molecular sieve (100–120 mesh) and unsupported Linde 5A zeolite crystals, obtained from Union Carbide. The gravimetric method of measurement is particularly sensitive to error at low pressures when the weight of hydrocarbon adsorbed is small and the influence of trace impurities is highest. Most of the measurements were therefore carried out at pressures within the range 20–400 torr. The range of temperatures is indicated in Fig. 1.

RESULTS AND DISCUSSION

The isotherms obtained from adsorption and desorption measurements agree well and no hysteresis was observed. When the sorbate concentration for the pellets is corrected to allow for the presence of 20% wt. clay binder, the isotherms for pellets and crystals become essentially coincident, except at the lowest temperatures at which significant capillary condensation in the macropores of the pellets may be expected (e.g. propane at −83°C). This implies that there is no essential difference between the adsorptive properties of the pellets and the corresponding zeolite crystals. The clay binder evidently acts merely as an inert diluent.

Figure 1 shows the characteristic curves, calculated from equation (1), for the sorption of methane, ethane propane and *n*-butane in 5A zeolite pellets. The corresponding curves for the crystals are essentially similar. Molar volumes were estimated from the values for the saturated liquid sorbates at the boiling point, extrapolated according to the method of Cook and Basmadjian[4]. Although qualitatively similar to Gaussian curves, these curves can be satisfactorily described by the Dubinin

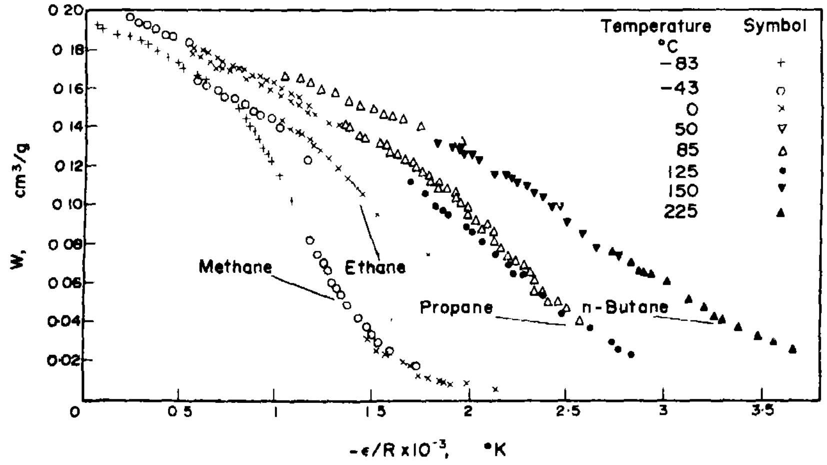

Fig. 1. Characteristic curves for sorption of light paraffins in Linde 5A pellets.

equation[1]:

$$\frac{W}{W_0} = e^{-(\alpha'\epsilon)^2} \qquad (2)$$

where α' is constant, only in the region near saturation ($W \to W_0, \epsilon \to 0$). The simple square law expression:

$$\frac{W}{W_0} = 1 - (\alpha'\epsilon)^2 \qquad (3)$$

to which equation (2) approximates in the saturation region, appears to give a more satisfactory representation of the characteristic curve which is a valid approximation over a somewhat wider range of sorbate concentration ($W_0 > W > 0{\cdot}4W_0$). Extrapolation of the characteristic curves on the basis of equation (3) yields, for the four sorbates, closely similar values for the limiting sorption volume W_0 (0·185–0·19 cc/g for pellets and 0·225–0·23 cc/g for crystals). The latter value may be compared with the specific free volume of the type A zeolite crystal lattice. Considering only the large central cavity which the sorbate molecules can penetrate, Dubinin has calculated, from crystallographic data, a free volume of 727 Å^3 per unit cell which is equivalent to a specific micropore volume of about 0·25 cc/g zeolite[5]. In view of the uncertainties in both the molar volumes of the sorbates and the effective free volume of the zeolite crystals, the agreement between these values (~ 10%) may be taken as additional evidence in support of the Dubinin–Polanyi theory.

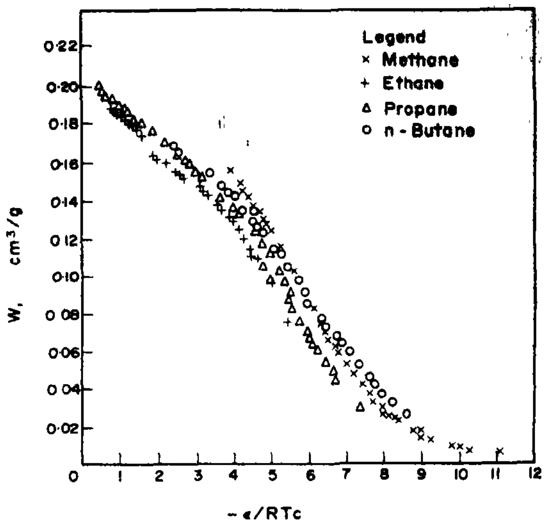

Fig. 2. Generalized characteristic curve for sorption of light paraffins in Linde 5A pellets.

The data of Fig. 1 are shown plotted against reduced adsorption potential (ϵ/RT_c where T_c = critical temperature of sorbate), in Fig. 2. It is evident that a single generalized characteristic curve gives an approximate representation (≃ 10%) for all four sorbates over the entire range of temperature and concentration. Within the range of concentration for which equation (2) is valid, the generalized curve may be represented by the expression:

$$\frac{W}{W_0} = 1 - \left(\frac{\alpha\epsilon}{RT_c}\right)^2 \qquad (4)$$

where $\alpha = \alpha' RT_c = 0{\cdot}130$. However, no completely satisfactory expression for the characteristic curve has been found which is valid over the entire range of concentration.

CONCLUSION

Dubinin has suggested[1] that the affinity coefficients (α') are directly related to the parachors of the sorbate species. Since, for the light paraffins, the parachors are approximately proportional to critical temperature, the present data support this contention. However, from the thermodynamic point of view, the correlation with critical temperature is more satisfactory. The generalized correlation of the equilibrium data in terms of reduced adsorption potential suggests that the sorbed species all obey the same reduced equation of state, to a degree of approximation which is comparable with the accuracy of the ordinary law of corresponding states. The predictive value of such a generalized correlation is obviously great. The present data are however limited to a series of closely related compounds, and further experimental data are required in order to ascertain whether such a correlation is valid for sorbates of different types.

K. F LOUGHLIN
D. M. RUTHVEN

Department of Chemical Engineering,
University of New Brunswick,
Fredericton,
New Brunswick,
Canada

REFERENCES

1. BERING B. P., DUBININ M. M. and SERPINSKY V. V., *J. Coll. Interface Sci.* **21**, 378 (1966).
2. DUBININ M. M., *J. Coll. Interface Sci.* **23**, 487 (1967).
3. LOUGHLIN K. F., *Ph.D. Thesis.*, University of New Brunswick, Fredericton, Canada (1970).
4. COOK W. H. and BASMADJIAN D., *Can. J. Chem. Engng* **42**, 146 (1964).
5. DUBININ M. M., *Dokl. Akad. Nauk. SSSR* **138**, 866 (1961).

J. Phys. Chem. Solids, 1971, Vol. 32, pp. 2455–2480. Pergamon Press. Printed in Great Britain

SOFT X-RAY BAND SPECTRA AND MOLECULAR ORBITAL STRUCTURE OF Cr_2O_3, CrO_3, CrO_4^{-2} AND $Cr_2O_7^{-2}$

D. W. FISCHER
Air Force Materials Laboratory (LPA), Wright-Patterson Air Force Base, Ohio 45433, U.S.A.

(*Received* 22 *January* 1971; *in revised form* 5 *April* 1971)

Abstract—A new experimental technique is described whereby the soft X-ray CrL_{III}, CrK and OK emission and absorption spectra are combined and used to construct empirically a complete molecular orbital diagram for simple chromium–oxygen compounds. All spectral components are assigned specific transitions associated with bonding, antibonding and nonbonding molecular orbitals. In Cr_2O_3 the spectra indicate that the three outermost electrons have t_{2g} symmetry and are involved in two distinct bonding mechanisms. One of these electrons is localized in a metal–metal covalent bond and the other two are associated with the Cr–O π bond. The results do not support the narrow *d*-band model which has been proposed for transition metal oxides. For CrO_4^{-2} the deduced MO structure does not agree well with previous calculations and a new interpretation is suggested for the optical absorption spectrum. Contrary to previous assumptions, it is concluded that the highest filled orbital in CrO_4^{-2} is $3t_2$ instead of t_1. Relationships between the X-ray spectra and various solid state phenomena such as coordination symmetry, bonding distances, valence state, and bonding character are discussed. It is concluded that the X-ray band spectra from compounds are best interpreted on the basis of molecular orbital theory.

1. INTRODUCTION

SOFT X-ray valence band spectra have for many years been recognized for their potential use in determining the electronic structure of solids. In actual practice, however, the direct utility of the spectra along this line has been severely limited. Over the years many correlations have been made between the spectra from simple compounds and certain physical and chemical properties. Typically such a correlation will involve a direct relationship between measured wavelength shifts or intensity variations in certain spectral components and a specific property such as bond character, bonding distance, electrical conductivity, heats of formation, and so on. While these properties are indeed indirect manifestations of the electronic structure of the material, they provide a very incomplete picture of that structure.

Ideally, X-ray band spectra should be capable of yielding a more complete structural picture than this. This expectation arises from the basic origin of the spectra, including both emission and absorption components. X-ray emission bands, according to classical descriptions, are due to electron transitions from the occupied valence/conduction band to an inner level vacancy. Conversely, the absorption spectra are due to the ejection of an inner level electron into one of the available vacant states in the outer regions of the atom. Since it is the structure of these outermost electronic levels that determines the properties of a material, then, so the reasoning goes, the X-ray band spectra should provide us indirectly with all sorts of information about why a material behaves the way it does. Unfortunately, the number of actual cases in which X-ray band spectra have been successfully used in this manner is disappointingly few. There are several reasons for this but in general they can be combined into two problem areas; (1) obtaining reliable band spectra and (2) interpretation of the spectra. It is the intention of this report to focus on these problems (primarily the latter one) for some simple chromium–oxygen compounds such as Cr_2O_3, CrO_3, CrO_4^{-2} and $Cr_2O_7^{-2}$.

Compounds of the first row transition metals are especially interesting from an electronic structure standpoint as reflected in their remarkably varied physical and chemical properties[1]. In attempting to unravel the complexities of the electronic structure of some of the more fascinating compounds in this group, many different types of experiments have been performed. It is a curious fact, however, that X-ray band spectra, despite their potential value in determining significant features of the electronic structure, have been virtually ignored in studying these materials. To be sure, there are problems in obtaining and using the spectra but there are distinct advantages, too. The present author has attempted to indicate this in some recent work on the soft X-ray spectra from some titanium and vanadium compounds[2–6].

One of the key points in two previous papers[4, 6] has been the use of a molecular orbital (MO) model to interpret the titanium and vanadium $L_{II,III}$ emission and absorption spectra. Recently, several other workers have also recognized the utility of MO theory in explaining certain features of X-ray band spectra which are difficult or impossible to rationalize by any other means[7–15]. There are still those, on the other hand, who claim that MO theory is fine for explaining the bonding in highly covalent materials such as transition metal complexes, but resist any effort to apply it to predominantly ionic materials such as Ti_2O_3, VO_2 and Cr_2O_3 or to metal-like compounds such as TiC or VC. Actually, however, MO theory is quite flexible in that it is capable of describing any degree of covalent-ionic bonding character so that in principle it is perfectly legitimate to apply it to simple inorganics such as oxides, nitrides and carbides. There is certainly a high degree of interaction between metal atom and nonmetal atom orbitals in these compounds so it seems only reasonable to use a bonding model which takes these interactions into account. If that model is also capable of accurately explaining the myriad of details in the soft X-ray emission and absorption band spectra better than any other model which has been advanced then it must be worth some consideration. One of the purposes of this paper is to demonstrate that the MO model is directly applicable to chromium–oxygen compounds in which chromium has either a +3 or +6 valence state and occupies either an octahedral or tetrahedral coordination site. The X-ray band spectra will then be used to construct empirically a complete MO energy-level diagram involving both occupied and vacant orbitals within 20 eV or so of the Fermi energy. No other experimental technique is capable of doing this.

In order to empirically determine the complete electronic structure of a transition metal compound, however, one needs more information than is contained in any one emission band or absorption spectrum. The reason for this is rooted in the symmetry characters of the outer orbitals and the dipole selection rules governing X-ray transitions. In forming a compound such as Cr_2O_3 the $3d$, $4s$ and $4p$ levels of the metal atom interact with the $2s$ and $2p$ levels of the nonmetal atom. According to MO theory, using a linear combination of atomic orbitals (LCAO), this interaction will result in a series of bonding and antibonding molecular orbitals such as shown later on in this report in Fig. 3. The important point to note here is that these outermost electron levels will consist of admixed s, p and d symmetries. Now a K X-ray emission band results from transitions of the outermost electrons to a vacancy created in the $1s$ core level. According to the dipole selection rules only electrons in levels having p symmetry can make such a transition. The K band, therefore, will reflect only the distribution of p symmetry in the outer levels and tell us nothing about the distribution of s and d symmetry. Conversely, the L or M band will reflect the distribution of s and d symmetry but not of p symmetry. Obviously, if we expect to obtain a complete pictute of the outer electronic structure it will be necessary to combine the information present in both K and L band spectra. Most X-ray band structure investigations of compounds have not been done from this viewpoint which makes the information obtained about the band structure very limited in scope. The importance of using the combined spectra has been recently demonstrated by this author for some titanium and vanadium compounds [5, 6]. In this report, the following spectra will be used for the chromium–oxygen compounds: chromium L_{III} (valence orbitals → $Cr2p^3/2$), chromium L_{II} (valence orbitals → $Cr2p^1/2$), chromium $K\beta_{2,5}$ (valence orbitals → $Cr1s$), oxygen K (valence orbitals → $O1s$) and their corresponding absorption spectra.

The investigation of these various band spectra from chromium–oxygen compounds is presented, therefore, with several objectives in mind. The primary objective is to empirically determine the complete outer electronic arrangement and energy positions of the bonding, antibonding, and nonbonding molecular orbitals. Also, the different valence states and coordination numbers of the chromium ion in various compounds should, according to MO theory, result in quite different energy-level arrangements and symmetry character of levels. This, in turn, should cause specific differences to appear in the X-ray band spectra and therefore give a valid indication of whether or not the MO model is capable of accurately explaining all the changes which occur in the spectra. It will be shown that this model is indeed applicable to the chromium–oxygen compounds. The empirical electronic structure obtained will be compared to other types of experimental data and to theoretical calculations, where possible.

It will be seen that the X-ray results do not agree very well with theoretical calculations of the electronic structure in some cases and reasons for the disagreement are suggested. New interpretations will be given for the optical absorption spectra of the CrO_4^{-2} ion based on the X-ray MO structure. In Cr_2O_3 two types of $3d$ (t_{2g}) electrons are observed and the results do not agree with the very narrow d model proposed elsewhere [1, 16].

2. EXPERIMENTAL

(a) *Instrumentation*

The plane single-crystal vacuum spectrometer used to obtain the spectra is the same as described previously [2]. Characteristic X-ray spectra are produced by direct electron beam bombardment of the target material. The interchangeable anode assembly of brass, copper or aluminum is constructed so that the X-ray takeoff angle is continuously variable between 0° and 90°. A flow-proportional detector with Formvar window and argon–methane flow gas is used at a reduced pressure of 120 torr. Spectrometer vacuum under normal operating conditions is about 1×10^{-6} torr.

Wavelength positions of the spectral features measured in this investigation have a probable error of $\pm 0{\cdot}02$ Å ($\pm 0{\cdot}3$ eV) but wavelength differences could be measured to $\pm 0{\cdot}005$ Å ($\pm 0{\cdot}1$ eV). The data points on the spectral curves have a statistical deviation of 2–3 per cent at the peak maxima and less than 1 per cent at the tails.

(b) *Dispersing crystal and resolution*

A rubidium acid phthalate crystal (RAP, $2d = 26{\cdot}118$ Å) was used in obtaining both the chromium L and oxygen K spectra [3]. The oxygen K bands were also obtained with a clinochlore crystal [$2d = 28{\cdot}393$ Å [2]] to aid in removing the anomalous high energy peak introduced by the RAP crystal [3].

The effective diffraction pattern of the spectrometer (window width) was tentatively determined although there is not universal agreement on the way to do this for a single plane-crystal spectrometer. The technique used here was to record the $K\alpha_1$ and $K\alpha_2$ lines of V, Cr, Mn, Fe, Co and Ni in various multiple orders and compare the measured half-widths to the so-called standard half-widths by the expression $W_m^2 = W_\lambda^2 + W_A^2$, where W_m = the half-width of the experimentally measured line, W_λ = the true half-width of the line and W_A = the half-width of the spectrometer window. For the RAP crystal the instrumental window was calculated to be 0·81 eV at the CrL_{III} band maximum (21·7 Å) and 0·53 eV at the oxygen K band maximum (23·6 Å). With the clinochlore crystal the window is 0·94 eV at the oxygen K band.

Due to the fact that the window width of the spectrometer varies with the wavelength and that the exact shape of the window is not known, the band spectra shown in this report have not been corrected for instrumental broadening. This is not considered to have any significant effect on the spectral interpretations which are offered.

The chromium K spectra which are used were not obtained by the author but were taken from the literature. The exact literature references are given later in the discussions of specific compounds and these spectra are also uncorrected for instrumental effects.

(c) *Sample preparation and spectral measurement*

To obtain the emission band spectra, target specimens of Cr_2O_3 were prepared by mixing a fine powder into a slurry with ethanol and painting it in a thin film on the anode surface. Specimens of CrO_3, the chromates and dichromates were prepared in a similar fashion except that the slurry liquid was H_2O instead of ethanol. After painting it on the anode surface, the specimen film was dried in air at 120°C, coated with a finely sprayed film of graphite and placed immediately into the spectrometer vacuum. When prepared in this fashion, all of the compounds, including CrO_3, remained chemically stable under normal excitation conditions.

Each of the sample materials was obtained from at least two different sources and checked by X-ray diffraction. One of the Cr_2O_3 specimens was a broken segment of a special high purity single crystal.

Obtaining the X-ray band spectra from these materials involved a tremendous amount of work. For each spectrum shown in this report, at least 20 complete runs were made. These runs were made under a wide variety of excitation conditions by varying parameters such as the bombarding electron beam voltage, the beam current, the sample chamber vacuum, and the length of time that the sample was subjected to the primary electron beam. Before any of the spectra were considered to be truly characteristic of the original sample material they had to be completely reproducible time after time. All of the chromium L and oxygen K spectra shown here satisfy this requirement. This is important because a typical bombarding electron beam voltage of 3–4 kV will only probe the first 100 layers or so below the surface. If any chemical change occurs at or near the surface during the excitation process, the soft X-ray band will not be characteristic of the starting material.

For the chromium L and oxygen K wavelength region it is extremely difficult to make absorption specimens which are both uniform enough and thin enough to transmit the continuum radiation in the usual manner. Successful films were made for only one of the compounds, Cr_2O_3. This was done by mixing an ultrafine powder in a dilute solution of parlodion in amyl acetate. Using an eyedropper, a few drops of this mixture were deposited on the surface of a shallow pan of water. The drops spread out to form a uniform film which can be picked up on a wire hoop. The film thickness can be varied by the amount of powder mixed in the solvent originally. An optimum thickness was determined by trial and error and for the CrL_{III} absorption in Cr_2O_3 it was found to be about 0·6 mg/cm^2.

The CrL_{III} and OK absorption spectra for all of the other materials were obtained by the differential self-absorption method which has been explained previously[2, 3]. Although one cannot obtain absolute absorption coefficients from these self-absorption spectra they have the advantage of being obtained from the same specimens and at the same time as the emission bands. This considerably simplifies the matching of emission and absorption energy scales and provides strong confidence that both types of spectra represent precisely the same chemical state of the target material.

3. RESULTS AND DISCUSSION

(a) *General comments*

The chromium compounds of particular interest in this investigation are the oxides Cr_2O_3 and CrO_3, the chromates (CrO_4^{-2}), and dichromates $(Cr_2O_7^{-2})$. In each of these materials the chromium ion is either octahedrally or tetrahedrally coordinated to the oxygen ligands. In Cr_2O_3, chromium has a +3 valence and occupies a slightly distorted octahedral site; in CrO_3, CrO_4^{-2} and $Cr_2O_7^{-2}$, chromium has a +6 valence and is tetrahedrally coordinated. This tetrahedron becomes quite distorted in progressing from CrO_4^{-2} to CrO_3 to $Cr_2O_7^{-2}$. As will be shown, this distortion has a significant effect on the X-ray band spectra, and is caused directly by gross variations in the chromium–oxygen and chromium–chromium interatomic distances. The various crystallographic parameters which influence the bonding, and hence the X-ray bands, are summarized in Table 1.

The chromium $L_{II,III}$ emission and absorption spectra from the compounds compared to that from the pure metal are illustrated in Fig. 1. Except for the pure Cr spectrum and Cr_2O_3 emission band, none of these spectra have ever been shown in the literature before. As can be seen, the total band spectrum covers the 550–590 eV (21·0 to 22·5 Å) energy region. Each of the emission bands (solid line spectra) are subject to serious distortion from self-absorption effects very similar to that shown previously for titanium and vanadium $L_{II,III}$ bands[2, 3, 5, 6]. Consequently, the bands illustrated in Fig. 1 were obtained under conditions of negligible self-absorption although multiple-vacancy satellite emission is at saturation[2]. The numbers placed on the high energy tails of the emission bands indicate the bombarding electron beam voltage, beam current and takeoff angle with which they were obtained. Each of the $L_{II,III}$ absorption spectra from the compounds (dashed curves) are self-absorption replicas obtained as described previously[2, 3, 6]. The pure metal spectrum is included only for reference purposes and will be discussed in detail in a subsequent report.

The oxygen K emission and absorption spectra from these same compounds are shown in Fig. 2. Here also, the emission bands (solid curves) were obtained with negligible self-absorption and are uncorrected for broadening effects. Absorption spectra (dashed curves) are self-absorption replicas. The relation between these oxygen spectra and the chromium $L_{II,III}$ and chromium K bands will later be compared in detail for each compound.

In Figs. 1 and 2 each of the emission maxima is denoted by a capital letter and each of the absorption maxima by a lower-case letter. The energy positions and relative intensities of these maxima are the basis of the molecular orbital interpretation which will follow. As mentioned earlier, each of the compounds represented in the figures result from different coordination symmetries and/or valence states

Table 1. Interatomic distances in some chromium–oxygen compounds

Compound	Cr co-ord no.	Structure	Cr–O distances (Å)	Shortest Cr–Cr distance (Å)
Cr metal	8	B.C.C.		2·50
Cr_2O_3 (Ref. [20])	6	Rhombohedral	$O_1, O_2, O_3 = 2{\cdot}02$ $O_4, O_5, O_6 = 1{\cdot}97$	2·65
CrO_3 (Ref. [40])	4	Orthorhombic	$O_1, O_2 = 1{\cdot}79$ $O_3, O_4 = 1{\cdot}81$	3·32
Na_2CrO_4 (Ref. [41])	4	Orthorhombic	$O_1, O_2, O_3, O_4 = 1{\cdot}60$	4·62
$(NH_4)_2Cr_2O_7$ (Ref. [41])	4	Monoclinic	$O_1 = 1{\cdot}55$ $O_2 = 1{\cdot}57$ $O_3 = 1{\cdot}78$ $O_4 = 1{\cdot}91$	3·22

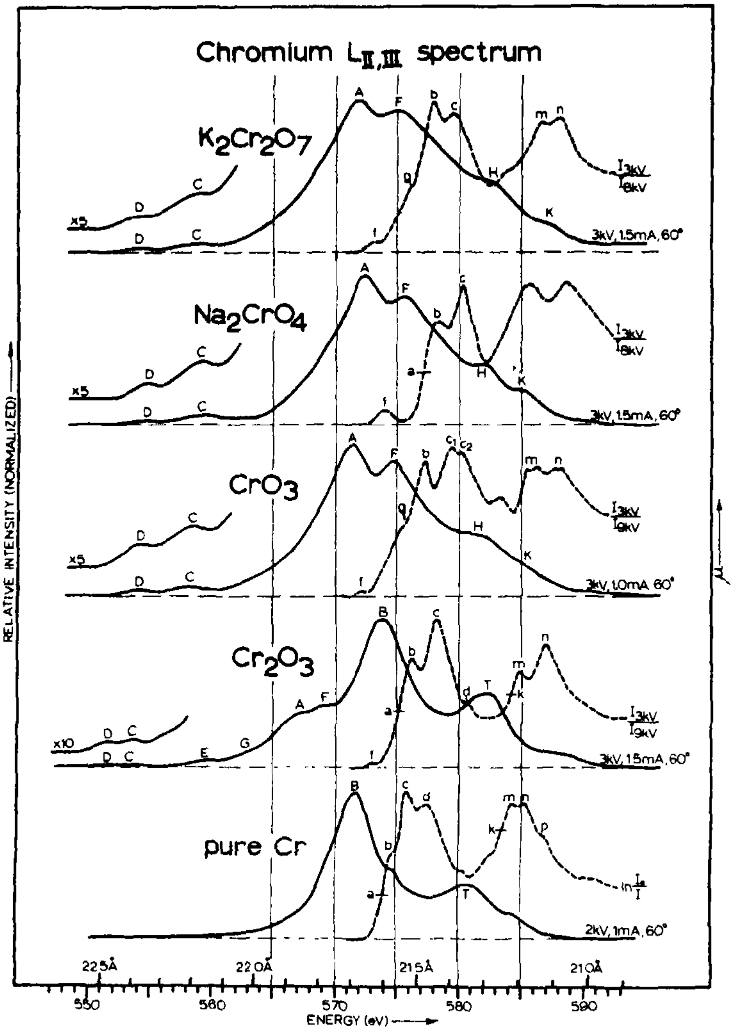

Fig. 1. Uncorrected chromium $L_{II,III}$ emission and absorption spectra from pure element and compounds. Emission bands obtained under negligible self-absorption conditions. Absorption spectra from compounds are self-absorption replicas. All spectra normalized to same height for comparison purposes.

of the chromium ion. According to MO theory, each of these symmetries should lead to a different interaction between the chromium and oxygen outer orbitals and therefore produce different MO energy-level arrangements. This in turn should result in specific differences in the X-ray emission and absorption bands and provide a reasonably good test of whether or not the proposed MO interpretation of the spectra is at least qualitatively correct. The interpretation which is offered here follows along the same lines developed previously for titanium and vanadium compounds[4, 6]. The derivation and formation of molecular orbitals for various coordination symmetries is text book information[17, 18] and will not be detailed here. It is of interest, however, to know what type of MO diagram

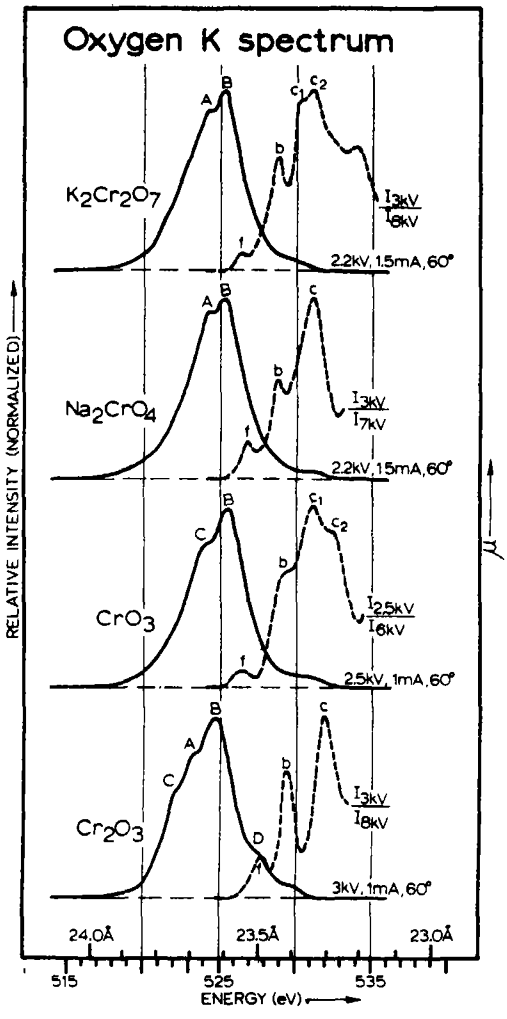

Fig. 2. Uncorrected oxygen *K* emission and absorption spectra. Emission bands obtained under negligible self-absorption conditions. Absorption spectra are self-absorption replicas. All spectra normalized to same height for comparison purposes.

is to be expected, in general, for a transition metal ion in octahedral and tetrahedral symmetry sites. This is indicated schematically in Fig. 3. These diagrams are adapted from Ballhausen and Gray's book[17] and are based on the assumption that the metal ion 3*d*, 4*s* and 4*p* atomic orbitals interact in the LCAO approximation with the oxygen 2*s* and 2*p* orbitals. As such, they are only qualitatively correct but they provide a firm starting point for interpreting the individual X-ray spectra. The idea now is to assign each X-ray spectral maximum as being due to an electron transition between a specific MO and core level. Actually, this is considerably easier to do for X-ray spectra than for optical spectra because in the X-ray case the inner level is essentially atomic in character and can be considered to have a constant energy value for a given compound. If such MO assignments can be made with a reasonable degree of confidence for both the X-ray emission and absorption spectra then obviously these spectra will form a strong empirical foundation for deducing a complete and accurate molecular-orbital structure for each compound. Since no other experimental technique has been proven capable of doing this, the results could have far-reaching significance as to the virtually untapped potential of the soft X-ray band spectra from compounds.

For the chromium and oxygen band spectra discussed in this report the MO interpretations rely heavily on the usual dipole selection rules. By taking into account the relative peak intensities and their relative energy positions for each spectral series, therefore, we might expect to make reasonably confident assignments for each component. This will be done and explained in detail for each type of compound in the sections which follow. Included with the schematic MO diagrams in Fig. 3 are vertical lines indicating which MO's would most likely be expected to contribute to the CrL$_{III}$ and OK spectra. The MO's contributing to the CrL$_{III}$ band contain at least some 3*d* or 4*s* admixture while those involved in the OK band contain 2*p* states. Table 2 contains the peak assignments for the CrL$_{II,III}$ spectra shown in Fig. 1. Table 3 lists the experimentally measured energy positions for these peak maxima. Tables 4 and 5 give comparable data for the oxygen *K* spectra. These tables will be frequently referred to in the following sections and although the reasoning behind the specific electron transition assignments

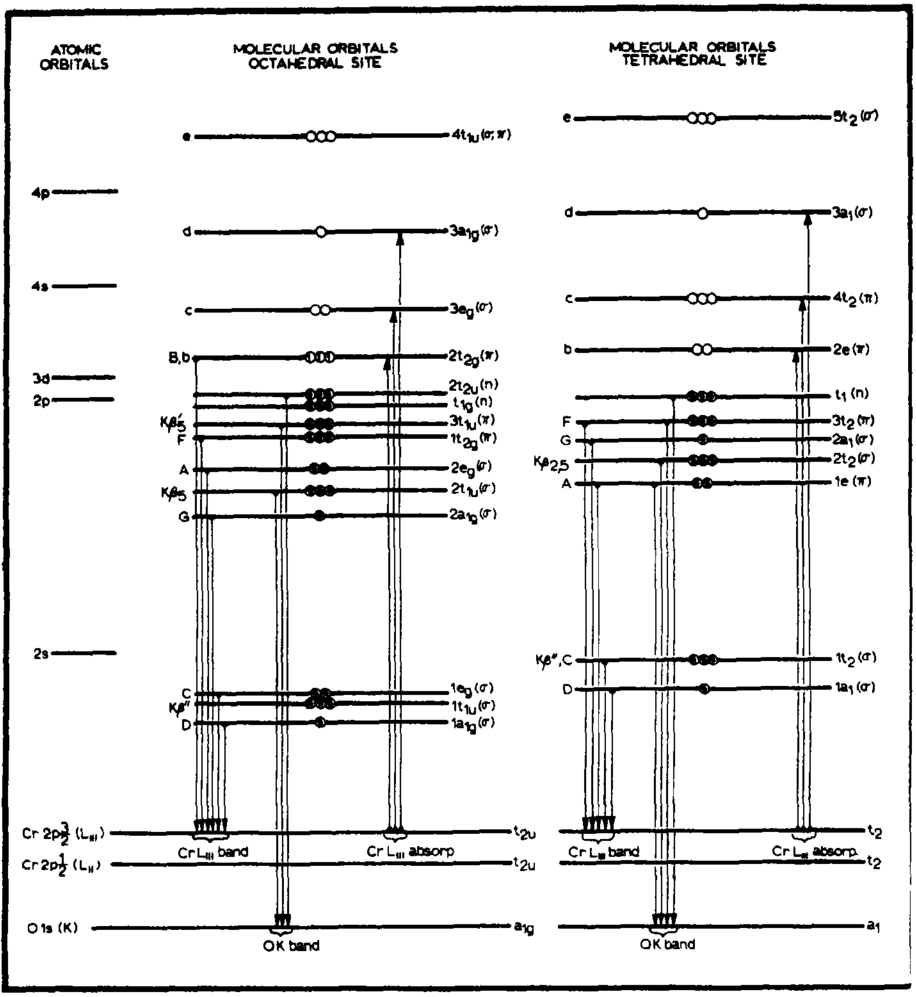

Fig. 3. Schematic molecular-orbital energy-level diagrams for chromium in octahedral and tetrahedral symmetry sites with oxygen anion. Vertical lines indicate electron transitions most likely to contribute to specific spectra. Diagrams adapted from Ballhausen and Gray[17]. Not drawn to scale.

may not be apparent at this point, it will be later on.

Each of the CrL$_{III}$ and OK band spectra illustrated in the following sections have been unfolded into their constituent components by means of the DuPont Model 310 Curve Resolver. Since complicated spectra can often be resolved into almost as many components as the operator has the patience to attempt, two basic points were adhered to for the spectra shown here; (1) both Gaussian and Lorentzian unfolds were tried for each spectrum and (2) the simplest solution was sought, i.e., the spectra were resolved into as few components as possible. As a result it was found that the CrL$_{III}$ spectra (both emission and absorption) were best approximated by Gaussian components and the OK spectra by Lorentzian components. This was the case for every compound, including many which are

Table 2. Suggested electronic transitions responsible for intensity maxima observed in chromium $L_{II,III}$ *emission and absorption spectra from compounds*

Emission spectra

Peak	Electron transition Octahedral site	Electron transition Tetrahedral site	
B	$2t_{2g} \rightarrow 2p\frac{3}{2}$	not observed	L_{III} components
F	$1t_{2g} \rightarrow 2p\frac{3}{2}$	$3t_2 \rightarrow 2p\frac{3}{2}$	
A	$2e_g \rightarrow 2p\frac{3}{2}$	$1e \rightarrow 2p\frac{3}{2}$	
G	$2a_{1g} \rightarrow 2p\frac{3}{2}$	$2a_1 \rightarrow 2p\frac{3}{2}$	
C	$1e_g \rightarrow 2p\frac{3}{2}$	$1t_2 \rightarrow 2p\frac{3}{2}$	
D	$1a_{1g} \rightarrow 2p\frac{3}{2}$	$1a_1 \rightarrow 2p\frac{3}{2}$	
T	$2t_{2g} \rightarrow 2p\frac{1}{2}$	not observed	L_{II} components
K	$1t_{2g} \rightarrow 2p\frac{1}{2}$	$3t_2 \rightarrow 2p\frac{1}{2}$	
H	$2e_g \rightarrow 2p\frac{1}{2}$	$1e \rightarrow 2p\frac{1}{2}$	
E	$1a_{1g}, 1e_g \rightarrow 2p\frac{1}{2}$		

Absorption spectra

Peak	Electron transition Octahedral site	Electron transition Tetrahedral site	
a	L_{III} edge	L_{III} edge	L_{III} components
b	$2p\frac{3}{2} \rightarrow 2t_{2g}$	$2p\frac{3}{2} \rightarrow 2e$	
c	$2p\frac{3}{2} \rightarrow 3e_g$	$2p\frac{3}{2} \rightarrow 4t_2$	
g		$2p\frac{3}{2} \rightarrow en$	
k	L_{II} edge	L_{II} edge	L_{II} components
m	$2p\frac{1}{2} \rightarrow 2t_{2g}$	$2p\frac{1}{2} \rightarrow 2e$	
n	$2p\frac{1}{2} \rightarrow 3e_g$	$2p\frac{1}{2} \rightarrow 4t_2$	
f	exciton (?)	exciton (?)	

Table 3. Energy positions of peak maxima in chromium $L_{II,III}$ *emission and absorption spectra. All values given in* eV *with probable error of* ± 0·2 eV

Emission spectra

Material	*B*	*F*	*A*	*G*	*C*	*D*	*T*	*H*	*K*
Cr metal	571·5	—	—	—	—	—	580·8	—	—
Cr_2O_3	[572·1 573·8]	569·2	566·4	563·4	553·2	551·3	582·3	—	—
CrO_3	—	574·7	571·5	569·3	558·0	553·8	—	580·8	584·0
Na_2CrO_4	—	575·7	572·5	569·3	558·9	554·6	—	581·6	584·7
$Na_2Cr_2O_7$	—	573·9	571·7	570·3	558·7	553·8	—	581·5	586·2

Absorption spectra

Material	*f*	*a*	*b*	*c*	*d*	*g*	*k*	*m*	*n*
Cr metal	—	573·8	574·6	575·7	577·2	—	583·3	584·2	585·2
Cr_2O_3	572·9	575·0	576·0	578·1	580·5	—	584·0	584·9	586·9
CrO_3	572·1	—	577·1	[578·9 580·4]	—	575·9	—	586·2	588·2
Na_2CrO_4	573·9	576·9	577·9	580·2	—	—	—	—	—
$Na_2Cr_2O_7$	572·9	—	577·7	579·7	—	575·9	—	586·5	588·9

Table 4. Suggested electronic transitions responsible for intensity maxima observed in chromium K and oxygen K X-ray spectra from chromium–oxygen compounds

Spectrum	Peak	Electron transition Octahedral site	Electron transition Tetrahedral site
Cr *K* Emission	$K\beta_{2,5}$ (or $K\beta_5$)	$2t_{1u} \to 1s$	$2t_2 \to 1s$
	K_5'	$3t_{1u} \to 1s$	not observed
	$K\beta''$	$1t_{1u} \to 1s$	$1t_2 \to 1s$
Cr *K* Absorption	*b*	$1s \to 2t_{2g}$	not observed
	c	$1s \to 3e_g^*$	$1s \to 4t_2$
	d	$1s \to 3a_{1g}$	$1s \to 3a_1$
	e	$1s \to 4t_{1u}$	$1s \to 5t_2$
O *K* Emission	*A*	$1t_{2g} \to 1s$	—
	B	$t_{1g}, t_{2u} \to 1s$	$t_1 \to 1s$
	C	$2t_{1u} \to 1s$	$1e \to 1s$
	D	$2t_{2g} \to 1s$	—
O *K* Absorption	*a*	*K* edge	*K* edge
	b	$1s \to 2t_{2g}$	$1s \to 2e$
	c	$1s \to 3e_g$	$1s \to 4t_2$
	f	exciton (?)	exciton (?)

Table 5. Energy positions of peak maxima in oxygen K emission and absorption spectra. All values given in eV *with probable error of* ± 0·2 eV

	Emission				Absorption		
Material	*A*	*B*	*C*	*D*	*f*	*b*	*c*
Cr_2O_3	523·0	524·7	521·7	527·7	527·5	529·3	531·9
CrO_3	—	525·5	523·6	—	526·4	529·1	[531·0 532·4]
Na_2CrO_4	523·8	525·2	522·6	—	526·5	528·5	530·9
$Na_2Cr_2O_7$	523·9	525·5	522·6	—	526·3	528·6	[530·1 530·8]

not shown in this report. Why the different spectra should unfold into different symmetry components is not clear to the author. Inner levels are generally believed to be Lorentzian in shape while outer levels (molecular-orbitals) are often assumed to have a Gaussian shape[19]. At any rate, whether coincidental or not, the unfolding procedure used here results in precisely the correct number of components predicted by the MO model for both octahedral and tetrahedral compounds. With certain reservations, these unfolded components can be used not only to accurately position the individual electronic orbitals but to give some indication of their width as well.

With these points in mind, let us now proceed to examine the X-ray band spectra from some individual compounds.

(b) Cr_2O_3

Cr_2O_3 crystallizes in the corundum structure in which the chromium–oxygen octahedraon is slightly distorted[20]. Along the threefold axis the chromium ions (cations) form pairs and are ordered antiferromagnetically up to the Neel temperature of about 45°C[21]. It is an insulator both above and below this temperature. Apparently no calculations have been made of the electronic band structure for Cr_2O_3 but some work has been done on the isostructural compounds Ti_2O_3 and V_2O_3 [1, 16, 22, 23]. It will be assumed here that certain features of the band structure for these three sesquioxides (corundum phase) are very similar, the main difference being the number of $3d$ electrons.

The $CrL_{II,III}$ emission and absorption spectra obtained from Cr_2O_3 are shown in Fig. 1. According to the dipole selection rules these spectra should reflect primarily the distribution of $3d$ symmetry in the outermost levels of the compounds. Since it is these d electrons that are mainly responsible for many of the important properties (e.g. conductivity, magnetism), the $L_{II,III}$ spectra should contain some important information about the structure. It is obvious in Fig. 1 that the appearance of the emission band from Cr_2O_3 is considerably different than that from elemental Cr. New components labeled *F*, *A*, *G*, *C*, *D* and *E* are observed in the oxide but not at all in the pure metal. This is exactly what was observed previously for the $L_{II,III}$ bands from titanium and vanadium oxides[4]. The extra components in those oxides were interpreted as being due to the presence of ligand $2p$ and $2s$ orbitals and the same explanation is used here for Cr_2O_3. It will be noticed in Fig. 1 that the $L_{II,III}$ absorption spectrum does not change as much as the emission band in going from metal to oxide. The exact energy positions of each of the emission and absorption maxima referred to are listed in Table 3.

In order to interpret the $L_{II,III}$ spectrum from Cr_2O_3 it is necessary to have also at hand the CrK and OK band spectra. It is also helpful to refer to the schematic MO energy-level diagram for octahedral symmetry shown in Fig. 3. The method of relating the X-ray spectra to the MO structure is illustrated in Fig. 4. Shown here are CrL_{III} and OK spectra obtained in this work and CrK band spectrum taken from Menshikov and Nemnonov[24]. The zero of energy is arbitrarily placed at the Fermi energy which is here assumed to be the CrL_{III} absorption edge. Each of the spectra is positioned on the relative energy scale by lining up peaks *b* and *c* in the absorption spectra. The reason for this will become apparent shortly.

As mentioned earlier, the CrL_{III} spectrum has been resolved into Gaussian components and the OK spectrum into Lorentzian components. Before unfolding the L_{III} emission band, everything on the high energy side of the L_{III} absorption edge was subtracted away. It is assumed that any emission components which occur on this side of the edge are L_{III} multiple ionization satellites and L_{II} band features and can therefore be ignored in determining the MO structure. Also, all the absorption features which occur to the high energy side of maximum *d* (see Fig. 1) are ignored since they are L_{II} absorption transitions involving the same outer orbitals represented by the L_{III} components (see Table 2). The CrK spectrum has not been unfolded because it has been replotted from a Russian publication and not enough is known about the experimental conditions used to obtain it.

Now, referring to Figs. 3 and 4, let us examine the CrL_{III} emission band. Since this spectrum should reflect primarily the distribution of $3d$ states we will assume that the main components are due to transitions from the occupied orbitals which contain a significant amount of $3d$ character. Peaks *B*, *F* and *A* are therefore assigned as originating in the $2t_{2g}$, $1t_{2g}$ and $2e_g$ MO's respectively. The $2t_{2g}$ orbital is only partially occupied so it should be involved in the absorption spectrum also. In fact, it is assumed that the first two absorption maxima represent the two lowest vacant MO's which are $2t_{2g}$ and $3e_g$. These two orbitals consist mostly of $3d$ character but there is also expected to be some p character present because of the chromium–oxygen orbital overlap. Indeed, both the CrK and OK absorption spectra contain *b* and *c* maxima and it is the alignment of these peaks in all three spectra which dictates their relative

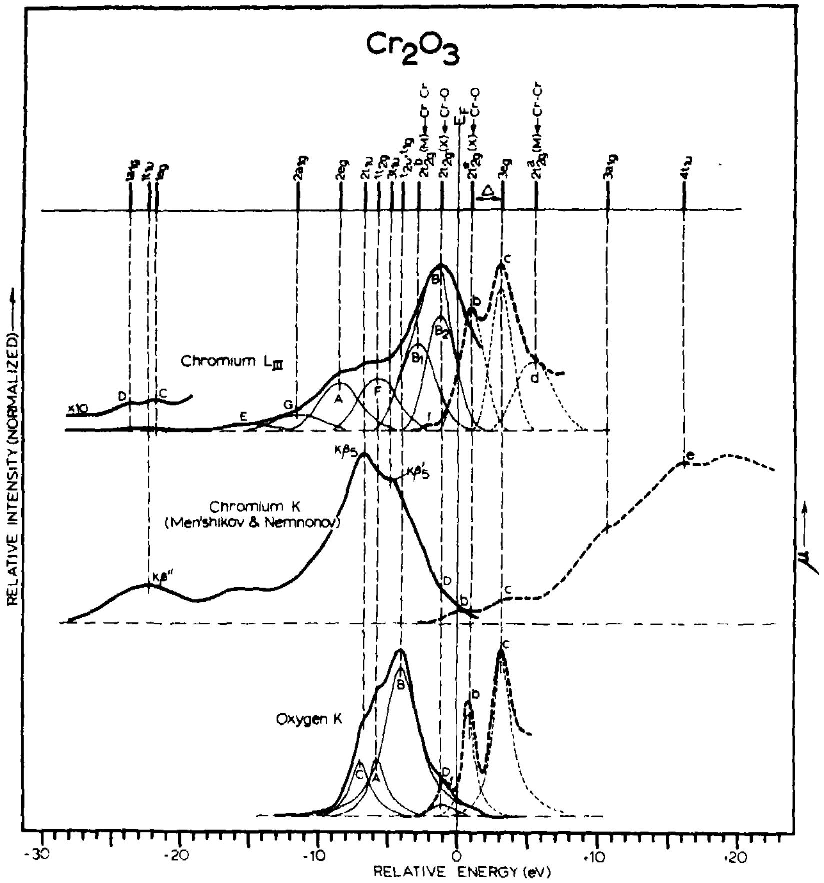

Fig. 4. Empirical deduction of MO structure of Cr_2O_3 by combining the chromium L, chromium K and oxygen K X-ray band spectra.

positions on the energy scale. In the chromium K emission band the two strongest peaks are assumed to originate in orbitals consisting of some $4p$ symmetry, which in this case would be the $2t_{1u}$ and $3t_{1u}$ orbitals. It is further assumed that the main oxygen K emission component originates in the t_{2u} and t_{1g} non-bonding $2p$ 'lone-pairs'. Peaks C and D in the L_{III} band and $K\beta''$, in the K band would then be due to the $1e_g$, $1a_{1g}$ and $1t_{1u}$ levels which are associated primarily with 0 $2s$ states. As can be seen in Fig. 4, one of the really attractive features of such an MO interpretation is that orbitals such as $1t_{2g}$, $2t_{2g}$ and $3e_g$ which consist of admixed $3d$ and $2p$ states contribute components to both the CrL_{III} and OK spectrum. Furthermore, the relative intensities of the peaks reflect the relative degrees of admixture which would be intuitively expected from the normal assumptions made about the individual orbitals as being either strongly bonding or slightly bonding and as being localized primarily on either the metal ion or ligand. The MO assignments for all the peaks are summarized in Table 2.

One of the more significant consequences of the peak assignments discussed above is brought to light by a closer examination of peaks B, b and d in the CrL_{III} spectrum. Peak B actually consists of two components B_1 and B_2. It is suggested here that all four of these components, B_1, B_2, b and d involve $2t_{2g}$

orbitals. This is a consequence of the two different but simultaneous kinds of bonding involving the $3d$ (t_{2g}) electrons. In the corundum structure, c-axis cation–cation pairs are formed and strong t_{2g}–t_{2g} covalent bonding can occur between the cations (in this case chromium) forming the pair[22, 25, 26]. The other type of bond is the t_{2g}–$p\pi$ (chromium–oxygen) bond. In order for these two types of bonding to be clearly observable in the L_{III} spectrum the $2t_{2g}$ orbitals would be required to become non-degenerate and split apart considerably in energy. Some splitting will occur as a consequence of the trigonal field in the corundum structure. Also, the chromium atoms forming the c-axis pairs have the closest cation–cation distances in the structure (see Table 1) and the t_{2g} orbitals associated with the covalent bonding in this pair could exhibit a rather large bonding–antibonding splitting[22, 25]. The antiferromagnetic ordering could further contribute to the splitting. Therefore it is suggested that CrL$_{III}$ components B_1 and d represent the bonding and antibonding set of the $2t_{2g}$ orbital associated with chromium–chromium covalent bond. These components are labeled $2t^b_{2g}(M)$ and $2t^a_{2g}(M)$ respectively (Fig. 4) and are assumed to be single electron states. The $2t^b_{2g}(M)$ orbital is occupied, the $2t^a_{2g}$ (M) orbital is vacant. Components B_2 and b would then represent the occupied and vacant two-electron states associated with the $3d$–$2p\pi$ bond. They are labeled $2t_{2g}(X)$ and $2t^*_{2g}(X)$ in Fig. 4.

The three outermost electrons in Cr_2O_3 are therefore involved in two distinct bonding mechanisms. One of the electrons is localized in a metal–metal covalent bond and the other two are associated with the metal–oxygen π bond. Whether or not this latter orbital has a true energy gap between the occupied and vacant states is not clear from the X-ray spectra but the Fermi energy is assumed to be in this region. There is no obvious evidence of a collectivized orbital.

The above interpretation is further supported by the fact that since components B_1 and d represent the metal–metal covalent bond, they should consist of pure $3d$ character (more or less) and therefore should not contribute to either the CrK or OK spectra. As can be seen in Fig. 4 there are indeed no components in either of the K spectra corresponding to the energy positions of B_1 and d. On the other hand since components B_2 and b in the L_{III} spectrum are interpreted as being due to the $3d$–$2p\pi$ bond, they should also contribute something to the oxygen K spectrum and perhaps also to the Cr K spectrum. It is seen in Fig. 4 that these contributions do actually occur as evidenced by peaks D and b in both the O K and Cr K spectra. These spectral relations are also evident in Table 6.

Actually, the above interpretation of peaks B, b and d in the L_{III} spectrum is not based solely on the results obtained for Cr_2O_3. Much consideration was also given to the TiL_{III} spectrum from Ti_2O_3 and the VL$_{III}$ spectrum from V_2O_3 which have been shown previously [2–4]. It is an experimental fact that the relative intensity of emission component B and also absorption component b in these oxides is directly proportional to the number of $3d$ electrons while the intensities of components F, A and G remain virtually unchanged with respect to each other. It must be concluded, therefore, that components B and b are associated with the partially occupied $2t_{2g}$ orbital and that components F, A and G are associated with orbitals which are filled in all cases (see Table 2).

The CrK band shown in Fig. 4 has been interpreted by Menshikov and Nemnonov[24] in terms of two different types of d electrons but their interpretation is not in agreement with the one presented here. They concluded that the $K\beta'_5$ peak was associated with the collectivized (conduction) d electrons, the $K\beta_5$ peak with the localized d electrons, and the $K\beta''$ peak as due to a crossover transition of the oxygen valence electrons to the chromium K level. According to the MO model of Fig. 4, however, all three of the $K\beta$ peaks are

Table 6. Line widths and relative intensities of unfolds in $\mathrm{Cr_2O_3}$ *band spectra. The values have not been corrected for spectrometer window or internal level width*

Spectrum	Component	Assigned MO	$W\frac{1}{2}$ (eV)	Relative integrated intensity (emission)
$\mathrm{Cr}L_{\mathrm{III}}$ (Gaussian) $3d$ character	B_1	$2t_{2g}^{b}$ (M) cation–cation	3·0	89
	B_2	$2t_{2g}$ (X) cation–anion	2·4	100
	F	$1t_{2g}$	3·3	62
	A	$2e_g$	3·4	60
	G	$2a_{1g}$	3·8	21
	b	$2t_{2g}^{*}(X)$ cation–anion	2·4	—
	c	$3e_g$	2·1	—
	d	$2t_{2g}^{a}(M)$ cation–cation	3·0	—
OK (Lorentian) $2p$ character	B	t_{2u}	2·8	100
	A	$1t_{2g}$	1·6	21
	C	$2t_{1u}$	1·7	23
	D	$2t_{2g}(X)$	1·8	5
	b	$2t_{2g}^{*}(X)$	1·1	—
	c	$3e_g$	1·5	—

seen to be associated with localized orbitals consisting partially of chromium $4p$ character. Peak $K\beta_5'$ arises from the $4p$–$2p\pi$ bond, peak $K\beta_5$ from the $4p$–$2p\sigma$ bond, and peak $K\beta''$ from the $4p$–$2s$ bond. This interpretation is more in accord with the dipole selection rules than that offered by Menshikov and Nemnonov. It serves, however, as a good example of the advantage gained in using the combined K and L spectra for structure determinations instead of relying on one spectrum alone.

Adler and Brooks[16] have postulated that the d bands in transition metal oxides, such as $\mathrm{Ti_2O_3}$ and $\mathrm{V_2O_3}$, are extremely narrow, being on the order of a few tenths of an eV in width. From their arguments one would also expect the narrow band model to apply to $\mathrm{Cr_2O_3}$. In fact, if anything, the d bands in $\mathrm{Cr_2O_3}$ would likely be even narrower than in the corresponding titanium and vanadium oxides because when moving across the $3d$ series the d orbitals are contracted by the increased nuclear charge and nearest-neighbor overlap would not be as great[26]. The X-ray band spectra, however, do not appear to support the narrow band model. In the case of $\mathrm{Cr_2O_3}$, the $\mathrm{CrL_{III}}$ emission band has been resolved into 5 components and the $\mathrm{L_{III}}$ absorption into 3 components as shown in Fig. 4. The measured half-widths and relative integrated intensities of these components are listed in Table 6. Before trying to relate the measured component widths to the actual electron orbital widths, they must first be corrected for various broadening effects. The two primary effects to consider here are the width of the instrumental window and the width of the core level. For the experimental arrangement used to obtain the $\mathrm{CrL_{III}}$ band, the spectrometer window width is approximately 0·8 eV. The chromium $\mathrm{L_{III}}$ level is believed to have a width of about 0·4 eV[27]. This means that the experimental probe has a total full-width at half-maximum of about 0·9 eV. Molecular vibrations and spin-orbit coupling may also cause some level broadening but probably amount to no more than a few tenths of an eV. As can be seen in Table 6, the uncorrected component widths are considerably larger than the sum of the broadening distortions just mentioned. The B_1 and d components, for instance, which are associated with the d orbitals of the cation–cation bond have a measured half-width of 3·0 eV. Assuming a conservatively large correction of 1·3 eV, there is still at least a 1·7 eV width which remains. Similarly, the d orbitals of the cation–

anion bond (components B_2 and b) would have a corrected half-width of about 1 eV. While these values contain some uncertainties, it is nevertheless apparent that the d orbitals in Cr_2O_3 are considerably broader than is proposed in the Adler–Brooks model[16]. This is also the case in the X-ray band spectra of the titanium and vanadium oxides shown previously[2–4, 6] Some recent photoemission studies on TiO_2 and VO_2 by Derbenwick also fail to support the narrow d band model[28].

The components of the oxygen K spectrum tend to be narrower than those of the CrL_{III} spectrum as indicated in Table 6. This is mainly due to the fact that both the spectrometer window width (0·5 eV) and inner level width (0·2 eV) are smaller for the oxygen spectrum. All of the individual molecular orbitals in Cr_2O_3 appear to have half-widths on the order of 1 to 2 eV. Some solid-state broadening should be expected due to electron interactions between atoms in neighboring octahedra. Also, the distortion from ideal octahedral symmetry may cause unresolved splitting of degenerate orbitals which would make levels appear broadened.

If the method of unfolding the spectra, especially the CrL_{III} band, is accepted as being reasonably correct then the relative intensities of the components can be used to provide a general indication of the amount of $3d$ character in the e_g and t_{2g} valence orbitals. The results are given in Table 7. In determining the values in the last column of the table, it was first assumed that the single-electron $2t_{2g}$ orbitals associated with the chromium–chromium covalent bond (components B_1 and d) represented 100 per cent d character. These components were assigned an arbitrary intensity value of 100 and the other component intensities then scaled on a relative basis to them. The relative intensity values were then divided by the number of electron states appropriate to the orbital. It is difficult to assess the accuracy of the results since they depend primarily on the unfolding procedure. It must first of all be assumed that the transition probability remains constant throughout the band. In addition, there are certain reservations about relating the intensities of absorption components on the same basis as emission components. Nevertheless, the results given in Table 7 are interesting in that they confirm, in a general quantitative way, the expected degree of cation and anion contributions to the various t_{2g} and e_g orbitals. The bonding orbitals ($2e_g$ and $1t_{2g}$) are seen to be strongly polarized toward the oxygen ions whereas the antibonding orbitals ($3e_g$ and $2t_{2g}$) are polarized toward the chromium ions. According to the intensity values given in Table 7, there are $3{\cdot}5d$ electrons in the occupied orbitals of Cr_2O_3. In principal, this same technique could be applied to the K bands for determining the relative percentages of $2p$ and $4p$ character in the appropriate orbitals. In fact, if the relative intensities of all components in the K and L_{III} spectra were known, the relative contribution of all the atomic orbitals to each of the valence molecul-

Table 7. Relative percentages of 3d character in e_g and t_{2g} valence orbitals of Cr_2O_3 as determined from unfolded CrL_{III} band spectrum

Component	Number of electron states (n)	Relative integrated intensity	I/n = % d character	
$B_1(2t_{2g}Cr–Cr)$	1	100	100	occupied states (total $3{\cdot}5d$ electrons)
$B_2(2t_{2g}Cr–O)$	2	112	56	
$F(1t_{2g})$	6	70	12	
$A(2e_g)$	4	67	17	
$b(2t_{2g}Cr–O)$	2	176	88	vacant states
$c(3e_g)$	4	205	51	
$d(2t_{2g}Cr–Cr)$	1	100	100	

ar orbitals could be empirically determined. For the particular case of Cr_2O_3, however, not enough is known about the various parameters involved in the CrK band measurement[24] to attempt a meaningful unfolding of the spectrum. The authors spectrometer does not have the necessary resolution at this short wavelength (2·1 Å) to permit an accurate *K* band measurement.

According to the MO interpretation which has just been suggested, all of the individual molecular orbitals of Cr_2O_3 can be empirically placed on a relative energy scale as in Fig. 4. The energy values of each X-ray component are listed in Tables 3 and 5. This data could be placed on an absolute scale if accurate binding energies were obtained for the inner subshells by electron spectroscopy measurements. This author is unaware of any such work done for Cr_2O_3 but the usefullness of the measurements has been demonstrated by Anderman and Whitehead[15] for some sulfur and chlorine compounds.

There is one other piece of experimental evidence that can be used to gauge the correctness of the empirical MO structure of Fig. 4. That evidence is found in the optical absorption spectrum of α-Cr_2O_3 measured by Neuhaus[29]. The first prominent peak in that spectrum is at 2·1 eV and is believed to be a measure of Δ, the ligand field splitting parameter. In Cr_2O_3 Δ would correspond to the energy separation between the $2t_{2g}^*$ and $3e_g$ orbitals. From Fig. 4, however, it is seen that both these orbitals (absorption peaks *b* and *c*) are vacant and so no electrons are normally available to give rise to an optical transition between them. It is also seen from Fig. 4 (and Table 3) that the energy separation between the highest occupied orbital (B_2) and the lowest vacant orbital (*b*), both of which have $2t_{2g}$ symmetry, is 2·2 eV. This is in good agreement with the optical value and apparently it is this separation and not Δ that the optical absorption spectrum is measuring.

It is also of some interest to note that the MO structure of Fig. 4 indicates that the oxygen 2*s* levels are involved in the bonding in Cr_2O_3. The presence of peaks *C* and *D* in the L_{III} band and peak $K\beta''$ in the *K* band cannot be readily accounted for unless there is assumed to be slight interaction between the 02*s* level and the Cr 3*d*, 4*s* and 4*p* levels.

From the preceeding discussions we are now in a position to list several points in support of the MO interpretation which has been suggested for the X-ray band spectra of Cr_2O_3. The facts of note are:

(1) Individual X-ray spectra. The main peaks in each spectrum follow the expected selection rules, i.e., main peaks in the *L* band arise only from orbitals having considerable *d* or *s* character; main peaks in the *K* band arise only from orbitals having considerable *p* character.

(2) Combined X-ray spectra. Orbitals which consist of admixed chromium 3*d* and oxygen 2*p* symmetries (1*e*, 2*e*, $2t_{2g}$ . . .) contribute to both the chromium *L* and oxygen *K* bands. Orbitals which are virtually atomic in character (t_{2u}, cation pair t_{2g}) contribute only to the appropriate spectrum of the element involved.

(3) The intensities of CrL_{III} spectral components associated with the bonding and antibonding t_{2g} and e_g orbitals show the expected relative contributions of 3*d* and 2*p* symmetries.

(4) The separation between the highest occupied and lowest vacant orbitals as measured by the X-ray spectra is in good agreement with that measured by the optical absorption spectrum.

(5) There are no 'left-over' components in the unfolded spectra. Each component can be logically assigned to a specific molecular orbital.

In addition to the above points, it is found that the empirically deduced energy positions of the individual orbitals in Cr_2O_3 are in reasonable agreement with calculations made for other octahedrally coordinated chromium complexes, e.g., CrF_6^{3-}[30]. The ordering of the orbitals is slightly different in the empirical structure but the relative energy ranges in which they occur show tolerable agreement. Further support for the MO method will be found in the following sections on tetrahedral chromium–oxygen compounds.

(c) CrO_4^{-2}

In the CrO_4^{-2} ion the chromium atom is surrounded by a regular tetrahedral arrangement of oxygen atoms. This tetrahedral field will result in a different molecular orbital structure than that of octahedral Cr_2O_3 as illustrated in Fig. 3. Consequently, considerable differences should also be observed in the CrL_{III}, CrK and OK X-ray band spectra.

In obtaining the X-ray bands, three different chromates were studied; Na_2CrO_4, K_2CrO_4 and $PbCrO_4$. As expected, they each yielded virtually identical spectra. Both the emission and absorption spectra shown in this report are from Na_2CrO_4.

The CrL_{III} X-ray spectrum from CrO_4^{-2} is shown in Fig. 1. Notice that it is indeed quite different in appearance from the Cr_2O_3 spectrum. The oxygen K spectrum is shown in Fig. 2. These two spectra are then combined with Best's CrK band[8] in Fig. 5. The object of Fig. 5 is to empirically deduce the CrO_4^{-2} MO structure in a manner similar to what was done in the previous section for Cr_2O_3. A general schematic of the type of MO structure we might expect to obtain is illustrated in Fig. 3. Lining up each of the spectra in Fig. 5 on a common energy scale is accomplished by positioning the absorption maxima *c* directly in line with each other. The reasoning behind this will become apparent shortly. The zero of energy is arbitrarily placed at the L_{III} absorp-

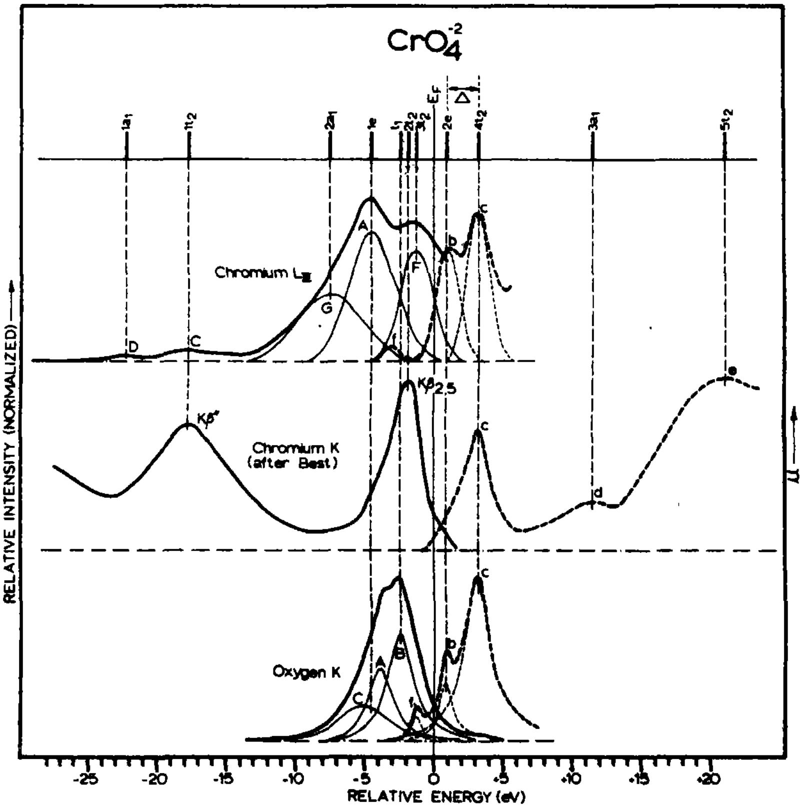

Fig. 5. Empirical deduction of MO structure of CrO_4^{-2} by combining the chromium *L*, chromium *K* and oxygen *K* X-ray band spectra from Na_2CrO_4.

tion edge which is assumed to be the position of the Fermi energy.

As was done with Cr_2O_3, it is assumed that the dipole selection rules dictate the main peak assignments in the CrO_4^{-2} spectra. The CrL_{III} band should therefore reflect primarily the distribution of $3d$ states and we will begin by assigning emission component A in Fig. 5 as due to a transition from a filled molecular orbital made up of mostly $3d$ symmetry. From the schematic diagram of Fig. 3, we find that the $1e$ level satisfies this condition. Similarly, the strongest peak in the CrK emission band ($K\beta_{2,5}$) should arise from a filled orbital consisting mostly of p symmetry, which is identified here as the $2t_2$ orbital. In the CrL_{III} and OK absorption spectra the first two maxima are assumed to represent the two lowest empty MO's which are the $2e$ and $4t_2$. According to electron spin resonance measurements, the $2e$ is below $4t_2$[31] and the X-ray results support this. The CrK absorption spectrum shows only one distinct maximum in this region and is assumed to be associated with the $4t_2$ level. The $2e$ level should not contribute significantly to the K spectrum because it consists of mostly $3d$ symmetry. This is why the absorption peaks c were lined up at the same energy position and labeled $4t_2$. Having now placed the $1e$, $2e$, $2t_2$, and $4t_2$ orbitals on the energy scale, the only one remaining which could be reasonably expected to contribute to peak F in the CrL_{III} band is $3t_2$. It is further assumed that the primary oxygen K emission component is due to transitions from the t_1 nonbonding $2p$ orbitals. The other assignments follow logically as explained previously for the VO_4^{-3} structure[6]. The energy positions and MO assignments of each of the components are summarized in Tables 2, 3, 4 and 5. As a result of the above interpretation all of the CrO_4^{-2} valence molecular orbitals are accounted for.

Best has also interpreted his CrK spectrum from CrO_4^{-2} on the basis of an MO model[8]. It is basically the same as the interpretation offered here except for one point. Best concludes that the $K\beta_{2,5}$ peak arises from transitions from the $3t_2$ orbitals instead of the $2t_2$ orbital as suggested in Fig. 5. If that was correct, then component F in the L_{III} band could not be accounted for. This is a further example of the advantage of using the combined K and L bands instead of depending on any one spectrum by itself.

The MO structure of CrO_4^{-2} as shown in Fig. 5 has no partially occupied orbital as Cr_2O_3 does (Fig: 3). In tetrahedral compounds, Cr has a +6 valence state so that all the bonding orbitals are exactly filled and all the antibonding orbitals completely empty. This is reflected in the CrL_{III} emission bands of Fig. 1. There is a peak labeled B in the Cr_2O_3 spectrum but not in the spectra of the three tetrahedral compounds. The presence of peak B in a CrL_{III} band from a compound always signifies that the lowest antibonding orbitals is partially occupied.

Now that we have shown how the MO structure of CrO_4^{-2} can be determined empirically from X-ray spectra it is of interest to see how this structure compares with some experimental data and theoretical calculations made by others. The CrO_4^{-2} optical absorption spectrum has two primary peaks at 3·32 and 4·54 eV[32]. These peaks have been interpreted in at least four different ways. In 1952, Wolfsberg and Helmholz[33] calculated an MO structure for CrO_4^{-2} in which the highest filled orbital was t_1 and the lowest empty orbital was $4t_2$. On this basis, they interpreted the optical spectrum as indicated in Table 8, column 2. Later, Ballhausen and Liehr [34] disagreed with the Wolfsberg–Helmholz scheme, suggesting that the lowest empty orbital was $2e$ instead of $4t_2$. They then reinterpreted the optical spectrum as being due to the transitions listed in column 3 of Table 8. That the lowest empty orbital is indeed $2e$ was further supported by Carrington and Schonland's ESR measurements. Another MO calculation was made by Viste and Gray [35] using certain simplifying assumptions which resulted in their calling the structure 'pseudo' CrO_4^{-2}. They then interpreted the optical spectrum in yet a third way as indicated in column 4 of Table 8. Oleari *et al.*[36] performed a self-consistant MO calculation for CrO_4^{-2} and interpreted the optical spectrum in terms of multiple transitions for each peak as indicated in column 5 of Table 8. They justified their multiple assignments by pointing out that the absorption bands are quite broad and that the second band actually has a shoulder. Surprisingly, the X-ray results do not agree completely with any of these previous interpretations. The problem stems from the assumed MO structure in the vicinity of the Fermi energy. All of the previous workers assumed that the highest filled orbital was the nonbonding t_1. The X-ray spectra in Fig. 5 indicate that this is not correct and that the highest filled orbital is actually $3t_2$. This X-ray deduced structure is compared with the calculated Viste–Gray and Oleari *et al.* structures in Fig. 6. All three structures are placed on the same relative scale by arbitrarily placing the zero energy point at the t_1 nonbonding level. The Wolfsberg–Helmholz calculation is not included in the figure because it comes nowhere close to agreeing with the X-ray results and is, at any rate, generally considered to be incorrect. As can be seen in Fig. 6, the X-ray results are in terrible agreement with the Oleari *et al.* calculations despite the fact that they are supposedly self-consistent. They made two calculations, for chromium charge numbers of 0 and +1. The diagram shown in Fig. 6 is for the +1 charge. The 0 charge diagram shows even worse agreement. A rather odd odd feature of the results of Oleari *et al.* is the extremely large energy separation (~ 9 eV) between the highest filled and lowest empty orbitals. Much better agreement is found in comparing the X-ray results with the Viste–Gray calculations which were considered very rough to begin with[35]. Perhaps the disagreements should not be very surprising in light of Fensky and Sweeny's conclusion [37] that the final outcome of the calculations depends very strongly on the initial assumptions made in determining symmetry characters of hybridized orbitals.

The X-ray deduced MO structure of CrO_4^{-2} is further supported by a different interpretation of the optical absorption spectrum. On the basis of the orbital positions determined in Fig. 5, the optical peaks at 3·32 and 4·54 eV can be assigned to the transitions $t_1 \rightarrow 2e$ and $3t_2 \rightarrow 4t_2$, respectively. It is emphasized that these orbital energy differences agree *exactly* with the optical peak positions which is often not the case in the other work referred to. According to Ballhausen and Liehr's interpretation, for example, the $2e$ and $4t_2$ orbitals would be separated by only 1·2 eV. This is certainly too small as indicated by the CrL_{III} X-ray absorption spectrum, the OK absorption spectrum and the optical spectra of other, similar compounds[35, 38]. This energy separation is also known as Δ, the ligand field splitting parameter. The X-ray spectra shown

Table 8. Electron transition assignments for two principle maxima in optical absorption spectrum of CrO_4^{2-}

Peak position[32]	Wolfsberg and Helmholz[33]	Ballhausen and Liehr[34]	Viste and Gray[35]	Oleari *et al.*[36]	This work (X-ray)
3·32 eV	$t_1 \rightarrow 4t_2$	$t_1 \rightarrow 2e$	$t_1 \rightarrow 2e$	$t_1 \rightarrow 4t_2$ $t_1 \rightarrow 2e$	$t_1 \rightarrow 2e$ (3·3 eV)
4·54 eV	$3t_2 \rightarrow 4t_2$	$t_1 \rightarrow 4t_2$	$3t_2 \rightarrow 2e$	$3t_2 \rightarrow 4t_2$ $3t_2 \rightarrow 2e$	$3t_2 \rightarrow 4t_2$ (4·5 eV)
Highest occupied orbital	t_1	t_1	t_1	t_1	$3t_2$
Lowest vacant orbital	$4t_2$	$2e$	$2e$	$3a_1$	$2e$
Δ (eV)	1·6	1·2	3·1	0·5	2·3

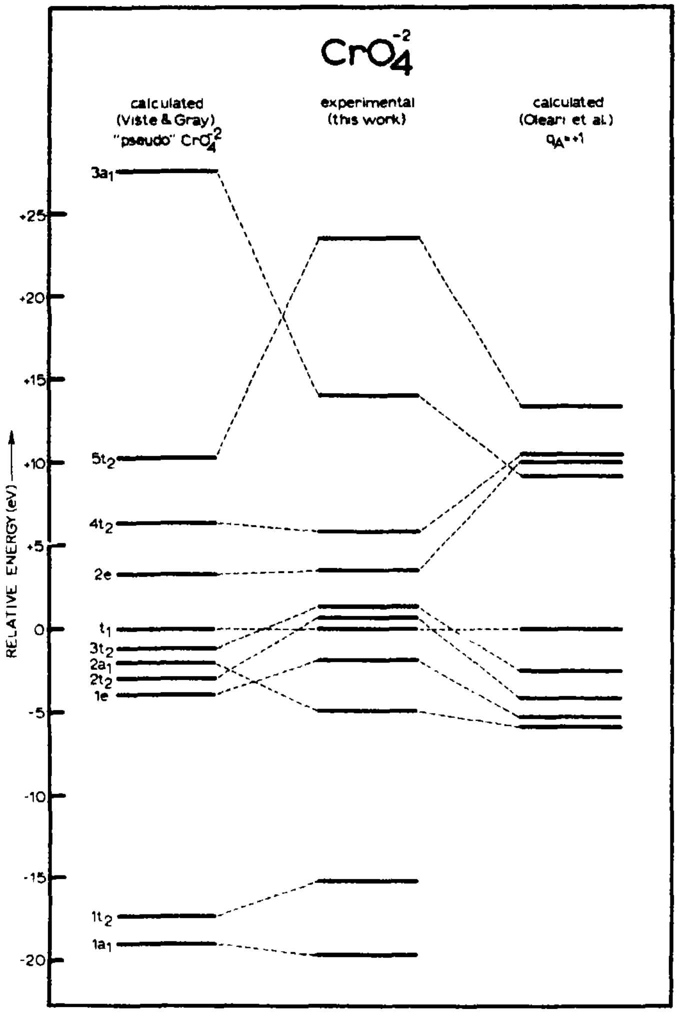

Fig. 6. Comparison of relative MO energy positions of CrO_4^{2-} determined in this work and calculated by Viste and Gray[35] and Oleari *et al.*[36]. Zero of energy arbitrarily placed at t_1 non-bonding level to facilitate comparison.

here indicate a Δ value of 2·3 eV. The X-ray results also indicate that each of the two absorption peaks has a unique transition assignment and that multiple assignments such as suggested by Oleari *et al.*[36] are incorrect. Table 8 summarizes the CrO_4^{-2} situation.

Oleari *et al.*[36] have also stated that during a charge–transfer excitation the antibonding MO energy separation ($4t_2 - 2e$) changes and that it is therefore impossible to derive from experimental data (specifically optical absorption) an imperical evaluation of the $4t_2 - 2e$ energy separation. This seems questionable and most certainly does not hold true for the experimental X-ray data. As seen in Fig. 5, both the CrL_{III} and oxygen *K* absorption spectra directly give the $4t_2 - 2e$ energy separation as reflected in peaks *b* and *c*. If the 2*e* and $4t_2$ orbitals are considered to be localized primarily on the Cr atom, then the oxygen *K* absorption could be thought of as arising from a charge-transfer excitation while the CrL$_{III}$ absorption represents an intra-atomic transition. Both spectra are seen to give the same energy separation for peaks *b* and *c*, and hence the same $4t_2-2e$ energy separation. These two orbitals are also involved in optical absorption transitions and the agreement between the optical and X-ray data was discussed in the preceeding paragraph.

It may have been noticed by the reader that component *A* in the oxygen *K* emission band of Fig. 5 has not been assigned to any particular orbital. This is due to the fact that component *A* does not appear to have anything to do with the CrO_4^{-2} ion. In the chromates, the oxygens are involved in bonding to two different metal ions. In Na_2CrO_4, for instance, there are Cr–O and Na–O bonds, the latter probably being highly ionic. After observing the oxygen *K* band from several different chromates it appears that component *A* is associated with the oxygen bond to the other metal ion, although it is much more intense than would normally be expected. The reason for this is not clear at present.

Viste and Gray[35] have emphasized the importance of including the oxygen 2*s* level in any MO calculation of the valence orbitals in tetrahedral oxyanions. The X-ray band spectra shown here support their point because peaks *C* and *D* in the L$_{III}$ spectrum and $K\beta''$ in the *K* spectrum could not be accounted for without assuming 02*s* participation in the bonding. This was also the case in the VO_4^{-3} spectra[6]. Furthermore, in Fig. 6 it is obvious that the X-ray MO structure is in much closer agreement with the calculations of Viste and Gray who included 2*s* participation than it is with the calculations of Oleari *et al.* who did not.

There is no indication from the X-ray spectra of a significant energy gap between the top of the highest filled and the bottom of the lowest empty orbitals in CrO_4^{-2}. Since these orbitals are highly localized on the molecule a gap is not necessary to explain the lack of electrical conductivity. If a gap is present, it would probably not be detectable by the X-ray spectra anyway because of the presence of multiple ionization satellite structure at the emission edge which would completely mask the true position of the edge. The only way this problem could be overcome would be to obtain the L$_{III}$ band at threshold excitation[39] which is too difficult to be practial in this case.

The CrL$_{III}$ band in Fig. 5 was resolved into the Gaussian components by the method described in Section 3(a). Since there is believed to be no significant interaction between neighboring tetrahedral units, in CrO_4^{-2} [8], the individual orbitals should not be broadened to quite the extent observed in Cr_2O_3. With the exception of component *G* the CrO_4^{-2} orbitals do indeed appear to be somewhat narrower. The width of component *G* is probably greatly exaggerated in Fig. 5 because an attempt was made to make the unfolds match the low energy tail of the L$_{III}$ band without introducing another component. Extended tailing due to Auger transitions, certain types of excitation states, etc.[14] could therefore make component *G* (and to a lesser extent, component *A*) appear much broader than it really is. This is also true for components *G* and *E* in the Cr_2O_3 spectrum in Fig. 4.

(d) CrO_3

In CrO_3, the oxygen atoms form distorted tetrahedra around the Cr atoms[40]. As indicated in Table 1, both the Cr–O and Cr–Cr interatomic distances are considerably different than in CrO_4^{-2}. Even though the CrO_3 tetrahedra are distorted, the soft X-ray band spectra would be expected to be similar in appearance to the CrO_4^{-2} spectra. To a large degree this similarity is actually observed as seen in Figs. 1 and 2. The specific spectral differences which occur are attributed to the symmetry distortion as explained below.

The CrL$_{III}$ and OK spectra from CrO_3 are displayed on the same energy scale in Fig. 7. These spectra are aligned with each other by the method described in the previous section

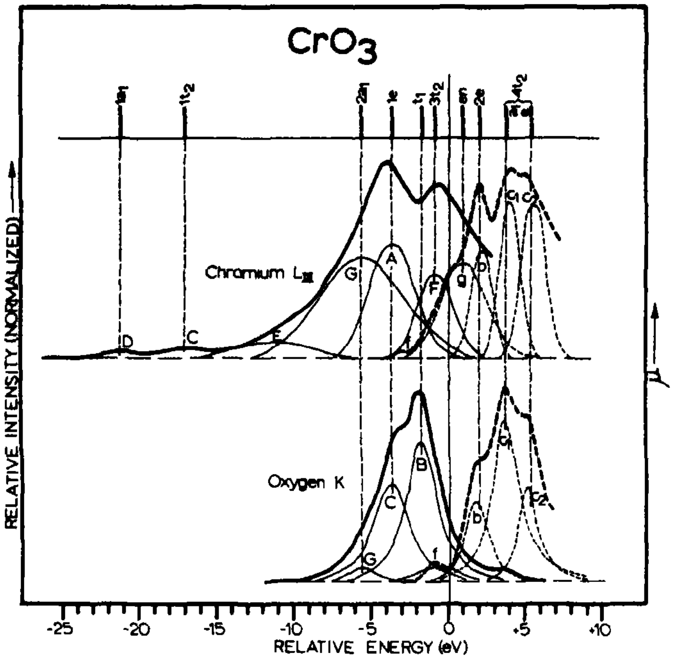

Fig. 7. Empirical deduction of partial MO structure of CrO_3 by combining the chromium L and oxygen K X-ray band spectra.

concerning Fig. 5. No CrK spectrum is shown because apparently no one has ever published it. The author's spectrometer does not have sufficient resolution at 2 Å to obtain a detailed K band which would be needed here. Without the CrK band, unfortunately, the complete MO structure of CrO_3 cannot be deduced. Nevertheless, considerable information is still present in the combined CrL_{III} and OK spectra of Fig. 7. The unfolding of the spectra into individual components follows the method described in Section 3(a). In making assignments for the spectral components, the same MO term symbols are used for CrO_3 as for a regular tetrahedral structure. This is not strictly permissible because the distorted symmetry will result in a splitting of the triply degenerate orbitals into a singlet and a doublet $(e+a_1)$. It is very convenient, however, to retain the original term symbols for making comparisons of the CrO_3 spectra with what was previously shown for CrO_4^{-2}. In many cases, the symmetry distortion is reflected in the spectra only as a band broadening anyway.

The CrL_{III} emission band is essentially the same as obtained from CrO_4^{-2} except that the components are broadened as seen in Fig. 7. Peaks F, A, G, C and D are therefore interpreted in the same way (Table 2). In the oxygen K emission band component B is again assigned as arising from the t_1 non-bonding orbital. Components C and G correspond to the A and G components of the L_{III} band. The big difference in CrO_3 as compared to CrO_4^{-2} occurs in the absorption spectra. The most noticeable change is the appearance of a new L_{III} component, labeled g. It is suggested that component g is associated with non-bonding chromium e orbitals since the tetrahedral distortion is such that some of the e orbitals could not form bonds with the oxygen $2p$ orbitals[40]. This interpretation is reinforced by the fact that there is no corresponding component observed in the oxygen K spectrum. Another noticeable aspect of the absorption spectra is that peak c has apparently split into two easily separated components, c_1 and c_2. This splitting occurs in both the CrL_{III} and OK spectra and may indicate the a_1 and e components of the original $4t_2$ orbital. The energy positions of each spectral component are listed in Tables 3 and 4.

It would be helpful to have some other experimental data for CrO_3 with which to compare the X-ray results but none could be found. Apparently the optical absorption spectrum has not been published and no electronic structure calculations have been made. The MO interpretation of the X-ray band spectra however, does appear to be supported by what is known about CrO_3. It is concluded that the empirically deduced MO structure is similar to that obtained for CrO_4^{-2} (Fig. 5) except that the tetrahedral distortion has caused some obvious splitting of the $4t_2$ orbital and has also caused the formation of non-bonding chromium e orbitals.

(e) $Cr_2O_7^{-2}$

The ammonium, sodium and potassium dichromates crystallize in a monoclinic structure in which the oxygen atoms form extremely distorted tetrahedra around the chromium atoms[41]. As indicated in Table 1, the Cr—O bonding distances (and angles) vary considerably. Such extreme distortion may cause a splitting of all degenerate orbitals although no calculations have been made on this sort of structure. As in the case of CrO_3, the regular tetrahedral term symbols are used for the sake of convenience in interpreting the X-ray band spectra.

The CrL_{II} spectrum from $K_2Cr_2O_7$ is shown in Fig. 1. The sodium and ammonium salts give spectra virtually identical to this. As can be seen, this spectrum looks very much like that obtained from CrO_3 and CrO_4^{-2}. The oxygen K spectrum is shown in Fig. 2, and is matched to the CrL_{III} spectrum in Fig. 8. No

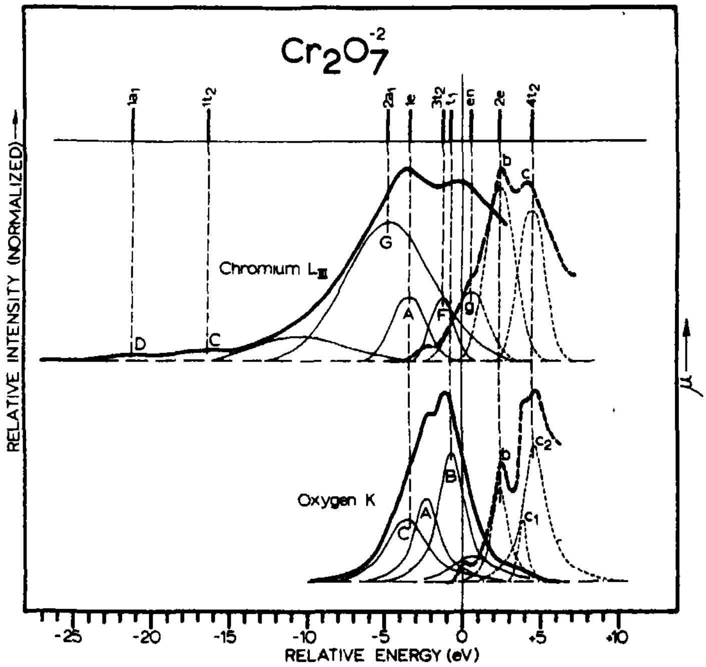

Fig. 8. Empirical deduction of partial MO structure of $Cr_2O_7^{2-}$ by combining the chromium L and oxygen K X-ray band spectra from $K_2Cr_2O_7$.

CrK spectrum is available for comparison. Due to the extreme symmetry distortion and lack of other experimental data, no clearcut arguments can be offered in support of the empirical MO structure for $Cr_2O_7^{-2}$ shown in Fig. 8. Since the spectra have the same general appearance as shown earlier for CrO_4^{-2} and CrO_3, the only reasonable approach is to make an analogous interpretation. Energy positions of each of the components and their assignments are listed in Tables 2–5.

4. SUMMARY AND CONCLUSIONS

It has been shown that a complete valence molecular orbital structure can be empirically deduced for chromium–oxygen compounds by combining the information present in the CrL_{III}, CrK and OK X-ray band spectra. MO assignments are made on the basis of the energy positions and relative intensities of the unfolded X-ray components in conjunction with other experimental data and theoretical calculations. All of the emission and absorption components are seen to be logically explained in terms of bonding, antibonding and non-bonding molecular orbitals.

In Cr_2O_3, the L_{III} X-ray spectrum indicates that the three outermost electrons have t_{2g} symmetry and are involved in two distinct bonding mechanisms. One of these electrons is localized in a metal–metal covalent bond (c-axis pairing) and the other two are associated with a Cr–O π bond. There is no obvious evidence of a collectivized d orbital. After corrections for broadening effects, the predominantly $3d$ orbitals of Cr_2O_3 are found to have a half-width on the order of 1 to 1·5 eV. The narrow d-band model of Adler and Brooks [16] is therefore not supported. Relative intensities of the CrL_{III} spectral components can be used to indicate the approximate amount of $3d$ contribution to each of the bonding and antibonding e_g and t_{2g} orbitals in Cr_2O_3 (Table 7). The X-ray absorption spectra indicate that Δ, the ligand field splitting parameter, is 2·1 eV in Cr_2O_3 but that the optical absorption spectrum does not measure Δ as is often assumed. It is probably the separation between the highest occupied and lowest empty orbitals, both of which have t_{2g} symmetry in Cr_2O_3, that the optical spectrum is measuring.

The empirically deduced MO structure of CrO_4^{-2} is not in good agreement with previous calculations (Fig. 6). At least four different interpretations have been previously suggested for the optical absorption spectrum of CrO_4^{-2} but none of them are consistent with the X-ray results. A different interpretation therefore, is offered here (Table 8). It is concluded that, contrary to previous assumptions, the highest filled orbital in CrO_4^{-2} is $3t_2$ instead of t_1. The X-ray absorption spectra support ESR measurements [31] in indicating that the lowest empty orbital is $2e$. It is determined that Δ is 2·3 eV.

In going from CrO_4^{-2} to CrO_3 to $Cr_2O_7^{-2}$, the tetrahedral symmetry becomes increasingly distorted. This is mirrored in the X-ray band spectra as a broadening and splitting of certain orbitals and by the formation of non-bonding chromium e orbitals in CrO_3 and $Cr_2O_7^{-2}$. These spectral variations are expected on the basis of MO theory and provide additional support for interpreting the spectra in MO terms.

The presence of peaks C and D in the CrL_{III} band and peak $K\beta''$ in the CrK band show that the oxygen $2s$ orbitals are involved in the bonding in each of the compounds discussed here.

To obtain a complete valence molecular-orbital diagram of transition metal compounds it is necessary to use the combined K and L x-ray bands of the metal ion and anion as in Figs. 4 and 5. No one spectrum by itself is sufficient. This is because the valence orbitals contain a strong admixture of p, d and s symmetries and the dipole selection rules prevent certain transitions from occuring in each X-ray state.

Although the molecular orbital structures determined in this report are strongly empirical in nature they nevertheless point out the great value of X-ray valence band spectra in studying the electronic structure and chemical bonding in solids. Molecular orbital assignments can be made quite confidently for the various spectral components from simple considerations of peaks positions and relative intensities in conjunction with the usual dipole selection rules. It is always helpful, of course, to have theoretical calculations and other types of experimental data at hand for comparison purposes. The great advantage of X-ray spectra over other experimental techniques is evident in both their simplicity and completeness. The combination of emission and absorption spectra makes it possible to locate both occupied and vacant orbitals within 20 eV or so of the Fermi energy. In addition, the relative contributions of the various atomic orbitals to each molecular orbital plus the energy width of each molecular orbital can be empirically determined from good, reliable X-ray data. Also, the atomic character of the inner vacancy considerably simplifies the problem of unambiguously assigning an electron transition to each spectral component. This overall simplicity, completeness and flexibility cannot even be approached by any other single experimental technique. The real beauty of the MO interpretation as illustrated in Figs. 4 and 5 is that it ties together very effectively the various cation and anion emission and absorption spectra with the chemical interactions which must occur between anion and cation in forming a compound. Strong relationships are seen between the X-ray spectra and various solid state phenomena such as coordination symmetry, bonding distances, valence state, bonding character and many of the resulting physical properties. Certainly more complete work needs to be done in certain areas, particularly in persuading theoreticians to do more careful MO structure calculations which can be directly compared with the experimental data that can now be obtained. Even with the present state of affairs, however, it is quite apparent that soft X-ray band spectroscopy is an extremely powerful tool for probing the electronic structure of compounds.

REFERENCES

1. ADLER D., *Rev. mod. Phys.* **40**, 714 (1968).
2. FISCHER D. W. and BAUN W. L., *J. appl. Phys.* **39**, 4757 (1968).
3. FISCHER D. W., *J. appl. Phys.* **40**, 4151 (1969).
4. FISCHER D. W., *J. appl. Phys.* **41**, 3561 (1970).
5. FISCHER D. W., *J. appl. Phys.* **41**, 3922 (1970).
6. FISCHER D. W., *Appl. Spectrosc.* **25**, 263 (1971).
7. DODD C. G. and GLEN G. L., *J. appl. Phys.* **39**, 5377 (1968).
8. BEST P. E., *J. chem. Phys.* **44**, 3248 (1966).
9. BEST P. E., *J. chem. Phys.* **49**, 2797 (1968).
10. SEKA W. and HANSON H. P., *J. chem. Phys.* **50**, 344 (1969).
11. MANNE R., *J. chem. Phys.* **52**, 5733 (1970).
12. LAWRENCE D. F. and URCH D. S., *Spectrochim. Acta* **25B**, 305 (1970).
13. URCH D. S., *J. Phys. Soc. C* **3**, 1275 (1970).
14. NAGEL D. J., *Adv. X-Ray Anal.* **13**, 182 (1970).
15. ANDERMAN G. and WHITEHEAD H. C., *Adv. X-Ray Anal.* **14**, 453 (1971).
16. ADLER D. and BROOKS H., *Phys. Rev.* **155**, 826 (1967).
17. BALLHAUSEN C. J. and GRAY H. B., *Molecular Orbital Theory*, W. A. Benjamin, New York (1964).
18. FIGGIS B. N., *Introduction to Ligand Fields*, John Wiley, New York (1966).
19. JORGENSEN C. K., *Absorption Spectra and Chemical Bonding in Complexes*, Pergamon Press, New York (1962).
20. NEWNHAM R. E. and DEHAAN Y. M., *Z. Kristallogr.* **117**, 235 (1962).
21. BROCKHOUSE B. N., *J. chem. Phys.* **21**, 961 (1953).
22. ADLER D., FEINLEIB J., BROOKS H. and PAUL W., *Phys. Rev.* **155**, 851 (1967).
23. NEBENZAHL I. and WEGER M., *Phys. Rev.* **184**, 936 (1969).
24. MENSHIKOV A. Z. and NEMNONOV S. A., *Bull. Acad. Sci. U.S.S.R. (Phys. Ser.)* **27**, 402 (1963).
25. GOODENOUGH J. B., *Phys. Rev.* **117**, 1442 (1960).
26. MORIN F. J., *J. appl. Phys.* **32**, 2195 (1961).
27. PARRATT L. G., *Rev. mod. Phys.* **31**, 616 (1959).
28. DERBENWICK G. F., Stanford Electronic Laboratories, Tech. Rept. 5220-2 (1970).
29. NEUHAUS A., *Z. Kristallogr.* **113**, 195 (1960).
30. Reference [17], page 130.
31. CARRINGTON A. and SCHONLAND D. S., *Mol. Phys.* **3**, 331 (1960).
32. CARRINGTON A. and SYMONS M. C. R., *J. chem. Soc. Lond.* 889 (1960).
33. WOLFSBERG M. and HELMHOLZ L., *J. chem. Phys.* **20**, 837 (1952).
34. BALLHAUSEN C. J., and LIEHR A. D., *J. mol. Spectr.* **2**, 342 (1958).
35. VISTE A. and GRAY H. B., *Inorg. Chem.* **3**, 1113 (1964).

36. OLEARI L., DeMICHELIS G. and DiSIPIO L., *Mol. Phys.* 10, 111 (1965).
37. FENSKY R. F., and SWEENY C. C., *Inorg. Chem.* 3, 1105 (1964).
38. CARRINGTON A. and JORGENSEN C. K., *Mol. Phys.* 4, 395 (1961).
39. LIEFELD. R. J., In *Soft X-Ray Band Spectra* (Edited by D. J. Fabian), pp. 133–149, Academic Press, New York (1968).
40. BYSTROM A. and WILHELMI K., *Acta Chem. Scand.* 4, 1131 (1950).
41. WYCKOFF R. W. G., *Crystal Structures*, Interscience, New York (1953).

J. Phys. Chem. Solids, 1971, Vol. 32, pp. 2481–2486. **Pergamon Press. Printed in Great Britain**

INFRARED REFLECTIVITY OF InP

F. KÖHL
Physikalisches Institut, Universität Frankfurt/Main, Germany

(*Received* 30 *September* 1970; *in revised form* 5 *April* 1971)

Abstract—Reflectivity measurements at normal incidence have been made on several InP samples doped with Te such that the plasma frequency is smaller than, close to, and greater than the optical lattice frequency. For heavily doped samples the free-carrier effective mass has been determined by the dependence of the reflectivity-minimum upon carrier concentration at 77 and 300 K. The measured reflectivity deviates from theory near the plasma edge; surface effects may be responsible.

1. INTRODUCTION

IN THE i.r. region the complex dielectric constant of a semiconductor is given by the following expression[1, 2]:

$$\epsilon(\omega) = \epsilon_\infty + \frac{\epsilon_0 - \epsilon_\infty}{1 - \omega^2/\omega_t^2 - i\Gamma_1\omega/\omega_t^2} - \frac{\epsilon_\infty \omega_P^2}{\omega^2 + i\Gamma_2\omega} \qquad (1)$$

where ϵ_0 is the static dielectric constant, ϵ_∞ the high-frequency dielectric constant, Γ_1 the damping coefficient of the phonons, Γ_2 the damping coefficient of the free carriers, ω the frequency of the incident light, ω_t the transverse optical frequency, and ω_P the plasma frequency. This equation includes the contributions of both the free carriers and the optical phonons. The reflectivity at normal incidence of an absorbing medium is given by

$$R = \left|\frac{\sqrt{\epsilon} - 1}{\sqrt{\epsilon} + 1}\right|^2. \qquad (2)$$

An interaction takes place between the free carriers and the optical phonons which is strong when the plasma frequency is close to the longitudinal optical frequency ω_L[1–4]. Substitution of equation (1) into equation (2) usually gives a good fit to the observed reflection spectra[5–7]. If $\omega_P \gg \omega_L$ or $\omega_L \gg \omega_P$ the two first terms of equation (1) can be included in a constant, ϵ_L, the dielectric constant of the lattice. In this case the real and the imaginary parts of the dielectric constant assume the forms

$$\epsilon_1 \equiv Re(\epsilon) = \epsilon_L[1 - \omega_P^2/(\omega^2 + \Gamma_2^2)] \qquad (3)$$

$$\epsilon_2 \equiv Im(\epsilon) = \epsilon_L\omega_P^2\Gamma_2/[\omega(\omega^2 + \Gamma_2^2)]. \qquad (4)$$

In equations (3) and (4) the plasma frequency ω_P takes the form

$$\omega_P = [4\pi N e^2/(\epsilon_L m^*)]^{1/2} \qquad (5)$$

where N is the carrier density, e the elementary charge and m^* the effective mass of the free carriers. With the aid of equations (2), (3) and (4) the following polynomial of fourth order has been derived in order to determine the plasma frequency from the reflectivity minimum[8]:

$$x^4 - Ax^3 + Bx^2 + Cx + D = 0. \qquad (6)$$

where

$$A = \tfrac{2}{3}[(3\epsilon_L - 1) - y^2(\epsilon_L - 1)]/(\epsilon_L - 1)$$

$$B = [4\epsilon_L(3\epsilon_L - 2) - 5y^2(3\epsilon_L - 1)(\epsilon_L - 1)]/[12(\epsilon_L - 1)^2]$$

$$C = [2\epsilon_L y^2(3\epsilon_L - 2) - y^4(3\epsilon_L - 1)(\epsilon_L - 1)]/[12(\epsilon_L - 1)^2]$$

$$D = \epsilon_L^2 y^2/[12(\epsilon_L - 1)^2]$$

$$x = (\omega(R = \text{min.})/\omega_P)^2; \qquad y = \Gamma_2/\omega_P.$$

Here $\omega(R = \text{min.})$ is the frequency at the minimal reflectance. For different ϵ_L the dependence of x upon y can be closely determined by the polynomial (6). Moreover, the amount of the minimal reflectivity is fixed by the values of x and y and the equations (2), (3) and (4). Conversely, obtaining the minimal reflectance by experiment, we can determine both the plasma frequency ω_P and the damping Γ_2 of the free carriers with these equations[8]. From ω_P in turn, N or m^* can be calculated.

2. EXPERIMENTAL

The measurements were performed with a grating spectrometer (Beckman IR12) in the region between 2·5 and 50 μ. An auxiliary reflection apparatus has been built with an average angle of incidence of 13 deg so that formula (2) can still be used. A cryostat has been constructed to make reflectivity measurements at room temperature, liquid nitrogen and hydrogen temperatures, respectively. Measurements were performed in the single-beam system. In order to obtain the reflectivities the experiment had to be made both with sample and refererence mirror. The reflectivity of aluminium mirror used was calculated by the Hagen–Rubens-Relation, where the static conductivity σ of the evaporated layer was assumed to be $\sigma = 3{\cdot}178 \,.\, 10^{17}[\mathrm{s}^{-1}]$[9]. Sample and mirror were mounted on a cold finger which could be revolved in order to introduce either one into the beam. Low temperature measurements were only possible for stationary chopper between sample and monochromator. The experimental arrangement was equipped with a digital data system for rapid evaluation. We are able to investigate very small samples, down to 2 mm². The optical resolution was better than 5 cm⁻¹.

The samples were n-type InP crystals grown in an In-solution[10]; they are doped with Te. The surfaces of the samples were polished and etched with bromine–methanol.

3. RESULTS AND DISCUSSION

Experimental reflection spectra at room temperature are shown in Fig. 1. The minima of the reflectivity curves were used to determine the effective masses by the procedure outlined before and described in detail elsewhere[8]. The resulting dependence of N on m^* is given in Fig. 2. The experimental values are represented by circles. The effective mass increases rapidly for heavily doped samples. This increase is explained by deviation from the parabolicity of the conduction band. The two curves in Fig. 2 are calculated according to the theory of Cardona [11, 12]. For $T = 0$ K. Cardona derived the following expressions for m^* and N[12]:

$$1/m^* = \delta^2/((E_F+\Delta)\hbar^2) \tag{7}$$

$$N = E_F{}^{3/2}(E_F+2\Delta)^{3/2}/(3\pi^2\delta^3) \tag{8}$$

δ is a constant, E_F the Fermi-energy and 2Δ the energy of the band gap. The constant δ is evaluated for four pairs of values m^* and N

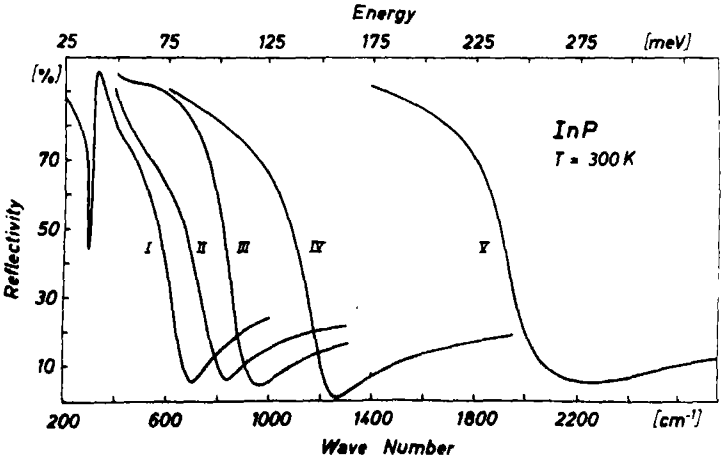

Fig. 1. I.r.-reflection spectra at room temperature. The carrier densities of the samples I–V are: (I): 5·8 . 10¹⁸; (II): 9·5 . 10¹⁸; (III): 1·1 . 10¹⁹; (IV): 1·8 . 10¹⁹; (V): 6·5 . 10¹⁹ cm⁻³.

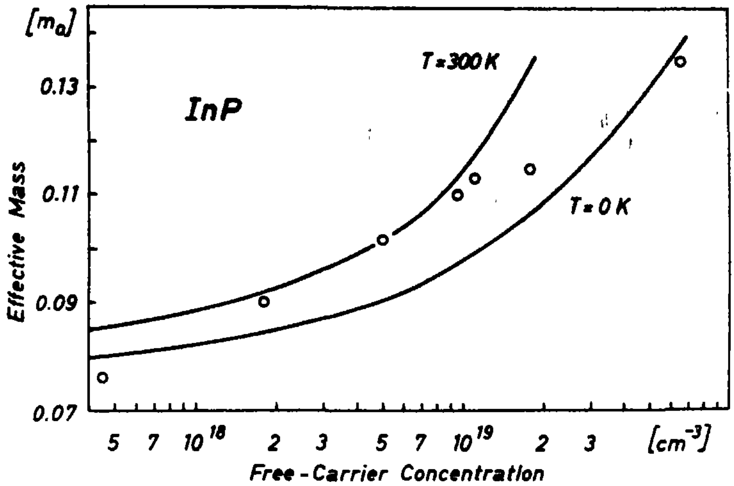

Fig. 2. Dependence of the effective mass m^* on the free-carrier concentration N. Circles represent experimental results at room temperature, solid lines give theory for temperatures indicated.

from equations (7) and (8) (Table 1)[13]. The lower curve of Fig. 2 is obtained by the same equations with the arithmetical average of the four values of δ; the upper curve is valid for 300 K and is evaluated from equation (5) of Ref. [11] and includes the appropriate averaging over the Fermi function.

The ratio ω_P/ω_L is 1·7 for curve I in Fig. 1. In this case an interaction of plasmons and phonons takes place, and the effective mass can be obtained only by a fit according to equation (1). This fit for curve I is shown in Fig. 3. The fit parameters were: $\omega_t = 37{\cdot}6$ meV, $\omega_P = 75{\cdot}9$ meV, $\epsilon_\infty = 13{\cdot}7$, $\epsilon_0 = 17{\cdot}7$, $\Gamma_1 = 0{\cdot}005\omega_t$ and $\Gamma_2 = 0{\cdot}1\omega_P$. Shown in Fig. 3 are the eigenfrequencies ω_+ and ω_- of the coupled oscillations according to Yokota[3].

Table 1. *Effective masses m^* at different free-carrier densities N and the constants δ evaluated from equations* (7) *and* (8)[13]

N [cm^{-3}]	m^*	$\delta \,.\, 10^{40}$
$6{\cdot}1 \,.\, 10^{15}$	0·077	178·2
$1{\cdot}0 \,.\, 10^{16}$	0·073	188·1
$8{\cdot}2 \,.\, 10^{18}$	0·066	210·5
$1{\cdot}4 \,.\, 10^{17}$	0·10	138·8

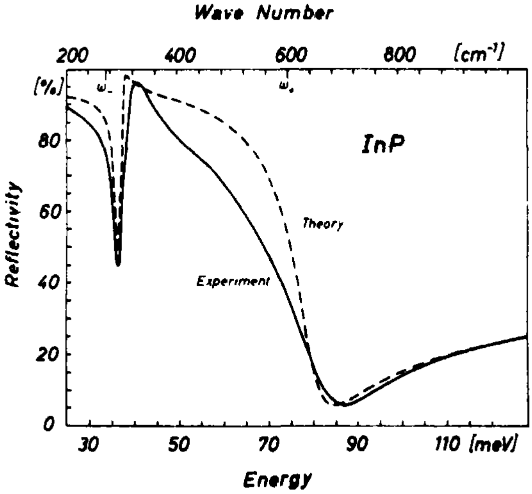

Fig. 3. Fit of a Plasmon–Phonon–Coupling; $\omega_P/\omega_L \approx 1{\cdot}7$ (The solid line is identical with curve I in Fig. 1).

If $\omega_L \approx \omega_P$, the coupling between plasmons and phonons is very strong. The experimental spectrum of such a strong coupling is represented in Fig. 4 for 300 K (solid line) and 77 K (dashed line); N was here $1{\cdot}8 \,.\, 10^{18}$ cm^{-3}. At

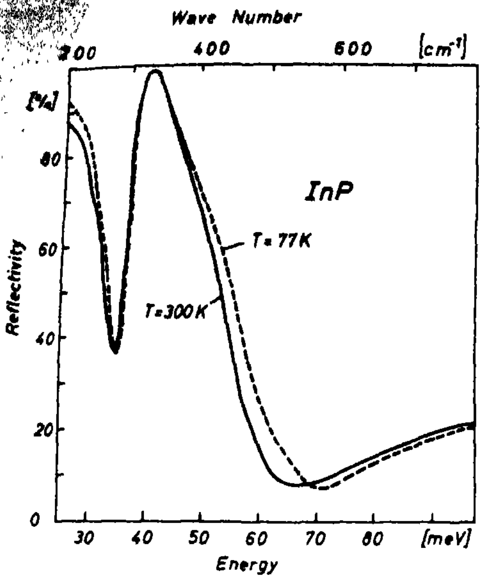

Fig. 4. Plasmon-Phonon-Coupling at 300 and 77 K: $\omega_P/\omega_L \approx 1$.

low temperatures the reflectivity minimum is shifted towards higher energies. The same phenomenon is shown in Fig. 5 for a plasma reflection spectrum of a sample with a ratio $\omega_P/\omega_L = 3{\cdot}15$. The effect can be explained by a decrease of m^* with decreasing temperature. The magnitude of this effect depends on how far the tails of the Fermi-function penetrate into the nonparabolic parts of the conduction band[12]. The Reststrahlen band at a ratio $\omega_P/\omega_L = 0{\cdot}6$ is presented in Fig. 6. At this ratio the influence of the free carriers on the Reststrahlen band is still so strong that the peak is broadened at decreasing temperature by the same effect. The damping coefficient Γ_2, and from it in turn the mobility $\mu = e/(m^*\Gamma_2)$, can be determined by the minimal reflectance, e.g. 1070 cm²/(Vs) is obtained as the mobility for curve IV of Fig. 1. The values of μ evaluated by reflectance and Hall measurements differ less than 5 per cent.

Excellent fit on the high energy side and in the minimum is achieved with equations (2–5). However, near the plasma edge there are systematic deviations of the measured spectra from theoretical predictions. Figures 3 and 7 show examples of such fits for curves I and IV, respectively, of Fig. 1. Attempts to explain the experimental spectrum with an energy-dependent damping were unsatisfactory, since they led to complicated functions $\Gamma(\omega)$.

We suggest that surface-plasmon effects are responsible for the reduced reflectivity

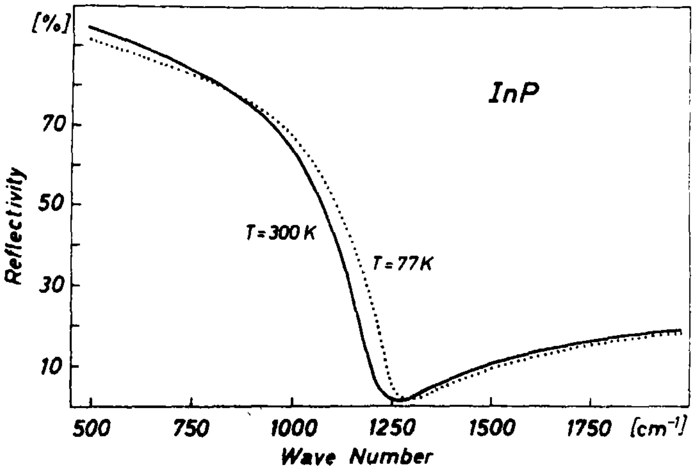

Fig. 5. Reflection Spectra at 300 and 77 K; $\omega_P/\omega_L = 3{\cdot}15$ (Solid line is identical with curve IV in Fig. 1).

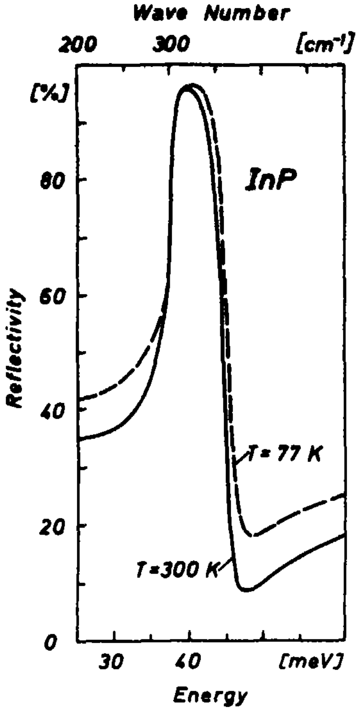

Fig. 6. Reflection Spectra of Reststrahlen Band at 300 and 77 K; $\omega_P/\omega_L = 0{\cdot}6$.

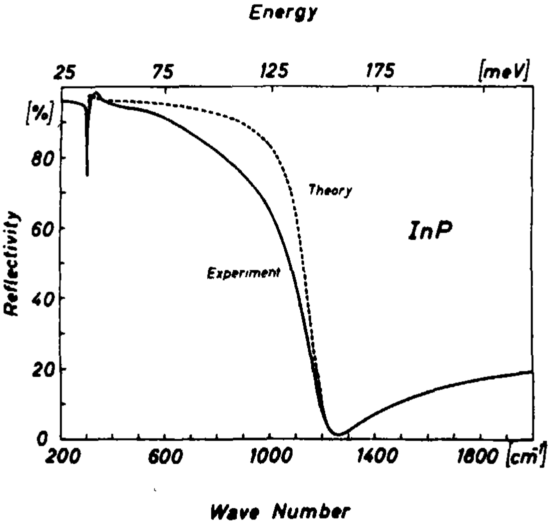

Fig. 7. Fit of a Plasma-Reflection Spectrum at 300 K; $\omega_P/\omega_L = 3{\cdot}15$ (The solid line is identical with curve IV in Fig. 1).

below the plasma edge, because even the polished surfaces are not absolutely flat. Surface plasmons have been discussed in connection with the reflectivity of rough metal surfaces[14–19]. Semiconductors have recently been considered[20]. The maximal surface plasmon energy ω_s in semiconductors is only a few per cent smaller than the bulk plasmon energy[21], because of their large lattice dielectric constants. The maximal deviation between experimental and theoretical reflectivity can be explained with the formulas for metals[15–16], adjusted for the dielectric constant of InP. However, the overall fit is still unsatisfactory. It seems likely that the assumption of highly damped surface plasmons might lead to better agreement; work is in progress in this laboratory[22].

4. CONCLUSIONS

InP has similar properties as GaAs. The effective mass m^* is only slightly larger than that of GaAs. At high carrier densities m^* increases rapidly with increasing carrier concentration and decreases with decreasing temperature. The effective mass of the free carriers and their damping can be obtained relatively exactly by reflectivity measurements. Reduced reflectivities below the plasma frequency apparently result from surface plasmon effects.

Acknowledgements—I wish to thank Prof. Dr. H. J. Queisser for his helpful advice on the matters presented here, and Mr. N. Marschall for his support of the experimental construction. The financial support of the Fraunhofer Gesellschaft is greatly appreciated.

REFERENCES

1. VARGA B. B., *Phys. Rev.* **137**, A 1896 (1965).
2. SINGWI K. S. and TOSI M. P., *Phys. Rev.* **147**, 658 (1966).
3. YOKOTA I., *J. phys. Soc. Japan* **16**, 2075 (1961).
4. MOORADIAN A. and McWHORTER A. L., *Phys. Rev. Lett.* **19**, 849 (1967).
5. HASHIMOTO M. and AKASAKI I., *Phys. Lett.* **25A**, 38 (1967).
6. OLSON C. G. and LYNCH D. W., *Phys. Rev.* **177**, 1231 (1969).
7. McMAHON T. J. and BELL R. J., *Phys. Rev.* **182**, 526 (1969).

8. KÖHL F., *Opt. Commun.*, **2**, 157 (1970); references to previous mathematical treatments are given in this publication.
9. BENNET H. E., SILVER M. and ASLEY E. J., *J. Opt. Soc.* **A53**, 1089 (1963).
10. RÖDER O., HEIM U. and PILKUHN M., *J. Phys. Chem. Solids* in press.
11. CARDONA M., *Prague Conference of Semiconductors*, p. 388 (1960).
12. CARDONA M., *Phys. Rev.* **121**, 752 (1961).
13. PALIK E. D. and WRIGHT G. B., in *Semiconductors and Semimetals* (Edited by R. K. Willardson and A. C. Beer) Vol. 3, Academic Press, New York and London (1967).
14. KRETSCHMANN E. and RAETHER H., *Z. Naturf.* **23a**, 2135 (1968).
15. KRETSCHMANN E., *Z. Phys.* **227**, 412 (1969).
16. BEAGLEHOLE D., *Phys. Rev. Lett.* **22**, 708 (1969).
17. ENDRIZ J. G. and SPICER W. E., *Phys. Rev. Lett.* **24**, 64 (1970).
18. RITCHIE R. H., WILEMS R. E., *Phys. Rev.* **178**, 373 (1969).
19. SCHRÖDER E., *Opt. Comm.* **1**, 13 (1969).
20. FISCHER B. and MARSCHALL N., *Proceeding of the Tenth International Conference on Semiconductors*, Cambridge, Massachusetts (1970). (Edited by S. P. Keller *et al.*). p. 845.
21. See, for example, ANCKER-JOHNSON B. in *Semiconductors and Semimetals*, (Edited by R. K. Willardson and A. C. Beer) Vol. I, Academic Press, New York and London (1966).
22. FISCHER B. and MARSCHALL N., private communications.

J. Phys. Chem. Solids, 1971, Vol. 32, pp. 2487–2492. Pergamon Press. Printed in Great Britain

MAGNETIC STATES IN AMORPHOUS Fe–Pd–Si ALLOYS*

R. HASEGAWA
W. M. Keck Laboratory of Engineering Materials, California Institite of Technology, Pasadena, Calif. 91109, U.S.A.

(*Received* 15 *March* 1971)

Abstract – Low temperature measurements of electrical resistivity, magnetic susceptibility and magnetoresistivity for the amorphous $Fe_x(Pd_{82}Si_{18})_{100-x}$ alloys where x is changed between 0·1 and 0·9 are reported. The amorphous alloys were prepared by rapid quenching from the liquid state. The polarization of the *d*-electrons of Pd atoms around a Fe atom is found to persist down to the lowest Fe concentration. No giant moment was observed in the present alloys. The effect of the spin polarization on the Kondo type *s–d* scattering is absent or very small. Interactions between the *d*-electrons of the Fe atoms, resulting in the superparamagnetic behavior of the alloys seem to take place below a characteristic temperature T_d and only at higher fields. This is found to be consistent with the magnetoresistivity data. The results of both electrical and magnetic measurements are in quantitative agreement.

1. INTRODUCTION

A TRANSITION metal like Fe, Co or Ni, when dissolved in Pd or Pt, tends to polarize the surrounding Pd or Pt atoms via conduction electrons. Spin polarization of this sort has been observed in magnetic susceptibility, electrical resistivity, specific heat, Mössbauer effect, neutron scattering, NMR and EPR measurements[1]. The spin polarization seems to originate from the nearly ferromagnetic, itinerant character of the Pd or Pt *d*-band. Iron[2] or cobalt[3] in Pd have received much attention, since they form a well-defined ferromagnetic state for very low concentrations (~0·1 at.%). In addition the range of the spin polarization around the magnetic atom has been shown to vary from 10 to 1 Å when the Fe or Co concentration increases from ~0·5 to 4 at.%[4]. The polarization range probably extends even further than 10 Å when the magnetic atom concentration is decreased below 0·5 at.%, since the value of the local magnetic moment reaches as high as 12 μ_B at 0·28 at.% Fe[2].

The situation is somewhat different in the amorphous Pd–Si alloys containing iron[5]. The major differences are that the amorphous Pd–Si host alloy is weakly paramagnetic while crystalline Pd is strongly paramagnetic and the *d–d* exchange interactions are weaker in the amorphous alloys than in the crystalline alloys. In the vicinity of a Fe atom, however, the neighboring Pd atoms are polarized by the magnetic atoms as in the case of the Fe–Pd crystalline alloys. The amorphous Fe–Pd–Si alloys containing from 0·5 to 7 at.% Fe tend to become superparamagnetic at low temperatures and become ferromagnetic when the Fe concentration is large (e.g. $Fe_7Pd_{73}Si_{20}$). For these alloys a Kondo type resistivity minimum has been found[6]. The crystalline Fe–Pd alloys do not exhibit any Kondo effect due to the appearance of a well-defined ferromagnetism. In these alloys it is therefore not possible to study the effect (if any) of the spin polarization on the Kondo type *s–d* scattering. The results previously published on the FePdSi amorphous alloys[5, 6] have now been extended to Fe concentrations varying from 0·1 to 0·9 at.%. The main points of interest include the effect of decreasing Fe concentration on the local magnetic moments and on the persistence of the superpara-

---

*Work supported by the U.S. Atomic Energy Commission.

magnetism, and the influence of the spin polarization on the Kondo effect. The amorphous alloys were prepared by rapid quenching from the liquid state and the experimental methods were similar to those described in Ref. [7].

2. RESULTS

2.1 *Electrical resistivity*

Measurements of the electrical resistivity were made on the amorphous samples with Fe concentrations of 0·1, 0·2, 0·3, 0·5, 0·7 and 0·9 at.% in the temperature range 1·4–300°K. The results of the measurements are shown in Fig. 1 for $1{\cdot}4 \leq T \leq 100$°K. It was found that the total resistivity for temperatures below 50°K can be fitted to a form

$$\rho(T) = \alpha + \delta T^2 + \gamma \ln T \qquad (1)$$

in which α, δ and γ are as described in Ref. [6]. The temperature dependent part of the spin resistivity, $\rho_{\text{spin}}(T)$, corresponding to the third term in equation (1), can be obtained by subtracting from the total resistivity the resistivity of the host $Pd_{82}Si_{18}$ alloy which has a temperature dependence similar to that of Fig. 1 in Ref. [7]. The results for $\rho_{\text{spin}}(T)$ per at.% Fe are plotted as a function of temperature in Fig. 2. Equation (1) gives a resistivity temperature at

$$T_m = (-\gamma/2\delta)^{1/2}. \qquad (2)$$

Substituting the values of γ obtained from Fig. 2 and $\delta \cong 2{\cdot}8 \times 10^{-4}\,\mu\Omega$-cm into equation (2), the values of T_m can be calculated and are listed in Table 1 together with the values of γ and those for T_m shown in Fig. 1.

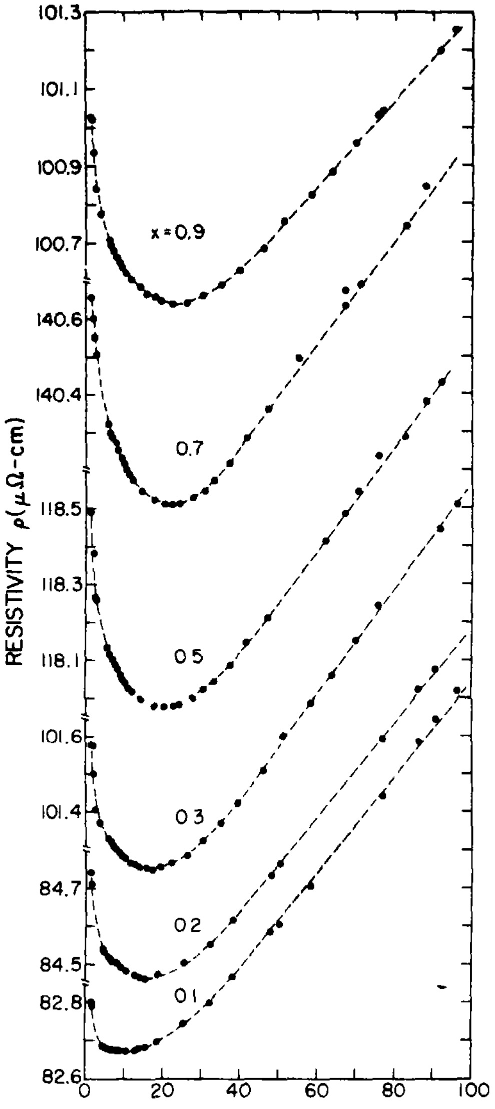

Fig. 1. Electrical resistivity vs. temperature for the amorphous $Fe_x(Pd_{82}Si_{18})_{100-x}$ alloys.

2.2 *Magnetic susceptibility*

A pendulum-type magnetometer[8] was used to measure the magnetic moments of the amorphous alloys with a magnetic field up to 8·4 kOe and in a temperature range 1·7–300°K. The contribution of the Fe atoms to the total magnetic moments was obtained by subtracting the moments of the host $Pd_{82}Si_{18}$ amorphous alloy from those observed for the $Fe_x(Pd_{82}Si_{18})_{100-x}$ alloys. The corrected magnetic moments were found to be linearly proportional to the applied magnetic field above the characteristic temperature T_d[5]. Below T_d, the magnetization M vs. magnetic field H curves resemble those of a

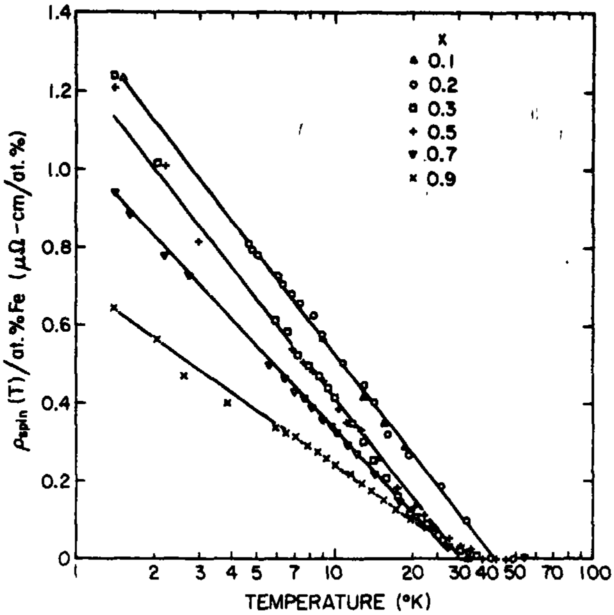

Fig. 2. Temperature dependent part of the spin resistivity per at. % Fe vs. temperature.

Table 1. *Values of* γ, $(T_m)_{cal}$, *calculated by using equation (2) and* $(T_m)_{obs}$, *observed in Fig.* 1., *for the amorphous* $Fe_x(Pd_{82}Si_{18})_{100-x}$ *alloys*

x (at. %)	γ/at. % Fe ($\mu\Omega$-cm)	$(T_m)_{cal}$ (°K)	$(T_m)_{obs}$ (°K)
0·1	−0·40±0·02	8·5	10
0·2	−0·41±0·01	12	15
0·3	−0·40±0·01	15	17·5
0·5	−0·41±0·01	19	22·5
0·7	−0·30±0·01	19	21
0·9	−0·20±0·01	18	23

typical superparamagnetic alloy [9]. The initial susceptibility $\chi_i = (dM/dH)_{H=0}$, however, obeys the Curie–Weiss law which holds above T_d. The inverse of the high field susceptibility contributed from the Fe atoms alone is plotted against temperature between 1·4 and 40°K in Fig. 3. The data points shown by crosses indicate the inverse of the initial susceptibility. These results can be expressed by $\chi = C/(T-\theta_p)$ where C is the Curie constant and θ the paramagnetic Curie temperature. The local moments, $\mu = gS$, are calculated from the values of C and are listed in Table 2 together with the values of θ_p and T_d[10].

2.3 *Magnetoresistivity*

Since the magnetoresistivity at 295 and 77°K is not large enough to be measured accurately, the data at 4·2°K are presented here. The observed magnetoresistivity, ρ_H(Fe–Pd–Si), is corrected by subtracting that of the host Pd–Si alloy, ρ_H(Pd–Si), from ρ_H(Fe–Pd–Si) as previously [6]. The results are shown in Fig. 4 in the form of $\Delta\rho_H/\rho_{H=0}$

Table 2. *Results of the magnetic measurement* (*the value of g is taken as* 2·0)

x (at. %)	$\mu = gS(\mu_B$/Fe atom)	θ_p(°K)	T_d(°K)
0·1	3·9	~0	~4
0·2	4·2	~2	~6
0·3	4·5	~6	~6
0·5	4·6	~0	~6
0·7	4·8	~1·5	~8

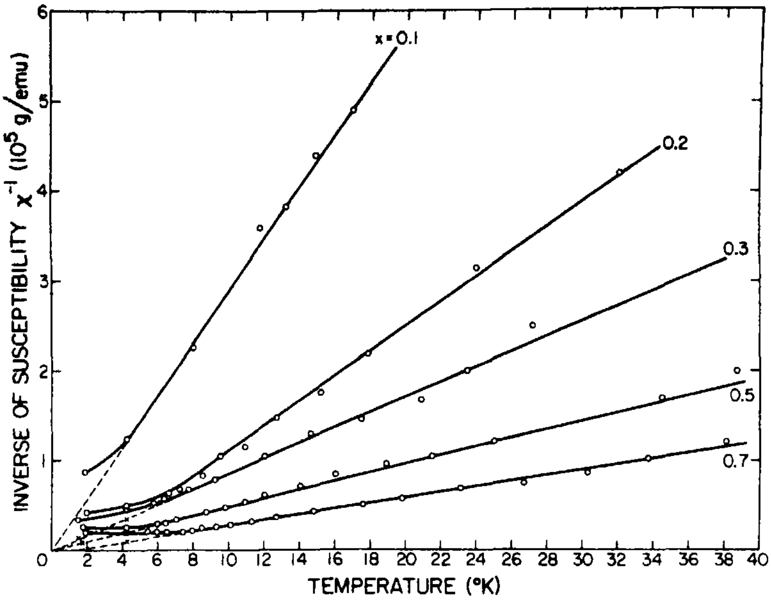

Fig. 3. Inverse of the high field susceptibility per gram of the amorphous $Fe_x(Pd_{82}Si_{18})_{100-x}$ alloy vs. temperature. The susceptibility is corrected by subtracting that of the host Pd–Si alloy from the total one. The crosses correspond to the low field susceptibilities.

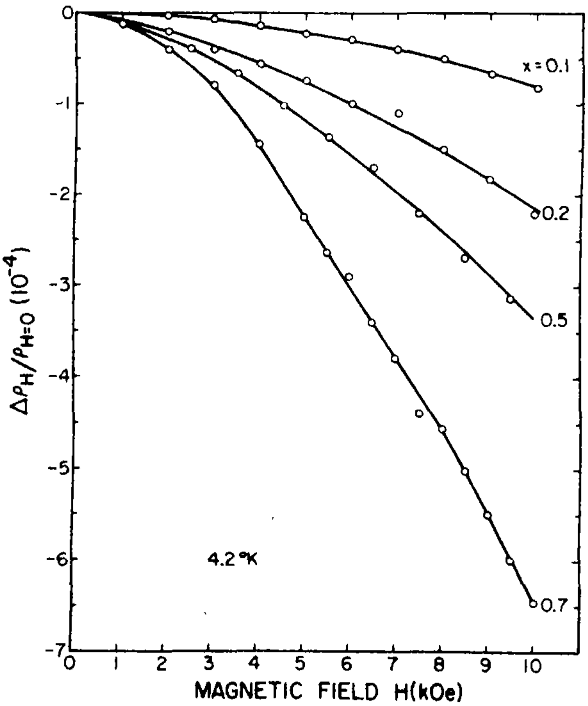

Fig. 4. Magnetoresistivity vs. magnetic field for $x = 0{\cdot}1$, $0{\cdot}2$, $0{\cdot}5$, and $0{\cdot}7$ at $T = 4{\cdot}2$°K.

vs. H, where $\Delta\rho_H = \rho_H - \rho_{H=0}$ and $\rho_H = \rho_H$ (Fe–Pd–Si) $- \rho_H$(Pd–Si). A best fit of the results for $H \geqslant 4$ kOe was made to a relation

$$\Delta\rho_H/\rho_{H=0} = -qH^n \quad (H \text{ in kOe}) \qquad (3)$$

where the values of q and n are listed in Table 3[11]. A meaningful fit of the data for $H < 4$ kOe to equation (3) is difficult to obtain for the alloys containing less than 0·5 at.% Fe due to the uncertainty in the measurements. For the alloy containing 0·7 at.%, however, $\Delta\rho_H$ is large enough to find that $q = 9{\cdot}4 \times 10^{-6}$ and $n = 2{\cdot}0$ for $H < 4$ kOe.

Table 3. Values of q and n in equation (3)

x (at.%)	$q(10^{-6})$	n
0·1	8·0	2·0
0·2	6·8	1·5
0·3	8·4	1·5
0·5	10·4	1·5
0·7	20·4	1·5

3. DISCUSSION

The invariance of the value of γ/at.% Fe for $0{\cdot}1 \leqslant x \leqslant 0{\cdot}5$ (Table 1) may indicate that the direct interactions between Fe atoms are negligible. For this concentration range of Fe, both $(T_m)_{\text{obs.}}$ and $(T_m)_{\text{cal.}}$ vary approximately as $30x^{1/2}$. Above the Fe concentration of 0·5 at.%, the value of γ/at.% Fe decreases with increasing x. This may be understood as a result of the reduction of the number of free paramagnetic ions, as pointed out previously[6], since equation (1) describes the resistivity data fairly well without adding any term such as proposed by Silverstein[12].

The nature of the s–d scattering in the present alloys becomes clearer when the magnetic properties are compared with the resistivity results. As seen in Table 2, the local moment per Fe atom is larger than the value $\mu_{\text{Fe}} = 3\,\mu_B$ assuming $S = 3/2$[5]. This shows persistence of the spin polarization down to a concentration of 0·1 at.% Fe. No giant moment as obtained in dilute Fe–Pd crystalline alloys[2] was observed in the present alloys. This is probably linked with the fact that the host Pd–Si amorphous alloy is weakly paramagnetic. Taking $\mu_{\text{Fe}} = 3{\cdot}0\,\mu_B$ and assuming that one Fe atom has 11·6 nearest neighbors of either Pd or Si atom[5], we obtain

$$\mu_{\text{Pd}} \sim 0{\cdot}23\,x^{0{\cdot}4}\,\mu_B \quad (0 < x < 0{\cdot}7).$$

The non-linear dependence of μ_{Pd} on x may suggest that the range of spin polarization changes with the Fe concentration as in the case of crystalline Fe–Pd alloys[4]. An interesting statement can be made with respect to the effect of the spin polarization on the Kondo type s–d scattering. This effect seems to be quite small or absent, since γ/at.% Fe (Table 1) is constant in the Fe concentration range 0·1–0·5 at.% in which both the magnitude and the range of the polarization seem to vary significantly. Even though the high field susceptibility deviates from the Curie–Weiss relation below T_d (Table 2), low field susceptibility obeys the same relation below T_d (see Fig. 3). This may indicate that interactions between the Fe atoms take place below T_d and above a certain field (which depends on the temperature and on the concentration of Fe). This interpretation is consistent with the fact that there is no change in the value of γ at T_d. Further evidence for this explanation is given by the results of the magnetoresistivity (see Table 3). For $x = 0{\cdot}1$, the negative magnetoresistivity measured at 4·2°K is proportional to the square of the field. Other alloys with larger concentrations of Fe exhibit the negative magnetoresistivity which is approximately proportional to $H^{3/2}$ for $H \geqslant 4$ kOe and is proportional to H^2 for $H < 4$ kOe (e.g. $\text{Fe}_{0\cdot7}(\text{Pd–Si})_{99\cdot3}$). The H^2 dependence of the negative magnetoresistivity is due to the paramagnetic nature of the magnetic atoms [13, 14] while the $H^{3/2}$ dependence could be attributed to the presence of superparamagnetism[6, 15]. It is noticed that the value of $q(\cong 8\times 10^{-6})$ for $x = 0{\cdot}1$ is close to that for $x = 0{\cdot}7$ $(q \simeq 9\times 10^{-6})$ in a field $H < 4$ kOe. This is qualitatively consistent with the values of γ for the corresponding alloys in the sense that the number of free paramagnetic ions decreases with increasing Fe concentration. Since the results of the magnetic measurements indicate that the amorphous alloy with 0·1 at.% Fe is paramagnetic at 4·2°K and at higher fields, the results of both electrical and magnetic measurements are consistent. If we take $E_F = 3{\cdot}5$ eV and $J_{sd} = -0{\cdot}62$ eV as obtained previously[6], equation (34) of Ref. [14] gives $\Delta\rho_H \simeq -0{\cdot}10\ \mu\Omega$-cm at $H = 8{\cdot}4$ kOe for $x = 0{\cdot}1$ by using $M(H = 8{\cdot}4) \simeq 1{\cdot}53\ \mu_B/$Fe atom and $\mu_{\text{eff}} = 4{\cdot}8\ \mu_B/$Fe atom. From the magnetoresistivity data for $x = 0{\cdot}1$ (Table 3), we obtain $\Delta\rho_H \simeq -(8\times 10^{-6}H^2)\rho_{H=0} = -0{\cdot}06\ \mu\Omega$-cm at $H = 8{\cdot}4$ kOe. The discrepancy (of about 40%) between the two values of $\Delta\rho_H$ is probably due to the uncertainty in the value of M, since the amount of Fe impurities in Pd used in the present study ranges from 50 to 300 ppm corresponding to an uncertainty of 5 to 30% in the Fe concentration for the $\text{Fe}_{0{\cdot}1}(\text{Pd–Si})_{99{\cdot}9}$ alloy. As it is noticed in equation (34) of Ref. [14], an error of 20% in the value of M results in an error of about 40% in the value of $\Delta\rho_H$.

The present results can be summarized as follows. The spin polarization via the conduction electrons around the Fe atoms persists to a Fe concentration as low as 0·1 at.%. No giant moment, however, was observed in the present alloys. The amount of the polarization increases monotomically with the Fe concentration up to 0·5 at.% and levels off above this concentration. This may indicate that the range of the polarization changes with the Fe concentration similarly to the case of crystalline Fe–Pd alloys. For the Fe concentration range 0·1–0·5 at.%, the coefficient of the Kondo logarithmic term of the resistivity is proportional to the Fe concentration. This demonstrates that the spin polarization plays little or no part in the Kondo type s–d scattering. Below the characteristic temperature T_d, the alloys tend to be superparamagnetic at high fields. This result is found to be consistent with the magnetoresistivity data. A satisfactory consistency has been found among the results of the electrical and magnetic measurements, if the uncertainty of the Fe impurities in Pd is taken into consideration.

Acknowledgements – The author is grateful to Prof. Duwez for his interest and support of the present study. The resistivity and the magnetoresistivity measurements were made by E. Wheatley during his NSF summer (1970) research project.

REFERENCES

1. For a recent development of the various experimental works, see for example, *J. appl. Phys.* **41**, No. 3 (1970).
2. CRANGLE J. and SCOTT W. R., *J. appl. Phys.* **36**, 921 (1965).
3. BOZORTH R. M., WOLFF P. A., DAVIS D. D., COMPTON V. B. and WERNICK J. H., *Phys. Rev.* **122**, 1157 (1961).
4. LOW G. G. and HOLDEN T. M., *Proc. Phys. Soc. Lond.* **89**, 119 (1966); HICKS T. J., HOLDEN T. M. and LOW G. G., *J. phys. Soc. C: Phys. Soc. Proc.* **1**, 528 (1968).
5. HASEGAWA R., *J. appl. Phys.* **41**, 4096 (1970).
6. HASEGAWA R. and TSUEI C. C., *Phys. Rev. B* **3**, 214 (1971).
7. HASEGAWA and TSUEI C. C., *Phys. Rev. B* **2**, 1631 (1970).
8. WEINER M. E., Ph.D. thesis, California Institute of Technology 1968 (unpublished).
9. See, for example, Fig. 1 of Ref. [5].
10. There seems to exist a spread in the values of T_d, since the previous measurements (Ref. [5]) give $T_d \sim 1{\cdot}7$°K for $x = 0{\cdot}5$.
11. Since ferromagnetism does not appear in the present Fe concentration range, a fit to a relation $\Delta\rho_H/\rho_{H=0} = -pH - qH^2$ described in Ref. [6] was not attempted. For $x = 0{\cdot}05$. Table 3 of Ref. [6] gives $\Delta\rho_H/\rho_{H=0} = -(1{\cdot}36H + 0{\cdot}075H^2)\times 10^{-5}$ which can be fitted also to $\Delta\rho_H/\rho_{H=0} = -qH^n$ with $q = 8{\cdot}0\times 10^{-6}$ and $n = 1{\cdot}5$ in satisfactory agreement with the corresponding values in Table 3 of this paper.
12. SILVERSTEIN S. D., *Phys. Rev. Lett.* **16**, 466 (1966).
13. YOSIDA K., *Phys. Rev.* **107**, 396 (1957).
14. BÉAL-MONOD M. T. and WEINER R. A., *Phys. Rev.* **170**, 552 (1968).
15. However, we cannot explain the result that the Fe–Fe interaction energy kT_d is about ten times larger than $\mu_B H$ with $H \sim 4$ kOe.

J. Phys. Chem. Solids, 1970, Vol. 32, pp. 2493–2498. Pergamon Press. Printed in Great Britain

THE ORIGIN OF THE $K\beta_5$ LINE IN THE X-RAY EMISSION SPECTRUM OF K^+ IN KF, KCl AND KBr

J. UTRIAINEN and M. LINKOAHO
Laboratory of Physics, Helsinki University of Technology, Otaniemi, Finland

(*Received* 28 *December* 1970; *in revised form* 11 *March* 1971)

Abstract–The relative energy and intensity of the potassium $K\beta_5$ line in KF, KCl and KBr have been measured in fluorescence. The energy and intensity calculations indicate this line to be a cross transition between the K^+1s state and the anion valence state with mixing of K^+3p wave function. The appearence of this line is thus connected with the covalency of the crystal.

1. INTRODUCTION

THE HYPOTHESIS of the existence of cross transitions between the energy levels of two unlike neighbouring atoms has been discussed frequently. For instance, Mendel[1], Mendel and Koster[2] have interpreted the $K\beta'$ satellites in some compounds of the elements Na, Mg, Al and Si using this hypothesis in an atomic model. A similar mechanism was recently discussed also by Linkoaho *et al.* [3]. On the other hand, more detailed considerations by Åberg *et al.*[4] for the $K\beta_1$ line in sodium halides and by Urch[5], Lawrence and Urch[6] for $K\beta'$ satellites show that the atomic model is unsatisfactory. A molecular model is needed to explain the energies and intensities of these lines, for instance, the $K\beta_1$ line in sodium halides seems to be caused by the covalency in the crystal only[4].

As early as in 1938 Valasek[7] proposed that the $K\beta_5$ line of potassium in KCl is due to the cross transition of electrons from the chlorine $3p$ band filling $1s$ vacancies in the potassium ion. More recently Deslattes[8] has measured the $K^+K\beta_5$ line in KCl and he has provided supporting evidence for the cross-transition hypothesis by comparing his results with band structure calculations. As far as we know there are no measurements of the integrated intensity for the $K\beta_5$ line in other potassium halides. For this reason we have measured the $K^+K\beta$ spectrum of KF, KCl and KBr by secondary excitation. We have also compared our energy and intensity data with calculations based on the assumption that the $K^+K\beta_5$ line is a cross transition.

2. THE MEASUREMENTS

The spectra were measured by a vacuum plane-crystal spectrometer and the third-order reflection from an ammonium dihydrogen phosphate (ADP) crystal. The specimens were excited by the radiation from a chromium anode X-ray tube operating at 50 kV and 36 mA. The detector was an argon–methane flow-proportional counter with a 2μm Makrofol window. For optimum resolution two Soller slits were employed. The entrance slit limited the horizontal divergence to 0·40° and the receiving slit limited it further to 0·15°. The recording system and the X-ray generator were commercial Siemens equipments and have been described earlier[9]. The specimens were pressed from fine powders (Merck, pro analysi). Crystalline water was removed from the KF samples by heating. Each spectrum was recorded at least three times and some results are shown in Fig. 1. The time of measurement per step of

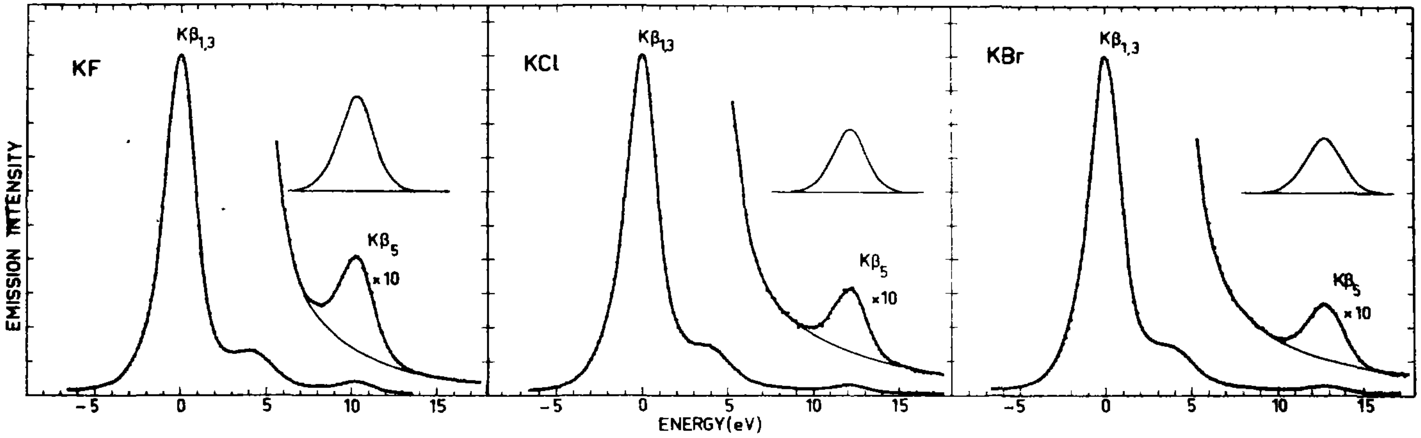

Fig. 1. The $K\beta$ X-ray spectrum of the K^+ ion in various halides recorded in secondary excitation with an ammonium dihydrogen phosphate (ADP) crystal in the third order. The $K\beta_5$ line is shown also in enlarged scale and with the background subtracted.

0·02° (in 2θ) was 4 or 10 min. The positions of the peaks were determined with a step of 0·005°. The energies of the $K\beta_5$ line were determined relative to those of the $K\beta_{1,3}$ line. The experimental energy differences $EK\beta_5$–$EK\beta_{1,3}$ and the relative integrated intensities $IK\beta_5/IK\beta_{1,3}$ are shown in Table 2. On the high-energy side of the $K\beta_{1,3}$ line the KM satellite contribution[8] was separated under the assumption that the $K\beta_{1,3}$ line is symmetric. In the calculation of the energy differences the peak values were used, and a value of 10·648 Å for the spacing $2d$ of the ADP crystal was assumed.

The trend in the measured energy differences is in agreement with the photographic recordings of Kiyono[10] for KCl and KBr.

3. THE ENERGY OF THE $K\beta_5$ LINE

Howland[11] has shown that the Hartree–Fock (HF) one-electron energies $E_i(\bar{k})$ in an ionic crystal can be written as

$$E_i(\bar{k}) = E_{0i} \pm E_M + f_i(\bar{k}) \tag{1}$$

Here E_{0i} is the HF energy of the i^{th} electron in the free ion and E_M is the Madelung energy. The plus sign corresponds to the anion and the minus sign to the cation. The $f_i(\bar{k})$ term represents the $\bar{k}$-dependent spread of the band. Instead of $f_i(\bar{k})$ we can use f_i, which is the distance from $E_{0i} \pm E_M$ to the energy corresponding to the maximum value of the product $P(E)N(E)$, $P(E)$ being the transition probability to the $K^+ 1s$ state and $N(E)$ the density

Table 1. *The estimated* (*equation* (1)) *limiting values of the band spread* f_i *and the values of the polarization energy* E_{pi} *in equations* (2) *and* (3) *for* K^+ *and* Cl^- *in KCl*

		3p band		Estimated range of	
	$E_{0i} \pm E_M$ eV	Lower limit eV	Upper limit eV	f_i eV	E_{pi} eV
K^+3p	23·8	23·5	23·9	−0·3 −0·1	2·0
Cl^-3p	12·1	10·7	12·2	−1·4* −0·1	1·4

*Note an error in Ref. [4].

Table 2. *The measured and calculated energies and intensities of the* $K^+K\beta_5$ *line relative to those of the main* $K\beta_{1,3}$ *line*

	$\Delta E = E\beta_5 - E\beta_{1,3}$ (eV)					$I\beta_5/I\beta_{1,3}$ (%)	
	Expt	Calc	Expt-Calc	ESCA	Kiyono	Expt	Calc
KF	10·2±0·1	9·5	0·7	†	–	2·2±0·3	1·5
KCl	12·1*±0·1	12·2	−0·1	12·1	12·7	1·5* ±0·2	0·9
KBr	12·7±0·1	13·2	−0·5	12·9	13·5	1·4±0·2	–
KI	–	14·5	–	13·8	14·2	–	–

*The values of Deslattes[8] are 12·0±0·1 eV and 1·5 per cent.

†Stephan *et al.*[15] have obtained values 9·75 and 10·15 eV from the reflectance spectra.

of states. Taking into account the polarization and the correlation in the ion and the energy of interaction E_{pi} of the hole due to the electronic polarizability of the neighbouring ions, we obtain instead of equation (1)

$$E_i = B_i \pm E_M + f_i - E_{pi}, \tag{2}$$

where B_i is the real ionization energy of the free ion. B_i, E_M and E_{pi} are here considered positive. Supposing that

$$f_{3p}(K^+) - f_{np}(X^-) + E_{p,np}(X^-) - E_{p,3p}(K^+) = 0 \tag{3}$$

we get for the energy difference $E\beta_5 - E\beta_{1,3}$ in the $K^+K\beta$ spectra of potassium halides

$$E\beta_5 - E\beta_{1,3} = B_{3p}(K^+) - B_{np}(X^-) - 2E_M. \tag{4}$$

We can estimate the accuracy of the assumed relation (3) in KCl, where the calculations by Howland[10] for the Cl^-3p and K^+3p bands are available. The results are shown in Table 1. For the polarization energies E_{pi} we have used the values of du Pré *et al.*[12]. For the limiting values of the left hand side of equation (3) we get $-1{\cdot}0$ and $+0{\cdot}9$ eV and thus the accuracy of equations (3) and (4) is about ± 1 eV in this case.

In Table 2 we show the values obtained for the energy differences $E\beta_5 - E\beta_{1,3}$ from equation (4) where we have used $B_{3p}(K^+) = 31{\cdot}8$ eV[13] and the electron affinities $B_{np}(X^-)$ measured by Berry and Reimann[14]. We see that the agreement between the measured and the calculated values is good.

According to the photoelectron measurements by ESCA (Electron Spectroscopy for Chemical Analysis) group[15] the energy separation between the K^+3p and the anion valence state np in KCl and KBr crystals shown in Table 2 is in agreement with our measured value. In KF the energy gap between the K^+3p and F^-2p states obtained from the reflectance spectra[16] is also quite near our measured value. These results support our cross-transition hypothesis. A comparison between the measured and calculated values in Table 2 indicates that the influence of neglecting the differences in the polarization energy and in the band spread in equation (4) is small (< 1 eV). There is, however, a systematic trend in the values of $\Delta E_{\text{expt}} - \Delta E_{\text{calc}}$ of Table 2, which is similar to that in Ref. [4].

4. THE INTENSITY OF THE $K\beta_5$ LINE

A value of approximately 10^{-3} per cent is obtained when the relative integrated intensity of the $K\beta_1$ line in the sodium halides is calculated without mixing of the Na^+2p wave function with the anion valence-shell wave functions[4]. Urch[5] makes a similar estimate of the relative intensity of the $K\beta'$ line to that of the main $K\beta_{1,3}$ line in silicium oxides obtaining 10^{-2} per cent. The experimental values are about 2 per cent in the former and 15–25 per cent in the latter case. Thus we cannot explain the intensities of these cross-transition lines using a purely ionic model. We have, therefore, chosen a molecular orbital model in calculating the relative intensity of the potassium $K\beta_5$ line.

Following Åberg *et al.*[4] we have calculated the values of the integrals

$$I_c = \frac{1}{3N}\left\{\left|\int_0^\infty R_{1s}(r)\beta_p(r;\sigma,a)r^3\,\mathrm{d}r\right|^2 + 2\left|\int_0^\infty R_{1s}(r)\beta_p(r;\pi,a)r^3\,\mathrm{d}r\right|^2\right\} \tag{5}$$

where N is the square of the radial integral

$$\int_0^\infty R_{1s}(r)R_{3p}(r)r^3\,\mathrm{d}r.$$

We have used the radial $1s$ and $3p$ single-electron wave functions of K^+[17] and the radial p-symmetric SCF-LCAO-MO potassium orbitals $\beta_p(r;\sigma,a)$ and $\beta_p(r;\pi,a)$ from Matcha[18]. We obtain only an estimate for the relative intensity, because the wave functions of Matcha are calculated for molecules, not for crystals. The results are shown in Table 2 and they indicate that the molecular model is satisfactory. It is interesting to note that the model gives the change in the intensity between KF and KCl correctly.

If we examine the measured emission spectra (Fig. 1), we see an additional contribution between the KM satellite and the $K\beta_5$ line. This is also detectable in the spectra measured by Parratt and Jossem[19] and Deslattes[8]. Possible sources for this contribution are, according to Deslattes' energy calculations[8], the $KM_1-M_1M_{2,3}$ $({}^3S-{}^3P)$ transition at 6·5 eV and KM^2-M^3 type transitions around 11·3 eV. The KM^2 triple-hole excitation states may be caused by simultaneous M-shell excitation and K-shell ionization or by $KL-KM^2$ Auger transitions and they may, for example, decay to M^3 or LM^2 states. It is, consequently, very difficult to calculate the relative intensities of the various components of the KM^2 structure. As in the papers of Åberg[20, 21], the relative production probability of the KM^2 states can be estimated to 1·4 per cent without the effect of the $KL-KM^2$ Auger transitions included. We can also calculate the term splitting of the KM^2-M^3 structure from the atomic energy levels derived from the analysis of optical spectra[13]. If we use the $Z+1$ approximation for the KM^2 state, we need only the energies of various terms of the Ca $3s^23p^4$ and $K\ 3s^23p^3$ structures relative to the energies of the ground state of Ca $3s^23p^6$ and $K\ 3s^23p^5$. This way we have obtained ten terms with energies 7–16 eV relative to the main $K\beta_{1,3}$ peak. About one half of the total intensity accumulates at 11–12 eV.

We have seen that a part of the measured $K\beta_5$ intensity in Table 2 may be due to the triple-hole excitations. The energies and intensities of the triple-hole KL^2-L^3 satellites in sodium are independent of the chemical bond[4]. The position and intensity of the $K\beta_5$ line, however, clearly differ in KF and KCl. This line seems to be symmetric and its measured line width at half maximum is about the same in KF, KCl and KBr. Thus there is no evidence of an additional line on the high-energy side of the $K\beta_5$ line in KF and on the low-energy side of this line in KBr. For metallic potassium the unpublished measurements of Jossem (cf. Ref. [8]) show less than 10 per cent of the intensity in KCl at the wavelength corresponding to $K\beta_5$. Therefore we conclude that the intensity of the $K\beta_5$ line in KF, KCl and KBr is mainly determined by the cross transition due to the mixing of the K^+3p wave function with the anion valence shell wave function.

Note added in proof: a thorough discussion of $K\beta_5$ line in the emission spectrum of KCl has been recently given by BEST P. E., *Phys. Rev.* **B3**, 4377 (1971).

Acknowledgements—We would like to thank Dr. T. Åberg for stimulating discussions and for his help with the computations. The financial support of the National Research Council for Sciences is gratefully acknowledged.

REFERENCES

1. MENDEL H., *Proc. K. Ned. Acad. Wet.* **B70**, 276 (1967).
2. MENDEL H. and KOSTER A. S., *J. Phys. C: Solid State Phys.* 3, 855 (1970).
3. LINKOAHO M., ÅBERG T., GRAEFFE G. and UTRIAINEN J., *Z. Naturf.* **24a**, 775 (1969).
4. ÅBERG T., GRAEFFE G., UTRIAINEN J. and LINKOAHO M., *J. Phys. C: Solid State Phys.* 3, 1112 (1970).
5. URCH D. S., *J. Phys. C: Solid State Phys.* 3, 1275 (1970).
6. LAWRENCE D. F. and URCH D. S., *Spectrochim. Acta* **25B**, 305 (1970).
7. VALASEK J., *Phys. Rev.* **53**, 274 (1938).
8. DESLATTES R. D., *Phys. Rev.* **133**, A390 (1964); **133**, A399 (1964).
9. UTRIAINEN J., LINKOAHO M., RANTAVUORI E., ÅBERG T. and GRAEFFE G., *Z. Naturf.* **23a**, 1178 (1968).
10. KIYONO, S., *Sci. Rep. Tôhoku Univ.* [1], **39**, 129 (1956).
11. HOWLAND L. P., *Phys. Rev.* **109**, 1927 (1958).
12. DU PRÉ F. K., HUTNER R. A. and RITTNER E. S., *J. chem. Phys.* **18**, 379 (1950).
13. MOORE C. E., Atomic Energy Levels, Vol. I,

Nat. Bur. Stand. Circ. 467. U.S. Govt. Printing Office, Washington (1949).
14. BERRY R. S. and REIMANN C. W., *J. chem. Phys.* **38**, 1540 (1963).
15. SIEGBAHN K. *et al.*, *Nova Acta R. Soc. Scient. upsal.* [IV], **20**, 72 (1967).
16. STEPHAN G. and RODIN S., *C.R. Acad. Sci. Paris* **267**, 1286B (1968).
17. CLEMENTI E., Tables of Atomic Functions (Supplement to IBM *J. Res. Dev.* **9**, 2 (1965).
18. MATCHA R. L., *J. chem. Phys.* **49**, 1264 (1968); **53**, 485 (1970).
19. PARRATT L. G. and JOSSEM E. L., *Phys. Rev.* **97**, 916 (1955).
20. ÅBERG T., *Phys. Rev.* **156**, 35 (1967).
21. ÅBERG T., *Ann. Acad. Sci. Fenn.* [AVI], **308**, 1 (1969).

J. Phys. Chem. Solids, 1971, Vol. 32, pp. 2499-2516. Pergamon Press. Printed in Great Britain

DESCRIPTION OF THE HYDROGEN-METAL INTERACTION BY A MORSE POTENTIAL FUNCTION

D. R. OLANDER
Inorganic Materials Research Division of the Lawrence Radiation Laboratory and the Department of Nuclear Engineering, University of California, Berkeley, Calif. 94720, U.S.A.

(*Received* 3 *November* 1970; *in revised form* 11 *March* 1971)

Abstract—The interaction between hydrogen atoms adsorbed on the surface or dissolved in the interstices of a metal and the atoms of the host crystal is represented by a pairwise additive Morse potential function. This interaction is summed over all metal atoms surrounding the hydrogen atom. Interactions between hydrogen atoms are not considered. The three force constants of the potential function are determined from three experimental values of the hydrogen-metal system: the heat of solution, the heat of adsorption and the activation energy for bulk migration. Relaxation of the metal lattice surrounding the dissolved hydrogen and reconstruction of the surface metal atoms next to the adsorbed hydrogen are considered in the calculation. The potentials so determined are long range-metal atoms many lattice constants distant from the hydrogen atom contribute to the binding and the metal atoms closest to a dissolved hydrogen atom are repulsive. Four metals are treated: b.c.c. iron and tantalum, and f.c.c. nickel and copper. For each metal, two surface planes are investigated. Although both tetrahedral and octahedral interstitial sites were tested as solution sites, only occupancy of octahedral sites satisfied the interaction energies upon which the calculation is based. Knowledge of the potential function permits other characteristics of the hydrogen-metal interaction, such as the activation energy for surface migration and the vibration frequency of dissolved hydrogen, to be computed. Agreement of these calculated properties with experimental data is satisfactory, but not quantitative. The extreme sensitivity to crystal structure (b.c.c. or f.c.c.) and the assumption that the nature of the binding of surface hydrogen is the same as that of bulk hydrogen limit the utility of the pairwise model to that of an interpolation scheme—as a means of utilizing known characteristics of the hydrogen-metal system to estimate parameters not experimentally available.

1. INTRODUCTION

CHARACTERISTICS of the interaction of hydrogen with the regular lattice of a metal are investigated analytically. The metal-hydrogen interaction is represented by summation of a central pairwise potential function over all the metal atoms surrounding a hydrogen atom in or on the lattice. The pairwise potential is assumed to be the Morse function. This function is applicable to the interaction of the two hydrogen atoms of the hydrogen molecule [1] and it has also been applied to the binding properties of the metal lattice[2]. The Morse potential (restricted to nearest neighbor interactions) has also been utilized to predict the equation of state of metals [3]. This study seeks to determine whether the mixed case of the metal-hydrogen system can be satisfactorily analyzed by the same type of potential function. An investigation similar in many aspects to the one undertaken here has been reported by Goodman[4], who used a Lennard-Jones 6-12 interatomic potential to investigate the binding of various adsorbed species on tungsten and nickel. Johnson *et al.*[5] used a cubic potential to investigate the properties of carbon in iron and vanadium. While Goodman's study was concerned solely with surface interactions, and the calculations of Johnson *et al.* dealt only with bulk properties, the present work examines both surface and bulk interactions of hydrogen and the host metal.

The calculation does not purport to be a fundamental representation of the nature of the hydrogen-metal bond. In fact, the notion of central pairwise additivity may not be applicable to such systems[4]; Tamm and Schmidt[6], for example, have been able to explain the structure of hydrogen adsorbed on the (100) plane of tungsten on the basis of nearest neighbor bonds between the hydrogen atom and the *d* electrons of the metal. The present calculation should be viewed as an interpolation scheme – as a method of utilizing three relatively easily obtainable characteristics of the binding in a metal–hydrogen system to deduce other features of the system which are not experimentally available. In order to perform such a function, it is necessary to be able to describe the energy of a hydrogen atom at various locations in or on the crystal. Only the pairwise interaction model with an adjustable-parameter interaction potential provides a sufficiently complete calculational framework for this purpose.

The three experimental parameters of the hydrogen–metal system are employed to deduce the three force constants in the Morse potential function:

$$\phi(r) = D\left\{\exp\left[-2\frac{m}{r_e}(r-r_e)\right] - 2\exp\left[-\frac{m}{r_e}(r-r_e)\right]\right\} \quad (1)$$

where $\phi(r)$ is the potential energy between the two atoms separated by a distance r, and r_e, m, and D are the force constants (r_e is the equilibrium separation of the two atoms and D is the energy of the interaction at the equilibrium separation distance). Knowledge of the interatomic potential function permits calculation of properties of the hydrogen–metal system other than the three used to determine the force constants. The validity of the method is assessed by comparing the predicted properties to available measurements. Auxiliary features of the interaction, such as relaxation of the host atoms around a dissolved hydrogen atom should affect the pressure dependence of the solubility. However, no such experiments have been reported.

Several additional assumptions concerning the behavior of hydrogen in the metal lattice are:

(1) Hydrogen is dilute in the metal; $H-H$ interactions either in the interior or on the surface of the metal are neglected. In concentrated solutions, this interaction must be considered[7, 8]. The dissolution equilibrium is assumed to follow Sievert's law, which implies hydrogen in atomic form in the bulk.

(2) The dissolved hydrogen behaves as a three dimensional Einstein oscillator in the interstitial site of the b.c.c. or f.c.c. lattice in which it is located. This model has been discussed by Ebisuzaki and O'Keefe[9] and applied to the solution and diffusion of hydrogen in nickel by Ebisuzaki, Kass and O'Keefe [10]. The assumption of an Einstein oscillator appears to be satisfactory for f.c.c. metals, but is on somewhat tenuous grounds for b.c.c. metals[9]. Nevertheless, it is assumed here to apply to hydrogen dissolved in both types of cubic structures.

(3) Dissolved hydrogen may reside in either the tetrahedral or octahedral interstices of the cubic lattices. No assumption concerning this point is made; the calculations are performed for both types of equilibrium sites.

(4) Binding of hydrogen on the surface is of the same type as that in the bulk.

(5) The measured heats of adsorption refer to polycrystalline material with unidentified surface structure. In order to perform the calculations, the exposed surface plane must be specified. The (100) and (110) planes of the b.c.c. lattice and the (110) and (111) planes of the f.c.c. lattice have been considered here. In each case, the heat of adsorption is assumed to apply to the surface face under consideration.

(6) The diffusional jump is assumed to be from one equilibrium site to another via the other type of interstitial site (e.g., octahedral–tetrahedral–octahedral). The difference between the energy of the hydrogen atom in octahedral and tetrahedral sites is the activation energy of diffusion.

There is some support for this idea from other studies of migration of interstitial impurities in b.c.c. lattices[5, 11]. As shown in Fig. 1, the straight line path between octahedral sites in the b.c.c. lattice passes through

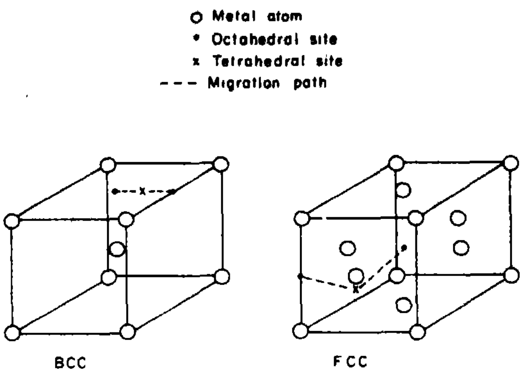

Fig. 1. Octahedral-octahedral migration paths via the tetrahedral site.

the tetrahedral interstitial site at the midpoint.

However, the octahedral–tetrahedral–octahedral path in the f.c.c. lattice is not a straight line, as shown in Fig. 1 (the tetrahedral site shown is at the (1/4, 1/4, 1/4) position). Nevertheless, the hydrogen-metal distance in the tetrahedral site ($\sqrt{3}a/4$, where a is the lattice constant) is larger than the hydrogen–metal distance at the midpoint of a straight line jump between two octahedral sites ($a/\sqrt{8}$), so that the path shown in Fig. 1 is not unreasonable. The diffusion of hydrogen in nickel has been shown to be in satisfactory agreement with an octahedral–octahedral jump mechanism[10].

The following aspects of the hydrogen-metal interaction are considered:

(1) the zero point energy of the dissolved hydrogen.

(2) relaxation of the host lattice about the dissolved and adsorbed hydrogen atoms.

(3) the difference between separation of planes in the bulk and the separation of the surface layer of metal atoms and the adjacent layer.

Four metals are considered: b.c.c. α-iron and tantalum and f.c.c. nickel and copper. The parameters of the Morse function for the metal–metal interactions have been taken from the calculations of Girifalco and Weizer [2]. The complete set of input parameters for the calculations are shown in Table 1. The lattice constant at room temperature is shown in the second column. The force constants for the metal–metal interaction are in columns 3–5. The sixth column contains the calculated relaxation of the surface layer obtained from the force constants shown in the preceding columns[12]. The quantity P is the difference between the calculated position of the surface plane and the position the surface would have

Table 1. *Input parameters*

		Metal force constants[b]				Hydrogen interaction parameters[d]		
Element	a, Å[a]	r_e/a	m	D[d]	P/a[c]	χ_a[e]	χ_s[f]	χ_d[g]
b.c.c. Fe	2·867	0·993	3·95	9·63	0·045(100) 0·048(110)	68	45	3·0
b.c.c. Ta	3·307	0·956	4·37	21·5	0·03 (110)	75	60	14·0
f.c.c. Ni	3·521	0·790	3·95	9·73	0·024(110) 0·017(111)	67	48	9·4
f.c.c. Cu	3·606	0·795	3·89	7·91	0·026(110) 0·018(111)	56	40	9·2

[a] SAMSONOV G. V., *Handbook of the Physicochemical Properties of the Elements*, Plenum, New York (1968).

[b] Ref. [2]; tantalum estimated from values for Mo and W.

[c] Ref. [12]; iron value scaled from corresponding nickel value; tantalum estimated.

[d] kcal/mole.

[e] EHRLICH G., *J. chem. Phys.* **31**, 1111 (1959).

[f] from Ref. [9] and FAST J. D., *Interaction of Metals and Gases*, Vol. 1, Academic Press, New York (1965).

[g] SMITHELLS C. J., *Metal Reference Book*, Vol. II, 4th Ed., Plenum Press (1967); except for tantalum which was taken from Ref. [15].

if the bulk interplanar spacing were maintained to the surface.

The three parameters of the hydrogen–metal interaction which were used in the calculations are shown in the last three columns. χ_a represents the binding energy of atomic hydrogen on the surface, χ_s represents the heat of solution of atomic hydrogen and χ_d is the activation energy for bulk diffusion. A survey of the available literature indicates general accord (to within one or two kcal/mole) on all of these values except for the activation energy for diffusion of hydrogen in tantalum. The NMR measurements of Pedersen *et al.*[13] on hydrides with hydrogen content exceeding $TaH_{0 \cdot 1}$ yield a value of 1·6 kcal/mole. The classic permeation experiments reviewed by Chandler and Walter[14] yield larger values. Although the activation energy from permeation experiments may be falsified by the existence of a rate-controlling surface step, the activation energy in concentrated *H*–Ta solutions may reflect *H–H* interactions. On balance, we have selected the 14·0 kcal/mole result of Klyachko[15], since it was obtained by experiments more closely reflecting the high temperature, dilute solutions to which the present calculations apply.

Parameters of the hydrogen–metal system used to check the reasonableness of the calculations were:

(a) Surface diffusion activation energy

(b) Effect of surface plane on the hydrogen binding energy

(c) The vibrational partition function for motion of the adsorbed hydrogen perpendicular to the surface

(d) Pre-exponential factor of the solubility (entropy of solution)

(e) The internal vibration frequencies of hydrogen in nickel and copper

(f) The effect of the lattice type on the solubility parameters (the solubility of hydrogen in both b.c.c. α-Fe and f.c.c. γ-Fe has been measured).

2. ANALYSIS

(a) *Heat of solution*

The ground state is the perfect metal lattice and free hydrogen atoms at rest. The dissolved state is the hydrogen atom in its lowest vibrational state at the center of an octahedral or tetrahedral interstice. The nearest and next nearest metal atom neighbors are allowed to relax. The energy released upon adding a hydrogen atom to the solid is given by:

$$\chi_s = -V_s - \Delta E_s - \tfrac{3}{2} h\nu_s \qquad (2)$$

where V_s is the potential energy of the hydrogen atom in the relaxed solution site. ΔE_s is the increase in the potential energy of the metal atoms surrounding the hydrogen atom due to relaxation. ν_s is the vibrational frequency of the hydrogen atom in the equilibrium solution site. The last term is the zero point energy of the dissolved hydrogen atom.

(b) *Binding energy of adsorbed hydrogen atoms*

The adsorbed hydrogen atom is assumed to be in its ground state with respect to vibration perpendicular to the surface on the surface site which maximizes the binding energy. The adsorption sites were taken to be those determined by Goodman[4] for each surface plane considered. The positions of the adjacent metal atoms and the distance of the hydrogen atom above the surface are adjusted to maximize the binding energy. The energy released on placing a free hydrogen atom on the surface is:

$$\chi_a = -V_a(z_{eq}) - \Delta E_a - \tfrac{1}{2} h\nu_a \qquad (3)$$

where $V_a(z_{eq})$ is the potential energy of the hydrogen atom at its equilibrium adsorption distance z_{eq} and ΔE_a is the energy required to reconstruct the surface. The third term on the right is the zero point energy for vibration of the hydrogen atom perpendicular to the surface. ν_a is the frequency of this mode of vibration. The lateral binding is assumed weak and the zero point energy of these vibrational modes is assumed to be negligible.

(c) *Activation energy for bulk diffusion*

The activation energy for diffusion is:

$$\chi_d = (V_d - V_s) - (\Delta E_s - \Delta E_d) \qquad (4)$$

where V_d is the potential energy of the hydrogen atom in the interstitial position chosen as the migration barrier and ΔE_d is the increase in lattice potential energy due to relaxation of the metal atoms about the hydrogen atom in this site. Transition state theory suggests that the right hand side of equation (4) should contain another term reflecting the zero point energies in the equilibrium and activated states. Ebusizaki *et al.*[10] have shown that this additional term is of the form:

$$-kT\left[\frac{3}{2}\left(\frac{h\nu_s}{kT}\right)\coth\left(\frac{h\nu_s}{2kT}\right) - \left(\frac{h\nu\dagger}{kT}\right)\coth\left(\frac{h\nu\dagger}{2kT}\right) - 1\right] \qquad (5)$$

where $\nu\dagger$ is the frequency of the two vibrational modes perpendicular to the migration path in the activated state. If $\nu_s = \nu\dagger$, the bracketed term in expression (5) is always positive. However, for hydrogen in nickel, Ebusizaki *et al.*[10] have measured $\nu\dagger/\nu_s = 1{\cdot}7$. In this case, the bracketed term is negative and expression (5) adds ~ 1 kcal/mole to the right hand side of equation (4). This correction is approximately 10 per cent of the energy of migration. Since the correction term of expression (5) may be either positive or negative and since it appears to be small compared to the remaining terms in equation (4), it has been neglected here. The treatment of diffusional migration energy is thus similar to that used by Burton and Jura[16] and Huntington [17].

(d) *Potential energy of hydrogen in the bulk metal*

The potential energies V_s and V_d are obtained by summing the interaction potential between the hydrogen atom and a metal atom over all metal atoms in the lattice. To simplify this procedure, the infinite sum is approximated by a finite sum over ~40 individual metal atoms closest to the hydrogen atom and an integral representing the interaction with the metal atoms at larger distances. The sums are accomplished by dividing the nearby metal atoms into spherical shells in which the metal atoms are equidistant from the central hydrogen atom.

The characteristics of these shells for the two interstitial sites in the two cubic lattices considered are shown in Table 2. The cut-off distance is chosen midway between the last shell of atoms included in the sum and the next shell further out. Beyond the cut-off distance, the central hydrogen is considered to interact with a continuum of atom density equal to that of the undisturbed solid. In seeking the maximum energy configuration, shells 1 and 2 are permitted to relax radially by factors of q_1 and q_2 respectively. The potential energy of the hydrogen atom in the interstitial site is:

$$V = \sum_{i=1}^{N} n_i \phi_{H-M}(q_i r_i^0) + 4\pi\gamma \int_{r_c}^{\infty} r^2 \phi_{H-M}(r)\,dr. \qquad (6)$$

In this formula, V refers either to V_s of equation (2) or V_d of equation (4). N is the number of shells over which the sum is carried ($N = 6$ for b.c.c. and 3 or 4 for f.c.c.), and n_i is the number of atoms in shell i. r_i^0 is the hydrogen–metal distance of an atom in unrelaxed shell i, shown in the last column of Table 2. q_i is zero for $i > 2$. The function ϕ_{H-M} is the Morse potential of equation (1). The last term in equation (6) represents the contribution of the continuum atom distribution at distances greater than the cut-off r_c to the total interaction energy. γ is the number of atoms in the unit cell of the metal (2 for b.c.c., 4 for f.c.c.).

(e) *Potential energy of hydrogen on the surface*

The potential energy of a hydrogen atom at

Table 2. Shells for computing lattice sums for dissolved hydrogen

Interstitial site	Shell number	Number of atoms in shell	4 times the H-metal distance in units of the lattice constant (unrelaxed)*
b.c.c.-octahedral	1	2	$\sqrt{4}$
	2	4	$\sqrt{8}$
	3	8	$\sqrt{20}$
	4	8	$\sqrt{24}$
	5	10	$\sqrt{36}$
	6	8	$\sqrt{40}$
	cut-off	—	$\sqrt{46}$
b.c.c.-tetrahedral	1	4	$\sqrt{5}$
	2	4	$\sqrt{13}$
	3	8	$\sqrt{21}$
	4	12	$\sqrt{29}$
	5	4	$\sqrt{37}$
	6	12	$\sqrt{45}$
	cut-off	—	$\sqrt{49}$
f.c.c.-octahedral	1	6	$\sqrt{4}$
	2	8	$\sqrt{12}$
	3	24	$\sqrt{20}$
	cut-off	—	$\sqrt{28}$
f.c.c.-tetrahedral	1	4	$\sqrt{3}$
	2	12	$\sqrt{11}$
	3	12	$\sqrt{19}$
	4	16	$\sqrt{27}$
	cut-off	—	$\sqrt{31}$

*The ratio of the distance of closest approach to the lattice constant is $\sqrt{3}/2$ for the b.c.c. lattice and $1/\sqrt{2}$ for the f.c.c. lattice.

a distance z over a particular surface site is determined by a sum over hemispherical shells of equidistant metal atoms plus a continuum contribution:

$$V_a(z) = \sum_{l=1}^{N} n_l \phi_{H-M}(r_l) + 2\pi\gamma \int_{r_c}^{\infty} r^2 \mathrm{d}r \int_0^{0} \times \phi_{H-M}[(z^2 + r^2 - 2rz\mu)^{1/2}]\mathrm{d}\mu. \quad (7)$$

The origin of the spherical coordinate system used in the integration is directly beneath the adsorbed atom on the surface plane which would exist in the absence of separation of the outer most layer of metal atoms. z is the distance of the adatom above this plane; r is the radial distance from the origin to a point in the continuum and μ is the cosine of the polar angle referred to the axis perpendicular to the surface and passing through the origin. The number of shells over which the sum is carried is chosen to give a cut-off radius r_c as close as possible to that used in the computation of the inter-action energy in the bulk. In general, the first term on the right of equation (7) includes one half as many metal atoms (~ 20) as the corresponding internal sum. Because of the lower degree of symmetry of the lattice below a hydrogen atom on the surface compared to a centrally placed hydrogen atom in an interstitial site, a larger number of shells are required. For the b.c.c. (100) and (110) surfaces and the f.c.c. (110) surface, the shells were structured in accord with Figs. 1 and 2 of Goodman's paper[4]. There are two potential adsorption sites in the f.c.c. (111) face. The adatom nestles in the crevice formed by three surface metal atoms. However, there may or may not be a metal atom directly beneath the adsorbed atom (these two situations are depicted as the B and C sites in Fig. 27(a) of Ref. [18]. Our calculations indicate only a few per cent difference in the binding energy on these two sites with the 'C' site (no metal atom directly below the adsorbed hydrogen) slightly more tightly bound. This site was taken as the adsorption site.

The foregoing considerations refer to the perfect crystal surface. To these calculations were added the separation of the entire outer layer of metal atoms from the bulk and the relaxation of the metal atoms close to the adsorbed hydrogen atom. The configurations of the surfaces for the four cases considered is shown in Fig. 2. On the b.c.c. (100) surface, the metal atom directly beneath the adatom is permitted to move vertically and the nearest neighbor metal atoms on the surface may relax radially and vertically. On the b.c.c. (110) surface, only radial and vertical relaxation of the nearest neighbor atoms on the surface is allowed. Relaxation of the f.c.c. (110) surface is equivalent to that on the b.c.c. (100) face. The three surface atoms closest to the adsorbed hydrogen atom on the f.c.c. (111) adsorption site relax radially and vertically. The three atoms in the next layer may relax in a radial direction only. These relatively restricted degrees of relaxations were designed to keep the calculations tractable yet still provide a qualitative estimate of the significance of surface reconstruction.

The shell distances r_i in equation (7) are functions of the hydrogen adsorption distance z. If the atoms considered are subject to relaxation or if the shell contains surface metal atoms, r_i also depends on the outer layer spacing P and the relaxation parameters s_1, s_2 and s_3.

(f) *Lattice relaxation energies*

The energy required for lattice relaxation about a hydrogen atom in the solution site or in the activated site (ΔE_s or ΔE_d) is a function of the relaxation the nearest and next-nearest neighbor shells surrounding the hydrogen atom (q_1 and q_2) and the Morse potential force constants for the metal–metal interaction. Following Burton and Jura[19], only radial relaxation is allowed.

The interaction energy between the N shells in which discrete atom positions are considered and between the discrete atom shells

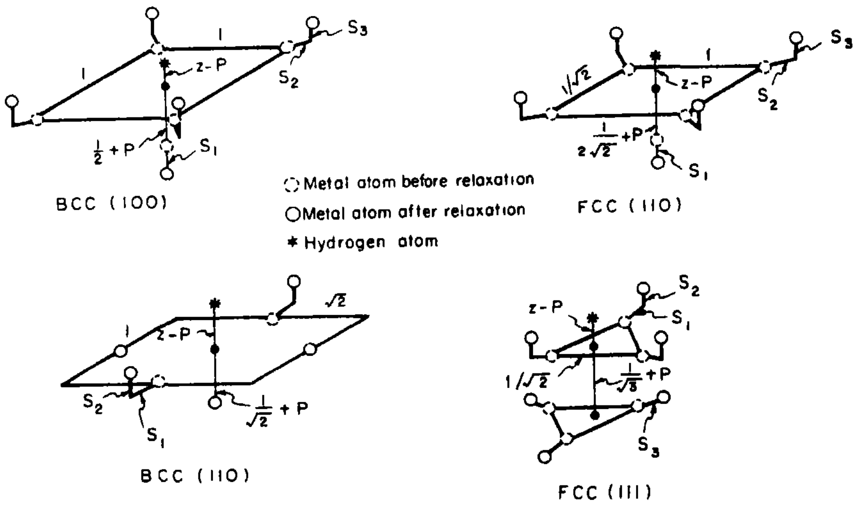

Fig. 2. Surface configurations after adsorption (distances in units of the lattice constant).

and the continuum is:

$$E_s(q_1, q_2) = \sum_{i=1,\neq 2}^{N} E_{1i}(q_1) + E_{12}(q_1, q_2)$$

$$+ E_{1c}(q_1) + \sum_{i=2}^{N} E_{2i}(q_2) + E_{2c}(q_2). \quad (8)$$

Interactions between atoms whose positions do not change during the relaxation process are not included in equation (8) since these cancel out in computing ΔE_s.

E_{ji} is the interaction energy between atoms in shells i and j and is given by:

$$E_{ji} = \sum \phi_{M-M}(r_{ij}), \quad (j = 1, 2) \quad (9)$$

where the summation runs over all bonds between atoms in shell i and shell j. For the self-energy of a single shell containing n_i atoms, there are $\frac{1}{2}n_i(n_i - 1)$ bonds. Between two different shells, there are $n_i n_j$ bonds. r_{ij} is the distance between a pair of atoms in the i and j shells, and is a function of the relaxation parameters q_1 and/or q_2. The Morse potential function in equation (9) utilizes the force constants appropriate to the metal under consideration (Table 1).

E_{1c} and E_{2c} denote the interaction energy between shells 1 and 2 and the continuum beginning at the cut-off distance r_c. The energy of interaction between shell j containing n_j atoms at a distance $q_j r_j^0$ from the hydrogen atom and the continuum is:

$$E_{jc}(q_j) = 2\pi\gamma n_j \int_{r_c}^{\infty} r^2 \mathrm{d}r^2 \int_{-1}^{1} \phi_{M-M}[\{(q_j r_j^0)^2$$

$$+ r^2 - 2r(q_j r_j^0)\mu\}^{1/2}]\mathrm{d}\mu, \quad (j = 1, 2)$$

$$(10)$$

where ϕ_{M-M} is again the metal–metal potential function, r_j^0 and r_c are taken from the last column of Table 2 and μ is the cosine of the polar angle in the spherical coordinate system with the origin at the hydrogen atom.

The suitability of this method for determining relaxation energies was tested by computing the energy of sublimation of the perfect metal lattice. In this test, the shells were constructed around a central metal atom and the sublimation energy computed by:

$$\Delta E_{\text{sub}} = -\frac{1}{2}\left\{\sum_{i=1}^{N} n_i \phi_{M-M}(r_i)\right.$$

$$\left. + 4\pi\gamma \int_{r_c}^{\infty} r^2 \phi_{M-M}(r)\mathrm{d}r\right\} \quad (11)$$

where n_i and r_i are the number of atoms in the ith shell and the distance of this shell from the central atom respectively. These parameters were taken from the compilation of Ref. [20]. The cut-off distance was taken mid-way between the Nth and the $(N+1)$th shells. For $N = 8$, the computed sublimation energy was within a fraction of a per cent of the value used by Girifalco and Weizer[2] to determine the force constants shown in Table 1. For $N = 4$, the number of discrete atoms considered in the lattice sum was ~ 40, as in the hydrogen–metal calculations. In this case, the computed sublimation energy was within 3–4 per cent of the correct value. This magnitude of error introduced by the continuum approximation to the lattice sum is considered acceptable for the calculations here.

Thus, for specified values of the first and second shell relaxation factors, the increase in the energy of the metal lattice surrounding the hydrogen atom is given by:

$$\Delta E_s = E_s(q_1, q_2) - E_s(1, 1). \quad (12)$$

The energy required to reconstruct the surface, ΔE_a, is computed in an entirely analogous fashion, with the surface relaxation parameters s_1, s_2 and s_3 replacing q_1 and q_2.

(g) *Vibration frequencies*

The vibration frequency of the interstitial hydrogen atom is determined by averaging out the angular dependence of the interaction energy between the hydrogen atom slightly displaced from its equilibrium position and the metal atoms in the N surrounding shells. This procedure forces the potential well to be spherically symmetric. The angle averaged potential between a hydrogen atom at a distance ρ from its equilibrium position and one of the atoms of shell i at a distance $q_i r_i^0$ from the center of the cell is given by:

$$\bar{\phi}_i(\rho) = \frac{1}{2}\int_{-1}^{1} \phi_{H-M}[\{\rho^2 + (q_i r_i^0)^2 - 2\rho(q_i r_i^0)\mu\}^{1/2}]\mathrm{d}\mu. \qquad (13)$$

The total potential energy of the hydrogen atom in the off center position is:

$$V(\rho) = \sum_{i=1}^{N} n_i \bar{\phi}_{i-(\rho)}(\rho) + 2\pi\gamma \int_{r_c}^{\infty} r^2 \mathrm{d}r^2 \int_{-1}^{1} \phi_{H-M}[(\rho^2 + r^2 - 2\rho r\mu)^{1/2}]\mathrm{d}\mu. \qquad (14)$$

The energies computed by equation (14) fit the parabolic form:

$$V(\rho) - V(0) = \tfrac{1}{2}\kappa_s \rho^2 \qquad (15)$$

to within a few per cent for displacements up to $\frac{1}{8}$ of a lattice parameter. The vibration frequency was determined from the value of κ_s obtained by fitting $V(\rho)$ according to equation (15):

$$\nu_s = \frac{1}{2\pi}\left(\frac{\kappa_s}{m}\right)^{1/2} \qquad (16)$$

where m is the mass of the hydrogen atom.

The frequency of perpendicular vibration of an adsorbed hydrogen atom, ν_a, was determined by fitting $V_a(z)$ of equation (7) to a parabola about the equilibrium adsorption distance z_{eq}.

(h) *Determination of the force constants*

The problem contains the following unknowns:

(a) The force constants m, r_e and D of the hydrogen–metal Morse potential function.

(b) The bulk relaxation parameters q_{1s} and q_{2s} for the solution site and q_{1d} and q_{2d} for the activated site.

(c) The equilibrium adsorption distance z_{eq}.

(d) The surface relaxation parameters s_1, s_2 and s_3.

Sufficient equations to determine these parameters are obtained by using equations (2–4) and the requirement that at equilibrium, the interaction energies must be a maximum. Applying the latter condition to the heat of solution expressed by equation (2) yields:

$$\frac{\partial V_s}{\partial q_{js}} + \frac{\partial \Delta E_s}{\partial q_{js}} = 0, \quad (j = 1, 2). \qquad (17)$$

Since the zero point energy term in equation (2) is small compared to the other terms, its variation with the relaxation parameters is neglected.

For the activated site the equilibrium condition is:

$$\frac{\partial V_d}{\partial q_{jd}} + \frac{\partial \Delta E_d}{\partial q_{jd}} = 0, \quad (j = 1, 2). \qquad (18)$$

The surface binding energy is maximized with respect to the adsorption distance:

$$\frac{\partial V_a}{\partial z} = 0 \quad \text{at} \quad z = z_{eq}. \qquad (19)$$

In obtaining this equation from equation (3) the effect of the relaxation energy of the lattice, ΔE_a, and the zero point energy, $\frac{1}{2}h\nu_a$, both of which are small compared to $V_a(z)$, have been neglected.

The surface binding energy is maximized with respect to the surface relaxation parameters:

$$\frac{\partial V_a}{\partial s_i} + \frac{\partial \Delta E_a}{\partial s_i} = 0, \quad (i = 1, 2, 3). \qquad (20)$$

Equations (2–4) and (17–20) constitute a set of 11 algebraic equations to be solved for 11 unknowns. The solution was effected numerically on a digital computer. Each of the metals in Table 1 was investigated. In each case, solution was attempted for the octahedral solution site-tetrahedral activated site and the reverse situation. For a specified metal and a particular solution site, two adsorption planes were considered. These planes are shown in Fig. 2 for the two lattice types.

3. RESULTS

(a) *Force constants*

Solutions were obtainable only for the combination of an octahedral solution site and a tetrahedral activated site. In no case did the *a priori* choice of the tetrahedral solution site yield a set of force constants which could reproduce the input interaction energies of Table 1. The results of the computations for the octahedral solution site are shown in Table 3.

Except for tantalum, solutions were obtained for both of the low index surface planes considered as adsorption sites in each of the cubic structures. The choice of adsorption plane had a minor effect on the computed force constants.

Again excepting tantalum, the hydrogen–metal interaction potentials are longer range $[(r_e)_{H-M} > (r_e)_{M-M}]$ and broader $(m_{M-H} < m_{M-M})$ than the host metal interaction parameters (compare Tables 1 and 3). Figure 3 illustrates the Fe-*H* Morse potential and the Fe–Fe potential taken from Ref. [2], as well as the positions of the first six shells of equidistant atoms surrounding the central atom. It can be seen that the first two shells of the Fe–*H* interaction are repulsive rather than attractive. Qualitatively, the reason for this behavior lies in the relative magnitude of the heats of solution and adsorption and the assumption that the metal–hydrogen forces in the bulk and on the surface are of the same type. Table 1 shows that in all cases the heat of solution is smaller than the hydrogen binding energy on the surface. Yet in the bulk, the hydrogen atom is surrounded by an infinite sea of metal atoms, while on the surface only a semi-infinite volume of metal atoms are available to bind the hydrogen. The only way that surface binding can be stronger than bulk binding when there are only half as many atoms with which to interact is for a substantial part of the bulk interaction to be non-binding (i.e. repulsive). Although the hydrogen–metal distances in an interstitial site are fixed by the lattice geometry (excluding relaxation for the moment), the surface hydrogen atom need only move away from the surface to escape the repulsive interaction characteristic of the interatomic distances separating the dissolved hydrogen atom and the first two interior shells. In the Fe–*H* case, the repulsive component of the first two shells is just cancelled by the attraction of the next four shells, and

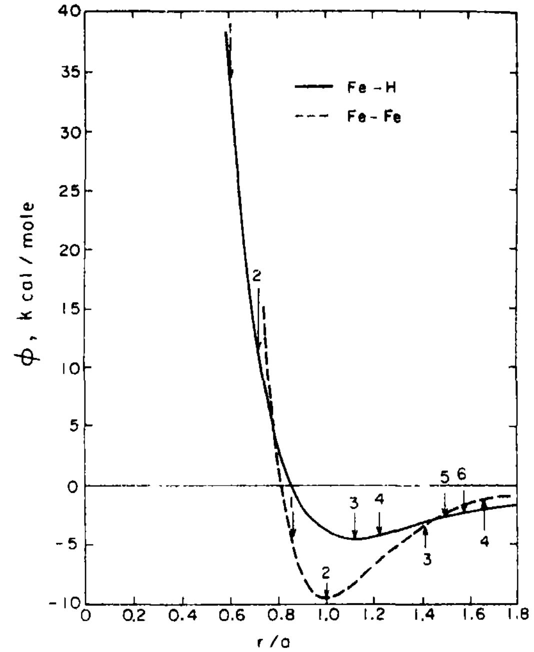

Fig. 3 The iron–iron interaction potential[2] and the hydrogen–iron interaction potential. Positions of shells surrounding central atom are marked. The shell positions in the Fe–*H* system are for the octahedral site. Shells 1 and 2 of the Fe–*H* system are in the relaxed configuration

Table 3. *Results – Octahedral solution site* (*all energies in kcal/mole*)

Metal	*H*-metal force constants			Internal relaxation						Surface relaxation						
				Octahedral site			Tetrahedral site									
	r_e/a	m	D	q_1	q_2	ΔE_s	q_1	q_2	ΔE_d	s_1	s_2	s_3	ΔE_a	$\frac{3}{2}h\nu_s$	$\frac{1}{2}h\nu_a$	z_{eq}/a
Fe(100)	1·12	2·96	4·6	1·199	1·019	33·8	1·118	0·999	34·3	−0·002	0·008	−0·020	1·4	6·0	1·1	0·58
Fe(110)	1·17	2·93	4·3	1·206	1·022	37·1	1·124	0·999	37·8	0·015	−0·087	—	2·7	5·8	1·2	0·73
Ta(110)	0·75	3·94	17·0	1·191	0·971	48·9	1·087	0·990	44·0	0·014	−0·044	—	2·8	10·9	1·9	0·45
Ni(110)	1·31	2·74	1·4	1·037	1·005	7·8	1·058	1·007	9·9	0·005	0·005	−0·019	0·8	3·4	0·8	0·64
Ni(111)	1·35	2·75	1·4	1·040	1·006	8·9	1·061	1·008	10·9	0·000	−0·004	0·000	0·2	3·4	0·8	0·80
Cu(110)	1·26	2·76	1·4	1·042	1·005	7·9	1·066	1·007	10·0	0·006	0·005	−0·021	0·8	3·2	0·7	0·62
Cu(111)	1·29	2·76	1·4	1·045	1·006	9·1	1·070	1·008	11·4	0·000	−0·005	0·000	0·2	3·3	0·8	0·78

the entire heat of solution is due to interaction of the hydrogen atom with the continuum of metal atoms beyond the cut-off distance.

Since the pairwise model used here results in interaction forces of quite long range, it is easy to see why hydrogen in the octahedral site is more stable than in the tetrahedral site. In the f.c.c. lattice, the nearest neighbors to a hydrogen atom in a tetrahedral site are significantly closer to the hydrogen atom than in the octahedral configuration. Consequently, the first shells are even more strongly repulsive in the tetrahedral case than in the octahedral case. The situation is not so clear cut in the b.c.c. lattice. In the unrelaxed configuration, the two metal atoms constituting the first shell of the b.c.c. octahedral interstice are closer to the central hydrogen atom than are the four metal atoms of the first shell of the tetrahedral site. However, the relaxation of the octahedral first shell is considerably greater than that of the tetrahedral first shell (since there are only two atoms in the former and four in the latter). The net result is that in the b.c.c. lattice, the first two shells of the octahedral site are somewhat less repulsive in nature than the first two shells of the tetrahedral site. Consequently, the binding energy is greater in the octahedral site.

Although Table 3 indicates that the computed force constants are relatively insensitive to the adsorption face, the effect of lattice type is very marked. The heats of solution and adsorption of the hydrogen-iron and hydrogen-nickel systems are very close, which suggests similar H-metal interaction potentials (the difference between the bulk migration energies is in the direction expected from the geometrical considerations discussed in the preceding paragraph). Yet Table 3 shows a distinct difference in the shapes of the Fe–H and Ni–H potential functions. The latter is even longer range and broader than the Fe–H potential. Because of this difference, and because of the closer packing of the f.c.c. lattice compared to the b.c.c. structure, the hydrogen atom in the nickel interstitial site interacts with many more metal atoms than in iron. Consequently, to give roughly the same binding energies, the bond energy, D, is appreciably less for the Ni–H interaction than the Fe–H interaction. This exaggerated influence of the crystal structure (which is even more dramatically illustrated by the computed difference in solubility of hydrogen in α and γ iron) is a defect in the pairwise model applied to such systems. From the previous arguments, this effect of structure would probably remain if other forms of the potential function were used.

It is a general feature of the model that the larger the bulk migration energy, the shorter range are the computed potentials. This is especially striking in comparing the Fe–H and Ta–H results. In the latter instance the equilibrium separation, r_e, is even smaller than that of the Ta–Ta potential function. However, because $\chi_a > \chi_s$ in the Ta–H system, the first shell surrounding the hydrogen atom in the octahedral site is still repulsive. In the f.c.c. lattice, the computed potentials are quite long range despite migration energies of ~ 9 kcal/mole. This is a reflection of the much smaller H–metal distance in the tetrahedral site than in the octahedral site for the f.c.c. of lattice compared to the b.c.c. lattice. Shorter range Ni–H or Cu–H forces would have required even larger migration energies.

(b) *Lattice relaxation*

Table 3 shows that the relaxation of the metal atoms in the octahedral site of the b.c.c. lattice is large; the first shell is displaced outward by ~ 20 per cent and the second shell contracts by 3 per cent in the case of tantalum and expands by 2 per cent in the case of iron. The relatively short range potential in the Ta–H system is similar to the potential employed for the Fe–C system by Johnson *et al.*[5], and the relaxations of the octahedral sites surrounding the impurity atom are also similar in magnitude. In addition, the relaxations of the first two shells of the octahedral site surrounding a dissolved carbon atom were found to be radially symmetric. In the Fe–*C*, Fe–*H* and Ta–*H* systems, the spherical configuration adjacent to the impurity atom is deformed into a prolate spheroid. Relaxation of the tetrahedral site in the present case is different from that in the carbon–iron analysis of Johnson *et al.*[5]. Although the maximum first shell tetrahedral relaxation of 11 per cent is of the same order of magnitude as that calculated for the hydrogen solute considered in this study, the Fe–*C* tetrahedral site relaxation was not of the purely radial displacement type. The effect of non-radial relaxation upon the Fe–*H* calculation was considered and found to be negligible (see Appendix).

Because of the longer range and greater width of the computed potentials in the f.c.c. systems considered here compared to the b.c.c. lattice, the forces on the nearest neighbors atoms are not as great in the former. Hence, the relaxation of the interstitial sites in the f.c.c. cases are less than in the b.c.c. systems.

Table 3 shows that the disruption of the surface by the adsorbed hydrogen is small. In all cases the surface atoms which are nearest neighbors to the adsorbed hydrogen atom are displaced radially outward and downward in the final configuration. When three degrees of relaxation are allowed, the displacements do not exceed 2 per cent of a lattice constant. The larger displacements in the b.c.c. (110) case are probably due to the fact that only two degrees of relaxation were allowed. The largest energy of surface relaxation is ~ 3 kcal/mole which is small compared to the adatom binding energy. Similarly, the zero point energy for adatom vibration perpendicular to the surface is small. The equilibrium adsorption distances are between $\frac{1}{2}$ and $\frac{3}{4}$ of a lattice constant. Although not shown in Table 3, sizeable variation of the first layer separation distance (*P* of Table 1) produced only minor changes in the computed force constants.

The zero point energy of vibration of the dissolved hydrogen constitutes ~ 15 per cent of the heat of solution for the b.c.c. metals and about 7 per cent for the f.c.c. metals.

4. COMPARISON WITH OTHER MEASUREMENTS

(a) *Activation energy for surface migration*

The measurement of interest here is the ratio of the activation energy for surface migration to the binding energy in the adsorption site, which is denoted by Q. This parameter has been determined by Gomer and co-workers to be 0·22 for hydrogen on tungsten[21] and 0·11 for hydrogen on nickel[22]. In calculating the surface migration energy from the potential functions, the migration sites were taken to be those utilized by Goodman[4]; for the f.c.c. (111) surface, the migration site was assumed to be the location midway over the line joining two surface metal atoms.

Because of the similarity of tantalum and tungsten and their very nearly equal hydrogen binding energies, the experimental *H*-*W* results may be compared to the *H*–Ta calculations. Only the (110) surface yielded a solution for the potential function in the *H*–Ta system. The Q value computed for this face of tantalum was 0·16, compared to the 0·22 experimental value for hydrogen on tungsten.

Although experimental measurements of Q are not available for the surface diffusion of hydrogen on iron, the calculations were performed for both the (100) and (110) faces. The corresponding Q values were 0·16 and 0·06 respectively. As expected, binding is much more uniform on the close packed (110) plane than on the rougher (100) plane, and the surface migration energy is lower on the former.

For f.c.c. nickel, the calculated Q value is 0·04 for the (100) face. This is significantly smaller than the experimental value of 0·11. However, the experimental observation of a lower value of Q for an f.c.c. crystal face compared to a b.c.c. surface is reflected in the calculations. The calculated binding energy on the migration site for the f.c.c. (111) face was negative by ~ 1 kcal/mole compared to the binding energy on the selected adsorption site. This means that the sites chosen as adsorption and migration positions should have been reversed. The energy difference between these two sites, however, is very slight (~ 2 per cent of the binding energy). The f.c.c. (111) surface is a good illustration of Ehrlich's description of a metal surface as one over which the hydrogen atom interacts continuously, with minor perturbations in the binding energy at adsorption sites[23].

The Q values for hydrogen on copper were essentially equal to those for hydrogen on nickel.

(b) *Effect of surface plane on the hydrogen binding energy*

It appears to be a general rule that binding of adatoms is weaker on close packed planes than on rougher ones[21]. In each of the cubic crystal systems investigated here, one of the two surfaces was the close packed plane (the (110) plane in the b.c.c. structure and the (111) plane in the f.c.c. lattice).

In the b.c.c. system, the difference between the binding energy of hydrogen on the (100) and (110) planes was 6 per cent of the binding energy for iron and 40 per cent for tantalum. On the b.c.c. (100) surface, the adatom can adjust its position above the surface to maximize the interaction energy with the four equidistant surface nearest neighbor metal atoms (see Fig. 2). On the b.c.c. (110) surface, however, the four surface metal atoms adjacent to the adsorbed atom are not equidistant from the latter. Consequently, the hydrogen–metal interaction cannot be optimized as efficiently as for the (100) surface, and binding is weaker on the (110) plane. As expected, the shorter range and narrower H–Ta interatomic potential accentuates this structural effect.

The effect of surface orientation is much less pronounced for the f.c.c. system than for the b.c.c. structure. The calculated hydrogen–metal forces are longer range and the substrate metal is more densely packed in the former. These two factors decrease the importance of the immediate environment of the adatom; a larger portion of the surface binding energy is due to the more distant atoms. The difference in the hydrogen binding energy on the (110) and (111) planes of the f.c.c. lattice is 3 per cent of the binding energy for both nickel and copper.

(c) *Vibration perpendicular to the surface*

Assuming that the adsorbed hydrogen atom behaves as a two-dimensional ideal gas, the rate constant for atom evaporation can be determined from the principle of detailed balancing[23]. The rate constant so calculated is inversely proportional to the partition function for adatom vibration perpendicular to the surface, which is:

$$j_\perp = \left[1 - \exp\left(-\frac{h\nu_a}{kT}\right)\right]^{-1}. \qquad (21)$$

Hickmott[24] has measured the rate of desorption of hydrogen atoms from tungsten. The experimental rate constant suggests a partition function $j_\perp \sim 1{\cdot}3$. Taking tantalum as a stand-in for tungsten and using the vibration frequency ν_a computed by the method described in Section 2(g), a value of $j_\perp$ of 1·2 is computed for a temperature of 1000°K. Both experiment and calculation suggest that on the refractory metals, the adsorbed hydrogen is very nearly in its ground vibrational state.

(d) *Pre-exponential factor in the solubility*

The Einstein oscillator model used to describe the behavior of hydrogen in an interstitial site in the metal forms the basis of the Fowler–Smithells solubility expression[25]:

$$\frac{c}{\sqrt{p_2}} = S_0 \exp\left(\frac{\chi_s - \frac{1}{2}D}{kT}\right) \qquad (22)$$

where c is the concentration of dissolved hydrogen in atoms/cm^3, p_2 is the pressure of molecular hydrogen gas in dynes/cm², and D is the dissociation energy of molecular hydrogen (103 kcal/mole).

The pre-exponential factor S_0 may be written as:

$$S_0 = \frac{\omega_g n_g j_g}{2^{3/4}(kTj_{2\mathrm{rot}})^{1/2}\lambda_1{}^{3/2}}\left(\frac{\lambda_1}{a}\right)^3 \qquad (23)$$

where $j_{2\mathrm{rot}}$ is the rotational partition function for molecular hydrogen gas, ω_g is the number of spin states available to the electron brought into the metal with the hydrogen atom and n_g is the number of solution sites per unit cell (12 and 6 for the b.c.c. tetrahedral and octahedral sites, respectively; 8 and 4 for the f.c.c. tetrahedral and octahedral sites, respectively). λ_1 is the thermal wave length of the hydrogen atom:

$$\lambda_1 = \frac{h}{\sqrt{2\pi mkT}} \qquad (24)$$

at $T = 1000°\mathrm{K}$, $\lambda_1 = 0{\cdot}55$ Å. j_g is the partition function of the dissolved hydrogen. For the Einstein oscillator model,

$$j_g = \left[1 - \exp\left(-\frac{h\nu_g}{kT}\right)\right]^{-3}. \qquad (25)$$

The internal vibration frequency, ν_g, is obtained by the methods of Section 2(g). The temperature dependent quantities in equation (23) were evaluated at 1000°K, which represents an average temperature of the solubility measurements. Table 4 compares the measured and calculated values of the pre-exponential factor S_0. The calculated values are all lower than the experimental ones. The discrepancies are probably due to the neglect of the excess entropy of mixing, which arises from the change in vibration frequency of the metal atoms adjacent to the dissolved continuum resulting from relaxation. Huntington *et al.* [26] have calculated an excess entropy of 0·8 k for a copper interstitial in copper; this provides a factor of ~ 2 increase in the pre-exponential factor of the solubility. Inclusion of the excess entropy in the hydrogen solubility expression of equation (23) undoubtedly would have driven the calculated values closer to the experimental ones.

Table 4. Pre-exponential factors in the solubility of hydrogen in metals

Metal	$S_0 \times 10^{-16}$, atoms/cm³/(dynes/cm²)$^{1/2}$ Calculated[a]	Experimental[b]
Fe	11	20 ± 2
Ta	4·8	4·9 ± 0·3
Ni	8	30 ± 3
Cu	8	40 ± 3

[a] These are average values for the two surface planes considered for each metal. The spin term in equation (23) was assumed to be unity.

[b] Taken from the compilation of Ref. [9] and FAST J. D., *Interaction of Metals and Gases*, Vol. I, Academic Press, New York (1965). The tantalum average also includes the measurement of Ref. [15]. The error indicates the spread among the sources used in obtaining the averages.

(e) *Internal vibration frequencies*

Comparison of the solubilities of hydrogen and deuterium in the same metal permits the internal vibration frequency of hydrogen in the metal to be determined[9]. Such experiments have been performed on nickel and copper; they yield values of the vibrational energy level spacing $h\nu_g$ of 2·7 and 3·1 kcal/mole for hydrogen in nickel and copper respectively[9]. The calculations here yield 2·3 and 2·2 kcal/mole respectively.

The calculated vibrational level spacings in the b.c.c. metals are significantly larger, being 3·9 and 7·2 kcal/mole for hydrogen in iron and tantalum, respectively. There are no directly comparable experimental values. Sakamoto[27] has measured the vibration frequency of hydrogen in the tetrahedral site of the face-centered tetragonal lattice of $TaH_{0{\cdot}7}$ by neutron diffraction. His result corresponds to an energy level spacing of 3·3 kcal/mole.

(f) *Hydrogen solubility in γ-iron*

The parameters of the hydrogen–iron Morse potential shown in Table 3 were determined from the b.c.c. structure of α-iron. This potential function was utilized to calculate the heat of solution of hydrogen in f.c.c. γ-iron. The octahedral site was assumed to be the solution site and an estimated value of the lattice constant of γ-iron at 300°K was utilized in order to keep the calculation on the same basis as that for α-iron. The calculated heat of solution is 56 kcal/mole. Experimentally, the heat of solution of hydrogen in γ-iron is essentially equal to the 45 kcal/mole value for α-iron[9]. The pairwise model calculation fails rather clearly on this point. This failure is more significant than, say, the five-fold difference between calculated and experimental solubilities in copper shown in Table 4. The prediction of the heat of solution in γ-iron involves only the potential function itself and is not obscured by unknown effects such as the excess entropy of solution which may account for some of the discrepancies in the figures in Table 4.

In the case of the disparity between the H–Fe and H–Ni potential functions discussed in Section 3, essentially similar binding energies yielded different potential functions. Here, the situation is one in which the same potential function yields significantly different binding energies for two different crystal structures of the same metal.

The heat of solution computed from equations (2) and (6) for a specified potential function is the difference between energy terms comparable in magnitude to the heat of solution itself. Such a calculation is quite sensitive to small errors in the computation of each term and to the input parameters. For example, a 1 per cent error in the estimated lattice constant of γ-iron produces a 2 kcal/mole change in the heat of solution.

The same sensitivity (and failure to obtain quantitative agreement) was observed by Johnson *et al.*[5] when their Fe–C potential function determined from the properties of carbon in α-iron was applied to predict the interaction energy of orthorhombic Fe_3C.

5. NEAREST NEIGHBOR INTERACTIONS ONLY

The results of Tamm and Schmidt[6] suggest that adsorbed hydrogen bonds only to adjacent metal atoms (on the (100) face of tungsten at least). To simulate this type of bonding (retaining the Morse potential function), the entire set of calculations were rerun with only nearest neighbor interactions permitted. In the bulk this amounted to restricting interactions to the first two shells of the b.c.c. octahedral site and the first shell of the other three interstices (see Table 2). On the surface, the hydrogen atom was permitted to interact only with the metal atoms shown in the sketches of Fig. 2 (except for the f.c.c. (111) face, where the three atoms in the second layer were replaced by a single atom directly beneath the adatom—the B site was used instead of the C site). All other aspects of the calculation were the same as in the case that hydrogen was permitted to interact with all surrounding atoms.

No solutions were found for the set of input hydrogen–metal interaction energies shown in Table 1. Bulk migration energies much larger than those shown in the last column of Table 1 would have been required to produce reasonable potential functions. The nearest-neighbor-only restraint renders the computation completely dependent upon the structure and distances of the metal atoms adjacent to the hydrogen atom. This extreme structural sensitivity is greatly mitigated by allowing longer range interactions, which was done in the original computations. The intermediate restraint employed by Johnson *et al.*[5] of forcing the potential to go to zero at some point between the second and third shells was not attempted.

6. CONCLUSIONS

The computational method of utilizing three parameters of the hydrogen–metal interaction to infer other characteristics of the system using the pairwise additive Morse potential function as a vehicle provides satisfactory qualitative results for b.c.c.

metals. It is an adequate interpolation technique for estimating some hard-to-measure features of the hydrogen–metal system. 'Fine-structure', such as the relative magnitude of the internal vibration frequencies in copper and nickel discussed in Section 6(e), is not faithfully reproduced. The method is excessively sensitive to the structure of the bulk crystal, and the results for f.c.c. crystals are discouraging. The adsorption face to which the surface binding energy is assumed to refer has little effect on the computed force constants.

The method is applicable only to dilute solutions. The pairing of hydrogen atoms in the metal, which has recently been shown to be important even at quite small hydrogen concentrations[28], is ignored. The actual state of dissolved hydrogen is not considered. Although hydrogen is believed to be ionized in metals[9], this fact affects the present calculations only in the rather inconsequential choice of the electron spin factor in equation (23). However, the long range of the potentials computed in this study (binding is due in large part to interaction of hydrogen with metal atoms many lattice constants distant) may be the manner that the pairwise model reflects coulombic forces between protons and the ion cores of a metal lattice.

The validity of the assumption that the nature of the binding on the surface is the same as that for dissolved hydrogen is not supported by experimental evidence. The fact that surface hydrogen binds more strongly to fewer atoms than does bulk hydrogen suggests that this assumption may need to be modified.

Given the qualitative nature of the entire procedure, some of the refinements employed in the calculations were, in hindsight, unnecessary. The zero point energies, the second shell internal relaxation, surface reconstruction and first layer surface separation all could have been omitted without markedly affecting the results.

The exclusive use of the Morse potential function to represent the energetics of the metal–hydrogen interaction does not permit explicit investigation of the effect of impurity introduction on the behavior of the electron gas in the metal. This aspect has received considerable attention in theoretical treatments of intrinsic point defects in metals [29, 30]. Application of a similar approach to hydrogen dissolution in metals was the subject of the review of Ebisuzaki and O'Keefe[9]. The status of these fundamental calculations, however, does not yet permit estimation of the types of properties which were the subject of the present paper.

However, long range electronic interactions are implicitly included in the Morse potential model in two ways: (a) Neglecting the free electron gas is partially compensated by requiring the force constants of the Morse function to be calculated from experimental energies of adsorption, solution, and bulk migration. (b) The attractive portion of the Morse function reflects the adhesive properties of the electrostatic terms. It was specifically to avoid a detailed consideration of the free electron effects that a potential with a repulsive *and* an attractive component was chosen.

REFERENCES

1. MOELWYN-HUGHES E. A., *Physical Chemistry*, 2nd Edition, MacMillan (1961).
2. GIRIFALCO L. A. and WEIZER V. G., *Phys. Rev.* **114**, 687 (1959).
3. PASTINE D. J., *J. appl. Phys.* **35**, 3407 (1964); NAUMANN R. J., NASA TN D-5892 (1970).
4. GOODMAN F. O., *Phys. Rev.* **164**, 1113 (1967).
5. JOHNSON R. A., DIENES G. J. and DAMASK A. C., *Acta. Metal.* **12**, 1215 (1964).
6. TAMM P. W. and SCHMIDT L. D., *J. chem. Phys.* **51**, 5352 (1969).
7. HOCH M., *Trans. AIME* **230**, 138 (1964).
8. BUCUR R. V. and CRISAN M., *J. Phys. Chem. Solids* **28**, 995 (1967).
9. EBISUZAKI Y. and O'KEEFE M., *Prog. Solid State Chem.* **4**, 187 (1967).
10. EBISUZAKI Y., KASS W. J. and O'KEEFE M., *J. chem. Phys.* **46**, 1373 (1967).
11. BESHERS D. N., in *Diffusion in Body-Centered Cubic Metals*, Amer. Soc. for Metals, p. 149 (1965).
12. BURTON J. J. and JURA G., *J. Phys. Chem.* **71**, 1937 (1967).
13. PEDERSEN B., KROGDEHL J. and STOKKELAND O. E., *J. chem. Phys.* **42**, 72 (1965).

14. CHANDLER W. T. and WALTER R. J., in *Refractory Metal Alloys*, (Edited by I. Machlin, R. T. Gegeley and E. D. Weisert), p. 197, Plenum Press (1968).
15. KLYACHKO I. A., KUNIN L. L., FEDOROV S. P. and LARIONOV I. N., *Akad. Nauk SSSR. Komissiia po Analiticheskoi Khimii. Trudy* **10**, 49 (1960). Also translated as UCRL-Trans-1375.
16. BURTON J. J. and JURA G., *J. Phys. Chem. Solids* **28**, 705 (1967).
17. HUNTINGTON H. B., *Phys. Rev.* **91**, 1092 (1953).
18. KITTEL C., *Introduction to Solid State Physics*, 3rd Edition, p. 29, John Wiley, New York (1967).
19. BURTON J. J. and JURA G., *J. Phys. Chem. Solids* **27**, 961 (1966).
20. HIRSCHFELDER J. O., CURTISS C. F. and BIRD R. B., *Molecular Theory of Gases and Liquids*, p. 1037, John Wiley, New York (1964).
21. GOMER R., WORTMAN R. and LUNDY R., *J. chem. Phys.* **26**, 1147 (1957).
22. WORTMAN R., GOMER R. and LUNDY R., *J. chem. Phys.* **27**, 1099 (1957).
23. EHRLICH G., *Transactions of the 8th Vacuum Symposium*, p. 126 Pergamon Press, New York (1962).
24. HICKMOTT T. W., *J. chem. Phys.* **32**, 810 (1960).
25. FOWLER R. H. and SMITHELLS C. J., *Proc R. Soc Lond.* **A160**, 37 (1937).
26. HUNTINGTON H. B., SHIRN G. A. and WAJDA E. S., *Phys. Rev* **99**, 1085 (1955).
27. SAKAMOTO M., *J. phys. Soc. Japan* **19**, 1862 (1964).
28. MCQUILLAN A. D., *J. chem. Phys.* **53**, (1970).
29. HUNTINGTON H. B. and SEITZ F., *Phys Rev.* **61**, 315 (1942).
30. TEWORDT L., *Phys. Rev.* **109**, 61 (1958).

APPENDIX

Effect of non-radial relaxation on lattice energies

Had complete freedom of motion of the metal atoms surrounding the hydrogen atom been permitted, the lattice distortion energy would have been smaller than that calculated by restricting relaxation to the radial direction only. The distortion of the f.c.c. lattices in the Cu-*H* and Ni-*H* systems studied here was so small that even appreciable nonradial distortion would not have affected the computed force constants. The relaxation of the first two shells of the octahedral side in the Fe-C system[5] was found to be exclusively radial. Consequently, the effect of non-radial relaxation about a hydrogen impurity was investigated only for the tetrahedral site of the b.c.c. lattice. Only the first shell was considered, since second shell relaxation was very small.

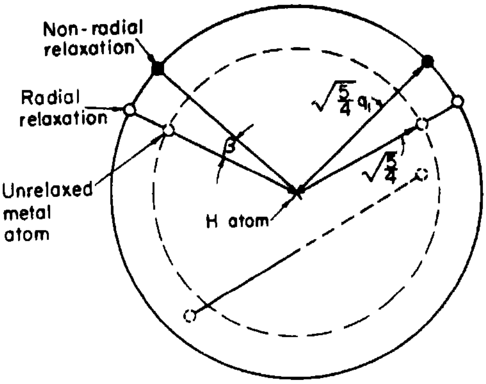

Fig. 4. Relaxation of the first shell around the tetrahedral site of the b.c.c. lattice.

The analysis of Johnson *et al.* [5] showed that the relaxation of the atoms in the first shell of the tetrahedral site occurred in the plane formed by the central impurity atom and two metal atoms of the surrounding tetrahedron (see Fig. 4). This type of distortion may be described by the radial component q_1 and the angle β denoting the non-radial component of the distortion. In the Fe-*C* system, the deviation from purely radial relaxation was $\beta = -1{\cdot}16°$ [5]. The Fe-*H* calculations were modified to permit this type of non-radial relaxation With q_1 fixed at 1·121 (the average of the Fe values for the tetrahedral site in Table 3), the minimum occurred at $\beta = -0{\cdot}4°$ and the lattice energy ΔE_s was 0·2 kcal/mole less than the value $\beta = 0$ (pure radial relaxation). An energy difference of this magnitude is well within the accuracy of the measured heats of solution or the migration energy. Consequently, the neglect of non-radial lattice distortion about the dissolved hydrogen atom is justified.

J. Phys. Chem. Solids, 1971, Vol. 32, pp. 2517–2528. Pergamon Press. Printed in Great Britain

CHARGE-TRANSFER LUMINESCENCE OF Cr^{3+} IN MAGNESIUM OXIDE

C.-C. CHAO*

Department of Chemistry, University of Minnesota, Minneapolis, Minn. 55455, U.S.A.

(*Received* 13 *October* 1970; *in revised form* 22 *February* 1971)

Abstract—Cr^{3+} impurity ions have been positively identified as one of the activators contributing to the thermoluminescence in MgO. It has been found that in undoped MgO crystals the major mechanism for Cr^{3+} X-ray fluorescence is a reaction between free holes and Cr^{2+} ions, i.e.

$$\text{Free hole} + Cr^{2+} \rightarrow Cr^{3+*}$$
$$Cr^{3+*} \rightarrow Cr^{3+} + h\nu.$$

The same mechanism produces the Cr^{3+} thermoluminescence in MgO. The free holes in thermoluminescence come from the destruction of V_1 centers. The destruction of V_1 centers is the rate determining step for the thermoluminescence and it follows first order kinetics. The activation energy of the thermoluminescence is $0{\cdot}80 \pm 0{\cdot}02$ eV.

1. INTRODUCTION

IT IS known that u.v. or x-irradiated, nominally pure MgO crystals give rise to a red thermoluminescence emission near 370°K. Several authors have characterized this thermoluminescence with various studies[1–7] but no direct identification was made. In this paper one of the components is identified by directly comparing the thermoluminescence spectrum with the high temperature Cr^{3+} fluorescence spectrum of the same crystal excited by visible light. The solid state reaction which is responsible for this thermoluminescence was determined by observing the effect of crystal treatment on the thermoluminescence, by monitoring the change in concentration of impurities and defect center at various stage of treatment and by analyzing the glow curve of the thermoluminescence.

This paper also includes evidence that in a nominally pure MgO crystal the major process responsible for Cr^{3+} X-ray fluorescence as well as the Cr^{3+} thermoluminescence is the reaction of a Cr^{2+} center with a hole.

The background knowledge needed for this study is readily at hand. The fluorescence spectrum of Cr^{3+} in MgO was first studied by Deutschbein[8], then extensively by Schawlow and his associates[9–13] and by Glass[14]. Most substitutional Cr^{3+} impurity ions in MgO exist in an octahedral symmetry. A fraction of Cr^{3+} ions associated with a next nearest neighbour cation vacancy ($Cr^{3+}O^{=}\square$, center) and some of the Cr^{3+} ions form doubly associated Cr^{3+} pairs ($Cr^{3+}O^{=}\square O^{=}Cr^{3+}$, T' center). The letter T is used to imply the tetragonal symmetry.

The octahedral Cr^{3+} ions can be excited to various low-lying excited states, but the ions relax rapidly to metastable ^2E state, and then emit a photon, returning to the $^4A_2$ ground state. At 77°K the sharp zero phonon line occurs at 698·1 nm (R line), and it has vibrational side bands near 712, 720 and 725 nm. The major absorption bands of Cr^{3+} are also its major fluorescence excitation bands. The lowest lying band is at 620 nm. In tetragonal symmetry the ground state $^4A_2$ and the ^2E state of Cr^{3+} are split into two levels. The splitting of the $^4A_2$ state is very small[15] and cannot be resolved in the fluorescence spectrum;

---

*Present Address: Department of Chemistry, Texas A&M University, College Station, Texas 77843, U.S.A.

therefore, the zero phonon line of Cr^{3+} splits into two lines (N lines). The T centers emit at 699·2 and 703·8 nm with vibrational side bands near 720, 726 and 732 nm. The T' centers emit at 698·9 and 703·4 nm with vibrational side bands near 720, 726 and 732 nm (13). Both T and T' centers have a fluorescence excitation band at 610 nm, which overlaps very much with the excitation band of the Cr^{3+} R line.

There are many different defect centers existing in nominally pure MgO crystals[16]. Most metal impurity ions either have an ionic radius considerably different to that of Mg^{2+} and thus precipitate out along dislocation lines and subgrain boundaries, or they cannot change their valence. In the events induced by ionizing irradiation, the transition metal ions of the iron group, and the intrinsic centers play the most important roles. Transition metal ions and most intrinsic centers are paramagnetic, hence, their concentration change can be monitored by ESR measurements. The centers which are of interest in this study all have been characterized by ESR. The ESR spectrum of Cr^{3+} centers in MgO were studied by Low[17] Wertz and Auzins[18–21]. The V_1 center, that is a hole trapped by a cation vacancy, was studied by Wertz and his associates[22, 23].

2. EXPERIMENTAL PROCEDURE

2.1 *Optical measurements*

For stimulating X-ray fluorescence, a G.E. CA7 Coolidge copper-target X-ray tube was used. It was usually operated at 40 kV and 18 mA. Cr^{3+} fluorescence was also excited by visible light. The light source was a Sylvania DWY 650 W tungsten–iodine lamp. After passing through a water filter to remove the i.r. component, the light was focused upon the entrance slit of a 0·25 meter Ebert monochromater made by Jarrell Ash. The exit beam of the monochromater was focused onto the sample. The exciting light band was centered at 620 nm and has a band width of 50 nm.

The crystals were mounted on the tail piece of an optical dewar. For taking low temperature fluorescence spectra, the dewar was filled with liquid nitrogen; for taking high temperature fluorescence spectra, the dewar was filled with ethylene glycol and heated by an immersion heater. The dewar was equipped with three suprasil windows and one aluminum foil window oriented at 90° to one another.

A Spex 1700-2 0·75 meter monochromater was used for spectroscopic analysis. The signal was detected by an EMI 9558Q photomultiplier.

The heated dewar was also used to heat up an x or u.v.-irradiated crystal to generate thermoluminescence for taking a thermoluminescence spectrum. For measuring the activation energy of the thermoluminescence, the Spex monochromater was set at 698·5 nm. The out-put of thermoluminescence at that wave length was monitored while the irradiated sample was heated up hyperbolically ($\mathrm{d}T/\mathrm{d}t = \beta_0 T^2$, T is temperature, t is time, β_0 is a proportional constant.) The hyperbolic heating apparatus was built according to Halperin's design[24].

All intensity measurements of fluorescence were made at 77°K. Since the irradiation induces changes in all samples, no standard can be used for X-ray fluorescence. For fluorescence excited by 620 nm light, an untreated nominally pure MgO crystal was mounted on the other side of the tail of the optical dewar, and the 698·1 nm line of this sample was used as a standard to calibrate the possible out-put change of the tungsten–iodine lamp.

2.2 *ESR measurements*

The concentration of Cr^{3+} and V_1 centers at various stages of treatment was monitored by ESR measurements. Two spectrometers were used. Most room temperature measurements were made in a reflection cavity homodyne type spectrometer with its klystron locked to the sample cavity. This spectrometer had a TE$_{104}$ rectangular dual sample cavity. A sample and a standard can be measured simultaneously in this cavity. The low temperature measurements were made in another reflection cavity homodyne type spectrometer which has a by-pass arm and balanced mixer. This spectrometer had a cylindrical TE_{111} cavity. The sample and standard were put in a sample holder and inserted along the wall of the cylinder.

For determination of spin number, the signal intensity of a particular center in the unknown was compared with the signal intensity of Cr^{3+} in a piece of ruby crystal. The Cr^{3+} content of the ruby crystal was, in turn, calibrated against $CuSO_4 \cdot 5H_2O$ and DPPH.

2.3 *Samples and sample treatments*

The single crystal MgO samples were obtained from W & C Spicer Limited, Muscle Shoals Electro Chemical Corp. and the Norton Company. Those crystals which were low in all other impurity ions but Cr^{3+} were classified as group *A*. The remaining crystals were called group *B*.

The crystals were treated cyclicly: *x* or u.v. irradiated at room temperature, then heated up to release the thermoluminescence. The X-ray treatments were done by a Machlett Thermax tube which was usually operated at 70 kV and 12 mA; the u.v. irradiations were made with an HP 290 Westinghouse sterilamp. The output of this lamp was largely the 253·7 nm mercury line. The crystals were put at about 1 cm away from the irradiation source. For heating, the sample crystal was placed in a test tube which was immersed in ethylene glycol or on a hot plate which was kept at 400°C. The point of termination of thermoluminescence was monitored by eyes.

Some of the crystals were heat-treated in drastic reducing atmospheres such as H_2 and Mg vapor. The hydrogen firing was done with an induction heater. The susceptor was a high purity graphite crucible. The upper part of it was recessed to accommodate an MgO crystal. Since at high temperature MgO started to sublime, the sample crystal was enclosed by a MgO box to preserve the optical quality of the surface. The MgO box in turn was placed in the cavity of the graphite crucible. The pressure of H_2 at room temperature was 85 torr. The temperature of the graphite cyclinder was monitored by an optical pyrometer. The treatments were carried out near 1200°C. The furnace for magnesium vapor treatment was built according to Hensley's design[25]. The treatments were carried out under Mg vapor of several atmospheric pressure with the sample near 2000°C.

3. RESULTS

3.1 *Spectra of luminescence*

Figure 1 is a Cr^{3+} fluorescence spectrum taken at 363°K. The spectrum was produced by exciting a Cr^{3+} rich but undoped MgO crystal with 620 mm light.

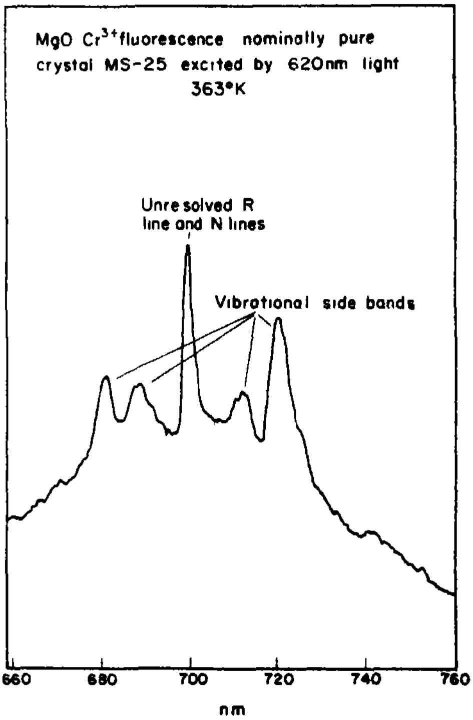

Fig. 1. Fluorescence spectrum of Cr^{3+} centers in MgO excited by 620 nm light at 363°K (Crystal MS-25).

The spectra of red thermoluminescence of most nominally pure MgO crystals looks like the one shown in Fig. 2. It is composed of emission lines which are due to Cr^{3+} centers and a broad band centered at 720 nm. Figure 3 is a red thermoluminescence spectrum of a nominally pure crystal which is rich in chromium and relatively free of manganese impurity ions. The spectrum is almost identical to the one that is presented in Fig. 1.

3.2 *Intensity variation of* Cr^{3+} *X-ray fluorescence*

For an untreated undoped MgO crystal, the first few cycles of *x*-irradiation and the subsequent heating to release the thermoluminescence enhanced the Cr^{3+} X-ray fluorescence intensity but the actual enhancement depended on the individual crystal. High temperature treatment of a crystal in an H_2 atmosphere or magnesium vapor did not diminish the intensity of the Cr^{3+} *R* line X-ray fluorescence. Some of the typical results are given in Table 1.

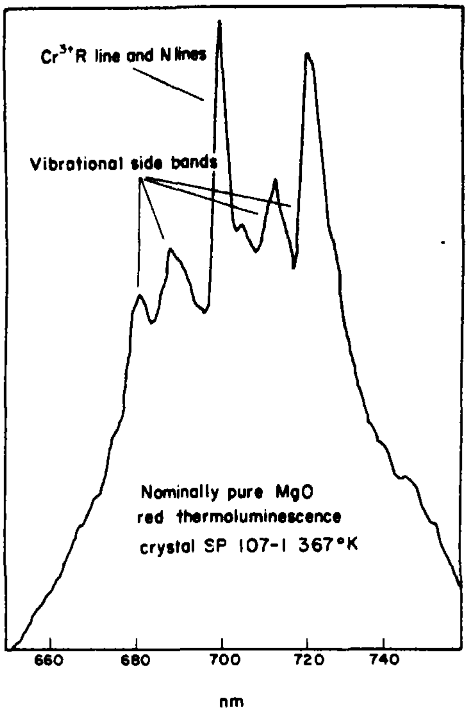

Fig. 3. Red thermoluminescence of a group A MgO crystal (SP 107-1).

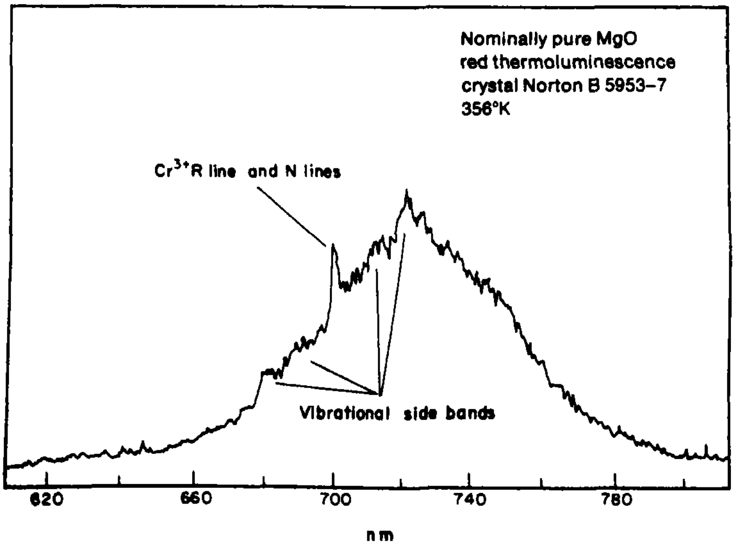

Fig. 2. Red thermoluminescence of a group B nominally pure MgO crystal (Norton B5953-7).

Table 1. *Effects of successive treatments on* Cr^{3+} *X-ray fluorescence intensity in nominally pure* MgO *at* 77°*K*

		Intensity	
		R line	*N* lines
Sample	Treatment	(in arbitrary unit)	
MS-24	None	92	93
	20 min. *x*-irr.	117	123
	1 min. at 400°C	130	173
	20 min. *x*-irr.	106	128
	1 min. at 400°C	160	213
	20 min. *x*-irr.	130	160
MS-37	none	63	54
	15 min. *x*-irr.	58	60
	heat to 180°C	116	113
	15 min. *x*-irr.	80	81
	22 hrs in H_2 at 1190°C	105	7
	15 min. *x*-irr.	59	6
	heat to 180°C	176	7
SP-107	*x*-irr. and heat to 180°C	45	31
	heat in Mg vapor (10^{18} atoms Mg/cm^3)	42	0

3.3 *Intensity variation of* Cr^{3+} *fluorescence excited by* 620 *nm light*

For an untreated undoped MgO crystal, the first few cycles of *x*-irradiation and heating reduces the intensity of Cr^{3+} fluorescence excited by 620 nm light. Some typical results are given in Table 2. In the table *X* and *H* means 10 mins *x*-irradiation followed by heating to 180°C to release the thermoluminescence. After the first few cycles the treatments only fluctuated the fluorescence intensity around a certain level.

Heating of a nominally pure MgO crystal in a hydrogen atmosphere significantly reduced the intensity of Cr^{3+} fluorescence excited by 620 nm light, and treatment in Mg vapor eliminated it completely. Table 3 gives the results of a crystal heated in H_2.

Table 3. *Effect of heating a nominally pure* MgO *crystal in* H_2 *atmosphere at* 1190°*C on the intensity of its fluorescence of* Cr^{3+} *excited by* 620 *nm light*

Treatment			
line position in nm	698·1	703·4	703·8
Before treatment	0·46	0·054	0·073
21 hr at 1190°C in H_2	0·069	0·017	0·018

3.4 *Variation of* Cr^{3+} *concentration monitored by ESR*

For the first few cycles, the combined effect of *x*-irradiation and heating reduced the concentration of all Cr^{3+} centers in an untreated, nominally pure MgO crystal. Such changes were monitored by spin number measurements and are presented in Table 4.

The decrease of the Cr^{3+} concentration stopped after the first few cycles; further treatments caused the Cr^{3+} concentration to fluctuate around a stable level. The type of fluctuation depended on the relative concentration of Cr^{3+} to other impurity ions. For crystals which were very pure, i.e., low in all other impurities but Cr^{3+} (group *A* crystals), *x*-irradiation diminished the Cr^{3+} concentration, and the subsequent heating increased it.

Table 2. *Combined effect of x-irradiation and heating on intensity of* Cr^{3+} *fluorescence excited by* 620 *nm light in nominally pure* MgO

		Intensity			
Crystal	Line	0 *X* & *H*	1 *X* & *H*	2 *X* & *H*	4 *X* & *H*
MS-24-5	698·1 nm	0·91	0·16	0·10	
MS-24-5	703·4 nm	0·21	0·12	0·08	0·07
MS-9-1	703·4 nm	0·24	0·17	0·09	0·04
MS-12-3	703·8 nm	0·28	0·22	0·19	0·15
MS-9-1	703·8 nm	0·33	0·29	0·23	0·18

(The intensities were calibrated against the 689·1 nm line of a reference MgO crystal.)

Table 4. Effect of first few x-irradiation and heating cycles on Cr^{3+} *concentration in untreated, nominally pure* MgO *crystals*

Crystal	Center	Spin number (Cr^{3+}/cm^3) $0\,X\,\&\,H$	$1\,X\,\&\,H$	$2\,X\,\&\,H$	$4\,X\,\&\,H$
MS-24-5	Octahedral Cr^{3+}	$6{\cdot}9\times10^{16}$	$7{\cdot}5\times10^{15}$	$4{\cdot}9\times10^{15}$	—
MS-24-5	T' centers	$1{\cdot}4\times10^{16}$	$9{\cdot}2\times10^{15}$	$6{\cdot}5\times10^{15}$	$5{\cdot}0\times10^{15}$
MS-9-1	T' centers	$9{\cdot}5\times10^{15}$	$7{\cdot}4\times10^{15}$	$3{\cdot}7\times10^{15}$	$1{\cdot}9\times10^{15}$
MS-9-1	T centers	$3{\cdot}0\times10^{16}$	$2{\cdot}6\times10^{16}$	$2{\cdot}2\times10^{16}$	$1{\cdot}8\times10^{16}$
MS-12-3	T centers	$3{\cdot}3\times10^{16}$	$3{\cdot}0\times10^{16}$	$2{\cdot}8\times10^{16}$	$1{\cdot}6\times10^{16}$

For crystals which had an iron content several times higher than its Cr^{3+} ions (group B crystals), the direction of Cr^{3+} concentration fluctuation was reversed. Examples of such changes are shown in Table 5. The irradiation history of a crystal can be erased by annealing at 400°C for several days.

Doping with magnesium metal eliminated the T and T' centers. Just after the Mg vapor treatment the concentration of octahedral Cr^{3+} ion was below the detectional level of the ESR spectrometer used (For the sample size used this was $2{\cdot}5\times10^{11}$ spin/cm^3.) The x-irradiation increased the Cr^{3+} concentration to a considerable level, as shown in Table 5. Heating at 400°C decreased the Cr^{3+} concentration. If the heating lasted more than a day, then the Cr^{3+} concentration again dropped below ESR detection limits.

3.5 *Variation of V_1 center concentration monitored by ESR*

V_1 centers can be produced in nominally pure MgO by X-ray or 5 eV light irradiation and can be bleached out by heating or visible light irradiation. It was found, as the data in Table 6 shows, that the thermal bleaching of V_1 centers and the emission of thermoluminescence occurred simultaneously. Heating at 70°C for 10 min destroyed about half of the V_1 centers and the same heating released about half of the red thermoluminescence. At 400°C all the thermoluminescent light was released in 1 min; also, the concentration

Table 5. Effect of x-irradiation and heating at 400°C 1 *min on octahedral* Cr^{3+} *in nominally pure and* Mg *doped* MgO *crystals which were preconditioned by x-irradiation and heating cycles*

Sample	Concentration (spin/cm^3) After 50 min x-irr.	After 1 min. at 400°C
SP 107-1 (group A)	$1{\cdot}7\times10^{16}$	$2{\cdot}7\times10^{16}$
MS-25-4 (group B)	$1{\cdot}2\times10^{16}$	$2{\cdot}0\times10^{15}$
SP 107-2 (10^{18} Mg atoms/cm^3)	$6{\cdot}2\times10^{15}$	$1{\cdot}1\times10^{15}$

Table 6. Number of V_1 centers in MgO *crystals*

Crystal/Treatment	V_1 center concentration 50 min x-irr.	70°C 10 min	400°C 1 min
SP 107-1 (group A)	$1{\cdot}7\times10^{17}$	$5{\cdot}4\times10^{16}$	$< 10^{13}$
MS-24-5 (group B)	$6{\cdot}8\times10^{16}$	$2{\cdot}6\times10^{16}$	$< 10^{13}$
SP 107-2 (Mg 2×10^{17})	$3{\cdot}6\times10^{17}$	$1{\cdot}7\times10^{17}$	$< 10^{13}$

of V_1 center was reduced to below the detection level of ESR.

Even after Mg doping x-irradiation always produced V_1 centers; however, for a crystal which was freshly doped with heavy dose of Mg (i.e. 10^{18} Mg atoms/cm^3 or more) 5 eV light could no longer produce V_1 centers.

3.6 *Glow curve of the* Cr^{3+} *thermoluminescence*

Figure 4 is a thermoluminescence glow curve of a group A crystal. The monochromater was set at 698·5 nm and the heating rate was hyperbolic. Figure 5 is the heating rate curve.

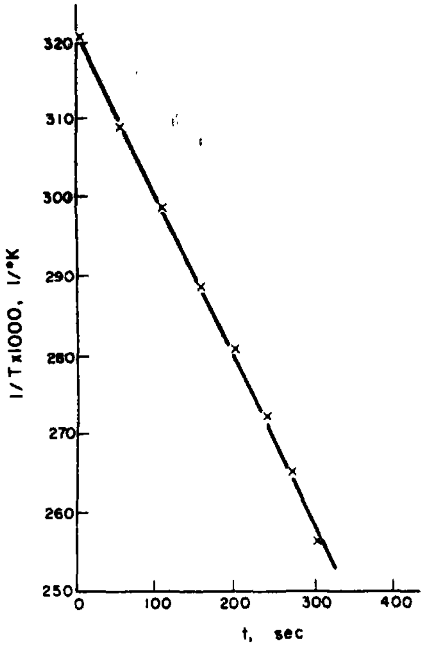

Fig. 5. Hyperbolic-heating-rate curve for the thermoluminescence in Fig. 4.

4. DISCUSSION

4.1 *Identification of the thermoluminescent activator*

The spectrum in Fig. 1 is a fluorescence spectrum excited by 620 nm light. In MgO crystals the 620 nm light can only excite Cr^{3+} fluorescence. Compared to spectrum taken at 77°K, at 363°K the fluorescence is weak and the lines are broadened and shifted. The central line at 699·5 nm is due to unresolved zero phonon lines of octahedral and tetragonal Cr^{3+} centers. Since at 363°K various phonon states are populated the photon-plus-phonon emission is possible. Vibrational

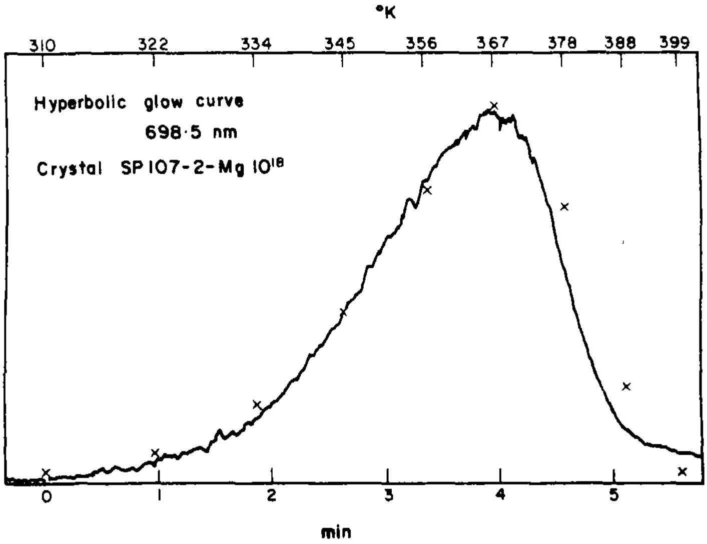

Fig. 4. Hyperbolic glow curve of the red thermoluminescence of a group A MgO crystal with the Spex monochromator set at 698·5 nm.

side bands are seen at both sides of the zero phonon line. The Stoke lines are at 712, 720 nm, the anti-Stoke lines are at 681, 690 nm. The spectra in Figs. 1 and 3 are essentially identical; therefore, there is little question that Cr^{3+} centers are the activators for the thermoluminescence in MgO observed in Fig. 3. In Fig. 2 those Cr^{3+} thermoluminescence peaks also can be clearly seen but they ride on a broad peak which centered at 720 nm. The broad emission band is due to manganese and the detail of assignment will be reported separately.

There were different assignments about the red thermoluminescence. Some authors attributed it to Fe^{3+} [2, 5] whereas others attributed it to Cr^{3+} [6, 7]. This report rules out the first assignment for good and also points out that manganese is a second contributor.

4.2 *The mechanism of* Cr^{3+} *X-ray fluorescence in a nominally pure* MgO

It was found that in MgO crystals the intensity of X-ray fluorescence of Cr^{3+} centers was not proportional to the concentration of these centers. The concentration of Cr^{3+} centers was minitored by two methods: (1) Measuring the intensity of ESR lines of corresponding centers. (2) Monitoring the intensity of the same fluorescence excited by 620 nm light. The 620 nm light, because of its low energy, has little ionizing effects in MgO. The intensity of Cr^{3+} fluorescence thus excited gives a good representation of the concentration of Cr^{3+} centers in the crystals. As the examples in Table 1 indicate, the combined effect of x-irradiation and a brief subsequent heating was to increase the intensity of Cr^{3+} R line X-ray fluorescence. Yet as indicated in Table 2 and 4, the concentration of octahedral Cr^{3+} was reduced to less than 10 per cent of the original value. Many samples were examined but no exception was found. This indicates that there exists some mechanism of X-ray fluorescence which starts with chromium in some valence state and produces Cr^{3+} only as the final product of the charge transfer process.

There are two mechanisms which will lead to the Cr^{3+} ions as the final products, namely:

$$\begin{aligned} &Cr^{4+} + e^- \rightarrow Cr^{3+*} \\ &Cr^{3+*} \rightarrow Cr^{3} + h\nu \end{aligned} \qquad (1)$$

$$\begin{aligned} &Cr^{2+} + \text{hole} \rightarrow Cr^{3+*} \\ &Cr^{3+*} \rightarrow Cr^{3+} + h\nu. \end{aligned} \qquad (2)$$

The latter case can be better illustrated by the diagram in Fig. 6. Free holes in the valence band are created by x-irradiation. These holes combined with Cr^{2+} ions to produce Cr^{3+} ions in an excited state, and the $^2E \rightarrow {}^4A_2$ transition of Cr^{3+} gives the fluorescence emission.

It is believed that x-irradiation reduces Cr^{3+} to Cr^{2+} in MgO. Fletcher *et al.* used ultrasonic paramagnetic resonance technique on nominally pure MgO crystals. They detected a signal that was induced by the x-irradiation and assigned it to Cr^{2+} [26]. The thermal magnets resistance measurements made by Challis and Williams [27] supported this assignment. If Cr^{3+} ions which disappeared during x-irradiation and heating were converted to Cr^{2+}, the second mechanism should be favored. However though Cr^{4+}

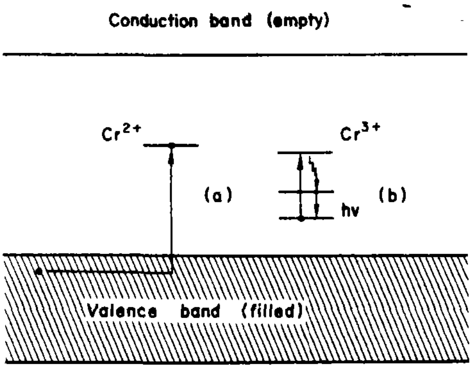

Fig. 6. Mechanism for X-ray fluorescence of octahedral Cr^{3+} ions in nominally pure MgO. (a) A free hole combines with a Cr^{2+} producing an excited Cr^{3+} ion. (b) The Cr^{3+*} emits a photon in undergoing the ^2E to $^4A_2$ transition and then return to the ground state.

was never detected there is no evidence against the production of Cr^{4+} ions in MgO by *x*-irradiation. It is known that Cr^{4+} can be produced in Al_2O_3 by irradiation[28].

To establish the existence of mechanism 2 several nominally pure MgO crystals were either heated in H_2 atmosphere at 1200°C for several hours or doped with Mg to see the effects of reducing treatments on the X-ray fluorescence.

Table 1 and 3 show that after high temperature treatment in H_2 the intensity of X-ray fluorescence increased significantly but the concentration of octahedral Cr^{3+} went down to 15 per cent of its original value. Doping a nominally pure MgO with Mg to a dose of 2×10^{17} Mg atmos/cm^3, or more, brought down the Cr^{3+} concentration to a level beyond the ESR detection. Yet as Table 1 indicates its X-ray fluorescence intensity was not significantly changed. After such strong reducing treatments one would not anticipate any Cr^{4+} to exist in a MgO crystal; therefore, in such crystals mechanism 2 is the exclusive one for fluorescence.

Table 1, 2 and 4 show the same discrepancy between X-ray fluorescence intensity and the concentration of the T and T' center of Cr^{3+}. Since the reduction of a Cr^{3+} ion in a T or T' center to Cr^{2+} by *x*-irradiation will not automatically cause the neighbouring cation vacancy to move away, it is anticipated that some Cr^{2+} ions at a tetragonal site will be produced by *x*-irradiation. It is reasonable to expect 2 is the dominant mechanism here too. Since now both a cation vacancy and a Cr^{2+} ion can capture a hole, there may be an increased probability for a hole to interact with a tetragonal Cr^{2+} ion. This was supported by the observation that the X-ray fluorescence due to T and T' centers was enhanced to a greater degree than R line emission by *x*-irradiation and heating.

3. *Mechanism for producing red thermoluminescence of octahedral* Cr^{3+} *in* MgO

The reaction between a hole and a Cr^{2+} ion appears to be established as the major mechanism for Cr^{3+} X-ray fluorescence. One would anticipate that the same reaction could be responsible for the Cr^{3+} thermoluminescence. Then the question is: Where does the hole come from? Several authors have pointed out that the V_1 centers which are destroyed might be the source of the holes[6, 7]. In this investigation it was verified that the destruction of V_1 centers and the emission of Cr^{3+} thermoluminescence occurred simultaneously. The results are tabulated in Table 6.

Doping with magnesium vapor produces a large quantity of F' centers (two electrons trapped in an anion vacancy). F' centers absorb strongly at 5 eV[16]. This led to another interesting observation about the Cr^{3+} thermoluminescence. For a crystal which was newly doped with a dose of 10^{18} Mg/cm^3 or more, the absorption of F' centers was very strong. As a result 5 eV irradiation could neither produce V_1 centers nor the Cr^{3+} thermoluminescence. This indicates that the existence of V_1 centers is the necessary condition for production of the Cr^{3+} thermoluminescence.

The product of the reaction between a Cr^{2+} ion and a hole is expected to be Cr^{3+}. It was observed, in rather pure and repeatedly *x*-irradiated and heated crystals, that the discharge of Cr^{3+} thermoluminescence was accompanied with an increase in the Cr^{3+} concentration (Table 5). However, for a newly cleaved crystal, as it was shown in the early part of this paper *x*-irradiation and heating only convert Cr^{3+} to Cr^{2+}. This indicates (1) Cr^{3+} ion has a large electron capture cross section. During irradiation the reaction of $Cr^{2+}+\text{hole}\rightarrow Cr^{3+}$ is competing with the reaction of $Cr^{3+}+e^-\rightarrow Cr^{2+}$. (2) In a newly cleaved crystal there exist some ions which have smaller electron capture cross section are losing electrons to Cr^{3+} ions during the irradiation. As for rather impure crystals and Mg doped crystal the number of such electron sources are large and some of them have their energy levels positioned very close to the conduction band. Therefore their behavior is different from the rather pure ones. As it is shown in Table 5, the irradiation increases the concentration of Cr^{3+} ion and the discharge of thermoluminescence decreases it. There is some evidence which supports such a hypothesis: It is known that the thermoluminescence is accompanied with a thermal electric charge release phenomenon (1). In the crystals studied in this research the V_1 centers are the only important hole source below 363°K. If the charges released are mainly holes then the quantity of released charges should be proportional to the concentration of V_1 centers. The experimental finding was that the concentration of V_1 centers of three different kinds of crystals had the same order of magnitude and followed the order that group *A* Mg doped > group *A* > group *B* (Table 6). But the quantity of electricity discharged by MS-24-5 was six times larger than SP-107-1 (group *A*), along with the Mg doped SP-107-2 discharged 1000 times more electricity than SP-107-1 (29). This is in agreement with the hypothesis that extra electron sources exist in the rather impure or Mg doped crystals. The nature of the electron source is still not clear.

Sibley *et al.*[7] also reported that Cr^{3+} concentration increased after emission of red thermoluminescence. The samples they used and the 'rather pure' samples used in this report were supplied by the same company. Presumably their measurements were made after samples been repeatedly X-rayed and heated.

In brief, since (1) the interaction of a hole with Cr^{2+} ion is the predominant mechanism for producing X-ray fluorescence of Cr^{3+} in MgO, (2) destruction of V_1 centers and emission of the Cr^{3+} thermoluminescence occur at the same temperature level, and Mg doping prevents both the formation of V_1 centers and production of the Cr^{3+} thermoluminescence by 5 eV irradiation. (3) after discharge of Cr^{3+} thermoluminescence, the concentration of Cr^{3+} increases in the fairly pure MgO crystals. The following solid state reaction steps are proposed

$$\begin{aligned} &V_1 \text{ center} \rightarrow \text{Free hole} + \text{cation vacancy} \\ &\text{Free hole} + Cr^{2+} \rightarrow Cr^{3+*} \qquad (3) \\ &Cr^{3+*} \rightarrow Cr^{3+} + h\nu. \end{aligned}$$

The thermal decomposition of V_1 centers should be the rate determining step for 3, and as a result the Cr^{3+} thermoluminescence should possess apparent first order kinetics. This was checked out on the glow curve of the thermoluminescence.

The analysis of glow curves is based on the assumption that the intensity of thermoluminescence is proportional to the rate of releasing of charge (C) which is needed in the luminescence process, that is:

$$I \sim -\frac{dC}{dt} = KC^n. \qquad (4)$$

Here n is a constant which depends on the mechanism, t is time, and K is a rate constant which has an exponential temperature (T) dependence, i.e.:

$$K = S \exp(^{-E}a/kT). \qquad (5)$$

Here S is preexponential factor, E_a is the activation energy.

Starting with 4 and 5, for the case with $n = 1$, and the heating rate is hyperbolic, that is $\beta_0 t = T_0^{-1} - T^{-1}$ (β_0 is a proportional constant, T_0 is the starting temperature of the heating program), Halperin[24] showed that the thermoluminescence glow curve should take the form of:

$$\ln \frac{I}{I_m} = 1 + x - e^x. \qquad (6)$$

Here

$$x = \frac{E_a \beta_0}{k}(t - t_m), \qquad (7)$$

where t_m is the time at which $I = I_m$. I_m means

I is at its maximum. At the half-intensity point, that is at $I/I_m = \frac{1}{2}$, equation (6) can be solved numerically to give $x_1 = -1{\cdot}462$, $x_2 = 0{\cdot}985$. By using the value of x_1, equation (7) and the hyperbolic thermoluminescence glow curve in Fig. 4, the activation energy of the thermoluminescence was calculated to be $0{\cdot}80 \pm 0{\cdot}02$ eV.

This value is significantly different from $1{\cdot}12 \pm 0{\cdot}05$ eV which was reported by Searles *et al.*[5]. The reason for this is: they assumed that the thermoluminescence is a biomolecular process. If one uses their data and their method of analysis (30) but changes the constant q (A factor determined by kinetics. $q \leqslant 1$ for unimolecular process, $1 \leqslant q \leqslant 2$ for bimolecular process) from 1·25 to 1, the activation energy of their glow curve drops down to 0·87 eV.

Our glow curves obey first order kinetics. By substituting 0·8 eV into the equation (6), a theoretical curve was calculated. As it is shown in Fig. 4 it fits to the experimental curve well. Searle *et al.* reported the thermal decay of V_1 center varied considerably from one crystal to another and could not be fitted into one exponential decay mechanism. This probably indicates that there are several mechanisms involved in the decomposition of V_1 centers; in some rather impure crystals a biomolecular process might be the main mechanism for the decay of V_1 center. But from our results it seems that the Cr^{3+} thermoluminescence is not produced by a reaction between V_1 center and Cr^{2+} ions.

It is known that V_1 centers can be bleached out by visible light. The efficiency of bleaching reaches its maximum at 2·5 eV[16]. The photon energy can be regarded as the optical activation energy for releasing a hole from a V_1 center. According to Mott the ratio of optical activation energy ($h\nu$) to thermal activation energy (E_a) is equal to the ratio of static dielectric constant (ϵ) to high frequency dielectric constant (ϵ_0)[28]:

$$\frac{h\nu}{E_a} = \frac{\epsilon}{\epsilon_0}. \tag{8}$$

For MgO $\epsilon = 9{\cdot}8$, $\epsilon_0 = 2{\cdot}95$[31]. Using $E_a = 0{\cdot}8$ eV then one gets $h\nu = 2{\cdot}64$ eV which is very close to the energy of the light which is most efficient in bleaching out the V_1 center. Similar results were also reported by Thomas and Houston[3].

In brief, the analysis of the thermoluminescence glow curve, and the comparison between the calculated optical activation energy and the experimental value indicate that the thermal decomposition of V_1 centers is the rate determining step for the Cr^{3+} thermoluminescence.

Acknowledgement—The author wishes to thank Prof. Wertz for his support and helpful discussions, and Mr. Dravnieks for permission to use some of his unpublished data.

REFERENCES

1. YAMAKA E., *Phys. Rev.* **96**, 293 (1954).
2. HANSLER R. L. and SEGELKEN W. G., *J. Phys. Chem. Solids* **13**, 124 (1960).
3. THOMAS B. and HOUSTON E., *Brit. J. appl. Phys.* **15**, 953 (1964).
4. HECHT H. G. and TAYLOR E. D., *J. Phys. Chem. Solids* **13**, 124 (1967).
5. SEARLE T. M. and GLASS A. M., *J. Phys. Chem. Solids* **29**, 609 (1968).
6. WERTZ J. E., HALL L. C., HEGELSON J., CHAO C. C. and DYKOSKI, W. A., *Interaction of Radiation and Solids* (Edited by A. Bishay) p. 617, Plenum Press, New York (1967).
7. SIBLEY W. A., KOLOPUS J. L. and MALLARD W. C., *Phys. Status Solidi* **31**, 223 (1969).
8. DEUTSCHBEIN O., *Ann. Phys. Ser.* **5**, **14**, 712 (1932).
9. SCHAWLOW A. L., WOOD D. L. and COGSTON A. M., *Phys. Rev. Lett.* **3**, 544 (1959).
10. SCHAWLOW A. L., *J. appl. Phys. Suppl.* **33**, 395 (1962).
11. SUGANO S., SCHAWLOW A. L. and VARSANYI F., *Phys. Rev.* **120**, 2045 (1960).
12. SCHAWLOW A. L., PIKSIS A. and SUGANO S., *Phys. Rev.* **122**, 1469 (1961).
13. IMBUSCH G. F., SCHAWLOW A. L., MAY A. D. and SUGANO S., *Phys. Rev.* **140**, A830 (1965).
14. GLASS A. M., *J. chem. Phys.* **46**, 2080 (1967).
15. WERTZ J. E. and AUZINS P., *Phys. Rev.* **106**, 484 (1957).
16. HERNDERSON B. and WERTZ J. E., *Adv. Phys.* **17**, 746 (1968).
17. LOW W., *Phys. Rev.* **105**, 793 (1957).
18. WERTZ J. E. and AUZINS P., *Phys. Rev.* **106**, 484 (1957).
19. WERTZ J. E. and ORTON J. W. and AUZINS P., *J. appl. Phys. Suppl.* **33**, 322 (1962).

20. AUZINS P. and WERTZ J. E., *J. chem. Phys.* **43**, 1129 (1965).
21. WERTZ J. E. and AUZINS P., *J. Phys. Chem. Solids* **28**, 1557 (1967).
22. WERTZ J. E., AUZINS P., GRIFFITHS J. H. E. and ORTON J. W., *Disc. Faraday Soc.* **28**, 136 (1959).
23. WERTZ J. E., SAVILLE G., AUZINS P. and ORTON J. W., *J. phys. Soc. Japan, Suppl. II.* **18**, 305 (1963).
24. HALPERIN A., LEIBOVITZ M., SCHLESINGER M., *Rev. Scient. Instrum.* **33**, 1168 (1962).
25. HENSLEY E. B., WARD W. C., JOHNSON B. P. and KROES R. L., *Phys. Rev.* **175**, 1227 (1968).
26. FLETCHER J. R., MARSHALL F. G., RAMPTON V. W., POWELL P. M. and STEVENS K. W. H., *Proc. Phys. Soc.* Lond. **88**, 127 (1966).
27. CHALLIS L. J. and WILLIAMS D. J., *Proc. Phys. Soc.* **88**, 131 (1966).
28. HOSKINS R. H. and SOFFER B. H., *Phys. Rev.* **133**, 490 (1964).
29. Dravnieks Fricis, unpublished data.
30. HALPERIN A. and BRANER A. A., *Phys. Rev.* **117**, 408 (1960).
31. MOTT N. F. and GURNEY R. W., *Electronic Process in Ionic Crystal*, Dover Publications, New York (1964).

J. Phys. Chem. Solids, 1971, Vol. 32, pp. 2529–2538. Pergamon Press. Printed in Great Britain

EPR OF SUBSTITUTIONAL AND CHARGE COMPENSATED Fe^{3+} IN ANATASE (TiO_2)*

M. HORN and C. F. SCHWERDTFEGER
Department of Physics, University of British Columbia Vancouver, Canada

(*Received* 19 *February* 1971)

Abstract—Paramagnetic resonances were observed in natural single crystals of anatase and are interpreted as due to regular substitutional Fe^{3+}(I) and to Fe^{3+} combined with an oxygen vacancy at a nearest neighbour site (II). The observed unusually strong temperature dependence of the spin-Hamiltonian parameter b_2^0 of (I) and the temperature dependence of the orientation of the magnetic axes of the spectrum (II) are both explained by assuming a shift within the unit cell of the equilibrium positions of the oxygen ions with temperature.

1. INTRODUCTION

ANATASE is a polymorphous form of rutile, brookite and the synthetic high pressure TiO_2II [1]. But whereas numerous EPR studies are reported on paramagnetic impurities and defects in rutile[2, 3], only a few EPR analyses of anatase and, to our knowledge, none on brookite have been made. The main reason is that one can grow good single crystals of rutile with a variety of appropriate dopings, but the technique to obtain synthetic crystals of anatase and brookite is still not well developed[4, 5].

The few EPR studies of anatase were therefore made with synthetic powders, in which the spectra of Cr^{3+}[6], Ti^{3+}[7, 8] and $(TiO)^{3+}$ [9] have been analysed. The only single crystal analysis was made by Gainon and Lacroix [10] who reported the EPR spectrum of Fe^{3+}, substituting Ti^{4+} in a natural single crystal of anatase.

Presented here are the results of an EPR analysis of natural single crystals of anatase supplemented with the analysis of synthetic polycrystalline anatase doped with iron. Some of the results, in as much as they reinterpreted the results of Gainon and Lacroix[10] were already presented in a previous short note[11] (henceforth noted as HSI).

2. CRYSTAL STRUCTURE AND PHASE TRANSFORMATION

In all polymorphous forms of TiO_2 the titanium ions are surrounded by six octahedrally coordinated oxygen ions. The difference between these forms lies in the stacking of the octahedra and in their distortion.

Anatase has tetragonal D_{4h} point symmetry and each unit cell contains four TiO_2 molecules. Figure 1 shows a unit cell. Cromer and Herrington[12] measured the room temperature cell dimensions $a = 3{\cdot}785$ Å, $c = 9{\cdot}514$ Å and the oxygen parameter $u = 0{\cdot}413$ Å. Rao *et al.*[13] determined the thermal expansion of anatase from 28 to 712°C. Over a temperature range of 500°C c increased 0·6 per cent and a, 0·3 per cent.

All Ti^{4+} ions in anatase have tetragonal site symmetry D_{2d} with their symmetry axes and planes parallel to each other. The oxygen octahedra are distorted with two long Ti^{4+}–O^{2-} bonds of 1·964 Å parallel to the [001]-crystal axis and four shorter bonds of 1·937 Å. The latter make an angle of $\alpha_0 = \pm 12° 34'$ with the (001)-crystal plane. Figure 1 displays one of these octahedra, formed by the Ti^{4+} ion S and the six O^{2-} ions A–F.

Each unit cell contains also four interstitial sites surrounded by oxygen octahedra, having the same symmetry with respect to the same axes as the Ti^{4+} sites. One of them is marked with I in Fig. 1. The only difference from the

---

*Research support by the National Research Council of Canada.

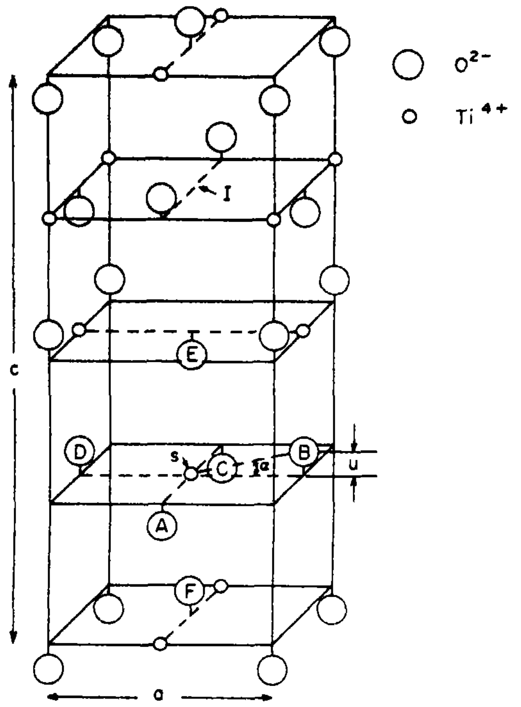

Fig. 1. The positions of the ions in a unit cell of anatase.

Ti^{4+} site is that the surrounding oxygen octahedra are longer along the [001]-axis with a I–O^{2-} distance of 2·792 Å.

Thermodynamically, pure anatase is unstable under any temperature–pressure condition[14]. By heating anatase transforms irreversible to rutile. This conversion is immeasurably slow below some threshold temperature, which varies between 400 and 1200°C, depending on the kind and concentration of the impurities. For spectroscopically pure anatase this threshold temperature is 610°C[15–19].

3. SPIN HAMILTONIAN AND CRYSTAL FIELD

In this chapter the spin Hamiltonian and the theoretical interpretation of its parameters will be discussed in as much as it is relevant to the observed EPR spectra of Fe^{3+} in anatase.

The general form of the spin Hamiltonian to describe the EPR spectra of Fe^{3+}, which has a ^6S-ground state, in a weak crystal field of arbitrary symmetry has the form [20]

$$\mathscr{H} = \beta\bar{H}\cdot\tilde{g}\cdot\bar{S} + \frac{1}{3}\sum_{m=-2}^{2} b_2^m O_2^m + \frac{1}{60}\sum_{m=-4}^{4} b_4^m O_4^m. \quad (1)$$

The O_n^m are operator equivalents[21], the b_n^m are experimental constants. Equation (1) neglects a possible interaction with surrounding nuclear spins or the nuclear spin of the 2 per cent abundant ^{57}Fe. The first term in (1) represents the magnetic field dependence. The spectroscopic splitting factor $\tilde{g}$ is found experimentally to be nearly isotropic and to differ at most a fraction of 1 per cent from the free electron value of 2·0023 in a variety of host lattices.

The constants b_n^m are related to D, E, a and F used in many EPR studies by the relations

$$b_2^0 = D \qquad b_4^0 = a/2 + F/3$$
$$b_2^2 = 3E \qquad b_4^4 = 5a/2. \quad (2)$$

Under rotation of the coordinate system the parameters b_n^m transform according to the formula given explicitly by Vinokurov *et al.* [22, 23] and Thyer *et al.* [24]. The number of necessary coefficients b_n^m can be reduced by choosing a special coordinate system and is further reduced according to the symmetry of the crystal field. In particular, a cubic field can be described by a single parameter $a = 2b_4^0 = \frac{2}{5}b_4^4$ provided one chooses the three fourfold axes as the reference system. All other b_n^m are then zero. If one uses, however, a fourfold axis as z-axis and the two perpendicular twofold axes as x- and y-axes, one obtains the cubic parameter a of opposite sign and an additional apparent axial distortion $F = -3a$. It is now apparent that Gainon and Lacroix[10] must have used this latter coordinate system to describe the EPR spectrum of substitutional Fe^{3+} in anatase resulting in an unusual negative value for a and a very large F.

In an axial crystal field, with the z-axis as symmetry axis, the spin Hamiltonian can be written

$$\mathscr{H} = g_{\parallel}\beta H_z S_z + \tfrac{1}{2}g_{\perp}\beta H_{\perp}(S_+ + S_-) + \tfrac{1}{3}b_2{}^0 O_2{}^0 + \tfrac{1}{60}b_4{}^0 O_4{}^0 + \tfrac{1}{60}b_4{}^4 O_4{}^4. \quad (3)$$

As already mentioned, the x- and y-axis are best chosen as the two perpendicular cubic fourfold axes.

If the only symmetry of the crystal field is a reflection plane, the appropriate coordinate system is given by two axes in this plane and the third axis perpendicular to it[20]. The directions of the two axes in the plane can be chosen so that $b_2{}^1 = 0$, this implies the choice of the principal axes of the second order tensor $b_2{}^m$ as coordinate axes. One obtains in this way the spin Hamiltonian

$$\mathscr{H} = \beta\bar{H}\,.\,\bar{g}\,.\,\bar{S} + \tfrac{1}{3}b_2{}^0 O_2{}^0 + \tfrac{1}{3}b_2{}^2 O_2{}^2 + \frac{1}{60}\sum_0^4 b_4{}^m O_4{}^m. \quad (4)$$

This form is especially appropriate if the terms $b_2{}^m$ are much larger than the fourth order terms $b_4{}^m$, because then the experimentally determined 'magnetic axes', defined by extreme positions of the EPR spectral lines, coincide with the coordinate axes.

By eventual permutation of the axes one can additionally limit the value of $b_2{}^2/b_2{}^0$ to the range $0 \leqslant b_2{}^2/b_2{}^0 \leqslant 1$ [25].

There exists a series of investigations to explain theoretically the parameters $b_n{}^m$, mainly $b_2{}^0$ and $b_4{}^4$ (D and a), for S-state ions [26–29]. The results for $b_2{}^0$ can be summarized in

$$b_2{}^0 = b_0 + c_1 B_2{}^0 + c_2(B_4{}^0)' + c_3(B_2{}^0)^2. \quad (5)$$

The $B_n{}^m$ are coefficients of a development of the electric crystal field V at the paramagnetic ion site in spherical harmonics $Y_n{}^m$

$$V = \sum_{n,m} \left(\frac{4\pi}{2n+1}\right)^{1/2} B_n{}^m r^n Y_n{}^m \quad (6)$$

$(B_4{}^0)'$ is the remaining part of $B_4{}^0$ after subtracting the part corresponding to a perfect cubic crystal field. b_0 accounts for covalent bonding and overlap of the electrons of the paramagnetic ion with the surrounding ligands and the c_i are constants determined by properties of the paramagnetic ion, such as spin–orbit coupling and orbital level splitting in a cubic crystal field. In some cases[26, 30] even the use of a point charge model to calculate $B_2{}^0$ and $(B_4{}^0)'$ while neglecting b_0 resulted in a calculated value of $b_2{}^0$ in reasonable agreement with the experiment. Sharma, Das and Orbach[26] calculated for Mn^{2+} in octahedral coordination of ZnF_2

$$b_2{}^0 = -0{\cdot}07B_2{}^0 + 0{\cdot}36(B_2{}^0)^2 + 4{\cdot}34(B_4{}^0)' \quad (7)$$

if $b_2{}^0$ is measured in cm^{-1} and $B_n{}^m$ in $e^2/2a_0{}^{n+1}$; e is the elementary charge, a_0, the atomic unit of length.

With a point charge model one can calculate[26]

$$B_2{}^0 = \sum_j q_j(3\cos^2\theta_j - 1)/R_j{}^3 \quad (8)$$

$$(B_4{}^0)' = \sum_j q_j\{\tfrac{1}{4}(35\cos^4\theta_j - 30\cos^2\theta_j + 3) - \tfrac{7}{4}\sin^4\theta_j \cos 4\phi_j\}/R_j{}^5 \quad (9)$$

where the external point charges $q_j|e|$ are situated at (R_j, θ_j, ϕ_j) with respect to an origin taken at the site of the paramagnetic ion.

Walsh *et al.*[31] analyse theoretically the temperature dependence of D and a. They divide it into an external and an implicit temperature dependence, where the implicit term accounts for the contribution produced by the expansion of the lattice. The implicit part should depend on the inter-ionic distance r as

$$D \propto r^7, \quad a \propto r^{-21}. \quad (10)$$

4. SAMPLES AND EXPERIMENTAL TECHNIQUE

The natural crystals of anatase studied in this work originated in Tavetch, Graubünden, Switzerland and Binntal, Wallis, Switzerland. They were kindly supplied to us by Harnik of the Crystallographic Institute of ETH, Zurich and Meagher of the Geology Department of UBC, Vancouver. Typical diameters were 1–3 mm. The two Tavetch crystals had pyramidal habit, opaque gray color and their EPR spectra, although qualitatively similar to those of the Binntal crystals showed broad and poor resolved lines. The three crystals of Binntal were yellow and transparent. They possessed different habits but always had clear recognizable {110}-planes which helped to orientate them. The orientation of the crystal axes was checked by Laue X-ray photographs. All the Binntal crystals showed the same EPR spectra and the results reported here are obtained with them.

The X-band EPR spectrometer was of standard design, with 100 kHz field modulation, AFC, phase sensitive signal detection and a Varian standard TE_{102} cavity.

For the room temperature measurements the crystal was mounted on a lucite sample holder permitting rotations about a horizontal and a vertical axis. For variable temperature measurements a smaller brass sample holder was used which permitted rotations only about a vertical axis, but could be inserted into a quartz dewar, passing through the cavity with temperature regulated N_2-gas flow. The temperature of the sample, measured with a chromel–alumel thermocouple, could be adjusted to any value between 78 and 900°K within ± 5°K.

The frequency of the microwaves was measured directly with a digital frequency meter and the magnetic field, with an NMR-gaussmeter.

To obtain the angular variations of the EPR lines in a particular crystal plane a new technique was employed. In this technique which has been recently reported[32], the magnetic field is locked to an EPR line by a feedback of the EPR signal to the magnet power supply. By slowly rotating the crystal with a motor one obtained on an X–Y plotter directly the angular dependence of the EPR transitions. A block diagram of this technique is given in Ref. [32].

To measure accurately relative angular positions of EPR lines the magnetic field was set to a constant value, the crystal slowly rotated with a synchronous motor and the EPR signal registered on a strip chart recorder. By selecting appropriate EPR lines the angle between the magnetic axis of different paramagnetic centres can be measured in this way to an accuracy of ± 0·01 deg.

In order to determine the absolute sign of the spin Hamiltonian parameters an EPR measurement at 1°K was made.

The single crystal studies were supplemented with synthetic powder studies. The powders were prepared by hydrolysis of $TiCl_4$, doped with 1 mol.% and 0·01 mol.% of $FeCl_3$, with NH_4OH. The precipitated TiO_2 powder was crystallized by heating for 24 hr at 400°C. A Debye–Scherrer X-ray analysis showed only anatase lines.

5. EXPERIMENTAL RESULTS

Two different paramagnetic spectra were identified in the anatase single crystals. By comparing these with the EPR spectra of the iron doped anatase powders both could be associated with iron impurities. The spectra did not appear in powders doped with other impurities.

The first spectrum which will be called type I, is interpreted as a regular substitutional Fe^{3+} site. In addition to this, there exist four strong spectra of type II, which are shown to be consistent with an Fe^{3+} ion, substituting also for Ti^{4+}, but with an oxygen vacancy at a nearest neighbour site. Other weaker EPR lines were observed, however their intensity did not permit even qualitative interpretation.

(a) *Spectrum* I

This spectrum is characterized by an effective spin $S' = 5/2$, a small zero field splitting compared with the Zeeman energy at X-band, and a tetragonal symmetry with respect to the [001] crystal axis. In HSI graphs showing the EPR spectra in three crystal planes are given. The center line has a line width of 10–12 G, depending on the orientation of the static field H. At 78°K the spectrum showed some saturation. Using the crystallographic [100], [010] and [001] axes as x, y, z axes respectively, the spectrum could be described by the spin Hamiltonian (3) with parameters given in Table 1 for 78 and 300°K. These values were obtained by fitting the transition fields with H parallel to [001], [100] and [110] to (3), evaluated to second order. The results were checked by direct diagonalization of the energy matrix with a computer programme.*

The most interesting feature of this spectrum is its temperature dependence. Figure 2 shows the temperature dependence of b_2^0 and b_4^0. b_2^0 decreases from 457×10^{-4} cm^{-1} at 1°K almost linearly with temperature over most of the analysed temperature range and passes through zero at 800 ± 10°K.

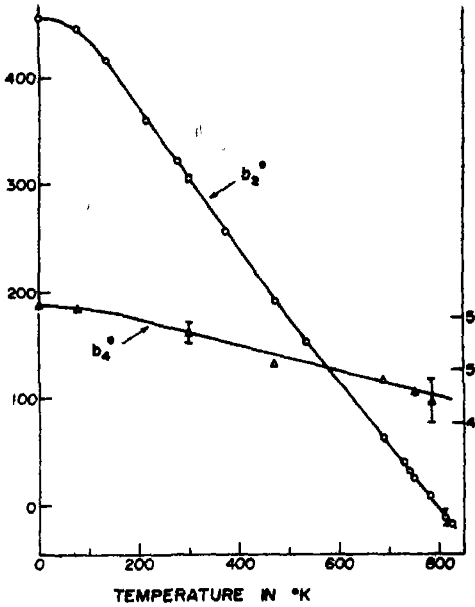

Fig. 2. Temperature dependence of b_2^0 and b_4^0 of spectrum I (substitutional Fe^{3+}) in anatase.

(b) *Spectra* II

In addition to the EPR lines of spectrum I, one observes in the anatase crystals several other rather intense EPR lines. Figure 3 shows these EPR lines in the (100)-crystal plane at room temperature and 9·19 GHz. They are characterized by a large anisotropy and strong angular dependent intensities. The intense lines between 1383 and 1783 G have a line width of 11–14 G at room temperature, are visible up to 300°C and show only a small saturation effect at 1°K.

These lines can be separated in four sets A–D which only differ from one another in

Table 1. *Spin Hamiltonian parameters. All energies are in* 10^{-4} cm^{-1}

	Spectrum I (Substitutional Fe^{3+}) 78°K	 300°K	Spectrum II (Charge compensated Fe^{3+}) 78°K	 300°K
$g_{\parallel}$	2·004 ± 0·001	2·005 ± 0·001	2·002 ± 0·005	
$g_{\perp}$	2·004 ± 0·002	2·005 ± 0·002		
b_2^0	+ 447 ± 1	+ 308·7 ± 1	− 5110 ± 30	− 4970 ± 30
b_2^2	—	—	−3540 ± 30	−3720 ± 30
b_4^0	+ 55·9 ± 1	+ 53·5 ± 1	− 26 ± 10	− 14 ± 10
b_4^2	—	—	+ 60 ± 50	+ 87 ± 50
b_4^4	+ 267 ± 3	+ 257 ± 3	+ 100 ± 10	+ 70 ± 10

---

*An unfortunate algebraic error in HSI resulted in slightly incorrect values for a and F. These values should read at room temperature $a = +103 \times 10^{-4}$ cm^{-1} and $F = +6 \times 10^{-4}$ cm^{-1}.

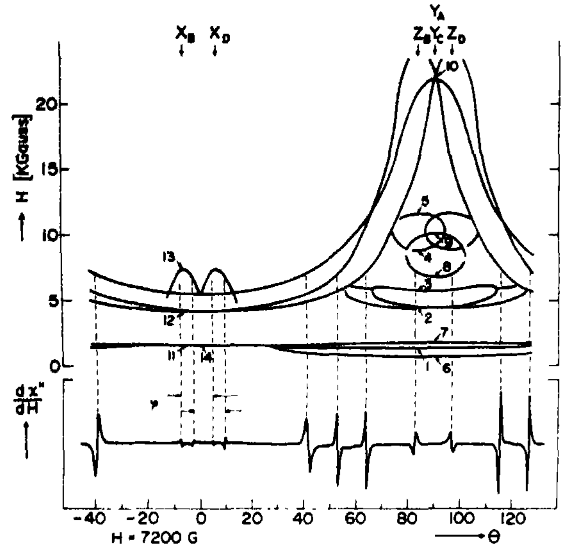

Fig. 3. Spectra II (charge compensated Fe^{3+}) in the (100)-crystal plane of anatase at room temperature and 9·19 GHz. 23 kG was the highest obtainable field. The lower part of the figure shows a spectrum obtained by rotating the crystal in the (100)-plane at a constant field $H = 7200$ G.

90° rotations of their magnetic axes about the [001] crystal axis. The magnetic axes of one of these sets, expressed in polar coordinates, are given in Table 2.

At the top of Fig. 3 are indicated these magnetic axes which lie in the (100)-plane. Y_A means the y-axis of center A, etc. In the lower part of Fig. 3 is shown a spectrum obtained by rotating the crystal at a constant field $H = 7200$ Gauss in the (100)-plane. From this spectrum one deduces an accurate value for φ, the angle which defines the orientation of the magnetic axes (Table 2).

Table 2. Directions of the magnetic axes for one spectrum II, expressed in polar coordinates (θ, ϕ). *The axes of the other three spectra II are obtained by successive rotations of* 90° *about the* [001] *crystal axis*

Magnetic axis	Direction in crystal (θ, ϕ)
x	$(\varphi, 0°)$
y	$(90°, 90°) = [010]$
z	$(90°+\varphi, 0°)$
	300°K: $\varphi = 6{\cdot}32 \pm 0{\cdot}01°$
	78°K: $\varphi = 6{\cdot}15 \pm 0{\cdot}01°$

The relatively small line widths at room temperature and the powder spectra indicate that these lines are also produced by Fe^{3+} with $S' = 5/2$. From the strong anisotropy of the lines one can infer that the zero field splitting is large. The quadrupolar terms b_2^m in the spin Hamiltonian (1) there have to be dominant and its principal axes will determine the orientation of the magnetic axes. Hence, an isotropic $g = 2{\cdot}0023$ was assumed and initially all b_4^m were set equal to zero. A first guess for the remaining b_2^0 and b_2^2 was obtained by using the graphs in Refs. [25], [33]. The axes in Table 2 are already chosen to give a fit with $0 \leq b_2^2/b_2^0 \leq 1$. An adjustment of these parameters was then made with a computer programme given by Hebden *et al.* [34]. With this programme the energy levels were directly obtained for the cases with H parallel to the three magnetic axes and are shown in Fig. 4. The observed transitions are marked identically as in Fig. 3. A final computer calculated least mean square fit was made on all lines in Fig. 4, including b_4^0, b_4^2 and b_4^4 in the spin Hamiltonian, which has then the form (4). The results are given in Table 1.

It should be pointed out that the b_4^m of Table 1 give only an order of magnitude since there exists no reason to suppose that the principal axes of the tensor b_4^m coincide with the principal axes of b_2^m, the latter being taken as defining the magnetic axes. But by including b_4^0, b_4^2 and b_4^4 the calculated transition fields agree with the measured ones to within the experimental error, which is ca. 0·1 per cent, and an additional inclusion of b_4^1 and b_4^3 did not seem warranted.

In order to obtain an estimate of the relative spin concentration of centers of type I and II, the spectra at room temperature with H parallel to the [001]-axis, where the four spectra II coincide, were used and the line intensities A of the center line $|+1/2\rangle \leftrightarrow$

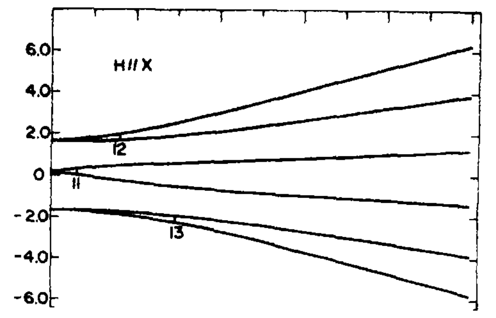

Fig. 4. Energy levels of charge compensated Fe^{3+} in anatase along the three magnetic axes. The observed transitions are indicated and numbered as in Fig. 3.

$|-1/2\rangle$ of I with the $|+3/2\rangle \leftrightarrow |-3/2\rangle$ line of II (line # 14 of Fig. 3) were compared. Using

$$\frac{N_I}{N_{II}} \approx \frac{N_{I,i}}{N_{II,i}} = \frac{A_I}{A_{II}} \cdot \frac{|\langle i|S^{II}_{100}|f\rangle|^2}{|\langle i|S^{I}_{100}|f\rangle|^2} \tag{11}$$

where $N_{I,II}$ is the total number of spins I, II in the sample, $N_{I,II,i}$ is the number of spins I, II in the state $|i\rangle$, and $|\langle i|S^{I,II}_{100}|f\rangle|^2$ is the transition probability between states $|i\rangle$ and $|f\rangle$ for the microwave magnetic field parallel to [100] with

$$\begin{aligned} &|\langle 1/2|S^{I}_{100}|-1/2\rangle|^2 = 9/4 \\ &|\langle 3/2|S^{II}_{100}|-3/2\rangle|^2 = 4{\cdot}4 \text{ (see Ref. [35])} \end{aligned} \tag{12}$$

a value $N_{II}/N_I = 0{\cdot}3 \pm 0{\cdot}1$ was obtained. (13)

The anatase crystals were heated several times up to 650°C. No new EPR lines, e.g. due to rutile, could be observed and all results reported in this chapter remained unchanged.

6. DISCUSSION

If Fe^{3+} substitutes for Ti^{4+} in anatase one expects a single paramagnetic spectrum with tetragonal symmetry along the [001]-axis. Spectrum I is interpreted as resulting from such a center. From the symmetry of the spectrum it is also possible that the Fe^{3+} ions are at interstitial sites such as I of Fig. 1. However, this would generate a strong local charge inequality. In addition, in rutile one observes paramagnetic impurities in interstitial sites, which have different symmetry axes than the substitutional sites, only if the paramagnetic impurities are too large to enter the substitutional site[2]. The Fe^{3+} ion is, however, smaller than Ti^{4+}.

There exist two main differences between the EPR spectra of substitutional Fe^{3+} in anatase and rutile[36, 37]: the zero splitting is much smaller in anatase and is strongly sensitive to temperature which is not the case in rutile.

According to Fig. 2, b_4^0 decreases 12·5 per cent by increasing the temperature 500°C. This can be explained with the implicit term of Walsh[31] as given in (10) if an increase in the interionic distance of 0·6 per cent is used. This is consistent with the increase of the lattice parameter c as measured by Rao[13]. According to (10) b_2^0 ($= D$) should increase with temperature. As a strong decrease of b_2^0 with temperature is observed, this cannot be explained by the lattice expansion.

Assuming a point charge model for anatase the lattice sums B_2^0 and $(B_4^0)'$ as defined by (8) and (9) were calculated with a computer programme. The oxygen parameter u (see

Fig. 1) was used as a variable. The results are given in Fig. 5. The crystal field was found to be very sensitive to small changes in u. An increase of u from 0·413 Å (its value at room temperature) to 0·452 Å decreases B_2^0 from 154×10^{-4} $e^2/2a_0^3$ to zero and $(B_4^0)'$ from $+4{\cdot}2\times10^{-4}$ to $-7{\cdot}3\times10^{-4}$ $e^2/2a_0^5$. Therefore it was concluded that the temperature dependence of b_2^0 is produced by a change in the equilibrium position of the oxygen ions. Also in support of this argument is the temperature dependent orientation of the magnetic axes of the spectra II as will be discussed below.

This shift of the oxygen ions does not change the symmetry of the crystal and changes essentially only the bond angles and not the bond lengths between a Ti^{4+} ion and its four nearest oxygen ions. In rutile this is not possible: there, a change of the oxygen parameter affects directly the nearest neighbour Ti^{4+}–O^{2-} distance and hence explains the absence of the temperature dependence of the EPR spectra in rutile.

An attempt to correlate the measured value of D using (7), with the calculated B_2^0 and $(B_4^0)'$ failed, however completely. As the numerical factors in (7) were calculated for Mn^{2+} they will not apply exactly in our case, but the same order of magnitude would be expected for Fe^{3+}. One possible explanation for this discrepancy is the high polarisibility of anatase, this would result in a deformation of the neighbouring oxygen ions and a change of their positions when replacing Ti^{4+} by the smaller charge of Fe^{3+}. This discrepancy exists also in rutile, where a point charge calculation gives $B_2^0=-45\times10^{-4}$ $e^2/2a_0^3$, $(B_4^0)'=-251\times10^{-4}$ $e^2/2a_0^5$, with the z axis parallel to [110].

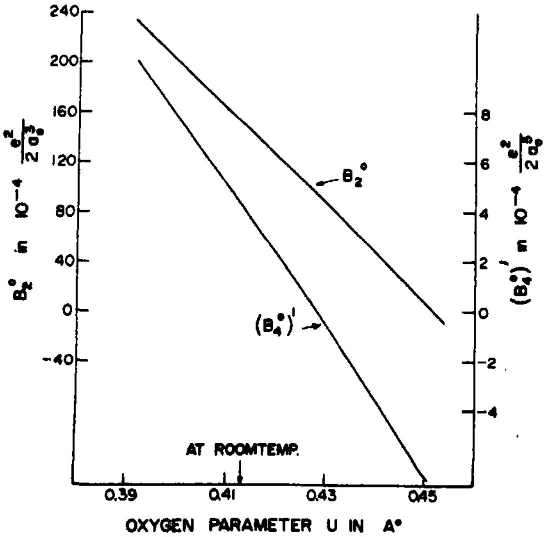

Fig. 5. Lattice sums B_2^0 and $(B_4^0)'$, calculated with a point charge model for anatase, as a function of the oxygen parameter u.

The most reasonable explanation of the spectra II is that Fe^{3+} replaces a Ti^{4+} ion and has an oxygen vacancy at a nearest neighbour site. This explains the four spectra II (vacancies at A–D of Fig. 1), their symmetries and the directions of their magnetic axes.

Similar EPR spectra of charge compensated Fe^{3+} have been observed in other crystal, e.g. $SrTiO_3$[38] which has the same basic structural blocks TiO_6 octahedra. In fact, there exists a great similarity between the EPR spectra of Fe^{3+} in anatase and in the tetragonal low temperature phase of $SrTiO_3$: b_2^0 of normal substitutional Fe^{3+} in $SrTiO_3$ is also strongly temperature dependent and the temperature dependent shift of the oxygen ions in $SrTiO_3$ could also be detected by a rotation of the axes of the charge compensated Fe^{3+} centers[39]. In rutile weak EPR spectra of charge compensated Cr^{3+}[40] and Co^{2+} [41] have been observed, however, not of Fe^{3+}.

From symmetry alone, it is possible that the oxygen vacancies are located one lattice distance farther in the same directions, it seems, however, unlikely that this could produce the large value of the crystal field at the Fe^{3+} site necessary to give the observed zero field splitting.

An interpretation of the temperature dependence of b_2^0 of spectrum I is a shift of the oxygen ions. This would imply that the axes of the crystal field of the charge compensated center should shift with temperature. An increase of u should increase φ and for $u=0$

one expects $\varphi = 0$. Lowering the temperature should therefore result in a decrease of φ. This decrease of φ with temperature was observed as shown in Table 2.

At room temperature we can empirically relate φ with the known value of α, the angle between the Ti^{4+}–O^{2-} bond and the (001)-plane:

$$\varphi = 0{\cdot}502\alpha.$$

If this relation remains valid also for other α, we get at 77°K: $\alpha_{77°} = 12{\cdot}26°$. This means that the oxygen parameter u should decrease from 0·413 to 0·401 Å by lowering the temperature from 300 to 78°K.

There remains the question as to why the charge compensation occurs only at the four oxygen ions A–D and not at E or F of Fig. 1. From symmetry one should expect that the magnetic axes of these latter paramagnetic centers coincide with the crystal axes and that the rhombic term (b_2^2) be relatively small. It is possible that the weaker lines which could not be identified would account for these paramagnetic centers.

Note added in proof:

(1) Since submission of this manuscript the temperature dependence of spectrum I has been measured up to 1230°K, where $b_2^{\circ} = -225 \times 10^{-4}\,\mathrm{cm}^{-1}$.

(2) The linewidths of the outer fine structure lines of spectrum I are very angular dependent. With H rotated in the (001)-plane, these lines are narrow when H is parallel to [110] but are poorly resolved with H parallel to [100]. This effect, which cannot be explained with a mosaic structure of the crystal, increases with increasing temperature.

Acknowledgements—The authors wish to thank the Ford Foundation and the Universidad Nacional de Ingenieria, Lima, Peru for the award of a fellowship to one of them (M.H.).

REFERENCES

1. SIMONS P. and DACHILLE F., *Acta crystallogr.* **22**, 334 (1967).
2. GERRITSEN H. J., In *Proceed. of 1st International Conference on Paramagnetic Resonance* (Edited by W. Low), Vol. 1, p. 3. Jerusalem (1962).
3. LOW W. and OFFENBACHER E. L., In *Solid State Physics* (Edited by F. Seitz and D. Turnball), Vol. 17, p. 135. Academic Press, New York (1965).
4. CZANDERNA A., CLIFFORD A. and HONIG J., *J. Am. chem. Soc.* **79**, 5407 (1957).
5. BACH H., *Naturwiss.* **51**, 10 (1964).
6. BARRY T. I., *Solid State Commun.* **4**, 123 (1966).
7. CHE M., GRAVELLE P. and MERIAUDEAU P., *C. R. Acad. Sci. Paris* **268C**, 768 (1969).
8. MERIAUDEAU P., CHE M. and JORGENSEN C., *Chem. Phys. Lett.* **5**, 131 (1970).
9. HAUSER C. and CORNAZ P., *Chem. Phys. Lett.* **5**, 226 (1970).
10. GAINON D. and LACROIX P., *Proc. Phys. Soc. Lond.* **79**, 658 (1962).
11. HORN M. and SCHWERDTFEGER C. F., *Solid State Commun.* **8**, 1741 (1970).
12. CROMER D. and HERRINGTON K., *J. Am. chem. Soc.* **77**, 4708 (1955).
13. RAO K. V., NAIDU N. and IYENGAR L., *J. Am. ceram. Soc.* **53**, 124 (1970).
14. NAVROTSKY A. and KLEPPA O. J., *J. Am. ceram. Soc.* **50**, 626 (1967).
15. SHANNON R. and PASK J., *J. Am. ceram. Soc.* **48**, 391 (1965).
16. SHANNON R., *J. appl. Phys.* **35**, 3414 (1964).
17. CZANDERNA A., RAO C. and HONIG J., *Trans. Faraday Soc.* **54**, 1069 (1958).
18. RAO C., *Can. J. Phys.* **39**, 498 (1961).
19. YOGANARASIMHAN S. and RAO C., *Trans. Faraday Soc.* **58**, 1579 (1962).
20. ABRAGAM A. and BLEANEY B., *EPR of Transition Ions*, p. 371, 667, Clarendon Press, Oxford (1970).
21. ORBACH R., *Proc. R. Soc. London* **264A**, 458 (1961).
22. VINOKUROV V. M., ZARIPOV M. M. and STEPANOV V. G., *Soviet Phys. solid State* **6**, 866 (1964).
23. VINOKUROV V. M., ZARIPOV M. M., and SEPANOV V. G., *Soviet Phys. solid State* **6**, 870 (1964).
24. THYER J. R., QUICK S. M., and HOLUJ F., *Can. J. Phys.* **45**, 3597 (1967).
25. TROUP G. J. and HUTTON D. R., *Brit. J. appl. Phys.* **15**, 1493 (1964).
26. SHARMA R., DAS T. and ORBACH R., *Phys. Rev.* **149**, 257 (1966).
27. SHARMA R., DAS T. and ORBACH R., *Phys. Rev.* **155**, 338 (1967).
28. SHARMA R., DAS T. and ORBACH R., *Phys. Rev.* **171**, 378 (1968).
29. HEUVELEN A. VAN., *J. chem. Phys.* **46**, 4903 (1967).
30. JA Y. H., *Australian J. Phys.* **23**, 299 (1970).
31. WALSH W., JEENER J. and BLOEMBERGEN N., *Phys. Rev.* **139**, A133 , (1965).
32. HORN M. and SCHWERDTFEGER C. F., *Rev. Scient. Instrum.* **42**, 880 (1971).
33. AASA R., *J. chem. Phys.* **52**, 3919 (1970).
34. BYFLEET C., CHONG D., HEBDEN J. and MCDOWELL C., *J. Mag. Res.* **2**, 69 (1970).
35. HOLUJ F., *Can. J. Phys.* **44**, 503 (1966).
36. LICHTENGERGER G. J. and ADDISON J. R., *Phys. Rev.* **184**, 381 (1969).

37. CARTER D. and OKAYA A., *Phys. Rev.* **118**, 1485 (1960).
38. KIRPATRICK E. S., MULLER K. A. and RUBINS R. S., *Phys. Rev.* **135**, A86 (1964).
39. MULLER K. and BERLINGER W., *Phys. Rev. Lett.* **26**, 13 (1971) and references quoted therein.
40. IKEBE M., MIYAKO Y. and DATE M., *J. phys. Soc. Japan.* **26**, 43 (1969).
41. MIYAKO Y., *Phys. Lett.* **24A**, 635 (1967).

J. Phys. Chem. Solids, 1971, Vol. 32, pp. 2539–2544. Pergamon Press. Printed in Great Britain

THERMAL PROPERTIES OF ALKALI METALS FROM STATIC AND DYNAMIC COMPRESSIBILITIES*

R. GROVER
Lawrence Radiation Laboratory, University of California, Livermore, Calif. 94550, U.S.A.

(*Received* 1 *February* 1971)

Abstract—A detailed comparison of the isothermal compression data of Vaidya *et al.* on the alkali metals in the preceding article is made with high temperature shock compression data. The comparison provides evidence for strong electronic *d*-band effects in the equation of state of Rb at high temperatures at pressures as low as 50 kbar.

1. INTRODUCTION

IN PREVIOUS work,[1],[2] it has been shown that for most metals there is excellent agreement between recent static compressibility data up to 45 kbar and dynamic compressibility data interpolated between shock velocity measurements at high pressure ($\gtrsim$ 100 kbar) and sonic velocity data at low pressures ($\lesssim$ 10 kbar). Apparently, agreement between static and dynamic data can be expected when shock velocity data extrapolates at low pressure closely to the measured sound velocity for the same phase and when irreversible heating accompanying shock compression is small.

In the immediately preceding paper by Vaidya, Getting and Kennedy (hereafter referred to as I), in which compressibility data for four highly compressible alkali metals is presented, the agreement with shock compression data is uneven. The disagreement is however, considerably less than the previously noted disagreement with various sets of Bridgman data[3]. In this paper the disagreement with shock data is attributed to the unusually low values of thermal pressure in the heavier alkali metals. An explanation of this behavior in terms of the influence of electric *d*-bands in the heavier alkali metal will be discussed as well as the possibility of confirming this explanation by additional shock wave data at very low pressures. Al'tshuler and Bakanova[4] have been led to similar conclusions by a study of the systematics of shock compressibility data for the metals in the periodic table which exhibit phase transitions.

2. COMPARISON OF STATIC AND DYNAMIC DATA

A graphical comparison of static and shock compression data is given in Fig. 1. The shock Hugoniot data extends down to pressures in the vicinity of 50 kbar while static isothermal data reaches up to about the same pressure. Extensions of the static isotherm above 45 kbar according to the preferred modified Murnaghan fit given in I are shown as dashed lines. The Hugoniot data of Rice as recently renormalized by the LASL group[5] has been extended to zero pressure by dashed lines for the purposes of comparing with the static data. The Hugoniot will normally lie above the isotherm due to the higher temperatures which arise from irreversible heating during shock compression. The two sets of data for Li are seen to be close to each other as is typically the case for metals of normal compressibility when shock heating is small [2]. As noted in I, the Hugoniot data for Na and K lies above the isothermal data by a reasonable amount, due to the thermal pressure generated by shock compression.

---

*Work performed under the auspices of the U.S. Atomic Energy Commission.

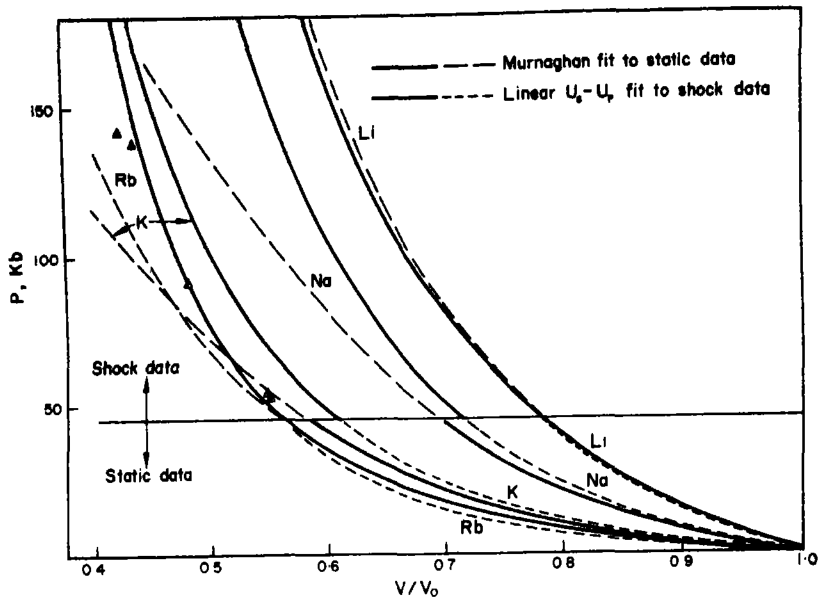

Fig. 1. Fits to static, isothermal and shock Hugoniot compression data. Δ-individual Hugoniot points for Rb.

Table 1. *Summary comparison of metal bulk modulus data and Gruneisen* γ. (*st*) *indicates quantities derived from static data,* (*so*) *from sonic velocity data and* (*sh*) *from shock data. Listed moduli are in units of kilobars.* $B' \equiv \mathrm{d}B/\mathrm{d}P$

Metal	γ_G^*	B_T	$B_s(st)$	$B_s(so)$	$B_s(sh)$	$B'_T(st)$	$B'_s(so)$	$B'_s(sh)$
Li	0·91	118·4	123·0	117·0	112·0	3·33	–	3·62
Na	1·16	61·2† (59·9)	64·3	65–69	63·6	3·68† (3·97)	3·6–3·7	3·97
K	1·32	31·4	34·4	33·8	32·0	3·63	3·98	3·75
Rb	1·42	26·2	29·2	(24–26)‡	21·4	3·39	(3·63)‡	3·93

*Calculated from tabulations of thermal expansion data in Handbook of Physics (American Institute of Physics, 1963) and specific heat data in *Selected Thermodynamic Properties of Metals and Alloys*, R. Hultgren, R. L. Orr, P. D. Anderson and K. K. Kelly (J. Wiley, New York, 1963) and Supplements.

†For Na, an average of two MME fits listed in Table 9 of 1 have been used instead of the combined fit shown in parentheses.

‡Extrapolated from data below 200°K.

In contrast, however, the extrapolated Hugoniot of Rb is considerably below the static isotherm below 45 kbar.

In order to evaluate this comparison, various sets of data on the initial adiabatic compressibility of these alkali metals are summarized in Table 1. The isothermal compressibility determined from best fits to static data are listed and converted to adiabatic bulk moduli with the use of the listed values of Gruneisen's γ_G. The listed value of γ_G, in turn, were made consistent with the static isothermal modulus, since these isothermal moduli are probably the most reliable of the available data. The listed bulk moduli obtained from room-temperature sonic velocity measurements in the alkali metal show a larger spread of values than is usual in metals, presumably because of the difficulty in measuring shear wave velocities near the melting temperature of a metal (see I for reference to sonic data). This problem is particularly severe for Rb in which shear wave have only been measured below 200°K. The shock data listed is obtained in the usual way[2] from a linear fit to shock velocity measurements.

For Na and K there is an acceptable, if somewhat poorer, agreement between sonic and shock moduli in view of the spread of the sonic data for Na. The static moduli reported in I are also consistent. In Li there is a larger discrepancy between shock and sonic data and a comparable spread between the shock data listed and two other available sets of shock wave data[6]. However, because of the smallness of the thermal corrections and the larger uncertainty in this low pressure data on Li, we shall not attempt to resolve these discrepancies. A much larger discrepancy exists between the extrapolation adiabatic modulus of Rb from shock data and the statically measured value. The sonic values extrapolated from low temperature data also indicate that the shock modulus is too small. In as much as the static modulus was measured to be the same in two very different static apparati in I, and is the only one of the three types directly measured, we must assume the static modulus to be correct. The larger disagreements between various measured values of the pressure derivatives of the bulk modulus, the B' in Table 1, are typical of the differences for normal metals[2].

The implication of the Rb discrepancy is that the extrapolation of shock data to zero pressure is incorrect in this case. The lowest shock data points for Rb which are shown in Fig. 1 also appear to deviate systematically from the single linear fit which is made to the entire range of the Rb shock data. For this reason, the initial compressibility data of I has been transformed into the shock-particle velocity plane (i.e., the $U_s - U_p$ plane) and is shown together with shock data points in Fig. 2. A best fit to this data is clearly a non-linear $U_s - U_p$ relation. It would be desirable to confirm this non-linearity by further shock velocity measurements at low pressure.

The upward curvature of the $U_s - U_p$ relation is only observed for metals in which there is a presumed change in electronic band structure. These effects have been discussed by Royce[7] as well as in [4]. In the latter reference, the authors actually included Rb in their collection of metals exhibiting electronic phase changes along the Hugoniot on the basis of an indication of a small amount of curvature in the original $U_s - U_p$ data on Rb.

3. DETERMINATION OF GRUNEISEN γ_G, FROM COMPRESSION DATA

By a simple subtraction at fixed volume it is possible to obtain an approximate average Gruneisen coefficient, $\bar{\gamma}_G$ between the

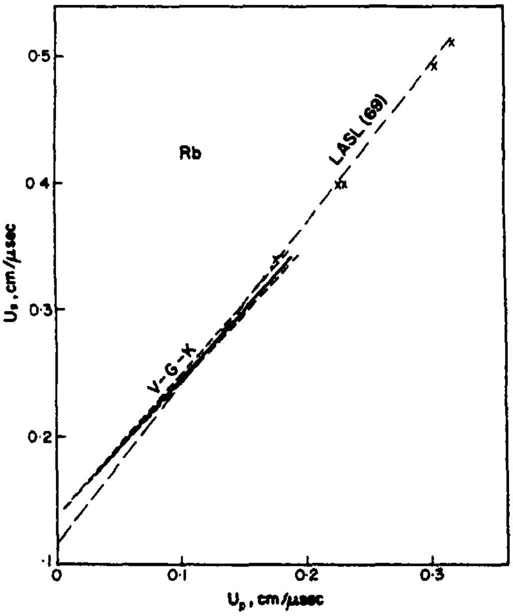

Fig. 2. Compression data in the shock velocity U-particle velocity U_p plane for Rb. x-individual shock points and fit from Ref.[5]. V-G-K-fits to static data from I.

Hugoniot and the static isotherm. The average $\bar{\gamma}_G$ is determined from Hugoniot and isothermal pressures, P_H and P_{T_0}, and internal energies, E_H and E_{T_0} according to

$$\bar{\gamma}_G(V) \equiv \frac{V[P_H(V)-P_{T_0}(V)]}{E_H(V)-E_{T_0}(V)}. \qquad (1)$$

$P_H(V)$ and $E_H(V)$ can be calculated directly from measured shock velocities by standard conservation equations. $E_{T_0}(V)$ can be calculated from $P_{T_0}(V)$ if the Mie-Gruneisen equation-of-state is assumed for the solid.

$$E_{T_0}(V) = \int_V^{V_0} P_0(V)dV - 3RT_0\int_V^{V_0} \gamma_G(V)\frac{dV}{V}. \qquad (2)$$

In principle $\gamma_G(V)$ can be calculated from compressibility data in the solid phase by an iterative solution of equations (2) and (1). However, at larger compressions the contribution of the second term in the right hand side of (2) becomes small and the solution is considerably simplified by making an approximate guess for $\gamma_G(V)$ in the integral. On the other hand at small compressions equations (1) and (2) are equivalent to determining $\gamma_G(V)$ from the difference between the initial adiabatic and isothermal bulk moduli. Clearly the moduli in Table 1 are not sufficiently reliable. For this reason we have used, as a first guess, a γ_G equal to its initial value (see Table 1) in equation (2) in order to calculate a γ_G at maximum compression from equation (1). A constant γ equal to the average of these two was then used in (2) to evaluate the final $\gamma_G(V)$ by equation (1). The resulting $\gamma_G(V)$ for Na and K over a restricted range of high densities is shown in Fig. 3. For Rb the necessary shock data below 45 kbar is unavailable as argued above. Therefore, a calculation of γ_G at the lowest shock points around 54 kbar (see Fig. 1) was done ignoring the second term of equation (2) giving a $\gamma_G \sim 0{\cdot}25$. The uncertainty even at large compression in the calculated γ_G for Na and K are large, $\sim \pm 20$ per cent, due to the subtraction of pressure and energy data in equation (1).

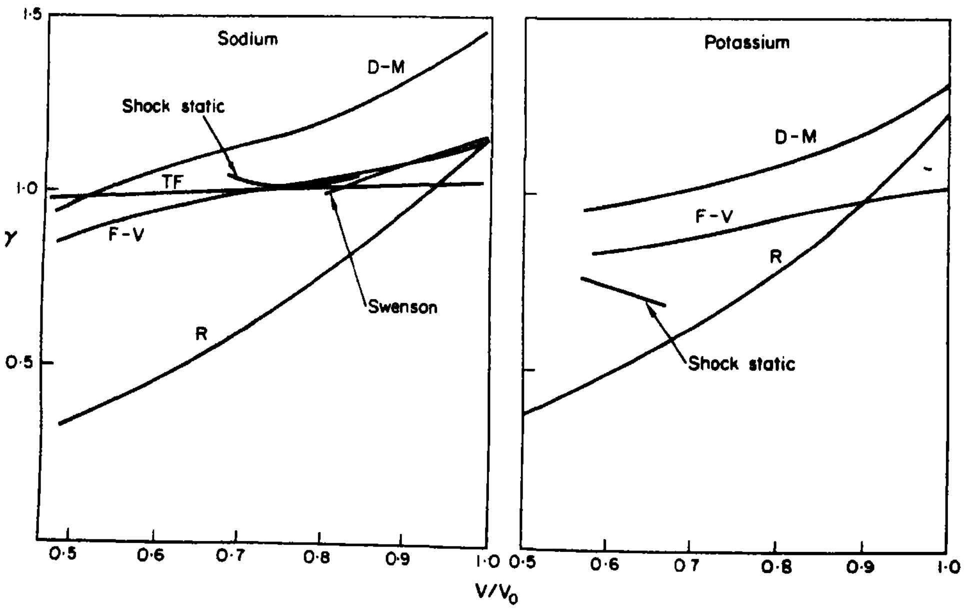

Fig. 3. Comparison of shock-static values of the Gruneisen coefficient with theoretical estimates discussed in Ref. [3].

For Rb the uncertainty of the estimated γ_G is even larger because of the closeness of the Hugoniot point to the static isotherm.

The average values of γ_G calculated above are averages at a fixed density over a range of temperatures in the solid, solid–liquid two phase and a portion of the liquid phase. For the simpler metals in which the electronic contributions to thermal properties are not too large, this averaged γ is not expected to differ by more than 20 per cent from the value of γ_G in the solid phase of the same density. However, the large and temperature dependent electronic effects which appear to be responsible for the small Gruneisen coefficient in the Rb data at high temperature do not permit us to determine γ_G for *solid* Rb.

The calculation values of γ_G for Na are seen in Fig. 3 to be reasonable agreement with other theoretical estimates (see Ref.[3] for review of these) and the data of Swenson. The calculated values for K and Rb at higher compressions are increasingly smaller than conventional estimates which deal primarily with the contributions of the motions of the atomic centers to the thermal equation of state.

4. *d*-BAND ELECTRONIC EXCITATIONS IN Rb AND K

The 5*d*-electron band has well-known effects in the heaviest alkali metal, Cs. An electronic phase transition which occurs around 45 kbar without a change in crystal structure has been shown by Sternheimer[8] to be due to the transfer of the outer 6*s*-electron to an inner 5*d*-electron shell. The corresponding transition in Rb should occur above 100 kbar according to theoretical estimates[8]. In Cs the transition occurs in the solid at high compression because of the elevation of the 6*s*-band energy level and the broadening of the 5*d*-band with compression. This transition is anticipated at a lower pressure (~ 25 kbar) by a maximum in the pressure dependence of the melting temperature. A similar maximum in the melting temperature curve of K and Rb has apparently been observed by Ref.[9] in the vicinity of 80 kbar. Scaling the phase transition to the maximum of the melting curve as in Cs results in a solid phase transition ~ 150 kbar for Rb and K.

Although the pressures are considerably less in the region under discussion, the proximity of inner *d*-band energy levels to the valence *s*-band can strongly affect the thermal properties at lower pressures. For instance, there are several ways in which the thermal excitation energy of electrons E_e can produce an abnormally small electron pressure P_e, i.e., the effective electronic Gruneisen coefficient, $\gamma_e = V(\partial P_e/dE_e)_V$ will be small. First of all, a part of this coefficient is proportional to the rate of change with specific volume of the density of electronic states in energy, $d\sigma_E/dV$, at the Fermi level. When the temperature is high enough to excite an appreciable number of electrons into the *d*-band $d\sigma_E/dV$ becomes negative reducing γ_e in magnitude. A second, related effect discovered by Ross[10] in the high temperature properties of X_e may be also operative here. Ross found that from simple thermodynamic arguments, that if the bottom of the excited bands decrease in energy with compression, the electronic pressure can also be considerably reduced at high temperature. Finally, a self-consistent, Hartree–Fock solution for electron-energy levels at high temperature may lead to a considerable rearrangement of the *d*- and *s*-band energy levels making a Cs-like transition possible at lower densities. This possibility arises from the fact that when excited *s*-electrons transfer to an inner *d* level they increase the shielding of the valence outer *s* band and thus raise its energy levels which in turn makes more likely the further transfer of electrons to the *d* band. This effect must make the metal softer at higher temperatures since the *d*-bands are smaller in radius and therefore effectively reduce the Gruneisen coefficient. If this effect occurs in the liquid phase the 'transition' can be expected to be smeared over a range of temperature and densities.

The reduction of γ_G with increasing temperature by any of the above mechanisms can explain the different behavior of γ in Rb and K. Rough estimates of the shock heating in[3] indicate that Rb is ~ 50 per cent hotter than K at shock pressures ~ 50 kbar. This large a difference in shock heating arises from the larger compressibility of Rb and its smaller specific heat. The apparent similarity of the $U_s - U_p$ data on Rb with the shock data in the rare earths[4] suggests furthermore, that the third, Hartree–Fock explanation above for a low γ is most correct. A more definite answer would be given by a detailed band theory calculation.

Acknowledgements—It is a pleasure to thank Professor G. C. Kennedy and his group for cooperation in evaluating the compressibility data and to Dr. M. Ross for discussions of their interpretation. Appreciation is also due Dr. R. McQueen and the GMX-6 group at LASL for supplying their renormalized data on the alkali metals.

REFERENCES

1. VAIDYA S. N. and KENNEDY G. C., *J. Phys. Chem. Solids* **31**, 2329 (1970).
2. GROVER R., *J. Phys. Chem. Solids* **31**, 2347 (1970).
3. GROVER R., KEELER R. N., ROGERS F. J. and KENNEDY G. C., *J. Phys. Chem. Solids* **30**, 2091 (1969).
4. AL'TSHULER L. V. and BAKANOVA A. A., *Soviet Phys. Usp.* **11**, 678 (1969).
5. GMX-6 Group, Los Alamos Sci. Lab., LA-4167-MS (1969) unpublished.
6. *Compendium of Shock Wave Data* Vols. 1 and 2 (UCRL-50108, 1966, plus Supplement 1967). (Edited by M. van Thiel and A. S. Kusubov.) Available from Clearinghouse for Federal and Technical Information, NBS, U.S. Dept. of Commerce, Springfield, Va. 22151.
7. ROYCE E. B. in *XLVII Course on Physics of High Energy Density* at International School of Physics "Enrico Fermi", Varenna, Italy 1969 (to be published) (also UCRL-71846 unpublished).
8. STERNHEIMER R., *Phys. Rev.* **78**, 235 (1950). ROSS, M. private communication.
9. LUEDEMANN H. D. and KENNEDY G. C., *J. geophys. Res.* **73**, 2795 (1968).
10. ROSS M., *Phys. Rev.* **171**, 777 (1968).

J. Phys. Chem. Solids, 1971, Vol. 32, pp. 2545–2556. Pergamon Press. Printed in Great Britain

THE COMPRESSION OF THE ALKALI METALS TO 45 KBAR*

S. N. VAIDYA, I. C. GETTING and G. C. KENNEDY
Institute of Geophysics and Planetary Physics, University of California, Los Angeles,
Calif. 90024, U.S.A.

(*Received* 10 *September* 1970; *in revised form* 8 *January* 1971)

Abstract—The volume compressions of lithium, sodium, potassium, and rubidium, have been determined in a piston cylinder apparatus to 45 kbars pressure. The results are at considerable variance with Bridgman's 1948 measurements. The bulk moduli and some of their pressure derivatives have been estimated by fitting a Murnaghan equation to the pressure volume data, and the results are compared with values obtained from ultrasonic measurements. The static compressions have also been compared with isothermal compressions calculated from the shock Hugoniot measurements.

1. INTRODUCTION

DETAILED measurements of the volume compressions of the alkali metals and many other solids were reported by Bridgman over a period of three decades. His early measurements on lithium, sodium, and potassium are quite consistent with those reported later, but there is a marked difference between earlier and later measurements on rubidium [1–4].

Swenson in 1955 measured the volumes of the alkali metals at liquid helium temperature up to 10 kbar pressure in a piston cylinder apparatus [5]. Experimental iostherms up to 20 kbar, ranging from liquid helium temperature to circa 350°K, have subsequently been reported by Swenson and his collaborators in lithium[6], sodium[7] and potassium [8].

Measurements of ultrasonic wave velocities along crystallographic directions in single crystal specimens of sodium, potassium, and rubidium[9–12] have been made in the low pressure range. These measurements give the low pressure bulk modulus and its pressure derivatives, adequate to formulate the low pressure P–V relations of these solids. Compressions have also been estimated from the measured shock wave and particle velocities. Rice[13] has reduced the shock Hugoniot pressures to isotherms assuming a particular variation of Gruneisen's parameter with the volume of the compressed solid. Keeler[14] and Grover *et al.*[15] using the Dugdale–MacDonald equation of state have also reduced the shock wave data. These reductions give results on volume compressions markedly different from each other and from Bridgman's results. The discrepancies between Bridgman's data and the data points calculated from shock studies seem to lie outside the limits of error involved. Grover *et al.*[15] concluded that the static measurements were responsible for the discrepancy. The measurements reported in this paper were undertaken to resolve the question.

2. EXPERIMENTAL METHOD

The data on alkali metal compression were obtained from piston displacement measurements in an end-loaded piston-cylinder apparatus. The apparatus and techniques have been previously described[16]. As in the earlier investigations our pressure chambers are of 883 grade Carboloy with 6 per cent cobalt bonder, and the pistons are of grade 999 Carboloy with 3 per cent cobalt bonder.

---

*Publication # 875 Institute of Geophysics and Planetary Physics, University of California, Los Angeles 90024.

Incidental to the work in these experiments it was noted that the life of our pressure vessels was short, apparently owing to the tendency of the alkali metals at high pressures to penetrate small microscopic cracks in the tungsten carbide. Lithium and rubidium seemed particularly deleterious. A number of runs during the course of these experiments had to be discarded owing to the failure of the pressure vessel.

The arrangement of the sample inside the pressure vessel is shown in Fig. 1. The alkali metal charge was retained by cups of aluminum alloy 6061-T6. The compressibility of this alloy has been previously determined and enters as a small correction in the final results[16]. The weight of the cups was approximately 0·11 g. The cups were backed by pyrophyllite mitre rings which serve to seal the contents in the assembly. In no case did we observe any reaction between the alkali metal and the aluminum cups.

The sample of the alkali metal was compacted in a small jig under mineral oil. The sample was then removed from the jig and the mineral oil washed off with dehydrated hexane. This sample was then quickly transferred to the pressure vessel. The aluminum cups, pyrophyllite mitre rings, and steel shims were weighed before the run was assembled.

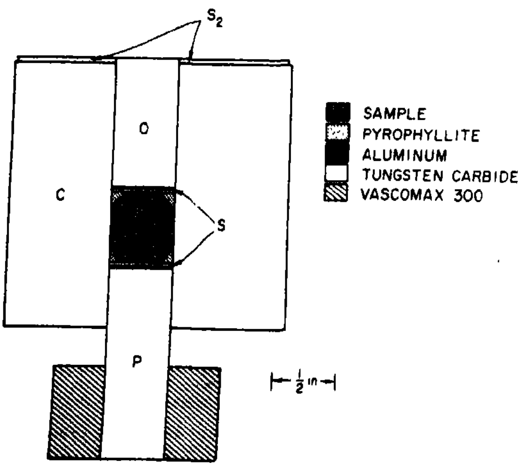

Fig. 1. Sample assembly.

After the experiment the entire contents of the pressure vessel were weighed and the weight of the sample was determined by the difference. The initial volume was then calculated by dividing the weight of the sample by the X-ray density.

3. DATA ANALYSIS

Experimenters tend to analyze their data in forms most convenient to the measurements they make. For example, Bridgman, who measured pressure and volume, expanded the expression, $\Delta V/V_0$, as a polynomial in pressure. Similarly, those who work with the shock wave equation of state and those who measure sound speed as a function of pressure find it most convenient to express their results in terms of the adiabatic bulk modulus.

Bridgman, who measured pressure and volume, found that most materials were adequately represented by an equation quadratic in pressure. Attempts to fit a polynomial to the data in Tables 1–4 show that such a representation is quite inadequate. The polynomial of the form

$$(V_0-V)/V_0 = aP+bP^2+cP^3+dP^4$$

$$+eP^5+fP^6+\cdots$$

does not fit the data until terms of fourth, fifth, or even the sixth power of pressure are included (Table 10). Further, as Gilvarry [17] has noted, the coefficient of the first order term, which determines the isothermal bulk modulus at zero pressure, varies as the number of terms in the series is changed. The derivation of the Slater equation for the Gruneisen gamma is based on the assumption that compression is adequately described by a polynomial quadratic in pressure. This equation is therefore inadequate to represent the Gruneisen gamma for materials such as the alkali metals. Thus, for lithium, sodium, potassium, and rubidium, a polynomial analysis, and the equation of state parameters derived from it, are unsatisfactory.

Table 1. *(V/V_0) of lithium from the compressibility experiments and the values calculated from the Murnaghan equation (ME) fit to the experimental data.* $\rho = 0{\cdot}533$ g/cc

Pressure (kb)	I Observed values	I Calculated values ME	II Observed values	II Calculated values ME
0	1·0000	1·0000	1·0000	1·0000
5	0·9610	0·9617	0·9611	0·9607
10	0·9285	0·9289	0·9281	0·9275
15	0·9011	0·9004	0·8994	0·8988
20	0·8756	0·8754	0·8738	0·8737
25	0·8526	0·8530	0·8518	0·8514
30	0·8333	0·8329	0·8313	0·8315
35	0·8141	0·8146	0·8123	0·8135
40	0·7983	0·7980	0·7966	0·7970
45			0·7829	0·7820
B_T (kbar)		119·97		116·38
B'_T		3·262		3·441
Standard deviation of V/V_0		0·0006		0·0008

Table 2. *(V/V_0) os sodium from the compressibility experiments and the values calculated from Murnaghan equation (ME) and the modified Murnaghan equation (MME) fit to the experimental data.* $\rho = 0{\cdot}97$ g/cc

Pressure (kb)	I Observed values	I Calculated values ME&MME	II Observed values	II Calculated values ME	II Calculated values NME
0	1·0000	1·0000	1·0000	1·0000	1·0000
5	0·9309	0·9308	0·9312	0·9324	0·9312
10	0·8781	0·8791	0·8795	0·8809	0·8799
15	0·8388	0·8384	0·8394	0·8397	0·8392
20	0·8054	0·8051	0·8058	0·8057	0·8057
25	0·7775	0·7771	0·7775	0·7769	0·7772
30	0·7528	0·7531	0·7524	0·7521	0·7525
35	0·7318	0·7321	0·7305	0·7304	0·7307
40	0·7138	0·7136	0·7113	0·7111	0·7111
45			0·6934	0·6938	0·6934
B_T (kbar^{-1})		61·14		63·50	61·34
B'		3·569		3·295	3·714
T					
B''_T (kbar^{-1})		0·000		0·000	−0·02286
Standard deviation of V/V_0		0·0006		0·0008	0·0002

Table 3. (V/V_0) of potassium from compressibility experiments and the values calculated from the Murnaghan equation (ME) and modified Murnaghan equation (MME) of the experimental data. $\rho = 0{\cdot}862$ g/cc

	I			II		
Pressure (kb)	Observed values	Calculated values ME	Calculated values MME	Observed values	Calculated values ME	Calculated values MME
0	1·0000	1·0000	1·0000	1·0000	1·0000	1·0000
5	0·8809	0·8852	0·8810	0·8809	0·8854	0·8827
10	0·8073	0·8100	0·8074	0·8087	0·8098	0·8079
15	0·7550	0·7553	0·7546	0·7537	0·7546	0·7538
20	0·7132	0·7130	0·7136	0·7118	0·7118	0·7119
25	0·6801	0·6789	0·6799	0·6784	0·6773	0·6778
30	0·6514	0·6505	0·6515	0·6490	0·6486	0·6492
35	0·6268	0·6264	0·6267	0·6243	0·6241	0·6246
40	0·6047	0·6056	0·6047	0·6032	0·6030	0·6030
45				0·5839	0·5844	0·5839
B_T (kbar)		33·87	31·02		34·13	32·35
B_T'		3·036	3·733		2·959	3·351
B_T'' (kbar^{-1})		0·000	−0·04400		0·000	−0·02221
Standard deviation of V/V_0		0·0024	0·0003		0·0020	0·0009
		III			IV	
0	1·0000	1·0000	1·0000	1·0000	1·0000	1·0000
5	0·8808	0·8850	0·8815	0·8810	0·8850	0·8809
10	0·8072	0·8099	0·8080	0·8061	0·8093	0·8065
15	0·7558	0·7553	0·7552	0·7528	0·7541	0·7530
20	0·7146	0·7131	0·7140	0·7118	0·7114	0·7116
25	0·6800	0·6791	0·6801	0·6781	0·6769	0·6778
30	0·6505	0·6508	0·6512	0·6493	0·6482	0·6493
35	0·6264	0·6268	0·6260	0·6246	0·6238	0·6246
40				0·6024	0·6027	0·6028
45				0·5836	0·5842	0·5833
B_T (kbar)		33·77	31·11		33·95	31·27
B_T'		3·054	3 773		2·971	3·573
B_T'' (kbar^{-1})		0·000	−0·05118		0·000	−0·03436
Standard deviation of V/V_0		0·0026	0·0009		0·0023	0·0003

The Murnaghan equation, which is derived by integrating an equation, in which the bulk modulus is represented by a linear equation in pressure, gives a superior fit to the data points. If the isothermal bulk modulus as a function of pressure is given by $B_T(P) = B_T + B_T' . P$ then the pressure-volume relationship is given by the Murnaghan equation

$$P = \frac{B_T}{B_T'} \cdot \left\{ \left(\frac{V_0}{V} \right)^{B_T'} - 1 \right\}. \qquad (1)$$

Alternatively, if the quadratic term in the expression for the bulk modulus is included:

$$B_T(P) = B_T + B_T' . P + \tfrac{1}{2} B_T'' . P^2,$$

then the pressure-volume relationship is[18]

$$\frac{2B_T + (\sqrt{B_T'^2 - 2B_T B_T''} + B_T')P}{2B_T - (\sqrt{B_T'^2 - 2B_T B_T''} - B_T')P} = \left(\frac{V_0}{V} \right)^{\sqrt{B_T'^2 - 2B_T\ B_T''}}. \qquad (2)$$

This modified Murnaghan equation (2) and the standard Murnaghan equation (1) were fit to the pressure-volume data by the method of least squares. Minimization of the sum of

Table 4. (V/V_0) of rubidium from the compressibility experiments and the values calculated from the Murnaghan equation (ME) and modified Murnaghan equation (MME) fit of the experimental data. $\rho = 1{\cdot}53$ g/cc

	I			II					
Pressure (kb)	Observed values	Calculated values		Observed values	Calculated values		Original value	Calculated value	
		ME	MME		ME	MME		ME	MME
0	1·0000	1·0000	1·0000	1·0000	1·0000	1·0000			
5	0·8614	0·8668	0·8648	0·8618	0·8651	0·8623			
10	0·7843	0·7857	0·7844	0·7818	0·7834	0·7817			
15	0·7293	0·7289	0·7284	0·7261	0·7265	0·7258			
25	0·6523	0·6519	0·6523	0·6492	0·6494				
20	0·6865	0·6860	0·6861	0·6839	0·6835	0·6836			
25	0·6523	0·6519	0·6523	0·6492	0·6494	0·6499			
30	0·6248	0·6239	0·6244	0·6219	0·6214	0·6220			
35	0·6002	0·6003	0·6006	0·5987	0·5978	0·5983			
40	0·5796	0·5800	0·5801	0·5776	0·5776	0·5776			
45	0·5623	0·5623	0·5619	0·5594	0·5599	0·5594			
B_T (kbar)		27·72	26·67		27·25	25·86			
B_T'		3·140	3·392		3·143	3·476			
B_T' (kbar^{-1})		0·140	−0·01471		0·000	−0·01943			
Standard deviation of V/V_0		0·0023	0·0016		0·0016	0·0005			
	III*			IV			V		
0	1·0000	1·0000	1·0000	1·0000	1·0000	1·0000	1·000	1·0000	1·0000
5	0·8615	0·8636	0·8617	0·8615	0·8627	0·8619	0·8614	0·8646	0·8630
10	0·7812	0·7823	0·7812	0·7806	0·7809	0·7805	0·7813	0·7829	0·7820
15	0·7249	0·7261	0·7257	0·7244	0·7244	0·7242	0·7263	0·7261	0·7259
20	0·6840	0·6839	0·6840	0·6820	0·6819	0·6820	0·6842	0·6832	0·6835
25	0·6516	0·6505	0·6508	0·6483	0·6484	0·6485	0·6501	0·6493	0·6496
30	0·6237	0·6231	0·6234	0·6210	0·6208	0·6210	0·6212	0·6214	0·6217
35	0·6000	0·6000	0·6002	0·5978	0·5977	0·5978	0·5974	0·5979	0·5980
40	0·5795	0·5802	0·5802	0·5778	0·5778	0·5778	0·5778	0·5777	0·5774
45	0·5629	0·5629	0·5625	0·5602	0·5604	0·5603			
B_T (kbar)		26·57	25·65		26·40	26·04		27·06	26·20
B_T'		3·264	3·490		3·237	3·324		3·165	3·392
B_T'' (kbar^{-1})		0·000	−0·01325		0·000	−0·00510		0·000	−0·01482
Standard deviation of V/V_0		0·0012	0·0006		0·0005	0·0002		0·0017	0·0011

*Sample completely enclosed in aluminum double cups.

the squares of the deviations was accomplished by an iterative descent method described by Fletcher and Powell[19] and available in the IBM Scientific Subroutine Package program (FMFP).

Values of V/V_0 were determined relative to the volume-pressure relation for gold derived from ultrasonic measurements. The final accuracy of these determinations depends in a very slight way on the accuracy of the gold data as the absolute compressibility of gold is very small in comparison to that of the alkali metals. It is estimated that the accuracy of our measurements is not far different from their reproducibility, approximately ±0·0015 in V/V_0 at the highest pressure.

4. DISCUSSION OF RESULTS

A compilation of the various compression parameters from this and other works is presented in Table 9. Final values of V/V_0 calculated from the Murnaghan parameters determined in this work are shown in Tables 5–8. Bridgman's results of 1938 and 1948, Swenson's data, and the values reduced from shock Hugoniot, are also shown.

Lithium

Lithium metal of 99·5 per cent stated purity was obtained from the A. D. Mackay Co. Specimens of the required dimensions were cut under mineral oil and scraped to obtain a clean and shiny surface. The results are shown in Table 1. The final result is shown in Table 5 and in Fig. 2, and is compared with previous measurements. These results are in excellent agreement with Bridgman's determinations. However, Swenson's values and the value determined by Keeler from reduction of the shock Hugoniot are lower.

Sodium

Baker's analyzed reagent grade sodium of 99·995 per cent stated purity was used. Results of two individual runs are shown in Table 2. Final results and those of other workers are summarized in Table 6 and plotted in Fig. 3. These results agree to 1 per cent with Swenson's work and with the shock wave data, but our compressibilities are lower than reported by Bridgman.

Potassium

Baker's analyzed reagent grade potassium

Table 5. *(V/V_0) of lithium obtained from various determinations*

Pressure (kb)	Bridgman (1938)	Bridgman (1948)	Shock	Swenson	This work
0	1·000	1·000	1·000	1·000	1·000
5	0·956	0·961	0·958	0·957	0·961
10	0·925	0·927	0·922	0·921	0·928
15	0·897	0·898	0·891	0·889	0·900
20	0·874	0·872	0·864	0·864	0·875
25	0·852	0·849	0·841		0·852
30	0·831	0·828	0·819		0·832
35	0·812	0·809	0·800		0·814
40	0·795	0·793	0·783		0·798
45	0·780		0·766		0·782

Table 6. *(V/V_0) of sodium obtained from various determinations*

Pressure (kb)	Bridgman (1938)	Bridgman (1948)	Shock	Swenson	This work
0	1·000	1·00	1·00	1·000	1·000
5	0·929	0·937	0·931	0·931	0·931
10	0·881	0·887	0·878	0·880	0·880
15	0·844	0·847	0·837	0·840	0·839
20	0·814	0·814	0·803	0·808	0·806
25	0·788	0·786	0·775		0·777
30	0·765	0·762	0·750		0·753
35	0·743	0·741	0·728		0·731
40	0·724	0·723	0·708		0·712
45	0·707		0·691		0·694

Table 7. (V/V_0) of potassium obtained from various determinations

Pressure (kb)	Bridgman (1938)	Bridgman (1948)	Shock	Swenson	This work
0	1·000	1·000	1·000	1·000	1·000
5	0·884	0·885	0·878	0·881	0·881
10	0·813	0·813	0·802	0·810	0·807
15	0·766	0·760	0·747	0·761	0·754
20	0·729	0·720	0·704	0·721	0·713
25	0·696	0·689	0·669		0·679
30	0·668	0·660	0·640		0·650
35	0·643	0·638	0·615		0·626
40	0·620	0·620	0·593		0·604
45	0·601	0·605	0·574		0·584

Table 8. (V/V_0) of rubidium obtained from various determinations

Pressure (kb)	Bridgman (1938)	Bridgman (1948)	Shock	This work
0	1·000	1·000	1·000	1·000
5	0·832	0·875	0·838	0·862
10	0·765	0·800	0·750	0·781
15	0·718	0·747	0·691	0·725
20	0·682	0·705	0·646	0·682
25	0·652	0·671	0·611	0·649
30	0·626	0·644	0·582	0·622
35	0·603	0·621	0·557	0·598
40	0·583	0·602	0·536	0·578
45	0·566		0·517	0·560

of 99·995 per cent stated purity was used to obtain the values reported in Table 3. The final results are compared with those of other experimenters in Table 7 and plotted in Fig. 4. The new results are intermediate between Bridgman's data and the reduced shock wave data, and while the disagreement at 40 kbar is less than 2 per cent in V/V_0, the difference appears to be significant.

Rubidium

Rubidium metal, sealed under argon in 5 g ampules, was obtained from the Research Organic and Inorganic Chemical Co. The stated purity was 99·5 per cent. The metal was melted and slowly resolidified in order to eliminate any voids in the sample. Data on five runs are shown in Table 4. Final values are compared with results of others in Table 8 and plotted in Fig. 5. Our results lie intermediate between Bridgman's 948 results and the data from the reduction of the shock Hugoniot. In three experiments (I–III) rubidium was completely encased in double aluminum cups, thus eliminating the possibility of creep into microscopic cracks in the pressure core while two other experiments (IV and V) employed aluminum cups at the two ends similar to the experiments with lithium, sodium, and potassium. Results of the runs made in these two different fashions are similar. As in the case of potassium, the newly determined room temperature isotherm is intermediate between Bridgman's results and the data from reduction of the shock wave measurements.

The initial bulk modulus of rubidium ($B_T = -V(\partial P/\partial V)_T$, $P \to 0$) estimated from our measurements is about 26·6 kbar, that from shock data is about 22 kbar. It is immediately clear that this large difference in values of B_T can account for the major discrepancy between the shock isotherm and the one obtained from the present work (Fig. 5). It is not possible to excite shear waves in rubidium at room temperatures so ultrasonic values of B_S are unavailable for comparison [20].

In order to resolve this discrepancy, an

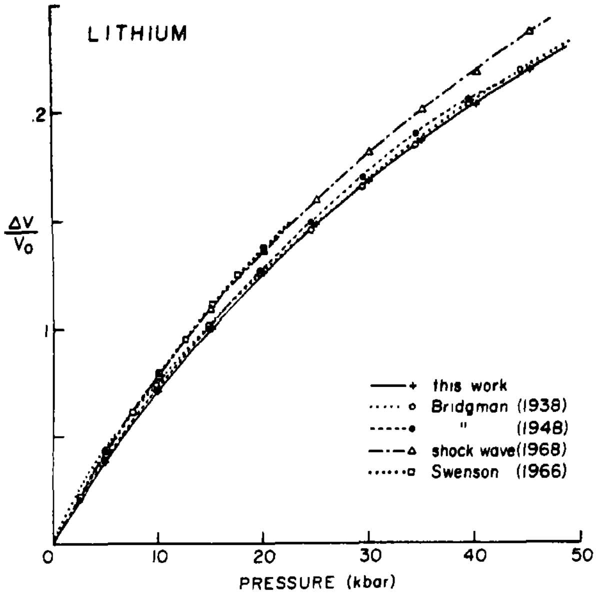

Fig. 2. Comparison of static isothermal compression data and the isotherm calculated from shock data for lithium.

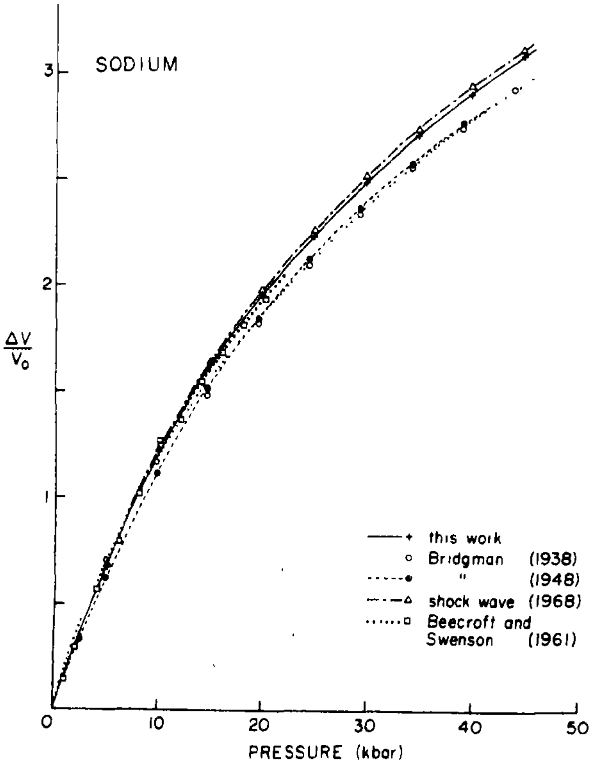

Fig. 3. Comparison of static isothermal compression data and the isotherm calculated from shock data for sodium.

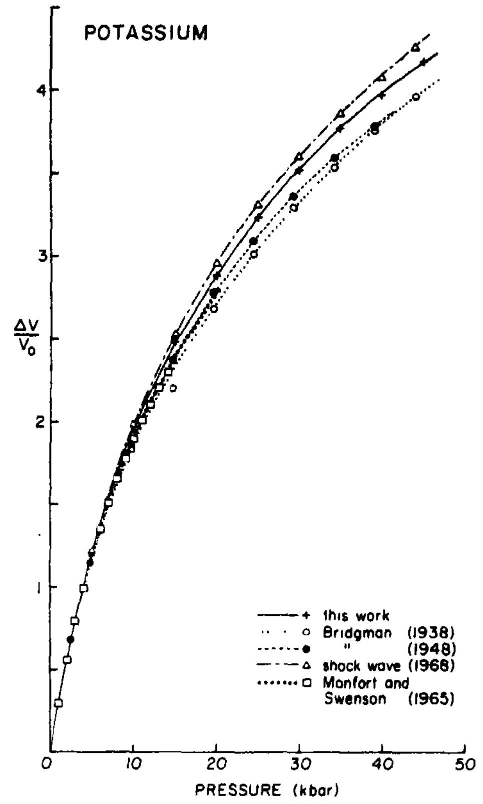

Fig. 4. Comparison of static isothermal compression data and the isotherm calculated from shock data for potassium.

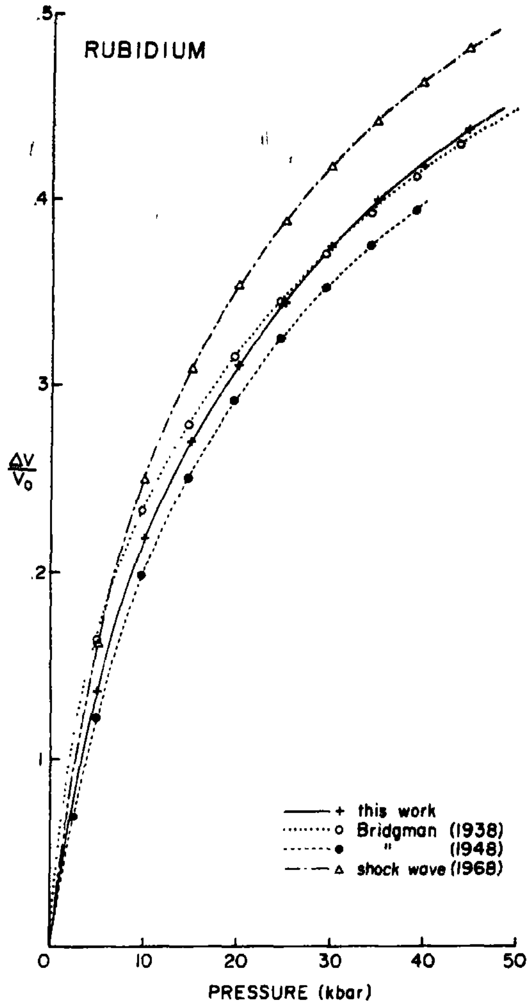

Fig. 5. Comparison of static isothermal compression data and the isotherm calculated from shock data for rubidium.

attempt was made to measure B_T directly. A hydrostatic volumeter originally designed and employed in the measurement of *PVT* relations for liquids at low pressures was used. Details of this apparatus and the methods of measurement have been previously described[21]. Mineral oil, free of all dissolved air and water was used as a pressure medium. An 16″ dia. 0–1400 bar range Heise-Bourdon tube gauge with graduations at 2 bar intervals was used for the measurements of pressure. The measurement consisted of observing the positions of a graduated piston, calibrated in terms of the volume of oil displaced, in two experiments—one with only mineral oil filling a certain volume of the volumometer and the other with the addition of a known volume of rubidium without altering the amount of mineral oil in the system. The *P-V* data for rubidium are then directly obtained from these difference measurements.

Rubidium for these low pressure experiments was purchased from the Aldrich Chemical Company and had a stated purity of 99+ per cent. Fluctuations in the ambient temperature gave rise to noticeable uneveness in the *P-V* plots, but hardly affected the estimation of B_T. Two independent experiments gave a B_T of 26·14 and 26·45 kbar which are in excellent agreement with values

Table 9. Compressibility parameters and Gruneisen constants of the alkali metals. Murnaghan equation (ME) and modified Murnaghan equation (MME) were fitted to all the experimental data

Element	Temp. (°K)	B_T (kbar)	B'_T	B''_T (kbar^{-1})	$\gamma^{[c]}_{\text{calc}}$	γ_{th}	Reference
Lithium	*RT*	118±2	3·33±0·09		1·50	0·89[d]	ME This work
	RT	111·9	3·33±0·09		1·64	0·81[13]	ME Bridgman[4]
	RT	112	3·6±0·25		1·6		Swenson[8]
	RT	109·1	3·06		1·36		ME Keeler[14]
	195	112·7					Nash & Smith[24]
	300	117					Jain[25]
	298	116[a]					Slotwinski & Trivisonno[26]
Sodium	*RT*	62±1	3·5±1		1·59	1·31[d]	ME This work
	RT	61·31±0·05	3·69±0·04	−0·019±0·006	1·68	1·17[13]	MME This work
	RT	66·9	3·4		1·55		ME Bridgman[4]
	RT	69·4	2·920	0·031	1·29		MME Bridgman[4]
	RT	63±2	3·95±0·02		1·80		Monfort & Swenson[f]
	RT	62·24	3·302		1·48		ME Keeler[14]
	RT	60·6	3·62	−0·017	1·64		MME Keeler[14]
	299±1	61·5[b]	3·59		1·62		Daniels[9]
	299	64·0[b]	3·79		1·73		Martinson[10]
	273·2	64·54±0·008	3·72±0·02		1·69		ME Ho &Ruoff[18]
	273·2	64·65±0·012	3·63±0·07	0·22±0·17	1·64		MME Ho & Ruoff[18]
	194·5	69·82±0·006	3·75±0·01		1·70		ME Ho & Ruoff[18]
	194·5	69·68±0·003	3·89±0·02	−0·37±0·05	1·77		MME Ho & Ruoff[18]
Potassium	*RT*	34·0±0·1	2·99±0·05		1·33	1·34[d]	ME This work
	RT	31·2±0·2	3·65±0·09	−0·039±0·006	1·66	1·23[13]	MME This work
	RT	33·25	3·43		1·55		ME Bridgman[4]
	RT	31·16	3·92	−0·028	1·79		MME Bridgman[4]
	RT	30·0±1·0	3·85±0·2		1·75		Monfort & Swenson[8]
	RT	33·90	2·75		1·21		ME Keeler[14]
	RT	29·70	3·68	−0·052	1·67		MME Keeler[14]
	295	30·87	3·98		1·82		Smith & Smith[11]
Rubidium	*RT*	26·6±0·2	3·23±0·02		1·45	1·80[d]	ME This work
	RT	26·0±0·1	3·37±0·06	−0·009±0·005	1·52	1·06[13]	MME This work
	RT	30·4	3·29		1·48	1·17[e]	ME Bridgman[4]
	RT	31·1	3·12	0·011	1·39		MME Bridgman[4]
	RT	22·7	2·90		1·27		ME Keeler[14]
	RT	21·0	3·34	−0·026	1·50		MME Keeler[14]
	195	26·3	3·79		1·72		Pauer[12]
	170	26·5					Gutman & Trivisonno[27]

[a] Calculated from extrapolation of the low temperature elastic constant data.

[b] Using $B_S/B_T = 1{\cdot}075$.

[c] Calculated from $\gamma_{SL} = 0{\cdot}5\ (B'_T - 0{\cdot}33)$.

[d] See Gschneidner (Ref. [23]).

[e] Calculated with $B_T = 26{\cdot}0$ kbar from our experimental data, instead of $B_S = 21{\cdot}4$ kbar used by Rice.

[F] This paper makes correction to the B_T, B'_T values earlier published by Beecroft and Swenson[7].

ranging from 25·6 to 27·7 kbar determined from our 45 kbar piston-cylinder measurements.

Ultrasonic data

The bulk modulus and its pressure derivatives can also be determined from ultrasonic velocities. These have been determined by Ho and Ruoff[18] who analyzed Martinson's data on sodium[10]. However, the standard deviation in the values of B_T'' estimated by Ho and Ruoff (Table 6 of Ref. [18]) from measurements at 273·2°K and 77·4°K are so large that even the sign of B_T'' cannot be determined with certainty. The data for 194·5°K is much more extensive than the rest and the sign of B_T'' is unquestionably negative[22]. A negative sign of B_T'' is also suggested by the results from our experiments on sodium (Table 2). The values of B_T'' for potassium and rubidium are also finite and negative, but an independent confirmation of this result from ultrasonic work is not yet available.

Gruneisen constant

The thermal Gruneisen gamma is defined by means of the thermodynamic identity

$$\gamma_{\text{th}} = \frac{V\,.\,\alpha\,.\,B_S}{C_p} = \frac{V\,.\,\alpha\,.\,B_T}{C_V}$$

where $\alpha = (1/V)(\partial V/\partial T)_p$, $B_S = -V(\partial P/\partial V)_S$, $B_T = -V(\partial P/\partial V)_T$ and C_p and C_V are the specific heats at constant pressure and at constant volume respectively. The Gruneisen gamma can also be evaluated from the relationship

$$\gamma_{\text{Calc}} = 0\cdot5(B_T' - 0\cdot33)$$

which is analogous to the Slater relation. Intercomparison of γ_{th} and γ_{calc} values in Table 9 shows that disparities among these values are similar to those previously noted by Gilvarry[17].

The volume dependence of γ can be obtained from equation (3) using experimental values of $V\alpha$, B_T and C_V at various pressures. A unique variation of γ with volume can also be derived from intercomparison of the static and shock measurements. Unfortunately, however, the static and shock measurements were not made over the same pressure interval. Hence in the absence of shock data, the Hugoniot must be extrapolated into the low pressure region and serious errors may result. The accuracy of shock data on lithium is not adequate for this calculation. The Hugoniot of rubidium is also unsuitable because of the peculiarities which may be due to the presence of electronic transitions similar

Table 10. *Coefficients of equation* $|\Delta V/V_0| = aP + bP^2 + cP^3 + dP^4 + eP^5 + fP^5$, *P in units of kbar*

Element	Data source	$a \times 10^2$	$-b \times 10^3$	$c \times 10^6$	$-d \times 10^7$	$e \times 10^8$	$-f \times 10^9$	Standard Deviation $\times 10^3$
Lithium	This work	0·80037	0·10097	0·67510				0·96
	Bridgman, 1948	0·86920	0·16962	3·4359	0·34965			0·40
	Keeler, 1969	0·89547	0·12795	0·99767				0·41
Sodium	This work	1·6240	0·54770	15·663	2·6677	0·19046		0·70
	Bridgman, 1948	1·4170	0·34067	5·7415	0·43823			0·07
	Keller, 1969	1·5694	0·42090	7·5423	0·56643			0·21
Potassium	This work	2·9713	1·4404	48·263	8·5874	0·60664		1·14
	Bridgman, 1948	2·7628	1·0789	23·576	1·9814			3·67
	Keeler. 1969	3·0409	1·4688	49·952	9·1636	0·67282		0·78
Rubidium	This work	3·6976	2·3517	111·32	31·837	4·8389	0·29875	1·36
	Bridgman, 1948	3·3580	2·1886	112·06	34·692	5·6595	0·37333	0·57
	Keeler, 1969	4·4335	3·0441	148·10	42·608	6·4559	0·39556	0·73

to those encountered in cesium. The volume dependence of γ has been estimated for sodium and potassium using the static and Hugoniot data. However, the details of these calculations will be presented elsewhere.

Acknowledgements—Our thanks are due to Mr. Geza Budai for assistance with the experiments and to Miss Sharon Bailey for the data processing and for several numerical calculations. Mr. J. Yamane did all the skillful and patient machining jobs and the upkeep of the apparatus is due to Mr. L. Faus and Mr. T. Thomas. This paper has benefited from illuminating discussions with Drs. G. H. Higgins, R. Grover and R. N. Keeler to whom our thanks are tendered. This work is supported by our Lawrence Radiation Laboratory and AEC contracts.

REFERENCES

1. BRIDGMAN P. W., *Proc. natn. Acad. Sci.* **8**, 361 (1922); *Proc. Am. Acad. Arts Sci.* **58**, 165 (1923).
2. BRIDGMAN P. W., *Proc. natn. Acad. Sci.* **21**, 109 (1935); *Proc. Acad. Arts Sci.* **70**, 71 (1935).
3. BRIDGMAN P. W., *Proc. Am. Acad. Arts Sci.* **72**, 207 (1938).
4. BRIDGMAN P. W., *Proc. Am. Acad. Arts Sci.* **76**, 71 (1940).
5. SWENSON C. A., *Phys. Rev.* **99**, 423 (1955).
6. SWENSON C. A., *J. Phys. Chem. Solids* **27**, 33 (1966).
7. BEECROFT R. I. and SWENSON C. A., *J. Phys. Chem. Solids* **18**, 327 (1961).
8. MONFORT C. E. III and SWENSON C. A., *J. Phys. Chem. Solids* **26**, 291 (1965).
9. DANIELS W. B., *Phys. Rev.* **119**, 1246 (1960).
10. MARTINSON R. H., *Phys. Rev.* **178**, 802 (1969).
11. SMITH P. A. and SMITH Ca. A., *J. Phys. Chem. Solids* **26**, 279 (1965).
12. PAUER L. A., *ONR Tech. Report* 11, Proj. NR 017-309, May 1968.
13. RICE M. H., *J. Phys. Chem. Solids* **26**, 483 (1965).
14. KEELER R. N., *Compressibilities* in American Institute of Physics Handbook (to be published).
15. GROVER R., KEELER R. N., ROGERS F. J. and KENNEDY G. C., *J. Phys. Chem. Solids* **30**, 2091 (1969).
16. VAIDYA S. N. and KENNEDY G. C., *Bull. Am. phys. Soc.* **14**, 734 (1969); *J. Phys. Chem. Solids* **31**, 2329 (1970).
17. GILVARRY J. J., *J. chem. Phys.* **23**, 1925 (1955).
18. HO P. S. and RUOFF A. L., *J. Phys. Chem. Solids* **29**, 2101 (1968).
19. FLETCHER R. and POWELL M. J. D., *Computer J.* **6**, 163 (1963).
20. ROBERTS C. A. and MEISTER R., *J. Phys. Chem. Solids* **27**, 1401 (1966).
21. NEWTON M. S. and KENNEDY G. C., *J. mar. Res.* **23**, 2 (1965).
22. Clarification of this topic was kindly made by Professor A. L. Ruoff in a private communication.
23. GSCHNEIDNER A., *Solid State Phys.* **10**, 276 (1964).
24. NASH H. C. and SMITH C. S., *J. Phys. Chem. Solids* **9**, 113 (1959).
25. JAIN A. C., *Phys. Rev.* **123**, 1234 (1961).
26. SLOTWINSKI T. and TRIVISONNO J., *J. Phys. Chem. Solids* **30** 1276 (1969).
27. GUTMAN E. J. and TRIVISONNO J., *J. Phys. Chem. Solids* **29**, 805 (1967).

J. Phys. Chem. Solids, 1971, Vol. 32, pp. 2557–2567. Pergamon Press. Printed in Great Britain

IONIC CONDUCTIVITY AND LOW FREQUENCY DISPERSION IN HEXAGONAL SILVER IODIDE*

G. COCHRANE† and N. H. FLETCHER
Department of Physics, University of New England, Armidale, N.S.W. Australia

(*Received* 29 *September* 1969; *in revised form* 6 *April* 1971)

Abstract—Measurements are reported for the temperature variation of ionic conductivity in single crystals of hexagonal silver iodide. Both nominally pure and Cu^{2+} doped crystals were studied and analysis of the measurements for conduction both parallel and normal to the *c*-axis leads to a formation energy for Frenkel defects of 0·60 eV, activation energies for diffusion of Ag^+ interstitials parallel and normal to the *c*-axis of 0·61 and 0·29 eV respectively and corresponding activation energies for Ag^+ vacancies of 0·50 and 0·39 eV. Similar measurements performed on thin films of AgI grown expitaxially on mica show varying behaviour but the activation energy for conduction is about 0·4 eV, which agrees with the value expected from the single-crystal results if the conductivity is vacancy controlled.

Dielectric measurements in the frequency range $10–10^6$ Hz at temperatures between 193 and 340°K show anomalous dispersion peaks at about 10^4 Hz for temperatures above 300°K which are tentatively interpreted in terms of trapped Frenkel defects and interfacial polarization. At temperatures below about 290°K a series of sharp resonant absorptions is observed whose origin is uncertain. The static dielectric constant approaches the value $6{\cdot}8 \pm 0{\cdot}2$ at temperatures below -40°C.

1. INTRODUCTION

THE ELECTRICAL and optical properties of the silver halides have received considerable attention over the past few decades; much of this interest has, however, been centred around silver chloride and silver bromide, a circumstance which can be attributed to the obvious commercial application and relative ease of obtaining large, pure, single crystals of these materials. A recent literature survey [1] revealed only one publication dealing with measurements of the electrical properties and none dealing with the optical properties of single crystals of AgI. It is proposed to present in this and following papers the results of a preliminary investigation on the optical and electrical properties of thin layers and single crystals of hexagonal silver iodide.

At atmospheric pressure silver iodide has been reported as trimorphic[2, 3, 4] with three further polymorphs appearing at elevated pressures[5]. Of those occurring at atmospheric pressure, two modifications coexist below a first order phase transition at about 147°C, namely a cubic sphalerite-type structure, designated γAgI, and a hexagonal wurtzite-type structure designated βAgI. The stability regions of the γ and β modifications have created considerable controversy.

Some authors[3] give γAgI as the stable phase at room temperature and βAgI as only metastable, while other authors[2, 4] give the reverse. Majumdar and Roy[6] doubt if γAgI even exists. It is generally agreed from X-ray diffraction studies that nearly all powder specimens of AgI at room temperature and atmospheric pressure consist of a mixture of the cubic and hexagonal phases in varying proportions depending on the method of preparation[7]. The original conjecture that βAgI is only metastable below 135°C was put forward by Bloch and Moller [3] in 1931 and this has since been quoted (but apparently not verified) by several authors. The results of Burley[2] and of

---

*Based on a thesis submitted by G. Cochrane for the Ph.D. degree of the University of New England.

†Present Address: Royal Military College, Duntroon, A.C.T., Australia.

Schneer and Whiting[4] show that γAgI undergoes a transformation to βAgI at temperatures as low as 90°C, while the reverse transition cannot be brought about below 147°C by thermal equilibration. An analysis of the experimental evidence suggests that the conclusions drawn by Bloch and Moller[3] are incorrect.

Unless special precautions are taken, the usual methods adopted for preparing AgI specimens suffer from several disadvantages which are often overlooked. These can be summarized as follows.

Powder compacts

The method of preparation is adequately covered in papers by Corrin and Storm[8] and by Jost and Oel[9]. A precaution which must be observed to maintain stoichiometry is the prevention of photolysis and consequent loss of iodine. Another disadvantage of powder compacts is that, if the compaction pressure exceeds about 100 bar, then, according to Burley[2], the final specimen will be predominantly γAgI, irrespective of the original proportions of βAgI and γAgI.

Solidification from the melt

Burley[2] observed that specimens obtained by quenching from the melt showed a predominance of the sphalerite structure, while those cooled slowly had the wurtzite structure. A difficulty always present when working with the melt is its tendency to decompose giving metallic silver and elemental iodine, again resulting in non-stoichiometric specimens.

Thin films

Layers deposited on a substrate have been used almost exclusively for optical work. A summary of thin film preparation is given elsewhere[1, 10]. The major difficulty is to prepare stoichiometric layers of a predetermined phase type.

Single crystals

To facilitate the interpretation of results it is usually desirable to work with specimens cut from single crystals. Recently, several methods have been described for growing single crystals of βAgI large enough to permit the undertaking of electrical and optical experiments. Two of the methods rely on slow diffusive dilution of either a saturated AgI-KI[11] solution or a AgI-HI[12] solution, while a third[13] method relies on convective circulation of a AgI-KI solution between two chambers held at different temperatures. In addition to the above a silica gel method has been described by Halberstadt [14].

2. IONIC CONDUCTIVITY MEASUREMENTS

The general theory of the electrical conductivity of ionic crystals, formulated in terms of the motion of Frenkel or Schottky defects, is well established[15]. In the case of pure βAgI the conductivity mechanism is generally agreed to involve the motion of Frenkel defects, while transport measurements[16] have established that only the Ag^+ ions contribute appreciably to the electric current, both I^- and electronic currents being negligible. Thus interstitial silver ions and their associated vacant lattice sites are primarily responsible for the conductivity.

Following an analysis given by Lidiard[15], the ionic conductivity results are presented by plotting $\ln(\sigma T)$ in terms of T^{-1}. In general the graph consists of two approximately linear segments. The upper segment extends from the melting point, or the highest temperature of stability of the solid phase of interest, to some lower temperature which is determined by the purity and perfection of the crystal. Normally, this region is an intrinsic property of the substance and measurements are quite reproducible. The low temperature conductivity, known as the extrinsic or structure sensitivity region, always displays a smaller slope. The magnitude of the conductivity in this region depends principally on the nature and magnitude of the impurity content and the thermal history of the specimen.

The complete ionic conductivity curve is therefore roughly a superposition of two lines, represented by

$$\sigma T = A_1 \exp(-E_1/kT)$$

for the high temperature or intrinsic region and

$$\sigma T = A_2 \exp(-E_2/kT)$$

for the low temperature or extrinsic region.

In the high-temperature regime the Frenkel defects are generated intrinsically with a formation energy W and the activation energy for conductivity can be written

$$E_1 = \tfrac{1}{2}W + U$$

where U is the activation energy for diffusion of an interstitial ion or of a vacancy, whichever is more mobile. In the low temperature regime the interstitial ions or vacancies are provided by the impurities and imperfections in the crystal, so that their concentration does not depend upon temperature and we can write

$$E_2 = U.$$

It is thus generally necessary to make measurements on crystals containing enough impurity that both linear regions can be adequately measured if we wish to determine both W and U. Alternatively, information about U can be obtained from self-diffusion studies using radioactive tracers[15], while an estimate of W can be made from specific heat measurements[17].

2.1 *Experimental*

Single crystal specimens were grown from a HI-AgI solution as described by Lakatas and Lieser[12] or alternatively from a KI-AgI solution as described by Cochrane[11]. Spectrochemical analysis showed the only detectable impurities to be traces of potassium and sodium, while a flame photometer test set the potassium impurity at about 20 ppm for crystals grown from KI-AgI solution. However, no differences were observed in the ionic behaviour of crystals obtained by the two methods. Plate-like specimens 0·27 to 0·88 mm thick were prepared by cleaving single crystals perpendicular to the *c*-axis with a razor blade. A specimen then had three electrodes applied to the freshly cleaved faces by evaporating silver through suitable masks. The lower specimen surface was completely coated to form one electrode while the upper surface had a central electrode, 0·088 cm in dia., concentrically surrounded by a guard electrode. An alternative arrangement, which gave identical results, was to use longer sections (1·0 to 4·0 mm) of prism-shaped crystals with each end face completely coated to form an electrode. For these specimens, in addition to silver, colloidal graphite (Aquadag) was also used as an electrode material. Since unwanted strains can readily be introduced into AgI specimens, no attempt was made to grind or alter the shape of the hexagonal cross-section. The samples were mounted in specimen holders fitted with beryllium copper contacts adjusted for the minimum contact pressure necessary to give noise-free behaviour.

For thin-film measurements, layers of βAgI were prepared by condensing silver on a mica substrate, held at room temperature in the presence of an iodine atmosphere. Electron diffraction studies[10] have shown that the films used were well oriented with the stacking direction normal to the substrate. Electrical contact to the film was made through silver or colloidal graphite electrodes deposited on the mica surface prior to the commencement of evaporation. The thickness of the films was measured by an optical interference method similar to that described by Tolansky[18].

All conductivity measurements were made under vacuum conditions with a pressure of about 10^{-4} torr. The specimen temperature was measured with a copper–constantan thermocouple clamped adjacent to and in a similar manner to the specimen. The specimen temperature was controlled to $\pm 0 \cdot 1$°C but quoted absolute temperatures are only accurate to ± 2°C.

All the conductivity measurements were made using a simple or a guarded two-electrode system as described and used either direct current or a low frequency (0·5 to 5 Hz) square wave. When using direct currents there was some evidence of the growth of silver dendrites from the electrodes, particularly for thin-film specimens at elevated temperatures, however, this was minimized by the use of very small currents (10^{-8} to 10^{-12} A) and by the limitation of measurement times to the minimum required to achieve stability.

2.2 *Results*

Initially current-voltage measurements were made on the longer sections of prismatic crystals to verify that the electrodes were truly ohmic. A typical set of room temperature results for a crystal with a pair of Aquadag electrodes is shown in Fig. 1. The initial curve, 1, was only obtained for a specimen which had not previously had a voltage applied across it. After measurements had been made at higher voltages, curve 1 could not be reproduced and the measurements followed curve 2 which was completely reproducible.

For temperatures above 260°K and below the 420°K transition point, silver electrodes were found to be completely ohmic in behaviour. Below 260°K silver electrodes exhibited ohmic behaviour only when the measuring voltage exceeded about one volt, below this current readings were very erratic. With thin-film specimens both silver and Aquadag electrodes exhibited ohmic behaviour.

Temperature dependence of the ionic conductivity for over 30 single crystal specimens was measured for a current flow in the direction of the c-axis. The results are summarized in Fig. 2(a).

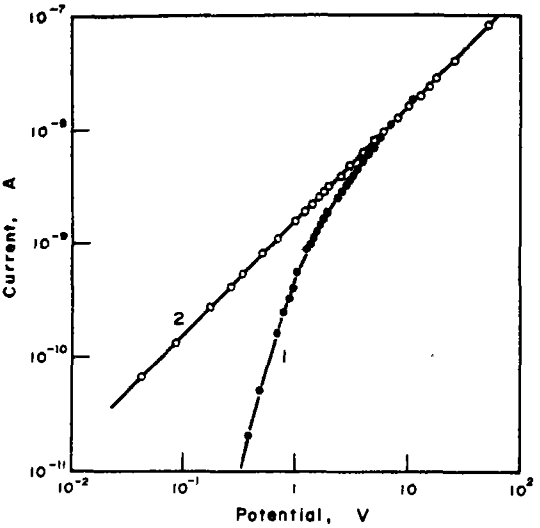

Fig. 1. Typical room temperature current-voltage characteristics for a single crystal specimen with colloidal graphite (Aquadag) electrodes. See text for explanation of curve 1 and curve 2.

In order to resolve the activation energy E into the two components U and W, attempts were made to grow crystals containing impurity cations. The required impurity in the form of the iodide was added to the KI-AgI growing solution. With the exception of Cu^{2+} ions, subsequent analysis either by X-ray fluorescence or atomic absorption failed to detect any traces of impurity. Atomic absorption measurements set the copper impurity at $0 \cdot 5 \pm 0 \cdot 1$ per cent by weight, although not all of this copper may be present as Cu^{2+}. Visibly the copper-doped crystals did not appear any different from pure βAgI; however, when attempts were made to cleave a prism-shaped crystal, it was noticeably more brittle and failed to cleave cleanly. Only one specimen containing Cu^{2+} ions proved sufficiently large for testing, the results for this specimen with a current flow in the c-axis direction are shown in Fig. 2(a).

Figure 3 shows the variation of ionic

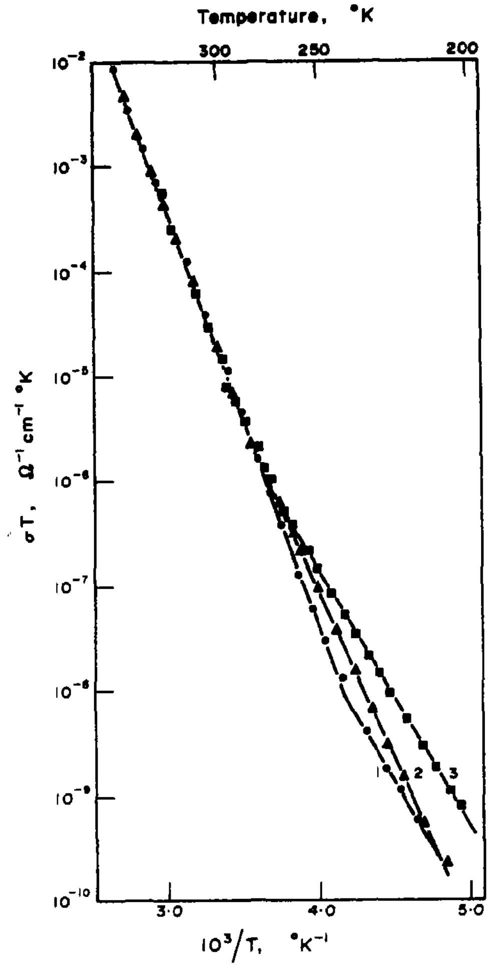

Fig. 2(a). Temperature dependence of the ionic conductivity of single crystals of βAgI with current flow parallel to the c-axis. (1) pure crystal with graphite electrodes; (2) pure crystal with silver electrodes and (3) crystal containing about 1/2 per cent by weight of Cu^{2+}.

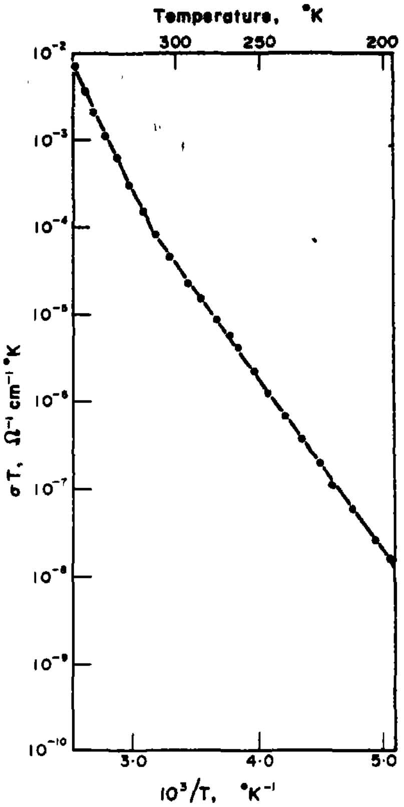

Fig. 2(b). Temperature dependence of the ionic conductivity of single crystals of βAgI with graphite electrodes and current flow perpendicular to the c-axis.

conductivity with temperature for a representative selection from over 40 thin-film specimens tested, ranging in thickness from 100 to 5000 Å. Apart from the measurement of film thickness, other experimental details were similar to those described for single-crystal specimens.

2.3 *Discussion of ionic conductivity results*

Measurements of the type reported show that metallic silver provides a good ohmic contact to βAgI at temperatures above 260°K. Colloidal graphite electrodes are initially non-ohmic but achieve ohmic behaviour after passage of an alternating current for a time at a reasonably high applied potential. Prolonged application of an alternating potential leads to growth of silver dendrites from both carbon electrodes; thus it is reasonable to assume that the conditioning process involves electrolytic build-up of silver so that the system becomes effectively |graphite |Ag|AgI|Ag| graphite|. With both electrode systems, then, we make the reasonable assumption that contact potential differences are negligible compared with 10V, the order of the potentials used in the measurements.

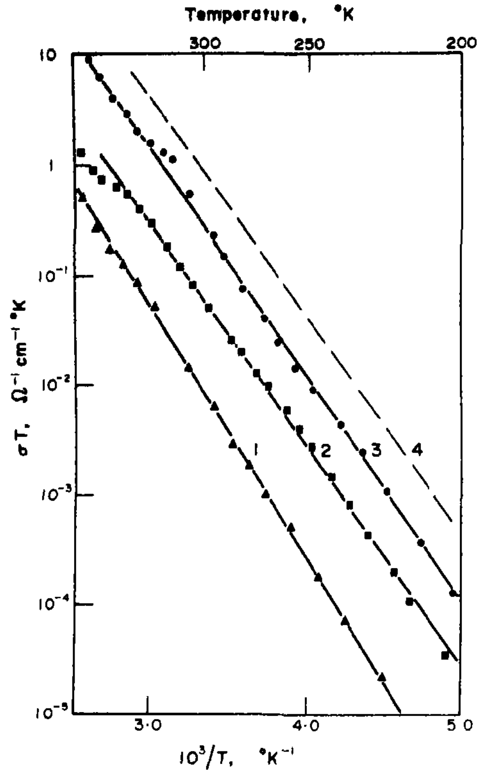

Fig. 3. Temperature dependence of ionic conductivity for a typical selection of AgI layers deposited on mica. Layer thickness (1) 1800 Å; (2) 4300 Å; (3) 100 Å; (4) represents an activation energy of 0·4 eV.

The ionic conductivity results in Fig. 2(a) illustrate that both nominally pure and copper doped single crystals with graphite electrodes display two distinct linear regions of similar slope. On the other hand, while nominally pure single crystals with silver electrodes have the same high temperature characteristics, the low temperature region is markedly different. Since all specimens tested with the current flowing parallel to the *c*-axis showed the same elevated temperature characteristics it seems reasonable to identify this portion of the curves as the intrinsic or structure insensitive region.

It is proposed that the low temperature regime for nominally pure crystals with graphite electrodes can be associated with the motion of excess Ag^+ vacancies. The additional Ag^+ vacancies are presumably generated when Ag^+ ions are electrolytically deposited during the electrode conditioning process.

The above proposal is supported by the low temperature results for a crystal doped with Cu^{2+} ions, where nominally the addition of each Cu^{2+} ion creates one Ag^+ vacancy. Normally little significance could be placed on the results from a single specimen; however, in the present context where the results for the copper doped crystal are only used in support of the other data the authors feel this is justified.

The results for nominally pure specimens with silver electrodes can be reconciled by attributing the low temperature regime to an increase in the interstitial Ag^+ ion concentration. The slight non-stoichiometry is assumed to be created by diffusion of silver from the electrodes.

In the intrinsic region $E_1 = \frac{1}{2}W + U$ and, since two possible values of U are available from E_{21} and E_{22}, two possible W values can be derived on the alternative assumptions that it is interstitials or vacancies which are the dominant carriers in the intrinsic region and *c*-axis direction. The former assumption gives the unlikely low value of 0·34 eV for W and we therefore accept the latter view and the W value of 0·60 eV, which is in better agreement with the other determinations shown in Table 2.

Figure 2(b) shows results for nominally pure crystals with aquadag electrodes and current flow normal to the *c*-axis. The use of aquadag electrodes implies that the low temperature region is associated with the motion of Ag^+ vacancies. Unfortunately we have no measurements on Cu^{2+} doped crystals in the *a* direction to yield direct confirmation of these assumptions. In the intrinsic region $E_1{}^a = \frac{1}{2}W + U$ and, since the value of W is independent of the current direction, U may be determined from $E_1{}^a$. However, the value of U calculated this way is considerably less than the value determined from the extrinsic region (where $E_2{}^a = U$), consequently conductivity in the intrinsic region must be associated with the motion of interstitial Ag^+ ions.

Accepting these interpretations and using the experimentally determined activation energies shown in Table 1, where superscript c refers to measurements in the c-axis direction and a to measurements normal to this direction, we derive the conclusions set out in the first line of Table 2. Here subscript + and − refer to Ag^+ interstitials and Ag^+ vacancies respectively.

Also shown in Table 2 are such values of these fundamental activation energies as can be derived from other work. Since these measurements were all on polycrystalline samples, some of the interpretations are uncertain and all have been derived in a variety of ways. The values of U^c and U^a ascribed to Jordan and Pochon[19], for example, are actually activation energies for diffusion of silver in hexagonal βAgI and cubic γAgI measured by a radioactive tracer technique. Lieser's value of W came from calorimetric measurements.

Table 1. *Experimentally determined activation energies (all in* eV*)*

E_1^c (all crystals)	0·79 ± 0·02
E_2^c (Cu^{2+} doped)	0·49 ± 0·02
E_{21}^c ('pure crystals', graphite electrodes)	0·50 ± 0·03
E_{22}^c ('pure crystals', silver electrodes)	0·62 ± 0·02
E_1^a ('pure crystals')	0·59 ± 0·02
E_2^a ('pure crystals' graphite electrodes)	0·39 ± 0·02

where values are shown spread between two or more columns, it is not clear from the nature of the experiment to which column they should be assigned, though the numerical result itself sometimes makes this obvious. The value of U given by Lieser[21] does not represent a direct measurement, but relies upon the assumption that his measured E is in fact E_1.

The only other reported measurements on single crystals of βAgI are those of Lakatos and Lieser[12] who found, for both axial directions, not two exponential conductivity segments but rather a continuously changing activation energy which increased with increasing temperature. The reason for this behaviour is not apparent.

It is noteworthy that the activation energies $U_\pm{}^c$ for diffusion in the c-axis direction are considerably greater than those for diffusion normal to this direction, $U_\pm{}^a$. It is easy to interpret this qualitatively since the wurtzite structure may be thought of in terms of alternating layers of positive and negative ions, each layer lying normal to the c-axis.

The present study indicates that for intrinsic material the conductivity can be attributed to the motion of silver ion vacancies in the c-axis direction and silver ion interstitials normal to this direction. It is not possible to conclude from these measurements alone if an interstitialcy type mechanism should be invoked, similar to that used to explain intrinsic conductivity in the other silver halides[15, 24]. The intrinsic conductivity

Table 2. *Fundamental activation energies for* βAgI *(all in* eV*)*

	E_1	E_2	W	$U_-{}^c$	$U_+{}^c$	$U_-{}^a$	$U_+{}^a$
Derivation			$2(E_1 - E_{21}^c)$	E_{21}^c	E_{22}^c	E_2^a	$E_1^a - \frac{1}{2}W$
This study	see Table 1		0·60	0·50	0·62	0·39	0·29
Jordan & Pochon[19]				hex. 0·62		cub. 0·38	
Murin[20]	0·86	0·38	0·96		---0·38---------		
Lieser[21, 22]	----0·49----		0·70		---0·14---------		
Takahashi *et al.*[23]				----0·41----		---0·30------	
Lakatos & Lieser[12]	c: 0·5 to 1·0 a: 0·3 to 1·1						

parallel and normal to the *c*-axis direction can be summarized by the following equations, (σ measured in Ω^{-1} cm^{-1} and kT in eV)

$$\sigma_{\parallel} = 8{\cdot}8 \times 10^{5} \exp(-0{\cdot}79/kT)$$
$$\sigma_{\perp} = 5{\cdot}7 \times 10^{2} \exp(-0{\cdot}59/kT).$$

Turning now to thin films, we find a variety of conductivity characteristics, a representative selection of which are shown in Fig. 3. Electron diffraction studies [1, 10] have shown that the films used are well oriented with the stacking direction normal to the substrate, so that it is relevant to compare the results with those for single crystals measured in the *a*-direction. Because of the large surface-to-volume ratio of thin films, it is reasonable to expect extrinsic behaviour and, indeed, the slope of the plots is quite close to the value $U_{-}^{a} = 0{\cdot}39$ eV expected from the single crystal results, if the majority carriers are silver ion vacancies rather than excess silver ions. There is little to be gained at present by any more detailed discussion of the curves. It is relevant to note, however, that the thin-film results show several points of similarity with those obtained on powder compacts [20, 25], which is, of course, expected because of the large surface-to-volume ratio in each case.

3. LOW-FREQUENCY DISPERSION

3.1 *Experimental*

Specimens approximately 0·15 cm long were cut from hexagonal prism-shaped single crystals grown from KI-AgI solution. Some specimens were mounted directly between two brass electrodes, while others first had Aquadag electrodes applied. Edge effects were reduced by arranging for the specimen to be smaller in diameter than the electrodes by at least twice its thickness. All of the six specimens tested over part or all of the temperature (−80 to +65°C) and frequency (20 Hz to 100 kHz) ranges, had the electric field applied parallel to the *c*-axis. Capacitance and loss measurements were made with a General Radio 1620A Capacitance Measuring Assembly which allowed accurate determination both of the real part ϵ' of the dielectric constant and of the loss factor tan δ. The amplitude of the alternating voltage applied across the specimen was 20 V peak-to-peak for all frequencies. Before testing specimens of βAgI, the assembly was checked over the complete temperature and frequency range using a specimen of polytetrafluoroethylene for which the dielectric properties are well known.

Measurement of the real part ϵ' of the dielectric constant is estimated to be correct to better than ±2 per cent for $\epsilon' < 20$. At low frequencies (< 1 kHz) and large values of ϵ' (> 500) the accuracy decreases to ±10 per cent.

3.2 *Results and discussion*

Typical plots of tan δ against frequency are shown in Fig. 4 and corresponding plots for

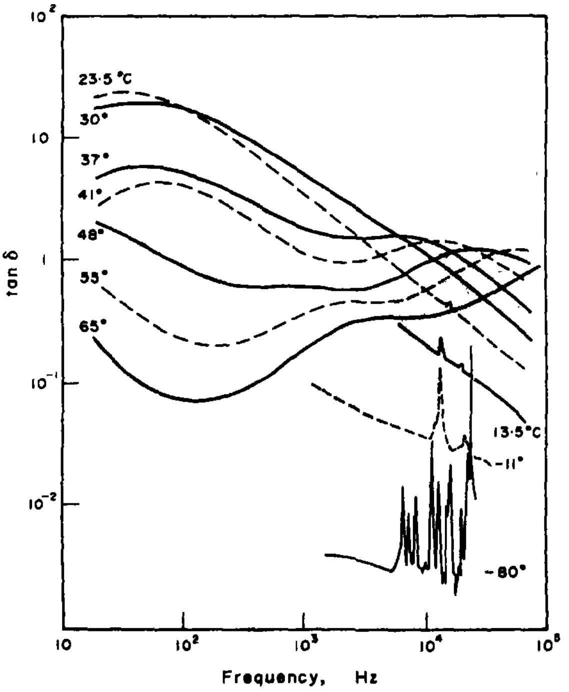

Fig. 4. Variation of the loss tangent with frequency in βAgI.

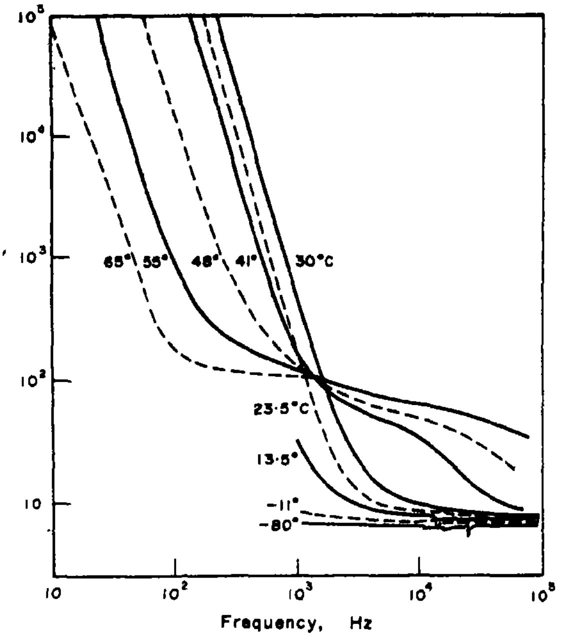

Fig. 5. Variation of the apparent dielectric constant ϵ' of βAgI with frequency.

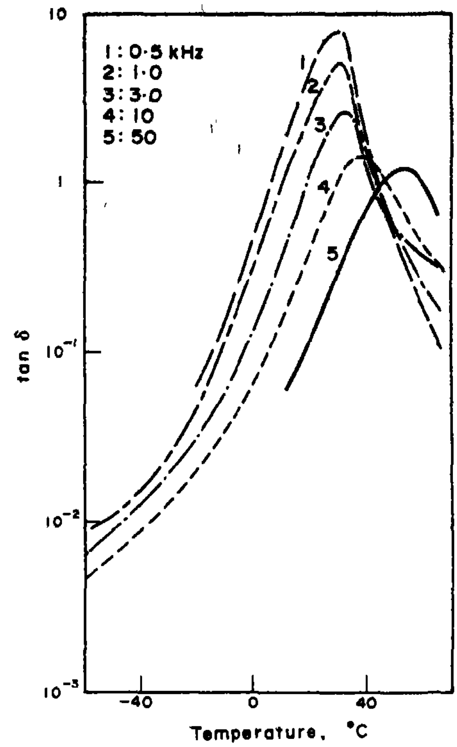

Fig. 6. Temperature dependence of the loss angle in βAgI derived from the results given in Fig. 4.

ϵ' in Fig. 5. When a specimen was held at a constant temperature above about 50°C, values of tan δ and ϵ' increased with time. The effect became more pronounced as the temperature increased until, at about 90°C, it was impossible to balance the bridge. On cooling the specimen to room temperature, the original values of tan δ and ϵ' were again obtained.

From Figs. 6 and 7 it is clear that the static dielectric constant at low temperatures, when space-charge effects are absent, has a value in the range 6 to 8, the precise result at −60°C being $6{\cdot}8 \pm 0{\cdot}2$. This result agrees well with the value $7{\cdot}0 \pm 0{\cdot}3$ reported by Bottger and Geddes[26] from measurements on powdered samples at 27°C in the frequency range 10^6 to 10^7 Hz but differs markedly from the results of Sathe *et al.*[27] who give a value of 33·86 from measurements on powder samples under unspecified conditions. Presumably in this latter case space charge effects were present.

The most reasonable interpretation of the behaviour shown in Figs. 6 and 7 is that, at low frequencies and high temperatures, ionic migration takes place and increases the measured dielectric constant ϵ' by the creation of space-charge layers at the electrodes.

Another interesting feature of the curves shown in Fig. 4 is the loss peak shown in the frequency range 10^4–10^5 Hz for temperatures above about 37°C. This is a rather broad peak which shifts steadily to higher frequencies as the temperature is raised, in the same way as does a simple Debye relaxation peak. A second somewhat similar peak appears in the frequency range 10^3–10^4 Hz for temperatures above about 50°C.

There seem to be three possible mechanisms which may be invoked to explain the observed relaxation spectra:

(i) Aliovalent impurities

(ii) Interfacial polarization
(iii) Reorientation of Frenkel defects.

Restricting our attention, for the moment, to the peak of higher frequency, we find that its shift with frequency implies an activation energy of 0·84 ± 0·05 eV. The magnitude of the peak above the interpolated base line provided by the conductivity losses increases with increasing temperature, which implies that the concentration of dipoles causing the relaxation also increases with temperature. At 55°C the value of tan $\delta_{\max}$ due to this loss mechanism is about 1 at a frequency of 50 kHz which, using the usual Debye treatment [28] as an approximation, implies a concentration n of contributing dipoles, each of moment μ, such that $n\mu^2 \sim 10^{-32}$ C^2 m^{-1}. For a typical ionic dipole having a length of the order of a lattice spacing, this leads to a dipole moment $\mu \sim 10^{-28}$ C m, which implies a dipole density $n \sim 10^{24}$ m^{-3}, compared with the total ion density $\sim 10^{28}$ m^{-3} in AgI. This concentration of dipoles is about two orders of magnitude greater than any expected aliovalent impurity ion and about an order of magnitude greater than the measured potassium impurity.

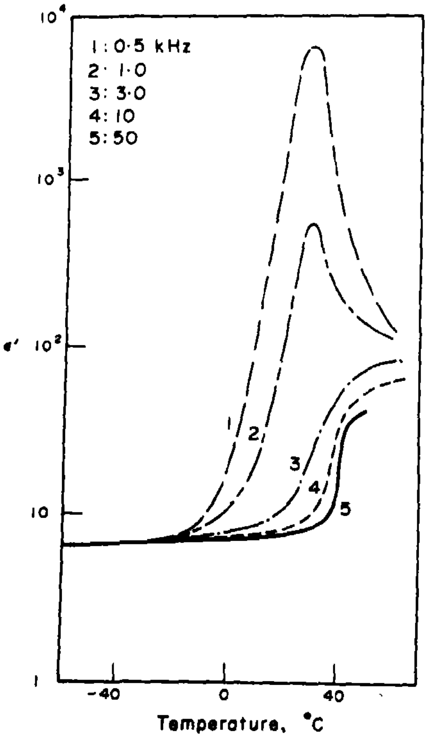

Fig. 7. Temperature dependence of the apparent dielectric constant ϵ' in βAgI, derived from the results given in Fig. 5.

Consider now the second possibility, interfacial polarization. Effects of this type have been observed in NaCl by Wimmer and Tallan[29] and by Kessler and Moriani[30], while similar effects have been observed in AgBr and explained theoretically by Friauf [31]. The present results for the loss peak of higher frequency show a marked similarity to the relaxation spectra of NaCl given by Wimmer and Tallan. In addition the activation energy of 0·84 eV, characteristic of ionic conduction in the region, suggests this peak is most probably caused by blocking at the electrodes. There is, however, still the problem of the second peak which it is difficult to explain by this argument.

The third possibility would involve the reorientation of vacancy pairs, which as pointed out by Greenwood[16] should involve two relaxation peaks in the case of Frenkel defects (i) normal lattice ion moving into a vacancy (ii) interstitial ion moving into a vacancy. At 55°C the apparent concentration of dipoles is of the same order of magnitude as the concentration of Frenkel defects, as calculated from the value of W given in Table 2. The occurrence of the second peak with an activation energy of 0·63 ± 0·03 eV tends to support this picture. There are, however, difficulties associated with such an interpretation. The activation energy involved in the relaxation should be that associated with the diffusion process alone which, from Table 2 is 0·50 eV for vacancies and 0·62 eV for interstitials, the c-axis direction being the relevant one in the present context. Neither of these energies is very close to the measured 0·84 eV for the higher frequency peak, although the lower frequency peak (0·63 eV) could well be associated with the motion of interstitial silver ions.

Finally we note the very sharp absorption peaks shown at low temperatures in Fig. 4. The corresponding behaviour of ϵ' in this range, as shown in Fig. 5, suggests that some sort of resonance phenomenon is being observed. To ensure that these peaks were not spurious, it was checked that they were not present when the specimen was replaced by a similarly sized block of NaCl, Calcite, Polythene or Teflon, their absence in these cases confirming them to be a genuine property of AgI.

Since the crystal structure of βAgI lacks a centre of symmetry, the natural interpretation is that these peaks arise from some piezoelectric resonance phenomenon. This conclusion is reinforced by the failure to observe the peaks in a differently prepared crystal with the field normal to the *c*-axis direction. The expected resonance frequency for a crystal of the size used is, however, around 400 kHz rather than the 10 kHz observed. Tests with a different sample holder reduced the probability that we were observing an incidental resonance of the apparatus excited by the crystal, but the position is not yet clear.

Acknowledgements—This work is part of a programme supported by the Australian Research Grants Committee and, in its earlier stages, by the C.S.I.R.O. Division of Radiophysics. One of us (G.C.) is grateful to the University of New England for a Teaching Fellowship, during tenure of which the work was done. It is also a pleasure to express our thanks to the technical staff of the Department for their valuable assistance.

REFERENCES

1. COCHRANE G., Ph.D. Thesis, University of New England 1968 (unpublished).
2. BURLEY G., *Am. Mineral.* **48**, 1266 (1963).
3. BLOCH R. and MOLLER H., *Z. Phys. Chem.* **A152**, 245 (1931).
4. SCHNEER C. J. and WHITING R. W., *Am. Mineral.* **48**, 737 (1963).
5. DAVIS B. L. and ADAMS L. W., *Science* **146**, 519 (1964).
6. MAJUMDAR A. J. and ROY R., *J. Phys. Chem.* **63**, 1858 (1959).
7. KOLKMEIJER N. H. and HENGEL J. W. A., *Z. Kristallogr.* **88**, 317 (1934).
8. CORRIN M. L. and STORM N. S., *J. Phys. Chem.* **67**, 1509 (1963).
9. JOST W. and OEL H. J., *Disc. Faraday Soc.* **23**, 137 (1957).
10. COCHRANE G., *J. Cryst. Growth.* **7**, 109 (1970).
11. COCHRANE G., *Brit. J. appl. Phys.* **18**, 687 (1967).
12. LAKATOS E. and LIESER K. H., *Z. Phys. Chem.* **48**, 228 (1966).
13. MILLS, D. R., PERROTT C. M. and FLETCHER N. H., *J. Cryst. Growth* **6**, 266 (1970).
14. HALBERSTADT E. S., *Nature Lond.* **216**, 574 (1967).
15. LIDIARD A. B., *Handbuch der Physik*, Vol. XX, 246 Berlin, (1957).
16. GREENWOOD N. N., *Ionic Crystals Lattice Defects and Nonstoichiometry*, Butterworths, London (1968).
17. JOST W. and NOLTING J., *Z. Phys. Chem.* **7**, 383 (1956).
18. TOLANSKY S., *Multiple Beam Interferometry of Surfaces and Films*, Clarendon Press, Oxford (1949).
19. JORDAN P. and POCHON M., *Helv. Phys. Acta.* **30**, 33 (1957).
20. MURIN A. N., LUR'E B. G. and TARLAKOV Yu P., *Fiz. tverd. Tela* **3**, 3299 (1961).
21. LIESER K. H., *Z. Phys. Chem.* **NF9**, 302 (1956).
22. LIESER K. H., *Z. Phys. Chem.* **NF2**, 238 (1954).
23. TAKAHASHI T., KUWABARA K. and YAMAMOTO O., *J. electrochem. Soc.* **116**, 357 (1969).
24. FRIAUF R. J., *Phys. Rev.* **105**, 843 (1957).
25. MRGUDICH J. N., *J. electrochem. Soc.* **107**, 475 (1960).
26. BOTTGER G. L. and GEDDES A. L., *J. chem. Phys.* **46**, 3000 (1967).
27. SATHE N. V., PHALNIKAR N. L. and BHIDE B. V., *J. Ind. Chem. Soc.* **22**, 29 (1945).
28. BRECKENRIDGE R. G., *J. chem. Phys.* **16**, 959 (1948).
29. WIMMER J. M. and TALLAN N. M., *J. appl. Phys.* **37**, 3728 (1966).
30. KESSLER A. and MARIANI E., *J. Phys. Chem. Solids* **29**, 1079 (1968).
31. FRIAUF R. J., *J. chem. Phys.* **22**, 1329 (1954).

J. Phys. Chem. Solids, 1971, Vol. 32, pp. 2569–2579. Pergamon Press. Printed in Great Britain

ELECTRON PARAMAGNETIC RESONANCE AND OPTICAL STUDIES OF MONOVALENT MANGANESE CENTER IN NaCl

M. IKEYA* and N. ITOH
Department of Nuclear Engineering, Nagoya University, Nagoya, Japan

(*Received* 10 *December* 1970; *in revised form* 5 *April* 1971)

Abstract—EPR and optical absorption spectra of Mn^+ center in NaCl are studied. EPR spectrum of Mn^+ at K-band frequency has a hyperfine coupling constant of $A = (231 \pm 1) \times 10^{-4}\,cm^{-1}$ and an isotropic g-value of $1{\cdot}9992 \pm 0{\cdot}0005$. Fine structures caused by second order hyperfine interaction at X-band frequency are analyzed by diagonalizing the matrix of the spin Hamiltonian which contains the Zeeman and the hyperfine terms. Shf structures are also observed for the magnetic field along $\langle 111 \rangle$. The temperature dependence of the hyperfine coupling constants of Mn^{2+}, Mn^+ and Mn^0-C is measured and explained by using theoretical formula based on the phonon-induced hyperfine coupling. It is concluded that the Mn^+ ion is located at the Na^+ site. An optical absorption band at 4·47 eV is ascribed to the transitions from the ground state $3d^54s(^7S)$ to the excited states $3d^54p(^7P)$ of the Mn^+ ion. Mn^+ ion are produced when the Mn^0 atom traps a positive hole or when the Mn^{2+} traps an electron.

1. INTRODUCTION

THE NATURE of the electronic configuration of impurity centers in ionic crystals has received a great deal of attention[1–3] and many works on EPR and optical absorption studies have been made. Comparison between the EPR and optical studies is useful in understanding the nature of the impurity center and has given much information for some paramagnetic centers, such as Cu^0, Ag^0 and Tl^0 [4, 5]. Such comparisons, however, can be made in a limited number of impurity centers since EPR measurements can be made only for the paramagnetic centers.

Impurities in rare earth and iron groups may offer several kinds of centers for which both EPR and optical absorption techniques are employed. It is also interesting to note that the same impurity with several valencies can be paramagnetic in such a case, which makes it feasible to compare the states of an impurity with different valencies in a crystal.

Recently, electron paramagnetic resonance studies on manganese with valencies other than divalent have been made[6–8]. Kasai has found sextets with a smaller hyperfine coupling constant and with a larger hyperfine coupling constant than that of divalent manganese in solid Argon matrix and ascribed them to an atomic and monovalent manganese centers[6]. Bettica *et al.* have found a few sextets with small A values in $NaCl:Mn^{2+}$ X-irradiated and bleached with F light at room temperature, and ascribed some of them to atomic manganese centers[7]. An EPR spectrum with $A = 231 \times 10^{-4}\,cm^{-1}$ at K-band frequency has been found by the present authors, who ascribed it to Mn^+ center in the electron configuration of $3d^54s(^7S)$ from the analysis of the fine structure splittings at X-band frequency caused by second order hyperfine interaction[9]. Theoretical calculation by Watson and Freeman[10] indicated that the hyperfine coupling constant of atomic manganese centers in the electron configuration of $3d^54s^2$ is smaller than that of Mn^{2+}, and that the hyperfine coupling constant of Mn^+ in the electron configuration of $3d^54s$ is much larger than that of Mn^{2+}: these results are consistent with the experimental observation. The reason why such changes in the hyperfine coupling constant occur is as follows: The hyperfine field caused by the core polarization is cancelled by the contribution of the 4*s* electrons in the case of Mn^0 and the net contribution of a 4*s* electron is much larger than that by core polarization in the case of Mn^+.

---

*Present Address: Department of Physics, University of North Carolina, Chapel Hill, N. C. 27514, U. S. A., on leave from Nagoya University.

In the previous study[11] correlation of the optical absorption bands and the EPR spectra for Mn^0 has been studied and optical absorption bands for Mn^0 associated with the transitions from $3d^54s^2(^6S)$ to $3d^54s4p(^6P)$ and $3d^54s5p(^6P)$ are assigned. Five different atomic manganese centers are found and tentative models for them are suggested[11, 12]. These are the Mn^0-*A* at Na^+ site, Mn^0-*B* at off-center displaced from Na^+ site, Mn^0-*C* located at the interstitial site, Mn^0-*D* located at the negative halogen site associated with a positive ion vacancy and Mn^0-*E* at off-center displaced from the halogen lattice site along ⟨100⟩.

In this paper, details of the analysis of the EPR spectrum of Mn^+ center and the optical studies are reported. It is concluded that the Mn^+ center is located at Na^+ lattice site and has an optical absorption band at 4·47 eV. Comparison of *A* values of manganese with various valencies are made, and the temperature dependence of *A* values of Mn^{2+}, Mn^+ and Mn^0-*C* is explained with the theory of the phonon-induced hyperfine coupling.

2. EXPERIMENTAL

Specimens of NaCl doped with several concentrations of Mn^{2+} were prepared with the method described elsewhere[13]. The methods of X-irradiation and optical absorption measurements are the same as described in a previous paper[11]. Optical bleaching was done with a diffraction type monochromator by using high pressure mercury lamp or 500 W Xe lamp. EPR measurements were made with JES-3B and JES-ME spectrometer at both *X*- and *K*-band frequencies. To measure EPR at temperatures between liquid nitrogen and room temperature, the specimen was set in a special holder to which cold gaseous nitrogen was flown.

3. EXPERIMENTAL RESULTS

(a) *EPR spectrum*

Figures 1(a) and 1(b) show the *K*-band and *X*-band EPR spectra, respectively, of the specimen of NaCl:Mn^{2+} X-irradiated at room temperature and then bleached with *F*-light at liquid nitrogen temperature. The direction of the magnetic field is along ⟨100⟩ and the manganese concentration of the specimen is about 0·01 mol %. The *K*-band spectrum consists of the sextets with $A = 15{\cdot}5 \times 10^{-4}$ cm^{-1}, $A = 83{\cdot}0 \times 10^{-4}$ cm^{-1} and $A = 231 \times 10^{-4}$ cm^{-1}. It is described already that these are associated with the Mn^0-*C* (interstitial Mn^0), Mn^{2+} (spectrum II′) and Mn^+, respectively [8, 11]. In the *X*-band spectrum, fine structures are observed instead of the sextet with $A = 231 \times 10^{-4}$ cm^{-1} that is observed at *K*-band frequency. The fine structures are nearly independent of the direction of the magnetic field. The lines in Fig. 1(b) indicate the expected position of the resonance lines of Mn^+ ion at the *X*-band frequency for a paramagnetic ion with ^7S state and $A = 231 \times 10^{-4}$ cm^{-1}.

Figure 2 shows a part of the *X*-band spectrum obtained at liquid nitrogen temperature with the magnetic field along ⟨111⟩ direction. Superhyperfine (shf) structure is clearly resolved. As the angle is deviated from ⟨111⟩ direction, the shf structure becomes broad and disappears completely when the magnetic field is along ⟨100⟩ direction. The splitting at ⟨111⟩ direction is about 4·5 G.

In the above experiments, the specimen is X-irradiated at room temperature and bleached with *F*-light at liquid nitrogen temperature to produce Mn^+. It is also interesting to see whether Mn^+ is produced by X-irradiation at liquid nitrogen temperature. The spectrum III[14] of Mn^{2+} remains after X-irradiation at liquid nitrogen temperature and Mn^+ may

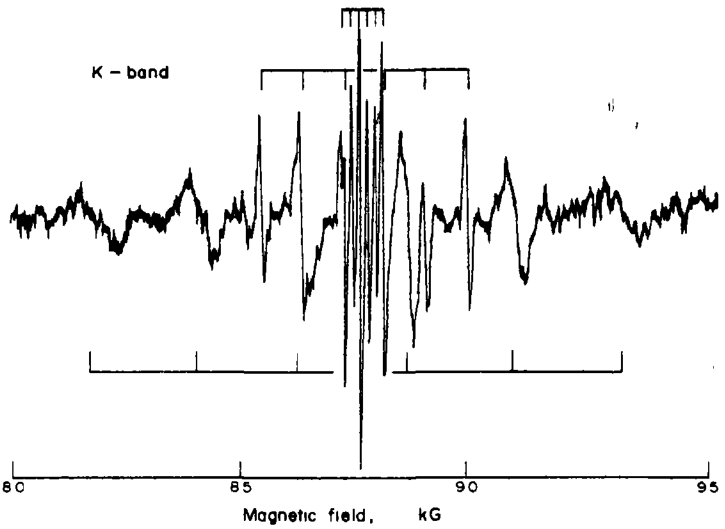

Fig. 1(a).

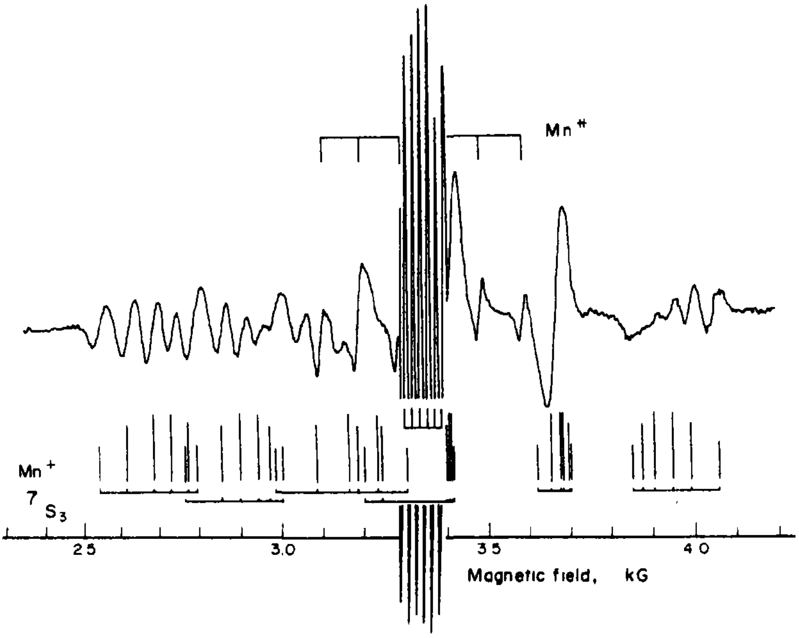

Fig. 1(b).

Fig. 1. EPR spectra of Mn^0, Mn^+ and Mn^{2+} centers in NaCl irradiated at room temperature and then bleached at liquid nitrogen temperature. Measurements were made at liquid nitrogen temperature with (a) *K*-band spectrometer and (b) *X*-band spectrometer. The sextets of Mn^0, Mn^+ and Mn^{2+} are indicated in the figure. In (b) the fine structures of the sextet associated with Mn^+ center are indicated with the lines whose height and the position of the magnetic field are the results of calculations discussed in the text.

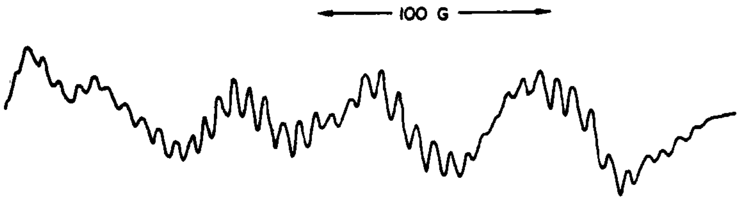

Fig. 2. Superhyperfine structures of Mn^+ center at X band frequency obtained with the magnetic field along $\langle 111 \rangle$.

not be identified in the EPR spectrum of a single crystal even if it is produced. Therefore powdered specimens of $NaCl:Mn^{2+}$ were used, in which the angular dependent fine structures for Mn^{2+} are eliminated. No EPR spectrum associated with Mn^+ is observed after X-irradiation at liquid nitrogen temperature. As the temperature is raised to −120°C, however, EPR spectra for Mn^+ and Mn^0-C are produced. Figure 3 shows the X-band EPR spectrum of the powdered specimen X-irradiated at liquid nitrogen temperature and warmed to −80°C. It is clear that this spectrum is nearly the same as that shown in Fig. 1(b). Fine structures are more clearly resolved in this case than in the case of single crystal. When the measurement is made at K-band frequency, the sextet with $A = 231 \times 10^{-4}\ cm^{-1}$ is observed.

Figure 4 shows the temperature dependence of the hyperfine coupling constant of Mn^+, Mn^{2+} and Mn^0-C. The curves in the figure are the best fitting of the theoretical formula of the phonon-induced hyperfine coupling[15, 16], which is discussed in the next section.

(b) *Optical absorption bands*

Studies of the optical absorption bands are also made. In Fig. 5, curve (a) shows the absorption bands of NaCl: Mn^{2+} X-irradiated at liquid nitrogen temperature for 1 min and

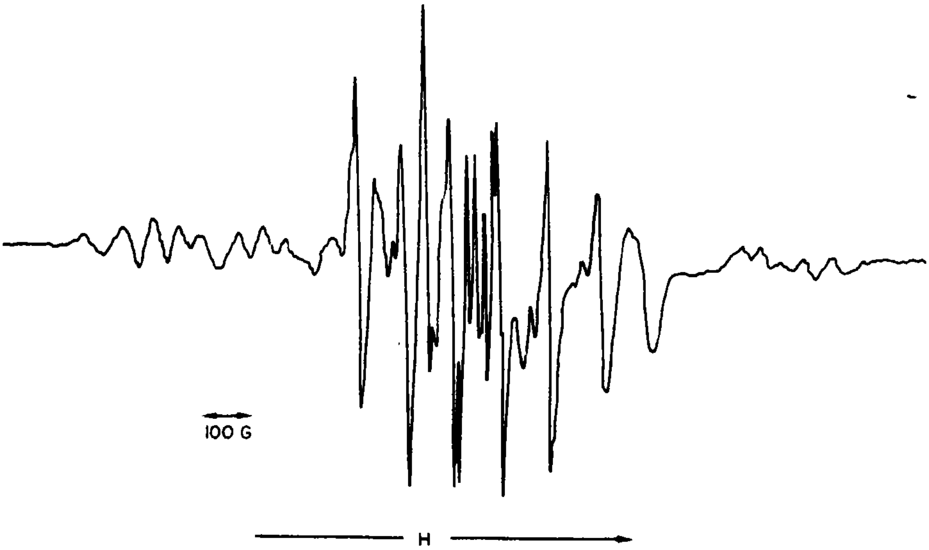

Fig. 3. EPR spectrum of the powdered specimen of $NaCl:Mn^{2+}$ X-irradiated at liquid nitrogen temperature and annealed at −80°C. Measurements were made at liquid nitrogen temperature.

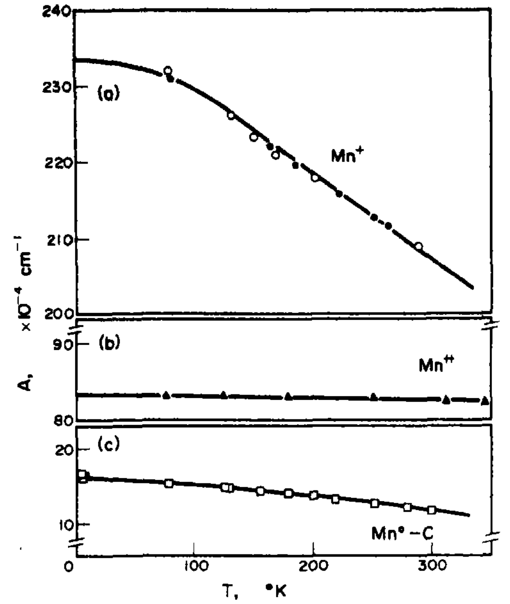

Fig. 4. Temperature dependence of the hyperfine coupling constant of (a) Mn$^+$, (b) Mn^{2+} and (c) Mn^0-C in NaCl. Curves in the figure are the best fittings of the theoretical formula of phonon-induced hyperfine field (see text).

the curve (b) is obtained at liquid nitrogen temperature after subsequent annealing at −80°C. As described in the work on atomic manganese centers, the bands around 3·0 eV are associated with the ^6S-^6P transitions in Mn^0-B center. As the temperature is raised, the bands associated with Mn^0-B are annealed out and new bands at 4·47 and 6·2 eV are formed. The procedure to produce these optical absorption bands is the same as that to produce the EPR spectrum associated with Mn$^+$ in powdered specimen (Fig. 3). The transition energies [17] in the free ion of Mn$^+$ from the ground state $3d^54s(^7S_3)$ to the excited states $3d^54p(^7P_2, {}^7P_3, {}^7P_4)$ are also shown in the figure, which is discussed in the following section.

Figure 6 shows the change in the optical absorption bands of the specimen X-irradiated at room temperature caused by bleaching with the F light at liquid nitrogen temperature. The band at 4·47 eV, as well as the band associated

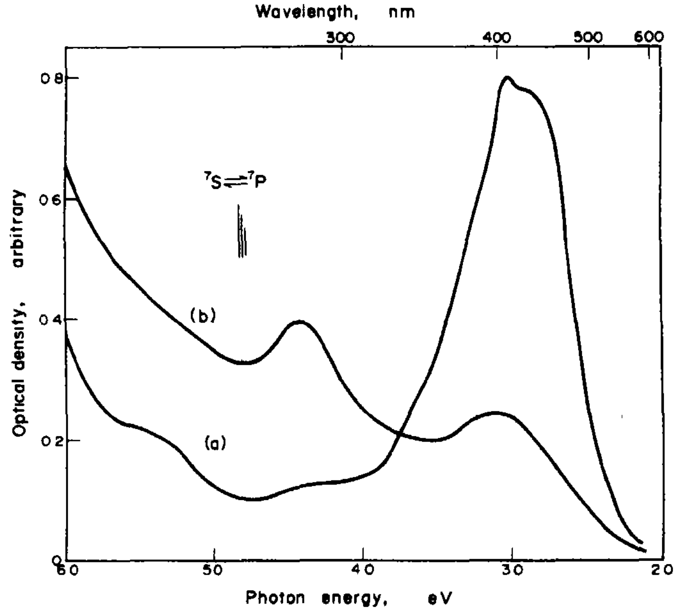

Fig. 5. Optical absorption spectra of NaCl:Mn^{2+}: (a) X-irradiated at liquid nitrogen temperature; (b) annealed at −80°C. Both measurements were made at liquid nitrogen temperature. The lines in the figure indicate the transition energies in free Mn$^+$ from the ground state $3d^54s(^7S)$ to the excited states $3d^54p(^7P)$, which is discussed in the text. The length of the lines indicates the strength of the absorption according to the J-sum file rule.

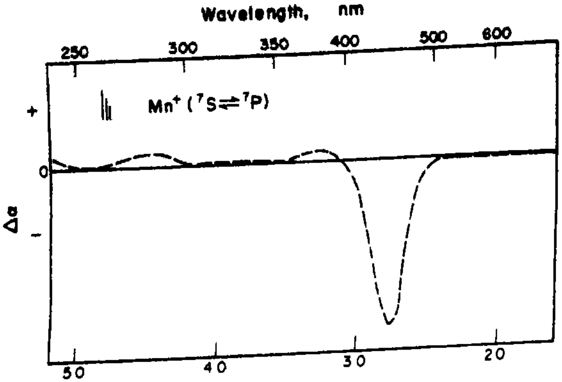

Fig. 6. Change in the optical absorption bands of NaCl:Mn^{2+} irradiated at room temperature by bleaching with the light in F band at liquid nitrogen temperature. The concentration of Mn^{2+} is about 0·01 mol. % and the radiation does is such that F centers less than about 5×10^{16} cm^{-3} are produced.

with Mn°-*C*[11] are produced. In the same specimen the EPR spectrum for Mn$^+$ shown in Fig. 1 is produced. When the concentration is lower (0·002 mol. %) and the irradiation dose is large enough to cause the saturation in the first stage coloration[18], the band at 4·47 eV is not formed and only the band associated with Mn^0-*C* center is formed. It is noted that the EPR spectrum for Mn$^+$ is not produced by *F*-bleaching in this case.

In Fig. 7 the curve (a) shows the optical absorption bands of NaCl:Mn^{2+} irradiated at room temperature and bleached with the *F* light at room temperature. An absorption band at 4·47 eV and a composite band at 3·7 eV* are formed. However, in the specimens with Mn^{2+} of 0·002 mol. %, the band at 4·47 eV is not formed by the same treatment as shown by curve (b). The optical absorption band at 4·47 eV decreases as the temperature is raised around 160°C.

4. DISCUSSION

Three sextets are observed in NaCl:Mn^{2+} irradiated at room temperature and bleached with *F* light at liquid nitrogen temperature. The sextet with $A = 83 \cdot 0 \times 10^{-4}$ cm^{-1} and with $A = 15 \cdot 5 \times 10^{-4}$ cm^{-1} are associated with Mn^{2+} (spectrum II′) and with Mn^0-*C* (interstitial

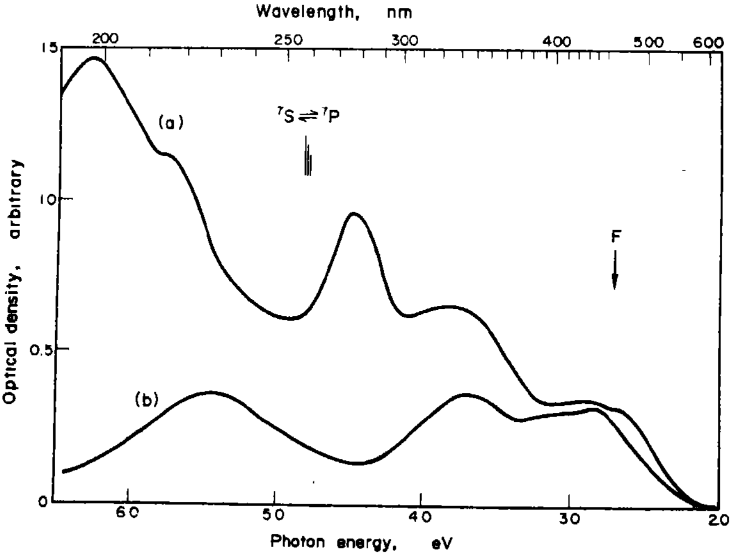

Fig. 7. Optical absorption bands of NaCl:Mn^{2+} irradiated at room temperature and then bleached with the *F* light at room temperature. Concentration of manganese is (a) 0·01 mol. % and (b) 0·0002 mol. %. The bands around 3·0 and at 3·7 eV are due to Mn^0-*C* and Mn^0-*D* centers, respectively.

---

*The nature of this band is discussed in a separate paper.

Mn°), respectively as described previously [11]. The sextet with $A = 231 \times 10^{-4}\,\text{cm}^{-1}$ measured at K-band frequency has been shown to be associated with Mn$^+$[9].

The X band spectrum for Mn$^+$ shows fine structure, which may be analyzed as follows. The spin Hamiltonian for Mn$^+$ may be written as

$$\mathscr{H} = g\beta \mathbf{H}\mathbf{S} + AS_zI_z + \frac{A}{2}(S_+I_- + S_-I_+), \quad (1)$$

where the notation has the usual meanings. The last term with shift operators, $S_\pm I_\pm$, produces non-zero off-diagonal matrix elements. There is a zero field splitting arising from the hyperfine structure quantum number $\mathbf{F} = \mathbf{I} + \mathbf{S}$, which ranges from $|S + I|$ to $|S - I|$. The hyperfine energies at zero field are

$$\bar{A}\mathbf{S}\mathbf{I} = \frac{A}{2}[F(F+1) - S(S+1) - I(I+1)]. \quad (2)$$

The $(2F+1)$-fold degeneracy of the energy level with quantum number F is lifted by the presence of the magnetic field. When the magnetic field is small the states are described with the quantum numbers $|F, m_F\rangle$. When the Zeeman term is much larger than the hyperfine term, the states can be described with $|M, m\rangle$. Perturbation theory may be applied to obtain energy levels in each extreme case. In the intermediate case, the matrix of the spin Hamiltonian (1) must be diagonalized directly to obtain the energy levels. Figure 8 shows the obtained energy levels, Breit–Rabi levels[19] for $S = 3$ and $I = 5/2$ obtained by diagonalizing the Hamiltonian of equation (1) numerically. For convenience, the energy and the magnetic field are divided by A and $(A/g\beta)$, respectively. In the absence of the magnetic field, six energy levels with $F = 11/2 \sim 1/2$ are present. Each level splits into $(2F+1)$ levels by the magnetic field. From the energy levels, one can obtain the positions of the magnetic field $H/(A/g\beta)$, where the energy difference between the states $|M, m_I\rangle$ and $|M+1, m_I\rangle$ is $h\nu/A$, that is, where the allowed

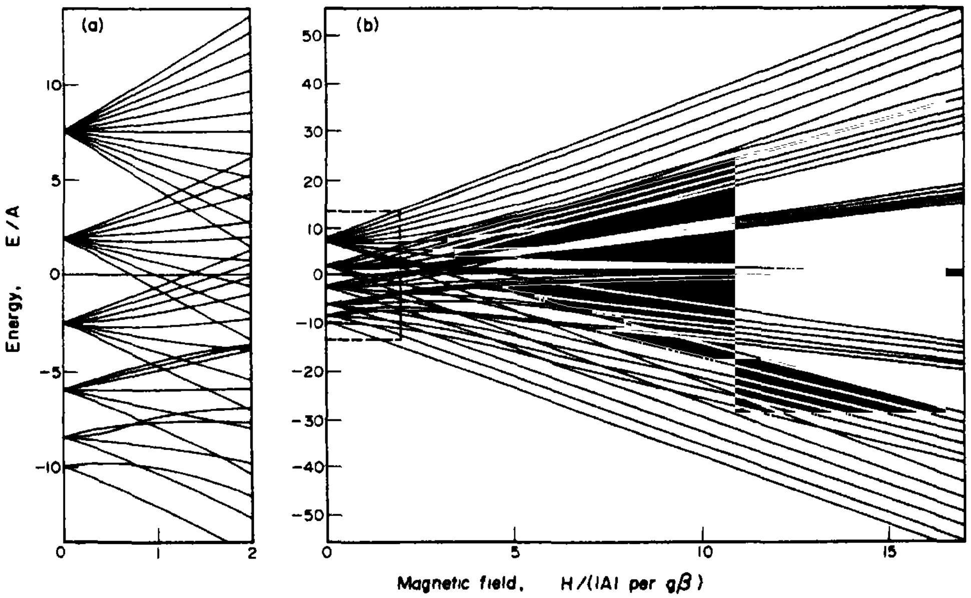

Fig. 8. Energy levels of Breit–Rabi for $S = 3$ and $I = 5/2$ obtained by the numerical diagonalization of the matrix of the spin Hamiltonian that is discussed in the text. (a) is the magnification of the part enclosed by dotted lines in (b).

transitions with $\Delta M = 1$ and $\Delta m_I = 0$ occur. The transition probability of the allowed transition from M to $M+1$ is proportional to $[S(S+1)-M(M+1)]$[20]. The positions of the magnetic field for the X-band spectrum was calculated using the A-value obtained from the K-band spectrum and shown in Fig. 1(b) by the lines whose length indicate the theoretical strength 3:5:6:6:5:3 of the transition probabilities. A group of six lines indicates the fine structure caused by the second order hyperfine splitting and belonging to the same m_I values. Six groups represent the hyperfine splitting of $m_I = \pm 5/2$, $m_I = \pm 3/2$ and $m_I = \pm 1/2$. In the calculation the fine structure produced by the cubic field is not included. A small discrepancy between the experimental and calculated energy may have been caused by the omission of the axial field or the cubic field splitting terms. The qualitative agreement between the experimental and calculated positions of the resonance lines indicate clearly that the Mn$^+$ has a ^7S configuration and that the spin Hamiltonian shown by equation (1) explains the fine structure splitting in the X-band frequency adequately. It is considered that the second order hyperfine coupling has made the outer lines of the K-band sextets wider.

The fact that the EPR spectrum for Mn$^+$ can be analyzed with a spin Hamiltonian which does not include the axial and rhombic field terms may indicate that the center is either in octahedral or in tetrahedral symmetry. The study of the shf structures may decide which is indeed the case. Syperhyperfine structures observed in each fine structure line are considered to be caused by the coupling of the electron spin with the nuclear spins of neighboring chlorine ions. The spin Hamiltonian for the shf structures may be written as

$$\mathscr{H}_{shf} = \sum_\alpha [A_s + A_p(3\cos^2\theta_\alpha - 1)]\mathbf{S}\,.\,\mathbf{I}_\alpha, \quad (3)$$

where θ_α is the angle between the direction of the magnetic field and the axis of the bond with the αth chlorine[19]. I_α is the nuclear spin operator for the αth chlorine. A_s denotes the contact interaction of the electron with the chlorine nucleus and A_p denotes the magnetic dipole–dipole interaction. In the case of Mn$^+$ the best resolution of shf structures is obtained when the magnetic field is along $\langle 111 \rangle$. If Mn$^+$ is at the substitutional site, θ_α at the magnetic field along $\langle 111 \rangle$ is $\cos^{-1}(1/\sqrt{3})$ for all neighboring chlorine nuclei and the anisotropic part of the shf structures vanishes. Thus it is again considered that Mn$^+$ in NaCl is located at the substitutional site. A_s is obtained from the splitting for $H/\!/\langle 111 \rangle$ and A_p is estimated from the angular dependence of the line width. The obtained parameters are

$$A_s = (4{\cdot}2 \pm 0{\cdot}2) \times 10^{-4}\,\text{cm}^{-1},$$

and

$$A_p = (0{\cdot}6 \pm 0{\cdot}2) \times 10^{-4}\,\text{cm}^{-1}.$$

The experimental values of hyperfine coupling constants, A, of manganese with various valencies in NaCl and in other materials are given in Table 1, together with the A values derived from the theoretical values of magnetic susceptibility calculated by Freeman and Watson. As is expected from the theory of core polarization, A values in the same material decrease as the number of d electrons decrease for Mn^{2+}, Mn^{3+} and Mn^{4+}. In the case of Mn$^+$, the net contribution of the 4s electron makes the A value larger than those of Mn^{2+}, Mn^{3+} and Mn^{4+}. For Mn^0, as discussed earlier, 4s electrons outside 3d electrons cancel the core polarization field of 1s, 2s and 3s electrons inside 3d electrons, and the A value is smaller than that of Mn^{2+}.

The A value of Mn$^+$ in NaCl obtained by extrapolation to $T = 0$°K, is $232{\cdot}6 \times 10^{-4}$ cm^{-1}, while that of Mn$^+$ in Ar at 4°K is $270{\cdot}4 \times 10^{-4}$ cm^{-1}. The A value in NaCl is about 86 per cent of that in Ar. For Mn^0, the A value in NaCl is reduced by about 59 per cent. This reduction would be the covalent reduction that is first discussed by Matsumura for Mn^{2+} [21] and recently by Simanek and Müller[22]

Table 1. Variation of the hyperfine coupling constant, A, of manganese with the degree of ionization

Valency	Configuration	$\chi_{\text{theo.}}$[a]	$A_{\text{theo.}}$	$\lvert A_{\text{exp.}}\rvert$(NaCl)	$\lvert A_{\text{exp.}}\rvert$
Mn^0	$3d^5 4s^2(^6S_{5/2})$	−0·64	−16·0	15·5(77°K)[b] 12·0(300°K)[c]	27·9 (Ar)[e]
Mn^+	$3d^5 4s(^7S_3)$	−3·35	−105·0	19·8(300°K)[C]	270·4 (Ar)[e]
Mn^{2+}	$3d^5(^6S_{5/2})$	−3·10 (−3·34)[f]	−91·5 (−99·0)	231(77°K) 82·3(300°K)[d]	81·3 (MgO)[g]
Mn^{3+}	$3d^4(^5D_0)$	−2·91	−86·0	—	84·5 and 52·8 (TiO_2)[g] 71·4 (MgO)[h]
Mn^{4+}	$3d^3(^4F_{3/2})$	−2·34	−60·8	—	72·8 and 70·3 (TiO_2)[g]

Both $A_{\text{theo.}}$ and $A_{\text{exp.}}$ are in the unit of $10^{-4}\ \text{cm}^{-1}$. $A_{\text{theo.}}$ is calculated from the value of $\chi_{\text{theo.}}$

[a] WATSON R. E. and FREEMAN A. J. (Ref. [10]).

[b] IKEYA M. and ITOH N. (Ref. [11]).

[c] BETTICA P., SANTUCCI S. and STEFANI A. (Ref. [7]).

[d] WATKINS G. D. (Ref. [14]).

[e] KASAI P. (Ref. [6]).

[f] The value in the parenthesis is the results from the exchange polarized contact term, others are from the spin polarized contact term.

[g] Taken from the Table given by LOW W. and OPPENBACHER E. L., *Solid State Physics* (Edited by F. Seitz and D. Turnbull), Vol. 17, p. 135, Academic Press (1965).

[h] DAVIES J. J., SMITH S. R. P. and WERTZ J. E., *Phys. Rev.* **178**, 608 (1969).

for iron group impurities. It is also interesting to note here that the A value of Cd^+ in NaCl [23] is considerably smaller than that in solid Argon.

The hyperfine coupling constant of Mn^+ decreases as the temperature increases as expected from the theory of the phonon-induced hyperfine coupling[15, 16]. Simanek and Orbach first proposed a mechanism in which excited configurations of the form $3d^4ns$ are admixed into the ground $3d^5$ configuration of Mn^{2+} by the orbit-lattice interaction[15]. They obtained a formula of the hyperfine coupling constant at temperature T as

$$A(T) = A(0)\left\{1 - CT^4 \int_0^{T_D/T} \frac{x^3}{e^x - 1}\mathrm{d}x\right\}, \quad (4)$$

where $A(0)$ is the hyperfine coupling constant at $T = 0°\text{K}$ and T_D is the averaged Debye temperature. C is related to the phonon-induced admixtures of the excited states. Later, Simanek and Huang adapted a covalent model to eliminate the discrepancy between the theory and experiment and arrived at the same equation[16]. In this case, the parameter C is related to the ns admixture coefficients due to both point-charge crystal field admixture and a covalent charge transfer contribution. From the experimental results shown in Fig. 4, the parameters $A(0)$ and C of manganese center are obtained by the best fitting to equation (4) and are given in Table 2. For Mn^{2+}, the results agree well with those obtained by Huang[24] who uses the experimental results by Wieringen and Rensen[25]. For Mn^0-C center that is located at the interstitial site, the results are reported already by Bianchini *et al.* and by the present authors

Table 2. Parameters for temperature dependence of the hyperfine coupling constants of manganese centers with various valencies in NaCl

Centers	A (0) ($\times 10^{-4}\ \text{cm}^{-1}$)	C (°K^{-4})
$Mn^{2+}(3d^5)$	83·5*	$8{\cdot}2 \times 10^{-12}$
$Mn^+(3d^5 4s)$	232·6	$7{\cdot}2 \times 10^{-11}$
Mn^0-$C(3d^5 4s^2)$	16·0†	$1{\cdot}8 \times 10^{-10}$†

*The value is in agreement with the value obtained by HUANG C. Y. (Ref. [24]).

†These values are same as those obtained by BIANCHINI *et al.* (Ref.[26]).

[26, 27]. The value of C increases as the valency decreases. So far as the C value of Mn^+ is concerned, it may be related with the admixture of $3d^5 4s(^7S)$ with the excited configuration $3d^6(^5D)$ and $3d^4 4s^2(^5D)$ by crystal-field and by spin-orbit interaction. Covalent charge transfer may also play a part in the admixture. The temperature dependence of the hyperfine coupling constant does not show any anomaly as in the case of Cu^0 in KCl and of Mn^0-E in NaCl. Thus it is concluded that Mn^+ is located at the lattice site and not at an off-center site.

The optical absorption band at 4·47 eV is formed by F bleaching at liquid nitrogen and room temperatures following X-irradiation at room temperature. By annealing of the specimen irradiated at liquid nitrogen temperature the absorption band is also formed, accompanied with the destruction of Mn^0-B center. It should be noted here that the EPR spectrum for Mn^+ is formed with the same treatments as those employed to create the 4·47 eV band.

The peak energy of the band at 4·47 eV is very close to the transition energies in free Mn^+ from the ground state $3d^5 4s(^7S_3)$ to the excited states $3d^5 4p(^7P_2, {}^7P_3, {}^7P_4)$, which occur at 4·75, 4·78 and 4·81, respectively[17]. These energies are indicated in Figs. 5, 6 and 7 with the lines whose length is proportional to $(2J+1)$, according to the J-sum file rule of the line strength[20]. Since the 4·47 eV band and the EPR spectrum for Mn^+ are obtained with the same treatments and the transition energy, 4·47 eV, is close to the transition energies in free Mn^+, we conclude that the 4·47 eV band is associated with transitions from ^7S to ^7P states in Mn^+. There is a red shift of 0·3 eV in the transition energy of Mn^+ upon entering into solids. The shift is about 6·5 per cent of the transition energy and it is comparable as the similar shift, 10 per cent, in Mn^0(Mn^0-A and Mn^0-B centers) [11] and much less than the shift in Ag^0 (23 per cent) and Cu^0 (28 per cent)[4, 5]. By comparing the intensities of the EPR spectrum and optical absorption bands for Mn^+ with those of Mn^0, it appears that the oscillator strength for the $^7S \rightarrow {}^7P$ transition in Mn^+ is much smaller than that for the $3d^5 4s^2(^6S) \rightarrow 3d^5 4s(^7S)4p$ transition in Mn^0. This is probably due to the exchange interaction of $4s$ electrons with $3d$ electrons as discussed already in connection with the $3d^5 4s^2(^6S) \rightarrow 3d^5 4s(^5S)4p$ transition in Mn^0.

Finally the formation process of Mn^+ is discussed. X-irradiation at room temperature and liquid nitrogen temperature alone does not produce a considerable amount of Mn^+. Irradiation at liquid nitrogen temperature produces Mn^0-B center[11] and subsequent warming the specimen to −120°C produces Mn^+ center. This is probably because the positive hole, V_K center, becomes mobile above −120°C and is trapped by the Mn^0-B center. When irradiation is made at room temperature, Mn^0 at the lattice site is not produced, but a considerable amount of isolated Mn^{2+} both at the substitutional and interstitial positions may be produced in this case[8]. By bleaching with F light at both liquid nitrogen and room temperature Mn^+ and Mn^0-C centers at the interstitial site are formed. So far Mn^+ at the interstitial site has not been detected. Most probably Mn^{2+} at the interstitial site will trap two electrons and Mn^0-C center will be formed. Mn^{2+} at the substitutional position may trap either one or two electrons to be converted into either Mn^+ or Mn^0-B centers. It is not very clear yet whether Mn^{2+} associated with a positive ion vacancy can capture an electron. Although the EPR spectra for Mn^+ are well analyzed with the spin Hamiltonian which does not include the axial and rhombic field terms, it might be possible that these spectra may represent Mn^+ associated with a positive ion vacancy if the crystal field parameters of lower symmetry for Mn^+ is small. Further works on the EPR of Mn^+ in the axial and rhombic fields may be of interest.

Acknowledgement—This work has been partially supported by the grant donated by Fuji-Photo Film Co.

Authors wish to thank Prof. H. Watanabe of Osaka City University for valuable discussions. Numerical calculation is made with HITAC 5020E, at the computer center, University of Tokyo.

REFERENCES

1. FOWLER W. B., *Physics of Color Centers* (Edited by W. B. Fowler), p. 53, Academic Press, New York (1968).
2. SCHULMAN J. H. and COMPTON W. D., *Color Centers in Solids*, McMillan, New York (1962).
3. McCLURE D. S., *Solid State Physics* (Edited by F. Seitz and D. Turnbull), Vol. 9, p. 399, Academic Press, New York (1959).
4. DELBECQ C. J., HAYES W., O'BRIEN M. C. and YUSTER P. H., *Proc. R. Soc.* **A271**, 243 (1963).
5. KRÄTZIG E., TIMUSK T. and MARTIENSSEN W., *Phys. Status Solidi* **10**, 709 (1965).
6. KASAI P. H., *Phys. Rev. Lett.* **21**, 67 (1968).
7. BETTICA P., SANTUCCI S. and STEFANINI A., *Nuovo Cim.* **48**, 316 (1967).
8. ITOH N. and IKEYA M., *Radiat. Effect* **4**, 161 (1970).
9. IKEYA M. and ITOH N., *Solid State Commun.* **7**, 355 (1969).
10. WATSON R. E. and FREEMAN A. J., *Phys. Rev.* **123**, 2027 (1961), and WATSON R. E. and FREEMAN A. J., *Hyperfine Interaction* (Edited by A. J. Freeman and R. B. Frankel), Chap. II. Academic Press, New York (1967).
11. IKEYA M. and ITOH N., *J. phys. Soc. Japan* **29**, 1295 (1970).
12. IKEYA M. and ITOH N., to be published.
13. IKEYA M., ITOH N. and SUITA T., *Japan J. appl. Phys.* **7**, 837 (1968).
14. WATKINS G. D., *Phys. Rev.* **113**, 79, 91 (1959).
15. SIMANEK E. and ORBACH R., *Phys. Rev.* **145**, 191 (1966).
16. SIMANEK E. and HUANG N. L., *Phys. Rev. Lett.* **17**, 699 (1966).
17. MOORE C. E., Circular of NBS, "Atomic Energy Level II" (1952).
18. IKEYA M., ITOH N. and SUITA T., *J. phys. Soc. Japan* **21**, 1304 (1966).
19. PAKE G. E., *Paramagnetic Resonance*, Benjamin, New York (1962).
20. CONDON E. U. and SHORTLEY G. H., *The Theory of Atomic Spectra* Chap. IX, Cambridge University Press (1964).
21. MATSUMURA O., *J. phys. Soc. Japan* **14**, 108 (1959).
22. SIMANEK E. and MÜLLER K. A., *J. Phys. Chem. Solids* **31**, 1027 (1970).
23. ZHITNIKOV R. A., NELNIKOV N. I. and BARANOV P. G., *Phys. Status Solidi* **35**, K81 (1969).
24. HUANG C. Y., *Phys. Rev.* **158**, 280 (1967).
25. WIERINGEN J. S. and RENSEN J. G., *Phillips Res. Repts* **20**, 659 (1965).
26. BIANCHINI A., SANTUCCI S. and STEFANINI A., *International Symposium on Color Centers*, Rome (1968) Abstract No. 22 (unpublished).
27. IKEYA M. and ITOH N., *International Symposium on Color Centers*, Rome (1968) Abstract No. 90 (unpublished).

J. Phys. Chem. Solids, 1971, Vol. 32, pp. 2581–2591. Pergamon Press. Printed in Great Britain

THEORY OF METALLIC CONTACTS ON HIGH RESISTIVITY SOLIDS (II) DEEP TRAPS

J. G. SIMMONS
Electrical Engineering Department, University of Toronto, Toronto, Canada

(*Received* 30 *November* 1970; *in revised form* 2 *April* 1971)

Abstract—The physics of injecting contacts on insulating solids is studied in detail for the case of discrete and distributed deep traps. It is shown that a shallow trap may be converted to a deep trap and vice versa when electrodes are applied to the insulator depending on the relative magnitudes of the insulator parameters and electrode work function. It is found that the insulator energy bands are severely distorted close to the interfaces and that screening lengths in the insulator are typically less than about $0{\cdot}5\mu$ for practical trap densities. Various combinations of blocking, ohmic and neutral metal-insulator contacts are discussed.

1. INTRODUCTION

GENERALLY speaking the physics of metal-insulator contacts have received very little attention in the literature. Often it is not recognised that considerable distortion of the insulator conduction band can occur at the interface, just as it occurs at a metal-semiconductor junction (Schottky barrier). However, the principle involved in forming the metal-insulator contact is different from that at the semiconductor junction in that traps are involved rather than donor or acceptor centers. (In the case of doped insulators, however, Schottky barriers can be formed at the interface)[1–3].

In an earlier paper a study was made of injecting contacts on insulating solids containing shallow traps. Here we consider the more general and important case of deep traps. As in the earlier paper[4] we concern ourselves with electron, rather than hole-injecting contacts, since these contacts are easier to visualize. However, it is a relatively simple task to extend the ideas discussed here to hole-injecting contacts.

2. THE INSULATOR IN ISOLATION (ELECTRODELESS INSULATOR)

In a perfect (trap-free) insulator the position of the Fermi level E_{Fi} is determined by the condition that the number of free electrons equal the number of free holes:

$$N_c \exp\left(\frac{E_{Fi}-E_c}{kT}\right) = N_v \exp\left(\frac{E_v-E_{Fi}}{kT}\right)$$

which yields for E_{Fi}

$$E_{Fi} = \frac{E_c+E_v}{2} + \frac{kT}{2}\ln\left(\frac{N_v}{N_c}\right)$$

$$= \frac{E_g}{2} + E_v + \frac{kT}{2}\ln\left(\frac{N_v}{N_c}\right) \qquad (1)$$

where N_c and N_v are respectively the effective density of states in the conduction and valence bands, E_c and E_v are respectively the energies of the bottom of the conduction and valence bands, E_g is the insulator energy gap, k is Boltzmann's constant and T is the absolute temperature. Normally, $(kT/2)\ln(N_v/N_c)$ is small compared to $E_g/2$ so that the intrinsic Fermi level lies close to the middle of the energy gap.

In practice an insulator abounds with traps. Traps positioned above the Fermi level are essentially empty (shallow) (see Figs. 1(a)–1(e)) while those positioned below the Fermi level are essentially filled (deep), see Figs. 1(a) and 1(e). In general, for this

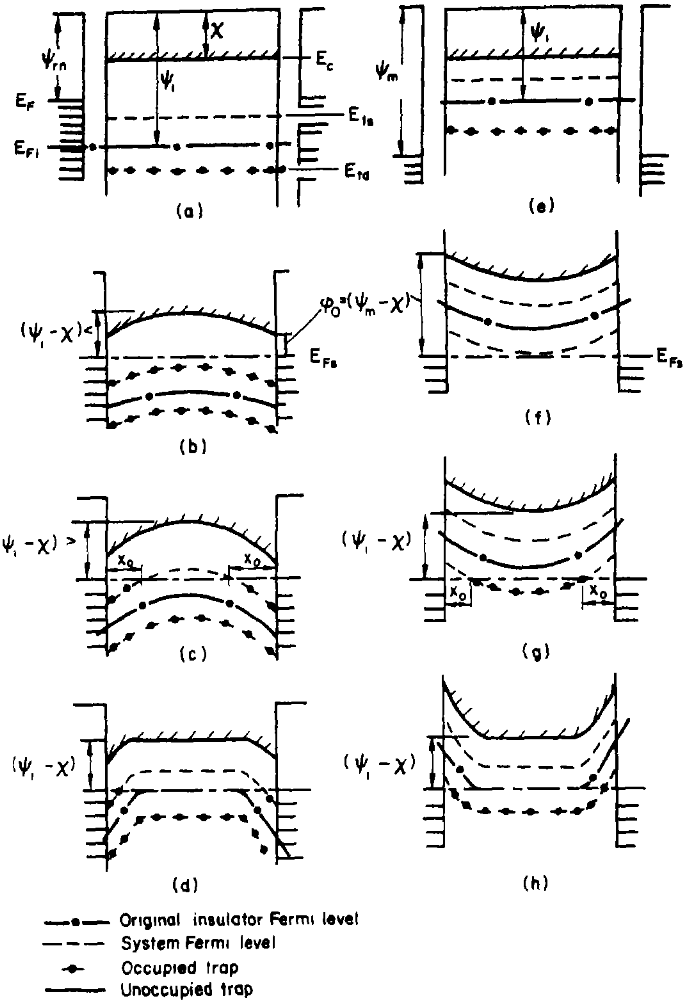

Fig. 1. Energy diagram of metal-insulator-metal system when the insulator contains a shallow trap (upper) level and a deep trap (lower) level. The figure illustrates the system: (a) before the electrodes are attached, and (b) (c) and (d) after the electrodes are attached and ohmic contacts are formed at the electrode-insulator interface. (b) illustrates the situation when the shallow traps have been totally converted to deep traps; (c) when the shallow traps have been converted to partially-filled traps and space charge exists throughout the insulator; and (d) when sufficient shallow traps have been converted to partially-filled traps so that the interior of the insulator is electrostatically screened from the surface. Fig. 1(e–h) are analogous to Figs. 1(a–d), respectively, except that blocking contacts are formed at the interfaces and the deep traps converted to shallow traps.

The dot-dash line marked E_{Fi} is the original insulator Fermi level, and the horizontal chain dotted line marked E_{Fs} is the system Fermi level.

case, the Fermi level will not be positioned close to mid-gap but will depend on the trap parameters.

It is convenient to consider a deep trap as a *donor-type* trap, that is, it is intrinsically neutral when it contains an electron; thus, the electrons do not have as their source the valence band. (If this were not the case, there would be free holes in the valence band essentially equal in number to the electrons residing in the traps and the material would be a relatively good conductor, even at absolute zero of temperature!) Furthermore, we will assume that the trap is monovalent and thus can be charged only positively (by giving up its electron). It is convenient also to assume that a shallow trap is acceptor-type; that is, it is intrinsically neutral when empty. Also this trap is assumed to be monovalent and is charged (negatively) by accepting one (and one only) electron.

In actual fact it is possible for a shallow trap to be donor-type and for a deep trap to be acceptor-type. In an insulator containing a combination of such traps, compensation occurs between these traps; that is, the electrons in the shallow donor-type traps are exchanged with the deep acceptor-type traps and the former are then positively charged and the latter negatively charged. Of course, the system remains electrically neutral and from a statistical point of view it is identical to that of an equivalent system in which all the centres are neutral. However, for clarity, throughout the remainder of this text we will assume that before the electrodes are applied all shallow traps are acceptor-type and all deep traps are donor-type[5].

2.1 *Discrete trap levels*

Consider an insulator containing a single discrete shallow and a single discrete deep trap level (Figs. 1(a)(e)). Non-degenerate equilibrium statistics require that

$$N_{td}\exp\left(\frac{E_{td}-E_{Fi}}{kT}\right)+N_v\exp\left(\frac{E_v-E_{Fi}}{kT}\right)=$$

$$N_{ts}\exp\left(\frac{E_{Fi}-E_{ts}}{kT}\right)+N_c\exp\left(\frac{E_{Fi}-E_c}{kT}\right) \qquad (2)$$

where N_{td} and N_{ts} are respectively the deep and shallow trap densities, and E_{td} and E_{ts} are respectively the energies of the deep and shallow trap levels.

For practical values of trap parameters we may neglect the two terms involving the conduction and valence band, and from the remaining two terms obtain the insulator Fermi energy:

$$E_{Fi}=\frac{E_{ts}+E_{td}}{2}+\frac{kT}{2}\ln\left(\frac{N_{td}}{N_{ts}}\right). \qquad (3)$$

From (3) it is seen that E_{Fi} is determined only by the trap parameters, and is normally positioned between the two traps levels. In the absence of deep traps (we may neglect the term involving the conduction band) we have from (2):

$$E_{Fi}=\frac{E_v+E_{ts}}{2}+\frac{kT}{2}\ln\left(\frac{N_v}{N_{ts}}\right). \qquad (4)$$

In this case the Fermi level lies about halfway between the shallow trap level and the top of the valence band. If shallow traps are absent (we may neglect the term involving the valence band) we obtain from (3):

$$E_{Fi}=\frac{E_c+E_{td}}{2}+\frac{kT}{2}\ln\left(\frac{N_{td}}{N_c}\right). \qquad (5)$$

For this case the Fermi level is positioned about halfway between the bottom of the conduction band and the deep trap level. In general, then, for the three cases discussed above, the insulator Fermi level will not be at the mid-gap of the insulator.

2.2 *Distributed traps*

In many instances the traps, rather than being discrete, are distributed[5] (uniformly, or otherwise) throughout the energy gap of the insulator. This is certainly the case for amorphous materials in which, due to the lack of long range order, the so-called density of states tail (localized levels) exist throughout the energy gap[6].

Consider the situation at absolute zero of temperature. Assume the insulator has been cooled sufficiently slowly so that the system was always in thermal equilibrium, then the *upper most filled* trap level defines the position of the Fermi level at absolute zero. In general the Fermi level is not positioned at mid gap, rather its position depends on the energy distribution of the traps and the number of filled traps. The position of the Fermi level is only a weak function of the temperature and can be approximated by

$$E_{Fi}(T) = E_{Fi}(0) - \frac{\eta_{Fi}}{6\eta'_{Fi}}(\pi kT)^2$$

where $E_{Fi}(0)$ defines the position of the Fermi level at absolute zero of temperature, and η_{Fi} and η'_{Fi} are the trap distribution and its derivative, respectively, evaluated at E_{Fi}.

3. METAL-INSULATOR-METAL SYSTEM

When electrodes are applied to the insulator, the underlying principle in determining the height of the potential barrier and the shape of the bottom of the insulator conduction band is that the vacuum and Fermi levels of the electrode and insulator are continuous across the interface. (Actually the electrode and insulator Fermi levels are now indistinguishable since they are now one and the same Fermi level: the system Fermi level.) The continuity of the vacuum levels determines the height of the interfacial barrier (see Figs. 1 and 2):

$$\phi = \psi_m - \chi$$

where ψ_m is the metal work function and χ the insulator affinity.

Normally before the electrodes are applied $\psi_m \neq \psi_i$, where ψ_i is the original work function of the insulator. Thus, when the electrodes are initially applied, charge is exchanged between the electrode and insulator such that the change in the position of the insulator Fermi level (resulting from the change in occupancy of the electron traps in the insulator) reduces the energy differential between the electrode and insulator Fermi levels. The charge exchange ceases when the two Fermi levels coalesce to form the discrete monoenergetic system Fermi level as shown in Figs. 1 and 2. Clearly, the number of electrons exchanged between the electrode and insulator is essentially equal to the number of traps positioned between the original insulator Fermi level (which is no longer spacially monoenergetic) and system Fermi levels[7]. Thus, if $\psi_m < \psi_i$ (Fig. 1(a), 2(a)), the original Fermi level lies below the system Fermi level (Fig. 1(b, c), 2(b)) which means electrons flowed out of the electrode into the insulator traps. The resulting build up of negative space charge within the insulator causes its conduction band edge to curve upwards, as shown in Figs. (1b–d) and 2(b, c). This type of contact is normally referred to as an ohmic contact (for electrons). Alternatively, if $\psi_m > \psi_i$ (Fig. 1(e), 2(d)) the original Fermi level lies above the system Fermi level (Figs. 1(f, g), a(e)), which means that electrons flow out of the insulator traps into the electrode. In this case the resulting build up of positive charge within the insulator causes its conduction band edge to curve downwards, as shown in Fig. 1(f–h) and 2(e, f). This type of contact is referred to as blocking contact (for electrons). Note that the conduction band edge and the original Fermi level are necessarily parallel.

At any plane in the insulator where the system and original Fermi levels do not coincide, the charge density will differ from that which existed before the electrodes were applied, thus space charge *must* exist at the plane under consideration. Therefore, when the two Fermi levels do not coincide at any point in the insulator (Figs. 1(b,c,f,g), 2(b,e)), space charge exists, and the energy bands are distorted, throughout the insulator. This is the case when either the trap density is too low or the insulator too thin. On the other hand if sufficient charge is injected into the insulator its original Fermi level in the interior of the insulator will be raised or lowered, as the case may be, so as to coincide

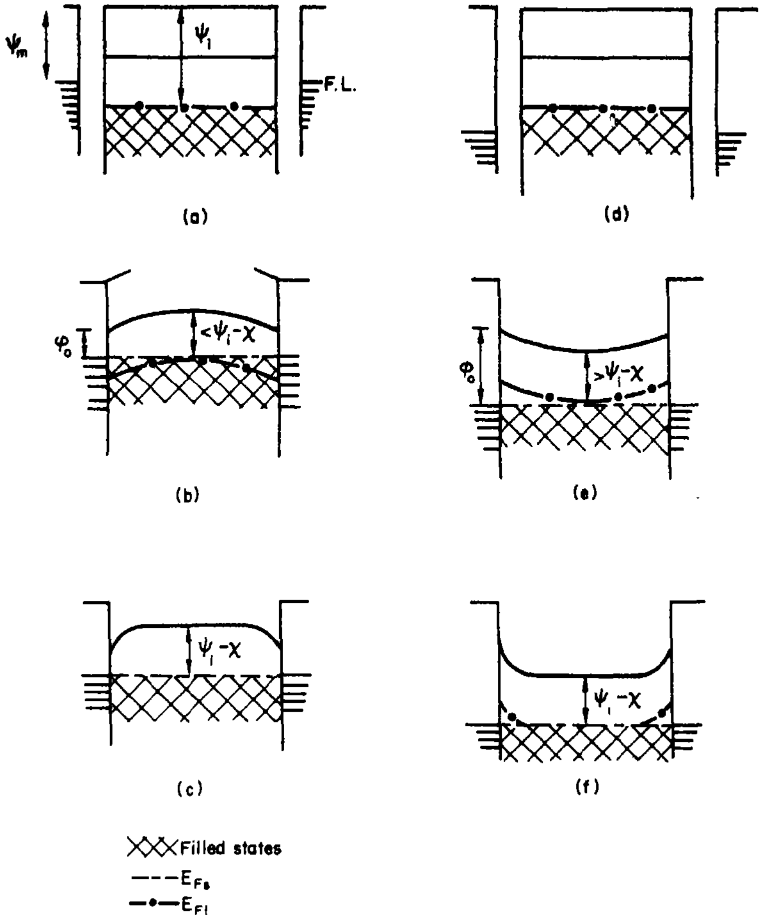

Fig. 2. Energy diagram of metal-insulator-metal system when the insulator contains trap levels distributed throughout its energy gap. The figure illustrates the system: (a) before electrodes are attached, and (b), (c) after the electrodes are attached, and (b), (c) after the electrodes are attached and ohmic contacts formed at the electrode-insulator interfaces. (b) illustrates the case when space charge exists throughout the insulator and (c) when sufficient charge exists in the insulator such that the interior of the insulator is electrostatically screened from the surface.

Figures 2(d)–(f) are analogous to Figs. 2(a)–(c), respectively, except that blocking contacts are formed at the interfaces.

with the system Fermi level over some region within the insulator. Where these two Fermi levels coincide there exists a space-charge-free, and hence field-free, region (Figs. 1 (d,h), 2(c,f)); in other words the space charge is localized just inside the surface of the insulator and *electrostatically shields* the interior of the insulator from its surface. Thus it will be apparent that the maximum extent to which the conduction band edge may be raised (or lowered) within the insulator due to space charge effects is $|\psi_i - \psi_m|$. The regions in which the negative and positive space charge are localised are referred to respectively as the *accumulation* and *depletion* regions.

A discrete trap (which is defined with respect to the insulator band edges) will have the same spacial variation in energy as the bottom of the conduction band after the electrodes are applied (Figs. 1(b–d)(f–k)). It follows then that if $\psi_m < (E_c - E_{ts} + \chi)$ a trap level which is shallow before the electrodes are applied can be converted to a deep level after the electrodes are applied (cf Figs. 1(a) and 1(b)). Similarly if

$$\psi_m > (E_c - E_{td} + \chi)$$

a trap level which is deep before the electrodes are applied may be converted to a shallow level when the electrodes are applied (cf Figs. 1(e) and 1(f)). Furthermore, it is possible for the level to be at once both deep and shallow (see Figs. 1(c–d, g–h)) within the definitions given above. We will subsequently refer to any such trap level as a *partially-filled* level. If

$$(E_c - E_{ts} + \chi) < \psi_m < (E_v - E_{td} + \chi)$$

the problem is one of shallow-trapping[1], with the result that distortion of the band edges are much less severe than when deep trapping occurs.

Generally speaking for the case of an insulator containing traps distributed throughout its band gap, distortion of the band edges will be fairly severe after electrodes are applied (Figs. 2(b,c,e,f)). Only when $\psi_i \simeq \psi_m$ will there be little distortion of the conduction band.

3.1 *Discrete trap levels*

(a) *Fully-charged traps.* Figure 1(b) illustrates the energy diagram for an insulator in which traps that were originally shallow (upper level) have been converted into deep fully-charged (negatively) traps after the application of ohmic contacts to the insulator surface. The occupancy and nature (deep) of the lower traps remain essentially unchanged after application of the electrodes. Thus in the subsequent discussion this level may be considered to play only a passive role (from a space charge point of view) compared to that of the converted (upper) trap. Hence, it follows that a constant negative space charge exists throughout the insulator.

If the trap density of the converted traps is N_{ts} per unit volume and ψ is the potential energy of the bottom of the conduction band with respect to the system Fermi level, we have from Poisson's equation

$$\frac{\mathrm{d}^2\psi}{\mathrm{d}x^2} = -\frac{e^2 N_{ts}}{\epsilon} \qquad (6)$$

where ϵ is the relative permittivity of the insulator and x is measured from the left-hand metal-insulator interface. Integrating (6) and using the boundary condition that $\psi = \phi_1$ and ϕ_2 at $x = 0$ and L (insulator thickness) respectively we obtain

$$\psi = \phi_1 + e^2 N_{ts} x(L-x)/2\epsilon + (\phi_2 - \phi_1)x/L. \qquad (7)$$

The maximum height, $\psi_{\max}$, of the bottom of the conduction band above the electrode Fermi level occurs at a distance

$$x_m = L/2 - (\phi_1 - \phi_2)\epsilon/e^2 L N_{ts} \qquad (8)$$

from the left-hand interface. Substituting this value for x in (7) yields the maximum height $\psi_{\max}$ of the conduction band above the electrode Fermi level. For similar electrodes (that is $\phi_1 = \phi_2 = \phi_0$)

$$\psi_{\max} = \phi_0 + e^2 N_{ts} L^2/8\epsilon. \qquad (9)$$

The maximum band bending that occurs in the insulator is given by the second term on the right hand side of (9). Therefore in order for the shallow traps to be converted to deep fully-charged traps requires that (cf Figs. 1(a) and (b))

$$e^2 N_{ts} L^2/8\epsilon < (E_{ts} - E_F)$$

or

$$L < [8\epsilon(E_F - E_{ts})/e^2 N_{ts}]^{1/2}. \qquad (10)$$

If it is arbitrarily assumed that $(E_F - E_{ts}) = \frac{1}{2}$ eV, $N_{ts} = 10^{22}$ m^{-3} and an insulator dielectric constant, K, of 5 then $L \simeq 3000$ Å, and it is corresponding less than this for higher values of trap density. Hence the fully-charged trap condition for practical trap densities is possible only in very thin insulators.

For the analogous case of an insulator in which traps that were originally deep and have been converted into shallow fully-charged (positively) traps after the application of *blocking* contacts ($\psi_m > \psi_i$) to its surfaces (see Fig. 2(f)), the equations corresponding to (6)–(9) are obtained by writing $(-N_t)$ for N_t in (6–9).

(b) *Partially-charged traps.* Figure 1(c) illustrates the energy diagram when the upper trap level has been converted from a shallow level to a *partially-filled* level upon application of ohmic contacts. The traps close to the surface have been converted to fully-charged (deep) traps. However, those traps positioned in the range $x_0 < x < L - x_0$ although still shallow, contain electrons that give rise to space charge, where x_0 is the distance from each interface that the partially-filled level cuts the system Fermi level. This is due to the fact that the portion of the trap level in the range $x_0 < x < (L - x_0)$ is positioned closer to the system Fermi level than the insulator Fermi level. Thus space charge and hence an electric field exist throughout the length of the insulator. On the other hand, Fig. 1(d) illustrates the case again of a partially-filled trap level but one in which there is sufficient charge inside the surfaces of the insulator ($x < x_0$, $x > L - x_0$) so that the interior ($x_0 < x < L - x_0$) is electrostatically-screened from conditions at the surface.

Figures 2(g)(h) are the corresponding counterparts to Figs. 1(c)(d) when blocking contacts are formed at the interfaces.

Poissons equations for Fig. 1(c) are to a good approximation:

$$\frac{d^2\psi_t}{dx^2} = -\frac{e^2N_t}{\epsilon}, \qquad x_0 > x < L - x_0 \quad (11)$$

$$\frac{d^2\psi_t}{dx^2} = -\frac{e^2N_t}{\epsilon}\exp\left(-\frac{\psi_t}{kT}\right), \qquad x_0 < x < L - x_0 \quad (12)$$

ψ_t is the potential energy of the trap level with respect to the system Fermi level. Using the appropriate boundary conditions (see Appendix) and assuming similar electrode work functions equation (11) integrates to,

$$L = 2x_0 + \pi\left(\frac{2kT\epsilon}{e^2N_t}\right)\exp\left(\frac{\psi_{t(\max)}}{2kT}\right) \quad (13)$$

where

$$x_0 = \left(\frac{2\epsilon}{e^2N_t}\right)^{1/2}\left[(kT + E_c - E_t - \phi_0)^{1/2} - (kT)^{1/2}\right]$$

and $\psi_{t(\max)}$ is the maximum height of the trap level above the system Fermi level. If $\psi_{t(\max)} < (E_t - E_{Ft})$, space charge exists throughout the insulator, with the result that the conduction band is distorted throughout its length, as shown in Fig. 1(c). If $\psi_{t(\max)} = (E_t - E_{Ft})$, the interior of the insulator is free of space charge; Fig. 1(d) illustrates the energy diagram for this case. Setting $\psi_{t(\max)} = E_t - E_{Ft}$ in (13), we find that for this condition to exist that L must satisfy the relationship

$$L \geqslant 2x_0 + \pi\left(\frac{2kT\epsilon}{e^2N_t}\right)^{1/2}\exp\left(\frac{E_t - E_{Ft}}{2kT}\right). \quad (14)$$

Assuming that $(E_t - E_{Ft}) = \frac{1}{2}$ eV, $N_t = 10^{22}\, m^{-3}$, $K = 5$, $\phi_0 = \frac{1}{2}$ eV and $T = 300$°K, then $L \geqslant 0{\cdot}25$ cm.

One half of the last term of (14) is the approximate width of the accumulation regions of Fig. 1(d) and of the depletion regions of Fig. 1(f).

3.2 *Distributed traps*

Figures 2(b)(c) illustrate energy diagrams for the system when the insulator contains traps distributed throughout its energy gap and ohmic contacts exist at the interfaces. Figure 2(b) corresponds to the situation when space charge exists throughout the insulator, and Fig. 2(c) to the case when the interior of the insulator is electrostatically screened from the surface.

Figures 2 (e)(f) are the corresponding counterparts to Figs. 2(b)(c) when blocking contacts exist at the interfaces.

Poisson's equation for the case shown in Fig. 2(b) can be written to a good approximation as (see Appendix)

$$\frac{d^2\psi}{dx^2}=\frac{-e^2\eta_t}{\epsilon}(\psi_i-\chi-\psi)\equiv-\beta^2(\psi_i-\chi-\psi) \tag{15}$$

where η_t is the trap density per unit energy per unit volume (assumed constant). Assuming similar electrode work functions (ψ_m) materials, yields the boundary conditions $d\psi/dx=0$ at $x=L/2$ and $\psi(0)=\phi_0$. Integrating (15) using these boundary conditions we have

$$\psi(x)=(\psi_i-\chi)-(\psi_i-\chi-\phi_0)\times\frac{\cosh[\beta(x-L/2)]}{\cosh(\beta L/2)}. \tag{16}$$

Noting that

$$(\psi_i-\chi-\phi_0)=(\psi_i-\psi_m)$$

we have from (16) that

$$\psi(L/2)=\psi_{\max}=(\psi_i-\chi)-(\psi_i-\psi_m)\operatorname{sech}(\beta L/2). \tag{17}$$

It is of interest to determine the minimum thickness of insulator L_t required in order for the interior to be electrostatically screened from conditions at the surface. This is the condition corresponding to the transitional stage between the two energy diagrams shown in Figs. 2(b) and 2(c). This situation occurs when the interior of the insulator is just electrostatically shielded from the surface; that is when the Fermi levels first coincide and $\psi_{\max}$ just reaches its maximum value of $(\psi_i-\chi)$. It is not possible to use $\psi_{\max}=(\psi_i-\chi)$ in (17) to determine L_t [the substitution yields $(\psi_i-\psi_m)\operatorname{sech}(\beta L/2)=0$] and this is because of the inadequacy of the approximation for the charge density used in (15) when ψ approaches $\psi_i-\chi$ (see A12 of the Appendix). However, we can obtain a sufficiently accurate value for L_t by using $\psi_{\max}=(\psi_i-\chi-kT)$ as the greatest value of $\psi_{\max}$ can attain, for which (15) is still valid. This approximation corresponds to the insulator Fermi level being within kT of the system Fermi level at their closest separation. Substituting this value in (17) yields

$$\cosh(\beta L_t/2)=\left(\frac{\psi_i-\psi_m}{kT}\right). \tag{18}$$

Normally $\exp(\beta L/2)\gg\exp(-\beta L/2)$ so that (18) reduces to

$$L_t\simeq\left(\frac{2}{\beta}\right)\ln\left[2\left(\frac{\psi_i-\psi_m}{kT}\right)\right]. \tag{19}$$

If it is arbitrarily assumed that $(\psi_i-\psi_m)=1$ eV, $\eta_t=10^{22}\,m^{-3}(\text{eV})^{-1}$ and $K=5$, then for $T=300°\text{K}$ we have that $L_t\simeq 4000$ Å and it is correspondingly smaller for greater values of N_t.

For the case of blocking contacts [Fig. 2(e)] the equations corresponding to (16) and (17) are:

$$\psi(x)=(\psi_i-\chi)+(\psi_i-\chi-\phi_0)\times\frac{\cosh[\beta(x-L/2)]}{\cosh(\beta L/2)} \tag{20}$$

and

$$\psi(L/2)=\psi_{\min}=(\psi_i-\chi)+(\psi_i-\psi_m)\times\operatorname{sech}(\beta L/2). \tag{21}$$

The width of the accumulation regions of Fig. 2(c) and the accumulation regions of Fig. 2(f) is equal to $L_t/2$ [see (19)].

3.3 *Other cases*

In light of the previous discussions and those of an earlier paper on shallow trapping [1] it is now possible to deduce the energy diagrams for any combination of insulator parameters and electrode work functions. It is instructive to consider a few of these combinations.

Figure 3(a) shows an insulator originally containing a deep and shallow trap level (Fig. 3(a)(i)) with blocking and ohmic contacts on opposite surfaces. The electrodes are such that (Fig. 3(a)(i))

$$\psi_{1m} > (\psi_i + E_{td} - E_{Fi})$$

and

$$\psi_{2m} < (\psi_i + E_{Fi} - E_{ts})$$

where ψ_{1m} and ψ_{2m} are respectively the work functions of the left hand (LH) and right hand (RH) electrodes. Thus a positive space charge exists in the LH surface of the insulator and a negative space charge in the RH surface, and both sets of traps are converted to partially-filled levels. If sufficient charge is transferred between each interface, that region of the interior of the insulator will be fully screened from the surface where the insulator and system Fermi levels are coincident, as shown in Fig. 3(a)(iii)). Otherwise, space charge exists, and the band edges distorted, throughout the insulator as shown in Fig. 3(a) (ii)).

Figures 3(c)(ii)(iii) correspond to those of Fig. 3(a)(ii)(iii) except that there is a continuous distribution of trap levels in the forbidden gap.

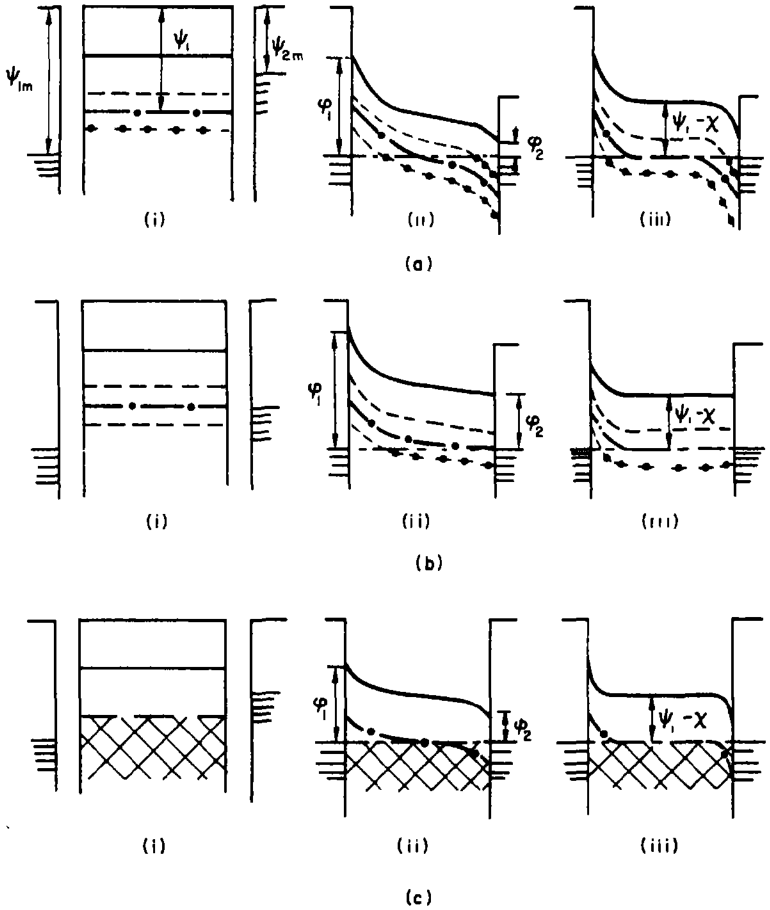

Fig. 3. Energy diagram of insulator with various combination of contacts. (See text for details).

Figure 3(b) illustrates the energy diagram for an insulator with a blocking and a *neutral* contacts[4] at the interface. In Fig. 3(b)(ii) insufficient positive charge reside in the insulator to electrostatically screen the RH interface from the LH interface. Figure 3(b) (iii) illustrates the situation when the RH interface is fully screened from the LH interface.

4. DISCUSSION

The cases that have been discussed refer to systems in thermal equilibrium. If the traps involved in charge exchange are very deep (> 1 eV below the conduction band at $T = 300°K$), the system may require some time to reach equilibrium after the electrodes are applied. The time taken for a trap to discharge its electron is $(\nu P)^{-1}$, where ν is the attempt-to-escape frequency and P $(= \exp [(E_t - E_c)/kT])$ is the escape probability of the electron. Assuming $\nu = 10^{13}\ s^{-1}$ and $(E_c - E_t) = 1\text{eV}$ then at room temperature $(\nu P)^{-1} = 10^4$ sec.

Also, if the trapping density is high, of the order $10^{26}\ m^{-3}\ (\text{eV})^{-1}$, as appears to exist in amorphous glassy semiconductors[9], the width of the depletion regions associated with blocking contacts is of the order 100 Å or less. Thus the depletion region barrier will be transparent to tunneling electrons. What this means is that the electrodes will appear to make a *neutral* contact[4] to the insulator; that is the potential barrier will appear essentially rectangular to electrons entering the insulator from the electrodes (see Fig. 4). Thus, blocking or rectifying contacts will not normally be possible on an amorphous solid [9, 10]. Hence, the present model leads to a neutral contact which, on the one hand, precludes blocking or rectifying effects and, on the other hand, also appears to preclude

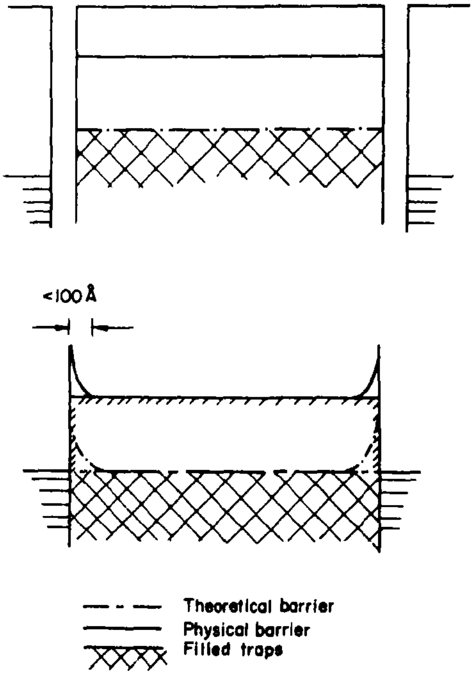

Fig. 4. Energy diagram showing the effective barrier to electrons when blocking contacts exist on an insulator containing a very high density of distributed traps.

injection effects of the sort frequently suggested[11] to support a double-injection model for switching.

REFERENCES

1. SIMMONS J. G., *Phys. Rev.* **166**, 912 (1968).
2. SIMMONS J. G., NADKARNI G. S. and LANCASTER M. C., *J. appl. Phys.* **41**, 538 (1970).
3. NADKARNI G. S. and SIMMONS J. G., *J. appl. Phys.* **41**, 545 (1970).
4. SIMMONS J. G., *J. Phys. Chem. Solids* (in press).
5. For an excellent account of trapping phenomena in defect insulators, see A. Rose Concepts in Photoconductivity (Interscience, 1963).
6. MOTT N. F., *Adv. Phys.* **16**, 49 (1967).
7. This is the reason for retaining the concept of the original insulator Fermi level as well as the system Fermi level after the electrodes are applied. The latter is of course the Fermi level of physical significance and the former merely an artifice for our convenience in determining the space charge.
8. Photoemissive measurements on Al-Al_2Ni_3-Al tunnel junctions [LEWICKI and MEAD C. A., *Appl. Phys. Lett.* **8**, 98 (1966)] suggest potential barriers of this form exist between the electrodes [SIMMONS J. G., *Phys. Rev. Lett.* **23**, 297 (1969)].
9. COHEN M. H., FRITZCHE H. and OVSHINSKY S. R., *Phys. Rev. Lett.* **22**, 1065 (1969).
10. OVSHINSKY S. R., EVANS E. J., NELSON D. L. and FRITZCHE H., *IEEE Trans. Nucl. Sci.* **NS-15**, 311 (1968).
11. HENISCH H. K., FAGEN E. A. and OVSHINSKY S. R., *J. non-Cryst. Solids* **4**, 538 (1970).

APPENDIX

(a) *Solution for partially filled traps*

Integrating (11) and using the boundary condition $d\psi_t/dx = eF_0$ at $x = 0$ we have

$$\frac{d\psi_t}{dx} = -\frac{e^2N_t}{\epsilon}x + eF_0. \qquad (A1)$$

Integrating (A1) and using the boundary condition $\psi_t = (\phi + E_t - E_c)$ at $x = 0$ yields

$$\psi_t = -e^2N_tx^2/2\epsilon + eF_0x + \phi_0 + E_t - E_c. \qquad (A2)$$

The distance x_0, measured from the electrode-insulator interface, that the trap level intersects the Fermi level of the system (see Fig. 1(c)), occurs at $\psi_t = 0$ in (A2), thus

$$eF_0 = e^2N_tx_0/2\epsilon + (E_c - E_t - \phi_0)/x_0. \qquad (A3)$$

Integrating (12) using the boundary condition $d\psi/dx = 0$ at $\psi = \psi_{tm}$ yields

$$\frac{d\psi_t}{dx} = (2e^2N_tkT/\epsilon)^{1/2}\left[\exp\left(-\frac{\psi_t}{kT}\right) - \exp\left(-\frac{\psi_{tm}}{kT}\right)\right]^{1/2} \qquad (A4)$$

where ψ_{tm} is the maximum height of the trap level above the system Fermi level. Integrating (A4) using the boundary condition $\psi = 0$ and ψ_{tm} at $x = x_0$ and L/2, we obtain

$$L/2 - x_0 = \left(\frac{2kT\epsilon}{e^2N_t}\right)^{1/2}\left\{\frac{\pi}{2} - \sin^{-1}\left[\exp\left(-\frac{\psi_{tm}}{2kT}\right)\right]\right\}\exp\left(\frac{\psi_{tm}}{2kT}\right). \qquad (A5)$$

For $\psi_{tm} > 4kT$, (A5) reduces to

$$L/2 = x_0 + \frac{\pi}{2}\left(\frac{2kT\epsilon}{e^2N_t}\right)\exp\left(\frac{\psi_{tm}}{2kT}\right) \qquad (A6)$$

In order to determine x_0 in (A6) we note that $d\psi/dx$ and ψ for the two regions $x \leq x \leq x_0$ and $x_0 \leq x \leq L/2$ are continuous at $x = x_0$. Hence equating (A1) and (A4) at $x = x_0$ (or at $\psi_t = 0$) we obtain

$$eF_0 = (2e^2kTN_t/\epsilon)^{1/2} + e^2N_tx_0/\epsilon. \qquad (A7)$$

Equating (A3) and (A7) and solving for x_0 we obtain

$$x_0 = (2\epsilon/e^2N_t)^{1/2}[(E_c + kT - E_t - \phi)^{1/2} - (kT)^{1/2}] \qquad (A8)$$

(b) *Charge density for distributed traps*

Charge density at any plane x is given by

$$\rho = \int_{E_{Fs}+\psi-(E_c-E_v)}^{E_{Fs}+\psi} \eta_t(E)\,[1 + e^{(E-E_{Fs})/kT}]^{-1}\,dE -$$

$$\int_{E_v}^{E_c} \eta_t(E)\,[1 + e^{(E-E_{Fi})/kT}]^{-1}\,dE \qquad (A9)$$

where $\eta_t(E)$ is the trap density per unit energy per unit volume, and ψ is the potential of the bottom of the conduction band with respect to the system Fermi level. The first and second terms on the right of (A9) are the charge densities in the system and the electrodeless insulator, respectively. Integrating (A9) assuming η_t is a constant in energy we have

$$\rho = (\eta_tkT)\ln\left\{\frac{1 + \exp[(E_c - E_v - \psi)/kT]}{1 + \exp(-\psi/kT)}\right\} -$$

$$(\eta_tkT)\ln\left\{\frac{1 + \exp[(E_{Fi} - E_v)/kT]}{1 + \exp[(E_{Fi} - E_c)/kT]}\right\}. \qquad (A10)$$

Generally speaking

$$\begin{aligned} 1 &\ll \exp[(E_{Fi} - E_v)/kT], \exp[(E_c - E_v - \psi)/kT] \\ 1 &\gg \exp[(E_{Fi} - E_c)/kT], \exp(-\psi/kT). \end{aligned} \qquad (A11)$$

Using the inequalities in (A10) yields

$$\rho \approx \eta_t(E_c - E_{Fi} - \psi) = \eta_t(\psi_i - \chi - \psi). \qquad (A12)$$

The quantity $(E_c - F_i - \psi)$ will be recognized as the energy difference between the system and the intrinsic Fermi levels (Fig. 2).

J. Phys. Chem. Solids, 1971, Vol. 32, pp. 2593–2603. Pergamon Press. Printed in Great Britain

TEMPERATURE AND PRESSURE DEPENDENCE OF THE DIELECTRIC CONSTANT AND SPONTANEOUS POLARIZATION OF FERROELECTRIC KNO_3 AND $NaNO_2$*†

J. T. LEONG and R. M. EMRICK
Department of Physics, University of Arizona, Tucson, Arizona 85721, U.S.A.

(*Received* 1 *February* 1971; *in revised form* 15 *March* 1971)

Abstract—Dielectric constant and spontaneous polarization (via hysteresis loops) measurements were made on ferroelectric KNO_3 (phase III) and $NaNO_2$ (phase III). The boundaries between the ferroelectric phases and adjacent regions received the most attention.

In KNO_3, the isothermal and isobaric I-III transitions exhibited sharp dielectric peaks at all pressures, with $\epsilon_{\max}$ increasing with pressure. KNO_3-I obeys a pressure Curie–Weiss law, with $(1/\epsilon(p))_{T'} = (p-p_0)/C^*$. At $T' = 160°C$, $C^* = -276$ kbar and $p_0 = 4·68$ kbar.

The KNO_3 II-III isobaric transition involves a small jump in ϵ (from 5 to 7·5 at $p = 1·7$ kbar) followed by a steady increase up to the III-I boundary.

The $NaNO_2$ isothermal III-IV transition was detected as a rather small break in the $\epsilon(p)$ curve, with the discontinuity increasing at higher temperatures. The $NaNO_2$ IV-III isobaric transition failed to show a similar anomaly in ϵ, although $\tan\delta$ has a maximum at the boundary.

Polarization loops were obtained in KNO_3-III, with $P_s(p)$ reaching a maximum of 8 μCoul/cm^2. Metastable KNO_3-III was observed at room temperature and room pressure after specimens had first been exposed to high pressures (1·7 to 4·0 kbar) while in region III. In KNO_3-I, $k' = dT_0/dp$ is approximately 25°C/kbar.

1. INTRODUCTION

POTASSIUM nitrate and sodium nitrite are of particular interest among ferroelectrics. Both show first order, order-disorder[1, 2] type transitions across the phase boundary between the low-temperature ferroelectric region and the high-temperature non-ferroelectric region. Moreover, the crystal structure of each is relatively simple, especially when compared with other order-disorder ferroelectrics (TGS and related compounds) [3].

The phase diagrams for $NaNO_2$ and KNO_3 are given in Figs. 1 and 2[4, 5]. $NaNO_2$ has received considerable attention because it possesses an antiferroelectric region (phase II) in which the ordering parameter of the NO_2^- ions in the a-plane changes sinusoidally along the a-axis with a period of 8 layers[6]. KNO_3's most distinguishing characteristic is the manner in which the ferroelectric phase must be approached at room pressure:

(a) by heating approximately 10°C above the I-II boundary and then cooling back down to around 120°C (Fig. 3—the ferroelectric phase appears only during cooling from region I)[7], or,
(b) by melting polycrystalline KNO_3 on a metal substrate[8].

In the latter case, KNO_3-III appears metastably at room temperature as well as at room pressure for periods up to a week.

From the KNO_3 phase diagram, we can see that KNO_3-III is stabilized at higher pressures. Taylor and Lechner [9] obtained ferroelectric hysteresis loops using hydrostatic pressure, but did not exceed 1·38 kbar. Dielectric measurements (Sawada *et al.*[1], Khodakov and Mirskaya [10], Chen and Chernow[11]), have been made across the I-II boundary at room pressure, but such studies have not been extended to high pressures.

Gesi, Ozawa, and Takagi[12] measured the dielectric constant across the III-II-I boundaries for $NaNO_2$ up to 10 kbar. Thus, Taylor and Lechner's[9] (KNO_3-hysteresis loops) and Gesi's ($NaNO_2$—dielectric constant) are the only high pressure studies of the dielectric properties of these two materials. However, differential thermal analysis, volume discontinuity, and X-ray studies have been made mainly to establish the location

---

*Supported in part by the U.S. Atomic Energy Commission.

†Part of a thesis submitted by J. T. Leong in partial fulfillment of the requirements for the Ph.D. degree.

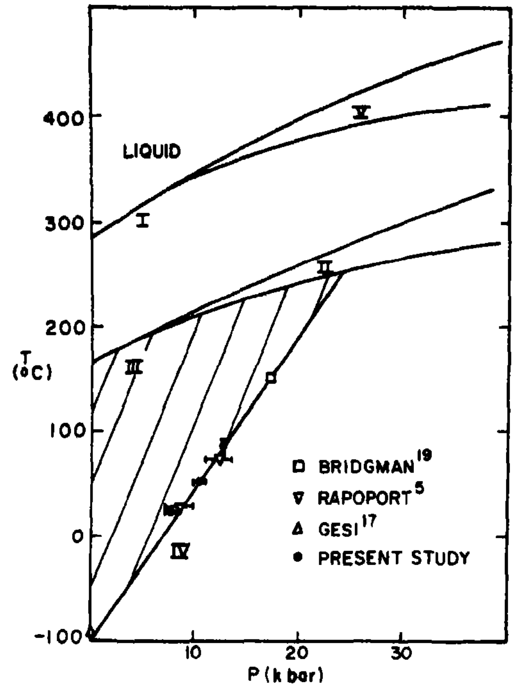

Fig. 1. Phase diagram of $NaNO_2$ (phase boundaries in diagram are from Rapoport[5]).

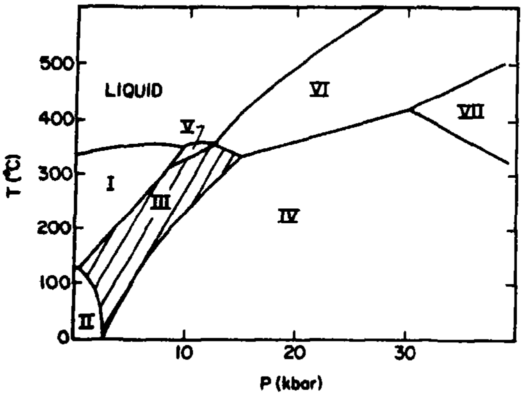

Fig. 2. Phase diagram of KNO_3 (Rapoport and Kennedy [4]).

of the phase boundaries.) The present work extends the two most direct methods of investigation (spontaneous polarization via hysteresis loops and dielectric measurements) into the high pressure regions. The main emphasis is on the behavior of the spontaneous polarization and dielectric constant at the boundaries between the ferroelectric region and all adjacent regions for both KNO_3 and $NaNO_2$.

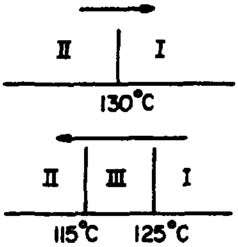

Fig. 3. Schematic diagram of location of metastable KNO_3-III. Upper: Upon increasing temperature, the transition II → I occurs directly. Lower: As the temperature is lowered from phase I, the sequence is I → III → II.

2. EXPERIMENTAL PROCEDURE

(a) *Sample preparation*

KNO_3 and $NaNO_2$ boules were obtained through the courtesy of G. A. Samara, Sandia Corporation, Albuquerque, New Mexico. The *c*-axis of KNO_3 and the *b*-axis of $NaNO_2$ are the directions along which spontaneous polarization occurs. All specimens were cut into thin rectangular plates, with the faces of the plates perpendicular to the ferroelectric axis.

The two KNO_3 boules were prepared by slow cooling of aqueous solutions of KNO_3. Slabs, 1·5 to 2 mm thick, were cut perpendicular to the *c*-axis (the long axis of the boule) with a Laser Technology diamond wire saw. Each slab was then cut into one or two rectangular plates, having area 0·1 to 0·2 cm². Each plate was glued onto a polishing jig and polished on 4/0 emery paper to a thickness of 0·05 to 0·07 cm.

Electrodes were applied to all samples by painting silver conductive paint on the faces of the plates and drying a day or so in a desiccator.

The $NaNO_2$ boules (about 4 cm long, with a cross section of approximately 0·2 cm²) were grown from melts by P. Wilcox at Sandia. Cutting, polishing and painting procedures were identical to those used in preparing KNO_3 samples.

(b) *Pressure systems and fluids*

The initial measurements for both KNO_3 and $NaNO_2$ were made at Sandia Corporation Laboratories using G. A. Samara's 30 kbar[13] (pentane–isopentane) and 14 kbar (Dow Corning 200 silicone oil, 3·0 cs) hydrostatic pressure systems. However, with the exception of the $NaNO_2$ dielectric constant data, all the results described here were obtained with two 10 kbar[14] systems at the University of Arizona. Silicone oil was used as the pressure fluid in the majority of the runs; hexane was used for some of the $NaNO_2$ runs around 10 kbar. Pressure was determined by Manganin resistance gauges calibrated against the freezing pressure of mercury at 0°C (7·492 kbar).

(c) *Bridge and looper*

A standard capacitance bridge (General Radio type 1620A) was used for all dielectric measurements. Most of the data presented here are based on measurements at 10 kHz, although a few of the earlier runs ($NaNO_2$ dielectric constant) at Sandia were made at 100 kHz. No appreciable differences were observed in using these two frequencies.

A modified Sawyer-Tower circuit was used for the hysteresis loop measurements. This circuit was designed at Sandia[15] and later modified (for reasons which will be discussed later) at The University of Arizona.

(d) *Specimen holder*

The inside diameter of the pressure vessel was 1 in with a chamber length of 6 in. Specimens were mounted in a holder consisting of two strips of linen-based phenolic, each with a small (0·05 cm²) capacitance plate in the center. The strips were flexible enough to provide light spring action, thus ensuring adequate contact between the capacitance plates and the electrodes painted on the specimen faces, while minimizing the external stresses applied to the crystal.

A chromel-alumel thermocouple was placed about 2 mm away from the sample. Specimen temperature was controlled by an internal furnace consisting of nichrome wire wound non-inductively on a lavite hollow cylinder. A copper braid shield enclosed the specimen holder, with the shield grounded to the pressure vessel.

3. DIELECTRIC BEHAVIOR

(a) KNO_3

Previous dielectric studies[1, 10, 11] of KNO_3 at room pressure were confined to the II-I boundary (with temperature increasing) and back down (temperature decreasing) across the I-III-II boundaries. These measurements were repeated in the present study; Fig. 4 shows a typical $p = 1$ bar, II-I transition at 10 kHz, along with the variation of the loss tangent, tan δ. The peak in the dielectric constant ($\epsilon_{max} = 74$), matches that of Chen and Chernow[11].

At $p = 0{\cdot}66$ kbar, the I-III transition gives a similar peak for ϵ, but the loss tangent has a broader and stronger peak (Fig. 5). At these low pressures (0·5 to 1·5 kbar), temperature hysteresis (approximately 4°C) was observed across the I-III boundary.

The Curie-Weiss behavior of KNO_3-I was investigated at 0·5, 1·0, and 1·5 kbar. In all these cases, region III was approached through the II-I, $p = 1$ bar, transition in order to avoid the more destructive (Taylor and Lechner[9]) III-I transition at high pressures.

Conductive losses in region I limited the

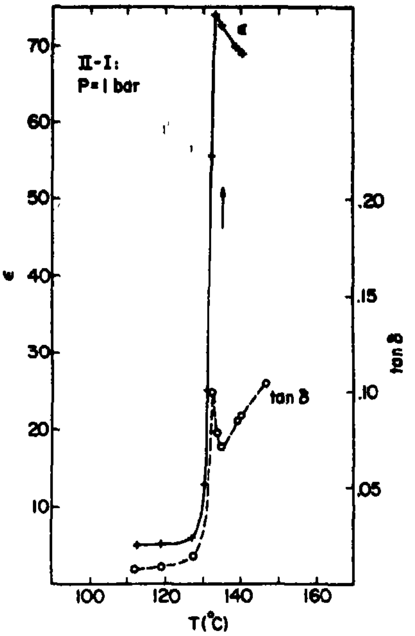

Fig. 4. Dielectric constant and loss tangent of KNO_3 across the II-I transition at $p = 1$ bar (increasing temperature).

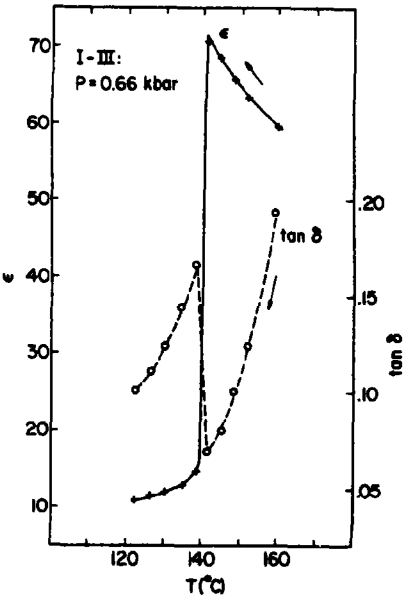

Fig. 5. Dielectric constant and loss tangent of KNO_3 across the I-III transition at $p = 0{\cdot}66$ kbar (decreasing temperature).

temperature range in which $(1/\epsilon)$ was linear. At 0·5 kbar, this range was approximately 12°C, and about 7°C at 1·5 kbar. Consequently, the extrapolated values for T_0, the Curie–Weiss temperature, are rather imprecise, especially because typical T_0 values are so far from the linear regions (Fig. 6). The values for the Curie constant, C, show a slight increase up to 1·0 kbar.

Figure 7 shows an isothermal ($T = 160{\cdot}0 \pm 0{\cdot}5$°C) KNO_3 I-III transition. The peak in ϵ is exceptionally sharp and is rather similar to the isobaric peaks. The inverse dielectric constant, $(1/\epsilon)$, is also plotted against pressure in Fig. 7, and follows a definite Curie–Weiss pattern: $\epsilon = C^*/(p-p_0)$, where $C^* = -276 \pm 3$ kbar and $p_0 = 4{\cdot}68 \pm 0{\cdot}07$ kbar (for Specimen A). At higher temperatures, C^* decreases slightly and p_0 increases: $C^* = -327 \pm 9$ kbar, $p_0 = 7{\cdot}3 \pm 0{\cdot}3$ kbar at 180°C (for Specimen C).

Dielectric behavior across the II-III boundary is shown in Fig. 8. A much smaller anomaly is evident, with ϵ jumping to a value of 7·5 at the boundary and then steadily increasing up to the III-I boundary. The reverse III-II transition exhibits a small temperature hysteresis (approximately 2°C). Both transitions (II-III and III-II) resemble the III-II (temperature decreasing) data of Sawada[1] at room pressure; however, the jump is much smaller (from 5 to 7·5) compared to the room pressure jump from 20 to 5.

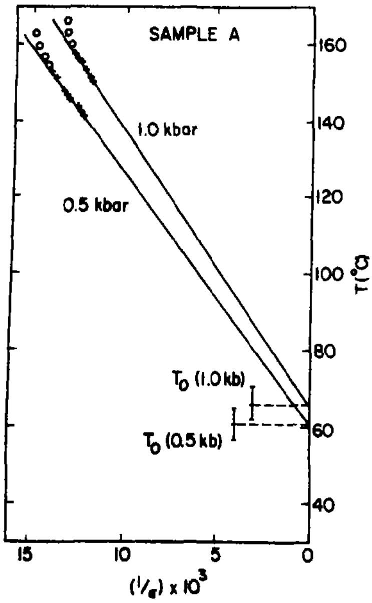

Fig. 6. Inverse dielectric constant vs. temperature for KNO_3-I, showing linear (crosses) and non-linear (circles) regions as determined by computer fit. Error bars are for extrapolated values of $T_0(p)$.

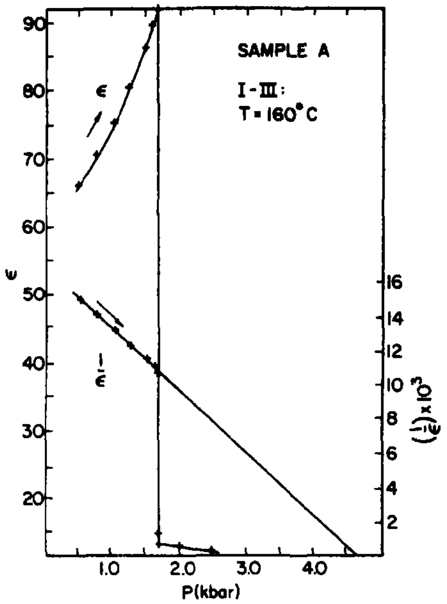

Fig. 7. Dielectric constant and inverse vs. pressure at 160°C for the KNO_3 I-III transition.

An isothermal run ($T = 60$°C) was made across the KNO_3 II-III-IV boundaries, but the extreme sluggishness[16] of these two transitions made reliable measurements impossible. The isobaric ($p = 5$ kbar) IV-III transition was also studied, but again, the transition turned out to be quite sluggish; phase III was evident long after the nominal boundary had been crossed (the existence of metastable phase III being confirmed by hysteresis loops).

(b) $NaNO_2$

Gesi, Ozawa and Takagi[12] were unable to measure C for $NaNO_2$I for p greater than

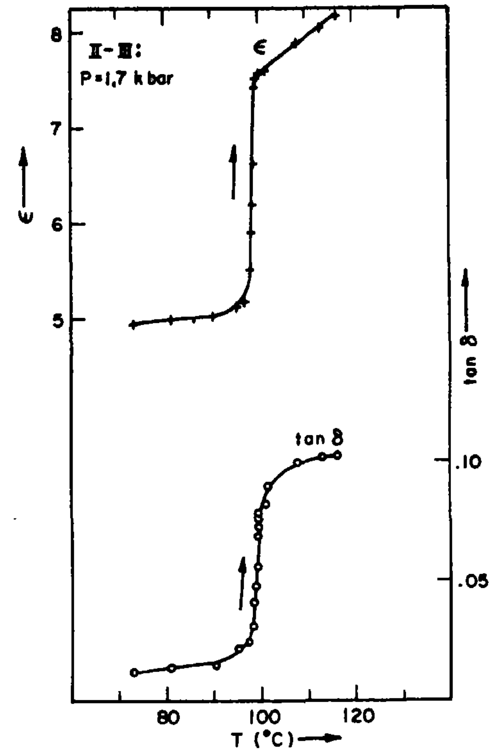

Fig. 8. Dielectric constant and loss tangent of KNO_3 at 1·7 kbar across the II-III transition (increasing temperature).

0·5 kbar, because the linear region of $(1/\epsilon)$ was too small. Since Gesi's III-II-I measurements extended to 10 kbar, the present study focused on the other ferroelectric boundary (the III-IV).

The III-IV transition is a much more gentle transition. Indeed, Rapoport[5] was able to detect isothermal ($T = 26°C$, and $T = 72°C$) transitions only by observing small volume discontinuities. At room pressure, Gesi[17] found the transition (at $-95°C$) in the form of a slight deviation in the linearity of $\epsilon(T)$.

The present study revealed that the isothermal III-IV dielectric anomaly at high pressures is also very slight (Fig. 9). The small jump in the $\epsilon(p)$ curve is somewhat larger at 50°C.

An isobaric ($p = 13·0$ kbar), IV-III, transition failed to show any distinctive discontinuity in $\epsilon(T)$, but the boundary (at $T = 85°C$) coincides with the top of a broad loss tangent peak (Fig. 10).

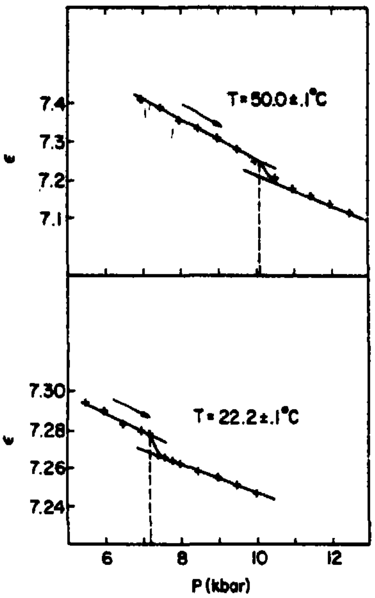

Fig. 9. Dielectric constant at 100 kHz vs. pressure for two isothermal $NaNO_2$ III-IV transitions (increasing pressure).

Anomalies in both ϵ and tan δ (much larger than the anomalies at the III-IV boundary) were observed at 3·5 to 4·0 kbar ($T = 25°C$). The location of these anomalies shifted to higher pressures as the temperature was increased. Since $NaNO_2$ is quite soluble in water, moisture sensitivity was suspected as the mechanism behind the anomalies. Therefore, samples were dried 24 hr in a desiccator (filled with molecular sieves) *after* being mounted, and then introduced directly into the pressure vessel (filled with silica-gel-dried silicone oil). Under these conditions, the anomaly at 3·5 kbar vanished. The effect (i.e., the appearance or disappearance of the anomaly) could be reproduced by exposing the crystals to different humidities before immersing them in the pressure fluid.

4. SPONTANEOUS POLARIZATION

(a) KNO_3

The hysteresis loop circuit was originally

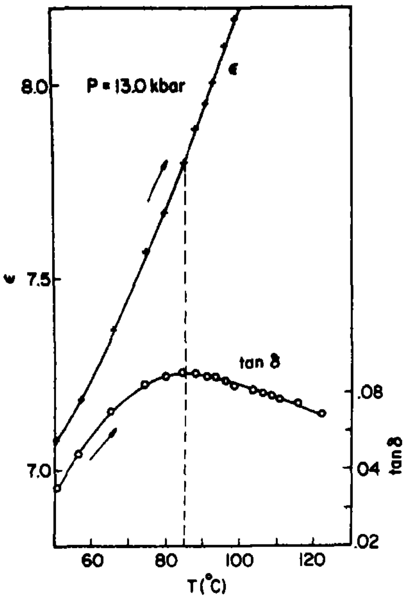

Fig. 10. Dielectric constant at 100 kHz and loss tangent vs. temperature for isobaric $NaNO_2$ IV-III transition (increasing temperature).

a single-cycle pulser. Initial measurements gave distorted, assymmetrical loops. The circuit was then modified to provide a two-cycle loop and a continuous loop. The second cycle loop was completely symmetric, unlike the distorted primary. In all subsequent measurements, the 60 Hz a.c. field was either applied for 3 sec (with the scope trace triggered for one complete cycle at the end of the 3 sec period), or, was applied continuously. Loops thus obtained were completely symmetrical, square, and saturated (i.e., increasing the applied field beyond approximately $2\times E_c$, the coercive field would not result in larger P_s, spontaneous polarization values).

Taylor and Lechner[9] reported a large increase in the maximum value of $P_s(T)$ as p was increased to 1·38 kbar. This effect was ascribed to a large increase in the dipole moment (associated with the displacement of the NO_3^- group with respect to the K^+ ion). If we plot $P_s(p)$ at $T = 130°C$ (which lies in the middle of the $P_s(T) = \text{maximum} \simeq$ constant region), we have a nearly linear $P_s(p)$ with an extremely large slope (Fig. 11).

However, all the P_s data of the present study failed to reproduce the rather large maximum P_s values of Taylor and Lechner. All isobaric runs showed the same fairly rapid increase of P_s (up to a nearly constant value) at the II-III transition, but the maximum P_s's attained were well below those of Taylor and Lechner. Figure 11 shows the 'flattening out' of the $P_s(p)$ curves ($T = 130°C$).

The lower curve in Fig. 11 shows P_s values obtained with 3-sec pulses; each point represents a virgin crystal (one that has just entered phase III along an isobar). The upper curve gives P_s values for a crystal that had been exposed continuously to the applied field; moderately greater values for P_s are evident, although the maximum P_s's are still far below those of Taylor and Lechner. The difference between the 3-sec pulse crystals and the continuous field crystals disappeared when the 3-sec pulse was increased to approximately 30 sec; then, each crystal

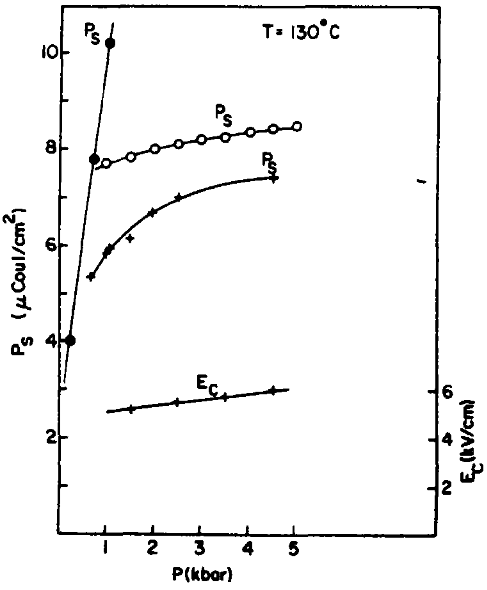

Fig. 11. Pressure dependence of spontaneous polarization and coercive field of KNO_3-III at 130°C. Data of: ● Taylor and Lechner[a]; + present study, 3 sec pulses; ○ present study, continuous loops.

would have the same higher P_s. However, the only P_s value that was close to the large Taylor and Lechner values was 10 μCoul/cm^2, obtained with a crystal that was deteriorating (the loop corners suddenly became round and breakdown occurred when an attempt was made to reach loop saturation).

All P_s data were obtained with virgin crystals. Attempts were made to use the same crystal after it had traversed the II-III boundary, crossed back down (III-II) and back up into the ferroelectric region, but invariably, such a procedure damaged the crystal. This could be seen from the round loop corners and from the fact that saturation could not be achieved; P_s would increase with applied field right up to breakdown (22 kV/cm), although P_s would still be less than the value attained with the virgin crystal.

Perfect loops could also be obtained by passing the crystal through the II-I, $p = 1$ bar, transition, increasing p, and then lowering T until phase III was reached. The maximum P_s values reached in this manner also coincided with the results in Fig. 13.

One of the more startling aspects of KNO_3 behavior is the ability of ferroelectric phase III to exist metastably at room pressure *and* room temperature. At 1·7 kbar, KNO_3 samples were lowered through the III-II boundary to 25°C, without affecting P_s. As Davis and Adams [16] have observed through X-ray studies, KNO_3III does *not* transform as a whole, but parts of the crystal remain in phase III long after the nominal boundary has been crossed. However, hysteresis loops were still observed after the pressure had been lowered to 1 bar. Even with the pressure vessel completely disconnected from the pump, loops would persist for 10 to 20 min before finally being degraded into loss loops.

Phase III seemed to be 'locked in' even longer when the crystal had been exposed to higher pressures (4·0 kbar) before being transferred back into region II. The same effect was observed for a crystal that was lowered into region IV (at 4·7 kbar) down to 40°C, then brought back across the IV-III-II-boundaries. Typical metastable values for P_s and E_c were 4·7 μCoul/cm^2 and 4·4 kV/cm compared to Nolta and Schubring's 3·5 μCoul/cm^2 and 6 kV/cm for polycrystalline KNO_3 melted on a metal substrate [8].

(b) *$NaNO_2$*

The $P_s(T)$ behavior of $NaNO_2$ at 1·0, 3·0, and 5·0 kbar is given in Fig. 12. In Fig. 13, the isothermal ($T = 164$°C) behavior of P_s is plotted as a function of p. At higher pressures, the loop degenerates into a loss ellipse.

In contrast to the case of KNO_3, the coercive field, E_c, of $NaNO_2$ is strongly dependent on the applied field. This has been previously mentioned by Sawada [2] and does not affect the P_s results.

Single-cycle $NaNO_2$ loops were distorted, but the loop assymmetry was less pronounced than in the case of KNO_3 single-cycle loops. Moreover, there was no discernible difference between the 3-sec loops and continuous loops.

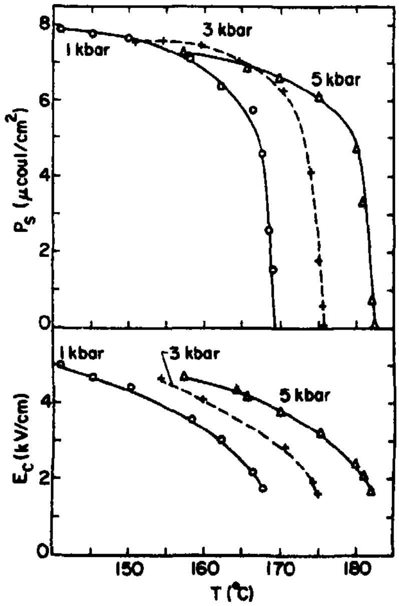

Fig. 12. Temperature dependence of spontaneous polarization and coercive field of $NaNO_2$-III on three isobars.

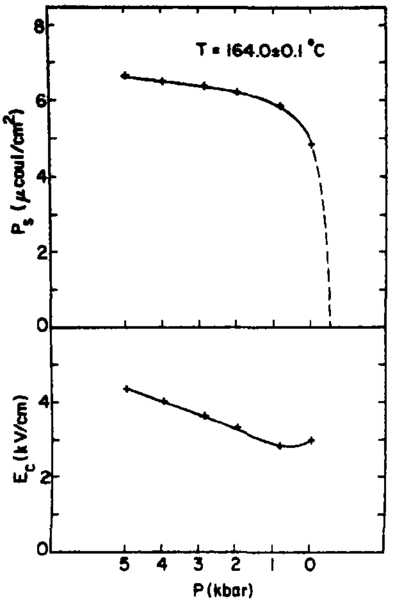

Fig. 13. Pressure dependence of spontaneous polarization and coercive field of $NaNO_2$-III.

5. DISCUSSION

(a) KNO_3

A reasonable assumption to make is:

$$C(p > 0{\cdot}5\ \text{kbar}) \approx C(p = 0{\cdot}5\ \text{kbar})$$
$$= 6440 \pm 110°\text{C},$$

using the data of Fig. 6. Let us further assume that $T_0(p)$ is linear:

$$T_0(p) = T_0(0) + k'p,$$

where

$$k' = \mathrm{d}T_0(p)/\mathrm{d}p.$$

Then,

$$\frac{1}{\epsilon(p)_{T'}} = \frac{(p-p_0)_{T'}}{C^*(T')} = \frac{T' - T_0(p)}{C}$$
$$= \frac{-k'p}{C} + \frac{(T' - T_0(0))}{C}.$$

This equation represents the intersection of the $1/\epsilon(p)_{T'}$ straight line with the entire family of

$$1/\epsilon(T)_p = \frac{T - T_0(p)}{C}$$

straight lines (for $p \geqslant 0{\cdot}5$ kbar).

Thus, $k' = -C/C^* = 23{\cdot}3 \pm 0{\cdot}6$°C/kbar and $T' - T_0(0) = (-p_0C)/C^*$ gives $T_0(0) = 50{\cdot}4 \pm 4{\cdot}5$°C, in contrast to the measured room pressure value of $T_0 = 40$°C, obtained from the data of Fig. 4. From the $\epsilon_{\max}$ data (Fig. 14) and the relation $1/\epsilon_{\max} = (T_c - T_0)/C$, we have $k' = 26{\cdot}7 \pm 1{\cdot}2$°C/kbar and an extrapolated $T_0(0)$ of $46{\cdot}8 \pm 2{\cdot}3$°C, again assuming that $C(p \geqslant 0{\cdot}5\ \text{kbar}) = 6440$°C. This is in rough agreement with the other value for k'. Both estimates are limited by the imprecise value of C.

The spontaneous polarization results show a large discrepancy between Taylor and Lechner's[9] $P_s(p)$ and $P_s(p)$ results of the present study. All results (3-sec pulses and continuous loops) indicate that $P_s(p)$ begins to level off at or before 1·5 kbar. The initial rise in $P_s(p)$ has been suggested[18] as evi-

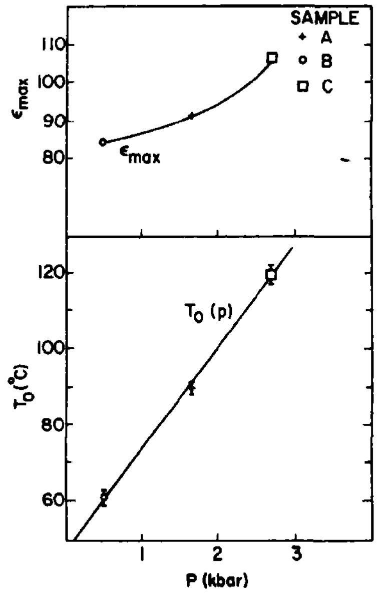

Fig. 14. Pressure dependence of maximum dielectric constant and Curie–Weiss temperature for KNO_3-I.

dence that the long range order in phase III is (initially) limited by the proximity of the I-III boundary.

Taylor and Lechner[9] reported that there were no appreciable differences between the polycrystalline and single-crystal results. Hence, we must rule out orientation error (in aligning the single-crystals) as the source of the discrepancy.

Attempts were made to determine the entropy change across the III-IV boundary by measuring the jump in P_s at the transition. However, phase III would persist metastably long after the nominal boundary had been passed.

(b) $NaNO_2$

The III-IV transition was interpreted by Gesi[17] as evidence of the activation of a NO_2^- ion vibro-rotatory state. Gesi's thermal expansion data and infrared reflectivity measurements (for determining the wave number shift of the ν_2 bending vibration mode) at −95°C and atmospheric pressure, show much smaller changes across the III-IV pressure results of Rapoport's[5] volume compression measurements.

The dielectric data of the present study support Gesi's suggestion that the anomalous change in physical properties across $NaNO_2$ III-IV is enhanced at higher pressures. Figure 9 shows the difference between the transition at 7·2–7·4 kbar (22°C) and the transition at 10·0–10·5 kbar (50°C). The corresponding points on the phase diagram are indicated in Fig. 1[5, 17, 19].

The isobaric transition (Fig. 10) is somewhat harder to detect, but the gradual variation of ϵ suggests a second order (or higher) transition. Indeed, the rather small anomalies across III-IV indicate that phase IV may not be appreciably different in structure from phase III. If so, an obvious question arises: Is phase IV also ferroelectric? At 140°C, P_s loops were observed to 5 kbar; the loop started unsaturated (round corners) at room pressure and gradually deteriorated into a loss ellipse around 5 kbar.

Next, an attempt was made to follow the loop development at 180°C. The loops first appeared at 1·4 kbar and were square and fully saturated. However, as the pressure was increased, P_s reached a maximum of approximately 7 μCoul/cm^2 (around 6 kbar) and then started to decrease. E_c increased throughout this pressure range at a rate comparable to that shown in Fig. 13.

Since the pressure system was limited to 9·5 kbar, the loops could not be followed out to the III-IV phase boundary at 20 kbar. Nevertheless, from the behavior of $E_c(p)$, one could predict that the loop would flatten out and close completely before reaching the boundary. Hence, the entropy change across the boundary cannot be found from loop measurements.

A similar situation exists at room pressure: As the temperature is decreased from T_c, the loop becomes more rounded, deteriorates into a loss ellipse (130°C) and is finally flattened out at 120°C. E_c increases at a rate of 0·05 kV/cm/°C[20]. However, P_s can be measured through pyroelectric measurements all the way down to room temperature [21]. Thus, the question of ferroelectricity in phase IV would best be answered through pyroelectric measurements.

The high pressure dielectric data of Gesi, Ozawa and Takagi[12] do not yield direct measurements (i.e., through $1/\epsilon(T)$) of C and T_0. Takagi and Gesi[22] interpreted the nonlinearity of $1/\epsilon$ above T_N as evidence that the (residual) short-range order of the antiferroelectric phase exists up to approximately $T_N + 15$°C.

Gesi, Ozawa and Takagi[12] obtained a pressure variation of the Néel temperature, $dT_N/dp = 5{\cdot}6$°C/kbar. From Gesi's phenomenological theory[23] $(dT_N/dp)/(dT_0/dp) = 1{\cdot}13$, based on X-ray measurements by Yamada *et al.*[6] and Gesi[23]. Then $dT_0(p)/dp = 4{\cdot}96$°C/kbar.

The expression

$$(1/\epsilon_{max})_p = \frac{T_N(p) - T_0(p)}{C}$$

is strictly true only if the Curie–Weiss law holds above T_N. However, we can use it to obtain a rough estimate of k' from Gesi's dielectric data[12]. The dielectric peaks (at the Néel temperature) at 0·57, 2·55, 4·00 and 5·95 kbar, are, respectively, 3220, 2810, 2010 and 1570. Using $C = 5130°C$[21] (and assuming that $C(p) =$ constant), we have $k' = dT_0/dp = 5{\cdot}28 \pm 0{\cdot}06°C/kbar$, $T_0(0) = 164{\cdot}1 \pm 0{\cdot}2°C$. This is surprisingly close to the other value of k' (and to Nomura's[21] $T_0(0) = 163°C$), but the close agreement should not be taken too seriously, since Curie–Weiss behavior begins only above $T_N + 15°C$.

Finally, we can utilize the P_s data. From Gesi's theory[23], $T/T_0 = (S_f + \Delta_0 S_f^3)/\tanh^{-1} S_f$, where S_f, the long range ordering parameter, $= P_s/N\mu$. N and μ are, respectively, the concentration and the dipole moment of the molecular dipoles. The parameter Δ_0 is related to the elastic energy contribution to the dipole interaction energy. Near the transition,

$$S_f^2 \approx \frac{3(1 - T/T_0)}{1 - 3\Delta_0};$$

using the P_s data, this yields $k' = 4{\cdot}2 \pm 0{\cdot}3°C/kbar$ (Fig. 15), a value moderately lower than the ones based on dielectric and X-ray data.

6. CONCLUSIONS

KNO_3-I exhibits Curie–Weiss behavior in pressure, with a well-defined pressure Curie constant and extrapolated Curie–Weiss pressure. The peak values of the dielectric constant at the I-III boundary, ϵ_{max}, increase with pressure. These two results permit a rough estimate of $k' = dT_0/dp$ to be made ($k' \simeq 25°C/kbar$).

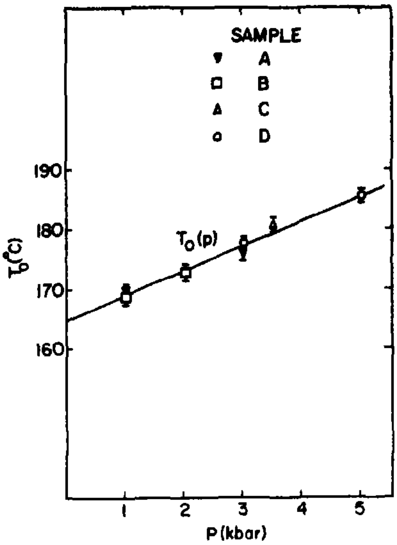

Fig. 15. Pressure dependence of Curie–Weiss temperature for $NaNO_2$.

In region III, $P_s(p)$ gave maximum values well below those reported previously[9]. Metastable KNO_3-III at room pressure and temperature could be induced by first exposing the crystal to high pressures (1·7 to 4·0 kbar) around 130°C. Typical P_s values for metastable KNO_3-III compare favorably with polycrystalline KNO_3 on metal substrate[8].

The $NaNO_2$ III-IV transition showed a slight discontinuity in the $\epsilon(p)$ curve, with the effect enhanced at higher temperatures. The question of ferroelectricity in phase IV could not be answered since $E_c(p)$ increases fairly rapidly. Calculations based on $P_s(T)$ at different pressures yield $k' = dT_0/dp = 4{\cdot}2°C/kbar$, a value somewhat lower than those provided by dielectric and X-ray measurements.

Acknowledgements—The present study was initiated at the suggestion of G. A. Samara, Sandia Corporation, Albuquerque, New Mexico. Preliminary measurements were conducted with G. A. Samara's high pressure systems at Sandia and with a Sandia-designed hysteresis loop circuit. B. E. Hammons and W. L. Chrisman provided valuable technical assistance in the initial runs at Sandia.

The looper circuit was modified repeatedly with the assistance of C. Simmons and P. Mioduski at The

University of Arizona. R. Lowell helped immeasurably in the maintenance of the two pressure systems.

The work at Sandia was supported by the U.S. Atomic Energy Commission; the major portion of this study was conducted at The University of Arizona and was supported in part by the U.S. Atomic Energy Commission.

REFERENCES

1. SAWADA S., NOMURA S. and ASAO Y., *J. phys. Soc. Japan* **16**, 2486 (1961).
2. SAWADA S., NOMURA S., FUJII S. and YOSHIDA I., *Phys. Rev. Lett.* **1**, 320 (1958).
3. SHIBUYA I. and MITSUI T., *J. phys. Soc. Japan* **16**, 479 (1961).
4. RAPOPORT E. and KENNEDY G. C., *J. Phys. Chem. Solids* **26**, 1995 (1965).
5. RAPOPORT E., *J. chem. Phys.* **45**, 2721 (1966).
6. YAMADA Y., SHIBUYA I. and HOSHINO S., *J. phys. Soc. Japan* **18**, 1594 (1963).
7. SAWADA S., NOMURA S. and FUJII S., *J. phys. Soc. Japan* **13**, 1549 (1958).
8. NOLTA J. P. and SCHUBRING N. W., *Phys. Rev. Lett.* **9**, 285 (1962).
9. TAYLOR G. W. and LECHNER B. J., *J. appl. Phys.* **39**, 2372 (1968).
10. KHODAKOV A. L. and MIRSKAYA E. Z., *Soviet Phys. crystallogr.* **7**, 382 (1962).
11. CHEN A. and CHERNOW F., *Phys. Rev.* **154**, 493 (1967).
12. GESI K., OZAWA K. and TAKAGI Y., *J. phys. Soc. Japan* **20**, 1773 (1965).
13. SAMARA G. A., *J. Phys. Chem. Solids* **26**, 121 (1965).
14. ABEY A. E. and TOMIZUKA C. T., *J. Phys. Chem. Solids* **27**, 1149 (1966).
15. McKINNEY I. D., Sandia Corporation Technical Manual # 29-63 (51).
16. DAVIS B. L. and ADAMS L. H., *J. Phys. Chem. Solids* **24**, 787 (1963).
17. GESI K., *J. phys. Soc. Japan* **26**, 953 (1969).
18. SAMARA G. A., *The Effects of Hydrostatic Pressure on Ferroelectric Properties.* Chapter 3 of Vol. III of *Advances in High Pressure Research.* (Edited by R. S. Bradley), Academic Press, New York (1969).
19. BRIDGMAN P. W., *Proc. Am. Acad. Arts Sci.* **72**, 45 (1937).
20. SONIN A. S. and ZHELUDEV I. S., *Soviet Phys. crystallogr.* **8**, 41 (1963).
21. NOMURA S., *J. phys. Soc. Japan* **16**, 2440 (1961).
22. TAKAGI Y. and GESI K., *J. phys. Soc. Japan* **22**, 979 (1967).
23. GESI K., *J. phys. Soc. Japan* **20**, 1764 (1965).

J. Phys. Chem. Solids, 1971, Vol. 32, pp. 2605–2611. **Pergamon Press. Printed in Great Britain**

SPECTRAL SENSITIZATION OF PHOTOCONDUCTIVITY ON THE SURFACE OF ZINC OXIDE CRYSTALS UNDER CLEAN CONDITIONS

W. BAUER and G. HEILAND
2. Physikalisches Institut, RWTH Aachen, 5100 Aachen, Germany

(*Received* 4 *February* 1971; *in revised form* 5 *March* 1971)

Abstract – A merocyanine dye is evaporated in ultrahigh vacuum onto the clean surface of ZnO single crystals. From absorption measurements the dye-coverage can be evaluated. The initial slope of photoconductivity is used to study the spectral distribution in a vacuum before and after dyeing and finally after admission of oxygen. Because of the short exposure to light photochemical changes of the state of the crystal surface are negligible.

The evaluated absolute quantum yield is limited by trapping of electrons. A density of states for these traps is estimated. The relative quantum yield of the sensitized photoconductivity referred to the yield in the intrinsic absorption region exceeds the number 1 by a factor of 2 resp. 5.

1. INTRODUCTION

PHOTOCONDUCTIVITY of ZnO has been observed in the fundamental absorption region, i.e. at wavelengths shorter than about 380 nm [1]. Because of the small penetration depth of about 10^{-5} cm the carriers are freed near the surface of the crystal and the photoconductivity depends on the surface conductivity in the dark. The mobile carriers are electrons in both cases. By adsorption of organic dyes the photoconductivity can be sensitized to longer wavelengths in the visible spectral region, where ZnO is transparent [2]. The light energy absorbed in the dye molecules is transferred to the crystal and causes an increase of carrier density near the surface. Several models have been proposed for explanation [4]. The purpose of the present paper is not a discussion in favour or against one of these mechanisms. We feel, that for understanding of the spectral sensitization it might be helpful to do some experiments under clean and well defined conditions. Therefore solvents and binders are avoided. Since sensitization by adsorbed molecules is a surface phenomenon, the dye is evaporated on clean surfaces of single crystals in an ultrahigh vacuum. Thus an influence of adsorbed gases can be excluded. The spectral distribution of photoconductivity is measured in the same vacuum.

2. EXPERIMENTAL

The crystals were grown in this laboratory from the vapor phase (Fig. 1). For lowering of the *n*-type conductivity which is caused by an excess of zinc about 10^{18} cm^{-3} Cu atoms were added during growth [1]. The surfaces were used as grown and cleaned by heating the crystal to about 400°C for a few minutes in an ultrahigh vacuum immediately before beginning of the measurements. During baking of the vacuum system (200°C) the dye was protected by water cooling (Fig. 2). For evaporation the Ni vessels were emptied magnetically and the dye fell down into the furnace. By turning the cylinder the crystals were moved between window and furnace. A sorption pump and a combination of ion and getter pumps generated a vacuum of 10^{-10} Torr.

Absorption measurements were performed with a spectrometer (Cary 15). The crystal was irradiated by a tungsten-iodine lamp through a monochromator with a quartz prism. The magnetically operated shutter had an opening time of 10^{-3} sec and was triggered

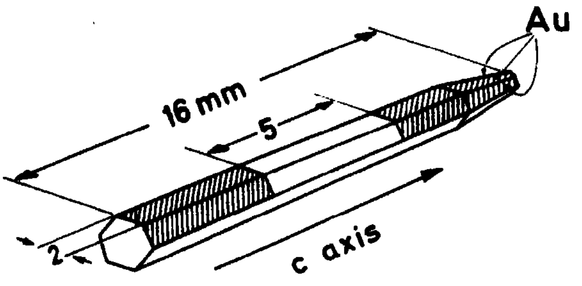

Fig. 1. ZnO crystal with electrodes of evaporated gold.

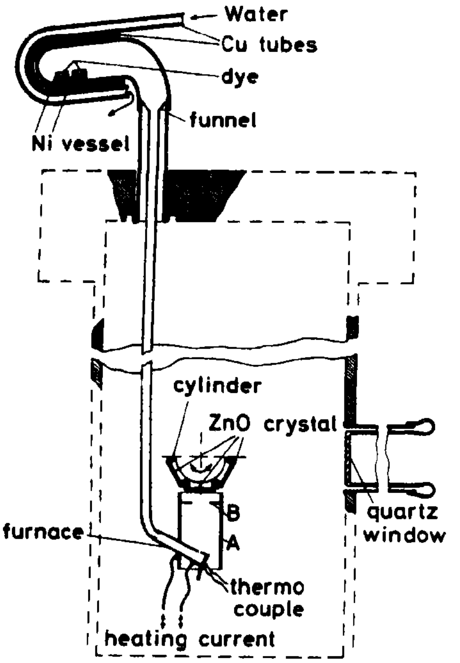

Fig. 2. Cross section of the vacuum vessel with the systems for cooling, transfer and evaporation of the dye.

by the oscilloscope. A thermocouple served for measurement of irradiation intensities. The change of conductance during irradiation was photographed by means of a Robot camera from an oscilloscope (Tektronix 543 with 1 A 7 plug in unit). The rise time of the electric outfit was 10^{-5} sec.

3. RESULTS AND EVALUATION

3.1 *Absorption and coverage*

The sensitizer was a merocyanine with the following structure:

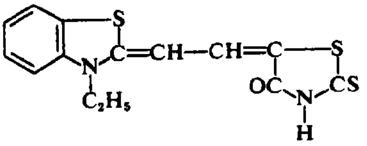

The broadening of the absorption band for the dye on the crystal surface[4] is also found after dyeing from solution (Fig. 3). Furthermore extended studies proved, that no change of absorption in ethanolic solution or of sensitization was induced by evaporation of the dye. Sublimation starts at about 100°C, decomposition becomes obvious at 250°C. After a check of Beer's law for the solution, absorption measurements were used for determination of coverage, i.e. of the number of dye molecules per cm² on the crystal surface. Since the orientation of the adsorbed molecules is not known, we do not attempt to estimate the number of monolayers.

The first method for determination of coverage is based upon the questionable assumption, that the absorbing crossection of the molecules as found in ethanolic solution is not changed very much by formation of an adsorbed layer on the ZnO surface. In the

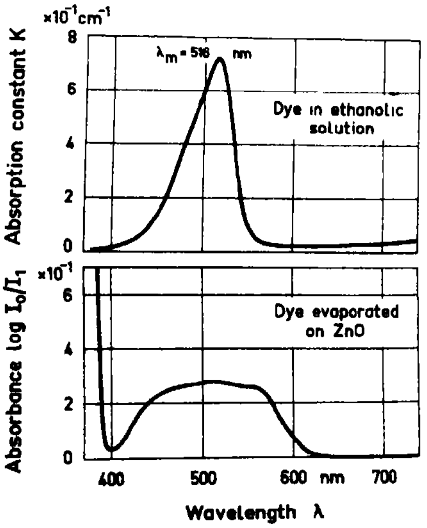

Fig. 3. Absorption spectrum of the dye in solution and after evaporation onto the crystals.

second method the dye is solved from the crystal by a small amount of ethanol under ultrasonic treatment. The absorption of this solution gives the coverage. Results of the two methods are shown in Table 1.

3.2 *Conductance of the crystals in the dark*

The bulk conductivity of the crystals was derived from the conductance in air. In this case the adsorbed oxygen creates a poorly conducting depletion layer whose thickness of about 10^{-5} cm is small compared to the diameter of the crystal. By the baking and heating procedures described in Section 2 the adsorbed oxygen is removed and a small surface conductivity of about $10^{-6} A/V$ is generated (Table 1, ΔN_0). For the surface conductivity $\Delta\sigma$ the following relations hold:

$$\Delta\sigma = (g - g_b) \times \frac{l}{w} = e \times \mu \times \Delta N, \qquad (1)$$

with $g = i/U = 1/R$ total conductance of the crystal (bulk and surface in parallel),

g_b = conductance of the crystal only from bulk conductivity,
l = length of the conducting surface between the electrodes, see Fig. 1.
w = width of the conducting surface,
e = electronic charge,
μ_S = surface mobility of conduction electrons in the accumulation layer,
ΔN = excess density of electrons per surface area, here: in the accumulation layer.

For a more precise definition see [6]. Since the bending of the bands at the surface was not as strong as to require a correction of mobility, the bulk value was used for evaluation of electron density ($\mu_b = 114\,\text{cm}^2/\text{Vsec}$[3]). From Table 1 it can be seen, that in every case the density of electrons at the surface in the dark is increased by evaporation of the dye.

3.3 *Spectral distribution of photoconductivity*

If good contacts are used the photocurrent is proportional to the applied voltage and confined to a thin surface layer. This has been shown for the case of intrinsic absorption[1] and holds as well for the sensitized photocurrent. Therefore the results will be given in terms of a surface conductivity.

An organic dye layer exhibits a photoconductivity itself[4, 7]. The resulting photoconductance might contribute to the observed

Table 1. *Experimental results for three* ZnO *crystals. The electron density* ΔN *is calculated using equation* (1). *The quantum yields per incident photon* η_i *and per absorbed photon* η_a *are explained in equations* (2) *and* (3). *Allowance is made for reflectivity:* 20 *per cent at* 370 nm *and* 10 *per cent at* 520 nm

crystal number → property ↓	3	9	8
Bulk conductivity $\sigma_b \left[\frac{A}{V \times \text{cm}}\right]$	9×10^{-5}	$1{\cdot}2 \times 10^{-4}$	$1{\cdot}1 \times 10^{-4}$
Excess surface electron density before dye evaporation ΔN_0 [cm^{-2}]	$2{\cdot}7 \times 10^{11}$	3×10^{11}	$2{\cdot}5 \times 10^{11}$
Excess surface electron density after dyeing ΔN_d [cm^{-2}]	$5{\cdot}1 \times 10^{11}$	$8{\cdot}8 \times 10^{11}$	1×10^{12}
Dye coverage [cm^{-2}] method 1	$<10^{13}$	3×10^{14}	$6{\cdot}5 \times 10^{14}$
method 2	not measurable	1×10^{15}	$6{\cdot}3 \times 10^{14}$
Relative quantum yield $\frac{\eta_i(520)}{\eta_i(370)}$	0·017	0·37	0·48
Relative quantum yield $\frac{\eta_a(520)}{\eta_a(370)}$	—	5·5	2·2

photoresponse. However an estimation using published data, showed, that this phenomenon should be negligible. An additional check was performed in this work: A glass plate with evaporated dye was studied instead of the ZnO crystal. Therefore the relative contribution of the dye layer should be less than 10^{-4}.

For evaluation of the spectral distribution not the steady state of photoconductivity was studied but the initial slope (Fig. 4). This method has several advantages: in many cases a steady state is reached only after prolonged irradiation. It can be questionable to specify a steady state at all[9]. The decay takes also a long time and may never become complete in a vacuum. These tedious phenomena can be attributed to photolysis[8]. Thereby oxygen is freed and donors of excess zinc are created at the surface. For observation of the initial slope only short light pulses are needed and there is no irreversible increase of surface conductivity. These measurements are not only time saving but also more reliable. Henceforth a quantum yield can be derived without knowing the life time of excited states. This question has been discussed already by Heiland and Neuhaus[9]. These authors also give comparisons for the spectral distribution of steady state and of initial slope of photocurrent.

Undyed crystals showed photoconductivity only in the intrinsic absorption region. After evaporation of the dye onto the clean surface a broad band of photoconductivity appeared at longer wavelengths. The spectral distribution corresponds to the absorption of the dyed crystal as measured after removal from the vacuum system. The intrinsic photoconductivity is not changed by dyeing. Figs. 5, 6 and 7 give examples for different coverage. Subsequent admission of oxygen does not cause any measurable change of the spectral distribution of the initial slope, whereas the total surface conductance in the dark decreases by a factor of 3 to 10.

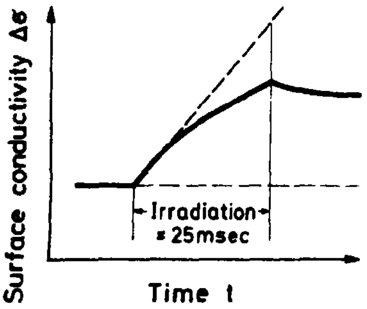

Fig. 4. Measurement of the initial slope of photoconductivity. Drawing after a photograph.

It was checked, that the initial slope is exactly proportional to the irradiation intensity. Thus a correction for equal current density of light quanta throughout the spectrum can easily be made. At λ = 520 nm the incident intensity was 18 times larger than at λ = 370 nm.

3.4 *Yield*

From the initial slope of photoconductivity

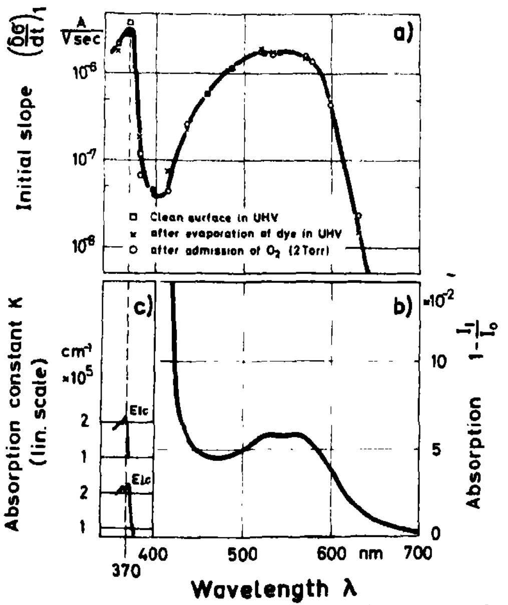

Fig. 5. ZnO crystal 9. (a) Spectral distribution for the initial slope of photoconductivity after various pretreatments, referred to an equal density of incident photons $I_0 = 1{\cdot}5 \times 10^{14}\,\mathrm{cm^{-2}\,sec^{-1}}$. (b) Absorption spectrum of the crystal after dyeing. (c) Absorption constant near the edge measured on a thin single crystal without doping and dye. After Liang and Yoffe[11].

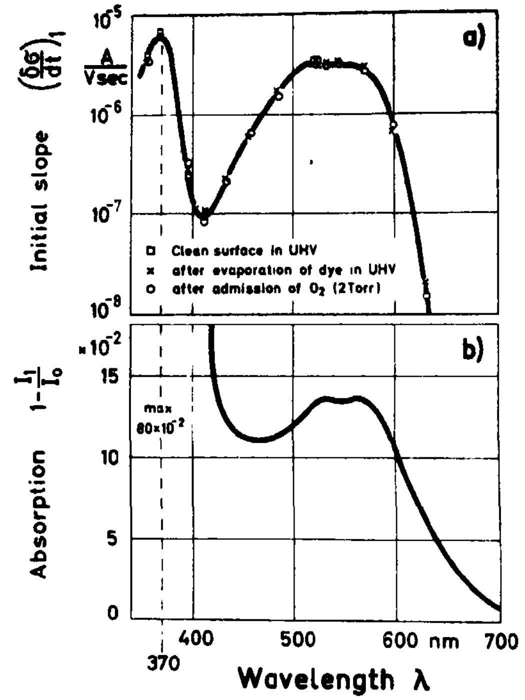

Fig. 6. ZnO crystal 8. (a) Spectral distribution of the initial slope of photoconductivity after various pretreatments, referred to an equal density of incident photons $I_0 = 1{\cdot}5\times10^{14}\,\mathrm{cm}^{-2}\,\mathrm{sec}^{-1}$. (b) Absorption spectrum of the crystal after dyeing.

a yield is derived with two different definitions:

$$\eta_i(\lambda) = \frac{\text{number of freed electrons per time and area}}{\text{number of } \textit{incident} \text{ photons per time and area}} = \left(\frac{\delta N}{\mathrm{d}t}\right)_1 \Big/ I_0 \qquad (2)$$

$$\eta_a(\lambda) = \frac{\text{number of freed electrons per time and area}}{\text{number of } \textit{absorbed} \text{ photons per time and area}} = \left(\frac{\delta N}{\mathrm{d}t}\right)_1 \Big/ I_a. \qquad (3)$$

The derived yields are of the order of 10^{-3} to 10^{-2}, also in the intrinsic absorption region. An explanation is given in the discussion. To check the efficiency of sensitization it may be helpful to relate the yield in the sensitized spectral region ($\lambda = 520$ nm) to the yield for intrinsic absorption ($\lambda = 370$ nm). These numbers are given in Table 1.

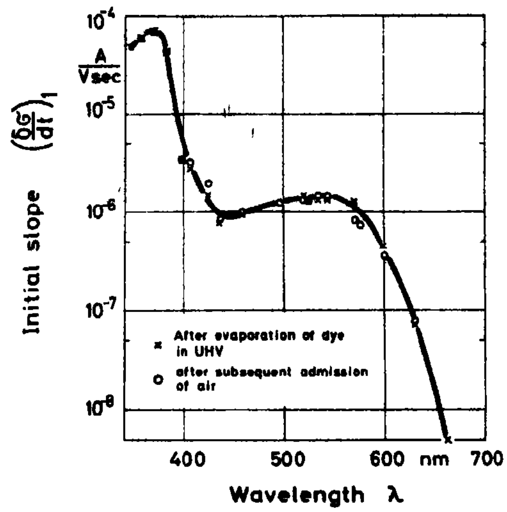

Fig. 7. ZnO crystal 3. Spectral distribution of photoconductivity after various pretreatments, referred to an equal density of incident photons $I_0 = 1{\cdot}5\times10^{14}\,\mathrm{cm}^{-2}\,\mathrm{sec}^{-1}$. The coverage is lower than for the other two crystals.

4. DISCUSSION

4.1 *Surface conductivity in the dark*

The evaporation of the dye always increases the electron density at the surface (Table 1). The increase remains several orders of magnitude below the coverage with dye molecules. However, the same electron traps might be effective for changes not only of photoconductivity (Section 4.3) but also of dark surface conductivity[14]. Under this assumption the electron density injected into surface traps by dyeing could exceed the increase of density in the conduction band ($\Delta N_d - \Delta N_0$) by orders of magnitude (Table 1). A similar result has been found with another dye on ZnO crystals. Thus for these two dyes the 'barrier model' can not hold, which has been proposed for some other dyes and ZnO[10]. According to this model electrons from the crystal surface are trapped at the dye molecules in the dark and freed again by illumination. Therefore dyeing should cause a decrease of the dark conductance of the ZnO. Furthermore the photoconductance should never exceed the initial decrease of dark conductance. Both predictions are not fulfilled for the two dyes studied on single crystals in this laboratory[9].

4.2 *Spectral distribution of photoconductivity*

Photoconductivity in the intrinsic absorption region is not influenced measurably by the dye. The absorption constant has been determined by Liang and Yoffe[11] with polarised light for thin platelets of ZnO (Fig. 5(c)). There are maxima for $E \parallel c$ at $\lambda = 368{\cdot}8$ nm and for $E \perp c$ at $\lambda = 372{\cdot}5$ nm. The maximum of the initial slope of photoconductivity in Figs. 5, 6 and 7 for irradiation with unpolarised light is situated at 370 nm. This corresponds to a quantum energy of 3·34 eV, whereas the gap from Faraday effect [12] is 3·35 eV ($E \perp c$) and from electroreflectance[13] 3·31 eV ($E \perp c$).

The spectral distribution of the sensitized photoconductivity follows the absorption. The broadening of the band is due to aggregates of molecules and possibly also due to an interaction with the surface (Figs. 3, 5, 6, 7).

In former work a strong influence of the adsorption of oxygen on the surface photoconductivity of ZnO has been observed[14]. With decreasing dark surface conductivity also the photoconductivity was diminished. The lack of a similar effect in the present work might be explained by a blocking action of the adsorbed dye against oxygen adsorption. The observed decrease of dark conductivity may be due mainly to parts of the crystal which are not covered by the dye (Figs. 1 and 2). The largest decrease by a factor of ten happened at the crystal with very low coverage (No. 3).

4.3 *Yield*

The low value of the absolute quantum yield in the order of 10^{-2} or 10^{-3} can be attributed to the trapping of electrons during the rise of photoconductivity. It has been shown some time ago that there exists a close relation between surface photoconductivity and field effect on ZnO crystals[14]. The field effect mobility increases through several orders of magnitude with the surface conductivity. This reproducible fact can only be explained by the assumption of surface states acting as traps for electrons. A drift mobility derived from photoconductivity follows closely the field effect mobility. Therefore the same traps should be effective in photoconduction. A density of states for the surface traps S_E can be estimated from data of the present work under the assumptions, that each absorbed photon initially frees one electron, and that there is a continuous distribution in energy near the Fermi level: $S_E \approx 1 \times 10^{15}\,\text{cm}^{-2}\,\text{eV}^{-1}$. According to the experimental method only traps with a response time below 10^{-3} sec are included. Also before dyeing the yield lies in the same order of magnitude for the intrinsic absorption region. Therefore the traps are due to the crystal and not to the dye. The exposure to oxygen does not change the estimated density of states on the dyed surface.

For information about the efficiency of sensitization it is reasonable to discuss the relative quantum yield (Table 1). If referred to an equal number of incident photons it should be especially sensible to the coverage. A more systematic study of this effect is planned. If only the absorbed quanta are counted for evaluation of the relative yield, it can be seen, that the efficiency for quanta absorbed in the dye is 2 resp. 5 times higher than for quanta absorbed in the crystal within a penetration depth of about 10^{-5} cm. At present not yet enough data are available for a more detailed discussion of the transfer of energy or charge.

5. CONCLUSION

Although no model is proposed, the present work may show that it is possible to study sensitization under clean conditions. No barrier layer and no adsorbed oxygen are required for the sensitization of photoconductivity on ZnO. By measuring the initial slope photochemistry is avoided and a quantum yield can be estimated. The clean surface of single crystals dyed in ultrahigh vacuum is open now for a variety of experimental methods which are approved in surface physics.

Acknowledgements—The authors would like to thank Dr. P. M. Cassiers, Gevaert-Agfa N.V., Antwerpen, for providing an especially pure dye and for discussions of its properties. Professor Dr. W. Mönch made helpful comments on experimental points.

REFERENCES

1. HEILAND G., MOLLWO E. and STOCKMANN F., In *Solid State Physics* (Edited by F. Seitz and D. Turnbull), Vol. 8, p. 191. Academic Press, New York (1959).
2. PUTZEIKO E. K. and TERENIN A. N., *Z. Fiz. Khim.* **23**, 676 (1949). TERENIN A. and AKIMOV I., *J. Phys. Chem.* **69**, 730 (1965).
3. BOGNER G., *J. Phys. Chem. Solids* **19**, 235 (1961).
4. MEIER H., *Spectral Sensitization*, p. 33. The Focal Press, London and New York (1968).
5. HEILAND G., *Z. Phys.* **138**, 459 (1954).
6. FRANKL D. R., *Electrical Properties of Semiconductor Surfaces*, p. 106, Pergamon Press, Oxford (1967); HEILAND G. and KUNSTMANN P., *Surface Sci.* **13**, 72, 75 (1969).
7. MATEJEC R., *Z. Phys. Chem. N. F.* **24**, 24 (1960).
8. COLLINS R. J. and THOMAS D. G., *Phys. Rev.* **112**, 388 (1958).
9. HEILAND G., BAUER W. and NEUHAUS M., *Int. Conf. on Photosensitization in Solids*, Sarlat, France (1971).
10. DUDKOWSKI S. J., KEPKA A. G. and GROSSWEINER L. I., *J. Phys. Chem. Solids* **28**, 485 (1967).
11. LIANG W. Y. and YOFFE A. D., *Phys. Rev. Lett.* **20**, 59 (1968).
12. EBINA A., KODA T. and SHIONOYA A., *J. Phys. Chem. Solids* **26**, 1497 (1965).
13. HOFFMANN B., *Z. Phys.* **219**, 354 (1969).
14. HEILAND G., *J. Phys. Chem. Solids* **22**, 227 (1961).

J. Phys. Chem. Solids, 1971, Vol. 32, pp. 2613–2619. Pergamon Press. Printed in Great Britain

PREPARATION AND PROPERTIES OF InAs$_{1-x}$P$_x$ ALLOYS*

A. G. THOMPSON and J. W. WAGNER
Electronic Materials Division, Bell & Howell, 360 Sierra Madre Villa, Pasadena,
Calif. 91109, U.S.A.

(*Received* 5 *March* 1971)

Abstract—Bulk ingots of InAs$_{1-x}$P$_x$ alloys have been prepared throughout the entire composition range by pulling from the melt using both the Gremmelmaier and liquid encapsulation methods. This paper reports on the growth and general characteristics of these alloys. The ingots were pulled from both stoichiometric and non-stoichiometric melts. In order to grow an alloy of a prespecified composition, the liquidus–solidus phase diagram was investigated. The resulting phase diagram differs substantially from that previously reported in the literature. The electrical properties of the as-grown alloys have been measured, and distribution coefficients and solubility limits of the major dopants were determined. The majority of the work focused on the 80–90 mole per cent InP range, since primary interest was in material suitable for light emission around 1·06 μ.

1. INTRODUCTION

THE InAs–InP alloy system has recently received attention since its bandgap range covers the near-i.r. spectral region which contains the neodymium-doped glass and YAG laser wavelengths. It has been used as a highly efficient photocathode[1], giving greater than an order of magnitude improvement over the S1 cathode at 1·06 μ. Similarly laser diodes have been fabricated[2] which emitted at 1·06 μ and which were matched to a Nd-doped glass amplifier[3]. The system has also been suggested as a prime candidate for Gunn oscillators[4] due to a favorable combination of main energy gap, intervalley gap and electron mobility.

Early attempts to prepare these alloys are summarized in a paper by one of us[5]. That work reported growth of small bulk crystals by a halogen vapor transport technique. Since that time two reports have been made of epitaxial growth using the arsine/phosphine vapor transport technique. In one of these the alloys were deposited on InAs substrates[6], which were lapped off to enable electrical measurements to be made. In the other depositions were made on GaAs and GaP high resistivity substrates[7, 8].

In this paper we report the growth and properties of single phase bulk InAs$_{1-x}$P$_x$ alloys across the entire alloy composition range. Although most of the ingots were polycrystalline, the results apply equally well to single crystal material. The earlier references to the photocathode[1] and laser[2, 3] applications used this large-grained polycrystalline material by effectively isolating single grains, so its utility for investigation programs has been good. Parts of this work have been presented previously[9, 10].

2. GROWTH

The bulk ingots were prepared by pulling from the melt using either the Gremmelmaier [11] or liquid encapsulation[12, 13] methods. Our initial experiments indicated that in both growth methods it was desirable to start with the compounds in the initial charge rather than the elements. The preparation of InAs was accomplished by casting in a two-zone furnace or by Czochralski pulling. However, the preparation of InP was complicated by the high phosphorus pressure needed over a stoichiometric melt. Therefore, a directional-freeze apparatus was used in preparing the InP. The phosphorus temperature was controlled close to 450°C, so that a phosphorus pressure of 1–2 atm was maintained in the chamber. The initial temperature of the main charge was held above the melting point of InP (1,060°C) for several hours allowing reaction with the phosphorus. The temperature of the furnace was then slowly cooled over a period of about two days until the entire charge was frozen. The material produced in this manner was polycrystalline with large grains and was quite suitable for use as source material in the growth of the alloys. A full account of the growth properties of InP is being published elsewhere[14].

---

*Work partially supported by the Office of Naval Research, Physics Branch, Washington, D.C. under Contract Nos. N00014-68-C-0219 and N00014-69-C-0415.

The starting charge in the Gremmelmaier sealed-tube method consisted of InAs, InP, and enough excess arsenic and/or phosphorus to establish a pressure of 1–3 atm over the melt. The apparatus used is shown in Fig. 1. The sealed quartz chamber was held at a temperature at least high enough to keep the excess arsenic and phosphorus in the vapor state. The melt was contained in a quartz crucible and was heated by a graphite susceptor coupled to a 450 KHz RF generator. The graphite susceptor was either baked out under vacuum (10^{-4} torr) for several hours at 900–1,000°C or sealed in quartz in order to minimize contamination.

The apparatus used in the B_2O_3 liquid encapsulation method has been reported previously[10, 15] and is shown in Fig. 2. A quartz tube was sealed at both ends by O-ring flanges so that a vacuum or positive pressure could be maintained in the growth chamber. The melt was covered with a layer (~ 1 cm thick) of boric oxide, and a pressure of 2–3 atms was maintained over the B_2O_3 surface in order to keep the volatile arsenic and phosphorus in the melt. Initially a resistance heater was used to bake out the boric oxide glass in situ at ~ 650°C under a vacuum of 10^{-4} torr. Then the system was pressurized with N_2 and an r.f. heater was substituted for melting the charge and subsequent pulling. Again a quartz crucible and graphite susceptor were used.

The pulled ingots were generally about one cm in diameter and 3–5 cm long, weighing 15–30 g. Grain sizes were often a few mm² by 5–10 mm long with the long axis parallel to the growth direction. Figure 3 shows typical

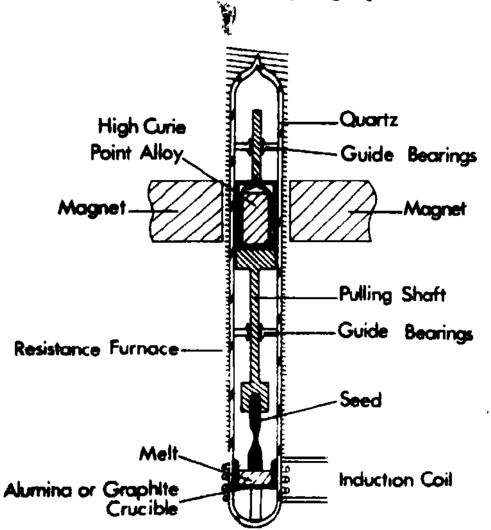

Fig. 1. Diagram of apparatus used for pulling crystals of [illegible] by the sealed Czochralski technique.

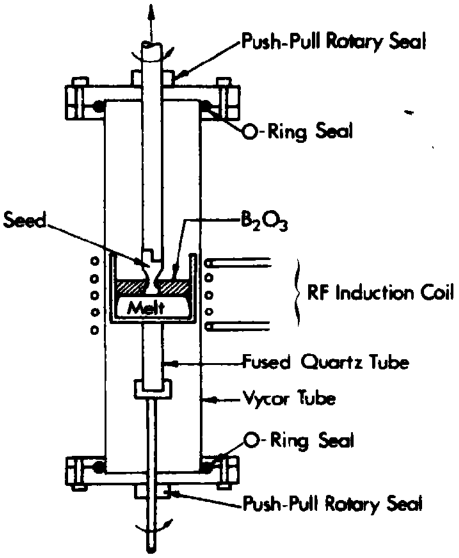

Fig. 2. Diagram of apparatus used for pulling crystals by the Czochralski technique under B_2O_3 glass.

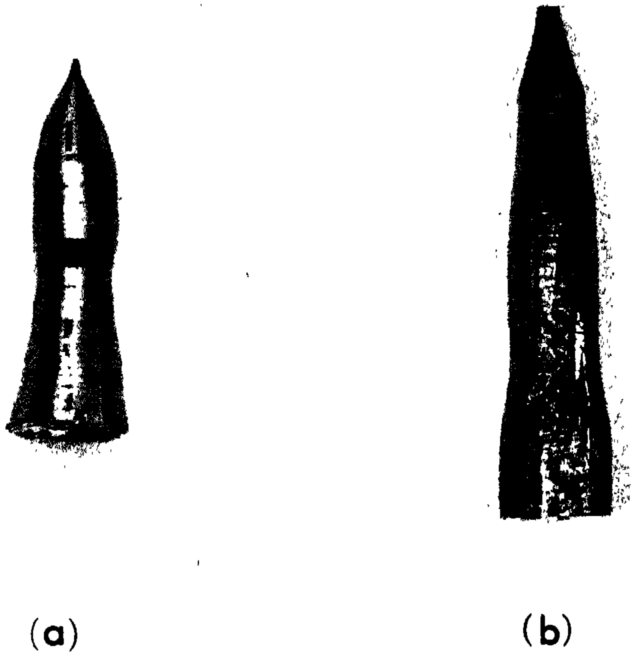

Fig. 3. Photographs of ingots of $InAs_{1-x}P_x$ ($x \sim 0{\cdot}8$) grown by (a) the sealed system and (b) the liquid encapsulation technique.

ingots having $x \sim 0{\cdot}8$ (i.e. InP rich) grown by the Gremmelmaier and liquid encapsulation methods. The scaliness at the base of the ingot grown using the liquid encapsulant is not due to poor crystalline quality, but rather is the region where the ingot was rapidly removed from the B_2O_3 and thus some glass froze on the ingot and upon cooling cracked the surface. The boric oxide encapsulation process was found to consistently yield larger-grained ingots than the sealed-tube technique.

When growing alloys from melts containing greater than 50 mole per cent InP by either method, it was necessary to use non-stoichiometric In-rich melts in order to keep the equilibrium melt pressure less than 3 atm, i.e., in order to prevent volatilization. Ingots were grown from non-stoichiometric melts which contained as much as 60 at.% indium. Pull speeds of about 1 mm per hour were used when pulling from non-stoichiometric melts, while more rapid rates (3–6 mm per hr) were suitable when growing from stoichiometric melts[16].

After experience with both systems the liquid encapsulation technique was selected as being the most satisfactory for several reasons. The pull speed needed for alloys from non-stoichiometric melts is very much smaller than that needed for the compounds, and under these circumstances the poorer mechanical stability of the seed rod in both height and rotation in the Gremmelmeier technique leads to vibrations which may cause the momentary effective pull speed to exceed that necessary for single phase crystal growth. Other advantages of the liquid encapsulation technique include the damping of melt surface vibrations, greatly improved thermal stability across the interface, better radial temperature gradients and simpler puller design and maintenance. Disadvantages are that strain may occur at the growth (liquid–solid) interface due to the presence of the B_2O_3, impurities floating on the melt cannot volatilize, reacting charges in situ is difficult and usually results in increased impurity levels and decreased visibility and certain dopants such as silicon cannot be used since they are gettered by the B_2O_3. However, where clean prereacted materials are available, as is usually the case for III–V's, most of these disadvantages do not apply. Therefore we feel that for many materials, especially those which have to be pulled slowly, the liquid encapsulation technique is superior.

3. PHASE DIAGRAM

The first-to-grow portion of each pulled alloy ingot was analyzed by X-ray powder diffraction techniques. The alloy composition x was then determined by assuming that the lattice parameter varies linearly with molecular composition, between the end compounds. Values for the latter are well established in the literature[17]. This assumption that Vegard's law applies is reasonable since most of the mixed III–V alloys follow it. Published work shows slight positive deviations from linearity[5, 6], but this is thought to be due to the preparation method used in one of these cases[5]. The maximum possible error in x incurred by our assumption is only 0·03 at $x \sim 0{\cdot}4$ and progressively decreases toward either compound.

A pseudobinary phase diagram has been established in the following manner. The starting composition of the melt was calculated and the composition of the first-to-freeze portion of the ingot (but away from the seed) determined in the manner described above. Since the liquidus–solidus spread is small a symmetrical shape was assumed. This procedure leads to the pseudo-binary phase diagram shown in Fig. 4. Also shown are the points obtained by Köster and Ulrich[18]—their much lower solidus is probably due to the use of inhomogeneous samples which would be expected with their technique. The slight difference between our liquidus and that of Ref. [18] is probably due to the different pressures and non-stoichiometric conditions used, and it should be stressed that our diagram applies only to alloys prepared in a

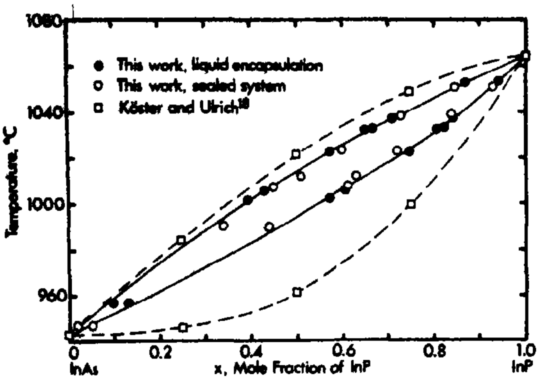

Fig. 4. Pseudobinary phase diagram of the $InAs_{1-x}P_x$ system.

similar manner to those described above. Recent theoretical work[19] shows the liquidus-solidus separation derived in the above manner to be reasonable. One should note that from a preparational standpoint this small spread is quite fortunate and permits homogeneous materials to be relatively easily grown throughout the entire alloy range.

Values of the starting composition of the melt and the initial ingot composition are shown in Table 1 for crystals grown by both the sealed system and liquid encapsulation techniques.

4. ELECTRICAL PROPERTIES

Hall bridges were ultrasonically cut from the first-to-grow sections of each ingot, and ohmic contacts were made by diffusing indium dots in a hydrogen atmosphere and soldering wires to these dots. Hall measurements were then made at 300 and 77°K using a field of 20,000 G. Carrier concentrations and Hall mobilities ($\mu = R\sigma$) were then calculated. The carrier concentrations of these undoped alloys ranged between $1-5 \times 10^{16}$ cm^{-3}.

Figure 5 is a plot of the electron mobilities in the undoped alloys at 300°K. Also plotted are the best experimental data of Tietjen *et al.*[6] obtained on vapor-epitaxially deposited layers from which the substrates had been removed, the experimental data of Weiss[20], and a theoretical curve which was calculated using the method of Ehrenreich [21] (assuming all of the factors affecting the mobility vary linearly with composition and using recent values for the lattice mobilities of the compounds). The values from Allen and Mehal[7] are not plotted since they are substantially lower than the above. One can see in the figure that the experimental data lie significantly below the theoretical curve but lie on a similarly shaped curve. Alloy scattering does not appear as a serious contribution to the alloy mobilities. Figure 6 shows the electron mobilities of the same undoped alloys at 77°K. Again the data on vapor-grown epitaxial materials[6] are included. The electrical data for individual ingots are listed in Table 1.

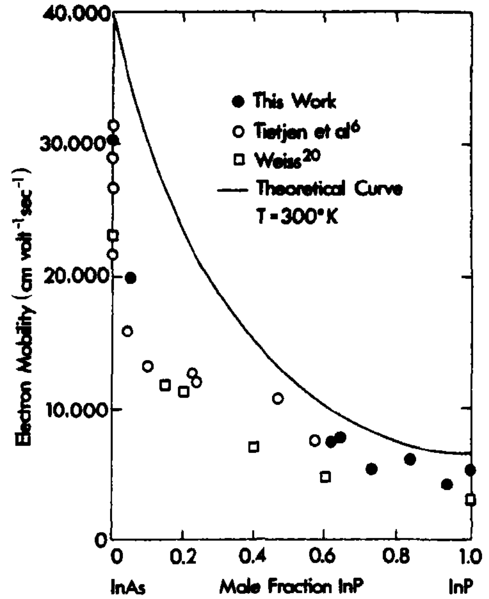

Fig. 5. Hall electron mobility of undoped $InAs_{1-x}P_x$ alloys as a function of composition at 300°K.

The variation of mobility with doping level was not investigated in detail except for InP, which is to be published elsewhere[14].

5. IMPURITIES

The distribution coefficients (defined as number of impurity atoms per cm^3 in the first-to-freeze portion of the ingot divided by the

Table 1. *Parameters for $InAs_{1-x}P_x$ ingots prepared by the sealed system and liquid encapsulation techniques*

Ingot No.	x Starting melt	x First to freeze (ingot)	Dopant	300°K $n(p)$ $cm^{-3} \times 10^{16}$	300°K μ $cm^2 V^{-1} sec^{-1}$	300°K ρ ohm-cm $\times 10^{-3}$	Comments
				Sealed system			
H1	0·34	0·44	none	120	4,400	1·2	
H2	0·45	0·61	none	0·87	6,800	110	
H5	0·51	0·63	none	2·4	7,300	36	Large ingot, x (bottom = 0·71)
H6	0·70	0·83	none	0·92	5,300	1·3	
H7	—	0·90	none	110	1,700	3·2	
H8	0·02	0·045	none	14	20,000	—	x (mass spec) = 0·03
H9	—	0·075	none	—	—	—	x (mass spec) = 0·11
H13	0·095	~0·15	Zn	2·4	5,600	47	n-type
H14	0·095	~0·15	Zn	(21)	90	340	
H18	0·73	0·855	Te	1,500	620	0·67	
H20	0·73	0·85	Te	940	1,300	0·51	x (mass spec) = 0·84
H21	0·72	0·835	Te	190	1,400	2·5	
H22	0·85	0·93	S	1,600	850	0·45	
H23	0·73	0·86	Se	670	1,200	0·77	x (mass spec) = 0·89

Ingot No.	x Starting melt	x First to freeze (ingot)	Dopant	300°K $n(p)$ $cm^{-3} \times 10^{16}$	300°K μ $cm^2 V^{-1} sec^{-1}$	300°K ohm-cm $\times 10^{-3}$	Initial melt stoichiometry, atomic fraction of In	Comments
					Liquid Encapsulation			
W6	0·87	0·945	none	4·0	3,800	39	0·60	x (mass spec) = 0·97
W8	0·65	0·825	Se	250	1,500	1·6	0·60	
W11	0·71	0·845	Se	330	1,900	1·0	0·60	
W13	0·10	0·130	Se	420	6,800	0·22	0·50	
W14	0·71	0·845	Se	1,400	1,300	0·34	0·60	
W18	0·71	0·845	Se	470	1,600	0·81	0·60	
W19	0·71	0·845	Se	1,200	1,400	0·37	0·60	
W20	0·71	0·845	Te	1,100	1,100	0·52	0·60	
W21	0·71	0·845	Se	1,000	790	0·80	0·60	
W22	0·71	0·845	Sn	130	2,200	2·2	0·60	
W23	0·71	0·845	Sn	63	2,200	4·6	0·60	
W101	0·71	0·85	Zn	(820)	40	20	0·60	
W102	0·71	0·85	Zn	(1,700)	30	13	0·60	
W103	0·575	0·75	Zn	(2,300)	25	13	0·59	
W104	0·430	0·605	none	18	4,400	8	0·55	
W105	0·670	0·805	Zn	(2,100)	35	9	0·57	
W106	0·390	0·575	Zn	(1,500)	25	16	0·52	

Note: A quantity that was not measured or is uncertain has been indicated with a dash.

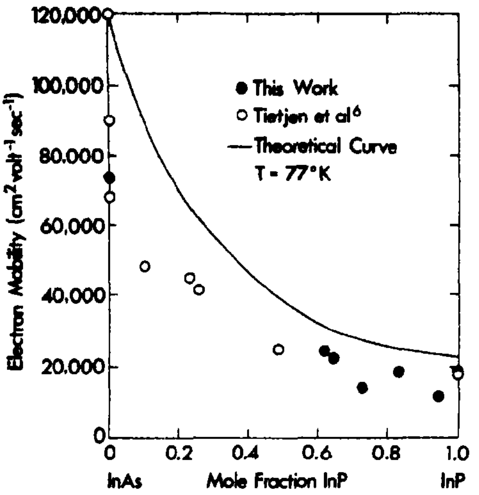

Fig. 6. Hall electron mobility of undoped $InAs_{1-x}P_x$ alloys as a function of composition at 77°K.

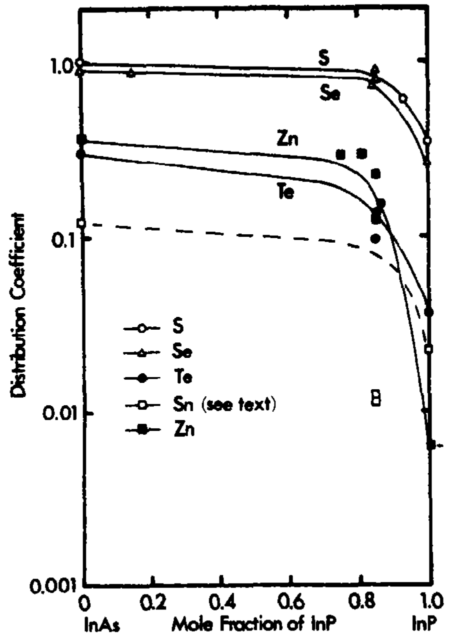

Fig. 7. Distribution coefficients for some common dopants in $InAs_{1-x}P_x$ alloys as a function of composition.

number of impurity atoms per cm³ in the initial melt) were calculated for S, Se, Te, Sn and Zn. The number of impurity atoms per cm³ in the first-to-freeze portion was determined by both carrier concentration measurements and by mass spectrometric analysis. Our data essentially show a one-to-one correspondence between the number of impurities per cm³ determined from mass spectrometer results and the measured carrier concentration providing the saturation limit was not exceeded. Figure 7 is a plot of the distribution coefficients in the alloys as a function of alloy composition. The large slope of the curves in the high phosphorus concentration alloys means that in this particular region the distribution coefficients are changing rapidly and therefore one will find it difficult to accurately predict the final carrier concentration of an ingot in this compositional range.

A notable exception to the general shape of the curves is noted for tin. A possible explanation is that the values for InP and InAs were derived from material prepared under a vapor pressure of the volatile component. The alloys however were grown by the liquid encapsulation technique using boric oxide (B_2O_3). It has been found in GaAs grown under B_2O_3 that silicon (and possibly oxygen) are 'gettered' or absorbed by the B_2O_3, which therefore acquires some borosilicate glass. It is possible that tin could act somewhat like silicon but to a lesser extent, permitting some to go into the ingot and some to form a tin oxide which either is absorbed by the B_2O_3 or sits between it and the melt surface. Since the tin oxides are usually transparent in the visible, it is impossible to tell visually that this is happening. It should be noted that the Sn-doped alloys all had $n < 1 \times 10^{18}\,cm^{-3}$ which is well below the limit at which the distribution coefficient begins to vary with concentration.

Injection laser studies [2] made on lasers fabricated from the materials grown in this study have indicated that the highest efficiencies are probably obtained from alloys having the highest carrier concentrations. Therefore, we have investigated the solubility limits of several of the dopants in the phosphorus-rich alloys. The solubility limits of S, Se and Te in InP were found to be 3·0, 2·0, and $1{\cdot}2 \times 10^{19}\,cm^{-3}$ respectively, which is consistent in that the larger atoms have the lower limits. These limits are really the maximum carrier concentration limits we have obtained and are perhaps not the true solubility limits in that we have chosen to ignore 'carrier freeze-out' (i.e. level at which concentration of dopant atoms starts to exceed carrier concentration). While we have not searched for the exact solubility limits for Sn and Zn, we have successfully doped with these to levels of $5 \times 10^{18}\,cm^{-3}$ and $3 \times 10^{19}\,cm^{-3}$ respectively. The values for the *n*-type dopants are substantially higher than those achieved in GaAs [22], and combined with good mobilities give low resistivities.

Mass spectrometric analysis techniques have been used to determine the level of impurities in the as-grown alloys. The major electrically active impurities were found to be silicon and sulfur, both of which have been shown to come from the elemental arsenic. These impurities are typically seen at levels of 1-2 ppm. The phosphorus-rich alloys were found to contain less impurities (particularly Si and S) since the starting materials were more pure and the distribution coefficients lower at the phosphorus-rich end.

6. SUMMARY

$InAs_{1-x}P_x$ ingots have been grown throughout the entire alloy composition range. A pseudobinary phase diagram for this alloy system has been postulated from the known liquidus and solidus values of x. The resulting phase diagram has a much smaller spread between the liquidus and solidus than that previously reported in the literature but agrees well with recent theoretical work. The electrical properties of the alloys were measured and the mobilities found to compare favorably with the literature. Distribution coefficients for the major dopants have been determined which change rapidly with composition in the 0·8-0·9 mole fraction phosphorus region. Solubility limits for the major dopants indicate that carrier concentrations in the $10^{19}\,cm^{-3}$ range can be achieved without carrier freeze-out.

Acknowledgements—The authors wish to express their appreciation to R. K. Willardson and J. H. Winkler for useful discussions and advice, and to H. M. Olsen, J. Nye, K. Schwartz and T. Tench for technical assistance.

REFERENCES

1. SONNENBERG H., *Appl. Phys. Lett.* **16**, 245 (1970).
2. ROSS B., *Bull. Am. phys. Soc.* **13**, 1640 (1968).
3. ROSS B. and SNITZER E., *IEEE J. Quant. Elec.* **QE-6**, 361 (1970).
4. HILSUM C. and REES H. D., *Electron. Lett.* **6**, 277 (1970).
5. THOMPSON A. G., ROWE J. E. and RUBENSTEIN M., *J. appl. Phys.* **40**, 3280 (1969).
6. TIETJEN J. J., MARUSKA H. P. and CLOUGH R. B., *J. electrochem. Soc.* **116**, 492 (1969).
7. ALLEN H. A. and MEHAL E. W., *J. electrochem. Soc.* **117**, 1081 (1970).
8. ALLEN H. A., *J. electrochem. Soc.* **117**, 1417 (1970).
9. WINKLER J. H., OLSEN H. M. and WAGNER J. W., *J. electrochem. Soc.* **115**, 244C (1968).
10. WAGNER J. W. and THOMPSON A. G., *J. electrochem. Soc.* **117**, 94C (1970).
11. GREMMELMAIER R., *Z. Naturf.* **11A**, 511 (1956).
12. METZ E. P. A., MILLER R. C. and MAZELSKY R., *J. appl. Phys.* **33**, 2106 (1962).
13. MULLIN J. B., STRAUGHAM B. W. and BRICKELL W. S., *J. Phys. Chem. Solids* **26**, 782 (1965).
14. THOMPSON A. G. and TENCH T., to be published.
15. WAGNER J. W. and WILLARDSON R. K., *Trans. Met. Soc. AIME* **242**, 366 (1968).
16. WAGNER J. W. and WILLARDSON R. K., *Trans. Met. Soc. AIME* **245**, 461 (1969).
17. MADELUNG O. in *Physics of* III-V *Compounds*, John Wiley, New York (1964).
18. KÖSTER W. and ULRICH W., *Z. Metallk.* **49**, 365 (1958).
19. STEININGER J., *J. appl. Phys.* **41**, 2713 (1970).
20. WEISS H. *Z. Naturf.* **11A**, 430 (1956).
21. EHRENREICH H., *J. Phys. Chem. Solids* **12**, 97 (1959).
22. WILLARDSON R. K. and ALLRED W. P., *Proceedings of the Conference on* GaAs, Reading, 1966 p. 35 (Inst. of Phys. and Phys. Soc. London (1967)).

J. Phys. Chem. Solids, 1971, Vol. 32, pp. 2621–2629. Pergamon Press. Printed in Great Britain

REVERSIBLE TEMPERATURE INDUCED INVERSION IN THE THERMIONIC EMISSION CURRENT ANISOTROPY PATTERN EMITTED BY ATOMICALLY CLEAN SILICON CATHODES

L. C. BURTON and A. H. MADJID
Department of Physics, Thermionic Emission Laboratory, The Pennsylvania State University, University Park, Penna. 16802, U.S.A.

(*Received* 10 *March* 1970; *in revised form* 26 *February* 1971)

Abstract—A reversible temperature induced inversion in the thermionic emission anisotropy pattern emitted by cylindrical silicon cathodes with axial direction [111] is described. At 1320°K both the {110} and the {112} facets yield emission minima. The {110} emission remains the pattern minimum throughout the temperature range investigated. But an inversion occurs for {112} so that at 1495°K, when this inversion is fully developed, the emission from these planes of silicon yield pronounced maxima in the anisotropy pattern of the thermionic emission current. The effect is completely reversible. When the temperature is lowered to 1320°K, the anisotropy again reverts to that at the starting point. The cycle can be repeated many times with identical results. The individual patterns are reproducible within limits of error set by the accuracy with which the temperature can be reset during the series of measurements. This reversibility allows the conclusion that irreversible changes in surface structure, such as those arising from diffusion and evaporation processes, can be ruled out as an explanation of the phenomenon.

In addition, the 'practical' emission parameters for the 'real' surfaces involved are compiled for both *n*-type and *p*-type silicon. 'Practical' and 'real' are used within this context to stress that the measurements do not necessarily pertain to ideal crystallographic planes, but, as is usual with all such thermionic data, are characteristic of those surface structures that result when single crystal cathodes are heated to incandescence. The measurements relating to *n*-type silicon represent first thermionic emission results. All previous data pertaining to thermionic emission from silicon that appeared in literature refers to electron emission from silicon cathodes of extreme boron doping.

WE WISH to report upon a completely reversible temperature induced inversion in the thermionic emission anisotropy of silicon. Such effects, as far as we known, have not previously been observed within the context of the variation of thermionic emission with crystalline direction.

Anisotropy measurements on silicon have first been reported by Baer, Busch and Madjid[1, 2]. But these authors did not deal with the temperature behaviour of the anisotropy. Their investigation was limited, (as was, indeed, all thermionic emission data for silicon published to date[2–5], to the investigation of the emission from silicon cathodes that are covered with strongly *p*-type surface layers. The reason for this is that all experiments cited were carried out in glass vacuum systems. Silicon surfaces invariably develop degenerate *p*-type layers of several micron thicknesses when heated within such systems. The contamination causing this layer formation is boron, the sources of which are glass components that are incorporated into the structure of these vacuum systems[2, 6, 7]. The present measurements were made in a system specifically constructed to avoid the contamination of silicon surfaces and the results presented in Figures 3, 4, 7 and 10, and in Table 2 constitute the first published data pertaining to thermionic emission from *n*-type silicon cathodes.

Several tests were carried out in order to demonstrate that the vacuum system constructed was indeed non-contaminating toward incandescent silicon surfaces. First, a moderately doped n-type silicon cathode was mounted in the system and the electrical conductivity of the silicon was measured as the sample was repeatedly heat-cycled above 1000°K. The results are shown in Fig. 1. The conductivity of the cathode is, here, plotted against the reciprocal absolute temperature for three runs, that is, for three cathode heating cycles. The results clearly indicate that, within the limits of error, the points representing the separate heating cycles all lie on the same curve which, in turn, closely represents the temperature dependence of the conductivity of 20 Ωcm silicon. The procedure outlined constitutes a very sensitive test for boron contamination of the silicon surface. Heating an identical silicon rod for only a few minutes in a glass vacuum system to similar temperatures results in a conductivity characteristic that is drastically altered as is also shown in Fig. 1 by the branch labled B. As a further precaution the room temperature conductivity and the 'type' of all silicon emitters was measured, using a 4-probe technique, before mounting the cylindrical cathodes in the experimental tube, and then again after the anisotropy runs were completed, and the emitters were removed from the apparatus. These results, which are summarized in Table 1, confirm that no contamination of the silicon surfaces investigated has taken place throughout the investigation.

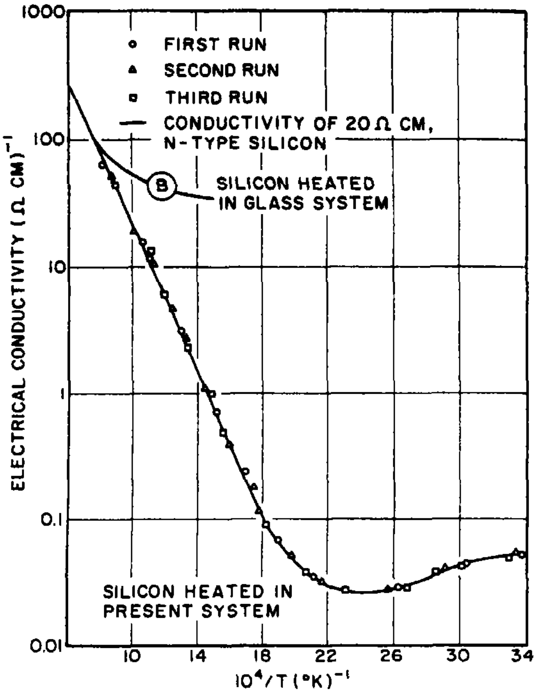

Fig. 1. Conductivity of a 20 Ωcm, n-type silicon cathode that was repeatedly heat-cycled above 1000°K in the experimental apparatus. The results show that the points, representing the successive runs, all lie on a curve that closely represents the temperature dependence of the conductivity of 20 Ωcm silicon. Branch B of the curve shows the consequence of heating an identical cathode for a few minutes in a vacuum system containing glass components.

Table 1. Room temperature conductivities of the thermionic silicon cathodes before and after the experiment

Electrical conductivity	
Before the experiment $(\Omega\text{cm})^{-1}$	After the experiment $(\Omega\text{cm})^{-1}$
n-type, 2·41 ± 0·05	n-type, 2·36 ± 0·05
p-type, 0·73 ± 0·05	p-type, 0·78 ± 0·05
n-type, 2·45 ± 0·05	n-type, 2·51 ± 0·05

The design of the anisotropy tube used in this experiment did not differ, in its geometry and also electrically, very much from the design described by Busch and Madjid[2] except in the avoidance of any construction materials that could contaminate the hot silicon surfaces, and in incorporating several improvements in the mechanical scanning system and the electrical collecting system. A schematic of the experimental tube is shown in Fig. 2. Dry runs with high work function cathodes indicated that the system was capable of rendering Richardson slopes corresponding to about 6 eV. This is an indication that the tube is reliable when used with surfaces that have Richardson work functions up to at least 5 eV. (A major consideration in the design of anisotropy tubes is the suppression of secon-

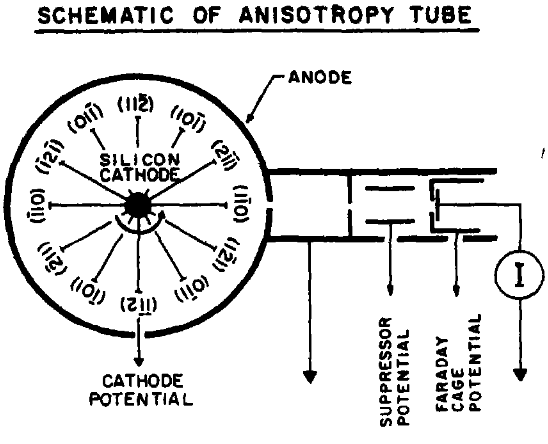

Fig. 2. Schematic of the anisotropy tube used for the measurements. The electrical potentials, in particular the suppressor potential, are chosen so as to minimize collection of slow secondary electrons liberated at the anode.

dary electrons in the collecting system[9]. These spurious currents tend to falsify the measurements by swamping the primary thermionic current when the latter is small. This condition is particularly serious if the emission current is sampled from a high work function face of the cathode. A good measure of the reliability of an anisotropy tube is, therefore, its upper limit capability of rendering Richardson work functions.)

The cathodes used were cylindrical single crystal silicon rods with axial direction [111]. They were 50 mm long and about 1 mm in dia. Such rods expose a six-fold symmetry in the (110) and (112) planes along the emission surface. The rods were cut from phosphorous doped and boron doped floating zone stock, ground to shape on a centerless grinder, etched in a mixture of HF-HNO_3, mounted, and flash-cleaned under ultra high vacuum conditions. Flash-cleaning silicon surfaces, (that is, heating the silicon for several minutes just below its melting point), has been carefully evaluated by Allen, Eisinger, Hagstrum and Law[10] by using oxidation and gas absorption techniques, by measuring the auger neutralization of He^+ at the silicon surface, and by external photoelectric and field emission studies. The conclusion that flash cleaning yields atomically clean silicon surfaces was corroborated by the thermionic emission studies of Busch and Madjid[2]. The present results tend to confirm these findings. Indeed one can easily monitor the cleaning-up of a freshly etched and mounted silicon rod by watching the anisotropy pattern settle with succeeding flashes from an initially erratic and disturbed pattern to one that closely reflects the six-fold symmetry of the single crystal cathode. An excerpt from the clean-up record of an *n*-type sample is shown in Fig. 3.

The temperature induced anisotropy inversion is shown in Figs. 4 and 5 for an *n*-type and a *p*-type silicon cathode respectively.

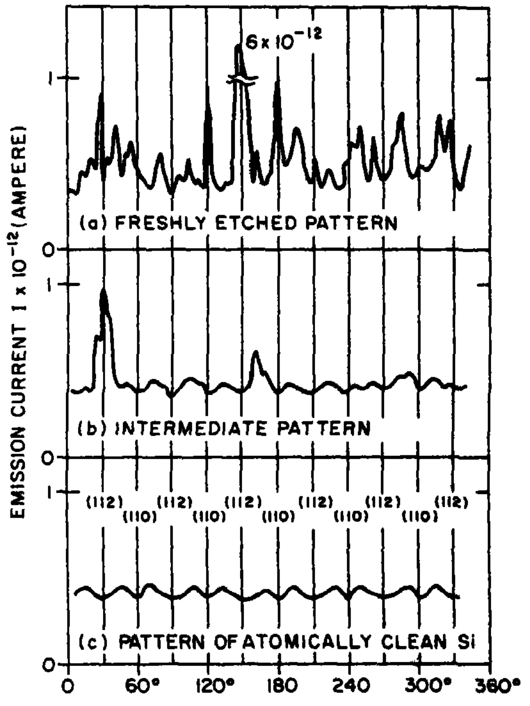

Fig. 3. Clean-up record of the surface of a 2·5 Ωcm *n*-type silicon cathode. The originally disturbed pattern of the freshly etched and mounted cathode, (a), is due to surface contamination. The pattern settles, after several minutes of flashing at a temperature near 1600°K, to the intermediary pattern (b), and finally to the pattern representative of clean silicon (c).

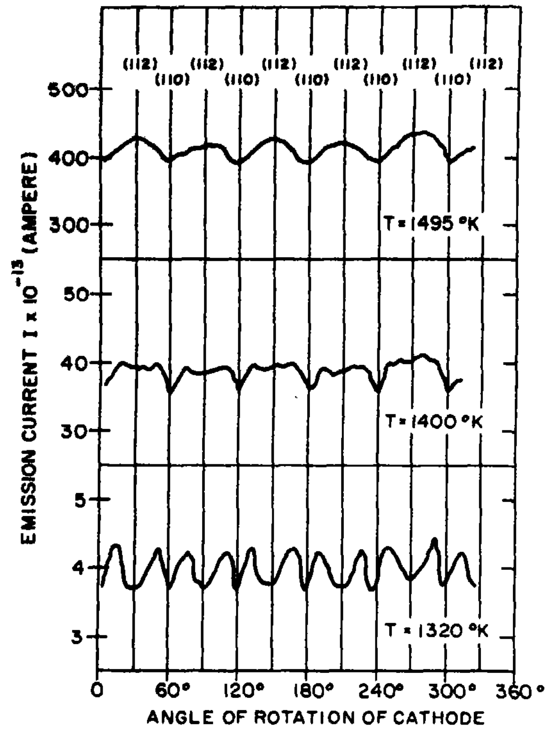

Fig. 4. Temperature induced inversion in the anisotropy pattern for a 2·5 Ωcm *n*-type silicon cathode. The (112) emission minima at 1320°K become emission maxima at 1495°K.

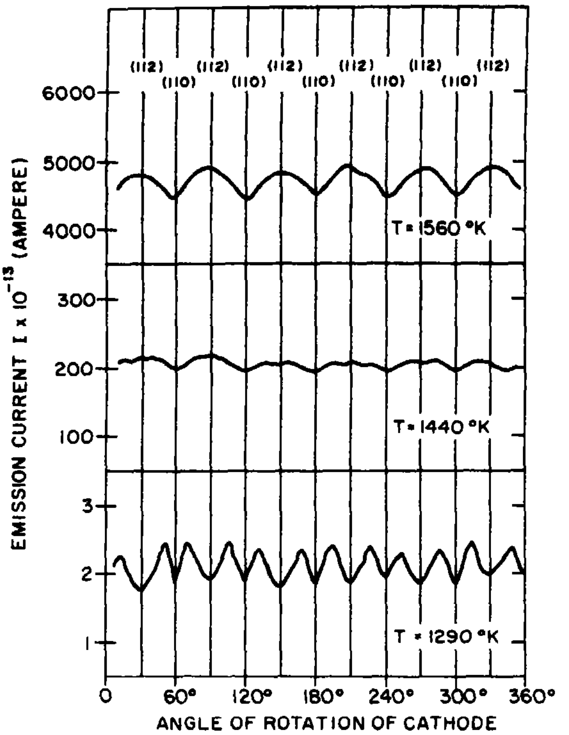

Fig. 5. The temperature induced inversion in the anisotropy pattern for a 0·75 Ωcm *p*-type cathode essentially parallels the behaviour of the *n*-type cathode shown in Fig. 3. This indicates that this inversion is characteristic of the silicon lattice and does not arise from surface contamination.

Referring to Fig. 4, the anisotropy curve at 1320°K shows almost equally deep emission minima for the (112) and the (110) planes. The (112) valleys are wider than the (110) troughs showing that the (112) facets on the surface of the cathode are broader. (These (112) planes, incidentally, can be located visually on floating zone crystals of silicon that are drawn in the [111] direction; they appear as three, or sometimes six, bright lines along the length of the crystal.) The emission maxima are emitted from higher index planes which were identified as the (541) faces of the crystal.

The pattern for 1400°K is appreciably different from that for 1320°K. The emission from the (112) faces draws even with the maxima of the previous pattern; and the emission is now fairly uniform over most of the cathode surface except for the interruptions represented by the narrow (110) minima.

At 1495°K the emission from the (112) facets is enhanced further. The emission from these planes, in fact, now yields maxima. Again the (110) surfaces contribute the least emission. In fact, these narrow valleys appear as the common feature in all the patterns considered.

The effect is completely reversible. When the temperature is lowered from 1495°K, through 1400°K, down to 1320°K, the anisotropy again regresses reversibly through all previously described temperature specific patterns finally to revert to the characteristic at the 1320°K starting point. The reproducibility of the patterns is within a limit of error that is consistent with the accuracy with which the cathode temperature can be reset during the measurements and the cycle can be repeated many times with identical results. This shows that the effect cannot be due to any irreversible change in the surface structure. For example, diffusion and evaporation processes, leading to changes in faceting structure, in surface ripple, in thermal etch-pit density, in d.c.-etch patterns, and in inhomogeneity and impurity clustering—may thus be ruled out unequivocally as an explanation for the anisotropy inversion observed. The effect must, instead, be due to a temperature induced, reversible, change in the anisotropy of the 'effective' surface dipole moment along the periodic succession of 'real' surfaces that is represented by the facet structure of the silicon cathode. 'Effective' and 'real' is used within this context because the processes responsible may not necessarily be due to the character of ideal, smooth, surface planes, but may conceivably arise out of the superposition of the characteristic irregularities, that are superimposed upon the ideal array of surface atoms, that is specific of the various crystallographic facets of the silicon cathodes.

The behaviour of boron doped *p*-type cathodes, Fig. 5, is similar to that of the *n*-type samples just considered. This indicates that the temperature dependent anisotropy changes can, neither, be caused by the presence of dopants at the silicon surface. Of course, the possibility that some persistent impurity, that reversibly migrates from one crystallographic site to another, is responsible for the effect observed may not be ruled out entirely, but the evidence cited in favor of flash-cleaning taken together with the fact that different samples of arbitrary doping flash clean to essentially identical patterns which are in accord with crystalline symmetry, is a strong argument in favor of the interpretation that the phenomenon presented is characteristic of silicon.

The anisotropy change can be represented more quantitatively by plotting the relative emission current anisotropy parameter $(\Delta I^{(x0)}/I^{(0)})$ against temperature. Since the (110) valley remains a constant feature in all runs, the variation of the emission current I with crystalline direction as a function of temperature in Fig. 6 has been plotted relative to that facet with the choice,

$$\frac{\Delta I^{(x0)}}{I^{(0)}} = \frac{I^{(110)} - I^{(541)}}{I^{(100)}} \tag{1}$$

and

$$\frac{\Delta I^{(x0)}}{I^{(0)}} = \frac{I^{(110)} - I^{(112)}}{I^{(110)}}, \tag{2}$$

for the (541) facet that yields the emission current maximum $I^{(541)}$ at 1320°K, and the (112) valley respectively. The results show that above 1410°K, $I^{(112)}$ exceeds the emission $I^{(541)}$ and thus supplants the latter as the emission maximum.

From the temperature dependence of the anisotropy it is possible to predict that the Richardson plots of $l[J^{(x)}/T^2]$ vs. $1/T$, based on the expression,

$$\frac{J^{(x)}}{T^2} = A_R{}^{(x)} \exp\left[-\frac{W_R{}^{(x)}}{kT}\right], \tag{3}$$

(with $J^{(x)}$ the emitted current density from the respective facet (x), and $W_R{}^{(x)}$ and $A_R{}^{(x)}$ the Richardson work function and emission constant for (x) respectively), will be non-linear in character.* That this is indeed the case is shown in Fig. 7 where two representative Richardson plots for an *n*-type and a *p*-type sample respectively, are displayed. Plotted on a larger scale, all such curves show definite curvature throughout the entire temperature range covered. But the nature of this curvature is such that within very reasonably limits of error each Richardson plot may be approxi-

---

*For a discussion of the meaning of equation (3), and the conditions under which non-linear Richardson plots occur, see Ref. [2].

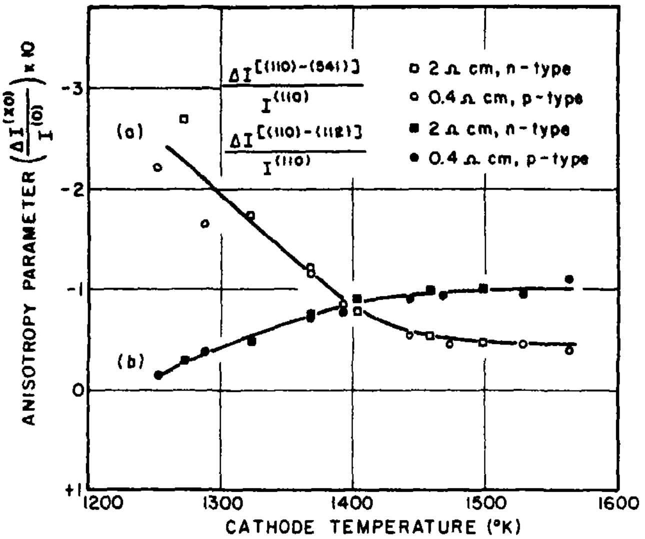

Fig. 6. Temperature dependence of the relative emission parameter $\Delta I^{(x0)}/I^0$ for (a) the (541) facet that yielded the emission maximum at 1320°K relative to the (110) facet; and (b) for $(x) = (112)$ also relative to $(0) = (110)$. The results show that the anisotropy parameters are virtually identical for *n*- and *p*-type silicon.

mated by two straight lines thus subdividing each curve into a high and a low temperature branch. The results of the A_R and W_R values thus determined are summarized in Table 2. The departures from linearity of the Richardson plots are, also, reproducible, within the estimated limits of error, when increasing and decreasing the cathode temperature in repeated cycles.

There remains to deal with the crystallographic facet structure that invariably develops when cylindrical silicon samples are heated to incandescence; and with the correlation of the geometry of these facets with the emission pattern of the cathodes.

Facets rapidly develop on incandescent single crystal samples, which have been machined or ground to arbitrary shapes, because of the inherent tendency of any finite solid to adjust its geometry toward an energetically more favorable surface configuration. Ideally, any fixed total volume of solid would thus assume the shape of a Wulff polyhedron [13–15]. That is a configuration that minimizes the sum over terms facet area times facet surface free energy[12]. In practical reality, however, the attainment of this equilibrium shape will be hampered by kinetic factors which come into play because the heating of the sample usually occurs under pronounced nonequilibrium conditions. The actual facet structure that develops will thus be a Wulff shape modified by such perturbations as evaporation, temperature gradients, initial shape, and any other conditions that determine the kinetics of macroscopic crystal growth.

It is clear that faceting around the circumference and parallel to the axis of the cylinder is to be expected in the present case where the shape is a long, slender cylinder. Indeed, the facet structure that develops when such silicon cylinders are heated in vacuum is rather simple comprising only the {112}, the {110}, and the {541} faces. This structure has been studied by observing the pattern of light that is scattered and specularly reflected as the cylindrical cathodes are rotated under

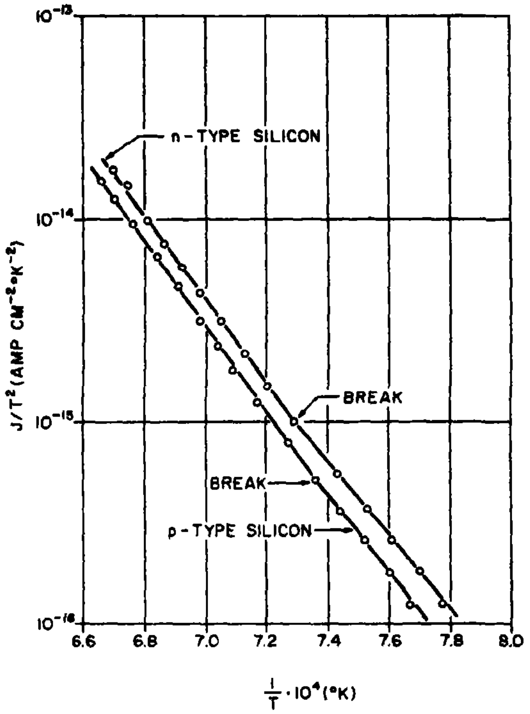

Fig. 7. Two representative Richardson plots for the n- and p-type cathodes described respectively in Figs. 3 and 4. A definite break occurs in both curves around 1400°K.

a low power microscope. The facet structure that developed was remarkably similar for all three samples considered. This is illustrated by the three different (112) faces shown in Fig. 8. In Fig. 9 a (112), a (110), and a (541) facet is displayed for comparison. In Fig. 9(b) the (110) facet is flanked on the right by the adjacent (541) face. In Fig. 9(c), the (541) facet is flanked on the left by the (110) plane. The {110} faces followed by {541} faces exhibit the smoothest surfaces. The {112} faces tend to be rougher and develop a hill and valley structure under very prolonged heating near the melting point of silicon, (particularly when heated in an oxygen ambient). The conclusion is, therefore, that the emission parameters cited for the different faces are probably reliable for the {110} and the {541} planes, but, because of surface roughness, should not, as yet, be considered to be unequivocally established for the {112} faces.

The correlation of the anisotropy of the thermionic emission with the facet structure turned out to be very satisfactory. In Figs. 10 and 11 the facet structure of a n-type, respec-

Table 2. The emission parameters of the (110), *the* (112), *and the facet that yields the low temperature emission maximum of cylindrical n and p-type silicon cathodes of axial direction* [111]

Cathode	Emission Parameter	(110)	(112)	(541)
	(1250°K W_R	3·76 ± 0·05	3·92 ± 0·05	3·74 ± 0·05
4 Ω-cm	to			
	1400°K) A_R	0·1 ± 0·03	0·3 ± 0·1	0·1 ± 0·03
	(1400°K W_R	4·14 ± 0·05	4·4 ± 0·1	4·3 ± 0·1
silicon	to			
	1625°K) A_R	3 ± 0·1	1 ± 0·3	2 ± 0·8
	(125°K W_R	3·17 ± 0·05	3·86 ± 0·05	3·67 ± 0·05
0·4 Ω-cm	to			
	1400°K) A_R	0·03 ± 0·01	0·2 ± 0·06	0·04 ± 0·01
p-type				
	(1400°K W_R	4·12 ± 0·05	4·10 ± 0·05	4·17 ± 0·05
	1625°K) A_R	1 ± 0·3	1 ± 0·3	2 ± 0·6

W_R in (eV) — A_R in (amp/cm²°K²)

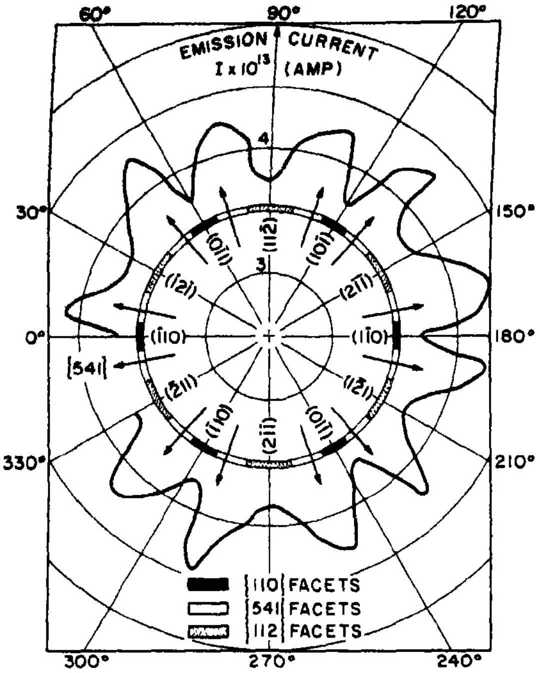

Fig. 10. Correlation of the emission anisotropy for n-type silicon with the crystallographic facet structure which develops when the, originally, cylindrical cathode is heated to incandescence.

tively p-type, cathode is delineated as to angular position and facet width; and this structure is correlated with the emission pattern of the respective cathode. The results clearly show the correlation to be unequivocally established.

We have reported upon an effect which may be of a practical significance in cases where electron emission is desired to be as uniform as possible over a macroscopic emitting area. One could hardly do any better, if this is the requirement, than to choose a (112) face of silicon at about 1400°K for either a planar or a cylindrical cathode geometry. As far as interpretation is concerned, any anisotropy of the thermionic emission current must arise either from the variation with crystalline direction of the surface dipole layer contribution to the work function, or else from a direction dependent electronic reflection coefficient. This

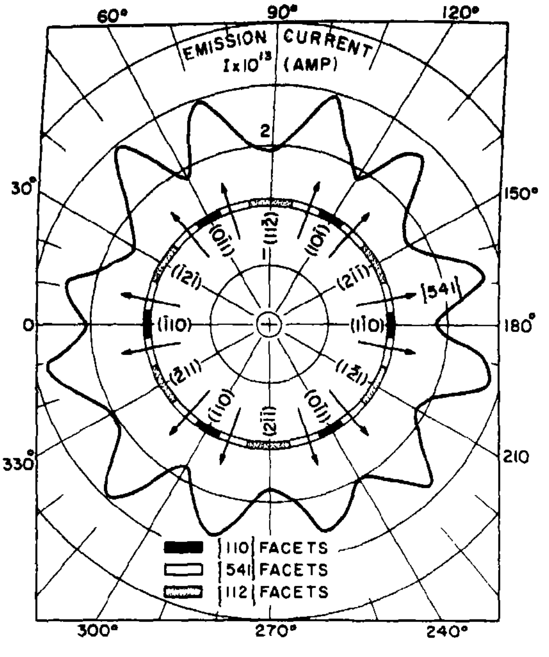

Fig. 11. Correlation of the emission anisotropy for p-type silicon with the crystallographic facet structure.

follows from arguments listed, among others, by Smoluchowski[11], Herring and Nichols [12], and Busch and Madjid[2]. A parallel argument applies to the temperature variation of the anisotropy of the three entities just listed. No quantitative data about the reflection coefficient for silicon surfaces has as yet been published. It is, therefore, not possible to apportion the present effect between dipole layer and reflection coefficient; and this report must for this reason remain on a phenomenological basis. But once quantitative reflection coefficient data becomes available, the present measurements may yield an important clue as to what is causing the temperature inversion of the thermionic emission current anisotropy and the pronounced breaks in the Richardson plots at around 1400°K for both p- and n-type silicon emitters.

Acknowledgements—The authors wish to express their appreciation to the Office of Naval Research and to the National Aeronautics and Space Administration for their

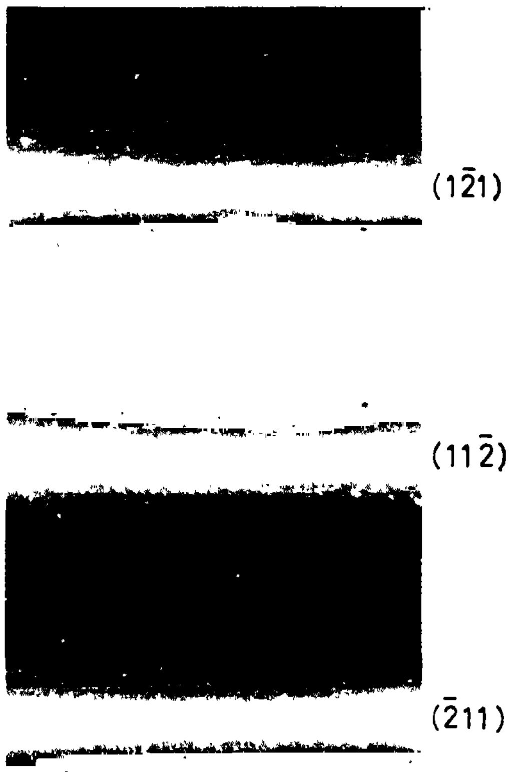

Fig. 8. Three different (112) facets that developed on the cylindrical silicon cathodes used in this experiment.

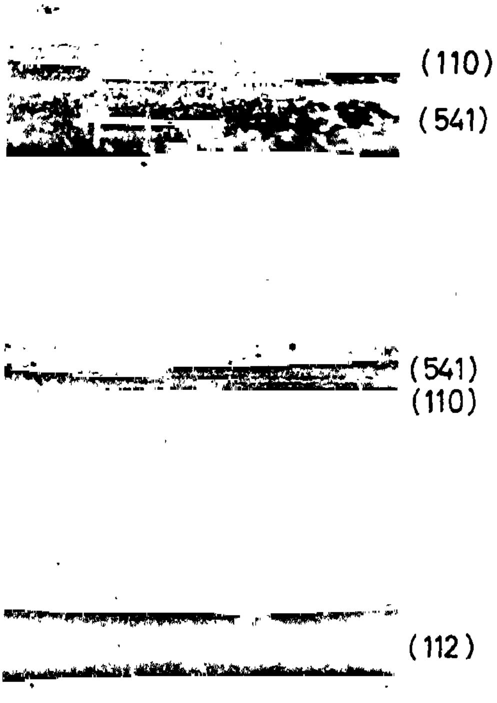

Fig. 9. Facets developed on the cylindrical silicon cathodes upon heating to incandescence. (a) a (112) face; (b) a (100) face flanked on the right by a (541) facet; (c) a (541) face flanked on the left by a (110).

support of this work; to H. Henry and T. Sauer for help with shop problems; and to Miss F. Fogle and Miss S. Wallace for preparing the manuscript.

REFERENCES

1. BAER Y., BUSCH G. and MADJID A. H.: Reported at the Spring Session of the Physikalische Gesellschaft Hessen-Mittelrhein-Saar e.V. at Saarbruecken/Germany (1962).
2. BUSCH G. and MADJID A. H., *Phys. Kondens. Mater.* **4**, 131 (1965).
3. BRAUN S. and BUSCH G., *Helv. Phys. Acta* **20**, 33 (1947).
4. ESAKI L., *J. phys. Soc. Japan* **8**, 347 (1953).
5. ALLEN F. G., *J. Phys. Chem. Solids* **8**, 119 (1958).
6. ALLEN F. G., BUCK T. M. and LAW J. T., *J. appl. Phys.* **30**, 979 (1960).
7. BUSCH G., SCHADE H., GOBBI A. and MARMIER P., *J. Phys. Chem. Solids* **23**, 513 (1962).
8. BURTON L. C. and MADJID A. H., *Phys. Rev.* **185**, 1127 (1969).
9. SMITH G. F., *Phys. Rev.* **94**, 295 (1954).
10. ALLEN F. G., EISINGER F., HAGSTRUM H. D. and LAW J. T., *J. appl. Phys.* **30**, 1563 (1959).
11. SMOLUCHOWSKI R., *Phys. Rev.* **60**, 661 (1941).
12. HERRING C. and NICHOLS M. G., *Rev. mod. Phys.* **21**, 185 (1949).
13. WULFF G., *Z. Kristallogr.* **34**, 449 (1901).
14. LIEBMANN H., *Z. Kristallogr.* **53**, 171 (1914).
15. LAUE M. V., *Z. Kristallogr.* **105**, 124 (1943).

J. Phys. Chem. Solids, 1971, Vol. 32, pp. 2631–2637. Pergamon Press. Printed in Great Britain

HOT CARRIER D.C. CONDUCTION IN A DEGENERATE MANY VALLEY SEMICONDUCTOR

M. S. SODHA*, V. K. TRIPATHI and JYOTI KAMAL

Department of Physics, Indian Institute of Technology, New Delhi-29, India

(*Received* 9 *December* 1970; *in revised form* 23 *February* 1971)

Abstract—The hot carrier d.c. conductivity of a degenerate many valley semiconductor has been investigated, using the effective carrier temperature approximation. Comparison of these results with earlier work on nondegenerate semiconductors shows that the effect of degeneracy is to reduce the anisotropy and carrier heating by d.c. field (thus making Ohm's law applicable up to higher fields). Further it is seen that degeneracy leads to increase of conductivity with increasing electric field; this is in contrast to the results for the nondegenerate case.

1. INTRODUCTION

IN A RECENT paper[1], designated as I here after, the transport phenomena in degenerate simple model semiconductors were studied using the effective carrier temperature approximation; the analysis also neglected the effect of optical phonon scattering and the dependence of Fermi energy on carrier temperature. Thus this treatment[1] was restricted to the case of highly degenerate semiconductors with spherical energy surfaces at low temperatures and low electric fields.

In this communication the authors have investigated the hot carrier d.c. conductivity in a many valley degenerate semiconductor (e.g. Ge), taking into account the carrier scattering by optical phonons and the dependence of Fermi energy on carrier temperature; thus this treatment is applicable to a wide range of temperature and electric field below the breakdown limit. In this communication we have limited ourselves to the study of the d.c. conductivity but the method could easily be extended, if required, to deal with the various galvanomagnetic and thermomagnetic effects.

The Boltzmann transfer equation has been solved in the relaxation time approximation for the carrier distribution function. Isotropic part of the distribution function in each valley has been taken to be the Fermi–Dirac function appropriate to the effective electron temperature in that particular valley; the electron temperature, which is a function of the electric field strength and depends on the angle between the electric field and the longitudinal axis of the particular valley under consideration, has different values in different valleys and is obtained by taking the acoustic and optical phonon scattering to be responsible for the energy loss of the electrons in the energy balance equation. The use of effective electron temperature is justified in the present case because of high carrier concentration[2]. Using this distribution function, expressions for current density have been obtained which, in turn, give expressions for conductivity tensor and Sasaki angle ψ (defined as the angle between the electric field and the current density). Some numerical results have been presented in the form of graphs. Comparison of these numerical results with those of earlier workers[3–8] for the nondegenerate case shows that the effect of degeneracy is to reduce the anisotropy and also to extend the ohmic regime to relatively higher electric fields.

---

*Present Address: Electrophysics Advanced Study Group Droxel University, Philadelphia, Pa. 19104, U.S.A.

2. DISTRIBUTION FUNCTION

The conduction band of germanium is characterised by energy minima at four equivalent points in the ⟨111⟩ directions [7, 9]. Around each minimum the constant energy surfaces are ellipsoids of revolution with their principal axes along the ⟨111⟩ directions. Let us consider the carriers in the i^{th} valley, where the energy (with respect to the valley minimum) is given by

$$\epsilon = \frac{\hbar^2}{2m_0}(\alpha_1 k_x^2 + \alpha_2 k_y^2 + \alpha_2 k_z^2); \tag{1}$$

k being the carrier wave vector in the ellipsoidal frame (with x axis along the principal axis of the ellipsoid). The ellipsoidal energy surfaces given by (1) can be transformed to spherical ones in terms of a variable $\mathbf{k}'$ i.e.

$$\epsilon = \frac{\hbar^2 k'^2}{2m_0}; \quad \mathbf{k}' = \boldsymbol{\alpha}^{1/2}.\mathbf{k},$$

where $\boldsymbol{\alpha}$ is the dimensionless inverse mass tensor. The distribution function of the carriers is governed by the Boltzmann equation, which on writing **k** in terms of $\mathbf{k}'$ becomes

$$\frac{\partial f^i}{\partial t} + \frac{\mathbf{F}^i}{\hbar}.\boldsymbol{\alpha}^{1/2}.\frac{\partial f^i}{\partial \mathbf{k}'} = \left(\frac{\partial f^i}{\partial t}\right)_{\text{coll.}} \tag{2}$$

with $\mathbf{F}^i$ as the externally applied force. The distribution function can be expanded as

$$f^i(\mathbf{k}') = f_0{}^i(k') + \frac{\mathbf{f}_1{}^i(k').\mathbf{k}'}{k'}. \tag{3}$$

Substititung equation (3) in equation (2) and solving it for $\mathbf{f}_1{}^i$ in the relaxation time approximation one gets

$$\mathbf{f}_1{}^i = \frac{e}{\hbar}[\boldsymbol{\nu}]^{-1}.[\boldsymbol{\alpha}^{1/2}.\mathbf{E}^i]\frac{\partial f_0{}^i}{\partial k'}, \tag{4}$$

where $\mathbf{E}^i$ is the electric field in the i^{th} valley and $\boldsymbol{\nu}$ is the inverse relaxation time tensor with xx and yy components respectively given as

$$\nu_{\parallel} = \nu_{\parallel\text{ac}} + \nu_{\parallel\text{op}} + \nu_{\parallel\text{ion}} \tag{5a}$$

and

$$\nu_{\perp} = \nu_{\perp\text{ac}} + \nu_{\perp\text{op}} + \nu_{\perp\text{ion}}. \tag{5b}$$

Subscripts ac, op and ion refer to collisions with acoustic phonons, optical phonons and ionized impurities respectively. The various components of the collision frequencies are [7, 10]

$$\nu_{\parallel\text{ac}} = \frac{1}{\gamma_2}\nu_{\perp\text{ac}}, \quad \nu_{\parallel\text{op}} = \nu_{\perp\text{op}}, \quad \nu_{\parallel\text{ion}} = \gamma_1 \nu_{\perp\text{ion}}$$

$$\nu_{\parallel\text{ac}} = W_0 T_0 \epsilon^{1/2},$$

$$\nu_{\parallel\text{ion}} = 9{\cdot}45 \times 10^{-3} N_i g(b) T_e^{-3/2} \frac{(m_\perp{}^2 m_\parallel)^{-1/6}}{m_0{}^{-1/2}} \times \left(\frac{\epsilon}{k_0 T_e}\right)^{-3/2},$$

$$\nu_{\text{op}} = \frac{\mathrm{B}\hbar\omega_0 W_0}{2k_0(\mathrm{e}^{\hbar\omega_0/k_0T_0} - 1)}\left[(\epsilon + \hbar\omega_0)^{1/2} + \mathrm{e}^{\hbar\omega_0/k_0T_0} Re(\epsilon - \hbar\omega_0)^{1/2}\right],$$

where γ_1 and γ_2 are anisotropy factors for ionized impurity and acoustic phonon scattering, $m_\perp$ and $m_\parallel$ are the electron masses perpendicular and parallel to the principal axes of the ellipsoid respectively, N_i is the concentration of ionized impurities, ϵ is the energy of the carrier, k_0 is the Boltzmann constant, T_e is the electron temperature,

$$g(b) = \frac{0{\cdot}253}{1{\cdot}66}\frac{(m_\perp{}^2 m_\parallel)^{-1/6}}{m_0{}^{-1/2}} T_e{}^{1/2}\frac{\epsilon}{k_0 T_e}\Big/ F_{-1/2}(\eta),$$

$$F_{-1/2}(\eta) = \int_0^\infty \frac{x^{-1/2}\,\mathrm{d}x}{1 + \mathrm{e}^{x-\eta}},$$

W_0 is a constant independent of temperature, determined from the experimental data of the lattice mobility in the low field region, $B = 0{\cdot}4$ is a constant as determined by Conwell[7], ω_0 is the characteristic frequency of optical phonons, T_0 is the lattice temperature and $Re(\epsilon - \hbar\omega_0)^{1/2}$ denotes the real part of $(\epsilon - \hbar\omega_0)^{1/2}$.

It may be worthwhile to point out here that the above mentioned relaxation times for the acoustic and optical phonons have been derived by Conwell[7] for nondegenerate semiconductors. However, it has been shown by Fistul[10] that in the case of semiconductors these expressions are true at all practically realizable carrier densities.

The expression for $\mathbf{f}_1$ (equation (4)) has been obtained in terms of f_0, the isotropic part of the distribution function which we take to be Fermi–Dirac at an effective electron temperature T_e appropriate to the valley under consideration:

$$f_0{}^i = \frac{1}{e^{\{\epsilon - \epsilon_F(T_e{}^i)\}/k_0 T_e{}^i} + 1}, \tag{6}$$

where $T_e{}^i$ and $\epsilon_F(T_e{}^i)$ are governed by the energy balance equation[1, 11]

$$\frac{\mathbf{J}^i \,.\, \mathbf{E}^i}{n} = \delta \langle \nu_{ac}(\epsilon - l)\rangle + \left\langle \frac{d\epsilon}{dt} - L \right\rangle_{op} \tag{7}$$

and the normalization condition,

$$n = \frac{2}{\pi^2} |J_a| \left(\frac{2m_0 k_0 T_e{}^i}{\hbar^2}\right)^{3/2} \int_0^\infty \frac{x^{1/2}\, dx}{1 + e^{x - \eta^i}}, \tag{8}$$

where $x = \epsilon/k_0 T_e{}^i$, $\eta^i = \epsilon_F(T_e{}^i)/k_0 T_e{}^i$, $|J_a| = (\alpha_2{}^2 \alpha_1)^{-1/3}$ is the Jacobian of transformation, $\mathbf{J}^i$ is the current density to be defined in the next section, δ is the fraction of energy loss of an electron in one collision with the acoustic phonons and may be written as[1, 7]

$$\delta = \frac{2(m_\perp{}^2 m_\parallel)^{1/3}}{M}.$$

M is the effective mass of the acoustical phonon ($\simeq k_0 T_0/c^2$, c is the appropriate mean of velocities of longitudinal and transverse acoustic modes), l and L are parameters which are determined by the condition that at $E = 0$, i.e. at $T_e = T_0$, the average energy lost by the carrier in collisions with acoustic and optical phonons is zero, ν_{ac} is the collision frequency of the carriers with the acoustic phonons. In n–Ge, for the temperature and field range where equipartition of energy is valid, it is a good approximation to use a single energy dependent relaxation time for the combined longitudinal and transverse acoustic scattering. Thus for ν_{ac} appearing in equation (7) one can use the average value of $\nu_{\parallel ac}$ and $\nu_{\perp ac}$. Equations (7) and (8) have been solved numerically for $T_e{}^i$ and $\epsilon_F(T_e{}^i)$ by assuming the electric field to be applied in the $\langle 1\bar{1}0\rangle$ plane at an angle θ to the $\langle 001\rangle$ direction. The results have been shown in Figs. (1) and (2).

3. CONDUCTIVITY AND SASAKI ANGLE

The current density in the ellipsoidal frame of reference may be defined as

$$\mathbf{J}^i = -\frac{e}{4\pi^3} \int \mathbf{v} f^i \, d\mathbf{k},$$

which on changing the variable gives

$$\mathbf{J}^i = -e\,|J_a| \frac{\hbar}{3\pi^2 m_0} \int \alpha^{1/2} \,.\, \mathbf{f}_1{}^i k'^3 \, dk'.$$

Substituting for $\mathbf{f}_1{}^i$ from equation (4) we can express the current density as

$$\mathbf{J}^i = \boldsymbol{\sigma}^i \,.\, \mathbf{E}^i, \tag{9}$$

where $\boldsymbol{\sigma}^i$ is a diagonal tensor with

$$\sigma_\parallel{}^i = A\alpha_1[K_1{}^i + K_2{}^i] \tag{10a}$$

and

$$\sigma_\perp{}^i = A\alpha_2[K_3{}^i + K_4{}^i]; \tag{10b}$$

$A = (e^2/3m_0\pi^2)|J_a|(2m_0 k_0 T_e{}^i/\hbar^2)^{3/2}$, K^i's have been defined in appendix A.

Having found the contribution to the current density from each valley the next step is the transformation of the coordinate system of each valley to the cubic frame of reference (for which, axes are along ⟨100⟩ directions) and then sum the resolved components of the current to obtain the total conductivity. If $(\mathbf{T}^i)^{-1}$ are the inverse transformation matrices then

$$\mathbf{J} = \sum_{i=1}^{4} [\mathbf{T}^i]^{-1} \cdot \mathbf{J}^i. \tag{11}$$

It, however, turns out that $\mathbf{T}^{-1} = \tilde{\mathbf{T}}$ where $\tilde{\mathbf{T}}$ is the transpose of $\mathbf{T}$[12].

Substituting for the appropriate components of current density equation (11) can be written as

$$\mathbf{J} = \boldsymbol{\sigma} \cdot \mathbf{E}, \tag{12}$$

where $\mathbf{E}$ is the electric field with respect to Lab. frame and

$$\sigma_{xx} = \sigma_{yy} = \sigma_{zz} = \tfrac{1}{3}\,[\sigma_{\parallel}{}^{\mathrm{I}} + 2\sigma_{\perp}{}^{\mathrm{I}} + \sigma_{\parallel}{}^{\mathrm{II}} + 2\sigma_{\perp}{}^{\mathrm{II}} + 2\sigma_{\parallel}{}^{\mathrm{III}} + 4\sigma_{\perp}{}^{\mathrm{III}}] \tag{13a}$$

$$\sigma_{xy} = \sigma_{yx} = \tfrac{1}{3}\,(\sigma_{\parallel}{}^{\mathrm{I}} - \sigma_{\perp}{}^{\mathrm{I}} + \sigma_{\parallel}{}^{\mathrm{II}} - \sigma_{\perp}{}^{\mathrm{II}} - 2\sigma_{\parallel}{}^{\mathrm{III}} + 2\sigma_{\perp}{}^{\mathrm{IV}}), \tag{13b}$$

$$\sigma_{xz} = \sigma_{zx} = \sigma_{yz} = \sigma_{zy} = \tfrac{1}{3}\,(\sigma_{\parallel}{}^{\mathrm{I}} - \sigma_{\perp}{}^{\mathrm{I}} - \sigma_{\parallel}{}^{\mathrm{II}} + 2\sigma_{\perp}{}^{\mathrm{II}}). \tag{13c}$$

In writing equations (13) the equality $T_e{}^{\mathrm{III}} = T_e{}^{\mathrm{IV}}$ (a direct consequence of equation (7)) has been used.

4. DISCUSSION

The electron temperature and Fermi energy have been computed numerically for each valley for various intensities and orientations, θ, of the electric field about the ⟨001⟩ direction in the ⟨1$\bar{1}$0⟩ plane. The results of Barrie and Burgess[3] for the nondegenerate case have also been shown in Fig. 1. (The ordinate should be multiplied by ten). A comparative study of these results shows that the rise in electron temperature for the degenerate case is much less pronounced. This may be attributed to the presence of significant amount of impurity scattering in degenerate semiconductor which results in reducing the mobility and hence the power absorption by the carriers. It is interesting to point out here that at still higher degeneracies where the ionized impurity scattering is the sole mechanism for momentum transfer, the rise in electron temperature becomes inversely proportional to the carrier concentration ($T_e - T \propto (1/n)$).

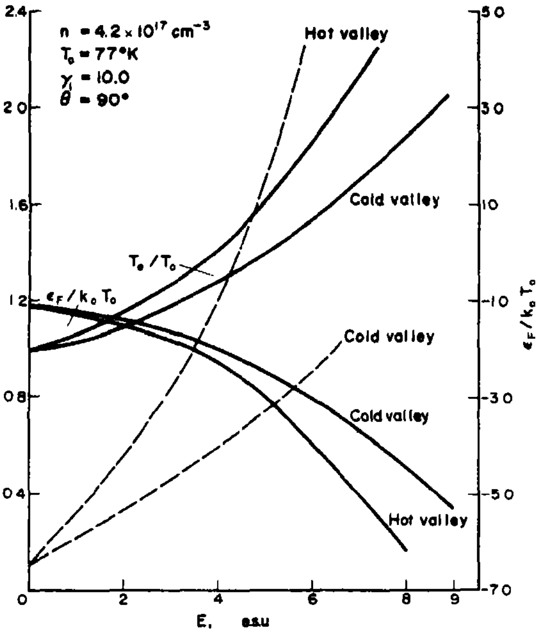

Fig. 1. Variation of T_e/T_0 and $\epsilon_F(T_e)/k_0T_0$ with electric field. Dashed line represents the theoretical results of Barrie and Burgess[3] for nondegenerate semiconductors for $\theta = 90°$ and $T_0 = 77°$K. *The ordinate for dashed curves is to be multiplied by* 10.

The Fermi energy as seen from Fig. 1 exhibits a wide variation with electric field in contrast to the implicit assumption of I, where the variation of Fermi energy with electric field was not accounted for. It is, however, found that the change in Fermi energy with the electric field becomes less pronounced as the degeneracy of the sample is increased. In Fig. 2 we have shown that for a given magnitude of electric field the temperature of the various valleys changes by different amounts with the angle θ. Heating of the $\langle 111\rangle$ valley is seen to be minimum. This is because the component of the electric field parallel to the principal axis of the $\langle 111\rangle$ valley is always greater than the perpendicular component, while in other valleys the reverse is true. Since the electrons have larger mass along the principal axis of the ellipsoid, they make a smaller contribution to the longitudinal current than to the transverse. Rise in the electron temperature in $\langle 1\bar{1}1\rangle$ and $\langle \bar{1}11\rangle$ valleys is the same as these are symmetrically oriented about the electric field i.e. $E_{\parallel}^{\mathrm{III}} = E_{\parallel}^{\mathrm{IV}}$ and $E_{\perp}^{\mathrm{III}} = E_{\perp}^{\mathrm{IV}}$. Same is true for $\langle 111\rangle$ and $\langle 11\bar{1}\rangle$ valleys at $\theta = 90°$. It is further seen from the figure that as the angle θ is increased, the electrons in $\langle \bar{1}11\rangle$ and $\langle 1\bar{1}1\rangle$ valleys get hotter than those in $\langle 11\bar{1}\rangle$ valley because the parallel component of the electric field in $\langle 11\bar{1}\rangle$ valley increases as θ is increased.

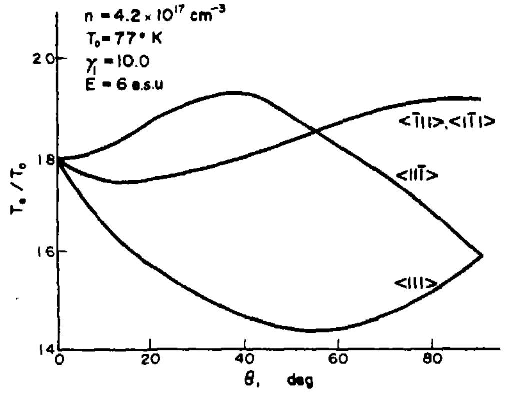

Fig. 2. Variation of T_e/T_0 with θ (the angle between E and $\langle 001\rangle$ direction in $\langle 1\bar{1}0\rangle$ plane).

In Figs. 3–4, the Sasaki angle has been plotted as a function of the electric field and the angle θ respectively. Comparison of our results with the experimental results of Sasaki *et al.*[4, 6] and the theoretical results of Conwell[3] for nondegenerate semiconductors reveals that the effect of degeneracy is to reduce the anisotropy; in our particular case it is reduced by an order of magnitude. For fields beyond 2000 V/cm the Sasaki angle tends to saturation in agreement with the results of earlier workers for nondegenerate case.

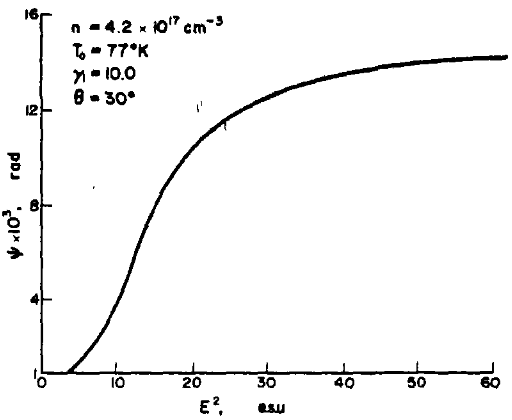

Fig. 3. Variation of Sasaki angle ψ with electric field.

The various components of the conductivity tensor have been plotted in Figs. 5–6 as a

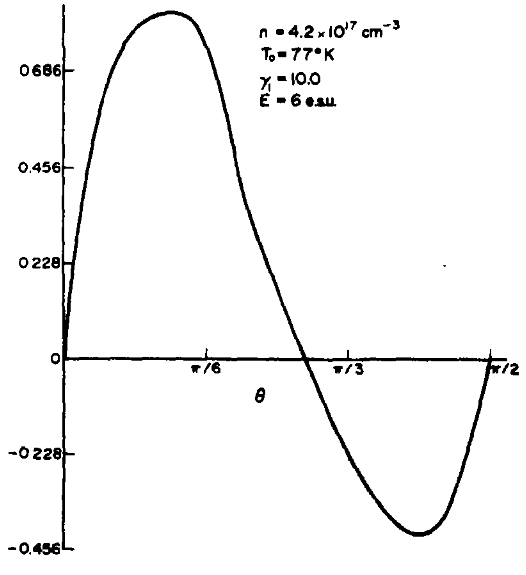

Fig. 4. Sasaki angle ψ as a function of the electric field orientation about $\langle 001\rangle$ axis in $\langle 1\bar{1}0\rangle$ plane.

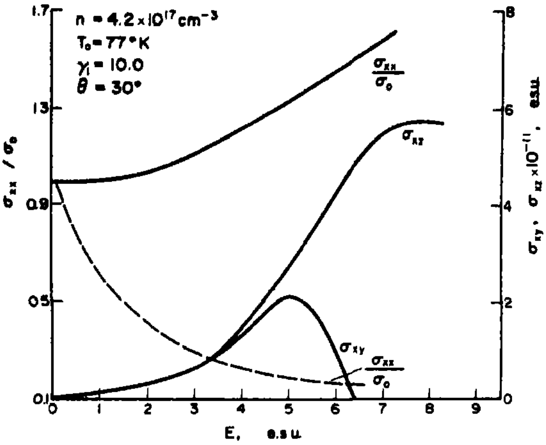

Fig. 5. Variation of various components of conductivity tensor σ with electric field. The dashed line represents the experimental results of Sasaki *et al.*[4] for nondegenerate semiconductors for $T_0 = 90$°K and $\theta = 30°$.

function of the electric field and the angle θ. Unfortunately, no experimental results appear to be available in the hot carrier regime for degenerate semiconductors with which we could compare our theory. Nevertheless, to assess the effect of degeneracy on conductivity, an attempt has been made to compare our results with the various experimental results [3–8] for nondegenerate semiconductors for $\theta = 0°$ and 30° (calculations were done for $\theta = 0°$ but they have not been shown for the sake of brevity). In particular, the results of Sasaki *et al.*[4] for $\theta = 30°$ have been plotted in Fig. 5 and it is seen that the ohmic region in our case extends up to relatively high electric fields. In addition to this, our results, in contrast to those of Sasaki *et al.*[4], show an increase of conductivity with electric field. This diversity in the behavior can be undoubtedly attributed to the dominance of ionized impurity scattering in degenerate semiconductors for which the collision frequency varies as $T_e^{-3/2}$.

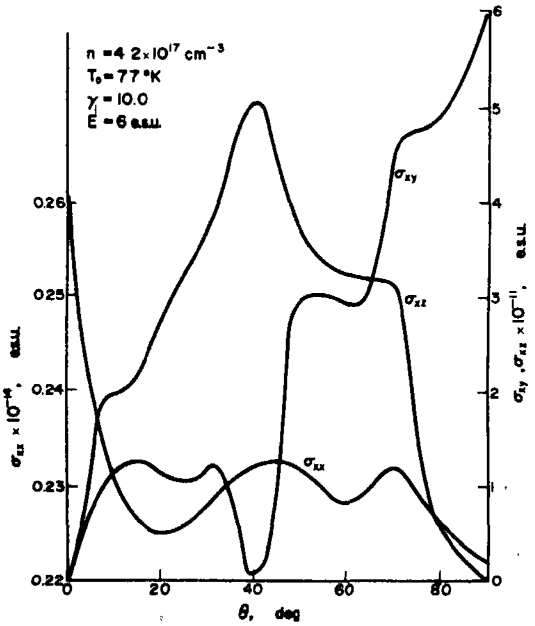

Fig. 6. Variation of the various components of the conductivity tensor σ with θ (the orientation of the electric vector about the $\langle 001\rangle$ direction in the $\langle 1\bar{1}0\rangle$ plane).

Table 1 shows a comparative study of our results and the experimental results of Nathan [5] for longitudinal anisotropy in nondegenerate semiconductors. It is evident from the table that for the same magnitude of electric field the anisotropy in Nathan's result is 40 per cent as against 13 per cent in our case. Thus we see that the longitudinal anisotropy in conductivity is suppressed as the carrier concentration is increased.

The analysis in the present paper inevitably suffers from certain simplifications; first in neglecting the intervalley scattering and second in assuming the number of electrons to be equal in all the valleys. The effect of former is to reduce the anisotropy and that of latter

Table 1. *Longitudinal anisotropy in many valley semiconductors (Ge)*

Direction	σ_{xx}/σ_{111} Nondegenerate (Exptl.)	Degenerate	Field
$\langle 111\rangle$	1	1	
$\langle 110\rangle$	1·3	0·95	1800 V/cm
$\langle 100\rangle$	1·4	1·13	

σ_{111} is the longitudinal conductivity when **E** is along $\langle 111\rangle$ direction.

to enhance it. It has, however, been mentioned by Yamashita and Inoue[13] that the contribution of intervalley scattering is rather small.

Acknowledgements—J.K. and V.K.T. are grateful to C.S.I.R., India and E.S.S.A., USA for financial support.

REFERENCES

1. KAMAL J., *Phys. Status Solidi* **35**, 801 (1969).
2. FRÖHLICH H., *Proc. R. Soc.* **A188**, 532 (1947).
3. BARRIE R. and BURGESS R. R., *Can. J. Phys.* **40**, 1056 (1962).
4. SASAKI W., SHIBUYA M., MIZUGUCHI K. and HATOYAMA G. M., *J. Phys. Chem. Solids* **8**, 250 (1959).
5. NATHAN M. I., *Phys. Rev.* **130**, 2201 (1963).
6. SASAKI W., SHIBUYA M. and MIZUGUCHI K., *J. phys. Soc. Japan* **13**, 456 (1958).
7. CONWELL E. M., *Solid State Phys. Suppl.* **9**, Chap. 3, (1967).
8. RYDER E. J., *Phys. Rev.* **90**, 766 (1953).
9. PAIGE E. G. S., *Progress in Semiconductors* Vol. 8, Temple Press Books (1964).
10. FISTUL V. I., *Heavily Doped Semiconductors*, Plenum Press, New York (1969).
11. SODHA M. S., KAMAL J. and DUBEY P. K., *J. phys. Soc. Japan* **28**, 1461 (1970).
12. TSUTSUMI O., *J. phys. Soc. Japan* **19**, 1290 (1964).
13. YAMASHITA J. and INOUE K., *J. Phys. Chem. Solids* **12**, 1 (1960).

APPENDIX A

The integral appearing in equation (10) are,

$$K_\gamma{}^i = \int_0^\infty I_\gamma{}^i(x)\phi_\gamma{}^i(x)\,\mathrm{d}x; \quad \gamma = 1,2,3,4 \tag{A.1}$$

$$I_1{}^i(x) = I_3{}^i(x) = \frac{x^{3/2}\,\mathrm{e}^{x-\eta^i}}{(1+\mathrm{e}^{x-\eta^i})^2}. \tag{A.2}$$

$$I_2{}^i(x) = I_4{}^i(x) = I_1{}^i(x+\hbar\omega_0/k_0T_e{}^i), \tag{A.3}$$

$$\phi_1{}^i = \frac{1}{\nu_1{}^i}, \quad \phi_2{}^i = \left(\frac{1}{\nu_2'^i} - \frac{1}{\nu_1'^i}\right),$$

$$\phi_3{}^i = \frac{1}{\nu_3{}^i}, \quad \phi_4{}^i = \left(\frac{1}{\nu_4'^i} - \frac{1}{\nu_3'^i}\right),$$

$$\nu_1{}^i = D^i\{x^{1/2} + B(x+x_0{}^i)^{1/2}\} + \nu^i_{\parallel\mathrm{ion}}(x), \tag{A.4}$$

$$\nu_2{}^i = D^iB\,\mathrm{e}^{x_0{}^i}(x-x_0{}^i)^{1/2} + \nu_1{}^i, \tag{A.5}$$

$$\nu_3{}^i = D^i\{\gamma_1 x^{1/2} + B(x+x_0{}^i)^{1/2}\} + \nu^i_{\perp\mathrm{ion}}(x) \tag{A.6}$$

$$\nu_4{}^i = \nu_3{}^i + \nu_2{}^i - \nu_1{}^i, \tag{A.7}$$

$$D^i = W_0T_0(k_0T_e{}^i)^{1/2}, \quad x_0{}^i = \hbar\omega_0/k_0T_e{}^i$$

and $\nu_1'^i$, $\nu_2'^i$, $\nu_3'^i$ and $\nu_4'^i$ are obtained from equation (A.4), (A.5), (A.6) and (A.7) respectively by replacing x by $x+x_0{}^i$.

J. Phys. Chem. Solids, 1971, Vol. 32, pp. 2639–2643. Pergamon Press. Printed in Great Britain

DETERMINATION DU SIGNE RELATIF DE A ET D A PARTIR D'UN SPECTRE DE R.P.E. D'UN ECHANTILLON A L'ETAT DE POUDRE CRISTALLINE

P. MIALHE, A. BRIGUET et B. TRIBOLLET
Laboratoire de Spectroscopie et Luminescence, Section de Spectroscopie Hertzienne,
Faculte des Sciences, 43, Bld du 11 Novembre 1918·69, Villeurbanne, France

(*Received* 3 *December* 1970; *in revised form* 12 *February* 1971)

Résumé – Nous montrons que le dédoublement des transitions hyperfines, observé sur un spectre de poudre, permet de déterminer le signe relatif de A et D. De plus le calcul de la forme de raies conduit à une méthode précise pour mesurer A.

Abstract – In a powder the observed doubling of the hyperfine transitions is shown to allow a determination of the relative sign of A and D. The shape of the lines permits a relatively high accuracy measurement of A on powder spectra.

1. INTRODUCTION

LES PARAMÈTRES de l'Hamiltonien de spin d'un ion présent à l'état d'impureté dans un réseau cristallin ont pu être déterminés en étudiant la forme des raies du spectre de R.P.E. d'un échantillon réduit à l'état de poudre. Bleaney et Rubins[1] ont montré que le dédoublement des transitions hyperfines, dans le cas d'un site à symétrie axiale et pour un tenseur spectroscopique g isotrope, est dû aux termes non diagonaux provenant des interactions électroniques et nucléaire. De Wijn et Balderen[2] ont noté que, pour des valeurs positives de l'interaction hyperfine isotrope mesurée par A, l'écart entre les composantes d'une raie dédoublée augmente lorsque le nombre quantique magnétique nucléaire m diminue.

Nous nous proposons, d'une part de donner une méthode permettant de déterminer A à partir de l'étude des raies de résonance, d'autre part de déterminer les signes relatifs des paramètres A et D en mesurant le dédoublement des transitions hyperfines observées sur un spectre de poudre cristalline.

2. THEORIE

L'Hamiltonien d'un ion dans un site axial peut s'écrire en fonction de l'angle θ qui repère l'axe du cristal par rapport à la direction Oz du champ magnétique appliqué H, sous la forme:

$$\begin{aligned}\mathscr{H} = {} & g\beta HS_z + \frac{D}{2}\left[S_z^2 - \frac{1}{3}S(S+1)\right] \\ & \times (3\cos^2\theta - 1) + \frac{D}{2}(S_zS_- + S_zS_+ \\ & + S_+S_z + S_-S_z)\cdot\cos\theta\sin\theta + \frac{D}{4} \\ & \times (S_+^2 + S_-^2)\sin^2\theta + AS_zI_z + \frac{A}{2} \\ & (S_-I_+ + S_+I_-). \qquad (1)\end{aligned}$$

Nous avons supposé le facteur spectroscopique g et l'interaction hyperfine A isotrope: dans ce cas souvent rencontré pour les ions dont l'état fondamental est un singulet orbital nous pourrons étudier l'influence des termes A et D sur la forme des raies de résonance. Les cinq derniers termes de l'Hamiltonien (1) étant considérés comme une perturbation de l'opérateur $g\beta HS_z$, nous avons calculé au troisième ordre la différence d'énergie des états $(\frac{1}{2}, m)$ et $(-\frac{1}{2}, m)$.

$$E_{1/2m}-E_{-1/2m}=g\beta H_0=g\beta H+Am+\frac{A^2}{2H}$$
$$+[I(I+1)-m^2]+\frac{D^2}{2H}$$
$$\times\sin^2\theta\cos^2\theta[3-4S(S+1)]$$
$$-\frac{D^2}{16H}\sin^4\theta[3-4S(S+1)]$$
$$-\frac{A^3}{2H^2}\Big[S(S+1)+I(I+1)$$
$$-m^2-\frac{5}{4}\Big]m-\frac{A^2D}{8H^2}$$
$$\times(3\cos^2\theta-1)[3-4S$$
$$\times(S+1)]m+\frac{AD^2}{16H^2}\sin^4\theta$$
$$\times[3-4S(S+1)]m-\frac{D^2A}{H^2}$$
$$\times\sin^2\theta\cos^2\theta[2S^2(S+1)^2$$
$$-S(S+1)-\tfrac{3}{8}]m \qquad (2)$$

(H_0 est la valeur du champ magnétique de résonance de l'électron libre).

L'approximation du 3ème ordre de l'expression H_m du champ magnétique de résonance des transitions hyperfines $(\frac{1}{2},m)\leftrightarrow(-\frac{1}{2},m)$, qui sont seules observables sur un spectre de poudre, peut être obtenue à partir de la relation (2) en remplaçant H par $H_0-Am/g\beta$[3] dans le dénominateur des ternes du 2ème ordre de (2).

$$H_m=H_{0m}-\frac{D'^2}{2H_0}\sin^2\theta\cos^2\theta\,[3-4S(S+1)]$$
$$+\frac{D'^2}{16H_0}\sin^4\theta\,[3-4S(S+1)]$$
$$-\frac{A'D'^2}{H_0^{\,2}}\sin^2\theta\cos^2\theta\Big[\frac{9}{8}-3S(S+1)$$
$$+S^2(S+1)^2\Big]m-\frac{3A'^2D}{8H_0^{\,2}}\sin^2\theta$$
$$\times[3-4S(S+1)]m. \qquad (3)$$

Introduisant les grandeurs A' and D' nous exprimons les mesures en gauss. Nous avons noté H_{0m} les termes indépendants de θ:

$$H_{0m}=H_0-A'm-\frac{A'^2}{2H_0}[I(I+1)-m^2]$$
$$+\frac{A'^3}{2H_0^{\,2}}\Big[S(S+1)-\frac{5}{4}\Big]m+\frac{A'^2D'}{4H_0^{\,2}}$$
$$\times[3-4S(S+1)]m. \qquad (4)$$

Forme des raies

Le facteur de forme $A(H)$ de la courbe d'absorption d'un échantillon contenant N moments magnétiques peut être défini par le relation:

$$A(H)=\frac{N}{2}\sin\theta\frac{d\theta}{dH}. \qquad (5)$$

En utilisant l'expression (3) du champ magnétique de résonance nous obtenons pour l'ion manganèse divalent:

$$A(H)=\frac{NH_0}{8D'^2}$$
$$\times\frac{1}{[\alpha_m\cos^2\theta-(\alpha_m+2\beta_m)\sin^2\theta]\cos\theta} \qquad (6)$$

avec

$$\alpha_m=8\Big[1-\frac{8A'}{H_0}m+\frac{3A'^2}{4D'H_0}m\Big] \qquad (7)$$

$$\beta_m=1-\frac{6A'^2}{D'H_0}m. \qquad (8)$$

Le facteur de forme $A(H)$ devient infini pour les deux valeurs de l'angle θ vérifiant $\theta=(\pi/2)$ et $\mathrm{tg}^2\theta=(\alpha_m/\alpha_m+2\beta_m)$ définissant les expressions H_{1m} et H_{2m} des champs magnétiques correspondant aux deux pics qui caractérisent le dédoublement de chaque transition hyperfine m. L'écart en champ entre les deux s'exprime au moyen de la relation:

$$\Delta H_m=H_{2m}-H_{1m}=\frac{D'^2}{2H_0}$$
$$\times\Big[\frac{\alpha_m^{\,2}+4\beta_m^{\,2}+4\alpha_m\beta_m}{\alpha_m+\beta_m}\Big]. \qquad (9)$$

Ces résultats sont différents de ceux de Bleaney et Rubins[1] par la présence du terme en $(A'^2/D'H_0)m$ dans les expressions de α_m et β_m. Ce terme provient de la contribution dû 3ème ordre en (A^2D'/H_0^2) $(3\cos^2\theta - 1)$ non considérée par ces auteurs dans le calcul de l'énergie de l'état Mm.

Signes relatifs de A et D

L'analyse du spectre de résonance électronique d'un ion placé dans un site cristallin axial ne permet de déterminer que les signes relatifs[4] des paramètres de l'Hamiltonien. Cette détermination peut être obtenue en mesurant les déplacements du 2ème ordre des raies hyperfines des transitions $(-\frac{1}{2}, m) \rightarrow (-\frac{3}{2}, m)$ et $(\frac{3}{2}, m) \rightarrow (\frac{1}{2}, m)$, et nécessite donc l'étude du spectre d'un monocristal. Les signes absolus sont alors déduits de la mesure de l'anisotropie de la susceptibilité magnétique[5] et de l'étude de la variation de l'intensité des raies à très basse température[6]. A notre connaissance aucun auteur n'a indiqué une méthode permettant dé déduire les signes relatifs de A et D, des données expérimentales obtenues sur un spectre de poudre. L'expression (9) dépend des seuls paramètres A et D de l'Hamiltonien dont les valeurs absolues peuvent être déterminées avec une incertitude inférieure à 2 pour cent sur un spectre de poudre. La mesure des écarts hyperfins permet d'obtenir la valeur de A, le paramètre D étant déduit des valeurs du dédoublement des raies. L'écart ΔH_m croît avec D et l'étude de l'expression (9) considérée comme une fonction de m montre que cet écart augmente avec le champ magnétique. Les raies les plus dédoublées correspondent donc aux valeurs positives de m pour A négatif et aux valeurs négatives de m pour A positif. De plus l'écart ΔH_m est une fonction de $x = (A/D)$, croissante pour ces raies les plus dédoublées et décroissante pour les raies les plus étroites. Ces résultats montrent que le plus fort dédoublement est observé en champ fort et lorsque A et D sont de même signe, les raies en champ faible étant alors les plus étroites possible. Le signe relatif de A et D peut donc être déduit simplement de la comparaison—pour des valeurs opposées de x—des différences des valeurs du dédoublement pour les transitions extrêmes avec les valeurs expérimentales.

3. RESULTATS EXPERIMENTAUX

Nous avons étudié le spectre de poudre de l'ion Mn^{2+} dans du carbonate de calcium.* La Fig. 1 reproduit un spectre complet analogue à celui qui a été publié par Hurd, Sachs et Hersberger[7] dans une étude de monocristaux qui a permis à ces auteurs de déterminer les valeurs de A et D: $(A' = 93{\cdot}95 \pm 0{\cdot}05\,G$ $D' = 81 \pm 0{\cdot}4\,G)$.

Le résultat du calcul de la forme des raies hyperfines est indiqué sur la Fig. 2 pour une distribution lorentzienne des fréquences de Larmor. L'étude des déformations de ces courbes avec la valeur $\Delta\nu$ de la largeur à mi-hauteur des raies individuelles nous a permis détablir une relation empirique pour déterminer les valeurs H_{1m} et H_{2m} à partir des valeurs expérimentales H_{1me} et H_{2me} des composantes d'une raie dédoublée:

$$H_{1m} = H_{1me} - \lambda\Delta\nu.$$

Bien que la valeur de λ soit un peu plus forte pour une raie gaussienne (0,47) que pour une raie Lorentzienne (0,44) la différence est trop faible pour permettre une distinction[8] entre ces deux distributions.

Dans le Tableau 1 nous indiquons les valeurs de $\Delta H_{|m|} - \Delta H_{-|m|}$ expérimentales, celles calculées pour A et D de même signe et de signe contraire.

Au vu des résultats nous déduisons que A et D sont de même signe.

Sur ces spectres la largeur des raies hyperfines, variant de 7–20G d'une extrémité à l'autre du spectre, rend très imprécise la mesure des écarts hyperfins. En effectuant le

---

*Ces produits ont été préparés par Amblard dans le laboratoire de M. R. A. Paris.

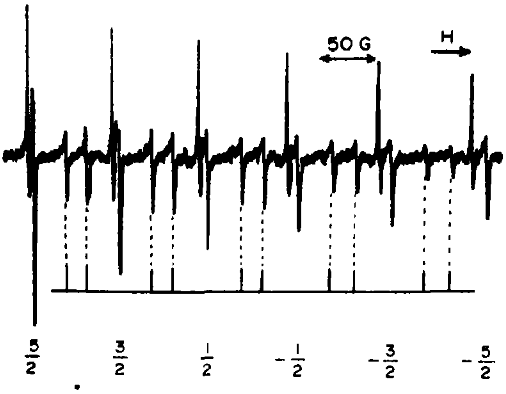

Fig. 1. Spectre de Mn^{2+} dans Ca CO_3. Les doublets marqués sont les transitions interdites $\Delta m = \pm 1$. Les transitions hyperfines sont indiquées par les valeurs de m. ($T = 77°K$).

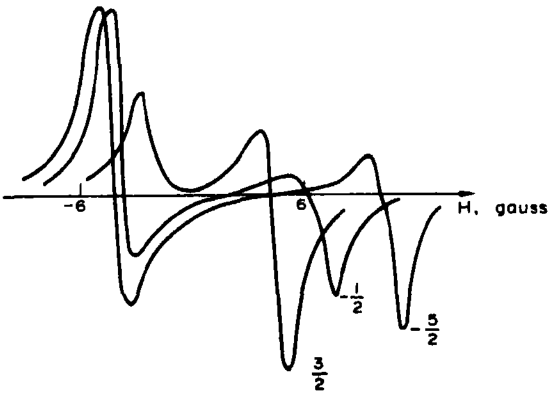

Fig. 2. Forme des raies correspondant aux transitions $m = \frac{3}{2}$, $m = -\frac{1}{2}$, $m = -\frac{5}{2}$ pour une distribution Lorentzienne des fréquences. L'origine du champ magnétique est H_{0m} pour chaque raie.

calcul de la forme de chaque raie nous avons choisi pour origine du champ magnétique la valeur de H_{0m}. Ainsi en prenant sur chaque raie cette valeur pour repère, nous déterminons la valeur de A par la mesure de l'écart hyperfin qui a l'expression:

$$H_{0m} - H_{0m-1} = -A' + \frac{A'^2}{2H_0}(2m-1) + \frac{15}{4}\frac{A'^3}{H_0^2} - \frac{8D'A'^2}{H_0^2}. \tag{8}$$

Les valeurs expérimentales et théoriques sont indiquées sur le Tableau 2.

Nous obtenons $|A'| = 94\,G \pm 0{,}6\,G$.

4. CONCLUSION

Nous avons donc montré que l'étude théorique de la forme des raies conduit à la mesure de l'interaction hyperfine isotrope, et à la détermination des signes relatifs de A et D sur un spectre de résonance paramagnétique

Tableau 2. Valeurs de $H_{0m} - H_{0m-1}$ exprimées en Gauss

$m-1$	m	Valeurs expérimentales	Valeurs théoriques
$\frac{3}{2}$	$\frac{5}{2}$	−88·7	−88·9
$\frac{1}{2}$	$\frac{3}{2}$	−91·4	−91·5
$-\frac{1}{2}$	$\frac{1}{2}$	−94·0	−94·2
$-\frac{3}{2}$	$-\frac{1}{2}$	−96·5	−96·8
$-\frac{5}{2}$	$-\frac{3}{2}$	−99·3	−99·8

Tableau 1. Comparaison du dédoublement des raies pour des transitions symétriques (même $|m|$)

Différence des écarts	Valeurs expérimentales (Gauss)	Valeurs calculées $\lvert A'\rvert = 94\,G$ $\lvert D'\rvert = 81\,G$	
		$\frac{A'}{D'} < 0$	$\frac{A'}{D'} > 0$
$\Delta H_{5/2} - \Delta H_{-5/2}$	11·3	10·9	6·4
$\Delta H_{3/2} - \Delta H_{-3/2}$	6·8	6·5	4
$\Delta H_{1/2} - \Delta H_{-1/2}$	2·3	2·2	1·3

électronique d'un échantillon à l'état de poudre cristalline. Ces résultats permettent la détermination, par R.P.E., des déformations d'un réseau cristallin consécutives à divers traitements chimiques ou physiques qui sont imposés au composé sous forme de poudre.

Remerciements—Nous remercions vivement Monsieur le Professeur Erbeia et Monsieur le Professeur Deimau pour les conseils qu'ils nous ont donnés au cours de cette étude.

REFERENCES

1. BLEANEY B. et RUBINS R. S., *Proc. Phys. Soc.* **77**, 103 (1961); **78**, 778 (1961).
2. DE WIJN H. W. et VAN BALDEREN R. F., *J. chem. Phys.* **46**, 1381 (1967).
3. DRUMHELLER J. E. et RUBINS R. S., *Phys. Rev.* **133**, A1099 (1964).
4. LOW W. et SUSS J. T., *Phys. Rev.* **119**, 132 (1960).
5. BLEANEY B. et INGRAM J. E., *Proc. R. Soc.* **A205**, 336 (1951).
6. LOW W., *Phys. Rev.* **105**, 793 (1957).
7. HURD F. K., SACHS M., et HERSBERGER W. D., *Phys. Rev.* **93**, 373 (1954).
8. SEARL J. W., SMITH R. C. et WYARD S. J., *Proc. Phys. Soc. Lond.* **A78**, 1174 (1961).

J. Phys. Chem. Solids, 1971, Vol. 32, pp. 2645–2646. Pergamon Press. Printed in Great Britain

TECHNICAL NOTES

Light-induced oxidation of $NbSe_2$ single crystals*

(*Received* 17 *December* 1970; *in revised form* 8 *April* 1971)

IT HAS been reported[1] that single crystals of groups IV and V transition metal-dichalcogenide compounds oxidize slowly in air. We have observed oxidation in $NbSe_2$ single crystals which were grown by iodine vapor transport[2], then stored in air on a laboratory bench directly under a fluorescent light. The crystal surfaces became discolored after several months; the color was dependent upon the angle of observation, suggesting an interference effect in a transparent surface layer. It was also observed that only the top surfaces of the platelets had become discolored, and that the portions of top surfaces that had been shielded by overlying crystals from direct illumination showed no such discoloration. Interior portions of the discolored crystals appeared normal when exposed by cleaving.

To test the assumption that the observed reaction, presumably with oxygen, was light-induced, four crystals were cleaved[3] to transparency, mounted on silica plates, and treated as follows: the optical transmission of selected areas was measured using light of wavelength $\lambda = 546$ nm; then two of the crystals were sealed in evacuated (5×10^{-6} torr) silica tubes, and the remaining two were placed in air-filled stoppered silica tubes. One air-filled tube and one evacuated tube were placed in direct sunlight, and the other two tubes were placed in an opaque enclosure. After ~60 days, the tubes were opened and the optical transmission of the selected areas of the crystals was again measured. Only the crystal which had been exposed to sunlight in air showed a significant change in optical transmission. Visual inspection showed that it had lost its characteristic reddish-orange color and had become completely colorless.

Figures 1(a) and 1(b) illustrate this transition on a somewhat thicker, incompletely reacted crystal. The appearance of this crystal suggests that oxygen may diffuse in from the edges and along faults in the structure, reacting with the crystal under the influence of light.

The thickness of an $NbSe_2$ crystal may be determined[4] from its optical density at $\lambda = 546$ nm. The above-mentioned colorless sample had optical densities in two areas, prior to exposure to sunlight, corresponding to crystal thicknesses of 630 and 990 Å. After treatment, the thicknesses of these areas were measured by multiple-beam interferometry and were found to be 1900 and 3500 Å, respectively. Such a thickness increase is reminiscent of the formation of lamellar compounds by intercalation[5].

It was not possible to weigh accurately these thin-cleaved samples to determine the net change in composition, so a whole crystal weighing 5420 μg was exposed to sunlight in air for ~90 days. At the end of this period, the crystal exhibited discoloration on its upper surface, indicating the formation of a reacted surface layer, and was found to weigh 4524 μg. A gain of 4 μg of material, concentrated in a surface film a few thousand Ångstroms in thickness, implies the formation of a selenate, or perhaps a mixture of oxides of Nb and Se, in the illuminated portions of the crystal.

In an effort to determine the wavelength region responsible for this light-induced effect, three thin-cleaved crystals covered respectively with Pyrex glass, a Corning CS3-69 filter (passing wavelengths greater than $\lambda =$

---

*Based on work performed under the auspices of the U.S. Atomic Energy Commission.

525 nm), and a Corning CS2-59 filter (passing wavelengths greater than $\lambda = 630$ nm), were exposed to light from a 150 W reflector floodlamp for ~90 days. Upon microscopic investigation, only the crystal which had been covered by the CS2-59 filter showed no colorless areas. As the ultraviolet output of a tungsten lamp is limited, and the u.v. cutoff for Pyrex is $\lambda \sim 300$ nm in any case, oxidation of $NbSe_2$ crystals appears to be induced by light in the wavelength region 300–630 nm. No effort was made to determine what, if any, specific wavelengths are responsible, or to ascertain a short wavelength cutoff.

To determine structural changes accompanying light-induced oxidation, a thin-cleaved $NbSe_2$ crystal was mounted on an electron microscope grid and exposed to sunlight in air for ~90 days. Figure 2(a) shows the 100 kV electron diffraction pattern of the unreacted crystal, and Fig. 2(b) shows the 80 kV electron diffraction pattern from a typical colorless area after treatment. A transition to complete lattice disorder is seen; this is consistent with observations[6] made on thermally oxidized $NbSe_2$ crystals.

Lee *et al.*[7] found less than 1 ppm iodine present in $NbSe_2$ crystals grown by chemical vapor transport; however, chemical analysis [8] of our crystals revealed iodine concentrations of the order of 100 ppm. Although this concentration is higher than that previously reported, it seems unlikely that the observed photolytic effects are due to the formation of an iodate; however, it may be that the presence of iodine sensitizes the photolysis. Simple attempts to reduce the iodine concentration have been unsuccessful, and we have therefore been unable to evaluate the effect, if any, of iodine on the observed photolytic behavior.

Inducement[9] and enhancement[10] of oxidation are well known effects of irradiation by light, and mechanisms have been postulated [11] to account for these effects.

The observations described in this note were made on ϵ-$NbSe_2$ single crystals, but similar effects were seen in single crystals of ϵ-$Nb_{1.04}Se_2$, ζ-$NbSe_2$, and ζ-$Nb_{1.04}Se_2$. We wish to advise other workers studying this material, and by inference other dichalcogenides of Nb (and possibly Ta), on the desirability of storing samples, particularly thin-cleaved crystals, in containers where they would be protected from light or oxygen, or both.

Argonne National Laboratory,
Argonne,
Illinois 60439,
U.S.A.

G. E. MYERS
G. L. MONTET

REFERENCES

1. WILSON J. A. and YOFFE A. D., *Adv. Phys.* **18**, 193 (1969).
2. MYERS G. E. and MONTET G. L., *J. appl. Phys.* **41**, 4642 (1970).
3. MYERS G. E. and MONTET G. L., *J. appl. Phys.* **37**, 4195 (1966).
4. MYERS G. E. and MONTET G. L., *Thin Solid Films* **6**, R7 (1970).
5. GAMBLE F. R., DISALVO F. J., KLEMM R. A. and GEBALLE T. H., *Science* **168**, 568 (1970).
6. MONTET G. L. (unpublished).
7. LEE H. N. S., McKINZIE H., TANNHAUSER D. and WOLD A., *J. appl. Phys.* **40**, 602 (1968).
8. Performed by the Analytical Group, Chemistry Division, Argonne National Laboratory.
9. GROSSWEINER L. I. and GORDON S., *J. chem. Phys.* **22**, 1139 (1954).
10. OREN R. and GHANDHI S., *J. appl. Phys.* **42**, 752 (1971).
11. See, for example, CALVERT J. G. and PITTS J. L., *Photochemistry*, John Wiley, New York (1966).

J. Phys. Chem. Solids Vol. 32, pp. 2646–2649.

Paramagnetic resonance of a diatomic nitrogen ion containing the N-15 isotope in barium azide

(*Received* 18 *December* 1970; *in revised form* 2 *March* 1971)

THE IRRADIATION of single crystals of barium azide ($Ba(N_3)_2$), sodium azide (NaN_3) and potassium azide (KN_3) with u.v. light or X-rays produces a five line ESR spectra which has been assigned to an N_2^- radical[1–4]. The assignment of the spectra to the N_2^- is not unambiguous. It is possible to account

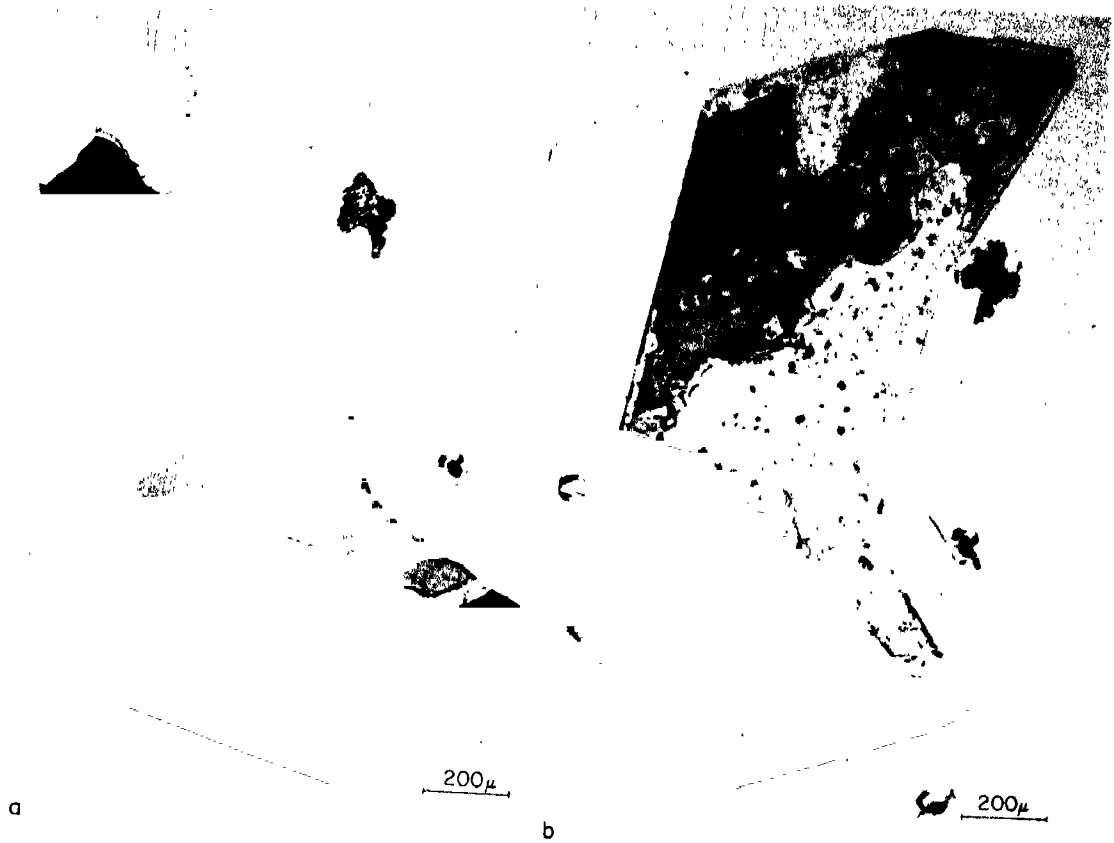

Fig. 1.

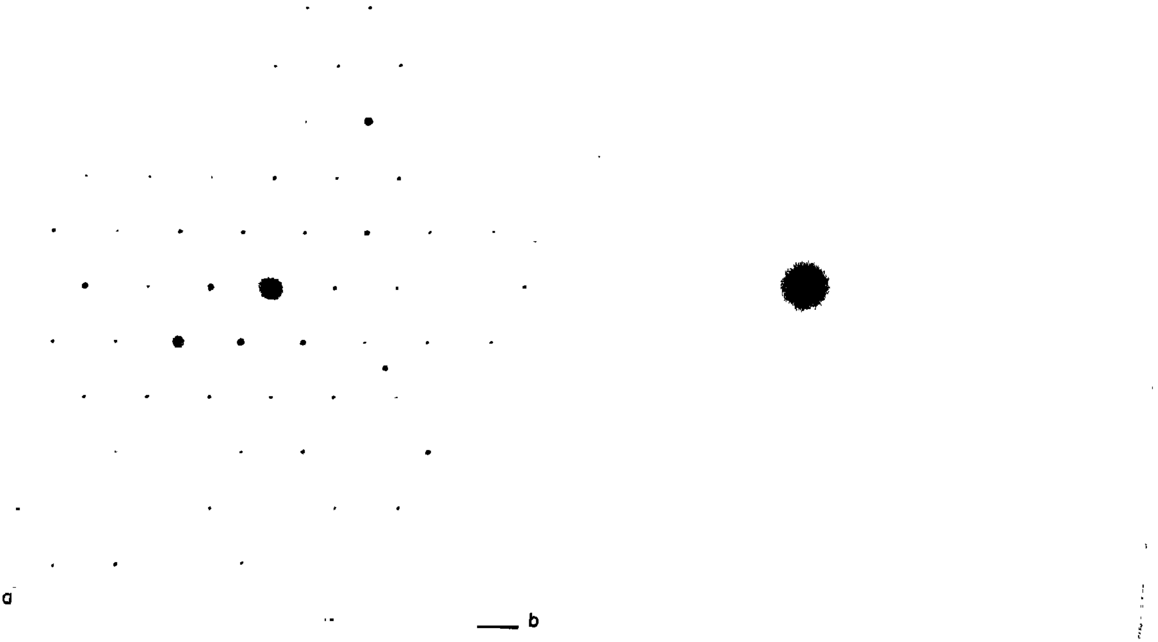

Fig. 2.

[*Facing page* 2646]

for the properties of the spectra with an N_3 neutral radical. In order to distinguish between the two models for the spectra single crystals of $Ba(N_3)_2$ were grown with the isotopic N-15 atom on one end of the triatomic linear azide ion. The ESR spectra of these crystals was then investigated after u.v. irradiation.

From a consideration of the energy levels of the N_2 molecule the valence configuration of the N_2^- would be expected to be $2\sigma_u$, $1\pi_u$, $2\pi_g^*$. The ESR data is consistent with the unpaired electron occupying a π_g^* molecular orbital because the unique and largest component of the hyperfine tensor is the A_y component. The y direction is perpendicular to the geometric axis of the molecule. The measured g shifts of the N_2^- are all negative. Recent calculations of the g shifts based on the above indicated valence configuration and using the formalism of Stone indicate that g_x should be shifted positively[4, 5]. It was pointed out however that this discrepency could be due to some covalency of the wavefunctions of the N_2^- with nearest neighbor barium cations[4]. It is interesting to note that in KN_3 no Raman vibrational bands have been observed that one might expect to be associated with an N_2^-[6].

Another equally plausible model for the spectra is an N_3 neutral radical. Based on the recently calculated molecular orbitals for the N_3^- the valence configuration of an N_3 neutral should be $4\sigma_g$, $3\sigma_u$, $1\pi_g$[7]. The unpaired electron would be in a π_g, molecular orbital which is consistent with the A_y component of the hyperfine tensor being the largest and the unique one. The probability density of this orbital is such that the electron would be localized primarily on the end two nitrogens of the linear N_3 neutral radical. Thus the unpaired electron would display a hyperfine interaction only with the two end nuclei. Since the nitrogen nuclei has a spin one, a five line ESR spectra with intensity ratio of 1:2:3:2:1 would result in agreement with what is experimentally observed. Also the magnitude of the hyperfine interaction is reasonable for the unpaired electron in this orbital. Further calculations of the g shifts based on the expected energy level scheme for an N_3 neutral radical indicate that the direction of the g shifts would be in agreement with those observed. Thus the N_3 neutral appears to provide an alternative model for the spectra.

Barium azide has a monoclinic unit cell[8]. The radical that gives rise to the spectra lies in one magnetic site in the lattice. The y principal axis of the g and the A tensor is parallel to the b axis of the unit cell.

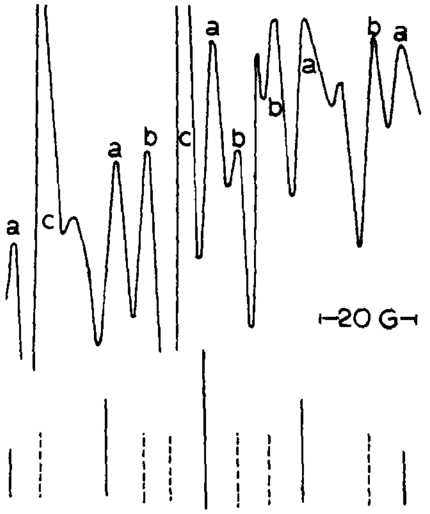

Fig. 1. The ESR spectrum obtained in barium azide in which the end nitrogen of the linear azide ion is the N-15 isotope. The d.c. H field is parallel to the b-axis of the unit cell. The resonances marked A arise from the N^{14}–N^{14} ion. The B labels the N^{14}–N^{15} radical and C indicates resonances that are not identified. The theoretically predicted spectrum is shown at the bottom of the figure. The dashed lines indicate the expected positions of the N^{15}–N^{14} resonances.

The ESR spectra obtained after room temperature u.v. irradiation of $Ba(N_3)_2$ containing N-15 on one end of the triatomic linear azide ion is shown in Fig. 1 at the top. The d.c. magnetic field for the illustrated spectra is parallel to the b crystal axis of the unit cell. The observed spectra can be accounted for by equal amounts of two kinds of radicals, an N^{14}–N^{15} species and an N^{14}–N^{14} radical. The resonances denoted by the letter A in Fig. 1 arise from the N^{14}–N^{14} species. These resonances consist of five lines with the intensity ratio of 1:2:3:2:1 indicating that the spectra is arising from the equal interaction of an unpaired electron with two nuclei of spin one. The separation K_{14} of the resonances from each other is 20 G. These results are in agreement with previously reported results for this orientation of the d.c. H field in non isotopically labled crystals [4].

The lines marked by the letter B are resonances due to the N^{14}–N^{15} species. In such a radical the unpaired electron interacts with the N^{14} nucleus which has a nuclear spin of one and with the N^{15} nucleus which has a spin of one half. The hyperfine splittings in this radical are given by

$$E = K_{14}M_s m_{14} + K_{15}M_s m_{15} \qquad (1)$$

where m and M refer to the nuclear and the electron magnetic quantum numbers. The energy level scheme due to the hyperfine interaction in the N^{14}–N^{15} radical is illustrated in Fig. 2. The ESR spectra of this radical should consist of six lines of equal intensity. The hyperfine coupling constant K_{15} due to the interaction with the N^{15} nucleus can be calculated from the ratio of the nuclear magnetic moments of the N^{15} and the N^{14} nuclei and the measured K_{14} splitting from the N^{14}–N^{14} ESR spectra. This calculation leads to a value of 27 G. for the K_{15} for the d.c. H field parallel to the b axis of the unit cell. The values of K_{14} and K_{15} can be used in equation (1) to predict the positions of the lines due to the N^{14}–N^{15} radical. The predicted positions of the lines are shown in the bottom of Fig. 1. The resonances labeled B appear to correspond to the positions predicted by the theory. Not all of the six lines of the N^{14}–N^{15} spectra are visible because of the presence of other resonances from unidentified radicals. The unidentified radicals are labeled by the letter C in the figure. That these lines are not due to the diatomic nitrogen radical is concluded from the fact that they have different annealing rates than the lines labeled A and B. The resonances labeled A and B all have the same annealing rates.

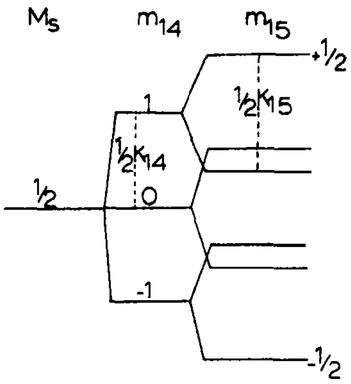

Fig. 2. The energy level scheme for the hyperfine interaction between an unpaired electron and an N^{14} and N^{15} nucleus. The electron is assumed to have an equal probability of being at either nucleus.

The major conclusion of the experiment is that the ultraviolet induced spectra in barium azide arises from a radical containing two nitrogen atoms. If the species were an N_3 neutral radical one would expect to get an ESR spectra in the isotopically labled barium azide only from an unpaired electron interacting with an N^{14} and an N^{15} nucleus. No spectra due to an N^{14}–N^{14} type radical should result. The fact that equal amounts of N^{14}–N^{14} and N^{15}–N^{14} type radicals result indicates that the radical is diatomic and formed from the linear N^{14}–N^{14}–N^{15} azide ion by the removal of an end nitrogen. Further it is indicated that the removal of either of the end nitrogens is equally probable. Thus the best model for the spectra appears to be the N_2^- radical.

Feltman Research Laboratories,
Picatinny Arsenal,
Dover,
N.J. 07801,
U.S.A.

F. J. OWENS

REFERENCES

1. WYLIE D. W., SHUSKUS A. J., YOUNG C. G., GILLIAM O. R. and LEVY P. W., *Phys. Rev.* **125**, 451 (1962).
2. HORST R. B., ANDERSON J. H. and MILLIGAN D. E., *J. Phys. Chem. Solids* **23**, 157 (1962).
3. GELERINTER E. and SILSBEE R. H., *J. chem Phys.* **45**, 1703 (1966).
4. MARINKAS P. L. and BARTRAM R. H., *J. chem Phys.* **48**, 927 (1968).
5. STONE A. J., *Proc. R. Soc. Lond.* **A271**, 424 (1963).
6. NAIR I. R. and HATHAWAY C. E., *Phys. Lett.* **30A**, 253 (1969).
7. BONACCORSI R., PETRONGOLO C., SCROCCO E. and TOMASI J., *J. chem. Phys.* **48**, 1500 (1968).
8. CHOI C. S., *Acta crystallogr.* **B25**, 2638 (1969).

J. Phys. Chem. Solids Vol. 32, pp. 2649–2652.

The simulation of a model of saturation of alkali halide crystals with *F* centres

(*Received* 23 *November* 1970; *in revised form* 16 *February* 1971)

1. INTRODUCTION

WHEN an alkali halide crystal is irradiated with an ionizing radiation, *F* centres are formed. In recent years, interest in the reactions following the primary creation event has steadily increased. These reactions are at the origin of the decrease of the formation rate of the centres with irradiation time, and of the saturation.

In [1], we described experiments made with 5 to 45 keV electrons at room temperature on KCl, KBr, KI and NaCl samples. It was found that all *F* centre growth curves can be described by the function:

$$n = n_0\left(1-\frac{1}{\sqrt{bt+1}}\right) \qquad (1)$$

with n the centre concentration, n_0 and b two adaptable parameters.

The saturation concentration is of the order of 10^{19} to 10^{20} cm^{-3} according to the nature of the sample.

The mechanisms proposed as causes of the saturation (or the decrease of the formation rate) may be divided into two groups:

(1) The formation rate decreases because an equilibrium which exists during irradiation between the formation and the destruction of centres shifts towards destruction when the concentration grows. Such models have been described by Wallis *et al.*[2], Sonder *et al.*[3], Durand *et al.*[4] and Farge[5], but only the latter investigators deduce an analytical representation of the growth curve from their model.

(2) The growth rate of the density decreases because the number of primary events diminishes. Such mechanisms have been proposed by Goldstein[6] and by Pooley[7]. According to Pooley, at the temperatures at which interstitials are mobile, there exists around every *F* centre a 'prohibited volume' inside which, when a Frenkel pair is created, the interstitial recombines, after a time of the order of the inverse of the lattice vibration frequency, with the *F* centre, and causes it to disappear. If an act of creation takes place outside the prohibited volumes, the interstitial disappears in an unspecified sink, and hence the corresponding *F* centre is stabilized. Because of its simplicity, this model leads to a growth curve which does not depend on different independent mechanisms, and which can be described by a small number of parameters, as in fact we have observed[1].

2. SIMULATION

To determine the analytical representation of their growth curves, most investigators, have used rate equations, i.e. equations whose variables are mean spatial values. Such a treatment of the processes is not convenient in every case, because it does not take into account correlated reactions, which, in fact, play a predominant role in the domain of high concentrations. We therefore used a Monte Carlo method to simulate colour centre growth curves.

By analogy with Pooley's proposition it is supposed, that around and F centre or a centre which is formed in a number equal or proportional to the number of F centres (V_3 at room temperature[8, 9]), there is a volume inside which another Frenkel pair cannot exist, because:

either it recombines immediately (Pooley's mechanism)

or the primary creation event cannot take place. This could be for the following reasons:

the displacement sequence[10] cannot occur because of the deformation of the lattice,

the electron-hole recombination necessary for the creation of the defect takes place via the centre to which the prohibited volume belongs, i.e., the centre acts as a recombination centre, a process of the same type as that suggested by Goldstein[6].

Outside the prohibited volumes Frenkel pairs can be created as in a virgin crystal.

We have carried out simulated experiments in one and three dimensions. The three-dimensional crystal is a primitive cubic lattice of 30^3 sites. Cyclic boundary conditions have been used. Irradiation is simulated in the following way: by means of random numbers, the coordinates of a lattice site are determined and the coordinates of the neighbouring sites, which determine its prohibited volume, are deduced from them. If the new volume overlaps with one already in existence the result of the attempt is ignored; if not, the coordinates of the prohibited volume are memorized and the attempt is considered a success. The number of attempts represents the irradiation dose, the number of successes the number of centres. The result of this calculation is given as a table of values for the coloration curve. Each experiment is repeated several times with other random numbers in order to diminish the statistical variations of the concentration values. The fact that random numbers are used implies that no correlation exists between the centres created along the trajectory of the ionizing particle. This is certainly true for the electronic irradiation we use. An electron of 10 keV has a range of some microns in the crystal and forms only 2 to 5 F centres along its path[1]: thus the distance between these centres is great compared to the average distance between neighbouring F centres at saturation (about ten interatomic spacings).

To compare the values given by the simulation with those yielded by the real experiment, they were treated in the same manner as the results of the measurements: the parameters n_0 and b in equation (1) were determined by applying a least squares method to the values of the simulation. (The method was applied to the logarithms of the concentration values, and time values were chosen in exponentially increasing intervals).

Several 'experiments' were carried out in one dimension in order to determine the influence of the boundaries and of the size of the prohibited volume. It was found that the shape of the coloration curve no longer varies (i) above a prohibited volume (which is a line segment in one dimension) of 5 sites for a fixed ratio prohibited volume-total volume, (ii) above a total volume of 30, the prohibited volume being 6 sites. It is supposed that this result can be generalized for three dimensions: it is not necessary, when a cubic prohibited volume is used, to have a side length of more than 6 sites.

The calculation in three dimensions show that about half of the total volume is occupied by the prohibited volumes when saturation is attained. As a real crystal saturated with F centres contains about one centre per 1000 anion sites, its prohibited volume is approximately 500 sites. The side length of the cube is thus about $\sqrt[3]{500} \approx 8$, i.e. more than 6 sites, and, as explained above, the calculations can be made with a side length of 6 sites.

The 'crystal' was 'bombarded' until the increase of concentration was less than 4 per cent when the 'irradiation time' doubled. This corresponds to 4096 attempts of which about 60 were successes. The result, which is the average over 5 runs, is shown on Fig. 1 as also is a function of type (1).

The figure further illustrates:

Experimental values obtained by irradiating a Korth KBr single crystal with an electron beam of 20 kV, 2 $\mu A/\text{cm}^2$. The scales are chosen in such a way that the function (1) fitted to these values is congruent with that obtained from the simulated experiment,

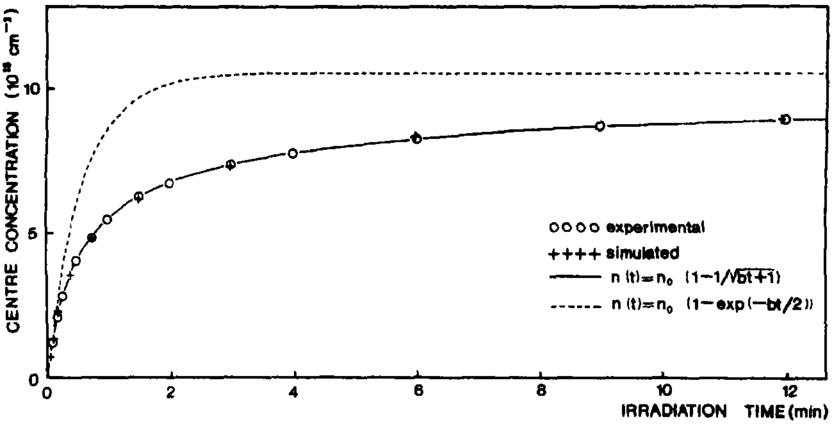

Fig. 1. Colour centre concentration plotted against irradiation time in a real experiment (Korth-KBr, 20 keV, 2 A/cm^2) and in a simulated experiment. The units correspond to the real experiment.

the function $n = n_0(1-e^{-bt/2})$, which has the same initial slope and saturation value as (1). It can be seen that the saturation obtained experimentally is attained much more slowly than that given by an exponential function.

3. DISCUSSION

The simulation yields a growth curve which is in close agreement with those obtained experimentally at room temperature by electron irradiation. The model at the basis of this calculation is purely geometric, for the physical processes at the origin of the prohibited volumes have not been considered. They must, however, be taken into account, if the calculations are to be improved, but at the moment, this does not seem possible, for the basic mechanism are not yet sufficiently well known.

Several modifications of the present form of the model might be suggested:

It has been supposed that a prohibited volume has a well-defined boundary, but the probability of formation will presumably decrease continuously when an already existing centre is approached,

the calculation implies that once a centre is created, it remains stationary. If the prohibited volumes belong to F centres, we will have to take into account the fact that, under irradiation they are transformed into M centres and vice versa,

if the interstitials stabilize as clusters, as suggested by Sonder *et al.*[11] and Durand *et al.*[4], then, if a new F centre is to be created, it is not enough for an interstitial to form at a sufficient distance from the existing centres, but it must also diffuse towards a cluster without recombining. In this case the diffusion has to be simulated in a random walk calculation[12].

If the hypothesis on which this model is based is true, this has important consequences for the distribution of the centres in the saturated crystal: mechanisms which can be treated by rate equations result in a statistical centre distribution while the prohibited volume mechanism provokes a more regular distribution. The distance between neighbouring centres at saturation is:

greater than the diameter of the prohibited volume,

less than twice the diameter of the prohibited volume (otherwise the crystal would not be saturated).

If such a distribution could be distinguished from a statistical distribution, a criterion for the validity of the model would have been found. However, we did not find a method sensitive enough for such an order to be made evident.

F. HERRMANN
P. PINARD

Laboratoire de Physique de la Matière,
Insitut National des Sciences Appliquées,
de Lyon,
Lyon,
France

REFERENCES

1. HERRMANN F. and PINARD P., *J. Phys. C* **3**, 1037 (1970).
2. WALLIS R. F. and FARADAY B. J., *Phys. Rev.* **133**, 1360 (1964).
3. SONDER E. and TEMPLETON L. C., *Phys. Rev.* **164**, 1106 (1967).
4. DURAND P., FARGE Y. and LAMBERT M., *J. Phys. Chem. Solids* **30**, 1353 (1969).
5. FARGE Y., *J. Phys. Chem. Solids* **30**, 1375 (1969).
6. GOLDSTEIN F. T., *Phys. Status Solidi* **20**, 379 (1967).
7. POOLEY D., *Brit. J. appl. Phys.* **17**, 855 (1966).
8. GOLDSTEIN F. T., *Solid State Commun.* **7**, 475 (1969).
9. HERRMANN F. and PINARD P., *Solid State Commun.* **8**, 791 (1970).
10. POOLEY D., *Proc. Phys. Soc. Lond.* **87**, 257 (1966).
11. SONDE[illegible] E., SIBLEY W. A., ROWE J. E. and NELSON C. M., *Phys. Rev.* **153**, 1000 (1967).
12. MEHRER H., *Z. Naturf.* **24a**, 358 (1969).

J. Phys. Chem. Solids Vol. 32, pp. 2652–2655.

Derivation of distribution functions from relaxation data

(*Received* 24 *September* 1970; *in revised form* 22 *January* 1971)

IN THE past few years, a sizable number of studies have been carried out on relaxation phenomena in glasses and glass-forming liquids. In most cases, the experimental data have indicated that the relaxation processes are complex – i.e. they are not describable in terms of a single relaxation time. Rather, a distribution of relaxation times is required to represent the data.

In the case of dielectric relaxation, the dielectric loss is then represented:

$$\epsilon''(\omega) = (\epsilon_R - \epsilon_U) \int_0^\infty \frac{G(\tau)\omega\tau d\tau}{1+\omega^2\tau^2} \quad (1)$$

where ϵ'' is the dielectric loss (the imaginary part of the complex dielectric constant); ϵ_R is the relaxed (low-frequency) dielectric constant; ϵ_U is the unrelaxed (high frequency) dielectric constant; ω is the frequency; τ is the relaxation time; and $G(\tau)$ is the distribution function of relaxation times.

In the case of mechanical relaxation, the corresponding expression is:

$$M''(\omega) = (M_U - M_R) \int_0^\infty \frac{F(\tau)\omega\tau d\tau}{1+\omega^2\tau^2} \quad (2)$$

where M'' is the mechanical loss; M_U is the unrelaxed (high-frequency) modulus; M_R is the relaxed (low-frequency) modulus; and $F(\tau)$ is the distribution function of relaxation times.

Experimental studies provide data on ϵ'' as a function of frequency as well as ϵ_R and ϵ_U, or on M'' as a function of frequency as well as M_U and M_R. The standard procedure (1, e.g.) then involves assuming various forms for the respective distribution functions – e.g., log normal distribution, Cauchy distribution, wedge distribution, box distribution, etc.—calculating the integrals in equations (1) or (2), and comparing the result with the experimental data on dielectric loss or mechanical loss as a function of frequency. If 'reasonable' agreement is found between experimental data and the calculated loss curve for a particular distribution of relaxation times, the data are then discussed in terms of the parameters characterizing that distribution. If, on the other hand, the agreement between calculated and experimental loss curves is poor, the investigator is faced with difficulties of real consequence and must frequently resort to discussion in terms of one of the distribution functions, which may fit the experimental data better than the other standard functions, but which fails to represent important features of the observed loss.

In the present brief paper, we shall describe an analytical technique which avoids these difficulties and permits the appropriate distribution function to be derived directly from the data.

Consider a general form of the relaxation expression:

$$P''(\omega) = P_0 \int_0^\infty \frac{H(\tau)\omega\tau d\tau}{1+\omega^2\tau^2} \qquad (3)$$

where P'' is the loss, P_0 is constant determined from experimental data, and $H(\tau)$ is the appropriate distribution function.

This can alternatively be represented in the form of a summation:

$$P''(\omega_i) = P_0 \sum_{j=1}^{n} \frac{H(\tau_j)\omega_i\tau_j\Delta\tau_j}{1+\omega_i^2\tau_j^2} \qquad (4)$$

where the precision of the representation depends on the number of terms, n, used in the sum.

The distribution function, $H(\tau_j)$, may be obtained from equation (4) by considering the frequency spectrum as divided into the same number of points, n, as the number of terms considered in the relaxation time spectrum. Then equation (4) corresponds to a series of n simultaneous equations, each with n terms:

$$\begin{aligned} P''(\omega_1) &= A_{11}H(\tau_1)+A_{12}H(\tau_2)+\cdots+A_{1n}H(\tau_n) \\ &\vdots \\ P''(\omega_i) &= A_{i1}H(\tau_1)+A_{i2}H(\tau_2)+\cdots+A_{in}H(\tau_n) \\ &\vdots \\ P''(\omega_n) &= A_{n1}H(\tau_1)+A_{n2}H(\tau_2)+\cdots+A_{nn}H(\tau_n) \end{aligned} \qquad (5)$$

where

$$A_{ij} = \frac{P_0\omega_i\tau_j\Delta\tau_j}{1+\omega_i^2\tau_j^2}. \qquad (6)$$

The terms A_{ij} can then be constructed into a matrix, M, such that

$$P'' = MH(\tau). \qquad (7)$$

Hence in terms of the reciprocal matrix, M^{-1}, we obtain:

$$H(\tau) = M^{-1}P''. \qquad (8)$$

Hence $H(\tau)$ can directly be determined from a knowledge of the loss, P'', and the parameters in the various A_{ij} terms.

The analysis of the preceding section has indicated that the distribution of relaxation times characterizing a given relaxation process can be obtained directly from experimental data. Corresponding distributions of activation energies can be derived from the distribution of relaxation times by the usual techniques. It is important, of course, that the experimental data be available over a wide range of frequency so that the resulting distribution functions can be specified with precision. In practice, a range of three decades or more in frequency around the maximum in the loss curve is generally sufficient.

As with previous techniques, the present analytical method does not permit by itself a ready differentiation to be made between a continuous distribution of relaxation times and a small number of discrete relaxation times. Such differentiation must be made, in cases where it is possible, on the basis of other information. In the present analysis, a continuous distribution is assumed [equations (1)–(3) above] and will be obtained from the matrix inversion.

It should also be noted that the present analytical method is used within the framework of a phenomenological description of relaxation data. Consequently, it does not by itself indicate whether the derived distribution of relaxation times reflects a distribution of molecular processes or results from nonlinearities in the system or other causes. Such distinctions must again be made on other grounds [See, for example, the discussion in Refs. [2] and [3]].

In carrying out the present analysis, the number of terms (n) used in the matrix should be large enough that the data can be faithfully represented and small enough that the inversion can be carried out with a reasonable expenditure of computer time. In most cases, 20–30 terms are sufficient to describe the data. In all cases, these terms should be spaced at sufficient intervals that the full range of the experimental results are represented; and in all cases the normalization integral, H_I, should be 0·99$^+$. Here

$$H_I = \int_{\tau_1}^{\tau_n} H(\tau)\mathrm{d}\tau.$$

While there are no formal restrictions on the selection of the τ_j and $\Delta\tau_j$, it is convenient in practice to select a range of τ_j which correspond to the frequency range of the experimental data. Using a suitable selection of ω_i to represent the range of the available data, the τ_j may then be selected as:

$$\tau_j = \frac{1}{\omega_i} \qquad (10)$$

and the $\Delta\tau_j$ as:

$$\Delta\tau_j = \frac{\tau_{j+1} - \tau_{j-1}}{2}. \qquad (11)$$

Adopting these procedures, a distribution of relaxation times can be obtained which provides a direct description of the experimental data. This distribution will not depend on the value of n or the spacing of terms selected, provided n is sufficiently large (and $\Delta\tau_j$ is sufficiently small) that the experimental data are well represented, and not so large (and $\Delta\tau_j$ not so small) that precision is lost during the matrix inversion. These conditions are satisfied for values of n which are convenient for the inversion, such as $n = 20$ to 30 or so, and experimental data covering some 3 or 4 decades in frequency. The derived distribution will, of course, reflect any errors which may be present in the original data (as will any phenomenological description).

It should be apparent from the preceding discussion that the present analytical technique is a simple and straightforward one. Its principal advantage over previous methods of analyzing relaxation data lies in the fact that no a priori assumptions concerning the form of the distribution function are involved in its application. In some cases, this can provide unique information; while in others, the experimental data may usefully be described in terms of one of the standard distribution functions. Consequently, it is suggested that the present method be used as a complement to rather than a substitute for the usual methods.

As an example of the use of this technique, let us analyze the dielectric relaxation data obtained in this laboratory on a 0·15 Cs_2O–0·85 SiO_2 glass at 125°C[1]. As shown in Fig. 1, the dielectric loss for this glass—as indeed for most glasses—is asymmetric to the high-frequency side of the peak. Distri-

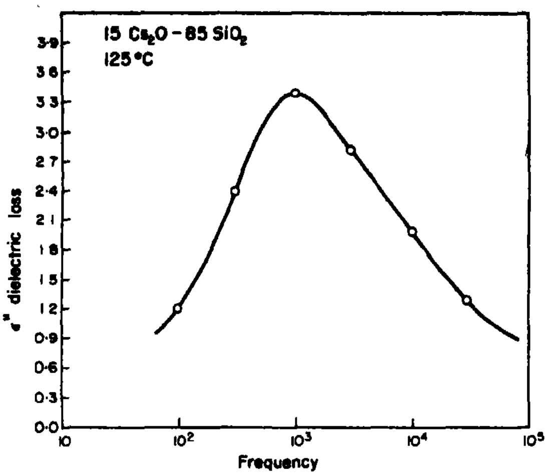

Fig. 1. Dielectric loss as a function of frequency.

bution functions of various forms can be assumed for describing the data and used with varying degrees of success. The distribution of relaxation times obtained by applying the analysis of the preceding section is shown in Fig. 2. In this application, the value of n was taken as 25, and the τ_j and $\Delta\tau_j$ for the matrix inversion were selected as outlined by equations (10) and (11). As expected, the derived distribution function provides a highly precise representation of the experimental data. The distributions of relaxation time derived from dielectric relaxation studies on this and other glasses will be discussed at length in a subsequent paper[4].

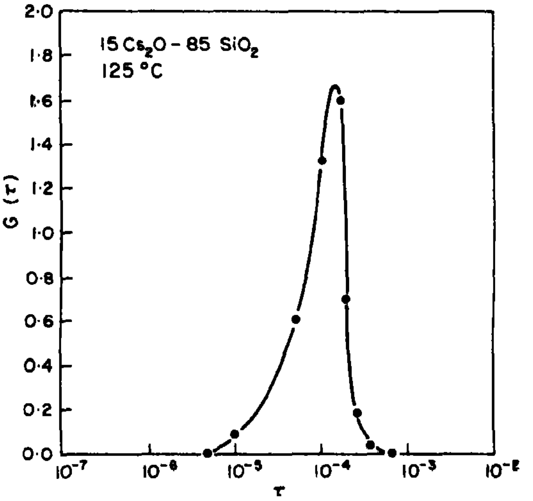

Fig. 2. Derived distribution of relaxation times.

The present paper has described a simple technique for deriving distribution functions of relaxation times directly from experimental data on relaxation phenomena. It is suggested that the technique can be employed with wide generality and that it can be particularly helpful when the standard distribution functions do not provide adequate representations of important features of the data.

Acknowledgements — Financial support for this work was provided by the United States Atomic Energy Commission and by the Advanced Research Projects Agency. This support is gratefully acknowledged, as is the assistance of R. Pronovost of Hydro-Quebec with the computer programming.

D. R. UHLMANN
R. M. HAKIM

Department of Metallurgy and Materials Science,
Center for Materials Science and Engineering,
Massachusetts Institute of Technology,
Cambridge, Mass. 02139, *U.S.A.*

REFERENCES

1. McCRUM N. G., READ B. E. and WILLIAMS G., *Anelastic and Dielectric Effects in Polymeric Solids*, Wiley, New York (1967).
2. KIMMEL R. M. and UHLMANN D. R., *J. appl. Phys.* 41, 592 (1970).
3. GOLDSTEIN M., in *Modern Aspects of the Vitreous State*, Vol. 3, (Edited by J. D. Mackenzie), Butterworths, London (1964).
4. HAKIM R. M. and UHLMANN D. R., *Dielectric Relaxation in Alkali Silicate Glasses*, to be published.

---

*Based in part on a thesis submitted by R. M. H. in partial fulfillment for the requirements for the ScD degree in Materials Science, June, 1968.

†Now with Hydro-Quebec Institute of Research, Varennes, Canada.

J. Phys. Chem. Solids Vol. 32, pp. 2656–2659.

A diffraction study of diffusion in the Mo–Cr system

(*Received* 29 *December* 1970)

A DIFFRACTION method for studying interdiffusion in powder compacts was first proposed by Duwez and Jordon[1], and later put on a quantitative basis by Rudman[2] and applied to the Cu–Ni system by Fisher and Rudman[3] and also be Heckel[4]. Diffraction method has also been applied to analyze diffusion under one dimensional conditions[5, 6]. The present work is concerned with an application of the Rudman–Duwez method to a b.c.c. system. Specifically, Mo–Cr system was chosen for this purpose as information relating to interdiffusion in this system is rather scanty and also somewhat conflicting: Pines and Smushkov[5] and Gruzin *et al.* [7] have reported parameters characterizing the diffusion of Cr in Mo (see Table 1; a summary of their original Russian paper appears in the Chemical Abstracts[6]). Proloshkin and Sidunova[8] and Arzhanyi and Volkova[9] from experiments with diffusion couples, on the other hand, have concluded that Mo and Cr do not form a continuous series of solid solutions and postulated the existence of an intermediate phase contrary to other works on this system[10]. The diffraction method for studying interdiffusion is suited to systems with complete range of solid solubility and our preliminary measurements were concerned with this question. We however failed to detect any intermediate phase or any other deviations from complete solid solubility in Mo-50%Cr powder compacts following successive diffusion anneals at 1050 or 1200°C.

Table 1. *Average diffusion parameters for b.c.c. binary systems*

System	D_0 (cm²/sec)	Q (k cal./mole)	Ref.
Mo–Cr	$2 \cdot 9 \times 10^{-3}$	61·4	This work
Mo–Cr	$2 \cdot 7 \times 10^{-3}$	58·0	7
Mo–Cr	$7 \cdot 5 \times 10^{-1}$	84·0	5
Mo–Ti	$1 \cdot 0 \times 10^{-3}$	66·0	12
Mo–Cb	$1 \cdot 0 \times 10^{+3}$	137	12
Cb–V	$5 \cdot 0 \times 10^{-2}$	68·0	12

For the diffusion runs, samples were prepared by mixing thoroughly high purity +325 mesh size Mo and Cr powders in equiatomic proportions. The mixture was compressed into 1 in. dia. billet forms under 35,000 psi pressure and given diffusion anneals at 1050 and 1200°C for times ranging from 50 to 1600 min under continuous flow of argon. Following each annealing treatment the sample surface was gound on 400 and 600 grit papers to remove any oxidized surface layer. The small degree of cold work introduced in this process was relieved by a short anneal (15 min) at a lower temperature (800°C). (In a separate run it was established that no measureable diffusion occurred at this temperature even after annealing for 1600 min. Following the strain anneal the sample was lightly ground and etched before making the diffraction runs. These consisted of recording the (200) diffraction profiles of Cr and Mo in a single continuous run following each diffusion anneal. Filtered Mo $K\alpha$ radiation was used and the peaks were scanned at 0.2°/min counter velocity in a $\theta - 2\theta$ scanning diffractometer equipped with a scintillation counter. Following Rudman[2], each measured profile was corrected for instrumental broadening and the remainder of the broadening attributed to composition fluctuation in the sample. The corrected profile $f(2\theta)$ may then be shown to be related to $N(c)$, the number of unit cells of composition c in the sample by the equation [2]

$$N(c) = Q(c) f(2\theta) \tag{1}$$

where

$$Q(c) = [kA^{-1} v d'(c) d_{hkl}^{-1}(c)] \times [c f_{\mathrm{Mo}} + (1 - c) f_{\mathrm{Cr}}]^{-2},$$

2θ is the scattering angle, c is the atom fraction Mo in the sample, $d_{hkl}(c)$ is the (hkl) interplanar spacing which is a function of c, $d'(c) = d(d_{hkl})/dc$, v is the volume of the unit cell, A is the absorption factor, the f's represent the atomic scattering factors for Cr and Mo corrected for anomalous dispersion and k is a constant. The lattice parameters for the Mo–Cr system, was taken from the work of Goldschmidt and Brand[11] which gives a linear variation between 3·145 Å for Mo to 2·880 Å for Cr from which $d'(c)$ was computed. In order to obtain the concentration–penetration profile, Rudman[2] defines a parameter x, equivalent to the penetration parameter used in conventional diffusion studies, in terms of $N(c)$

$$x = \left[\int_0^c N(c)\,\mathrm{d}c \Big/ \int_0^1 N(c)\,\mathrm{d}c\right]. \qquad (2)$$

Using equations (1) and (2), the measured (200) Mo–Cr diffraction profile after each diffusion anneal was reduced to a c–x profile. The results for the 1200°C diffusion runs are shown in Fig. 1. Similar curves were obtained for the 1050°C anneals. The concentration penetration curves (Fig. 1) have the expected shapes except near the regions $x \rightarrow 0, 1$ where there is a tendency for the curves to round off. Straight line extrapolations shown by the dashed lines in Fig. 1, however, appear more reasonable as it is unlikely to have a few isolated regions of pure metals in the sample nor instantaneous contamination of all metals at the earliest possible annealing time, as the rounding-off of the c–x curves would seem to indicate. Similar behavior has also been reported for the Cu–Ni system by Fisher and Rudman[3] who considered it as an artifact arising from the approximate nature of the instrumental broadening correction. It is possible to derive from these curves the time variation of the degree of interdiffusion which is defined by the ratio (m_t/m_∞), where m_t is the net mass transfer across the interface between the components at time t and m_∞ is the same quantity at infinite time[2, 3]. m_t is given by an integration over the c–x profile:

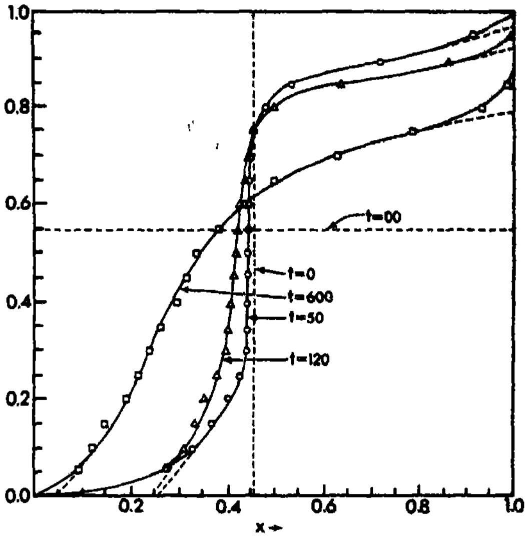

Fig. 1. Fraction Mo (c) as a function of the penetration parameter (x) for Mo–Cr powder samples interdiffused at 1200°C for the indicted times (t) in minutes.

$$m_t = \int_0^{c(x'=0)} x'\,\mathrm{d}c \qquad (3)$$

where $x' = 0$ defines the original interface between the components. The variation of (m_t/m_∞) with time is shown in Fig. 2 for the two interdiffusion temperatures used in this study. Assuming an Arrhenius type temperature dependence for m_t, an average activation energy Q for interdiffusion in the Mo–Cr system may be derived from this data; the result is listed in Table 1.

In addition to Q, it is also possible to derive information about the average D and hence D_0 from the c–x profiles (Fig. 1) by postulating a specific model for diffusion. From the works on the Cu–Ni system it appears that the concentric sphere model[3, 4] is perhaps the most appropriate one for describing interdiffusion in powder compacts. The validity of this model in the present work was determined by metallographic examina-

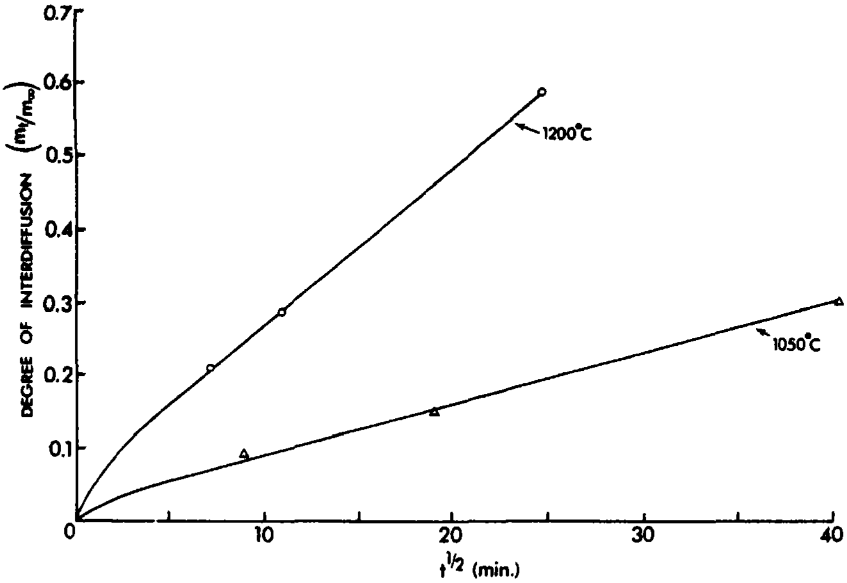

Fig. 2. Degree of interdiffusion as a function of (time)½ during annealing of Mo–Cr powder compacts at 1050 and 1200°C, respectively.

tions which revealed, quite early in the process, roughly spherical Cr rich regions in the sample surrounded by Mo rich material; this pattern continued until the entire Cr-rich core had been consumed. (A micrograph of the sample after 75 min at 1050°C is shown in Fig. 3.)

Adopting this model and with appropriate boundary conditions[3], the diffusion equation may be solved for $c(x)$ for different values of D and t. By comparing these curves with the experimental $c(x)$ curves a value of D is found which gives the best fit between the two sets for a given temperature. The results obtained in this manner are listed in Table 1 along with the D_0 and Q values for several other b.c.c. systems taken from the literature [12]. It is seen that the Q value for the Mo–Cr system follows the same, generally higher trend found for other b.c.c. systems while the D_0 values do not seem to show much correlation; the X-ray values and that of Gruzin *et al.*[7], however, are in good agreement. The X-ray analysis yields only the average diffusion parameters, corresponding to diffusion in a concentrated solution. It is possible, however, to draw some qualitative conclusions regarding the relative diffusivities of the two components. For example, the c–x profiles (Fig. 1) show that after 50 min at 1200°C no pure Mo is left in the sample while considerable Cr remains. This faster contamination of Mo by Cr may be indicative of a higher intrinsic diffusivity for Cr compared to Mo, a result which is expected to hold especially in concentrated solutions. Second, we note that despite the high interdiffusion temperatures used and the high Q value found in the present work indicating the dominance of volume diffusion, it is unlikely that some surface diffusion is not involved in the sintering of the powder compacts. In fact, the quick encircling of one metal by the other mentioned above does indicate the importance of surface diffusion during the early stages of annealing. However, the overall rate controlling process in achieving homogenization is volume diffusion and this is what the composition profiles and the D_0 and Q values derived from the diffraction data represent.

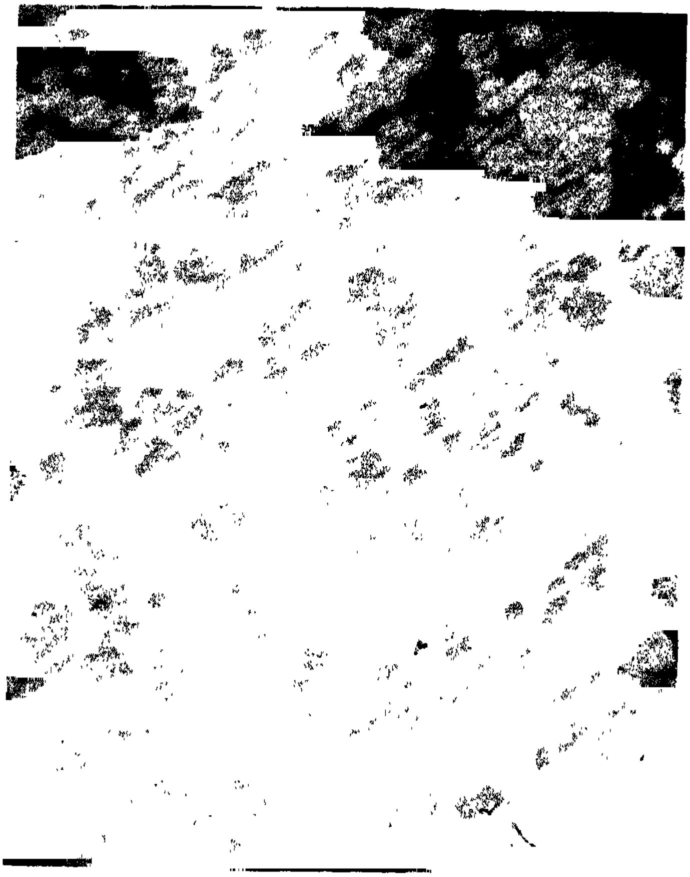

Fig. 3. Photomicrograph of Mo–Cr powder compact after interdiffusion at 1050°C for 75 min. Cr rich and Mo rich regions are in light and dark contrasts respectively. Mag. approx. 170*x*.

School of Engineering Science,
Florida State University,
Tallahassee,
Florida

P. H. HOLLOWAY*
G. P. MOHANTY

REFERENCES

1. DUWEZ P. and JORDAN C. B., *Trans. Am. Soc. Metals* **41**, 194 (1949).
2. RUDMAN P. S., *Acta crystallogr.* **13**, 905 (1960).
3. FISHER B. and RUDMAN P. S., *J. appl. Phys.* **32**, 1604 (1961).
4. HECKEL R. W., *Trans. Am. Soc. Metals* **57**, 443 (1964).
5. PINES B. Ia. and SMUSHKOV I. V., *Soviet Phys. Tech. Phys.* **28**, 626 (1958).
6. TENNEY D. R., CARPENTER J. A. and HOUSKA C. R., *J. Appl. Phys.* **41**, 69 (1970).
7. GRUZIN P. L., ZEMSKII S. V. and RODINA I. B., *Met. I. Metalloved. Chistykh Metal., Sb. Nauchn. Rabot.* **4**, 243 (1963); Summary in Chem. Abst., **60**, 2602 g.
8. PROKOSHKIN D. A. and SIDUNOVA O. I., *Izv. vyssh. ucheb. Zaved.*, Mashinostr. **5**, 101 (1960).
9. ARZHANYI P. M. and VOLKOVA R. M., *Russ. J. inorg. Chem.* **3**, 354 (1963).
10. HANSON M., *Constitution of Binary Alloys*, p. 537, McGraw-Hill (1958).
11. GOLDSCHMIDT H. J. and BRAND J. A., *J. less-common Metals* **3**, 44 (1961).
12. HARTLEY C. S., STEEDLY J. E. and PARSONS L. D., *Diffusion in Body Centered Cubic Metals*, p. 51, *J. Am. Soc. Metals* (1965).

---

*Now at the Rensselear Polytechnic Institute, Troy, N.Y., U.S.A.

J. Phys. Chem. Solids, 1971, Vol. 32, p. 2661. Pergamon Press. Printed in Great Britain

ERRATA

J. S. REID and T. SMITH: Improved Debye–Waller factors for some alkali halides. *J. Phys. Chem. Solids* **31**, 2689 (1970).

THE AUTHORS regret that in the appendix to the above article a factor of 2 has been misplaced in equations (7a), (9a), (10a) and (3a). However there are no changes in any of the results given in the article since they were obtained using the correct equations. These should read

$$B_k = \frac{8\pi^2}{3}\cdot\frac{1}{N}\sum_{\mathbf{q}j}\left(\frac{E}{\omega^2}\right)_{\mathbf{q}j}\left|\frac{\boldsymbol{\epsilon}(k/\mathbf{q}j)}{m_k{}^{1/2}}\right|^2 \tag{3a}$$

$$\langle x^2(lk)\rangle = 3B_k/8\,\pi^2 \tag{7a}$$

$$g\bar{m}\bar{B} = \frac{8\pi^2}{3}\cdot\frac{1}{N}\sum_{\mathbf{q}j}\left(\frac{E}{\omega^2}\right)_{\mathbf{q}j} \tag{9a}$$

$$\bar{B} = \frac{2h^2}{\bar{m}}\cdot\frac{3T^2}{k(\Theta^w)^3}\left[\int_0^{x_m}\frac{x\,\mathrm{d}x}{e^x-1}+\frac{x_m{}^2}{4}\right] \tag{10a}$$

$$\bar{B} = \frac{3h^2}{2\bar{m}k\Theta^w} \tag{13a}$$

L. L. ISAACS and D. J. LAM: The magnetic susceptibilities of hexagonal Tc–Ru, Tc–Rh, and Ru–Rh alloys *J. Phys. Chem. Solids* **31**, 2581 (1970).

THE LAST sentence in column 1, p. 2582, should read:

> 'Hence, the total diamagnetic contribution $\chi_{\mathrm{dia.}}$ for technetium is estimated as -30×10^{-6} emu/mole.'

The first paragraph in column 2, p. 2582, should read:

> 'The orbital paramagnetism $\chi_{\mathrm{orb.}}$ of *d*-electrons is difficult to calculate, but for technetium an estimated value of 60×10^{-6} emu/mole was derived from Knight shift data[5]. When the estimated values for the diamagnetic susceptibility and orbital paramagnetism were combined with the measured value of 120×10^{-6} emu/mole for technetium, we obtained an enhanced spin-susceptibility, $\chi_p/1-\phi N(E_F)$, value of 90×10^{-6} emu/mole.'

J. Phys. Chem. Solids, 1971, Vol. 32, pp. 2663–2672. Pergamon Press. Printed in Great Britain

ROTATIONAL PHASE TRANSITIONS IN MOLECULAR SOLIDS

D. S. WEBSTER* and M. J. R. HOCH†
University of Natal, Pietermaritzburg, South Africa

(*Received* 18 *January* 1971; *in revised form* 22 *April* 1971)

Abstract—Phase diagrams to 6 kbar have been obtained for solid cyclopropane, cyclohexane, and ethane. A new solid phase has been found in ethane. The results are discussed in terms of the Pople–Karasz theory for rotational phase transitions and fusion of molecular solids. In an effort to bring the theory into closer agreement with experiment the theory has been modified by choosing a central (28, 7) form for the intermolecular potential instead of the (12, 6) form used by Pople and Karasz. While there is some improvement in the comparison of experimental and theoretical phase diagrams the other thermodynamic predictions of the modified theory are in conflict with observations. The modification to the Pople–Karasz theory recently proposed by Amzel and Becka is also discussed.

1. INTRODUCTION

It is well known that a large number of molecular crystals exhibit one or more solid-state phase transitions, distinct from the melting transition, at atmospheric pressure. Such transitions correspond to the loss of some, or all, long-range orientational order. As might be expected, the molecular shape appears to be of importance in determining whether orientational and positional order disappear simultaneously in a single melting transition or separately in two or more transitions.

Pople and Karasz[1, 2] have extended the well-known Lennard–Jones and Devonshire [3, 4] theory of fusion to include orientational order–disorder transitions by allowing the molecules to take up two orientations on a lattice site. Coupled orientational and positional energy terms are included in the partition function and a parameter ν is introduced as a measure of the ratio of energy barriers for orientational and positional disorder. It is found that there are critical values for ν which the theory gives as 0·325 and 0·66. Three types of behaviour are predicted.

(a) For $\nu < 0{\cdot}325$ a rotational solid-state transition occurs before melting at all pressures. Furthermore, for values of ν between 0·17 and 0·325, a transition of this type should change from first to second order at high pressures while for $\nu < 0{\cdot}17$ the transition should always be of second order.

(b) For $0{\cdot}325 < \nu < 0{\cdot}66$, the two transitions coincide at zero pressure but separate at higher pressures.

(c) For $\nu \geqslant 0{\cdot}66$ a combined transition is predicted for all pressures.

Karasz and Pople[2] have compared the theoretical predictions with available experimental data for a number of substances which exhibit behaviour of types (a) and (c). Apart from the prediction concerning the change of order of transitions, the agreement is encouraging.

Clearly it would be of interest to seek materials which give behaviour of type (b). It is not possible to assign ν values to particular molecular systems on the basis of structural parameters alone. Most of the small diatomic (e.g. N_2, HCl), triatomic (e.g. H_2S) and tetrahedral polyatomic systems (e.g. CH_4) exhibit solid-state rotational transitions at zero pressure. According to the Pople–Karasz theory these have low ν values (less than 0·325) presumably corresponding in these cases to low barriers to reorientation because of the roughly spherical repulsion envelopes. We have determined the phase diagrams for ethane and cyclopropane which are fairly small hydrocarbon molecules with non-spherical repulsion envelopes. We have also made measurements for cyclohexane. Ethane was specifically suggested by Karasz and Pople [2] as a system which might exhibit behaviour of the type (b) given above, corresponding to a ν value in the range 0·325–0·66.

---

*Now at Research Department, African Explosives and Chemical Industries, P.O. Northrand, Transvaal, South Africa.

†Now at Department of Physics, University of the Witwatersrand, Jan Smuts Avenue, Johannesburg, South Africa.

Recently Amzel and Becka [5] have proposed a modification of the Pople–Karasz theory. They postulate that for each molecule on a lattice site there are not two but D possible orientations. The parameter D is chosen by considering the symmetry of molecule and lattice. The modified theory gives predictions which are physically more realistic than those of the unmodified theory in that for $D > 2$ all transitions are predicted to be of first order. Amzel and Becka show that by a suitable choice of ν, D, and the molecular force constants, it is possible to obtain good agreement with experimental data for a number of substances.

In Section 3 we propose a different modification to the Pople–Karasz theory involving a change in the intermolecular potential. Section 4 compares the experimental data with the different versions of the theory.

2. EXPERIMENTAL

The high pressure apparatus

A conventional high pressure apparatus of the piston-cylinder type involving a Bridgman unsupported-area seal was used. It is similar to that described by Stewart [6] for work on solidified gases. The maximum pressure for the present experiments was 6 kbar. Temperatures in the range 77–270°K were obtained using a reservoir type cryostat [7] in which liquid nitrogen was vapourised at a controlled rate in a copper spiral wound around the sample cylinder. Temperature measurements were made with a copper–constantan thermocouple. The stability and measurement accuracy was better than 1°K.

Sample pressures were obtained from the calculated multiplier ratio, and the hydraulic system pressure as measured on a Bourdon standard test gauge. The piston displacement was monitored using a sensitive Mercer dial gauge and phase transitions were detected as discontinuities in the P–V curve. The pressure calibration of the apparatus was checked by making measurements on the solid-state transition in RbI. The phase diagram obtained agreed to within 2 per cent with that of Pistorius [8].

Sample preparation

The ethane and cyclopropane samples were drawn from cylinders supplied by the Matheson Corporation and African Oxygen, respectively. Both were stated to be better than 99 per cent pure as supplied and were further purified by fractional distillation–condensation processes. The cyclohexane was BDH spectroscopic quality, and had a stated purity of better than 99 per cent (estimated to be of the order of 99·9 per cent) and was used without further purification. The gaseous samples were introduced into the high pressure cylinder through a small hole near the top (which led via a length of cupronickel tubing to a gas handling system) using essentially the technique described by Stewart [6]. The cyclohexane, being a liquid, was simply pipetted into the cylinder.

Measurements

The phase diagrams for the three substances investigated are depicted in Figs. 1, 2 and 3. Great difficulty was experienced in containing the ethane sample in the liquid phase. Even the use of an indium gasket and brass anti-extrusion rings [7] in the Bridgman unsupported area seal was not completely successful, and leakage generally occurred within 10 or so pressure cycles. Cyclopropane showed no signs of extrusion when teflon was used as the gasket material in the Bridgman seal, but

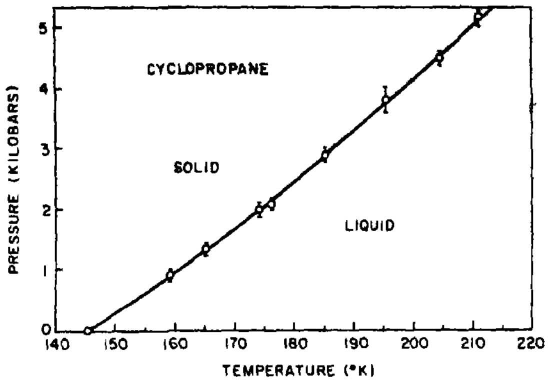

Fig. 1. Phase diagram for cyclohexane.

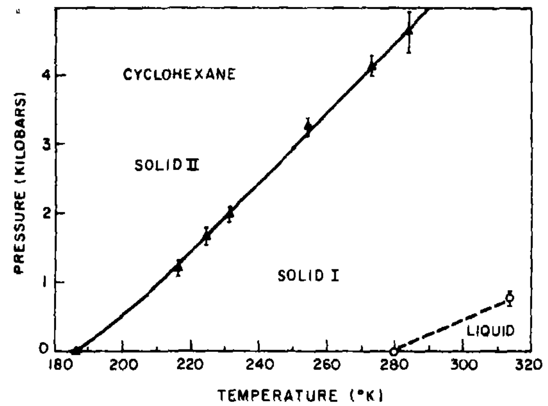

Fig. 2. Phase diagram for cyclopropane.

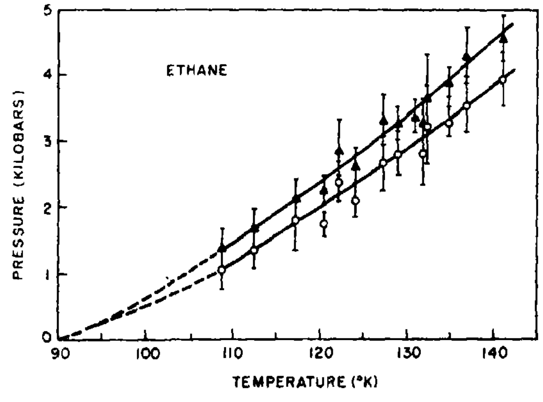

Fig. 3. Phase diagram for ethane.

this was found quite ineffective for ethane. Frictional effects were much more pronounced for ethane measurements than for the others.

The most realistic correction for friction is taken to be the average separation between the curves for increasing and decreasing pressure, at constant displacement, away from the transition (Bridgman[9], Stewart[6]). This value is assumed to apply over the transition discontinuity. Uncertainty bars shown were obtained from the hysteresis loop at the midpoint of the volume discontinuity after correction for frictional effects.

Only one point on the melting curve of cyclohexane was taken, and the curve drawn is that obtained by Deffet[10] as quoted by Babb[11]. No sign of any triple point was found with cyclopropane over the pressure range studied. Ethane, however, definitely has a solid-state transition at high pressure which must originate from a triple point on the melting curve. Unfortunately, the experimental difficulties of containing the sample at the lowest pressures and temperatures did not permit any successful experimental results at pressures low enough to establish the exact position of the triple point.

3. THEORY

Thermodynamic predictions of the Pople–Karasz theory using a (28,7) potential

The Pople–Karasz theory[1], as well as the Amzel–Becka modification[5], employs the (12, 6) intermolecular potential. Hamman and Lambert[12] have made the empirical observation that a (28, 7) potential fits the data for globular hydrocarbon molecules better than a (12, 6) potential. This is supported by Prigogine[13] who has considered various models of globular molecules and has shown that the assumption of a (12, 6) interaction between the outermost atoms gives a total central effect which is strongly modified from a (12, 6) form. The (28, 7) potential may be regarded as a better approximation. For the above reasons, and in an effort to improve the agreement between experimental and theoretical phase diagrams, we have modified the Pople–Karasz theory by introducing the (28, 7) potential instead of the (12, 6) potential.

The statistical model and the solution of the cooperative order–disorder problem have been treated in detail by Pople and Karasz[1]. We follow their notation.

The theory postulates two interpenetrating lattices, α and β, each of N sites with the molecules distributed among the $2N$ available sites. The total partition function Z is written as $Z = f^N\Omega$ where f^N is associated with the vibration of each molecule on a lattice site and Ω takes account of lattice disordering. The expression for Ω is

$$\Omega = \sum \exp\left[-\left(N_{\alpha\beta}W + N_{\alpha_1\alpha_2}W' + N_{\beta_1\beta_2}W'\right)/kT\right] \quad (1)$$

where the sum is over all orientations and arrangements of particles on the α and β lattice sites and W and W' are respectively the interaction energies for $\alpha\beta$ nearest neighbours and $\alpha_1\alpha_2$ (or $\beta_1\beta_2$) nearest neighbours. $N_{\alpha\beta}$ is the number of neighbours on α and β sites in any given configuration while $N_{\alpha_1\alpha_2}$ and $N_{\beta_1\beta_2}$ are, respectively, the number of α-site neighbours and β-site neighbours with unlike orientations. Using the Bragg–Williams approximation, Pople and Karasz obtained an expression for Ω in terms of two order parameters, Q, the fraction of molecules on α-sites, and S, the fraction in 1-orientations.

The Helmholtz free energy A and the pressure P are conveniently split into two parts

$$\begin{aligned} A &= A' + A'' \\ &= -NkT \log f - kT \log \Omega. \end{aligned} \quad (2)$$

$$\begin{aligned} P &= P' + P'' \\ &= -\left(\frac{\partial A'}{\partial V}\right)_T - \left(\frac{\partial A''}{\partial V}\right)_T. \end{aligned} \quad (3)$$

Evaluation of P' may be carried out using free volume theory. Pople and Karasz[1] and Amzel and Becka[5] used the thermodynamic functions tabulated by Wentorf *et al.*[14] on the basis of spherically smoothed three-shell calculations. This involves the (12, 6) intermolecular potential.

Some tables for the (28, 7) potential have been given by Hamman and Lambert[12] for values of V/V_0 appropriate for the gaseous phase. These have been extended by us to cover a wider range of values*. Our method was checked by regenerating the figures quoted by Hamman and Lambert.

In order to calculate P'' it is necessary to specify the volume dependence of W and W'. Assuming that the repulsive forces dominate in determining the volume dependence we take W/W' independent of volume and

$$W = W_0\left(\frac{V_0}{V}\right)^{28/3} \quad (4)$$

where W_0 is a constant proportional to ϵ_0.

The pressure P'' is found to be given by

$$\frac{P''V_0}{NkT} = \frac{28}{3}\frac{V_0}{V}\frac{ZW}{kT}\{Q(1-Q) + \nu S(1-S)\} \quad (5)$$

which differs only by a factor $\frac{7}{3}$ from the (12, 6) expression obtained by Pople and Karasz. The values of Q and S which maximise the partition function are readily obtained from expressions given by Pople and Karasz involving $\nu = Z'W'/ZW$ and ZW/kT. The factors Z and Z' are, respectively, the number of β sites which are nearest neighbours to an α site and the number of α sites which are nearest neighbours to an α site. In order to facilitate comparison with the Pople–Karasz and Amzel–Becka theories we have chosen $W_0/\epsilon_0 = 0{\cdot}977$.

A total isotherm is obtained by adding the two components P' and P''. Isotherms calculated in this way using both the (12, 6) and

---

*Tables of values of the compressibility factor $P'V/NkT$ as a function of the reduced temperature kT/ϵ_0 and reduced volume V/V_0 are available and will be supplied on request.

(28, 7) intermolecular potentials are compared in Fig. 4. The kinks correspond to the transitions at which orientational and positional order disappear. The equilibrium transition pressures may be obtained by applying the equal area principle to the sigmoid portion of an isotherm. A computer programme was drawn up to do this and to generate phase diagrams for given ν values. A series of phase diagrams are shown in Fig. 5 for both (28, 7)

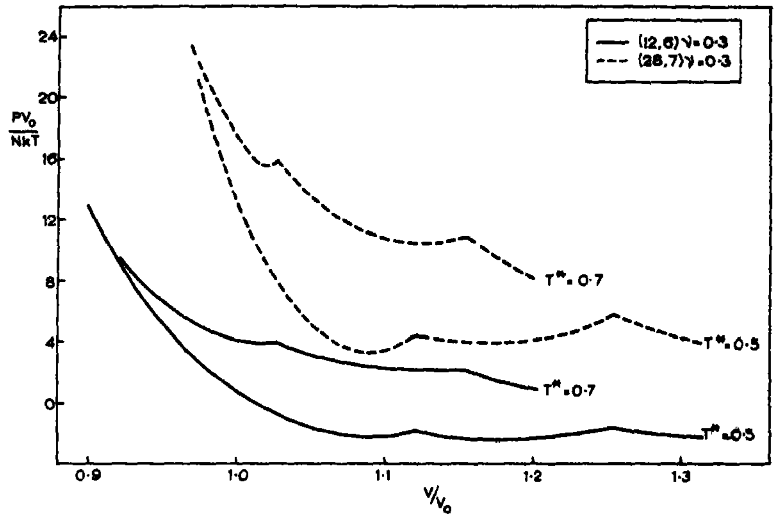

Fig. 4. Theoretical isotherm for (12, 6) and (28, 7) intermolecular potentials ($\nu = 0{\cdot}3$).

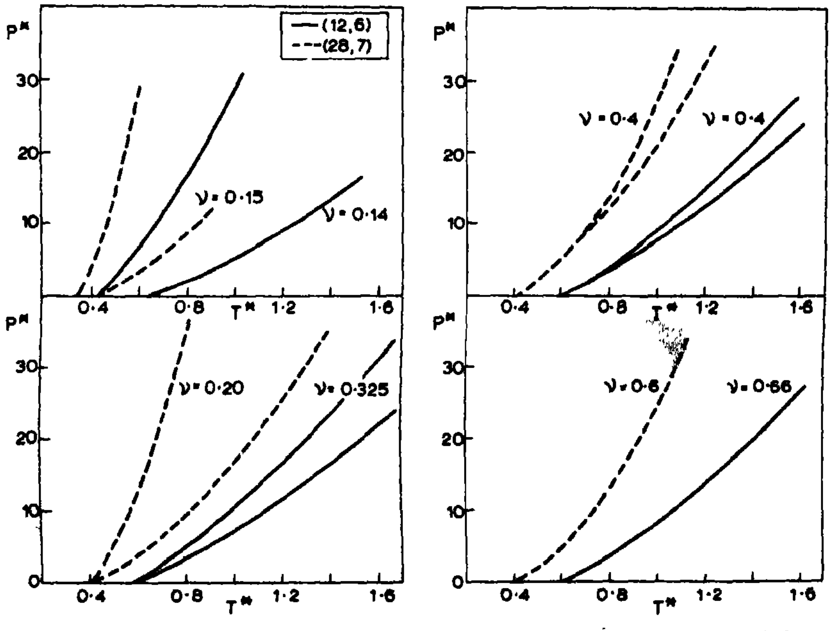

Fig. 5. Theoretical phase diagrams for (12, 6) and (28, 7) intermolecular potentials for various values of ν.

and (12, 6) potentials. The latter agree well with those given by Pople and Karasz for ν values which coincide.

For the (28, 7) model a critical value at $\nu = 0{\cdot}20$ is found below which the two transitions are distinct at zero pressure and above which they coincide at zero pressure but separate at higher pressures giving a triple point on the melting curve. For $\nu > 0{\cdot}6$ the theory predicts a combined transition for all pressures. For $\nu > 1{\cdot}0$ the transitions separate again, as is found in the (12, 6) case, with positional order disappearing before orientational order.

The zero pressure transition temperatures and the volume changes across the transitions are compared in Figs. 6 and 7 for the (28, 7) and (12, 6) cases. The (12, 6) model leads to the prediction that solid-state transitions should be of second order for $\nu < 0{\cdot}17$ while for $0{\cdot}17 < \nu \leq 0{\cdot}325$ they should become second order at elevated pressures. For the (28, 7) model all the solid-state transitions, corresponding to $\nu < 0{\cdot}2$, are predicted to be of second order even at zero pressure. However, when $0{\cdot}2 < \nu < 0{\cdot}6$, first order transitions, which separate at a triple point, are predicted.

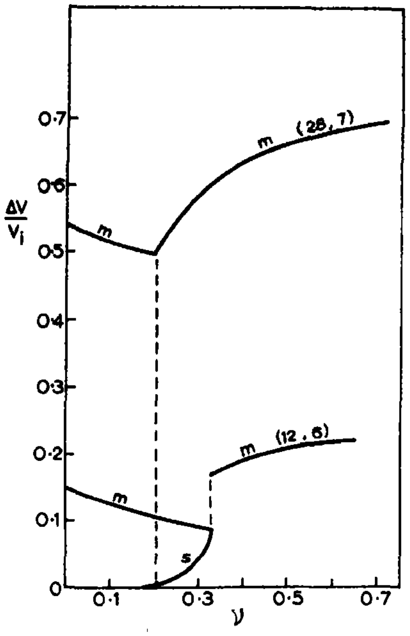

Fig. 7. Volume changes for melting (m) and solid (s) transitions, for (12, 6) and (28, 7) intermolecular potentials, as a function of ν.

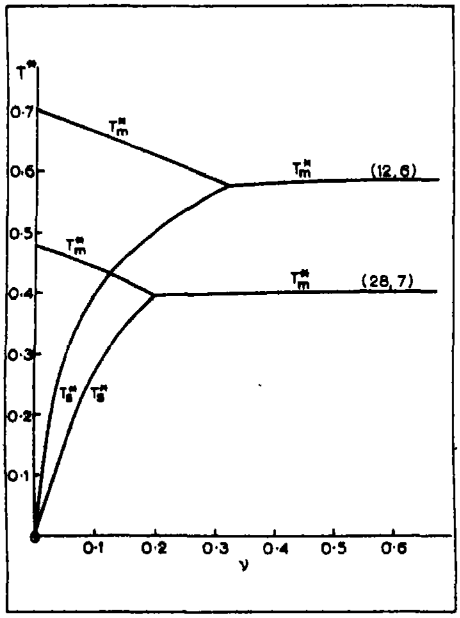

Fig. 6. Melting (m) and solid (s) transition temperatures, at zero pressure, for (12, 6) and (28, 7) intermolecular potentials, as a function of ν.

An important difference between the modification to the Pople–Karasz theory given here and that proposed by Amzel and Becka[5] is that changing the form of the central intermolecular potential alters primarily the P' contribution to P whereas introducing the parameter D alters the configurational terms and hence P''. In this connection it should be mentioned that the use of the Bragg–Williams approximation in calculating A'', and hence the thermodynamic functions derived from it, involves introducing certain errors. In comparing the trends predicted by the Pople–Karasz and Amzel–Becka theories it would be of interest to know how such trends are affected by the use of the Bragg–Williams approximation. In determining this the quasi-chemical approximation would probably be useful.

4. DISCUSSION

Cyclopropane and cyclohexane

Cyclopropane and cyclohexane belong to the family of cyclic hydrocarbons $(CH_2)_n$, $n = 3, 4, 5, 6$. These are fairly symmetrical molecules which will be spherical upon rotation, and fall into Timmermans[15] classification as 'globular' molecules. Solid-state transitions are known to occur in all except cyclopropane. The temperature range of the plastic crystal phase (solid I) increases going up the series C_4H_8 to C_6H_{12}.

The n.m.r. work for these substances has been reviewed by Hoch and Rushworth[16]. Effectively isotropic reorientation accompanied by some self-diffusion occurs in the plastic crystal phase for C_4H_8, C_5H_{10} and C_6H_{12}. In cyclopropane the molecules reorient about their 3-fold axes below the melting point. (Above 120°K the correlation time for this motion is less than 10^{-5} sec.) Reorientation about the molecular 3-fold axes also occurs in cyclohexane below the solid-state transition point.

Table 1 gives the transition entropies at atmospheric pressure for the substances studied. In cyclohexane, perhaps typical of substances forming plastic crystals, the solid-state transition is the major entropy transition. The slopes of the phase-equilibrium curves at zero pressure obtained from the phase diagrams (Figs. 1 and 2) and the corresponding volume changes calculated using the Clausius–Clapeyron equation are also tabulated. It is interesting to note that the total volume changes, expressed as a percentage of the effective size of the freely rotating molecule, are comparable for the different substances.

While it was thought that a triple point, accompanied by the appearance of a new plastic crystal phase, might occur on the melting curve of cyclopropane, this was not observed over the pressure range studied. According to the Pople–Karasz theory the ν value for cyclopropane exceeds 0·66. This may be interpreted to mean that the barrier to tumbling reorientation is high, compared to those for related substances, and/or the barrier to diffusion is comparatively low. It may be significant that cyclopropane is the only member of the $(CH_2)_n$ series which does not possess ring flexibility since this might inhibit cooperative effects involved in molecular reorientation. Dunning[17] has pointed out that, in the plastic crystal phase, the van der Waal's diameters of cyclobutane, cyclopentane, and cyclohexane are appreciably greater than the distances between molecular centres, as measured by X-ray diffraction methods.

The experimentally determined phase diagrams (in reduced coordinates) for cyclopropane and cyclohexane are compared in Fig. 8 with selected predictions of the Pople–Karasz theory using both the (12, 6) and (28, 7) potentials. The reducing constants are taken from Hirschfelder *et al.*[18] or calculated by their method from available viscosity data. The theoretically predicted phase diagrams used are chosen from the series as being most similar to the experimental figures. The solid-state transition intercepts at zero pressure are made to coincide. The agreement is not close but the (28, 7) model represents the slopes more closely in each case.

For cyclohexane the predicted entropy changes disagree with the experimentally

Table 1. Transition entropies and calculated volume changes at atmospheric pressure

Substance	Transition	Entropy (eu) (at atmos. pressure)	Initial slope dp/dT ((dynes/°K cm²) × 10^{-7})	ΔV (cm³/mole)	$\Delta V\%$
C_6H_{12}	S_I–S_{II}	8·6	4·62	0·85	0·73
	melting	2·2	1·85	0·32	0·27
C_3H_6	melting	8·9	7·34	0·51	0·81
C_2H_6	melting	7·6	6·19	0·51	0·92

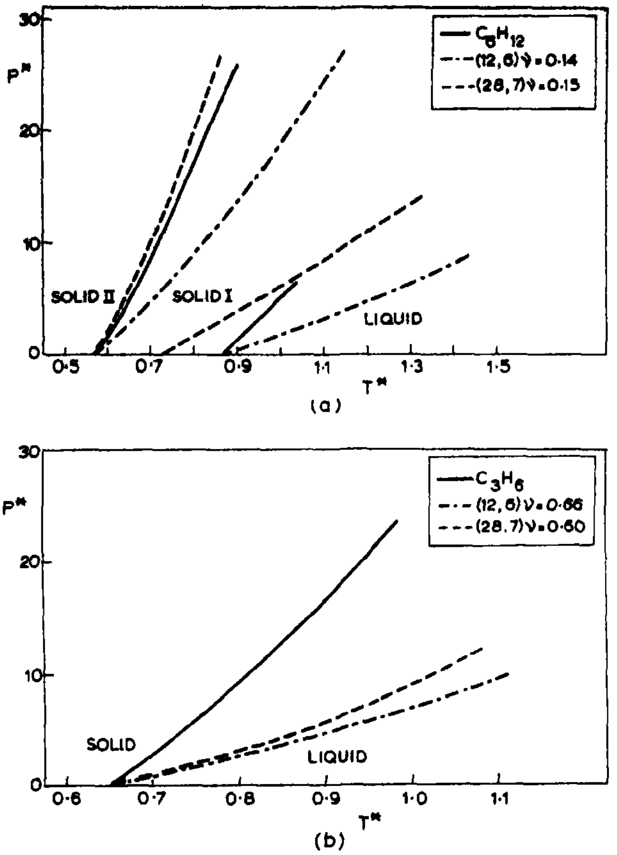

Fig. 8. Comparison of experimental and theoretical phase diagrams for (a) cyclohexane and (b) cyclopropane.

measured values quoted in Table 1. Our approximately determined relative volume changes give no indication of a trend towards second order of the solid-state transition with increasing pressure.

A comparison of the experimental phase diagrams for cyclohexane with selected predictions of the Amzel–Becka theory has been made but the agreement is not close. The assignment of a value for D is somewhat arbitrary. From the transition and melting entropy vs. T_t/T_m plots of Amzel and Becka [5] a value greater than 20 may be inferred and this was used in making the comparison.

It appears that the behaviour of C_6H_{12} is not particularly well described by any of the versions of the Pople–Karasz theory. Since no solid-state transition has been observed in C_3H_6, over the pressure range studied, it is not possible to infer very much concerning the applicability of the theory to this substance. As stated above the implication is that the parameter ν exceeds a critical value ($\nu > 0{\cdot}66$ for $D = 2$).

Ethane

The triple point on the melting curve of ethane (Fig. 3) appears to be the first experimental confirmation of the prediction of this type of behaviour by Pople and Karasz [1, 2]. From our data it is not possible to calculate the separate entropy changes for the transitions. However, the volume changes for the melting and solid-state transitions are roughly in the ratio 0·4 : 1 showing that for this substance the solid-state transition has the major entropy change. It is likely that phase I is a plastic crystal phase. Further measurements such as heat capacity and NMR measurements are needed to confirm this.

It is well known that certain members of the long chain hydrocarbon series exhibit rotational transitions in which molecular motion about the long axis sets in. This has also been found for *n*-butane (Hoch[19]). However, in *n*-butane the melting transition is accompanied by an entropy change twice as large as that of the solid-state transition. (It is, of course, necessary to have at least three carbon atoms in a chain in order that different orientations about the long axis may be distinguished.) It is safe to conclude that the behaviour found in ethane is of a different character to that found in the higher homologues.

The experimental results for ethane in reduced form are compared in Fig. 9 with selected predictions of the Pople–Karasz theory using both (12, 6) and (28, 7) potentials. The zero pressure intercepts are again chosen to coincide. The (28, 7) curves are in slightly closer agreement with experiment than are the (12, 6) curves.

A comparison of the data with a theoretical phase diagram given by Amzel and Becka[5] has been carried out. Since the transition entropies are not known it is not possible to assign a *D* value on this basis. Molecular symmetry suggests a value of 12 or lower and we have used the theoretical curve for $D = 12$ given by Amzel and Becka. The agreement between theory and experiment is not close and is only of qualitative significance.

We conclude that in ethane the molecules are sufficiently asymmetric to prevent reorientational disordering in the solid phase at zero pressure. However this type of disordering becomes possible at higher pressures. According to the Pople–Karasz theory and its modifications the effective ν value lies within a critical range. It is possible that

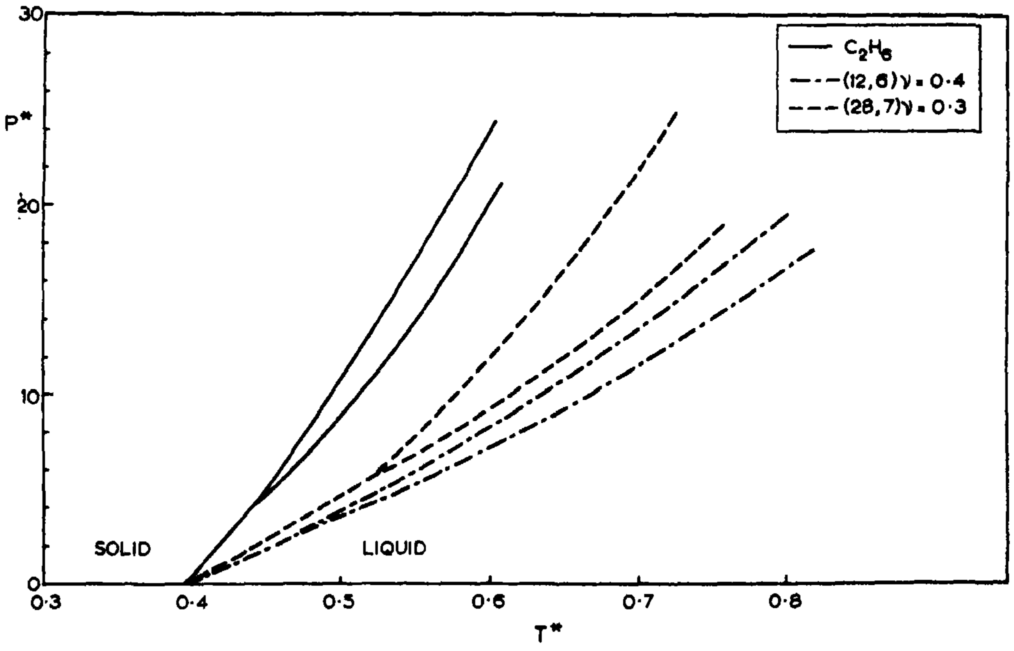

Fig. 9. Comparison of experimental and theoretical phase diagrams for ethane.

similar behaviour might be found in ethylene and other systems with molecules of similar shape.

5. CONCLUSION

The appearance of a new solid phase in ethane at elevated pressures appears to confirm the prediction of this type of behaviour by Pople and Karasz[1, 2]. The other experimental work on cyclohexane and cyclopropane yields results which are much less decisive in judging the Pople–Karasz theory.

The introduction of a (28, 7) intermolecular potential instead of the (12, 6) potential into the theory leads to some improvement in the correlation of experimental and theoretical phase diagrams but proves unsatisfactory in the prediction of other thermodynamic properties. The modification to the theory proposed by Amzel and Becka[5] appears to be able to describe a wide variety of situations reasonably well but does so at the expense of introducing an additional parameter. Further modifications, such as incorporating the (28, 7) potential into the Amzel–Becka theory are possibly worth carrying out, but the basic model does contain some rather artificial features.

Acknowledgements—We should like to acknowledge helpful comments and advice from Dr. D. C. Douglass and Dr. C. W. F. T. Pistorius. Financial support was provided by African Explosives and Chemical Industries Ltd., and the University of Natal Research Fund.

REFERENCES

1. POPLE J. A. and KARASZ F. E., *J. Phys. Chem. Solids* **18**, 28 (1961).
2. KARASZ F. E. and POPLE J. A., *J. Phys. Chem. Solids* **20** 294 (1961).
3. LENNARD-JONES J. E. and DEVONSHIRE A. F., *Proc. R. Soc.* **A169**, 317 (1939).
4. LENNARD-JONES J. E. and DEVONSHIRE A. F., *Proc. R. Soc.* **A170**, 464 (1940).
5. AMZEL L. M. and BECKA L. N., *J. Phys. Chem. Solids* **30**, 521 (1969).
6. STEWART J. A., *J. Phys. Chem. Solids* **1**, 146 (1956)
7. SWENSON C. A. and STAHL R. H., *Rev. scient. Instrum.* **25**, 608 (1954).
8. PISTORIUS C. W. F. T., *J. Phys. Chem. Solids* **25**, 1003 (1964).
9. BRIDGMAN P. W., *The Physics of High Pressure*. Bell, London (1952).
10. DEFFET L., *Bull. Belg. Chem. Soc.* **44**, 41 (1935).
11. BABB G. E., *Rev. mod. Phys.* **35**, 400 (1963).
12. HAMMAN S. D. and LAMBERT J. A., *Aust. J. Chem.* **7**, 18 (1953).
13. PRIGOGINE I., *Molecular Theory of Solutions*. North-Holland, Amsterdam (1957).
14. WENTORF R. H., BUEHLER R. J., HIRSCHFELDER J. O. and CURTISS C. F., *J. chem. Phys.* **18**, 1484 (1950).
15. TIMMERMANS J., *J. Phys. Chem. Solids* **18**, 1 (1961).
16. HOCH M. J. R. and RUSHWORTH F. A., in *Nuclear Magnetic Resonance in Chemistry* (Edited By B. Pesce), Academic Press, New York (1965).
17. DUNNING W. J., *J. Phys. Chem. Solids* **18**, 21 (1961).
18. HIRSCHFELDER J. O., CURTISS C. F. and BIRD R. B., *Molecular Theory of Gases and Liquids*, John Wiley, New York (1954).
19. HOCH M. J. R., to be published.

J. Phys. Chem. Solids, 1971, Vol. 32, pp. 2673–2684. Pergamon Press. Printed in Great Britain

THE SIMULTANEOUS DIFFUSION OF Pb^{2+} AND Cd^{2+} IN PURIFIED NaCL SINGLE CRYSTALS*

J. L. KRAUSE† and **W. J. FREDERICKS**
Department of Chemistry, Oregon State University, Corvallis, Oregon 97331, U.S.A.

(*Received* 19 *February* 1971; *in revised form* 22 *April* 1971)

Abstract—In this paper a technique for studying the simultaneous diffusion of two divalent ions in an alkali halide is described. The technique has several advantages over the usual single ion method. Equations are developed which show the effect of common ion interaction on the diffusion profile. The technique is applied to the diffusion of Pb^{2+} and Cd^{2+} in purified NaCl single crystals. The effect of effusion during quenching is examined and found not to distort the low concentration region of the penetration curve deeper in the crystal. The values of D_0, the migration energy U_0, the enthalpy $\Delta h'$ and entropy of association $\Delta S'$ measured in these experiments are given by

$$D_{g(\mathrm{Pb})} = 1{\cdot}40\times 10^{-2}\exp(-0{\cdot}982\,\mathrm{eV}/kT)\ \mathrm{cm^2/sec},$$
$$D_{g(\mathrm{Cd})} = 3{\cdot}57\times 10^{-3}\exp(-0{\cdot}857\,\mathrm{eV}/kT)\ \mathrm{cm^2/sec},$$
$$\Delta g'_{(\mathrm{Pb})} = -0{\cdot}775\,\mathrm{eV} + (5{\cdot}29\times 10^{-4}\,\mathrm{eV}/^{\circ}K)T,$$

and

$$\Delta g'_{(\mathrm{Cd})} = -0{\cdot}972\,\mathrm{eV} + (6{\cdot}65\times 10^{-4}\,\mathrm{eV}/^{\circ}K)T,$$

The primed quantities $\Delta g'$ and $\Delta s'$ have the configurational contribution to the entropy removed.

1. INTRODUCTION

THE ASSOCIATION between a substitutional divalent impurity cation and the vacancy it introduces in a univalent host crystal as proposed by Stasiw and Teltow[1] has been successful in explaining many of the transport properties of ionic solids. Lidiard[2] and Howard and Lidiard[3] have developed a detailed theory of the effect of association on the diffusion of divalent impurity ions in univalent crystals. Recent reviews[4, 5] of experimental work in this area are in general agreement with this model, but frequently the experimentally derived parameters for the same systems differ by more than experimental error.

These differences could arise from unsuspected interaction between anionic and cationic impurities in the host crystal. The reaction between anionic and cationic impurities is well known[6, 7]. However the effect of other divalent cations on the diffusant has only been discussed for the special case of a uniform concentration of the same impurity species as the diffusing species[3]. This is an idealised experimental situation. A more realistic case is that in which a low concentration of a species different from the diffusant is present. Its concentration distribution will be time dependent because it is effusing as the tracer diffuses. The two divalent impurity species interact through the common ion effect of their vacancies.

An experimental situation that can be obtained with sufficient control of boundary conditions is the diffusion of two different divalent species simultaneously into highly purified NaCl single crystals. This technique is unique in that over most of the diffusion profile aside from those vacancies introduced by the divalent diffusant itself, the major source of vacancies affecting the diffusant is the other diffusant. Since the concentration of diffusants can be measured, the total vacancy concentration in the environment of the individual diffusant is more accurately known than in single ion diffusion experiments.

---

*Research supported by the National Science Foundation under grant GP-6893 and based on a portion of a thesis submitted in partial fulfillment of the requirements for the degree Doctor of Philosophy.

†Present Address: Chemistry Department, Cornell University, Ithaca, N.Y. 14850, U.S.A.

The effect of these additional vacancies can be calculated through the common ion equilibrium of the two impurities. The conditions required for fitting the two profiles are more stringent than for single ions because the interaction of one diffusant with the other must be taken into account. This situation should provide more accurate estimates of diffusion and association parameters of both diffusants. If single ion and simultaneous ion diffusion experiments for the same divalent diffusant give the same values of enthalpy and entropy of association, it can be concluded that other impurities that interact with the diffusant are below concentrations that distort the diffusion profile. The simultaneous diffusion technique has the added advantage that data can be obtained for two diffusants with the same number of anneals, sectioning and weighing as required for a single diffusant.

This paper reports the results of a study of the simultaneous diffusion of Pb^{2+} and Cd^{2+} in purified sodium chloride single crystals. Some improvements in experimental detail are reported and the effect of too-slow quenching on observed diffusion profiles is discussed.

2. THEORY

If diffusion of a divalent cationic impurity occurs by a vacancy mechanism, then one of the 12 nearest neighbor cation sites of the NaCl lattice must be vacant just prior to the diffusion jump of the impurity. This configuration is the ground state of the Stasiw–Teltow complex. Lidiard[2] has shown that the complex can be treated as the diffusing species. Fick's first law can then be written as

$$J = -D_s\,\partial(Npc)/\partial x \qquad (1)$$

where J is the flux of complexes in the x direction, D_s is the diffusion coefficient, $\partial(Npc)/\partial x$ is gradient of the complex-concentration, N is the number of divalent cations per cm^3, p is the degree of association, and c is the mole fraction of the aliovalent impurity. On rearrangement equation (1) may be written as

$$J = -D_s[\partial(pc)/\partial c]\partial(Nc)/\partial x. \qquad (2)$$

From equation (2) the concentration dependent diffusion coefficient of the species is

$$D(c) = D_s\partial(pc)/\partial c. \qquad (3)$$

When all impurities are associated with a vacancy (i.e. $p = 1$), $D(c)$ equals D_s. For this reason D_s is called the saturation diffusion coefficient.

Equation (3) shows that the concentration dependence of the diffusion coefficient is a function of the degree of association p. The only extension of present theory required is to include the interaction of Cd^{2+} with p for Pb^{2+} and vice versa, then to solve Fick's law for simultaneous diffusion of cadmium and lead complexes.

The reactions necessary to form the two different complexes in the crystal are

$$Pb^{+} + V_c^{-} \rightleftharpoons PbV_c \qquad (4)$$

and

$$Cd^{+} + V_c^{-} \rightleftharpoons CdV_c. \qquad (5)$$

The charges have been assigned with respect to the lattice and V_c^- represents a cation vacancy. If c is the mole fraction of the species designated by the subscript, the mass action expressions for these reactions may be written as

$$c_{PbV_c}/(c_{Pb^+})(c_{V_c^-}) = 12\exp(-\Delta g'_{Pb}/kT) = K_{Pb}(T) \qquad (6)$$

and

$$c_{CdV_c}/(c_{Cd^+})(c_{V_c^-}) = 12\exp(-\Delta g'_{Cd}/kT) = K_{Cd}(T). \qquad (7)$$

The factor 12 is the configurational entropy and $\Delta g_i'$ is the Gibb's free energy of association from which the configurational entropy has been removed. In addition to the cation vacancies introduced by the divalent cation impurities the crystal will have an additional number of vacancies when in thermal equilibrium. In a pure crystal at equilibrium their concentration is given by the Schottky product

$$(c_{V_c^-})(c_{V_a^+}) = [B \exp(-h_s/kT)] = [K_s(T)] \tag{8}$$

where V_a^+ refers to anion vacancies, B is an entropy term and h_s is the enthalpy required to form a separated Schottky pair. To maintain electrical neutrality of the system the following defect balance is required

$$c_{V_c^-} = c_{\mathrm{Pb}} + c_{\mathrm{Cd}} - c_{\mathrm{Pb}V_c} - c_{\mathrm{Cd}V_c} + c_{V_a^+} \tag{9}$$

where the total concentrations of Pb^{2+} and Cd^{2+} are represented by c_{Pb} and c_{Cd} respectively.

If p_{Pb} and p_{Cd} are, respectively, the fraction of Pb^{2+} and Cd^{2+} associated with a vacancy, equations (6), (7) and (9) can be written:

$$c_{V_c^-} = p_{\mathrm{Pb}}/K_{\mathrm{Pb}}(1-p_{\mathrm{Pb}}) \tag{10}$$

$$c_{V_c^-} = p_{\mathrm{Cd}}/K_{\mathrm{Cd}}(1-p_{\mathrm{Cd}}) \tag{11}$$

$$c_{V_c^-} = (1-p_{\mathrm{Pb}})c_{\mathrm{Pb}} + (1-p_{\mathrm{Cd}})c_{\mathrm{Cd}} + c_{V_a^+}. \tag{12}$$

Equations (8), (10), (11) and (12) form a set that describe the effect of one cationic impurity on the association of the other and vice versa. In deriving these equations certain assumptions were required. For the mass action expressions to hold in the diffusion process a localized equilibrium must exist everywhere in the crystal. All interactions and aggregates except those specifically included are assumed negligible. At the temperatures and concentrations used in these studies, this is true. In applying the equations to a diffusion process we assume the diffusion proceeds by a vacancy mechanism and the diffusing species is the complex, not an isolated impurity ion. The mass of experimental evidence supports this assumption.

3. METHOD OF SOLUTION

The experimental results are treated quantitatively through the solution of Fick's second law of diffusion. Applied to two ions diffusing simultaneously Fick's second law gives two coupled equations when the diffusing species is the complex. These are

$$\partial(p_{\mathrm{Pb}}c_{\mathrm{Pb}})/\partial t = \partial\{D_{s(\mathrm{Pb})}\partial(p_{\mathrm{Pb}}c_{\mathrm{Pb}})/\partial x\}/\partial x \tag{13}$$

and

$$\partial(p_{\mathrm{Cd}}c_{\mathrm{Cd}})/\partial t = \partial\{D_{s(\mathrm{Cd})}\partial(p_{\mathrm{Cd}}c_{\mathrm{Cd}})/\partial x\}/\partial x. \tag{14}$$

The Schmidt method[8] of finite differences was used to solve simultaneously the coupled differential equations (13) and (14). The method is well known and was applied here in the following manner.

Fick's second law written in general form is

$$\partial c/\partial t = \partial(D\partial c/\partial x)/\partial x. \tag{15}$$

If D is constant and the following dimensionless parameters are introduced

$$X = x/b,\ Z = Dt/b^2,\ \text{and}\ C = c/C_0$$

equation (15) can be written as

$$\partial C/\partial Z = \partial^2 C/\partial X^2 \tag{16}$$

where b is a constant distance and C_0 is the surface concentration.

Let C_{m+1}, C_m, C_{m-1} be the average concentrations in the space intervals $(m+1)\delta X$, $m\delta X$, $(m-1)\delta X$, respectively, and C_m', C_m be the average concentrations in the space interval $m\delta X$ at the time intervals $(m+1)\delta Z$, $m\delta Z$, respectively. Expanding C_{m+1}, C_{m-1}, and C_m' in a Taylor series these concentrations can be expressed as

$$C_{m+1} = C_m + \delta X(\partial C/\partial X)_m + \tfrac{1}{2}(\delta X)^2(\partial^2 C/\partial X^2)_m + \ldots, \quad (17)$$

$$C_{m-1} = C_m - \delta X(\partial C/\partial X)_m + \tfrac{1}{2}(\delta X)^2(\partial^2 C/\partial X^2)_m - \ldots, \quad (18)$$

and

$$C'_m = C_m - \delta Z(\partial C/\partial Z)_m + \tfrac{1}{2}(\partial Z)^2(\partial^2 C/\partial Z^2)_m + \ldots. \quad (19)$$

If fourth and higher order terms are neglected on addition of equations (17) and (18) one obtains

$$(\partial^2 C/\partial X^2)_m = (C_{m+1} - 2C_m + C_{m-1})/(\delta X)^2. \quad (20)$$

By neglecting second and higher order terms in equation (19) one finds

$$(\partial C/\partial Z)_m = (C'_m - C_m)/\delta Z. \quad (21)$$

Substituting equations (20) and (21) in equation (16) and removing the dimensionless parameters gives the Schmidt solution to equation (15).

$$c'_m = c_m + [D\delta t/(\delta x)^2](c_{m+1} - 2c_m + c_{m-1}). \quad (22)$$

The validity of dropping higher order terms was checked by comparing one profile generated by equation (22) with another generated by using smaller time and space intervals. The two profiles agree in the fourth significant figure when using the parameters used in this study. The higher order terms are insignificant in this work. The solution is stable as long as the ratio $D\delta t/(\delta x)^2$ is one-half or less [9].

On introducing the impurity-vacancy complex as the diffusing species equation (22) becomes

$$(c_{\text{Pb}})'_m = (c_{\text{Pb}})_m + [D_{s(\text{Pb})}\,\delta t/(\delta x)^2] [(p_{\text{Pb}}c_{\text{Pb}})_{m+1} - 2(p_{\text{Pb}}c_{\text{Pb}})_m + (p_{\text{Pb}}c_{\text{Pb}})_{m-1}] \quad (23)$$

for the lead ions and

$$(c_{\text{Cd}})'_m = (c_{\text{Cd}})_m + [D_{s(\text{Cd})}\delta t/(\delta x)^2] [(p_{\text{Cd}}c_{\text{Cd}})_{m+1} - 2(p_{\text{Cd}}c_{\text{Cd}})_m + (p_{\text{Cd}}c_{\text{Cd}})_{m+1}] \quad (24)$$

for the cadmium ions. Apparently two symbols have been used for c_m: however, $(c_{\text{Pb}})'_m$ and $(c_{\text{Pb}})_m$ are simply accumulative terms and the diffusion process is governed by the remaining terms.

When identical time and space intervals are used in equations (23) and (24) the diffusion profiles generated are the simultaneous solutions of equations (13) and (14). The initial and boundary conditions are

$$c = 0 \text{ for } x \geq 0 \text{ at } t = 0, \quad (25a)$$

$$c = C_1 \text{ for } t > 0 \text{ at } x = 0, \quad (25b)$$

$$\partial c/\partial x = 0 \text{ at } x = \infty \text{ and } t = t_t \quad (25c)$$

where t_t is the total time of the diffusion anneal, and C_1 is a constant concentration.

The diffusion profiles are dependent on the degrees of association p_{Pb} and p_{Cd}. These can be calculated from equations (8), (10), (11) and (12). If $K_s(T)$ is taken from the literature this set of equations can be put in cubic form and solved. However, for computation in this work they were rewritten as

$$\xi = (1 - p_{\text{Pb}})c_{\text{Pb}} + (1 - p_{\text{Cd}})c_{\text{Cd}} \quad (26)$$

$$c_{v_a^+} = -\xi/2 + (\xi^2 + K_s)^{1/2}/2 \quad (27)$$

$$p_{\text{Pb}} = K_{\text{Pb}}(\xi + c_{v_a^+})[1 + K_{\text{Pb}}(\xi + c_{v_a^+})]^{-1} \quad (28)$$

$$p_{\text{Cd}} = K_{\text{Cd}}(\xi + c_{v_a^+})[1 + K_{\text{Cd}}(\xi + c_{v_a^+})]^{-1}. \quad (29)$$

At each experimental temperature K_{Pb} and K_{Cd} were calculated for trial values of $\Delta g'_{\text{Pb}}$ and $\Delta g'_{\text{Cd}}$ from equations (6) and (7). Values of K_s for the same temperatures were calculated from equation (8) using literature values for B and h_s. With these constants equations (26), (27), (28) and (29) were solved by a method of successive approximations for p_{Pb} and p_{Cd}. Values of p were accepted when successive approximations agreed in their sixth decimal place. With these p's, the experimental values of $(c_{\text{Pb}})_{x=0}$ and $(c_{\text{Cd}})_{x=0}$, using estimated values of $D_{s(\text{Pb})}$ and $D_{s(\text{Cd})}$ equations (23) and (24) were used to generate the Pb and Cd diffusion profiles at each temperature for annealing times equal to t_t with the δt and δx intervals chosen identically for each profile. The estimated values of $D_{s(\text{Pb})}$, $D_{s(\text{Cd})}$, $\Delta g'_{\text{Pb}}$, and $\Delta g'_{\text{Cd}}$ were varied until a satisfactory fitting of the calculated to the experimental profiles was obtained. In fitting the profiles the best fit was required in the region of deep penetration. The reason for this will be discussed later. The calculations were made with the aid of a CDC-3300 computer. It should be emphasized that these four parameters are obtained from two penetration curves and the interaction of the diffusants must be included to properly fit the profiles.

No analytical solution of the coupled differential equations exists. Therefore no direct test of the correctness of the generated profiles exists. However, the validity of this formulation in treating a concentration dependent diffusion coefficient can be demonstrated for the case of the diffusion of a single aliovalent impurity by setting $(c_{\text{Pb}})_{x=0} = 0$ and generating profiles for selected values of $\Delta g'_{\text{Cd}}$ and $D_{s(\text{Cd})}$ at same temperature and time. Then $D(c)$ is calculated from the profiles using Matano's method[10]. These agree within the scatter introduced by the graphical integrations and differentiations required in the Matano method.

4. EXPERIMENTAL

Single crystals of NaCl were grown from reagent grade salt that had been purified by ion-exchange[11]. The purified salt was dried by alternately adding HCl and evacuating while the salt was at 200°C. After the salt was dry, it was melted under an atmosphere of HCl. The crystals were grown by the Kyropoulas method from a melt contained in a General Electric semi-conductor grade quartz crucible under mixed argon and HCl at a total pressure slightly exceeding one atmosphere. The single crystals were annealed from 650°C to room temperature under ⅓ atmosphere of Cl_2.

The maximum concentration of OH^- in the NaCl was calculated to be 0·23 ppm by using the height of the absorption peak at 185 nm[12]. No other absorption bands in the wavelength range from 185 to 800 nm were observed. The results of preliminary analysis[13] of crystals grown by the above technique show only Br^- and OH^- to be present in quantities above the detection limit of the analytical technique. The ion for which an analysis was made, the detection limit of the ion when in a NaCl crystal, and the method of analysis are given in Table 1. To this extent initial condition 25a is established by use of suitable host crystals.

Table 1. *Analysis of* NaCl *crystals grown by the kyropoulas method from O.S.U. purified salt*

Impurity	ppm	Method
Ag^+	< 0·01	Optical Absorption (O.A.)
Br^-	0·95	Activation Analysis (A.A.)
K^+	< 1	A.A.
Mn^{2+}	< 0·004	A.A.
OH^-	0·23	O.A.
Pb^{2+}	< 0·01	O.A.
Tl^+	< 0·01	O.A.

Carrier free ^{210}Pb and ^{109}Cd were obtained from the new England Nuclear Corporation. The specific activity for the $Pb(NO_3)_2$ was 5·0 mC/mg and for the $CdCl_2$ was 3·8 mC/mg. A 99+% radioactive purity was listed for both isotopes. To assure that a condensed phase of each diffusant was always present in equilibrium with its vapor ten times the necessary quantity of each diffusant was used. This was to insure that the constant source boundary condition 25b was met.

$PbCl_2$ and $CdCl_2$ carrier and tracer solutions were evaporated to dryness in the bottom of a Vycor diffusion ampoule (8 cm long × 1·8 cm dia.) by flowing N_2 over the surface of the HCl solutions at 70°C. The tracer to carrier ratio was 0·080 mC/mg for the $PbCl_2$ and 0·129 mC/mg for the $CdCl_2$. A pedestal of Vycor tubing (3 cm long) provided support for one or two NaCl crystals (1·5 × 1·5 × 0·4 cm). It prevented contact between the solid diffusant in the bottom of the ampoule and the host crystals. The ampoule was sealed with one-sixth to one-third atmosphere of Cl_2 inside to prevent reduction of $CdCl_2$[14]. Two small projections on the outside of the ampoule 2 cm above its bottom were used to accurately position the ampoule in the diffusion furnace (see Fig. 1) by raising the ampoule (e) with support wire (c) until the projections engage graphite block (d).

Temperatures were measured with a Pt–Pt 13% Rh thermocouple which had been calibrated against a similar couple calibrated by N.B.S. The difference in temperature between the thermocouple at (b) and at the crystal position measured in an open ampoule was less than 1°C. The bottom of the ampoule was 5°C cooler than the crystal. This temperature gradient is used to prevent condensation of the diffusant on the crystal during the diffusion anneal. The temperature of the sample was held constant within ±1°C during the diffusion and the temperature of the sample was known to within 1°C.

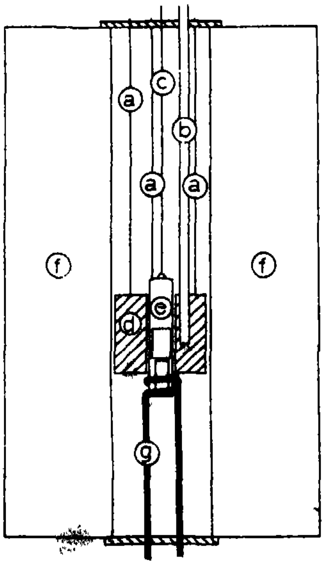

Fig. 1. Diffusion anneal apparatus. a. Support wires for carbon block. b. Thermocouple. c. Support wire for ampoule. d. Carbon block. e. Ampoule. f. Furnace. g. Cooling coil.

After the diffusion anneal the crystals were removed from the ampoule. To insure the samples would be of a one-dimensional diffusion two-millimeter sections were cleaved from the edges of the crystals after which the area of the surface was measured with a micrometer. Either two crystals were initially placed in the diffusion ampoule, or more often, a single crystal was cleaved in half after removing the edges to produce two one-dimensional diffusion samples. The samples were sectioned with an American Optical Company Model 960 microtome. Each section was collected in a clean preweighed vial. Both samples and vials were dried at 110°C for 3 hr, then weighed on a microbalance and thickness of the section calculated.

The gamma radiation of ^{210}Pb and ^{109}Cd was counted with a Packard Model 410 A auto-gamma spectrometer. The 86 Kev photopeak of ^{109}Cd and the 46 keV photopeak of the ^{210}Pb were counted while using a 20 KeV window. There was a slight overlap of the two peaks. The corrected activity was calculated by use of standard activity samples (Cd St. and Pb St.) in the following manner:

$$A_{Pb} = A_{46KeV} - A_{86KeV} A_{46KeV}(\text{Cd St.})/A_{86KeV}(\text{Cd St.}) \quad (30)$$

$$A_{Cd} = A_{86KeV} - A_{46KeV} A_{86KeV}(\text{Pb St.})/A_{46KeV}(\text{Pb St.}) \quad (31)$$

where A is the activity and the subscript indicates which channel was counted.

One problem encountered during these experiments is illustrated in Fig. 2. The two crystals from the same diffusion anneal have differing surface concentrations of Cd^{2+}. Apparently this problem occurs because the crystal requires longer to reach furnace temperature than does the diffusant. Thus during warm up the diffusant transfers from the bottom of the ampoule to the cooler crystal surface. To prevent this a water cooled coil [(g) of Fig. 1] was used to keep the diffusant at a low temperature (100 to 150°C) while the crystal reached the anneal temperature. 15 to 20 min after insertion of the ampoule into the pre-heated furnace the cooling coil was lowered and this time recorded as $t = 0$. The profiles agreed within experimental error in all later experiments except two (360 and 409°C). The reason for these exceptions was not specifically investigated. It is interesting to note that they all occur in the low temperature experiments.

With the coil in place, not only is the diffusant cooled but also the bottom of the pedestal supporting the crystals. Thus, radiant transfer of heat is the more important process in heating the crystal and is much more efficient at higher temperatures. Possibly at these lower temperatures the coil was not left around the ampoule long enough for the crystals to reach temperature. All penetration profiles exhibiting this behavior occur below 423°C which is the peritectic temperature of $2NaCl{\cdot}CdCl_2$[15]. Below this temperature $CdCl_2$ could be condensed on the surface of the crystal due to a chemical potential difference caused by the formation of $2NaCl{\cdot}CdCl_2$. This could account for the difference between the behavior of $CdCl_2$ and $PbCl_2$ (Fig. 2). There is doubt as to the existence of cadmium complexes in the melt [16] and if no complexes exist above 423°C, the system would behave normally (Fig. 3).

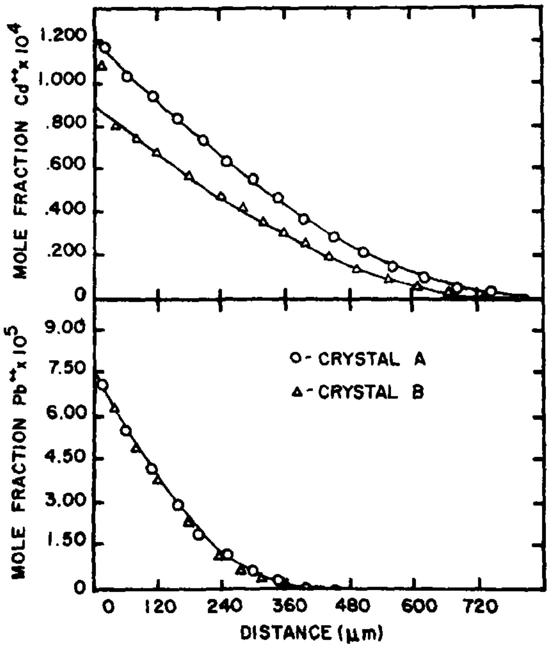

Fig. 2. Penetration profiles for the diffusion of cadmium and lead ions in NaCl at 360°C. $t_f = 1{\cdot}2890 \times 10^6$ sec. Liquid quenched. Solid curves are profiles generated by finite differences using the following parameters.

(a). $D_{s(Cd)} = 5{\cdot}80 \times 10^{-10}$ cm²/sec $\Delta g'_{Cd} = -0{\cdot}550$ eV
(b). $D_{s(Cd)} = 5{\cdot}00 \times 10^{-10}$ cm²/sec $\Delta g'_{Cd} = -0{\cdot}550$ eV
(a),(b). $D_{s(Pb)} = 1{\cdot}90 \times 10^{-10}$ cm²/sec $\Delta g'_{Pb} = -0{\cdot}440$ eV.

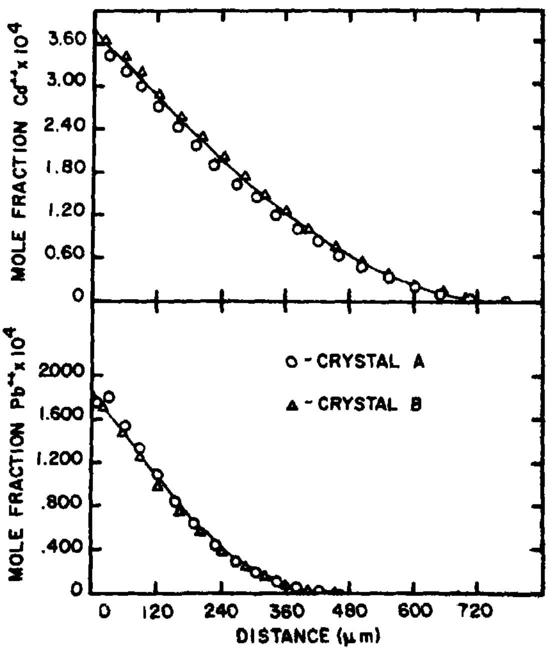

Fig. 3. Penetration profiles for the diffusion of cadmium and lead ions in NaCl at 460°C. $t_f = 1{\cdot}674 \times 10^5$ sec. Liquid quenched. Solid curves are profiles generated by finite differences using the following parameters.

$D_{s(Cd)} = 4{\cdot}10 \times 10^{-09}$ cm²/sec $\Delta g'_{Cd} = -0{\cdot}485$ eV
$D_{s(Pb)} = 2{\cdot}30 \times 10^{-08}$ cm²/sec $\Delta g'_{Pb} = -0{\cdot}388$ eV.

This violation of boundary conditions in the early portion of the experiment did not change the Δg which depends on the shape of the profile but did introduce a slight variation in D_g as will be seen in the Results Section.

A related problem occurs when the ampoule is removed from the furnace. The walls of the ampoule cool rapidly and the diffusant vapor condenses on them while the crystal remains hot. Thus the chemical potential of the diffusant surrounding the crystal falls below that in the crystal and the impurity desorbs from the host until it cools below temperatures at which the impurity is mobile. Experimentally the desorption is observed as a lower diffusant concentration near the surface than expected. The magnitude of the effect increases with increasing anneal temperatures and with slower cooling rates. This effect can be minimized by effective quenching. With systems which must remain sealed to avoid extraneous reactions, quenching is difficult. With the exceptions noted the sealed ampoules were immersed in ice water immediately on removal from the furnace, then in liquid N_2. One of the ampoules from the highest temperature anneal was allowed to cool clowly to produce a large amount of desorption to investigate its effect on Δg and D_g derived from such experiments.

5. EXPERIMENTAL RESULTS

Diffusion profiles of Pb^{2+} and Cd^{2+} in NaCl were measured at eight temperatures in the range from 347 to 569°C. At all temperatures except 569°C two samples were sectioned. The results of three of these measurements are shown in Figs. 2 through 4. The curves shown as solid lines in these figures are diffusion profiles calculated as described above using the D_g and $\Delta g'$ values for each ion given in the figure caption. Dreyfus and Nowick's[15] data show the Schottky product, $K_s(T)$, to be negligible in the range of these NaCl experiments and these profiles were calculated without considering this contribution to the vacancy concentration.

The profiles show the characteristics discussed in the experimental section with the lower temperature measurements exhibiting differences in surface concentrations; the middle temperature range was well behaved; the higher temperature measurements showed desorption during the quench. The different surface concentrations which developed during the lower temperature diffusion anneals cause the values of D_g to vary but do not affect $\Delta g'$ a detectable amount. The abnormally low concentrations near the surface found in the high temperature anneals (Fig. 4) were neglected in calculating the profile shown. Assuming the crystal to remain at the anneal temperature for a finite time after quenching has reduced the vapor pressure of the diffusants to zero, desorption

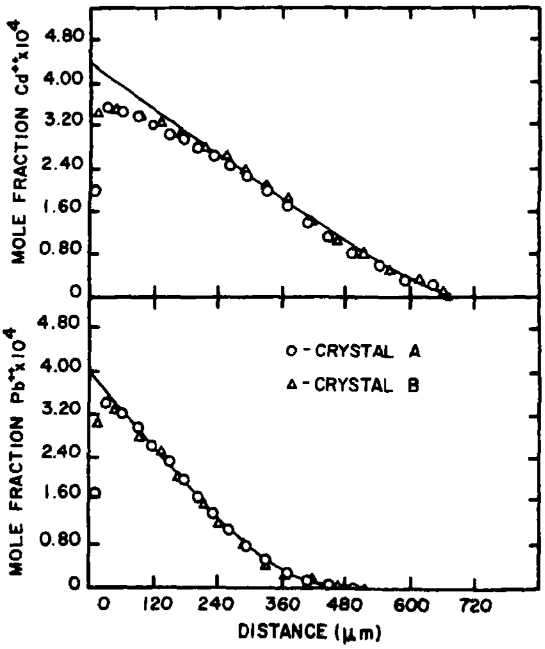

Fig. 4. Penetration profiles for the diffusion of cadmium and lead ions in NaCl at 553°C. $t_t = 4\cdot368\times10^4$ sec. Liquid quenched. Solid curves are profiles generated by finite differences using the following parameters.

$$D_{g(Cd)} = 2\cdot40\times10^{-08}\ \mathrm{cm^2/sec}\ \Delta g'_{Cd} = -0\cdot424\ \mathrm{eV}$$
$$D_{g(Pb)} = 1\cdot50\times10^{-08}\ \mathrm{cm^2/sec}\ \Delta g'_{Pb} = -0\cdot342\mathrm{eV}.$$

profiles were calculated for various times using the values of D_s and $\Delta g'$ for the 553°C anneal. These desorption profiles are shown together with the diffusion profile in Fig. 5. While this calculation does not realistically represent the quenching process, it suggests the low concentrations near the surface are primarily due to desorption. More important, however, is that the desorption does not affect the shape of the penetration curve in the region used to derive $\Delta g'$ and D_s.

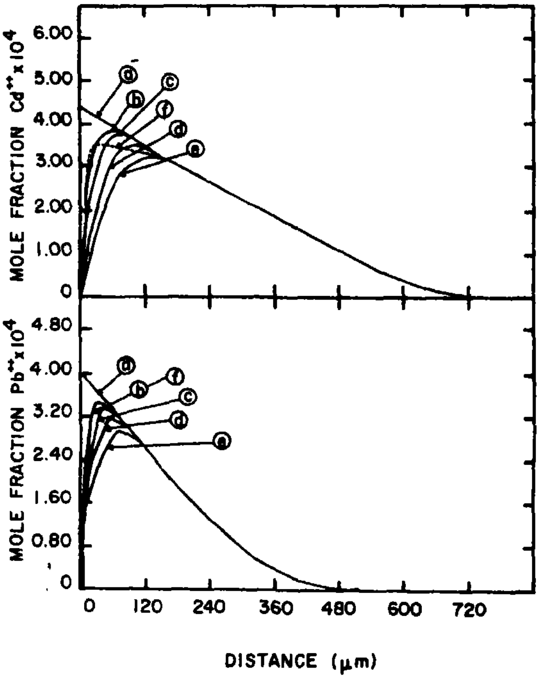

Fig. 5. Penetration profiles for the desorption of cadmium and lead from NaCl at 553°C for short periods of time. Calculated by finite differences using the following parameters.

$D_{s(\mathrm{Cd})} = 2{\cdot}40 \times 10^{-08}\ \mathrm{cm^2/sec}\ \Delta g'_{\mathrm{Cd}} = -0{\cdot}424\ \mathrm{eV}$

$D_{s(\mathrm{Pb})} = 1{\cdot}50 \times 10^{-08}\ \mathrm{cm^2/sec}\ \Delta g'_{\mathrm{Pb}} = -0{\cdot}342\ \mathrm{eV}.$

(a). 0 min (b). 2 min (c). 4 min (d). 10 min (e). 20 min (f). average of experimental points.

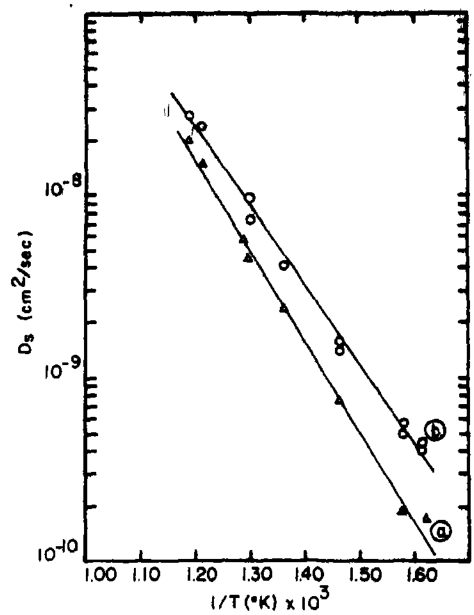

Fig. 6. Log D_s vs $1/T$ from diffusion in NaCl. The Pb^{2+} results are fit by line a. and those of Cd^{2+} by line b.

All parameters calculated from each diffusion anneal are given in Table 2 along with some experimental conditions of each anneal. Plots of log D_s vs. $1/T$ are given in Fig. 6. The solid lines are the least squares fit to the data of Table 2 and are given by the expressions

$$D_{s(\mathrm{Pb})} = 1{\cdot}40 \times 10^{-2} \exp\left(-0{\cdot}982\ \mathrm{eV}/kT\right)\ \mathrm{cm^2\,sec^{-1}} \quad (32)$$

and

$$D_{s(\mathrm{Cd})} = 3{\cdot}57 \times 10^{-3} \exp\left(-0{\cdot}857\ \mathrm{eV}/kT\right)\ \mathrm{cm^2\,sec^{-1}} \quad (33)$$

where the activation energy of migration of the Pb^{2+} vacancy complex is 0·982 eV, and that of the Cd^{2+} vacancy complex is 0·857 eV.

The Gibbs free energies of association less the configurational entropies can be expressed by

$$\Delta g'_{\mathrm{Pb}} = -0{\cdot}775\ \mathrm{eV} + (5{\cdot}29 \times 10^{-4}\ \mathrm{eV/°K})T \quad (34)$$

and

$$\Delta g'_{\mathrm{Cd}} = -0{\cdot}972\ \mathrm{eV} + (6{\cdot}65 \times 10^{-4}\ \mathrm{eV/°K})T. \quad (35)$$

Table 2. Values of D_S and $\Delta g'$ used to generate diffusion of Pb^{2+} *and* Cd^{2+} *in* NaCl

T(°C)	$D_{s(Pb)}$ (cm²/sec)	$D_{s(Cd)}$ (cm²/sec)	$\Delta g'_{Pb}$ (eV)	$\Delta g'_{Cd}$ (eV)	Notes
347	$1{\cdot}70 \times 10^{-10}$	$4{\cdot}10 \times 10^{-10}$	−0·445	−0·560	[a], [d]
347	$1{\cdot}70 \times 10^{-10}$	$4{\cdot}50 \times 10^{-10}$	−0·445	−0·560	[b], [d]
360	$1{\cdot}90 \times 10^{-10}$	$5{\cdot}80 \times 10^{-10}$	−0·440	−0·550	[a], [c]
360	$1{\cdot}90 \times 10^{-10}$	$5{\cdot}00 \times 10^{-10}$	−0·440	−0·550	[b], [c]
409	$7{\cdot}60 \times 10^{-10}$	$1{\cdot}60 \times 10^{-09}$	−0·415	−0·520	[a], [c]
409	$7{\cdot}60 \times 10^{-10}$	$1{\cdot}45 \times 10^{-09}$	−0·415	−0·520	[b], [c]
460	$2{\cdot}30 \times 10^{-09}$	$4{\cdot}10 \times 10^{-09}$	−0·388	−0·485	[a], [b], [c]
497	$4{\cdot}60 \times 10^{-09}$	$7{\cdot}50 \times 10^{-09}$	−0·370	−0·455	[a], [b], [c]
502	$5{\cdot}80 \times 10^{-09}$	$1{\cdot}00 \times 10^{-08}$	−0·367	−0·453	[a], [b], [d]
553	$1{\cdot}50 \times 10^{-08}$	$2{\cdot}40 \times 10^{-08}$	−0·342	−0·424	[a], [b], [c]
569	$2{\cdot}00 \times 10^{-08}$	$2{\cdot}75 \times 10^{-08}$	−0·323	−0·414	[a], [d]

[a] Crystal *A*.
[b] Crystal *B*.
[c] Cooling coil used, crystal quenched after diffusion anneal.
[d] No cooling coil used, crystal air quenched.

These enthalpies and entropies of formation for the Pb^{2+} and Cd^{2+} complexes were derived by a least squares fit to the $\Delta g'$ vs. T data shown in Fig. 7.

6. DISCUSSION

Comparison of the diffusion and association parameters for Pb^{2+} and Cd^{2+} obtained from these simultaneous diffusion measurements with those obtained in single ion measurements are given in Table 3. All three values of the migration energy U_0 of Pb^{2+} in NaCl are in excellent agreement. In the two earlier studies[16, 17] of Pb^{2+} diffusion the free energy of association $\Delta g'$ was not considered by the authors to be measured precisely enough to warrant extracting the enthalpy and entropy of association. However the results of the present experiments (Fig. 7) were significantly better. Table 3 gives Δh and $\Delta s'$ along with the correlation factor r for a linear regression fit of n data for these experiments and for the earlier work. For Pb^{2+} all data reported in the earlier papers were used. In the case of Cd^{2+} the earlier experiments extended to considerably lower temperatures than did the dimultaneous diffusion studies and exhibited an unusual curvature at the lower temperatures[14]. For this reason the enthalpy and entropy given in Table 3 were calculated with data[14] from 328 to 520°C.

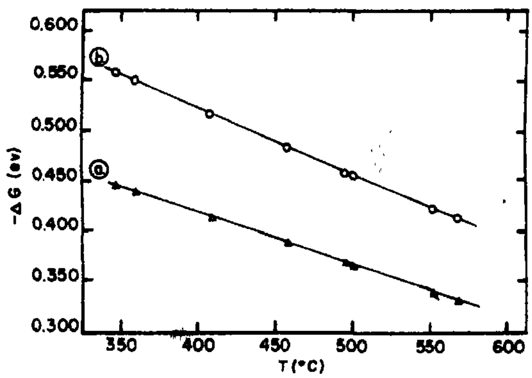

Fig. 7. Gibbs free energies of association of impurity-vacancy complexes in NaCl. The Pb^{2+} results are fit by line a. and those of Cd^{2+} by line b.

The agreement of the Pb^{2+} data measured in purified NaCl is excellent, well within the experimental errors. However, the single ion diffusion measurements in Harshaw crystals lead to a $-\Delta h$ which is 0·14 eV lower and a $-\Delta s'$ lower by a factor of two than those obtained with purified crystals. Similar discrepancies occur between the diffusion parameters for Cd^{2+} in purified and Harshaw NaCl. However with Cd^{2+} both

Table 3. Values of D_0, the migration energy U_0, the enthalpy of formation Δh and the entropy of formation $\Delta s'$ of Pb^{2+} *and* Cd^{2+} *complexes in* NaCl

Cation	[a]D_0(cm²/sec)	[a]U_0(eV)	[b]Δh (eV)	[b]$\Delta s'$ (eV)	[c]r	[d]n	[e]method	Crystal	Ref.
Pb^{2+}	$1·5 \times 10^{-2}$	0·98	−0·632	$-2·60 \times 10^{-4}$	0·8816	8	D1	Harshaw	18
Pb^{2+}	$1·75 \times 10^{-2}$	0·98	−0·780	$-5·31 \times 10^{-4}$	0·829	9	D1	OSU	19
Pb^{2+}	$1·40 \times 10^{-2}$	0·982	−0·775	$-5·29 \times 10^{-4}$	0·9973	16	D2	OSU	this work
Cd^{2+}	$2·06 \times 10^{-2}$	0·92	−1·085	$-8·95 \times 10^{-4}$	0·9536	12	D1	Harshaw	14
Cd^{2+}	$3·57 \times 10^{-3}$	0·857	−0·972	$-6·65 \times 10^{-4}$	0·9989	16	D2	OSU	this work
Pb^{2+}		0·80					DE	[f]CSIRO	21
Cd^{2+}			[g]−0·34				C	Harshaw	24
Cd^{2+}	1·2	0·64					D3	[h]Halle	23
Cd^{2+}		0·50					itc	[j]IFU	44

Notes: [a] $D_s = D_0 \exp(-U_0/1sT)$

[b] $\Delta g = \Delta h - T\Delta s'$

[c] $r = \sum_{j=1}^{n} (X_i - X)(Y_i - Y)\left[\sum_{j=1}^{n} (X_i - X)^2 \sum (Y_i - Y)^2\right]^{-1/2}$

[d] nts number of data

[e] D1 is single ion diffusion by directly measured profile
D2 is simultaneous diffusion
DE is dielectric relaxation
C is ionic conductivity
D3 is diffusion from an indirect profiled by color center formation
itc is ionic thermal currents.

[f] CRIRO – grown at CSIRO, Sydney, Australia

[g] Calculated from the data of Ref.[25]

[h] Halle refers to natural NaCl crystals from Halle Company, Germany

[j] IFU – grown at Istituto di Fisica dell Universita, Parma, Italia, total Co, Cu, Mn, Ni, Zn and Pb content less than 0·3 ppm.

$-\Delta h$ and $-\Delta s'$ are larger in Harshaw crystals than in the purified crystals. The only significant difference between these experiments is the host crystals. The most probable cause of these discrepancies in U_0, Δh and $\Delta s'$ are interactions between the tracers and unknown impurities in the Harshaw crystals.

Comparison of the results of various methods of measuring U_0, Δh or $\Delta s'$ are complicated by the use of host crystals of unknown or varying purity. Some of these results have been considered in previous papers[14]. Crawford[20] has discussed the interpretation of migration energies obtained from various dipole relaxation measurements [21, 22]. Since the present work illustrates the interaction of two known aliovalent cations through a common ion effect, and others [6, 7] have shown that cation–anion reactions occur between impurity ions in alkali halides, it appears unlikely that further comparison of various results is useful at present.

Although Table 1 shows that these crystals contain very low concentrations of those ions for which specific analyses were made, the question of the concentration of other impurities is not directly answered. However, if other impurities which affected the tracer impurity-vacancy complex equilibrium were present in the host crystal, then the addition of another ion, such as during the simultaneous diffusion experiments, would shift the equilibrium through a common ion effect not taken into account in either the single ion or simultaneous diffusion equilibrium calculations. Since both experiments employed purified host crystals and the experiments required different assumptions about the equilibrium conditions yet gave good agreement for the diffusion parameters of Pb^{2+}, we concluded that the unintentional impurity concentration is too low to affect these experiments. Therefore, the values of U_0, Δh and $\Delta s'$ reported here are the best values we have been able to obtain from direct measurement of a diffusion profile in NaCl.

In comparing parameters obtained from these measurements one should note that they are measured under ideal solution conditions. It was not necessary to include Debuy–Hückel terms in the equilibrium equations to account for long range forces. The U_0 obtained are for $D_s(p \rightarrow 1)$ and may be different than those measured from experiments which yield $D_s(c \rightarrow \infty)$ because in this latter case impurity aggregates of various kinds may form.

REFERENCES

1. STASIW O. and TELTOW J., *Ann. Phys.* (*Leipzig*) **1**, 261 (1947).
2. LIDIARD A. B., *Handbuch der Physik* (Edited by S. Flügge), Vol. 20, pp. 246–349, Springer-Verlag, Berlin (1957).
3. HOWARD R. W. and LIDIARD A. B., *Rep. Prog. Phys.* **27**, 161 (1964).
4. SÜPTITZ P. and TELTOW J., *Phys. Status Solidi* **23**, 9 (1967).
5. BARR L. W. and LIDIARD A. B., *Defects in Ionic Crystals, Physical Chemistry–An Advanced Treatise*; (Edited by Eyring, Henderson and Jost), Vol. 10, pp. 151–228, Academic Press, New York (1970).
6. FRITZ B., LÜTY F. and ANGER J., *Z. Phys.* **174**, 240 (1963).
7. ALLEN C. A. and FREDERICKS W. J., *Phys. Status Solidi* (a) **3**, 143 (1970).
8. SCHMIDT E., *Föppls Festschrift*. Springer, Berlin (1924).
9. DUSINBERRE G. M., *Heat-Transfer Calculations by Finite Differences*. International Textbook, Scranton (1961).
10. MATANO C., *Japan J. Phys.* **8**, 109 (1933).
11. FREDERICKS W. J., SCHUERMAN L. W. and LEWIS L. C. *An Investigation of Crystal Growth Processes*. Corvallis 1966 (Final Reports AF-AFOSR 217-63 and AF-AFOSR-217-66).
12. GIE T. I. and KLEIN M. V., *Bull. Amer. phys. Soc.* **8**, 230 (1963).
13. FREDERICKS W. J. and SCHUERMAN L. W., unpublished data.
14. KENESHEA F. J. and FREDERICKS W. J., *J. Phys. Chem. Solids* **26**, 501 (1965).
15. BRAND H., *Neuses Jahrb. Min.* **32**, 627 (1911).
16. BOARDMAN N K., PALMER A. R. and HEYMANN E., *Trans. Faraday Soc.* **51**, 277 (1955).
17. DREYFUS R. W. and NOWICK A. S., *J. appl. Phys.* **33**, 473 (1962).
18. ALLEN C. A., IRELAND D. T. and FREDERICKS W. J., *J. chem. Phys.* **46**, 2000 (1967).
19. MANNION W. A., ALLEN C. A. and FREDERICKS W. J., *J. chem. Phys.* **48**, 1537 (1968).
20. CRAWFORD J. H., Jr., *J. Phys. Chem. Solids* **31**, 399 (1970).
21. DRYDEN J. S. and HARVEY G. G., *J. Phys. C.* (*Solid State Phys.*) **2**, 603 (1969).
22. CAPELLETTI R. and DEBENEDETTI E., *Phys. Rev.* **165**, 981 (1968).
23. IKEDA T., *J. phys. Soc. Japan* **19**, 858 (1964).
24. LIDIARD A. B., *Phys. Rev.* **94**, 29 (1954).
25. ETZEL H. W. and MAURER R. J., *J. chem. Phys.* **18**, 1003 (1950).

J. Phys. Chem. Solids, 1971, Vol. 32, pp. 2685–2692. Pergamon Press. Printed in Great Britain

INFLUENCE OF THE CHEMICAL BOND ON THE *K* EMISSION SPECTRUM OF OXYGEN AND FLUORINE

A. S. KOSTER*
Department of Physics, University of Arizona, Tucson, Arizona 85721, U.S.A.

(*Received* 18 *May* 1970; *in revised form* 20 *April* 1971)

Abstract—The *K* emission spectrum of oxygen and fluorine from a number of simple oxides and fluorides is divided into three to six sub-peaks. The spectra of many of these oxides and fluorides resemble one another owing to their basically ionic bonding. Certain sub-peaks, however, are ascribed to cross-over transitions and partially covalent energy levels. The different fluorine spectrum of Teflon is due to the hybrid nature of its covalent bonds.

1. INTRODUCTION

FOLLOWING early reports of Tyrén[1] and O'Bryan and Skinner[2] in 1940 on oxygen and fluorine *K* bands from different compounds, the first extensive investigation of these spectra was undertaken by Fischer in 1965[3]. He showed that they were influenced by composition, crystal structure, valence and coordination, but his data were too ill-defined to permit definite conclusions. Another report on oxygen and fluorine spectra was given by Mattson and Ehlert[4] who also made no attempt to interpret them. Chun and Hendel[5] obtained results on a number of oxides of di- and trivalent metals which indicated some correlation between the electronegativity of the metal and the position of satellites, but they too offered no explanation of the spectra. Krause and White[20] made a comprehensive survey of oxygen X-ray emission band shifts from oxides and indicated a relation between the wavelength of the main band and the valence of the cation on an empirical basis. Since then several isolated oxygen spectra have been described, for instance by Fischer and Baun for titanium oxides[6], by Fischer for vanadium oxides[7], by Fomichev for aluminum oxide[8] and magnesium oxide[9], by Chun and Klein for aluminum oxides[10].

In the investigation of Koster and Mendel [11, 12] on the relation of 3*d*-transition metal *K*β spectra to chemical bonding, oxygen and fluorine spectra taken from the literature were used to construct composite energy diagrams. Many of the required spectra were either not available or of unsatisfactory quality, however, and the present work aims to fill this gap.

2. EXPERIMENTAL

The light element X-ray spectrometer used and the experimental technique have been described in previous publications[13–15] from this laboratory. The specimen is the secondary target in a cold cathode X-ray tube. Excitation under these conditions is so mild that there is no significant rise in temperature. All of the compounds investigated here, except MnO_2, were stable for the period of an experiment; for this dioxide a number of ten minute runs were used. Oxygen spectra were recorded with a potassium acid phthalate (*KAP*), fluorine spectra with a mica crystal, both in the first order. The flow counter was filled with a 50-50 helium–methane mixture. Wavelength calibration was carried out by means of Al $K\alpha_{1,2}$ ($\lambda = 8{\cdot}339$ Å) in the 2nd and 3rd orders for oxygen, and by means of K $K\alpha_{1,2}$ ($\lambda = 3{\cdot}742$ Å) and Ca $K\alpha_{1,2}$ ($\lambda = 3{\cdot}360$ Å) in the 5th order for fluorine. For most measurements the power applied was 10–15 kV at 5–10 mA, giving peak intensities of 30–60 c/s for oxygen and 60–200 c/s for fluorine.

---

*Permanent Address: Laboratory for Physical Chemistry, Technische Hogeschool, Eindhoven, The Netherlands.

3. RESULTS

Oxygen

Typical oxygen *K* bands are reproduced in Figs. 1–3. In order to save space, some spectra resembling these are omitted; comparable oxygen spectra were obtained from the following substances: MgO, Al_2O_3 and BeO; NO_3^- and $CO_3^=$; TiO_2, $Cr_2O_7^=$ and MnO_4^-; Cr_2O_3 and Fe_2O_3. In some cases, as for BeO and Li_2CO_3, separation between the main and smaller peaks is large enough so that the band spectrum can easily be split into its constituent parts. The resulting sub-peaks are quite symmetrical and have a similar half-width of 3 to 3-1/2 eV. The main band in compounds of the 3*d*-transition metals, on the other hand, is broader and obviously contains sub-peaks. The spectra of these compounds could be satisfactorily accounted for by splitting them into three or four sub-peaks using the profiles of the bands of Li_2CO_3 or BeO. The positions of the maxima of the sub-bands and their relative intensities obtained in this way are given in Table 1.

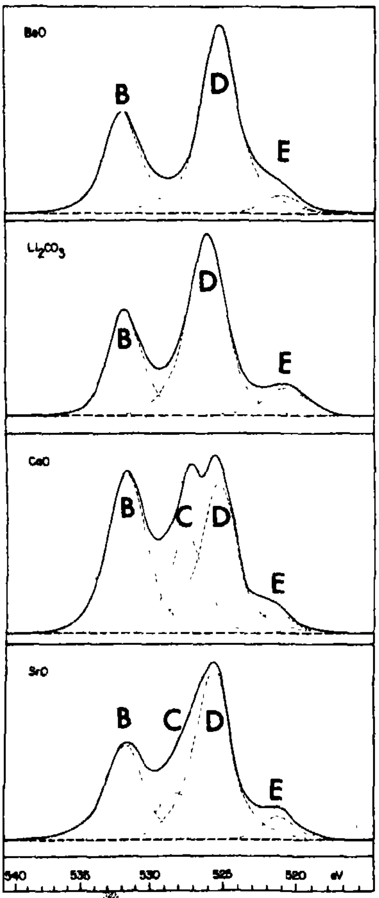

Fig. 1. The first order oxygen *K* bands from BeO, Li_2CO_3, CaO and SrO. In this and subsequent figures the observed peak is the full line, the sub-peaks into which it has been broken down are dashed. Background is also dashed. Ordinates are the intensities in counts per second.—

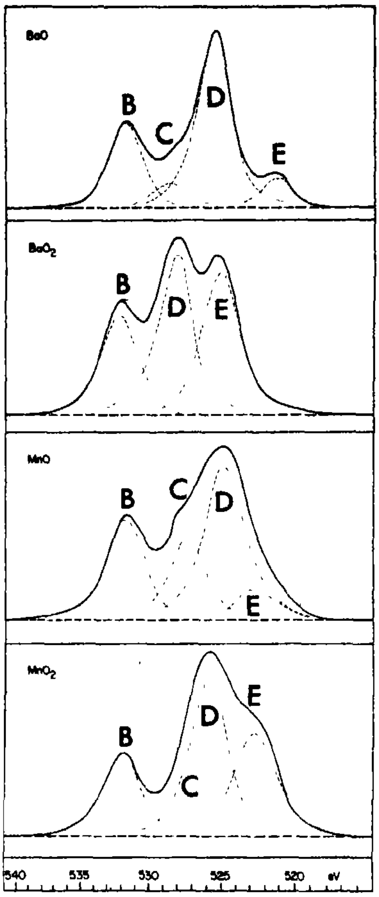

Fig. 2. The oxygen *K* bands from BaO, BaO_2, MnO and MnO_2.

Peak *D* is obviously the main peak of the spectrum and may be ascribed to the transition

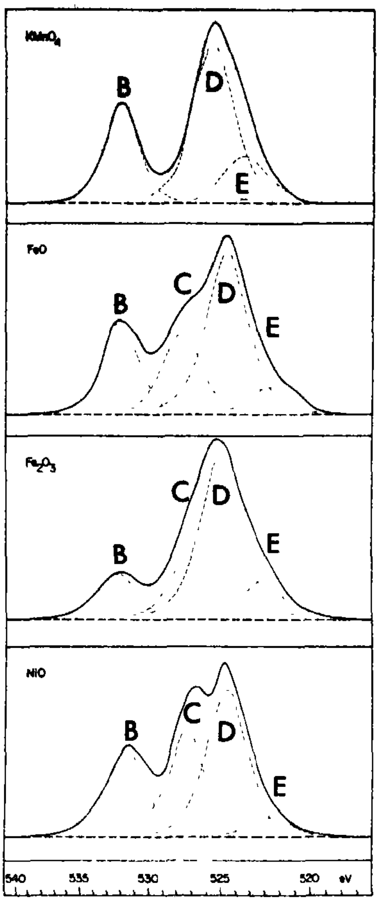

Fig. 3. The oxygen *K* bands from $KMnO_4$, FeO, Fe_2O_3 and NiO.

of a valence band electron:$2p(O^{2-}) - 1s(O^{2-})$. For the predominantly ionic substances like BeO, MgO, Al_2O_3, CaO, SrO and BaO, the energy of this sub-peak is 525 eV. The residual charge in electron units, calculated using Pauling's electronegativity values, is −1·6 to −1·8 e.u. for these substances. Much the same value is found in the lower oxides of the 3*d*-transition metals. In the compounds where the residual charge is less negative, due to a weaker ionic bond, the energy of peak *D* is higher; this is observed in the spectra of CO_3^{2-}, NO_3^-, $Cr_2O_7^{2-}$, and MnO_4^-. In BaO_2, the ion O_2^{2-} is present; each oxygen thus carries a formal charge of −1 e.u., which because of the partially covalent character of the compound is reduced to −0·7 to −0·8 e.u. residual charge. This leads to a shift to still higher energy. A tentative plot of residual charge vs. position of peak *D* is given in Fig. 4.

Peak *B* is the most constant in position. Whereas the other peaks shift over a range of 2–3 eV, it remains at 532·0 ± 0·3 eV. It has already been reported[4, 7] that its height depends upon the analyzing crystal. We found the same effect. The position of *B* remains the same, but its intensity as compared to the intensity of peak *D* is three times less for a lead stearate pseudocrystal than for a *KAP* crystal, other conditions being unchanged. Liefeld, Hanzely, Kirby and Mott[17] have shown that the prominence of this peak is due to a line-like reflectivity structure at 532 eV which *KAP* exhibits; it is not clear, however, whether only continuum radiation or also a true emission peak is enhanced. Other analyzers containing oxygen may exhibit the same phenomenon. Many investigators, using various crystals and gratings, found a more or less pronounced peak in the 530–532 eV region. Holliday[18], comparing the O *K* spectrum from BeO obtained with a grating with that from a *KAP* crystal, found no peak at 532 eV. O'Bryan and Skinner[2] and Chun and Hendel[5], likewise using a grating, detected a peak at this position, however. In the spectra of Fischer and Baun[6], who used a clinochlore crystal, a hump can be detected

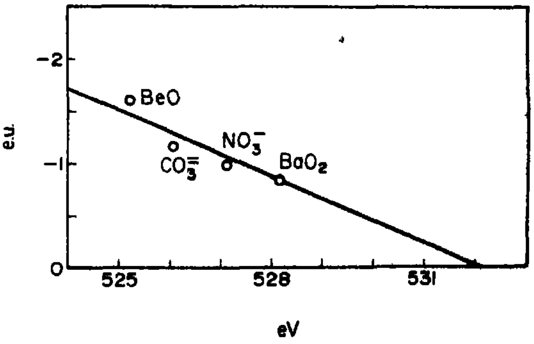

Fig. 4. Graph of the residual charge on the O ion plotted against the position of the main O *K* band.

Table 1. Energies in eV of the bands of the oxygen K spectrum and peak intensities relative to peak D

	B	C	D	E	I_B/I_D	I_C/I_D	I_E/I_D
BeO	532·1		525·2	521·2	0·57		0·10
MgO	532·0		525·4	522·2	0·68		0·10
Al_2O_3	532·1		525·3	521·3	0·60		0·18
Li_2CO_3	531·9		526·1	520·7	0·55		0·15
$LiNO_3$	532·1		527·1	520·7	0·30		0·13
CaO	531·7	527·5	525·3	521·5	1·06	0·66	0·11
SrO	531·9	528·3	525·5	521·4	0·56	0·27	0·16
BaO	531·8	528·6	525·4	521·3	0·47	0·13	0·14
BaO_2	532·2		528·1	525·0	0·65		0·90
TiO_2	532·0		525·9	523·3	0·57		0·34
Cr_2O_3	532·3	528·2	525·3	522·5	0·38	0·24	0·28
$K_2Cr_2O_7$	532·3		526·0	523·8	0·55		0·28
MnO	531·9	527·5	524·9	522·6	0·60	0·49	0·16
MnO_2	532·3	527·7	525·6	523·1	0·50	0·22	0·60
MnO_4^-	532·1		525·8	523·6	0·58		0·30
FeO	532·1	527·7	524·6	521·8	0·55	0·50	0·15
Fe_2O_3	532·2	527·2	525·0	522·1	0·30	0·37	0·24
NiO	531·9	527·4	524·6	521·6	0·60	0·70	0·13
Estimated error	±0·3	±0·4	±0·2	±0·4	±10%	±20%	±20%

at 530–531 eV. Probably the oxygen spectrum does contain a peak here, but in some experiments this peak is enhanced by the crystal chosen while in other experiments it is suppressed by absorption or by other modes of excitation. High-energy satellites are often due to multiple ionization; in this case peak *B* can be ascribed to a transition from a KL^2 triplehole state, which is generally called the $K\alpha_{5,6}$ satellite. The triplehole electron configuration of the oxygen ion present in the substances investigated corresponds to a state of neutral oxygen. The data available for the main peak *D* suggest that a peak found at 531–532 eV can indeed be attributed to a neutral oxygen atom (Fig. 4). The exact location of the $K\alpha_{5,6}$ peak cannot be deduced from our spectra, however, the band *B* being enhanced by the analyzing crystal.

The presence of peak *C* depends on the metal ion. For the oxides of the lighter elements, as BeO, MgO, Al_2O_3, $CO_3^=$ and NO_3^-, it is absent. Significantly it is also absent in the spectra of $Cr_2O_7^=$ and MnO_4^-, but present in the spectra of Cr_2O_3, MnO and MnO_2. This peak may be ascribed to the cross-over transition of an electron of the metal ion to the oxygen *K* level. The occurrence of this type of cross-over transition was predicted by Koster and Mendel in their work on the 3*d*-transition metal *Kβ* spectra[11], where proof was given of the reality of the cross-over transition from the oxygen or fluorine *L* level to the metal *K* level. The existence of cross-over transitions was first recognized by Vainshtein, Bril' and Staryi[19]. No unbonded 3*d* electrons remain in the ions $Cr_2O_7^=$ and MnO_4^-, and thus peak *C* of the lower oxides of Cr and Mn and also of FeO, Fe_2O_3 and NiO can be attributed to the transition of valence band electrons mainly characterized as metal 3*d* electrons admixtured with 4*s* and perhaps 4*p* electrons. The intensity of peak *C*, in rough agreement with this interpretation, is highest in FeO and NiO. Oxides like CoO, Co_3O_4, etc., were not investigated but they also should show peak *C* rather strongly.

According to the present interpretation, peak *C* should show fine structure; this has been found by several authors[1, 2, 4, 5] though our spectrometer did not resolve it. Chun and Hendel[5], for instance, show in the series CaO-SrO-BaO that the two components, separated from each other by about 1 eV, are sharper than the oxygen main band, and the more so if the metal is heavier. This agrees with the notion that these two lines are associated with metal ion valence electrons. The same authors found a small single peak in the case of MgO as would be predicted for a Mg atom having only 3*s* electrons.

Peak *E* is generally weak; but in BaO_2 it is nearly as intense as the main peak and in MnO_2, TiO_2, MnO_4^- and $Cr_2O_7^=$ it is also rather prominent. It is less pronounced in NaCl type compounds like MgO, CaO, MnO, FeO, NiO. We attribute it to the transition of electrons involved in covalent bonding, in much the same way as specific energy levels due to the covalent bond were assigned for hydroxides (Mendel and Koster[16]). The two oxygen atoms in the O_2^{2-} ion are held together by a single bond of the σ type, its electronic structure being $\underline{:\ddot{\underset{..}{O}}:}\,\underline{:\ddot{\underset{..}{O}}:}$; a similar bond is presumably present in MnO_2 (certainly not an ionic crystal), which accounts for its high *E* peak, to a lesser extent in TiO_2, MnO_4^-, $Cr_2O_7^=$ and still less in Cr_2O_3 and Fe_2O_3.

Composite diagrams of oxides

When explaining the $K\beta$ spectra of compounds of the 3*d*-transition metals and of other elements, Mendel and Koster[11, 12, 16] constructed composite energy diagrams. A composite energy diagram consists of series of energy levels that belong to the various constituting atomic and molecular orbitals, and it represents the energetic state of the compound. During emission of X-ray quanta, transitions are possible not only between levels of the orbitals of one atom, but transitions between a molecular orbital and an atomic orbital level and cross-over transitions (which can be regarded as an extreme form of a M.O.-A.O. transition) can also occur. The composite energy diagrams as proposed for CaO, TiO_2, Cr_2O_3, CrO_3, MnO, MnO_2, MnO_4^-, FeO and Fe_2O_3[11] are fully confirmed by the present experiments, and some details can now be added*. Table 2 gives the relevant energy levels.

Table 2. Energy levels in the composite diagrams, in eV

	Metal $M_{IV,V}$, N_I	Oxygen $L_{II,III}$	Oxygen K
CaO	4–5	7	532
TiO_2	6–7	7	532
Cr_2O_3	4–5	7	532
$Cr_2O_7^=$		7	533
MnO	5	7	532
MnO_2	6	7	532
MnO_4^-		7	533
FeO	4	7	532
Fe_2O_3	5	7	532

*The $M_{IV,V}$, N_I level at 8 eV in Cr_2O_3 was based upon an incorrect spectrum by Fischer and should be

Fluorine

Most of the fluorine *K* spectra investigated here are comparable with the oxygen *K* spectra, and their interpretation can follow that of the preceding section. The only exception is the F *K* spectrum of Teflon, a tetrafluoroethylene polymer, which has a different appearance caused by its covalent bonding. Typical fluorine *K* bands are shown in Figs. 4 and 5. Analogous spectra have been omitted, CsF being like NaF, K_2TiF_6, K_3MnF_6, K_2MnF_6, and CrF_2 like CaF_2, and CoF_2 like NiF_2. Table 3 gives the positions of the maxima of the sub-peaks and their relative intensities.

Peak *B*, less prominent than in the oxygen *K* spectra, occurs at 680·7 ± 0·3 eV and can be ascribed to neutral fluorine atoms, as was already suggested by O'Bryan and Skinner [2]. A neutral atom is the result of the removal of an electron from the *L* shell, and accordingly peak *B* can be called the $K\alpha_{3,4}$ satellite, which is due to a double-hole *KL* transition. Its energy is 4 eV greater than the main

---

*See Table 2.

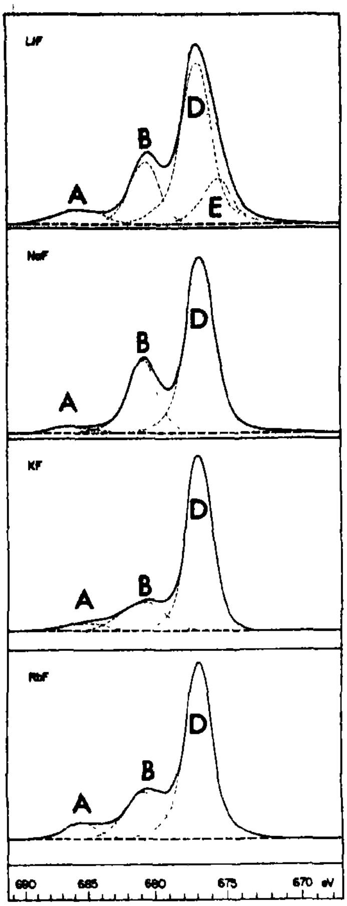

Fig. 5. The first order fluorine K bands from LiF, NaF, KF and RbF.

fluoride ion peak, as would be expected for an emitter whose charge is one electron unit higher (cf. the section on oxygen spectra). At high resolution several authors[3, 4] found this peak to be a doublet, the separation between the components being about 1 eV. The same was found for the $K\alpha_{5,6}$ peak (peak B) of the oxygen spectra[5]. Among the alkali fluorides the intensity of peak B is somewhat irregular; it is low and broad in KF and to a lesser extent in RbF. Fischer[3] states that it is absent in KF, but it is definitely present.

We have found peak A only in fluorides although it has been reported in oxygen spectra[4]. It is very weak in the fluorides and since the oxygen spectra are less intense than those for fluorine, it could have been missed. This high energy band is also due to multiple ionization at a fluorine site, it is presumably the $K\alpha_{5,6}$ satellite.

The maximum of the main fluoride ion band D, at 676·9 ± 0·1 eV, is remarkably constant in position because of the high electronegativity of fluorine. This value was predicted by Koster and Mendel[12] for those compounds for which no data were available. This peak is very sharp for all the alkali halides except LiF, which shows a neighboring low energy band. In the other compounds

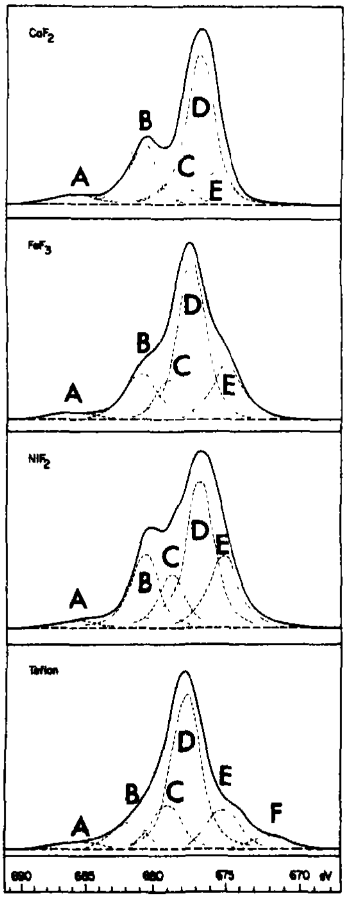

Fig. 6. The fluorine K bands from CaF$_2$, FeF$_3$, NiF$_2$ and Teflon.

Table 3. *Energies in eV of the sub-bands of the fluorine K spectrum and peak intensities relative to peak D*

	A	*B*	*C*	*D*	*E*	*F*	I_A/I_D	I_B/I_D	I_C/I_D	I_E/I_D	I_F/I_D
LiF	686·1	680·6		677·0	675·5		0·08	0·39		0·26	
NaF	686·6	680·9		676·9			0·04	0·39			
KF	685·6	681·0		676·9			0·05	0·16			
RbF	685·6	680·7		676·9			0·09	0·25			
CsF	685·0	681·0		677·0			0·09	0·39			
CaF_2	686·1	680·9	678·5	676·8	675·6		0·06	0·39	0·18	0·21	
K_2TiF_6	686·0	681·0	678·2	677·0	675·4		0·06	0·39	0·16	0·28	
CrF_2	685·0	680·5		676·9	675·5		0·08	0·41		0·37	
K_3MnF_6	686·3	681·0	678·4	676·9	675·5		0·06	0·26	0·18	0·30	
K_2MnF_6	685·3	680·5	678·0	676·9	675·4		0·06	0·34	0·17	0·35	
FeF_3	685·3	681·0	679·0	677·3	674·9		0·04	0·28	0·24	0·36	
CoF_2	685·2	680·5	678·3	676·8	675·1		0·07	0·46	0·31	0·45	
NiF_2	686·1	680·7	678·9	676·9	675·2		0·04	0·38	0·36	0·48	
$(CF_2)_n$	685·6	681·7	679·2	677·7	675·2	671·8	0·05	0·16	0·28	0·26	0·07
Estimated error	±0·6	±0·3	±0·4	±0·1	±0·4	±0·4	±30%	±10%	±20%	±20%	±20%

examined it is broader, both on the low and the high energy side. In FeF_3, for instance, a definite hump can be detected on the low energy side. Peaks *C* and *E* were obtained by subtracting the standard *D* profile (from RbF or CsF) from the observed *D* band.

Peak *C* is absent for the alkali fluorides and becomes more prominent as the number of 3*d* electrons increases. Accordingly it can be attributed, like the peak *C* of oxygen, to the cross-over transition of a metal $M_{IV,V}$, N_I electron to the fluorine *K* level. Unfortunately the accuracy with which this peak can be defined, both in intensity and in position, is limited.

Among the alkali halides peak *E* is seen only for LiF. In this compound the covalent contribution to the bonding is greatest and this is probably enhanced by the mutual contact of its fluoride ions. In the series of transition metal fluorides, the relative intensity of peak *E* increases with the electronegativity of the metal. Thus, as with oxygen, there is a correlation between the appearance of peak *E* and the covalency of bonding.

Teflon yields a totally different spectrum. A maximum appears at approximately the position of the fluoride ion peak; on the low energy side two humps yield two peaks, while on the high energy side peak *A* appears together with a very broad sub-peak, which was tentatively divided into two components of comparable half-widths. The C-F bond is sufficiently polar so that peaks *A* and *D* may be presumed to have the same meaning as for the inorganic fluorides. Peak *D* is shifted to higher energy, because the lesser negative charge on the fluorine atom increases the absolute value of its F *K* level. The remaining four peaks are attributed to the sp^3 hybrid covalent bond. The carbon *K* band emission spectrum of Teflon has already been determined[15]; besides a very weak high energy peak, which presumably is analogous to the fluorine peak *A*, it shows four sub-peaks occupying approximately the same positions as those in the fluorine spectrum. It appears probable that four levels in the valence band (attributed to the fine structure of the sp^3

Table 4. Energy levels in the composite diagrams, in eV

	Metal $M_{IV,V}$, N_I	Fluorine $L_{II,III}$	Fluorine *K*
CaF_2	6	8	685
MnF_6^{3-}	6·5	8	685
MnF_6^{2-}	7	8	685
FeF_3	6	8	685

hybrid molecular orbital) give rise to these peaks in both spectra.

Composite diagrams of fluorides

Information from the spectra described above add some agreeing details to the composite diagrams given by Koster and Mendel [12]. This is indicated in Table 4 showing the relevant levels; note for instance the position of the metal $M_{\mathrm{IV,V}}$, N_{I} level in the series of manganese oxygen and fluorine compounds.

Acknowledgement—This investigation has been carried out in the laboratory of Prof. Ralph W. G. Wyckoff. The author is indebted to him and to Franklin D. Davidson for valuable discussions. This work has been supported by Grant No. NsG 120 from the National Aeronautics and Space Administration to Prof. Wyckoff.

REFERENCES

1. TYRÉN F., *Nova Acta R. Soc. Scient. Upsal.* **12**, 7 (1940).
2. O'BRYAN H. M. and SKINNER H. W. B., *Proc. R. Soc. Lond.* **A176**, 229 (1940).
3. FISCHER D. W., *J. chem. Phys.* **42**, 3814 (1965).
4. MATTSON R. A. and EHLERT R. C., *Advances in X-ray Analysis*, Vol. 9, p. 471, Plenum Press, New York (1966).
5. CHUN H. U. and HENDEL D., *Z. Naturforsch.* **22a**, 1401 (1967).
6. FISCHER D. W. and BAUN W. L., *J. appl. Phys.* **39**, 4757 (1968).
7. FISCHER D. W., *J. appl. Phys.* **40**, 4151 (1969).
8. FOMICHEV V. A., *Fiz. tverd. Tela* **8**, 2892 (1966); *Soviet Phys. solid State* **8**, 2312 (1967).
9. FOMICHEV V. A., ZIMKINA T. M. and ZHUKOVA I. I., *Fiz. tverd. Tela* **10**, 3073 (1969); *Soviet Phys. solid State* **10**, 2421 (1969).
10. CHUN H. U. and KLEIN G. *Phys. Lett. A*, **1968**, 28.
11. KOSTER A. S. and MENDEL H., *J. Phys. Chem. Solids*, **31**, 2511 (1970).
12. KOSTER A. S. and MENDEL H., *J. Phys. Chem. Solids*, **31**, 2523 (1970).
13. DAVIDSON F. D. and WYCKOFF R. W. G., *Norelco Repr* **14**, 3 (1967).
14. DAVIDSON F. D. and WYCKOFF R. W. G., *Advances in X-ray Analysis*, Vol. 9, p. 344, Plenum Press, New York (1966).
15. KOSTER A. S., *Proc. K ned. Akad. Wet.* **73**, 228 (1970).
16. MENDEL H. and KOSTER A. S., *J. Phys. C* (*Proc. Phys. Soc.*) **3**, 855 (1970).
17. LIEFELD R. J., HANZÉLY S., KIRBY T. B. and MOTT D., *Advances in X-ray Analysis*, Vol. 13, p. 373, Plenum Press, New York (1970).
18. HOLLIDAY J. E., *Norelco Repr* **14**, 84 (1967).
19. VAINSHTEIN E. E., BRIL' M. N. and STARYI I. V., *Izv. Akad. Nauk SSSR* **20**, 784 (1956).
20. KRAUSE B. and WHITE E. W., U.S. Clearinghouse Fed. Sci. Techn. Inf. 1968, AD 673321.

J. Phys. Chem. Solids, 1971, Vol. 32, pp. 2693–2698. Pergamon Press. Printed in Great Britain

ON THE SCATTERING OF X-RAYS BY STRUCTURES CONTAINING A RANDOM DISTRIBUTION OF DEFECTS*

D. T. KEATING
Brookhaven National Laboratory, Upton, N.Y. 11973, U.S.A.

(*Received* 18 *February* 1971)

Abstract – A recent treatment of the diffuse scattering of X-rays by defect structures (Keating 1968) has been shown to contain an approximation which is incorrect in the first order of the concentration of the defects (Hall 1969). When correctly treated the diffuse scattering is referred to the mean (dilated) lattice and the diffuse scattering attenuated by the same factor as the Bragg reflections. This treatment avoids expanding any exponential in powers of its argument.

1. INTRODUCTION

IN A RECENT paper (Keating[1]) the scattering of X-rays by a crystal containing a random array of defects was considered. This treatment shows that there is a dilation of the average crystal lattice, and the Bragg peaks are displaced by a corresponding amount and weakened by an attenuation factor, first introduced by Krivoglaz[2]. The diffuse scattering was given approximately as the square of the appropriate Fourier transform of a single defect referred to the original (undilated) crystal lattice whose atomic scattering factors were not weakened by an attenuation factor. Hall[3] has shown that this prediction regarding the undilated lattice and absence of an attenuation factor is incorrect due to a neglect of terms which are of first order in the concentration of defects. In order to demonstrate this error the exponentials like exp (ix) were expanded to second order and appropriate terms regrouped.

It is the purpose of this paper to correct this error without the expansion of such exponentials and give the correct expression for the diffuse scattering. The diffuse scattering is found to be referred to the average (dilated) lattice and weakened by the same attenuation factor as the Bragg peaks. This attenuation factor is not that due to an artificial temperature factor involving the mean square atomic displacements. The attenuation factor for static displacements may in fact be quite different (Krivoglaz[4]). The results of a computer calculation are presented to demonstrate this difference.

2. CALCULATIONS

In order to simplify notation we define the following quantities:

$$s_j = (\exp(i\boldsymbol{\kappa}\,.\,\boldsymbol{\mu}_{mj}) - 1) \tag{1a}$$

$$t_j = (\exp(-i\boldsymbol{\kappa}\,.\,\boldsymbol{\mu}_{nj}) - 1). \tag{1b}$$

The notation is that used by Keating and Hall, where atoms initially at $\mathbf{r}_m$ and $\mathbf{r}_n$ are displaced by the amounts $\boldsymbol{\mu}_{mj}$ and $\boldsymbol{\mu}_{nj}$ due to the presence of a defect at the j-th defect site. Here $\boldsymbol{\kappa}$ is the difference in wavevectors of the scattered and incident X-ray beams. For the sake of clarity only the scattering by the matrix atoms is considered in detail. The attenuation and change in phase of the scattering of a matrix atoms is (Keating[1]).

$$A_m\,e^{i\Phi_m} = \prod_j A_{mj} = \prod_j (1 + ps_j), \tag{2}$$

where p is the fraction of defect sites occupied by defects. The attenuation factor A_m is essentially independent of the site m and the phase Φ_m arises from the mean displacement of an atom originally at $\mathbf{r}_m$ to the position $\mathbf{r}'_m$ on the mean (dilated) lattice. The diffuse intensity is the difference between the expectation of the intensity and the product of the expectation of the scattering amplitude and its conjugate. The diffuse intensity scattered by the matrix atoms is then found by Keating (see equation (31)) and Hall (see equation (2)) to be

---

*Work supported by the U.S. Atomic Energy Commission.

$$I_m = f_a{}^2 \sum_m \sum_n \mathrm{e}^{i\kappa.(\mathbf{r}_m-\mathbf{r}_n)} \{\prod_j [1+p(s_j+t_j+s_jt_j)] - \prod_j [1+ps_j][1+pt_j]\}. \quad (3)$$

The products are to be taken over all defect sites. Factoring out the last product which represents the attenuation factor and phase factor representing the change to the mean (dilated) lattice we may write for equation (3),

$$I_m = f_A{}^2 A_m{}^2 \sum_m \sum_n \mathrm{e}^{i\kappa.(\mathbf{r}'_m-\mathbf{r}'_n)} \times \left\{\prod_j \left[1+\frac{p(1-p)s_jt_j}{(1+ps_j)(1+pt_j)}\right] - 1\right\}. \quad (4)$$

Using the expansion formula for a product (Keating equation (18) or Hall equation (3)) we write equation (4) as

$$I_m = f_A{}^2 A_m{}^2 \sum_m \sum_n \mathrm{e}^{i\kappa.(\mathbf{r}'_m-\mathbf{r}'_n)} \left\{ \sum_j \frac{p(1-p)s_jt_j}{A_{mj}A_{nj}} + \frac{1}{2!} \sum\sum_{j\neq k} \frac{p^2(1-p)^2 s_jt_js_kt_k}{A_{mj}A_{nj}A_{mk}A_{nk}} + \frac{1}{3!} \sum\sum\sum_{j\neq k\neq 1} \frac{p^3(1-p)^3 s_jt_js_kt_ks_1t_1}{A_{mj}A_{nj}A_{mk}A_{nk}A_{m1}A_{n1}} + \cdots \right\}. \quad (5)$$

The N terms with $m = n$ in equation (3) yield $Nf_A{}^2A_m{}^2(A$[illegible]$-1)$. This would be the expression for the diffuse scattering if there were no correlation between the displacements at sites m and n when defects are present. We can view the series within the braces in equation (5) as contributions to the diffuse scattering arising from correlations between sites m and n due to respectively one defect, two defects, three defects, etc. For $m = n$ this series within the braces must be equal to $(A_m{}^{-2}-1)$. The magnitude of these terms for $m = n$ serves as an appropriate criteria for the importance of single, double, and triple defect scattering etc. We note that the first term within the braces in equation (5) with $m = n$ can be expressed as

$$-p(1-p)\frac{\mathrm{d}\ln A_m{}^2}{\mathrm{d}\,(p(1-p))} = -p(1-p)A_m{}^{-2}\frac{\mathrm{d}A_m{}^2}{\mathrm{d}\,(p(1-p))}. \quad (6)$$

The ratio of this first term to $(A_m{}^{-2}-1)$ or the relative importance of the single defect scattering term is

$$-p(1-p)(1-A_m{}^2)^{-1}\frac{\mathrm{d}A_m{}^2}{\mathrm{d}\,(p(1-p))}. \quad (7)$$

If we consider the first and second terms in equation (5), (the second and third terms in the expansion of the product) the term analagous to the term in square brackets in Hall's equation (5) (keeping terms of first order in the arguments of exponentials) is

$$1+p(1-p) \times \sum_{k\neq j} \frac{(\boldsymbol{\kappa}\,.\,\boldsymbol{\mu}_{mk})(\boldsymbol{\kappa}\,.\,\boldsymbol{\mu}_{nk})}{[1+ip(\boldsymbol{\kappa}\,.\,\boldsymbol{\mu}_{mk})][1-ip(\boldsymbol{\kappa}\,.\,\boldsymbol{\mu}_{nk})]}. \quad (8)$$

Clearly, this is not linear in the displacements and hence cannot represent a lattice dilatation.

We also recognize the first term in equation (5) as the square of the magnitude of a sum written as

$$p(1-p) \sum_j \left| \sum_m f_A A_m \frac{(\mathrm{e}^{i\kappa.\mu_{mj}}-1)}{A_{mj}} \mathrm{e}^{i\kappa.\mathbf{r}'_m} \right|^2. \quad (9)$$

This is analagous to Hall's equation (7) except that his Debye–Waller factor is replaced by A_m and there is the additional complex factor A_{mj} appearing in the denominator of equation (9). To be certain that the complex factor A_{mj} does not contain a term representing a lattice dilation multiply numerator and denominator by A^*_{mj}. If the defect has a center of symmetry the result is

$$-p(1-p)\sum_j f_A{}^2 A_m{}^2\left|\sum_m \frac{\sin(\boldsymbol{\kappa}\,.\,\boldsymbol{\mu}_{mj})\sin(\boldsymbol{\kappa}\,.\,\mathbf{r}'_{mj})+2(1-2p)\sin^2(\boldsymbol{\kappa}\,.\,\boldsymbol{\mu}_{mj}/2)\cos(\boldsymbol{\kappa}\,.\,\mathbf{r}'_{mj})}{[1+4p(1-p)\sin^2(\boldsymbol{\kappa}\,.\,\boldsymbol{\mu}_{mj}/2)]}\right|^2. \tag{10}$$

Equation (10) is clearly expressed in terms of the vectors $\mathbf{r}'_{mj}$ of the mean (dilated) lattice. For sufficiently small p, A_{mj} in equation (9) may be replaced by unity.

The other terms in equation (31) of Keating can be treated in a similar manner to give an expression similar to equation (32). The main terms in that equation can be written as

$$\begin{aligned} I_D = p\sum_j\ &(1-A_j{}^2)f_B{}^2 \\ &+p(1-p)\sum_j\left|A_j f_B\right. \\ &+\sum_m A_m f_A\,\mathrm{e}^{i\boldsymbol{\kappa}.\mathbf{r}'_{mj}}\frac{(\mathrm{e}^{i\boldsymbol{\kappa}.\boldsymbol{\mu}_{mj}}-1)}{A_{mj}} \\ &\left.+p\sum_i A_i f_B\,\mathrm{e}^{i\boldsymbol{\kappa}.\mathbf{r}'_{ij}}\frac{(\mathrm{e}^{i\boldsymbol{\kappa}.\boldsymbol{\mu}_{ij}}-1)}{A_{ij}}\right|^2. \end{aligned} \tag{11}$$

The primed vectors are expressed in terms of the mean lattice. The terms not included in equation (11) are of the order p^2 and are discussed in the appendix.

3. DISCUSSION

Hall is correct. The diffuse intensity should be referred to the mean (dilated) lattice and be attenuated by the same factor as the Bragg peaks. However, this method of proof avoids the procedure of expanding the exponential, grouping terms, and identifying them. Furthermore, if only quadratic terms in the arguments of the exponentials are retained then the attenuation factor is identified as a Debye–Waller factor or artificial temperature factor $2M' = \langle(\boldsymbol{\kappa}\,.\,\boldsymbol{\mu}_{mj})^2\rangle$, Hall (see equation (7)). The attenuation factor used in this treatment is not related to the mean square atomic displacements unless $\boldsymbol{\kappa}\,.\,\boldsymbol{\mu}_{mj}$ is small for *all* the displacements. The reason for this lies in the fact that the probability distribution for static displacements is not described by a Gaussian distribution as it is in the case of thermal displacements in the harmonic approximation (Krivoglaz[4]). The disparity between exp $(-2M')$ and $A_m{}^2$ is illustrated in Fig. 1 for a case in which the displacements are large. The case is that of a hcp crystal with the ideal c/a ratio and a Poisson's ratio of 0·3 containing basal plane dislocation loops of 148 atoms each. The displacements were calculated with a Control Data CDC-6600 computer using the expressions given by Keating and Goland [5] for the displacement field. Displacements less than 0·005 of the largest displacement were set equal to zero, or the displacements of 1,192,830 atoms were taken into consideration. The weakening factors exp $(-2M')$ and $A_m{}^2$ for several (HK . L) reflections are plotted vs. $2p$ in Fig. 1, where p is the concentration of loops expressed as a fraction of matrix atoms present in the form of loops.

Because the displacements are largest in the direction of the hexagonal axis, the $(\boldsymbol{\kappa}\,.\,\boldsymbol{\mu}_{mj})$'s are largest when $\boldsymbol{\kappa}$ is in this direction, and there is a strong dependence of the weakening factors on the Miller index L. Thus for a given concentration the figure is a good illustration of the discrepancy between $A_m{}^2$ and exp $(-2M')$ as the magnitude of the $(\boldsymbol{\kappa}\,.\,\boldsymbol{\mu}_{mj})$'s are varied. As long as the $(\boldsymbol{\kappa}\,.\,\boldsymbol{\mu}_{mj})$'s are all small the two weakening factors give similar results; when this is not the case, as in the case

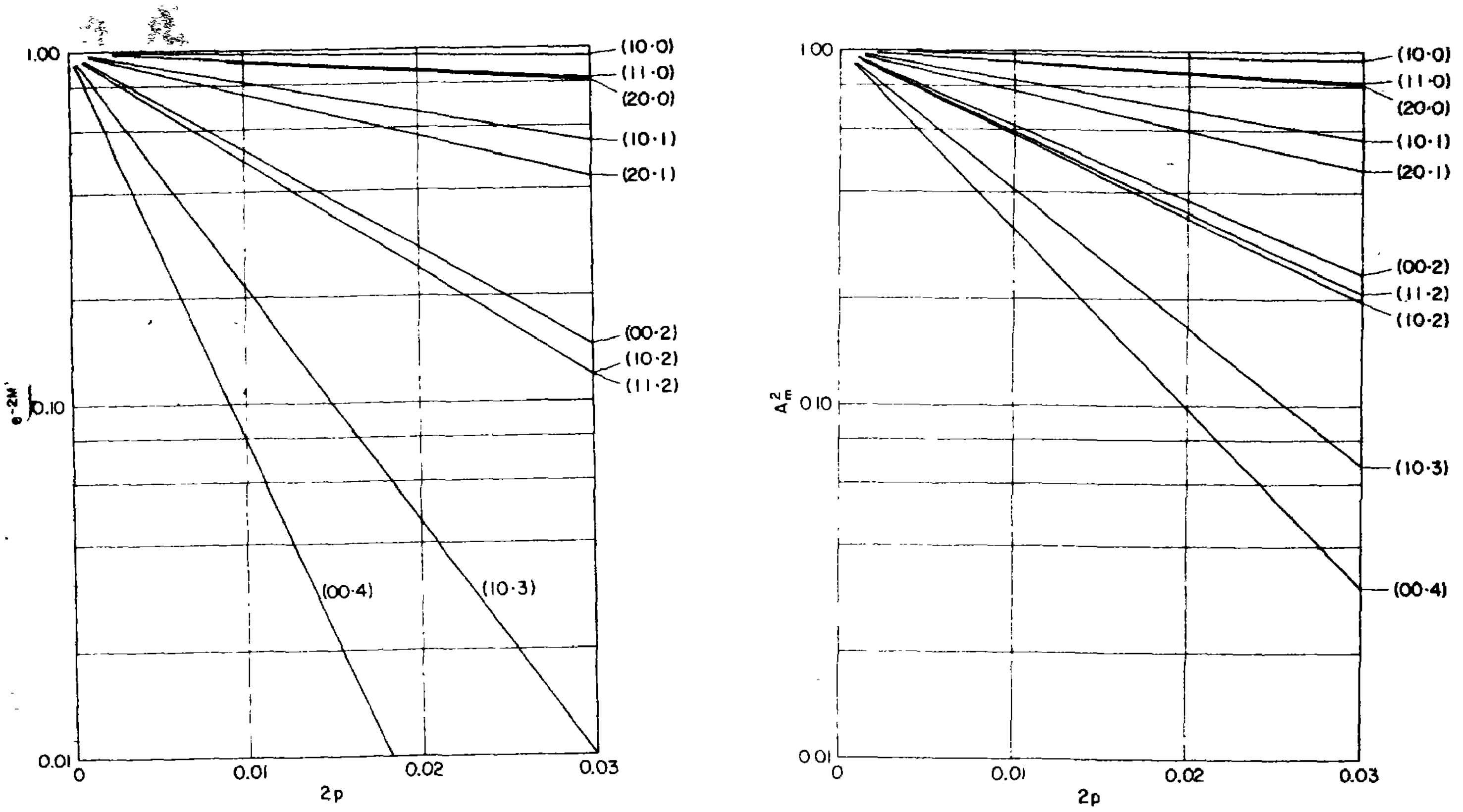

Fig. 1. The weakening factors (a) exp $(-2M')$ and (b) $A_m{}^2$ as a function of $2p$, a measure of the concentration of basal plane dislocation loops in a h.c.p. crystal. If the $(\kappa . \mu_{mj})$'s are all small the two factors are similar (compare the two for the (10·0) reflection). The disparity between the two increases when this condition is not met (compare the two (00·4) reflections), and (a) overestimates the weakening.

of the (00·4) reflection $\exp(-2M')$ overestimates the weakening. This can be understood from the fact that $|e^{i\kappa\cdot\mu_{\ast}}-1|\leq 2$ while $(\kappa\,.\,\mu_{mj})^2$ has no bound. This treatment has an advantage in the interpretation of the terms in equation (5) according to the powers of $p(1-p)$ as single, double, triple defect scattering, etc. Furthermore, a criterion for the relative importance of the single defect scattering is established in equation (7). For example, in Fig. 1 $A_m{}^2$ is essentially exponential in the concentration so that to a good approximation equation (7) becomes $(-\ln A_m{}^2)/(A_m{}^{-2}-1)$. That is, for $A_m{}^2 = 0{\cdot}8, 0{\cdot}4$, and $0{\cdot}1$ the relative contribution of the single defect scattering is respectively 89·3%, 61·1%, and 25·6% of the total diffuse scattering. However, it should be stressed that the criterion is not exact in the sense that the relative contribution of the single defect scattering is given exactly for any value of κ. Rather if the fraction is small then it would be prudent to consider the effects of the other terms in equation (5).

In the experimental observations of BeO and diamond considered by Keating the diffuse intensity appears to be stronger on the high angle side of the reflections as if it were centered at the undilated lattice position rather than at the mean dilated lattice position. In a computer simulation of an interstitial defect in the bcc position of a simple cubic lattice (Keating and Goland[6]) it is found that when the strength of the defect is large, the diffuse scattering is larger on the high angle side of the reflections (see the (b) parts of the figures). It is possible that a complex defect or cluster with a large effective strength is the explanation of the apparent displacement of the diffuse scattering to the high angle side of the reflections in BeO and diamond.

Acknowledgements—The author is grateful to Mrs. Lydia Bargiuk and Mrs. Patricia Moll for their programming of the weakening factors shown in Fig. 1.

REFERENCES

1. KEATING D. T., *J. Phys. Chem. Solids* **29**, 771 (1968).
2. KRIVOGLAZ M. A., *Phys. Metal. Metallogr.* **7**, No. 5, 11 (1959).
3. HALL C. R., *J. Phys. Chem. Solids* **30**, 919 (1969).
4. KRIVOGLAZ M. A., *Theory of X-ray and Thermal Neutron Scattering by Real Crystals*, p. 228, Plenum Press, New York (1969).
5. KEATING D. T. and GOLAND A. N., *J. appl. Phys.* **39**, 6018 (1969).
6. KEATING D. T. and GOLAND A. N., *Acta crystallogr.* **A27**, 134 (1971).

APPENDIX

There are other terms in the diffuse scattering equation (31) of Keating which can be treated in the same manner as the scattering from the matrix atoms. If only those terms corresponding to single defect scattering are retained and the fact that $\mu_{lj}=-\mu_{jl}$ is used, then the single defect scattering can be written as

$$\begin{aligned}
I_D &= p\sum_l\,(1-pA_l{}^2)f_B{}^2\\
&+p^2(1-p)\sum_{lk}\left\{A_lA_kf_B{}^2\,e^{i\kappa.r'_{lk}}\frac{(e^{i\kappa.\mu_{lk}}-1)}{A_{lk}^2}+\text{Conj.}\right\}\\
&+p^2(1-p^2)\sum_{lk}A_lA_kf_B{}^2\,e^{i\kappa.r'_{lk}}\frac{(e^{i\kappa.\mu_{lk}}-1)^2}{A_{lk}^2}\\
&+p^3(1-p)\sum_j\sum_{l\neq k}A_lA_kf_B{}^2\,e^{i\kappa\cdot r'_{lk}}\\
&\times\left(\frac{e^{i\kappa\cdot\mu_{lk}}}{A_{lk}}\right)^2\frac{(e^{i\kappa\cdot\mu_{lj}}-1)}{A_{lj}}\frac{(e^{-i\kappa\cdot\mu_{kj}}-1)}{A_{kj}}\\
&+p(1-p)\sum_{ml}\left\{A_mA_lf_Af_B\,e^{i\kappa\cdot r'_{ml}}\frac{(e^{i\kappa\cdot\mu_{ml}}-1)}{A_{ml}}+\text{Conj.}\right\}\\
&+p^2(1-p)\sum_j\sum_{ml}\left\{A_mA_lf_Af_B\,e^{\,i\kappa\cdot r'_{ml}}\right.\\
&\times\left.\left(\frac{e^{i\kappa\cdot\mu_{ml}}}{A_{ml}}\right)\frac{(e^{i\kappa\cdot\mu_{mj}}-1)}{A_{mj}}\frac{(e^{-i\kappa\cdot\mu_{lj}}-1)}{A_{lj}}+\text{Conj}\right\}\\
&+p(1-p)\sum_j\sum_{mn}A_mA_nf_A{}^2\,e^{i\kappa\cdot r'_{mn}}\\
&\times\frac{(e^{i\kappa\cdot\mu_{mj}}-1)}{A_{mj}}\frac{(e^{-i\kappa\cdot\mu_{nj}}-1)}{A_{nj}}.
\end{aligned}\tag{A.1}$$

The factors A_{lj} etc. are defined as A_{mj} in equation (2). When equation (A.1) is compared term by term with equation (11), the difference is

$$\begin{aligned}
&p^2(1-p)\sum_{lk}\left\{A_lA_kf_B{}^2\,e^{i\kappa.r'_{lk}}\right.\\
&\times\left.(A_{lk}^{-1}-1)\frac{(e^{i\kappa.\mu_{lk}}-1)}{A_{lk}}+\text{Conj}\right\}\\
&+p^2(1-p^2)\sum_{lk}A_lA_kf_B{}^2\,e^{i\kappa.r'_{lk}}\frac{(e^{i\kappa.\mu_{lk}}-1)^2}{A_{lk}^2}
\end{aligned}$$

$$+p^2(1-p)\sum_j\sum_{l\neq k}A_lA_kf_B^2\,e^{i\kappa\cdot r'_{lk}}$$

$$\times\left[\left(\frac{e^{i\kappa\cdot\mu_{lk}}}{A_{lk}}\right)^2-1\right]\frac{(e^{i\kappa\cdot\mu_{lj}}-1)}{A_{lj}}\,\frac{(e^{-i\kappa\cdot\mu_{lk}}-1)}{A_{lk}}$$

$$+p^2(1-p)\sum_j\sum_{ml}\left\{A_mA_lf_Af_B\,e^{i\kappa\cdot r'_{ml}}\right.$$

$$\left.\times\left[\left(\frac{e^{i\kappa\cdot\mu_{ml}}}{A_{ml}}\right)-1\right]\frac{(e^{i\kappa\cdot\mu_{mj}}-1)}{A_{mj}}\,\frac{(e^{-i\kappa\cdot\mu_{lj}}-1)}{A_{lj}}+\text{Conj}\right\}.$$

These terms are of order p^2, and for the most part contain factors like $(A_{lk}^{-1}-1)$ which further reduce their importance.

J. Phys. Chem. Solids, 1971, Vol. 32, pp. 2699–2710. Pergamon Press. Printed in Great Britain

ETUDE DE LA REORIENTATION DES COMPLEXES LACUNE-IMPURETE DIVALENTE DANS NaCl DOPE*

P. DANSAS
Laboratoire de Physique Electronique, Bâtiment 220, Faculté des Sciences, 91-Orsay, France

(*Received* 15 *February* 1971)

Résumé – On étudie par la méthode des thermocourants de dépolarisation, la réorientation des complexes lacune-impureté dans les cristaux de NaCl dopés par Ca^{2+}, Cd^{2+}, Mn^{2+} et Mg^{2+}. On met en évidence un pic d'absorption principal monoénergétique qu'on attribue aux lacunes en position de premier voisin et un second, plus faible, caractérisable par plusieurs temps de relaxation, attribuable aux lacunes plus éloignées. Cette interprétation, donnée en considérant trois couches d'occupation pour la lacune autour de l'impureté, est généralisée au cas de NaCl dopé par une impureté divalente quelconque, en tenant compte des résultats publiés par d'autres auteurs pour Be^{2+}, Co^{2+}, Sr^{2+}, ainsi que de ceux obtenus par diffusion, conductivité et RPE.

Abstract – We study, by means of the depolarization thermocurrent method (I.T.C.), the reorientation of impurity-vacancy complexes in NaCl containing divalent substitutional ions such as Ca^{2+}, Cd^{2+}, Mn^{2+} and Mg^{2+}. Two thermocurrent peaks are noticeable: the greater one (monoenergetic) is ascribed to vacancies in nearest neighbour positions; the other (not compatible with a single relaxation time) to vacancies in more distant sites. This interpretation (given using a three-shell model) is extended to the case of NaCl doped with any divalent impurity: for this purpose, it is taken account of the results published by other authors concerning Be^{2+}, Co^{2+}, Sr^{2+}, and those obtained from diffusion, conductivity and E.P.R. measurements.

INTRODUCTION

LA RÉORIENTATION des complexes lacune-impureté divalente dans des monocristaux d'halogénures alcalins dopés a déjà fait l'objet de nombreux travaux expérimentaux. Comme on peut associer à ces complexes un moment dipolaire, l'étude de leur réorientation a souvent été effectuée par l'analyse de la polarisation acquise sous l'action d'un champ électrique. Les méthodes utilisées sont soit celle des pertes diélectriques[1], soit celle des courants transitoires[2], soit encore, plus récemment, celle des thermocourants de dépolarisation (initialement appelé ITC par Bucci et ses collaborateurs[3]).

Si l'on dispose d'un nombre assez élevé de résultats expérimentaux, fort peu de modèles par contre, ont été proposés pour expliquer le mécanisme de réorientation de ces complexes.

Le plus complet d'entre eux a été proposé par Dreyfus[2] pour expliquer les résultats expérimentaux qu'il a obtenus sur NaCl dopé par Sr^{2+}, Ca^{2+}, Cd^{2+}, Mn^{2+}, Zn^{2+} et Mg^{2+}, dont les rayons ioniques sont voisins ou différents de celui de l'ion substitué. Selon l'auteur les phénomènes de polarisation peuvent être convenablement interprétés en tenant compte de deux couches d'occupation pour la lacune: 12 positions de premier voisin (p–v), distantes de $a\sqrt{2}$ de l'impureté; 6 positions de second voisin (s–v), distantes de $2a$ de l'impureté (a étant le demi pas du réseau). Ce modèle prévoit, entre autres, que la majorité des lacunes est soit en position de p–v, lorsque le rayon R de l'impureté est grand devant celui R_0 de l'ion substitué, soit en position de s–v, dans le cas contraire; dans les deux situations évoquées on est conduit à prévoir une polarisation basse fréquence prépondérante. Or il faut remarquer qu'un certain nombre de résultats parus postérieurement au travail de Dreyfus vont à l'encontre de cette prévision (totalement ou en partie seulement):

---

*Ce travail fait partie d'une thèse de Doctorat es-Sciences présentée à la Faculté des Sciences d'Orsay par P. Dansas.

Bucci[4, 7] sur NaCl dopé par Sr^{2+} ($R > R_0$) et Be^{2+} ($R \ll R_0$) observe une polarisation haute fréquence prépondérante; en ce qui concerne NaCl dopé par Sr^{2+} on peut noter d'autre part que l'ensemble des résultats expérimentaux ne sont pas concordants: mise en évidence de trois phénomènes de relaxation par Dreyfus, de deux seulement par Bucci.

A partir de leurs mesures effectuées en haute température Jain et Lal[6] concluent, en utilisant ce modèle, à l'existence d'une majorité de lacunes en position de s–v; on arrive à une conclusion différente (majorité de lacunes en position de p–v) si on considère les résultats de Capelletti[5] obtenus à basse température (cas de Co^{2+}).

Tels sont quelques exemples de désaccord entre des résultats expérimentaux et le modèle proposé par Dreyfus.

En ce qui concerne le modèle lui-même, il convient de faire un certain nombre de remarques. Il existe, en effet, dans l'argumentation de Dreyfus, un point qui, sans paraître a priori déraisonnable, est néanmoins suceptible d'être remis en cause.

Dans ses expériences Dreyfus met en évidence trois phénomènes de polarisation, celui situé en plus basse fréquence n'étant par monoénergétique. Il attribue ce dernier aux lacunes présentes dans des sites plus éloignés que ceux de second voisin; les deux autres phénomènes de relaxation sont alors analysés en ne tenant compte cette fois, que des lacunes en position de p–v et s–v. En procédant ainsi, il n'a pu être vérifié que l'importance et la position du phénomène de polarisation basse fréquence (attribué aux lacunes présentes dans des sites plus éloignés que ceux de s–v) étaient bien compatibles avec celles des autres phénomènes de polarisation (attribués aux lacunes situées en position de p–v et s–v). Cette dernière remarque a conduit Franklin[9] à réexaminer en partie le modèle de Dreyfus. En adoptant des hypothèses qui concordent avec celles de Dreyfus (dans le cas précis de NaCl dopé par Mn^{2+}) et tenant compte en outre des lacunes en position de troisième voisin (t–v) (distantes de $a\sqrt{6}$ de l'impureté), prévoit des phénomènes de polarisation dont les grandeurs respectives ne concordent pas avec celles observées par Dreyfus.

Etant donné qu'il existe certaines contradictions, tant en ce qui concerne les expériences que le modèle lui-même, il nous a paru souhaitable:

De reprendre, d'une part, des mesures de polarisation sur des cristaux déjà étudiés par Dreyfus (NaCl dopé par Ca^{2+}, Cd^{2+}, Mn^{2+} et Mg^{2+}) celles sur NaCl dopé par Be^{2+}, Co^{2+} et Sr^{2+} ayant été obtenus[4–7] récemment. Il est en effet très important de préciser si tous les phénomènes de polarisation observés par Dreyfus sont bien attribuables à la relaxation de complexes lacune-impureté.

D'autre part de calculer, en considérant trois couches d'occupation pour la lacune, les temps de relaxation et les polarisations correspondantes, sans se limiter, comme l'a fait Franklin à un calcul numérique (dans le seul cas de NaCl dopé par Mn^{2+}) qui ne revêt aucune généralité.

1. ETUDE EXPERIMENTALE DES COMPLEXES LACUNE-IMPURETE DANS DES CRISTAUX DE NaCl DOPES PAR Ca^{2+}, Cd^{2+}, Mn^{2+} et Mg^{2+}

(1.1) *Echantillons et conditions experimentales*

Les monocristaux utilisés* sont faiblement dopés, les concentrations en impuretés (déterminées par spectrophotométrie d'absorption atomique) sont indiquées dans le Tableau 1.

Pour étudier les propriétés diélectriques de ces cristaux, nous avons utilisé la méthode des thermo-courants de dépolarisation[3]. Nous

---

*Ces échantillons nous ont été fournis par le Prof. Korth Laboratoire de Physique, Kiel, Allemagne.

Tableau 1. *Enérgie d'activation et facteurs pré-exponentiels dans* NaCl *dopé*

Impuretés	$E_{(eV)}$	$1/\tau_0(S^{-1})$	Concentration atomique	Rayon (Å) (Pauling)
Ca^{2+}	0,695	$1,2\times 10^{14}$	$1,5\times 10^{-5}$	0,99
Cd^{2+}	0,65	$1,5\times 10^{13}$	$3,5\times 10^{-4}$	0,97
Mn^{2+}	0,67	$1,1\times 10^{14}$	7×10^{-5}	0,80
Mg^{2+}	0,63	$3,4\times 10^{13}$	7×10^{-6}	0,65

ne rappellerons ici que brièvement le principe de cette méthode. Lorsqu'une substance contient des dipôles, un certain nombre d'entre eux peuvent être orientés sous l'action d'un champ électrique continu. Une trempe à une température très basse, pour laquelle le temps de relaxation est devenu extrèmement grand, permet de 'geler' la polarisation acquise; le champ peut alors être coupé sans que l'état de polarisation de la substance se trouve modifié. Si on fait remonter la température à une vitesse contrôlée, on obtient un pic de thermocourant (correspondant à la désorientation progressive des dipôles), dont les caractéristiques peuvent être reliées aux grandeurs cherchées: énergie d'activation, facteur pré-exponentiel, polarisation. Etant donné la nécessité l'opérer à basse température, cette méthode permet de mieux séparer expérimentalement les différents phénomènes de polarisation. Nous avons utilisé, pour la mesure du courant, un électromètre Cary 401 dont la résolution est de 10^{-17} A.

Les échantillons (dont les faces sont peintes à l'aide d'une laque à l'argent) sont, avant la mesure, chauffés pendant quelques heures, à des températures voisines de 400°C puis rapidement portés à une température inférieure à 0°C, pour laquelle la cinétique de disparition des dipôles est lente[10], en particulier si les cristaux sont faiblement dopés.

Les échantillons sont généralement polarisés par des champs de l'ordre de 10 Kv/cm, pendant quelques minutes, à une température voisine de celle pour laquelle le thermocourant est maximal. Les enregistrements sont effectués pour des vitesses de remontée de la température voisines de 0, 1°KS^{-1}.

(1.2) *Résultats obtenus sur* NaCl *dopé par* Ca^{2+}, Cd^{2+}, Mn^{2+} *et* Mg^{2+}

On a regroupé sur la Fig. 1 les thermocourants de dépolarisation observés pour les quatre impuretés utilisées. Sauf pour Ca^{2+} où il n'existe qu'un seul pic, l'enregistrement de thermocourant présente deux pics, presque dissociés dans le cas de Mg^{2+} et Cd^{2+}, fortement imbriqués dans le cas de Mn^{2+}. Les pics

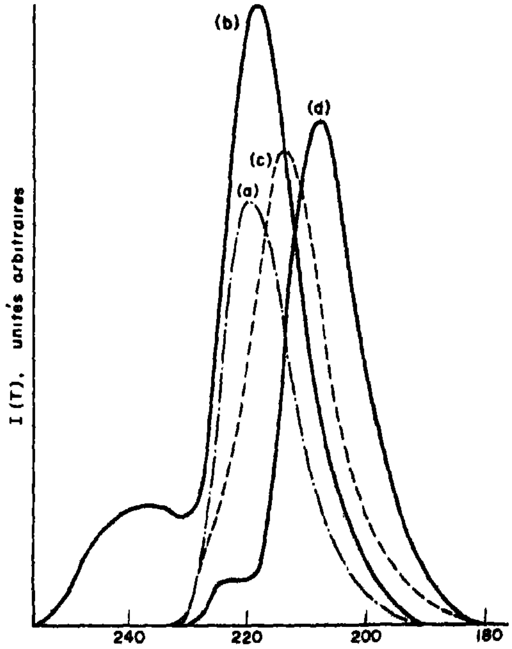

Fig. 1. Thermocourants de dépolarisation en fonction de la température, pour NaCl dopé par: Ca^{2+}(a); Cd^{2+}(b); Mn^{2+}(c); Mg^{2+}(d).

obtenus pour une même impureté sont trop dissemblables pour qu'on puisse analyser le pic le plus petit avec une précision suffisante. On peut cependant affirmer qu'il n'est pas à temps de relaxation unique (la courbe Log $P/I = \varphi(1/T)$ n'est pas une droite; on appelle P la valeur de la polarisation de l'échantillon et I celle du thermocourant à la température T)[3]. Le pic principal est, par contre, monoénergétique et a les caractéristiques indiquées sur le Tableau 1. Si l'on compare nos résultats à ceux de Dreyfus, on retrouve bien un phénomène de polarisation principal à temps de relaxation unique (les valeurs des énergies d'activation étant concordantes) ainsi qu'un second phénomène de polarisation (de plus faible amplitude) qui ne l'est pas. Par contre nous ne mettons pas en évidence le troisième phénomène de polarisation observé par Dreyfus (qui, dans nos expériences, devrait se traduire par l'existence d'un pic supplémentaire situé à une température inférieure à celle du pic principal), bien que la méthode de mesure utilisée soit au moins aussi sensible que celle employée par Dreyfus.

2. DETERMINATION DES MODES DE RELAXATION, FREQUENCES DE RELAXATION ET POLARISATIONS

(2.1) *Modes de relaxation électriques*

Pour faire cette détermination, il faut, selon une méthode tout à fait classique, établir le bilan dynamique des populations des sites possibles pour la lacune, à partir des fréquences d'échanges entre ces sites. Le principe de ce calcul est donné dans l'Annexe 1.

Nous considérerons ici trois couches d'occupation pour la lacune, soit 42 sites possibles: 12 dans la position de p–v (distants de $a\sqrt{2}$ de l'impureté), 6 dans la position de s–v (distants de $2a$ de l'impureté), 24 dans la position de t–v (distants de $a\sqrt{6}$ de l'impureté) qui, dans une représentation par rapport à un système d'axes 0, x, y, z (l'impureté étant placée à l'origine) se répartissent comme l'ind[illegible] Tableau 2.

Tableau 2. Répartition des différents sites considérés pour la lacune

	Sites équivalents				
Plan	Nombre				Position
$Z = \pm 2a$	1(+)	1(−)	1(+)	10(−)	$s-v$
	4(+)	4(−)	2(+)	9(−)	$t-v$
$Z = \pm a$	4(+)	4(−)	3(+)	8(−)	$p-v$
	8(+)	8(−)	4(+)	7(−)	$p-v$
$Z = 0$	4		5		$p-v$
	4		6		$s-v$

On appellera w_{ij} la fréquence de saut de la lacune d'un site en position de $i^{\text{ème}}$ voisin vers un site en position de $j^{\text{ème}}$ voisin, w_{10} celle relative à l'échange lacune-impureté et on posera: $w_0 = w_{11} + w_{10}$. On supposera d'autre part, que les échanges entre deux sites distants de plus de $a\sqrt{2}$ sont impossibles.

Les quatre fréquences de relaxation possibles sont les valeurs propres de la matrice A donnée en Annexe 1.

(2.2) *Fréquences de relaxation et polarisations*

Hypothèses

Nous effectuerons le calcul dans le cas où la majorité des lacunes est en position de premier voisin (les résultats de celui-ci seront utilisés lors de l'identification des phénomènes de relaxation). On peut considérer dans ce cas que les valeurs de la fréquence de saut $w_{n,n+1}$ et celle $w_{n+1,n}$ du saut inverse vont varier lentement et progressivement lorsque n croît, et atteindre, pour n assez grand, la valeur de la fréquence de saut relative à la lacune libre. Ceci peut se traduire dans un modèle à trois couches, par les inégalités suivantes:

$w_{12} > w_{23}$ (éloignement de la lacune)

$w_{32} < w_{21}$ (rapprochement de la lacune)

$w_{23} < w_{32}$; $w_{12} < w_{21}$; $w_{13} < w_{31}$

$w_{13} < w_{12}$; $w_{33} < w_{32} < w_{31}$.

Nous avons supposé que $w_{n,n+1}$ est de la forme $w_{n,n+1} = A \exp -(E_{n,n+1}/kT)$, $E_{n,n+1}$

désignant la barrière qui sépare un site en position de $n^{\text{ème}}$ voisin d'un site en position de $(n+1)^{\text{ème}}$ voisin; elle tend vers 0,8 eV [11] pour n grand (énergie de migration de la lacune libre). Les énergies relatives à la migration d'une lacune autour de l'impureté obtenues à partir de mesures de pertes diélectriques donnent des valeurs systématiquement plus faibles d'au moins 0,1 eV.

On peut raisonnablement penser que la barrière s'opposant à l'échange t–$v \rightarrow t$–v est suffisamment grande devant celle qui s'oppose au retour direct d'un site t–v vers un site p–v, pour qu'on ait en particulier à basse température, $w_{33} \ll w_{31}$.

Il est difficile de préciser a priori les valeurs respectives de w_{13}, w_{23} d'une part et w_{21}, w_{31} d'autre part; tout au plus peut on dire qu'elles sont voisines deux à deux.

Nous supposerons d'autre part, que w_0 peut prendre des valeurs différentes suivant l'impureté utilisée, mais qu'on aura toujours pour une impureté donnée:

$$w_0 \gg w_{31}, w_{32}, w_{21}$$

(w_0 désignant la fréquence de saut la plus grande de toutes).

Si on adopte ces hypothèses on est amené à prévoir un phénomène de polarisation haute fréquence prépondérant, à temps de relaxation unique, attribuable aux lacunes en position de p–v et un phénomène de polarisation basse fréquence, caractérisable par plusieurs temps de relaxation voisins, rendant compte de l'existence des lacunes en position de s–v et t–v simultanément (voir Annexe 2).

3. IDENTIFICATION DES PHENOMENES DE RELAXATION

La situation que nous avons décrite ci-dessus (polarisation basse température prépondérante) est bien celle observée dans nos expériences sur NaCl dopé par Ca^{2+}, Cd^{2+}, Mn^{2+} et Mg^{2+} et dans celle de Bucci sur NaCl dopé par Sr^{2+}. Néanmoins cette concordance ne suffit pas à justifier les hypothèses que nous avons adoptées, tant que nous n'aurons pas expliqué la différence entre nos résultats joints à ceux de Bucci et ceux de Dreyfus (existence d'un phénomène supplémentaire pour cet auteur).

Ceci peut être fait en considérant le cas de NaCl dopé par Mn^{2+}, exemple pour lequel Watkins[19] a montré par R.P.E. que la majorité des lacunes est en position de p–v. Lorsque cette situation existe, les fréquences de relaxation relatives au s–v et t–v ne peuvent être que voisines (voir leur expression Annexe 2). C'est en effet ce qui ressort de nos calculs ainsi que de ceux de Franklin, bien que ce dernier fasse sur w_0 une hypothèse très différente de la nôtre. Il ne semble donc pas qu'il soit possible, comme le fait Dreyfus, d'attribuer aux s–v et voisins plus éloignés (t–v en particulier) des fréquences de relaxation très différentes, tout en supposant que la majorité des lacunes est en position de p–v.

Nous sommes donc conduits à penser que la polarisation haute fréquence mise en évidence par Dreyfus (et qui correspondrait dans nos expériences, à l'existence d'un pic supplémentaire situé à des températures plus basses que celles où nous observons le pic basse température) ne peut être attribuée aux seconds voisins. Il faut remarquer néanmoins qu'un tel phénomène de polarisation supplémentaire peut exister[12, 13] mais présente la particularité de n'apparaître qu'au cours d'un recuit; il ne semble donc pas qu'il s'agisse d'un phénomène de polarisation ayant la même origine que ceux dont nous avons discuté précédemment. Nous n'avons pas d'ailleurs reporté ici les résultats obtenus sur des cristaux de NaCl dopés par Zn^{2+} et Ni^{2+}, pour lesquels il y a apparition d'un tel pic supplémentaire: celui-ci disparaît après chauffage suivi de trempe, mais réapparaît très rapidement au cours d'un recuit, même à la température ambiante; simultanément le pic principal diminue. Il semble donc que ce soit un phénomène de ce genre que Dreyfus a observé.

Cette précision étant donnée, on peut dire que nos expériences et celles de Bucci sur NaCl dopé par Sr^{2+} sont en accord avec celles de Dreyfus pour les mêmes impuretés.

Dans ces conditions se trouve justifiée l'hypothèse suivant laquelle $w_0 \gg w_{21}, w_{31}, w_{32}$, la majorité de lacunes étant en position de premier voisin, ce qui entraîne nécessairement l'existence d'un phénomène de polarisation haute fréquence prépondérant. La réciproque est d'ailleurs vraie, puisque dans un modèle à deux couches seulement, l'existence d'un phénomène de polarisation haute fréquence prépondérant entraîne nécessairement: $w_0 > w_{21} > w_{12}$ (majorité des lacunes en position de *p–v*). Si on introduit alors les *t–v*, le phénomène de polarisation basse fréquence à considérer n'est plus monoénergétique, mais caractérisable par plusieurs temps de relaxation voisins et tient compte de l'existence des lacunes en position de *s–v* et *t–v* simultanément.

Les hypothèses que nous avons adoptées permettent donc de rendre compte de l'ensemble des résultats expérimentaux relatifs à NaCl dopé par Sr^{2+}, Ca^{2+}, Cd^{2+}, Mn^{2+}, Mg^{2+}, Co^{2+}, Be^{2+} (existence d'une polarisation basse température prépondérante).

4. INTERPRETATION DES RESULTATS EXPERIMENTAUX

(4.1) *Pic basse température*

Nous sommes conduits à attribuer ce phénomène de polarisation aux lacunes en position de *p–v*, avec une fréquence de relaxation:

$$\lambda_1 \simeq 2w_0 = 2(w_{11} + w'_{10}).$$

Le pic correspondant étant à temps de relaxation unique, il convient de déterminer la fréquence prépondérante dans l'expression de w_0. A partir de mesures diélectriques, on peut atteindre la plus grande d'entre elles et à partir de mesures de diffusion la plus faible (limitation par le mécanisme le plus lent [14, 15]. Ceci signifie que si dans l'expression de w_{11} et de w_{10} les facteurs préexponentiels ne sont pas très différents, on atteint à partir de mesures de pertes diélectriques le phénomène d'énergie la plus faible. Nous examinerons d'abord le cas des impuretés pour lesquelles les mesures de diffusion existantes sont ici utilisables. Les résultats obtenus à partir de mesures de diffusion[15–17] peuvent ainsi être résumés:

$$w_{DCa^{2+}} = 2{,}3 \cdot 10^{13} \exp\left(-\frac{0{,}96}{kT}\right);$$

$$w_{DCd^{2+}} \propto \exp\left(-\frac{0{,}92}{kT}\right)$$

$$w'_{DMn^{2+}} = 6{,}3 \cdot 10^{11} \exp\left(-\frac{0{,}71}{kT}\right).$$

Les valeurs de l'énergie et du facteur préexponentiel sont sensiblement modifiées lorsqu'on passe d'une impureté à l'autre.

On fait la constatation inverse à partir des mesures obtenues par relaxation diélectrique (voir Tableau 1).

On peut expliquer les différences obtenues entre les deux séries de résultats en admettant que par diffusion, on atteint l'échange direct lacune-impureté. On conçoit en effet que ce soit la fréquence de saut relatif à l'échange direct qui puisse être considérablement modifiée lorsque l'ion divalent change (l'interaction à courte distance entre l'ion divalent et les six ions Cl^- qui l'entrourent joue en effet un rôle prépondérant dans le mécanisme d'échange direct). On conçoit parallèlement que le saut de la lacune autour de l'impureté ne soit affecté qu'au 'second ordre' par le changement d'impureté, surtout si ces impuretés sont de rayons voisins

$$(R_{Ca^{2+}} = 0{,}99\ \text{Å};\ R_{Mn^{2+}} = 0{,}80\ \text{Å};\ R_{Cd^{2+}} = 0{,}97\ \text{Å}).$$

Dans ces conditions, nous pensons que la polarisation haute fréquence mise en évidence pour Ca^{2+}, Cd^{2+} et Mn^{2+} est dûe à la relaxation des premiers voisins (et plus particulièrement à l'échange entre premiers voisins) et que les grandeurs respectives de w_{11} et w_{10} sont celles schématisées sur la Fig. 3(a).

On admet généralement que l'échange lacune-impureté ne peut devenir prépondérant que si le rayon de l'impureté est suffisamment petit devant l'ion substitué et on justifie cette hypothèse à partir des considérations suivantes: l'énergie mise en jeu pour l'échange $Z^{2+} \rightleftarrows \boxed{Na^+}$ est plus grande que pour l'échange $\boxed{Na^+} \rightleftarrows Na^+$; l'ion Z^{2+} ayant une charge de plus que l'ion Na^+, la barrière de potentiel à franchir est plus grande, du fait de l'augmentation des forces de répulsion à courte distance avec les six ions Cl^- qui l'entourent; lorsque le rayon de l'ion Z^{2+} est petit (devant celui de l'ion Na^+) ces forces deviennent inférieures à celles qui existeraient pour un ion Na^+ dans la même position.

Pour traiter le cas de Mg^{2+}, nous ferons au préalable deux remarques:

Le terme d'énergie trouvé par relaxation diélectrique varie peu lorsqu'on passe de Ca^{2+} ($R = 0{,}99$ Å) à Mg^{2+} ($R = 0{,}68$ Å) bien que le rayon de Mg^{2+} commence à être assez différent de celui de Na^+ (0,95 Å).

L'énergie trouvée par diffusion décroît très rapidement quand on change l'ion divalent. Cette énergie passe de 0,96 eV pour Ca^{2+} à 0,71 eV pour Mn^{2+}, pour atteindre 0,46 eV pour Zn^{2+} (Chemla [18]).

Compte tenu de la grandeur de $R_{Mg}{}^{2+}$ on est en droit de penser, en examinant le diagramme des énergies de la Fig. 2, que l'énergie d'échange lacune-impureté sera plus faible que celle relative au saut p–$v \rightarrow p$–v, auquel cas on comprend mal que ce soit la valeur de l'énergie obtenue par relaxation diélectrique qui soit la plus élevée, à condition, bien entendu, que les facteurs préexponentiels dans l'expression de w_{10} et w_{11} aient des valeurs peu différentes.

On peut essayer de donner une réponse en examinant les résultats obtenus par Bucci [7] sur NaCl dopé par Be^{2+}. $R_{Be}{}^{2+}$(0,31 Å) étant très petit devant $R_{Na}{}^{2+}$, la possibilité d'échange direct peut devenir grande. Bucci trouve, par la méthode TCD, deux pics:

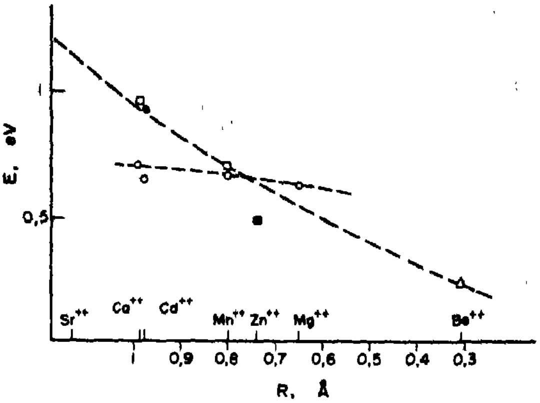

Fig. 2. Variation de l'énergie de rotation de la lacune et de l'énergie d'échange lacune-impureté dans NaCl dopé obtenues par: Diffusion: ■ (18); □ (15)(16); ● (17). Relaxation délectrique: ○ (+); △ (7).

Pic BT: fréquence de relaxation

$$f_1 = 2 \cdot 10^8 \exp\left(-\frac{0{,}26}{kT}\right)$$

Pic HT: fréquence de relaxation

$$f_2 = 6{,}5 \cdot 10^{12} \exp\left(-\frac{0{,}5}{kT}\right).$$

Il trouve bien comme nous, un pic BT supérieur en amplitude au pic HT. Il est vraisemblable que dans ce cas, le pic BT est attribuable à l'échange lacune-impureté; c'est tout au moins la conclusion que l'on peut formuler, si l'on admet, comme nous l'avons déjà fait, le processus d'identification suivant: des deux fréquences de saut w_{11} et w_{10}, c'est la dernière qui peut être la plus modifiée, lorsqu'on change d'impureté. En effet le facteur préexponentiel est 10^4 à 10^5 fois plus faible qu'il ne l'était dans le cas de Ca^{2+} ou Mn^{2+}; quant à l'énergie elle est devenue faible (0,26 eV au lieu de 0,96 et 0,71 eV pour Ca^{2+} et Mn^{2+}). Et parallèlement, pour l'autre fréquence de relaxation (qui ne concerne pas un saut faisant intervenir directement l'ion Be^{2+}) le facteur préexponentiel reste de l'ordre de ceux obtenus pour des ions plus gros.

On voit donc qu'en ce qui concerne la fréquence de relaxation des premiers voisins, le terme correspondant au saut d'énergie le plus élevé peut tout de même être prépondérant si l'on tient compte du fait que le facteur preexponentiel, dans l'expression de la fréquence d'échange direct, peut être très faible. C'est certainement le cas lorsque l'impureté est Mg^{2+}; les grandeurs respectives de w_{11} et w_{10} sont probablement celles schématisées sur la Fig. 3(b) pour Mg^{2+} et sur la Fig. 3(c) pour Be^{2+}.

On peut donc dire que dans NaCl, pour des ions de substitution allant de Ca^{2+} à Be^{2+}, ce phénomène de relaxation haute fréquence est attribuable à la rotation de la lacune autour de l'impureté (à l'exception de Be^{2+} pour lequel l'échange direct est prépondérant) et que la barrière d'énergie correspondante diminue progressivement lorsqu'on passe de Ca^{2+} à Mg^{2+} (cette variation est néanmoins peu importante: écart maximum 0,07 eV).

(4.2) *Pic haute température*

Lors de l'identification des phénomènes de relaxation, nous avons été conduits à attribuer cette polarisation basse fréquence ou haute température (P_{HT}) aux lacunes en position de s–v et t–v simultanément. Son importance par rapport à la polarisation basse température (P_{BT}) s'exprime par le rapport Q (voir Annexe 2):

$$Q = P_{HT}/P_{BT} \simeq w_{12}/w_{21} + 6w_{13}/w_{31}.$$

Si on appelle E_n l'énergie d'association du complexe, la lacune étant en position de $n^{\text{ème}}$ voisin (soit à une distance $a\sqrt{2n}$ de l'impureté), Q s'écrit:

$$Q \simeq \exp-(E_1-E_2)/kT + 6\exp-(E_1-E_3)/kT.$$

L'importance de cette polarisation basse température rend donc compte de la façon dont l'énergie d'association du complexe diminue lorsque la lacune est dans des sites de plus en plus éloignés de l'impureté et par là même de la population de ces différents sites.

Les courbes d'énergie d'association représentées sur la Fig. 4 vont nous permettre d'illustrer ce propos. La courbe a, relative à l'énergie d'association du complexe lacune-impureté dans NaCl dopé par Mn^{2+}, est obtenue par Franklin, de la façon suivante: il suppose que lorsque l'impureté et la lacune sont suffisamment éloignées, l'énergie d'association du complexe peut être obtenue avec une bonne approximation à partir de l'énergie coulombienne (courbe *b*) de deux charges de signes opposés, distantes de *d* et plongées dans un milieu de permittivité ϵ (ici celle de NaCl). Il adopte ensuite un lissage consistant à faire passer une courbe par les points expérimentaux E_1 et E_2 (ce sont les énergies d'association déduites du travail de Watkins), laquelle rejoint la courbe *b* au niveau du 5° voisin.

On se rend compte d'après ces courbes que les différences E_1-E_2 et E_1-E_3 seront

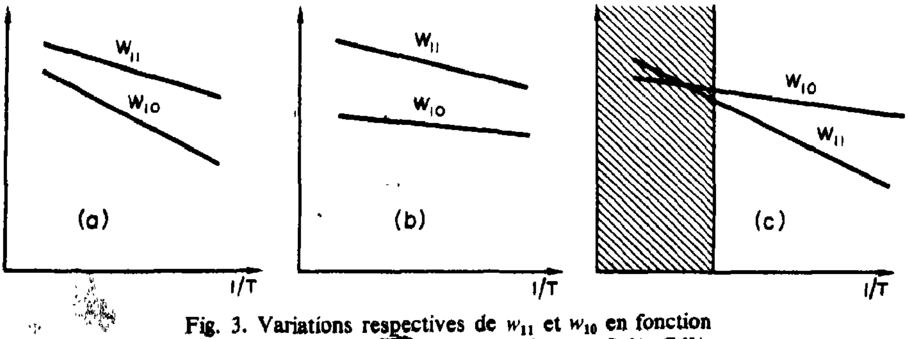

Fig. 3. Variations respectives de w_{11} et w_{10} en fonction de $1/T$ pour les différentes impuretés: (a): Ca^{2+}, Cd^{2+}, Mn^{2+}; (b): Mg^{2+}; (c): Be^{2+}; partie non hachurée.

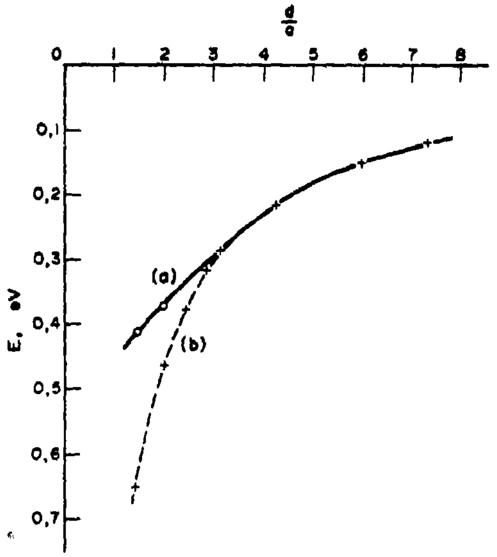

Fig. 4. Diagrammes d'énergie d'association (a): d'après Franklin[9] dans le cas de NaCl dopé par Mn^{2+}; O: points obtenus à partir des résultats de Watkins[19], (b): énergie d'association coulombienne; +: points calculés.

d'autant plus faibles que E_1 sera faible, ce qui favorisera l'importance du pic haute température.

On peut alors essayer de relier nos résultats à ceux obtenus à partir de mesures de diffusion ou de conductivité. En effet pour analyser celles-ci, on est amené à définir une enthalpie d'association, qui, dans un modèle de simple association n'est autre que E_1 (on considère par simplification que la lacune peut occuper deux états: associée ou libre).

L'enthalpie d'association, déterminée à partir de mesures de diffusion par Banasevich et ses collaborateurs[15, 16], est de 0,67 eV pour le complexe $\boxed{Na^+}$ Ca^{2+}; cette valeur est très proche de l'énergie d'association coulombienne (0,65 eV); dans ces conditions, l'énergie de liaison de la lacune décroît très rapidement lorsque celle-ci passe de la position de *p–v* à celle de *s–v*, puis à celle de *t–v*.

Il s'ensuit qu'aux températures où nous opérons et étant donné les différences E_1-E_2 et E_1-E_3 (Fig. 4(b)), les rapports w_{12}/w_{21} et w_{13}/w_{31} sont $\ll 1$; ce qui est parfaitement cohérent avec le fait qu'on n'observe pas de pic haute température.

En ce qui concerne Mn^{2+}, les mesures de Banasevitch et ses collaborateurs indiquent que l'enthalpie d'association du complexe $\boxed{Na^+}$ Mn^{2+} est de 0,7 eV. Cette valeur apparaît trop élevée, étant donné qu'elle conduirait à ne pas observer de contribution haute température comme dans le cas de Ca^{2+}. La valeur de 0,41 eV déterminée par Watkins[19] apparaît plus valable.

En ce qui concerne Mg^{2+} et Cd^{2+}, l'enthalpie d'association devrait être du même ordre que pour Mn^{2+}; c'est ce que confirment d'ailleurs Brown et Hoodless[20] en tout cas pour Cd^{2+}.

Dans le cas de Co^{2+}, Sr^{2+} et Be^{2+}[4, 5, 7] l'importance de la polarisation haute température est plus grande que pour les impuretés considérées jusqu'ici.

Il semble donc que seulement dans le cas de Ca^{2+} la lacune soit très fortement associée à l'impureté.

Il est possible de dégager une autre conclusion: la contribution *HT* à la polarisation totale tendant à se différencier de la contribution *BT* lorsque le rayon de l'impureté diminue, la différence entre les énergies E_{32}, E_{31}, E_{21} et E_{11} tend à s'accroître (on désigne par E_{ij} la barrière d'énergie s'opposant au saut du site *i* vers le site *j*).

5. CONCLUSION

Nous avons proposé un modèle qui permet d'expliquer d'une part nos résultats relatifs à NaCl dopé par Ca^{2+}, Cd^{2+}, Mn^{2+} et Mg^{2+} d'autre part, ceux (obtenus par d'autres auteurs sur NaCl dopé par Be^{2+}, Co^{2+}, Sr^{2+}) qui n'étaient pas interprétables à partir du modèle de Dreyfus.

Nous pensons avoir montré que:

Le phénomène de relaxation principal est dû à la rotation de la lacune en position de premier voisin (position de la majorité des lacunes); de tous les sauts possibles, c'est bien celui entre premiers voisins qui est le plus probable sauf dans le cas de Be^{2+} et non pas le saut second voisin premier voisin comme le suppose Dreyfus pour un certain nombre d'impuretés (Ca^{2+}, Cd^{2+}, Mn^{2+}).

Le phénomène de relaxation situé en plus haute température rend compte de l'influence des lacunes en position de second et troisième voisin simultanément.

Dans le cas où l'impureté est Ca^{2+} (dont le rayon est très voisin de celui de Na^+), où le réseau est le moins déformé, l'energie de liaison de la lacune décroît très vite lorsqu'on s'eloigne de l'impureté, si bien que l'influence des lacunes occupant des sites plus éloignés que ceux de premiers voisins peut être négligée. Pour les autres impuretés les distorsions locales du réseau autour de l'impureté sont plus importantes, ce qui semble se traduire par une décroissance moins rapide de l'énergie de liaison. Toutefois, ces modifications ne sont pas suffisamment importantes pour que la majorité des lacunes occupe une position de second voisin lorsque la taille de l'impureté devient assez faible devant celle de l'ion substitué; il n'y aurait donc pas, comme le suppose Dreyfus, une inversion de population entre les sites de premier et second voisins lorsqu'on passe d'impuretés de grande taille à des impuretés de petite taille.

La considération de la seule variation du rayon de l'impureté ne peut permettre de rendre compte de celles des grandeurs caractérisant les phénomènes de polarisation observée (en particulier l'importance du phénomène de relaxation haute température ne varie pas d'une facon régulière avec le rayon de l'impureté).

Dans le cas de NaCl dopé par Sr^{2+} ($R_{Sr^{2+}} > R_{Na^+}$) Bucci[4] met aussi en évidence une polarisation basse fréquence non négligeable devant la polarisation haute fréquence prépondérante. On voit donc que lorsque la taille de l'impureté est différente de celle de l'ion substitué (situation dans laquelle le réseau est localement plus déformé), le nombre de lacunes dans des positions plus éloignées que celles de p–v est plus grand.

Nous ferons, pour terminer, une remarque concernant les résultats publiés sur NaCl dopé par Co^{2+}, par Jain et Lal[6] et par Capelletti[5].

Jain et Lal observent, pour des températures supérieures à 370°K, une polarisation basse fréquence supérieure à la polarisation haute fréquence. L'extrapolation à basse température de l'hypothèse adoptée par eux (et d'après le modèle de Dreyfus) suivant laquelle le site de second voisin est le plus stable, doit conduire à observer vers 200°K une polarisation basse fréquence prépondérante. Or, autour de 200°K, Capelletti[5] observe par la méthode *TCD*, un pic basse température (haute fréquence) d'amplitude supérieure à celle du pic haute température (basse fréquence). Ces deux résultats expérimentaux ne sont pas incompatibles si on les interpréte dans le cadre du modèle à trois couches tel que nous l'avons proposé. Le rapport Q peut en effet devenir < 1 quand la température croît, principalement à cause de l'augmentation de w_{13}/w_{31}. Cet exemple montre bien qu'il est toujours souhaitable de considérer un nombre assez important de couches d'occupation pour la lacune, a fortiori lorsqu'on suppose en même temps que la majorité d'entre elles est en position de s–v.

Nous pensons donc que le modèle à trois couches, tel que nous l'avons présenté, est valable, d'une façon générale, pour NaCl dopé par des impuretés divalentes, mais seulement pour NaCl. Il faudrait en effet reconsidérer les grandeurs respectives des fréquences de saut dans le cas de NaF dopé [8] par exemple, pour lequel on sait qu'au moins dans le cas de Mn^{2+}, la majorité des lacunes est en position de s–v.

ANNEXE 1

Considérons par exemple p sites notés $1, \dots, p$ et supposons que les échanges à partir d'un site puissent se faire avec les $(p-1)$ autres sites. Appelons k_{ij} les fréquences de saut du site i vers le site j.

Si on appelle N_i la population du site i, celle N_1 du site noté 1 s'écrit:

$$\frac{dN_1}{dt} = -(k_{12} + \cdots + k_{1p})N_1 + k_{21}N_2 + \cdots + k_{p1}N_p.$$

On peut de la même manière écrire les $(p-1)$ équations différentielles restantes et les fréquences de relaxation seront données par les valeurs propres de la matrice M du système différentiel.

Telle est la façon dont on peut faire le calcul d'une façon générale.

Si maintenant on veut effectuer celui des modes de relaxation dans le cas de trois couches d'occupation pour la lacune autour de l'impureté, il faudra en principe considérer 42 sites.

En fait comme l'indique le Tableau 2, un certain nombre d'entre eux sont équivalents: le champ étant appliqué suivant **Oz** il suffit de considérer la population d'un site de chaque catégorie dans des plans perpendiculaires à **Oz**.

En utilisant les notations du Tableau 2, on a par raison de symétrie:

$$0 = \frac{dN_6}{dt} = \frac{dN_5}{dt} = \frac{d(N_1 + N_{10})}{dt} = \frac{d(N_2 + N_9)}{dt} = \frac{d(N_3 + N_8)}{dt} = \frac{d(N_4 + N_7)}{dt}$$

il suffira donc de considérer le système:

$$\frac{d}{dt}\begin{vmatrix} N_1 - N_{10} \\ N_2 - N_9 \\ N_3 - N_8 \\ N_4 - N_7 \end{vmatrix} = (A) \times \begin{vmatrix} N_1 - N_{10} \\ N_2 - N_9 \\ N_3 - N_8 \\ N_4 - N_7 \end{vmatrix}$$

avec:

$$A = \begin{vmatrix} -4w_{21} & 0 & 4w_{12} & 0 \\ 0 & -2(w_{31} + w_{33}) & 2w_{13} & 2w_{33} \\ w_{21} & 2w_{31} & -2(w_0 + w_{12} + w_{13}) & 0 \\ 0 & w_{33} & 0 & -(w_{32} + w_{13} + w_{33}) \end{vmatrix}$$

On ne retrouve pas exactement la matrice donnée par Franklin[9], pour la raison suivante: il ne peut y avoir comme le suppose implicitement l'auteur, d'échanges supplémentaires dûs au champ dans un plan perpendiculaire à celui-ci, même entre sites non énergétiquement équivalents.

ANNEXE 2

D'après les approximations faites au paragraphe (2.3), les quatre fréquences de relaxation ont pour expressions:

$$\lambda_1 \simeq 2w_0; \quad \lambda_2 \simeq 4w_{21}; \quad \lambda_3 \simeq 2w_{31}; \quad \lambda_4 \simeq w_{31} + w_{32}.$$

Les populations instantanées des différents sites s'écrivent:

$$N_{1,10} = n_0 \pm \sum_i n_i\, e^{-\lambda_i t};$$

$$N_{2,9} = m_0 \pm \sum_i m_i\, e^{-\lambda_i t}\ (i = 1, \ldots, 4)$$

$$N_{3,8} = p_0 \pm \sum_i p_i\, e^{-\lambda_i t};$$

$$N_{4,7} = q_0 + \sum_i q_i\, e^{-\lambda_i t}\ (i = 1, \ldots, 4).$$

Si l'on néglige les échanges *t–v* → *t–v*, la population relative au $i^{\text{ème}}$ mode de relaxation s'exprime par:

$$P_i = 8eap_i + 16eam_i + 4ean_i\ (i = 1, 2, 3)$$

$P_4 \simeq 16eaq_4$ (e: charge de l'électron).

Si toutes les fréquences de relaxation avaient des valeurs très différentes, il serait intéressant de calculer tous les n_i, m_i, p_i (existence d'un mode dominant pour chaque site).

Nous nous sommes bornés à montrer que:

$$|p_1| \gg |n_1|, |m_1| \text{ et } p_1 \gg p_2 + p_3$$

---

si bien que

$$p_1 \simeq A = (eEa/kT)N$$

avec

$$N = \left(\frac{N_i}{6}\right)\left(2+\frac{w_{12}}{w_{21}}+\frac{4w_{13}}{w_{31}}\right)$$

(n_i: n^{bre} d'impuretés par unité de volume; E: champ électrique). On trouve, dans ces conditions:

$$P_1 \simeq 8eaA;\ P_2+P_3 \simeq 32eaA\frac{w_{13}}{w_{31}}+8eaA\frac{w_{12}}{w_{21}};$$

$$P_4 \simeq 16eaA\frac{w_{13}}{w_{31}}.$$

L'importance de la polarisation relative aux lacunes en position de s–v et t–v par rapport à celle attribuable aux lacunes en position de p–v peut alors être mesurée par le rapport:

$$(P_2+P_3+P_4)/P_1 = \frac{w_{12}}{w_{21}}+6\,\frac{w_{13}}{w_{31}}$$

BIBLIOGRAPHIE

1. DRYDEN J. S. and MEAKINS R. J., *Disc. Faraday Soc.* **23**, 29 (1957).
2. DREYFUS R. W., *Phys. Rev.* **121**, 1675 (1961).
3. BUCCI C. and FIESCHI R., *Phys. Rev. Lett.* **12**, 16 (1964).
4. BUCCI C., FIESCHI R. and GUIDI G., *Phys. Rev.* **148**, 816 (1966).
5. CAPPELETTI R., FIESCHI R., MARTEGANI G. and PIROLA L., *J. Phys.* 130 (1967).
6. JAIN S. C. and LAL K., *Proc. Phys. Soc. Lond.* **92**, 990 (1967).
7. BUCCI C., *Phys. Rev.* **164**, 1200 (1967).
8. LAJ C., Thèse ORSAY (1969).
9. FRANKLIN A. D., SHORB A. and WACHTMANN J. B., *J. Res. natn. Bur. Stand.* **68A**, 425 (1964).
10. COOK J. S., DRYDEN J. S. and DRYDEN J. S., *Proc. Phys. Soc. Lond.* **80**, 479 (1962).
11. DREYFUS R. W. and NOWICK A. S., *J. appl. Phys. Suppl.* **33**, 473 (1962).
12. COOK J. S. and DRYDEN J. S., *Aust. J. Phys.* **13**, 260 (1960).
13. DANSAS P. and SIXOU P., *C.R. Acad. Sci. Paris* **266**, 568 (1968).
14. LIDIARD A. B., *Handbuch der Physik*, Berlin, Vol. 20 (1957).
15. MURIN A. N., BANASEVITCH S. M. and GRUSHKO Yv. S., *Soviet Phys. solid State* **3**, 1762 (1962).
16. LUR'E B. G., MURIN A. N. and BRIGEVICH R. F., *Soviet Phys. solid State* **4**, 1432 (1963).
17. ALLEN C. A., IRELAND D. T. and FREDERICKS W. J., *J. chem. Phys.* **47**, 3068 (1967).
18. CHEMLA M., *Ann. Phys.* **1**, 959 (1956).
19. WATKINS G. D., *Phys. Rev.* **113**, 79 (1959).
20. BROWN N. and HOODLESS I. M., *J. Phys. Chem. Solids* **28**, 2297 (1967).

J. Phys. Chem. Solids, 1971, Vol. 32, pp. 2711–2716. Pergamon Press. Printed in Great Britain

ANGULAR CORRELATION MEASUREMENTS OF ANNIHILATION RADIATION IN ORDERED β BRASS*

W. TRIFTSHÄUSER† and A. T. STEWART
Queen's University, Kingston, Canada

and

R. TAYLOR
National Research Council, Ottawa, Canada

(*Received* 28 *December* 1970)

Abstract – The angular correlation of radiation from positrons annihilating in β' CuZn single crystals has been measured. The crystals were oriented in the (100), (110) and (111) directions and the measurements yield information intimately related to the areas of slices through the Fermi surface normal to these directions. These cross sections were obtained from a theoretical calculation by Taylor using results of de Haas–van Alphen measurements for β' CuZn. The experimental data are directly compared with these calculated values. We find a remarkable good agreement between theory and experiment and most of the anisotropy in the electron momentum distribution can be ascribed to the topology of the Fermi surface.

1. INTRODUCTION

It is very well known that the usual solid state techniques used in determining the topology of Fermi surfaces are restricted to pure metals, very dilute alloy systems and alloys which possess a long range order. Therefore most of the theory of the electronic structure of alloys remains to be tested in more detail.

Positron annihilation experiments yield directly the density of electrons in k-space and the results are approximately independent of the electron mean free path. Thus it can be used to examine the electron structure of alloys, which because of electron scattering cannot be examined by the more usual transport techniques. It is therefore of great importance to understand and to investigate the extent to which positron annihilation experiments are directly relevant to the topology of the Fermi surface in metal alloys.

For a number of years, positron angular correlation experiments have been used to obtain information about the shape of the Fermi surface of pure metals. The possibility of measuring momentum anisotropies in oriented single crystals has first been shown by Berko and Plaskett for copper and aluminum[1]. Measurements on other metals have been reported by several authors[2–7]. In this paper we present observations on single crystals of β' brass in order to examine how well this technique can be used for the determination of electron states in alloys and to what extent the results can be analyzed directly in terms of cross-sectional areas of the Fermi surface. We chose ordered β' brass as a 'test alloy' because the Fermi surface of this material is very well known from de Haas-van Alphen measurements and from studies of the high field magneto-resistance [8, 9]. The β' phase of this alloy is ordered forming the CsCl structure and contains approximately equal numbers of each constituent material. A preliminary account of this work has already been given[10].

---

*Work supported by the National Research Council of Canada.

†New Address: Institut für Festkörperforschung, KFA Jülich, Germany.

2. PHOTON MOMENTUM DISTRIBUTION

The technique of using positron annihilation to obtain the momentum distribution of electrons has often been described[11]. If the annihilating electron is in the state ψ_k the probability that a pair of photons will be emitted with momentum $\hbar\mathbf{k}$ is proportional to[12]

$$\rho(\mathbf{k}) = \sum_{k'} \left| \int \psi_+(\mathbf{r})\psi_{k'}(\mathbf{r})\, e^{-i\mathbf{k}\cdot\mathbf{r}}\, d^3\mathbf{r} \right|^2 \qquad (1)$$

where ψ_+ is the positron wave function and the summation extends over all occupied states in k-space. The coincidence counting rate measured by the conventional long-slit apparatus is proportional to

$$N(k_z) = \int_{-\infty}^{\infty} \int_{-\infty}^{\infty} \rho(\mathbf{k})\, dk_x\, dk_y \qquad (2)$$

In the lowest approximation of free electrons and a positron in its lowest energy state, $N(k_z)$ is directly proportional to the cross-sectional areas of the Fermi surface in the extended zone scheme. For a less simplified situation, the importance and influence of the positron wave function, the higher momentum components of the electron wave functions and the core electrons has been discussed already earlier[4, 12].

3. EXPERIMENTAL ARRANGEMENT

In the experimental arrangement we used a long-slit geometry with 30 cm long NaI(Tl) detectors, the slits subtending 0·325 mrad at the specimen. Figure 1 shows the schematic of the experimental setup. The β' CuZn single crystal had been oriented by X-rays and was afterwards spark cut to rectangular pieces of 6 × 6 × 12 mm keeping the accuracy of the orientation within one half of a degree. After cutting, the surface of the specimens was carefully etched to remove possible distortions due to spark machining. The experiments were performed with the samples at 78°K in order to reduce the thermal motions of the positrons and its broadening influence on the instrumental resolution[13] The finite resolution due to the positron motion can be approximated by

$$A(k) = \exp\left(-\frac{\hbar^2 k_+^{\,2}}{2m^* k_B T}\right) \qquad (3)$$

where k_+ is the positron wave number, m^* the effective mass of the positron and k_B the Boltzmann constant. Since $\Theta_z = \hbar k_+/mc$ one can

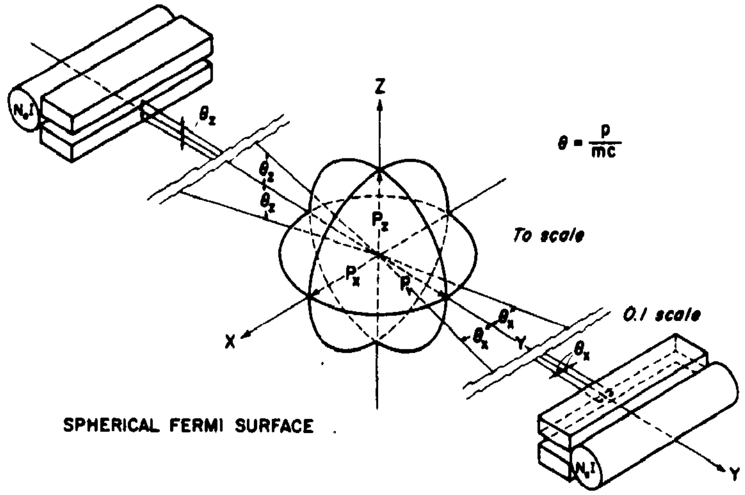

Fig. 1. Schematic experimental arrangement using a long-slit geometry. The maximal cross sections of a spherical Fermi surface are indicated.

write equation (3) in the form

$$A(\Theta_z) = \exp\left(-\frac{\Theta_z^2 mc^2}{3k_B T}\right) \tag{4}$$

taking an average value of $1{\cdot}5m_e$ for the effective mass. For $T = 78°\text{K}$ we obtain a full width at half maximum (FWHM) of 0·33 mrad for the positron motion alone. In the experiment, however, one has to take into account also a triangular resolution function determined by the geometry of the apparatus, especially by the slit width.

$$G(\Theta_z) = H\left(1-\frac{\Theta}{\Theta_0}\right) \tag{5}$$

where $|\Theta_z| \leq \Theta_0$ and H being determined by choosing the condition that the areas of the two resolution functions are equal. Thus the total (phenomenological) resolution function is the convolution of $G(\Theta_z)$ with $\Theta_0 = 0{\cdot}325$ mrad and $A(\Theta_z)$, which is a pure mathematical procedure and therefore is not shown here in detail. It results in a new function with FWHM of 0·46 mrad. As a positron source we used about 180 mCi of ^{58}Co deposited electrolytically onto a very thin copper foil. Through annealing afterwards, most of the radioactive material diffused into the copper. The foil was sealed by a 0·005 mm-thick nickel window to avoid possible contamination[14]. The coincidence counts were collected automatically and corrected for source decay and accidental coincidence background. The coincidence resolving time of the electronic device was 80 nsec.

4. RESULTS AND DISCUSSION

The results of the measurements are shown in Fig. 2. The three curves represent the angular distributions for the (100), (110) and (111) directions (k_z was parallel to these directions) normalized to equal areas. The lines represent the best visual fit through the data points. The statistical accuracy at the peak was about ±0·65 per cent. In the region from 0 to about 6 mrad there are marked differences in the angular distributions and all clearly differ from an ideal parabolic distribution. In the higher momentum tail of the angular distribution, the differences in the three curves are almost completely smoothed out. As regards to the tail of the angular correlation curves, i.e. the absence of a sharp cutoff at the Fermi momentum, this is partly due to zone boundary effects, but mostly due to annihilations with the ion core electrons in high momentum events. The special role of the 3d electrons of the Cu atom is known to survive in the alloy, making the band structure of the β' CuZn similar to that of pure Cu

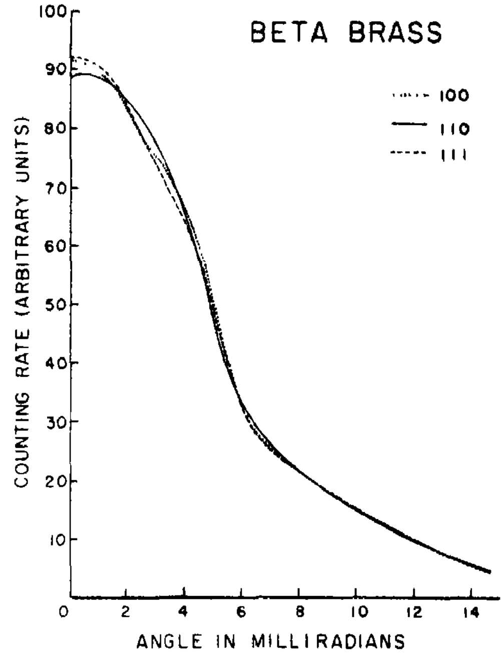

Fig. 2. Experimental angular correlation curves for (100), (110) and (111) directions in β' CuZn at liquid nitrogen temperature. The chemical composition of this alloy was (51·24±0·06)% Cu and (48·74±0·06)% Zn. k_z was parallel to these crystallographic directions. The three curves are normalized to equal areas. The statistical accuracy of the data points at the peak is 0·65 per cent. The lines represent the best visual fit through the data points.

which is not free-electron like [1]. However the d-band of the alloy is only half as wide as the d-band of pure Cu and it lies farther below the position of the Fermi level than in pure Cu because of the larger electron-atom ratio and hence the larger Fermi energy of the alloy. Consequently the hybridization of the free-electron-like sp-bands near the Fermi level with the tight-binding d-band is much weaker in the alloy than in pure Cu. In addition, the positron is excluded from the inner core region by its coulomb repulsion by the positively charged nucleus. Therefore it is a good approximation that primarily the $3d$-electrons contribute to the high momentum annihilations.

Table 1. *Theoretical geometric cross-sectional areas of the Fermi surface of* β' CuZn *normal to the* (100), (110) *and* (111) *directions as obtained through calculations by Taylor*[15]. *The Fermi surface was confined to the first two zones. The areas are given in units of* $(2\pi/a)^2$ *with the lattice constant* $a = 2{\cdot}945$ Å.

Momentum k_z in units of $(2\pi/a)$	Cross section of β' CuZn Fermi Surface in Units of $(2\pi/a)^2$		
	(100)	(110)	(111)
0	1·5477	1·5773	1·5978
0·025	1·5470	1·5776	1·5967
0·050	1·5398	1·5711	1·5888
0·075	1·5350	1·5592	1·5778
0·10	1·5231	1·5454	1·5747
0·125	1·5079	1·5336	1·5781
0·15	1·4886	1·5310	1·5831
0·175	1·4649	1·5117	1·5744
0·20	1·4326	1·4839	1·5290
0·225	1·3975	1·4496	1·4712
0·25	1·3388	1·3978	1·3753
0·275	1·2955	1·3465	1·2981
0·30	1·2721	1·2933	1·2337
0·325	1·2633	1·2403	1·1714
0·35	1·2435	1·1863	1·1125
0·375	1·2079	1·1280	1·0572
0·40	1·1626	1·0678	1·0073
0·425	1·1081	1·0012	0·9660
0·45	1·0443	0·9306	0·9247
0·475	0·9714	0·8637	0·8641
0·50	0·8512	0·8013	0·7942
0·525	0·7289	0·7348	0·7182
0·55	0·6526	0·6305	0·6364
0·575	0·5670	0·4955	0·5508
0·60	0·4774	0·3988	0·4615
0·625	0·3732	0·3183	0·3717
0·65	0·2116	0·2540	0·2749
0·675	0	0·2080	0·1606
0·70		0·1863	0·0902
0·725		0	0·0507
0·75			0·0093
0·775			0

In order to evaluate the part of the angular correlation curve due to conduction electrons, we subtracted the higher momentum tail from 'the angular distribution by fitting a Gaussian function in the region from about 7 mrad to 14 mrad (see Fig. 2). The fitting was done for the measured (100) distribution and the same curve was then subtracted from the measured data of all three distributions. The resultant data points are shown in Fig. 3 together with a solid line drawn through the points. This line results from the values given in Table 1 after being corrected for the total resolution of our system. The convolution integral was performed numerically. The numbers in Table 1 are calculated geometrical cross-sectional areas of the Fermi surface of β' CuZn along the (100), (110) and (111) directions. The expression for the Fermi surface was obtained through calculations by Taylor, who fitted the results from de Haas–van Alphen measurements to a six parameter description of the Fermi surface of β' CuZn using non-local pseudo-potentials. The comparison of the calculated curves with the experimental data indicates that the overall shape of the angular distribution stems principally from the topology of the Fermi surface. The (110) necks and the (111) holes, lying at different positions for each of the three orientations, are almost entirely responsible for the structure in these curves. More details, however, are exhibited by the first derivative of these angular correlation curves. From the corrected experimental data of Fig. 3, the derivative was calculated by taking the difference of adjacent points. The same procedure was applied to the calculated values. The results are shown in Fig. 4 where again values from the cross-sectional areas are represented by the solid drawn lines. As seen, these theoretical curves agree remarkably well with the experiment but they also exhibit some differences in certain regions. The burden of accounting for these small differences falls on the effects not considered in the approximation used in equation (1), e.g. anisotropy of the ground state positron wave function, more accurate consideration of higher momentum components of the electron wave function, including the influence of the nearlyfree-electron theory[1, 16], and many-body-correlation effects, leading to a k-dependent annihilation probability[17, 18]. In spite of these small discrepancies the results show clearly that the positron annihilation technique can be used to yield information about the Fermi surface of alloys. However, higher accuracy in the experimental data as well as in the theoretical calculations, especially in anisotropy and manybody effects, is necessary to account for the fine details present in the electron momentum distributions.

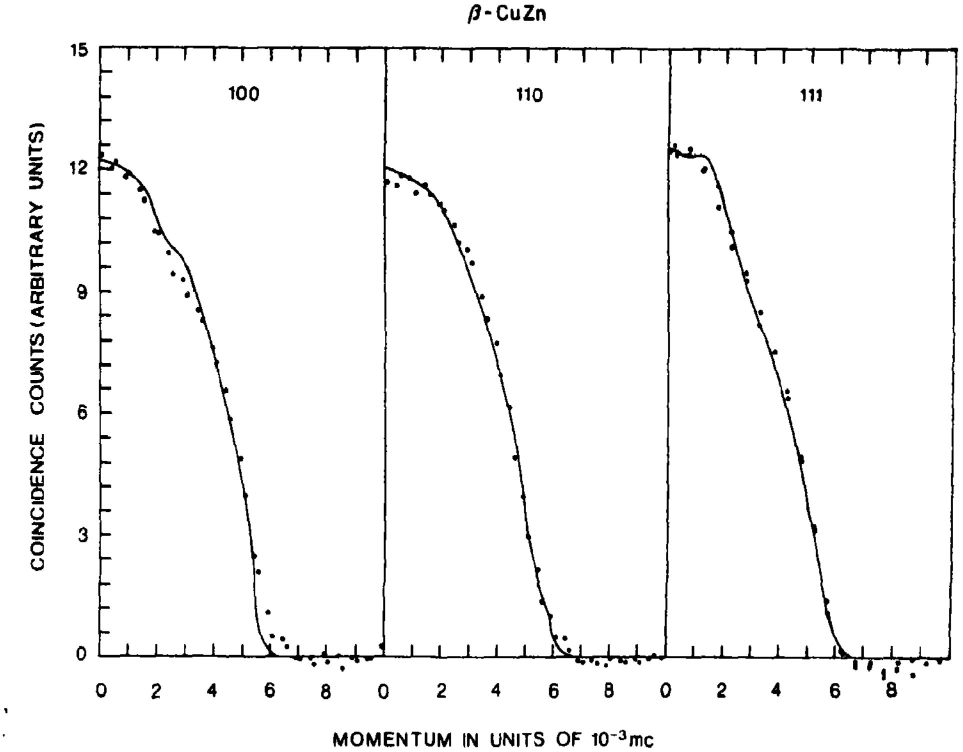

Fig. 3. Experimental data of (100), (110) and (111) directions after subtraction of the contribution due to annihilations with core electrons. In the free-electron approximation the Fermi level of this alloy is at $5{\cdot}83 \times 10^{-3}$ mc. The solid lines through the data points are from the values given in Table 1 after correction for the total resolution of the apparatus.

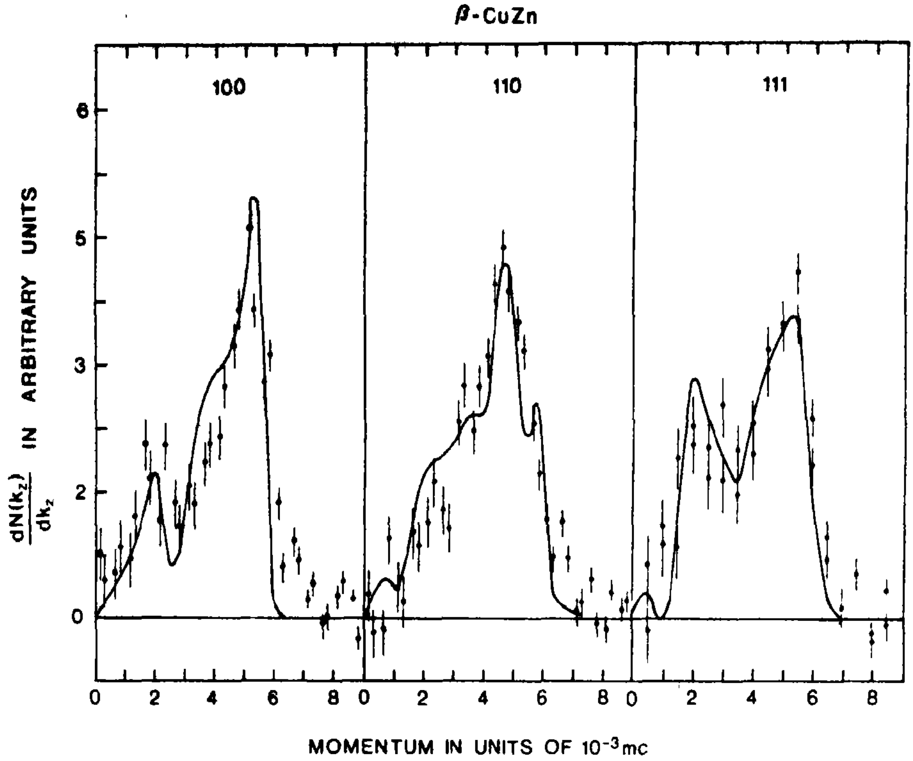

Fig. 4. Electron momentum distribution in β' CuZn. These data points are obtained from Fig. 3 by taking the difference of adjacent points. The theoretical difference curves are obtained from the values of Table 1 after being corrected for resolution as discussed in the text.

REFERENCES

1. BERKO S. and PLASKETT J. S., *Phys. Rev.* **112**, 1877 (1958).
2. STEWART A. T., SHAND J. B., DONAGHY J. J. and KUSMISS J. H., *Phys. Rev.* **128**, 118 (1962).
3. BERKO S., *Phys. Rev.* **128**, 2166 (1962).
4. DONAGHY J. J. and STEWART A. T., *Phys. Rev.* **164**, 396 (1967).
5. DEKHTYAR YA. and MIKHALENKOV V. S., *Dokl. Akad. Nauk SSSR* **136**, 63 (1961) *Dokl. Akad. Nauk SSSR* **140**, 1293 (1961).
6. WILLIAMS R. W., LOUCKS T. L. and MACKINTOSH A. R., *Phys. Rev. Lett.* **16**, 168 (1966).
7. LOUCKS T. L., *Phys. Rev.* **144**, 504 (1966).
8. JAN J. P., PEARSON W. B. and SAITO Y., *Proc. R. Soc. London* **A297**, 275 (1967).
9. SELLMYER D. J., AHN J. and JAN J. P., *Phys. Rev.* **161**, 618 (1967).
10. TRIFTSHÄUSER W. and STEWART A. T., *Proceedings Electronic Density of States*, National Bureau of Standards, Washington D.C. (1969).
11. See *Positron Annihilation* (Edited by A. T. Stewart and L. O. Roellig) Academic Press, New York (1967)
12. DE BENEDETTI S., COWAN C. E., KONNECKER W. R. and PRIMAKOFF H., *Phys. Rev.* **77**, 205 (1950).
13. STEWART A. T., SHAND J. B. and KIM S. M., *Proc. R. Soc. London* **88**, 1001 (1966).
14. The radioactive source was supplied by the International Chemical and Nuclear Corporation.
15. TAYLOR R., *Proc. R. Soc. London* **A312**, 495 (1969).
16. MOTT N. F. and JONES H., *Properties of Metals and Alloys*, Clarendon Press, Oxford (1936).
17. KAHANA S., *Phys. Rev.* **117**, 123 (1960) and CARBOTTE J. and KAHANA S., *Phys. Rev.* **139**, 213 (1965).
18. CARBOTTE J., *Phys. Rev.* **155**, 197 (1967).

J. Phys. Chem. Solids, 1971, Vol. 32, pp. 2717–2722. Pergamon Press. Printed in Great Britain

POSITRON ANNIHILATION ANGULAR CORRELATION MEASUREMENTS IN DISORDERED SYSTEMS: α BRASS*

W. TRIFTSHÄUSER† and **A. T. STEWART**
Department of Physics, Queen's University, Kingston, Canada

(*Received* 28 *December* 1970)

Abstract – We performed angular correlation measurements of positrons annihilating in αCuZn single crystals. The orientation of the specimens was parallel to the (100), (110) and (111) directions. The results are compared with a model calculation for the Fermi surface of this alloy, assuming that every Zn atom adds two electrons to the total number of conduction electrons. The cross-sectional areas normal to the (100), (110) and (111) axes of the Fermi surface constructed in this way are compared with the experimental data. According to the evidence and conclusions in Ref. [1], we interpret the experimental results in terms of the topology of the Fermi surface. For a 77·7% Cu 22·3% Zn concentration alloy we find a radius for the necks along the (111) directions of 0·27 ± 0·02 in units of the Fermi momentum.

1. INTRODUCTION

IN PREVIOUS papers it has been shown that the positron annihilation technique, if applied with sufficient angular resolution, can reveal important information about the topology of the Fermi surface (F.S.) of pure metals and ordered and disordered alloys[1, 2]. The method is especially useful in the case of disordered alloy systems for studies of anisotropies of Fermi surfaces. For pure Cu it is known that the F.S. makes contact with the (111) Brillouin zone boundaries. In alloying other metals to copper one expects changes in the Fermi surface and particularly in the size of the necks, and positron angular correlation experiments should provide information about these changes. Other methods[3] of studying these changes are restricted to concentrations of about 0·1 per cent or less, but the positron annihilation technique imposes no such restrictions. In this paper we present results of measurements on single crystals of αCuZn. After having verified and discussed the advantages as well as the limits of this method in the case of β′ CuZn[1] where the F.S. was already known, we also wanted to explore the technique for a case where the Fermi surface is only approximately known. The α phase in CuZn alloys has the fcc structure as does pure copper and this phase is stable up to about 33% Zn. The analysis of the alloy used for the measurements revealed a composition of (77·7 ± 0·2)% Cu and (22·3 ∓ 0·2)% Zn. A preliminary report of this work has already been given[4].

2. THE α CuZn FERMI SURFACE

The F.S. of pure Cu has been known for some time and various methods have been applied for its determination[5]. In recent investigations[2, 6] the six parameter description of Roaf[7] for the copper F.S. has been used. It is therefore well established that the Fermi surface forms eight necks at the (111) Brillouin zone boundaries. The radius of the necks was determined to 0·201 in units of k_F. By alloying divalent Zn to the monovalent Cu the number of conduction electrons should increase according to the rigid-band model. Consequently the F.S. should expand and

---

*Work supported by the National Research Council of Canada.

†Now at Institut für Festkörperforschung, KFA Jülich, Germany.

therefore also the size of the necks. Under these assumptions we have set up a model with its basic features shown in Fig. 1. The Fermi surface of α CuZn is assumed to consist of a sphere with eight necks superimposed along the (111) axes. The necks intersect the zone boundary at right angles and join smoothly the rest of the sphere. The total volume is normalized to the number of free electrons one would anticipate for the above copper–zinc concentration. From Fig. 1 which shows $\frac{1}{8}$ of the Fermi surface we obtain the following relations:

$$\Gamma M = \frac{\sqrt{3}}{2} b$$

where $b = 2\pi/a$. a is the lattice constant for this alloy[8], b is the absolute value of the reciprocal lattice vector, MN is the neck radius, NO and OT are of equal length, and $\tan \Phi = MO/\Gamma M$. Under these conditions it is possible to determine various configurations leaving the angle Φ as a parameter in the calculations. A computer program was written to map out the F.S. and to obtain cross-sectional areas normal to the (100), (110) and (111) directions as a function of Φ, limited to the first Brillouin zone.

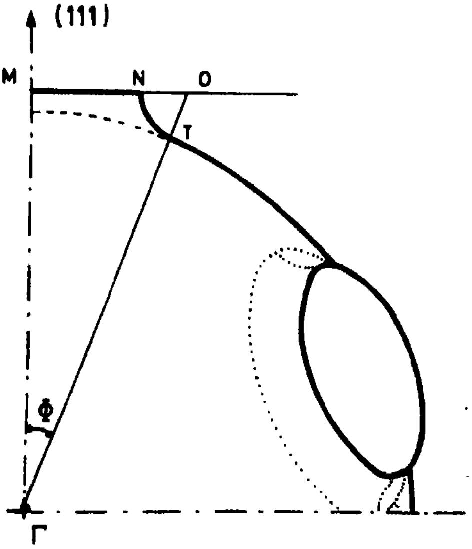

Fig. 1. Model of $\frac{1}{8}$ of the proposed Fermi surface of αCuZn. The geometrical relations and the basic assumptions of the model are discussed in the text.

The calculations were performed in the interval from $\Phi = 15°$ to $\Phi = 30°$ in steps of one degree[9]. Figure 2 shows the proposed F.S. for α CuZn oriented parallel to the (100), (110) and (111) axes. Indicated by dashed lines is also the first Brillouin zone (truncated octahedron).

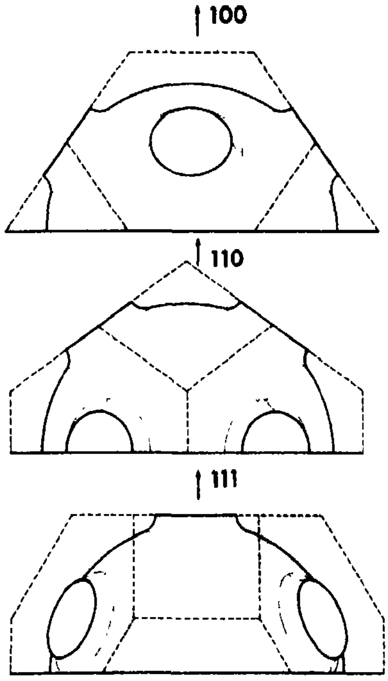

Fig. 2. Fermi surface of αCuZn for $\Phi = 20°$, oriented parallel to the (100), (110) and (111) direction respectively. The Fermi surface makes contact with the first Brillouin zone, indicated by dashed lines, along the (111) directions.

3. EXPERIMENTAL RESULTS AND DISCUSSION

The experimental arrangement (long-slit geometry) as well as the preparation of the single crystal specimens of α CuZn was the same as described in Ref. [1]. The experiments were performed with the samples at 78°K. The results of the measurements are shown in Fig. 3. The three curves represent the angular distributions for the (100), (110) and (111) directions normalized to equal

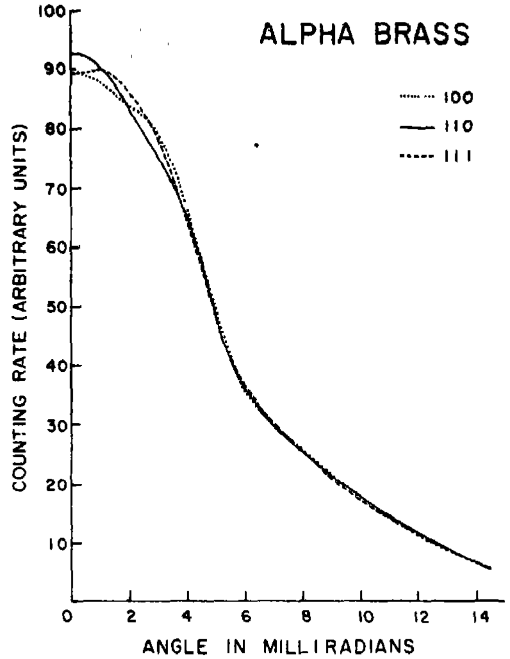

Fig. 3. Experimental angular correlation curves for the (100), (110) and (111) directions in αCuZn at liquid nitrogen temperature. The chemical composition of this alloy was (77·7 ± 0·2)% Cu and (22·3 ∓ 0·2)% Zn. k_z was parallel to these crystallographic directions. The three curves are normalized to equal areas. The statistical accuracy of the data at the peak is 0·67 per cent. The lines *represent the best visual fit through the data points.*

areas. The data at angles $\Theta < 0$ are folded over onto the data at angles $\Theta > 0$. The statistical accuracy at $\Theta = 0$ was about ±0·67 per cent. As in the case of pure Cu[6] and β'CuZn [1] there are marked differences in the three curves here too, especially in the region from 0 to about 6 mrad. Again there is an appreciable number of annihilations with core electrons. It should be noted that the relative number of core annihilations in α brass is larger than in β' brass because of the higher copper concentration. In order to display better the part due to annihilations with conduction electrons, the core annihilation contribution was eliminated by the same procedure as discussed previously [1]. The resultant data points after subtraction of annihilations due to the ion core electrons are shown in Fig. 4. These experimental values are now compared with the calculations of Section 2. In Table 1 are the results of this calculation for $\Phi = 19°$. All calculated values are corrected for the total resolution of the experimental arrange-

Table 1. *Calculated cross-sectional areas of the model Fermi surface of αCuZn for $\Phi = 19°$ normal to the* (100), (110) *and* (111) *directions. The basic assumptions of the model are given in Fig.* 1 *and are discussed in the text. The Fermi surface was confined to the first Brillouin zone. The areas are given in units of $(2\pi/a)^2$ with the lattice constant $a = 3{\cdot}666$ Å* [8].

Momentum k_z in units of $(2\pi/a)$	Cross sections of αCuZn model-Fermi surface for $\Phi = 19°$ in units of $(2\pi/a)^2$ (100)	(110)	(111)
0	2·1552	2·2807	2·1551
0·025	2·1532	2·2778	2·1545
0·05	2·1473	2·2698	2·1534
0·075	2·1375	2·2562	2·1562
0·10	2·1234	2·2368	2·1675
0·125	2·1061	2·2114	2·1605
0·15	2·0845	2·1796	2·1445
0·175	2·0590	2·1402	2·1221
0·20	2·0295	2·0903	2·0944
0·225	1·9961	2·0201	2·0620
0·25	1·9599	1·9638	2·0252
0·275	1·9229	1·9176	1·9843
0·30	1·8872	1·8724	1·9393
0·325	1·8563	1·8233	1·8902
0·35	1·8519	1·7703	1·8368
0·375	1·8050	1·7134	1·7769
0·40	1·7494	1·6525	1·7159
0·425	1·6875	1·5877	1·6468
0·45	1·6204	1·5190	1·5696
0·475	1·5488	1·4464	1·4776
0·50	1·4730	1·3693	1·3849
0·525	1·3928	1·2855	1·2893
0·55	1·3081	1·1999	1·2048
0·575	1·2180	1·1092	1·1165
0·60	1·1206	1·0837	1·0242
0·625	1·0121	0·9947	0·9280
0·65	0·8792	0·8980	0·8279
0·675	0·7238	0·7959	0·7238
0·70	0·6158	0·6894	0·6158
0·725	0·5039	0·5785	0·5039
0·75	0·3880	0·4619	0·3880
0·775	0·2683	0·3347	0·2683
0·80	0·1446	0·1784	0·1818
0·825	0·0169	0·0440	0·1531
0·85	0	0	0·1412
0·875			0

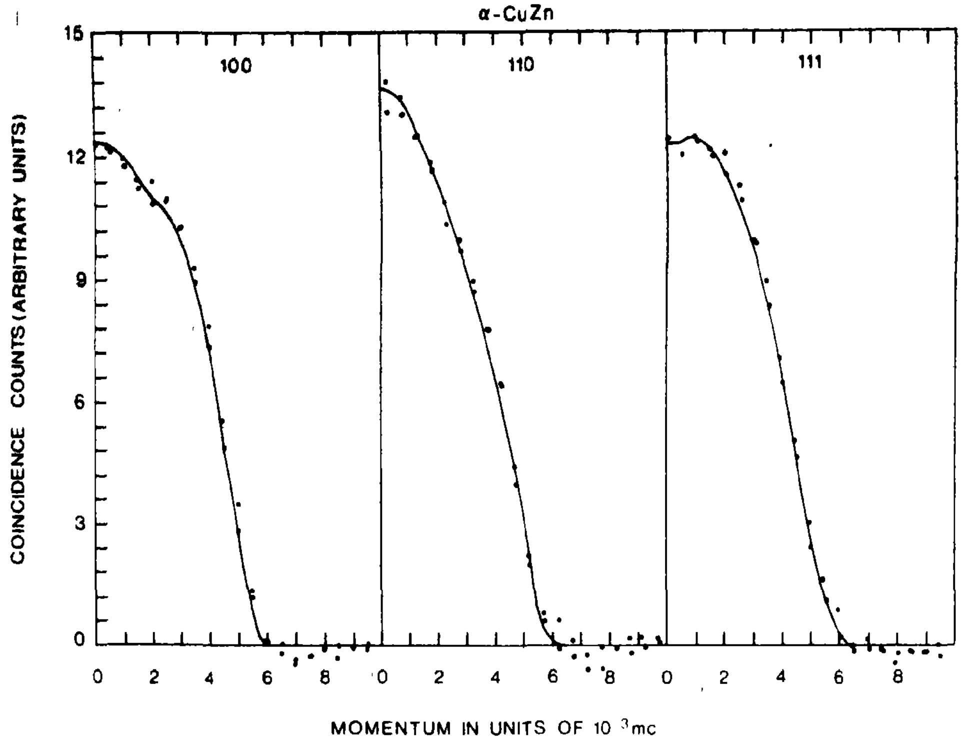

Fig. 4. Experimental data of the (100), (110) and (111) directions after subtraction of the contribution due to annihilations with core electrons. In the free-electron approximation the Fermi level of this alloy is at $5{\cdot}53 \times 10^{-3}$ mc. The solid lines through the data points represent the calculated values for $\Phi = 20°$ after correction for the total resolution of the apparatus.

ment (0·46 mrad FWHM). The best fit of the theoretical values with the experimental data for all three orientations was obtained for $19° < \Phi < 21°$. The solid lines in Fig. 4 correspond to the cross-sectional areas for $\Phi = 20°$. The agreement with the experimental values is remarkably good. More details in the structure of the curves are exhibited by looking at the slopes of these curves. That is done by taking the difference of adjacent points and these results are shown in Fig. 5. The derivatives for the three orientations are clearly different from each other and all show deviations from a straight line (spherical F.S.) at different values of k_z. Murray *et al.*[2] published recently results of positron annihilation experiments on various copper alloys. In particular they used a single crystal of composition 78% Cu and 22% Zn, which is almost identical to the Cu–Zn concentration we had for our experiments. However their measurements were performed only for the (110) direction and they observe no marked structure but a rather smooth distribution. This is in contrast to our experimental results.

We do not understand the discrepancies in the two measurements. However, our results agree well with the predictions of the rigid-band model and also with the Fermi momentum k_F to be at 5·53 mrad. Furthermore we can deduce from the fairly narrow interval of the parameter Φ the radius of the necks to be ($0{\cdot}27 \pm 0{\cdot}02$) in units of k_F. This corresponds to an angle of about ($1{\cdot}5 \pm 0{\cdot}1$) mrad. The neck radius for pure copper is 0·201 in units of k_F[7]. This indicates that in 77·7% Cu and 22·3% Zn the neck radius is about 35 per cent larger than for pure Cu. But considering our simple model as well as the validity of the rigid-band model at these concentrations we

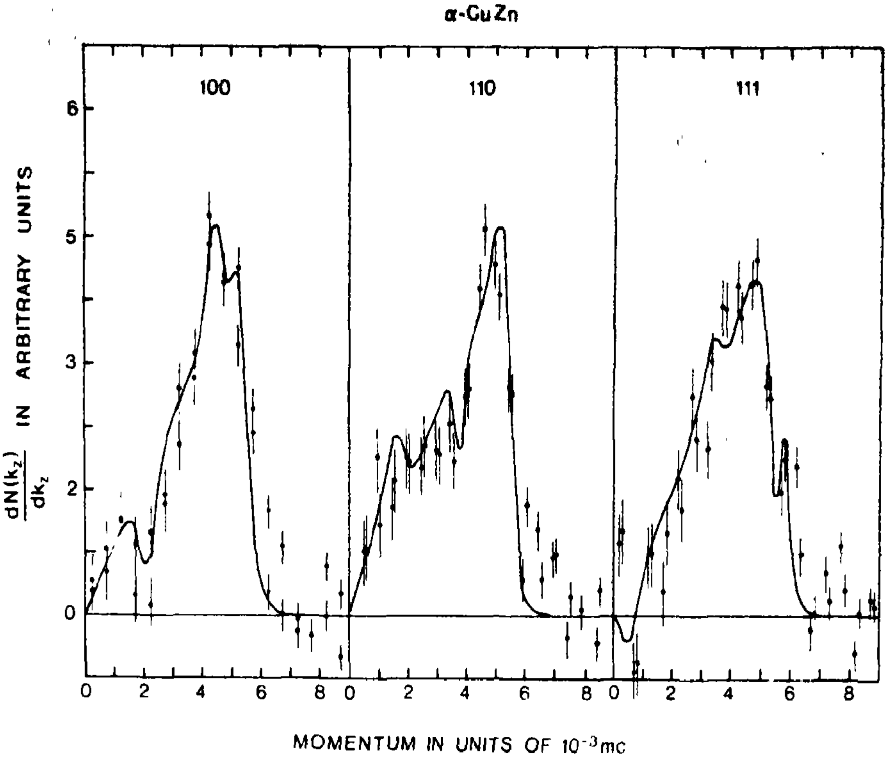

Fig. 5. Electron momentum distribution in αCuZn. These points are obtained from the data shown in Fig. 4 by taking the difference of adjacent points. The derivative for the calculated values is obtained by the same procedure and is shown as a solid line.

think that the total uncertainty of the neck radius should rather be set to $\pm 0{\cdot}04\,k_f$. Williams *et al.*[10] reported only a 30 per cent increase in the neck radius when copper was alloyed with 30 per cent zinc. Our measurements would predict a much higher value for the neck radius increase. However without a thorough investigation of the details of their experiments it is difficult to explain the contradiction.

4. CONCLUSIONS

We have shown that the positron annihilation technique can be used to yield information about the occupation in k-space of electrons in alloys. The long-slit geometry in particular is superior to a crossed-slit system [10–12] in cases where the overall shape of the Fermi surface is approximately known, because of its higher available resolution in the z-direction. For all measurements with a long-slit apparatus however, a model for the Fermi surface has to be set up first. In some favorable cases then this model can be established by the experiment. Furthermore our measurements indicate that with high statistical accuracy at good angular resolution there is sufficient sensitivity to detect details of the Fermi surface of alloy systems.

REFERENCES

1. TRIFTSHÄUSER W., STEWART A. T. and TAYLOR R., *J. Phys. Chem. Solids*, **32**, 2711 (1971).
2. MURRAY B. W. and McGERVEY J. D., *Phys. Rev. Lett.* **24**, 9 (1970).
3. CHOLLET L. F. and TEMPLETON I. M., *Phys. Rev.* **170**, 656 (1968).
4. TRIFTSHÄUSER W. and STEWART A. T., *Proceedings Electronic Density of States*, National Bureau of Standards, Washington D.C. (1969).

5. PIPPARD A. B., *Dynamics of Conduction Electrons*, Gordon and Breach (1965).
6. BERKO S., CUSHNER S. and ERSKINE J. C., *Phys. Lett.* **27A**, 668 (1968).
7. ROAF D. J., *Phil. Trans. Roy. Soc. Lond.* **A255**, 135 (1962).
8. PEARSON W. B., *Handbook of Lattice Spacings and Structures of Metals and Alloys* Vol. 2, Pergamon Press, London (1958).
9. The calculations of the cross-sectional areas reported recently [4] contain a small error in the approximation of the higher momentum components of the electron wave functions.
10. WILLIAMS D. L., BECKER E. H. and PETIJEVICH P., *Bull. Am. Phys. Soc.* **14**, 402 (1969).
11. FUJIWARA K. and SUEOKA O., *J. phys. Soc. Japan* **21**, 1947 (1966).
12. FUJIWARA K., SUEOKA O. and IMURA T., *J. phys. Soc. Japan* **24**, 467 (1968).

J. Phys. Chem. Solids, 1971, Vol. 32, pp. 2723–2735. Pergamon Press. Printed in Great Britain

ORIGINE DE LA RESISTIVITE DANS LE COBALT ET SES ALLIAGES DILUES

B. LOEGEL
Laboratoire de Physique électronique, Collège Scientifique Universitaire rue des Frères, Lumière,
68 Mulhouse France

et

Laboratoire de Physique des Solides*, Institut de Physique,
4, rue Blaise Pascal 67, Strasbourg, France

et

F. GAUTIER
Laboratoire de Physique des Solides*, Institut de Physique,
4, rue Blaise Pascal 67, Strasbourg, France.

(*Received* 16 *April* 1970; *in revised form* 3 *May* 1971)

Résumé—Des mesures de résistivité à basse température sur des alliages dilués de cobalt avec des métaux de transition des trois séries ont permis de préciser la structure électronique du cobalt et des impuretés dissoutes dans ce métal.

L'analyse des déviations à la loi de Matthiessen entre 4°K et 77°K d'alliages du type Co Tr (Tr = Os, Ru, Ir, Fe, Re, Cr) permet de séparer, pour chaque température, les diverses contributions à la résistivité de la matrice et de ses alliages dilués dans un modèle à deux bandes couplées. Les résistivités de chaque sous-bande s ($\sigma = \uparrow, \downarrow$) du cobalt pur sont analysées en termes de diffusions *s-s*, *s-d*, électrons–électrons et électrons–magnons. De plus, le terme de mélange de spin est détermine d'une façon quantitative dans un large domaine de température.

Abstract—Low temperature resistivity measurements on cobalt-based alloys with transitional elements gives informations on the electronical structure as well for pure cobalt as for impurities dissolved in the matrix.

Deviations from Matthiessen's rule from 4 up to 77°K are analyzed for Co Tr alloys (Tr = Os, Ru, Ir, Fe, Re, Cr), and the various contributions to the total resistivity, at each temperature, are given for the matrix and dilute alloys in a coupled two band model. The resistivity of each sub-band $s_\sigma(\sigma = \uparrow, \downarrow)$ are analyzed for pure cobalt in terms of *s-s*, *s-d*, electrons–electrons and electrons-magnons scattering. Furthermore, the spin-mixing term is quantitatively determined in a wide temperature range.

INTRODUCTION

DES ÉTUDES récentes ont montré que la résistivité d'alliages ferromagnétiques dilués de métaux de transition à base de Fer[1], de nickel[2, 3] et de cobalt[4, 5] présente de fortes déviations à la loi de Matthiessen à basse température. Ces résultats s'interprètent bien, dans un modèle à deux bandes suggéré par Mott[6] où la conduction est essentiellement assurée par les électrons s et limitée par les transitions *s-d*. Dans un métal ferromagnétique, les bandes $d_\sigma(\sigma = \uparrow, \downarrow)$ étant décalées en énergie par les interactions magnétiques, les bandes $s_\sigma(\sigma = \uparrow, \downarrow)$ présentent des résistivités ρ_σ dépendant fortement de la direction de spin σ.

Ce modèle permet d'interpréter le comportement de la résistivité résiduelle d'alliages ferromagnétiques ternaires et cela en ne faisant aucune hypothèse sur la matrice[7]. Cependant, les variations de résistivité à basse température d'alliages binaires ou de matrices ferromagnétiques pures ne satisfont pas à ce modèle. Il est nécessaire d'introduire un terme supplémentaire $\rho_{\uparrow\downarrow}$ traduisant l'ensemble des processus de couplage entre les bandes $s\uparrow$ et $s\downarrow$ provenant des diffusions électrons–électrons et électrons–magnons. Ces contributions à la résistivité varient proportionnellement au carré de la température T. L'effet de désordre de spin doit se traduire par une saturation de $\rho_{\uparrow\downarrow}$ à température suffisamment élevée[8].

---

*Equipe de recherche sur la structure électronique des solides, associée au CNRS n° 100.

Nous nous proposons de déterminer ici la dépendance en température des différents termes $\rho_{m\uparrow}$, $\rho_{m\downarrow}$, $\rho_{\uparrow\downarrow}$ contribuant à la résistivité du cobalt à basse température. Pour cela, nous couplerons les résultats de mesures de résistivité (1) sur des alliages ternaires à basse température ($T = 4{,}2$°K) (2) sur des alliages binaires entre 4–50°K.

Dans le paragraphe 1, nous présentons les résultats des mesures sur les alliages ternaires: celles-ci permettent de déterminer les résistivités des impuretés de transition dissoutes dans le cobalt $\rho_{0\sigma}$ associées à la bande parallèle ($s\uparrow$) ou antiparallèle ($s\downarrow$) au spin des électrons de la bande 'd' pleine; les résultats ainsi obtenus pour $\rho_{0\sigma}$ sont en accord avec ceux qui ont été obtenus à 77–300°K en étudiant la variation de l'écart à la loi de Matthiessen avec la concentration[5]. Ces résultats, associés à ceux que nous obtenons sur les alliages binaires, permettent d'effectuer la séparation des différentes contributions à la résistivité ρ_m du *cobalt pur* (paragraphe 2). Enfin, dans le paragraphe 3, après avoir examiné la cohérence des résultats, nous proposons une interprétation de ceux-ci (ordre de grandeur, origine du comportement $\rho_m \alpha AT^2 + BT^5$, comparaison des résistivités $\rho_{m\sigma}$ avec celles d'un métal noble, . . .) et nous identifions les contributions des processus fondamentaux participant à la résistivité électrique: processus électrons–électrons, électrons–magnons et électrons–phonons intrabandes et interbandes ($s\uparrow - s\downarrow$, $s\uparrow - d\downarrow$, $s\downarrow - d\downarrow$). Nous mettons en évidence, en particulier, un terme de Baber $s\downarrow d\downarrow$ $s\downarrow d\downarrow$ important pour les électrons de la bande $d\downarrow$ et un terme de diffusion électrons–phonons $s\downarrow d\downarrow$ bloqué à basse température. Nous montrons que l'interprétation directe du comportement de la résistivité en termes de processus de diffusion n'a de sens qu'après la séparation de la résistivité en ses diverses composantes, chacun des termes A et B n'ayant qu'un sens phénoménologique.

(1) *Structure électronique des impuretés de transition dissoutes dans le cobalt*

Si l'on dissout deux éléments de transition en faible quantité dans une matrice ferromagnétique et si l'alliage ternaire ainsi constitué suit la loi de Matthiessen, la résistivité de celui-ci $\rho(c_1, c_2)$ doit obéir à une loi du type:

$$\rho(c_1, c_2) = c_1\rho_{01} + c_2\rho_{02} \quad \text{(M.R.)} \qquad (1.1)$$

où c_1 et c_2 sont les concentrations atomiques d'impuretés 1,2 et où ρ_{01} et ρ_{02} sont les résistivités résiduelles des alliages binaires correspondants.

Les alliages ternaires **Co** Ir Fe, **Co** Ru Fe, **Co** Os Fe présentent une forte déviation à la loi de Matthiessen et suivent une loi du type:

$$\frac{\rho(c_1, c_2)}{c_1} = f\left(\frac{c_2}{c_1}\right) = f(\lambda) \qquad (1.2)$$

$$\frac{\rho(c_1, c_2)}{c_2} = g\left(\frac{c_1}{c_2}\right) = g(\lambda^{-1}) \qquad (1.3)$$

en accord avec les résultats d'un modèle à deux bandes[7].

Nous avons vérifié par ailleurs[9, 10], que les interactions entre impuretés sont négligeables: en effet, les mesures d'aimantation moyenne d'un alliage $\bar{\mu}(c_1, c_2)$ suivent une loi de superposition:

$$\bar{\mu}(c_1, c_2) = \mu_{\text{Co}} + c_1\left(\frac{\mathrm{d}\bar{\mu}_1}{\mathrm{d}c_1}\right)_{c_1=0} + c_2\left(\frac{\mathrm{d}\bar{\mu}_2}{\mathrm{d}c_2}\right)_{c_2=0}. \qquad (1.4)$$

Dans (1,4)μ_{Co} désigne l'aimantation du cobalt pur, $(\mathrm{d}\bar{\mu}_1/\mathrm{d}c_1)_{c_1=0}$ et $(\mathrm{d}\bar{\mu}_2/\mathrm{d}c_2)_{c_2=0}$ représentent les variations d'aimantation des alliages binaires correspondants dans la limite d'une dilution infinie.

Connaissant les fonctions f et g, nous avons déterminé les résistivités des bandes ↑ et ↓ associées à chaque impureté dissoute dans le cobalt en utilisant la méthode proposée par Léonard *et al.*[7]. La résistivité pour chaque bande et pour chaque impureté est donnée par:

$$\rho_{01}{}^{\uparrow}_{\downarrow}=2\rho_{01}\left[1{}^{+}_{-}\sqrt{\left\{1+\frac{4\rho_{01}(\rho_{02}-\beta_1)^2(\rho_{01}-\beta_2)}{(\beta_1\beta_2-3\rho_{01}\rho_{02})^2+4(\beta_1\rho_{01}^2\rho_{02}+\beta_2\rho_{02}^2\rho_{01}-3\rho_{01}^2\rho_{02}^2)}\right\}}\right]^{-1} \qquad (1,5)$$

$$\rho_{02}{}^{\uparrow}_{\downarrow}=2\rho_{02}\left[1{}^{-}_{+}\sqrt{\left\{1+\frac{4\rho_{02}(\rho_{01}-\beta_2)^2(\rho_{02}-\beta_1)}{(\beta_1\beta_2-3\rho_{01}\rho_{02})^2+4(\beta_1\rho_{01}^2\rho_{02}+\beta_2\rho_{02}^2\rho_{01}-3\rho_{01}^2\rho_{02}^2)}\right\}}\right]^{-1} \qquad (1,6)$$

où $\beta_1 = \mathrm{d}f(\lambda = 0)/\mathrm{d}\lambda$ et $\beta_2 = \mathrm{d}g(\lambda^{-1} = 0)/\mathrm{d}\lambda^{-1}$ représentent les pentes à l'origine des fonctions f et g.

Le Tableau 1 résume les résultats de cette décomposition à 4,2°K. Il y est porté en même temps les valeurs obtenues à 77 et à 300°K[5] par une autre méthode de décomposition. L'ensemble des valeurs obtenues est cohérent, tant du point de vue de l'ordre de grandeur, que du point de vue de la variation en température; on notera, la très faible variation des résistivités $\rho_{0\uparrow}, \rho_{0\downarrow}$ associées à chaque bande entre 4–77°K. Ceci justifie donc à postériori, l'hypothèse utilisée par Durand selon laquelle les écarts à la loi de Matthiessen dans chaque bande σ sont négligeables. Notons enfin, que les valeurs obtenues pour les résistivités $\rho_{0\sigma}(\sigma = \uparrow, \downarrow)$ du fer sont indépendantes du type d'alliage ternaire étudié (cf. Tableau 1). Nous ne discuterons pas ici les valeurs obtenues pour $\rho_{0\sigma}$ en fonction de la structure électronique des impuretés, reportant pour celà à la discussion détaillée qui est faite dans la Réf. [5].

(2) *Séparation des diverses contributions à la résistivité du cobalt pur*

Les alliages binaires étudiés ont été choisis de sorte que les déviations à la loi de Matthiessen soient assez fortes ainsi que le suggèrent les mesures de moments magnétiques[9] et de résistivité résiduelle[5] qui ont été faites par ailleurs. Rappelons que, si $\rho_{\mathrm{all}}(T,c)$ désigne la résistivité à la température T de l'alliage de concentration c en impureté, $c\rho_0$ sa résistivité résiduelle et $\rho_m(T)$ la résistivité de la matrice, la déviation à la loi de Matthiessen est définie par:

$$\Delta\rho(T) = \rho_{\mathrm{all}}(T,c) - c\rho_0 - \rho_m(T).$$

Dans un modèle à deux bandes couplées la résistivité de l'alliage s'écrit[3]:

$$\rho_{\mathrm{all}} = \frac{(\rho_{m\uparrow}+c\rho_{0\uparrow})(\rho_{m\downarrow}+c\rho_{0\downarrow})+\rho_{\uparrow\downarrow}\{\rho_{m\uparrow}+\rho_{m\downarrow}+c(\rho_{0\uparrow}+\rho_{0\downarrow})\}}{\rho_{m\uparrow}+\rho_{m\downarrow}+c(\rho_{0\uparrow}+\rho_{0\downarrow})+4\rho_{\uparrow\downarrow}}. \qquad (2.1)$$

Remarquons que dans cette relation:

– on néglige les termes de couplages interbandes dus à l'impureté;

– on définit $\rho_{m\sigma}$ comme la résistivité de la matrice pure associée à la bande σ en tenant compte de l'ensemble des termes de couplages interbandes s-s;

– $\rho_{0\sigma}$ contient tous les termes de modification de la résistivité dans la bande σ dus à l'impureté.

Si l'on se place dans la limite $\rho_{0\uparrow}, \rho_{0\downarrow} \gg \rho_{m\uparrow}, \rho_{m\downarrow}, \rho_{\uparrow\downarrow}$, les déviations à la loi de Matthiessen se mettent sous la forme:

$$\Delta\rho(T) = \frac{\rho_{m\uparrow}}{\mu+1}\left[\frac{\mu-\alpha}{1+\alpha}\right]^2+\rho_{\uparrow\downarrow}\left[\frac{1-\alpha}{1+\alpha}\right]^2 \qquad (2,2)$$

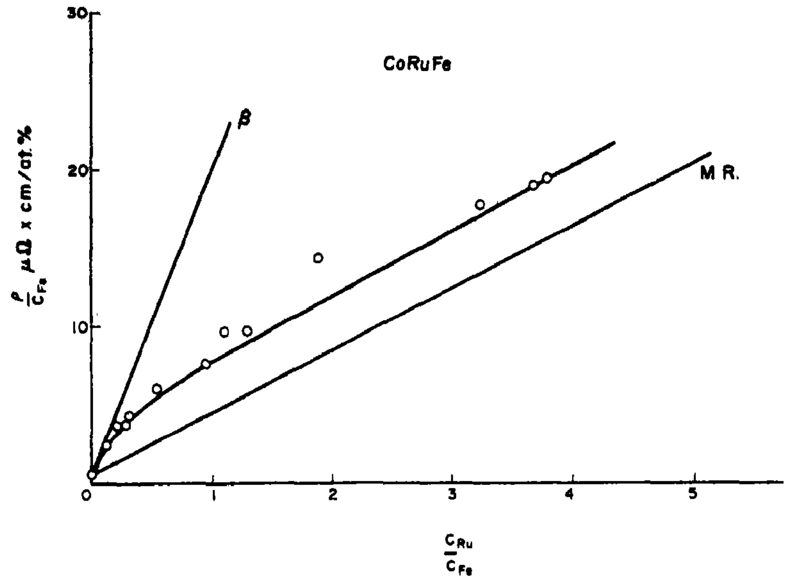

Fig. 1. ρ/c_1 en μΩ cm/at.% pour l'alliage ternaire Co Ru Fe en fonction du rapport $\lambda = c_2/c_1$. M.R.: loi de Matthiessen. β: pente à l'origine.

Tableau 1. *Résistivités (exprimées en* μΩ *cm/% at.) associées à chaque bande pour les impuretés de transition dissoutes dans le cobalt.* (*) *Valeurs à* 77°K *et* 295°K *d'après*[5]

		4,2°K		4,2°K	77°K*	295°K*
Co Ir Fe	$\rho_{Fe\uparrow}$	0.54	$\rho_{Ir\uparrow}$	11,7	11,85	16,40
	$\rho_{Fe\downarrow}$	6,62	$\rho_{Ir\downarrow}$	3,82	3,75	3,45
	α_{Fe}	$12{,}2_5$	α_{Ir}	0,327	0,316	0,213
Co Ru Fe	$\rho_{Fe\uparrow}$	0,54	$\rho_{Ru\uparrow}$	22,4	23,8	35,4
	$\rho_{Fe\downarrow}$	6,67	$\rho_{Ru\downarrow}$	4,86	4,80	4,50
	α_{Fe}	$12{,}3_2$	α_{Ru}	0,217	0,202	0,127
Co Os Fe	$\rho_{Fe\uparrow}$	0,54	$\rho_{Os\uparrow}$	23,55	23,75	34,0
	$\rho_{Fe\downarrow}$	6,72	$\rho_{Os\downarrow}$	6,84	6,80	6,40
	α_{Fe}	$12{,}4_2$	α_{Os}	0,290	0,286	0,188

avec

$$\mu = \frac{\rho_{m\downarrow}}{\rho_{m\uparrow}} \quad \alpha = \frac{\rho_{0\downarrow}}{\rho_{0\uparrow}} \tag{2,3}$$

Les déviations par rapport à la loi de Matthiessen d'alliages binaires tels que Co Ru, Co Os, Co Ir, Co Fe, Co Re, Co Cr satisfont entre 4–30°K à une loi phénoménologique du type (Figs. 3–5):

$$\Delta\rho(T) = AT^2 + BT^5. \tag{2,4}$$

On ne peut cependant pas assimiler directement le coefficient A à la contribution à la résistivité du terme de mélange de spin $\rho_{\uparrow\downarrow}$. En effet, A dépend de l'impureté de transition dissoute dans la matrice et les résistivités ρ et ρ peuvent aussi comporter un terme en T^2.

Pour effectuer la séparation des diverses

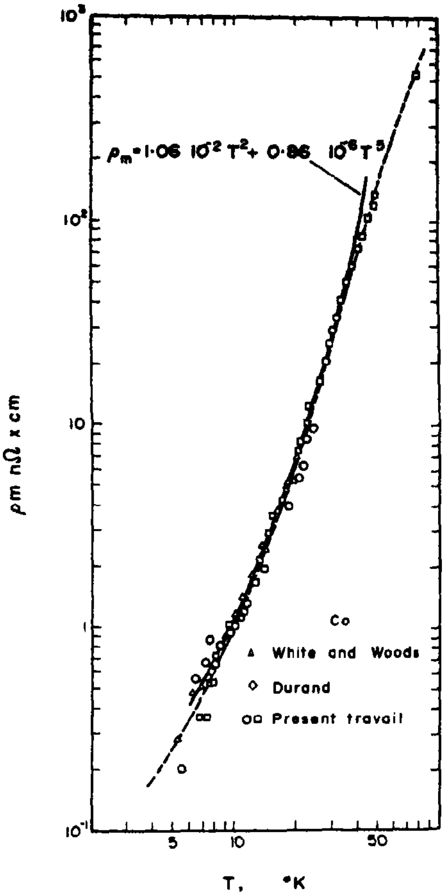

Fig. 2. Résistivité du cobalt pur $\rho_m(T) = \rho_{Co}(T) - \rho_{Co}(0)$ en fonction de la température.

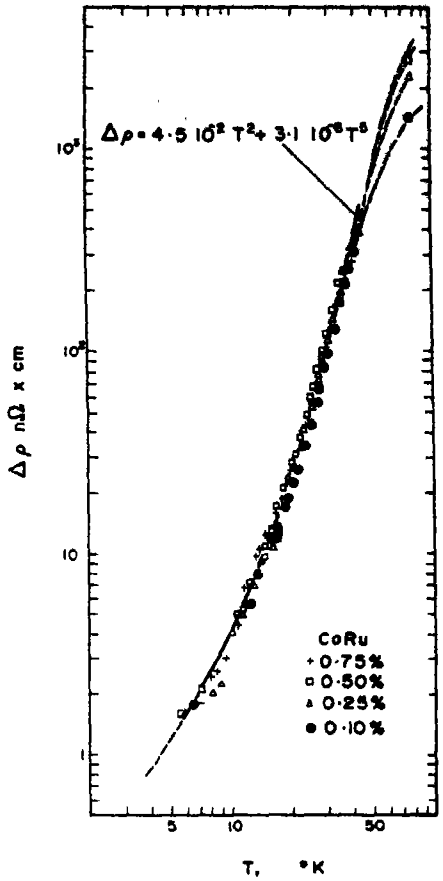

Fig. 3.

contributions, nous avons utilisé la relation (2,2):

pour une température et un alliage donné, α est connu grâce aux *mesures de résistivités résiduelles sur les alliages ternaires*; on recherche les valeurs de $\rho_{m\uparrow}$, $\rho_{\uparrow\downarrow}$ et μ concordant le mieux avec les résultats expérimentaux concernant la matrice (ρ_m) et les déviations à la loi de Matthiessen de quatre alliages binaires ($\Delta\rho$(CoRu), $\Delta\rho$(CoIr), $\Delta\rho$(CoOs), $\Delta\rho$(CoFe)).

On a ainsi pu déterminer les valeurs de μ, $\rho_{m\uparrow}$, $\rho_{\uparrow\downarrow}$ entre 4–50°K, l'accord entre les déviations calculées et expérimentales étant réalisé à mieux de 10 pour cent (Fig. 6) si l'on accepte le cas des alliages Co Fe pour $T >$ 15°K. Pour ces derniers, les écarts à la loi de Matthiessen dépendant déjà fortement de la concentration à 20°K, la relation (2,2) n'est plus valable, et le calcul doit être fait en utilisant la formule générale (2,1); cependant, on ne peut obtenir qu'un ordre de grandeur, d'une part en raison de la faible déviation observée pour $\Delta\rho$(Co Fe), d'autre part en raison de l'imprécision subsistant sur la concentration et la résistivité résiduelle extrapolée à 0°K.

Afin de compléter cette étude, nous avons repris les valeurs obtenues pour les binaires à 77–295°K[5] et nous avons déterminé l'ordre de grandeur des termes $\rho_{m\uparrow}$, $\rho_{m\downarrow}$, $\rho_{\uparrow\downarrow}$ à

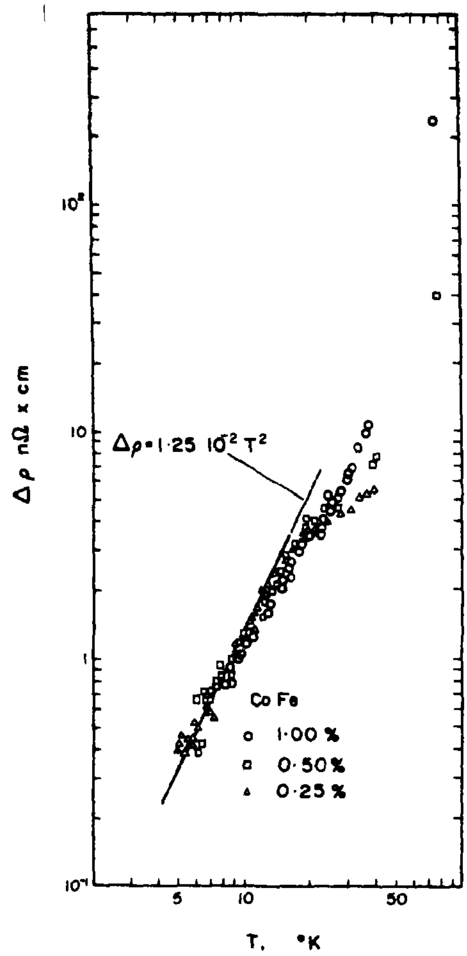

Fig. 4.

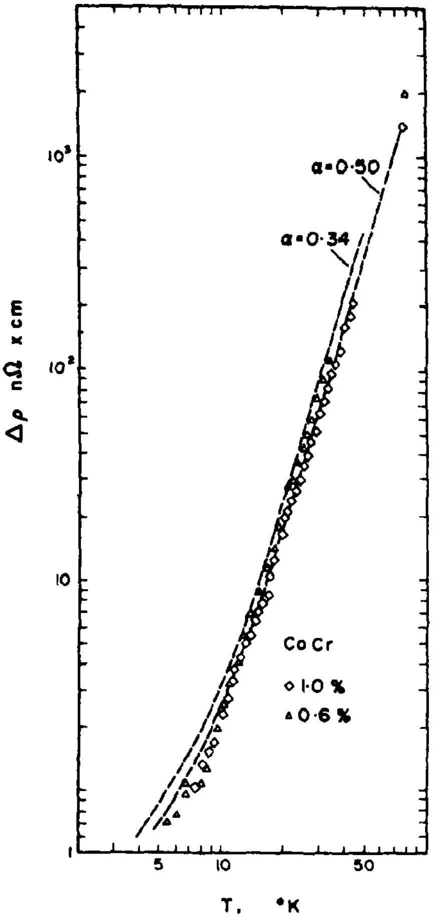

Fig. 5.

Figs. 3, 4, 5. Déviations à la loi de Matthiessen des alliages binaires $\Delta\rho = \rho_{\text{all}}(T) - \rho_m(T) - c\rho_{\text{all}}(0)$ pour différentes concentrations. En trait plein: loi phénoménologique en $AT^2 + BT^5$. En pointillé: valeurs correspondant à la decomposition effectuée à la Section 2.

ces températures. La méthode utilisée étant toutefois différente, car, à ces températures, les déviations à la loi de Matthiessen—de même que pour l'alliage Co Fe à partir de 15°K—ne sont plus indépendantes de la concentration et la condition $\rho_{0\uparrow}, \rho_{0\downarrow} \gg \rho_{m\uparrow}, \rho_{m\downarrow}, \rho_{\uparrow\downarrow}$ n'est plus vérifiée d'une façon satisfaisante. En partant de la relation générale (2,1) nous avons recherché un couple de valeurs $\rho_{m\uparrow}, \rho_{\uparrow\downarrow}$, en prenant diverses valeurs de μ, donnant le meilleur accord pour toutes les concentrations considérées. Cet accord doit aussi se faire pour les autres alliages binaires à toutes concentrations ($0{,}1\% \leq c \leq 1\%$).

Le Tableau 2 résume l'ensemble des résultats de cette étude. L'accord réalisé est satisfaisant, compte tenu des hypothèses faites dans l'utilisation de la relation (2,1) ($\rho_{\uparrow\downarrow}$ indépendant de $c, \ldots$).

(3) *Discussion et interprétation des résultats obtenus*

Dans ce paragraphe, la cohérence de la méthode employée est discutée brièvement; les variations thermiques des diverses contributions à la résistivité du cobalt pur sont

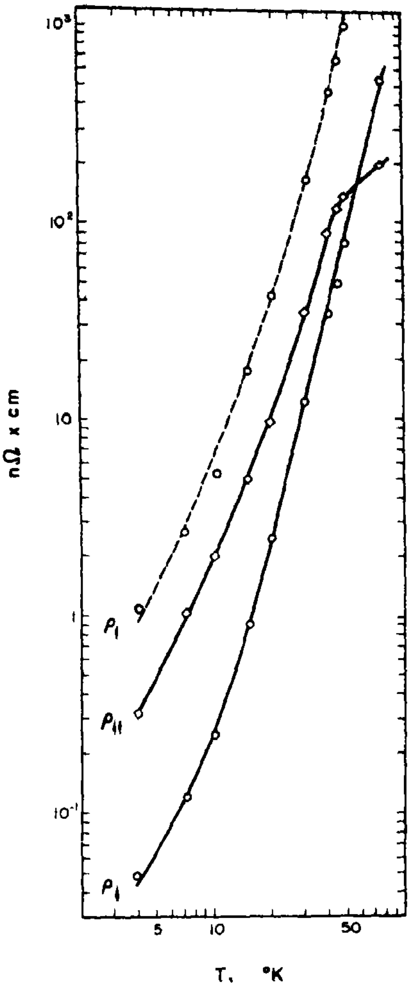

Fig. 6. $\rho_{m\uparrow}$, $\rho_{\uparrow\downarrow}$, $\rho_{m\downarrow}$ en fonction de la température pour le cobalt. Valeur à 77°K d'après (5).

interprétées en tenant compte des mécanismes de relaxation électrons-électrons et électrons-magnons intrabande et interbande.

3.1 *Cohérence des résultats obtenus.* La cohérence des méthodes employées pour séparer les différentes contributions à la résistivité du cobalt et de ses alliages est vérifiée par les tests suivants (10):

(a) Pour une température fixée, μ, $\rho_{\uparrow\downarrow}$ et $\rho_{m\uparrow}$ sont indépendants de l'impureté dissoute dans la matrice.

(b) Les déviations expérimentales à la loi de Matthiessen des alliages qui n'ont pas été utilisés pour effectuer la séparation exposée au paragraphe 2 (par exemple Co Cr et Co Re entre 4–50°K) sont en accord avec les valeurs calculées à l'aide de $\rho_{m\uparrow}$, $\rho_{\uparrow\downarrow}$, $\mu = f(T)$ en prenant $\alpha_{\mathrm{Re}} = 0{,}44$ et $\alpha_{\mathrm{Cr}} = 0{,}50$; ces valeurs sont du même ordre de grandeur que celles obtenues par J. Durand[5] ($\alpha_{\mathrm{Re}} = 0{,}43$, $\alpha_{\mathrm{Cr}} = 0{,}34$), quoique cet accord soit moins bon pour le chrome. Cependant ce dernier, présente parmi les métaux de la première série de transition un comportement particulier, apparaissant aussi bien dans les mesures de moments magnétiques moyens que de résistivité résiduelle, et il est nécessaire de préciser sa structure électronique par de nouvelles mesures.

3.2 *Interprétation des résultats.* La méthode de séparation exposée précédemment (Section 2) montre que les termes $\rho_{m\uparrow}$, $\rho_{\uparrow\downarrow}$, $\rho_{m\downarrow}$ suivent une loi phénoménologique du type $aT^2 + bT^5$ et cela au moins jusqu'à 30°K:

Tableau 2. Résistivités (exprimées en nΩ cm) associées à chaque bande et terme de mélange de spin dans le cobalt pur entre 4–77°K

T°K	4	7	10	15	20	30	40	45	50	77
μ	23	22	21	18	17	15	13,5	13	12,5	11
$\rho_{m\uparrow}$	0,046	0,12	0,25	0,9	2,5	11	35	50	80	400 à 700
$\rho_{\uparrow\downarrow}$	0,32	1,04	2,0	5,0	10	35	90	120	140	< 2500
$\rho_{m\downarrow}$	1,06	2,6	5,25	16,2	42,5	165	473	650	1000	4400 à 7700

$$\begin{aligned}\rho_{m\uparrow} &= 0{,}27\ 10^{-2}T^2+3{,}8\ 10^{-7}T^5 \qquad (n\Omega\,\mathrm{cm})\\ \rho_{\downarrow\uparrow} &= 2{,}0\ 10^{-2}T^2+6{,}0\ 10^{-7}T^5\\ \rho_{m\downarrow} &= 5{,}8\ 10^{-2}T^2+56\ 10^{-7}T^5. \qquad (3{,}1)\end{aligned}$$

Si l'on reporte ces valeurs dans l'expression de la résistivité de la matrice (cf. (2,1) pour $c=0$) nous obtenons une fraction rationnelle dont la dépendance en température est complexe, alors que la décomposition faite directement sur les résultats expérimentaux donne une fonction de la forme:

$$\rho_m(T) = 1{,}06\ 10^{-2}T^2+8{,}6\ 10^{-7}T^5. \qquad (3{,}2)$$

Cependant, les deux fonctions présentent le même comportement au moins entre 4–30°K, *aucun des termes du développement (2,1) (3,1) n'étant négligeable dans ce domaine de température.*

De même, nous retrouvons un résultat analogue pour les alliages dilués de métaux de transition; ainsi, dans le cas du Co Ru la décomposition expérimentale directe donne, pour l'écart à la loi de Matthiessen:

$$\Delta\rho(\mathrm{Co\ Ru}) = 4{,}5\ 10^{-2}T^2+3{,}1\ 10^{-6}T^5 \qquad (3{,}3)$$

tandis que la décomposition obtenue donne:

$$\Delta\rho(\mathrm{Co\ Ru}) = \frac{50{,}6\ 10^{-4}T^2+7{,}32\ 10^{-7}T^5+3{,}27\ 10^{-11}T^8}{8{,}9\ 10^{-2}+87{,}6\ 10^{-7}T^3}. \qquad (3{,}4)$$

Là encore, les deux fonctions (3,3) et (3,4) prennent les mêmes valeurs pour $4°\mathrm{K} \leq T \leq 30°\mathrm{K}$, aucun terme de (3,4) n'étant négligeable dans le domaine de température étudié.

Les lois $(\alpha a T^2+bT^5)$ que suivent la résistivité du cobalt et les déviations à la loi de Matthiessen d'alliages dilués de métaux de transition, ne sont que phénoménologiques: *la variation en T^2 ne traduit pas uniquement la contribution du terme de mélange de spin $\rho_{\downarrow\uparrow}$, et le comportement en T^5 à plus haute température ne correspond pas directement au phénomène de diffusion du type Bloch-Grüneisen.*

Dans la suite de ce paragraphe, nous allons étudier directement l'origine des résistivités $\rho_{m\sigma}$, $\rho_{\downarrow\uparrow}$ en fonction des processus fondamentaux de diffusion.

3.3 *Séparation des processus électrons-magnons, électrons-phonons, électrons-électrons.* Dans un ferromagnétique fort, c'est-à-dire un ferromagnétique dont l'une des bandes $d(d\uparrow)$ est pleine, l'expression de la résistivité associée à chaque bande σ est de la forme: [5]

$$\begin{aligned}\rho_{m\uparrow} &= \bar{\rho}^{M}_{\downarrow\uparrow}+\rho^{\circ M}_{\uparrow d}+\rho^{\circ}_{m\uparrow}\\ \rho_{m\uparrow} &= \bar{\rho}^{M}_{\downarrow\uparrow}+\rho^{\circ B}_{\downarrow d}+\rho^{\circ}_{\downarrow d}+\rho^{\circ}_{m\downarrow}.\end{aligned} \qquad (3{,}5)$$

En effet, dans chaque bande $s_\sigma(\sigma=\uparrow,\downarrow)$, le terme $\rho^{\circ}_{m\sigma}$ représente la résistivité de la bande σ supposée seule, et traduit les transitions électrons-phonons $s_\sigma-s_\sigma$. La présence de la bande $s_{-\sigma}$ introduit un terme de couplage $\bar{\rho}^{M}_{\downarrow\uparrow}$ dû aux mécanismes de diffusion électrons-magnons $s_\sigma-s_{-\sigma}$. De plus, l'existence d'une bande $d\downarrow$ incomplètement remplie entraîne: (i) dans la bande $s\uparrow$, des transitions $s\uparrow-d\downarrow$ dus au couplage électrons-magnons $\rho^{\circ M}_{\uparrow d}$; (ii) dans la bande $s\downarrow$, des transitions électrons électrons du type Baber $(\rho^{\circ B}_{\downarrow d})$ et des transitions électrons-phonons $(\rho^{\circ}_{\downarrow d})$.

Nous nous proposons de discuter les variations de $\rho_{m\sigma}(\sigma=\uparrow,\downarrow)$ avec la température et de mettre en évidence la contribution de chacun de ces processus à la résistivité $\rho_{m\sigma}$ à partir des formules (3,5).

(i) *Variation de $\rho_{m\uparrow}$ avec la température.* Dans la bande $s\uparrow$, $\rho^{\circ}_{m\uparrow}$ doit être un terme de diffusion $s-s$ obéissant à une loi de Bloch-Grüneisen; les autres termes proviennent des magnons; ils doivent présenter une variation proportionnelle à T^2 sur tout le domaine de température étudié ($T<77°\mathrm{K}$) puisque la température maximum du spectre de magnons est très supérieure aux températures considérées ($\theta_s \leq 2000°\mathrm{K}$)[11, 12].

Pour $T \ll \theta_D$, θ_s (i.e. pour $T<30°\mathrm{K}$) nous obtenons expérimentalement la loi:

$$\rho_{m\uparrow} = 0{,}27\ 10^{-2}T^2 + 3{,}8\ 10^{-7}T^5. \quad (T < 30°\text{K})$$

Le terme variant proportionnellement à T^2 est considéré comme provenant des interactions électrons–magnons; cette interprétation doit être justifiée a posteriori par la variation du terme $\rho^\circ_{m\uparrow}$ qui doit suivre, en principe, une loi de Bloch–Grüneisen.

De fait, les résultats expérimentaux montrent que, dans tout le domaine étudié ($T \ll \theta_s$) la résistivité $\rho_{ss}(T) = \rho_{m\uparrow} - 0{,}27\ 10^{-2}T^2$ suit une loi de Bloch–Grüneisen:

$$\rho_{ss}(T) = 2{,}24\ 10^4 \left[J_5\left(\frac{\theta_D}{T}\right)\right]\left(\frac{T}{\theta_D}\right)^5 \qquad (n\Omega\ \text{cm})$$

avec

$$\theta_D = 380°\text{K}$$

$\rho_{ss}(T)$ doit être identifié avec le terme $\rho^\circ_{m\uparrow}$. *Sur tout le domaine de température étudié (Fig. 7) le comportement de la résistivité associée à la bande $s\uparrow$, $\rho_{ss}(T) = \rho^\circ_m$, est identique à celui d'un métal noble tel que le cuivre ou l'argent, et peut donc être identifié avec la résistivité dûe aux transitions $s\uparrow - s\uparrow$ dues aux phonons.*

(ii) Variation de $\rho_{m\downarrow}$ avec la température. Dans la bande $s\downarrow$, l'expression phénoménologique de $\rho_{m\downarrow}$, valable pour $T < 30$°K, est donnée par:

$$\rho_{m\downarrow} = 5{,}8\ 10^{-2}T^2 + 56\ 10^{-7}T^5.$$

La grande valeur du coefficient du terme en T^2, par rapport à celui qu'on a mis en évidence dans la bande ↑ s'explique par la présence du terme de diffusion de Baber[13]. Ce terme est approximativement proportionnel au carré de la densité d'états '*d*' au niveau de Fermi, et est, pour cela, plus important que tout autre terme en T^2 à basse température. Il s'en suit que le coefficient du terme en T^2 doit être proportionnel au carré de la chaleur spécifique ce qui a été assez bien vérifié par Rice[14], pour les éléments de transition tels que Os, Re, Pt, Pd. Si l'on adopte ce schéma pour le cobalt-en faisant intervenir la chaleur spécifique par bande de spin- on obtient un coefficient de 4 $10^{-2} n\Omega$ cm $(°\text{K})^{-2}$ qui est du même ordre de grandeur que celui que nous avons obtenu $\rho^{B}_{\downarrow d} = 5{,}8\ 10^{-2} n\Omega\ \text{cm}\ (°\text{K})^{-2}$.

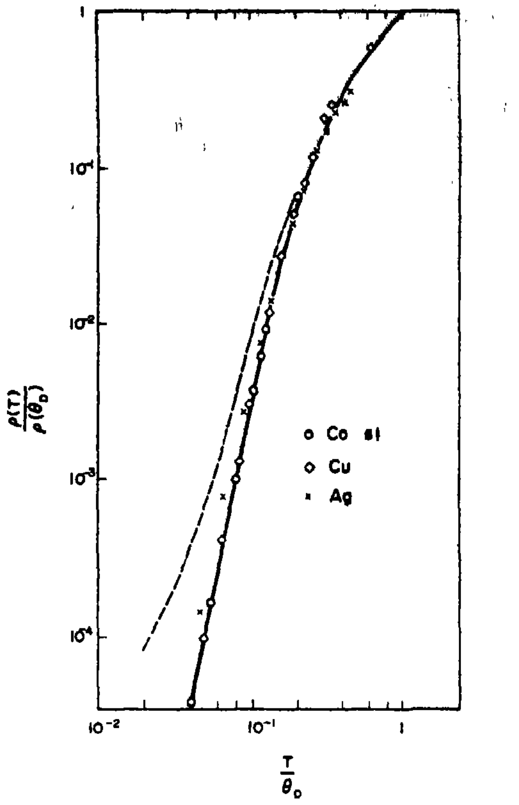

Fig. 7. $\rho(T)/\rho(\theta_D)$ en fonction du rapport T/θ_D pour le cuivre, l'argent et la bande $s\uparrow$ du cobalt. Pour ce dernier, on a représenté $[\rho_m(T) - 0.27\ 10^{-2}T^2]/[\rho_m\cdot(\theta_D) - 0{,}27\ 10^{-2}\theta_D^2]$ en pointillé $\rho(T)/\rho(\theta_D)$ pour le cobalt sans séparation des diverses contributions.

Par contre, le coéfficient du terme en T^5 est nettement trop grand si l'on admet que dans la bande $s\downarrow$, le terme $\rho^\circ_{m\downarrow}$ est du même ordre de grandeur que $\rho^\circ_{m\uparrow}$, et qu'il suit de même une loi de Bloch–Grüneisen.

Ce désacord s'explique par le fait que le terme phénoménologique en T^5 contient à la fois le terme de diffusion électrons–phonons *s-s* ($\rho^\circ_{m\downarrow}$) et le terme de diffusion *s-d* ($\rho^\circ_{\downarrow d}$).

Dans le modèle proposé par Wilson[15], la contribution des transitions électrons–

phonons $s\downarrow$-$d\downarrow$ est donnée par

$$\rho^{\circ}_{\downarrow d}(T) = \left(\frac{T}{\theta_D}\right)^3 \left\{C\left[J_3\left(\frac{\theta_D}{T}\right) - J_3\left(\frac{\theta_E}{T}\right)\right]\right\} \quad (3{,}6)$$

où C est une constante, θ_D est la température de Debye et $k_B\theta_E$ est l'énergie minimum des phonons induisant des transitions s-d, $J_n(x)$ désigne l'intégrale du type Debye:

$$J_n(x) = \int_0^x \frac{y^n}{(e^y - 1)(1 - e^{-y})}\,\mathrm{d}y.$$

Dans ce modèle, on ne considère que des processus de diffusion normaux et on admet que les surfaces de Fermi s et d sont sphériques.

$\rho^{\circ}_{\downarrow d}$ varie comme T^3 tant que la température T est grande devant la température de blocage du processus θ_E. Au contraire, à très basse température ($T \ll \theta_E$), les transitions s-d sont inefficaces et la résistivité $\rho^{\circ}_{\downarrow d}(T)$ tend vers zéro comme $e^{-\theta_E/T}$.

Nous pouvons avoir un ordre de grandeur du terme $\rho^{\circ}_{\downarrow d}$ si on admet que, les bandes s_σ- ($\sigma = \uparrow, \downarrow$) étant très semblables, les termes de diffusion s-s $\rho^{\circ}_{m\uparrow}$ et $\rho^{\circ}_{m\downarrow}$ *sont égaux:* il s'agit là d'une hypothèse vraisemblable puisque l'on sait que les bandes de spin s ne sont que très légèrement décalées l'une par rapport à l'autre par l'intermédiaire du potentiel d'échange. Par ailleurs, les résultats que nous obtenons ci-dessous sont indépendants de la valeur précise donnée à la résistivité $\rho^{\circ}_{m\downarrow}$, pourvu qu'elle soit du même ordre de grandeur que $\rho^{\circ}_{m\uparrow}$.

Sur la Fig. 8, nous reportons la variation en fonction de la température de

$$\bar{\rho}_{m\downarrow} = \rho_{m\downarrow} - 2{,}24\,10^4\left[J_5\left(\frac{\theta_D}{T}\right)\right]\left(\frac{T}{\theta_D}\right)^5 \quad (n\Omega\,\mathrm{cm}).$$

Le terme $\bar{\rho}_{m\downarrow}$ contient en principe (cf. 3,5) les contributions électrons–électrons, électrons–magnons et électrons–phonons s-d. Ainsi qu'on peut le voir sur la figure, ce terme présente uniquement un comportement en T^2 jusqu'à $T = 15°\mathrm{K} = \theta_E$ (température de blocage des transitions s-d). Au-delà, apparaît un terme supplémentaire en T^3 que nous

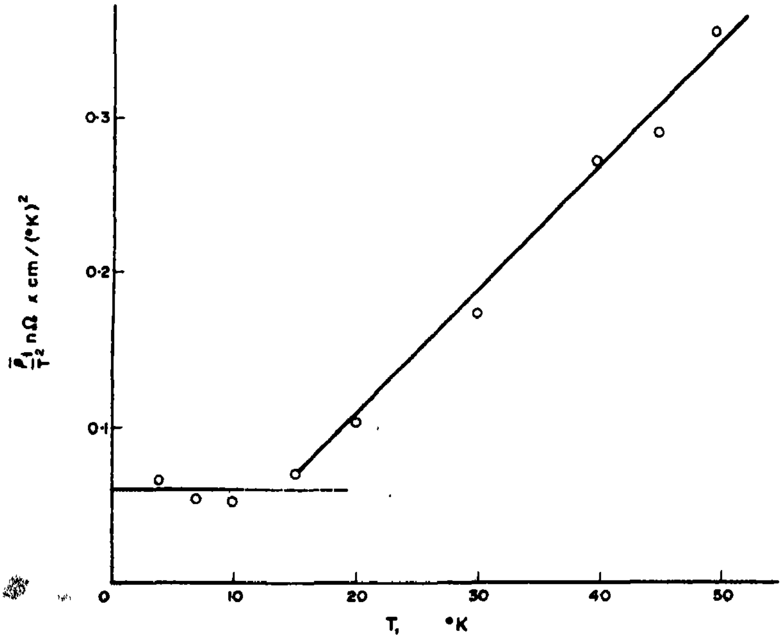

Fig. 8. $\bar{\rho}_{m\downarrow}/T^2$ en fonction de la température.

attribuons aux transitions électrons–phonons s-d.

En conclusion, la grande résistivité de la bande $s\downarrow$ par rapport à la bande $s\uparrow$ s'explique donc par la présence, dans cette dernière, de phénomènes de diffusion électrons–électrons du type Baber (pour $T < 15°K$) et de phénomènes de diffusion électrons–phonons s-d (pour $T > 15°K$). Ces derniers sont bloqués à très basse température parce que les surfaces de Fermi $s\downarrow$ et $d\downarrow$ ne se coupent pas. la distance moyenne entre surface $s\downarrow$ et $d\downarrow$ étant de l'ordre de $\delta k/k_s = \theta_E/\theta_D \# 4\ 10^{-2}$ où k_s est le rayon de la sphère de Wigner.

Remarquons enfin qu'une méthode telle que celle proposée par Colquitt[16], permettant de déterminer l'ordre de grandeur de θ_E n'est pas quantitativement applicable: parce que les bandes s et d n'ont pas de surfaces de Fermi sphériques, la variation thermique de $\rho^\circ_{\downarrow d}\ \alpha T^3$ restant valable tant que l'élément de matrice des transitions électrons–phonons $\langle k|V^{ep}|k'\rangle$ ne dépend que de la différence k-k' des vecteurs d'ondes incidents et diffusés par les phonons. D'autre part, nous ne disposons pas de données expérimentales suffisamment détaillées dans le domaine où les transitions s-d sont dominantes ($T > 77°K$). Enfin cette séparation ne peut être faite que directement sur chacune des résistivités partielles $\rho_{m\sigma}$ et non sur la résistivité mesurée.

(iii) Ordre de grandeur et variation de $\mu = \rho_{m\downarrow}/\rho_{m\uparrow}$ avec la température. Les valeurs élevées de μ, obtenues à basse température (à 4°K, $\mu = 23$), sont en accord avec un modèle de Mott: les transitions du type Baber sont dominantes et n'existent que pour la bande $d\downarrow$, qui est partiellement vide. La décroissance de μ, lorsque la température croît, est en accord avec les résultats déjà obtenus à 77–295°K[5].

(iv) Variation de $\rho_{\downarrow\uparrow}$ avec la température. L'interprétation des variations en température du terme de mélange de spin est plus délicate en raison des différentes contributions qui y participent (électrons–magnons, électrons–électrons) et de l'allure particulière des résultats expérimentaux (saturation de $\rho_{\downarrow\uparrow}$ à haute température, Fig. 9). On peut néanmoins remarquer que les interactions électrons–magnons et électrons–électrons présentent un comportement en T^2: la détermination expérimentale de $\rho_{\downarrow\uparrow}$ présente bien un tel comportement pour 4°K < T <

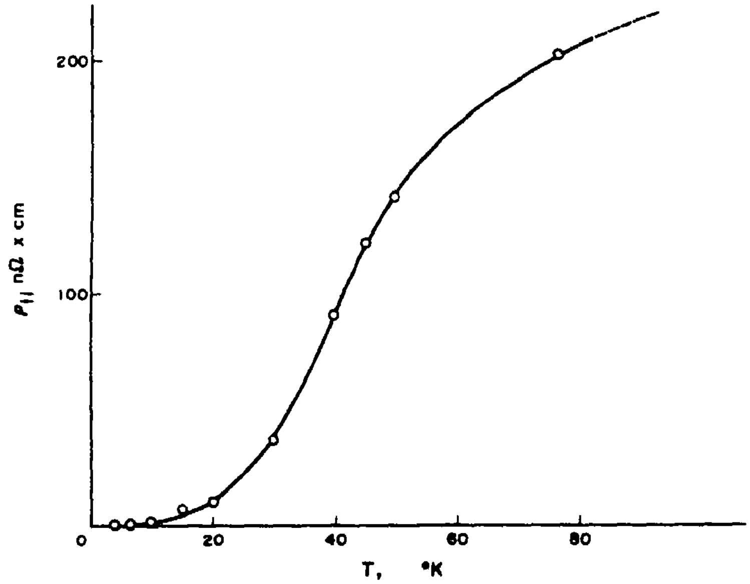

Fig. 9. Variation du terme de mélange de spin $\rho_{\downarrow\uparrow}$ en fonction de la température.

20°K. D'autre part, *la saturation du terme de mélange de spin* pour des températures supérieures à 50°K *ne peut être attribuée comme dans le fer*[17] *à des processus de blocage* $s\uparrow s\downarrow$.

En effet, en admettant des relations de dispersion quadratique pour les électrons des deux directions de spin, décalés par échange, des surfaces de Fermi sphériques et en introduisant une température caractéristique $\theta_1 = \hbar^2 q^2/2k_B\mu$, Fert[17] obtient:

$$\rho_{\uparrow\downarrow} \alpha (k_B T)^2 F\left(\frac{\theta_1}{T}\right).$$

Dans cette formule, q est le vecteur d'onde minimum du magnon effectuant une transition $s\uparrow s\downarrow$, μ est la masse effective du magnon et $F(x)$ est définie par:

$$F(x) = x\left[\frac{xe^x}{e^x-1} - \mathrm{Log}\,(e^x-1)\right].$$

La fonction F passe par un maximum pour $T \# 0{,}9\theta_1$ (Fig. 10). Les transitions électrons magnons sont bloquées à basse température ($T \ll \theta_1$, $F(\theta_1/T) = 0$) puisqu'il faut fournir l'énergie minimum $k_B\theta_1$ pour faire passer un électron d'une surface de Fermi s_σ à l'autre $s_{-\sigma}$. Dans le cas présent du cobalt, le modèle précédent n'est pas applicable puisque $\rho_{\uparrow\downarrow}/T^2$ ne tend pas vers zéro avec la température (du moins pour $T > 4$°K, Fig. 10); la variation de $\rho_{\uparrow\downarrow}$ ne peut être obtenue qu'en supposant qu'au moins l'un des termes qui contribuent au couplage interbande n'est pas bloqué. D'autre part, une estimation de la température de blocage des ondes de spin θ_B montre que celle-ci doit être très petite ($\theta_B \#$ 1–2°K) de sorte que les processus électrons–magnons ne sont pas bloqués pour $T > 4$°K et que le maximum de $\rho_{\uparrow\downarrow}/T^2$ vers 50°K ne peut être convenablement attribué à ces transitions.

La variation de $\rho_{\uparrow\downarrow}$ avec la température reste donc incomprise dans l'état actuel de la théorie; des expériences à plus haute température s'avèrent nécessaire pour permettre une meilleure compréhension de ce phénomène.

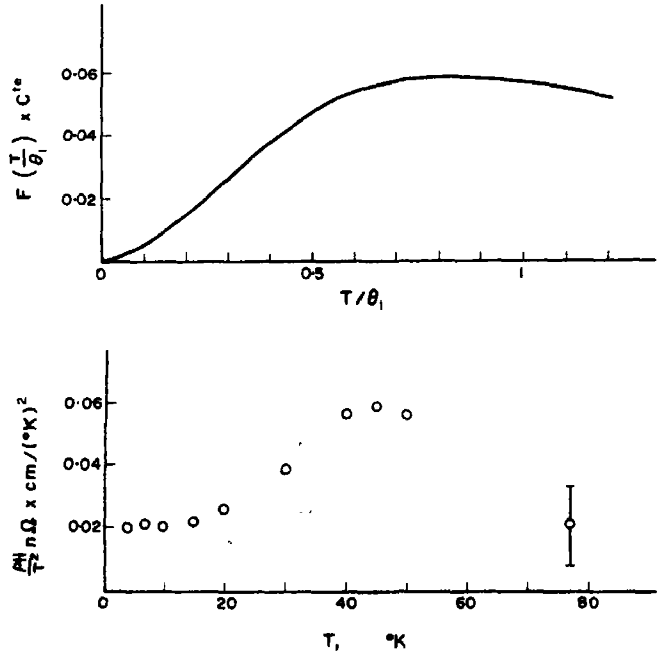

Fig. 10. $\rho_{\uparrow\downarrow}/T^2$ et 0,06 $F(\theta_1/T)$ en fonction de la température ($\theta_1 = 70$°K).

CONCLUSION

Cette étude met en évidence dans le cobalt:

—un terme de diffusion s-s dans la bande $s\uparrow$, identique à celui d'un métal noble (Cu, Ag).

—un terme de Baber du même ordre de grandeur que celui d'un métal paramagnétique et un terme s-d électrons–phonons (bloqué à basse température) dans la bande $s\downarrow$.

—l'existence d'un terme de mélange de spin.

Elle a permis la détermination quantitative, dans un large domaine de température, des résistivités associées à chaque bande de la matrice, ainsi que du terme de mélange de spin.

Elle explique l'origine physique d'un comportement du type $\Delta\rho$, $\rho_M = AT^2 + BT^5$ pour la matrice et ses alliages dilués et montre que les résultats expérimentaux ne peuvent être interprétés directement pour en déduire la nature, l'ordre de grandeur et la variation en température du terme de mélange de spin.

Enfin, tout en justifiant l'effet de période dans les éléments de transition, elle montre la validité du modèle à deux bandes couplées pour un ferromagnétique fort. Elle doit être poursuivie d'une part par des mesures de magnéto-résistance, et d'effets Hall, d'autre part en étendant le domaine de température étudié.

Remerciements—Nous remercions M. le Prof. C. Robert dont l'aide et les conseils nous ont été précieux ainsi que les Drs J. Durand et M. C. Cadeville pour de fructueuses discussions. Nous remercions également les Drs I. A. Campbell et A. Fert qui nous ont communiqué avant publication certains résultats sur leurs travaux en cours.

BIBLIOGRAPHIE

1. CAMPBELL I. A., FERT A. and POMEROY A. R., *Phil. Mag.* **15**, 977 (1967).
2. SCHWERER F. C. and SILCOX J., *Phys. Rev. Lett.* **20**, 101 (1968); FARREL T. and GREIG D., *J. Phys. C.* **1**, 1359 (1968).
3. FERT A. and CAMPBELL I. A., *Phys. Rev. Lett.* **21**, 1190 (1968).
4. WHITE G. K. and WOODS S. B., *Phil. Trans. R. Soc. (Lond.)* **251A**, 273 (1959).
5. DURAND J. and GAUTIER F. *J. Phys. Chem. Solids* **31**, 2773 (1970); DURAND J. Thèse 3ième cycle, Strasbourg (1969).
6. MOTT N. F., *Proc. Phys. Soc.* **47**, 571 (1935); *Proc. Phys. Soc.* **153A**, 699 (1936a); *Proc. Phys. Soc.* **156A**, 368 (1936b).
7. LEONARD P., CADEVILLE M. C., DURAND J. and GAUTIER F., *J. Phys. Chem. Solids* **30**, 2169 (1969).
8. KASUYA T., *Prog. theor. Phys.* **16**, 45 (1956); **16**, 58 (1956).
9. LOEGEL B., *J. Phys. C, Metal Phys. Suppl.* **3**, S355 (1970).
10. LOEGEL B. Thèse 3ième cycle, Strasbourg (1969).
11. SHIRANE G., MINKIEWICZ V. J. and NATHANS D., *J. appl. Phys.* **39**, 383 (1968).
12. WOLFARTH E. P., *J. appl. Phys.* **41**, 1205 (1970).
13. BABER W. G., *Proc. R. Soc. A* **158**, 383 (1937).
14. RICE M. J. *Phys. Rev. Lett.* **20**, 1439 (1968).
15. WILSON A. M., *Proc. R. Soc. (Lond.)* **A167**, 580 (1938).
16. COLQUITT L. Jr., *J. appl. Phys.* **36**, 2454 (1965).
17. FERT A., *J. Phys. C.* **2**, 1784 (1969).

J. Phys. Chem. Solids, 1971, Vol. 32, pp. 2737–2747. Pergamon Press. Printed in Great Britain

LOCALIZED MODE FREQUENCY FOR SUBSTITUTIONAL IMPURITIES IN ZINC BLENDE TYPE CRYSTALS*

S. P. GAUR and J. F. VETELINO
Department of Electrical Engineering, University of Maine, Orono, Maine 04473, U.S.A.

and

S. S. MITRA
Department of Electrical Engineering, University of Rhode Island, Kingston, R. I. 02881, U.S.A.

(*Received* 15 *April* 1971)

Abstract – A mathematical model which employs a Green's function technique in the mass defect approximation is utilized to calculate the lattice dynamics of the imperfect crystal. This model makes direct use of the eigenfrequencies and eigenamplitudes of vibration of the phonons in the perfect lattice calculated by the modified rigid ion model introduced earlier. The phonon density of states is calculated for a number of II–VI and III–V type compounds that crystallize in the zinc blende structure. Next the variation of local mode frequency as a function of the defect mass is obtained for these crystals. The existence of a new type of localized gap mode, which corresponds to the replacement of the heavy host atom by a yet heavier substitutional atom, is predicted. The results are found to compare favorably with available experimental data on local mode frequencies obtained by infrared, Raman, and other optical measurements.

1. INTRODUCTION

SUBSTITUTIONAL impurities are known to affect the lattice vibrational spectrum of a crystal. In addition to modifying the frequency distribution of the host lattice, certain new features known as the localized modes of vibration are introduced in certain cases. In a diatomic crystal, when the substituent is lighter than both the host lattice atoms, one expects resonance modes due to the localized vibrations of the impurity to occur with frequencies above the optic band of the host lattice. If the host lattice phonon frequency spectrum possesses a gap between the optic and acoustic bands, then localized modes in the gap, known as gap modes, may also occur for certain substitutional impurities.

A large amount of experimental data have recently appeared[1–22] on localized modes due to substitutional impurities in zinc blende compounds. Theoretically, the solution for the local mode problem can be expressed in terms of the eigenvalues and the eigenvectors of all phonon states in the host lattice by using a Green's function technique [23]. Actual calculations have, however, been rather sparse[15, 17, 24, 25] due to the lack of a consistent lattice dynamical model for the zinc blende crystals. Where neutron scattering data did exist, which is for only a relatively few zinc blende crystals[26–30], local mode calculations have been performed[25] assuming a molecular model[31] with the eigenvalues and the eigenvectors of the phonon states as determined by an elaborate shell model calculation. The calculated results are however fitted to the infrared maxima. Recently an elementary linear diatomic chain model[17] has been phenomelogically utilized to predict local mode behavior with fair success.

In this work, the eigenvalues and the eigenvectors of the phonons are determined by using a modified rigid ion model[32]. This

---

*Work supported in part by the Research Corporation.

model does not require neutron scattering data but only the three elastic constants, C_{11}, C_{12} and C_{44}, and the two long-wavelength optic mode phonon frequencies as input data in order to determine the eigenvalues and the eigenvectors of the phonon states. In the past for SiC and ZnS, the phonon dispersion predicted[32, 33] by this model displays good agreement with experimental data. In the case of ZnS, where neutron scattering data is available[29, 30] and a reasonable number of calculations have been performed, [29, 30, 33, 34] a comparison between the different models is possible. For the acoustic mode frequencies the modified rigid ion model predicts phonon dispersion which in some cases is superior to that of some force fitted models. In the case of the optic mode frequencies, this model is consistently superior to the results predicted[29, 30, 34] by other lattice dynamical models. It also has been previously discussed[35] that the resulting frequency distribution function calculated by the modified rigid ion model, even though approximate, may in fact be superior to that calculated by a force fit model. Further, the application of a shell model and its modifications to zinc blende crystals has in fact been questioned[36, 37] on fundamental grounds. The applicability of our model to zinc blende crystals has also been discussed[35] in terms of an invariance relation between the elastic constants and the long-wavelength zone center phonon frequencies. This model also predicts [38] the coefficient of thermal expansion in ZnTe well. The present model has however certain drawbacks. Whenever experimental data have been available the present model predicts[32, 33, 35] zone boundary TA mode frequencies which are slightly high. This, however, is not expected to have a large effect on the local mode or gap mode prediction.

As already pointed out, a considerable interest has recently been evidenced[1–22] in the measurement of local and gap mode phonons in zinc blende type crystals. Many new measurements are in progress. Since the knowledge of the host lattice phonon frequency distribution is essential to proper interpretation of these data, it is felt that the presentation of the phonon density of states and the local and gap mode behavior for mass defects for all zinc blende type crystals for which relevant data are available will be useful.

In this paper the eigenvalues and the eigenvectors of the phonon states as determined by the modified rigid ion model are incorporated into the framework of the Green's function technique[23] in order to predict the local mode and gap mode behavior in a large class of zinc blende crystals. In the Green's function approach, it is assumed that the only significant change introduced in the lattice by the substitutional impurity is the change in mass. A condition for the appearance of a new localized gap mode, which corresponds to the replacement of the heavy host atom by a yet heavier substitutional atom, is predicted.

Explicit calculations have been carried out for GaP, GaAs, GaSb, InAs, InSb, InP, AlSb, CdTe, ZnS, ZnSe, ZnTe, HgTe and SiC. These results are then compared to existing experimental data whenever possible.

2. FREQUENCY DISTRIBUTION FUNCTION

In the harmonic approximation for the rigid ion model, the eigenvalues, ω^2, and the eigenvectors, $\sigma = \mathbf{u}e^{i\omega t}$, of the phonon states of the perfect lattice are given[32] by the solution to the following equations of motion,

$$\mathbf{Lu} = (\mathbf{R} + \mathbf{ZCZ})\mathbf{u} - \mathbf{M}\omega^2\mathbf{u} = 0. \qquad (1)$$

The matrices **R** and **C** are Hermitian and represent the short range and long range interactions respectively, while the matrices **M** and **Z** are diagonal matrices representing the particle masses and the charge number. The eigenvalues of the phonon states, $\omega_j(\bar{k})$, where the index, j, represents the normal mode and the index, $\bar{k}$, the wave vector, result from the solution to the secular equation,

$$|\mathbf{R}+\mathbf{ZCZ}-\mathbf{M}\omega^2| = 0. \qquad (2)$$

The eigenvectors are orthogonal and are normalized so that

$$\sum_{\alpha} \sigma_\alpha^{*j}(\bar{k})\sigma_\alpha^{j'}(\bar{k}) = \delta_{jj'}$$

and

$$\sum_{j} \sigma_\alpha^{*j}(\bar{k})\,\sigma_\beta^{j}(\bar{k}) = \delta_{\alpha\beta}, \qquad (3)$$

where the subscripts, α and β, refer to the x, y and z components of the eigenvectors.

This model incorporates short range non-central interactions for nearest neighbors and equal central interactions for next nearest neighbors and long range Coulomb interactions among ions of appropriate effective ionic charge. There are essentially four model parameters, three short range force constants and an effective ionic charge number. The model parameters are then determined by relating them to the three independent elastic constants, C_{11}, C_{12}, and C_{44}, and the long wavelength longitudinal and transverse optic mode phonons[32].

The distribution of the phonon frequencies of the perfect lattice, $G(\omega)$, was calculated for a mesh of 4,096 wave vector points in the first Brillouin zone. Due to the symmetry properties of the Brillouin zone for the zinc blende structure, one need only consider the determination of the eigenvalues of the phonon states at the non-equivalent points in $\bar{k}$-space defined as,

$$\bar{k} = \frac{\pi}{8a}(q_x, q_y, q_z),$$

where

$$16 \geqslant q_x \geqslant q_y \geqslant q_z \geqslant 0$$

$$q_x + q_y + q_z \geqslant 24. \qquad (4)$$

and

$$a = \text{lattice constant.}$$

This particular mesh of $\bar{k}$ points gave a total of 24,576 frequencies from which a histogram of $G(\omega)$ was obtained as a function of frequency. The frequency sampling width used was $\Delta\omega = 0{\cdot}1 \times 10^{13}\,\text{sec}^{-1}$. Figures 1–4 present $G(\omega)$ for GaP, GaAs, GaSb, InAs, InSb, CdTe, ZnS, ZnSe, ZnTe, InP, AlSb and HgTe. The frequency distribution function for SiC is reported elsewhere[32]. It may be noted that the distribution functions conform with the Debye model of the solid at low frequencies in each case. In the case of GaP, GaSb, InAs, ZnTe, ZnS, InP, AlSb, HgTe and SiC, a frequency gap is noted, as is expected from the consideration of relative mass.

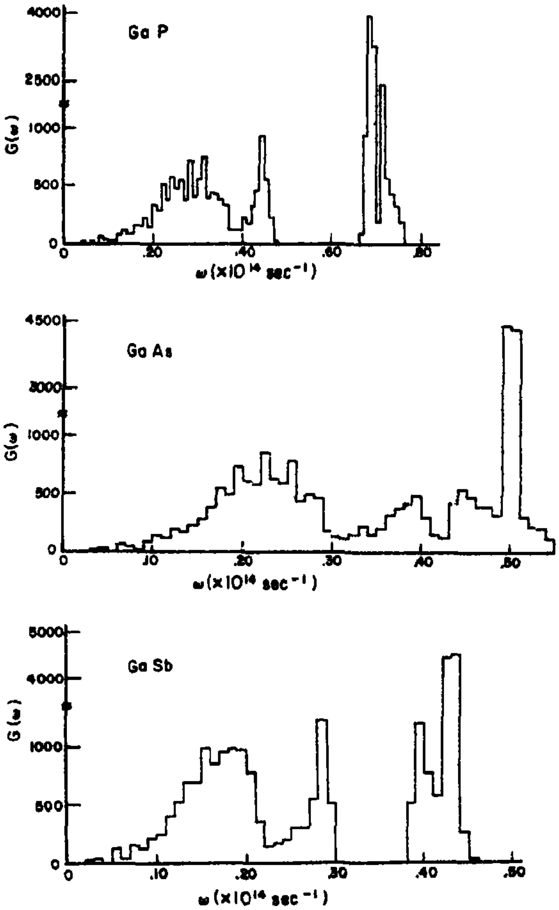

Fig. 1. Frequency distribution, $G(\omega)$, of GaP, GaAs and GaSb. Histograms are calculated with frequency interval $\Delta\omega = 0{\cdot}1 \times 10^{13}\,\text{sec}^{-1}$.

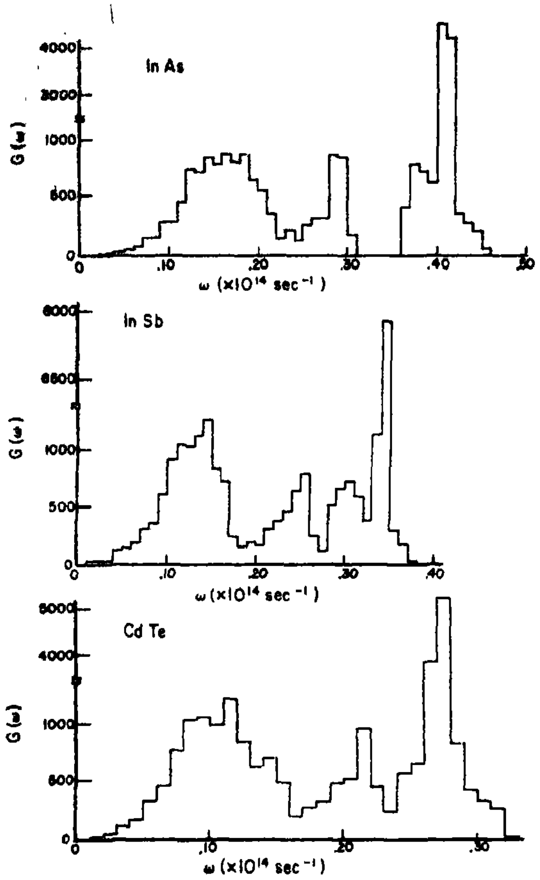

Fig. 2. Frequency distribution, $G(\omega)$, of InAs, InSb and CdTe. Histograms are calculated with frequency interval $\Delta\omega = 0{\cdot}1 \times 10^{13}\ \mathrm{sec}^{-1}$.

3. LOCAL MODE BEHAVIOR

The introduction of a substitutional impurity for one of the atoms of the host lattice, modifies the dynamical behavior of the lattice in that region. It is assumed that the force constants remain unchanged from the perfect lattice in the vicinity of the defect and that only the mass parameter is changed. Under these assumptions the equations of motion become,

$$\mathbf{L}\mathbf{u}' = (\mathbf{R}+\mathbf{ZCZ})\mathbf{u}' - \mathbf{M}\omega'^2\mathbf{u}' = \mathbf{S}\mathbf{u}', \quad (5)$$

where **S** is a matrix of low rank incorporating the mass defect approximation. Due to the fact that the spatial extension of the mass defect is limited, the Green's function method [39] can be used to solve the problem. Noting that the Green's function matrix, **G**, is defined by **LG** = **E**, where **E** is the identity matrix, the equations of motion can be formally expressed as,

$$\mathbf{u}' = \mathbf{GSu}' = [\mathbf{R}+\mathbf{ZCZ}-\mathbf{M}\omega'^2]^{-1}\,\mathbf{Su}'$$

or

$$u'_\alpha = \sum_\beta g_{\alpha\beta} \sum_\gamma s_{\beta\gamma} u'_\gamma, \qquad (6)$$

where $g_{\alpha\beta}$ and $s_{\beta\gamma}$ are elements of the matrices **G** and **S** respectively. The elements of the matrix **G** are functions of the phonon frequencies of both the perturbed and the unperturbed lattice. The condition for the

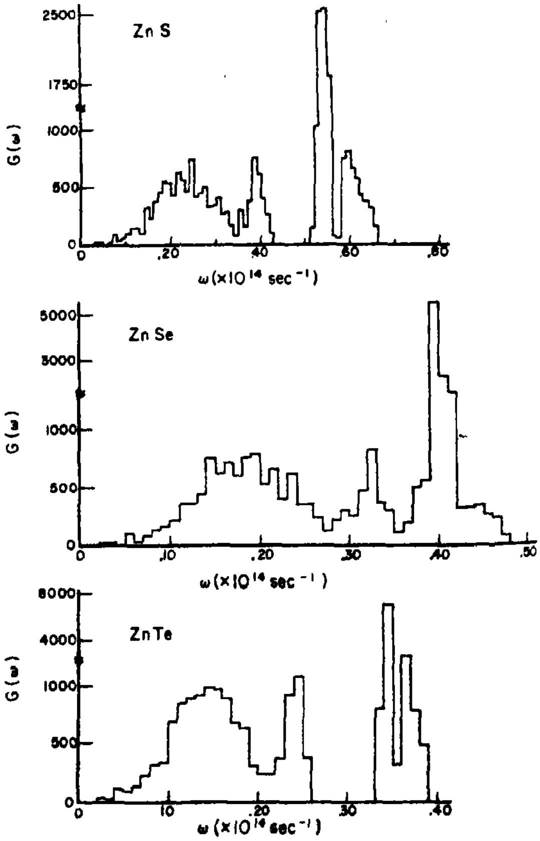

Fig. 3. Frequency distribution, $G(\omega)$, of ZnS, ZnSe and ZnTe. Histograms are calculated with frequency interval $\Delta\omega = 0{\cdot}1 \times 10^{13}\ \mathrm{sec}^{-1}$.

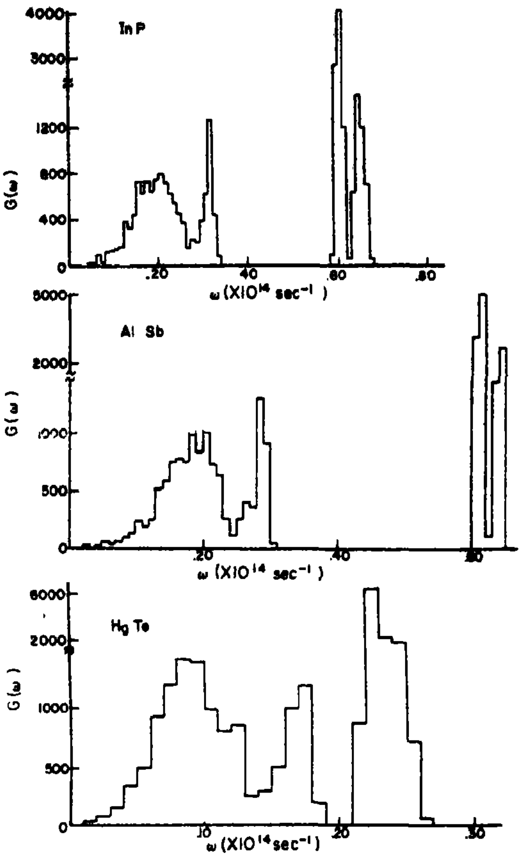

Fig. 4. Frequency distribution, $G(\omega)$, of InP, AlSb and HgTe. Histograms are calculated with frequency interval $\Delta\omega = 0{\cdot}1 \times 10^{13}\,\text{sec}^{-1}$.

existence of a nontrivial solution for the eigenvectors of the phonon states in the perturbed lattice reduces to the following secular equation,

$$|\mathbf{GS}-\mathbf{E}| = 0. \tag{7}$$

Using equations (1), (3) and (6) it can be shown that the elements of the Green's function matrix are

$$g_{\alpha\beta} = \sum_{k}\sum_{j} \frac{\sigma_{\alpha}^{*j}(\bar{k})\sigma_{\beta}^{j}(\bar{k})}{\omega_j^2(\bar{k}) - \omega'^2}, \tag{8}$$

where ω' is the eigen frequency of the perturbed phonon state. Under the mass defect approximation, the defect matrix, **S**, is directly related to the mass defect which is defined by,

$$\epsilon(K) = \frac{m_K - m_{K'}}{m_K}. \tag{9}$$

m_K is the mass of the particle to be substituted for, and $m_{K'}$ is the mass of the substitutional impurity. It can then be shown[23] for the zinc blende structure, which is cubic, that the secular equation for the eigenvalues of the perturbed phonon state produced by the substitutional impurity reduces to the

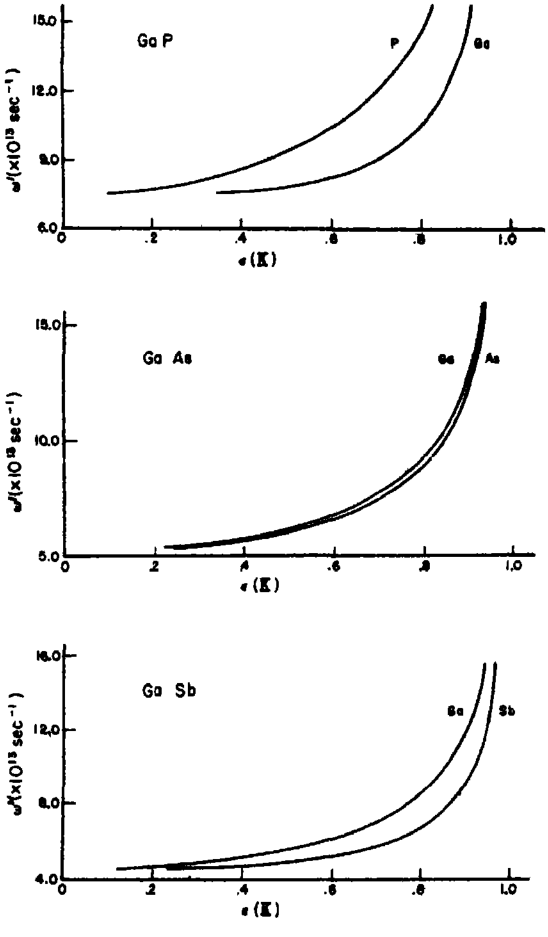

Fig. 5. Localized mode frequency, ω', as a function of the mass defect parameter, $\epsilon(K)$, for GaP, GaAs and GaSb.

following,

$$1+\frac{\epsilon(K)\omega'^2}{N}\sum_{\bar{k}}\sum_{j}\frac{|\sigma_\alpha^j(\bar{k},K)|^2}{\omega_j^2(\bar{k})-\omega'^2}=0, \quad (10)$$

where N is the total number of wave vectors. The eigenvector, $\sigma_\alpha^j(\bar{k},K)$, corresponds only to the particular particle of mass m_K. Local modes are usually defined above the optic branches and correspond to the condition that $m_{K'}$ is smaller than the host lattice atomic masses. Gap modes occur when $m_{K'}$ may be heavier or lighter than one or both of the host lattice masses.

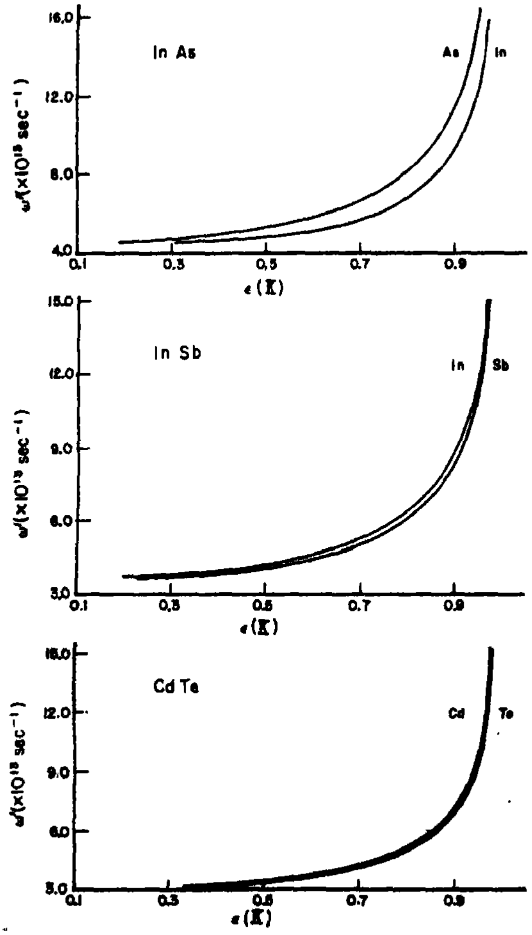

Fig. 6. Localized mode frequency, ω', as a function of the mass defect parameter, $\epsilon(K)$, for InAs, InSb, and CdTe.

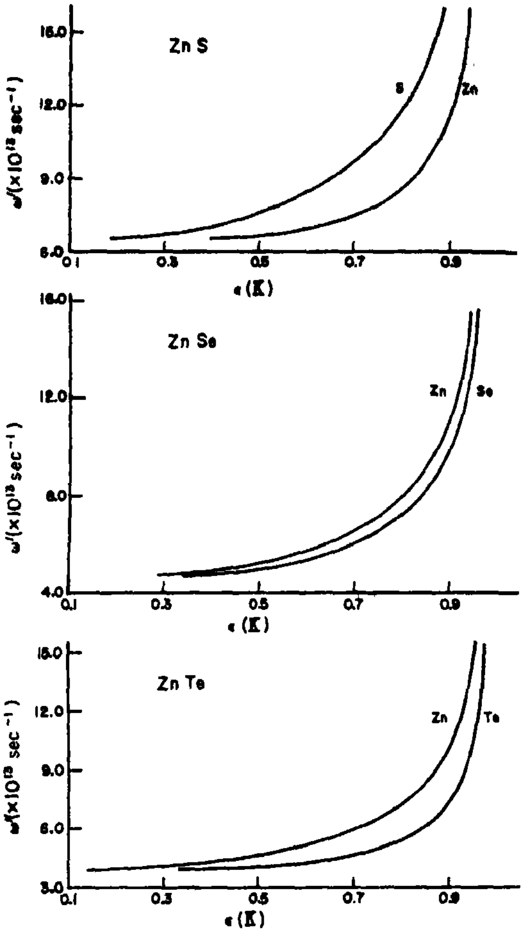

Fig. 7. Localized mode frequency, ω', as a function of the mass defect parameter, $\epsilon(K)$, for ZnS, ZnSe and ZnTe.

Utilizing the phonon frequencies of the perfect lattice in terms of the frequency distribution function and also utilizing the corresponding eigenvectors for the 4,096 wave vector points, the above equation was solved numerically to obtain a functional relationship between the mass defect parameter and the local mode and gap mode frequency due to the impurity. Calculations have been made for replacement of either the anion or cation atoms of the zinc blende compounds. The variation of the local and gap mode frequencies as a function of the mass defect parameter is presented in Figs. 5–13 for GaP, GaAs, GaSb, InAs, InSb, CdTe,

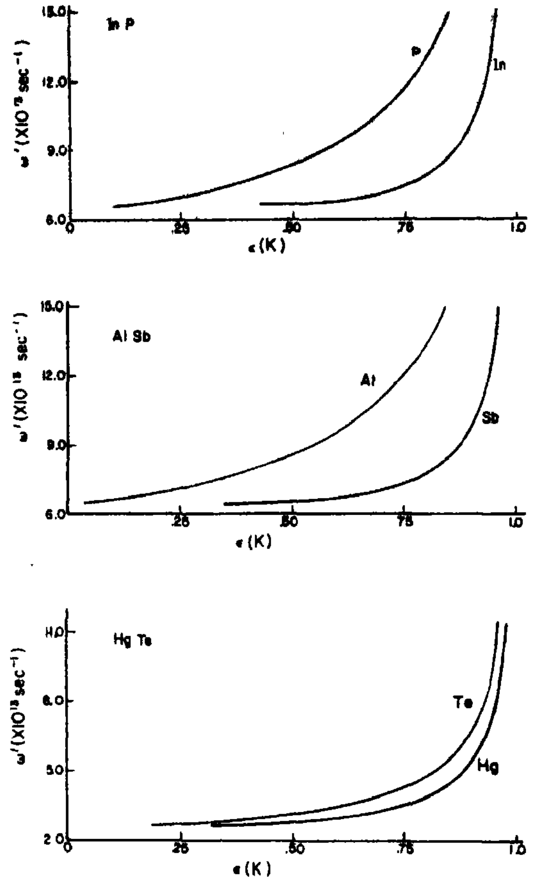

Fig. 8. Localized mode frequency, ω', as a function of the mass defect parameter, ε(K), for InP, AlSb and HgTe.

ZnS, ZnSe, ZnTe, InP, AlSb, HgTe and SiC. The available experimental data are compared to the calculated results in Tables 1 and 2.

The localized modes above the optic branch correspond to the condition that the substitutional atom is less than some critical mass. Depending upon the substitution made, this critical mass is less than either the heavy or light host atom mass.

The calculation shows localized modes in the frequency gap are possible for three different kinds of mass defect. For the replacement of the lighter of the host atoms by a substitutional atom of heavier mass, the model predicts a localized gap mode for which the allowed values of the defect mass are bounded by two critical masses. If the heavy atom is replaced by a lighter substitutional atom a localized gap mode is predicted subject to the mass of the substituent atom becoming smaller than some critical mass. Finally, the third condition for the existence of the gap mode corresponds to the case when the heavier of the host atoms is replaced by an atom of yet heavier mass, with a lower bound of critical mass.

The condition for localized modes above the optic branch and the first and second condition for the localized gap modes conform with previous predictions[40]. We believe

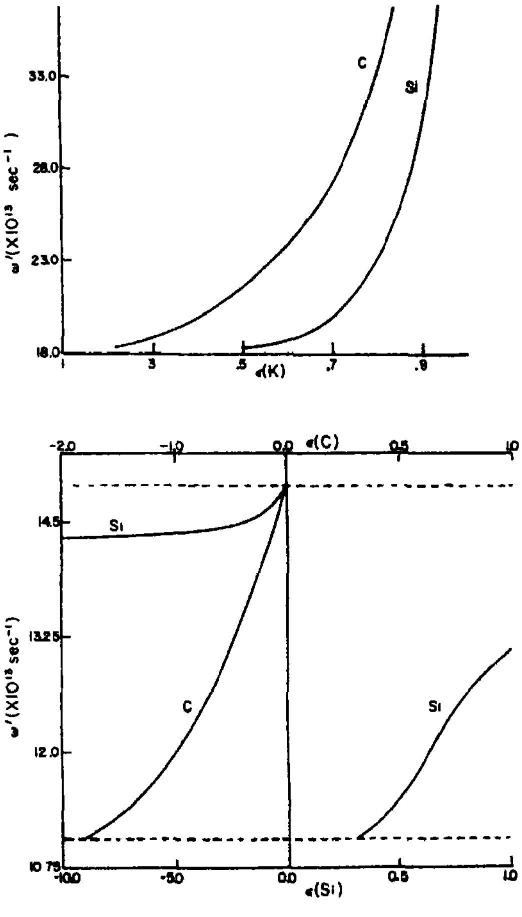

Fig. 9. Localized mode and gap mode frequency, ω', as a function of the mass defect parameter, ε(K), for SiC. The gaps in the frequency spectra are shown by dotted lines.

Table 1. Comparison of calculated and experimental values of local mode frequencies (in cm^{-1}*) for various zinc blende compounds*

Compound[a]	Calculated local mode frequency	Experimental local mode frequency	Reference for experimental data
GaP:Si	437·4	453	13
GaP:^{11}B	611·6	569, 571	13, 15
GaP:^{10}B	636·6	592, 594	13, 15
GaP:Al	442·2	443	13
GaP:^{12}C	563·1	527, 606·2	13, 16
GaP:^{14}C	525·2	564	16
GaP:0	494·4	464	13
GaP:^{14}N	525·2	488	15
GaP:^{15}N	509	472	15
GaAs:Si	362·9	384	7
GaAs:Si	365	399	7
GaAs:P	351	355·4, 351	5, 10
GaAs:Al	368·9	362	4
GaAs:^{7}Li	685·9	422·2	2
GaAs:^{6}Li	739	451·4	2
GaSb:Al	333	316·7	1
GaSb:P	327·3	324	1
GaSb:As	248	240	17
InAs:Ga	244	240	11
InSb:Al	307	295·7	3, 5
InSb:As	206·6	200	17
InSb:Ga	209·8	196	20
ZnS:Al	362·6	437·9	12
ZnS:Be	543	486	21
ZnSe:S	285·9	297	9
ZnSe:^{7}Li	563	383	6
ZnSe:^{6}Li	606·6	412	6
ZnSe:Al	301·9	359	8
ZnSe:Be	498	450	6
ZnSe:^{24}Mg	317·2	352	6
ZnSe:^{25}Mg	312	345	6
ZnSe:^{26}Mg	306·6	334	6
ZnTe:Al	274·5	312·6	12
ZnTe:S	266·5	269 to 272	19
ZnTe:Be	461·5	411	21
CdTe:Be	426	391	14
CdTe:Se	171·6	170	19
CdTe:Mg	266·3	248	18

[a] Atom in bold type has been replaced.

Table 2. Comparison of calculated and experimental values of gap mode frequencies (in cm^{-1}*) for impurities in* GaP *and* SiC

Compound[a]	Calculated gap mode frequency	Experimental gap mode frequency	Reference for experimental data
GaP:^{10}B	289·2	293·8	15
GaP:^{11}B	287·9	284·2	15
GaP:As	275	270	15
SiC:He(?)	676	670	22

[a] Atom in bold type has been replaced.

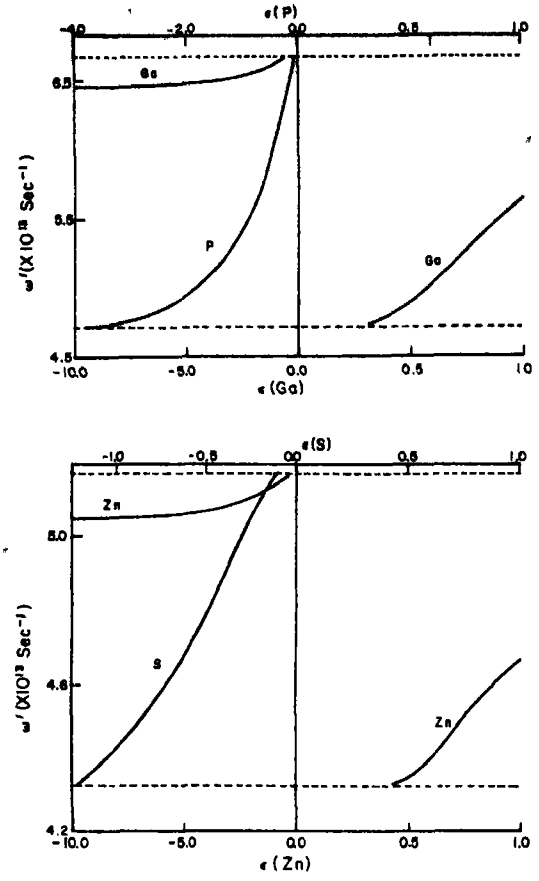

Fig. 10. Gap mode frequency, ω', as a function of the mass defect parameter, $\epsilon(K)$, for GaP and ZnS. The gaps in the frequency spectra are shown by dotted lines.

that the third condition, under which a gap mode may appear, constitutes a new condition hitherto unnoticed. A search of the literature has not revealed any experimental data for this type of mode, but in view of the scarcity of experimental data for gap modes, this is not surprising. For the third condition the lower bound of critical mass for the localized gap mode corresponds to a physically realizable substituent mass in all compounds studied except GaSb and InAs. In the latter two compounds the lower bound of critical mass is quite large and would no doubt correspond to a physically unrealizable mass for the substituent atom. It may be pointed out that a linear chain model is unable to predict such a gap mode[17]. It will be of interest to find out if this is a pecularity of the zinc blende structure or such a mode may be expected in other diatomic cubic crystals with frequency gaps like some alkali halides.

The agreement with available experimental measurements for the cases where the impurity atom and the atom substituted belong to the same group of the periodic table is fairly good and is comparable to a recent phenomenological calculation using a linear chain model[17]. The relatively poor agreement with the experimental measurements on the Li substitutional impurity replacing Zn in ZnSe and Ga in GaAs respectively can

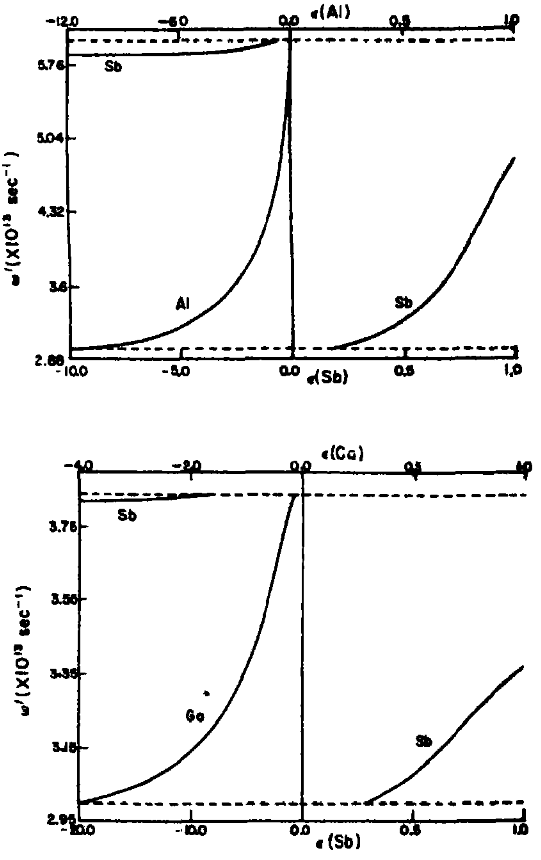

Fig. 11. Gap mode frequency, ω', as a function of the mass defect parameter, $\epsilon(K)$, for AlSb and GaSb. The gaps in the frequency spectra are shown by dotted lines.

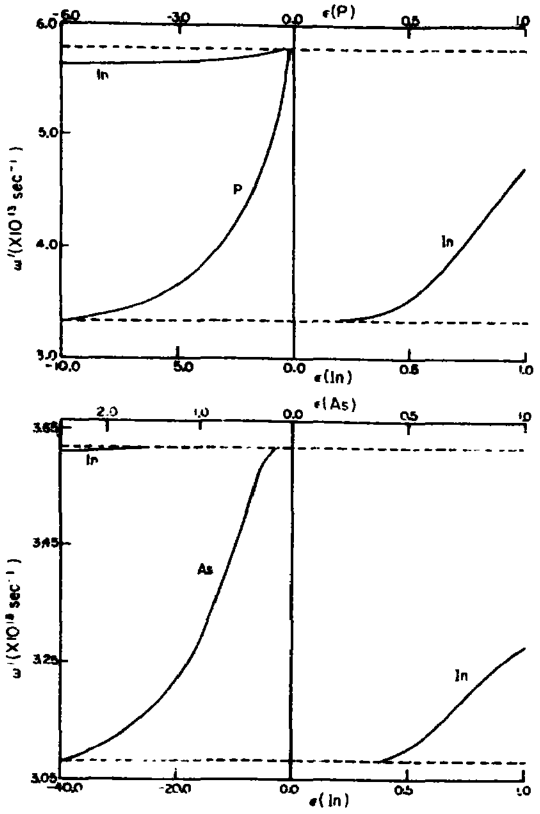

Fig. 12. Gap mode frequency, ω', as a function of the mass defect parameter, $\epsilon(K)$, for InP and InAs. The gaps in the frequency spectra are shown by dotted lines.

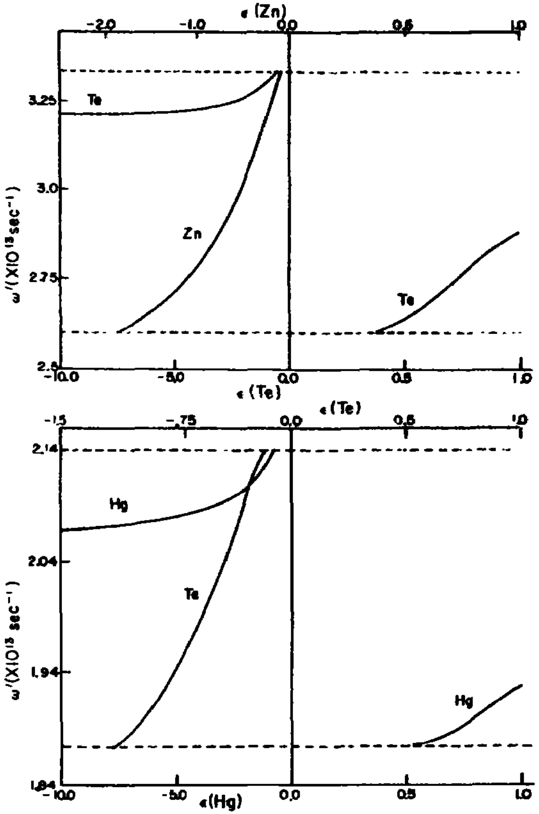

Fig. 13. Gap mode frequency, ω', as a function of the mass defect parameter, $\epsilon(K)$, for ZnTe and HgTe. The gaps in the frequency spectra are shown by dotted lines.

be attributed to the fact that no force constant change was incorporated into the model. The difference in the valence states of the substituting and the substituted atoms will no doubt have a significant effect on the force constant parameters in the neighborhood of the defect. Our model also does not include effects due to charge compensation when the effective ionic charges are very different.

Acknowledgements—The authors extend their appreciation to the University of Maine Computer Laboratory where all the computation was performed.

REFERENCES

1. HAYES W., *Phys. Rev. Lett.* **13**, 275 (1964).
2. HAYES W., *Phys. Rev.* **138**, 1227 (1965).
3. GOODWIN A. R. and SMITH S. D., *Phys. Lett.* **17**, 203 (1965).
4. LORIMOR O. G., SPITZER W. G. and WALDNER M., *J. appl. Phys.* **37**, 2509 (1966).
5. SMITH S. D., CHADDOCK R. E. V. and GOODWIN A. R., *Proceedings of the International Conference on the Physics of Semiconductors*, p. 67, Kyoto, (1966).
6. MITSUISHI A., MANABE A., YOSHINAGA H., IBUKI S., and KOMIYA H., *Progress of Theoretical Physics*, Supplement 45, (1970).
7. LORIMOR O. G. and SPITZER W. G., *J. appl. Phys.* **37**, 3687 (1966).
8. IBUKI S., KOMIYA H., MITSUISHI A., MANABE A. and YOSHINAGA H., *II–VI Semiconductor Compounds* (Edited by D. G. Thomas), p. 1140 Benjamin, New York (1967).
9. BRAFMAN O., CHANG I. F., LENGYEL G. and MITRA S. S., *Phys. Rev. Lett.* **19**, 1120 (1967).
10. SPITZER W. G., *J. Phys. Chem. Solids* **28**, 33 (1967).
11. BRODSKY M. H. and LUCOVSKY G., *Phys. Rev. Lett.* **21**, 990 (1968).
12. IBUKI, S. KOMIYA H., MITSUISHI A., MANABE A. and YOSHINAGA, H., *International Conference on Semiconductors*, p. 1047 Moscow, (1968).
13. SPITZER W. G., ALLRED W., BLUM S. E. and CHICOTKA R. J., *J. appl. Phys.* **40**, 2589 (1969).
14. SENNET C. T., BOSOMWORTH D. R., HAYES W. and SPRAY A. R. L., *J. Phys. C (Solid State Phys.)* **2**, 1137 (1969).
15. HAYES W., MacDONALD H. F. and SENNET C. T., *J. Phys. C (Solid State Phys.)* **2**, 2402 (1969).
16. HAYES W., WILTSHIRE M. C. K. and DEAN P. J., *J. Phys. C. (Solid State Phys.)* **3**, 1762 (1970).
17. LUCOVSKY G., BRODSKY M. H. and BURSTEIN E., *Phys. Rev. B* **2**, 3295 (1970).
18. MARPLE D. T. F., Unpublished.
19. BALKANSKI M., BESSERMAN R. and VODOPIANOV L. K., *Localized Excitations in Solids* (Edited by R. F. Wallis) p. 154 Plenum Press, New York (1968).
20. BRODSKY M. H., LUCOVSKY G., CHEN M. F. and PLASKETT T. S., *Phys. Rev. B* **2**, 3303 (1970).
21. MITSUISHI, A., *Solid State Commun.* (to be published).
22. CHOYKE W. J. and PATRICK L., *Bull. Am. phys. Soc.* **16**, 397 (1971).
23. DAWBER P. G. and ELLIOTT R. J., *Proc. R. Soc. Lond.* **A273**, 222 (1963).
24. GOVINDRAJAN J. and HARIDASAN T. M., *Phys. Lett.* **29A**, 387 (1969).
25. KRISHNAMURTHY N. and HARIDASAN T. M., *Ind. J. Pure Phys.* **7**, 89 (1969).
26. WAUGH J. L. T. and DOLLING G., *Phys. Rev.* **132**, 2410 (1963).
27. YARNELL J. L., WARREN J. L., WENZEL R. G. and DEAN P. J., *Neutron Inelastic Scattering*, Vol. I, p. 301, International Atomic Energy Agency, Vienna.
28. JOUFFROY J., *Compt. Rend.* **265**, 67 (1967); PONS-CORBEAU J. and JOUFFROY J., *Bull. Soc. Franc. Miner. Crist.* **90**, 498 (1967).
29. FELDKAMP L. A., VENKATARAMAN G. and KING J. S., *Solid State Commun.* **21**, 1571 (1969); KING J. S., Private Communication.
30. BERGSMA J., *Phys. Lett.* **32A**, 324 (1970).
31. JASWAL S. S., *Phys. Rev.* **140**, 687 (1965).
32. VETELINO J. F., and MITRA S. S., *Phys. Rev.* **178**, 1349 (1969).
33. VETELINO J. F., MITRA S. S., BRAFMAN O. and DAMEN T. C., *Solid State Commun.* **7**, 1809 (1969).
34. KUNC K., BALKANSKI M. and NUSIMOVICI M., *Phys. Status Solidi* **41**, 491 (1970).
35. VETELINO J. F. and MITRA S. S., *Solid State Commun.* **7**, 1181 (1969).
36. COCHRAN W., in *Lattice Dynamics* (Edited by R. F. Wallis) pp. 75–84, Pergamon Press, New York (1965).
37. DICK G. G., in *Lattice Dynamics* (Edited by R. F. Wallis), pp. 159–174, Pergamon Press, New York (1965).
38. VETELINO J. F., MITRA S. S. and NAMJOSHI K. V., *Phys. Rev. B* **2**, 967 (1970).
39. LIFSHITZ I. M., *Nuovo Cim. Suppl.* **3**, 716 (1956).
40. See for example, MAZUR P., MONTROLL E. W. and POTTS R. B., *J. Wash. Acad. Sci.* **46**, 2 (1956).

J. Phys. Chem. Solids, 1971, Vol. 32, pp. 2749–2753. Pergamon Press. Printed in Great Britain

EFFECT OF THE NON-EQUIVALENT INTERVALLEY SCATTERING ON THE HIGH-FIELD CONDUCTIVITY CHARACTERISTICS OF *n*-Ge

D. CHATTOPADHYAY and B. R. NAG
Institute of Radio Physics and Electronics, University of Calcutta, Calcutta 9, India

(*Received* 4 *February* 1971; *in revised form* 12 *April* 1971)

Abstract—Room-temperature velocity-field characteristics of *n*-type germanium have been calculated taking into account the effect of non-equivalent intervalley scattering in addition to that of intravalley acoustic, optical and equivalent intervalley phonon scattering. The analysis has been made on the assumption of a field-dependent displaced Maxwellian distribution function for the electrons in the ⟨111⟩ valleys and field-independent mobility for the electrons in the ⟨100⟩ valleys. The calculated values are found to agree with the results of Monte Carlo calculations to within 10 per cent.

It is also found that the calculated characteristic agrees with experiments very closely if the values of the deformation potential constant for the intravalley optical phonon scattering and for the non-equivalent intervalley scattering are taken to be $0{\cdot}5 \times 10^9$ and $0{\cdot}5 \times 10^8$ eV cm^{-1}, respectively. The non-equivalent intervalley scattering introduces saturation in the velocity-field characteristics and at the same time reduces the temperature of the electrons in the ⟨111⟩ valleys sufficiently to eliminate the possibility of breakdown.

1. INTRODUCTION

ELECTRONS in *n*-type germanium attain a drift velocity at high electric fields almost independent of the magnitude of the field[1–4]. Attainment of a field-independent drift velocity may be explained theoretically if it is assumed that the electrons lose energy only through intravalley optical phonons[2, 5, 6], and the theoretically calculated values of the drift velocity agree with the experiment if the deformation potential constant, D_0, for the optical phonon scattering is taken to be $0{\cdot}5 \times 10^9$ eV cm^{-1}. In spite of this agreement there remain some theoretical difficulties which need further clarification. First, the theoretical value of the average energy of the electrons is comparable to the band gap and one would therefore expect a breakdown which is not, however, experimentally observed[7]. Secondly, the above value of D_0 is about half that required to fit the temperature dependence of low-field mobility[7]. Thirdly, the contribution of the intravalley acoustic mode scattering to energy loss of the electrons, though negligible at low fields, becomes significant compared to that of the optical phonons at high fields. When this contribution is included in the analysis the drift velocity is, however, found to increase with increasing electric field[2, 6]. The difficulties mentioned above may arise from two approximations made in the theory. First, the effect of non-parabolicity of the band structure and non-classical acoustic phonon excitation may be important in the saturation region. Secondly, the effect of scattering of the electrons to the ⟨100⟩ valleys from the normally occupied ⟨111⟩ valleys may also be important. Calculated velocity-field curves using the non-parabolic band and non-classical acoustic phonon distribution have been presented recently by Dumke[8]. It would appear from his results that the saturation velocity calculated by taking into account the effect of non-parabolicity and the non-classical acoustic phonon distribution agrees to within 10 per cent with the experimental value at 300°K[4]. The required value of D_0 is also found to be about $0{\cdot}7 \times 10^9$ eV cm^{-1} and is in fair agreement with the value required to explain the temperature variation of low field mobility including the effect of non-parabolicity. However, it is not clear whether the effect of the band anisotropy on the coupling constants for the momentum and energy exchange between electrons and the acoustic phonons has been taken into account[9]. The values of the parameters in Table 1 of his paper are also confusing as apparently the parameter values have not been correctly reproduced against the corresponding symbols. The low-field mobility calculated with the parameter values when this table is plausibly interpreted is not in agreement with the experimental value at 300°K. Our calculations indicate that the effect of acoustic phonon scattering has been overestimated in momentum exchange and underestimated in the energy exchange due to the choice of the parameter values. In addition, in spite of the agreement found between theory and experiment it remains of interest to investigate if the scattering to the ⟨100⟩ valleys may be important.

Recently, calculations have been performed by the Monte Carlo method[10] in which the scattering of the electrons to the ⟨100⟩ valleys from the ⟨111⟩ valleys is taken into account. The characteristic for the temperature of 300°K shows a field-independent drift velocity region, but the magnitude of the drift velocity is about $0{\cdot}82 \times 10^7$ cm sec^{-1}, whereas most of the experimental values lie within 0·55 and $0{\cdot}62 \times 10^7$ cm sec^{-1}. Also, the value of the field at which the drift velocity is saturated is higher than the experimental value. However, these results may significantly change when the coupling constants for the various scattering mechanisms are altered. It is almost an impossible task to apply the Monte Carlo method for the purpose of studying the effect of change in the values of the coupling constants as it involves lengthy numerical computations. On the other hand, the simple, analytic methods based on the assumption of displaced Maxwellian or Maxwellian distribution functions give results not much different from that obtained by the Monte Carlo method and may be conveniently used to study the effect of the choice of the parameters on the average energy of the carriers and on the magnitude of the drift velocity. We present in this paper results which were obtained by such methods to examine the effect of scattering to ⟨100⟩ valleys and the choice of parameters on the velocity-field characteristic in the saturated region.

2. METHOD OF ANALYSIS

The band structure related to the ⟨111⟩ minima as also the coupling constants for the acoustic and for the equivalent intervalley scattering processes are fairly accurately known[7]. On the other hand, there are no direct experimental data about the band parameters of the ⟨100⟩ valleys and the coupling constant for the non-equivalent intervalley phonons. In order to limit the number of adjustable parameters we have taken the mobility of the electrons when in the ⟨100⟩ valleys to be 700 cm^2 V^{-1} sec^{-1} and independent of the applied field. The above value was obtained from an earlier analysis for explaining BNDC results under uniaxial stress[11]. The effect of changing this value may, however, be easily estimated from the results corresponding to this value. The assumption that the mobility is independent of the field introduces the limitation that the calculations will not be valid for very high fields. But in the field range of 4–6 kV cm^{-1} over which the onset of saturation in the drift velocity occurs this assumption should not introduce any serious error. With the above assumptions we have only two unknowns, namely, the value of the deformation potential constant for the intravalley optical phonons, D_0, and that for the non-equivalent intervalley phonons, D_{neq}. As the mobility of the electrons in the ⟨100⟩ valleys has been assumed to be independent of the applied field the velocity-field curve may be obtained by solving the energy and momentum balance equations for only the ⟨111⟩ electrons. However, in contrast with the earlier analyses, these equations should include the energy and momentum loss due to scattering by the equivalent and non-equiva-

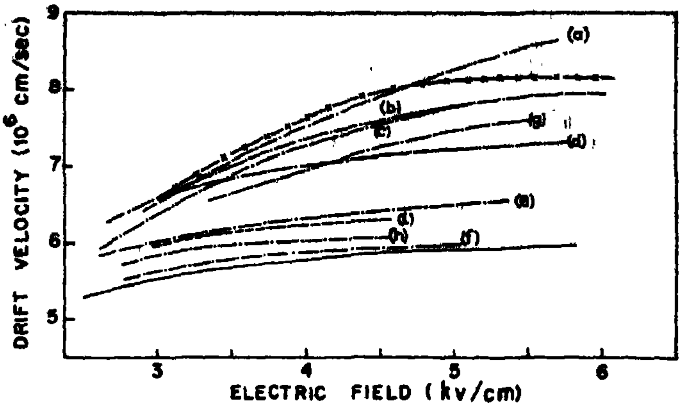

Fig. 1. Drift velocity —— electric field curves. ———, experimental curve[4]. —x—x—, theoretical curve obtained by the Monte Carlo method[10]. —·—·—, theoretical curves obtained with a displaced Maxwellian distribution function. ——, theoretical curve obtained with a Maxwellian distribution function. The values of D_0 are respectively 1·0, 1·0, 0·9, 0·8, 0·6, 0·5, 0·5, 0·5 and $0{\cdot}5 \times 10^9$ eV cm^{-1} in curves (a–i). The values of D_{neq} are 2·0, 1·0 and $1{\cdot}0 \times 10^8$ eV cm^{-1} in curves (a), (c) and (g). Transfer to the ⟨100⟩ valleys has been neglected in curve (h) and in the rest of the curves D_{neq} is assumed to be $0{\cdot}5 \times 10^8$ eV cm^{-1}.

lent phonons. In addition, we are also required to solve the number conservation equation to determine the number of the carriers transferred to the ⟨100⟩ valleys. As the equations involved in the analyses are well-known[2, 5], we shall not repeat them here, but only present the results. It should, however, be noted that in the results presented here the band has been assumed to be parabolic.

3. RESULTS AND DISCUSSION

We show in Fig. 1 the velocity-field characteristic obtained for the different combination of the values of D_0 and D_{neq}, and assuming the field to be applied in the ⟨100⟩ direction.

We first note that the values of the drift velocity obtained from the present analysis [curve (c)] using the parameters employed by Paige[10] agrees to within 6 per cent with his Monte Carlo calculations. It is therefore expected that the present calculations would not differ from Monte Carlo calculations by more than 10 per cent.

The values of the drift velocity are altered by large amounts due to the change in the values of D_0 and D_{neq}. On considering the different curves we find that agreement with experimental results may be obtained when the effect of scattering to the ⟨100⟩ valleys is taken into account if we choose $D_0 = 0{\cdot}5 \times 10^9$ eV cm^{-1} and $D_{neq} = 0{\cdot}5 \times 10^8$ eV cm^{-1} even if the band is assumed to be parabolic.

It is interesting to note that inclusion of the effect of scattering to the ⟨100⟩ valleys gives slightly better agreement with experiments, but to get the experimental value of the drift velocity D_0 has to be given the same value as required when this effect is neglected. The curves obtained by including and by excluding the effect are nearly identical in the field-independent drift velocity region. This result is contrary to that surmised earlier. It was surmised that the transfer of the carriers to the ⟨100⟩ valleys should reduce the saturation drift velocity by large amounts. But the transfer of carriers to the ⟨100⟩ valleys affects the results in two ways. The velocity of the transferred carriers is less than that of the carriers in the ⟨111⟩ valleys. But in the process of transfer the electron system in the ⟨111⟩

valleys loses energy and the average energy of the carriers in the ⟨111⟩ valeys is thereby reduced. Hence the drift velocity of the carriers in the ⟨111⟩ valleys is higher when the non-equivalent scattering is taken into account than when it is neglected. The reduction of the average drift velocity due to the lower velocity of the transferred electrons is almost compensated by the increased velocity of the carriers in the ⟨111⟩ valleys.

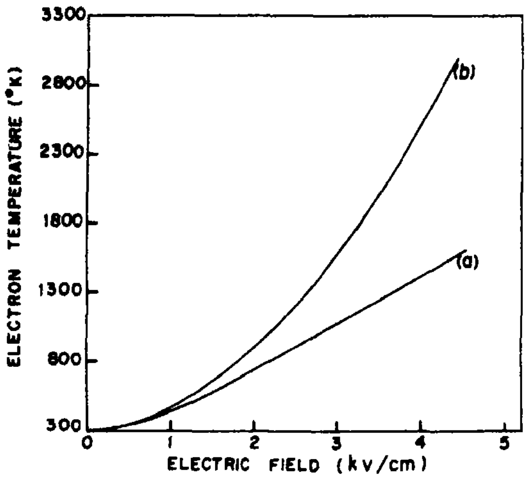

Fig. 2. Variation of the electron temperature in a ⟨111⟩ valley with electric field. (a) present analysis, (b) earlier analysis neglecting scattering to the ⟨100⟩ valleys.

The result discussed above is further evident when we consider the electron temperature-field curves obtained in earlier analysis [2] taking into account only the energy loss due to the intravalley optical phonons, and in the present analysis, as shown in Fig. 2. We note that at a field of 4·5 kV cm^{-1} the present analysis indicates an electron temperature of about 1600°K whereas the earlier analysis indicates an electron temperature of about 3000°K. The value of the electron temperature is reduced somewhat if the energy loss due to the acoustic phonon scattering is taken into account in the earlier analysis[2] but then the velocity-field characteristic does not saturate. Thus the inclusion of the effect of scattering to the ⟨100⟩ minima in addition to the effect of intravalley optical and acoustic phonon scattering reduces the electron temperature to ranges where breakdown would not be expected, but produces the experimentally observed field-independent drift velocity region. One of the main shortcomings of the earlier theory as discussed before is thereby removed. However, we note that the value of D_0 is required to be $0{\cdot}5 \times 10^9$ eV cm^{-1} as in the earlier analysis. This value is affected by the value of the mobility of the electrons in the ⟨100⟩ valleys. There is experimental evidence [12] which suggests that the mobility may be somewhat higher than the value assumed in our analysis, but when a higher value is taken for this mobility the value of D_0 would have to be reduced further for explaining the experimental results. It should also be mentioned that the calculations based on a Maxwellian distribution function gives almost identical results but to fit the experimental values of the drift velocity, D_0 is required to be $0{\cdot}4 \times 10^9$ eV cm^{-1}.

It may be concluded on the basis of the results presented here that the saturation region of the velocity-field characteristic of n-Ge at 300°K may be fitted with theory by including the effect of scattering to ⟨100⟩ valleys even if the bands are assumed to be parabolic, but the required value of the intravalley optical phonon deformation potential constant is $0{\cdot}5 \times 10^9$ eV/cm.

Acknowledgements—The authors are thankful to the authorities of the Indian Statistical Institute, Calcutta, for computer facilities. Financial assistance of CSIR (India) is gratefully acknowledged.

REFERENCES

1. GUNN J. B., *J. Electron.* **2**, 87 (1956).
2. BARRIE R. and BURGESS R. R., *Can. J. Phys.* **40**, 1056 (1962).
3. NATHAN M. I., *Phys. Rev.* **130**, 2201 (1963).
4. SMITH J. E., *Phys. Rev.* **178**, 1364 (1969).
5. REIK H. G. and RISKEN H., *Phys. Rev.* **126**, 1737 (1962).
6. MEYER N. I. and JØRGENSEN M. H., *J. Phys. Chem. Solids* **26**, 823 (1965); CHOU S., *J. Phys Chem. Solids* **31**, 2549 (1970).

7. See, for example, PAIGE E. G. S., *Progress in Semiconductors*, Vol. 8, Heywood, London (1964).
8. DUMKE W. P., *Phys. Rev.* **B2**, 987 (1970).
9. REIK H. G. and RISKEN H., *Phys. Rev.* **124**, 777 (1961).
10. PAIGE E. G. S., *IBM J. Res. Dev.* **13**, 562 (1969).
11. CHATTOPADHYAY D. and NAG B. R., *Phys. Status Solidi* **39**, 341 (1970).
12. JAYARAMAN A. and KOSICKI B. B., *Proc. 9th Int. Conf. on Phys. Semiconductors*, Vol. 1, p. 53, Nauka, Leningrad, (1968).

J. Phys. Chem. Solids, 1971, Vol. 32, pp. 2755–2759. Pergamon Press. Printed in Great Britain

INFLUENCE OF THE CRYSTALLINE ELECTRIC FIELD ON THE KONDO RESISTIVITY OF $Ce_xLa_{1-x}Pd_3$ TERNARIES*

V. U. S. RAO, R. D. HUTCHENS and J. E. GREEDAN

Department of Chemistry, University of Pittsburgh, Pittsburgh, Penna. 15213, U.S.A.

(*Received 5 April* 1971)

Abstract—The electrical resistivities of the cubic $Ce_xLa_{1-x}Pd_3$ ternary alloys have been measured from 2° to 300°K. The alloys were found to consist of single phases except in the region $0{\cdot}3 < x < 0{\cdot}5$. The resistivities indicated the presence of the Kondo phenomenon in all the alloys containing cerium. In some alloys a maximum in the resistivity-temperature curve was found and also an additional minimum at low temperatures. This behavior is interpreted as arising due to the influence of the cubic crystalline field on the cerium ions.

1. INTRODUCTION

THE CRYSTALLINE electric field has been shown to have considerable influence on the spin-disorder resistivity by Rao and Wallace [1] who have calculated the effect in the first Born approximation for Ce^{3+} in a cubic environment (e.g. $CeAl_2$) and by Maranzana[2] who evaluated the contribution in the second Born approximation for Ce^{3+} in the hexagonal compound $CeAl_3$. The latter author has shown the existence of divergences in the relaxation rate for conduction electron energies away from the Fermi level. These side divergences which he termed 'Kondo sidebands' result in one or more maxima in the resistivity (ρ) temperature (T) curve, in addition to the minimum usually associated with a Kondo effect. This viewpoint has been exploited by van Daal *et al.*[3, 4] in the interpretation of the ρ-T behavior of a number of cerium alloys.

In this paper we wish to present the results of our measurement on electrical resistivity of $Ce_xLa_{1-x}Pd_3$ ternary intermetallics measured in the temperature range 2°K to about 300°K. The lattice parameters of these compounds which are cubic (Cu_3Au type) are presented and their correlation with the resistivity behavior is discussed. Certain features of the Kondo resistivity that may be expected for cerium ions subjected to a *cubic* crystal field are described and compared with the ρ-T behavior of some of the compounds.

2. EXPERIMENTAL

The starting materials from which the compounds were made were elements of 99·9 per cent purity. The elements were melted together under a purified argon atmosphere to form the compounds using induction heating and a water-cooled copper boat similar in design to that described by Sterling and Warren[5]. Using this technique melts could be easily maintained for periods of one or two minutes with vigorous stirring and virtually no contamination from the cold boat. Well-homogenized compounds cast in a form convenient for the cutting of resistivity samples were consistently obtained. The samples were then annealed for two weeks at 750°C.

The lattice parameters were measured with a Picker Nuclear X-ray powder diffractometer using a Cu-$K\alpha$ radiation.

The samples for the resistivity measurements were cut in the shape of elongated bars ($\sim 1{\cdot}5\ \text{cm} \times 1\ \text{mm}^2$) with the help of a Servomet spark cutter. The resistivity was measured

---

*This work was supported by the U.S. Atomic Energy Commission and by NASA through a traineeship to one of us. (RDH).

using a standard four-probe method.

3. RESULTS

The X-ray measurements (Fig. 1) showed that the solubility range existed from $x = 0$ to $x \approx 0{\cdot}3$ and again from $x \approx 0{\cdot}5$ to $x = 1$. Between $x \approx 0{\cdot}3$ and $x \approx 0{\cdot}5$ the X-ray diffraction patterns clearly showed the existence of two phases which had lattice parameters (a_0) similar to those found at the limiting compositions for solid solubility. In the two single phase regions which we shall call regions I and II (see Fig. 1), a_0 was found to show a linear dependence on x.

The resistivity vs. temperature curves for the compositions corresponding to $x = 0$, 0·1 and 0·2 belonging to region I are shown in Fig. 2. $LaPd_3$ exhibits a normal $\rho - T$ behavior expected of a metal with no local moments. The compositions $Ce_{0\cdot1}La_{0\cdot9}Pd_3$ and $Ce_{0\cdot2}La_{0\cdot8}Pd_3$ show well defined minima at about 32 and 170°K respectively.

The $\rho - T$ curves for $x = 0{\cdot}95$, 0·99 and 1·0 belonging to region II are shown in Fig. 3.

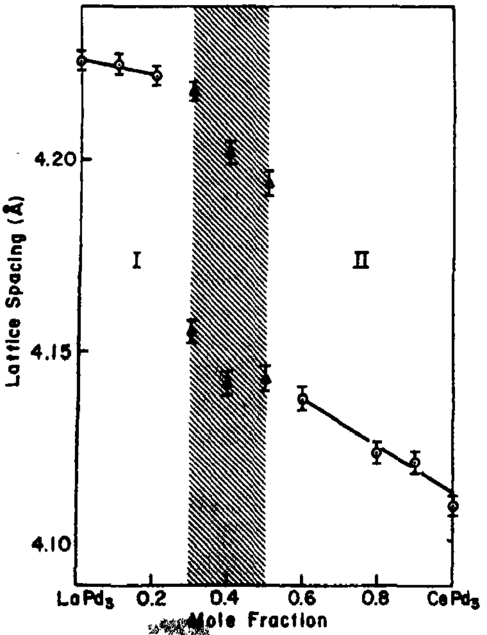

Fig. 1. Lattice parameter a_0 as a function of composition (x) in $Ce_xLa_{1-x}Pd_3$ ternaries. The shaded area represents a two phase region.

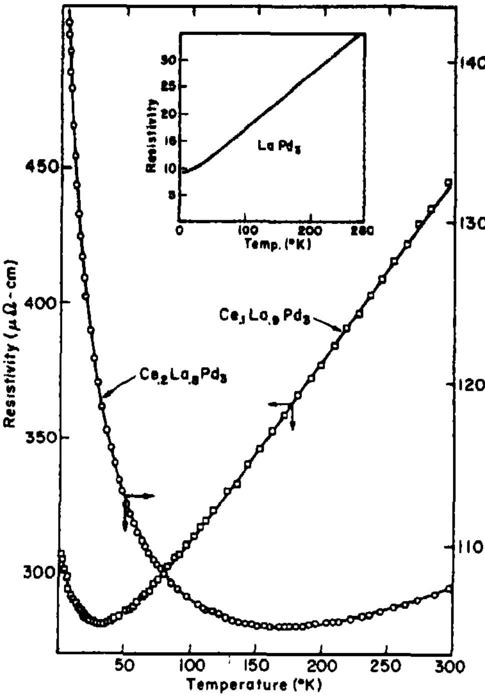

Fig. 2. Resistivity vs. temperature curves for $LaPd_3$ (inset), $Ce_{0\cdot1}La_{0\cdot9}Pd_3$, and $Ce_{0\cdot2}La_{0\cdot8}Pd_3$.

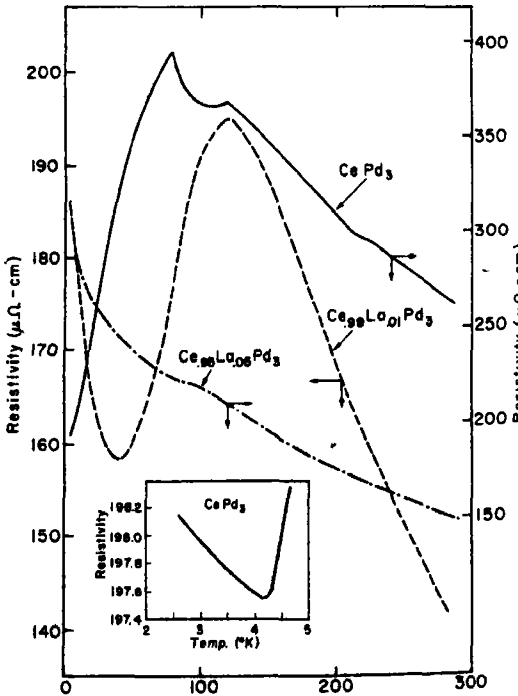

Fig. 3. Resistivity vs. temperature curves for $CePd_3$ (shown also on expanded scale in the inset to reveal upturn below 4·2°K), $Ce_{0\cdot99}La_{0\cdot01}Pd_3$, $Ce_{0\cdot95}La_{0\cdot05}Pd_3$.

These samples are characterized by a negative coefficient of resistance near room temperature. As noted previously no minimum in the $\rho - T$ curve could be seen in $CePd_3$ up to a temperature as high as 660°K. A noteworthy feature is the additional upturn in the resistivity at low temperature seen clearly in the compositions $Ce_{0\cdot99}La_{0\cdot01}Pd_3$ and $CePd_3$. The results on $CePd_3$ were presented earlier[6] but since those earlier measurements were made only above 4·2°K the second upturn was not seen. The present measurements which were carried out down to 2°K, however, revealed the upturn (see Fig. 3, inset). Measurements were also performed on the samples with $x = 0{\cdot}6$, $0{\cdot}8$ and $0{\cdot}9$ all of which showed decreasing ρ with increasing T, somewhat like the $x = 0{\cdot}95$ composition.

4. DISCUSSION

Normally the Kondo effect is encountered in systems in which the influence of the crystalline electric field on the local moments is unimportant. In the absence of a magnetic field the sublevels of the magnetic ion are degenerate. It is well known[7] that in this case when the conduction electron relaxation times (τ_k) due to spin–spin scattering are evaluated in the second Born approximation, the inverse relaxation times (τ_k^{-1}) at low temperatures show a logarithmic divergence as the conduction electron energy approaches the Fermi surface. This situation is shown schematically in Fig. 4(a). This divergence at the Fermi level is responsible for the -ln T term in the resistivity at low temperatures as indicated qualitatively in Fig. 4(a).

When one is considering the Kondo effect associated with Ce^{3+} ions ($J = \frac{5}{2}$) where normally crystal field splittings of the order of 100°K are encountered, the influence of these splittings on the Kondo resistivity has to be considered. Maranzana[2], who was the first to treat these effects theoretically, has considered the case of Ce^{3+} ions subjected to a hexagonal crystal field in $CeAl_3$. This crystal field splits the $J = \frac{5}{2}$, ${}^2F_{5/2}$ ground level of Ce^{3+} into three doublets $|\pm\frac{5}{2}\rangle$, $|\pm\frac{3}{2}\rangle$ and $|\pm\frac{1}{2}\rangle$. In order to explain the ρ vs. T behavior of this compound which shows a broad maximum at 35°K in addition to a minimum at higher temperatures, the $|\pm\frac{1}{2}\rangle$ level was assumed to be the lowest lying level with $|\pm\frac{3}{2}\rangle$ the next higher level and separated by ΔE from $|\pm\frac{1}{2}\rangle$. The spin–flip scattering of the conduction electrons takes place due to the terms $s_\pm J_\mp$ in the Hamiltonian $(g-1)\mathscr{J}(\mathbf{r}-\mathbf{R})\mathbf{s}\cdot\mathbf{J}$ which represents the exchange interaction between the rare-earth and conduction electron moments. The exchange of energy between the conduction electron and the rare-earth moments that takes place in some of the scattering terms gives rise to divergences in τ_k^{-1} for conduction electrons whose energies are away from the Fermi level by amounts $\pm\Delta E$ (side-bands), where ΔE is the extent of the crystal field splitting. This is shown schematically in Fig. 4(b). In the

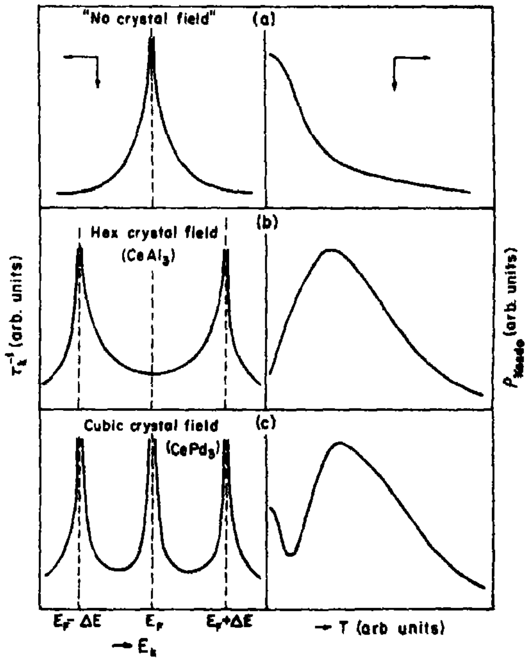

Fig. 4. Schematic relationship between inverse relaxation time and conduction electron energy at $T = 0$ (left side) and Kondo resistivity vs. T (right side) for (a) no crystal field (b) Ce^{3+} in hexagonal crystal field (c) Ce^{3+} in cubic crystal field.

case of Ce^{3+} in a hexagonal field, the choice of the energy level scheme made by Maranzana[2] led to a situation such that at low temperatures one could obtain only the sidebands but not the usual divergence at the Fermi level. The $\rho - T$ curve predicted by such a picture would show a maximum and a positive $d\rho/dT$ at the low temperature side as shown in Fig. 4(b). The upturn in the $\rho - T$ curve at the lowest temperatures seen in a normal Kondo phenomenon is absent because of the lack of the divergence at the Fermi level.

We shall now consider the case of Ce^{3+} ions in a cubic crystal field as in $CePd_3$. It is known[8] that a cubic crystal field splits the ground multiplet of the Ce^{3+} ion into a Γ_7 doublet and a Γ_8 quartet shown schematically in Fig. 5. The sign of the crystal field decides whether Γ_7 or Γ_8 is lower. The wave functions of the crystal field states are given by[8]

$$|\Gamma_7\rangle = a|\pm\tfrac{5}{2} - b|\pm\tfrac{3}{2}\rangle,$$

$$|\Gamma_8\rangle = b|\pm\tfrac{5}{2}\rangle + a|\mp\tfrac{3}{2}\rangle,$$

$$\text{and } |\pm\tfrac{1}{2}\rangle,$$

where $a = 0{\cdot}4083$ and $b = 0{\cdot}9129$.

It can now be seen that a divergence at the Fermi level is always present whether the Γ_7 or the Γ_8 level is lower. This is because spin–flip resonances can take place without the need for energy exchange since the $s_{\pm}J_{\mp}$ terms in the Hamiltonian can connect states within a Γ_7 or a Γ_8 manifold. We therefore expect a divergence in τ^{-1} for electrons at the Fermi level, in addition to the sidebands at $\pm\Delta E$ away from the Fermi level as shown in Fig. 4(c). This would lead to an upturn in the $\rho - T$ curve at the lowest temperatures followed also possibly by a maximum at higher T as shown in Fig. 4(c). These qualitative expectations are in agreement with our resistivity measurements in the $Ce_xLa_{1-x}Pd_3$ ternary alloys, in all of which an upturn *was* observed at the lowest temperature. In addition, in two compositions viz. $CePd_3$ and $Ce_{0{\cdot}99}La_{0{\cdot}01}Pd_3$ maxima in the $\rho - T$ curve are observed.

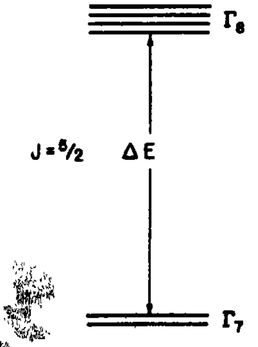

Fig. 5. Schematic diagram showing the cubic crystal field splitting of the ground state ($J = \frac{5}{2}$) of the Ce^{3+} ion.

It is also worth noting here the rather strong dependence of the position of the resistance minimum with x in $La_{1-x}Ce_xPd_3$, the temperature at the minimum increasing sharply with increasing x. Such effects were absent in the $La_{1-x}Ce_xAl_2$ system reported previously[9]. The detailed $\rho - T$ behavior is sensitively dependent on at least three major factors: (a) the size of the crystal field splitting, (b) the magnitude of the exchange interaction between the rare-earth and conduction electron spins and (c) the density of states at the Fermi level. Efforts are being made to obtain more information on factors (a) and (c) through heat capacity measurements.

Finally, it is pertinent to make some remarks about the variation of the lattice parameter with composition x. Harris and Raynor [9] who measured the lattice parameters of several RPd_3 (R = rare-earth) intermetallic compounds, noted that the lattice parameter of $CePd_3$ showed a negative deviation from the lattice parameter vs. atomic number curve for this series. They suggested that this possibly meant that cerium ions in $CePd_3$ were in a valence state higher than three. Our magnetic measurements[6] on this compound showed that the susceptibility was well below that expected for an assemblage of tripositive cerium ions. It has been argued from an analysis of the magnetic susceptibility of cerium metal by Edelstein[11] that the transition from the γ to α phase accompanied by a decrease in lattice parameter is caused by the transition into a spin-compensated state. We believe that a similar effect is responsible for the smaller volume of the $CePd_3$ unit cell. This conjecture is supported by our observation that in region II of our system the Kondo temperatures seem to be quite high (well above room temperature).

In region I and Kondo temperatures are considerably lower (near or well below room temperature). The lattice parameters (which were all measured at room temperature) reveal that there is a much smaller volume contraction, compared to compositions in region II.

Acknowledgements—The authors wish to thank Profs. W. E. Wallace and R. S. Craig for several valuable discussions and encouragement.

REFERENCES

1. RAO V. U. S. and WALLACE W. E., *Phys. Rev.* 2, 4616 (1970).
2. MARANZANA F. E., *Phys. Rev. Lett.* 25, 239 (1970).
3. VAN DAAL H. J. and BUSCHOW K. H. J., *Phys. Status. Solidi.* (to be published).
4. VAN DAAL H. J., MARANZANA F. E. and BUSCHOW K. H. J., *Proc. Int. Conf. Magn.*, Grenoble, 1970. *J. Phys.* 32, C1-424 (1971).
5. STERLING H. F. and WARREN R. W., *Metallurgia* 67, 301 (1963).
6. HUTCHENS R. D., RAO V. U. S., GREEDAN J. E., WALLACE W. E. and CRAIG R. S., *J. appl. Phys.* 42, 1293 (1971).
7. KONDO J., *Prog. Theor. Phys.* 32, 37 (1964); *Solid State Physics* (Edited by F. Seitz and D. Turnbull) 23, 184 (1969).
8. LEA K. R., LEASK M. J. M. and WOLF W. P., *J. Phys. Chem. Solids* 23, 1381 (1962).
9. BUSCHOW K. H. J. and VAN DAAL H. J., *Phys. Rev. Lett.* 23, 408 (1969).
10. HARRIS I. R. and RAYNOR G. U., *J. less-common Metals* 9, 263 (1965).
11. EDELSTEIN A. A., *Phys. Rev. Lett.* 19, 1184 (1967).

J. Phys. Chem. Solids, 1971, Vol. 32, pp. 2761–2763. Pergamon Press. Printed in Great Britain

CRYSTAL STRUCTURE OF KCN IV AT 50 KBAR

C. W. F. T. PISTORIUS

Chemical Physics Group of the National Physical and National Chemical Research Laboratories,
South African Council for Scientific and Industrial Research, P.O. Box 395, Pretoria, South Africa

(*Received* 23 *March* 1971)

Abstract—KCN IV near 25°C and 50 kbar is rhombohedral, space group $D_{3d}^5-R\bar{3}m$, with $a_{rh} = 3{\cdot}727$ Å, $\alpha = 85° 58'$ and $Z = 1$. The structure appears to be the same as that of CsCN II, with the cyanide ions behaving as ellipsoids of rotation with radii of 2·22 and 1·69 Å closely similar to those obtaining in CsCN II. KCN IV cannot be thermodynamically stable at high pressures near absolute zero.

1. INTRODUCTION

POTASSIUM cyanide is richly polymorphic, with seven different solid phases, two of which appear to be metastable, known in the pressure range to 40 kbar[1–3]. At 25°C KCN I, which is cubic, space group O_h^5-Fm3m[4] with the NaCl-type structure, reversibly transforms to KCN IV at 19·72 ± 0·43 kbar[1, 5]. KCN IV is ~ 10 per cent denser than KCN I at the transition pressure [1], and reversibly transforms to KCN III, which is very slightly less dense than KCN IV at the IV/III phase boundary[1, 2], upon raising the temperature.

KCN I is cubic due to the fact that the cyanide ions are either freely rotating[4], or undergo a hindered rotation, with preferential positions in the directions of the four body-diagonals of the unit cell[3]. The entropy change for the KCN I/III transition is negligible[1]. This led to the prediction[2] that KCN III will be cubic, space group O_h^1-Pm3m with the CsCl-type structure. At lower temperatures, the disordered cyanide ions of KCN III will evidently become more ordered, and it was suggested[2] that KCN IV would crystallize with a CsCl-type structure slightly distorted by the partial ordering of the rod-shaped cyanide ions. KCN IV would then probably possess the rhombohedral CsCN II structure[6], space group $D_{3d}^5-R\bar{3}m$.

2. EXPERIMENTAL

The KCN was BDH Analar grade, containing 0·5% KCl and 1–2% K_2CO_3.

The high-pressure X-ray diffraction cell was similar to that described by Perez–Albuerne *et al.*[7], but used 1·25 cm dia. pistons with 0·4 cm dia. flats in order to obtain good control over the low-pressure range (0–80 kbar). No markers were used in view of the reservations expressed elsewhere[8], but sample pressures were calculated from the observed unit-cell volumes by using Bridgman's volume compressibility data[9]. Filtered Mo K_α radiation ($\lambda = 0{\cdot}7069$ Å) was used, and the diffraction patterns recorded on a flat-film camera 8·5 cm from the sample position. Exposure times were ~ 30 hr.

3. RESULTS

Patterns at 25°C were obtained at 0, ~ 25·5 and ~ 49 kbar. The diffraction pattern at atmospheric pressure was used to correct for film shrinkage and absorption effects. The pattern at 25·5 kbar was quite different from that at atmospheric pressure, and showed that the KCN I/IV transition had occurred, but the peaks were of poor quality. The third pattern at ~ 49 kbar yielded sharp diffraction peaks which could be indexed without trouble. The data are given in Table 1. KCN IV at 25°C, ~ 49 kbar is rhombohedral with

$$a_{rh} = 3{\cdot}727 \pm 0{\cdot}010\ \text{Å}$$

$$\alpha_{rh} = 85°58' \pm 10;\ Z = 1,\ \rho_{\text{calc}} = 2{\cdot}103\ \text{g cm}^{-3}.$$

At 25°C, ~ 25·5 kbar the unit-cell constants

$$a_{rh} = 3{\cdot}811 \pm 0{\cdot}015\ \text{Å}$$

$$\alpha_{rh} = 86°58' \pm 20;\ \rho_{\text{calc}} = 1{\cdot}96\ \text{g cm}^{-3}$$

were obtained. The error limits are estimated from the fit at high angles only.

Table 1. *Powder pattern of* KCN IV *at* 25°C, ~ 49 *kbar* (Mo K_α *radiation*)

d_{obs} in Å	d_{calc} in Å	*hkl* (rhombohedral)	I
3·69	3·710	001	vw
2·75[a]	2·714	011	vs
2·545	2·541	01$\bar{1}$	m
2·096	2·096	11$\bar{1}$	s
1·856	1·855	002	vw
1·698	1·704	012	m
1·58[b]	1·605	112	vvw
1·465	1·467	11$\bar{2}$	vw
1·361	1·357	022	vw
1·315	1·316	122	w
1·223	1·237, 1·202	22$\bar{1}$, 12$\bar{2}$	vw broad

[a] The precision of data obtainable with a flat-film camera drops very rapidly at low diffraction angles. The present discrepancy between d_{obs} and d_{calc} in the case of the 011 peak is ascribed to this effect.

[b] It was not possible to measure the 112 peak accurately due to its extreme weakness.

The observed selection rules (no restriction) rule out the space groups $R3c$ and $R\bar{3}c$. It is not possible to make a definite decision as to the correct space group out of the remaining five from powder data alone. However, the following considerations do apply. CsCN II is rhombohedral, space group $D^5_{3d}-R\bar{3}m$, with[6]

$$a_{rh} = 4{\cdot}23\ \text{Å}$$

$$\alpha_{rh} = 86°21',\ Z = 1.$$

The structure is a slight deformation of the CsCl-type structure (in which $\alpha = 90°$), with the Cs$^+$ ion at (0, 0, 0) and the CN$^-$ ion along the trigonal axis. Heat capacity data[10] indicate that there is no distinction between the heads and tails of the cyanide ions, and that CsCN II still has a residual orientational entropy of Rln 2. The transition entropy of the KCN IV/III transition is equal to or slightly less than that of the CsCN II/I transition[11]. However, since KCN I is fully disordered [3–4] and the entropy of the KCN I/III transition is negligible[1], KCN III must also be fully disordered. The residual orientational entropy for KCN IV is therefore Rln 2 as in the case of CsCN II, indicating not only no distinction between the heads and tails of the cyanide ions, but also no further disorder than this. This particular disorder can only be found in the space group $D^5_{3d}-R\bar{3}m$, with the indistinguishable C and N atoms at (x, x, x) and $(\bar{x}, \bar{x}, \bar{x})$. The conclusion that KCN IV is isostructural with CsCN II is therefore inescapable on the basis of entropy considerations.

The mean positions of the C and N atoms are located at $x = 0{\cdot}43$ if the C-N separation is taken to be ~ 1 Å, as compared to a separation of 1·05 Å at atmospheric pressure [14]. The CN^- ions must be considered as ellipsoids of rotation. The ionic radius of an eight-coordinated K^+ ion at 100 kbar is $\simeq$ 1·13 Å,[12, 13] i.e. ~ 1·22 Å at ~ 49 kbar. From packing considerations it then follows that the ellipsoid of rotation has a length of ~ 4·45 Å and a diameter of ~ 3·38 Å. In CsCN II at −60°C and atmospheric pressure the values ~ 4·44 and ~ 3·35 Å, respectively, are obtained, in very good agreement. The ellipsoids of rotation in KCN IV and CsCN II are elongated in comparison with that found in KCN V at −105°C and atmospheric pressure[14], viz., 4·30 Å by 3·56 Å. The proposed structure of KCN IV is illustrated in Fig. 1. The observed intensities are not sufficiently reliable to justify a determination of calculated intensities for comparison purposes.

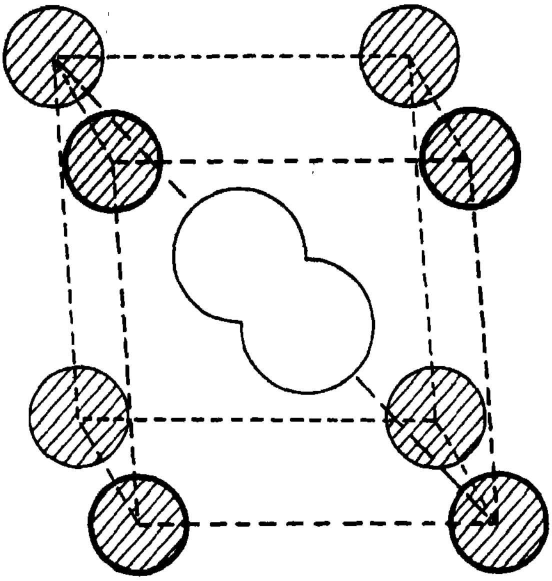

Fig. 1. Proposed structure of KCN IV. K^+ ions are shaded.

4. DISCUSSION

Due to its residual orientational entropy of Rln 2, CsCN II cannot be thermodynamically stable at absolute zero. No phase transition to a more stable completely ordered phase occurs[10] down to 10 K, however, and it was concluded[11] that the non-occurrence of the expected transition is due to the cyanide ions being 'frozen' in orientations where there is a random distribution between the heads and tails of these ions. At and near absolute zero CsCN II is therefore metastable. KCN IV also has a residual entropy of Rln 2,[2, 11] and a similar expected transition should occur at low temperatures and high pressures, failing which KCN IV will be metastable at very low temperatures. These, at present hypothetical, phases may very possibly have a structure similar to that of tetragonal KN_3. Even if the presumed static disorder of CsCN II and KCN IV at low temperatures does not allow complete ordering to occur at moderate pressures, it is possible that, if the ordered forms are somewhat denser than the partly disordered forms, the ordered forms may be obtained at extremely high pressures where the transition partial disorder → complete order will occur at higher temperatures. Once found, these phases should, at low temperatures, not revert when quenched to lower pressures and temperatures within the eight-coordinated phase field.

At 25°C RbCN I transforms to a dense disordered phase RbCN II at 5·6 kbar[15]. RbCN II was suggested[15] to have the CsCl-type structure. If this is indeed the case, a phase similar to CsCN II and KCN IV should occur above ~ 5 kbar at low temperatures in the phase diagram of RbCN.

TlCN has the same structure[16] as CsCN I. This substance, also, should undergo one or more ordering transformations at lower temperatures.

Acknowledgements—The author would like to thank Prof. H. Drickamer of the University of Illinois, and Drs J. C. A. Boeyens and J. de Villiers of this laboratory, for valuable discussions. The apparatus was constructed and maintained by J. Erasmus and his staff and A. de Kleijn and his staff. The powder patterns were indexed and fitted on the IBM 360/65 H of the National Research Institute for Mathematical Sciences, using programs written by Martha C. Pistorius.

REFERENCES

1. BRIDGMAN P. W., *Proc. Am. Acad. Arts Sci.* **72**, 45 (1937).
2. PISTORIUS C. W. F. T., CLARK J. B. and RAPOPORT E., *J. chem. Phys.* **48**, 5123 (1968).
3. SUGA H., MATSUO T. and SEKI S., *Bull. Chem. Soc. Japan* **38**, 1115 (1965).
4. ELLIOTT N. and HASTINGS J., *Acta crystallogr.* **14**, 1018 (1961).
5. KENNEDY G. C. and LAMORI P. N., *J. geophys. Res.* **67**, 851 (1962).
6. LELY J. A., Dissertation, Utrecht University (1942).
7. PEREZ-ALBUERNE E. A., FORSGREN K. F. and DRICKAMER H. G., *Rev. scient. Instrum.* **35**, 29 (1964).
8. JAMIESON J. C. and OLINGER B., *NBS Spec. Publ.* **326**, 321 (1971).
9. BRIDGMAN P. W., *Proc. Am. Acad. Arts Sci.* **76**, 71 (1948).
10. SUGISAKI M., MATSUO T., SUGA H. and SEKI S., *Bull. Chem. Soc. Japan* **41**, 1747 (1968).
11. RICHTER P. W. and PISTORIUS C. W. F. T., *J. chem. Phys.* **54**, 5436 (1971).
12. HALL H. T., *Prog. Inorg. Chem.* **7**, 1 (1966).
13. GOLDSCHMIDT V. M., *Skrifter utgitt av det Norske Vidensk.* Ak. Oslo I.M.N.Kl., pp. 57–69 (1926).
14. BIJVOET J. M. and LELY J. A., *Recl. Trav. chim. Pays-Bas* **59**, 908 (1940).
15. CLARK J. B. and PISTORIUS C. W. F. T., *Solid State Commun.* **7**, 787-9 (1969).
16. STRADA M., *Rend. Accad. Lincei* **19**, 809 (1934).

J. Phys. Chem. Solids, Vol. 32, pp. 2765–2771. Pergamon Press. Printed in Great Britain

ETUDE EXPERIMENTALE DE LA SUSCEPTIBILITE MAGNETIQUE DES SOLUTIONS SOLIDES DE METAUX DE LA PREMIERE SERIE DE TRANSITION DANS L'ALUMINIUM

J. F. SADOC
Laboratoire de Physique des Solides*, Faculté des Sciences, Orsay-91, France

(*Received* 16 *December* 1970; *in revised form* 3 *March* 1971)

Résumé – L'étude expérimentale de la susceptibilité magnétique des solutions solides de métaux de la première série de transition dans l'aluminium a été rendue possible par préparation d'échantillons par trempe ultra-rapide (Splat-cooling). Les mesures ont mis en évidence une forte contribution paramagnétique des métaux du centre de la série de transition. Cette observation confirme les prévisions théoriques faites sur ces alliages. Par contre, l'existence d'un important terme diamagnétique reste inexpliqué théoriquement.

1. INTRODUCTION

L'ÉTUDE des solutions solides métalliques à faible concentration permet d'obtenir des renseignements sur la structure électronique des métaux. C'est dans ce but que le laboratoire de Physique des Solides d'Orsay a entrepris une étude sur les solutions solides des métaux de la première série de transition dans l'aluminium. Plusieurs types d'études ont été menés:

- Variation des paramètres des solutions AlT[1]
- Etude, par diffusion centrale des rayons X, de l'ordre et de la précipitation dans ces solutions
- Propriétés mécaniques
- Résonance magnétique nucléaire.

Le présent travail a été consacré à la mesure de la susceptibilité magnétique des alliages: AlTi, AlV, AlCr, AlFe, AlMn, AlCo et AlNi, entre 80°K et 300°K.

La solubilité naturelle des métaux de transition dans l'aluminium étant très faible, nous avons utilisé des solutions solides sursaturées, préparées grâce à une technique de trempe ultra-rapide[2]. Nous avons pu dissoudre jusqu'à 5 pour cent d'atomes de transition dans l'aluminium.

La mesure de la susceptibilité a été faite avec une balance magnétique suivant le principe de Faraday–Curie.

2. PREPARATION DES ECHANTILLONS

La pureté des constituants de l'alliage est un facteur fondamental pour pouvoir faire une étude précise sur la susceptibilité magnétique. Les alliages ont été obtenus à partir de métaux contenant moins de 100 p.p.m. d'impuretés. Tout au long de la préparation des échantillons, des précautions ont été prises pour éviter la contamination.

Les alliages ont d'abord été préparés à la concentration voulue dans un four à induction. Puis, pour obtenir des solutions solides sursaturées, nous avons procédé à une trempe ultra-rapide avec l'appareil mis au point par Dixmier[3] qui permet de tremper une goutte d'alliage en l'écrasant entre deux plaques métalliques de grande diffusivité thermique. On obtient ainsi des petits morceaux d'alliage trempé de quelques mm^2 de surface et de 1 à 100 μ d'épaisseur[1].

C'est lors de l'opération de trempe que l'on doit prendre les plus grandes précautions pour

---

*Laboratoire associé au C.N.R.S.

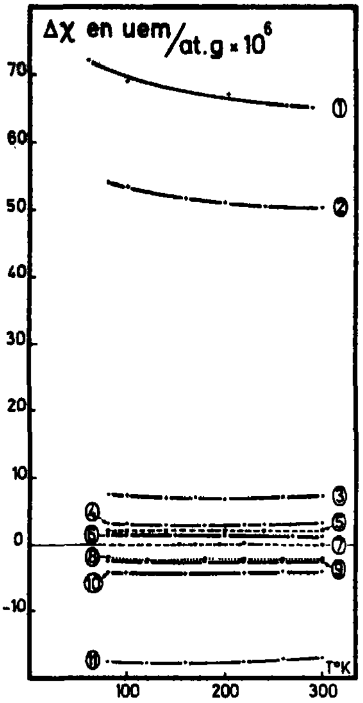

Fig. 1. Variation de la susceptibilité des impuretés diluées de métal de transition. Δχ est la différence entre la susceptibilité des alliages et la susceptibilité de l'aluminium pure pour les alliages suivants:

1 AlMn 4,8 at. %
2 AlMn 3,5 at. %
3 AlMn 0,5 at. %
4 AlFe 3 at. %
5 AlCr 0,5 at. %
6 AlFe 1 at. %
7 AlCO 3 at. %
8 AlTi 0,5 at. %
9 Al V 0,5 at. %
10 Al Ni 1 at. %
11 Al Ni 4,5 at. %.

éviter l'introduction d'impuretés. Les deux plaques entre lesquelles sont écrasées les gouttes d'alliage liquide doivent être très propres. Les impuretés les plus gênantes sont les traces de métaux ferromagnétiques déposées sur la surface des échantillons. Il est à noter que les impuretés introduites après la trempe sont plus nuisibles que celles introduites avant la trempe. En effet ces dernières sont bloquées sous forme de solutions solides non ferromagnétiques alors que les impuretés de surface restent ferromagnétiques.

La concentration en métal de transition des alliages trempés a été mesurée à la microsonde électronique de Castaing qui donne des mesures précises et permet en outre de vérifier l'homogénéité de la trempe. Voici, par exemple, les valeurs relevées pour divers échantillons d'alliage trempé d'Al Mn

9,5% 9,2% 9,4% 9,6% 9,8% 9,6%
9,7% 9,2%

soit une moyenne de 9,5%±0,2% de la concentration en poids, c'est-à-dire 4,8%±0,1% de la concentration atomique.

Il était très important d'éliminer les échantillons dans lesquels pouvait rester du métal de transition non dissous. La technique de diffraction des rayons X a permis de faire le tri. Le fait de dissoudre un métal de transition dans l'aluminium provoque une variation du paramètre cristallin, fonction de la concentration. Nous avons utilisé le montage très dispersif de Seeman–Bohlin. Pour mettre en évidence le déplacement de paramètre nous avons fait deux clichés, un de l'échantillon seul et un du même échantillon recouvert par évaporation d'une couche d'aluminium pur. Le second cliché permet de mesurer le déplacement, le premier de voir si la dissolution est totale ou partielle. Quand la dissolution est partielle il reste une raie à l'emplacement de la raie de l'aluminium pur qui correspond à des grains dans lesquels une phase intermédiaire Al *T* a précipité. En étudiant la fraction d'impureté non dissoute en fonction de l'épaisseur des morceaux d'alliage trempé, nous avons pu trier ces morceaux et connaître la limite supérieure de l'incertitude sur la proportion de métal de transition dissous.

La mesure de la susceptibilité nécessite un échantillon de poids relativement important (0, 5 g) par rapport aux quelques mg d'alliage obtenus dans l'appareil à trempe rapide. Nous avons aggloméré, par pressage, les petits morceaux d'alliage pour en faire des échantillons cylindriques de 6 mm de diamètre, faciles à manipuler, ce qui a rendu plus aisées les mesures de susceptibilité.

3. MESURES MAGNETIQUES

Nous avons utilisé une balance mise au point par MM. Poix et Bernier au laboratoire du Centre d'Etudes de Chimie Métallurgique de Vitry.

4. INCERTITUDES ET CORRECTIONS

Les mesures sont perturbées par des traces non dissoutes de métaux ferromagnétiques*; une correction des mesures est donc nécessaire. Nous supposons que le moment magnétique M_s dû à ces traces est saturé par le champ utilisé (5000 à 10000 G). Le moment total est alors $M = N\chi H + M_s N$. D'où la susceptibilité effectivement mesurée:

$$\chi_H = \chi + \frac{M_s}{H}.$$

En extrapolant à partir de plusieurs mesures de χ_H pour différents champs on déduit χ, susceptibilité de l'échantillon pur. Cette méthode n'est justifiée que si la correction n'est pas trop importante. De plus, elle accroît l'incertitude sur la mesure de la susceptibilité.

5. INCERTITUDE SUR LES MESURES

Deux causes principales d'incertitudes sont à retenir:

l'incomplète dissolution des métaux de transition dans l'aluminium,
la correction due aux traces de métaux ferromagnétiques.

L'étude aux rayons X nous a permis d'estimer l'incertitude maximale sur la concentration en métal de transition non dissous (donc sous forme de phase intermédiaire) et ainsi de calculer l'incertitude maximale sur la mesure de susceptibilité. L'incertitude relative due aux impuretés de métal de transition non dissous est de l'ordre de 1 à 5 pour cent.

L'incertitude, liée à l'extrapolation à un champ infini, des mesures faites en champs finis est de 10 à 20 pour cent.

6. RESULTATS DES MESURES

Nous nous sommes particulièrement intéressés à la variation de susceptibilité atomique rapportée à 1 pour cent de métal de transition car elle correspond à la susceptibilité des électrons excédants provenant des impuretés.

Nous avons en outre étudié les variations de la susceptibilité des alliages avec la température, (ce qui a permis de constater que l'on avait affaire à une susceptibilité de Pauli et par conséquent qu'il n'y avait pas de moment localisé sur les impuretés) et avec la concentration en élements de transition (études faites pour Al Mn, Al Fe, Al Ni).

(a) *Mesures sur les alliages* **Al** Ti, **Al** V *et* **Al** Cr

Un échantillon de Al Ti de 0,306 g et un échantillon de Al V de 0,284 g ont été préparés à la concentration unique de 0,5 pour cent. En effet, à une concentration supérieure la température de fusion totale de l'alliage est très élevée et lors de la trempe il y a fusion des rondelles de cuivre servant à écraser les gouttes de liquide.

Nous avons échelonné des mesures en fonction de la température entre 80 et 300°K, en utilisant plusieurs valeurs du champ magnétique pour faire la correction d'impuretés magnétiques.

L'écart $\Delta\chi$ entre la susceptibilité de l'aluminium et celle des alliages ne présente pas de variation avec la température, supérieure aux incertitudes de mesures.

La masse réduite des échantillons et la faible concentration laissent une incertitude importante sur les valeurs de l'écart $\Delta\chi$ rapporté à une concentration de 1 pour cent

Al Ti $\Delta\chi_{1\%} = (-5 \pm 1,5) \times 10^{-6}$ uem/at . g%

Al V $\Delta\chi_{1\%} = (-4,5 \pm 1,5) \times 10^{-6}$ uem/at . g%

---

*Ces traces proviennent probablement de la contamination de la surface des échantillons par des poussières de fer. Leur masse est extrêmement réduite (quelques p.p.m.) mais le moment magnétique du fer étant très grand leurs effets sont importants.

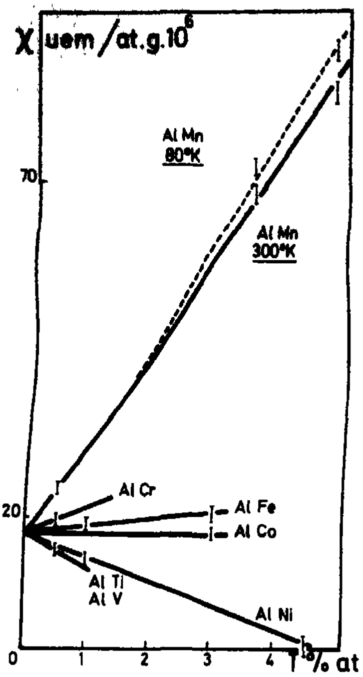

Fig. 2. Variation de la susceptibilité des alliages avec la concentration en métal de transition dissous.

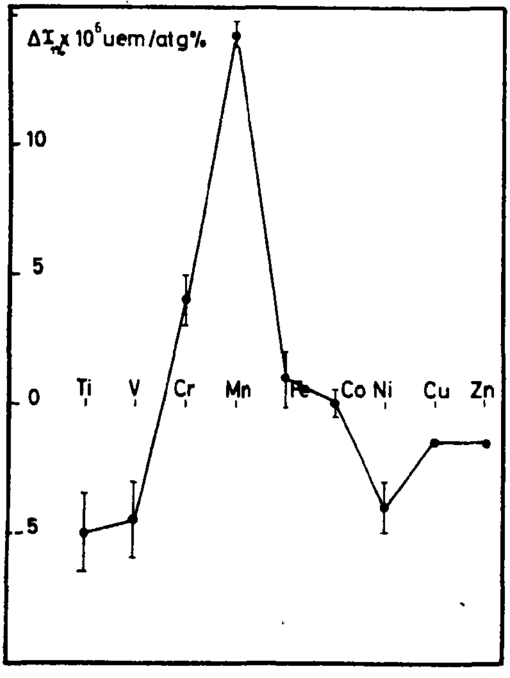

Fig. 3. Susceptibilité $\Delta\chi_{1\%}$ des métaux de transition dissous dans l'aluminium. $\Delta\chi_{1\%}$ étant la différence entre la susceptibilité de l'alliage rapporté à 1 at. % de métal de transition, et celle de l'aluminium pure.

L'échantillon de l'alliage Al Cr préparé contenant 0,5 pour cent de chrome, avait une masse de 0,458 g. Nous n'avons pas observé de variation de $\Delta\chi_{1\%}$ avec la température.

$$\text{Al Cr} \quad \Delta\chi_{1\%} = (4 \pm 1) \times 10^{6}\ \text{uem/at.g\%}$$

(b) *Mesures sur l'alliage* **Al Mn**

Trois échantillons de 0,350 g, 0,506 g et 0,279 g aux concentrations respectives de 0,5%-3,5% et 4,8%.

Ces mesures nous ont permis d'étudier la variation de $\Delta\chi$ avec la concentration et avec la température.

Pour l'alliage de 0,5 pour cent on n'observe pas de variation avec le température, mais pour les alliages à plus fortes concentrations, $\Delta\chi$ décroît lorsque T augmente. Cette décroissance est toujours plus lente qu'une décroissance en $1/T$.

A la température ambiante la variation de $\Delta\chi$ est linéaire pour les concentrations étudiées. Mais à température plus basse on observe une variation de $\Delta\chi$ légèrement plus rapide que la variation linéaire. Ceci peut provenir du fait que pour une concentration de 5 pour cent la distance entre deux atomes de manganèse voisins est de trois distances interatomiques. Beaucoup d'atomes de manganèse sont donc voisins et des couplages importants apparaissent.

Nous donnons les valeurs dans le Tableau 1.

(c) *Mesures sur les alliages* Al Fe, Al Co *et* Al Ni

Nous avons utilisé deux échantillons de Al Fe de 0,370 et 0,412 g aux concentrations respectives de 1 et 3 pour cent. La variation de $\Delta\chi$ avec la température est inférieure aux incertitudes de mesures pour les deux échantillons. La variation avec la concentration semble linéaire.

Nous donnons les valeurs dans le Tableau 2.

L'échantillon d'Al Co de 0,287 g avait une concentration de 3 pour cent.

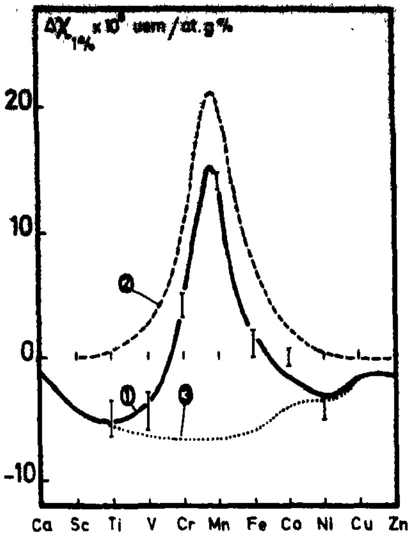

Fig. 4. Comparaison entre les résultats expérimentaux et les prévisions théoriques: (1) Susceptibilité $\Delta\chi_{1\%}$ expérimentale des impuretés. (2) Susceptibilité paramagnétique théorique de 1 at.% d'impureté de transition, avec un facteur d'augmentation maximum de 17. (3) Différence entre les courbes 1 et 2 permettant d'estimer l'allure de la susceptibilité diamagnétique des impuretés diluées.

Nous avons mesuré une susceptibilité identique à celle de l'aluminium pour toutes les températures de 80 à 300°K

$$\Delta\chi_{1\%} = 0 \pm 0{,}5 \text{ uem/at. g\%}.$$

Deux échantillons de 0,270 et 0,313 g aux concentrations respectives de 1 et 4,5 pour cent ont été utilisés.

Nous n'avons pas observé de variation notable avec la température.

Il semble que la variation avec la concentration soit quasi linéaire jusqu'à 4,5 pour cent, mais l'incertitude sur la bonne dissolution du nickel dans l'alliage à 4,5 pour cent étant importante, nous ne pouvons pas être très affirmatif.

Nous donnons les valeurs dans le Tableau 2.

1. COMPARAISON AVEC LES PREVISIONS THEORIQUES

Du point de vue théorique, les résultats obtenus peuvent s'interpréter par la théorie des états liés virtuels de Friedel. Avec l'Hamiltonien d'Anderson et en tenant compte de la dégénérescence orbitale on obtient pour la susceptibilité par impureté:

$$\Delta\chi_P = \frac{2\mu^2(2l+1)\rho(E_F)}{1-U'\rho(E_F)}$$

où $\rho(E_F)$ est la densité d'état des électrons 'd' au niveau de Fermi sur l'impureté et U' l'énergie de répulsion coulombienne entre états 'd', le facteur $s = [1-U'\rho(E_F)]^{-1}$ est le facteur d'augmentation dû à l'échange.

Si $\langle n\rangle$ est l'occupation moyenne des orbitales 'd' on a, avec une courbe lorentzienne:

$$\rho(E_F) = \frac{\sin^2 \pi\langle n\rangle}{\pi\Delta}.$$

Des courbes $\Delta\chi$ ont été tracées pour différentes valeurs des paramètres U' et Δ en supposant que $\Delta\chi_P$ était environ 2000 uem/at. g pour les impuretés de manganèse. Puis nous avons tracé les courbes $\Delta\chi_0$, différence entre la courbe expérimentale et la courbe du paramagnétisme théorique. Le choix d'une courbe diamagnétique de forme simple (présentant un minimum d'oscillation) permet de faire un choix pour Δ et U'. Nous prenons $\Delta = 1$ eV et pour facteur d'augmentation maximum ($\langle n\rangle = \frac{1}{2}$)

$$s = \left(1-\frac{U'}{\pi\Delta}\right)^{-1} = 17.$$

L'allure de la courbe expérimentale indique que le maximum est situé entre le Cr et le Mn ce qui signifie que les impuretés de manganèse ont plus de 5 électrons localisés. Ceci a déjà été observé lors de l'expérience de résonance nucléaire[4]. Le maximum de la courbe théorique a été déplacé pour le faire coïncider avec celui de la courbe expérimentale.

Remarquons que le terme d'augmentation pour le manganèse est de 15 avec $\langle n\rangle = 5{,}3$. Cette valeur est celle observée lors des expériences de résonance[4, 5].

Tableau 1. *$\Delta\chi$ et $\Delta\chi_{1\%} \times 10^6$ (en uem/at. g) dans les alliages* Al Mn

Alliages Al Mn		0,5%	3,5%	4,8%
300°K	$\Delta\chi$	$7,1 \pm 1$	$50,2 \pm 1,5$	$70 \pm 2,5$
	$\Delta\chi_{1\%}$	$14,2 \pm 2$	$14,3 \pm 0,5$	$14,6 \pm 0,5$
80°K	$\Delta\chi$	$7,1 \pm 1$	$54 \pm 1,5$	$77 \pm 2,5$
	$\Delta\chi_{1\%}$	$14,2 \pm 2$	$15,4 \pm 0,5$	$16 \pm 0,5$

Tableau 2. *$\Delta\chi$ et $\Delta\chi$ $\times 10^6$ (en uem/at. g) dans les alliages* Al Fe *et* Al Ni

Alliage Al Fe	1%	3%
$\Delta\chi$	$1,3 \pm 1$	$3,2 \pm 3$
$\Delta\chi_{1\%}$	$1,3 \pm 1$	$0,94 \pm 1$
Alliage Al Ni	**1%**	**4,5%**
$\Delta\chi$	-4 ± 1	-17^{+2}_{-4}
$\Delta\chi_{1\%}$	-4 ± 1	-4 ± 1

La courbe diamagnétique obtenue par différence entre les courbes expérimentale et théorique est purement hypothétique mais on peut malgré tout affirmer qu'elle est symétrique et que son amplitude est d'environ 6 à 7×10^6 uem/at. g.

Il semble qu'au terme paramagnétique de Pauli $\Delta\chi_p$, explicable théoriquement, soit superposé un terme diamagnétique $\Delta\chi_0$ symétrique en fonction de $\langle n \rangle$.

Ce terme diamagnétique est important (environ le tiers de la susceptibilité au milieu de la série). Il est difficile de l'évaluer théoriquement. Pour des impuretés normales (zinc dans le cuivre par exemple) Kohn et Luming [6] ont tenté de calculer ce terme, mais ils ont trouvé des résultats 10 à 20 fois trop faibles.

Nous avons repris la même méthode de calcul pour Al*T*. Nous avons trouvé des résultats qui – comparés aux résultats expérimentaux – sont environ 25 fois trop faibles.

Le problème du diamagnétisme des impuretés dans les métaux reste donc à expliquer.

8. CONCLUSION

Nous pouvons comparer nos résultats pour Al V, Al Cr et Al Mn avec ceux obtenus par différents auteurs dans le Tableau 3.

Ces résultats sont compatibles.

Il est à noter cependant que les résultats

Tableau 3. *Comparaison des valeurs données pour $\Delta\chi_{1\%} \times 10^6$ (en uem/at. g) par différents auteurs*

	Al V	Al Cr	Al Mn	Remarques
Flynn [7], Rigney et Gardner $\Delta\chi_{1\%}$	$(+2 \pm 0,5)10^{-6}$	$(7 \pm 0,5)10^{-6}$	$(11,15 \pm 0,3)10^{-6}$	Alliages liquides
Taylor [8] et Burger $\Delta\chi_{1\%}$	$(-5,5 \pm 1)10^{-6}$	$(3,1 \pm 0,5)10^{-6}$	$(12,4 \pm 1)10^{-6}$	
Colling [9] et Hedgcock $\Delta\chi_{1\%}$			$(12,4 \pm \ )10^{-6}$	
Aoki [10] et Otsuka $\Delta\chi_{1\%}$	$(-4,3 \pm 1,6)10^{-6}$	$(7,3 \pm 1,4)10^{-6}$	$(14,6 \pm 2)10^{-6}$	
Sadoc $\Delta\chi_{1\%}$	$(-4,5 \pm 1,5)10^{-6}$	$(4 \pm 1)10^{-6}$	$(14,2 \pm 0,5)10^{-6}$	

obtenus pour des alliages liquides sont assez différents de ceux que nous avons obtenus pour les alliages en solutions solides, particulièrement au début et à la fin de la série de transition. En effet $\Delta\chi$ est toujours positif pour les alliages liquides. Le terme diamagnétique disparaît donc à l'état liquide.

La mesure de susceptibilité d'un certain nombre d'alliages Al T permet de dégager des lois générales.

(1) Aux concentrations inférieures à 5 at. % la loi de variation de $\Delta\chi$ en fonction de la concentration est linéaire.

(2) Les variations de $\Delta\chi$ avec la température sont très faibles pour des concentrations inférieures à 3 at. %. Pour des concentrations plus importantes $\Delta\chi$ décroît en fonction de T beaucoup plus lentement que $1/T$. (Mesures sur Al Mn).

(3) Pour les éléments de transition proches des extrémités de la série, $\Delta\chi$ est négatif, alors qu'il devient positif pour Cr, Mn, Fe.

La mesure des variations de la susceptibilité de l'aluminium avec la concentration en impureté de transition a donc fourni des valeurs expérimentales dans un domaine où n'existaient que des calculs théoriques.

Les résultats sont peu conformes aux prévisions théoriques car une contribution diamagnétique considérable a été mise en évidence. Il n'est malheureusement pas encore possible de trouver une explication théorique satisfaisante au diamagnétisme.

BIBLIOGRAPHIE

1. BLETRY J. Thèse de 3ème Cycle, Orsay (Avril 1968); *J. Phys. Chem. Solids* 31, 6, 1263 (1970).
2. DUWEZ P. et WILLENS R. H., *Trans Met. Soc. AIME* 227, 362 (Avril 1963).
3. DIXMIER J. et GUINIER A., *Mém. Sci. Rev. Metall.* LXIV, 1, 53 (1967).
4. BRETELL J. M. and HEEGER A. J., *Phys. Rev.* 153, 319 (1967).
5. LAUNOIS H., Thèse d'Etat, Orsay (Mai 1969).
6. KOHN W. et LUMING M., *J. Phys. Chem. Solids* 24, 851 (1963).
7. FLYNN G. P., RIGNEY D. A. et GARDNER J. A., *Phil. Mag.*, 15, 1255 (1967).
8. TAYLOR A. et BURGER J. P., *J. Phys.* 20, 829 (1959).
9. COLLING E. W. et HEDGCOCK F. T., *J. de Phys.* 126, 1654 (1962).
10. AOKI et OTSUKA (en cours de publication).

J. Phys. Chem. Solids, 1971, Vol. 32, pp. 2773–2777. Pergamon Press. Printed in Great Britain

SPECIFIC HEATS OF $LaIn_3$, $CeIn_3$ AND $PrIn_3$ AT TEMPERATURES BETWEEN 1·5 AND 4·2°K*

S. NASU,† A. M. VAN DIEPEN,‡ H. H. NEUMANN and R. S. CRAIG
Department of Chemistry, University of Pittsburgh, Pittsburgh, Penn. 15212, U.S.A.

(*Received* 10 *February* 1971)

Abstract – The specific heats of $LaIn_3$, $CeIn_3$ and $PrIn_3$ have been measured at temperatures between 1·5–4·2°K. In $LaIn_3$ and $PrIn_3$ they showed the usual temperature dependence expressed in the formula $C = \gamma T + \beta T^3$, where $\gamma = 6{\cdot}28 \pm 0{\cdot}10$ mj°K^{-2} mole^{-1}, $\beta = 1{\cdot}06 \pm 0{\cdot}01$ mj°K^{-4} mole^{-1} (Debye temperature $\theta = 194{\cdot}4$°K) for $LaIn_3$ and $\gamma = 11{\cdot}42 \pm 0{\cdot}09$ mj°K^{-2} mole^{-1}, $\beta = 0{\cdot}94 \pm 0{\cdot}01$ mj°K^{-4} mole^{-1} ($\theta = 202{\cdot}3$°K) for $PrIn_3$. The specific heat of $CeIn_3$ is an order of magnitude higher. Because of the complex behavior of C_p/T vs. T^2 in this compound γ and β were not determined. The electron–phonon enhancement factors for $LaIn_3$ and $PrIn_3$ as determined from experiment, were found to be 0·59 and 0·54, respectively.

1. INTRODUCTION

STUDIES of the magnetic properties of the rare-earth metals and their intermetallic compounds have long been a subject of great interest. One interesting class of systems is that of the RIn_3 compounds (R = rare earth) which have the cubic Cu_3Au structure. The magnetic behavior of $CeIn_3$ reveals antiferromagnetism below 11°K; $PrIn_3$, on the other hand, exhibits Van Vleck paramagnetism below about 30°K[1, 2]. The rare earths possess a well-localized 4*f* magnetic moment, and are influenced by crystal field effects. In the case of $PrIn_3$ magnetic ordering is prevented by the crystalline field.

Previous studies have been made of the specific heat of $LaIn_3$, $CeIn_3$ and $PrIn_3$ by van Diepen *et al.* at temperatures in the range 8–300°K[3]. In the course of the specific heat measurements on $CeIn_3$ a lambda-type anomaly was found near 11°K which was associated with the antiferromagnetic transition. Both $CeIn_3$ and $PrIn_3$ showed a Schottky anomaly around 60 and 36°K respectively, from which overall crystal field splittings of 155°K (Γ_7 doublet lowest) and ~ 170°K (Γ_1 singlet lowest, $-0{\cdot}8 \leq x \leq -0{\cdot}6$) were derived, respectively.

It is well known [4] that the electron–phonon interaction provides an important mechanism for the renormalization of the effective electron mass which influences the specific heat. Unfortunately, no theoretical studies of the electron band structures of these compounds have been reported. However, since $LaIn_3$ shows superconductivity below 0·70°K[5], it is possible to obtain an empirical electron–phonon enhancement factor from the Debye temperature and the superconducting transition temperature [6].

In this light we have investigated the specific heats of $LaIn_3$, $CeIn_3$ and $PrIn_3$ in the temperature range between 1·5 and 4·2°K. In Section 2, we give a brief experimental description of this study, in Section 3 we present the result of our measurements, and in Section 4 we attempt to provide a qualitative understanding.

2. EXPERIMENTAL

The samples used in this investigation, 7 to 9 g per compound, were prepared by levitation melting, followed by stress annealing under an

---

*Support for this work was provided by the U.S. Atomic Energy Commission, by the National Aeronautics and Space Administration and by the Army Research office, Durham.

†On leave of absence from Japan Atomic Energy Research Institute, Tokai-mura, Naka-hun, Ibaraki-Ken, Japan.

‡Present Address: Philips Research Laboratories, Eindhoven, The Netherlands.

argon atmosphere at 500°C for about 1 hr. The purity of the indium metal was stated to be 99·999 per cent while the rare-earths had a stated purity of 99·9 per cent. This figure, furnished by the manufacturer, refers only to metallic impurities. No information is available on the presence of hydrogen, oxygen, nitrogen, etc. X-ray diffraction showed the three compounds to have the Cu_3Au structure with lattice parameters in good agreement with the reported values[2]. The heat capacity measurements were carried out in a calorimeter in which the energy was supplied to the sample as a pulse of about 1 sec. duration and was measured by means of an integrating digital voltmeter. Temperature measurements were made with a germanium resistance thermometer calibrated against the vapor pressure of He_4. Details of the calorimetric procedure will be published elsewhere[7].

3. RESULTS

The temperature range covered in the measurements was from about 1·6 to 4°K. If only electronic contributions and lattice vibrations are involved, the specific heat may be represented in this range by the equation

$$Cp = \gamma T + \beta T^3, \qquad (1)$$

where the first term γT corresponds to the electronic contribution and the second term βT^3 to the lattice contribution.

The measured electronic specific heat coefficient γ is related to the apparent density of states $N(E_F)$ at the Fermi surface by the equation

$$\gamma = (\pi^2/3)k^2 N(E_F)L, \qquad (2)$$

where L is the number of atoms per mole, k is the Boltzmann constant. At low temperature ($T \ll \theta$) the Debye temperature θ can be determined using the following expression:

$$\beta = (12/5)\pi^4 kL/\theta^3. \qquad (3)$$

The electronic specific heat coefficient γ, the term β, the apparent density of states $N(E_F)$, the bare density of states $N(E_F)_0$ (which will be discussed in Section 4) and the Debye temperature θ are listed in Table 1.

The experimental results for $LaIn_3$ and $PrIn_3$ are shown in Fig. 1 in the usual C/T vs. T^2 format. The data appear to be satisfactorily represented by equation (1). The data for $CeIn_3$ are given in a similar format in Fig. 2. $CeIn_3$, being an antiferromagnet, might be expected to show a simple T^3 temperature dependence for the magnetic contribution to its specific heat. The situation is, however,

Table 1. Data derived from heat capacity measurements

	$LaIn_3$	$PrIn_3$
γ (mj°K^{-2} mole^{-1})	6·28 ± 0·10	11·42 ± 0·09
β (mj°K^{-4} mole^{-1})	1·06 ± 0·01	0·94 ± 0·01
θ°K	194·4	202·3
$N(E_F)$ (eV^{-1} atom^{-1})	0·666	1·211
$N(E_F)_0$ (eV^{-1} atom^{-1})	0·419	
λ_{ph}	0·59	0·54

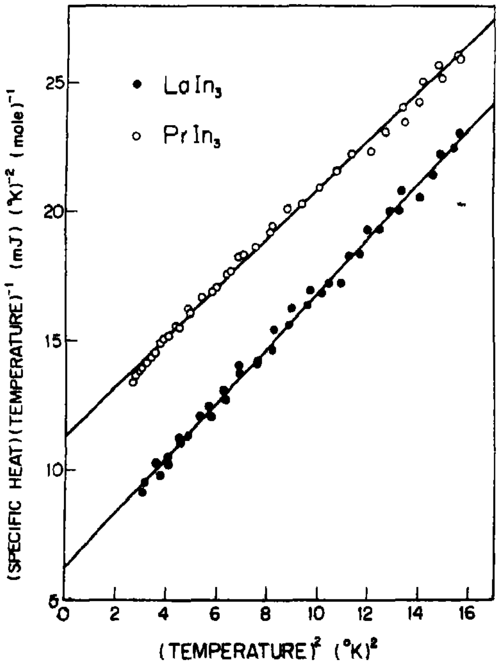

Fig. 1. Experimental heat capacity points for $LaIn_3$ and $PrIn_3$ plotted in the C/T vs. T^2 format.

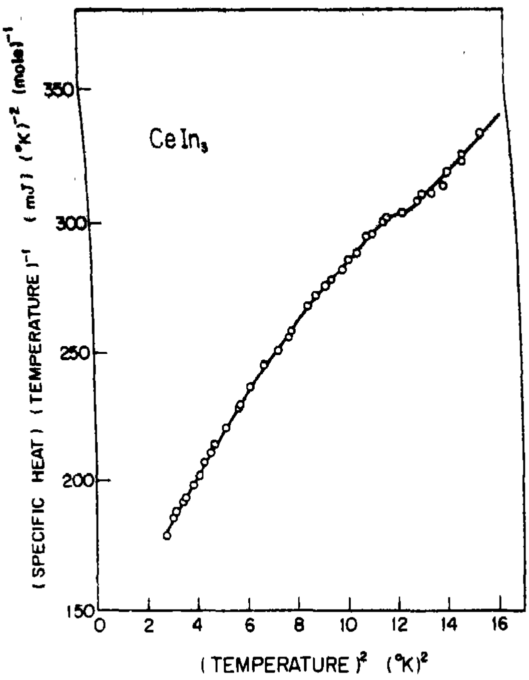

Fig. 2. Experimental heat capacity results for CeIn$_3$ plotted in the C/T vs. T^2 format.

complicated by the proximity of the Néel point and by the operation of a crystal field effect. It is clear from Fig. 2 that the specific heat behavior of CeIn$_3$ is somewhat more complex, with a small hump around 3°K.

4. DISCUSSION

(a) LaIn$_3$

LaIn$_3$ is superconducting with the transition temperature $T_c = 0{\cdot}70$°K[5]. The transition temperature for metallic lanthanum (4·9°K for h.c.p. structure, 6·05°K for f.c.c. structure) is much higher than that for LaIn$_3$. The value of γ for LaIn$_3$ in Fig. 1 and Table 1 is about two-thirds the value for metallic lanthanum (10·1 mj deg^{-2} mol^{-1}). There seems little doubt that the fall of the transition temperature in LaIn$_3$ is due to a decreasing electron–phonon interaction if the mechanism responsible for superconductivity is the electron–phonon interaction.

Our measurements of the electronic specific heat allow us to determine the apparent density of states through equation (2). The magnitude of the density of states so determined, however, is affected by several important many-body interactions. In particular, the electron–electron, the electron–phonon and the paramagnon interactions cause γ to be enhanced from the one electron value by the mass enhancement factor m^*/m

$$\gamma = \frac{m^*}{m}\gamma_0 = (1 + \lambda_e + \lambda_{ph} + \lambda_p)\gamma_0$$

$$= \frac{m^*}{m}\frac{\pi^2}{3}kN(E_F)_0 \qquad (4)$$

here λ_e, λ_{ph} and λ_p are the enhancements due to electron–electron, electron–phonon, and paramagnon interactions respectively, $N(E_F)_0$ is the bare or unenhanced density of states such as could be obtained, in principle, from a band structure calculation and γ_0 is the bare electronic specific heat coefficient. The changes in self-energy induced by these three interactions are assumed to be additive. Although this assumption is not strictly true equation (4) is sufficiently accurate for the qualitative arguments which follow below. Unfortunately, no band structure calculations, such as those employing the augmented-plane-wave method, have been reported. However, we can estimate the electron–phonon interaction enhancement factor, which seems to be the most important, using experimental data.

McMillan[6] showed that an empirical electron–phonon enhancement factor can be obtained from the experimentally determined superconducting transition temperature T_c and the Debye temperature θ by the relation

$$\lambda_{ph} = \frac{1{\cdot}04 + \mu^* \ln(\theta/1{\cdot}45T_c)}{(1 - 0{\cdot}62\mu^*)\ln(\theta/1{\cdot}45T_c) - 1{\cdot}04}. \qquad (5)$$

Using the value 0·13 for the coulomb pseudopotential strength μ^* (see Ref. [6]) and taking the superconducting transition temperature T_c to be 0·70°K for LaIn$_3$, we obtain a value of 0·59 for λ_{ph}. If, in the case of $LaIn_3$, the enhancement due to the electron–electron and the paramagnon interactions may be neglected, we obtain a mass enhancement factor $m^*/m = 1{\cdot}59$ and the bare density of states is 0·418 eV^{-1} $atom^{-1}$. The value of λ_{ph} for $LaIn_3$ is smaller than that for metallic lanthanum (0·94 experimentally, 1·33 theoretically[8]), which seems to support our earlier arguments.

(b) $CeIn_3$

The cubic crystal field splits the $J = \frac{5}{2}$ level in $CeIn_3$ into a doublet Γ_7 and a quartet Γ_8. The specific heat measurements by van Diepen *et al.*[3] show that the ground state is the doublet and that the overall energy separation is 155°K. The Schottky specific heat calculated from this splitting is found to be six orders of magnitude smaller ($2{\cdot}24\times 10^{-6}$ *j.* $°K^{-1}$ mol^{-1} at 4·2°K) than the value observed in this study (1·33 *j.* $°K^{-1}$ mol^{-1} at 3·98°K) and hence is negligible.

The Néel point T_N for $CeIn_3$ was observed at 11°K. In addition to the Néel point the curve of inverse magnetic susceptibility vs. temperature exhibits a maximum at approximately $T_N/3$. According to simple spinwave theory [8], the magnetic specific heat C_M of an antiferromagnetic compound, at temperatures well below the Néel temperature, may be written $C_M \propto T^3$. However, the situation in $CeIn_3$ is complex because of the anisotropy energy, and because of the low-lying doublet, the energy separation of which may vary with the degree of magnetic order below the Néel point. Other antiferromagnets have shown departures from the T^3 dependence at comparable temperatures relative to the Néel point[9].

The specific heat of $CeIn_3$ in the liquid helium range is an order of magnitude larger than that of the other two compounds in this study. Two factors may contribute to this excess heat capacity: the magnetic contribution mentioned above; and a high density of states resulting from the proximity of the 4*f* band to the Fermi surface. A high density of states, connoting a high specific heat in the helium range, has also been found in $YbIn_3$ [10].

The heat capacity data for $CeIn_3$ shows a hump on the C/T vs. T^2 curve centered at about 3°K (Fig. 2). This hump may well be connected with the above mentioned minimum in the susceptibility at about $T_N/3$. This minimum in susceptibility also occurs in other RIn_3 compounds. Its origin is at present not understood.

(c) $PrIn_3$

In $PrIn_3$ the value of γ is about twice as large as that in the Pauli paramagnetic $LaIn_3$, which implies that there is still some interaction between the 4*f* level and the Fermi surface. We take for isostructural compounds a rough estimate of λ_{ph} to be given by the following expression[11]

$$\lambda_{ph} = C/M\theta^2 \qquad (6)$$

where M is the average atomic mass and C is a constant. Using M, θ and λ_{ph} for $LaIn_3$ we obtain $1{\cdot}07\times 10^7$ as an estimate of C in equation (6). Using this value of C, we find the value of λ_{ph} for $PrIn_3$ to be 0·54. If we assume that the bare density of states is the same in $PrIn_3$ as in $LaIn_3$ and if we neglect the electron–electron enhancement factor we arrive at a paramagnon enhancement factor of 1·64 in $PrIn_3$. This assumption may considerably overestimate the mass renormalization factor. The large specific heat of $PrIn_3$ is probably due to a change in the bare density of states as well as to the electron–phonon and paramagnon enhancements.

Acknowledgements—The authors wish to express their appreciation to Prof. W. E. Wallace for his interest, helpful discussion and encouragement throughout the course of this work, to Dr. C. Bechmann for his aid in computer programming and to Mr. N. Marzouk for his part in preparing samples.

REFERENCES

1. TSUCHIDA T. and WALLACE W. E., *J. chem. Phys.* **43**, 3811 (1965).

2. BUSCHOW K. H. J., DE WIJN H. W. and VAN DIEPEN A. M., *J. chem. Phys.* **50**, 137 (1969).
3. VAN DIEPEN A. M., CRAIG R. S. and WALLACE W. E., *J. Phys. Chem. Solids* **32**, 1867 (1971).
4. KITTEL C., Introduction to *Solid State Physics*, John Wiley, New York (1966).
5. HAVINGA E. E., *Phys. Lett.* **28A**, 350 (1968).
6. MCMILLAN W. L., *Phys. Rev.* **167**, 331 (1968).
7. CRAIG R. S., NASU S. and NEUMANN H. H., to be published.
8. VAN KRANENDONK J. and VAN VLECK J. H., *Rev. mod. Phys.* **30**, 1 (1958).
9. MIEDEMA A. R., WIELINGA R. F. and HUISKAMP W. J., *Physica* **31**, 835 (1965).
10. MIEDEMA A. R. and CHANG H. K., private communication.
11. JENSEN M. A., *Superconductivity* (Edited by P. R. Wallace), Gordon and Breach, *Proceedings of the Advance Summer Study Institute*, McGill University, Montreal.

J. Phys. Chem. Solids, 1971, Vol. 32, pp. 2779–2783. Pergamon Press. Printed in Great Britain

SPECIFIC HEATS OF $LaNi_5$, $CeNi_5$, $PrNi_5$, $NdNi_5$ AND $GdNi_5$ BETWEEN 1·6 AND 4°K*

S. NASU†, H. H. NEUMANN, N. MARZOUK, R. S. CRAIG and W. E. WALLACE
Department of Chemistry, University of Pittsburgh, Pittsburgh, Penna. 15213, U.S.A.

(*Received* 10 *February* 1971)

Abstract—The specific heats of $LaNi_5$, $CeNi_5$, $PrNi_5$, $NdNi_5$ and $GdNi_5$ have been measured at temperatures between 1·6 and 4° K. The specific heats of $LaNi_5$, $CeNi_5$ and $PrNi_5$ can be represented by the expression $Cp = \gamma T + \beta T^3$, where $\gamma = 34{\cdot}33 \pm 0{\cdot}13$ mj °K^{-2} mole^{-1} for $LaNi_5$, $40{\cdot}01 \pm 0{\cdot}11$ mj °K^{-2} mole^{-1} for $CeNi_5$ and $37{\cdot}02 \pm 0{\cdot}16$ mj °K^{-2} mole^{-1} for $PrNi_5$; and $\beta = 0{\cdot}294 \pm 0{\cdot}014$ mj °K^{-4} mole^{-1} ($\theta = 340{\cdot}9$°K) for $LaNi_5$, $0{\cdot}279 \pm 0{\cdot}012$ mj °K^{-4} mole^{-1} ($\theta = 347{\cdot}1$°K) for $CeNi_5$ and $0{\cdot}309 \pm 0{\cdot}017$ mj °K^{-4} mole^{-1} ($\theta = 333{\cdot}5$°K) for $PrNi_5$. The γ and β for $NdNi_5$ and $GdNi_5$ were not determined because of the complex behavior of C_p/T vs. T^2 relations due to anomalies and large magnetic contributions.

1. INTRODUCTION

STUDIES of the magnetic properties of rare-earths and their intermetallic compounds have recently been a subject of great interest. Rare-earth atoms possess a well-localized 4-*f* magnetic moment. A strong indirect-exchange mechanism provided by the conduction electrons is reponsible for the magnetic ordering of these materials. One interesting class of systems is that represented by the formula RNi_5 (R = rare-earth atoms). These are isostructural with the RCo_5 compounds which are currently of great technological interest because of the useful magnetic properties of several members of the series, particularly $SmCo_5$. The crystallographic and the magnetic properties of RNi_5 including Mössbauer studies have been extensively investigated by various authors[1–5]. Little attention, however, has been paid to the specific heat study in these compounds.

For these compounds the ordering of the magnetic sublattice (Ni or Co) is important. In RCo_5 moments are observed at Co sites; on the contrary, there seem to be practically no moments on Ni sites. It is thought that the three valence electrons of the rare-earth atom have filled the 3*d* shell of the nickel giving it the configuration $3d^{10}$. It will be interesting to compare the specific heat of RNi_5 with that of RCo_5. Toward this objective, we have investigated the specific heats of $LaNi_5$, $CeNi_5$, $PrNi_5$, $NdNi_5$ and $GdNi_5$ in the temperature range between 1·6–4°K.

2. EXPERIMENTAL

The samples used in the present investigation, 6 to 10 g for each compound, were prepared by levitation melting, following which they were sealed in Vycor tubes under an argon atmosphere and heated for several weeks at 800–900°C. The structures and magnetic characteristics of the samples were established and found to be in good agreement with results observed in earlier studies. The rare earth metals were stated by the manufacturer to be of 99·9 per cent purity with respect to metallic impurities, while the nickel (Johnson–Matthey spectrographically standardized grade) had an impurity level of about 10 ppm, the principal contaminants being silver, copper, iron and silicon. The

---

*This work was assisted by the U.S. Atomic Energy Commission and the National Aeronautics and Space Administration.

†On leave of absence from Japan Atomic Energy Research Institute, Tokai-mura, Naka-gun, Ibaraki-Ken, Japan.

specific heat measurements were carried out in the temperature range between 1·6 and 4·2°K employing an experimental procedure reported in another paper[6].

3. RESULTS

The temperature range covered in the measurements was from 1·6 to 4°K. In this range the specific heats of the samples may be represented by the equation

$$Cp = \gamma T + \beta T^3 \qquad (1)$$

where the first term γT corresponds to the contribution of the electrons to the specific heats and the second term βT^3 corresponds to the lattice vibration.

The experimental results for $LaNi_5$, $CeNi_5$ and $PrNi_5$ are presented in Fig. 1 in the usual Cp/T vs. T^2 format. The Cp vs. T relations for $NdNi_5$ and $GdNi_5$ are also presented in Figs. 2 and 3 respectively. It is clear from Fig. 1 that the present data for $LaNi_5$, $CeNi_5$ and $PrNi_5$ exhibit only the simple temperature dependence which is usually found for the specific heat of metals at low temperatures, although the temperature dependence of electrical resistivity for $CeNi_5$ shows something like a Kondo anomaly[7]. It is clear from Fig. 2 and 3 that the specific heats of $NdNi_5$ and $GdNi_5$ are extremely large and exhibit some anomalies.

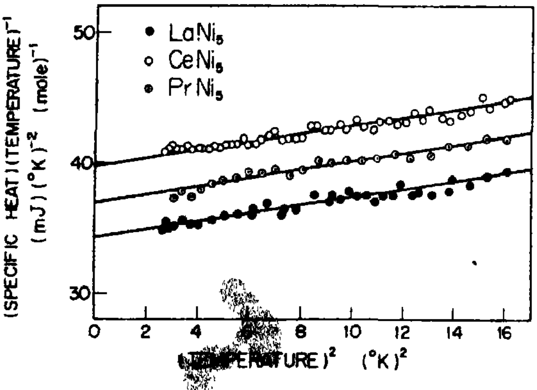

Fig. 1. The specific heat of $LaNi_5$, $CeNi_5$ and $PrNi_5$ in the temperature range 1·6–4°K as Cp/T vs. T^2.

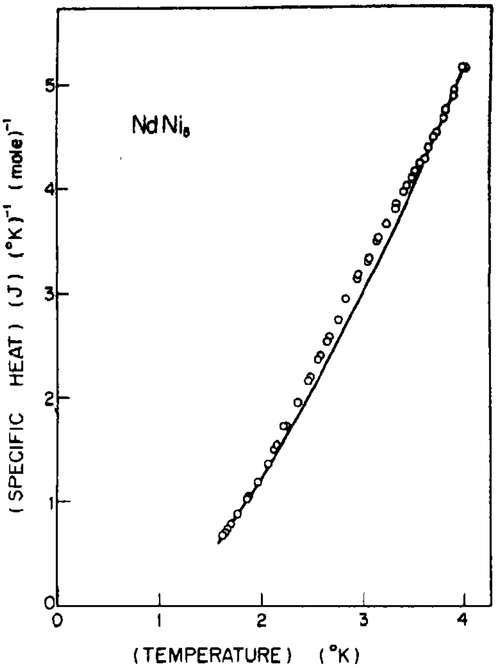

Fig. 2. The specific heat of $NdNi_5$ in the temperature range 1·6–4°K.

The experimentally determined electronic specific heat coefficient γ is related to the apparent density of states $N(E_F)$ at the Fermi surface,

$$\gamma = (\pi^2/3)k_B{}^2N(E_F) \qquad (2)$$

where L is the number of atoms per mole, k_B is the Boltzmann constant. At low temperatures, the Debye temperature θ can be estimated using the following expression:

$$\beta = (12/5)\pi^4 k_B L/\theta^3. \qquad (3)$$

4. DISCUSSION

It is well known that the magnetic properties of rare earth metals and compounds are significantly influenced by the interaction between the rare earth ion and the crystal field. The high temperature heat capacity behavior is also known[8] to be affected by the crystal field interaction. The question arises as to whether the heat capacities in

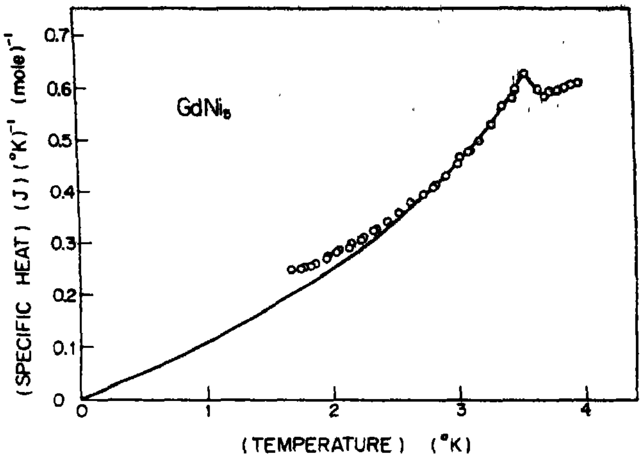

Fig. 3. The specific heat of GdNi$_5$ in the temperature range 1·6–4°K.

the temperature covered in this study also contain a crystal field contribution. Although this question cannot be answered rigorously, it appears that this effect is insignificant. A rigorous answer requires knowledge of the crystal field spectrum for the ions in question which is as yet unavailable.

We can indicate the reasoning which leads us to conclude that the crystal field contribution is negligible by considering the case of Ce^{+3} in $CeNi_5$. In a crystal field of hexagonal symmetry the six-fold degenerate ground state of Ce^{+3} is split into 3 doublets, the relative positions of which depend upon the strength of the crystal field interaction and the relative importance of the second and fourth order terms. Point charge calculations including first and second Ce^{+3} neighbors (Ni is ignored since it is in the $3d^{10}$ configuration) shows a ground state doublet and excited states at 190 and 452°K. Location of the first excited state at 100°K or more is confirmed by unpublished higher temperature heat capacity measurements[9] on $CeNi_5$ which shows that the Schottky type heat capacity anomaly associated with excitation within the crystal field states is inappreciable below 50°K. The Schottky tail for splittings of this magnitude is entirely negligible in the liquid helium range. The linearity of C/T vs. T^2 (Fig. 1) for $CeNi_5$ supports this conclusion and similar data for $PrNi_5$ and $NdNi_5$ make it appear that the crystal field interaction is negligible in these cases as well.

Although the values of γ for $LaNi_5$, $CeNi_5$ and $PrNi_5$ are smaller than the sum of γ for the constituent atoms, ~ 43 mj. K^{-2} $mole^{-1}$ they would be regarded as large compared to most γ values. The large values of γ for these compounds seem to come from the rare-earth component since nickel is in a $3d^{10}$ configuration. This suggests that for $LaNi_5$, $CeNi_5$ and $PrNi_5$ narrow $4f$ bands are near the Fermi surface.

The simplest approach to interpreting the variation of γ with atomic number is in terms of atomic volume. The band splitting is greater the smaller the atomic volume. Since the density of states at the Fermi level $N(E_F)$ is inversely proportional to the band width, it follows that $N(E_F)$ should vary directly with atomic volume. (This is of course subject to the assumption of a constant band shape, which may be invalid.) The volumes of the unit cells of $LaNi_5$, $CeNi_5$ and $PrNi_5$ are 86·70, 82·53 and 84·73, A^3, respectively. On this basis we expect the highest γ for $LaNi_5$ and the lowest for $CeNi_5$. Examination of

Table 1 shows that this is not correct, indicating that size variation alone cannot account for the differences in γ.

Assuming a constant band structure for $LaNi_5$, $CeNi_5$ and $PrNi_5$, which may not be correct, we could attribute the variation of γ to the variation in Fermi energy within the band. However, there are other effects which could influence γ. $LaNi_5$ is a Pauli paramagnet. $CeNi_5$ seems to be a Kondo system. $PrNi_5$ exhibits complex magnitude behavior at low temperatures and may be a Van Vleck parmagnet[10]. Hence, there may be varying paramagnetic enhancements of the electronic specific heats in these compounds. Also there may be significant and variable (from compound-to-compound) electron–phonon enhancement effects. Unfortunately, band calculations for RNi_5 compounds are nonexistant so the electron-phonon enhancement factor (λ_{ph}) is uncertain. However, we can approximate it using Jensen's expression[11]

$$\lambda_{ph} = c/M\theta^2 \tag{4}$$

where c is a constant, M is the mass and θ is the Debye characteristic temperature. Lacking information concerning the constant, we take it to be that of elemental Zr, which is also hexogonal, $3{\cdot}6\times10^6$. M is one sixth of the gram formula weight. This gives λ_{ph} values of 0·72, 0·69 and 0·74, respectively for the La, Ce and Pr compounds, which is again inconsistent with the trend of γ values.

The Debye temperature varies inversely as the square root of the effective mass. Since the mass of these compounds varies only slightly, we expect little variation in θ. The data in Table 1 confirms this expectation.

Results for $NdNi_5$ are different, and more complex than those observed for the La, Ce and Pr compounds. This compound exhibits a λ-type thermal anomaly[9] peaking at about 6·5°K. This is though to be an impurity effect, perhaps associated with oxides contamination by oxides (*vide infra*).

The specific heat of $GdNi_5$ is also very large. Wallace *et al.*[8] found two λ-type thermal anomalies peaking at 30·6 and 30°K, which, it was suggested, might correspond to the paramagnetic to antiferromagnetic and antiferromagnetic to ferromagnetic transitions, respectively. It appears that the magnetic contribution is also the major contribution to the specific heat for this compound. The results in Fig. 3 show a λ-type anomaly peaking at 3·55°K and a departure from the smooth curve below 2·8°K. Measurements by Crane[12] on elemental gadolinium showed two λ-type thermal anomalies, peaking at 1·66 and 3·4°K. It appears that these are impurity effects associated with the presence of oxygen and/or nitrogen. The anomaly at 3·6°K and the excess heat capacity below 2·8°K probably stem from the same source. Similar phenomena probably exist with the other RNi_5 compounds but because of the smaller R moments (for Pr, etc.) the interactions are weaker so that these impurity effects become evident only below the temperature range covered in the present measurements.

Table 1. *Specific heat parameters and densities of states for* RNi_5 *compounds*

	$LaNi_5$	$CeNi_5$	$PrNi_5$
(mj °K^{-1}mole^{-1}) γ	$34{\cdot}33\pm0{\cdot}13$	$40{\cdot}01\pm0{\cdot}11$	$37{\cdot}02\pm0{\cdot}16$
(mj °K^{-4}mole^{-1}) β	$0{\cdot}299\pm0{\cdot}014$	$0{\cdot}279\pm0{\cdot}012$	$0{\cdot}309\pm0{\cdot}017$
(eV^{-1} atom^{-1}) $N(E_F)$	2·43	2·83	2·62
(°K) θ	340·9	347·1	333·5

Acknowledgement—The authors would like to express their appreciation to Dr. C. Bechman for his aid in computer programming.

REFERENCES

1. WERNICK J. H. and GELLER S., *Acta. crystallogr.* **12**, 662 (1959).
2. NESBITT E. A., WILLIAMS H. J., WERNICK J. H. and SHERWOOD R. C., *J. appl. Phys.* **33**, 1674 (1962).
3. ABRAHAM S. C., BERNSTEIN J. L., SHERWOOD R. C., WERNICK J. H. and WILLIAMS H. J., *J. Phys. Chem. Solids* **25**, 1069 (1964).
4. NOWICK I. and WERNICK J. H., *Phys. Rev.* **140**, A131 (1965).
5. WALLACE W. E., *Progress in Rare Earth Science and Technology* (Edited by A. Eyring), Vol. 3 p. 1 (1968).
6. CRAIG R. S., NASU S. and NEUMANN H. H., to be published.
7. MARZOUK N., WALLACE W. E. and CRAIG R. S., Unpublished measurements.
8. WALLACE W. E., CRAIG R. S., THOMPSON A., DEENADAS C., DIXON M., AOYAGI M. and MARZOUK N., *International Colloquium of the French National Center of Scientific Research*, Vol. II, p. 427, CNRS, Paris (1970).
9. MARZOUK N., CRAIG R. S. and WALLACE W. E., Unpublished measurements.
10. WALLACE W. E. and AOYAGI M., Unpublished measurements.
11. JENSEN, M. A., *Superconductivity* (Edited by P. R. Wallace), Gordon and Breach, Proceedings of the Advanced Summer Study Institute, McGill University, Montreal.
12. CRANE L. T., *J. chem. Phys.* **36**, 10 (1962).

J. Phys. Chem. Solids, Vol. 32, pp. 2785–2786. Pergamon Press. Printed in Great Britain

TECHNICAL NOTES

Enhanced electrical conduction in ZnO crystals by excited oxygen molecules

(*Received* 1 *April* 1971)

SINCE Putzeiko and Terenin[1] found that photoconductivity of zinc oxide was sensitized to longer wavelengths by adsorption of dyes, a number of papers have been devoted to discuss whether the photocarriers are generated by 'the energy transfer mechanism' or 'the electron transfer mechanism'. We found that ZnO single crystals showed an enhanced conduction when they were exposed to excited oxygen molecules produced by the chemical reaction[2].

$$NaOCl + H_2O_2 = NaCl + H_2O + O_2^* \quad \text{(singlet oxygen).}$$

This is believed to offer a direct evidence for existence of the excitation energy transfer to ZnO surface traps.

Vapor grown hexagonal crystals of ZnO here employed were approximately 3 mm long and 1·5 mm² in cross section, and had a slightly yellowish color. Lead wires were connected through vacuum deposited gold on surface of crystals. Measurements were made with an electrochemical cell,

$$\text{Nesa} \mid H_2O_2 + \text{electrolyte} \mid \text{ZnO}.$$

The electrolyte solution was 0·05 M KCl buffered at pH 4·6 with sodium acetate and acetic acid. Near the crystal, 0·25 ml of NaOCl solution (0·125 ml of '12% Cl' NaOCl and 0·125 ml of the electrolyte solution) was injected through a capillary into the cell, in about 0·5 sec. Only when NaOCl solution was added almost on the surface of crystal (approximately 1 mm apart), the conductivity jumped up to a higher level and then followed a rapid decay (Fig. 1). The current depended on the concentration of H_2O_2 as is illustrated in Fig. 2. In order to examine the possibility that the jump was brought about by ground state oxygen, oxygen gas was bubbled in at the crystal surface, in place of NaOCl solution. No response was observed.

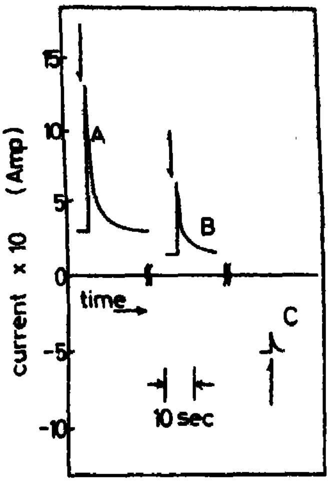

Fig. 1. Current jump induced by singlet oxygen
Applied voltage *A*: 0·16 v . . . ZnO(+)
B: 0·0 v
C: 0·25 v . . . ZnO(−).

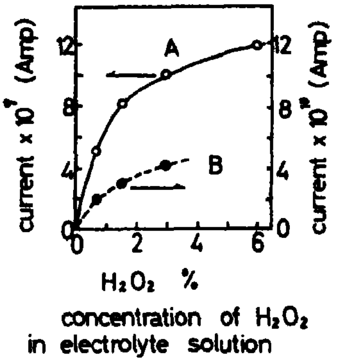

Fig. 2. Dependence of enhanced current on concentration of H_2O_2
Applied voltage *A*: 0·65 v . . . ZnO(+)
B: 0·14 v . . . ZnO(−).

These facts indicate that chemically produced excited oxygen molecules ($^1\Delta_g$ or $^1\Sigma_g{}^+$) are responsible for the enhanced electrical conduction in ZnO. This was further confirmed by observing the influence of a quencher for singlet oxygen. Trimethylene diamine is known as an effective quencher[3]. When it is dissolved in the electrolyte solution in concentration of $1{\cdot}2\times10^{-2}M$, the enhanced current decreased to $\frac{1}{4}$ to $\frac{1}{5}$.

The voltage-current curves of the cell with (*A*) and without (*A*′) H_2O_2 are shown in Fig. 3. The curve *A* crosses the abscissa at −0·22 v, while the curve *A*′ at −0·31 v. This may be a result of some action of H_2O_2 on ZnO surface. However, the resemblance of the curve *A* and *A*′ is apparent within the experimental region of voltage. It does not seem, therefore, that the above conclusion is affected by the partly destroyed surface condition of ZnO.

The current enhancement by singlet oxygen provides a strong evidence for the existence of energy transfer in dye sensitized photoconductivity of ZnO. On ZnO surface, there are a number of traps, a great part of which are oxygen ions adsorbed over a wide range of energy depth[4].

The energy donatable from singlet oxygen (0·96 eV for $^1\Delta_g$, 1·60 eV for $^1\Sigma_g{}^+$) would be sufficient to inject some electrons from these surface traps into ZnO bulk. The same process would also be realized by excited dye molecules instead of singlet oxygen molecules. On the other hand, the electron transfer-like process, $O_2 \rightarrow O_2{}^+ + e$ does not seem plausible for the explanation of the present finding, because of the large ionization energy of O_2 ($^1\Delta_g$ or $^1\Sigma_g{}^+$).

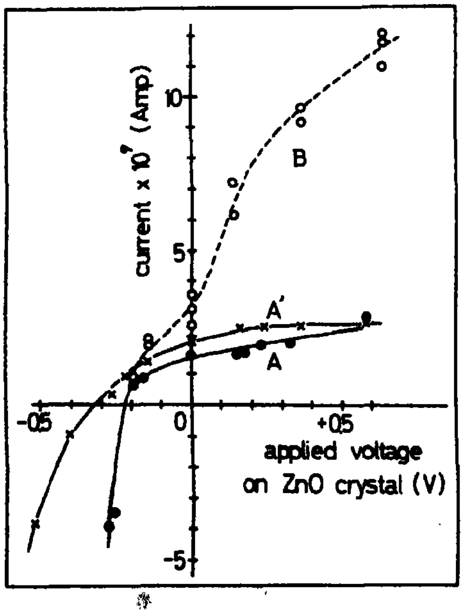

Fig. 3. V-I curves of cell
A′ Nesa | 0·05M KCl (pH 4·6) | ZnO
A Nesa | 0·05M $KCl_{aq} + H_2O_2$ | ZnO
B Nesa | 0·05M $KCl_{aq} + H_2O_2$ + injected NaOCl | ZnO.

Imaging Science and Engineering Laboratory, Tokyo Institute of Technology., Ohkayama, Meguroku, Tokyo, 152, Japan

H. KOKADO
T. NAKAYAMA
E. INOUE

REFERENCES

1. PUTZEIKO E. K. and TERENIN A. N., *Z. Fiz. Khim.* **23**, 676 (1949).
2. KHAN A. U. and KASHA M., *J. Am. Chem. Soc.* **92**, 3293 (1970).
3. OUANNES C. and WILSON T., *J. Am. Chem. Soc.* **90**, 6527 (1968).
4. WILLIAMS R. and WILLIS A., *J. appl. Phys.* **39**, 3731 (1968).

J. Phys. Chem. Solids, Vol. 32, pp. 2786–2788.

The heat capacity of indium antimonide — II*

(*Received* 23 *December* 1969; *in revised form* 22 *February* 1970)

In 1962, Darnell and Libby[1] succeeded in retaining a high pressure metallic polymorph of indium antimonide [InSb(II)] at atmospheric pressure and temperatures below 210°K. Since indium and antimony bracket tin in the Periodic Table, InSb is isoelectronic with tin and the transition between InSb(I) and InSb(II) which occurs at 23 kbars at room temperature is analogous to the grey-tin-to-white-tin transition which occurs at atmospheric pressure and 13°C. Both grey tin and

---

*This research was supported in part by the Chemical Directorate of the United States Air Force, Office of Scientific Research, Grant No. AFOSR-1255-67.

InSb(I) are semiconductors with four-neighbored tetrahedral crystal structures and similar lattice parameters. Darnell and Libby [2] found that not only do metallic InSb(II) and white tin also have the same crystal structure, but that the lattice parameters of the two are identical within experimental error at liquid–nitrogen temperatures. Moreover, InSb(II) and β-tin were found to be miscible in all proportions and to form solid solutions with no change in lattice parameters across the entire composition range. Because of these similarities, we decided to measure the heat capacity of InSb(II) to see if we could further extend the analogy between the two isoelectronic systems.

We determined the heat capacity at constant pressure of InSb(II) between 80–100°K using the standard method of changing a known amount of electrical work into heat by means of a heating coil and then measuring the resulting temperature rise. Since InSb(II) can be retained at atmospheric pressure only below 210°K, we were forced to wind the heating coil around a thin-walled (0·003″) cylindrical copper container instead of directly around the samples. The samples were then pressed into this container under a liquid-nitrogen bath.

Fairly large pieces of InSb(II) were needed and we started with ½″ dia. and 1″ long cylinders of InSb (99·99+% purity). These were pressurized to 28 kbars and heated to ~ 375°C (M.P. at 28 kbars ≈ 350°C) in a piston-cylinder apparatus with an internal graphite furnace. They were then cooled to − 140°C with liquid-nitrogen and the pressure was slowly released. The samples were removed from the pressure vessel and directly transferred into a liquid-nitrogen bath at which temperature they remained metastable. The diameter of the samples was now slightly larger than the 0·460″ inner diameter of the copper container and this insured a tight fit and good thermal contact. The container was 0·930″ high and about 14 g of InSb(II) were needed to fill it for each experiment.

Confirmation that the samples were completely converted to InSb(II) was obtained by two independent methods. First, many small pieces of material were randomly chipped off the samples and allowed to warm. All showed the characteristic dramatic reversion to InSb(I) at about −60°C. Secondly, the superconducting transition temperature was determined. The prepared samples showed a broad transition in the temperature range of about 1·5°–2·0°K. This agrees well with the reported values for InSb(II) [3,4].

The calorimeter was calibrated using copper, nickel and tin cylinders. Then, eighty-five runs were made on three independent InSb(II) samples and the Cp was obtained as a function of temperature between 80–100°K. This function was approximated by a straight line obtained by the method of linear regression on an IBM 360/75 computer. The equation of this straight line is:

$$\mathrm{Cp}\ (\text{in calories}/g\text{-atom}^\circ\mathrm{K}) = 1{\cdot}860 \times 10^{-2}T + 3{\cdot}441.$$

This equations gives values for the Cp of InSb(II) (in calories/*g*-atom°K) of 4·93, 5·11 and 5·30 at 80, 90 and 100°K respectively. Each of these values has an estimated standard deviation of ±0·10 or about 2 per cent.

These values are shown in Table 1 along with the values for white tin and it is apparent that, within experimental error, the heat

Table 1. *Heat capacity data (cal/g-atom°C)*

Temp (°K)	InSb(II) (±0·10)	β-Sn	InSb(I)	α-Sn
50		3·68	2·69	2·67
60		4·20	3·19	3·20
70		4·59	3·63	3·71
80	4·93	4·90	4·00	4·04
90	5·11	5·11	4·31	4·35
100	5·30	5·32	4·56	4·64
150		5·86	5·29	5·44
200		6·10	5·61	5·81
250		6·26	5·81	6·01
298		6·50	6·06	6·16
Reference		5,6,7	8,9,10	6,11,12

capacities of InSb(II) and white tin are identical within this temperature range. The Cp data for InSb(I) and α-tin are also presented in Table 1. As can be seen from the table, the heat capacities of InSb(I) and grey tin are also practically identical over a much larger temperature range. These data indicate that the lattice dynamics of the $A^{\mathrm{II}}B^{\mathrm{V}}$ compounds are very similar to the Group IV elements in both the semiconducting and metallic forms.

The experiment also shows that it is feasible for a similar method to be used to determine the electronic heat capacity of InSb(II) at liquid helium temperatures.

Acknowledgements—We would like to thank Mr. C. Bayer for assistance in designing and fabricating the calorimeter and Dr. H. L. Luo for his assistance with the superconducting measurements. The press used was financed by National Aeronautics and Space Administration Grant No. 237-63.

Department of Chemistry,†
University of California,
Los Angeles,
Calif.
U.S.A.

H. KATZMAN
J. MOSS
W. F. LIBBY

REFERENCES

1. DARNELL A. J. and LIBBY W. F., *Science* **139**, 1301 (1963).
2. DARNELL A. J. and LIBBY W. F., *Phys. Rev.* **135**, A1453 (1964).
3. TITTMAN B. R., DARNELL A. J., BOMMEL H. E. and LIBBY W. F., *Phys. Rev.* **135**, A1460 (1964).
4. STOMBERG T. F. and SWENSON C. A., *Phys. Rev.* **134**, A21 (1964).
5. CETAS T. C., HOLSTE J. C. and SWENSON C. A., *Phys. Rev.* **182**, 679 (1969).
6. HULTGREN R., ORR R. L., ANDERSON P. D. and KELLEY K. K., *Selected Values of Thermodynamic Properties of Metals and Alloys*, p. 262, John Wiley and Sons, New York (1963).
7. *Handbook of Chemistry and Physics*, 46th edition, (Edited by R. C. WEAST, D85, Chemical Rubber Company, Cleveland, Ohio (1966)
8. PIESBERGEN V., *Z. Naturforsch.* **18a**, 141 (1963).
9. CETAS T. C., TILFORD C. R. and SWENSON C. A., *Phys. Rev.* **174**, 835 (1968).
10. LICHTER B. C. and SOMMELET P., *Trans. AIME* **245**, 99 (1[illegible]
11. HILL R. W. and PARKINSON D. H., *Phil. Mag.* **43**, 309 (1951).
12. GSCHNE[illegible]R Jr., K. A., *Solid State Phys.* **16**, 275 (19[illegible]

---

†Contribution No. 2784.

J. Phys. Chem. Solids, Vol. 32, pp. 2788–2790.

Specific heats of $LaNi_2$ and $NdNi_2$ between 1·6 and 4° K*

(*Received* 10 *February* 1971)

IN EARLIER measurements in this laboratory by Wallace *et al.*[1] the heat capacity of the series RNi_2 (R = La (unpublished), Ce, Pr, Nd) was measured between 7–300° K and for $CeNi_2$ and $PrNi_2$ also below 4° K. To complete measurements on these systems we have determined the heat capacity of $LaNi_2$ and $NdNi_2$ between 1·7°–4·1°K. These alloys occur in the $MgCu_2$-structure.

The samples for the measurements were prepared by levitation melting, using Johnson-Matthey nickel (total impurity content about 10 ppm) and La and Nd which were stated by the manufacturers to be of 99·9 per cent purity with respect to metallic contaminants. After annealing for several days at approximately 800° C under an argon atmosphere the X-ray pattern for the alloys showed the pure $MgCu_2$ structure. The measurements were carried out on samples of 8–9 g. using a procedure which will be published elsewhere[2].

In the temperature range investigated the specific heat may be represented as

$$Cp = \gamma T + \beta T^3 \qquad (1)$$

if only electronic and vibrational contributions are involved. The electronic heat coefficient γ is related to the apparent density of states $N(E_F)$ at the Fermi surface by the equation

$$\gamma = (\pi^2/3) k_B{}^2 N(E_F) L \qquad (2)$$

where k_B is the Boltzman constant and L the number of atoms per mole. At low temperatures ($T \ll \theta$) the Debye temperature

---

*This work was assisted by the U.S. Atomic Energy Commission and the National Aeronautics and Space Administration.

θ can be determined with the equation

$$\theta = (2{\cdot}4\pi^4 k_B L/\beta)^{1/3}. \tag{3}$$

In Fig. 1 the experimental results of both alloys are shown in the usual Cp/T vs. T^2 format.

the loss of ferromagnetism. T_c from magnetic measurements is 16° K[3]. Since the temperature range investigated is relatively close to T_c one must expect a magnetic contribution. This is also suggested by the fact that the specific heat is an order of magnitude higher than that for $LaNi_2$.

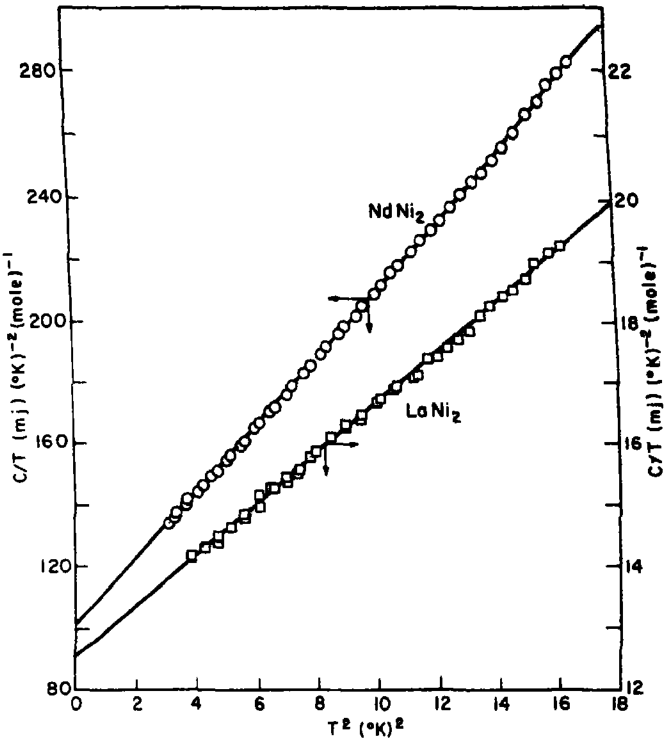

Fig. 1. Heat capacities of $LaNi_2$ and $NdNi_2$ plotted in the C/T vs. T^2 format. The scales for $LaNi_2$ and $NdNi_2$ are on the right and left ordinates respectively.

The $LaNi_2$ data follow equation (1) and we find that $\gamma = 12{\cdot}52 \pm 0{\cdot}03\, mj\, K^{-2}\, mole^{-1}$ and $\theta = 0{\cdot}413 \pm 0{\cdot}003\, mj\, K^{-4}\, mole^{-1}$. The Debye temperature is calculated to be 242° K and the density of states to be $1{\cdot}77\, eV^{-1}\, atom^{-1}$.

Through $NdNi_2$ also gives a straight line with $Cp/T = (101{\cdot}1 \pm 0{\cdot}2) + (10{\cdot}8 \pm 0{\cdot}02)T^2$, the specific heat cannot be associated with electronic and lattice contributions only for the following two reasons:

(a) Wallace *et al.*[1] report a λ-type anomaly at about 10° K which is associated with

(b) The $J = 9/2$ level is split by the crystal field with an overall splitting of 431° K[1] which could also give some contribution to the specific heat.

Thus, the specific heat is a sum of electronic, lattice, magnetic and crystal field contributions.

$$Cp = C_E + C_L + C_N + C_K. \tag{4}$$

In a first approximation it is assumed that C_E and C_L are equal for $LaNi_2$ and $NdNi_2$. For the calculation of C_K relative values of the crystal field energy levels where determined after Schumacher and Hollingsworth [4] and then adjusted to the experimentally found overall splitting of 431° K. The computed C_K was only 0·3 mj mole^{-1} deg^{-1} at 4° K and so negligible below this temperature. Hence, the magnetic contribution seems to be the difference of the specific heat of $NdNi_2$ and $LaNi_2$:

$$C_M = 88{\cdot}6\,T + 10{\cdot}4\,T^3. \qquad (5)$$

The error in this equation is probably small even if C_E and C_L for both alloys are not accurately the same because $C_M \gg C_{LaNi_2}$.

The simple spin-wave theory[5] predicts for ferromagnetic materials well below the Curie-point that C_M is proportional to $T^{3/2}$. For a region nearer to T_c Dyson[6] gives for the magnetization a power law with additional terms of $T^{5/2}$ and $T^{7/2}$. We tried therefore to find an equation of the form

$$C_M = AT^{3/2} + BT^{5/2} + CT^{7/2}. \qquad (6)$$

This attempt was unsuccessful. At present it is not understood why C_M follows an equation with T and T^3.

Acknowledgements—The authors wish to express their appreciation to Dr. V. U. S. Rao for many worthwhile discussions.

Department of Chemistry,
University of Pittsburgh,
Pittsburgh,
Penna. 15213,
U.S.A.

H. H. NEUMANN
S. NASU*
R. S. CRAIG
N. MARZOUK
W. E. WALLACE

REFERENCES

1. WALLACE W. E., *et al.* in Les Élémentes des Terres Rares, Tome II, S. 427–441, Paris-Grenoble, 1969.
2. CRAIG R. S., NASU S. and NEUMANN H. H., to be published.
3. FARELL J. J. and WALLACE W. E., *Inorg. Chem.* **5**, 105 (1966).
4. SCHUMACHER D. P. and HOLLINGSWORTH C. A., *J. Phys. Chem. Solids* **23**, 1381 (1962).
5. VAN KRANENDONK J. and VAN VLECK J. H., *Rev. mod. Phys.* **30**, 1 (1958).
6. DYSON F. J., *Phys. Rev.* **102**, 1217, 1230 (1956).

---

*On leave of absence from Japan Atomic Energy Research Institute, Tokai-mure, Naka-gun, Ibaraki-Ken, Japan.

J. Phys. Chem. Solids, 1971, Vol. 32, p. 2791. Pergamon Press. Printed in Great Britain

ERRATUM

A. CASALOT, P. DOUGIER and P. HAGENMULLER: Sur l'évolution des propriétés physiques de la perovskite $GdCoO_3$ entre 77–1200 K. *J. Phys. Chem. Solids* **32**, 407 (1971).

THE AUTHOR regrets that a small omission was made: Tables 1 and 2, cited in the text, were not included. They are enclosed herewith.

Tableau 1. *Propriétés magnétiques de* $GdCoO_3$

Intervalle de température	$77 \leq T \leq 270$ K	$270 \leq T \leq 580$ K	$580 \leq T \leq 1200$ K
Constante de Curie C_{exp}	7,90	8,80	10,90
Température de Curie θ_c	0 K	−30 K	−175 K
Concentration x en Co^{III}	1,0	0,7	0

Tableau 2. *Energies d'activation de* $GdCoO_3$

Intervalle de température	ΔE (eV)
$77 \leq T \leq 135$ K	$0{,}080 \pm 0{,}005$
$230 \leq T \leq 500$ K	$0{,}19 \pm 0{,}01$
$590 \leq T \leq 770$ K	$0{,}57 \pm 0{,}04$
$T > 1150$ K	≈ 0

J. Phys. Chem. Solids, 1971, Vol. 32, p. i. Pergamon Press. Printed in Great Britain

PAPERS TO BE PUBLISHED IN FUTURE ISSUES

PH. GERMAIN, D. CALECKI ET G. COSTE: Oscillations quantiques des coefficients de pouvoir thermoélectrique et de conductivité thermique: Théorie et mésures dans Cd_3As_2

G. E. PALMA AND R. M. GAGOSZ: Optical absorption in fused silica during irradiation: Radiation annealing of the C-band

J. DEVOS: Proprietes magnétiques dans des alliages de vanadium avec des métaux de transition

R. J. BIRGENEAU: Transition probabilities for *f*-electron *J*-multiplets in cubic crystal fields

A. T. FROMHOLD, JR.,: Parabolic oxidation of metals in homogeneous electric fields

L. R. SARAVIA AND L. CASAMAYOU: Interpretation of the optical and photoemissive properties of CdTe

F. KÖRMENDI: On the nondirect optical transition characteristics in the photon-enhanced field emission spectra

B. R. APPLETON AND L. C. FELDMAN: Investigation of interstitial Zn concentrations in additively colored ZnO using the uni-directional channeling and blocking technique

P. L. YOUNG and A. BIENENSTOCK: A phenomenological theory of time dependent fluctuations above T_c.

R. D. POPP and R. B. MURRAY: Diffusion of the V_k-polaron in alkali halides: Experiments in NaI and RbI

NOTES FOR CONTRIBUTORS

I. GENERAL

1. Submission of a paper to *The Journal of Physics and Chemistry of Solids* will be taken to imply that it represents original research not previously published (except in the form of an abstract or preliminary report), that it is not being considered for publication elsewhere, and that if accepted it will not be published elsewhere in the same form, in any language, without the consent of the Editor-in-Chief. It should deal with original research work in the field of the physics and chemistry of solids.

2. Papers should be submitted to the appropriate regional editor (all English-language papers to be sent to the U.S. editor).

3. Short communications may be published as "Technical Notes" and will receive somewhat more rapid handling than full length articles. Short communications requiring the maximum speed of publication should be submitted to one of the editors of *Solid State Communications*.

II. SCRIPT REQUIREMENTS

1. **Papers** submitted should be concise and written in a readily understandable style. Scripts should be typed and double spaced with good margins on one side of the paper only and submitted in duplicate to facilitate refereeing.

It will be appreciated if authors clearly indicate any special characters used. An abstract not exceeding 200 words, should be provided in the language of the paper. French and German papers should be submitted with English abstract and titles, but if this is not possible the abstract will be translated by the publishers. To conserve space, **authors are requested to mark less important parts of the paper,** such as details of experimental technique, methods, mathematical derivations, etc. **for printing in small type.** The technical description of methods should be given in detail only when such methods are new. Authors will receive proofs for correction when their papers are first set, and **alterations must be restricted to printer's errors.** Other than these, any substantial changes may be charged to the authors.

2. **Illustrations** should not be included in the typescript of the paper, and legends should be typed on a separate sheet. Line drawings which require redrawing should include all relevant details and clear instructions for the draughtsman. If figures are already well drawn it may be possible to reproduce them direct from the originals, or from good photo-prints if these can be provided. It is not possible to reproduce from prints with weak lines. Illustrations for reproduction should normally be about twice the final size required. The lettering should be sufficiently large and bold to permit this reduction. Photographs should only be included where they are essential.

3. **Tables and figures** should be so constructed as to be intelligible without reference to the text. Every table and column should be provided with an explanatory heading. Units of measure must always be clearly indicated. The same data should not be published in both tables and figures. The following standard symbols should be used on line drawings since they are easily available to the printers: ○, ●, +, ×, □, ■, △, ▲, ◇, ◆, ▽, ▼.

4. **References** are indicated in the text by numbers on the line in brackets, and the full reference should be given in a list at the end of the paper in the following form:

1. BARNES R. G., BORSA F. and PETERSON D., *J. appl. Phys.* **36**, 940 (1965).
2. KNIGHT W. D., In *Solid State Physics* (Edited by F. Seitz and D. Turnbull), Vol. 2, p. 93. Academic Press, New York (1957).

Abbreviations of journal titles should follow those given in *World List of Scientific Periodicals* (4th Edn.). It is particularly requested that authors' initials, and appropriate volume and page numbers, should be given in every case.

Footnotes, as distinct from literature references, should be indicated by the following symbols—*, †, ‡, §, commencing anew on each page; they should *not* be included in the numbered reference system.

5. Due to the international character of the journal no rigid rules concerning notation and spelling will be observed, but each paper should be consistent within itself as to symbols and units.

THE JOURNAL OF PHYSICS AND CHEMISTRY OF SOLIDS
VOLUME 32 NUMBER 9 1971 SEPTEMBE

CONTENTS

S. P. Murarka and R. A. Swalin: Cation self-diffusion in barium oxide(BaO) 201
M. J. Taylor, D. J. Marshall and H. Evans: Infra-red spectra of photochromic sodalites . . 202
S. Bloom: Band structures of GaN and AlN 2027
Marie-Martine Dujardin and Marie-Luce Theye: Investigation of the optical properties of Ag by means of thin semi-transparent films 2033
C. Taupin, M. Lambert et Ch. Mazière: Résonance électronique dans le lithium liquide . . 2045
J. D. Wiley: Donor-acceptor pairing in the system GaP(Zn, O) 2053
P. Weinberger, K. Schwarz and A. Neckel: Electronic band structure of ScN 2063
J. E. A. Alderson and C. M. Hurd: Spin component of the Hall effect and transverse magnetoresistance in dilute alloys containing magnetic solutes 2075
A. Gerard, P. Imbert, H. Prange, F. Varret and M. Wintenberger: Fe^{2+} impurities, isolated and in pairs, in ZnS and CdS studied by the Mössbauer effect 2091
J. Gilchrist and P. Monceau: Resistivity of superconducting alloys in the mixed state in a weak field 2101
P. T. Gallagher and W. A. Oates: Vibrational entropies of hydrogen in palladium–silver–hydrogen alloys by the isotopic solubility ratio method 2105
C. H. Bennett and B. J. Alder: Persistence of vacancy motion in hard sphere crystals . . 2111
F. P. Larkins: Isolated single vacancy in diamond—II. Jahn–Teller effect 2123
J. B. Holt, M. Y. Almassy and R. W. Crawford: Helium diffusion in LiH 2129
Nguyen van Doan: Vacancy flow effect on electromigration in silver 2135
D. L. Huber: Spin–spin relaxation near the Curie point 2145
C. L. Dick, Jr. and B. Ancker-Johnson: Impact ionization in p-type InSb 2151
Paul H. E. Meijer: A study of the crystal field parameters in thulium garnets 2163
G. Busch, M. Campagna, F. Hulliger and H. C. Siegmann: Electronic energy levels in ferromagnetic Eu_3P_2 and Eu_2As_2 2173
V. A. M. Brabers: Cation migration, cation valencies and the cubic-tetragonal transition in $Mn_xFe_{3-x}O_4$ 2181
I. Filinski, B. Wojtowicz-Natanson and J. M. Hvam: Spontaneous and stimulated emmission from CdSe at high excitation levels 2193
F. T. J. Smith: A high temperature study of native defects in ZnTe 2201
R. H. Doremus: Delayed elasticity resulting from periodic stress-induced atomic diffusion . . 2211
J. Edwards and R. F. Frindt: Anisotropy in the resistivity of $NbSe_2$ 2217
A. E. Whiteman, J. J. Martin and H. R. Shanks: Thermal conductivity of cubic sodium tungsten bronzes 2223
U. T. Höchli: Theory of local oscillation of substitutional defects near a free surface . . . 2231
C. A. Coulson and F. P. Larkins: Isolated single vacancy in diamond—I. Electronic structure . 2245

Technical Notes:
C. Basu and U. S. Ghosh: Estimation of bonding parameters and overlap integrals in octahedral iron group complexes from magnetic susceptibility and anisotropy data 2259
K. Hess and H. Kahlert: Harmonic mixing and energy relaxation of warm electrons in n-GaAs at low temperatures 2262

Printed by A. Wheaton & Co., Exeter, England